Transactions of the ASME®

Journal of Heat Transfer

Published Quarterly by The American Society of Mechanical Engineers

VOLUME 111 • NUMBER 2 • MAY 1989

Transactions of the ASME, Journal of Heat Transfer (ISSN 0022-1481) is published quarterly (Feb., May, Aug., Nov.) for $155 per year by The American Society of Mechanical Engineers, 345 East 47th Street, New York, NY 10017. Second class postage paid at New York, NY and additional mailing offices. POSTMASTER: Send address changes to Transactions of the ASME, Journal of Heat Transfer, c/o THE AMERICAN SOCIETY OF MECHANICAL ENGINEERS, 22 Law Drive, Box 2300, Fairfield, NJ 07007-2300.
CHANGES OF ADDRESS must be received at Society headquarters seven weeks before they are to be effective. Please send old label and new address.
PRICES: To members, $29.00, annually; to nonmembers, $155.00. Add $15.00 for postage to countries outside the United States and Canada.
STATEMENT from By-Laws. The Society shall not be responsible for statements or opinions advanced in papers or . . . printed in its publications (B7.1, para. 3).

INDEXED by Applied Mechanics Reviews and Engineering Information, Inc.

ANNOUNCEMENTS

TECHNICAL PAPERS

(Contents Continued on p. 242)

(Contents continued)

TECHNICAL NOTES

Analysis of Order of the Sequential Regularization Solutions of Inverse Heat Conduction Problems

E. P. Scott
Graduate Assistant.
Student Mem. ASME

J. V. Beck
Professor.
Fellow ASME

Heat Transfer Group,
Department of Mechanical Engineering,
Michigan State University,
East Lansing, MI 48824

Various methods have been proposed to solve the inverse heat conduction problem of determining a boundary condition at the surface of a body from discrete internal temperature measurements. These include function specification and regularization methods. This paper investigates the various components of the regularization method using the sequential regularization method proposed by Beck and Murio (1986). Specifically, the effects of the regularization order and the influence of the regularization parameter are analyzed. It is shown that as the order of regularization increases, the bias errors decrease and the variance increases. Comparatively, the zeroth regularization has higher bias errors and the second-order regularization is more sensitive to random errors. As the regularization parameter decreases, the sensitivity of the estimator to random errors is shown to increase; on the other hand, the bias errors are shown to decrease.

Introduction

The direct heat conduction problem involves the determination of the temperature distribution throughout a body with time when the initial and boundary conditions are given. In contrast, the Inverse Heat Conduction Problem (IHCP) involves the determination of a time-variable boundary condition from the initial condition and discrete transient internal temperature measurements. The latter problem is ill-posed.

Many methods have been proposed to solve the inverse problem. Exact analytical solutions, requiring continuously differentiable data, were developed by Burgraff (1964) and Langford (1976). Stolz (1960) provided one of the earliest solutions to the IHCP, which was found to be unstable with small time steps. A similar method involving the numerical inversion of a convolution integral and utilizing future time steps was developed by Beck (1968). This method provides a solution at each time step, and is called the sequential function specification method. Other integral methods using Laplace transforms have been demonstrated in one-dimensional form by Imber and Khan (1972), and in two-dimensional form by Imber (1974). Weber (1981) replaced the traditional heat conduction equation by a hyperbolic one to obtain a well-posed problem with established solution techniques.

Regularization methods were proposed by Miller (1970) and Tikhonov and Arsenin (1977). These methods provide stability by the addition of smoothing factors and reduce the influence of measurement errors in the data. The influence of the regularization component is determined by the magnitude of a regularization parameter. Different criteria are found in the literature for the selection of this parameter. Tikhonov and Arsenin (1977) and Reinsch (1967) base their criteria on measurement errors, while Murio (1985) considers, in addition, a bound based on the square of the L_2 norm of the heat flux vector. Hills and Mulholland (1979) applied the method of Backus and Gilbert (1970) to a transient heat conduction problem. This method, adapted from geophysics, also utilizes smoothing functions to stabilize the solution.

Difference methods have been used to solve the nonlinear IHCP, which cannot be solved using integral methods. Methods utilizing finite differences were demonstrated by Blackwell (1981), Beck (1970, 1982), and Williams (1977). In Beck's methods the same concepts used for the convolution-based methods were also used to develop the numerical algorithms. A stabilizing matrix was utilized by Hensel and Hills (1984) in developing a space marching finite difference algorithm. Finite elements were incorporated in the solution by Krutz et al. (1978) and Bass (1980). It is important to note that the solutions of the linear IHCP with the function specification and/or regularization methods are independent of the method of solution of the heat conduction equation; irrespective of whether numerical convolution, finite differences, or finite elements are used, nearly identical solutions are obtained (provided accurate approximations are used in each case).

Beck and Murio (1986) presented a new method that combines the sequential function specification procedure with the regularization method. This method differs from the global regularization methods in that the solution is found sequentially, greatly improving computational efficiency. This method was shown to be very competitive with the global regularization methods in terms of the heat flux estimates.

Beck (1979) presented and demonstrated the use of a number of criteria for comparing these different methods for solving the IHCP.

The objective of this paper is to investigate the various components of the regularization method. Specifically, this study is an analysis of the effects of the regularization order and the influence of the regularization parameter.

The sequential-regularization procedure proposed by Beck et al. (1985) is used in this investigation, due to its greater computational efficiency over global regularization methods. The primary terms investigated are common to both global and sequential methods. A brief derivation of this method is presented. Several test cases using exact and random simulated data are used to compare the various regularization orders and to determine the influence of the regularization parameter. The scope of this study is limited to the investigation of the regularization parameter, and the various regularization orders; the influence of other variables, such as the time step, is left for future studies. The test cases presented were chosen as simple building blocks on which other more complicated cases can be built.

Methodology

Derivation of the Sequential-Regularization Method. The regularization method is a modification of the sum of squares function with the addition of the regularization terms. These

Contributed by the Heat Transfer Division and presented at the ASME Winter Annual Meeting, Miami Beach, Florida, November 17–21, 1985. Manuscript received by the Heat Transfer Division January 29, 1988. Paper No. 85-WA/HT-43. Keywords: Conduction, Numerical Methods, Transient and Unsteady Heat Transfer.

terms have a smoothing effect on the heat flux components, acting to minimize the effects of noisy data.

The modified least-squares function is

$$S=(\mathbf{Y}-\mathbf{T})^T(\mathbf{Y}-\mathbf{T})+\alpha\sum_{j=0}^{2}R_j \tag{1}$$

where $\mathbf{Y}$ and $\mathbf{T}$ are the measured and estimated temperature vectors, respectively, and the terms in the summation (R_0, R_1, R_2) represent the zeroth, first, and second-order regularization components, respectively. The scalar term α is the regularization parameter, which is adjusted to determine the influence of the regularization terms on the least-squares function.

Based on suggestions by Tikhonov and Arsenin (1977) the following regularization terms were proposed by Beck et al. (1985):

$$R_0 = W_0\sum_{i=1}^{r}(q_{M+i-1})^2 \tag{2}$$

$$R_1 = W_1\sum_{i=1}^{r}(q_{M+i+1}-q_{M+i})^2 \qquad r\geq 1 \tag{3}$$

$$R_2 = W_2\sum_{i=1}^{r}(q_{M+i-1}-2q_{M+i}+q_{M+i+1})^2 \qquad r\geq 2 \tag{4}$$

The r in the summation terms is the number of future times to be used for estimating q_M. Note that the regularization terms are finite difference approximations for the jth derivative. The zeroth order regularization term tends to minimize the magnitude of the heat flux components, biasing the q values toward zero, while the first-order regularization term results in a minimization of the difference between heat flux values, causing the q components to be biased toward a constant value. In the second-order regularization term, the q components are forced toward a constant slope by the minimization of the finite difference approximation of the second derivative. Thus, if $\alpha \cdot W_2 \to \infty$, the estimated q function becomes linear with time.

The expressions for the regularization terms in equations (2), (3), and (4) can be written in matrix formulation as follows:

$$R_j=(\mathbf{H}_j\mathbf{q})^T W_j\mathbf{H}_j\mathbf{q} \tag{5}$$

The $\mathbf{H}_j$ matrices contain the coefficients for the finite difference approximations of the heat flux components in equations (2), (3), and (4) (Beck et al., 1985), and W_j are scalar weighing coefficients.

The linear IHCP is now considered. For such cases, superposition and Taylor series with only one correction term give the same result. Using either method, the $\mathbf{T}$ matrix is substituted by the following expression involving $\mathbf{q}$, the sensitivity coefficient matrix $\mathbf{X}$, and previously estimated components, $\hat{\mathbf{T}}|_{\mathbf{q}=0}$ (Beck et al., 1985):

$$T=\mathbf{X}\mathbf{q}+\hat{\mathbf{T}}|_{\mathbf{q}=0} \tag{6}$$

The sensitivity coefficient matrix $\mathbf{X}$ is an $r\times r$ matrix that describes the influence of the heat flux on the temperature. The components of the matrix are given by

$$X_{ij}=\frac{\partial T_i}{\partial q_j} \tag{7}$$

Since a temperature calculated at any given time is independent of future heat flux values, the matrix components in equation (7) above the diagonal are equal to zero. Thus, with a constant heat flux assumption over each time step, the components of the $\mathbf{X}$ matrix are equal to $\phi_{k+1}-\phi_k$, where ϕ_k is the temperature rise for a unit step increase in the surface heat flux, and $k=0$ along the diagonal, $k=1$ for the second diagonal, etc. For the special case of a one-dimensional slab of length L, heated at $x=0$, and with a temperature sensor at x, ϕ_k is given (Beck et al., 1985) as

$$\phi_k = \phi(x,t_k)$$

$$= \frac{L}{k}\left[\frac{\kappa t}{L^2}+\frac{1}{3}-\frac{x}{L}+\frac{1}{2}\left(\frac{x}{L}\right)^2 - \frac{2}{\pi^2}\sum_{n=1}^{\infty}\frac{1}{n^2}\exp\left(-\frac{n^2\pi^2\kappa t}{L^2}\right)\cos\left(\frac{n\pi x}{L}\right)\right] \tag{8}$$

where κ is the thermal diffusivity.

Differentiating equation (1) with respect to $\mathbf{q}$, using equation (6) for $\mathbf{T}$, setting the resulting equation equal to zero, and rearranging yields

$$\left[\mathbf{X}^T\mathbf{X}+\alpha\sum_{j=0}^{2}W_j\mathbf{H}_j^T\mathbf{H}_j\right]\mathbf{q}=\mathbf{X}^T(\mathbf{Y}-\hat{\mathbf{T}}|_{\mathbf{q}=0}) \tag{9}$$

where $\hat{\mathbf{T}}|_{\mathbf{q}=0}$ are the estimated temperature values with q_M, $q_{M+1}, \ldots, q_{M+r-1}$ temporarily set equal to zero. This matrix equation represents a set of r linear, algebraic equations for the estimated $\mathbf{q}$ vector, which is denoted $\hat{\mathbf{q}}$. It is called the matrix normal equation.

In the global regularization method, $\hat{\mathbf{T}}|_{\mathbf{q}=0}$ is equal to the initial temperature; r is equal to n, the total number of measurements; and M is equal to 1. This solution involves an $n\times n$ matrix requiring a number of computations proportional to n^3. In the sequential method where r, the number of future time steps for calculating q_M, is much less than n, the solution of equation (9) involves an $r\times r$ matrix requiring computations proportional to $n\cdot(r\cdot r)$ for a total of n times. Thus, the sequential method greatly improves computational efficiency by a very large reduction in the number of computations.

Nomenclature

D = deterministic error
$\mathbf{H}$ = regularization matrix
k = thermal conductivity
L = slab thickness
m^* = one half n, where n is even
M = present time step
n = total number of time steps
q_o = nominal heat flux
q = heat flux
$\mathbf{q}$ = heat flux vector
r = number of future time steps
R = regularization component
S = least-squares function
S_e = mean squared error
t = time
T_i = temperature at time t_i
$\mathbf{T}$ = temperature vector
V = variance
W = weighing coefficient
x = position
$\mathbf{X}$ = sensitivity coefficient matrix
$\mathbf{Y}$ = measured temperature vector
α = regularization parameter
κ = thermal diffusivity
σ_q = standard deviation of estimated heat flux
σ_Y = standard deviation of temperature
ϕ = step rise in temperature for unit step rise in heat flux

Superscripts

$\hat{}$ = estimated
$+$ = dimensionless
T = transpose of matrix
e = random measurement errors included

Problem Statement. A one-dimensional planar slab of thickness L is considered in analyzing the various terms in the regularization procedure. A temperature sensor is simulated at the insulated boundary at $x=L$, and a prescribed heat flux is imposed on the other surface at $x=0$.

The analytical solution is used to generate simulated temperature data to calculate the heat flux history. The thermal properties are assumed to be constant; hence, the problem in linear.

The heat conduction problem is summarized below:

$$\frac{\partial T}{\partial t}=\kappa\frac{\partial^2 T}{\partial x^2} \qquad 0<x<L; \quad t>0 \tag{10a}$$

$$T(L, t)=Y(t) \qquad t>0 \tag{10b}$$

$$-k\frac{\partial T}{\partial x}\bigg|_{x=L}=0 \qquad t>0 \tag{10c}$$

$$T(x, 0)=T_o \qquad 0<x<L \tag{10d}$$

where T is temperature and T_o is the constant initial temperature.

In nondimensional terms, the problem is

$$\frac{\partial T^+}{\partial t^+}=\frac{\partial^2 T^+}{\partial x^{+2}} \qquad 0<x^+<1; \quad t^+>0 \tag{11a}$$

$$T^+(1, t^+)=Y^+(t^+) \qquad t^+>0 \tag{11b}$$

$$\frac{\partial T^+}{\partial x^+}\bigg|_{x^+=1}=0 \qquad t^+>0 \tag{11c}$$

$$T^+(1, 0)=0 \qquad 0<x^+<1 \tag{11d}$$

where

$$T^+(x^+, t^+)=\frac{(T-T_o)}{q_oL/k} \tag{11e}$$

$$Y^+(t^+)=\frac{(Y-T_o)}{q_oL/k} \tag{11f}$$

$$x^+=x/L; \tag{11g}$$

$$t^+=\kappa t/L^2; \tag{11h}$$

$$q^+=q/q_o \tag{11i}$$

and q_o is a nominal surface heat flux value. The + superscripts are omitted in the subsequent discussions.

The following three test cases are used for the input heat flux $q(t)$:

1. Pulse heat flux

$$q(t)=\begin{cases}1 & t_{i-1}<t<t_i\\ 0 & \text{otherwise}\end{cases} \tag{12}$$

2. Square heat flux (from $t=0.75$ to $t=1.25$)

$$q(t)=\begin{cases}0 & t<0.75\\ 1 & 0.75\le t\le 1.25\\ 0 & t>1.25\end{cases} \tag{13}$$

3. Triangular heat flux (from $t=0.5$ to $t=1.5$)

$$q(t)=\begin{cases}0 & t<0.5\\ t-0.5 & 0.5\le t<1.0\\ 1.5-t & 1.0\le t<1.5\\ 0 & 1.5\le t\end{cases} \tag{14}$$

The effects of a single temperature measurement are determined in the fourth test case by imposing the following condition at $x=1$:

4. Single temperature measurement error at time t_i

$$Y(t_i)=\begin{cases}1 & i=r\\ 0 & i\neq r\end{cases} \tag{15}$$

For the linear heat conduction problem, any heat flux history can be represented by the sum of a number of pulse heat fluxes using the principle of superposition. The pulse heat flux is obtained by assuming a constant heat flux over a single time step. Thus, the pulse heat flux test case (Case 1) represents the basic building block for the solutions of the square heat flux and the triangular heat flux test cases.

Results and Discussion

Two criteria, the deterministic bias and the variance, are used in comparing the various regularization orders in the different test cases; see Beck et al. (1985) and Raynaud and Beck (1988). The deterministic bias is defined as a measure of the bias or error in the estimator, when the random measurement errors are set equal to zero. The variance is a measure of the estimators sensitivity to random errors. It is desired to minimize both the deterministic bias and the variance in obtaining the estimator; however, these objectives tend to conflict with each other.

The deterministic bias for the ith time step is defined as

$$D_i=E(\hat{q}_i)-q_i \tag{16}$$

where q_i is the true heat flux, $E(\cdot)$ is the expected value operator, and $E(\hat{q}_i)$ is the expected value of the estimated heat flux, found from the case when the random errors equal zero. The variance of the estimated heat flux is found from

$$V(\hat{q}_i)=E(\hat{q}_i^2)-E^2(\hat{q}_i) \tag{17}$$

The mean squared error, S_e^2, is the sum of the variance and the square of the deterministic error

$$S_{ei}^2=V(\hat{q}_i)+D_i^2 \tag{18}$$

The first test case (pulse heat flux) is used as a measure of the deterministic error, and the fourth test case (single temperature measurement error) is used to estimate the variance.

The pulse heat flux is considered first. The pulse heat flux was chosen at the midpoint of the total number of time steps to avoid interference from the beginning and ending time steps. In this example, the total number of time steps n equaled 20, but a larger value has no effect on the results. The weighing coefficients W_j equaled one or zero, depending on the regularization order being considered. The regularization orders were compared using $\Delta t=0.1$, $r=4$, and $\alpha=0.05$. A relatively large value for the regularization parameter α was chosen to exaggerate the effects of the various regularization orders.

For a single pulse heat flux, the deterministic error may be estimated from the sum of squares of the deviations of the estimated q values from the input values. For a pulse heat flux at the m^*th time step, this estimate of the dimensionless deterministic error is stated as follows:

$$D=\left[\sum_{\substack{i=1\\ i\neq m^*}}^{M}(\hat{q}_i)^2+(\hat{q}_{m^*}-1)^2\right]^{1/2} \tag{19}$$

In this example, the dimensionless input pulse heat flux was

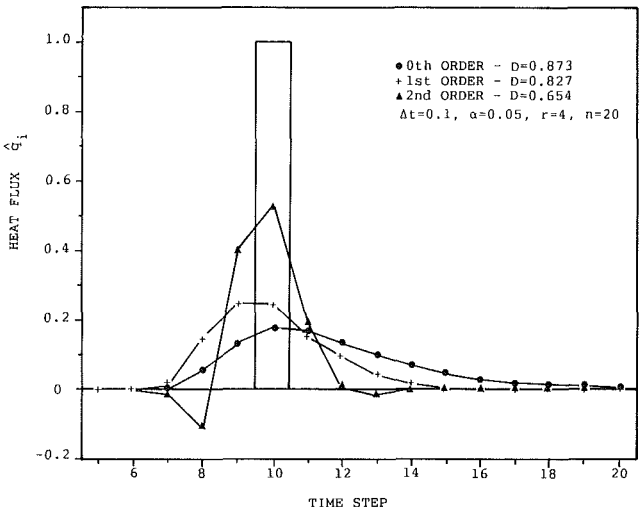

Fig. 1 Pulse heat flux at $t_{n/2}$

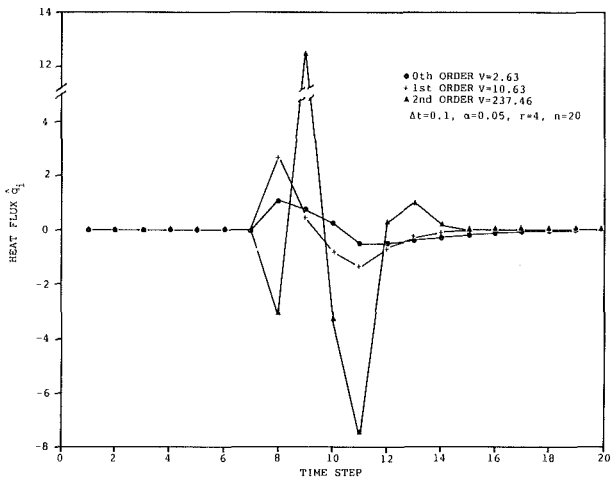

Fig. 2 Single temperature measurement error at $t_{n/2}$

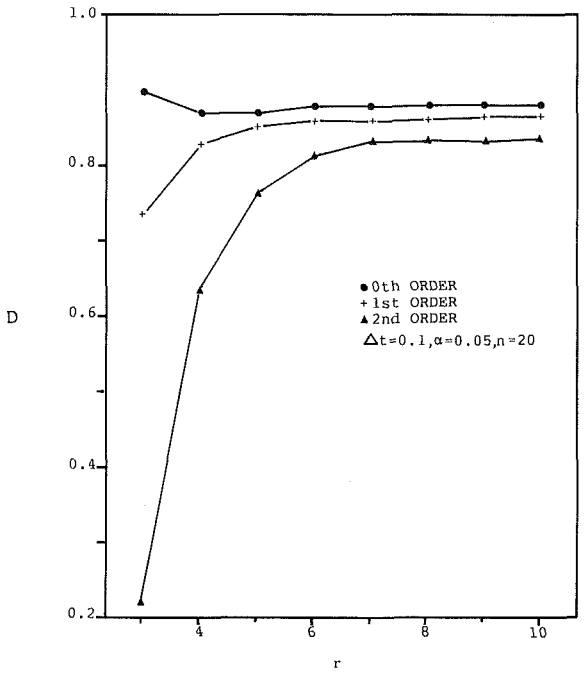

Fig. 3 Deterministic error D as a function of r for a pulse heat flux

equal to one, and m^* was equal to ten, the midpoint of the total number of time steps.

Results for three regularization orders are shown for $r=4$, $\Delta t=0.1$, and $\alpha=0.05$, in Fig. 1. The second-order regularization gave the best approximation to the pulse heat input. However, in achieving this, the heat flux solution oscillated before and after the pulse heat flux. The first-order regularization showed no oscillations, but it anticipated the heat flux, resulting in a curve skewed to the left. The zeroth order regularization provided a damped solution, resulting in a high deterministic error. This is a result of the zeroth order's tendency to force the estimated heat fluxes toward zero.

In all cases energy is conserved. If a sufficiently large number of time steps are used, the sum of the estimated heat fluxes over all time steps is exactly equal to the input pulse heat flux.

The variance of the different regularization orders can be estimated from the fourth test case of a single temperature measurement error. Beck et al. (1985) present an expression for $\hat{q}$ in the form of a digital filter, which is a convenient for the direct determination of the variance. Using the single temperature measurement error of the fourth test case, Beck et al. (1985) demonstrate that the proportionality constants of the digital filter can be expressed in terms of the resulting $\hat{q}$ values of the fourth test case as follows:

$$\hat{q}_M = \sum_{i=1}^{M+r-1} f_{M-i}(Y_{M+r-i} - T_o) \tag{20}$$

where Y_i are the measured temperatures and f_{M-i} are the filter coefficients, which are the $\hat{q}_{M+r-i}$ estimates from the fourth test case. Equation (20) provides a basis for an expression for the variance. If it is assumed that the random errors in the measured temperatures are additive, have zero mean with a constant variance, and are uncorrelated, the variance of $\hat{q}_M$ is given by

$$V(\hat{q}_M) = \sum_{i=1}^{M+r-1} f_{M-i}^2 V(Y_{M+r-i} - T_o) = \sigma_Y^2 \sum_{i=1}^{M+r-1} f_{M-i}^2 \tag{21}$$

where σ_Y^2 is the variance of Y_i. Dividing by σ_Y^2 results in the dimensionless variance of

$$V^+(\hat{q}_M) = \frac{V(\hat{q}_M)}{\sigma_Y^2} = \sum_{i=1}^{M+r-1} f_{M-i}^2 \tag{22}$$

As M becomes large, V^+ approaches a constant and is independent of the time index M.

Using the fourth test case also with $\Delta t=0.1$, $\alpha=0.05$, and $r=4$, the estimated heat fluxes for the three regularization orders are shown in Fig. 2. The results clearly indicate that the zeroth regularization order is the least sensitive to measurement errors, while the second order was the most sensitive to measurement errors. These results are in contrast with those for case 1, in which the second-order regularization was the best estimator.

The deterministic errors calculated from equation (19) and the variance determined from equation (22) are shown as functions of the number of future times, r, in Figs. 3 and 4. In all of the regularization orders, both the variance and the deterministic errors had little dependence on r for $r>7$. The deterministic errors are shown to decrease as r decreases. The second-order regularization method showed the smallest deterministic error, while the errors using the zeroth order varied little with r. In contrast to the deterministic errors, the dimensionless standard deviation of $\hat{q}$, $(\sigma_q^+ = V^{+1/2})$, increased as the order decreased; the second-order regularizer was the most sensitive to measurement errors, especially for $r<5$. This indicates limited use of the second-order regularization method for $r<5$ and $\Delta t=0.1$, if random measurement errors are present.

The square heat flux of the second test case demonstrated the use of superposition of the pulse heat flux. This test case is

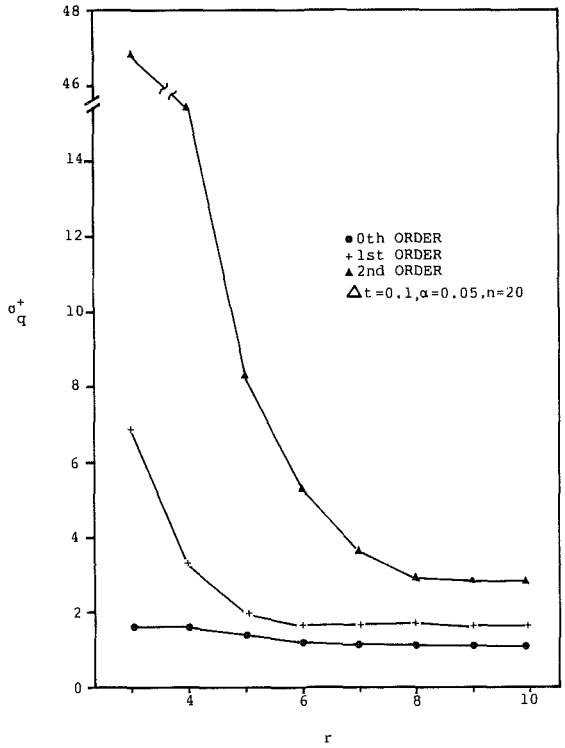

Fig. 4 Standard deviation σ_q^+ of the estimated heat flux as a function of r

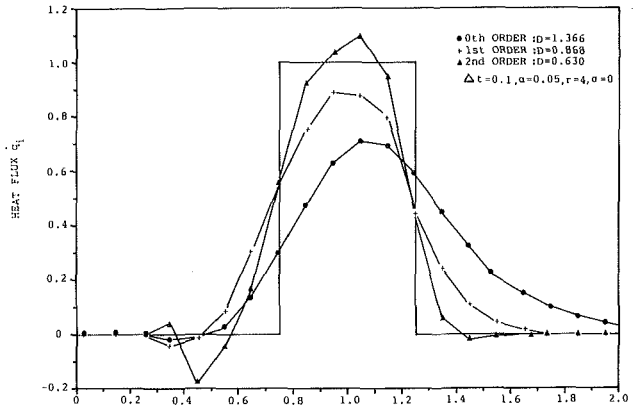

Fig. 5 Square heat flux

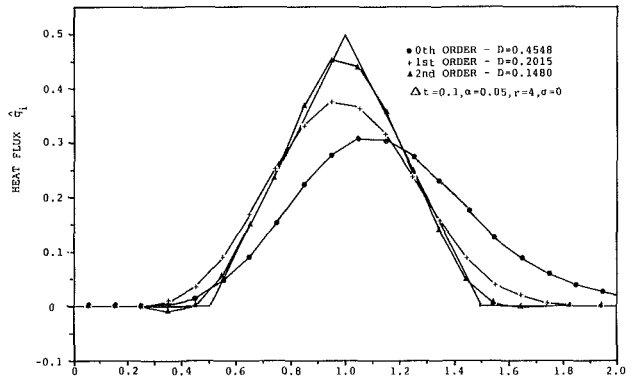

Fig. 6 Triangular heat flux

also important because it is typical of many actual heat flux estimation problems. The input heat flux was equal to one from $t=0.75$ to $t=1.25$ and equal to zero otherwise. In this instance, the time step, $\Delta t=0.1$, $r=4$, $\alpha=0.05$, and exact data were used. As with the pulse heat flux, the square heat flux provided insight into the estimators ability to predict abrupt changes in a "realistic" heat flux. The various regularization orders were compared by examining the bias or deterministic error. The square of the deterministic error is approximated by (Beck et al., 1985)

$$D^2=\sum_{i=1}^{n}(\hat{q}_i-q_i)^2 \tag{23}$$

where $\hat{q}_i$ and q_i are the estimated and input heat fluxes, respectively.

Results for the square heat flux shown in Fig. 5 are similar to those obtained for the pulse heat flux. The second-order regularization method provided the lowest deterministic error, but not without a fluctuation prior to the input heat flux. The first-order regularization method was also a good estimator, with only a small fluctuation at the onset of the square heat flux. This curve is slightly skewed to the left, but not to the same extent as was shown for the pulse heat flux. The zeroth regularization order provided a solution similar in shape to that obtained with the pulse heat flux; however, the deterministic error was higher, compared with the other regularization orders, than was seen in the pulse heat flux case.

An understanding of the estimator's ability to predict linear increasing and decreasing functions is provided by the triangular heat flux of the third test case. The time step, Δt, equaled 0.1, $\alpha=0.05$, and $r=4$ as in the previous example. The results shown in Fig. 6 possess the same characteristics found in the square heat flux case; however, there was a much smaller fluctuation at the onset of the heat flux input for the second-order regularization method and no fluctuations for the other orders. The zeroth order estimator attempted to drive the estimated heat flux values toward zero, minimizing the magnitude of the estimated curve, and shifting the estimated values to the right. The second-order result had the lowest deterministic error, and was clearly a better estimator than the other two orders shown in Fig. 6. This is consistent with the tendency of the second order to cause the heat flux to vary linearly with time.

The second and third test cases were repeated using normally distributed random temperature measurement errors with a standard deviation $\sigma=0.01$. The time step Δt was equal to 0.1, the regularization parameter α was equal to 0.05, and the number of future time steps r was equal to 4 as before. The results were compared with the previous examples for the second and third test cases without random errors by comparing the deterministic errors shown in Figs. 5 and 6 with the mean squared error S_e. The mean squared error defined by Beck et al. (1985) is found from

$$S_e^2=\sum_{i=1}^{n}(\hat{q}_i-q_i)^2+\frac{1}{n-1}\sum_{i=1}^{n}(\hat{q}_i^e-\bar{\hat{q}}_i^e)^2 \tag{24}$$

where the first term is an approximation for the deterministic error, and is found from the pulse heat flux test case (first test case) with no random errors; the second term is an approximation for the variance, found from using many sets of random errors in the input data. Note that the superscript e indicates that random errors were used in the input data. In this study, the mean squared error was approximated as follows:

$$S_e^2=\sum_{i=1}^{n}(\hat{q}_i^e-q_i)^2 \tag{25}$$

where $\hat{q}_i^e$ are the estimated heat fluxes determined with random temperature errors, and q_i are the "true" heat fluxes.

The results for the second and third test cases comparing S_e and D are shown in Fig. 7. The difference between S_e and D is an indication of the sensitivity of the estimator to random errors. The second regularization order provided the best

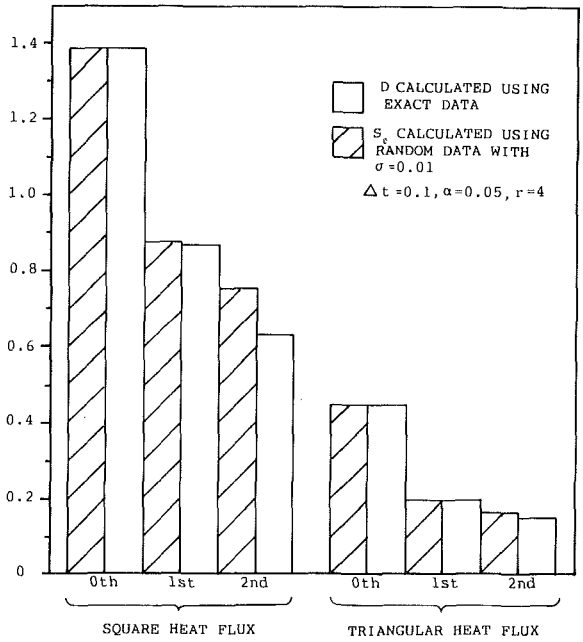

Fig. 7 Comparison of D and S_e for two test cases

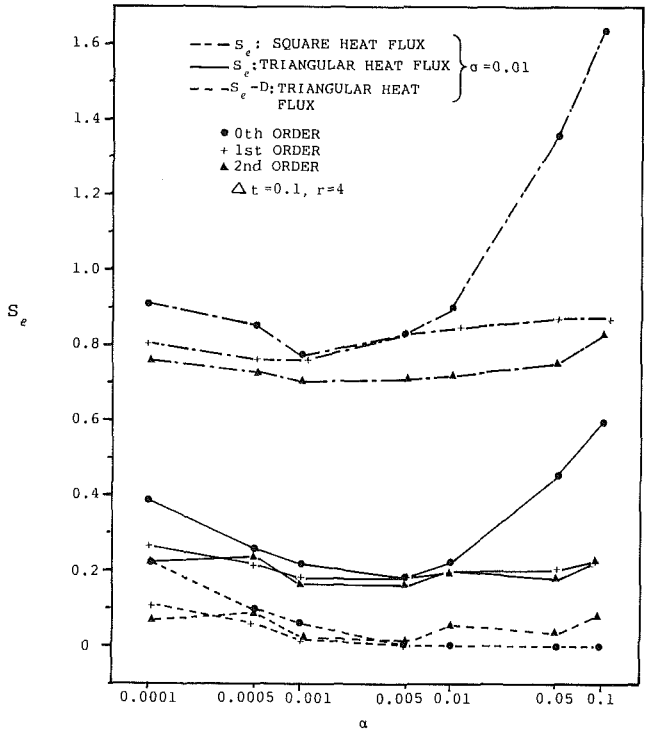

Fig. 8 Mean squared error S_e as a function of α

estimator in all cases; however, it is also the most sensitive to random temperature measurement errors. The zeroth regularization order was least sensitive to random temperature errors. In all cases the differences between S_e and D are small, therefore random errors had relatively little effect compared with the biased errors, using $\alpha=0.05$ and $\sigma=0.01$.

The second objective of this paper is to investigate the influence of the regularization parameter α. Various techniques for selecting α are found in the literature. The criteria for selecting α proposed by Tikhonov and Arsenin (1977) require the residual sum of squares to be equal to the sum of squares of the errors in the measurements. The criteria given by Reinsch (1967) require the residual to be between $[n-(2n)^{1/2}]\cdot\sigma_Y^2$ and $[n+(2n)^{1/2}]\cdot\sigma_Y^2$. If there are no random errors, or if the random errors are small, these criteria require α to equal zero or to be very small. In these cases, the solution can be unstable; thus the above criteria are not appropriate for extremely small errors. An alternative criteria is to choose α where S_e, or D for the case of no random errors, is a minimum; this criterion is valid even if the errors are very small.

Test runs using exact and random analytic data were compared for various magnitudes of α. Values chosen for α were 0.0001, 0.0005, 0.001, 0.005, 0.01, 0.05 and 0.1. Results were compared for the various regularization orders using the triangular and square heat flux cases with r equal to 4, 6, and 8, and Δt equal to 0.1.

The mean squared error S_e was determined from equation (25) for the various values of α. Results are shown in Fig. 8 for $r=4$; similar results were obtained for $r=6$ and 8. The upper two sets of curves are the values of S_e obtained using random normal, uncorrelated errors, with $\sigma=0.01$ for the square and triangular heat flux. The lower set of curves represents the difference in S_e calculated using random data and D obtained from using exact data for the triangular heat flux case. This is an indication of the value of the variance.

Mean squared errors tended to increase as α decreased below 0.001. This was a result of the increasing variance as shown for the triangular heat flux. The variance also contributed to the fluctuations in S_e for the second-order regularization. This again indicates the greater sensitivity of the second-order regularization to random errors. The magnitude of S_e for the zeroth order regularization increased sharply for $\alpha>0.01$. Noting the small difference between S_e and D for the zeroth order for $\alpha>0.01$ in Fig. 8, this increase was a result of the deterministic error. This large deterministic error was previously shown for the first regularization order using $\alpha=0.05$ in Fig. 7.

Minimum errors are found with $0.001<\alpha<0.005$ for all regularization orders (using the dimensionless time step of $\Delta t=0.1$). The mean squared errors increased with decreasing regularization order in this region. The first and second-order regularization orders were relatively insensitive to α compared with the zeroth order throughout the range for α investigated, as shown in Fig. 3.

Summary and Conclusions

Several components of the regularization methods were investigated using the sequential-regularization method proposed by Beck and Murio (1986). The orders of the regularization terms were compared using four different test cases. These included a pulse, a square, and a triangular heat flux imposed on a finite slab, and a single temperature measurement error. Exact and random simulated data were used for the square and triangular heat flux. The effectiveness of the different regularization orders as estimators was compared with respect to the combined errors of the deterministic or estimator bias, and the variance. The influence of the number of future time steps used in the sequential procedure was also shown.

The magnitude of the regularization parameter was investigated using the square and triangular input heat flux with exact and random analytic data. The mean squared errors of the various regularization orders were compared for various magnitudes of α using random data. Differences in the mean squared error using exact and random data were shown for the triangular heat flux case.

Several conclusions may be drawn from this study. As the order of regularization decreases, the deterministic errors tend to increase; however, as the regularization order increases, the variance increases. Therefore, the zeroth order has inherently higher deterministic errors, while the second-order regulariza-

tion is more sensitive to measurement errors. In the case where experimental errrors are known to be high, the zeroth order regularization method might be preferred, while if experimental errors are known to be very low, the second order might be the better choice. The first-order regularization method would be preferred in the case where no prior information is known about the data because of this method's relatively low biased errors compared with the zeroth order, and its relatively low deterministic errors compared with the second-order regularization method. The differences between the orders are amplified at smaller values of the number of future temperatures r, and become negligible for $r>6$. The variance and deterministic errors both approach a constant as r becomes large for all regularization orders.

The sharp change encountered in the square heat flux test case is much more difficult to estimate than the linear function of the triangular heat flux case. The deterministic error is much higher with all three regularization orders, and the second-order regularization is much more sensitive to variance errors in the square heat flux test case.

The influence of the magnitude of the dimensionless regularization parameter α on the solution depends on the regularization order used. For small $\alpha<0.001$, the stabilizing effects of the regularization components are decreased, increasing the sensitivity of the estimators to measurement errors. As α increases above 0.01, the deterministic errors of the zeroth order regularization increase dramatically; the first and second orders are relatively insensitive to α. The optimum values of dimensionless α appear to be between 0.001 and 0.005 for all regularization orders in these cases studied, which had the dimensionless time step of $\Delta t=0.1$.

In conclusion, the zeroth order regularization method provides a solution that is relatively insensitive to random measurement errors, but has relatively high deterministic errors. The second-order regularization method has relatively low deterministic errors and it is the most sensitive to random measurement errors. The first-order regularization method offers a solution with low deterministic error, which compared with the zeroth order, and low variance, when compared with the second-order regularization solution. In addition, a very large optimum range for α can be found that minimizes the sum of the deterministic errors and the variance.

References

Backus, B., and Gilbert, F., 1980, "Uniqueness in the Inversion in Inaccurate Gross Earth Data," *Phil. Trans. R. Soc., Lond.*, Vol. 266, pp. 123–192.

Bass, B. R., 1980, "Application of the Finite Element Method to the Nonlinear Inverse Heat Conduction Problem Using Beck's Second Method," ASME *Journal of Engineering for Industry*, Vol. 102, pp. 168–176.

Beck, J. V., 1968, "Surface Heat Flux Using an Integral Method," *Nuclear Engr. & Design*, Vol. 7, pp. 170–178.

Beck, J. V., 1970, "Nonlinear Estimation Applied to the Nonlinear Inverse Heat Conduction Problem," *Int. J. Heat and Mass Trans.*, Vol. 13, pp. 703–716.

Beck, J. V., 1979, "Criteria for Comparison of Methods of Solution of the Inverse Heat Conduction Problem," *Nuclear Engr. & Design*, Vol. 53, pp. 11–22.

Beck, J. V., Litkouhi, B., and St. Clair, C. R., Jr., 1982, "Efficient Sequential Solution of the Nonlinear Inverse Heat Conduction Problem," *Numerical Heat Transfer*, Vol. 5, pp. 275–286.

Beck, J. V., and Murio, D. A., 1986, "Combined Function Specification-Regularization Procedure for Solution of Inverse Heat Conduction Problem," *AIAA Journal*, Vol. 24, pp. 180–185.

Beck, J. V., Blackwell, B., and St. Clair, C. R., Jr., 1985, *Inverse Heat Conduction: Ill-Posed Problems*, Wiley, New York.

Blackwell, B. F., 1981, "Efficient Technique for the Numerical Solution of the One-Dimensional Inverse Problem of Heat Conduction," *Numerical Heat Transfer*, Vol. 4, pp. 229–238.

Burggraf, O. R., 1964, "An Exact Solution of the Inverse Problem in Heat Conduction Theory and Applications," ASME JOURNAL OF HEAT TRANSFER, Vol. 86, pp. 373–382.

Hensel, E. C., and Hills, R. G., 1984, "A Space Marching Finite Difference Algorithm for the One Dimensional Inverse Conduction Heat Transfer Problem," ASME Paper No. 84-HT-48.

Hills, R. G., and Mulholland, G. P., 1979, "The Accuracy and Resolving Power of One Dimensional Transient Inverse Heat Conduction Theory as Applied to Discrete and Inaccurate Measurements," *Int. J. Heat and Mass Transfer*, Vol. 22, pp. 1221–1229.

Imber, M., 1974, "Temperature Extrapolation Mechanism for Two-Dimensional Heat Flow," *AIAA Journal*, Vol. 12, No. 8, pp. 1089–1093.

Imber, M., and Khan, J., 1972, "Prediction of Transient Temperature Distribution With Embedded Thermocouples," *AIAA Journal*, Vol. 10, No. 6, pp. 784–788.

Krutz, G. W., Schoenhals, R. J., and Hore, P. S., 1978, "Application of the Finite-Element Method to the Inverse Heat Conduction Problem," *Numerical Heat Transfer*, Vol. 1, pp. 489–498.

Langford, D., 1976, "New Analytical Solutions of the One-Dimensional Heat Equation for Temperature and Heat Flow Rate Both Prescribed at the Same Fixed Boundary (With Applications to the Phase Change Problem)," *Quarterly of Applied Mathematics*, Vol. 24, No. 4, pp. 315–322.

Miller, K., 1970, "Least Squares Methods for Ill-Posed Problems With a Prescribed Bound," *SIAM J. Math. Anal.*, Vol. 1, No. 1, pp. 52–74.

Murio, D. A., 1985, "On the Characterization of the Solution of the Inverse Heat Conduction Problem," ASME Paper No. 85-WA/HT-41.

Raynaud, M., and Beck, J. V., 1988, "Methodology for Comparison of Inverse Heat Conduction Methods," ASME JOURNAL OF HEAT TRANSFER, Vol. 110, pp. 30–37.

Reinsch, C. H. J., 1967, "Smoothing by Spline Function," *Numerische Mathematik*, Vol. 10, pp. 177–183.

Stolz, G., Jr., 1960, "Numerical Solutions to an Inverse Problem of Heat Conduction for Simple Shapes," ASME JOURNAL OF HEAT TRANSFER, Vol. 82, 1960, pp. 20–26.

Tikhonov, A. N., and Arsenin, V. Y., 1977, *Solutions of Ill-Posed Problems*, V. H. Winston and Sons, Washington, DC.

Weber, C., 1981, "Analysis and Solution of the Ill-Posed Inverse Heat Conduction Problem," *Int. J. Heat and Mass Trans.*, Vol. 24, No. 11, pp. 1783–1792.

Williams, S. D., and Curry, D. M., 1984, "An Analytical and Experimental Study for Surface Heat Flux Determination," *J. Spacecraft*, Vol. 14, No. 10, pp. 632–637.

Wave Characteristics of Heat Conduction Using a Discrete Microscopic Model

K. J. Cheng[1]
Department of Mechanical Engineering,
Duke University,
Durham, NC 27706

The wave properties of heat conduction are studied using a discrete velocity microscopic model. In this model, molecules move with two possible speeds along one of six allowable directions, and the molecular dynamics are governed by the Boltzmann transport equation. Macroscopic quantities such as temperature and density are extracted from the distribution of molecules among various possible states. It is found that at a low degree of rarefaction (low Knudsen number), an initial temperature pulse simply spreads out with time without exhibiting any wavelike behavior. But at a high degree of rarefaction (high Knudsen number), an initial temperature pulse propagates as a highly damped temperature ripple at almost constant speed. The thermal propagation speed thus obtained agrees with the value predicted from macroscopic equations. This propagation of temperature pulse is then compared with the propagation of density disturbance (sound wave) using the same model.

1 Introduction

The classical heat conduction equation

$$\frac{\partial T}{\partial t} - \alpha \nabla^2 T = 0 \tag{1}$$

has the peculiar property that any perturbation in temperature is propagated with infinite speed. An easy way to see this peculiarity is to consider the conduction problem in an infinite medium subject to the initial condition

$$T(r,\ t=0) = \text{const} \times \delta(r)$$

where δ is the Kronecker delta function. According to equation (1), the solution for this problem is

$$T(r,\ t) = \text{const} \times 2(\pi\alpha t)^{1/2} \exp(-r^2/4\alpha t) \tag{2}$$

A consequence of this solution is that at $t = 0+$, the temperature is nonzero everywhere except at infinity (Landau and Lifshitz, 1959); in other words, the initial temperature pulse is propagated at infinite speed. This paradox has been discussed extensively in the literature.

One of the first studies to resolve this paradox was by Zeldovich and Kompaneets (1950). They showed that the velocity of propagation is finite if the conductivity is a function of the temperature that vanishes at $T = 0$ (absolute temperature). A different but more commonly used approach to resolve the paradox, as first suggested by Morse and Feshbach (1953), is to replace equation (1) by the hyperbolic heat equation (also called the telegraph equation)

$$\frac{\alpha}{w_h^2}\frac{\partial^2 T}{\partial t^2} + \frac{\partial T}{\partial t} - \alpha \nabla^2 T = 0 \tag{3}$$

where w_h is the heat propagation speed. This equation may be regarded as the wave equation with an absorption (or resistive loss) term, $\partial T/\partial t$; or it may be regarded as the usual heat conduction equation with a relaxation term, $\partial^2 T/\partial t^2$, which causes a finite propagation speed.

The concepts of wavelike behavior and finite propagation speed in heat conduction have been further discussed by many other authors. Vernotte (1958) and Cattaneo (1958) are among the first to show that equation (3) can be obtained by using a modified Fourier law of heat conduction, which was originally introduced by Maxwell (1867) and has the form

$$\tau \frac{\partial q}{\partial t} + q = -k \nabla T \tag{4}$$

where τ is the relaxation time, q the heat flux, and k the thermal conductivity.

Nettleton (1960, 1963) studied the inertial effects in heat conduction based on the classical Onsager thermodynamics. Kaliski (1965) and Luikov (1966) discussed the physical basis of the hyperbolic heat equation, also from the viewpoint of the classical Onsager thermodynamics. Weymann (1967) and Taitel (1972) used random walk models to derive the hyperbolic heat equation. A general integro-differential equation for heat conduction that exhibits wavelike properties was derived by Gurtin and Pipkin (1968) based on the laws of thermodynamics and certain constitutive relations for the internal energy and heat flux. An application of this integro-differential equation was later given by Amos and Chen (1970). Lambermont and Lebon (1973) showed that the heat conduction speed is finite if the entropy per unit volume is a function not only of the internal energy, but also of the heat flux. Bubnov (1976) and Luikov et al. (1976) derived the hyperbolic heat equation by considering the motion of isotherms. By using a modified collision term in the Boltzmann equation and then calculating the heat flux from the molecular distribution function, Berkovsky and Bashtovoi (1977) derived a power heat conduction law that possesses a finite propagation speed. Sieniutycz (1979, 1981a, 1981b) studied the wave equations for the more general case of simultaneous heat and mass transfer.

Solutions of equation (3) for the transient temperature distribution in various situations that show wave characteristics and finite propagation speed have been obtained by many authors. For example, Baumeister and Hamill (1969) used the hyperbolic heat equation to study the propagation of a temperature pulse in a semi-infinite medium, whereas Vick and Ozisik (1983) and Ozisik and Vick (1984) used the equation to study the propagation of a heat pulse. These studies, however, serve more as illustrations of the properties of the hyperbolic heat equation, rather than as a demonstration of the wavelike and finite speed properties of heat conduction from basic principles.

The purpose of this paper is to show that heat conduction indeed possesses wavelike properties and a characteristic finite

[1]Current address: AT&T Bell Laboratories, Whippany, NJ 07981.

Contributed by the Heat Transfer Division for publication in the JOURNAL OF HEAT TRANSFER. Manuscript received by the Heat Transfer Division September 17, 1987. Keywords: Conduction, Modeling and Scaling.

propagation speed, without resorting to the hyperbolic heat equation or any macroscopic equation. This is achieved by studying the propagation of a temperature disturbance in a fluid by solving the Boltzmann transport equation in a discrete velocity microscopic model.

In this model the speed of each molecule takes a discrete value of either c or $2c$. The molecular motion is along one of the six allowed directions in a two-dimensional space, as shown in Fig. 1. The translational motion of the molecules and the collisions between molecules are responsible for the propagation of a temperature disturbance. This model is used in the present work to compare the propagation of a temperature disturbance with the propagation of a density disturbance (sound wave) in a fluid. The model shows that like the propagation of density disturbance, the propagation of temperature disturbance also possesses wave characteristics (propagation of ripples). However, the wave characters of heat conduction is observable only at a degree of rarefaction below the continuum regime (Knudsen number less than 0.001).

Before proceeding to develop the discrete velocity microscopic model in Section 3.1, the theoretical value of the heat propagation speed as predicted by the hyperbolic heat equation is first given in Section 2. This will be used for later comparison with the results of the discrete velocity microscopic model.

2 Propagation Speed According to the Hyperbolic Heat Equation

Equation (3) can be rigorously derived from the kinetic theory by solving the Boltzmann transport equation to the third approximation using the moment method. (The second approximation leads to equation (1).) This has been done by Grad (1949) and Chapman and Cowling (1970). Grad's original result for the heat flux q in a gas at rest is

$$\frac{\partial q}{\partial t} + \frac{5}{2} p \nabla (RT) + \frac{2}{3} \beta \rho q = 0 \tag{5}$$

where R is the universal gas constant, and β is a parameter related to the intermolecular potential (Harris, 1971). Combining this equation with $\rho c_v \, \partial T/\partial t = -\nabla \cdot q$ gives the hyperbolic heat equation

$$\frac{3}{2\beta\rho} \frac{\partial^2 T}{\partial t^2} + \frac{\partial T}{\partial t} - \frac{15pR}{4\beta\rho^2 c_v} \nabla^2 T = 0 \tag{6}$$

On comparing equation (6) with equation (3), it is seen that heat conduction propagation speed w_h is given by

$$w_h^2 = \frac{15pR}{4\beta\rho^2 c_v} \Big/ \frac{3}{2\beta\rho} = \frac{5}{2}\left[\frac{c_p}{c_v} - 1\right] RT \tag{7}$$

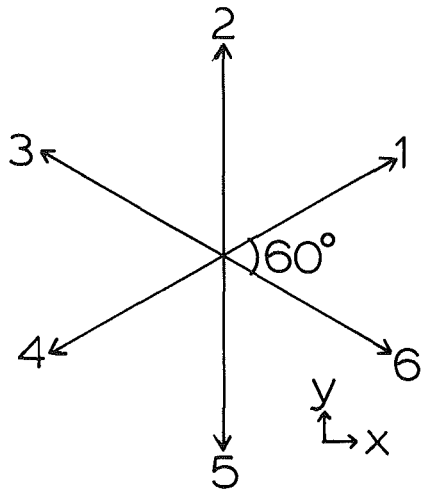

Fig. 1 The six allowable directions of molecular motion

In writing equation (7), the thermodynamic relations $c_p - c_v = R$ and $p/\rho = RT$ have been used. For comparison, the speed of sound w_s is $[c_p/c_v \, RT]^{1/2}$, and the root-mean-square molecular speed w_{rms} is $[3kT/m]^{1/2} = (3RT)^{1/2}$. Here, k is the Boltzmann constant and m is the mass of a molecule. For a diatomic gas c_p/c_v is approximately 1.4, and this results in the following ratios: $w_h/w_{rms} = 0.58$; $w_s/w_{rms} = 0.68$. (For future reference, note that in a two-dimensional case, $w_{rms} = [2RT]^{1/2}$, $w_h/w_{rms} = 0.71$, $w_s/w_{rms} = 0.84$.)

3 Heat Conduction Using the Discrete Velocity Microscopic Model

Heat and fluid flow processes can be described on three levels. At the macroscopic level the fluid is treated as a continuum, and the fluid behavior is governed by equations such as the diffusion equation and the Navier-Stokes equation. The next lower level of description is usually referred to as the kinetic theory. The Boltzmann transport equation (Lifshitz and Pitaevski, 1981) belongs to this level. Here the behavior of aggregates of molecules from the point of view of collisions between them is considered using distribution functions. Processes at this level and at the macroscopic level are in general irreversible. At the lowest level the behavior of individual molecules is considered; at this level the motion is Hamiltonian and reversible.

Nomenclature

c = unit molecular speed
$\bar{c}$ = mean molecular speed
c_v = specific heat at constant volume
c_p = specific heat at constant pressure
d = characteristic length
f = distribution function
k = thermal conductivity, or Boltzmann constant
m = mass of a molecule
n_i^j = N_i^j/N_o
p = pressure
q = heat flux
t = time
t^* = td/c = dimensionless time
x, y = spatial coordinates
y^* = y/d = dimensionless y
w_h = heat propagation speed
w_s = sound propagation speed
w_{rms} = root-mean-square molecular speed
$C(f)$ = collision integral
N_i^j = number of molecules per unit volume with speed j along direction i
N_o = initial total number of molecules per unit volume
R = universal gas constant (per unit mole)
S = collision cross section
T = absolute temperature
T^* = T/mc^2 = dimensionless absolute temperature
$\mathbf{U}$ = mean molecular velocity vector
$\mathbf{V}_i$ = velocity vector for particle moving along direction i
V_x, V_y = x, y components of velocity
α = thermal diffusivity
β = intermolecular potential parameter
θ = angle between direction of motion and x axis
λ = mean free path
ρ = density
τ = relaxation time
ϕ = collision frequency
$\binom{j}{i}$ = symbol for particle moving with speed j along direction i

Table 1 x **and** y **velocity components of particles with speed** c

Direction	1	2	3	4	5	6
V_x	$\sqrt{3}c/2$	0	$-\sqrt{3}c/2$	$-\sqrt{3}c/2$	0	$\sqrt{3}c/2$
V_y	$c/2$	c	$c/2$	$-c/2$	$-c$	$-c/2$

While a lower level description can be patched together to give a macroscopic description of heat and fluid flow processes, there is little advantage in using a low level description if the process can be adequately described by a macroscopic equation, since the lower level approach requires more computation in general. However, there are situations where the macroscopic equations are not applicable (e.g., problems involving a highly rarefied medium, or the determination of shock wave structure), or they lead to paradoxical results (e.g., infinite propagation speed that follows from the parabolic heat conduction equation). In these cases, it is necessary to refine the macroscopic equations from a lower level consideration, as in the refinement of the heat conduction equation using Grad's solution of the Boltzmann equation. Or one may give up the macroscopic equations altogether and use a low level description from start to finish; this is done in Section 3.1.

3.1 A Discrete Velocity Model for Heat Flow Processes. Discrete velocity models of gas have been used by several authors to study fluid flow processes. Broadwell (1964a, 1964b) was one of the first to use this type of model in his study of shear flow and shock wave structure in a rarefied gas. Similar models were used by Cabanees (1976) to study Couette flow and by Longo and Moriaco (1985) to study Rayleigh flow in gas mixtures. Some general theories on the discrete velocity models for a gas have been formulated by Gatignol (1975a, 1975b, 1987).

In this work a two-dimensional hexagonal two-speed model is used to study the propagation of a temperature pulse. In this model all molecules have the same mass and a speed of either c or $2c$, and move along one of the six allowable directions in a two-dimensional space, as shown in Fig. 1. The x and y components of the speed c particles moving along each of the six directions are shown in Table 1. The allowable collisions are those that conserve the number of particles, momentum, and energy. This dual speed model is the simplest discrete velocity model that is capable of describing heat conduction phenomenon. (Some other dual speed models are described in the work of Gatignol, 1975b.) Furthermore, only binary collisions are considered in the present work; collisions involving three or more particles are ignored.

The only allowable collisions between particles of the same speed are the head-on collisions. Using the notation $\binom{j}{i}$ to denote a particle with speed j ($=c$ or $2c$) along direction i (between 1 and 6), these collision rules can be written as

$$\binom{1}{1}+\binom{1}{4}\leftrightarrow\binom{1}{2}+\binom{1}{5}\leftrightarrow\binom{1}{3}+\binom{1}{6} \tag{8a}$$

$$\binom{2}{1}+\binom{2}{4}\leftrightarrow\binom{2}{2}+\binom{2}{5}\leftrightarrow\binom{2}{3}+\binom{2}{6} \tag{8b}$$

For example, the first double arrow in equation (8a) says that the collision between a particle with speed 1 moving along direction 1 and a particle with speed 1 moving along direction 4 can give rise to two speed 1 particles, with one along direction 2 and the other along direction 5; and vice versa. The allowable collisions between particles of different speeds are

$$\binom{1}{1}+\binom{2}{5}\leftrightarrow\binom{1}{4}+\binom{2}{6} \tag{9a}$$

$$\binom{1}{2}+\binom{2}{6}\leftrightarrow\binom{1}{5}+\binom{2}{1} \tag{9b}$$

$$\binom{1}{3}+\binom{2}{1}\leftrightarrow\binom{1}{6}+\binom{2}{2} \tag{9c}$$

$$\binom{1}{4}+\binom{2}{2}\leftrightarrow\binom{1}{1}+\binom{2}{3} \tag{9d}$$

$$\binom{1}{5}+\binom{2}{3}\leftrightarrow\binom{1}{2}+\binom{2}{4} \tag{9e}$$

$$\binom{1}{6}+\binom{2}{4}\leftrightarrow\binom{1}{3}+\binom{2}{5} \tag{9f}$$

The above six formulas can be generalized as

$$\binom{1}{i}+\binom{2}{i+4}\leftrightarrow\binom{1}{i+3}+\binom{2}{i+5} \tag{9g}$$

where $i = 1, 2, \ldots, 6$, and the addition in the subscript is cyclic about 6. For example, if $i = 3$, then $i + 3 = 6$, $i + 4 = 1$. In all the above collisions, the total energy is trivially conserved. It can be easily verified that the total momentum is also conserved.

The basic equation governing the heat conduction process in this model is the Boltzmann transport equation

$$\frac{\partial f}{\partial t}+\mathbf{v}\cdot\nabla f=C(f) \tag{10}$$

where f is the distribution function, $\mathbf{v}$ is the velocity, and $C(f)$ is the collision integral, which gives the change in f due to collisions.

Following the procedures Broadwell (1964a, 1964b) used to approximate the Boltzmann equation in his single speed discrete velocity model, the Boltzmann equation can be applied to each of the twelve types (two speeds and six directions) of particle and be approximated by following two equations:

$$\frac{\partial N_i^1}{\partial t}+c\sin\theta_i\frac{\partial N_i^1}{\partial y}=\frac{2}{3}cS(N_{i+1}^1N_{i+4}^1+N_{i+2}^1N_{i+5}^1-2N_i^1N_{i+3}^1)+\frac{\sqrt{7}}{2}cS(N_{i+3}^1N_{i+5}^2+N_{i+3}^1N_{i+1}^2-N_i^1N_{i+4}^2-N_i^1N_{i+2}^2) \tag{11a}$$

$$\frac{\partial N_i^2}{\partial t}+2c\sin\theta_i\frac{\partial N_i^2}{\partial y}=\frac{4}{3}cS(N_{i+1}^2N_{i+4}^2+N_{i+2}^2N_{i+5}^2-2N_i^2N_{i+3}^2)+\frac{\sqrt{7}}{2}cS(N_{i+5}^1N_{i+1}^2+N_{i+1}^1N_{i+5}^2-N_{i+4}^1N_i^2-N_{i+2}^1N_i^2) \tag{11b}$$

where $i = 1, 2, \ldots, 6$. Here the notation N_i^j refers to the number of particles with speed j along direction i per unit volume. For example, N_6^1 refers to the number of particles with speed c along direction 6 per unit volume. Also, S is the effective cross section of collision (with dimension m^2), and θ_i is the angle between the i direction and the x axis. For example, $\theta_1 = 30$ deg, $\theta_3 = 150$ deg (see Fig. 1). In writing the above equations, it is assumed that the problem of interest is one-dimensional so that $\partial/\partial x = 0$.

The terms following the equality signs in equations (11a) and (11b) are the collision terms corresponding to $C(f)$ in equation (10). The positive terms are the gain terms due to collisions that result in the creation of the particle type being considered. For example, in equation (11a), which determines the time evolution of N_i^1, the products $N_{i+1}^1N_{i+4}^1$ and $N_{i+2}^1N_{i+5}^1$ are due to the colliding pairs $\binom{1}{i+1}+\binom{1}{i+4}$ and $\binom{1}{i+2}+\binom{1}{i+5}$, both of which can give rise to $\binom{1}{i}$; and the products $N_{i+3}^1N_{i+5}^2$ and $N_{i+3}^1N_{i+1}^2$ are due to the colliding pairs $\binom{1}{i+3}+\binom{2}{i+5}$ and $\binom{1}{i+3}+\binom{2}{i+1}$, both of which can also give rise to $\binom{1}{i}$. The negative terms are the loss terms due to collisions that result in the loss of the particle type being considered. Also, the term preceding the parenthesis $\left(\frac{2}{3}cS, \frac{4}{3}cS \text{ or } \frac{\sqrt{7}}{2}cS\right)$ is the product of the collision cross section and the relative speed between colliding particles.

Notice that when the N_i^j are all equal, all the terms following

the equality signs in equations (11*a*) and (11*b*) reduce to zero; this is expected from the fact that at thermal equilibrium when the N_i^j are all equal, molecular collisions will no longer change the distribution function. Notice also that in all the collision terms in equations (11*a*) and (11*b*), mod_6 (sum of subscripts) = 0. For example, in the first collision term of equation (11*a*), the sum of subscripts = $i + 1 + i + 4 + i + 2 + i + 5 - 2(i + i + 3) = 6$; and $\text{mod}_6\ 6 = 0$. This is a consequence of the spatial symmetry along the six directions.

Equations (11*a*) and (11*b*) can be nondimensionalized by introducing the following three dimensionless quantities: $t^* = tc/d$, $y^* = y/d$, and $n_i^j = N_i^j/N_o$, where d is the characteristic length of the problem, and N_o is the initial total number of particles of all types per unit volume.

The product SN_o can be related to the mean free path λ of the particles using the following consideration. At thermal equilibrium, all molecules can be regarded as having the same mean speed $\bar{c}$ with equal probability along all the allowable directions. The collision rate for the molecules along direction 1, for instance, is

$$\phi = \bar{c}S(N_1N_2 + N_1N_6 + 2N_1N_4 + \sqrt{3}(N_1N_3 + N_1N_5)) \quad (12)$$

Note that in the above formula, the superscript $j = 1, 2$ has been dropped since all molecules are now assumed to have the same mean speed. The coefficient of each product in the equation is simply the relative speed of the colliding pair. At thermal equilibrium, motions along all allowable directions are equally probable. This gives $N_1 = N_2 \ . \ . \ . = N_6$. The collision frequency is then $\phi/N_1 = (4 + 2\sqrt{3})\bar{c}SN_1$. The mean free path is $\lambda = \bar{c}/(\phi/N_1) = 1/(4+2\sqrt{3})SN_1$. Since $N_1 = N_o/6$, this gives $\lambda = 6/(4+2\sqrt{3})SN_o = 0.804/SN_o$. It is well known from kinetic theory tht $\lambda \sim 1/SN_o$ (Lifshitz and Pitaevski, 1981).

Equations (11*a*) and (11*b*) can now be rewritten as

$$\frac{\partial n_i^1}{\partial t^*} + \sin\theta_i \frac{\partial n_i^1}{\partial y^*} = \frac{2}{3} 0.804 \frac{d}{\lambda} (n_{i+1}^1 n_{i+4}^1 + n_{i+2}^1 n_{i+5}^1 - 2n_i^1 n_{i+3}^1) + \frac{\sqrt{7}}{2} 0.804 \frac{d}{\lambda} (n_{i+3}^1 n_{i+5}^2 + n_{i+3}^1 n_{i+1}^2 - n_i^1 n_{i+4}^2 - n_i^1 n_{i+2}^2) \quad (13a)$$

$$\frac{\partial n_i^2}{\partial t^*} + 2\sin\theta_i \frac{\partial n_i^2}{\partial y^*} = \frac{4}{3} 0.804 \frac{d}{\lambda} (n_{i+1}^2 n_{i+4}^2 + n_{i+2}^2 n_{i+5}^2 - 2n_i^2 n_{i+3}^2) + \frac{\sqrt{7}}{2} 0.804 \frac{d}{\lambda} (n_{i+5}^1 n_{i+i}^2 + n_{i+1}^1 n_{i+5}^2 - n_i^2 n_{i+4}^1 - n_i^2 n_{i+2}^1 \quad (13b)$$

Notice that aside from the initial conditions and boundary conditions, which have yet to be formulated, the above two equations are characterized by one parameter: d/λ. This parameter is a measure of the degree of rarefaction of the medium, and its reciprocal is usually referred to as the Knudsen number.

3.2 Propagation of a Temperature Pulse Using the Discrete Velocity Model. Equations (13*a*) and (13*b*) are now used to determine the temperature distribution in an infinite medium subject to an initial temperature pulse. The initial condition is: at $t = 0$, $T(y, 0) =$ const everywhere, except at $y = 0$ where $T(0, 0) = 4 \cdot$ const. The subsequent temperature distribution can be determined by solving equations (13*a*) and (13*b*) using the finite difference method.

The procedure for this solution is as follows. First the region of interest is divided into a large number of length cells. Then the initial condition is implemented by setting $n_i^1 = 1.0/6$ and $n_i^2 = 0.0$ at every cell, except at the length cell corresponding to $y = 0$ where $n_i^1 = 0.0$ and $n_i^2 = 1.0/6$ ($i = 1, 2, \ldots, 6$). This is just a mathematical statement that says that the molecular speed is c everywhere, except at the middle length cell where it is $2c$. The time evolution of the temperature distribution is then obtained by writing equations (13*a*) and (13*b*) in explicit finite difference form and marching forward in time. The absolute temperature at a particular point is proportional to the average thermal energy of the molecules, and is related to n_i^j by

$$T(y) = \left[\frac{mc^2}{2} \sum_{i=1}^{6} n_i^1 + 2mc^2 \sum_{i=1}^{6} n_i^2 \right] \Big/ \sum_{i=1}^{6} (n_i^1 + n_i^2) \quad (14)$$

(More correctly, the thermal energy of a molecule is $(m/2)(\mathbf{V}_i - \mathbf{U})^2$ where $\mathbf{V}_i$ is the molecular velocity and $\mathbf{U}$ is the mean molecular velocity. But in this problem $|\mathbf{V}_i| \gg |\mathbf{U}|$, and so $(m/2)(\mathbf{V}_i - \mathbf{U})^2 \cong (m/2) V_i^2 \cong (m/2) c^2$ or $2mc^2$ depending on the molecular speed. Also, in equation (14) the Boltzmann constant has been omitted since it is of no interest here.) A dimensionless absolute temperature can then be defined as $T^* = T/mc^2$.

Figure 2 gives some of the computed results, showing T^* as a function of length steps at various time steps. In particular, it shows the effect of the degree of rarefaction, d/λ, on the behavior of the temperature profiles.There each length step corresponds to $\delta y^* = \delta y/d = 10^{-3}$, and each atime step corresponds to $\delta t^* = \delta tc/d = 2.5 \times 10^{-4}$. The convergence of these numerical results has been checked by decreasing the size of the length and time steps.

It is seen that at $d/\lambda = 5 \times 10^3$, the temperature pulse simply spreads out without showing any wavelike characteristics. This is the same behavior as expected from the parabolic heat conduction equation. At $d/\lambda = 10^3$, the initial pulse propagates as a ripple for a short time and then disappears. Thenceforth, the maximum temperature stays at the location of the initial pulse. Incidentally, $d/\lambda > 10^3$ (Knudsen number smaller than 10^{-3}) is usually regarded as the continuum domain at which continuum equations (such as the Navier–Stokes equation or the conduction equation) are applicable (Isachenko et al., 1977). At $d/\lambda = 100$ and 50, distinct temperature ripples are seen to propagate from the site of the initial pulse. Moreover, in each case the mother ripple gives rise to a smaller baby ripple at the front. These temperature ripples are highly damped. The speed of propagation of the mother ripple is almost constant at about one length step per four time steps. If this speed is identified as the heat conduction propagation speed w_h, we then have $w_h \approx (10^{-3}/(4 \times 2.5 \times 10^{-4}))c$, or $w_h \approx c$. Since $w_{rms} = \sqrt{(1+4)/2}c = 1.58c$, we also have $w_h/w_{rms} = 0.63$. This is in fair agreement with the predicted value of $w_h/w_{rms} = 0.71$ given in Section 2.

(The propagation speed here refers to that of the peak of a ripple. It may be more useful to talk about the propagation speed of the temperature front, i.e., the speed at which the region with temperature higher than the initial unperturbed value spreads out. But this is impractical in a numerical scheme, because the value of such a speed is largely determined by the roundoff error of the computer.)

Temperature solutions to the hyperbolic heat equation with a pulsed heat source that show the propagation and damping of distinctive temperature ripples have also been obtained by Vick and Ozisik (1983) and Ozisik and Vick (1984). As expected, the temperature ripples in their solutions propagate at the theoretically predicted speed in accordance with equation (3). A merit of the solutions in the present work is that these solutions are not based on the hyperbolic heat equation, yet

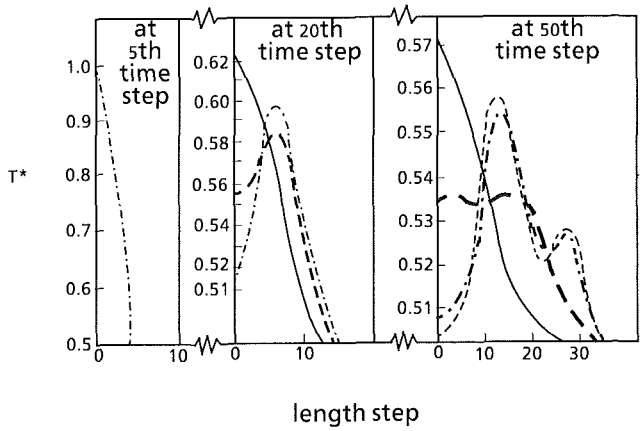

Fig. 2(*a*) At 5th, 20th, and 50th time steps. At 5th time step, all profiles are indistinguishable. At 20th time step, the profiles for $d/\lambda = 50$ and 100 are indistinguishable.

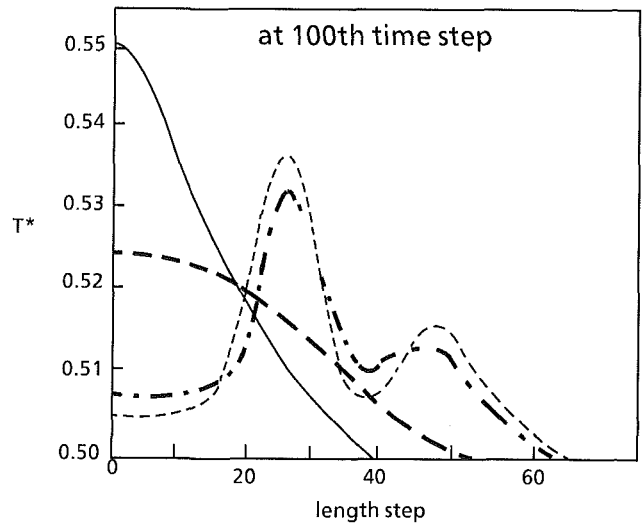

Fig. 2(*b*) At 100th time step

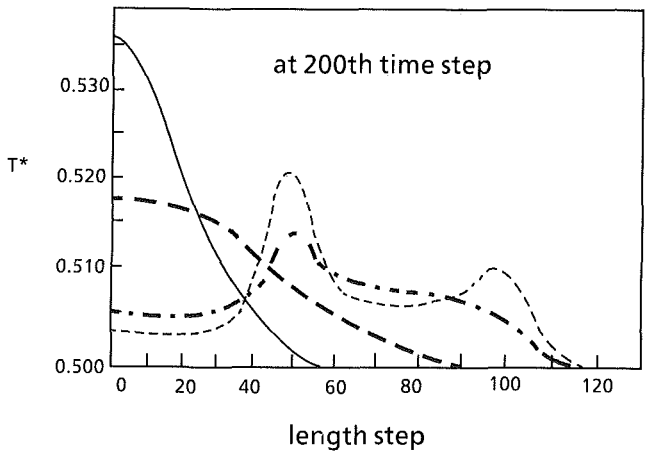

Fig. 2(*c*) At 200th time step

Fig. 2 Dimensionless temperature profiles at various time steps: —— $d/\lambda = 5000$; —— —— $d/\lambda = 1000$; —— - —— $d/\lambda = 100$; ------ $d/\lambda = 50$

they give a propagation speed in fair agreement with the value predicted by the hyperbolic heat equation (in a two-dimensional world).

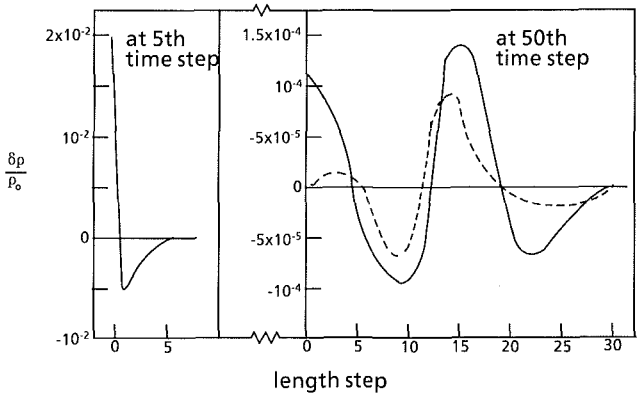

Fig. 3(*a*) At 5th and 50th time steps. At 5th time step, the two profiles are indistinguishable.

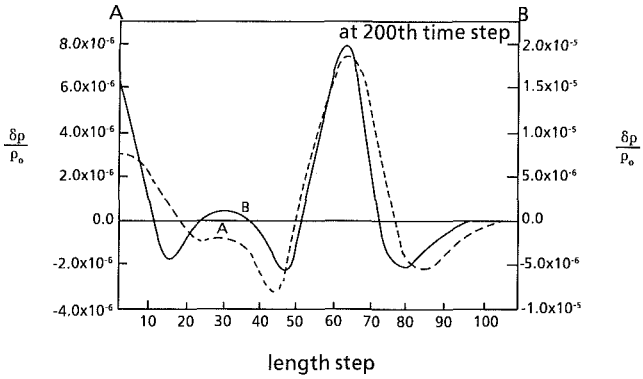

Fig. 3(*b*) At 200th time step

Fig. 3 Density profiles at various time steps: ——— $d/\lambda = 5000$; ------ $d/\lambda = 1000$

3.3 Comparison of Propagation of Temperature Disturbance With That of Density Disturbance. For comparison, equations (13*a*) and (13*b*) are now used to study a similar process of the propagation of density disturbance (sound wave). In this case the initial condition is implemented in finite difference form as follows. At $t = 0$, $n_i^1 = n_i^2 = 1/12$ everywhere, except at the three length cells in the middle. At the center length cell, $n_i^1 = n_i^2 = 1/12 + 0.01$, and at the steps neighboring the center step $n_i^1 = n_i^2 = 1/12\text{-}0.005$. This simulates a compression at the center length step and rarefactions at the two neighboring steps. (Note that the sum of Σn_i^j over the three middle length cells is 3, which is also equal to the sum of Σn_i^j over any three unperturbed length cells.) The density at any point is proportional to Σn_i^j.

Some of the computed results are given in Fig. 3, showing the change in density, $\delta\rho/\rho_o = (\rho - \rho_o)/\rho_o$, as a function of length steps, where ρ_o is the initial density of the unperturbed gas. There the value of δy^* for a length step and the value of δt^* for a time step are the same as in Section 3.2. It is seen that the density ripples, though still highly damped, are more persistent than the temperature ripples. For example, while no temperature ripple is seen at $d/\lambda = 5 \times 10^3$, a distinct density ripple is seen to propagate at this same d/λ. The propagation speed of the density ripple is almost constant at 0.34 length step per time step, which amounts to about 1.36*c*. Identifying this speed as the speed of sound w_s then gives $w_s/w_{rms} \approx 1.36/1.58 \approx 0.86$, in reasonable agreement with the value of 0.84 given in Section 2.

(It should be noted that the initial condition used in Section 3.2 also produces density ripples in addition to the temperature ripples. These density ripples, however, are a consequence of the temperature fluctuations; they propagate with the same speed and phase as the temperature ripples. The density ripples considered in this section are the "pure" density waves under almost isothermal conditions.)

4 Discussion

Although the discrete microscopic model was presented here for the study of the propagation of temperature and deWity pulses in a gas, this type of modeling is also useful in the study of other heat flow processes where the usual continuum equations are not applicable. These include, for example, the heat flow in a rarefied medium and the temperature across a shock wave front. An advantage of this model is that the governing equations are characterized by one parameter d/λ. This enables the effect of the degree of rarefaction on fluid and heat flow processes to be studied conveniently.

While both the hyperbolic heat equation and the discrete Boltzmann equation (equations (11*a*) and (11*b*)) in this work predict the existence of temperature waves, there are fundamental differences between the two. The hyperbolic heat equation is a macroscopic continuum equation for the temperature, whereas the Boltzmann equation is a lower level general equation for the distribution function. The latter equation makes no direct reference to the temperature or any macroscopic variable. But from the distribution function, various macroscopic quantities such as temperature, density, and fluid velocity can be deduced. Unlike the hyperbolic heat equation, equations (11*a*) and (11*b*) can also be used to study fluid flow. (The difference between the hyperbolic heat equation and the Boltzmann equation is somewhat analogous to the difference between a high level programming language such as FORTRAN and a low level language such as an assembly language. The former is easier to use but application specific, whereas the latter is more clumsy to use but more general.)

Some authors (Baumeister and Hamill, 1969; Vick and Ozisik, 1983; Ozisik and Vick, 1984) have drawn a parallel between the wave nature of heat conduction and the propagation of undamped temperature oscillation (the so-called second sound wave) in helium II below its λ-point (Peshkov, 1944, 1946), at which helium II becomes a superfluid. This is a misleading parallel, since the nature of heat flow in a superfluid is fundamentally different from ordinary heat conduction. The second sound observed in helium II is essentially a quantum-mechanical effect, involving a quantum fluid that can simultaneously execute two kinds of motion: a superfluid flow and a normal flow. (Details are given in Chap. 16 of the textbook by Landau and Lifshitz, 1959.) This second sound is not a limiting case of the ordinary thermal conduction process, and in fact has no connection with the damped temperature "wave" as described by equation (3) or the results presented in Section 3.2. The propagation of temperature oscillation wave may also occur in a solid in the absence of Umklapp processes (Lifshitz and Pitaevski, 1981). But again, this wave motion is unrelated to ordinary thermal conduction; it is not even capable of establishing thermal equilibrium (Kittel, 1976).

5 Concluding Remarks

The propagation of an initial temperature pulse is studied by solving the Boltzmann transport equation in a discrete velocity microscopic model. It is found that at a low degree of rarefaction (small Knudsen number), an initial temperature pulse simply spreads out without showing any wavelike character. But at a high degree of rarefaction (high Knudsen number), the temperature pulse propagates as a ripple at nearly constant speed. Moreover, the temperature ripple becomes more pronounced and persistent as the degree of rarefaction increases. The thermal propagation speed obtained from this model agrees fairly well with the value predicted from macroscopic equations.

References

Amos, D. E., and Chen, P. J., 1970, "Transient Heat Conduction With Finite Wave Speeds," ASME *Journal of Applied Mechanics*, Vol. 37, pp. 1145–1146.

Baumeister, K. J., and Hamill, T. D., 1969, "Hyperbolic Heat Conduction Equation—a Solution for the Semi-infinite Body Problem," ASME JOURNAL OF HEAT TRANSFER, Vol. 91, pp. 543–548.

Berkovsky, B. M., and Bashtovoi, V. G., 1977, "The Finite Velocity of Heat Propagation From the Viewpoint of the Kinetic Theory," *Int. J. Heat Mass Transfer*, Vol. 20, pp. 621–626.

Broadwell, J. E., 1964a, "Study of Rarefied Shear Flow by the Discrete Velocity Model," *Journal of Fluid Mechanics*, Vol. 19, pp. 401–414.

Broadwell, J. E., 1964b, "Shock Structure in a Simple Discrete Velocity Gas," *Physics of Fluids*, Vol. 7, pp. 1243–1247.

Bubnov, V. A., 1976, "Wave Concepts in the Theory of Heat," *Int. J. Heat Mass Transfer*, Vol. 19, pp. 175–184.

Cabannes, H., 1976, "Couette Flow for a Gas With a Discrete Velocity Distribution," *Journal of Fluid Mechanics*, Vol. 76, pp. 273–287.

Cattaneo, C., 1958, "Sur une Forme de l'equation de la Chaleur eliminant le Paradoxe d'une Propagation Instantanee," *C. R. Hebd. Seanc. Acad. Sci., Paris*, Vol. 247, pp. 431–433.

Chapman, S., and Cowling, T. G., 1970, *The Mathematical Theory of Non-uniform Gases*, Cambridge University Press, Cambridge, United Kingdom.

Gatignol, R., 1975a, "Kinetic Theory for a Discrete Velocity Gas and Application to Shock Structure," *Physics of Fluids*, Vol. 18, pp. 153–161.

Gatignol, R., 1975b, "Theorie Cinetique des Gaz a Repartition Discrete de Vitesses," *Lecture Notes in Physics*, Vol. 36, Springer-Verlag, Berlin.

Gatignol, R., 1987, "The Hydrodynamical Description for a Discrete Velocity Model of Gas," *Complex Systems*, Vol. 1, pp. 709–725.

Grad, H., 1949, "Kinetic Theory of Rarefied Gas," *Communications in Pure and Applied Math*, Vol. 2, pp. 331–407.

Gurtin, M. E., and Pipkin, A. C., 1968, "A General Theory of Heat Conduction With Finite Wave Speeds," *Arch. Rational Mech. Anal.*, Vol. 31, pp. 113–126.

Harris, S., 1971, *An Introduction to the Theory of the Boltzmann Equation*, Holt, Rinehart and Winston, New York.

Isachenko, V. P., Osipova, V. A., and Sukomel, A. S., 1977, *Heat Transfer*, MIR Publishers, Moscow.

Kaliski, S., 1965, "Wave Equation of Heat Conduction," *Bull. Acad. Polon. Sci.*, Vol. 13, pp. 211–219.

Kittel, C., 1976, *Introduction to Solid State Physics*, 5th ed., Wiley, New York, p. 145.

Lambermont, J., and Lebon, G., 1973, "On a Generalization of the Gibbs Equation for Heat Conduction," *Physics Letters*, Vol. 42A, pp. 499–500.

Landau, L. D., and Lifshitz, E. M., 1959, *Fluid Mechanics*, Pergamon, London.

Lifshitz, E. M., and Pitaevski, L. P., 1981, *Physical Kinetics*, Pergamon, London.

Longo, E., and Moriaco, R., 1985, "Analytical Solutions of the Discrete Boltzmann Equation for Rayleigh Flow Problem for Gas Mixtures," *Physics of Fluids*, Vol. 26, pp. 2730–2734.

Luikov, A. V., 1966, "Application of Irreversible Thermodynamics Methods in Investigation of Heat and Mass Transfer," *Int. J. Heat Mass Transfer*, Vol. 9, pp. 139–152.

Luikov, A. V., Bubnov, V. A., and Soloviev, I. A., 1976, "On Wave Solutions of the Heat-Conduction Equation," *Int. J. Heat Mass Transfer*, Vol. 19, pp. 245–248.

Maxwell, J. C., 1867, "On the Dynamical Theory of Gases," *Phil. Trans. Roy. Soc.*, Vol. 157, pp. 49–88.

Morse, P. M., and Feshbach, H., 1953, *Methods of Theoretical Physics*, McGraw-Hill, New York, p. 865.

Nettleton, R. E., 1960, "Relaxation Theory of Thermal Conduction in Liquids," *Physics of Fluids*, Vol. 3, pp. 216–226.

Nettleton, R. E., 1963, "Inertial Effects in the Phenomenological Theory of Thermal Diffusion in Liquids," *Nuovo Cimento*, Vol. 28, pp. 952–969.

Ozisik, M. N., and Vick, B., 1984, "Propagation and Reflection of Thermal Waves in a Finite Medium," *Int. J. Heat Mass Transfer*, Vol. 27, pp. 1845–1854.

Peshkov, V. P., 1944, "Second Sound in Helium II," *J. Phys. (USSR)*, Vol. 8, p. 381.

Peshkov, V. P., 1946, "Determination of Velocity Propagation of Second Sound in Helium II," *J. Phys. (USSR)*, Vol. 10, pp. 389–398.

Sieniutycz, S., 1979, "The Wave Equations for Simultaneous Heat and Mass Transfer in Moving Media-Structure Testing, Time-Space Transformations and Variational Approach," *Int. J. Heat Mass Transfer*, Vol. 22, pp. 585–599.

Sieniutycz, S., 1981a, "Action Functionals for Linear Wave Dissipative Systems With Coupled Heat and Mass Transfer," *Physics Letters*, Vol. 84A, pp. 98–102.

Sieniutycz, S., 1981b, "The Thermodynamic Stability of Coupled Heat and Mass Transfer Described by Linear Wave Equations," *Chemical Engineering Science*, Vol. 36, pp. 621–624.

Taitel, Y., 1972, "On the Parabolic, Hyperbolic and Discrete Formulation of the Heat Conduction Equation," *Int. J. Heat Mass Transfer*, Vol. 15, pp. 369–371.

Vernotte, P., 1958, "Les Paradoxes de la Theorie Continue de l'equation de la Chaleur," *C. R. Hebd. Seanc. Acad. Sci., Paris*, Vol. 246, pp. 3154–3155.

Vick, B., and Ozisik, M. N., 1983, "Growth and Decay of a Thermal Pulse Predicted by the Hyperbolic Heat Conduction Equation," ASME JOURNAL OF HEAT TRANSFER, Vol. 105, pp. 902–907.

Weymann, H. D., 1967, "Finite Speed of Propagation in Heat Conduction, Diffusion, and Viscous Shear Motion," *American Journal of Physics*, Vol. 35, pp. 488–496.

Zeldovich, Ya., and Kompaneets, A. S., 1950, "On the Theory of Heat Propagation at Heat Conduction Depending on Temperature," collected articles dedicated to the 70th birthday of A. F. Ioffe, *Izd. Akad. Nauk SSSR*, Moscow.

On the Thermal Shock Wave Induced by a Moving Heat Source

D. Y. Tzou
Assistant Professor,
Department of Mechanical Engineering,
University of New Mexico,
Albuquerque, NM 87131

Analytical solutions for the temperature field around a moving heat source in a solid with finite speed of heat propagation are obtained via the method of Green's functions. When the speed of the moving heat source is equal to or faster than that of the thermal wave propagated in the solid, the thermal shock wave is shown to exist in the thermal field. The shock wave angle is obtained as $\sin^{-1}(1/M)$ *for* $M \geq 1$. *Orientation of crack initiation in the vicinity of the heat source is also estimated by considering the temperature gradient* $T_{,\theta}$ *along the circumference of a continuum circle centered at the heat source. Such an orientation is established as a function of the thermal Mach number in the subsonic, transonic, and supersonic regimes, respectively.*

Introduction

The major difference between hyperbolic and diffusion models in heat conduction lies in the heat-affected zone in the transient stage. In the diffusion model, it is assumed that the speed of heat propagation in the solid is infinite such that the existence of a thermal agent (including heat sources, initial and boundary conditions) at infinity can be detected right after its application. The hyperbolic model, on the other hand, simulates the process of energy transfer in the solid by thermal waves. Depending on the speed of heat propagation through the multicrystalline lattice, the heat-affected zone is spread through the solid with the same speed as the thermal wave, and consequently, the characteristic dimension of the heat-affected zone is finite and increases as a function of time. Consider a hyperbolic equation with finite speed of heat propagation C (Morse and Feshbach, 1953):

$$\nabla^2 T = (1/\alpha) T_{,t} + (1/C^2) T_{,tt} \tag{1}$$

Traditionally, the importance of considering the wave nature in a heat transport process is evaluated by weighing the relative contributions of the two coefficients on the right-hand side of this equation. The criterion obtained in this manner is a function of intrinsic properties of the solid medium. Chester (1963) established a critical frequency (inversely proportional to the relaxation time) for thermal fluctuation above which heat transport proceeds by wave propagation rather than by diffusion. Later, in 1965, Weymann further identified the analogy between random walk and diffusion, and extended the study to the problems of mass diffusion and viscous shear motion. Boley (1964) and Baumeister (1969) concluded that except for the existence of a distinct wave front, or under a circumstance with very low temperature or very short response time, the effect of finite speed correction to the diffusion process is negligible in most practical engineering problems.

A more general evaluation on the importance of the wave phenomena represented by equation (1) can be made by taking the rate change of temperature into consideration. If we directly compare the two terms on the right-hand side of the equation, an inequality

$$\Delta\psi/\psi >> (C^2/\alpha)\Delta t, \quad \text{with } \psi = T_{,t} = \text{rate change of temperature} \tag{2}$$

can be rendered for the dominance of wave nature in the process of heat transport. In addition to the conditions considered in the past, i.e., small value of C, or large value of α, we notice that equation (2) also induces the rate change of temperature in the criterion. In a situation where C is large or α is small in a relative sense, equation (2) states that the wave phenomena can still be important if the rate change of temperature in a short time interval is high. A typical example where this occurs is in laser sparkling oriented technology. Because the intensity of energy supplied to the solid is high and the application time is extremely short, a very high rate of temperature increase in the neighborhood of the localized heat source usually results. Consideration of the wave model in the heat transport process becomes even more important if some irreversible physical processes, such as crack or void initiation in the solid, occurs in the transient stage. Under the application of an energy source with sufficiently high intensity, these local defects could be initiated in a shorter time interval than that required for the diffusion behavior to be retrieved, and the orientation of crack initiation, for example, must be predicted according to the hyperbolic wave model.

It is the intention of the present study to investigate the thermal field under this condition. The temperature distributions are obtained in closed-from solutions according to the moving velocity of the energy source. With reference to the speed of heat propagation in the solid, all three cases containing subsonic, transonic, and supersonic modes of heat transfer are studied. In the transonic and supersonic modes, we further show the formation of thermal shock waves attached to the moving heat source. This is a salient feature unique in the hyperbolic model that is not able to be predicted by the diffusion model. The fracture angle initiated in the vicinity of the heat source is also approximately estimated according to the temperature gradient thereby. The deviation between the results predicted by the wave model and those by the diffusion model are presented in terms of the thermal Mach number. In all cases under consideration, this deviation is by no means negligible.

Formulation of the Problem

As shown in Fig. 1, consider a point heat source with intensity Q moving at a constant speed v along the x_1 axis. The dimensions of the solid are assumed to be large such that the edge effects on the local thermal field around the heat source can be neglected. It is well known that the edge effects introduced through boundary conditions only influence the intensity of the local field solutions while the characteristics of the solutions are not affected (Tzou, 1985a). The energy and the constitutive equations for the thermal wave propagated in the solid with a finite speed C can be written as (Frankel et al., 1985)

$$-\nabla \cdot \mathbf{q} + S = \rho C_p T_{,t} \tag{3}$$

$$(\alpha/C^2)\mathbf{q}_{,t} + \mathbf{q} = -k\nabla T \tag{4}$$

Contributed by the Heat Transfer Division for publication in the JOURNAL OF HEAT TRANSFER. Manuscript received by the Heat Transfer Division December 4, 1987. Keywords: Conduction.

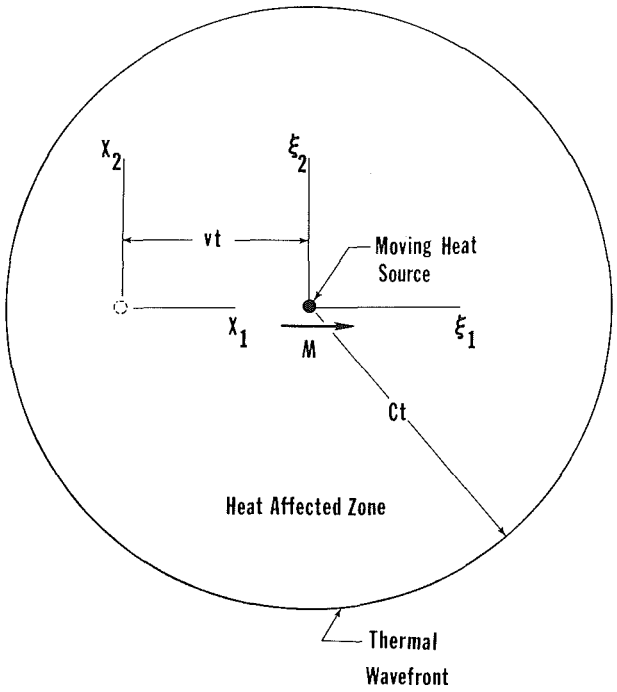

Fig. 1 Thermal waves emanating from a moving heat source and the coordinate system

By eliminating $\mathbf{q}$ from these equations, we obtain a single equation for T

$$\alpha\nabla^2 T + (1/\rho C_p)[S + (\alpha/C^2)S_{,t}] = (\alpha/C^2)T_{,tt} + T_{,t} \quad (5)$$

where the apparent heat source term differs from the real heat source applied to the solid by a term of $(\alpha/\rho C_p C^2)S_{,t}$.

Now, for a point heat source with its position simulated by Dirac delta functions

$$S(x_1, x_2, t) = Q\delta(x_1 - vt)\delta(x_2) \quad (6)$$

equation (5) can be reduced to the form of

$$\alpha\nabla^2 T - (\alpha/C^2)T_{,tt} - T_{,t} = -(Q/\rho C_p)[\delta(x_1 - vt) + (\alpha/C^2)\delta_{,t}(x_1 - vt)]\delta(x_2) \quad (7)$$

Since the heat source is assumed to be moving at a constant speed, the Galilei transformation

$$x_1 = \xi_1 + vt$$
$$x_2 = \xi_2 \quad (8)$$

can be applied, and the equation governing the quasi-stationary temperature field observed from the moving coordinate system $\xi_i (i = 1, 2)$ can be obtained by applying the chain rule to the differentiations in equation (7), which yields

$$\alpha[(1 - \mathrm{M}^2)T_{,11} + T_{,22}] + 2c\alpha T_{,1} = -(Q/\rho C_p)\{\delta(\xi_1)\delta(\xi_2) - (\mathrm{M}^2/2c)\delta_{,1}(\xi_1)\delta(\xi_2)\} \quad (9)$$

where $\mathrm{M} = v/C$ is the thermal Mach number of the moving heat source with reference to the speed of heat propagation in the solid.

The advantage of using equation (9) in the present study is quite obvious. Through the introduction of a single parameter M, the effect of the speed of the moving heat source is weighed with respect to the heat propagation speed in the solid. The characteristics of the solution for equation (9) depend on the thermal Mach number of the heat source. In the subsonic case with $\mathrm{M} < 1$, the equation is elliptic, while in the transonic ($\mathrm{M} = 1$) and supersonic cases ($\mathrm{M} > 1$), the equation is transmitted to parabolic and hyperbolic types, respectively. This is a situation similar to the equation governing the aerodynamic velocity potential in a mixed flow field (Shapiro, 1954, for example). After equation (9) is solved for T, the heat flux vector $\mathbf{q}$ in the ξ_i coordinates can be obtained by solving the transformed equation

$$(\mathrm{M}^2/2c)q_{,1} - q = k\nabla T \quad (10)$$

As the speed of heat propagation approaches infinity, i.e., M approaches zero, equations (9) and (10) reduce to those defined in the diffusion model. The transitional behavior due to different types of thermal wave equation in different sonic ranges are investigated systematically in this work. Due to the presence of extra terms containing $T_{,1}$ and $\delta_{,1}$ in equation (9), the approach used in the present analysis is quite different from that in the classical theory of aerodynamics. In the following section, the energy equation (9) will be first transformed, for every case of M, to a form for which Green's function can be found. Closed-form solutions for T in the sub-

Nomenclature

c = $v/2\alpha$ = a parameter used in the thermal wave equation, 1/m
C = speed of heat propagation in the solid, m/s
C_p = heat capacity, kJ/kg-K
f = spatial distribution in the transformation on the dependent variables
f_g = Green's function used in the subsonic and supersonic cases
G = Green's function for the transformed equation of f
I_n = modified Bessel function of the first kind of order n
k = thermal conductivity, W/m-K
K_n = modified Bessel function of the second kind of order n
M = v/C = thermal Mach number
$\mathbf{q}, q_1, q_2$ = heat flux vector and its components, W/m^2
Q = intensity of the heat source, W/m
r = transformation function for the independent variables, m
r^0, r_η = radial position of the heat source, m
R = radial distance from the heat source, m
S = general heat source term, W/m
t = physical time, s
T = temperature, K
T_g = Green's function for the transonic case
v = speed of the moving heat source, m/s
x_1, x_2 = stationary coordinates, m
α = thermal diffusivity, m^2/s
θ = angle in the polar coordinate system, deg
θ_M = thermal shock angle, deg
ξ_1, ξ_2 = moving coordinates with the heat source, m
ξ_1^0, ξ_2^0 = position of the heat source, m
ρ = mass density, kg/m^3
ϕ = angle measured from negative ξ_1-axis, deg
∇ = gradient operator, 1/m
$(\ )_{,i}$ = $\partial/\partial\xi_i$, $i = 1, 2$
$\bar{(\ )}$ = dimensionless quantity

sonic, transonic, and supersonic ranges are then followed by direct integrations. The influences of finite speed of heat propagation on the thermal field are more explicitly displayed in this manner.

Temperature Field Around the Heat Source

Because equation (9) varies intrinsically as a function of the thermal Mach number, the temperature field should be investigated individually for $M<1$, $M=1$, and $M>1$. In all cases, the temperature and its gradient are assumed to vanish at infinity.

(a) Subsonic Cases: $M<1$. Let us consider a transformation on the dependent variable $T(\xi_i)$

$$T(\xi_i)=\exp[-c\xi_1/(1-M^2)]f(\xi_i), \qquad \text{for } M<1 \tag{11}$$

By substituting equation (11) into (9), an equation governing $f(\xi_i)$ can be found as

$$(1-M^2)f_{,11}+f_{,22}-[c^2/(1-M^2)]f = -(Q/\rho C_p\alpha)\exp[c\xi_1/(1-M^2)]\cdot \{\delta(\xi_1)\delta(\delta_2)-(M^2/2c)\delta_{,1}(\xi_1)\delta(\xi_2)\} \tag{12}$$

By applying another transformation on the independent variables from ξ_i to r

$$r=\sqrt{\xi_1^2/(1-M^2)+\xi_2^2}, \qquad \text{for } M<1 \tag{13}$$

which stretches a circle on the ξ_i plane to an ellipse, equation (12) can be further cast in the form of

$$f_{,rr}+\frac{1}{r}f_{,r}-[c^2/(1-M^2)]f = -(Q/\rho C_p\alpha)\exp[c\xi_1/(1-M^2)]\delta(\xi_1)\delta(\xi_2) + (QM^2/2c\rho C_p\alpha)\exp[c\xi_1/(1-M^2)]\delta_{,1}(\xi_1)\delta(\xi_2) \tag{14}$$

where the independent variables ξ_i in the nonhomogeneous terms of the equation are temporarily retained for later use. The solution of equations (14) consists of two parts. One is the contribution from the real heat source applied to the solid; the other results from the effect of finite speed of heat propagation. For both cases, the solutions can be found if the Green's function $f_g(r|r_\eta)$ satisfying the equation

$$f_{g,rr}+\frac{1}{r}f_{g,r}-[c^2/(1-M^2)]f_g=\delta(r-r_\eta) \tag{15}$$

is sought. The operator in equation (15) is identified as the modified Bessel operator. The Green's function for this type of equations is (Arfken, 1970)

$$f_g(r|r_\eta)=\frac{1}{A}K_0[c|r-r_\eta|/(1-M^2)^{1/2}] \tag{16}$$

where $r_\eta=[\eta_1^2/(1-M^2)+\eta_2^2]^{1/2}$ and the constant A comes from the Wronskian

$$I_0(z)K_0'(z)-I_0'(z)K_0(z)=\frac{A}{z} \tag{17}$$

which is obviously equal to -1. Using equation (16) as the Green's function for equation (14), and noticing the integral properties of the Dirac delta function (Morse and Feshback, 1953)

$$\int G[r(\xi_1,\xi_2)|r^0(\xi_1^0,\xi_2^0)]\delta(\xi_1^0)\delta(\xi_2^0)d\xi_1^0d\xi_2^0 = G[r(\xi_1,\xi_2)|r^0(0,0)]$$

$$\int G[r(\xi_1,\xi_2)|r^0(\xi_1^0,\xi_2^0)]\delta_{,1}(\xi_1^0)\delta(\xi_2^0)d\xi_1^0d\xi_2^0 = -\left\{\frac{\partial}{\partial\xi_1^0}G[r(\xi_1,\xi_2)|r^0(\xi_1^0,0)]\right\}_{\xi_1^0\to 0} \tag{18}$$

the solution of equation (14) for $f(r)$ is

$$f(r(\xi_i))=(Q/\rho\alpha C_p)\left\{\frac{2-M^2}{2(1-M^2)}K_0[cr/(1-M^2)^{1/2}] - \frac{M^2}{2(1-M^2)}K_1[cr/(1-M^2)^{1/2}]\right\} \tag{19}$$

and the temperature $T(\xi_i)$ in the subsonic range is thus obtained from equation (11)

$$T(\xi_i)/(Q/\rho\alpha C_p)=\exp[-c\xi_1/(1-M^2)] \left\{\frac{2-M^2}{2(1-M^2)}K_0[cr/(1-M^2)^{1/2}] - \frac{M^2}{2(1-M^2)}K_1[cr/(1-M^2)^{1/2}]\right\}, \qquad M<1 \tag{20}$$

The heat flux vector $\mathbf{q}$ with components q_1 and q_2 in the ξ_i coordinate system can be obtained by solving equation (10). The result is

$$\{q_1, q_2\}=\frac{2ck}{M^2}\exp(2c\xi_1/M^2) \int\exp(-2c\xi_1/M^2)\{T_{,1}, T_{,2}\}d\xi_1 \tag{21}$$

By direct differentiation on $T(\xi_i)$, $i=1, 2$ yields

$$T_{,1}/(Q/\rho\alpha C_p)=\exp[-c\xi_1/(1-M^2)] \left\{\left[\frac{M^2c\xi_1}{2r(1-M^2)^{5/2}}-\frac{(2-M^2)}{2(1-M^2)^2}\right]K_0[cr/(1-M^2)^{1/2}] + \left[\frac{M^2c}{2(1-M^2)^2}-\frac{(2-M^2)c\xi_1}{2r(1-M^2)^{5/2}} + \frac{M^2\xi_1}{2r^2(1-M^2)^2}\right]K_1[cr/(1-M^2)^{1/2}]\right\} \tag{22}$$

$$T_{,2}/(Q/\rho\alpha C_p)=\exp[-c\xi_1/(1-M^2)] \left\{\left[\frac{M^2c\xi_2}{2r(1-M^2)^{3/2}}\right]K_0[cr/(1-M^2)^{1/2}] + \left[\frac{M^2\xi_2}{2r^2(1-M^2)}-\frac{(2-M^2)c\xi_2}{2r(1-M^2)^{3/2}}\right]K_1[cr/(1-M^2)^{1/2}]\right\} \tag{23}$$

Note that as $M\to 0$, equation (20) is reduced to the expression for the diffusion model, while reduction for the heat flux vector to that of the Fourier solid must be made from equation (10) rather than equations (22) and (23).

(b) Supersonic Case; $M>1$. As $M>1$, equation (9) can be reduced to the following form:

$$\alpha[(M^2-1)T_{,11}-T_{,22}]-2c\alpha T_{,1} = (Q/\rho C_p)\{\delta(\xi_1)\delta(\xi_2)-(M^2/2c)\delta_{,1}(\xi_1)\delta(\xi_2)\} \tag{24}$$

In this case, the transformations on the dependent (from T to f) and independent (from ξ_i to r) variables are taken to be

$$T(\xi_i)=\exp[c\xi_1/(M^2-1)]f(\xi_i), \qquad r=[\xi_1^2/(M^2-1)-\xi_2^2]^{1/2}, \qquad \text{for } M>1 \tag{25}$$

The corresponding equation governing the function $f(\xi_i)$ becomes

$$f_{,rr}+\frac{1}{r}f_{,r}-[c^2/(M^2-1)]f = (Q/\rho C_p\alpha)\exp[-c\xi_1/(M^2-1)]\delta(\xi_1)\delta(\xi_2) - (QM^2/2c\rho C_p\alpha)\exp[-c\xi_1/(M^2-1)]\delta_{,1}(\xi_1)\delta(\xi_2) \tag{26}$$

and the Green's function in this case is

$$f_g(r|r_\eta)=K_0[c|r-r_\eta|/(M^2-1)^{1/2}] \tag{27}$$

By employing the same procedure as that used in the previous case, the temperature and its gradient can be obtained as

$$T(\xi_i)/(Q/\rho\alpha C_p) = -\exp[c\xi_1/(M^2-1)] \left\{\frac{2-M^2}{2(M^2-1)} K_0[cr/(M^2-1)^{1/2}] - \frac{M^2}{2(M^2-1)} K_1[cr/(M^2-1)^{1/2}]\right\}, \quad M>1 \tag{28}$$

$$T_{,1}/(Q/\rho\alpha C_p) = \exp[c\xi_1/(M^2-1)] \left\{-\left[\frac{M^2 c\xi_1}{2r(M^2-1)^{5/2}} + \frac{(2-M^2)c}{2(M^2-1)^2}\right] K_0[cr/(M^2-1)^{1/2}] + \left[\frac{M^2 c}{2(M^2-1)^2} + \frac{(2-M^2)c\xi_1}{2r(M^2-1)^{5/2}} - \frac{M^2\xi_1}{2r^2(M^2-1)^2}\right] K_1[cr/(M^2-1)^{1/2}]\right\} \tag{29}$$

$$T_{,2}/(Q/\rho\alpha C_p) = \exp[c\xi_1/(M^2-1)] \left\{\left[\frac{M^2 c\xi_2}{2r(M^2-1)^{3/2}}\right] K_0[cr/(M^2-1)^{1/2}] + \left[\frac{M^2\xi_2}{2r^2(M^2-1)} - \frac{(2-M^2)c\xi_2}{2r(M^2-1)^{3/2}}\right] K_1[cr/(M^2-1)^{1/2}]\right\} \tag{30}$$

Unlike the subsonic case, we first notice that the radial distance r defined in equation (25) restricts the applicable range of equations (28) to (30) to the domain satisfying the condition

$$\xi_1^2/(M^2-1) > \xi_2^2. \tag{31}$$

The physical interpretation of equation (31) can be nicely made if we represent the condition in terms of polar coordinates (R, θ) centered at the heat source, as shown in Fig. 4. The equivalent expression of equation (31) is

$$|\tan\theta| < [1/(M^2-1)]^{1/2} \tag{32}$$

or in a more familiar form

$$0<\theta<\sin^{-1}(1/M) \text{ or } \pi-\sin^{-1}(1/M)<\theta<\pi \tag{33}$$

where the ranges for θ in the third and fourth quadrant are omitted due to symmetry of the problem. In equation (33), the first domain is that for the heat-affected zone with an energy source moving leftward, while the second is that with an energy source moving rightward. The latter is the case for the present study under the Galilei' transformation defined in equation (8). The temperature field outside this domain stays undisturbed as the heat source moves rightward with a supersonic speed. The existence of a thermal shock wave forming a shock angle $\theta_M = \sin^{-1}(1/M)$ with the negative x_1 or ξ_1 axis is obvious, and discontinuity of the thermal field across the shock wave is thus expected.

(c) Transonic Case; M = 1. As the heat source moves at the same speed as the heat propagation speed in the solid, a normal shock with $\theta_M = 90$ deg exists according to equation (33). In this case, equation (9) degenerates into a parabolic equation

$$T_{,22} + 2cT_{,1} = -(Q/\rho\alpha C_p)\{\delta(\xi_1)\delta(\xi_2) - (M^2/2c)\delta_{,1}(\xi_1)\delta(\xi_2)\} \tag{34}$$

whose Green's function can be found as (Carslaw and Jaeger, 1959)

$$T_g(\xi_i|\xi_i^0) = [-1/(8\pi c)^{1/2}]\exp[-c(\xi_2-\xi_2^0)^2/2|\xi_1-\xi_1^0|]/[|\xi_1-\xi_1^0|]^{1/2} \tag{35}$$

where ξ_i^0, $i=1, 2$ denote the location of the heat source. The temperature distribution and its derivatives in the heat-affected zone with $90<\theta<180$ deg can be obtained in the same fashion as that in the previous cases. The results are

$$T/(Q/\rho\alpha C_p) = [1/(8\pi c)^{1/2}]\exp(c\xi_2^2/2\xi_1) [1/(-\xi_1)^{1/2} + (c\xi_2^2+\xi_1)/4c(-\xi_1)^{5/2}] \tag{36}$$

$$T_{,1}/(Q/\rho\alpha C_p) = [1/(8\pi c)^{1/2}]\exp(c\xi_2^2/2\xi_1) [1/8c(-\xi_1)^{7/2}]\{c(4\xi_1^2+5\xi_2^2)+3\xi_1 + (c\xi_2^2/\xi_1)[c(4\xi_1^2+\xi_2^2)+\xi_1]\} \tag{37}$$

$$T_{,2}/(Q/\rho\alpha C_p) = [-1/(8\pi c)^{1/2}]\exp(c\xi_2^2/2\xi_1) [\xi_2/4(-\xi_1)^{7/2}][c(4\xi_1^2+\xi_2^2)+3\xi_1]$$

Qualitative Assessment of the Possible Failure Site

The location of crack initiation around the moving heat source is an interesting phenomenon to be studied. As a first-order approximation that neglects the Poisson effect from the radial direction, such a location can be found from the location on the circumference of a continuum circle centered at the point heat source where the temperature gradient $T_{,\theta}$ reaches the maximum value. The radius of this circle depends on the scale of observation for the failure initiation. It should be, however, sufficiently large such that the continuum formulation for the hyperbolic wave model is valid. The material continuum at such a location experiences the largest volume change due to thermal expansion, and consequently, the stress component σ_θ also reaches the maximum. According to the maximum stress criterion in fracture mechanics, as clearly discussed by Tzou and Sih (1985b) for example, a macroscopic crack tends to be initiated at such a location and propagated along the radial direction perpendicular to that of σ_θ.

Numerical Results

The temperature distribution in the neighborhood of the moving heat source is presented graphically for the thermal Mach number in the subsonic, transonic, and supersonic ranges. The radius of the continuum circle centered at the heat source is taken to be 10^{-4} m. This threshold value is the lower bound of continuum mechanics beyond which the microscopic lattice structure of the medium can be neglected in the formulation. The thermal material properties are assumed to be

$$\rho = 2.72\times10^3 \text{ kg/m}^3, \quad k = 220 \text{ W/m-K}, \quad C_p = 0.895 \text{ kJ/kg-K} \tag{38}$$

and the speed of heat propagation C in the solid is taken as 20 m/s. Under the present formulation, it should be noticed from equations (20), (28), and (36) that the parametric value of C is absorbed in the thermal Mach number M in the temperature distributions. It only serves as a reference value for estimating the relative speed of the moving heat source in the parameter c.

Figure 2 shows the temperature distribution represented by equation (20) for the subsonic case ($M<1$). In comparing the curves with different values of M, we observe that the temperature level decreases as the values of M increases. This means, as either the speed of the moving heat source is high, or the speed of heat propagation in the solid is low, the material continua in the vicinity of the heat source do not have sufficient time to build up the temperature before the source moves ahead. For a curve with a fixed value of M, we notice that the temperature increases slowly as θ is small. As the trailing edge of the heat source is approaching, it tends to increase with a much higher rate and for all the cases under consideration, the temperature reaches its maximum at $\theta = 180$ deg.

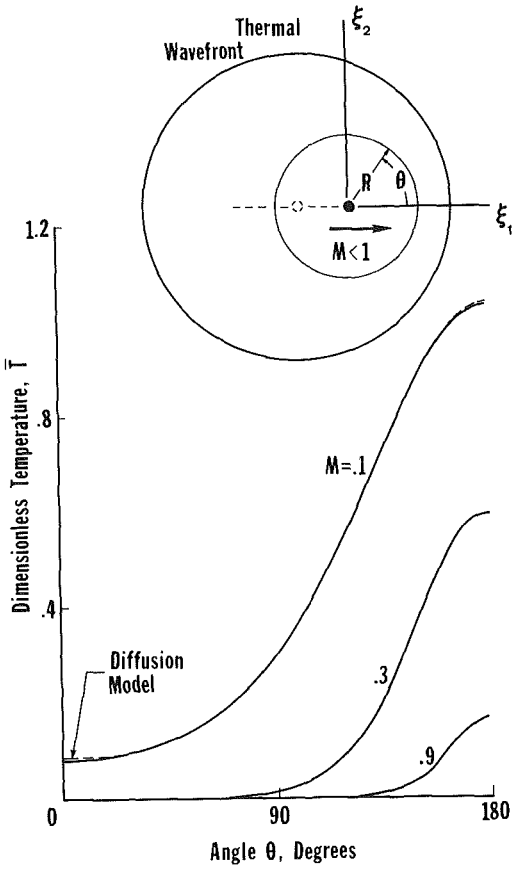

Fig. 2 Temperature distribution along the circumference of the continuum circle centered at the heat source: subsonic case, M<1; $\bar{T} = T/(Q/\rho\alpha C_p)$

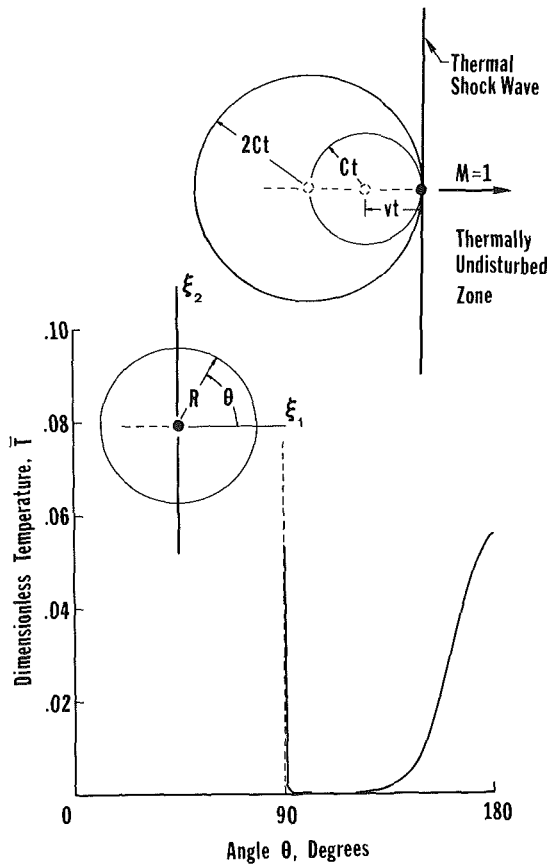

Fig. 3 Temperature distribution and shock formation at transonic stage, M = 1

Also, we notice that as the thermal Mach number approaches the transonic range, a thermally undisturbed zone is gradually formed. It is reflected by the presence of a domain of θ (for M = 0.3 and 0.9) within which only a minor temperature increase is observed. This domain increases as the value of M increases. In tribology with a high-speed friction load, the thermal Mach number can reach as high as 0.4 to 0.6 (Ju and Liu, 1987). According to the temperature distributions shown in Fig. 2, significant deviations between the results predicted by the thermal diffusion and the thermal wave models are observed for M in this range.

As M = 1, the temperature distribution represented by equation (36) is shown in Fig. 3. A normal shock is formed and attached to the heat source. The thermal field in the domain $0 < \theta < 90$ deg stays undisturbed as the heat sources moves ahead. We observe that except for the singularity existing at the thermal shock wave, the relative maximum of the temperature at $\theta = 180$ deg continuously decreases in comparison with those in the subsonic range. The temperature distribution represented by equation (28) for the supersonic case is displayed in Fig. 4. Distinct shock waves are formed at $\phi = 30$, 11.54, and 7.18 deg for M = 2, 5, and 8, respectively. The domain for the thermally undisturbed zone dramatically increases from 90 to 150 deg as the thermal Mach number increases from 1 to 2, but the rate of increasing gradually tapers off as the value of M further increases. By comparing the distributions at M = 2, 5, and 8, we also notice that the temperature level gradually builds up as the heat-affected zone becomes smaller. In summary, we have found a swinging phenomenon for the temperature field in the solid with finite speed of heat propagation. In the subsonic range with M < 1, the temperature level decreases as M increases. While entering

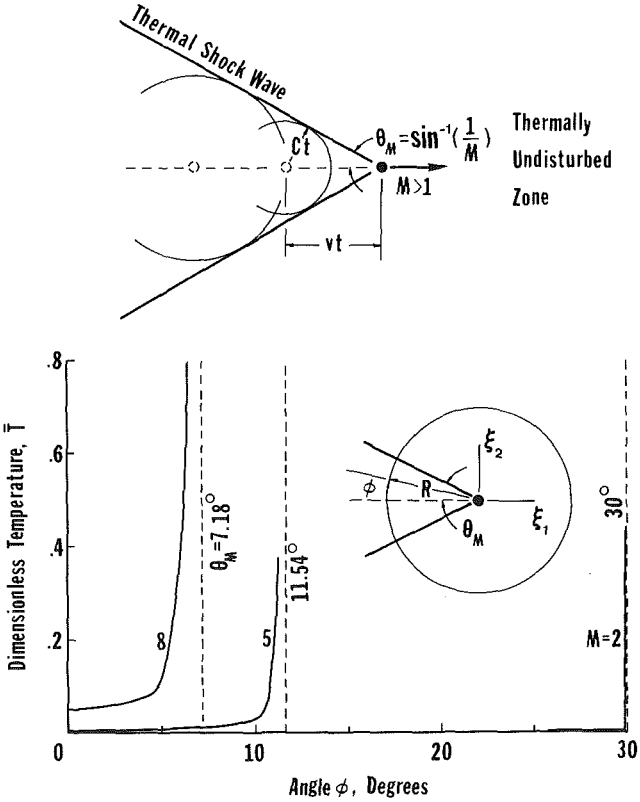

Fig. 4 Formation of the oblique thermal shock wave and temperature distribution in the heat-affected zone: supersonic case, M>1

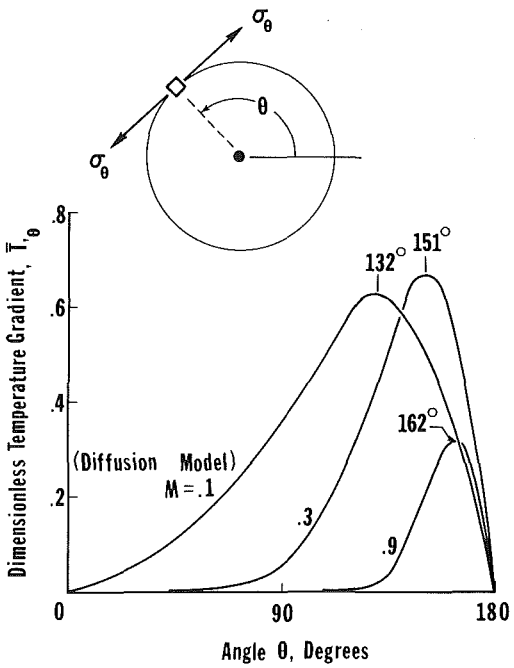

Fig. 5 Variations of temperature gradient $T_{,\theta}$ along the circle in the subsonic case, $M<1$; $\bar{T}_{,\theta} = T_{,\theta}/(Q/\rho\alpha C_p)$

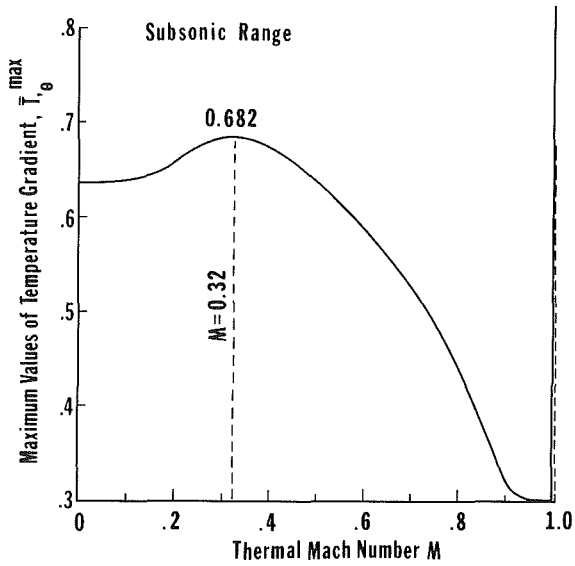

Fig. 6 Variation of $T_{,\theta}^{max}$ versus the thermal Mach number M in the subsonic range; $\bar{T}_{,\theta}^{max} = T_{,\theta}^{max}/(Q/\rho\alpha C_p)$

the supersonic range with $M>1$, the temperature level increases as M increases. Together with the phenomenon of shock formation, this is also a salient feature in the hyperbolic wave model of heat conduction.

Under the present quasi-stationary approach, the wave-dominance condition represented by equation (2) can be expressed in terms of the rate change of temperature versus the space variable ξ_1

$$|\psi_{,1}/\psi| >> 2c/M^2, \qquad \text{with } \psi = T_{,1} \tag{39}$$

Except for the case of thermal diffusion with $M=0$, the magnitude of $|\psi_{,1}/\psi|$ increases as the thermal Mach number increases and the dominance of the wave nature becomes more significant, as shown in Fig. 2. For the transonic and supersonic cases shown in Figs. 3 and 4, this phenomenon is even more pronounced due to the presence of the singularity existing at the location of the thermal shock wave.

Qualitative patterns of material failure are shown in Figs. 5 to 8. According to the chain rule, the temperature gradient $T_{,\theta}$ along the circumference of the continuum circle can be obtained as

$$T_{,\theta} = R[T_{,2}\cos(\theta) - T_{,1}\sin(\theta)] \tag{40}$$

with T being the temperature field in the subsonic, transonic, and supersonic cases, respectively. By substituting equations (22) and (23) into (39), the variation of $T_{,\theta}$ for $M<1$ is shown in Fig. 5. The location possessing a maximum value of $T_{,\theta}$ shifts toward the trailing edge of the heat source as the thermal Mach number increases. It is important to notice that the maximum value of $T_{,\theta}$ first increases from $M=0$ to 0.3, and then decreases as the transonic range is approached. Since $T_{,\theta}$ is a quantity that increases with the amount of thermal expansion of the continua, this phenomenon indicates the existence of a specific value of M in the subsonic range at which the volume expansion induced by the thermal field is maximum. Figure 6 shows this phenomenon more explicitly. At $M\simeq 0.32$, the maximum value of $T_{,\theta}^{max}/(Q/\rho\alpha C_p)$ is found to be 0.682 and occurs at $\theta \simeq 152$ deg. Figure 7 shows the corresponding variations of $T_{,\theta}$ with the values of M in the transonic and supersonic ranges. Notice that all the values of $T_{,\theta}$ are negative in these cases. As expected, the maximum value occurs in the

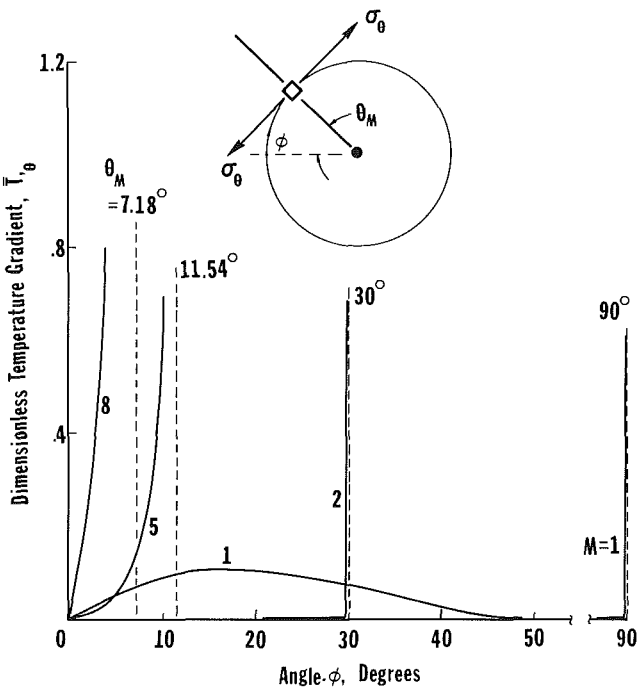

Fig. 7 Variations of temperature gradient $T_{,\theta}$ along the circle in the transonic and supersonic cases, $M\geq 1$

vicinity of the thermal shock wave in every case, and the fracture angle is obviously at $\theta = \pi - \theta_M$ for $M\geq 1$. Also, larger values of $T_{,\theta}$ developed at higher values of the thermal Mach number indicate the development of larger thermal strain in the narrower heat-affected zone. In this study, due to the absence of a general consideration given to the coupling between thermal and deformation fields, we do not intend to make a general conclusion about the sign change of $T_{,\theta}$ from the subsonic to the transonic and supersonic ranges. But it is obvious that the stress field is switched from tension to compression (or vice versa) as M is transmitted from the subsonic to the supersonic ranges. Again, this is another physical phenomenon peculiar to the wave model. Figure 8 shows the variation of failure angle versus the thermal Mach number estimated in this approximate fashion. A more detailed

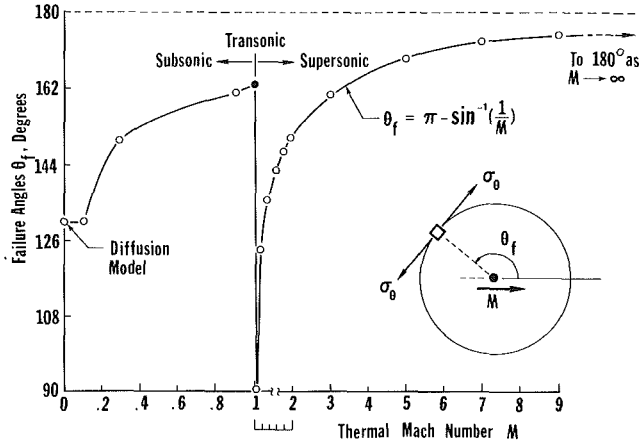

Fig. 8 The direction of failure initiation varies as a function of the thermal Mach number in the subsonic, transonic, and supersonic regimes; a qualitative assessment

analysis employing the thermoelastic/plastic approaches has been made by Tzou (1988a, 1988b). It shows that the fracture angle estimated in this analysis is still reliable on a qualitative basis, but material damage by softening should also be addressed in the vicinity of thermal shock waves due to large temperature gradients existing nearby.

Summary and Conclusions

Formation of the thermal shock wave is an interesting phenomenon in the hyperbolic theory of heat conduction. When the heat source moves at a speed equal to or faster than that of the heat propagation in the solid, a large amount of thermal energy accumulates in the neighborhood of the moving heat source. Such accumulated energy can not be efficiently transferred to the surrounding media before the heat source moves away. As a consequence, a large temperature gradient exists thereby, which results in significant deviations between the thermal diffusion and the thermal wave models. In this study, we have shown that as $M \geq 1$, the thermal shock wave develops in the physical domain that separates the heat-affected zone from the thermally undisturbed zone. The thermal shock angle is obtained as $\sin^{-1}(1/M)$ inclining to the trailing edge of the moving heat source. It is found that the temperature in the heat-affected zone strongly depends on the thermal Mach number and the deviation between the two models increases as the thermal Mach number increases. Besides, the swining phenomenon found for the temperature field in transition of the thermal Mach number from the subsonic to the supersonic range is also unique for the thermal wave model. Such a phenomenon cannot be depicted by the thermal diffusion model.

Characteristics of thermal waves in the vicinity of a moving crack tip have also been studied by the author (Tzou, 1988c). An analogy between the thermal shock angles, namely $\sin^{-1}(1/M)$, has been established for the two problems with different origin of moving sources. For the problem with a moving crack, the concept of thermal Mach number can be introduced as well, while the speed of the moving heat source is replaced by that of the crack propagation. The strength of the thermal shock in the vicinity of the crack tip is not as strong as that in the neighborhood of a moving heat source. Because temperature is bounded at the crack tip, only a finite but discontinuous change of temperature is observed across the surface of the shock wave.

Lastly, in the use of a hyperbolic theory of heat conduction, the regular equation governing the thermoelastic displacement potential Φ (Jakubowska, 1984, for example) is modified to the following form:

$$M^2\Phi_{,11} - 2c\Phi_{,1} = \epsilon\beta[\Phi_0(\xi_i) + T] \tag{41}$$

where ϵ is the coefficient of thermal expansion, β a function of the Poisson ratio, Φ_0 a function of ξ_i resulting from the apparent heat source, and T the corresponding temperature in the subsonic, transonic, and supersonic ranges. A modified term containing $\Phi_{,11}$ appears in the equation, which also takes the highest order of the differential operator. Dramatic changes in the characteristics of the solution for Φ (from the diffusion model with $M = 0$ in equation (41)), and hence for the thermal stress field are thus expected. Discussions on this topic will appear in the near future.

References

Arfken, G., 1970, *Mathematical Methods for Physicists*, Academic Press, New York, Chap. 16, p. 763.

Baumeister, K. J., and Hamill, T. D., 1969, "Hyperbolic Heat-Conduction Equation—A Solution for the Semi-infinite Body Problem," ASME JOURNAL OF HEAT TRANSFER, pp. 543-548.

Boley, B. A., 1964, "The Analysis of Problems of Heat Conduction and Melting," *High Temperature Structures and Materials*, Pergamon Press, New York, pp. 260-315.

Carslaw, H. S., and Jaeger, J. C., 1959, *Conduction of Heat in Solids*, Oxford University Press, Chap. X, pp. 255-257.

Chester, M., 1963, "Second Sound in Solids," *The Physical Review*, Vol. 131, pp. 2013-2015.

Frankel, J. I., Vick, B., and Ozisik, M. N., 1985, "Flux Formulation of Hyperbolic Heat Conduction," *Journal of Applied Physics*, Vol. 58, pp. 3340-3345.

Jakubowska, M., 1984, "Kirchhoff's Formula in Thermoelasticity With Finite Wave Speeds," *J. Thermal Stresses*, Vol. 7, pp. 259-283.

Ju, F. D., and Liu, J. C., 1987, "Effect of Peclet Number in Thermo-Mechanical Cracking Due to High-Speed Friction Load," ASME *Journal of Tribology*, Vol. 21, pp. 1-5.

Morse, P. M., and Feshbach, H., 1953, *Methods of Theoretical Physics*, Vol. 1, McGraw-Hill, New York, Chap. 7, pp. 865, 837-839.

Shapiro, A., 1954, *The Dynamics and Thermodynamics of Compressible Fluid Flow*, Vol. 1, The Ronald Press, New York, pp. 304-308.

Tzou, D. Y., 1985, "Intensification of Externally Applied Magnetic Field Around a Crack in Layered Composite," *Journal of Theoretical and Applied Fracture Mechanics*, Vol. 4, pp. 191-199.

Tzou, D. Y., and Sih, G. C., 1985, "Discussion on Critieria for Brittle Fracture in Biaxial Tension," *Journal of Engineering Fracture Mechanics*, Vol. 21, pp. 977-981.

Tzou, D. Y., 1988a, "Elastic Deformation Induced by Thermal Shock Waves," ASME *Journal of Applied Mechanics* (submitted for publication).

Tzou, D. Y., 1988b, "Material Damage by Softening in the Vicinity of a Thermal Shock Wave," ASME *Journal of Applied Mechanics* (to be published).

Tzou, D. Y., 1988c, "Thermal Shock Waves Induced by a Moving Crack," ASME JOURNAL OF HEAT TRANSFER, in press.

Weymann, H. D., 1967, "Finite Speed of Propagation in Heat Conduction, Diffusion, and Viscous Shear Motion," *American Journal of Physics*, Vol. 35, pp. 448-496.

L. W. Hunter
Chemist.

J. R. Kuttler
Mathematician.

The Johns Hopkins University,
Applied Physics Laboratory,
Laurel, MD 20707

The Enthalpy Method for Heat Conduction Problems With Moving Boundaries

The purpose of this paper is to demonstrate how an enthalpy method for heat conduction problems with moving boundaries associated with phase changes can be combined with Kirchhoff and coordinate transformations to put these problems in a particularly simple form. All nonlinearities in density, conductivity, and specific heat can be concentrated in the functional relation between enthalpy and the generalized temperature. Convection in the fluid is neglected. A simple numerical example is included.

Introduction

Moving boundary problems were studied as early as 1831 by Lamé and Clapeyron (1831). The sequence of papers written by Stefan (1889, 1891) has given his name to this type of problem. Because of applications as diverse as metal casting, petroleum exploration in the arctic, corrosion-resistant coatings, and preparation of frozen foods, there is a vast literature on the subject. The books by Luikov (1968) and Rubenstein (1971), the survey article by Bankhoff (1964), and the reviews by Muehlbauer and Sunderland (1965) and by Murray and Landis (1959), pretty well summarize the work done through the early 1960s. The conference proceedings (Ockendon and Hodgkins, 1975; Wilson et al., 1978) contain a number of interesting papers. More recent results are surveyed in Crank (1981), Furzeland (1980), Gladwell and Wait (1979), and Schulze et al. (1983). The book by Cannon (1984) has an extensive collection of references, and Shih (1982) is a list of recent literature.

The earliest paper to suggest using an enthalpy approach to avoid a nonlinearity in a heat conduction problem may be Eyres et al. (1946). The earliest use of a finite-difference method applied to an enthalpy formulation appears to be Rose (1960). A nice overview of enthalpy approaches is in the recent book by Crank (1984).

Despite this extensive literature, the compact formulation presented in equation (11) has apparently not explicitly appeared before.

The Enthalpy Equation

Consider a material that can occur in two or more phases. The material initially occupies the slab, $0 < x < a$, and its temperature T depends on time t and one space variable x. The enthalpy H per unit mass is the sum of the sensible heat and the internal (or chemical) heat. Within a phase

$$\frac{\partial H}{\partial T} = C \tag{1}$$

where C is the specific heat of the phase (which may depend on T). At a phase boundary, H has a jump discontinuity equal to the latent heat of the phase transition

$$[H] = L \tag{2}$$

where the bracket denotes the right-hand limit minus the left-hand limit at the jump.

Let $x_i = x_i(t)$, $i = 1, 2$, be the locations of two points fixed to the material. The basic relation that governs both the heat transfer and the phase-transition processes is

$$\frac{d}{dt}\int_{x_1(t)}^{x_2(t)} \rho\, H\, dx = k\frac{\partial T}{\partial x}\Bigg|_{x_1(t)}^{x_2(t)} \tag{3}$$

where ρ is the density and k is the thermal conductivity (both of which may also be variables depending on T).

It is easily shown (see, e.g., Shamsundar and Sparrow, 1976) that equation (3), along with conservation of mass, is equivalent to both the following: within a single phase

$$\rho C\left(\frac{\partial T}{\partial t} + v\frac{\partial T}{\partial x}\right) = \frac{\partial}{\partial x}\left(k\frac{\partial T}{\partial x}\right), \tag{4}$$

where v is the material velocity due to density changes; and, across a phase boundary at $x = S(t)$, the heat balance

$$\rho L\left(\frac{dS}{dt} - v\right) = -\left[k\frac{\partial T}{\partial x}\right] \tag{5}$$

In equation (5) ρ and v are the values either to the left or to the right of the interface. Either interpretation is valid because of the mass balance across S (see Hunter and Kuttler, 1987, for a more detailed discussion).

Transformations to Fundamental Equation

The enthalpy equation (3) can be transformed into a much simpler form. First, if the point $x = 0$ on the slab remains motionless throughout the process, then

$$\xi = \frac{1}{\rho_0}\int_0^x \rho(x', t)\,dx' \tag{6}$$

defines a new space coordinate fixed to the material (Hunter, 1981; Hunter and Kuttler, 1983). Here ρ_0 is some convenient reference density (such as the density at a time when the entire slab is at a uniform temperature, so laboratory and material coordinates will coincide at that time). In this new coordinate equation (3) becomes

$$\frac{d}{dt}\int_{\xi_1}^{\xi_2} \rho_0 H\, d\xi = \frac{k\rho}{\rho_0}\frac{\partial T}{\partial \xi}\Bigg|_{\xi_1}^{\xi_2} \tag{7}$$

In the ξ coordinate, the length of the slab remains fixed at the length b, where

$$b = \frac{1}{\rho_0}\int_0^a \rho\, dx'$$

Next, make the Kirchhoff transformation (Kirchhoff, 1894)

$$\theta = \frac{1}{\rho_0 k_0}\int_{T_c}^{T} \rho\, k\, dT' \tag{8}$$

where k_0 is a reference conductivity and T_c is the critical temperature at which the phase transition occurs. Now equation (7) becomes

Contributed by the Heat Transfer Division for publication in the JOURNAL OF HEAT TRANSFER. Manuscript received by the Heat Transfer Division June 5, 1987. Keywords: Conduction, Phase-Charge Phenomena.

$$\rho_0 \frac{d}{d\tau} \int_{\xi_1}^{\xi_2} H \, d\xi = k_0 \frac{\partial \theta}{\partial \xi} \Bigg|_{\xi_1}^{\xi_2} \tag{9}$$

Finally, the time coordinate can be scaled by defining

$$\tau = k_0 t / \rho_0 \tag{10}$$

Then the fundamental equation has the elegant form

$$\frac{d}{d\tau} \int_{\xi_1}^{\xi_2} H \, d\xi = \frac{\partial \theta}{\partial \xi} \Bigg|_{\xi_1}^{\xi_2} \tag{11}$$

which is solved with appropriate initial and boundary conditions (which are now imposed on fixed boundaries).

After solving for θ in the coordinates ξ and τ, the temperature T can be expressed in lab-fixed coordinates x and real time t by inverting equations (6), (8), and (10). Because ρ and k are strictly positive, the relations in equation (6) connecting x and ξ, and equation (8) connecting T and θ, are strictly monotone, and so have inverses that may be expressed as

$$x = \rho_0 \int_0^{\xi} \frac{d\xi'}{\rho(\xi', t)} \tag{12}$$

$$T = T_c + \rho_0 k_0 \int_0^{\theta} \frac{d\theta'}{\rho(\theta') k(\theta')} \tag{13}$$

(When ρ, k are piecewise constants as in the example below, these relations are explicit piecewise linear functions.)

Temperature Versus Enthalpy

All of the nonlinearities of the moving boundary problem have been combined into the explicitly known relation between the enthalpy H and the generalized temperature θ, as shown in Fig. 1(*a*). H has a jump discontinuity equal to the latent heat of fusion L at the critical temperature, which corresponds to $\theta = 0$. However, if the axes of the graph are rotated as in Fig. 1(*b*), the simple but very important observation is made that θ is a well-defined, continuous function of H (Elliot and Ockendon, 1982).

Numerical Example

A very simple example with ice and water will be presented, mainly to show the effect of the density change, and how it is treated very naturally by the above formulation. The motion of the material due to the change in density might be the phenomenon of most interest to, say, a petroleum engineer concerned with frost heave of his pipeline in the Arctic (Hayes and Diller, 1983).

The case of a semi-infinite slab with a fixed temperature specified at the boundary has an exact solution, given in Carslaw and Jaeger (1959), from which the values of the physical parameters are taken. Here a finite slab will be considered with forced convection at one boundary. A similar problem in two dimensions was treated by Shamsundar and Sparrow (1976), with the restriction that initially the material was uniformly at the transition temperature T_c. So here the initial temperature will be assumed to be different from T_c.

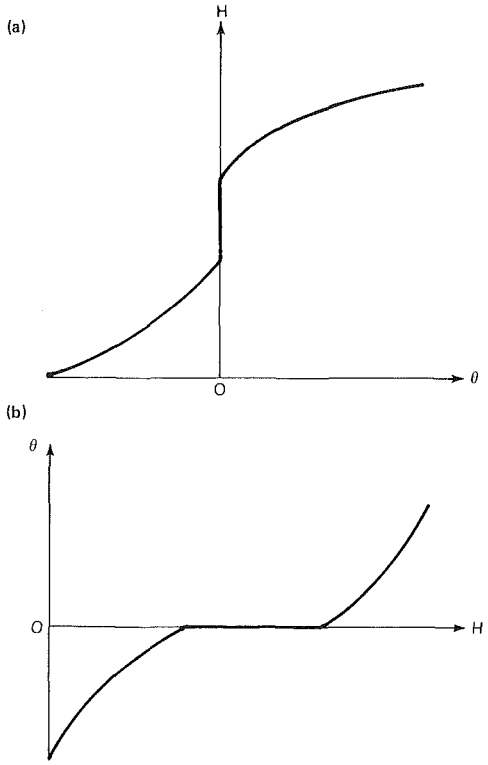

Fig. 1 The relation between enthalpy H and generalized temperature θ

Thus, let the system be initially all water, occupying $0 < x < a$, and at a constant temperature 50 K above freezing ($T_c = 273.15$ K). Heat is withdrawn by forced convection

$$k \frac{\partial T}{\partial x} = h(T - T_f) \text{ at } x = 0 \tag{14}$$

where the parameter h is the convective heat transfer coefficient, and the driving temperature T_f is taken to be 50 K below freezing. The other face is insulated, so $\partial T/\partial x = 0$ there, but its position moves in laboratory coordinates. The density, specific heat, and conductivity can be assumed to be step functions, constant within each phase, so for ice and water, respectively, let

$$\rho_I = 917 \text{ kg/m}^3, \quad C_I = 2.10 \text{ kJ/kg-K}, \quad k_I = 2.22 \text{ W/m-K}$$
$$\rho_W = 1000 \text{ kg/m}^3, \quad C_W = 4.18 \text{ kJ/kg-K}, \quad k_W = 0.602 \text{ W/m-K}$$

In equation (6) let the reference density ρ_0 be ρ_I so the fixed length b of the slab in ξ coordinates corresponds to the final length when all the material is frozen and

$$0.917\, b = a$$

The reference conductivity of k_0 will be taken to be k_I and the latent heat is given by $L = 336$ kJ/kg. The enthalpy H can be defined by

Nomenclature

a = initial thickness of slab
b = mass-weighted thickness of slab
B^* = Biot number = hb/k_I
C = specific heat
h = convective heat transfer coefficient
H = enthalpy per unit mass
H^* = defined in equation (16)
k = thermal conductivity
L = latent heat
t = time
T = temperature
v = material velocity
x = lab-fixed space coordinate
$\Delta\xi$ = increment in ξ^*
$\Delta\tau$ = increment in τ^*
θ^* = defined in equation (16)
θ_f^* = $C_I(T_f - T_c)/L$
ξ = body-fixed space coordinate
ξ^* = defined in equation (16)
ρ = density
τ^* = defined in equation (16)

Subscripts

0 = reference state
c = critical, phase transition
f = fixed ($x = 0$)
I = ice
W = water

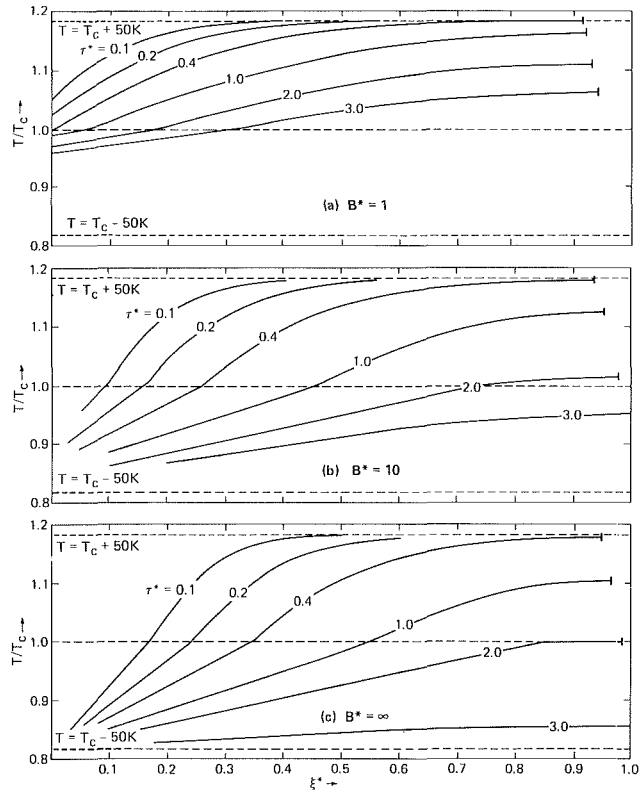

Fig. 2 Temperature profiles in ice-water system at various times

$$H = \begin{cases} C_I(T - T_c), & T < T_c \\ C_W(T - T_c) + L, & T > T_c \end{cases} \tag{15}$$

After the transformations in equations (6), (8), and (10), the problem can be nondimensionalized by the normalizations

$$\xi^* = \xi/b, \quad H^* = H/L, \quad \theta^* = C_I\theta/L, \quad \tau^* = \tau/b^2C_I \tag{16}$$

Then the completely dimensionless equations become

$$\frac{d}{d\tau^*}\int_{\xi_1^*}^{\xi_2^*} H^* d\xi^* = \frac{\partial\theta}{\partial\theta^*}\Big|_{\xi_1^*}^{\xi_2^*}, \quad 0 < \xi_1^* < \xi_2^* < 1 \tag{17}$$

$$\frac{\partial\theta^*}{\partial\xi^*} = \begin{cases} B^*(\theta - \theta_f^*) & \text{at } \xi = 0 \\ 0 & \text{at } \xi = 1 \end{cases} \tag{18}$$

$$H^* = H^* \quad \text{at } \tau^* = 0, \tag{19}$$

along with the nonlinear relation

$$\theta^* = \begin{cases} H^*, & H^* \le 0 \\ 0 & 0 \le H^* \le 1 \\ \dfrac{C_I k_W \rho_W}{C_W k_I \rho_I}(H^* - 1), & 1 \le H^* \end{cases} \tag{20}$$

In the above, B^* is the dimensionless Biot number defined by $B^* = hb/k_I$, and $\theta_f^* = C_I(T_f - T_c)/L$.

Equations (17)–(19) were solved by a Crank–Nicolson type finite-difference scheme (Crank and Nicolson, 1947; Forsythe and Wasow, 1960). If the space increment $\Delta\xi = 1/N$, N is an integer, and $\Delta\tau$ is a time increment, let

$$H_{i,j} = (\Delta\xi)^{-1}\int_{(i-1)\Delta\xi}^{i\Delta\xi} H^*(\xi, j\Delta\tau)d\xi,$$

$$\theta_{i,j} = \theta^*((i - 1/2)\Delta\xi, j\Delta\tau) \tag{21}$$

Then equation (17) is approximated by

$$H_{i,j+1} - H_{i,j} = (\theta_{i+1,j+1} - 2\theta_{i,j+1} + \theta_{i-1,j+1} + \theta_{i+1,j} - 2\theta_{i,j} + \theta_{i-1,j})/(2\Delta\xi^2\Delta\tau) \tag{22}$$

along with analogs of the boundary and initial conditions (18) and (19). This is an implicit scheme because $\theta_{i,j+1}$ depends on $H_{i,j+1}$, so equation (20) is used in the form

$$\theta_{i,j+1} = A_{i,j+1}H_{i,j+1} + B_{i,j+1} \tag{23}$$

When this is used in equation (22) a tridiagonal system of equations results, which is easily solved at each time step using standard software packages (Dongarra et al., 1979) in a number of operations proportional only to N. However, it must be iterated a few times to establish the values of $A_{i,j+1}$, $B_{i,j+1}$, which also depend on $H_{i,j+1}$. Explicit front-tracking is avoided; the location of the front is implicit in the value of H. Complete details of the numerical procedure may be found in Hunter and Kuttler (1987).

Numerical results are shown in Fig. 2 for various values of the dimensionless Biot number B^*. When the Biot number is very large, Fig. 2(*c*), the cooled face of the slab quickly drops to the driving temperature, $\theta^* = \theta_f^*$. For times $\tau^* \le 0.4$, the temperature profiles agree with the analytic formulas for semi-infinite slabs (Carslaw and Jaeger, 1959) within 0.5 percent for step sizes $\Delta\xi = 0.01$ and $\Delta\tau = 0.01$.

With a finite Biot number, Figs. 2(*a*) and 2(*b*), there is an initial delay until freezing begins. The temperature of the cooled face drops quickly to the freezing point $\theta^* = 1$, but its subsequent drop toward $\theta^* = \theta_f^*$ is much slower. The temperature distribution in the ice phase is approximately linear from the cooled face to the moving freeze front.

The quantity θ_f^* in equation (18) is essentially the Stefan number. If this quantity were smaller in magnitude, the slab would take longer to freeze completely.

Concluding Remarks

A unified approach to moving boundary value problems has been presented, incorporating enthalpy, Kirchhoff, and coordinate transformations. The resulting equation (11) has a particularly simple form. All of the many nonlinearities possible in such problems are concentrated in the relation between generalized temperature and enthalpy (Fig. 1*b*). Here a simple finite-difference scheme was exhibited for a simple problem, but the virtue of this formulation is its suitability for various numerical approaches and for a wide variety of problems.

The formulation applies to materials with more than two phases, or, since there is no front-tracking, to cases of multiple phase fronts, as in the interesting paper by Schneider and Row (1984), which also uses an enthalpy approach. It can also be adapted to single-phase, ablation-type problems, which will be the subject of a future paper.

The formulation can also be extended to two or more space dimensions. However, the analog of the density transformation (6) would only make sense for special problems, e.g., where the phases are a liquid and a gas, or where the solid phase is convex and remains so, as in the problem treated in Shamsundar and Sparrow (1976). Otherwise stresses generated by thermally dependent density may fracture the solid, as when an ice cube is dropped into a glass of water. Higher dimensional problems will also be a topic for future investigations.

References

Bankhoff, S. G., 1964, "Heat Conduction or Diffusion With Change of

Phase," *Advances in Chemical Engineering*, Vol. 5, T. B. Drew, J. W. Hoopes, Jr., and T. Vermeulen, eds., Academic Press, New York, pp. 75–150.

Cannon, J. R., 1984, "The One-Dimensional Heat Equation," *Encyclopedia of Mathematics and Its Applications*, Vol. 23, Addison-Wesley, Menlo Park, CA.

Carslaw, H. S., and Jaeger, J. C., 1959, *Conduction of Heat in Solids*, 2nd ed., Oxford.

Crank, J., 1981, "How to Deal With Moving Boundaries in Thermal Problems," *Numerical Methods in Heat Transfer*, L. W. Lewis, K. Morgan, and O. C. Zienkiewicz, eds., Wiley, New York, pp. 177–200.

Crank, J., 1984, *Free and Moving Boundary Value Problems*, Clarendon Press, Oxford, Chap. 6.

Crank, J., and Nicolson, P., 1947, "A Practical Method for Numerical Evaluation of Solutions of Partial Differential Equations of the Heat Conduction Type," *Proc. Cambridge Philos. Soc.*, Vol. 43, pp. 50–67.

Dongarra, J. J., Bunch, J. R., Moler, C. B., and Stewart, G. W., 1979, *Linpack User's Guide*, SIAM, Philadelphia.

Elliott, C. M., and Ockendon, J. R., 1982, *Weak and Variational Methods for Moving Boundary Problems*, Pitman, London.

Eyres, N. R., Hartree, D. R., Ingham, J., Jackson, R., Sarjant, R. J., and Wagstaff, J. B., 1946, "The Calculation of Variable Heat Flow in Solids," *Phil. Trans. Royal Soc.*, Vol. A240, pp. 1–57.

Forsythe, G. E., and Wasow, W. R., 1960, *Finite-Difference Methods for Partial Differential Equations*, Wiley, New York, Chap. 2.

Furzeland, R. M., 1980, "A Comparative Study of Numerical Methods for Moving Boundary Problems," *J. Inst. Math. Appl.*, Vol. 26, pp. 411–429.

Gladwell, I., and Wait, R., 1979, *A Survey of Numerical Methods for Partial Differential Equations*, Clarendon Press, Oxford, Chap. 20.

Hayes, L. J., and Diller, K. R., 1983, "Implementation of Phase Change in Numerical Models of Heat Transfer," ASME *Journal of Energy Resources Technology*, Vol. 105, pp. 431–435.

Hunter, L. W., 1981, "Transient Thermal Expansion of Solids During Inert Heating Phase Change and Gasification," ASME JOURNAL OF HEAT TRANSFER, Vol. 103, pp. 601–602.

Hunter, L. W., and Kuttler, J. R., 1983, "Cooling of a Slab With Thermal Contraction and Progressive Loss of Contact With a Cold Surface," ASME JOURNAL OF HEAT TRANSFER, Vol. 105, pp. 936–938.

Hunter, L. W., and Kuttler, J. R., 1987, "The Enthalpy Method for Moving Boundary Problems," The Johns Hopkins University Applied Physics Laboratory, Memo BBP 87-47, Feb. 19.

Kirchhoff, G., 1894, *Vorlesungen uber die theorie der Warme*, Barth, Leipzig.

Lamé, G., and Clapeyron, B. P. E., 1831, "Memoire sur la Solidification par Refroidissment d'un Globe Solid," *Ann. Chem. Phys.*, Vol. 47, pp. 250–256.

Luikov, A. V., 1968, *Analytical Heat Diffusion Theory*, Academic Press, New York, Chap. II.

Muehlbauer, J. C., and Sunderland, J. E., 1965, "Heat Conduction With Freezing or Melting," *Applied Mech. Rev.*, Vol. 18, pp. 951–959.

Murray, W. D., and Landis, F., 1959, "Numerical and Machine Solutions of Transient Heat-Conduction Problems Involving Melting or Freezing. Part I—Method of Analysis and Sample Solutions," ASME JOURNAL OF HEAT TRANSFER, Vol. 81, pp. 106–112.

Ockendon, J. R., and Hodgkins, W. R., eds., 1975, *Moving Boundary Problems in Heat Flow and Diffusion*, Clarendon Press, Oxford.

Rose, M. E., 1960, "A Method for Calculating Solutions of Parabolic Equations With a Free Boundary," *Math. Comput.*, Vol. 14, pp. 249–256.

Rubenstein, L. I., 1971, *The Stefan Problem*, American Mathematical Society, Providence, RI.

Schneider, G. E., and Raw, M. J., 1984, "An Implicit Solution Procedure for Finite Difference Modeling of the Stefan Problem," *AIAA J.*, Vol. 22, pp. 1685–1690.

Schulze, H. J., Beckett, P. M., Howarth, J. A., and Poots, G., 1983, "Analytical and Numerical Solutions to Two-Dimensional Moving Interface Problems With Applications to the Solidification of Killed Steel Ingots," *Proc. Royal Soc. London*, Vol. A385, pp. 313–343.

Shamsundar, N., and Sparrow, E. M., 1976, "Effects of Density Change on Multidimensional Conduction Phase Change," ASME JOURNAL OF HEAT TRANSFER, Vol. 98, pp. 550–557.

Shih, T. M., 1982, "A Literature Survey on Numerical Heat Transfer," *Numerical Heat Transfer*, Vol. 5, pp. 369–420.

Stefan, J., 1889, *S. B. Wien Akad. Mat. Natur*, Vol. 98, pp. 173–184; 616–634; 965–983, 1418–1442.

Stefan, J., 1891, "Uber die Theorie der Eisbildung, inbesondere uber die Eisbildung im Polarmeer," *Ann. Phys. Chem.*, Vol. 42, pp. 269–286.

Wilson, D. G., Solomon, A. D., and Boggs, P. T., eds., 1978, *Moving Boundary Problems*, Academic Press, New York.

Calculated Temperature and Stress Distribution in the Edge Cladding of a Pulsed-Laser Slab

Y. J. Lee

H. L. Julien

Kaiser Engineers, Inc.,
P.O. Box 23210,
Oakland, CA 94623

The efficiency of solid-state laser amplifiers can be improved significantly by using an absorbing edge cladding on the laser slab to reduce parasitic light oscillation within the slab. An analytic solution for the conduction and thermal stress problem in a simply supported cladding has been developed for a periodic incident-light energy source in order to evaluate the influence of amplifier design variables on cladding stress. An approximate relationship between pulse frequency and the absorptivity corresponding to a minimum difference in thermally induced stresses is shown to be in agreement with this solution.

Introduction

Parasitic light oscillations in a slab laser amplifier can be reduced by adding an absorbing cladding to the edge of the slab (Trenholme, 1972; Glaze et al., 1974). However, the energy absorbed is significant and, in a pulsed laser slab, the imposed cyclic thermal stresses in the cladding may exceed material limits. Accordingly, the development of an efficient high-average-power laser system includes the design and performance assessment of this edge cladding system.

Figure 1 is a sketch of an edge cladding system currently in use on slab laser amplifiers that are being developed at the Lawrence Livermore National Laboratory, LLNL (Emmett et al., 1984). The cladding is fastened to a water-cooled housing and is both thermally and mechanically isolated from the slab by a transparent elastomer support. An adjustment in the temperature level of the coolant water can easily keep the elastomer and cladding temperature levels below material limits. The design of the system consists of matching the indices of refraction for the slab and elastomer to achieve optimal optical performance, and specifying the requisite thickness and material properties of the cladding to keep cladding stress below the ultimate stress level. The cladding is anticipated to be thin, and for practical purposes it is simply supported in this system; consequently, it is amenable to analysis with a one-dimensional thermal stress model, and the cladding thickness and material characteristics can be selected on the basis of parametric studies performed with such a model.

Extensive studies of periodic heat conduction problems have been reported, with the most recent and complete being those of Arpaci (1966), Wang et al. (1961), and Luikov (1968). Arpaci (1966) and Wang et al. (1961) considered both sinusoidal cyclic temperature boundary conditions and sinusoidal cyclic heat generation in an adjacent convective boundary layer. Luikov (1968) summarizes transient heat conduction problems, including cyclic internal heat generation. However, the results of these and past studies could not be applied to a heat conduction problem with an arbitrary cyclic heat generation function, such as that found in an absorbing edge cladding, and a more direct solution had to be developed.

This paper describes the model, the attending generalized analytic solution of the one-dimensional cyclic heat transfer equation, and the evaluation of the stress induced by the temperature fluctuations. One of the optimal design conditions, where the difference in thermally induced stress becomes minimal, is shown to be well represented by an approximate relationship when compared with this solution.

Contributed by the Heat Transfer Division for publication in the JOURNAL OF HEAT TRANSFER. Manuscript received by the Heat Transfer Division February 27, 1987. Keywords: Conduction, Laser Processing.

Model and Generalized Solution

Heat Transfer. High-average-power laser systems are generally operated at a well-controlled constant pulse frequency; after a large number of pulses, the cladding system reaches a cyclic quasi-steady thermal condition where light energy is absorbed by the cladding during the pumping pulse and an equal amount of energy is conducted to the surroundings between pulses. The attained temperature variation in the cladding can be evaluated by solving the cyclic thermal diffusion problem for the cladding.

The governing one-dimensional equation for the temperature $T(x, t)$ in the cladding is

$$\frac{\partial T}{\partial t} = \alpha \frac{\partial^2 T}{\partial x^2} + \frac{g(x, t)}{\rho c_p} \tag{1}$$

where g is the heat generation rate due to light absorption. This generation rate is cyclic in time and spatially dependent on the absorption characteristics of the cladding. The applicable cyclic boundary conditions are

$$\frac{\partial T(x, t)}{\partial x} = A(t) \qquad \text{at } x = 0$$

and

$$T(x, t) = B(t) \qquad \text{at } x = L \tag{2}$$

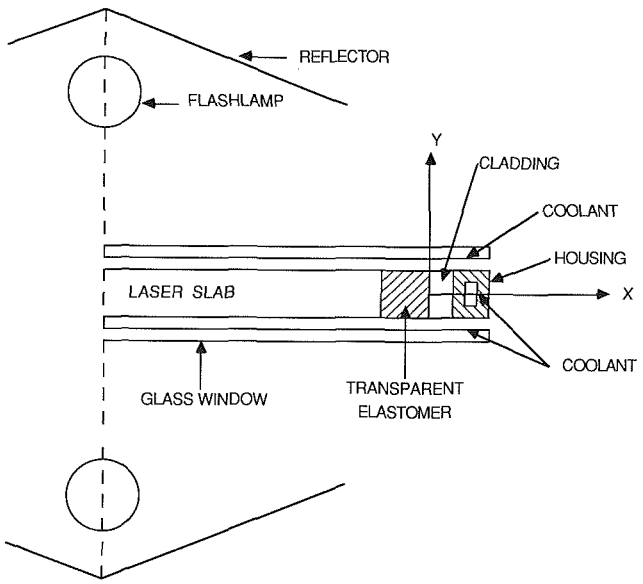

Fig. 1 Edge cladding system in laser amplifier

Here, L is the thickness of cladding, and the terms $A(t)$ and $B(t)$ are periodic functions of time that are dependent on the thermal diffusion characteristics of the adjacent elastomer and housing, respectively. Since the temperature variation is periodic, a cyclic condition also applies, i.e.,

$$T(x, 0) = T(x, t_I) \tag{3}$$

Equations (1), (2), and (3) represent a complete mathematical statement of the general inhomogeneous problem.

This problem can be transformed to one with homogeneous boundary conditions (Berg and McGregor, 1966) by introducing the function $u(x, t)$, where

$$u(x, t) = T(x, t) - B(t) + (L - x)A(t) \tag{4}$$

Substituting equation (4) into equations (1), (2), and (3), the problem statement obtained is

$$\frac{\partial u}{\partial t} = \alpha \frac{\partial^2 u}{\partial x^2} + \frac{g(x, t)}{\rho c_p} + (L-x)\frac{dA}{dt} - \frac{dB}{dt} \tag{5}$$

$$\frac{\partial u}{\partial x} = 0 \qquad \text{at } x = 0$$

$$u = 0 \qquad \text{at } x = L \tag{6}$$

and

$$u(x, 0) = u(x, t_I) \tag{7}$$

For this transformation to be valid, the functions $A(t)$ and $B(t)$ must be differentiable between pulses ($0 \le t \le t_I$); this is necessarily true because temperatures must always change at a finite rate.

The general solution (Berg and McGregor, 1966) of equations (5), (6), and (7) is

$$u(x, t) = \sum_{n=0}^{\infty} \left[C_n e^{-\lambda_n \alpha t} + \int_0^t e^{-\lambda_n \alpha (t-\tau)} P_n(\tau) d\tau \right] \cos \sqrt{\lambda_n}\, x \tag{8}$$

where the eigenvalues λ_n are

$$\lambda_n = \left(n + \frac{1}{2}\right)^2 \left(\frac{\pi}{L}\right)^2 \qquad n = 0, 1, 2, \ldots \tag{9}$$

The function $C_n(t)$ is determined from the cyclic condition, equation (7), and the function $P_n(t)$ is defined as follows:

$$P_n(t) = \frac{2}{L} \int_0^L \left[\frac{g(x, t)}{\rho c_p} - xA' + LA' - B' \right] \cos \sqrt{\lambda_n}\, x\, dx \tag{10}$$

where A' and B' refer to the first derivatives of the functions $A(t)$ and $B(t)$. A more specific form of solution can be attained by considering the characteristics of the energy source function $g(x, t)$.

Energy is delivered to the cladding only during the pulse, and for this study the incident light intensity is assumed to be constant over the pulse as an approximation. The source function then becomes

$$g(x, t) = \begin{cases} G(x) & \text{for } 0 < t \le t_p \\ 0 & \text{for } t_p < t \le t_I \end{cases} \tag{11}$$

where t_p is pulse interval. Adopting this form for the source function in equation (10) and evaluating the integral on the right-hand side, equation (10) can be written

$$P_n(t) = F_n(t) + \frac{2}{L\sqrt{\lambda_n}} \left[\frac{A'}{\sqrt{\lambda_n}} + (-1)^{n+1} B' \right] \tag{12}$$

where

$$F_n(t) = \begin{cases} \dfrac{2}{L} \displaystyle\int_0^L \frac{G(x)}{\rho c_p} \cos \sqrt{\lambda_n}\, x dx & \text{for } 0 < t \le t_p \\ 0 & \text{for } t_p < t \le t_I \end{cases} \tag{13}$$

Then, the solution given by equation (8) can be written

$$u(x, t) = \sum_{n=0}^{\infty} \left[C_n + I_F(t) + \frac{2}{L\lambda_n} I_A(t) + \frac{2(-1)^{n+1}}{L\sqrt{\lambda_n}} I_B(t) \right] e^{-\lambda_n \alpha t} \cos \sqrt{\lambda_n}\, x \tag{14}$$

where the operators I_F, I_A, and I_B are defined by

Nomenclature

$A(t), B(t)$ = functions defined by boundary condition, equation (2)
$C_n(t)$ = coefficient in solution defined on the basis of cyclic condition, equation (3)
c_p = specific heat of cladding
E_0 = intensity of incident light at the cladding/elastomer interface
E = Young's modulus for cladding material
f = pulse frequency
$F_n(t)$ = coefficient defined by equation (23)
I_F, I_A, I_B = integral operators defined by equations (15), (16), and (17)
L = thickness of cladding
$P_n(t)$ = coefficient in eigenvalue solution defined by equation (10)
$g(x, t)$ = internal heat generation per unit volume in cladding
$G(x)$ = assumed function for $g(x, t)$ during pulse, given by equation (22)
$T(x, t)$ = temperature
t = time
$u(x, t)$ = transformation variable defined by equation (4)
x = distance from elastomer/cladding interface, Fig. 1
y, z = Cartesian coordinates, orthogonal to x coordinate
α = thermal diffusivity of cladding material
α_a = absorptivity of cladding material
α_T = coefficient of thermal expansion for cladding material
λ_n = eigenvalue defined by equation (9)
ν = Poisson's ratio for cladding material
ρ = density of cladding material
σ = stress in cladding material

Subscripts

1, 2 = refers to conditions in laser amplifier
I = refers to period between pulses
n = refers to nth number of eigenvalue
p = refers to length of flashlamp pulse
u = refers to ultimate level

$$I_F(t) = \int_0^t e^{\lambda_n \alpha \tau} F_n(\tau) d\tau \tag{15}$$

$$I_A(t) = \int_0^t e^{\lambda_n \alpha \tau} A'(\tau) d\tau \tag{16}$$

and

$$I_B(t) = \int_0^t e^{\lambda_n \alpha \tau} B'(\tau) d\tau \tag{17}$$

Also, by imposing the cyclic conditions with equation (14), the definitive equation for the coefficient C_n is obtained; here,

$$C_n = \frac{I_F(t_p) + \dfrac{2}{L\sqrt{\lambda_n}} I_A(t_I) + \dfrac{2(-1)^{n+1}}{L\sqrt{\lambda_n}} I_B(t_I)}{e^{\lambda_n \alpha \tau_I} - 1} \tag{18}$$

Finally, substituting equation (14) into equation (4) for $u(x, t)$, the general solution obtained for the cladding temperature is

$$T(x, t) = \sum_{n=0} \left[C_n + I_F(t) + \frac{2}{L\sqrt{\lambda_n}} I_A(t) + \frac{2(-1)^{n+1}}{L\sqrt{\lambda_n}} I_B(t) \right] e^{\lambda_n \alpha t} \cos\sqrt{\lambda_n}\, x - (L - x)A(t) + B(t) \tag{19}$$

In the currently reported work, only the homogeneous case was considered; that is, $A(t) = 0$ and $B(t) = 0$. This case, however, closely approximates the physical condition of the cladding in the high-average-power lasers of current interest. Here, the cladding is isolated from the slab by an elastomer, with a very low thermal conductivity that can be modeled as an insulated surface; and it is cooled on the opposite side through a metal housing, with a high conductivity that can be modeled as an isothermal surface. For this restricted case equation (13) reduces to

$$T(x, t) = \sum_{n=0}^{\infty} [C_n + I_F(t)] e^{-\lambda_n \alpha \tau} \cos\sqrt{\lambda_n}\, x \tag{20}$$

with

$$C_n = \frac{I_F(t_p)}{e^{\lambda_n \alpha t_I} - 1} \tag{21}$$

and the integral I_F becomes

$$I_F(t) = \begin{cases} \dfrac{F_n}{\lambda_n \alpha} [e^{\lambda_n \alpha t} - 1] & \text{for } 0 < t \le t_p \\ \dfrac{F_n}{\lambda_n \alpha} [e^{\lambda_n \alpha t_p} - 1] & \text{for } t_p < t \le t_I \end{cases} \tag{24}$$

The corresponding analytic solution is

$$T(x, t) = \begin{cases} \displaystyle\sum_{n=0}^{\infty} \frac{F_n}{\lambda_n \alpha} \left[\frac{e^{\lambda_n \alpha t_p} - 1}{e^{\lambda_n \alpha t_I} - 1} + e^{\lambda_n \alpha t} - 1 \right] e^{-\lambda_n \alpha t} \cos\sqrt{\lambda_n}\, x & \text{for } 0 < t \le t_p \\ \displaystyle\sum_{n=0}^{\infty} \frac{F_n}{\lambda_n \alpha} \left[\frac{e^{\lambda_n \alpha t_p} - 1}{1 - e^{-\lambda_n \alpha t_I}} \right] e^{-\lambda_n \alpha t} \cos\sqrt{\lambda_n}\, x & \text{for } t_p < t \le t_I \end{cases} \tag{25}$$

For relatively short duration pulses, the energy input to the cladding could have been treated as instantaneous, leading to an even more simple solution; however, this solution would have applied to low pulse frequencies only and, therefore, was considered only as one way of predicting trends in this frequency regime.

Stress. The relationship between temperature distribution and the induced thermal stress in an unrestrained slab (Timoshenko and Goodier, 1951) is

$$\sigma_y = \sigma_z = -\frac{\alpha_T E T}{1 - \nu} + \frac{1}{L(1 - \nu)} \int_0^L \alpha_T E T dx + \frac{12x}{L^3(1 - \nu)} \int_0^L \alpha_T E x T dx \tag{26}$$

where σ_y and σ_z are the stress in the y and z directions, which are normal to the x coordinate.

Substituting equation (25) into equation (26), and integrating over x, the induced thermal stresses can be expressed

$$\sigma_y = \sigma_z = \begin{cases} \dfrac{\alpha_T E}{1 - \nu} \displaystyle\sum_{n=0}^{\infty} \frac{F_n}{\lambda_n \alpha} \left[\frac{(-1)^n}{L\sqrt{\lambda_n}} - \cos\sqrt{\lambda_n} x + 12\left\{\frac{x}{L} - \frac{1}{2}\right\}\left\{\frac{(-1)^n}{2L\sqrt{\lambda_n}} - \frac{1}{L^2 \lambda_n}\right\}\right] \left[\frac{e^{\lambda_n \alpha t_p} - 1}{e^{\lambda_n \alpha t_I} - 1} + e^{-\lambda_n \alpha t} - 1 \right] e^{-\lambda_n \alpha t} & \text{for } 0 < t \le t_p \\ \dfrac{\alpha_T E}{1 - \nu} \displaystyle\sum_{n=0}^{\infty} \frac{F_n}{\lambda_n \alpha} \left[\frac{(-1)^n}{L\sqrt{\lambda_n}} - \cos\sqrt{\lambda_n} x + 12\left\{\frac{x}{L} - \frac{1}{2}\right\}\left\{\frac{(-1)^n}{2L\sqrt{\lambda_n}} - \frac{1}{L^2 \lambda_n}\right\}\right] \left[\frac{e^{\lambda_n \alpha t_p} - 1}{1 - e^{-\lambda_n \alpha t_I}} \right] e^{-\lambda_n \alpha t} & \text{for } t_p < t \le t_I \end{cases} \tag{27}$$

Furthermore, the spatially varying heat generation rate $G(x)$ was determined from the known absorptivity of the cladding and $I_F(t)$ was evaluated accordingly. Incident light energy E_0 is absorbed in the cladding exponentially via Beer's law; and considering both incident light and light reflected off the metal housing, the derived expression for the heat generation rate is

$$g(x) = \alpha_a E_0 e^{-\alpha_a x} [1 + e^{-2\alpha_a (L - x)}] \tag{22}$$

Then equation (13) becomes

$$F_n = \begin{cases} \left[\dfrac{2\alpha_a E_0}{L \rho c_p} \right] \dfrac{2(-1)^n \sqrt{\lambda_n} e^{-\alpha_a L} + \alpha_a (1 - e^{-2\alpha_a L})}{\alpha_a^2 + \lambda_n} & \text{for } 0 < t \le t_p \\ 0 & \text{for } t_p < t \le t_I \end{cases} \tag{23}$$

This is the equation used to evaluate the suitability of alternative cladding materials and thicknesses. Specifically, calculated stresses were compared with stress limits for the cladding materials.

Application—Results and Discussion

With light energy absorbed in the cladding in accordance with Beer's law, the ratio of incident and returning light intensity is $e^{-2\alpha_a L}$. Consequently, the most important cladding design requirement is to keep this ratio below a certain value or, equivalently, impose a minimum value for $\alpha_a L$. This requirement can be met by selecting either a thick cladding with a low absorptivity or a thin cladding with higher absorptivity. However, the temperature and stress responses during the pulse are quite different for these two cases, with other variables,

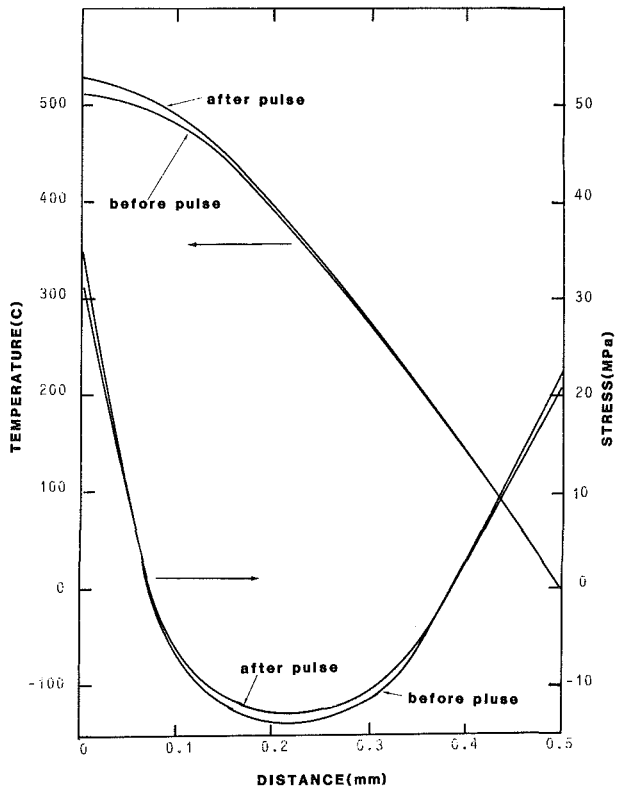

Fig. 2 Temperature and stress variation in thick cladding at 250 Hz with $\alpha_a L = 3$

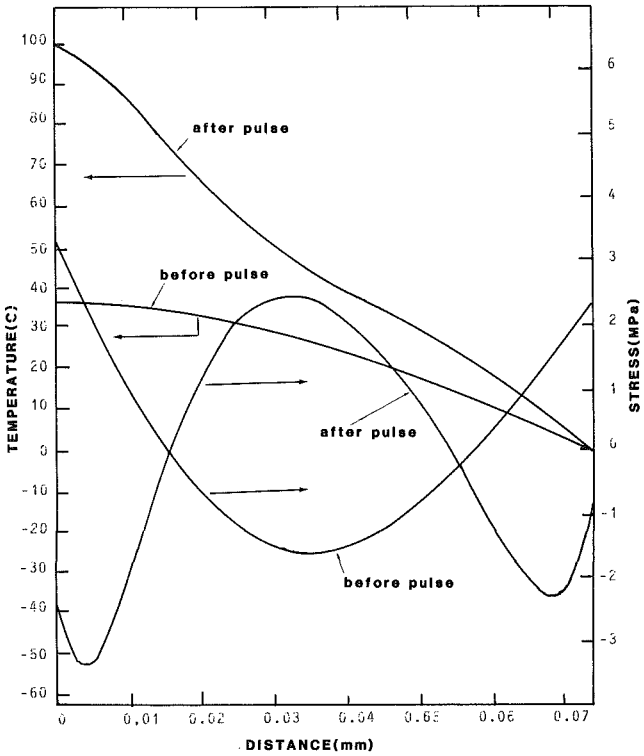

Fig. 4 Temperature and stress variation in cladding of intermediate thickness at 250 Hz with $\alpha_a L = 3$

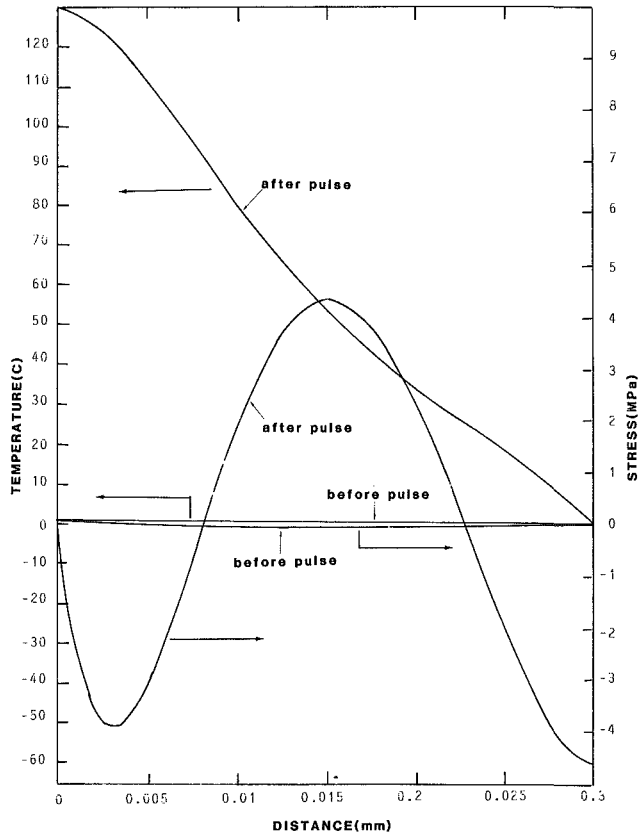

Fig. 3 Temperature and stress variation in thin cladding at 250 Hz with $\alpha_a L = 3$

such as physical properties and pulse characteristics, constant. For the thick cladding with low absorptivity, the temperature variation through the thickness is significant but the change in temperature between pulses is small. For the thin cladding with high absorptivity, the temperature variation through the thickness is negligible but the temperature rises sharply during the pulse.

Numerical examples have been developed for a typical cladding material and typical operating conditions for a high-average-power laser to demonstrate this relative influence of thickness and absorptivity. The physical properties of the cladding material are those for the absorbing glass used in test amplifiers at LLNL; specifically,

$$\alpha_T = 8.4 \times 10^{-6}\ ^\circ\mathrm{C}^{-1}$$
$$\sigma_u = 70.0\ \mathrm{MPa}$$
$$E = 5.116 \times 10^{10}\ \mathrm{Pa}$$
$$\nu = 0.27$$
$$\rho = 6.4 \times 10^{3}\ \mathrm{kg/m^3}$$
$$c_p = 2.9 \times 10^{2}\ \mathrm{J/kg^\circ C}$$
$$\alpha = 4.39 \times 10^{-7}\ \mathrm{m^2/s}$$

The other fixed design parameters are

$$t_p = 9.0 \times 10^{-5}\ \mathrm{s}$$
$$E_0 = 3.94 \times 10^{7}\ \mathrm{W/m^2}$$

with pulse frequency extending to 250 Hz (t_p/t_l extending to 0.0225).

Figure 2 presents calculated temperature and stress variations for a thick cladding, $L = 5.0 \times 10^{-4}$ m, with a low absorptivity, $\alpha_a = 6.0 \times 10^{3}\ \mathrm{m}^{-1}$, yielding an absorption parameter $\alpha_a L = 3.0$. Distributions before and after a pulse are shown; there is a very small difference between them and, for all practical purposes, the distribution can be considered steady state. Temperatures in the cladding are high, exceeding 500°C at the interface with the elastomer. Also, the stresses at each end surface are high and compressive, while moderate tensile stresses exist at the center.

Figure 3 presents calculated temperature and stress varia-

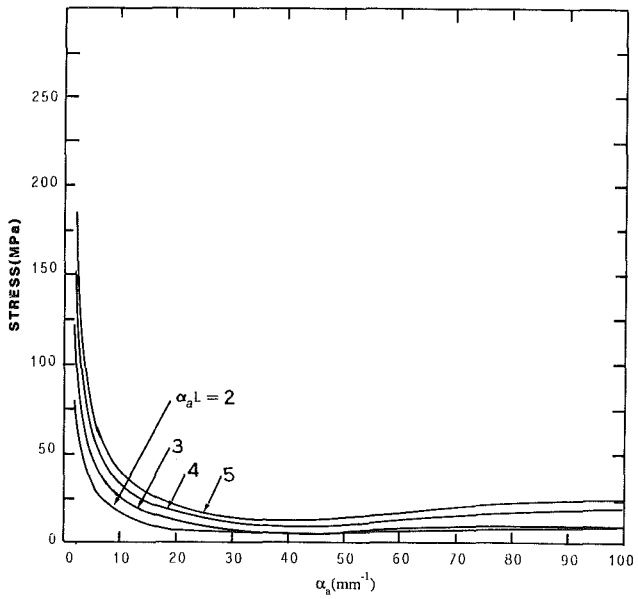

Fig. 5 Maximum stress difference in cladding at 250 Hz

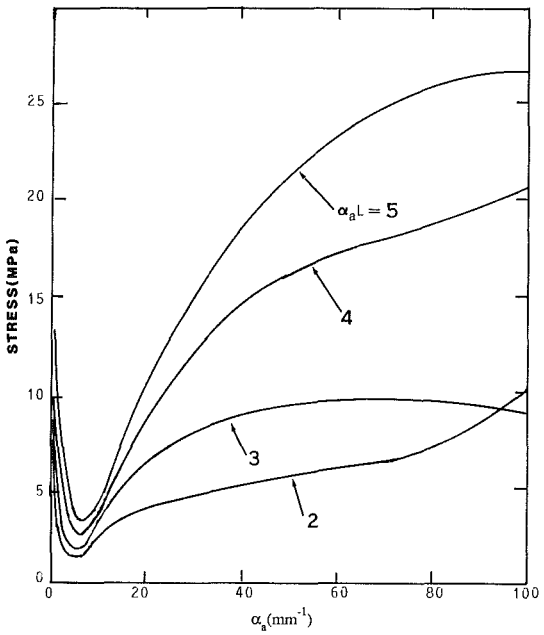

Fig. 6 Maximum stress difference in cladding at 10 Hz

tions for a thin cladding, $L = 3.0 \times 10^{-5}$ m, and a high absorptivity $\alpha_a = 10^5$ m^{-1}, yielding the same absorption parameter α_aL of 3.0. Flat temperature and stress variations before the pulse are shown to rise sharply after the pulse, with moderate tensile stresses at each end surface and compression stresses at the center.

Figure 4 presents calculated temperature and stress variations for a cladding of intermediate thickness, $L = 7.5 \times 10^{-5}$ m with the same absorption parameter α_aL of 3.0. These results are in between the thick and thin cladding results. However, local stresses are shown to oscillate between compressive and tensile stresses and the stress distribution near the end surface after a pulse is more complex in this intermediate case.

The optimal cladding design limits the average temperature and minimizes the stress variation in the cladding by properly selecting the thickness and absorptivity of the cladding to achieve the predetermined absorption parameter α_aL. It is also

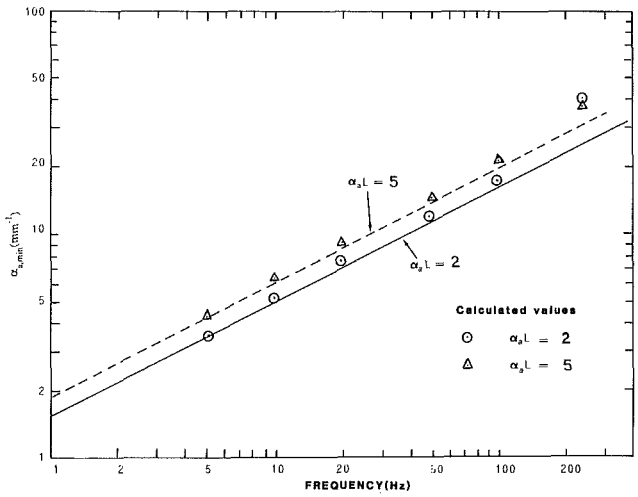

Fig. 7 Absorptivity for minimum stress variation in cladding

important to minimize tensile stress at the surface of the cladding. As demonstrated in Figs. 2, 3, and 4, the stress variations can change character, and this optimum is generally sought by calculating and analyzing a number of trial cases. Figure 5 shows the maximum stress variations evaluated on this basis for $\alpha_aL = 2$, 3, 4, and 5 at a constant frequency of 250 Hz. As expected, a minimum variation exists at an intermediate value of α_a for each α_aL value; for example, the minimum stress for $\alpha_aL = 3$ occurs at $\alpha_a = 4.4 \times 10^4$ m^{-1}.

Figure 6 is a similar plot of the maximum stress variations at a constant frequency of 10 Hz. These data illustrate the trends much more dramatically than the data for 250 Hz. Also, the α_a value at which the minimum stress variation occurs at 10 Hz is much smaller than that at 250 Hz. These comparatively different results demonstrate the importance of pulse frequency in cladding design.

In a parallel study (Trenholme, 1986), it was deduced that a good approximate relationship between pulse frequency and the α_a value corresponding to minimum stress variation can be obtained by considering an instantaneous pulse found at low pulse frequencies where the maximum stress can be shown to be a function only of the Fourier number for the pulse period t_I; in other words the optimal design condition for a given α_aL is obtained at fixed ratios of the diffusion length to cladding thickness. Consequently, the ratios for pulse frequencies f_1 and f_2 at the same value of α_aL are equal or

$$\left[\frac{\alpha t_I}{L_{\min}}\right]_{f_1} = \left[\frac{\alpha t_I}{L_{\min}}\right]_{f_2} \tag{28}$$

where $L_{\min}$ is the cladding thickness with the minimum stress variation. Since α_aL is a constant and

$$t_I = \frac{1}{f} \tag{29}$$

equation (28) can also be written

$$\frac{(\alpha_{a,\min})_{f_1}}{(\alpha_{a,\min})_{f_2}} = \frac{f_1}{f_2} \tag{30}$$

where $\alpha_{a,\min}$ is the cladding absorptivity at the minimum stress difference. Equation (30) is exact when $t_p = 0$ and a good approximation when $t_p \ll t_I$.

Figure 7 is a comparison of equation (30) with the absorptivities at minimum stress difference determined with the more general solution given by equation (27). There is good agreement between the calculated $\alpha_{a,\min}$ and $\alpha_{a,\min}$ predicted by equation (30) until the frequency reaches 250 Hz, where t_I approaches t_p.

Experimental Verification

Test amplifiers using glass edge absorbers have been successfully operated at LLNL, but not with sufficient light intensity or pulse frequency to test severely the validity of this design model. Although no thermal stress failure has been observed for the imposed light intensities, estimated to be low, and pulse frequencies up to 100 Hz, these results are not considered sufficient to validate application of the model in edge cladding design.

Concluding Remarks

A one-dimensional cyclic quasi-steady conduction problem for an arbitrary internal heat generation function has been solved and the solution used to predict the temperature and thermal stress distributions in the edge cladding of a solid-state laser slab. The results of analysis show that:

1 The thermal stress variations in the cladding, for a given pulse frequency and absorption parameter $\alpha_a L$, can be minimized by selecting proper absorptivity of the cladding material.

2 An approximate relationship between pulse frequency and absorptivity corresponding to the minimum thermal stress variation is reliable at pulse frequencies less than 250 Hz.

References

Arpaci, V. S., 1966, *Conduction Heat Transfer*, Addison-Wesley Publishing Co., New York, pp. 324–335.

Berg, P. W., and McGregor, J. L., 1966, *Elementary Partial Differential Equation*, Holden-Day, Inc., New York, pp. 102–107.

Emmett, J. L., Krupke, W. F., and Sooy, W. R., 1984, "The Potential of High-Average-Power Solid State Lasers," UCRL-53571.

Glaze, J. A., Guch, S., and Trenholme, J. B., 1974, "Parasitic Suppression in Large Aperture Nd:Glass Disk Laser Amplifiers," *Applied Optics*, Vol. 13, pp. 2808–2811.

Luikov, A. V., 1968, *Analytical Heat Diffusion Theory*, Academic Press, New York, pp. 363–365.

Timoshenko, S., and Goodier, J. N., 1951, *Theory of Elasticity*, 2nd ed., McGraw-Hill, New York, p. 401.

Trenholme, J. B., 1972, "Fluorescence Amplification and Parasitic Oscillation Limitations in Disc Laser," Naval Research Laboratory, Washington, DC, NRL Memorandum Report 2480.

Trenholme, J. B., 1986, Lawrence Livermore National Laboratory, Personal Communication.

Wang, W. J., Clark, J. A., and Arpaci, V. S., 1961, "Dynamic Response of Heat Exchangers Having Internal Heat Source—Part IV," ASME JOURNAL OF HEAT TRANSFER, Vol. 83, p. 321.

ERRATUM

John H. Lienhard
Heat Transfer/Phase Change Laboratory
Mechanical Engineering Department
University of Houston
Houston, Texas 77204-4792

Many of us (see, e.g., Ramilison and Lienhard, 1987, "Transition Boiling Heat Transfer and the Film Transition Regime," JOURNAL OF HEAT TRANSFER, Vol. 109, No. 3, pp. 746–752) have credited an important discovery to the wrong authors. This was the discovery that the surface temperature of certain ostensibly surface-temperature-controlled boiling heaters is actually strongly dependent on the local heat flux. We have referred to G. Hesse (1973, "Heat Transfer in Nucleate Boiling, Maximum Heat Flux and Transition Boiling," *Int. J. Heat Mass Transfer*, Vol. 16, pp. 1611–1627), who detailed the phenomenon and attributed it to work in the late sixties by Stephan, Kovalev, Grassman, and Ziegler.

Actually, E. Adiutori (1964, "New Theory of Thermal Stability in Boiling Systems," *Nucleonics*, Vol. 22, No. 5, pp. 92–101) clearly diagnosed this experimental shortcoming, and he followed it up with more specifics in a letter published in the Dec. 1964 issue of *Nucleonics*. This was before any of Hesse's sources were published. To the best of my knowledge, Adiutori should be credited with discovering this subtle influence.

Thermal Constriction Resistance of Sphere/Layered Flat Contacts: Theory and Experiment

N. J. Fisher
Chalk River Nuclear Laboratories,
Atomic Energy of Canada Limited,
Chalk River, Ontario, Canada

M. M. Yovanovich
UW Microelectronics Heat Transfer Laboratory,
Department of Mechanical Engineering,
University of Waterloo,
Waterloo, Ontario, Canada

The effect of surface layers on the thermal constriction resistance of contacts is of interest to the thermal analyst. This paper investigates analytically and experimentally the thermomechanical problem of a sphere in elastic contact with a flat coated with a layer. An approximate solution is developed that utilizes the solution to the thermal portion of the problem and the Hertzian limits of the mechanical portion. The approximation shows good agreement with the full solution for two examples that represent extremes in elastic properties for common metallics. Thermal constriction resistance measurements for a steel sphere contacting a nickel flat coated with a silver layer are compared to theoretical predictions. Resistance predictions from both full and approximate solutions show good agreement with measurements for light loads within the elastic load range. For heavy loads, the resistance is overpredicted due to plastic yielding of the nickel substrate.

Introduction

The use of surface layers within components is increasing as designers search for more variety and flexibility in material properties. Uses of layers include improving wear resistance, strength and corrosion resistance, modifying electrical and thermal conductivities, reducing weight, and conserving resources (Texas Instruments, 1983).

The development of computers with high chip densities makes efficient heat removal increasingly important. The Thermal Conduction Module (TCM), a key component of the IBM 3081 computer, is shown in Fig. 1 (Bar-Cohen et al., 1983). Each module contains an array of surface-mounted chips. The heat generated within each chip is removed through a spring-loaded aluminum piston, which presses onto the chip surface. A typical piston/chip contact is detailed in Fig. 2 (Chu et al., 1982). Heat transfer occurs through both the solid contact and the helium-filled gap. One technique to increase the heat removal rate is to add a thermally conductive layer to the piston/chip interface.

The purpose of this paper is to develop a simple model to predict the effect of a surface layer on the thermal constriction resistance of the piston/chip contact and to verify the model by comparing experimental resistance measurements to theoretical predictions.

Analysis

Idealized Model. The piston/chip contact is idealized as a nominal point contact between smooth surfaces, as shown in Fig. 3(*a*). The piston is modeled as a spherical indenter and the chip as a flat. Both bodies are idealized as half-spaces because the dimensions of the contact area are small as compared to the overall body dimensions. The indenter radius ρ_I is the reduced radius combining the radii of both bodies.

The addition of a layer to the piston/chip interface is modeled by including a layer on the flat, as shown in Fig. 3(*b*). This assumption does not restrict the applicability of the model. The layer can be added to either the piston or chip since both are assumed to be half-spaces in this analysis.

The complete model of the contact including the layer is shown in Fig. 4. The indenter (subscript *I*) is loaded onto a flat composed of a layer (subscript *L*) of thickness *t*, bonded to a substrate (subscript *S*).

In general, heat transfer can occur through both the contact and the surrounding gap. Heat transfer across the gap occurs by two different modes: conduction or convection, and radiation. The relative contributions of the two modes, for a gap size similar to this problem, have been investigated by Kitscha

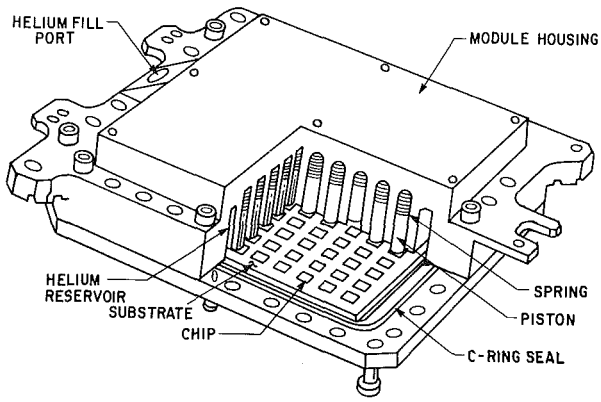

Fig. 1 Thermal conduction module

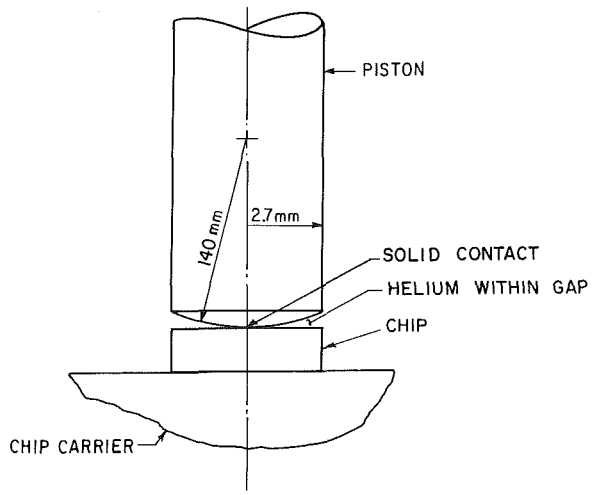

Fig. 2 Piston/chip contact

Contributed by the Heat Transfer Division and presented at the 4th AIAA/ASME Thermophysics and Heat Transfer Conference, Boston, Massachusetts, June 2–4, 1986. Manuscript received by the Heat Transfer Division November 30, 1987. Keywords: Conduction.

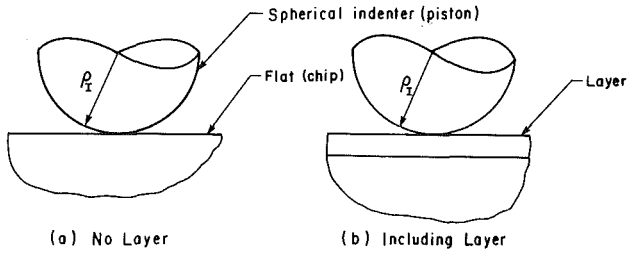

Fig. 3 Idealized piston/chip contact

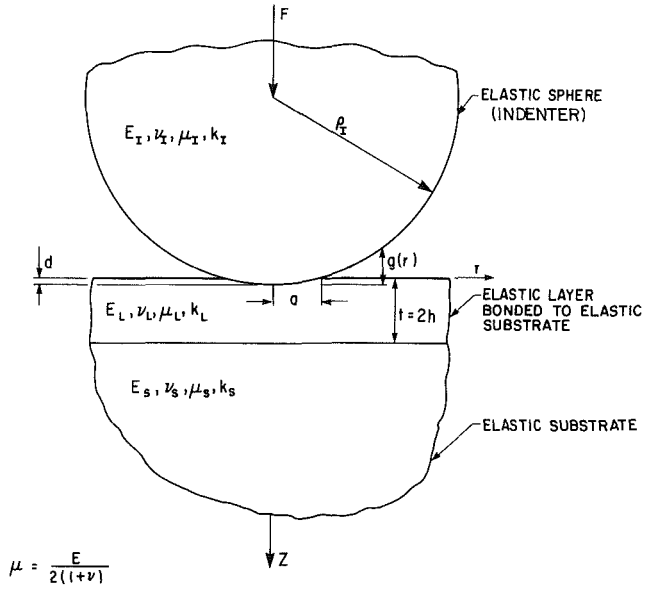

Fig. 4 Model of contact

and Yovanovich (1975), Ogniewicz and Yovanovich (1978), and Turyk and Yovanovich (1985).

Heat transfer by natural convection is found to be negligible. Models have been developed for conduction and radiation across the gap and, by comparison with experimental measurements for bare flats, these models have been shown to predict the heat transfer rate through the gap adequately.

The addition of a layer to the interface significantly affects the conductive heat transfer rate through the solid contact. Since the two heat transfer pathways (solid contact and gap) are coupled, changes in the temperature field and heat transfer rate across the solid contact will affect the temperature field and heat transfer rate across the gap. However, because this coupling is weak, the heat transfer rate through the gap is only slightly affected by the addition of a layer. Therefore, to simplify this analysis, heat transfer across the gap is neglected and only steady-state conduction heat transfer through the solid contact is considered.

The following assumptions further simplify the analysis: The mechanical and thermal properties of the bodies are assumed to be constant, the contact is assumed to form elastically, the bodies are assumed to be smooth with negligible surface roughness, the temperature drop across the contact is assumed to be small so thermal strain effects are negligible, and the heat flux distribution over the contact area is assumed to be equivalent isothermal, which is that flux distribution that results in an isothermal contact spot on a homogeneous half-space.

Analytical Solution. Heat flowing between the idealized bodies must flow through the solid contact area. The constriction and subsequent spreading of the heat flow lines gives rise to a thermal constriction resistance defined as the temperature difference across the contact divided by the total heat flow rate through the contact. This constriction resistance depends upon the load, geometry, and thermophysical properties of the contact.

The thermal constriction resistance for a sphere in elastic contact with a bare flat was investigated by Kitscha and Yovanovich (1975). They experimentally verified the analytical solution for the elastic load range. Antonetti and Yovanovich (1985) studied the problem of a rough conforming surface in contact with a smooth coated surface and developed an analytical solution for the constriction resistance, which they verified against experimental measurements.

The contact of a sphere and a flat consisting of a layer bonded to a substrate is a complicated problem. To predict the thermal constriction resistance of the contact, both mechanical and thermal portions of the problem must be solved. First, the mechanical portion is solved to find the radius a of the circular area of contact. Then, using the contact radius, the thermal portion is solved to find the constriction resistance.

The mechanical portion is a complex problem in axisymmetric elasticity governed by the following differential equation:

Nomenclature

a = contact radius
$\tilde{a}$ = arithmetic average of bounding contact radii (equation (10))
d = approach or penetration
E = elastic modulus
F = load
$g(r)$ = indenter profile
h = layer half-thickness
H = hardness (Pa) or H_b (kg/mm^2)
k = thermal conductivity
m = mean asperity slope
r = radial coordinate
R = thermal constriction resistance
R^* = dimensionless resistance $= R\tilde{a}k_s$
Q = heat flow rate
t = layer thickness
T = temperature
ΔT = contact temperature drop
z = axial coordinate
α = ratio of contact radius bounds (equation (6))
γ = ratio of reduced elastic moduli (equation (3))
κ = ratio of thermal conductivities (equation (3))
μ = shear modulus (Fig. 4)
ν = Poisson ratio
ρ = body radius
ρ_I = reduced radius (Fig. 4)
σ = rms surface roughness
τ = relative layer thickness (equation (3))
$\bar{\tau}$ = average relative layer thickness (equation (11))
ϕ = stress function
$\psi(\tau)$ = constriction parameter for an isothermal contact spot, Dryden's solution (equation (A1))

Superscripts

* = dimensionless or reduced
$\bar{}$ = average

Subscripts

AP = approximate solution
E = experimental measurement
I = indenter
L = layer
m = from measured plastic indentation
S = substrate

$$\nabla^2 \nabla^2 \phi = 0 \tag{1}$$

where ϕ is the stress function (Timoshenko and Goodier, 1951) and ∇^2 is the Laplacian. The boundary condition is mixed, with the surface deflection prescribed within the contact area and the normal stress prescribed outside. For layered bodies, equation (1) cannot be solved to yield a closed-form solution for the contact radius. Instead, an iterative procedure is used in which an initial guess at the contact radius is continually updated until the calculated supported load equals the given load to some relative error criterion. Two solution procedures have been used to find the load supported by the contact of given radius.

With the integral transform method, the problem is formulated as a dual integral equation that is reduced to a Fredholm integral equation. The equation is then solved by expanding the kernel into a series of base functions. The shortcoming of the method is in the evaluation of the resulting integrals because they are slow to converge at the top surface of the layer near the boundary of the loaded region, especially for thin layers.

Chen and Engel (1972) circumvented this convergence difficulty with their general approximate method (GAM), in which they replaced the unknown stress condition within the contact area with an assumed set of base functions. The functions are assembled such that the displacement within the contact area approximates the real displacement boundary condition in accordance with an integral least-squares residual error criterion. The shortcoming of their method is that many numerical integrations are necessary to evaluate the displacement due to the assumed set of base functions.

The governing differential equation for the thermal portion is the Laplace equation

$$\nabla^2 T = 0 \tag{2}$$

The boundary condition is mixed with the temperature prescribed within the contact area and the flux prescribed outside. Dryden (1983) removed the mixed boundary condition by replacing the unknown flux condition within the contact area with the equivalent isothermal flux distribution, which is the flux distribution that results in an isothermal contact spot on the surface of a homogeneous half-plane.

For thick layered half-spaces, $\tau \geq 10$, Negus et al. (1985) have shown that the equivalent isothermal flux condition is a good approximation to the true isothermal condition. However, for thin resistive layers, $\tau < 1$ and $\kappa < 1$, the uniform flux condition is a better approximation, while for thin conductive layers, $\tau < 1$ and $\kappa > 1$, the resistance due to the true isothermal condition is somewhat lower than the equivalent isothermal flux result and much lower than the uniform flux result. Application of Negus et al.'s superposition technique to this problem to solve for the true isothermal condition would be beneficial.

Dryden solved Laplace's equation using Hankel transforms to yield an integral expression for the constriction resistance, which he further simplified into simple closed-form expressions for the limiting cases of very thin and very thick layers and a series solution for intermediate layer thicknesses.

The combination of Chen and Engel's (1972) solution to the mechanical portion and Dryden's (1983) solution to the thermal portion forms a complete solution to the contact resistance problem of a spherical indenter contacting a layered, elastic half-space with an equivalent isothermal flux distribution over the contact area. As the layer thickness approaches zero, the resistance approaches that of an indenter contacting a half-space composed entirely of substrate material, and as the thickness approaches infinity, the resistance approaches that of an indenter contacting a half-space composed entirely of layer material. At these bounds, the equivalent isothermal distribution accurately represents the flux distribution for an isothermal contact. For intermediate layer thicknesses, the resistance predicted by this combined solution lies between these two bounding resistances.

Although the mechanical portion of the contact problem cannot be solved in closed form for layered bodies, a closed-form solution is available for the contact of unlayered bodies (Hertzian contact theory). By combining the Hertzian contact solution with Dryden's thermal solution, an approximate closed-form solution for the constriction resistance of the layered contact can be developed.

Resistance Bounds. Three important parameters influence the thermomechanical behavior of a flat composed of a layer bonded to a substrate (hereafter called a "layered flat"): ratio of elastic moduli γ, conductivity ratio κ, and relative layer thickness τ.

$$\gamma = \frac{E_L^*}{E_S^*} \qquad \kappa = \frac{k_L}{k_S} \qquad \tau = \frac{t}{a} \tag{3}$$

For a thin layer ($\tau \to 0$), the general layered contact reduces to the Hertzian contact of an indenter and a flat composed of substrate material. The contact radius a_S corresponding to the substrate bound is

$$a_S = \left[\frac{3}{4} \frac{F\rho_I}{E_S^*}\right]^{1/3} \tag{4}$$

where the reduced elastic modulus for the substrate bound E_S^* is

$$\frac{1}{E_S^*} = \frac{1-\nu_I^2}{E_I} + \frac{1-\nu_S^2}{E_S} \tag{5}$$

For a thick layer ($\tau \to \infty$), the general contact reduces to the Hertzian contact of an indenter and a flat composed of layer material. The contact radius a_L corresponding to the layer bound is

$$a_L = \left[\frac{3}{4} \frac{F\rho_I}{E_L^*}\right]^{1/3} \tag{6}$$

where the reduced elastic modulus for the layer bound E_L^* is

$$\frac{1}{E_L^*} = \frac{1-\nu_I^2}{E_I} + \frac{1-\nu_L^2}{E_L} \tag{7}$$

For all other values of τ, the contact radius a will lie between the two bounding radii, a_S and a_L. If the difference between the bounds is small, then they can be used to estimate the contact radius.

We define the ratio of the bounding radii α as

$$\alpha = \frac{a_L}{a_S} \tag{8}$$

Then α depends upon γ to the $-1/3$ power

$$\alpha = \gamma^{-1/3} \tag{9}$$

When γ is unity, the difference between the bounds is zero. As γ differs from unity, the difference between the bounds widens. For common metallics, the range of γ is

$$0.2 \leq \gamma \leq 5 \tag{10}$$

Therefore

$$1.7 \geq \alpha \geq 0.6 \tag{11}$$

or the bounding radii differ by less than a factor of two. For this condition, the arithmetic mean of the bounds $\bar{a}$ is a good estimate of the contact radius a

$$\bar{a}=\frac{a_S+a_L}{2} \tag{12}$$

and the average relative layer thickness $\bar{\tau}$ is a good estimate of the relative layer thickness τ

$$\bar{\tau}=\frac{t}{\bar{a}} \tag{13}$$

The harmonic and geometric means of the bounding radii were also examined as possible estimates of the contact radius. The three means differ by less than 3.5 percent for the particular case of $\gamma=0.37$. Therefore, the arithmetic mean is arbitrarily chosen as a convenient estimate.

The total constriction resistance R of the system shown in Fig. 4 equals the sum of two constriction resistances in series: the resistance of an isothermal contact spot on the indenter and the resistance of an isothermal contact spot on the layered flat

$$R=\frac{1}{4a\,k_I}+\frac{\psi(\tau)}{4a\,k_S} \tag{14}$$

where the contact spot radius a must be calculated from the mechanical portion of the contact problem. The constriction parameter $\psi(\tau)$ for an isothermal contact spot on a layered flat is given by Dryden (1983).

The bounds on the constriction resistance, R_S and R_L, can be easily calculated from the bounding contact radii, a_S and a_L. The substrate resistance bound is

$$R_S=\frac{1}{4a_S k_I}+\frac{\psi(\tau_S)}{4a_S k_S}$$

where

$$\tau_S=\frac{t}{a_S} \tag{15}$$

and the layer resistance bound is

$$R_L=\frac{1}{4a_L k_I}+\frac{\psi(\tau_L)}{4a_L k_S}$$

where

$$\tau_L=\frac{t}{a_L} \tag{16}$$

Note that $\psi(\tau)$ is defined with respect to the substrate conductivity k_S (see Appendix).

Approximate Resistance. The bounding resistances approximate the constriction resistance of the system for small and large relative layer thicknesses. However, for intermediate layer thicknesses, the resistance lies between the bounds. For this range, an approximation combining the bounds is required.

For several layer-substrate combinations the dimensionless constriction resistance R^* was plotted versus the common logarithm of the average relative layer thickness $\bar{\tau}$. The dimensionless resistance is defined with respect to the average contact radius $\bar{a}$ and the substrate conductivity k_S

$$R^*=R\bar{a}k_S \tag{17}$$

The average contact radius is chosen as the nondimensionalizing length because it is load dependent and can be easily calculated from the bounding contact radii. The dimensionless bounding resistances are

$$R_S^*=\frac{\bar{a}}{4a_S}\left(\frac{k_S}{k_I}+\psi(\tau_S)\right) \tag{18}$$

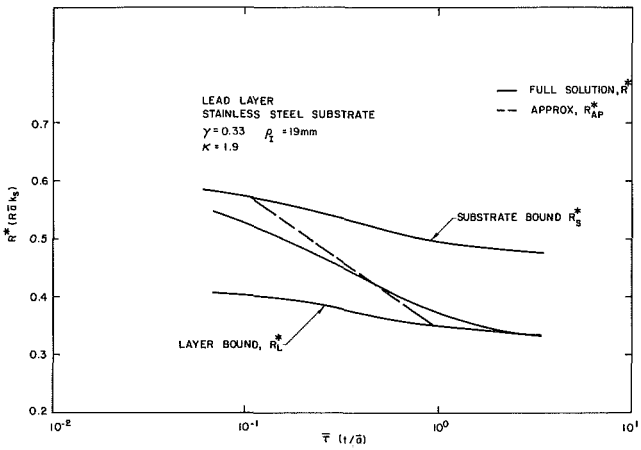

Fig. 5 R^* versus $\bar{\tau}$ for lead layer example

$$R_L^*=\frac{\bar{a}}{4a_L}\left(\frac{k_S}{k_I}+\psi(\tau_L)\right) \tag{19}$$

For the examined combinations, the following behavior was observed. For $\bar{\tau}$ less than 0.1, R^* approached the substrate bound, R_S^*, while for $\bar{\tau}$ greater than 1.0, R^* approached the layer bound R_L^*. Within the intermediate range, R^* varied logarithmically with $\bar{\tau}$. Therefore, the dimensionless resistance can be approximated as

$$R_{AP}^*=\begin{cases} R_S^* & \bar{\tau}\le 0.1 \\ R_{1.0}^*+(R_{1.0}^*-R_{0.1}^*)\log_{10}(\bar{\tau}) & 0.1<\bar{\tau}<1.0 \\ R_L^* & \bar{\tau}\ge 1.0 \end{cases} \tag{20}$$

where $R_{0.1}^*$ and $R_{1.0}^*$ are transition points defined as

$$R_{0.1}^*=\frac{\bar{a}}{4a_S}\left(\frac{k_S}{k_I}+\psi(0.1)\right) \tag{21}$$

$$R_{1.0}^*=\frac{\bar{a}}{4a_L}\left(\frac{k_S}{k_I}+\psi(1.0)\right) \tag{22}$$

In dimensional terms, the approximate resistance is

$$R_{AP}=\frac{R_{AP}^*}{\bar{a}\,k_S} \tag{23}$$

Analytical Results. The approximate dimensionless resistance R_{AP}^* is compared to the dimensionless resistance calculated using the full mechanical and thermal solutions R^* for two layer-substrate examples that represent relative extremes in elastic properties for common metallics.

The first example is a layered flat consisting of a lead layer on a stainless steel substrate in contact with a stainless steel sphere. The dimensionless parameters are $\gamma=0.33$ and $\kappa=1.9$, so the effect of the lead layer is to lower the constriction resistance. The dimensionless resistances are plotted versus $\bar{\tau}$ in Fig. 5.

The approximation overpredicts the resistance for $\bar{\tau}$ less than 0.5 and underpredicts for $\bar{\tau}$ greater than 0.5. The largest differences of 8 and -5 percent (relative to R^*) occur at the transition points $\bar{\tau}=0.1$ and $\bar{\tau}=1.0$, respectively, because the approximate resistance curve changes slope abruptly at these points, while the full solution curve changes slope gradually. The greater difference at the small transition point indicates that this transition point is less accurate. The approximation

Table 1 Properties of bare specimens

	Material	ρ_I, mm	E, GPa	ν	k, W/mK	σ, μm	Hardness
Flat 13A	Ni 200	∞	204	0.3	79.3	0.06	H_b^* 103
Flat 15A	Keewatin TS	∞	204	0.3	33.5	<0.05	$H_c^\dagger$ 60
Indenter (sphere)	Carbon Steel	38.1	207	0.3	45.7	<0.05	H_c 35

*H_b is Brinell hardness (kg/mm^2).
†H_c is Rockwell C hardness number.

Table 2 Properties of layered specimens

	Silver layer							Nickel substrate		
Test	t, μm	E, GPa	ν	k, W/mk	σ, μm	m	Hardness	E, GPa	ν	Hardness
14B	60	75	0.3	427	0.09	0.03	H_B* 65	204	0.3	H_b 103
14D	900	75	0.3	427	0.04	0.02	H_B 83	204	0.3	H_b 103

*H_B is Rockwell B hardness number.

would be improved for this example by shifting the small $\bar{\tau}$ transition point to $\bar{\tau}=0.05$.

The second example is a layered flat consisting of a chromium layer on an aluminum substrate in contact with an aluminum sphere. The dimensionless parameters are $\gamma=1.6$ and $\kappa=0.39$, so the chromium layer increases the constriction resistance. The dimensionless resistances are plotted versus $\bar{\tau}$ in Fig. 6.

The approximation underpredicts the resistance for $\bar{\tau}$ less than 0.12 and overpredicts for $\bar{\tau}$ greater than 0.12. The maximum difference of 5 percent occurs at $\bar{\tau}=0.2$. The small $\bar{\tau}$ transition point is again less accurate than the large $\bar{\tau}$ transition point. For this example the approximation would be improved by shifting the small $\bar{\tau}$ transition point to $\bar{\tau}=0.2$.

As noted in the two examples, the approximation could be improved by shifting the small $\bar{\tau}$ transition point. However, the position of this transition appears to depend on the relative properties of the particular layer/substrate combination. For the conductive layer, the recommended shift is toward smaller $\bar{\tau}$ and for the resistive layer, the shift is toward larger $\bar{\tau}$. The position of the transition point ($\bar{\tau}=0.1$) appears to be a reasonable compromise.

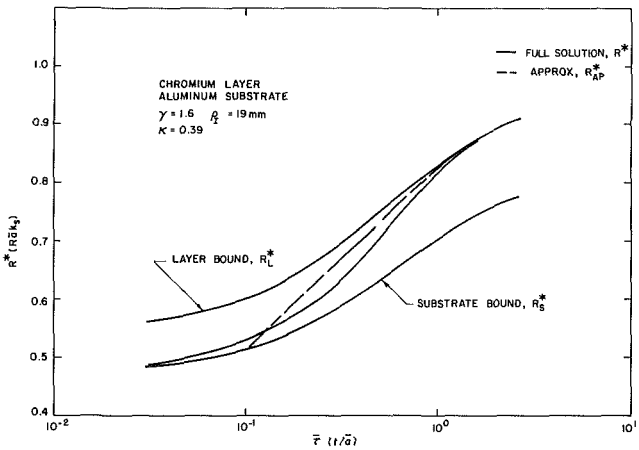

Fig. 6 R^* versus $\bar{\tau}$ for chromium layer example

Experiment

To verify the analytical models, an experimental test program was conducted to provide thermal constriction resistance measurements for comparison with theoretical predictions.

Apparatus and Procedure. A test column consisting of four sections was used in the experimental program: source, test, sphere, and sink. The source and sink specimens were heat flow meters, used to measure the heat flow rate above and below the contact. The temperature distributions within the test and sphere specimens were extrapolated to the contact plane to determine the temperature difference across the contact.

Axial loads were applied directly to the test column by a dead weight loading system, with a load range from 23.9 N to 688 N.

Heat was supplied to the column by a pair of resistive cartridge heaters positioned within the source specimen. The heat flowed axially down the column and was removed at the heat sink by a cold water bath. The column was wrapped in Fibrax insulation and aluminum foil to reduce heat losses in the radial direction.

Tests were conducted at a pressure less than 1×10^{-5} torr to eliminate convective and conductive heat transfer across the contact gap and radially, from the test column. The source and test specimens were maintained at temperatures below 373 K by using a low heat flow rate (approximately 1 W). In this manner, radiative heat transfer across the gap and radiative heat loss from the upper half of the test column were minimized. At this temperature level, the radiative heat flow rate across the gap was less than 1 percent of the total heat flow rate across the contact and could be neglected. The small temperature difference across the contact also reduced the effect of thermal strain at the sphere/flat interface.

To remove surface films, the sphere and test specimens were ultrasonically cleaned before each test in soapy deionized water and the contact surfaces were wiped with 1,1,1-trichloroethane ($C_2H_3Cl_3$) as recommended by Hegazy (1985).

Test specimens were fabricated from a single rod of commercially pure nickel (Nickel 200). The specimen for Test 15A was made from Keewatin Tool Steel. The ends of each specimen were ground and lapped smooth, and a silver layer was electroplated on one end. The layer surface was lapped smooth and uniform.

The properties of the bare flat specimens and the steel sphere are listed in Table 1. A smooth sphere was used so surface roughness effects could be neglected. The properties of the layered flat specimens are listed in Table 2. Handbook values (Baumeister, 1978) were used for the elastic modulus E, and Poisson ratio ν. The rms surface roughness σ, and mean asperity slope m, were measured with a surface profilometer.

Hardness values were measured for the bare and layered nickel flats using Brinell and Rockwell B hardness testers. Hardness values measured by McGee et al. (1985) and Kitscha and Yovanovich (1975) are listed for the bare Keewatin TS flat and the steel sphere. The layer thickness t was measured at the edge of the layered specimens by SEM. For one specimen, the thickness close to the contact spot was measured using eddy current techniques. The measurements from both techniques at both locations were of similar magnitude. X-ray energy spectroscopy of several layered specimens verified that the layer composition was at least 99 percent silver.

The temperature variation through each specimen was small. Consequently, the thermal conductivity was assumed uniform throughout each specimen, dependent only upon the average specimen temperature T. It was not possible to measure the conductivity of the thin silver layers, so the handbook value for pure silver at temperatures below 373 K was used (see Table 2).

The experimental contact resistance R_E was defined as the temperature difference across the contact ΔT divided by the heat flow rate through the contact Q

$$R_E = \frac{\Delta T}{Q} \tag{24}$$

The contact temperature difference was the difference in the extrapolated average contact plane temperatures, T_{e_1} and T_{e_2},

$$\Delta T = T_{e_1} - T_{e_2} \tag{25}$$

where T_{e_1} and T_{e_2} corresponded to the test specimen and sphere, respectively. These temperatures were calculated by extrapolating the specimen temperature distributions to the contact plane. For the layered specimens, the contact plane temperature T_{e_1} was assumed to equal the extrapolated temperature at the layer-substrate interface because the layer was thin and of high thermal conductivity. The interface resistance at the layer-substrate bond was neglected because the layer was deposited on a clean, smooth substrate. The resistance of this bond should be about two orders of magnitude less than the constriction resistance of the contact.

Heat flow rates were measured in both source and sink heat flow meters. The heat flow rate measured in the source was always greater than that measured in the sink since heat loss occurred along the test column. The sink heat flow rate was used to estimate Q since minimal heat loss occurred on the sink side of the contact (McGee et al., 1985). Equation (24) yields the conservative upper limit on the contact resistance because the sink heat flow rate is the minimum heat flow rate through the contact.

Experimental Results and Discussion

Bare Flats. Experiments were conducted with bare flats to establish the accuracy of the experimental procedure by comparison to the analytical model previously verified by Kitscha and Yovanovich (1975). Also, the bare nickel flat measurements (Test 13A) provided the upper bound on the constriction resistance for the subsequent tests with silver-nickel layered flats.

The theoretical resistance for the bare specimens is

$$R = \frac{1}{4k_I a} + \frac{1}{4k_S a} \tag{26}$$

If the contact behavior is elastic, the contact spot radius a can be calculated using Hertzian elastic theory

$$a = \left[\frac{3F\rho_I}{4E^*}\right]^{1/3} \tag{27}$$

where the reduced elastic modulus E^* is defined as

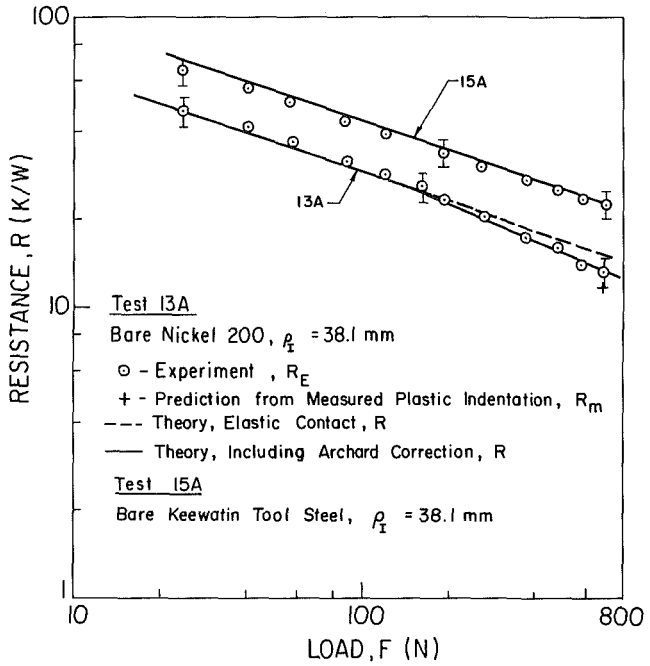

Fig. 7 Resistance versus load for bare flats

$$\frac{1}{E^*} = \frac{1-\nu_I^2}{E_I} + \frac{1-\nu_S^2}{E_S} \tag{28}$$

Experimental and theoretical resistances are plotted versus the applied load in Fig. 7 for the two tests with bare specimens: Nickel flat (13A) and Keewatin TS flat (15A). The probable experimental error in the measured resistance was ±8.5 percent and the probable error in the theoretical resistance due to uncertainty in the material properties is ±7 percent. The probable difference between the resistances is ±11 percent and this error bound is included on representative data points.

The agreement between the theoretical resistance based on Hertzian elastic theory and the experimental resistance is excellent for Test 15A. However, Hertzian theory overpredicts the measured resistance for the high load portion of Test 13A due to plastic deformation of the nickel flat. At the maximum load of 688 N, the experimental resistance is 14 percent less than the elastic theoretical prediction.

Archard (1980) developed a simple technique to estimate the load ranges for elastic and plastic contact behavior. The ranges of pure elastic and plastic behavior are defined in terms of the critical load F_c, where the elastic and plastic theories predict the same value for the contact radius

$$F_c = \frac{9\pi^3}{16} H^3 \left(\frac{\rho_I}{E^*}\right)^2 \tag{29}$$

The hardness H is the hardness of the softer material in pressure units. The three load ranges are:

$$\left.\begin{array}{ll} \text{(1) pure elastic} & F \le \dfrac{1}{15} F_c \\ \text{(2) elastic-plastic transition} & \dfrac{1}{15} F_c < F < 15 F_c \\ \text{(3) pure plastic} & F \ge 15 F_c \end{array}\right\} \tag{30}$$

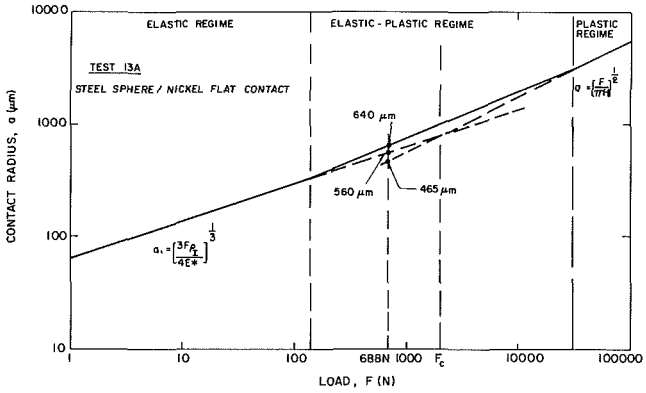

Fig. 8 Contact radius versus load: Nickel 200 flat

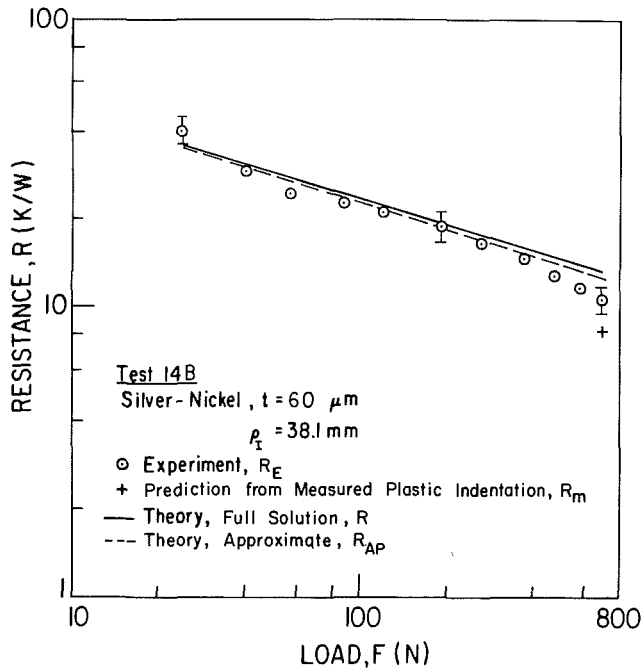

Fig. 9 Resistance versus load for silver-nickel flat; $t = 60$ μm

For Test 13A, the nickel flat is the softer material and determines the onset of plastic behavior. The critical load F_c is 2050 N and the elastic-plastic transition load range begins at 135 N. The onset of plastic behavior for Test 15A is controlled by the hardness of the steel sphere, which is softer than the Keewatin TS flat. For this test, F_c is 67.6 kN and the transition load range begins at 4500 N. After Test 13A, the nickel flat had an indentation of about 750 μm radius at the contact spot, but after Test 15A, neither the Keewatin TS flat nor the hardened steel sphere had any discernible plastic deformation.

The load range used in the experiments extended from 23.9 N to 688 N. Therefore, for Test 13A the contact behavior is elastic from 23.9 N to 135 N, and elastic-plastic from 135 N to 688 N. For Test 15A, the contact behavior is elastic for the full load range.

For loads greater than 135 N, the effect of elastic-plastic contact behavior must be included in the theoretical resistance predictions for Test 13A. The contact radius within the elastic-plastic load range is larger than predicted by either elastic or plastic theory. Archard (1980) recommended that simple curve fitting blending the theoretical curves for pure elastic and plastic deformation be used to estimate the contact radius within this range.

The theoretical curves for Test 13A are shown in Fig. 8. Within the elastic-plastic transition range, a straight line joining the elastic and plastic theoretical curves is chosen as a convenient estimate of the contact behavior. Actually, this estimate should provide the upper bound on the contact radius within this range. The extended curves for elastic and plastic deformation provide the lower bound for loads less than and greater than F_c, respectively.

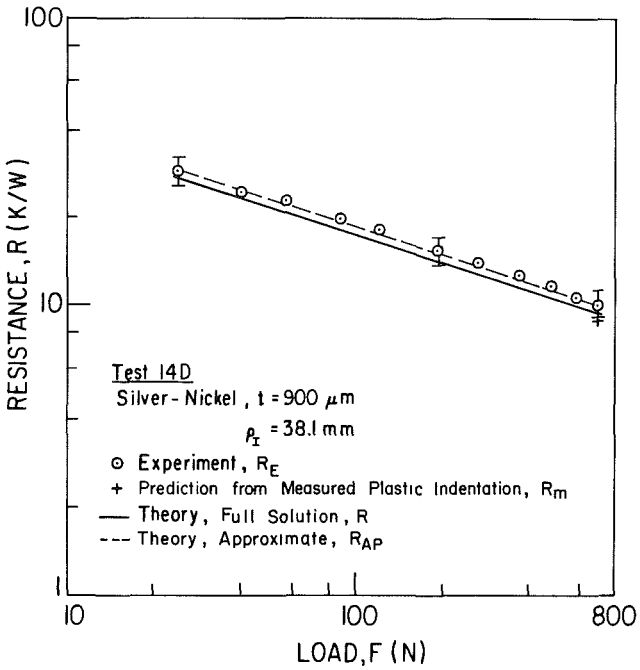

Fig. 10 Resistance versus load for silver-nickel flat; $t = 900$ μm

The theoretical curve including Archard's correction for elastic-plastic behavior is shown as the solid line on Fig. 7 for Test 13A. In the elastic-plastic load range, the agreement between this corrected prediction and the experimental resistance is excellent, with a maximum difference of 3 percent. The pure elastic curve is shown as a dashed line for loads greater than 135 N.

After each test the radius of the resulting plastic indentation, a_m, was measured. The predicted resistance R_m, calculated from a_m, is plotted with a plus (+) sign in Fig. 7.

Layered Flats. Nickel test specimens with silver layers of differing thickness were thermally tested in contact with a steel sphere. In Figs. 9 and 10, experimental resistances are compared to theoretical resistances predicted using the full solution: Chen and Engel's solution to the mechanical portion and Dryden's solution to the thermal portion. For Test 14B (Fig. 9) $\kappa = 5.4$ and $0.1 \leq \tau \leq 0.3$, while for Test 14D (Fig. 10) $\kappa = 5.4$ and $1.35 \leq \tau \leq 4.0$. The probable error bound (±11 percent) is included on representative data points. The theoretical resistance R_m, calculated using the measured plastic indentation a_m, is plotted with a plus (+) sign.

In general, the agreement between the theoretical and experimental resistances is good for the layered tests. For loads less than 135 N, the experimental data are in good agreement with the theoretical predictions. For loads greater than 135 N, the contact behavior for Test 14B (Fig. 9) is elastic-plastic due to plastic yielding of the softer nickel substrate (see Tables 1 and 2). Test 14D does not exhibit this behavior because the hard silver layer is relatively thick. The end of the pure elastic load range for Test 14B is consistent with the bare nickel test (13A), at approximately 135 N, verifying that the soft nickel substrate controls the onset of plastic deformation for this test.

Archard's elastic-plastic correction cannot be directly applied to the layered tests because the layer and substrate

materials have different hardness values. Antonetti and Yovanovich (1985) demonstrated that the contact theory for bare rough conforming surfaces is applicable to coated rough conforming surfaces if the effective hardness of the layer–substrate combination is used. The effective hardness is obtained from the hardness distribution for the particular combination. Therefore, to apply Archard's technique to the layered tests, it is suggested that the effective hardness of the silver/nickel combination be used to predict the critical load. To estimate the elastic-plastic contact radius for a given load, several iterations would be required since the effective hardness and contact radius are interrelated.

Conclusions

A simple analytical model has been developed to approximate the thermal constriction resistance of a sphere in elastic contact with a layered flat. The approximation utilizes the limiting cases of the mechanical portion of the contact problem incorporated with Dryden's solution to the thermal portion. For two examples representing relative extremes in elastic properties for common metallics, the approximation compares favorably to results obtained using the full mechanical and thermal solutions to calculate the constriction resistance.

The analytical models have been verified by comparing experimental resistance measurements to theoretical predictions.

Two different bare flats were tested in contact with a steel sphere: Nickel 200 and Keewatin TS. Excellent agreement is observed between the experimental resistances and theoretical predictions for light loads within the elastic load range. For the nickel test, elastic theory overpredicts the measured resistance at heavy loads due to plastic deformation of the nickel flat. With the theoretical predictions corrected for elastic-plastic contact behavior, excellent agreement between experiment and theory is obtained for the full load range.

Two nickel test specimens with silver layers of different thickness were tested in contact with a steel sphere. Good agreement is observed between the experimental measurements and theoretical predictions for light loads. For heavy loads, elastic theory overpredicts the resistance due to plastic deformation of the nickel substrate. It is suggested that the technique used to correct for elastic-plastic behavior of the bare nickel contact could be applied to the layered contact by introducing the effective hardness of the layer/substrate combination.

Acknowledgments

The authors acknowledge R. Kaptein for technical assistance with the design of the experimental apparatus, A. Hodgson for fabrication of experimental hardware, A. Hegazy for surface roughness measurements, and C. Lane for thermal measurements in Test 15A. N. J. Fisher acknowledges financial support received under the Natural Sciences and Engineering Research Council of Canada Postgraduate Scholarship and the Ontario Graduate Scholarship.

References

Antonetti, V. W., and Yovanovich, M. M., 1985, "Enhancement of Thermal Contact Conductance by Metallic Coatings: Theory and Experiment," ASME JOURNAL OF HEAT TRANSFER, Vol. 107, pp. 513–519.

Archard, J. F., 1980, "Wear Theory and Mechanisms," *Wear Control Handbook*, M. B. Peterson and W. O. Winer, eds., ASME, New York, pp.35–80.

Bar-Cohen, A., Kraus, A. D., and Davidson, S. F., 1983, "Thermal Frontiers in the Design and Packaging of Microelectronic Equipment," *Mechanical Engineering*, pp. 53–59.

Baumeister, T., 1978, *Marks' Standard Handbook for Mechanical Engineers*, 8th ed., McGraw-Hill, New York.

Chen, W. T., and Engel, P. A., 1972, "Impact and Contact Stress Analysis in Multilayer Media," *Int. J. Solids Structures*, Vol. 8, pp. 1257–1281.

Chu, R. C., Hwang, U. P., and Simons, R. E., 1982, "Conduction Cooling for an LSI Package: A One-Dimensional Approach," *IBM J. Res. Develop.*, Vol. 26, No. 1, pp. 45–54.

Dryden, J. R., 1983, "The Effect of a Surface Coating on the Constriction Resistance of a Spot on an Infinite Half Plane," ASME JOURNAL OF HEAT TRANSFER, Vol. 105, No. 2, pp. 408–410.

Hegazy, A. A., 1985, "Thermal Joint Conductance of Conforming Rough Surfaces: Effect of Surface Micro-Hardness Variation," Ph.D. Thesis, University of Waterloo, Canada.

Incropera, F. P., and DeWitt, D. P., 1981, *Fundamentals of Heat Transfer*, Wiley, New York.

Kitscha, W. W., and Yovanovich, M. M., 1975, "Experimental Investigation on the Overall Thermal Resistance of Sphere-Flat Contacts," *Heat Transfer With Thermal Control Applications*, M. M. Yovanovich, ed., Vol. 39, Progress in Astronautics and Aeronautics, AIAA, MIT Press, Cambridge, MA, pp. 93–110.

Negus, K. J., Yovanovich, M. M., and Thompson, J. C., 1985, "Thermal Constriction Resistance of Circular Contacts on Coated Surfaces: Effect of Contact Boundary Conditions," AIAA85-1014, 20th Thermophysics Conference, Williamsburg, VA; accepted for publication in *Journal of Thermophysics and Heat Transfer*.

McGee, G. R., Schankula, M. H., and Yovanovich, M. M., 1985, "Thermal Resistance of Cylinder–Flat Contacts: Theoretical Analysis and Experimental Verification of a Line-Contact Model," *Nuclear Engineering and Design*, Vol. 86, pp. 369–381.

Ogniewicz, Y., and Yovanovich, M. M., 1978, "Effective Conductivity of Regularly Packed Spheres: Basic Cell Model With Constriction," *Heat Transfer and Thermal Control Systems*, L. S. Fletcher, ed., Vol. 60, Progress in Astronautics and Aeronautics, AIAA, New York, pp. 209–228.

Texas Instruments, 1983, "Tl Clad Metals."

Timoshenko, S., and Goodier, J. N., 1951, *Theory of Elasticity*, 2nd ed., McGraw-Hill, New York.

Turyk, P. J., and Yovanovich, M. M., 1985, "Modified Effective Conductivity Models for Basic Cells of Simple Cubic Packed Beds," *Heat Transfer in Porous Media and Particulate Flows*, HTD-Vol. 46, ASME, New York, pp. 9–19.

APPENDIX

Constriction Parameter for a Layered Half-Space

The constriction parameter $\psi(\tau)$ is defined in terms of the substrate thermal conductivity k_S, and is dependent upon the relative layer thickness τ and the conductivity ratio κ

$$\psi(\tau) = 4k_S aR \tag{A1}$$

Dryden (1983) reports expressions for three different ranges of relative layer thickness. For thin layers ($\tau \le 0.01$), a linear approximation is given

$$\psi(\tau) = 1 + \frac{4\tau}{\pi\kappa}(1-\kappa^2), \qquad \tau \le 0.01 \tag{A2}$$

and for thick layers ($\tau \ge 2$), a logarithmic approximation is provided

$$\psi(\tau) = \frac{1}{\kappa} - \frac{2}{\pi\tau\kappa}\ln\left(\frac{2}{1+\kappa}\right), \qquad \tau \ge 2 \tag{A3}$$

For intermediate layer thicknesses ($0.01 < \tau < 2$), Dryden presents a series solution

$$\psi(\tau) = 1 + \frac{4\tau}{\pi\kappa}(1-\kappa^2) + \frac{8}{\pi\kappa}\sum_{j=1}^{\infty}\left[\frac{\kappa-1}{\kappa+1}\right]^j N(\theta_j), \qquad 0.01 < \tau < 2 \tag{A4}$$

where

$$N(\theta_j) = \left[1-e^{-2\phi}\right]^{1/2}\left[e^{\phi} - \frac{e^{-\phi}}{2}\right] + \frac{1}{2}\sin^{-1}(e^{-\phi}) - \frac{\pi}{4} \tag{A5}$$

$$\phi = \ln\left(\frac{\theta_j}{2} + \left[\frac{\theta_j^2}{4}+1\right]^{1/2}\right) \tag{A6}$$

$$\phi_j = 2j\tau \tag{A7}$$

Theory of Rolling Contact Heat Transfer

A. Bejan
Department of Mechanical Engineering
and Materials Science,
Duke University,
Durham, NC 27706
Fellow ASME

This paper addresses the fundamentals of the phenomenon of steady heat transfer by rolling contact between two bodies at different temperatures. The contact region is modeled according to the classical Hertz theory, by which the bodies undergo elastic deformation and the contact area has the shape of an ellipse. In the first part of the study it is shown that when the two bodies make contact continuously over the elliptical area, the overall heat transfer rate is proportional to the square root of the Peclet number based on the ellipse semiaxis parallel to the tangential (rolling) velocity. In the same case the heat transfer rate increases as the square root of the normal force (F) *between the two bodies. The second part of the study treats the case when the rolling contact is made through a large number of asperities (contact sites) distributed over the elliptical contact area. The heat transfer rate is again proportional to the square root of the Peclet number. When the asperities are distributed randomly, the heat transfer rate increases as* $F^{5/6}$. *In the case of regularly distributed asperities that undergo elastic deformation, the heat transfer rate is proportional to* $F^{13/18}$. *The high Peclet number domain covered by this study is discussed in the closing section of the paper.*

1 Background

In this paper we examine the fundamentals of heat transfer by "rolling contact," that is, the steady heat exchange between a roller (cylinder, sphere, torus) and its substrate when a finite temperature difference exists between the two. This very interesting heat transfer phenomenon depends not only on the motion and the thermal properties of the two bodies but also on the size and shape of the "flat spot" over which the rolling contact is made. Furthermore, when at least one of the rolling surfaces is rough, the heat transfer process depends greatly on the distribution of pressure over the contact region. For these reasons we find it appropriate to begin with a brief review of the classical mechanics description of the rolling contact region.

According to Heinrich Rudolf Hertz' (1895) classical theory concerning the pressure between two elastic bodies in contact, the contact area has the shape of an ellipse, while the pressure distribution is represented by a semi-ellipsoid constructed on the contact area. These key features are sketched in Fig. 1, in which the contact surface lies in the plane x–y. It is assumed that the linear dimension of this contact region is considerably smaller than the smallest of the principal radii of curvature of the two body surfaces that come in contact, so that the contact surface is practically plane regardless of the relative elasticity of the two bodies.

The focus is on the heat transfer interaction between the two bodies as they touch and roll without slip over the elliptical contact spot. The effect of heat generation by friction at the contact interface is assumed to be negligible. This effect was investigated by Cameron et al. (1965) in the case of two rolling cylinders having the same temperature.

Let U be the peripheral velocity with which both bodies sweep this area, and let x represent the axis parallel to the peripheral velocity. Sufficiently far from the contact area the temperatures of the two bodies are uniform (T_1 and T_2). The elastic and thermal properties of the upper body ("body No. 1") are generally not the same as those of the lower body ("body No. 2"). In the present analysis the two sets of properties are distinguished by the subscripts $(\,)_1$ and $(\,)_2$, while each property symbol is defined in the Nomenclature.

We begin with the observation that the "elasticity" problem of determining the size of the contact area is decoupled from the heat transfer problem addressed in this study. Key results of the Hertz theory are two formulas for calculating the size of the semiaxes of the contact area (see also Timoshenko and Goodier, 1970)

$$a = M\left[\frac{3\pi(K_1+K_2)}{4(A+B)}F\right]^{1/3} \tag{1}$$

$$b = N\left[\frac{3\pi(K_1+K_2)}{4(A+B)}F\right]^{1/3} \tag{2}$$

where F is the total force with which one body pushes against the other, and where

$$K_1 = \frac{1-\nu_1^2}{\pi E_1} \text{ and } K_2 = \frac{1-\nu_2^2}{\pi E_2} \tag{3}$$

Parameters A and B are purely geometric, and are given by the relations

$$2(A+B) = \frac{1}{R_1}+\frac{1}{R_1'}+\frac{1}{R_2}+\frac{1}{R_2'} \tag{4}$$

$$2(B-A) = \left[\left(\frac{1}{R_1}-\frac{1}{R_1'}\right)^2+\left(\frac{1}{R_2}-\frac{1}{R_2'}\right)^2 + 2\left(\frac{1}{R_1}-\frac{1}{R_1'}\right)\left(\frac{1}{R_2}-\frac{1}{R_2'}\right)\cos 2\psi\right]^{1/2} \tag{5}$$

where (R_1, R_1') and (R_2, R_2') are the principal radii of curvature of the two body surfaces in the vicinity of the rolling

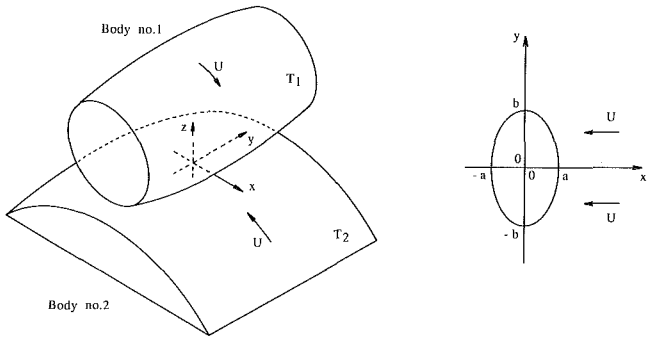

Fig. 1 The elliptical contact area between two elastic bodies in rolling contact

Contributed by the Heat Transfer Division for publication in the JOURNAL OF HEAT TRANSFER. Manuscript received by the Heat Transfer Division November 30, 1987. Keywords: Conduction, Materials Processing and Manufacturing Processes.

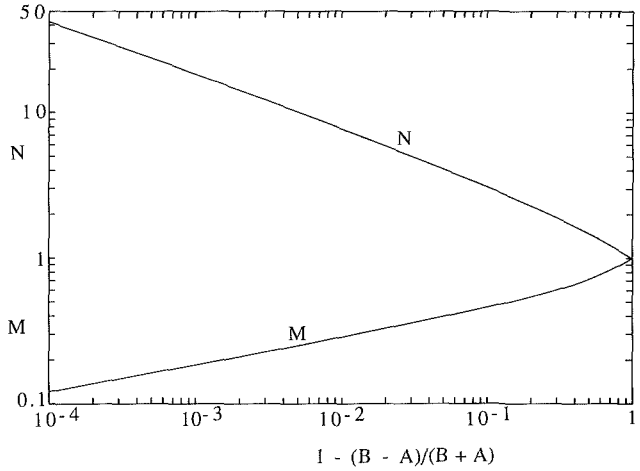

Fig. 2 The dimensionless coefficients proportional to the semiaxes of the elliptical area of elastic contact, equations (1) and (2)

contact region, and where ψ if the angle between the normal planes containing the curvatures $1/R_1$ and $1/R_2$. In these expressions a curvature term such as $1/R_1$ is considered positive if the center of curvature from which the radius R_1 is drawn is located inside body No. 1. According to this convention, in the first sketch of Fig. 1 all the curvatures are positive.

Finally, the coefficients M and N of equations (1) and (2) are geometric also, as they depend only on the dimensionless group $(B-A)/(A+B)$. This dependence is tabulated for small values of this group in Timoshenko and Goodier (1970) and for large values in Kornhauser (1951). In order to make the present heat transfer theory self standing, I combined the information from these two sources to construct Fig. 2 as a means for evaluating M and N. The use of the double logarithmic grid and, especially, the group $[1-(B-A)/(B+A)]$ on the abscissa makes the M and N curves appear almost as straight lines over the entire domain.

The pressure distribution over the elliptical contact area is given by

$$P(x,y)=P_0\left[1-\left(\frac{x}{a}\right)^2-\left(\frac{y}{b}\right)^2\right]^{1/2} \tag{6}$$

where P_0 is the maximum pressure located in the center of the contact spot

$$P_0=\frac{3}{2}\left(\frac{F}{\pi ab}\right) \tag{7}$$

Worth noting at this stage is the size of the contact area, πab, and the average pressure exerted on this area, $F/(\pi ab)$. Simpler versions of these results can be written by inspection for those two-body arrangements involving cylinders (for body No. 1, for example, $R_1'=\infty$), spheres ($R_1=R_1'$) and plane surfaces ($R_1=R_1'=\infty$). They can also be found in the elasticity textbooks and handbooks. The important conclusion to retain as we investigate the heat transfer problem is that the geometry and pressure distribution of the rolling (elliptical) contact spot are known.

2 Continuous Contact

Consider now the case where the two surfaces are polished to such an extent that they make contact at every point over the elliptical contact area sketched in Fig. 1. Figure 3 shows what appears in the cut made by a plane that is parallel to the x axis and perpendicular on the x-y plane. The two bodies touch as they travel with the same speed the distance

$$L(y)=2a\left[1-\left(\frac{y}{b}\right)^2\right]^{1/2} \tag{8}$$

Note that the longitudinal coordinate ξ of Fig. 3 points in the negative x direction and has as origin the leading edge of the elliptical contact spot shown in Fig. 1.

There is a range of sufficiently high speeds U in which the temperature distributions on both sides of the contact line are of the boundary layer type. This range is identified at the end of this section [see equations (21)]. Looking at the upper body first, we recognize the energy equation for boundary layer convection in a constant property solid, which reduces to

$$U\frac{\partial T}{\partial \xi}=\alpha_1\frac{\partial^2 T}{\partial z^2} \tag{9}$$

Nomenclature

a,b = semiaxes of elliptical elastic contact area, equations (1) and (2)
A, B = geometric parameters, equations (4) and (5)
c = specific heat, appearing always in the group "ρck"
c = radius of contact site disk, Fig. 4
e = outer radius of annular area in which the bodies do not touch, Fig. 4
E = modulus of elasticity
E^* = effective modulus of elasticity, equation (30)
F = normal contact force
G = function, equation (32)
H = microhardness of the softer material
k = thermal conductivity
K = elasticity parameter, equation (3)
L = length of sweep, equation (8)
m = dummy variable
M, N = coefficients of the ellipse semiaxes, equations (1) and (2) and Fig. 2
P = nominal pressure
P_0 = maximum pressure (the value of P at $x=y=0$)
Pe = Peclet number based on the a semiaxis, equation (19)
q = heat transfer rate, W
q' = heat transfer rate per unit length, W/m
q'' = heat flux, W/m^2
$\tilde{q}''$ = heat flux, W/m^2, equation (23)
Q = heat transfer interaction, J
R, R' = radii of curvature
t = time
T = temperature
T_0 = contact temperature, or interface temperature, equation (16)
U = peripheral velocity with which both bodies sweep the elliptic contact area
x = direction parallel to U, pointing against U
y = direction normal to x, also in the plane of the elliptic contact spot
z = direction normal to the plane x-y, pointing toward body No. 1
α = thermal diffusivity
Δ = amplitude of regular two-dimensional wave roughness
κ_s = mean curvature of the asperity summits
ν = Poisson's ratio
ξ = longitudinal coordinate, Fig. 3
ρ = density
σ_s = standard deviation of the asperity heights
ψ = angle defined under equation (5)
$()_1$ = property of body No. 1
$()_2$ = property of body No. 2

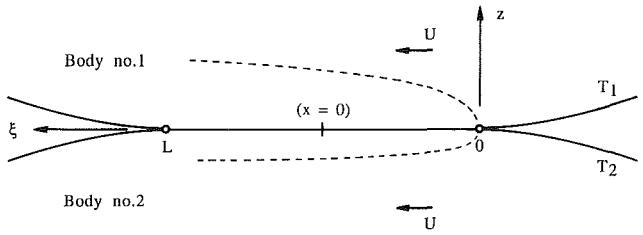

Fig. 3 Conjugate parallel boundary layers on the two sides of the continuous contact surface

where the longitudinal velocity U is constant. The temperature boundary conditions are

$$T = T_1 \text{ at } \xi = 0 \text{ and } z > 0 \tag{10}$$

$$T \to T_1 \text{ as } z \to \infty \tag{11}$$

$$T = T_0 \text{ at } z = 0 \tag{12}$$

in which we assume further that the interface temperature T_0 is constant (i.e., ξ independent). This assumption will be verified later by the requirement that the wall heat flux distributions of the two boundary layers solutions must match at the interface [see equation (16)].

In the field of convection, the problem stated in equations (9)–(12) is analytically the same as that of forced convection boundary layer heat transfer over an isothermal surface imbedded in a saturated porous medium, or the zero-Prandtl-number limit of the Pohlhausen solution (Bejan, 1984). Its solution is analogous to the much older solution for transient conduction into a semi-inifinite solid (Carslaw and Jaeger, 1959)

$$\frac{T - T_0}{T_1 - T_0} = \text{erf}\left[\frac{z}{2}\left(\frac{U}{\alpha_1 \xi}\right)^{1/2}\right] \tag{13}$$

Of greater interest here is the corresponding result for the heat flux distribution along the interface (the heat flux leaving body No. 1)

$$q_1'' = \pi^{-1/2} k_1 (T_1 - T_0)\left(\frac{U}{\alpha_1 \xi}\right)^{1/2} \tag{14}$$

The same solution can be invoked in connection with the slug-flow boundary layer problem that resides on the underside of the interface. The heat flux received by body No. 2 from the interface is therefore

$$q_2'' = \pi^{-1/2} k_2 (T_0 - T_2)\left(\frac{U}{\alpha_2 \xi}\right)^{1/2} \tag{15}$$

The heat flux continuity condition at the interface, $q_1'' = q_2''$, indicates that the interface attains a special (constant) temperature between T_1 and T_2, such that

$$\frac{T_0 - T_2}{T_1 - T_2} = \frac{(\rho c k)_1^{1/2}}{(\rho c k)_1^{1/2} + (\rho c k)_2^{1/2}} \tag{16}$$

Worthy of note is that the value of the contact temperature level T_0 is ruled by the dimensionless group $(\rho ck)_1/(\rho ck)_2$; this feature is found also in the calculation of the contact temperature between two semi-infinite solids that are placed suddenly in contact along a perfectly smooth plane (Grigull and Sandner, 1984).

What remains now is to calculate the total heat transfer rate through the elliptical contact spot. The heat transfer rate collected over the contact line of length $L(y)$ is, cf. equation (14),

$$q'(y) = \int_0^L q_1'' d\xi = 2\pi^{-1/2} k_1 (T_1 - T_0)\left(\frac{UL}{\alpha_1}\right)^{1/2} \tag{17}$$

The total heat transfer rate is obtained by integrating this last result in the transverse direction along the contact spot

$$q = \int_{-b}^{b} q'(y)\,dy = 2.789 k_1 b (T_1 - T_0)\text{Pe}_1^{1/2} \tag{18}$$

in which Pe_1 is the Peclet number based on the longitudinal semiaxis (a) and on the thermal diffusivity of the upper body,

$$\text{Pe}_1 = \frac{Ua}{\alpha_1} \tag{19}$$

Recalling equation (16), the same conclusion can be catalogued in the form of an overall conductance to heat transfer through the elliptical contact spot

$$\frac{q}{T_1 - T_2} = 2.789 \frac{(\rho ck)_2^{1/2}}{(\rho ck)_1^{1/2} + (\rho ck)_2^{1/2}} k_1 b \text{Pe}_1^{1/2} \tag{20}$$

Since both semiaxes increase as $F^{1/3}$ [see equations (1) and (2)], we learn now that the thermal conductance increases as $F^{1/2}$.

The conjugate boundary layer arrangement on which this analysis is based (Fig. 3) is valid when both boundary layers are sufficiently "slender." One can see from the argument of the similarity error-function solution (13) that the boundary layer thickness scales are $(\alpha_1 a/U)^{1/2}$ above and $(\alpha_2 a/U)^{1/2}$ below the interface; therefore, the slenderness conditions translate into the following simultaneous requirements

$$\text{Pe}_1 \gg 1 \text{ and } \text{Pe}_2 \gg 1 \tag{21}$$

Another assumption that has been made implicitly in writing equation (9) is that the effect of transversal thermal diffusion (in the y direction) is negligible relative to that in the vertical direction. The temperature solution (13) depends on y through ξ, which has its origin on the leading edge of the contact region. The elliptical shape suggests that the gradient $\partial/\partial y$ becomes significant near the lateral extremities of the contact region ($y = \pm b$). Writing Δy for the segment $(b - y)$ near the $y = b$ extremity, it is easy to show that in body No. 1 the assumption of negligible lateral diffusion ($\partial^2/\partial y^2 \ll \partial^2/\partial z^2$) breaks down in an end region of length scale

$$\Delta y \sim b\left(\frac{b}{a}\text{Pe}_1\right)^{-2} \tag{22}$$

In view of the first of the inequalities (21) we conclude that Δy is negligible when compared with b, in other words, that the boundary layer solutions developed in this section apply over practically the entire contact region. A similar conclusion is reached when analyzing the validity of neglecting lateral diffusion in body No. 2, for which Pe_2 replaces Pe_1 in the conclusion represented by equation (22). The high-Pe conditions (21) are discussed further in section 4.

An alternative derivation of the heat transfer formula (20) was suggested by one of the reviewers of the original manuscript of this paper. This alternative begins with the observation that to an observer who rides on body No. 1, the conduction effect is unidirectional, that is, in the direction normal to the contact surface. This feature is due to the neglect of conduction in the x and y directions in the boundary layer formulation of Fig. 3. Relative to the observer, the instantaneous heat flux experienced by body No. 1 at a point of contact is given by the classical formula for transient heat conduction between two semi-infinite solids (Grigull and Sandner, 1984)

$$\tilde{q}_1''(t) = k_1 (T_1 - T_0)(\pi \alpha_1 t)^{-1/2} \tag{23}$$

The instantaneous distribution of heat flux over the contact area, $\tilde{q}_1''(x, y)$, is obtained by noting that the life of the transient conduction phenomenon (23) begins when the contact point enters the elliptical area (i.e., at $\xi = 0$ in Fig. 3), and ends when the point leaves this area [at $\xi = L(y)$]. The relationship between time and the longitudinal position of the contact point is $t = \xi/U$, which can be substituted into equation (23),

to obtain $\tilde{q}_1''(\xi)$. Next, integrating $\tilde{q}_1''(\xi)$ from $\xi=0$ to $\xi=L(y)$ leads to exactly the same heat transfer rate per unit length result $q'(y)$ as in equation (17). The final step in this alternative analysis is identical to the one taken between equations (17) and (20). The numerical coefficient in equation (20) is the result of evaluating the following integral numerically:

$$\left(\frac{32}{\pi}\right)^{1/2}\int_0^1 (1-m^2)^{1/4}dm = 2.789 \tag{24}$$

3 Discrete Contact

The rolling contact heat transfer phenomenon is considerably more complicated when the contact is effected through the asperities of the two surfaces involved. This aspect comes into play not only when at least one of the surfaces is "rough," but also when the surfaces are relatively smooth and the normal load F approaches zero.

The issue of how an array of asperities impedes the conduction between two stationary bodies has been treated extensively in the heat transfer subfield titled "Thermal Contact Resistance." The problem has been studied both in the steady state (e.g., Fenech and Rohsenow, 1963; Cooper et al., 1969; Yovanovich, 1969; Mikic and Carnasciali, 1970) and in the unsteady state that follows the establishment of a sudden light-pressure contact between two stationary bodies (e.g., Davies, 1959; Heasley, 1965; Schneider et al., 1977). Overviews of this field can be found in monographs by Yovanovich (1975) and Fletcher (1978), and in a recent review by Yovanovich (1986).

Plastic Deformation. In the original version of this paper (Bejan, 1988) I relied on a discrete-contact model that has been used frequently in the past. The model consists of a *uniform* distribution of asperities (Fig. 4), the peaks of which are flattened by plastic deformation. Each contact site is represented by a circular area of radius c, surrounded by an annular area of radius e, in which the two bodies do not touch. The vertical force balance over the area of one contact site requires $\pi e^2 P = \pi c^2 H$, where P is the local nominal pressure [equation (6)] and H is the microhardness of the softer of the two materials. This model contains therefore the assumption that the real contact area is proportional to the nominal pressure P

$$\frac{\text{real contact area}}{\text{unit nominal area}} = \frac{P(x,y)}{H} \tag{25}$$

The variation of P with both x and y across the Hertz ellipse (Fig. 1) was accommodated by allowing the radius of each contact site (c) to vary (Fig. 4). The final heat transfer result produced by this analysis is discussed at the end of this subsection.

In place of the analysis based on the model of Fig. 4 (Bejan, 1988), in this section I outline two more direct alternatives that have been suggested by the reviewers. The first alternative is based on the observation that if equation (20) represents the overall heat transfer rate through the elliptical contact area, then the heat transfer rate in the present case can be calculated approximately by multiplying equation (20) by the area ratio (25). Using instead of $P(x, y)$ the ellipse-averaged pressure $2P_0/3$, equation (7), the answer to the discrete-contact heat transfer problem becomes

$$\frac{q}{T_1-T_2} \cong 1.860\frac{(\rho ck)_2^{1/2}}{(\rho ck)_1^{1/2}+(\rho ck)_2^{1/2}} k_1 b \mathrm{Pe}_1^{1/2}\frac{P_0}{H} \tag{26}$$

The second alternative is based on the more modern view that the size of one contact site is insensitive to pressure changes, and that the higher nominal pressures near the center of the ellipse are accommodated by the formation of a denser population of contact sites (see Johnson, 1985, and references

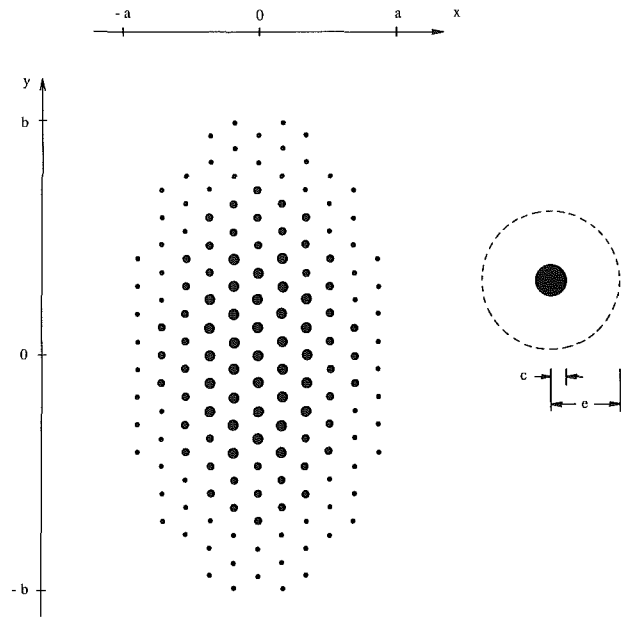

Fig. 4 Uniform distribution of disk-shaped contact sites over the elliptical elastic contact area of Fig. 1

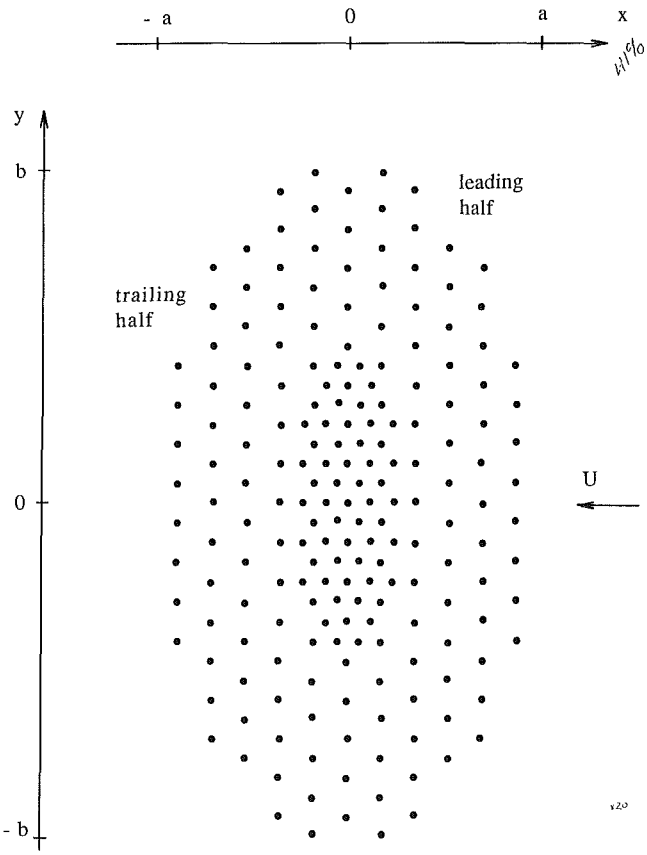

Fig. 5 Nonuniform distribution of contact sites over the elliptical elastic contact area of Fig. 1

therein; e.g., Nayak, 1971; Whitehouse and Phillips, 1978, 1982; Greenwood, 1984). This new model is illustrated in Fig. 5 by means of only two different asperity densities; the contact sites travel to the left with the velocity U, across the elliptical image. New contact sites are being generated over the entire half-ellipse $x>0$, while the trailing half is the area over which the contact sites expire.

The analysis consists of applying the unidirectional tran-

sient heat conduction result (23) to each contact site that "lives" inside the elliptical area, and then integrating the result over all the contact sites that are generated per unit time in the leading half of the ellipse. According to equation (25), any nominal area element $dxdy$ of the ellipse contains "$(P/H)dxdy$)" real contact area. This real contact area content varies from one point (x, y) to the next, particularly in the longitudinal direction x. The derivative $-\partial(P/H)/\partial x$ is proportional to the increase in contact site density as the eye sweeps the leading half of the ellipse from right to left. The local rate of new contact area formation [m^2/s] at a point in the leading half of the ellipse ($x>0$) is therefore $[-\partial(P/H)/\partial x]U\,dxdy$.

Each contact site that is generated at a point (x, y) in the leading half expires "symmetrically" at the point $(-x, y)$ in the trailing half of the ellipse. Its lifetime is therefore equal to $2x/U$, and its total contribution [J/m^2] to the heat transfer between the two bodies is obtained by integrating equation (23) from $t=0$ to $t=2x/U$. Multiplying the result of this integration with the rate of new contact area formation that concluded the preceding paragraph, we obtain the heat transfer rate [W] contributed by the nominal area element $dxdy$

$$\frac{2^{3/2}}{\pi^{1/2}}(T_1-T_0)[U(\rho ck)_1]^{1/2}\frac{P_0}{a^2H}\left[1-\left(\frac{x}{a}\right)^2-\left(\frac{y}{b}\right)^2\right]^{-1/2}x^{3/2}dxdy \tag{27}$$

Finally, integrating this result over the $x>0$ half of the elliptical area yields the total heat transfer rate between the two bodies

$$\frac{q}{T_1-T_2}=\frac{2^{5/2}\pi^{1/2}}{5}\frac{(\rho ck)_2^{1/2}}{(\rho ck)_1^{1/2}+(\rho ck)_2^{1/2}}k_1 b\mathrm{Pe}_1^{1/2}\frac{P_0}{H} \tag{28}$$

The leading numerical coefficient in this final result is equal to 2.005. The heat transfer rate estimate based on equation (28) is therefore only 7.2 percent higher than the approximate result based on equation (26). The original analysis (Bejan, 1988) produced a heat transfer rate formula similar to equations (26) and (28), except that in it the leading numerical coefficient is 1.76. Among these three alternatives, the preferable one is equation (28) because it is based on the most realistic model (Fig. 5), and because it accounts accurately for the heat transfer contributed by each contact site during its life in the elliptical contact region.

Elastic Deformation of Random Asperities. The method centered on Fig. 5 is to be preferred also because of its versatility. Consider a case in which the nominal pressure is sufficiently low so that the two bodies experience elastic deformations around their mutual and random contact sites. A good correlation for the real contact area in this regime is (Greenwood and Williamson, 1966; also in Johnson, 1985)

$$\frac{\text{real contact area}}{\text{unit nominal area}}=\left(\frac{\pi}{\sigma_s\kappa_s}\right)^{1/2}\frac{P}{E^*} \tag{29}$$

where E^* is the effective modulus of elasticity of the two solids

$$\frac{1}{E^*}=\frac{1-\nu_1^2}{E_1}+\frac{1-\nu_2^2}{E_2} \tag{30}$$

σ_s is the standard deviation of the asperity heights, and κ_s is the mean curvature of the asperity summits. Comparing equation (29) with equation (25), we see that the analysis of the present case leads to a final result just like equation (28), in which H is now replaced by the quantity $(\sigma_s\kappa_s/\pi)^{1/2}E^*$. Criteria for distinguishing between elastically and plastically deformed asperities are discussed by Johnson (1985, pp. 415–416).

Elastic Deformation of Regular Asperities. It is found that when the asperities are arranged in a regular array the real contact area is not proportional to the nominal pressure P, as was the case in equations (25) and (29). (In Figs. 4 and 5, the "regular" array of dots was used only for the purpose of simplifying the drawings). In the case of two-dimensional wavy roughness undergoing elastic deformation, the real contact area increases as $P^{2/3}$ (Johnson, 1985):

$$\frac{\text{real contact area}}{\text{unit nominal area}}=\left(\frac{P}{G}\right)^{2/3} \tag{31}$$

The symbol G is shorthand for the expression

$$G=1.503(\kappa_s\Delta)^{3/4}E^* \tag{32}$$

in which Δ is the amplitude of the wave.

The analytical steps outlined en route to equations (27) and (28) can be repeated, by starting in this case with equation (31) instead of equation (25). The end result of this new analysis is the overall heat transfer rate formula

$$\frac{q}{T_1-T_2}=2.19\frac{(\rho ck)_2^{1/2}}{(\rho ck)_1^{1/2}+(\rho ck)_2^{1/2}}k_1 b\mathrm{Pe}_1^{1/2}\left(\frac{P_0}{G}\right)^{2/3} \tag{33}$$

in which the numerical coefficient is based on evaluating two integrals numerically

$$2.19=\frac{2^{7/2}}{3\pi^{1/2}}\left(\int_0^1\frac{dm}{(1-m^2)^{2/3}}\right)\left(\int_0^1\frac{m^{3/2}dm}{(1-m^2)^{1/6}}\right) \tag{34}$$

4 Observations

(*i*) The discrete-contact heat transfer results developed in the preceding section do not depend on the actual size of one contact site (radius c in Fig. 4). This feature is due to the unidimensionality of the transient heat conduction process, when it is viewed in a frame of reference attached to the contact site. When the "local" conduction phenomenon is unidirectional (i.e., at high Peclet numbers; see (*v*) below), all parts of the contact site area contribute equally to the heat transfer through that site. What is important is not the size and shape of each contact site, but the distribution of real contact area per unit nominal area, equations (25), (29), and (31).

(*ii*) The discrete-contact heat transfer rate depends strongly on the total normal force F. Note first that the semiaxes a and b increase as $F^{1/3}$, which means that the maximum pressure P_0 increases as $F^{1/3}$ also. In the case of plastically flattened asperities, equation (28), these trends imply that the heat transfer rate increases as $F^{5/6}\cong F^{0.83}$. The normal force has the same effect on the heat transfer rate when the contact is made through random asperities that undergo elastic deformations, equation (29).

In the case of regular two-dimensional asperities under elastic deformation, equation (33), the total heat transfer rate q increases as $F^{13/18}\cong F^{0.72}$. The effect of F is therefore slightly less pronounced than in the random-asperity cases reviewed in the preceding paragraph.

(*iii*) It has been assumed throughout section 3 that the presence of discrete contact sites (asperities) does not affect the size and shape of the macroscopic region (the Hertz ellipse, Fig. 1). Greenwood and Tripp (1967) showed that this assumption holds at sufficiently high loads, for example, when the combined roughness of the two surfaces (σ_s) is less than 5 percent of the bulk elastic compression of the touching bodies (Johnson, 1985, p. 420).

(*iv*) Another assumption that has been adopted throughout the preceding analyses is that the elastic deformations that produce the Hertz ellipse (Fig. 1) are not coupled to the temperature variations that occur in the vicinity of the contact region. In real life, the temperature gradients induce thermal stresses that, in turn, influence the equilibrium shape of the contact region. The coupled problem of "thermoelastic

contact'' has received considerably less attention in the mechanics literature than the isothermal (Hertzian) contact problem on which the present heat transfer study is built. An overview of this relatively unexplored area is presented by Johnson (1985, Chap. 12). For example, the thermoelastic contact with heat generation between a cylinder sliding on a flat surface was studied recently by Hills and Barber (1986). The formulation of the continuous contact problem of section 2 as a problem of thermoelastic contact may be a worthy topic for furture research, particularly in the field of thermoelasticity.

(*v*) The most critical limitation of the analytical results developed in this paper stems from the high Peclet numbers (high peripheral speeds, large contact areas) that are being assumed. In the continuous contact problem, equation (21), the high Peclet numbers are necessary in order to preserve the slenderness of the boundary layer structure of Fig. 3, or the unidirectionality of the transient conduction process discussed before equation (23).

In the case of rolling via discrete contact, the high Peclet number conditions are even more restrictive than the inequalities (21). The unidirectionality of the single-site transient conduction process analyzed in section 3 is maintained as long as the Fourier numbers based on site radius (c) are small

$$\frac{\alpha_1 t}{c^2} \ll 1, \qquad \frac{\alpha_2 t}{c^2} \ll 1 \tag{35}$$

Schneider et al. (1977) have shown that three-dimensional conduction effects become predominant when these numbers are of the order of 1 or greater than 1. In the present problem, the lifetime of an individual contact site is of the order of a/U or smaller; therefore, the inequalities (35) become

$$\mathrm{Pe}_1^{1/2} \gg \frac{a}{c}, \qquad \mathrm{Pe}_2^{1/2} \gg \frac{a}{c} \tag{36}$$

Since the ratio a/c is considerably greater than one, this new set of inequalities is more stringent than in equations (21).

(*vi*) The high-Pe limitations emphasized above may raise questions about the practical applicability of the present heat transfer results. I became interested in the present topic while thinking about the heat transfer process that occurs between an automobile tire and the road surface. This is why as a first model for the discrete-contact problem I chose Fig. 4. In general, the rolling-heating or cooling of a body of rubber can be quite complicated, if one considers simultaneously the conduction in the two solids, the heat generated by friction, the convection to the atmosphere and, as in the case of a car driving on ice or packed snow, the superficial melting and lubrication.

I decided then to study this complicated process one phenomenon at a time, with the thought that only in the end—when all the pieces of the puzzle are known—I can assess the relative importance of the individual phenomena. In my first paper in this area I focused exclusively on the melting and lubrication phenomenon (Bejan, 1989). In this second paper I focused exclusively on the heat transfer *through* the region of contact. From my point of view, the practical application of this study is that it contributes to building a reasoned theoretical description for what can be a very complicated phenomenon.

As an aside, the work that I am beginning with these two papers is a comment on what I think the heat transfer community can contribute to the field of tribology. One approach to the study of a complex phenomenon is to compose the most ''realistic'' (i.e., complicated) model, and to watch what happens when the many relevant parameters are allowed to vary. Such an approach obscures the theoretical reasons for why the process responds in certain ways when certain parameters vary. The alternative approach—the one that I have adopted—is to study one facet of the process, and to understand it before moving on to the next facet.

Returning to the tire-on-road example mentioned earlier, the Peclet numbers Pe_1, Pe_2 can have extremely high values. For example, taking $U \sim 50$ km/h and $a = 10$ cm as representative orders of magnitude, the Peclet numbers for vulcanized soft rubber, asphalt, and ice are $(2.4)10^7$, $(4.4)10^7$, and $(1.4)10^6$, respectively. These calculations are based on the thermal diffusivity information provided by Incropera and DeWitt (1985). Peclet numbers of order 10^6–10^7 are compatible with the validity criteria (21) and (36).

Another potential application that came to my attention recently (Zumbrunnen, 1988) is the high-speed casting and cooling of a continuous metal slab. The speed of the slab is of order 50 km/h or higher. Assuming $a \sim 1$ cm for the steel-on-steel contact between the hot slab and one cold roller, the calculated Peclet numbers are both of order $(1.4)10^4$.

Acknowledgments

This work was supported by the National Science Foundation through Grant no. CBT-8711369.

I appreciate very much the constructive suggestions that were made by the three reviewers of the original manuscript. Their suggestions have been identified in sections 2 and 3 of the present text.

References

Bejan, A., 1984, *Convection Heat Transfer*, Wiley, New York, pp. 52, 357.

Bejan, A., 1988, ''Theory of Rolling Contact Heat Transfer,'' Report DU-AB-7, Department of Mechanical Engineering and Materials Science, Duke University, Durham, NC.

Bejan, A., 1988, ''The Process of Melting by Rolling Contact,'' *International Journal of Heat and Mass Transfer*, Vol. 31, pp. 2273–2283.

Cameron, A., Gordon, A. N., and Symm, G. T., 1965, ''Contact Temperatures in Rolling/Sliding Surfaces,'' *Proc. Royal Society*, Vol. A286, pp. 45–61.

Carslaw, H. S., and Jaeger, J. C., 1959, *Conduction of Heat in Solids*, 2nd ed., Oxford University Press, Oxford, United Kingdom, p. 51.

Cooper, M. G., Mikic, B. B., and Yovanovich, M. M., 1969, ''Thermal Contact Conductance,'' *International Journal of Heat and Mass Transfer*, Vol. 12, pp. 279–300.

Davies, W., 1959, ''Thermal Transients in Graphite-Copper Contacts,'' *British Journal of Applied Physics*, Vol. 10, pp. 516–522.

Fenech, H., and Rohsenow, W. M., 1963, ''Prediction of Thermal Conductance of Metallic Surfaces in Contact,'' ASME JOURNAL OF HEAT TRANSFER, Vol. 85, pp. 15–24.

Fletcher, L. S., ed., 1978, *Heat Transfer and Thermal Control Systems*, (Progress in Astronautics and Aeronautics, Vol. 60), AIAA, New York.

Greenwood, J. A., 1984, ''A Unified Theory of Surface Roughness,'' *Proc. Royal Society*, Vol. A393, pp. 133–157.

Greenwood, J. A., and Tripp, J. H., 1967, ''The Elastic Contact of Rough Spheres,'' ASME *Journal of Applied Mechanics*, Vol. 34, pp. 153–159.

Greenwood, J. A., and Williamson, J. B. P., 1966, ''Contact of Nominally Flat Surfaces,'' *Proc. Royal Society*, Vol. A295, pp. 300–319.

Grigull, U., and Sandner, H., 1984, *Heat Conduction*, translated by J. Kestin, Springer-Verlag, Berlin, p. 81.

Heasley, J. H., 1965, ''Transient Heat Flow Between Contacting Solids,'' *International Journal of Heat and Mass Transfer*, Vol. 8, pp. 147–154.

Hertz, H. R., 1895, *Gesammelte Werke*, J. A. Barth, Leipzig, Vol. 1, p. 155.

Hills, D. A., and Barber, J. R., 1986, ''Steady Sliding of a Circular Cylinder Over a Dissimilar Thermally Conducting Half-Plane,'' *Int. J. Mech. Sci.*, Vol. 28, pp. 613–622.

Incropera, F. P., and DeWitt, D. P., 1985, *Fundamentals of Heat and Mass Transfer*, 2nd ed., Wiley, New York, pp. 765–766.

Johnson, K. L., 1985, *Contact Mechanics*, Cambridge University Press, Cambridge, United Kingdom, Chap. 13.

Kornhauser, M., 1951, ''A Note on Elastic Surface Deformation,'' ASME *Journal of Applied Mechanics*, Vol. 18, pp. 251–252.

Mikic, B., and Carnasciali, G., 1970, ''The Effect of Thermal Conductivity of Plating Material on Thermal Contact Resistance,'' ASME JOURNAL OF HEAT TRANSFER, Vol. 92, pp. 475–482.

Nayak, P. R., 1971, ''Random Process Model of Rough Surfaces,'' ASME *Journal of Lubrication Technology*, Vol. 93, pp. 398–407.

Schneider, G. E., Strong, A. B., and Yovanovich, M. M., 1977, ''Transient Thermal Response of Two Bodies Communicating Through a Small Circular Contact Area,'' *International Journal of Heat and Mass Transfer*, Vol. 20, pp. 301–307.

Timoshenko, S. P., and Goodier, J. N., 1970, *Theory of Elasticity*, 3rd ed., McGraw-Hill, New York, p. 416.

Whitehouse, D. J., and Phillips, M. J., 1978, "Discrete Properties of Random Surfaces," *Phil. Trans. Royal Society*, Vol. A290, pp. 267–298.

Whitehouse, D. J., and Phillips, M. J., 1982, "Two-Dimensional Discrete Properties of Random Surfaces," *Phil. Trans. Royal Society*, Vol. A305, pp. 441–468.

Yovanovich, M. M., 1969, "Overall Constriction Resistance Between Contacting Rough, Wavy Walls," *International Journal of Heat and Mass Transfer*, Vol. 12, pp. 1517–1520.

Yovanovich, M. M., ed., 1975, *Heat Transfer With Thermal Control Applications* (Progress in Astronautics and Aeronautics, Vol. 39), MIT Press, Cambridge, MA.

Yovanovich, M. M., 1986, "Recent Developments in Thermal Contact, Gap and Joint Conductance Theories and Experiment," *Heat Transfer 1986*, Vol. 1, C. L. Tien, V. P. Carey, and J. K. Ferrell, eds., Hemisphere, Washington, DC, pp. 35–45.

Zumbrunnen, D. A., 1988, "A Study of Heat Transfer From Moving and Stationary Plates Cooled by Planar Jets of Water," seminar given in the Dept. Mechanical Eng. Materials Sci., Duke University, Durham, NC, Feb. 25, based on a Ph.D. thesis, School of Engineering, Purdue University, West Lafayette, IN.

Comprehensive Room Transfer Functions for Efficient Calculation of the Transient Heat Transfer Processes in Buildings

J. E. Seem
S. A. Klein
W. A. Beckman
J. W. Mitchell

Solar Energy Laboratory,
University of Wisconsin-Madison,
Madison, WI 53706

This paper describes a method in which the transfer functions describing heat flows in building elements can be combined into a single transfer function for an enclosure, referred to as a comprehensive room transfer function (CRTF). The method accurately models long-wave radiation exchange and convection in an enclosure through an approximate network, referred to as the "star" network. Resistances in the star network are determined from a network that uses view factors to model long-wave radiation exchange. The Padé approximation and bilinear transformation are used to reduce the number of coefficients in a CRTF.

Introduction

Year-long simulations of the heating and cooling loads of buildings are important for sizing heating, ventilating, and air conditioning equipment, determining the effect of a design change or retrofit on energy usage, and developing optimal control strategies. Accurate calculation of building loads involves the long-time solution of transient conduction, convection, and radiation heat transfer processes. Calculation of these loads requires significant computational effort.

Transfer function methods are more efficient for solving long-time transient heat transfer problems than Euler, Crank-Nicolson, or other classical techniques. Transfer functions relate the output of a linear, time-invariant system to a time series of current and past inputs, and past outputs. Inputs are modeled by a continuous, piecewise linear curve or equivalently, a series of triangular pulses.

The definition of transfer function used in the field of heat transfer in buildings is different from that used in the field of automatic controls. In automatic controls, a transfer function is the Laplace or z transform of the output divided by the Laplace or z transform of the input. In heat transfer, a transfer function is a difference equation that relates the outputs of a linear, time-invariant system to a time series of current and past inputs, and a time series of past outputs. In this paper, the latter definition will be used. Also, this paper uses Laplace transfer function as the definition for the Laplace transform of the output divided by the Laplace transform of the input and z-transfer function as the definition for the z transform of the output divided by the z transform of the input.

There are a number of methods available for calculating transfer functions. Stephenson and Mitalas (1971) present a method for determining transfer functions for one-dimensional heat transfer through multilayered slabs by solving the conduction equation with Laplace and z-transform theory. Mitalas and Arsenault (1971) wrote a program for computing transfer function coefficients based upon the method of Stephenson and Mitalas. Transfer function coefficients computed from Mitalas and Arsenault's program for 40 roof, 103 wall, and 47 interior partition constructions are listed in the ASHRAE Handbook of Fundamentals (1977, 1981, 1985). Ceylan and Meyers (1980) and Seem et al. (1987) present methods for calculating transfer function coefficients for multidimensional heat transfer. A discussion of two methods that use transfer functions to calculate building loads follows.

ASHRAE (1977, 1981, 1985) discusses the energy balance method (ASHRAE refers to this as the heat balance method) for calculating sensible heating or cooling loads for buildings. An energy balance equation is written for every surface in a room and the room air. For a room with N surfaces, these energy balance equations can be formulated in the matrix equation.

$$\mathbf{AT} = \mathbf{B} \tag{1}$$

where $\mathbf{A}$ is an $(N+1)$ by $(N+1)$ matrix, which contains transfer function coefficients, convection coefficients, and linearized long-wave radiation resistances; $\mathbf{T}$ is a vector of temperatures with all rows equal to an interior surface temperature, except the last row, which is the room air temperature; and $\mathbf{B}$ is a vector of current inputs, past inputs, past interior surface temperatures, and transfer function coefficients. After solving the matrix equation for the $\mathbf{T}$ vector, the load due to convective heat transfer between surfaces and the room air can be calculated. The computational effort is reduced when the $\mathbf{A}$ matrix is time invariant, i.e., convection coefficients and linearized long-wave resistances are constant. Mitalas (1965) shows that the cooling loads for a room are quite insensitive to changes in the interior convection coefficient. Walton (1980) shows that long-wave radiation exchange between surfaces in a room can be linearized without introducing significant errors. Assuming long-wave radiation resistances are constant does not introduce significant errors because the average temperature of surfaces in a room is fairly constant. Estimating exterior convection coefficients that vary with time is difficult due to the large number of factors (e.g., building size, building shape, building surrounding, wind direction, local wind velocity) that affect convective heat transfer from exterior surfaces.

Madsen (1982) develops a comprehensive room transfer function (CRTF) by using linear regression on results from an energy balance simulation. A CRTF is a single transfer function equation for computing loads or floating indoor air temperatures in a room or zone. CRTF simulations require less computational effort than energy balance simulations because only outputs of interest are computed.

This paper describes a method in which the transfer functions describing heat flows in building elements can be combined into a CRTF for an enclosure. The first section of this paper presents the derivation of the equations for combining

Contributed by the Heat Transfer Division and presented at the ASME/AIChE National Heat Transfer Conference, Pittsburgh, Pennsylvania, August 9-12, 1987. Manuscript received by the Heat Transfer Division November 20, 1987. Keywords: Building Heat Transfer, Numerical Methods.

transfer functions with parallel heat transfer paths. The second section of this paper is devoted to a method for accurately modeling the convection and radiation heat transfer processes in an enclosure by a star network. A star network allows individual transfer functions for building elements to be easily combined for rooms. The third section of this paper presents equations for combining transfer functions for a room model based on a star network. A method that can be used to reduce the number of coefficients in a transfer function equation is presented in the fourth section. The last section of this paper compares the computational effort of energy balance simulations with CRTF simulations that use reduced coefficients.

Parallel Path Combination

Equations for combining transfer functions for walls with parallel heat transfer paths, as shown in Fig. 1, are derived in this section. The transfer function equation for the heat flux for wall a is

$$q''_{t,a} = \sum_{n=0} (a_{n,a} T_{t-n\delta,o} + b_{n,a} T_{t-n\delta,i}) - \sum_{n=1} (c_{n,a} q''_{t-n\delta,a}) \quad (2)$$

The upper limits on the summations in equation (2) are dependent upon the method used to obtain the transfer function coefficients.

Equation (2) can be expressed in terms of the backshift operator B as

$$\left(\sum_{n=0} c_{n,a} B^n\right) q''_{t,a} = \left(\sum_{n=0} a_{n,a} B^n\right) T_{t,o} + \left(\sum_{n=0} b_{n,a} B^n\right) T_{t,i} \quad (3)$$

where $c_{o,a} = 1.0$. The backshift operator (Box and Jenkins, 1976) is defined as

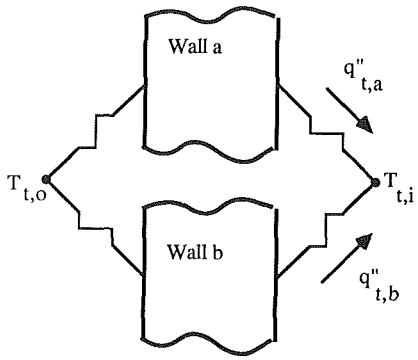

Fig. 1 Walls with parallel heat transfer paths

$$Bz_t = z_{t-\delta} \quad (4)$$

Dividing by the summation on the left side of equation (3) results in

$$q''_{t,a} = \frac{\left(\sum_{n=0} a_{n,a} B^n\right) T_{t,o} + \left(\sum_{n=0} b_{n,a} B^n\right) T_{t,i}}{\left(\sum_{n=0} c_{n,a} B^n\right)} \quad (5)$$

A similar equation for wall b is

$$q''_{t,b} = \frac{\left(\sum_{n=0} a_{n,b} B^n\right) T_{t,o} + \left(\sum_{n=0} b_{n,b} B^n\right) T_{t,i}}{\left(\sum_{n=0} c_{n,b} B^n\right)} \quad (6)$$

Nomenclature

a = outdoor temperature transfer function coefficient for a wall; input transfer function coefficient
$\bar{a}$ = input coefficient for Laplace transfer function, input coefficient for w transfer function
A = area
A_w = window area
$\mathbf{A}$ = $(N+1)$ by $(N+1)$ matrix, equation (1)
b = indoor temperature transfer function coefficient for a wall; output coefficient for transfer function
$\bar{b}$ = input coefficient for Laplace transfer function, input coefficient for w transfer function
B = backshift operator, equation (4)
$\mathbf{B}$ = $(N+1)$ vector of inputs, equation (1)
c = transfer function coefficient for past heat fluxes for a wall, input coefficient for reduced transfer function
$\bar{c}$ = coefficient for power series expansion of Laplace transfer function
d = outdoor temperature transfer function coefficient, output coefficient for reduced transfer function
$\bar{d}$ = input coefficient for reduced Laplace transfer function coefficient, input coefficient for reduced w transfer function
e = star or indoor air temperature transfer function coefficient, output coefficient for reduced transfer function
$\bar{e}$ = output coefficient for reduced Laplace transfer function, output coefficient for reduced w transfer function
f = solar radiation transfer function coefficient
f_a, f_b = area fraction for walls a and b, respectively, equation (7)
g = radiation transfer function coefficient
h = transfer function coefficient for past outputs
G_{i-j} = absorption factor between surfaces i and j, equation (15)
$G(s)$ = Laplace transfer function in Appendix A
$G_r(s)$ = reduced Laplace transfer function in Appendix A
I = incident solar radiation
N = number of surfaces in enclosure or room
R = resistance between star node and room air, equation (28)
R_{i-j} = resistance between surfaces i and j in the view factor network, when other nodes are floating, equation (20)
R_{i-r} = resistance between surface i and the room air in the view factor network when other nodes are floating, equation (22)
R_k = resistance between interior surface of wall k and star node, equation (23)

The heat flux for walls a and b combined, $q''_{t,\chi}$, is

$$q''_{t,\chi} = \frac{A_a}{A_a + A_b} q''_{t,a} + \frac{A_b}{A_a + A_b} q''_{t,b} = f_a q''_{t,a} + f_b q''_{t,b} \tag{7}$$

Substituting equations (5) and (6) into equation (7) gives

$$q''_{t,\chi} = f_a \left[\frac{\left(\sum_{n=0} a_{n,a} B^n \right) T_{t,o} + \left(\sum_{n=0} b_{n,a} B^n \right) T_{t,i}}{\left(\sum_{n=0} c_{n,a} B^n \right)} \right] + f_b \left[\frac{\left(\sum_{n=0} a_{n,b} B^n \right) T_{t,o} + \left(\sum_{n=0} b_{n,b} B^n \right) T_{t,i}}{\left(\sum_{n=0} c_{n,b} B^n \right)} \right] \tag{8}$$

Multiplying by the denominators of the terms on the right-hand side of equation (8) results in

$$\left(\sum_{n=0} c_{n,a} B^n \right) \left(\sum_{n=0} c_{n,b} B^n \right) q''_{t,\chi} = \left[f_a \left(\sum_{n=0} a_{n,a} B^n \right) \left(\sum_{n=0} c_{n,b} B^n \right) \right] T_{t,o} + \left[f_b \left(\sum_{n=0} a_{n,b} B^n \right) \left(\sum_{n=0} c_{n,a} B^n \right) \right] T_{t,o} + \left[f_a \left(\sum_{n=0} b_{n,a} B^n \right) \left(\sum_{n=0} c_{n,b} B^n \right) \right] T_{t,i} + \left[f_b \left(\sum_{n=0} b_{n,b} B^n \right) \left(\sum_{n=0} c_{n,a} B^n \right) \right] T_{t,i} \tag{9}$$

Carrying out the algebra and combining common powers of the backshift operator yields

$$\left(\sum_{n=0} c_{n,\chi} B^n \right) q''_{t,\chi} = \left(\sum_{n=0} a_{n,\chi} B^n \right) T_{t,0} + \left(\sum_{n=0} b_{n,\chi} B^n \right) T_{t,i} \tag{10}$$

where

$$a_{n,\chi} = \sum_{i=0}^{n} (f_a a_{i,a} c_{n-i,b} + f_b a_{i,b} c_{n-i,a}) \tag{11}$$

$$b_{n,\chi} = \sum_{i=0}^{n} (f_a b_{i,a} c_{n-i,b} + f_b b_{i,b} c_{n-i,a}) \tag{12}$$

$$c_{n,\chi} = \sum_{i=0}^{n} (c_{i,a} c_{n-i,b}) \tag{13}$$

Using the definition of the backshift operator, equation (10) can be rewritten in a form that looks exactly like equation (2)

$$q''_{t,\chi} = \sum_{n=0} (a_{n,\chi} T_{t-n\delta,o} + b_{n,\chi} T_{t-n\delta,i}) - \sum_{n=1} c_{n,\chi} q''_{t-n\delta,\chi} \tag{14}$$

where equations (11), (12), and (13) define the transfer function coefficients. The number of previous time steps in the combined transfer function equation is equal to or greater than the number of previous time steps for each individual transfer function.

Nomenclature (cont.)

$R_{i-j,\text{rad}}$ = resistance to radiation exchange between surfaces i and j, equation (15)
$R_{i,\text{conv}}$ = resistance to convective heat transfer between surface i and room air
$R_{k,\text{out}}$ = resistance to convective heat transfer between exterior surface of wall k and outdoor air
s = complex Laplace transform variable
T = temperature
$\bar{T}$ = average temperature of surfaces in a room, equation (15)
$\mathbf{T}$ = $(N+1)$ vector of temperatures, equation (1)
u = input
w = complex variable that results from bilinear transformations
$x_{(i,j)}$ = element in row i and column j of the $\mathbf{X}$ matrix, equation (18)
$x_{(i,j),\text{inv}}$ = element in row i and column j of the inverse of the $\mathbf{X}$ matrix
$\mathbf{X}$ = $(N+1)$ by $(N+1)$ matrix, equation (18)
$y_{(i)}$ = element in row i of $\mathbf{Y}$ vector, equation (18)
y = output
$\mathbf{Y}$ = $(N+1)$ vector, equation (18)
z = complex variable
$z_{(i)}$ = element in row i of $\mathbf{Z}$ vector, equation (18)
$\mathbf{Z}$ = $(N+1)$ vector, equation (18)
q = heat flow
q'' = heat flux
α = solar absorptance
ϵ = emittance
σ = Stefan–Boltzmann constant
ϕ_ρ = fraction of radiation gains from people, equipment, and lights that is absorbed at the internal surface of building element k
ψ_1 = dimensionless error function, equation (25)
ψ_2 = weighted error function, equation (26)
$\overline{(\tau\alpha)}_k$ = fraction of incident solar radiation that is absorbed at the interior surface of building element k

Subscripts

a = wall a
amb = ambient temperature
b = wall b
i = inside
I = solar radiation
k = building element k
load = heating or cooling load for building
n = transfer function coefficient for n time steps prior to time t
o = outside
r = room air
rad = radiation gains from people equipment and lights
sa = sol-air temperature, equation (30)
$t-n\delta$ = input or output n time steps prior to time t
χ = combined

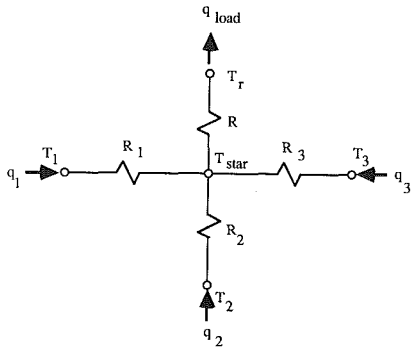

Fig. 2 Star network for a room with three surfaces

The Star Network

Direct combination of individual wall transfer functions into a CRTF when view factors are used to model long-wave radiation in the room requires the manipulation of polynomial matrices (Chen, 1984), an area of research in systems analysis. Approximating the actual radiation and convection heat transfer processes in a room by a star network allows for each combination (i.e., no manipulation of polynomial matrices) of transfer functions. Figure 2 shows a star network for an enclosure with three surfaces. This section presents a computationally easy method for determining the resistances in a star network that uses wall-to-wall view factors to model long-wave radiation exchange, i.e., a view factor network. (Davies (1983) presents a method for modeling the radiation heat transfer processes in a room with a star network. The star network developed in this paper models both the radiation and convection heat transfer processes in a room.)

Figure 3 shows a view factor network for an enclosure with three surfaces. The resistance to long-wave radiation exchange between surfaces in the view factor network is

$$R_{i-j,\text{rad}} = \frac{1}{\epsilon_i A_i G_{i-j} \sigma 4 \bar{T}^3} \tag{15}$$

The absorption factor (Gebhart, 1971), G_{i-j}, is the fraction of energy emitted by surface i that is absorbed by surface j.

Two main steps are involved in determining the resistances in the star network from the resistances in the view factor network. First, the resistance between each pair of nodes in the view factor network is determined when all other nodes are floating. A floating node is defined as one in which heat transfer occurs only by convection to the air or by long-wave radiation exchange with other surfaces in the enclosure. As a result, conduction through building elements, solar radiation gains, and radiation gains from people, equipment, and lights do not affect floating surface nodes, and infiltration or convection gains from people, equipment, and lights do not affect the floating room air node. Second, an approximation is used to determine the resistances in the star network from the resistances between nodes in the view factor network.

To compute the resistances between nodes in the view factor network, an energy balance must be performed on each surface in the enclosure and on the air in the enclosure. An energy balance for surface i in an enclosure with N surfaces is

$$\frac{(T_1 - T_i)}{R_{1-i,\text{rad}}} + \frac{(T_2 - T_i)}{R_{2-i,\text{rad}}} + \ldots + \frac{(T_N - T_i)}{R_{N-i,\text{rad}}} + \frac{(T_r - T_i)}{R_{i,\text{conv}}} + q_i = 0 \tag{16}$$

where q_i is the energy input to surface i other than by convection to the air or long-wave radiation exchange with other surfaces in the room, e.g., absorbed solar energy. An energy balance for the air in the room is

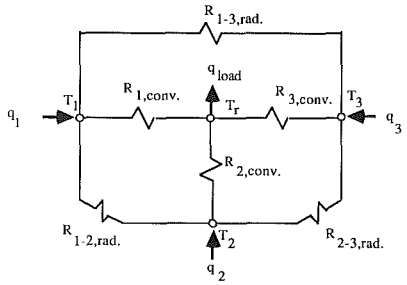

Fig. 3 View factor network for a room with three surfaces

$$\frac{(T_1 - T_r)}{R_{1,\text{conv}}} + \frac{(T_2 - T_r)}{R_{2,\text{conv}}} + \ldots + \frac{(T_N - T_r)}{R_{N,\text{conv}}} = q_{\text{load}} \tag{17}$$

The N energy balances for every surface in the room and the energy balance on the room air can be combined into the matrix equations

$$\mathbf{XY} = \mathbf{Z} \tag{18}$$

where (for $i = 1$ to N and $j = 1$ to N)

$$x_{(i,i)} = -\left(\sum_{j=1}^{N} \frac{1}{R_{i-j,\text{rad}}}\right) - \frac{1}{R_{i,\text{conv}}}$$

$$x_{(i,j)} = x_{(j,i)} = \frac{1}{R_{i-j,\text{rad}}}$$

$$x_{(i,N+1)} = 0$$

$$x_{(N+1,i)} = \frac{1}{R_{i,\text{conv}}}$$

$$x_{(N+1,N+1)} = -1$$

$$y_{(i)} = T_i - T_r$$

$$y_{(N+1)} = q_{\text{load}}$$

$$z_{(i)} = -q_i$$

$$z_{(N+1)} = 0$$

To compute the resistance R_{i-j} between surfaces i and j when all other nodes are floating, arbitrarily let q_i be unit y so that

$$q_i = -q_j = 1.0 \text{ [W or Btu/h]} = \frac{T_i - T_j}{R_{i-j}} \tag{19}$$

then

$$R_{i-j} = (T_i - T_r) - (T_j - T_r) = y_{(i)} - y_{(j)} = x_{(i,j),\text{inv}} + x_{(j,i),\text{inv}} - x_{(i,i),\text{inv}} - x_{(j,j),\text{inv}} \tag{20}$$

To compute the resistance R_{i-r} between surface i and the room air, again let

$$q_i = q_{\text{load}} = \frac{(T_i - T_r)}{R_{i-r}} = 1.0 \text{ [W or Btu/h]} \tag{21}$$

then

$$R_{i-r} = T_i - T_r = -x_{(i,i),\text{inv}} \tag{22}$$

A number of approximations could be used to obtain the unknown resistances in the star network from the resistances between nodes in the view factor network. For example, nonlinear regression could be used to minimize the error in heat flow between nodes, or linear regression could be used to minimize the resistance to heat transfer between nodes. An approximation that accurately models the heat transfer processes in a room and requires less computational effort than linear or nonlinear regression is as follows.

The net heat flow to the air (i.e., load) for steady-state

temperature differences between enclosure surfaces and the air will be the same for the star network and the view factor network if the following N equations are satisfied:

$$R_1 + R = R_{1-r}$$
$$R_2 + R = R_{2-r}$$
$$\vdots$$
$$R_N + R = R_{N-r} \tag{23}$$

One more equation is needed to provide $N+1$ equations with $N+1$ unknowns. The last equation is selected so that the heat transfer between surfaces for the star network approximates the heat transfer between surfaces in the view factor network. The difference in resistance to heat transfer between surface nodes i and j when other nodes are floating for the view factor network and the star network is

$$R_i + R_j - R_{i-j} = R_{i-r} + R_{j-r} - R_{i-j} - 2R \tag{24}$$

Squaring a dimensionless form of this error in resistance between all surface nodes gives the function

$$\psi_1 = \sum_{i=2}^{N} \sum_{j=1}^{i-1} \frac{(R_{i-r} + R_{j-r} - R_{i-j} - 2R)^2}{R_{i-j}^2} \tag{25}$$

Surfaces with a lower resistance (R_{i-j}) between them have a larger heat transfer for the same temperature difference. The following error function will place more weight on resistances between surfaces with a smaller R_{i-j}:

$$\psi_2 = \sum_{i=2}^{N} \sum_{j=1}^{i-1} \frac{(R_{i-r} + R_{j-r} - R_{i-j} - 2R)^2}{R_{i-j}^3} \tag{26}$$

Other weighting functions could be used to obtain ψ_2, but as will be shown, this weighting function results in accurate modeling of the heat transfer processes for rooms with a wide variety of thermal physical properties, resistances to long-wave radiation exchange, and resistances to convective heat transfer. The derivative of ψ_2 with respect to resistance R between the star node and the air is

$$\frac{d(\psi_2)}{dR} = \sum_{i=2}^{N} \sum_{j=1}^{i-1} \frac{-4(R_{i-r} + R_{j-r} - R_{i-j} - 2R)}{R_{i-j}^3} \tag{27}$$

Setting the derivative ψ_2 with respect to R equal to zero gives

$$R = \frac{\sum_{i=2}^{N} \sum_{j=1}^{i-1} \frac{R_{i-r} + R_{j-r} - R_{i-j}}{R_{i-j}^3}}{2 \sum_{i=2}^{N} \sum_{j=1}^{i-1} \frac{1}{R_{i-j}^3}} \tag{28}$$

The second derivative of ψ_2 with respect to R will be positive for all positive values of R. Therefore, ψ_2 will be a minimum when R is positive. The other N unknown resistances in the star network can be obtained from equation (23) after equation (28) is used to compute the resistance between the star node and the room air node. Seem (1987) shows that this method results in an exact transformation for a room with two surfaces and for rooms that have the same resistance to long-wave radiation exchange and resistance to convective heat transfer for all surfaces.

Loads with the star and view factor networks were compared for a three-surface room and an eight-surface room. To test the star network, building elements with a wide range of thermal physical properties, resistances to long-wave radiation exchange, and resistances were used. The three-surface room contained the following building elements:

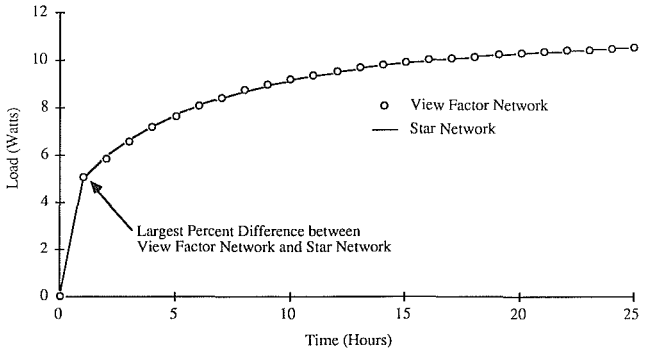

Fig. 4 Response to 0.56°C (1°F) step change in outdoor temperature for eight-surface room

Table 1 Percent difference in steady-state loads between the star and view factor networks

Input	Three-Surface Room	Eight-Surface Room
Temperature Difference	0.45 percent	0.69 percent
Solar	0.12 percent	0.36 percent
Radiation	0.006 percent	0.17 percent

1) 3 m^2 of exterior glazing
2) 3 m^2 of an exterior frame wall with 80 mm of insulation
3) 30 m^2 of 0.3 m heavy concrete interior partition

The eight-surface room contained the following building elements:

1) 6 m^2 of exterior glazing
2) 1 m^2 of the stud path of an exterior frame wall
3) 5 m^2 of the insulation path of an exterior frame wall
4) 12 m^2 of an 0.2 m low-weight concrete floor deck
5) 6 m^2 of a frame partition with 30 mm wood
6) 12 m^2 of interior partition consisting of an 0.2 m clay tile with 20 mm plaster
7) 6 m^2 of interior partition consisting of 0.1 m clay tile with 20 mm plaster
8) 12 m^2 of a 0.1 m wood deck with false ceiling

Loads resulting from step changes in outdoor temperature, indoor temperature, solar radiation gains, and radiation gains from people, equipment, and lights were computed for the star and view factor networks for both rooms. A one-hour time step was used. The time step with the largest percent difference in loads between the networks is shown in Fig 4. Table 1 contains the percent difference in steady-state loads between the star and view factor networks for the following inputs: temperature difference between the ambient and indoor air, solar radiation gains, and radiation gains from people, equipment, and lights. Figure 4 and Table 1 demonstrate that the star network accurately models the heat transfer processes for both rooms and all inputs.

This section described a method for determining the resistances in a star network from a network that uses view factors to model long-wave radiation exchange. Locations of room surfaces are needed to compute view factors. Carroll (1980) developed a mean radiant temperature (MRT) network for modeling the long-wave radiation exchange in rooms. There are two advantages of the MRT network over the view factor network. First, no information concerning the location of room surfaces is required. Second, it is easier to include furnishings in a MRT network (Walton, 1984). The resistances in the star network could also be obtained from a MRT network.

Transfer Function Combination for a Star Network

This section presents a method for combining individual

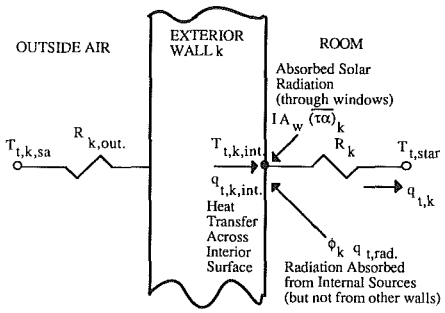

Fig. 5 Energy flows for an exterior wall

building component transfer functions into a single transfer function for an enclosure modeled by a star network. This method requires three main steps. First, transfer functions are developed for each building component (e.g., wall, floor, ceiling) that relate heat flow to the star node with the inputs. Second, transfer functions for each building component are combined in order to relate the total heat flow to the star node with the inputs. Third, the star temperature is removed from the combined transfer function equation by relating the building load to the temperature difference between the star node and the room air temperature.

A transfer function equation for an exterior wall will be developed that will relate the heat flow to the star node with solar radiation gains (from one direction), outdoor temperature, star temperature, and radiation gains from people, equipment, and lights as indicated in Fig. 5. The methods previously discussed can be used to calculate the coefficients for a transfer function equation of the form

$$q_{t,k,\text{int}} = \sum_{n=0} (a_{n,k} A_k T_{t-n\delta,k,sa} + b_{n,k} A_k T_{t-n\delta,k,\text{int}}) - \sum_{n=1} c_{n,k} q_{t-n\delta,k,\text{int}} \tag{29}$$

The sol-air temperature (Mitchell, 1983) for wall k is

$$T_{t-n\delta,k,sa} = T_{t-n\delta,\text{amb}} + I_{t-n\delta} \alpha_k R_{k,\text{out}} A_k \tag{30}$$

An energy balance on the interior surface results in the following equation for heat flow to the star node from wall k:

$$q_{t-n\delta,k,\text{int}} = q_{t-n\delta,k} - \phi_k q_{t-n\delta,\text{rad}} - I_{t-n\delta} A_w \overline{(\tau\alpha)}_k \tag{31}$$

The interior surface temperature is related to the star temperature and heat flow to the star node by

$$T_{t-n\delta,k,\text{int}} = R_k q_{t-n\delta,k} + T_{t-n\delta,\text{star}} \tag{32}$$

Substituting equations (30), (31), and (32) into equation (29) results in

$$q_{t,k} = \sum_{n=0} (d_{n,k} T_{t-n\delta,\text{amb}} + e_{n,k} T_{t-n\delta,\text{star}} + f_{n,k} I_{t-n\delta} + g_{n,k} q_{t-n\delta,\text{rad}}) - \sum_{n=1} h_{n,k} q_{t-n\delta,k} \tag{33}$$

where

$$d_{n,k} = \frac{a_{n,k} A_k}{1 - b_{0,k} A_k R_k} \tag{34}$$

$$e_{n,k} = \frac{b_{n,k} A_k}{1 - b_{0,k} A_k R_k} \tag{35}$$

$$f_{n,k} = \frac{c_{n,k} A_w \overline{(\tau\alpha)}_k + a_{n,k} \alpha_k R_{k,\text{out}} A_k^2}{1 - b_{0,k} A_k R_k} \tag{36}$$

$$g_{n,k} = \frac{c_{n,k} \phi_k}{1 - b_{0,k} R_k A_k} \tag{37}$$

$$h_{n,k} = \frac{c_{n,k} - b_{n,k} R_k A_k}{1 - b_{0,k} R_k A_k} \tag{38}$$

Equation (33) relates the heat flow to the star node for exterior wall k with the inputs. Seem (1987) develops similar transfer functions for heat flow to the star node from an interior partition and a window. The equations for an interior partition are similar to the equations for an exterior wall, but the surface temperature on both sides of the interior partition are identical. For a window, there are no past time steps involved in the transfer function equation because the thermal capacitance of glass is small.

The transfer functions for heat flow from each building element to the star node can be combined in a nested fashion (i.e., combine the transfer functions for building elements 1 and 2, then combine the transfer function for building element 3 with the combined transfer function for building elements 1 and 2, and continue). The backshift operator can be used to combine any two transfer functions to give the combined heat flow $q_{t,\chi}$:

$$q_{t,\chi} = \sum_{n=0} (d_{n,\chi} T_{t-n\delta,\text{amb}} + e_{n,\chi} T_{t-n\delta,\text{star}} + f_{n,\chi} I_{t-n\delta} + g_{n,\chi} q_{t-n\delta,\text{rad}}) - \sum_{n=1} h_{n,\chi} q_{t-n\delta,\chi} \tag{39}$$

where

$$q_{t-n\delta,\chi} = q_{t-n\delta,1} + q_{t-n\delta,2} \tag{40}$$

$$d_{n,\chi} = \sum_{j=0}^{n} (d_{n-j,1} h_{j,2} + d_{j,2} h_{n-j,1}) \tag{41}$$

$$e_{n,\chi} = \sum_{j=0}^{n} (e_{n-j,1} h_{j,2} + e_{j,2} h_{n-j,1}) \tag{42}$$

$$f_{n,\chi} = \sum_{j=0}^{n} (f_{n-j,1} h_{j,2} + f_{j,2} h_{n-j,1}) \tag{43}$$

$$g_{n,\chi} = \sum_{j=0}^{n} (g_{n-j,1} h_{j,2} + g_{j,2} h_{n-j,1}) \tag{44}$$

$$h_{n,\chi} = \sum_{j=0}^{n} (h_{j,1} h_{n-j,2}) \tag{45}$$

Combining heat flows from every surface to the star node gives

$$q_{t,\chi} = ((\ldots(((q_{t,1} + q_{t,2}) + q_{t,3}) + q_{t,4}) + \ldots + q_{t,n-1}) + q_{t,n}) = q_{t,\text{load}} \tag{46}$$

The load is related to the temperature difference between the star node and the air node simply by

$$q_{t,\text{load}} = \frac{T_{t,\text{star}} - T_{t,r}}{R} \tag{47}$$

Substituting equations (46) and (47) into equation (39) gives

$$q_{t,\text{load}} = \sum_{n=0} (d_n T_{t-n\delta,\text{amb}} + e_n T_{t-n\delta,r} + f_n I_{t-n\delta} + g_n q_{t-n\delta,\text{rad}}) - \sum_{n=1} h_n q_{t-n\delta,\text{load}} \tag{48}$$

where

$$d_n = \frac{d_{n,\chi}}{1 - Re_{0,\chi}} \tag{49}$$

$$e_n = \frac{e_{n,\chi}}{1 - Re_{0,\chi}} \tag{50}$$

$$f_n = \frac{f_{n,\chi}}{1 - Re_{0,\chi}} \tag{51}$$

$$g_n = \frac{g_{n,\chi}}{1 - Re_{0,\chi}} \tag{52}$$

$$h_n = \frac{h_{n,\chi} - Re_{n,\chi}}{1 - Re_{0,\chi}} \tag{53}$$

Equation (48) is a CRTF, which relates the load for an enclosure to past and current inputs and past loads. The next section presents a method for reducing the computational effort of CRTF simulations.

Model Reduction

The multiple input CRTF given by equation (48) involves more coefficients than required for any of the individual building components. Not all of these coefficients are needed, however, and computational effort can be significantly reduced by model reduction, i.e., find a smaller set of coefficients (i.e., requiring less past information) that provides nearly the same results. Model reduction techniques for multiple input CRTF are complex. A simpler approach to model reduction is to use superposition to decompose the multiple input CRTF into single input CRTF's. Performing a simulation with the single input CRTF's would require more computational effort than would be required with the multiple input CRTF [equation (48)], but the model reduction method discussed in this section can be used to obtain a reduced set (i.e., fewer coefficients) of single input CRTF's, which greatly reduces the necessary computational effort.

The following four single input CRTF's are required to compute the same building loads as given by the multiple input CRTF, equation (48):

$$q_{t,\text{load,amb}} = \sum_{n=0} (d_n T_{t-n\delta,\text{amb}}) - \sum_{n=1} (h_n q_{t-n\delta,\text{load,amb}}) \tag{54}$$

$$q_{t,\text{load},r} = \sum_{n=0} (e_n T_{t-n\delta,r}) - \sum_{n=1} (h_n q_{t-n\delta,\text{load},r}) \tag{55}$$

$$q_{t,\text{load},I} = \sum_{n=0} (f_n I_{t-n\delta}) - \sum_{n=1} (h_n q_{t-n\delta,\text{load},I}) \tag{56}$$

$$q_{t,\text{load,rad}} = \sum_{n=0} (g_n q_{t-n\delta,\text{rad}}) - \sum_{n=1} (h_n q_{t-n\delta,\text{load,rad}}) \tag{57}$$

The net heating or cooling load for a room is

$$q_{t,\text{load}} = q_{t,\text{load,amb}} + q_{t,\text{load},r} + q_{t,\text{load},I} + q_{t,\text{load,rad}} \tag{58}$$

Shamash (1980) said that the Padé approximation is a popular method for reducing single-input Laplace transfer functions because it requires little computational effort, cancels common factors if they exist, and matches the steady-state response of the original and reduced Laplace transfer functions for polynomial inputs. This section extends the Padé approximation to model reduction for single-input transfer functions.

The following single-input transfer function relates the inputs of a system to the outputs:

$$y_t = \sum_{j=0}^{n} (a_j u_{t-j\delta}) - \sum_{j=1}^{n} (b_j y_{t-j\delta}) \tag{59}$$

Taking the z transformation (Jury, 1964) of equation (59) results in

$$\left[\sum_{j=0}^{n} (b_j z^{-j})\right] Y(z) = \left[\sum_{j=0}^{n} (a_j z^{-j})\right] U(z) \tag{60}$$

From equation (60), the z transfer function is

$$G(z) = \frac{Y(z)}{U(z)} = \frac{\sum_{j=0}^{n} a_j z^{-j}}{\sum_{j=0}^{n} b_j z^{-j}} \tag{61}$$

Equation (61) is a z transfer function that relates the z transform of the input to the z transform of the output, and it is unstable if there are poles outside the unit circle. (Poles are roots of the denominator of a transfer function.) To reduce z transfer functions, the bilinear transformation (Kuo, 1980)

$$z = \frac{1 + \text{w}}{1 - w} \tag{62}$$

is used to transform a z transfer function into a w transfer function. (A w transfer function is a ratio of polynomials of the complex variable w.) The bilinear transformation maps the unit circle on the z plane into the left half of the w plane. A w transfer function behaves like a Laplace transfer function because both transfer functions are unstable if they have poles in the right half of their complex planes. Substituting equation (62) into equation (61) gives the following w transfer function:

$$G(w) = \frac{\sum_{j=0}^{n} a_j \left(\frac{1+w}{1-w}\right)^{-j}}{\sum_{j=0}^{n} b_j \left(\frac{1+w}{1-w}\right)^{-j}} = \frac{\sum_{j=0}^{n} a_j \left(\frac{1-w}{1+w}\right)^{j}}{\sum_{j=0}^{n} b_j \left(\frac{1-w}{1+w}\right)^{j}}$$

$$= \frac{\sum_{j=0}^{n} a_j (1-w)^j (1+w)^{n-j}}{\sum_{j=0}^{n} b_j (1-w)^j (1+w)^{n-j}} \tag{63}$$

Appendix A describes an algorithm for determing the $\nu_{i(j,n)}$ coefficients in the following equation:

$$(1-w)^j (1+w)^{n-j} = \sum_{i=0}^{n} \nu_{i(j,n)} w^i \tag{64}$$

Substituting equation (64) into equation (63) gives

$$G(w) = \frac{\sum_{j=0}^{n} a_j \left(\sum_{i=0}^{n} \nu_{i(j,n)} w^i\right)}{\sum_{j=0}^{n} b_j \left(\sum_{i=0}^{n} \nu_{i(j,n)} w^i\right)} = \frac{\sum_{i=0}^{n} \left(\sum_{j=0}^{n} a_j \nu_{i(j,n)}\right) w^i}{\sum_{i=0}^{n} \left(\sum_{j=0}^{n} b_j \nu_{i(j,n)}\right) w^i} \tag{65}$$

Equation (65) is a ratio of polynomials of the complex variable w. Appendix B contains equations for reducing Laplace transfer functions with the Padé approximation. The Padé approximation can also be used to reduce w transfer functions. To use the equations in Appendix B to reduce w transfer functions, the coefficient for w^0 in the denominator of equation (65) must be set equal to one.

Table 2 Transfer function coefficients for exterior wall 17

	ASHRAE		Reduced	
i	a_i, W/(m^2-K)	c_i	a_i, W/(m^2-K)	c_i
0	0	1	−0.00505	1
1	0.00006	−2.35214	0.02339	−2.13547
2	0.00125	1.98104	−0.03895	1.47238
3	0.00511	−0.73353	0.03486	−0.32658
4	0.00454	0.12178		
5	0.00108	−0.00859		
6	0.00006	0.00021		

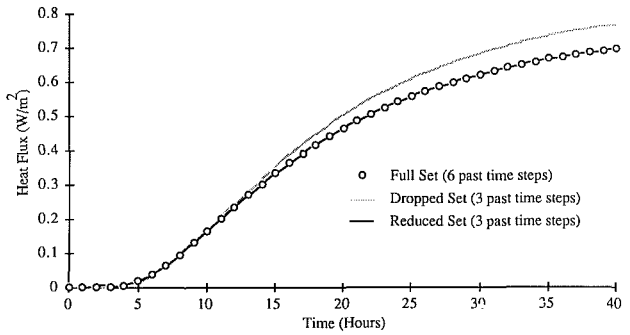

Fig.6 Response to 0.56°C (1°F) step change in outdoor temperature for ASHRAE exterior wall 17

$$G(w)=\frac{\sum_{i=0}^{n}\bar{a}_i w^i}{\sum_{i=0}^{n}\bar{b}_i w^i} \tag{66}$$

where

$$\bar{a}_i=\frac{\sum_{j=0}^{n}a_j\nu_{i(j,n)}}{\sum_{j=0}^{n}b_j\nu_{0(j,n)}} \tag{67}$$

$$\bar{b}_i=\frac{\sum_{j=0}^{n}b_j\nu_{i(j,n)}}{\sum_{j=0}^{n}b_j\nu_{0(j,n)}} \tag{68}$$

The Padé approximation described in Appendix B can be used to obtain a reduced w transfer function of the following form:

$$G_r(w)=\frac{\sum_{i=0}^{m}\bar{d}_i w^i}{\sum_{i=0}^{m}\bar{e}_i w^i} \tag{69}$$

where

$\bar{e}_0=1$

m = number of past time steps in reduced transfer function

Next, the reduced w transfer is transformed into a reduced z transfer function by using the bilinear transformation

$$w=\frac{z-1}{z+1}=\frac{1-z^{-1}}{1+z^{-1}} \tag{70}$$

Substituting equation (70) into equation (69) results in

$$G_r(z)=\frac{\sum_{i=0}^{m}\bar{d}_i\left(\frac{1-z^{-1}}{1+z^{-1}}\right)^i}{\sum_{i=0}^{m}\bar{e}_i\left(\frac{1-z^{-1}}{1+z^{-1}}\right)^i}=\frac{\sum_{i=0}^{m}\bar{d}_i(1-z^{-1})^i(1+z^{-1})^{m-i}}{\sum_{i=0}^{m}\bar{e}_i(1-z^{-1})^i(1+z^{-1})^{m-i}} \tag{71}$$

The algorithm described in Appendix A can be used to compute the $\nu_{j(i,m)}$ coefficients in the following equation:

$$(1-z^{-1})^i(1+z^{-1})^{m-i}=\sum_{j=0}^{m}\nu_{j(i,m)}z^{-j} \tag{72}$$

Substituting equation (72) into equation (71) gives

$$G_r(z)=\frac{\sum_{i=0}^{m}\bar{d}_i\left(\sum_{j=0}^{m}\nu_{j(i,m)}z^{-j}\right)}{\sum_{i=0}^{m}\bar{e}_i\left(\sum_{j=0}^{m}\nu_{j(i,m)}z^{-j}\right)}=\frac{\sum_{j=0}^{m}\left(\sum_{i=0}^{m}\bar{d}_i\nu_{j(i,m)}\right)z^{-j}}{\sum_{j=0}^{m}\left(\sum_{i=0}^{m}\bar{e}_i\nu_{j(i,m)}\right)z^{-j}} \tag{73}$$

Equation (73) can be rewritten as

$$G_r(z)=\frac{\sum_{j=0}^{m}d_j z^{-j}}{\sum_{j=0}^{m}e_j z^{-j}} \tag{74}$$

where

$$d_j=\frac{\sum_{i=0}^{m}\bar{d}_i\nu_{j(i,m)}}{\sum_{i=0}^{m}\bar{e}_i\nu_{0(i,m)}} \tag{75}$$

$$e_j=\frac{\sum_{i=0}^{m}\bar{e}_i\nu_{j(i,m)}}{\sum_{i=0}^{m}\bar{e}_i\nu_{0(i,m)}} \tag{76}$$

Transforming equation (76) back into the time domain gives the following reduced transfer function:

$$y_t=\sum_{j=0}^{m}d_j u_{t-j\delta}-\sum_{j=1}^{m}e_j y_{t-j\delta} \tag{77}$$

ASHRAE contains tables of single input transfer functions for walls, roofs, and interior partitions.The Padé approximation and bilinear tranformation can be used to obtain a reduced set of coefficients that closely model the response of the full set of coefficients listed in ASHRAE. As an example, Table 2 contains transfer function coefficients for exterior wall 17 (4-in. face brick, 8-in. common brick with air space) listed in ASHRAE. Table 2 also contains reduced transfer function coefficients for three time steps back rather than six as given by ASHRAE. Figure 6 is a plot of the response to a 0.56°C (1°F) step input for the full set of coefficients, the reduced set of coefficients, and a dropped set of the coefficients, i.e., the ASHRAE coefficients for three time steps back. The reduced coefficients closely reproduce the full set of ASHRAE coefficients while the dropped set results in errors.

When combining transfer functions for building elements, the number of past time steps in the resulting transfer function increases. Fortunately, the number of past time steps required to perform a simulation accurately can be significantly reduced by using the Padé approximation and bilinear transformation. Figure 7 shows the response to a 0.56°C (1°F) step change in outdoor temperature for full and reduced sets of single input CRTF's for the eight-surface room.

Comparison of Methods

Table 3 contains the number of mutiplications required per time step for energy balance simulations of view factor net-

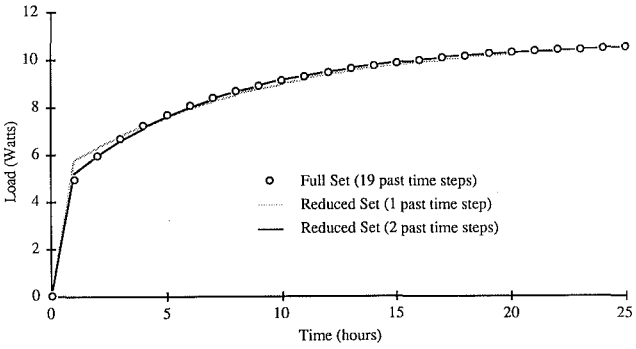

Fig.7 Response to 0.56°C (1°F) step change in outdoor temperature for eight-surface room

works with time-independent **A** matrices, multiple-input CRTF simulations, and single-input CRTF's simulations with reduced coefficients for the rooms previously described. For the methods compared in Table 3, the number of additions required per time step is close to the number of multiplications required per time step. Table 3 demonstrates that the computational savings of using reduced single-input CRTF's increase with the complexity of the zone, i.e., the larger the number of surfaces the greater the computational savings.

Table 3 shows that the computational effort of single-input CRTF simulations with reduced coefficients is less than the computational effort of energy balance simulations with time-independent **A** matrices. Sowell and Walton (1980) determined that the execution times are similar for energy balance simulations with time-dependent **A** matrices and DOE 2.1 (1980). (DOE 2.1 is an advanced weighting factor program, which assumes that heat transfer processes are linear and time-invariant.) The computational effort of energy balance simulations with time-independent **A** matrices is less than the computational effort of energy balance simulations with time-dependent **A** matrices. Therefore, reduced CRTF simulations should require significantly less effort than DOE 2.1 simulations.

Conclusion

A procedure for accurately and efficiently computing loads and floating room temperatures in buildings is presented in this paper. Three main steps are involved in this procedure. First, the resistances for a star network are computed from the resistances for a view factor network. Second, transfer functions for individual building elements of a star network are combined. Third, the Padé approximation and bilinear transformation are used to reduce the number of coefficients in the combined transfer function equation.

Acknowledgments

Financial support for this work has been provided by Lawrence Berkeley Laboratory, University of California and the Solar Heating & Cooling Research Development Branch, Office of Conservation and Solar Applications, U.S. Department of Energy.

References

ASHRAE Handbook of Fundamentals, 1985, American Society of Heating, Refrigerating and Air-Conditioning Engineers, Inc., Atlanta, GA, pp. 25.28-25.35, 1977; pp. 26.35-26.36, 1981; and p. 26.32.

Box, G. E. P., and Jenkins, G. M., 1976, *Time Series Analysis Forecasting and Control*, Holden Day, San Francisco, CA, p. 8.

Carroll, J. A., 1980, "An MRT Method for Computing Radiant Exchange in Rooms," *Proceedings of the Second Systems & Economic Analysis Conference*, San Diego, CA, pp. 343-348.

Ceylan, H. T., and Myers G. E., 1980, "Long-Time Solutions to Heat-Conduction Transients With Time-Dependent Inputs," ASME JOURNAL OF HEAT TRANSFER, Vol. 102, No. 1, pp. 115-20.

Table 3 Number of multiplications required per time step

	Energy balance	Multiple-input CRTF	Reduced single-input CRTF's
Three-surface room	35	38	20
Eight-surface room	152	109	20

Chen, C.-T., 1984, *Linear System Theory and Design*, Holt, Rinehart and Winston, New York, pp. 587-622.

Conte, S. D., and de Boor, C., 1980, *Elementary Numerical Analysis an Algorithmic Approach*, McGraw-Hill, New York.

Davies, M. G., 1983, "Optimal Designs for Star Circuits for Radiant Exchange in a Room," *Building and Environment*, Vol. 18, No. 3, pp. 135-150.

DOE-2, 1980, "DOE-2 Reference Manual, Version 2.1," Report LBL-8706, Revision 1, Lawrence Berkeley Laboratory, CA.

Gebhart, G., 1971, *Heat Transfer*, 2nd ed., McGraw-Hill, New York, pp. 150-158.

Jamshidi, M., 1983, *Large-Scale Systems Modeling and Control*, North-Holland Series in System Science and Engineering, Series Vol. 9, pp. 72-74.

Jury, E. I., 1964, *Theory and Application of the z-Transform Method*, Wiley, New York.

Kuo, B. C., 1980, *Digital Control Systems*, Holt, Rinehart and Winston, New York, pp. 286-287.

Madsen, J. M., 1982, "Modeling Heat Transfer in Rooms Using Transfer Function Methods," M.S. Thesis, University of Wisconsin—Madison, WI.

Mitalas, G. P., 1965, "An Assessment of Common Assumptions in Estimating Cooling Loads and Space Temperatures," *ASHRAE Transactions*, Vol. 71, Part II, pp. 72-80.

Mitalas, G. P., and Arseneault, J. G., 1971, "Fortran IV Program to Calculate z-Transfer Functions for the Calculation of Transient Heat Transfer Through Walls and Roofs," *Proceedings of the Conference on Use of Computers for Environmental Engineering Related to Buildings*, Gaithersburg, MD, NBS Building Science Series 39, Oct.

Mitchell, J. W., 1983, *Energy Engineering*, Wiley, New York, p. 82.

Sedgewick, R., 1983, *Algorithms*, Addison Wesley Publishing Company, Boston, MA.

Seem, J. E., 1987, "Modeling of Heat Transfer in Buildings," Ph.D. Thesis, University of Wisconsin—Madison, WI.

Seem, J. E., Klein, S. A., Beckman, W. A., and Mitchell, J. W., 1987, "Transfer Functions for Efficient Calculation of Multi-dimensional Transient Heat Transfer," *Heat Transfer in Buildings and Structures*, ASME HTD-Vol. 78, New York, pp. 25-33.

Shamash, Y., 1980, "Failure of the Routh-Hurwitz Method of Reduction," *IEEE Transactions on Automatic Control*, Vol. AC-25, No. 2, pp. 313-314.

Sowell, E. F., and Walton, G. N., 1980, "Efficient Calculation of Zone Loads," *ASHRAE Transactions*, Vol. 86, Part 1, pp. 49-72.

Spiegel, M. R., 1968, *Mathematical Handbook of Formulas and Tables, Schaum's Outline Series*, McGraw-Hill, New York, p. 236.

Stephenson, D. G., and Mitalas, G. P., 1971, "Calculation of Heat Conduction Transfer Functions for Multi-layer Slabs," *ASHRAE Transactions*, Vol. 77, Part II, pp. 117-126.

Walton, G. N., 1980, "A New Algorithm for Radiant Interchange in Room Loads Calculations," *ASHRAE Transactions*, Vol. 86, pp. 190-208.

Walton, G. N., 1984, "Developments in the Heat Balance Method for Simulating Room Thermal Response," Workshop on HVAC Controls, Modeling and Simulation, Georgia Institute of Technology, Atlanta, GA.

APPENDIX A

Extension of Pascal's Triangle

Numerical analysis textbooks (Conte and de Boor, 1980; Sedgewick, 1983) contain algorithms for multiplying polynomials. These algorithms could be used to obtain the $\nu_{j(i,n)}$ coefficients in the following equation:

$$(1-x)^i(1+x)^{n-i} = \sum_{j=0}^{n} \nu_{j(i,n)} x^j \tag{78}$$

This appendix contains a numerically efficient algorithm for determining the $\nu_{j(i,n)}$ coefficients in equation (78). The algorithm is numerically efficient because no multiplications or divisions are required. The following algorithm for computing the coefficients in equation (78) is based upon an extension of Pascal's triangle (Spiegel, 1968):

$\nu_{0(i,n)} = 1$

For $k = 1$ to i with a step size of 1

$\nu_{k(i,n)} = -\nu_{k-1(i,n)}$

For $j = (k-1)$ to 1 with a step size of -1

$\nu_{j(i,n)} = \nu_{j(i,n)} - \nu_{j-1(i,n)}$

Next j

Next k

For $k = (i+1)$ to n with a step size of 1

$\nu_{k(i,n)} = \nu_{k-1(i,n)}$

For $j = (k-1)$ to 1 with a step size of -1

$\nu_{j(i,n)} = \nu_{j(i,n)} + \nu_{j-1(i,n)}$

Next j

Next k

APPENDIX B

Padé Approximation

Jamshidi (1983) presented equations for reducing Laplace (i.e., continuous) transfer functions when the order of the numerator is equal to or less than the order of the denominator. In this paper, equations for reducing Laplace transfer functions when the order of the numerator is equal to the order of the denominator are needed. Therefore, this appendix contains equations for reducing single-input Laplace transfer functions with the Padé approximation when the order of the numerator is equal to the order of the denominator.

The reduced Laplace transfer function

$$G_r(s) = \frac{\bar{d}_0 + \bar{d}_1 s + \bar{d}_2 s^2 + \ldots + \bar{d}_m s^m}{1 + \bar{e}_1 s + \bar{e}_2 s^2 + \ldots + \bar{e}_m s^m} \tag{79}$$

is the Padé approximation of

$$G(s) = \frac{\bar{a}_0 + \bar{a}_1 s + \bar{a}_2 s^2 + \ldots + \bar{a}_n s^n}{1 + \bar{b}_1 s + \bar{b}_2 s^2 + \ldots + \bar{b}_n s^n} \tag{80}$$

(where m is less than n) if the power series expansion for $G_r(s)$ is equal to the power series expansion of $G(s)$ for terms of order s^0 to s^{2m}. Next, the equations for calculating the power series of

$$G(s) = \bar{c}_0 + \bar{c}_1 s + \bar{c}_2 s^2 + \bar{c}_3 s^3 + \ldots \tag{81}$$

will be formulated. The following equation results from equating equation (81) with equation (80):

$$\bar{a}_0 + \bar{a}_1 s + \bar{a}_2 s^2 + \ldots + \bar{a}_n s^n = (1 + \bar{b}_1 s + \bar{b}_2 s^2 + \ldots + \bar{b}_n s^n)(\bar{c}_0 + \bar{c}_1 s + \bar{c}_2 s^2 + \ldots \tag{82}$$

Multiplying the terms on the right-hand side of equation (82) together and combining common powers of the Laplace transform variable s results in

$$\bar{a}_0 + \bar{a}_1 s + \bar{a}_2 s^2 + \ldots + \bar{a}_n s^n = \bar{c}_0 + (\bar{c}_0 \bar{b}_1 + \bar{c}_1) s + (\bar{c}_0 \bar{b}_2 + \bar{c}_1 \bar{b}_1 + \bar{c}_2) s^2 + \ldots \tag{83}$$

The $\bar{c}_i$ coefficients for the power series expansion of $G(s)$ are determined by equating the coefficients of equal powers of s in equation (83).

$$\bar{c}_0 = \bar{a}_0$$

$$\bar{c}_1 = \bar{a}_1 - \bar{c}_0 \bar{b}_1$$

$$\bar{c}_2 = \bar{a}_2 - \bar{c}_0 \bar{b}_2 - \bar{c}_1 \bar{b}_1$$

$$\bar{c}_i = \bar{a}_i - \sum_{j=0}^{i-1} \bar{c}_j \bar{b}_{i-j} \tag{84}$$

To calculate the Padé approximation for $G(s)$, the power series for $G(s)$ is set equal to the Laplace transfer function $G_r(s)$. The following equation results from combining equal powers of s when the numerator of $G_r(s)$ is set equal to the denominator of $G_r(s)$ times $G(s)$:

$$\begin{aligned}\bar{d}_0 + \bar{d}_1 s + \bar{d}_2 s^2 + \ldots + \bar{d}_m s^m &= \bar{c}_0 + (\bar{c}_1 + \bar{e}_1 \bar{c}_0) s \\ &+ (\bar{c}_2 + \bar{e}_1 \bar{c}_1 + \bar{e}_2 \bar{c}_0) s^2 + \ldots \\ &+ (\bar{c}_m + \bar{e}_1 \bar{c}_{m-1} + \bar{e}_2 \bar{c}_{m-2} + \ldots + \bar{e}_m \bar{c}_0) s^m \\ &+ (\bar{c}_{m+1} + \bar{e}_1 \bar{c}_m + \bar{e}_2 \bar{c}_{m-1} + \ldots + \bar{e}_m \bar{c}_1) s^{m+1} \\ &+ (\bar{c}_{m+2} + \bar{e}_1 \bar{c}_{m+1} + \bar{e}_2 \bar{c}_m + \ldots + \bar{e}_m \bar{c}_2) s^{m+2} + \ldots \\ &+ (\bar{c}_{2m} + \bar{e}_1 \bar{c}_{2m-1} + \bar{e}_2 \bar{c}_{2m-2} + \ldots + \bar{e}_m \bar{c}_m) s^{2m} + \ldots\end{aligned} \tag{85}$$

A set of m linear equations with m unknown denominator coefficients ($\bar{e}_i$) of the Padé approximation can be formulated by equating powers of s from $(m+1)$ to $(2m)$ in equation (85).

$$\begin{bmatrix} \bar{c}_m & \bar{c}_{m-1} & \ldots & \bar{c}_2 & \bar{c}_1 \\ \bar{c}_{m+1} & \bar{c}_m & \ldots & \bar{c}_3 & \bar{c}_2 \\ \cdot & \cdot & \cdot & \cdot & \cdot \\ \cdot & \cdot & \cdot & \cdot & \cdot \\ \cdot & \cdot & \cdot & \cdot & \cdot \\ \bar{c}_{2m-2} & \bar{c}_{2m-3} & \ldots & \bar{c}_m & \bar{c}_{m-1} \\ \bar{c}_{2m-1} & \bar{c}_{2m-2} & \ldots & \bar{c}_{m+1} & \bar{c}_m \end{bmatrix} \begin{bmatrix} \bar{e}_1 \\ \bar{e}_2 \\ \cdot \\ \cdot \\ \cdot \\ \bar{e}_{m-1} \\ \bar{e}_m \end{bmatrix} = \begin{bmatrix} -\bar{c}_{m+1} \\ -\bar{c}_{m+2} \\ \cdot \\ \cdot \\ \cdot \\ -\bar{c}_{2m-1} \\ -\bar{c}_{2m} \end{bmatrix} \tag{86}$$

The denominator of the Padé approximation is determined by solving equation (86) for the $\bar{e}_1, \bar{e}_2, \ldots, \bar{e}_m$ coefficients. After determining the denominator of the Padé approximation, numerator coefficients of the Padé approximation are determined by equating powers of s from 0 to m in equation (85).

$$\bar{d}_0 = \bar{c}_0$$

$$\bar{d}_1 = \bar{c}_1 + \bar{e}_1 \bar{c}_0$$

$$\bar{d}_2 = \bar{c}_2 + \bar{e}_1 \bar{c}_1 + \bar{e}_2 \bar{c}_0$$

$$\bar{d}_m = \bar{c}_m + \sum_{i=1}^{m} \bar{e}_i \bar{c}_{m-i} \tag{87}$$

G. E. Courville
Energy Division,
Oak Ridge National Laboratory,
Oak Ridge, TN 37831-6092

J. V. Beck
Heat Transfer Group,
Department of Mechanical Engineering,
Michigan State University,
East Lansing, MI 48824
Mem. ASME

Techniques for in Situ Determination of Thermal Resistance of Lightweight Board Insulations

Four techniques for determining the in situ thermal resistance of rigid board insulation installed in conventional low-sloped roofs are described and compared. All techniques use measured temperature distributions and heat fluxes in the roof systems. The limitations of the techniques are discussed. Test results are presented to allow a comparison of the methods.

1 Introduction

Thermal resistances (R-values) of roofs or other building envelope systems are normally obtained by a calculation based on the conductivity of the individual materials making up the components. For a one-dimensional layered geometry, e.g., an insulated low-slope roof, R is given by

$$R = \sum_i t_i/k_i \tag{1}$$

where t_i and k_i are, respectively, the thickness and thermal conductivity of the ith layer. For more complex geometries, i.e., multiple heat flow paths, other methods such as the ASHRAE Zone Method (*ASHRAE Handbook*, 1985) can be used. Frequently, these values are confirmed by laboratory hot box experiments (Mumaw, 1980; Van Geem, 1984) that can simulate the geometry of roof and wall components. The actual installed R-value of a system may differ significantly from a calculated or laboratory value due to material differences, aging, thermal bridging, moisture, the quality of construction, and other factors. Field measurement is the only unambiguous way to determine the in-place thermal resistance. However, there currently is no established, reliable technique for making field measurements of installed R-values of building envelope systems. The purpose of this paper is to describe and discuss several techniques for applicability of determining R-values from field data.

The motivation for this study arises from a need to provide measurements of heat transfer in building envelope systems under field conditions. These measurements are needed to assess the thermal performance of "as-built" envelope systems and to monitor the thermal properties of in-service systems that may change because of time or because of environmental conditions.

Two techniques based on averaging are discussed in Section 2, and two techniques based on the use of least squares are given in Sections 3 and 4. Section 5 provides experimental results and Section 6 gives the conclusions.

All techniques for determining the thermal resistance of field-mounted building insulation specimens require perivelic measurements of the temperature difference and the heat flow across the specimen over an extended period of time. Thermocouples are placed on either side of the specimen and a heat flux transducer is mounted within or at the boundary of the specimen. Sensor calibration is critical. Thermocouples cut from the same wire spools are preferred and ASTM procedures should be followed for the heat flux transducer (ASTM C1046-85).

2 Averaging Techniques for Determination of Thermal Resistance From in Situ Data

2.1 Averaging Technique. One method for determining the R-value of a building system in the field is the Averaging Technique (Flanders, 1980), which gives the ratio of the average temperature difference across a sample divided by the average heat flux. This expression for R-value can be derived from the one-dimensional transient heat conduction equation

$$\frac{\partial}{\partial x}\left(k\frac{\partial I}{\partial x}\right) = \rho c\frac{\partial T}{\partial t} \tag{2}$$

to show more clearly the limitations of the technique. In equation (2) x is the space coordinate, t is time, T is temperature, k is thermal conductivity, ρ is density, and c is specific heat. Use of equation (2) implies that the heat transfer is by conduction only (no radiation or convection). Integrating equation (2) over a layer of thickness L, from $x = 0$ to $x = L$, gives

$$k\frac{\partial T}{\partial x}\bigg|_{x=L} - k\frac{\partial T}{\partial x}\bigg|_{x=0} = \int_{x=0}^{L_{\rho c}} \rho c\frac{\partial T}{\partial t}\,dx \tag{3}$$

If this expression is then integrated over time for cyclic conditions, which somewhat approximates diurnal temperature variations, one obtains

$$\int_0^t k\frac{\partial T}{\partial x}\bigg|_{x=L} dt - \int_0^t k\frac{\partial T}{\partial x}\bigg|_{x=0} dt = 0 \tag{4}$$

The right side of equation (4) is zero because the integrand is the change in internal energy of the system, which, over one cycle, does not change. Since this result is true for a layer of any thickness, equation (4) can be rewritten to show that, under the conditions of the derivation, the average heat flux at any location in the system is a constant

$$\bar{q} = \frac{1}{t}\int_0^t q(t)dt = -\frac{1}{t}\int_0^t k\frac{\partial T}{\partial x}\,dt \tag{5}$$

Notice the similarity of equation (5) to the steady-state equation

$$q = -k\frac{\partial T}{\partial x} \tag{6}$$

In the Averaging Technique method, k in equation (5) is as-

Contributed by the Heat Transfer Division for publication in the JOURNAL OF HEAT TRANSFER. Manuscript received by the Heat Transfer Division October 30, 1987. Keywords: Conduction, Instrumentation, Measurement Techniques.

sumed to be a constant and $\partial T/\partial x$ is accurately approximated at time t_i by

$$\left.\frac{\partial T}{\partial x}\right|_{t_i} \approx \left.\frac{T_2 - T_1}{L}\right|_{t_i} = -\frac{\Delta T_i}{L}; \qquad \Delta T_i \cong (T_1 - T_2)_{t_i} \tag{7}$$

Measurements of q and ΔT are made at times t_i, $i = 1, 2, \ldots, n$ so that equation (5) can be approximated by

$$\sum_{i=1}^{n} q_i = \frac{k}{L} \sum_{i=1}^{n} \Delta T_i \tag{8}$$

Defining R as the thermal resistance

$$R = L/k \tag{9}$$

and solving equation (8) for R gives

$$R_{n,av} = \left[\sum_{i=1}^{n} \Delta T_i\right] \left[\sum_{i=1}^{n} q_i\right]^{-1} \tag{10}$$

where the subscript n indicates that n measurements are used, and av denotes the average. Equation (10) is the R equation for the Averaging Technique. A number of authors have discussed the Averaging Technique (Flanders, 1980; Orlandi et al., 1984; Reddy, 1986).

The advantages of using equation (10) are that it is simple to use and easy to understand, and that it is commonly accepted. The disadvantages are: (*a*) Difficulty in evaluation is encountered if Σq_i approaches zero as it typically does during the spring and fall seasons; (*b*) uncertainty is present in assigning an average temperature for R because it changes with the temperature level; (*c*) lack of treatment of the heat capacity of the layer causes errors, particularly when the average temperature drifts up or down; and (*d*) lack of treatment of heat capacity causes errors when rapid changes in ΔT occur.

An excellent discussion of the limitation of the Averaging Technique is given by Flanders (1980). He points out that "a major problem of on-site measurement is to *determine the minimum duration of measurement to obtain an accurate R-value.*" This is because the "building component not only *resists* the flow of heat, but also *stores* heat." Since equation (10) does not account for heat storage, the averaging period must be long enough to make net heat storage small compared to net heat transferred across the component. He also points out that the component is actually exposed to random as well as cyclic conditions. For these reasons it is necessary to cover more than one full cycle (i.e., one day). Typically, for lightweight wall or roof systems a period of three days is usually adequate. In experiments at Oak Ridge National Laboratory (ORNL), however, periods of even one week are not sufficient during the spring and fall; this is because the net heat transfer [i.e., the denominator of equation (10)] can be quite small, even for these long times. Other techniques to be described are not limited to conditions when Σq_i is near zero. Moreover, these techniques can also include the heat capacity of the component.

2.2 Absolute Value Technique. Lack of rapid convergence for conditions when the average heat transfer is near zero is the most inconvenient aspect of the Averaging Technique. Orlandi et al. (1984) suggested one procedure for circumventing the problem that involves an average of separate averages that are calculated for data points with all ΔT_i and q_i being positive and for data points with all ΔT_i and q_i being negative. In a variation of this technique, ORNL has defined the Absolute Value Technique in which one simply replaces the ΔT_i and the q_i in equation (10) by their absolute values (Courville et al., 1986)

$$R_{n,ab} = \sum_{i=1}^{n} |\Delta T_i| \Big/ \left[\sum_{i=1}^{n} |q_i|\right] \tag{11}$$

where the subscript ab denotes the absolute value.

Equation (11) gives the same results as the Averaging Technique for extreme weather conditions when both the ΔT_i and q_i values are always positive or always negative. More important, experiments have shown for lightweight roof systems that this method can provide a reliable, rapidly convergent R-value under most climatic conditions. Note, however, that since equation (11) is still an averaging technique, it is subject to the same uncertainties as the Averaging Technique regarding drifting average temperature levels and heat capacity effects.

2.3 Determination of Reporting Temperature. As will be seen in Section 5, the R-values determined by both the Averaging and the Absolute Value Techniques show seasonal variation. This is reasonable because there are significant changes in mean temperature over the year and R is a function of the mean temperature. This means that a unique value of R cannot be given. It has been recently shown (Sanders, 1987) that, while it may appear attractive and it is frequently done, it is inaccurate to report calculated in situ R-values at the average midplane temperature of the system defined by

$$T_m = \frac{1}{t}\int_0^t \frac{T_1 + T_2}{2}\, dt \tag{12}$$

where T_1 and T_2 are the temperatures on either side of the system for a given measurement. Sanders (1987) argued that a more appropriate expression is the Weighted Mean Temperature, defined by

$$T_{wm} = \frac{\int_0^t (T_2 - T_1)\,\dfrac{T_1 + T_2}{2}\, dt}{\int_0^t (T_2 - T_1) dt} \tag{13}$$

When the temperature dependence of R-values obtained by averaging techniques is discussed in this paper, it is always in terms of T_{wm} defined by equation (13).

3 Least-Squares Analysis Techniques for Determination of Thermal Resistance From in Situ Data

Least-squares methods can improve upon those given in Section 2. In this section, the steady-state model given by equation (6) is used. Two models are considered, one for constant k and the other for a linear temperature dependence for k.

3.1 Constant Thermal Conductivity. In this method, the sum of squares between the measured and calculated heat flux values (q_i and F_i, respectively)

$$S = \sum_{i=1}^{n} (q_i - F_i)^2 \tag{14}$$

is minimized with respect to the thermal conductivity k. The model for F_i is

$$F_i = k\Delta T_i/L \tag{15}$$

Introducing this expression into equation (14) and differentiating S with respect to k, replacing k by k_n (the estimate for n measurement times), and setting the equation equal to zero yields

$$\left.\frac{\partial S}{\partial k}\right|_{k_n} = 2\sum_{i=1}^{n}\left[q_i - k_n\frac{\Delta T_i}{L}\right]\left[-\frac{\Delta T_i}{L}\right] = 0 \tag{16}$$

Solving for k_n yields

$$k_n = L\left[\sum_{i=1}^{n} q_i \Delta T_i\right]\left[\sum_{i=1}^{n} \Delta T_i^2\right]^{-1} \tag{17}$$

or in the form involving the resistance

$$R_{n,ss1} = \left[\sum_{i=1}^{n} \Delta T_i^2\right]\left[\sum_{i=1}^{n} q_i \Delta T_i\right]^{-1} \quad (18)$$

This equation does not have as much difficulty with the denominator going to zero because the measured heat flux q_i and temperature difference ΔT_i almost always have the same sign. Equations (11) and (18) usually give very similar values of R. Both equations (11) and (18) give values of R that should be reported at T_{wm} (see Section 2.3).

3.2 Linear-With-Temperature Thermal Conductivity. If the thermal conductivity varies significantly over the experimental temperature range, the assumption of k being constant with T is not valid, which is revealed by the calculated values of k varying with time. This time variation of k may not be apparent in the average in one week but will appear for different seasons as the average temperature changes. Because R is inversely related to k', the calculated R (for $k = C$) is also a function of time. A more realistic model than assuming that k is a constant is for the thermal conductivity being a linear function of temperature

$$k = k_0 + \beta(T - T_0) \quad (19)$$

where k is the thermal conductivity at T, k_0 is the value at $T = T_0$, and β is a measure of the change of k with temperature. For the assumption of steady-state conditions, the calculated heat flux F is a constant so that equation (6) can be used with equation (19) and integrated over x to give

$$FL = -\int_{T_1}^{T_2} [k_0 + \beta(T - T_0)]dT \quad (20a)$$

$$= k_0(T_1 - T_2) + \beta T_0(T_2 - T_1) + \beta(T_1^2 - T_2^2)/2 \quad (20b)$$

$$= \Delta T\left\{k_0 + \beta\frac{T_1 + T_2}{2} - \beta T_0\right\}, \qquad \Delta T = T_1 - T_2 \quad (20c)$$

Equation (20c) is the second steady-state model.

In the roof tests, T_1 is nearly constant so that T_0 could be chosen to be T_1, which gives further simplification. This assumption is not necessary, however, since the heat flux at time t_i can be written as

$$F_i = \left[\frac{k_0}{L} + \frac{\beta}{2L}\Delta T_{0i}\right]\Delta T_i \quad (21a)$$

where ΔT_{0i} is defined to be

$$\Delta T_{0i} = (T_1 + T_2 - 2T_0)/2 \quad (21b)$$

There are now two parameters to estimate: k_0 and β. Introducing equation (21a) into equation (14), differentiating with respect to k_0, replacing k_0 and β with $\hat{k}_0$ and $\hat{\beta}$, and setting the equation equal to zero gives one algebraic equation for $\hat{k}_0$ and $\hat{\beta}$. The $\hat{}$ symbol over k_0 and β denotes an estimated value; in other words, $\hat{k}_0$ is an estimated value of the true conductivity k_0. The procedure is repeated with differentiation of S with respect to β to obtain another algebraic equation. These two equations can be written as

$$C_{11}[\hat{k}_0/L] + C_{12}[\hat{\beta}/2L] = H_1 \quad (22a)$$

$$C_{12}[\hat{k}_0/L] + C_{22}[\hat{\beta}/2L] = H_2 \quad (22b)$$

where

$$C_{11} = \sum_{i=1}^{n} \Delta T_i^2, \quad C_{12} = \sum_{i=1}^{n} \Delta T_i^2 \Delta T_{0i},$$

$$C_{22} = \sum_{i=1}^{n} \Delta T_i^2 \Delta T_{0i}^2 \quad (23a)$$

$$H_1 = \sum_{i=1}^{n} q_i \Delta T_i, \quad H_2 = \sum_{i=1}^{n} q_i \Delta T_i \Delta T_{0i} \quad (23b)$$

and the solution for the unknowns $\hat{k}_0$ and $\hat{\beta}$ in equations (21a) and (21b) yields

$$\hat{k}_0 = L(C_{22}H_1 - C_{12}H_2)/\Delta \quad (24a)$$

$$\hat{\beta} = 2L(C_{11}H_2 - C_{12}H_1)/\Delta \quad (24b)$$

$$\Delta T = C_{11}C_{22} - C_{12}^2 \quad (24c)$$

Difficulty in obtaining solutions using equations (22)–(24) can only be encountered if ΔT is zero or very small, which can only happen if the measured temperatures change only slightly with time, an unlikely possibility.

After calculating values of the parameters, $\hat{k}_0$ and $\hat{\beta}$, for n measurements, resistance at any temperature (inside the experimental range of T_i) can be found. In particular for the temperature T_{wm}, $R_{n,ss2}$ is given as

$$R_{n,ss2} = \frac{L}{k_{\text{mean}}} = \frac{L}{\hat{k}_0 + \hat{\beta}(T_{wm} - T_0)} \quad (25)$$

Notice that a linear-with-temperature variation of the thermal conductivity does not yield a linear-with-T relation for $R_{n,ss2}$. Advantages of this steady-state method include easy-to-evaluate expressions, no difficulties during the spring and fall, and the applicability to temperature-dependent resistance. Moreover, in the case of $R = R(T)$, such as discussed in Section 3.2, the temperature for reporting R is explicitly given and the relation to the thermal conductivity is clearly exhibited.

The least-squares method for the steady-state model eliminates two of the difficulties described earlier for the averaging techniques. These include the problem with Σq_i approaching zero and the problem with reporting R at some specific temperature. Problems do remain, however, that relate to the lack of treatment of the heat capacity of the layer.

4 Least-Squares Method for Transient Model

The heat capacity of the layer can be included in the analysis by using the heat conduction model, equation (2). The program PROPOR is a FORTRAN computer program developed by Beck at Michigan State University for estimating the thermal conductivity k and the product ρc from transient heat flux and temperature measurements (Beck and Arnold, 1977).

The concepts embedded in PROPOR are a natural extension of those described in connection with the steady-state least-squares methods. The sum of squares to be minimized is now

$$S = \sum_{i=1}^{n}\sum_{j=1}^{J} (Y_{ji} - T_{ji})^2 \quad (26)$$

where Y_{ji} is the measured temperature at time t_i and location x_j and T_{ji} is the corresponding calculated temperature. The T_{ji} values are calculated using Crank–Nicolson finite difference equations derived from the heat transfer equation (2), with appropriate boundary conditions. For the geometry shown in Fig. 2, the foam is the test material and the x domain starts at the lower side of the foam (at which the one thermocouple and the heat flux transducer are located) and ends at the upper side of the foam (at which another thermocouple is located). The boundary conditions used in calculating T_{ji} are the measured heat flux history at the lower surface and the measured temperature history at the upper surface. The program PROPOR can use temperatures for many interior locations in equation (26), but in the specimen shown in Fig. 2, the only location that can be used is for the thermocouple at the lower surface; hence for this case the upper j limit in equation (26) is $J = 1$. (A boundary condition temperature history included in equation (26) makes no contribution because $T_{ji} = Y_{ji}$ at the boundary.)

The calculated temperatures T_{ji} are functions of the thermal conductivity k of the test material. The function S is minimized by differentiating equation (26) with respect to the k com-

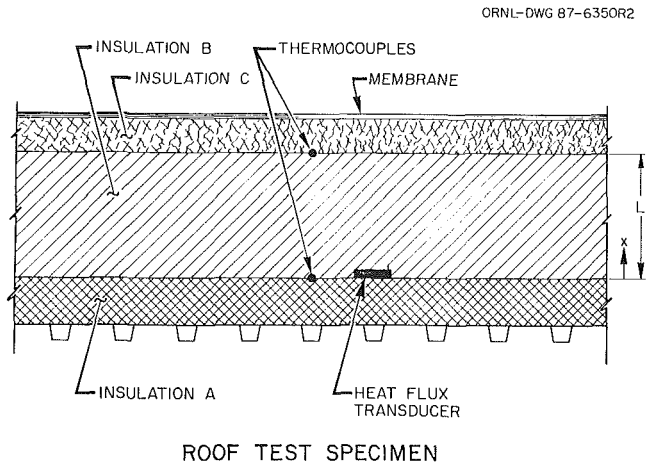

Fig. 1 Schematic drawing of the roof test specimen

ponents desired, set equal to zero and so on as mentioned in Section 3. The main difference is that T_{ji} is a nonlinear function of k even for the T-independent case. (See Beck and Arnold, 1977, Chapter 7, for details regarding treatment of nonlinear estimation problems.)

PROPOR was used to estimate a temperature-independent thermal conductivity k and a temperature-dependent k using the model

$$k = k_a + \frac{k_b - k_a}{T_b - T_a}(T - T_a) \tag{27}$$

where the unknown parameters are k_a and k_b, which are k at the selected temperatures T_a and T_b, respectively. Equation (27) is equivalent to equation (19). In the calculations, the ρc term in equation (2) was set equal to a certain value; its value has little effect on the results given below. (If necessary, the value of ρc can be determined using PROPOR. PROPOR is also capable of treating temperature variability of k and ρc.)

Notice that the program PROPOR eliminates all the disadvantages mentioned below equation (10): (*a*) There is no difficulty in the spring and fall where Σq_i approaches zero. (*b*) If the temperature-dependent model for k is used, equation (27), the temperature for k and hence R can be readily assigned. (*c*) The heat capacity is treated so that drifts in the average temperature have no effect. (*d*) Also, since the heat capacity is included, rapid transients should be amenable to treatment. There are further advantages. Since there is an attempt to describe all the relevant phenomena, deviations e_{ji} between the measured and calculated temperatures, which are called residuals, e_{ji}

$$e_{ji} = Y_{ji} - T_{ji} \tag{28}$$

can be examined to determine the adequacy of the heat conduction model, equation (2). If there are systematic deviations, the model might have to be improved to include other effects such as moisture movement and radiation heat transfer. Examination of the residuals can give insight both into the need to improve the model and into the types of improvement that should be considered.

5 Experimental Results

A detailed comparison of these techniques has been conducted using data obtained from the Roof Thermal Research Apparatus (RTRA), a facility of the Roof Research Center at Oak Ridge National Laboratory (Courville et al., 1984). The RTRA is a small building with replaceable panels in the roof. Roof systems, along with the sensors for particular tests, are assembled into panels. Panels are then transported and mounted into slots in the roof of the RTRA. Panels will hold roof

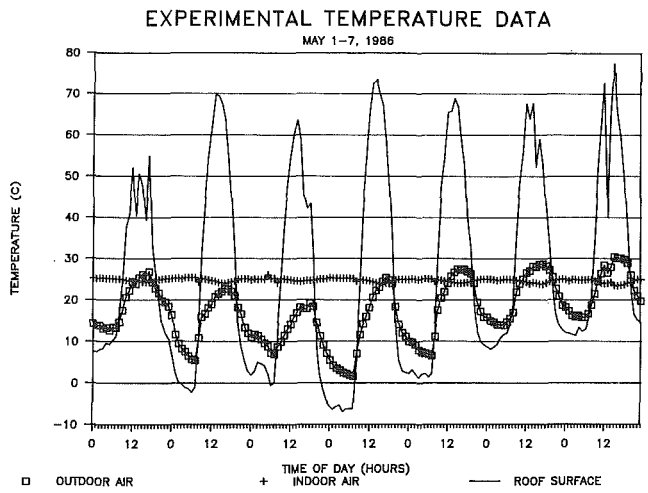

Fig. 2(*a*) Measured specimen surface temperatures during the week of May 1, 1986. Hour zero corresponds to midnight and hour 12 to noon. During this period the outdoor temperature was mostly below the indoor temperature, and the roof surface temperature was considerably above the outdoor air temperature during the days because of solar heating and below the outdoor air temperature during the nights because of radiation cooling.

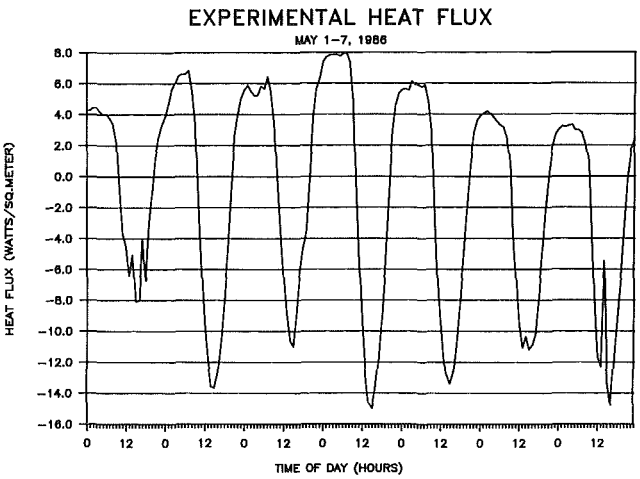

Fig. 2(*b*) The heat flux measured by the heat flux transducer positioned as shown in Fig. 1. THe data are for the same time period as Fig. 2(*a*).

systems that are 4 ft (1.2 m) by 8 ft (2.4 m) in dimensions. A computer analysis of this configuration has shown, for all roof systems for which tests are planned, that no significant thermal influence of the specimen holder extends more than about 1 ft (0.3 m) into the specimen. Thus, the thermal performance of the central 2 ft (0.6 m) by 6 ft (1.8 m) region is similar to that of a portion of a real roof of the same construction. Roof systems tested to date have all been one dimensional in the sensing region.

The particular roof construction for the tests described in this report is shown in Fig. 1. The deck is 0.047 in. (0.0012 m) galvanized steel. The bottom insulation board is 0.75 in. (0.019 m). Over this is one 2-in. (0.0508 m) insulation board. Next is a 1/2-in. (0.0127 m) top board. The waterproofing membrane is 0.06 in. (0.0015 m). All joints are staggered with no joints in the metering area. All thermocouples are copper-constantan and are taken from the same spool to minimize errors in temperature differences. Heat flux transducers are thermopile disks, 2 in. (0.05 m) by 2 in. (0.05 m) in area and 1/8 in. (0.0032 m) thick. (The heat flux transducers were made by Hy-Cal Engineering, Model BI-7-120-WP-T.) They are calibrated in situ by assembling the entire insulation assembly into its final configuration and placing it into an unguarded

hot screen laboratory steady-state thermal conductivity tester that has been shown to measure thermal conductivity to within one percent of the National Bureau of Standards guarded hot plate (Yarbrough et al., 1986). Heat flows are established and measured in the screen tester and a transducer voltage–heat flow calibration equation is developed over the temperature range of the screen tester. In addition to a calibration of the heat flux transducers, the screen tester also provides a base line laboratory measurement of the temperature dependence of the thermal conductance of the test specimen for temperatures above room temperature.

Typical data from sensors are shown in Fig. 2. Hourly data points are obtained by averaging over eleven 1-min readings from five minutes before to five minutes after the hour. As seen in Fig. 3(*a*), roof surface temperatures are considerably higher than outdoor air temperature during the day because of solar heating of the dark-colored membrane, and they are below air temperature during the night due to radiation loss to the cold sky. Sharp changes in surface temperature, for example in the seventh day in Fig. 2(*a*), have been correlated to cloud cover or to wind gusts, which can strongly influence the highly unstable surface-to-air temperature gradients. Heat flux q for the same time period is shown in Fig. 2(*b*). Heat flow out of the building is positive. Thus, during the night when the outside is cold relative to the inside, q is positive, and during the day when the temperature gradient reverses, this flow is negative. Time lags between peak exterior surface temperature and interior heat flux are small (about 1 hour) because this is a low mass, low R-value system.

All techniques for determining the thermal properties of in situ envelope systems require a data set of temperatures and heat fluxes over an extended time period. The length of this time period, which depends upon material properties and upon climatic conditions, is difficult to determine. For the RTRA, each data set contains 168 hours (7 days). For the Averaging Technique where the R-value is determined from the ratio of the average temperature difference to the average heat flux over a specified time period, this ratio is recalculated each hour for the entire 168 hours. Thus, it is possible to inspect the resultant R-value at each hour over the full time period for anomalous behavior. It has been determined from experience that 7 days is adequate to obtain reliable R-values, except when using the Averaging Technique in climates where the average heat flux is near zero at various times during the test period. An example of the importance of such an inspection is shown in Fig. 3.

Figure 3(*a*) is a plot of the average heat flux updated each hour during the test period

$$q_{\text{avg}} = \frac{1}{n}\sum_{i=1}^{n} q_n \tag{29}$$

and Fig. 3(*b*) shows the R-value calculated using the Averaging Technique and the Absolute Value Technique. These data were recorded during a mild period when the average heat flux was near zero, as can be seen from Fig. 3(*a*). Note that the R-value using the Averaging Technique appears very erratic especially when compared to the R-value using the Absolute Value Technique, which is not sensitive to small average heat flux. One benefit of a continuous display of the R-value is that it clearly shows that it would be difficult in this case to specify an R-value from the Averaging Technique for this time period.

The Absolute Value Technique, which is not influenced by near-zero values of the average heat flux, converges quickly to a single value. This distinction between the two techniques is observed routinely during transition seasons. As indicated in Section 2.1, this problem limits the usefulness of the Averaging Technique.

As mentioned in Section 4, PROPOR can let the thermal conductivity k vary linearly with temperature in a data set. The R-values are calculated in a manner analogous to equation (25). The temperatures T_a and T_b in equation (27) are chosen to cover the temperature range in an experiment; T_a could be the lowest observed temperature and T_b the highest. The R-values associated with T_a and T_b can be plotted in a similar fashion to those from the other techniques. As examples, Figs. 4 and 5 show these high and low-temperature R-values along with R-values determined by the Averaging Technique and the Absolute Value Technique. Figure 4 illustrates results under the best of conditions, namely a week of cold winter weather when the temperature difference across the sample is large most of the time and reversals in the heat flow over the period are minimal. Here, as one would expect, the R-values for the two averaging techniques agree and both are bounded by the PROPOR upper and lower limits.

Figure 5 shows what happens under transitional season conditions. PROPOR still provides upper and lower limits on the R-value and the R-value from the Absolute Value Technique is still within these limits. Now, however, the R-value from the Averaging Technique has not stabilized and is obviously not a reliable measure of system performance. Two other points

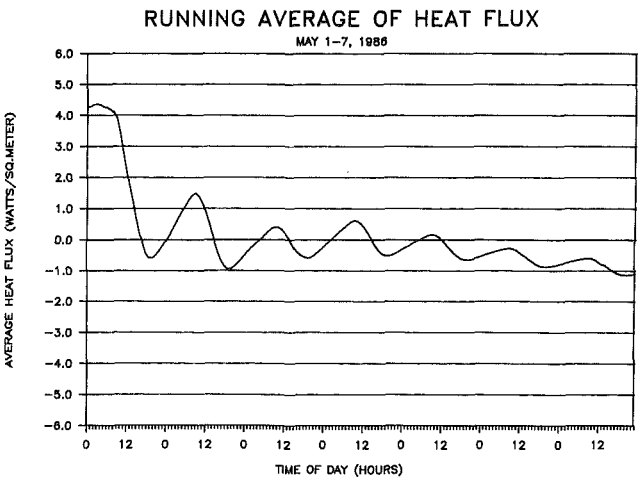

Fig. 3(*a*) A running average of the hourly heat flux shown in Fig. 2(*b*). The value at the far right represents the average hourly flux over the full 168-hour period. Note that this coverage is near zero and, for several days, oscillates above and below zero.

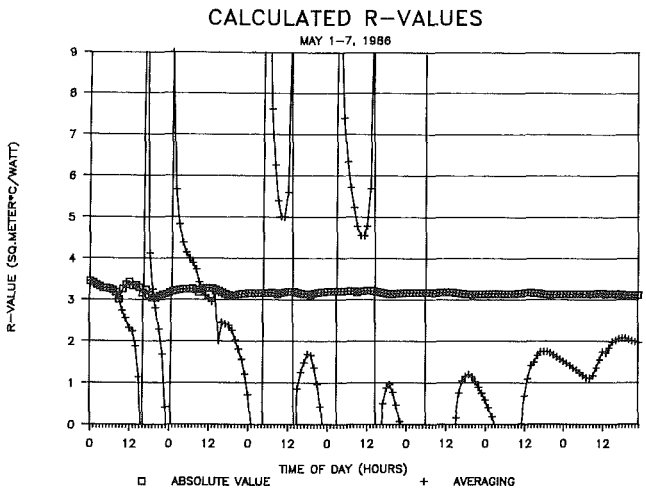

Fig. 3(*b*) Using the average heat flux shown in Fig. 3(*a*) and measured values of the temperature difference across the specimen, one can calculate R according to the Averaging Technique [equation (10)] and the Absolute Value Technique [equation (11)]. The dramatic lack of convergence in the Averaging Technique is due to uncertainties in equation (10) over much of the range.

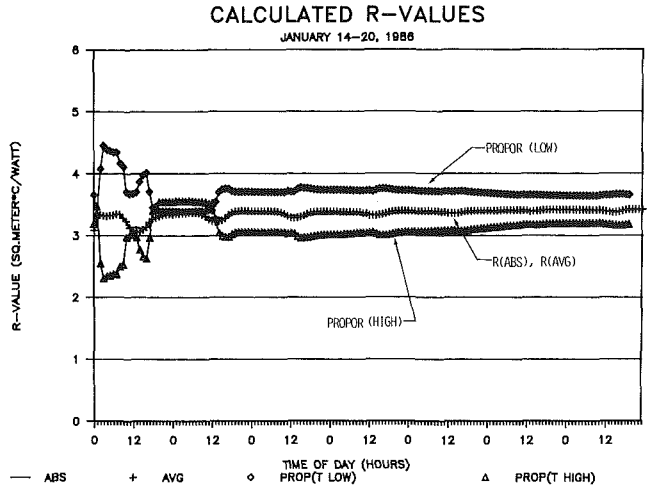

Fig. 4 Calculated *R*-values using different techniques for Jan. 14-20, 1986. The PROPOR method provides high and low values for *R*. These should, and do, bound the value calculated according to the Averaging Technique and the Absolute Value Technique. The latter two methods produce nearly identical results during very cold weather.

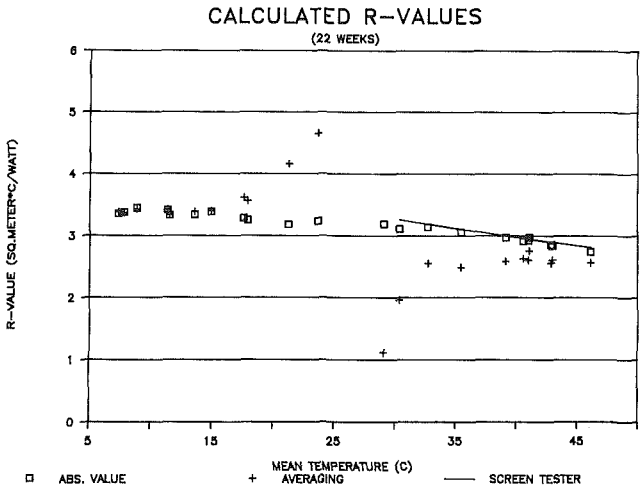

Fig. 6 *R*-values for the Averaging and the Absolute Value Techniques are plotted against weighted mean temperature. Each data point is the result of analysis of 1 week (168 hours) of data. Also plotted on this curve are laboratory steady-state data obtained from the ORNL Screen Tester Apparatus (Yarbrough et al., 1986).

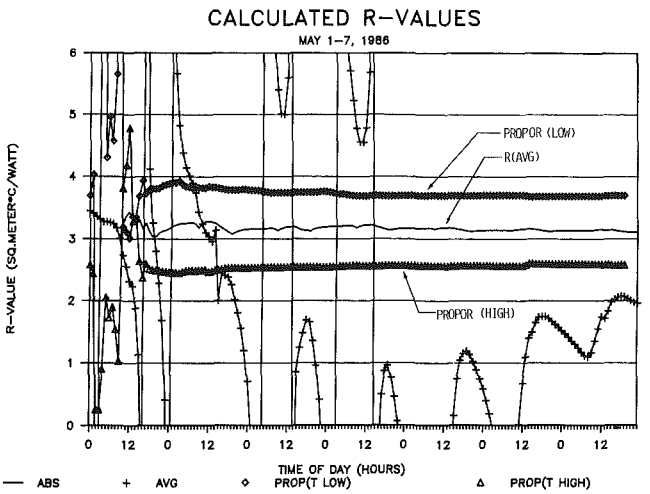

Fig. 5 Calculated *R*-values using the same techniques as in Fig. 4 for May 1-7, 1986. Note that the Averaging Technique gives very irregular results for this mild weather.

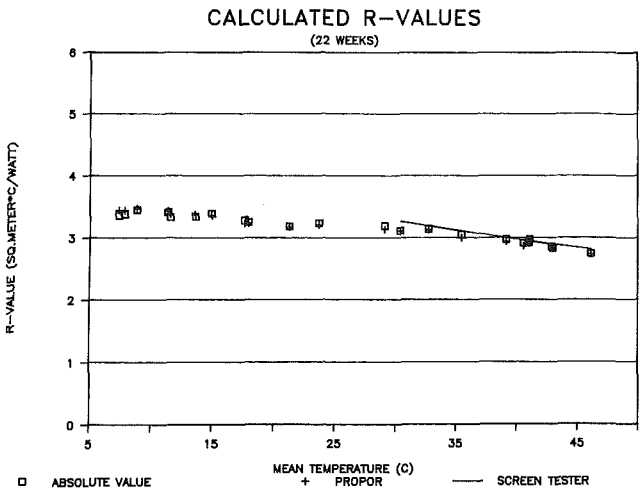

Fig. 7 A similar plot to Fig. 6. Here the *R*-values calculated by the Absolute Value Technique are compared to values calculated by PROPOR.

are worth noting in Figs. 4 and 5. First, the difference between the upper and lower PROPOR limits increases as the mean temperature in the specimen increases. This is because the *R*-value is a function of temperature and the range of temperatures increases during the summer. Second, the *R*-values change from figure to figure. This is again because *R*-value is a function of temperature and each curve represents a distinctly different temperature regime.

As mentioned in Section 2.3, care must be taken in comparing the results of the Averaging Technique and the Absolute Value Technique to laboratory results because laboratory results are recorded at a unique mean temperature and a field result is the average over a wide range of mean temperatures. Using the Weighted Mean Temperature defined in Section 2.3, *R*-values are plotted in Fig. 6 for both techniques along with results derived from laboratory measurements using the ORNL Screen Tester. Each field data point is the *R*-value after a 7-day averaging period (for example, the right abscissa intercepts on Fig. 3(*b*) are the values chosen for the week of May 1-7, 1986). Equation (13) is then used to determine the weighted mean temperature for the week and the *R*-values are plotted at this mean. Twenty-two one-week periods extending from December 14, 1985 through July 21, 1986 have been treated similarly. The agreement between the Absolute Value Technique and laboratory results is seen to be quite good in the region where the laboratory values were determined. As one would expect, there is considerable uncertainty in the results for the Averaging Technique in the region where the weighted mean temperature is near the building interior temperature, since this is where the average heat flux should be near zero. It is not clear at this time what causes the low values for *R*-value using the Averaging Technique at high weighted mean temperatures.

In Fig. 7 the *R*-values from the Absolute Value Technique and the Screen Tester are again plotted against the weighted mean temperature. This time, however, the additional data points are from the PROPOR calculations. The agreement is excellent.

This shows consistency between the PROPOR technique and laboratory results and it also offers additional confirmation of the usefulness of the Absolute Value Technique and of the usefulness of the definition of weighted mean temperature used in this study.

The Steady-State Least-Squares Technique has been applied to the same data set as the other techniques. The results, not shown in this paper, are in very good agreement with PROPOR and with the Absolute Value Technique. Note that the appli-

cation of equation (25), as with the PROPOR technique, does not have an ambiguity in reporting temperature.

6 Conclusions

There is a need for techniques that allow determination of the thermal resistance of in situ building envelope systems. Several promising techniques requiring temperatures on either side of a specimen and surface heat fluxes have been evaluated in this paper using data obtained from the Roof Thermal Research Apparatus at Oak Ridge National Laboratory. All these techniques give useful results provided they are used within bounds determined by their limitations.

The Averaging Technique as described by equation (10) requires the least sophistication and should be reliable provided:

(*a*) The average heat flux is not near zero during the testing period.

(*b*) The values of R-value obtained are reported at the weighted mean temperature. Results from this study support the use of equation (13) for determining the weighted mean temperature.

(*c*) Proper account is taken of the thermal mass of the system under test. This impacts on the time selected for the averaging period. For the lightweight roof systems in this study, the 7-day period was adequate.

(*d*) The mean temperature does not drift up or down significantly. The ORNL data do show a drift in the calculated R-value with time when the mean temperature is drifting. While noticeable, this drift has never amounted to more than a few percent.

Each of the other techniques defined in this paper addresses one or more of these limitations.

The Absolute Value Technique defined by equation (11) does not show a discontinuity when the average heat flux is zero. This technique has given R-values consistent with laboratory measurements and consistent with more theoretical techniques (e.g., PROPOR) for all the steel deck, low-mass systems tested to date.

The steady-state least-squares technique is simple to use and has the Absolute Value Technique advantage of having no difficulty when the average heat flux is zero. For this study, the steady-state least-squares technique, the Absolute Value Technique, and PROPOR all gave very nearly the same results, provided the weighted mean temperature is used to assign R-values. The temperature-dependent least-square equation, equation (25), and PROPOR both clearly and unambiguously relate R to temperature. In addition, the program PROPOR includes the heat capacity and potentially can give insight into the adequacy of the mathematical model and can suggest areas that need improvement. Such information cannot be obtained from the Averaging and Absolute Value techniques. Hence, the least-squares techniques, particularly PROPOR, retain much more of the information content of the measurements. In summation, for the data and techniques examined, all techniques (except the Averaging Technique) gave nearly the same results. For other cases when heat capacity is important, or an improved model is necessary to account for temperature dependence, radiation transfer, or moisture movement, least-square methods such as used in PROPOR are needed.

Acknowledgments

Research was sponsored by the Office of Buildings and Community Systems, Building Systems Division, U.S. Department of Energy under contract No. DE-AC05-840R21400 with Martin Marietta Energy Systems, Inc.

References

ASHRAE, 1984, *ASHRAE Handbook of Fundamentals*, Atlanta, GA, Chap. 23.

ASTM, 1986, *Annual Book of ASTM Standards*, Vol. 04.06, Philadelphia, PA.

Beck, J. V., and Arnold, K. J., 1988, *Parameter Estimation in Engineering and Science*, Wiley, New York.

Courville, G. E., Childs, K. W., and Griggs, I. E., 1984, "Thermal Performance Measurements of Insulated Roof Systems," ASTM C-16 Conference on Thermal Insulation, Materials and Systems, Dec. 2–6; to be published by ASTM.

Courville, G. E., Sanders, J. P., and Childs, P. W., 1986, "Dynamic Thermal Performance of Insulated Metal Deck Roof Systems," *Thermal Performance of the Exterior Envelopes of Buildings III*, ASHRAE SP 49, Atlanta, GA.

Flanders, S. N., 1980, "Time Constraints on Measuring Building R-Values," CRREL Report 80-15, U.S.A. Corps of Engineers, Cold Region Research and Engineering Laboratory, Hanover, NH.

Mumaw, J. R., 1980, "Thermal Research Facility—A Large Calibrated Hot Box for Horizontal Building Elements," STP 718, ASTM.

Orlandi, R. D., Derderian, G. D., Shu, L. S., Siadat, B., and Cirignano, P. C., 1984, "In Situ Thermal Performance Measurements of Some Roof Deck Systems," ASTM C-16 Conference on Thermal Insulations, Materials and Systems, Dec. 2–6; to be published as an ASTM STP.

Reddy, C. S., 1986, "Evaluation of a Method for Determining In Situ Insulation Values," ASME Paper No. 86-WA/HT-74.

Sanders, J. P., 1987, ORNL, Private Communication; to be published in an ORNL Technical Report.

Van Geem, M. G., 1984, *Calibrated Hot Box Test Results Data Manual—Vol. 1*, ORNL/Sub/79-42539/4. Oak Ridge National Laboratory.

Yarbrough, D. W., McElroy, D. L., and Graves, R. S., 1986, "Thermal Resistance of Roof Panels and In Situ Calibration of Heat Flux Transducers," *Thermal Performance of the Exterior Envelopes of Buildings III*, ASHRAE SP 49, Atlanta, GA.

An Experimental Determination of the Thermal Conductivity of a 304L Stainless Steel Powder Metallurgy Material

J. S. Agapiou
Senior Project Engineer,
General Motors Technical Center,
Warren, MI, 48090-9040
Assoc. Mem. ASME

M. F. DeVries
Professor of Mechanical Engineering,
University of Wisconsin—Madison,
Madison, WI 53706-1572
Fellow ASME

The thermal conductivity of a 304L stainless steel powder metallurgy (P/M) material was experimentally determined to support research aimed at understanding the poor machining characteristics of P/M austenitic stainless steels. Thermal conductivity measurements were made on samples having relative densities ranging between 64 and 90 percent of theoretical density since workpieces requiring machining are often fabricated in that density range. The measurements were also made over a temperature range of 50 to 300°C since workpiece temperatures can attain levels this high during the machining operation. The thermal conductivity was measured using an apparatus having a design based on the comparative method. The experimentally determined thermal conductivities were modeled by mathematical models found in the technical literature and modified for the present study. The thermal conductivity of this material increases with increasing relative density and temperature; it is also dependent on the matrix structure for a given porosity.

Introduction

The thermal conductivities of porous materials differ from those of fully dense materials since they are affected by the thermal conductivity of the base metal, the nature and amount of porosity, and the atmosphere present within the pores. These characteristics, and others, contribute to making the theoretical computation of the thermal conductivity of porous materials very difficult; thus experimental techniques are commonly used instead.

The mechanism of heat transfer in porous materials is complicated by the irregularity of the microstructure. In porous materials, heat is propagated by three processes: thermal conduction through the solid phase, radiation across the pores, and convention through the porous phase. Convection can be neglected for small pore sizes, while radiation is not a factor at low or intermediate temperatures, as noted by Luikov et al. (1968), Kingery and McQuarrie (1954), and Loab (1954).

In general, P/M materials have anisotropic thermal conductivity given by the tensor equation

$$\underset{\sim}{q} = -\underset{\approx}{K} \cdot \underset{\sim}{\nabla} T \tag{1}$$

The total thermal conductivity in a multiphase material will depend on the thermal conductivity of each phase, the proportions of each phase, and the way in which the phases are distributed (Kingery and McQuarrie, 1954). The distribution of the phases includes their size, shape, orientation, continuity relative to the heat flow direction, grain size, grain boundary thickness, and whether the phases are isometric or anisometric with ordered or random distribution. The conductivity is further dependent on the emissive and absorptive properties of the phases if there is any radiative heat transfer. If one of the phases is a void, such as the pores in a sintered P/M material, the thermal conductivity can be related to the conductivity of the completely dense material only if the effect of porosity is known.

There have been a number of porous material thermal conductivity predicting equations published based on theoretical studies; those most often cited are the ones by Loeb (1954), Russell (1935), and Eucken (1932). Their validity and accuracy were compared by Francl and Kingery (1954) using alumina ceramic materials having cylindrical, spherical, and ellipsoidal isometric-shaped pores. It was found that the mean deviation of the experimental data for the Loeb and Russell equations was about 2–3 percent, and a maximum error of 10 percent was present. The data fell substantially above the Eucken equation for pores oriented parallel to the heat flow. In the case where the cylindrical pore axes were perpendicular to the heat flow, the Eucken and the Russell equations do not apply, while the Loeb equation was in good agreement with the experimental data. The Russell equation was not applicable to anisometric pores, while Loeb's equations was applicable to both isometric and anisometric pores. Loeb (1954) suggested the following model:

$$\underset{\approx}{K} = \underset{\approx}{K}_B \cdot (\underset{\approx}{1} - \underset{\approx}{B} \cdot p) \tag{2}$$

The pore volume fraction p is equal to the pore fraction cross-sectional area for isometric pores. The term B is a second-order tensor depending upon the shape and distribution of the pores. The following discussion is concentrating on isotropic materials. At low temperatures and under the assumptions that (1) the solid matrix phase is continuous, (2) pores are isometric, (3) the distribution of the pores is uniform, and (4) the conductivity of the pores is zero, the Loeb equation reduces to

$$K = K_B \cdot (1 - p) \tag{3}$$

Other well-known models are that of Maxwell (1954)

$$K = K_B \cdot (1 - p)/[(1 + p)(C - 1)] \tag{4}$$

and Murabayashi's (1969) empirical relationship

$$K = K_B \cdot (2 - 3P_f) \cdot (1 - p)/(2 + p) \tag{5}$$

where

$$P_f = 1 - (1 - p)^n \tag{5A}$$

The Maxwell, Murabayashi, and Loeb models were evaluated experimentally by El-Fekey et al. (1978) on thoria compacts

Contributed by the Heat Transfer Division for publication in the JOURNAL OF HEAT TRANSFER. Manuscript received by the Heat Transfer Division February 26, 1988. Keywords: Measurement Techniques, Porous Media, Thermophysical Properties.

having porosities in the range of 19 to 46 percent and at temperatures ranging from 500 to 900°C. The pore shape was irregular. The Murabayashi relationship was found to be better than the Loeb and the Maxwell equations for explaining the experimental results.

More complex, although less frequently applied, thermal conductivity predicting relationships have been proposed for metal matrix materials other than those mentioned above. Kingery and McQuarrie (1954) discussed the effect of porosity on the thermal conductivity of ceramic materials and reported that the Eucken and Russell equations led to essentially identical results in that the thermal conductivity decreased almost linearly with the pore fraction as long as the solid phase was continuous. Cheng and Vachon (1970) developed a theoretical technique to predict the thermal conductivity of heterogeneous porous materials. They compared their equation with those of Russell, Eucken, and Loeb. All gave similar average percentage deviations from measured values of thermal conductivity. Marino (1971) studied the variation of the porosity shape and distribution correlation factor B, used in equation (2), with temperature and pore shape using the Ericke (1924) equation for the thermal conductivity of a two-phase medium considering the second phase as randomly distributed ellipsoids. Marino's model was applied to experimental data from ThO_2 and ThO_2–UO_2 specimens to obtain accurate B values. Brailsford and Major (1964) derived expressions for the thermal conductivity of two-phase media from a simple physical model involving various types of structures. They point out that completely general predictions of thermal conductivity cannot be made unless some knowledge of the degree of continuity of both phases is available. Equation (5) was obtained from the Brailsford and Major equation for continuous solid phase materials having pores that are either vacuum or filled with air. Kuzay (1980) compared some of the more complex developed correlations, including the Eucken and Russell equations, for two-components (solid and gas) porous systems. His comparison was made difficult owing to the large scatter in the data. Kelly et al. (1983) also evaluated the effective thermal conductivity for two component systems; firstly, based on the Luikov (1968) approach and secondly, on a method that linearly combines the effective conductivities of each component based on volume percent. Both methods yielded essentially the same results. Chiew and Glandt (1983) derived an expression for the thermal conductivity of materials with spherical pores that considers the effect of radiation within the pores. Their equation was similar to the original Maxwell equation. They also noted that the thermal conductivity is a strong function of the temperature, pore size, and number of pores. Zumbrunnen et al. (1986) developed a thermal conductance model for porous materials using geometric parameters characteristic of the matrix structure. They defined, in a probabilistic form, a unit cell for which an overall thermal resistance can be calculated from individual heat transfer mechanisms. They found that the thermal conductivity can increase or decrease with increasing porosity depending on the significance of radiation within the pores.

In NASA sponsored work (Koh, 1971; Tye, 1970), the thermal conductivity of porous materials, including 304L stainless steel Rigimesh wire, 304L stainless steel sintered spherical powders, and sintered spherical OFHC copper powders, was studied and correlated with density and temperature. Samples were made with porosity ranging between 9 and 38 percent. The effect of temperature on the thermal conductivity was represented by

$$K/K_{100} = 1 + a \cdot (T - 100) \tag{6}$$

A dimensionless or relative conductivity proposed by Koh (1971) is represented by the equation

$$K/K_B = (1 - p)/(1 + 10 \cdot p^2) \tag{7}$$

The validity of these models for microstructures produced by irregularly shaped powders is unknown.

The effect of temperature on thermal conductivity at different porosity levels was found to be small and within the experimental error of the thermal conductivity measurements for temperatures below 900°C (Koh, 1971; Luikov, 1968; Zumbrunnen, 1986). Francl (1954) reported a significant influence of the porosity level on conductivity for temperatures higher than 600°C on Al_2O_3 materials. Marino (1971) found that the effect of temperature on the constant C given in equation (4) is small and the same for different porosity levels in the temperature range of 300–1900°C for ThO_2 and ThO_2–UO_2 materials.

One of the best techniques for experimentally determining the thermal conductivity of a P/M material is the comparative method used by Stuckes and Chasmar (1956), Williams and Blum (1867), and Mirkovich (1965). A sample with unknown conductivity is placed between two reference specimens of known thermal conductivity. Steady-state heat flow is maintained throughout the column of reference and test specimens. The steady-state heat flow through each specimen should then be the same and Fourier's law of one-dimensional flow can be applied. As long as the temperature distribution along the guard cylinder is approximately equal to that along the specimens, the errors introduced by the comparative method are minimized (Flynn, 1969; Laubitz, 1969; Tye, 1969).

The 304L stainless steel sintered material made from irregular shape powder was chosen for the present study because it represents a commonly used engineering material. The results can also be compared to those for 304L stainless steel sintered materials formed from a Rigimesh matrix or spherical powders; this will help to evaluate the significance of the matrix structure on the thermal conductivity.

Experimental Procedure

Material and Samples. The test samples used in this study were prepared from standard commercial 100 mesh grade Pfizer Co. 304L atomized prealloyed stainless steel powder. The samples were produced by SSI Technologies, Inc. The chemical composition and bulk properties of the Pfizer powder are given in Table 1.

Cylindrical sintered specimens 19 mm in diameter were prepared at 64, 70, 73, 80, 84, and 90 percent relative density. The relative sintered density was calculated using a theoretical density of 7.8 mg/m^3 (Tye, 1969). The length and diameter of the sintered samples was chosen to be equal to minimize their

Nomenclature

a = a modeling constant $= 8.9 \times 10^{-4}$ for stainless steels
B = a constant depending on pore shape and distribution
C = a modeling constant
K = thermal conductivity of the P/M material
K_B = thermal conductivity of the fully dense material
K_{100} = thermal conductivity at 100°C
K^* = relative thermal conductivity
p = pore volume fraction
$\dot{q}$ = heat flux
ΔT = temperature difference for a given span
Δx = distance between two thermocouples for a given span
∇T = temperature gradient

Table 1 Chemical composition of the 304L stainless steel atomized metal powder, P304L (100)

Chemical composition, weight percent							
C	Ni	Cr	Fe	Si	Mn	S	P
0.018	11.72	18.98	Bal.	0.66	0.13	0.01	0.02
	Apparent density:			2.83 g/cc			
	Flow:			28.7 s/50 g			
	Green density:			6.82 g/cc			

variation in density. A detailed description of the microstructures of the base material for all relative density levels is available in the literature (Agapiou, 1985).

Thermal Conductivity Measurement Apparatus. Our apparatus, shown schematically in Fig. 1, is a version of the equipment described by Francl and Kingery (1954), Tye (1970), and Mirkovich (1965). A sintered cylindrical sample of unknown thermal conductivity (identified by the symbol II in Fig. 1) was placed between two Iconel 600 reference specimens (Wyrick, 1984) having a known thermal conductivity in the temperature range of 300 to 800 K.

The interfacial thermal resistance between the Inconel reference specimens and the unknown specimen was reduced by grinding and polishing their end surfaces and placing a thin (0.025 mm) silver foil between the contacting surfaces after coating both sides with a very thin layer of high-temperature silica paste. The advantage of this procedure is that it helps to improve uniform linear heat flow within the samples. Pressure was applied at the top on the specimen column through a spring to help ensure good contact. Unavoidably, some of the pores in the surface layers of the samples filled with metal due to the grinding and polishing processes. However, the effect of this very small layer of slightly higher density material was felt to be insignificant; the thermocouples on the sintered test specimens were attached about 1.3 mm away from the top and bottom specimen surfaces. The silica paste was not absorbed into the bulk material of the sample. Thus, the measured properties were those of the bulk properties of the specimen. The advantage of this procedure is that it helps to improve the uniform heat flow within the sample.

The four thermocouples on the sintered test specimens were attached by the condenser-discharge method so that the porosity of the unknown specimens at their surfaces in the junction areas would not be affected. The locations of the thermocouples were measured by an optical measuring microscope after they were attached.

There was no difficulty in maintaining a steady-state temperature during the experiments. A detailed description of the apparatus is available in the literature (Agapiou, 1985).

Determination of Thermal Conductivity. The thermal conductivity of the 304L stainless steel P/M material was determined for each of six different densities at four different temperature levels: 50, 100, 200, and 300° C. Temperatures were measured for the three spans identified in Fig. 1 as I, II, and III; the temperature gradient $\Delta T/\Delta x$ was determined for each span. For the specific measurement conditions used in this study, the interfacial temperature drop, temperature uniformity, and heat flow equality did not need to be rigorously established since the average of the heat flux through the top and bottom reference specimens was used as the heat flux through the unknown specimen. Three replicates of each run were performed with different density samples selected in random order. The thermal conductivity of the sample was calculated using Fourier's law. Steady-state conditions were considered achieved when the temperatures on the column did not vary more than 1 °C in one hour. When steady-state conditions were reached after some four to six hours, the temperatures of all thermocouples were recorded and then repeated twice at one hour intervals.

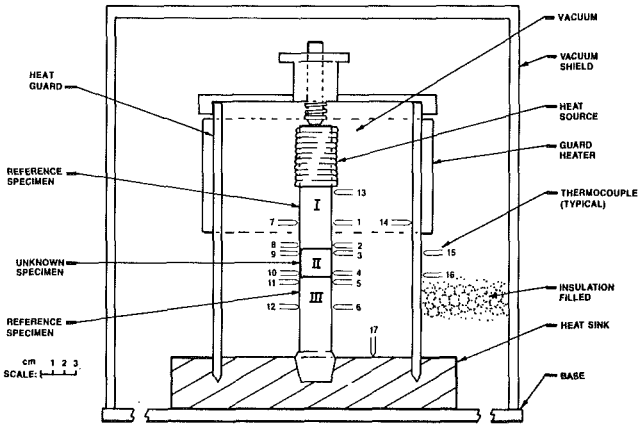

Fig. 1 An apparatus to measure thermal conductivity by longitudinal heat flow through two reference specimens with a test sample sandwiched between them

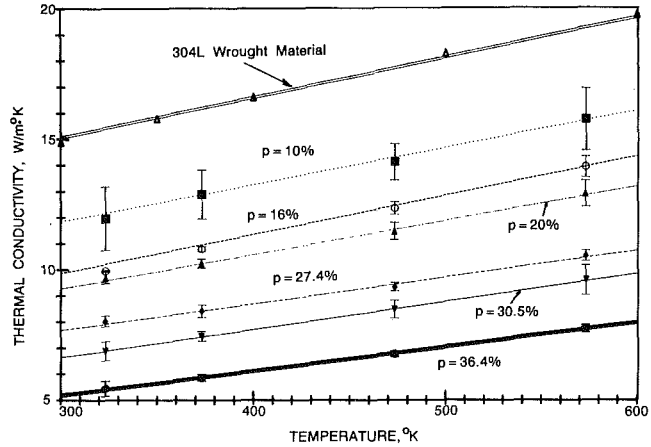

Fig. 2 Variation of the thermal conductivity with temperature for different density 304L stainless steel P/M materials

There were fixed and random errors in the experimental method used. The fixed errors were introduced through the calibration procedure of the device and by using a sample of supposedly known thermal conductivity. Random errors were introduced due the variation in the surface contact resistance between the various samples and the thermocouples, the heat losses at the interfaces between the reference specimens and the test sample, measurement errors in the distance between the thermocouples in the test samples resulting from the difficulty of knowing the exact center of the contact area, and the nonuniform distribution of the porosity. Six calibration runs were performed with Inconel specimens; the heat gain or loss was 1.1 ± 2.7 percent was neither consisted with nor correlated to the temperature level. The average error of the experimental thermal conductivity, as compared to that given by Wyrick (1984), was 1.83 ± 1.9 percent. For more details see Agapiou (1985). The experimental data have been corrected for the average heat loss of 1.1 percent.

Results and Discussion

The experimental thermal conductivities are given as a function of temperature in Fig. 2 for each of the densities studied. The conductivity of the wrought material is given for comparison (Ho, 1977). The percentage deviation in the average thermal conductivity of the replicated tests plus or minus one standard deviation is also given to quantify the results. It is assumed that the data can be fit by a normal distribution.

Uncertainties were present because the temperature gradient

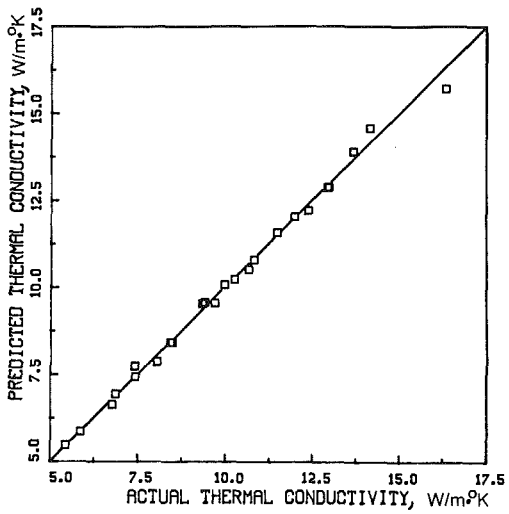

Fig. 3 Actual versus predicted thermal conductivity

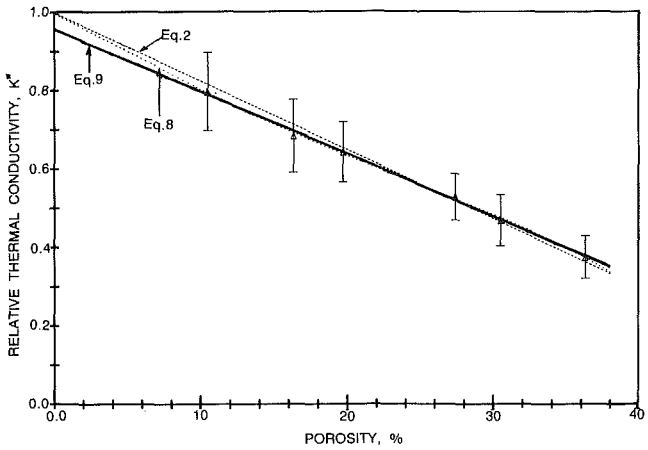

Fig. 4 Relative thermal conductivity for different density 304L stainless steel P/M materials

through the specimen column was not uniform due to the difference in the thermal conductivities of the reference specimens and the samples; however, the transition at the interfaces was smooth since this difference was small. There was some mismatch in the heat flux through the top and bottom reference specimens due to the heat loss at the interfaces or between the guard and the column. Under the specific experimental conditions, the percentage of heat gain or loss between the top and the bottom reference specimens was 3.6 ± 5.7 percent for the 72 tests at different porosities and temperatures.

Figure 2 shows that, in the range of 50 to 300°C (i.e., 323 to 573 K), the thermal conductivity increased in an approximately linear manner with increasing temperature. The experimental data were fitted to a linear model given by equation (6) at each density level. The model adequately represents the data at all density levels. The coefficient a increased slightly with increasing porosity. There was a small interaction between the density and temperature factors, as was confirmed by a two-way ANOVA analysis (Agapiou, 1985). However, the temperature coefficient a in equation (6) may be considered a constant independent of porosity and represents the average of the individual porosity coefficients. The thermal conductivity may be estimated by equation (6) with $a = 0.00132$. The comparisons of the predicted and experimental results are shown in Fig. 3. The coefficient obtained for the 304L sintered spherical powder material (Koh and Fortini, 1971) was 0.00089, a value somewhat lower than the one obtained here

Table 2 Models of thermal conductivity (K) as a function of porosity (p)

(1) $\dfrac{K}{K_B} = 1 - A_1 \cdot p$, Loeb (1954)

(2) $\dfrac{K}{k_B} = \dfrac{1-p}{(1+p)\cdot(A_2-1)}$, Maxwell (1954)

(3) $\dfrac{K}{K_B} = \dfrac{1-p}{1+A_3 \cdot p^2}$, Koh (1971)

(4) $\dfrac{K}{K_B} = \dfrac{1-A_1 \cdot p}{1+A_3 \cdot p^2}$

(5) $\dfrac{K}{K_B} = \dfrac{1-A_1 \cdot p}{1+A_2 \cdot p + A_3 \cdot p^2}$

for irregular particle shape powder. Equation (6) can be used safely at temperatures as high as 900°C based on the literature discussed in the Introduction.

While the density had a very small influence on the rate of thermal conductivity increase with temperature, as indicated by the nearly parallel slopes of the lines in Fig. 2 (parameter a in the model), the thermal conductivity did increase markedly with increasing density. The thermal conductivity of the wrought material was about three times larger than the least dense (64 percent) material tested. While there was scatter in the results from the three replicates of each test, the overall precision was adequate and less than the variation of conductivity with either the density or temperature at the levels selected. The variation of the thermal conductivity within replicates was not dependent on the temperature or density level.

The effect of porosity on the thermal conductivity is shown in Fig. 4. The relative thermal conductivity K^*, the ratio of the conductivity of the porous material to that of the fully dense wrought material, is presented as a function of porosity. Both porosity and temperature have a significant influence on the conductivity as discussed above.

The dimensionless relative thermal conductivity data were fitted to the five mathematical models given in Table 2; the first three models were proposed by other researchers, as presented in this paper by equations (2), (4), and (7), respectively, while Models 4 and 5 were proposed by the authors as the residual plots indicated strong evidence of the inadequacy of the first three models. The Loeb equation, i.e., equation (2), is given by the linear Model 1 with $A_1 = 1.755$ as shown in Fig. 4. Model 5 is the best fit expression of the data shown in Fig. 4; with constants inserted, it is given by

$$K^* = \frac{K}{K_B} = \frac{1 - 1.88 \cdot p}{1 + 0.38 \cdot p - 2.3 \cdot p^2} \tag{8}$$

The dependence of the thermal conductivity on both the porosity and temperature was investigated because there was some indication of an interaction effect between them. Five extended models, obtained by multiplications of the five models in Table 2 by the linear relationship $A_4 + A_5 \cdot T$, were fitted to the data. The results of this fitting are shown in Table 3. Extended Model 5 provided the best fit since it had the lowest residual sum of squares (RSS) and is similar to the model given by equation (8). However, if Extended Model 1 is compared to Extended Model 5 in Table 3, Extended Model 1 has only a slightly higher residual sum of squares. Hence, the linear Extended Model 1 is both adequate and appropriate to represent the relationship between the thermal conductivity and material porosity and temperature. Furthermore, the parameter A_5 of Extended Model 1 is very small ($= 0.0002$) as shown in Table 3 and can be neglected. Extended Model 1 then reduces to the linear model shown in Fig. 4 as

Table 3 F-test comparison of the five extended models fitted to the thermal conductivity data

Extended Model	Parameters						
	A_1	A_2	A_3	A_4	A_5	*RSS*	*Fdof*
1	1.65	—	—	0.95	0.0002	0.0459	0.56
2	—	3.90	—	0.82	0.0002	0.1143	4.80
3	—	—	2.0	0.84	0.0002	0.0474	0.65
4	1.71	—	−0.39	0.86	0.0002	0.0459	0.59
5	2.05	0.68	−4.20	0.93	0.0003	0.0444	0.52

$$K^* = \frac{K}{K_B} = 0.95 - 1.57 \cdot p \tag{9}$$

The effect of temperature on thermal conductivity for various levels of porosity is similar since the coefficients of the nondimensional fitted models for the temperature parameters are very small and can be neglected. Equation (2) (Loab, 1954) overpredicts at porosity levels lower than 25 percent, and underpredicts for higher porosity levels. On the other hand, equation (9) gives results similar to equation (8) over the porosity range of 10 to 40 percent. However, equations (2), (8), and (9) all fall within the 95 percent confidence level of the results.

Some available experimental data of relative thermal conductivity for various materials together with the authors' data are shown in Fig. 5 for comparison. Figure 5 shows the variation in the conductivity for 304L materials made of Regimesh, spherical powder, and the author's irregular shape powder. There is a significant difference in thermal conductivity at porosity levels higher than 20 percent. Similarly, the conductivity of the Al_2O_3 powder varied with pore shape as shown by Francl for isometric and cylindrical pores and by McClelland for irregular pores. The matrix structure is found to affect the thermal conductivity strongly. Figure 5 also shows that equation (7) would underestimate the conductivity for 304L sintered irregular powder while Loeb's equation (3) for uniform pore distribution would overestimate the conductivity. Experimental data for these materials at low porosities are not available. Model (3) could be more appropriate than an Extended Model (5) when conductivity at porosity levels higher than 35 percent needs to be predicted.

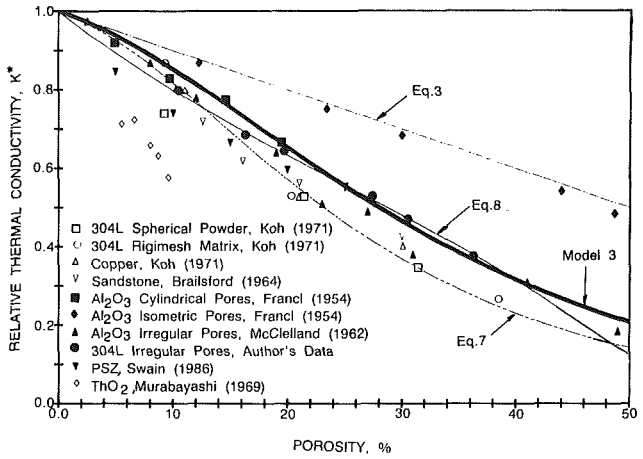

Fig. 5 Relative thermal conductivity for different density P/M materials

Conclusions

From this work, the following conclusions may be drawn concerning the effect of porosity on the thermal conductivity of powder metallurgy 304L stainless steel:

1 The thermal conductivity of the P/M material at a given temperature strongly depends on porosity.

2 The effect of temperature on thermal conductivity for various levels of porosity is similar.

3 The thermal conductivity of sintered 304L stainless steel materials increases with increasing density and temperature.

4 The thermal conductivity of porous material can be computed from the knowledge of the thermal conductivity of its wrought material as a function of temperature.

5 The influence of density and temperature on the relative conductivity for the 304L stainless steel can be best described by equations (8) and (9) for porosities up to 40 percent.

6 The matrix structure of the material becomes an important variable in the prediction of the thermal conductivity for a given porosity.

Acknowledgments

The authors express their appreciation to SSI Technologies, Inc. of Janesville, WI for their donation of the test samples and to Huntington Alloys, Inc. for their donation of the Inconel alloy material. Thanks are due to Professor G. W. Halldin for encouraging this work and to Professor G. E. Myers for his review of the manuscript.

References

Agapiou, J. S., 1985, "An Experimental Investigaton of Various Factors on the Machinability of Powder Metallurgy Austenitic Stainless Steels," Ph.D. Thesis, University of Wisconsin—Madison, Madison, WI.

ASTM, "Thermal Conductivity of Whiteware Ceramics," ASTM Designation C408-76, pp. 329-333.

Brailsford, A. D., and Major, K. G., 1964, "The Thermal Conductivity of Aggregates of Several Phases Including Porous Materials," *J. Applied Physics*, Vol. 15, pp. 313-319.

Brun, E. A., 1975, *Engineering Laboratories*, The Unesco Press, Paris, p. 110.

Cheng, S. C., and Vachon, R. I., 1970, "A Technique for Predicting the Thermal Conductivity of Suspensions, Emulsions and Porous Materials," *Int. J. Heat Mass Transfer*, Vol. 13, pp. 537-46.

Chiew, Y. C., and Glandt, E. D., 1983, "Simultaneous Conduction and Radiation in Porous and Composite Materials: Effective Thermal Conductivity," *Industrial Engineering Chemistry Fundamentals*, Vol. 22, pp. 276-282.

El-Fekey, S. A., et al., 1978, "Mathematical Analysis of the Dependence of Thermal Conductivity on Porosity," *Powder Metallurgy International*, Vol. 37, pp. 80-81.

Ericke, H., 1924, *Physics Review*, Vol. 24, pp. 575-587.

Eucken, A., 1932, "Thermal Conductivity of Ceramic Refractory Metals; Calculation From Thermal Conductivity of Constituents," *Forsch. Gebiete Ingenieurw.*, B3, Forschungsheft No. 353, p. 16; *Ceramic Abstract*, Vol. 11, 1932, p. 576.

Flynn, D. R., 1969, "Thermal Conductivity of Ceramics in Mechanical and Thermal Properties of Ceramics," NBS Spec. Publ. 303, p. 104.

Francl, J., and Kingery, W., 1954, "Thermal Conductivity: IX Experimental Investigation of Effect of Porosity on Thermal Conductivity," *J. American Ceramic Society*, Vol. 37, No. 2, pp. 99-107.

Francl, J., and Kingery, W., 1954, "Thermal Conductivity: IV Apparatus for Determining Thermal Conductivity by a Comparative Method," *J. American Ceramic Society*, Vol. 37, No. 2, pp. 80-84.

Ho, C. Y., et al., 1977, "Electrical Resistivity and Thermal Conductivity of Nine Selected AISI Stainless Steels Thermophysical and Electronic Properties Information Analysis, Cindas-45, AD-A129-160.

Kelly, J. E., et al., 1983, "Heat Transfer Characteristics of Dry Porous Particulate Beds With Internal Heat Generation," ASME/JSME *Thermal Engineering Joint Conference Proceedings*, Honolulu, HI, Mar. 20-24, pp. 81-91.

Kingery, W. D., and McQuarrie, M. C., 1954, "Thermal Conductivity: I. Concepts of Measurement and Factors Affecting Thermal Conductivity of Ceramic Materials," *J. American Ceramic Society*, Vol. 37, No. 2, pp. 67-72.

Koh, J. C. Y., and Fortini, A., 1971, "Thermal Conductivity and Electrical Resistivity of Porours Material," NASA, Report No. NAS3-12012, CR-120854.

Kuzay, T. M., 1980, "Effective Thermal Conductivity of Porous Solid-Gas Mixtures," ASME Paper No. 80-WA/HT-63.

Laubitz, M. J., 1969, in: *Thermal Conductivity*, R. P. Tye, ed., Vol. 1, Academic Press, London.

Loab, A. L., 1954, "Thermal Conductivity: VIII, A Theory of Thermal Conductivity of Porous Materials," *J. American Ceramic Society*, Vol. 37, No. 2, pp. 96-99.

Luikov, A. V., et al., 1968, "Thermal Conductivity of Porous Systems," *Int. J. Heat Mass Transfer*, Vol. 11, pp. 117-140.

Marino, G. P., 1971, "The Porosity Correction Factor for the Thermal Conductivity of Ceramic Fuels," *J. Nuclear Materials*, Vol. 38, pp. 178-190.

McClelland, J. D., 1962, "Materials and Structures Physical Measurements Program," Aerospace Corporation Report No. TDR-930 (2240-64) TR-1.

Maxwell, J. C., 1954, A Treatise on Electricity and Magnetism, 3rd ed., Vol. 1, Clarendon Press, Oxford.

ASM, 1980, *Metals Handbook*, Vol. 3.

Mirkovich, V. V., 1965, "Comparative Method and Choice of Standards for Thermal Conductivity Determinations," *J. American Ceramic Society*, Vol. 48, No. 8, pp. 387–391.

Murabayashi, M., et al., 1969, "Effect of Porosity on the Thermal Conductivity of ThO_2," *J. Nuclear Science and Technology*, Vol. 6, pp. 47–52.

Rusell, H. W., 1935, "Principles of Heat Flow in Porous Insulators," *J. American Ceramic Society*, Vol. 8, No. 1, pp. 1–5.

Stuckes, A. D., and Chasmar, R. P., 1956, "Measurement of the Thermal Conductivity of Semiconductors," *Report of the Meeting of Semiconductors*, (Phys. Soc., London), pp. 119–25.

Sugawara, A., 1968, "The Precise Determination of Thermal Conductivity of Pure Fused Quartz," *J. Applied Physics*, Vol. 39, No. 13, pp. 5994–5997.

Swain, M. V., et al., 1986, "Thermal Diffusivity, Heat Capacity and Thermal Conductivity of Porous Partially Stabilized Zirconia," *J. Materials Science Letters*, Vol. 5, No. 8, pp. 799–802.

Touloukian, Y. S., et al. 1970, "In Thermophysical Properties of Matter: Experimental Determination of Thermal Conductivity," *The TPRC Data Series*, Vol. 1, p. 13*a*.

Tye, R. P., 1969, *Thermal Conductivity*, Vol. 2, Academic Press, London.

Tye, R. P., 1970, "An Experimental Investigation of the Thermal Conductivity and Electrical Resistivity of Three Porous 304L Stainless Steel RIGIMESH Materials to 1300 K," NASA Report No. NAS3-12012, CR-72710.

Watson, T. W., and Robinson, H. E., 1968, "Thermal Conductivity of Some Commercial Iron-Nickel Alloys," ASME JOURNAL OF HEAT TRANSFER, Vol. 90, pp. 403–408.

Williams, D. R., and Blum, H. A., 1967, "Thermal Conductivities of Several Methods: An Evaluation of a Method Employed by the NBS," *Proceedings of the 17th Conference on Thermal Conductivity*, NBS 302, No. 13–16, pp. 349–354.

Wyrick, M. D., 1984, Huntington Alloys Inc, Private Communication, "Data of Thermal Conductivity of Inconel Alloy 600 as a Function of Temperature," Heat No. NX3717.

Zumbrunnen, D. A., et al., 1986, "Heat Transfer Through Porous Solids With Complex International Geometries," *Int. J. Heat Mass Transfer*, Vol. 29, No. 2, pp. 275–284.

Optimal Heat Exchangers

M. Kovarik
Division of Building, Construction and Engineering, Commonwealth Scientific and Industrial Research Organisation, Highett, Victoria, 3190 Australia

The design of optimal heat exchangers is formulated as the solution of five simultaneous equations. The analysis of these equations yields general properties of optimal crossflow heat exchangers; in particular, an upper bound of 1/3 is given for the fractional cost of maintaining the flow through the heat exchanger. Some of these general properties also apply in the presence of a simple constraint. It is shown that some technically feasible designs cannot be optimal under realistic costs and others under any costs.

Introduction

The task of a heat exchanger is to transfer heat from one stream of fluid to another. An optimal heat exchanger is defined as one that, while satisfying imposed constraints, achieves the required task at the lowest possible cost. The cost is defined, for this purpose, as the annual equivalent of all the present value of expenditure necessarily incurred in acquiring and operating any equipment over its useful lifetime.

The task may be defined, in the simplest case, by the rate of flow of an extensive thermodynamic quantity associated with one or both of the streams, e.g., free energy, enthalpy, free enthalpy, and others. In this paper, the performance of the task will be measured by the mean *rate of energy added to the colder of the two streams.*

A survey of earlier work by Shah et al. (1978) recognizes the problem as one suitable for nonlinear programming techniques and recommends several types of numerical methods as appropriate for corresponding classes of optimization problems.

The application of numerical methods to the optimization problem presupposes the existence of a solution. Since an important factor determining the performance of a heat exchanger, the effectiveness ϵ, is usually a transcendental function of design variables, the existence of an optimal solution is neither necessary nor obvious. A direct discussion of existence would be difficult, but some light will be cast on the subject by a brief analysis of the complementary problem: Given a heat exchanger design, which cost factors make it an optimal design? It will be shown that a technically feasible design may require negative cost factors for optimality. In the neighborhood of such design, real optimal solutions do not exist and numerical methods with given positive cost factors cannot find them.

The main purpose of this paper is not to add to the available methods of numerical optimization, but rather to examine the results of analysis and show some general properties of optimal designs. Prominent among them will be the well-defined proportion between the costs related to the size of the heat transfer area (capital cost) and those related to the pumping effort (running cost) for a given rate of energy transfer. Another general property to be shown is the independence of optimal design from the cost of heat transferred, and so from the cost of fuel.

Performance

The rate of heat transferred by heat exchanger is

$$H = \epsilon C_{MI} \Delta_M \tag{1}$$

where, as shown by Kays and London (1984), the effectiveness ϵ depends on the flow arrangement and on two dimensionless parameters. Excepting the simplest cases, the relationship between ϵ and the type of heat transfer surface is largely empirical; no reliable mathematical procedures exist for prediction of performance of a new, untested surface. Therefore the choice of the type of surface for the design from some catalog of patterns of known performance will be left to the designer and the optimization process will operate on a reduced set of design variables. Effectiveness depends on only two parameters:

$$\epsilon \equiv \epsilon(\alpha_1, \alpha_2) \tag{2}$$

where the α are dimensionless

$$\alpha_1 \equiv N_{TU} \tag{3}$$

$$\alpha_2 \equiv C_{MI}/C_{MA} \tag{4}$$

The overall number of heat transfer units N_{TU} depends on the Stanton number, surface temperature effectiveness η_0, and dimensions of both sides as shown by Kays and London (1984)

$$N_{TU} = \left(\frac{1}{z_{MA}} + \frac{1}{z_{MI}}\right)^{-1} \tag{5}$$

where

$$z_{MA} = \alpha_2^{-1} \eta_{0MA} (L/r_h)_{MA} \mathrm{St}_{MA} \tag{6}$$

and

$$z_{MI} = \eta_{0MI} (L/r_h)_{MI} \mathrm{St}_{MI} \tag{7}$$

The subscripts denote the side of major (MA) and minor (MI) capacity rates in the flow.

Stanton number is a heat transfer characteristic of a given surface and flow; for a range of known cases, it can be obtained from Kays and London (1984). In the vicinity of an operating point characterized by the Reynolds number, St is

$$\mathrm{St} = b \cdot \mathrm{Pr}^{-\frac{2}{3}} \mathrm{Re}^{\gamma} \tag{8}$$

where Pr depends on fluid properties alone, γ is the slope of the St curve on logarithmic graphs in Section 10 of Kays and London (1984), and b is a constant obtainable from the same graph.

Cost

The cost of owning and operating a heat exchanger is the sum of the cost of providing and maintaining the heat transfer surfaces with their supporting structures, the cost of maintaining the flow through it, and the cost of heating or cooling effect supplied. The cost related to the heat transfer surface is usually taken as proportional to its area A; see, e.g., Peters and Timmerhaus (1968), Yarzebski (1984), or Nishimura (1980). However, graphs of average costs, given by Peters and Timmerhaus (1968), Buchanan and Sinclair (1966), and Gregorig (1959), extrapolate to a positive intercept for zero area, indicating that there is a component in the cost related to size that does not depend on A. This part of the cost corresponding to $A = 0$ will be taken as representing the cost of

Contributed by the Heat Transfer Division for publication in the JOURNAL OF HEAT TRANSFER. Manuscript received by the Heat Transfer Division October 19, 1987. Keywords: Heat Exchangers.

terminal supports for the flow passages and the cost of the manifolds or plenum chambers distributing the flow between parallel passages. Their size is proportional to the frontal area A_p and the total size-related cost is

$$c_s = \alpha a_1 V + a_2 A_{p,MA} + \nu a_2 A_{p,MI} \tag{9}$$

where α is the ratio of heat transfer area to the volume of the heat exchanger.

The cost of maintaining the flow through both sides of the exchanger is related to the power expended on the operation of pumps or fans and includes the annualized cost of this equipment and its maintenance. It will be represented by an amount proportional to the power used on both sides

$$c_p = a_3 p_{MA} + \omega a_3 p_{MI} \tag{10}$$

Finally, the cost of heating or cooling effect supplied to the heat exchanger will be represented by an amount proportional to the rate of heat transferred

$$c_H = a_4 H \tag{11}$$

When the energy price undergoes a major change, reflected in the value of a_4, the possible influence of this change on exchanger design creates uncertainties. In the next section it will be shown that energy cost does not influence optimal design.

Objective Function

The aim of optimization is to find the maximum of the objective function J. This is defined as the ratio of performance to cost

$$J = \frac{H}{c_s + c_p + c_H} \tag{12}$$

From equation (12)

$$J = \frac{1}{(c_s + c_p)/H + a_4} \tag{13}$$

Clearly, the position of the maximum of J coincides with the minimum of the first term in the denominator of the right-hand side of equation (13), and is independent of the value of the energy cost factor a_4. Therefore an optimal heat exchanger is optimal for any cost of energy. In the following, the analysis will proceed under the simplifying assumption

$$c_H = 0 \tag{14}$$

It will be understood that all subsequently asserted relations between costs apply to costs excluding the c_H component.

A necessary condition for J to reach its maximum is the simultaneous vanishing of its partial derivatives with respect to all free variables. For any variable X_i, this means

$$\left(\frac{\partial H}{\partial X_i} c_T - \frac{\partial c_T}{\partial X_i} H\right) \Big/ c_T^2 = 0 \tag{15}$$

where c_T is the total cost

$$c_T = c_s + c_p \tag{16}$$

As H and c_T are inevitably positive, equation (15) implies

$$H_i = \frac{X_i \partial c_T}{c_T \partial X_i} \tag{17}$$

where H_i is the logarithmic derivative of H wih respect to X_i:

$$H_i \equiv \frac{X_i \partial H}{H \partial X_i} \tag{18}$$

H_i is defined as the sensitivity of output to variable X_i. The free variables can be flow lengths and capacity rates. In a crossflow exchanger, the flow lengths are independent and the optimization scheme can be applied with greater generality than with a parallel-flow case.

Crossflow Heat Exchanger

The model to be analyzed is a section that is rectangular and prismatic in shape, consisting of passages bordered by heat transfer surfaces of known properties. The hydraulic radii are fixed.

The independent variables are identified in Fig. 1. The common dimension of both cross-sectional areas is taken as unity and may be scaled up or down to give the desired quantity of heat. The remaining two lengths and capacity rates will be the optimization variables; they will be considered as four components of the vector $\mathbf{X}$. The volume and frontal areas of the exchanger are then

$$V = X_1 X_2 \cdot L_R^3 \tag{19}$$

$$A_{p,MA} = X_2 \cdot L_R^2 \tag{20}$$

$$A_{p,MI} = X_1 \cdot L_R^2 \tag{21}$$

The size-related component of total cost in equation (9) can now yield the logarithmic derivatives

Nomenclature

A = exchanger total heat transfer area on reference side
A_C = exchanger minimum free-flow area $= \beta A_p$
A_p = frontal area
a_1 = unit cost for the total heat transfer area, annual equivalent
a_2 = unit cost for the frontal area on the side of the major capacity rate, annual equivalent
a_3 = unit cost for the pumping power on the side of the major capacity rate, annual equivalent
a_4 = unit cost of thermal energy
b = constant defined by equation (8)
c_E = annual cost of pumping, component related to entrance, exit, and acceleration losses
c_F = annual cost of pumping, component related to friction losses
c_s = cost component related to heat exchanger size, annual equivalent
c_p = cost component related to the pumping power, annual equivalent
c_H = cost component related to the supply of heating or cooling effect to the exchanger
c_T = total cost of heat exchanger, annual equivalent
C = flow-stream capacity rate
C_C = flow-stream capacity rate of cold side fluid
C_H = flow-stream capacity rate of hot side fluid
C_{MA} = the greater of C_C, C_H
C_{MI} = the smaller of C_C, C_H
f = friction factor
f_0 = coefficient in the friction factor equation (24)
G = mass velocity
H = rate of heat transferred by the heat exchanger
H_i = logarithmic derivative of H with respect to variable X_i, equation (18)

$$\frac{X_1 \partial c_s}{c_T \partial X_1} = (\alpha a_1 V + a_2 A_{p,MA})/c_T \tag{22}$$

$$\frac{X_2 \partial c_s}{c_T \partial X_2} = (\alpha a_1 V + \nu a_2 A_{p,MI})/c_T \tag{23}$$

with the remaining two derivatives with respect to X_3, X_4 equal to zero.

The cost components related to pumping power (or fan power) will be separated into those resulting from friction pressure drop and those related to flow acceleration, entrance, and exit effects. The latter three are proportional to the cube of mass velocity, the friction component depends further on the friction factor given by

$$f = f_0 \, \mathrm{Re}^{\psi} \tag{24}$$

The exponent ψ varies between -1 for laminar flow and higher values in turbulence. The values of f_0 and ψ applicable to the neighborhood of the operating point of a particular surface may be obtained as the intercept and slope of the tangent of logarithmic in Chap. 10 of Kays and London (1984). The friction component depends also on the length of passage. Details of the cost related to pumping are in Appendix 1; in the optimization analysis, the relevant factors are only their logarithmic derivatives. These reflect the exponents of the free variables represented as factors in the expressions for c_p

$$c_p = c_{E,MA} + c_{F,MA} + c_{E,MI} + c_{F,MI} \tag{25}$$

where c_E is the pumping cost related to the entrance, exit, and acceleration losses and c_F arises from friction losses.

Applying the logarithmic derivative to both sides of equation (25) yields, with reference to Appendix 1

$$\frac{X_1 \partial c_p}{c_T \partial X_1} = [c_{F,MA} - 2c_{E,MI} - (2 + \psi_{MI}) c_{F,MI}]/c_T \tag{26}$$

Here, the first term represents the linear dependence of the friction loss of the major stream on the major passage length; the (-2) in the second term is due to the inverse effect of the increase of X_1 on the flow velocity in the minor stream, velocity being involved in the second power; the third term is the inverse effect of the increase in X_1 to the friction loss of the minor stream. For constant capacity rates X_3, X_4, the flow velocities vary inversely as the flow cross-section areas and these are in turn proportional to the flow length of the other stream, as evident from Fig. 1. The derivative with respect to the other flow length (X_2) can be written by analogy to equation (26).

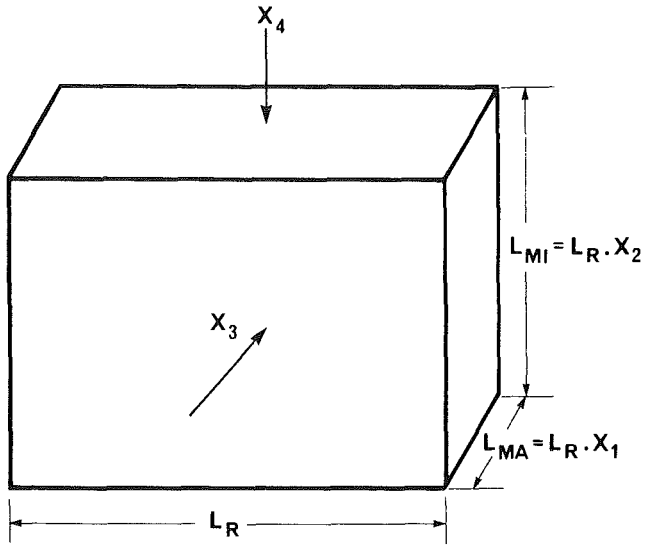

Fig. 1 Crossflow heat exchanger: independent variables

The derivatives with respect to capacity rates are, referring again to Appendix 1

$$\frac{X_3 \partial c_p}{c_T \partial X_3} = [3c_{E,MA} + (3 + \psi_{MA}) c_{F,MA}]/c_T \tag{27}$$

and likewise for X_4 and the minor stream.

The Fractional Cost Equation

In equations (22), (23), (26), and (27), the partial costs are always divided by the total cost. Therefore, the partial derivatives of cost can be expressed in terms of fractional costs defined as follows:

$$\Gamma_1 = \alpha a_1 V/c_T \tag{28}$$

$$\Gamma_2 = a_2 A_{p,MA}/c_T \tag{29}$$

$$\Gamma_3 = \nu a_2 A_{p,MI}/c_T \tag{30}$$

$$\Gamma_4 = c_{E,MA}/c_T \tag{31}$$

$$\Gamma_5 = c_{F,MA}/c_T \tag{32}$$

Nomenclature (cont.)

k_i = cost component divided by unit cost $= c_j/a_i$
L = total heat exchanger flow length
L_R = reference length, Fig. 1
p = power expended on maintaining flow through the exchanger
Pr = Prandtl number
Re = Reynolds number
r_h = hydraulic radius $= A_C L/A$
St = Stanton number
V = volume of heat exchanger
v_i = specific volume of fluid at point i
X_1, X_2 = dimensionless length in the direction of major (minor) capacity rate; $X_1 = L_{MA}/L_R$
X_3, X_4 = major (minor) capacity rate
z = heat transfer parameter, equations (6), (7)
α = ratio of total heat transfer area to the volume of the heat exchanger, equation (9)
$\alpha_{1,2}$ = dimensionless parameters of effectiveness, equations (2), (3), (4)
β = ratio of minimum free-flow area to frontal area
γ = slope of log (St $\mathrm{Pr}^{2/3}$) as a function of log Re, equation (8)
Γ_i = component of the fractional cost vector $\mathbf{\Gamma}$, equations (28) to (35)
Δ_M = temperature difference between the hottest and coldest fluids
ϵ = exchanger effectiveness
ϵ_i = see equations (37) and (38)
η_0 = total surface temperature effectiveness, equations (6), (7)
ν = ratio of unit costs related to frontal areas, equation (9)
ψ = exponent of the friction factor, equation (24)
ω = ratio of unit costs related to pumping power, equation (10)

$$\Gamma_6 = c_{E,MI}/c_T \tag{33}$$

$$\Gamma_7 = c_{F,MI}/c_T \tag{34}$$

and

$$\sum_1^7 \Gamma_i = 1 \tag{35}$$

because Γ represents all the cost components. The five simultaneous equations following from equation (17) by substitution from equations (28) to (35) for the cost components can be presented in matrix-vector form, the fractional costs forming components of the fractional cost vector Γ.

$$\begin{bmatrix} 1 & 0 & 1 & 0 & 1 & -2 & -(2+\psi_{MI}) \\ 1 & 1 & 0 & -2 & -(2+\psi_{MA}) & 0 & 1 \\ 0 & 0 & 0 & 3 & 3+\psi_{MA} & 0 & 0 \\ 0 & 0 & 0 & 0 & 0 & 3 & 3+\psi_{MI}) \\ 1 & 1 & 1 & 1 & 1 & 1 & 1 \end{bmatrix}$$

$$\bullet\Gamma = \begin{bmatrix} H_1 \\ H_2 \\ H_3 \\ H_4 \\ 1 \end{bmatrix} \tag{36}$$

The above equation is in dimensionless terms; the 5×7 matrix contains only constants, Γ is a function of $\mathbf{X}$. The fifth row represents the normalizing condition, equation (35). The logarithmic derivatives on the right-hand side are transcendental functions of $\mathbf{X}$ depending on the expression for temperature effectiveness apporopriate to the chosen flow arrangement. In view of the above properties, the existence of a solution and its uniqueness cannot be taken for granted; nevertheless all numerical methods of optimal design of heat exchanger are equivalent to an attempt to solve equation (36) or, independently, some of its rows.

As equation (36) states the necessary conditions for the optimal designs, properties derived from it must obtain in such design, if it exists. In manipulating the rows of the matrix, it is helpful to use the following definitions:

$$\epsilon_1 = \frac{\alpha_1 \partial \epsilon}{\epsilon \partial \alpha_1} \tag{37}$$

is the sensitivity of effectiveness to N_{TU},

$$\epsilon_2 = \frac{\alpha_2 \partial \epsilon}{\epsilon \partial \alpha_2} \tag{38}$$

is the sensitivity of effectiveness to the capacity rate ratio, and the consequent equations for the output sensitivities, following from equations (2) to (8), are

$$H_1 = \alpha_1 \epsilon_1 (1/z_1 - \gamma_{MI}/z_2) \tag{39}$$

$$H_2 = \alpha_1 \epsilon_1 (1/z_2 - \gamma_{MA}/z_1) \tag{40}$$

$$H_3 = \alpha_1 \epsilon_1 (1+\gamma_{MA})/z_1 - \epsilon_2 \tag{41}$$

$$H_4 = 1 - \alpha_1 \epsilon_1 (1/z_1 - \gamma_{MI}/z_2) + \epsilon_2 \tag{42}$$

The relations between the H_i's are

$$H_1 + H_4 = 1 + \epsilon_2 \tag{43}$$

$$H_2 + H_3 = \epsilon_1 - \epsilon_2 \tag{44}$$

$$H_1 + H_2 + H_3 + H_4 = 1 + \epsilon_1 \tag{45}$$

and

$$H_3 + H_4 = 1 + \alpha_1 \epsilon_1 (\gamma_{MA}/z_1 + \gamma_{MI}/z_2) \tag{46}$$

Moreover, if

$$\gamma_{MA} = \gamma_{MI} = \gamma \tag{47}$$

then

$$H_3 + H_4 = 1 + \epsilon_1 \gamma \tag{48}$$

Summing the first four rows of equation (36) and subtracting the fifth row from the result yields

$$\Gamma_1 + \Gamma_5 + \Gamma_7 = \epsilon_1 \tag{49}$$

or the fractional cost of heat transfer surface and friction losses equals the sensitivity of effectiveness to N_{TU}.

The sensitivity ϵ_1 decreases with increasing N_{TU} in all flow configurations; therefore, high values of N_{TU} are optimal only if the incremental costs of heat transfer area and friction losses are low.

Subtracting the last result from the fifth row of equation (36) gives an equation for the remaining fractional costs

$$\Gamma_2 + \Gamma_3 + \Gamma_4 + \Gamma_6 = 1 - \epsilon_1 \tag{50}$$

On the left-hand side is the sum of partial costs related to the frontal areas and those resulting from pumping to overcome nonfriction losses.

The fractional cost of pumping, defined by

$$\Gamma_{P,MA} = \Gamma_4 + \Gamma_5 \tag{51}$$

for the major capacity side and

$$\Gamma_{P,MI} = \Gamma_6 + \Gamma_7 \tag{52}$$

for the other, follows from rows 3 and 4

$$\Gamma_{P,MA} = \frac{1}{3}(H_3 - \psi_{MA}\Gamma_5) \tag{53}$$

and

$$\Gamma_{P,MI} = \frac{1}{3}(H_4 - \psi_{MI}\Gamma_7) \tag{54}$$

The above properties of optimal heat exchangers are valid without restrictions concerning flow arrangement or values of the parameters γ and ψ. Some further properties can be derived if these parameters satisfy two conditions:

1 symmetry

$$\psi_{MA} = \psi_{MI} = \psi \tag{55}$$

2 the analogy due to Colburn (1933), which implies

$$\gamma = \psi \tag{56}$$

Equality of friction factors on both sides of the exchanger is not required here; only the slope of the log (f) curve plotted against log (Re) must be equal. As for the second condition, the surfaces that violate it always have the ratio of friction factor to the Stanton number increasing with Re. At higher values of Re, extended surface elements decrease their contribution to heat transfer as their temperature approaches that of the surrounding fluid, without diminishing their contribution to the friction loss. This characteristic is clearly increasing the ratio of cost to performance and thus those flow conditions where the Colburn analogy is substantially violated should not be used in design.

With symmetry and the Colburn analogy satisfied, equations (53), (54), and (48) yield

$$\Gamma_P = \frac{1}{3}\left[1 + \psi(\epsilon_1 - \Gamma_5 - \Gamma_7)\right] \tag{57}$$

and, by substitution from equation (49)

$$\Gamma_P = \frac{1}{3}\left(1 + \psi\Gamma_1\right) \tag{58}$$

which relates the fractional costs of pumping and of heat transfer area. Where ψ is negative with a lower bound of -1 (laminar flow), the cost of pumping is bounded by

$$\Gamma_P \leq 1/3 \tag{59}$$

the equality corresponding to zero cost of heat transfer area.

Example 1

A typical case of plain plate-fin surface (type 3.97 of Kays and London, 1984) illustrates the use of equation (58). A heat exchanger using the above surface has an assumed fractional cost of 0.05 associated with the frontal areas. The fractional cost associated with the heat transfer area is then

$$\Gamma_1 = 1 - 0.05 - \Gamma_P \tag{60}$$

The average slope of the $\log f - \log \mathrm{Re}$ curve (p. 224 or Table 10.3) between $\mathrm{Re} = 3000$ and $\mathrm{Re} = 4000$ is $\psi = -0.2$ and equation (58) gives

$$\Gamma_P = \frac{1}{3}\left(1 - 0.2\,\Gamma_1\right) \tag{61}$$

and, after substitution from equation (60)

$$\Gamma_P = 0.27$$

Thus, if the pumping costs exceed 27 percent of total cost in their annual equivalent, a heat exchanger of larger heat transfer area and lower pumping cost is economically preferable.

Constrained Optimum

The four variables used in optimization are not always fully independent. Any relation $F(X_1, X_2, X_3, X_4) = 0$ imposed upon some or all of them leads to a reformulation of equation (12) to

$$J = H/(c_s + c_p) + \lambda F \tag{62}$$

where λ is the Lagrange multiplier. The resulting problem has an augmented set of variables $[\mathbf{X}\,|\,\lambda]$ and an additional equation to satisfy

$$F(\mathbf{X}) = 0 \tag{63}$$

If the constraint consists of a fixed capacity rate ratio α_2

$$F \equiv \alpha_2 - X_4/X_3 = 0 \tag{64}$$

which is frequently the case, λ is easily eliminated.

The logarithmic derivative operation $(X_i \partial J/J\partial X_i)$, which produced the first four rows of equation (36) from equation (12), is now applied to equation (62). As the adjoint factor λF does not contain any X_1 or X_2, the first two rows of equation (36) remain unchanged; for $i = 3$ and $i = 4$, the logarithmic derivative of the adjoint factor produces $(\lambda X_4/X_3)$ and $(-\lambda X_4/X_3)$, respectively. By adding the resulting rows, this term cancels out and the third row of equation (65) is obtained:

$$\begin{bmatrix} 1 & 0 & 1 & 0 & 1 & -2 & -(2+\psi_{MI}) \\ 1 & 1 & 0 & -2 & -(2+\psi_{MA}) & 0 & 1 \\ 0 & 0 & 0 & 3 & 3+\psi_{MA} & 3 & 3+\psi_{MI} \\ 1 & 1 & 1 & 1 & 1 & 1 & 1 \end{bmatrix}$$

$$\cdot \boldsymbol{\Gamma} = \begin{bmatrix} H_1 \\ H_2 \\ H_3 + H_4 \\ 1 \end{bmatrix} \tag{65}$$

This leads to a simplification of the numerical solution process.

The analytical results remain unchanged in their majority: equations (49), (50) are valid as before, but (53) and (54) only in their sum

$$\Gamma_P = \frac{1}{3}\left(H_3 + H_4 - \psi_{MA}\Gamma_5 - \psi_{MI}\Gamma_7\right) \tag{66}$$

Subject to the condition of symmetry (55) and the Colburn analogy (56) the relations (58), (59) are preserved in the case constrained by a given capacity rate ratio.

The Inverse Problem

Given a complete design of a heat exchanger, it may be of interest to know for which cost factors, if any, that design is optimal. The cost factors are related to the fractional costs by

$$\Gamma_i = (ak)_{\Gamma_i}/c_T \tag{67}$$

where k is the quantity of which one unit costs a dollars per annum equivalent. Whereas there are seven fractional costs, there are fewer independent cost factors. In particular, the cost of pumping against a unit of friction resistance and nonfriction resistance are equal. Moreover, the unit cost related to pumping in the major and minor stream are related by a nondimensional proportionality factor, and both can be represented by a_3 and ωa_3, respectively. Likewise, the unit costs related to cross-sectional area can be written as a_2, νa_2 for the major and minor stream; see equations (29), (30). With these simplifications the matrix-vector equation (65) can be modified to

$$\begin{bmatrix} k_1 & k_3 & k_5 - 2k_6 - (2+\psi_{MI})k_7 \\ k_1 & k_2 & -2k_4 - (2+\psi_{MA})k_5 + k_7 \\ 0 & 0 & 3k_4 + (3+\psi_{MA})k_5 + 3k_6 + (3+\psi_{MI})k_7 \end{bmatrix}$$

$$\cdot \begin{bmatrix} a_1 \\ a_2 \\ a_3 \end{bmatrix} = \begin{bmatrix} H_1 \\ H_2 \\ H_3 + H_4 \end{bmatrix} \tag{68}$$

This was achieved by

1 leaving out the fifth row of equation (65), as the normalizing condition only applies to Γ_i;

2 adding the second and third column, as they have the common multiplier a_2;

3 adding the last four columns, representing the sensitivity of pumping work. These have the same cost factor a_3;

4 adding the third and fourth row. The terms k_6 and k_7 contain the proportionality factor ω (possibly unity) between the cost of unit pumping efforts in the major and minor stream.

5 setting the total cost c_T arbitrarily at unity, thus to obtain a set of a's representing the proportions of cost factors only, and not their actual values. There is no loss of generality involved in this step, as it amounts to expressing all costs in a currency such that $c_T = 1$.

Equation (68) is of the form

$$\mathbf{M} \cdot \mathbf{a} = \mathbf{h} \tag{69}$$

which is linear in **a**. It uniquely determines **a** unless the 3×3 matrix M is singular, which is the case only if $k_2 = k_3$. Thus a given design is always optimal for some unique set of cost factors **a** with the exception of the singular case.

In the case of a singularity, the equations represented by (68) are either inconsistent and no solution exists, or linearly dependent. In the latter case, the top two elements of all the three columns, as well as on the right-hand side, must be equal. Then, a_3 is given uniquely by the third row and a_1, a_2 contain an arbitrary common factor.

In either case, singular or not, a_3 is inevitably positive, whereas one or both of a_1, a_2 may be negative. Consequently, a technically feasible design may be optimal for

(*a*) a set of positive cost factors;
(*b*) a set of cost factors of which one or two are negative;
(*c*) a positive unit pumping cost and a loosely constrained pair of capital cost factors—case of linear dependence;
(*d*) no set of cost factors—case of singularity where the first two rows of equation (68) are not linearly dependent.

Example 2

Results of type (*b*) are obtained by analysis of a Direct-Transfer Regenerator, used as Example 2 of Kays and London (1984). It is a regenerator for a 3.7 MW open-cycle gas turbine plant. The entering temperatures are 175°C/430°C air/gas side, with pressures 9.1×10^5 Pa/103×10^3 Pa. The core dimensions are 2.09 m^2/4.18 m^2 frontal areas air/gas and the volume is 3.82 m^3. The principal dimensions-optimization variables are $L_{MA} = 0.91$ m, $L_{MI} = 1.83$ m, the reference length 2.29 m with the capacity rates $X_3 = 26.7$ kW/K (gas) and $X_4 = 25.5$ kW/K (air). The efficiency with the chosen surface types is 0.75 and $N_{TU} = 4.25$.

With the above parameters, assuming equal unit cost of pumping and of cross-sectional area on both sides, the design is optimal for the following cost factors:

$$a_1 = -0.064, \quad a_2 = 200, \quad a_3 = 45.6.$$

The negative cost factor related to the heat transfer area indicates that the design is not optimal for realistic costs. This appears to be due to:

(*a*) the unavoidable constraint on the capacity rate ratio, given by the combustion process;
(*b*) the aim of the designer for high effectiveness, leading to the choice of high N_{TU} and consequently an uneconomically large area for heat transfer.

Alternatively, the high effectiveness could be achieved by the Multipass Overall-Counterflow Arrangement of Kays and London (1984). In two passes, effectiveness of 0.59 per unit is sufficient to give $\epsilon = 0.75$ overall; but for the lower effectiveness, only an N_{TU} of 1.8 per stage is needed, reducing the total heat transfer area to 85 percent for unchanged capacity rate. With a triple pass arrangement, the required effectiveness is only 0.49 in each pass, leading to an N_{TU} of approximately 1.2, or a combined area of 3.6, yielding no further improvement. The area reduction to 85 percent offers further economies by allowing increased flow velocities for unchanged pumping powers, so that further increases of the performance index J will be achieved by several iterations. The actual values of J do, of course, depend on the true cost factors, which are not known in this case. Assuming the following values of cost factors, Table 1 gives the comparisons of optimal designs constrained to $\epsilon = 0.75$, $\alpha_2 = 0.955$.

Table 1 Optimal multipass overall-counterflow heat exchangers. Fluids mixed between passes, overall effectiveness = 0.75. Cost factors: $a_1 = 10$, $a_2 = 50$, $a_3 = 0.045$.

No. of passes	Effectiveness per stage	N_{TU} per stage	J per stage	J overall
1	0.75	4.30	0.688	0.688
2	0.59	1.34	1.72	1.090
3	0.49	0.878	2.12	1.085

Discussion

The approach to the optimization of heat exchangers outlined in this paper can serve as a convenient formal basis to numerical calculations of optimal design, starting with equation (36). The results stated in equations (49), (50), (53), and (54) can be used to analyze existing or proposed heat exchanger designs and their associated cost estimates to reveal major departures from optimality; as in Example 2, they may lead to a search for preferable alternatives.

The general validity of fractional cost relations expressed in equations (57), (58), (59), and (66) allows the assessment of potential tradeoffs between heat transfer and friction performance of heat transfer surfaces to be examined in future research.

Conclusion

The relations between all major components of the cost of an optimal heat exchanger and the output sensitivities of such heat exchanger with respect to its principal design variables are expressed by the five dimensionless constants (1, −2, 3, ψ_{MA}, ψ_{MI}) of the first four rows of equation (36). For every operating heat exchanger, there are unit cost factors that render it optimal in the sense defined here, with the exception of singular cases. Such cost factors are not necessarily realistic; indeed, some of them may turn out to be negative. Numerical optimization methods may not proceed smoothly from an absurd starting point. By observing the numerical relations derived here, a search for optimal design using known heat transfer surface may be initiated, guided, and accomplished.

Acknowledgments

Many colleagues of the author contributed to this work. Those most frequently consulted were P. F. Lesse and A. N. Stokes in the area of mathematics, P. J. Banks, D. J. Close, and M. C. Welsh on heat transfer, and C. Y. L. Chan on economic factors. J. G. van Leersum produced the first proof of independence of optimality and energy cost.

References

Bird, R. B., Stewart, W. E., and Lightfoot, E. N., 1960, *Transport Phenomena*, Wiley, New York.

Buchanan, R. H., and Sinclair, C. G., 1966, *Costs and Economics of the Australian Process Industries*, West Publishing Corporation, Sydney.

Colburn, A. P., 1933, "A Method of Correlating Forced Convection Heat Transfer Data and Comparison With Fluid Friction," *Trans. AIChE*, Vol. 29, pp. 174-210.

Gregorig, R., 1959, "Waermeaustauscher," Verlag, H. R. Sauerlaender & Co., Aarau und Frankfurt am Main.

Jarzebski, A. B., 1984, "Dimensioning of Spiral Heat Exchangers to Give Minimum Costs," ASME JOURNAL OF HEAT TRANSFER, Vol. 106, pp. 633-637.

Kays, W. M., and London, A. L., 1984, *Compact Heat Exchangers*, McGraw-Hill, New York.

Nishimura, H., 1980, "A Theory for the Optimal Synthesis of Heat Exchanger," *J. of Optimization Theory and Applications*, Vol. 30, pp. 423-450.

Peters, M. S., and Timmerhaus, K. D., 1968, *Plant Design and Economics for Chemical Engineers*, McGraw-Hill, New York.
Shah, R. K., Afimiwala, K. A., and Mayne, R. W., 1978, *Heat Exchanger Optimization*, Proceedings of the Sixth International Heat Transfer Conference, Toronto, Vol. 4, pp. 185–191.

APPENDIX

Pumping Costs and Their Derivatives

The annual equivalent of the present value of the pumping cost of a stream through the heat exchanger will be taken as proportional to the power required to overcome the pressure difference opposing the flow. It consists of two components differing in their relation to the mass velocity G. The friction component is proportional to fG^3, where f is the friction factor, dependent on Re and thus on G. The second component is simply proportional to G^3. The total cost of pumping on the side of major capacity rate is

$$c_{P,MA} = a_3 p_{MA} \tag{70}$$

where the pumping power p is the product of the volume flow rate and of the pressure drop

$$p_{MA} = v_{1,MA} G_{MA} \times \Delta P_{MA} \tag{71}$$

and

$$\Delta P_{MA} = \Delta P_{E,MA} + \Delta P_{F,MA} \tag{72}$$

or the sum of nonfriction and friction-dependent pressure drops.

The nonfriction part consists of the entrance, flow acceleration and the exit effects

$$\Delta P = \frac{1}{2} G^2 v_1 \Big[\underbrace{(K_C + 1 - \sigma^2)}_{\text{entrance}} + \underbrace{2\left(\frac{v_2}{v_1} - 1\right)}_{\text{acceleration}} \underbrace{- (1 - \sigma^2 - Ke)\frac{v_2}{v_1}}_{\text{exit}} \Big]$$

The friction part depends on $f(\mathrm{Re})$ and the area ratio

$$\Delta P_F = \frac{1}{2} G^2 v_m f A/A_C \tag{74}$$

The friction factor is given in the vicinity of the operating point as

$$f = f_0 \, \mathrm{Re}^{\psi} \tag{75}$$

the constants being obtainable from graphs or tables in Kays and London (1984) or formulas by Bird et al. (1960).

The mass flow rates and Re are proportional to the optimization variables X_3 and X_4; the mass velocities are inversely proportional to free flow areas and thus to the transverse dimensions. Consequently, the partial derivatives are

$$\frac{X_1 \partial c_{E,MA}}{c_{E,MA} \partial X_1} = 0 \tag{76}$$

$$\frac{X_2 \partial c_{E,MA}}{c_{E,MA} \partial X_2} = -2 \tag{77}$$

since the pumping power increases with the cross-section area and the cube of velocity, but the velocity decreases with the transversal dimensions X_2. For the side of minor capacity rate, the indices 1, 2 are reversed.

The sensitivity of nonfriction pumping costs to the capacity rates is

$$\frac{X_3 \partial c_{E,MA}}{c_{E,MA} \partial X_3} = 3 \tag{78}$$

$$\frac{X_4 \partial c_{E,MA}}{c_{E,MA} \partial X_4} = 0 \tag{79}$$

with the obvious permutation of indices for the minor stream.

Friction-related pumping costs depend on velocities in an analogous manner, and, in addition, on the slope ψ of the friction factor, and on the length of passages; thus

$$\frac{X_1 \partial c_{F,MA}}{c_{F,MA} \partial X_1} = 1 \tag{80}$$

as the length X_1 affects the pumping power proportionally. The increase of transverse dimension reduces the flow velocity and friction pressure drop, giving

$$\frac{X_2 \partial c_{F,MA}}{c_{F,MA} \partial X_2} = -(2 + \psi_{MA}) \tag{81}$$

The capacity rate appears in the pumping power formula with the exponent $(3 + \psi)$:

$$\frac{X_3 \partial c_{F,MA}}{c_{F,MA} \partial X_3} = 3 + \psi_{MA} \tag{82}$$

and

$$\frac{X_4 \partial c_{F,MA}}{c_{F,MA} \partial X_4} = 0 \tag{83}$$

On the side of minor capacity rate, subscripts change to give $MA \rightarrow MI$, $X_1 \leftrightarrow X_2$, $X_3 \leftrightarrow X_4$. These sensitivities enter as elements into the matrix in equation (36).

All results in this appendix are based on the pressure drop equations stated by Kays and London (1984).

Relation Between the Thermal Effectiveness of Overall Parallel and Counterflow Heat Exchanger Geometries

A. Pignotti

TECHINT S. A.,
1001 Buenos Aires, Argentina

A simple relation is established between the thermal effectiveness of two heat exchanger configurations that differ from each other in the inversion of either one of the two fluids. Using this relation, if the expression for the effectiveness of a configuration, as a function of the heat capacity rate ratio, and the number of heat transfer units, is known, the corresponding expression for the "inverse" configuration is immediately obtained. The relation is valid under the assumptions of temperature independence of the heat transfer coefficient and heat capacity rates, when one of the fluids proceeds through the exchanger in a single, mixed stream. The property is illustrated with several examples from the available literature.

Statement of the Problem

Expressions for the thermal effectiveness P of a heat exchanger, as a function of the heat capacity rate ratio R, and of the number of heat transfer units NTU, have been reported in the literature for a wide variety of geometries, under the assumptions of temperature independence of the heat transfer coefficient and the heat capacity rates involved. Many such relations are listed in the review work of Shah and Mueller (1985), where reference to the original papers can be found.

In order to alleviate the task of finding such expressions for as yet unsolved geometries, it is useful to establish relations between P-R-NTU formulas for different configurations. The statement of flow reversibility, for example, implies that any two geometries that differ from each other in the inversion of the direction of flow of both fluids share the same P-R-NTU relation (Pignotti, 1984b). Although in some cases with special symmetry, the inversion of both fluids does not alter the geometry, and, therefore, this property is trivially satisfied, there are instances in which it leads to interesting results, and a deeper insight into the nature of the problem. There are no exceptions to the validity of this property, as long as the above-stated assumptions hold.

The purpose of this work is to establish a correspondence between the P-R-NTU relations of two different configurations, which differ from each other in the inversion of the direction of flow of only one of the fluids. Because we know that inverting both fluids leaves the effectiveness invariant, as far as the present work is concerned, it is immaterial which one of the two fluids is inverted.

Whereas the inversion of both fluids often does not alter the geometry, the inversion of only one of them usually leads from one configuration to an entirely different one, as is the case in going from a pure parallel-flow to a pure counterflow arrangement. In general, it leads from a configuration that, loosely speaking, may be characterized as "overall parallel-current," to an "overall countercurrent" geometry. Nonetheless, the expression for the effectiveness of one configuration can be immediately derived from that of the other one through the simple relation

$$\hat{P}(R, \text{NTU}) = P(-R, \text{NTU})/[1 + R\,P(-R, \text{NTU})] \qquad (1)$$

where P denotes the effectiveness of a given arrangement, and $\hat{P}$ that of the same one, with one fluid reversed. The only additional restriction for the validity of equation (1) is that one of the two fluids is required to go through the exchanger in a single stream, perfectly mixed in its transverse direction. In equation (1), we have chosen the variables P, R, and NTU to be referred to the other, unrestricted (i.e., possibly split or unmixed) fluid, which we call fluid 1. The fluid that is necessarily mixed will correspondingly be referred to as fluid 2.

Equation (1) relates the effectiveness value $\hat{P}$ of the "inverted" exchanger for physical (i.e., positive) values of R, to the expression of P for the original exchanger at "unphysical" (negative) values of the heat capacity rate ratio. Such unphysical values for P are, however, mathematically perfectly well defined, and equation (1) can be viewed as a relation between different functional forms which describe physically different arrangements. Alternatively, we can think of the function $P(R, \text{NTU})$ as describing one configuration for $R > 0$, and, through equation (1), the configuration with one fluid inverted, when analytically continued to negative values of R.

An elementary example may help to clarify the meaning of equation (1). Consider the well-known expression for the effectiveness of a parallel-flow configuration

$$P(R, \text{NTU}) = \{1 - \exp[-\text{NTU}(1+R)]\}/(1+R) \qquad (2)$$

and let us derive from it the expression for the effectiveness of a pure counterflow configuration, which we denote $\hat{P}(R, \text{NTU})$. Equation (1) is applicable, because the counterflow geometry is obtained from parallel flow by inverting the direction of flow of one of the fluids, and the condition that at least one of the fluids should be mixed throughout the exchanger is satisfied. Indeed, after replacing R by $-R$ in equation (2), and performing the elementary algebraic operations indicated in equation (1), we obtain

$$\hat{P}(R, \text{NTU}) = \{1 - \exp[-\text{NTU}(1-R)]\}/\{1 - R\exp[-\text{NTU}(1-R)]\} \qquad (3)$$

which is the well-known expression for the effectiveness of the counterflow configuration.

Table 1 shows a compilation of examples of the property discussed here. Observe that five cases in which the inversion of one fluid is immaterial, namely, single-pass mixed-mixed or unmixed-mixed crossflow exchange, the 1-2 and 1-4 TEMA E configurations, and the 1-2 TEMA J exchanger, have been in-

Contributed by the Heat Transfer Division and presented at the National Heat Transfer Conference, Pittsburgh, Pennsylvania, August 9–12, 1987. Manuscript received by the Heat Transfer Division September 14, 1987. Keywords: Heat Exchangers, Heat Recovery.

cluded. In these cases, equation (1) must preserve the functional form for the effectiveness, i.e.,

$$\hat{P}(R, \text{NTU}) = P(R, \text{NTU}) \tag{4}$$

This can be easily verified using equation (1) and the corresponding formulas in Table 1.

Observe also that the inversion of one fluid leads from a parallel flow connection to a counterflow one, but, likewise, from the latter to the former. Therefore, equation (1) can be used to go from the first to the second column of formulas in Table 1, as well as vice versa.

The transformation property of equation (1) can also be expressed in terms of the variables referred to the mixed fluid, namely,

$$\mathbf{P} = R\,P, \quad \mathbf{R} = 1/R, \quad \mathbf{NTU} = R\,\text{NTU} \tag{5}$$

in which case it reads

$$\hat{\mathbf{P}}(\mathbf{R}, \mathbf{NTU}) = -\mathbf{P}(-\mathbf{R}, -\mathbf{NTU})/[1-\mathbf{P}(-\mathbf{R}, -\mathbf{NTU})] \tag{6}$$

This equation is exactly equivalent to equation (1), and holds whenever equation (1) does.

Finally, we point out that equation (1) has no immediate direct implication on the numerical values of the effectiveness for the two related configurations. Indeed, equation (1) holds for such widely different circumstances as those for which $\hat{P} = P$, i.e., for which the inversion of one fluid does not alter the effectiveness, to the extreme case of pure parallel flow, which, upon inversion of one fluid, turns into the drastically different pure counterflow configuration.

Formalism

In order to derive equation (1), we recall the basic features of the matrix formalism to be used. An exchanger with two inlet and two outlet streams is described by the thermal matrix (Domingos, 1969)

$$M(R, \text{NTU}) = \begin{bmatrix} 1-R\,P(R, \text{NTU}) & R\,P(R, \text{NTU}) \\ P(R, \text{NTU}) & 1-P(R, \text{NTU}) \end{bmatrix} = \begin{bmatrix} M_{00} & M_{01} \\ M_{10} & M_{11} \end{bmatrix} \tag{7}$$

which relates the outlet temperatures to the inlet ones, through the equation

$$\begin{vmatrix} T' \\ t' \end{vmatrix} = M(R, \text{NTU}) \begin{vmatrix} T \\ t \end{vmatrix} \tag{8}$$

If equation (8) is solved for T and t' as functions of T' and t, we obtain

$$\begin{vmatrix} T \\ t' \end{vmatrix} = H(R, \text{NTU}) \begin{vmatrix} T' \\ t \end{vmatrix} \tag{9}$$

with

$$H(R, \text{NTU}) = [1-R\,P(R, \text{NTU})]^{-1} \begin{bmatrix} 1 & -R\,P(R, \text{NTU}) \\ P(R, \text{NTU}) & \det M(R, \text{NTU}) \end{bmatrix} \tag{10}$$

From equations (7) and (10) we see that equation (1) is equivalent to

$$\hat{M}(R, \text{NTU}) = H(-R, \text{NTU}) \tag{11}$$

In words, this means that, whenever equation (1) holds, the thermal matrix for the inverted process is equal to the H matrix for the original one, with R replaced by $-R$.

Because one of the fluids may be split or unmixed, we must use a generalized matrix formalism to allow for multiple streams for that fluid (Pignotti, 1984a). Correspondingly, we write

$$\begin{vmatrix} T' \\ t'_1 \\ . \\ . \\ t'_{n'} \end{vmatrix} = M \begin{vmatrix} T \\ t_1 \\ . \\ . \\ t_n \end{vmatrix} \tag{12}$$

and

$$\begin{vmatrix} T \\ t'_1 \\ . \\ . \\ t'_{n'} \end{vmatrix} = H \begin{vmatrix} T' \\ t_1 \\ . \\ . \\ t_n \end{vmatrix} \tag{13}$$

where n and n' are the number of inlet and outlet streams of the split fluid, and M and H are rectangular $(n'+1)\times(n+1)$ matrices, with

$$\begin{aligned} H_{00} &= 1/M_{00} \\ H_{0i} &= -M_{0i}/M_{00} \\ H_{j0} &= M_{j0}/M_{00} \\ H_{ji} &= M_{ji} - M_{j0}\,M_{0i}/M_{00} \end{aligned} \tag{14}$$

In these expressions, and those that follow, the subscripts used for the elements of the matrices M or H are based on the expansions of equations (12) or (13), with the convention that 0 denotes the mixed fluid stream. For instance, M_{ji} is the coefficient of t_i in the expansion of t'_j; M_{0i} the coefficient of t_i in the expansion of T'; H_{j0} that of T' in the expansion of t'_j, etc.

An overall parallel-current assembly of two exchangers A and B, coupled as shown in Fig. 1(*a*), in which there are arbitrary numbers of inlet and outlet streams of one of the

Nomenclature

A = heat transfer surface area, m^2
c, C = fluid 1 and fluid 2 heat capacity rates, W/°C
H = matrix relating left-hand to right-hand temperatures as in equation (13)
M = matrix relating outlet to inlet temperatures
n, n' = inlet and outlet number of streams of fluid 1
NTU = UA/C = number of heat transfer units referred to fluid 1
NTU = UA/C = number of heat transfer units referred to fluid 2
P = $(t'-t)/(T-t)$ = fluid 1 effectiveness
P = $(T'-T)/(t-T)$ = fluid 2 effectiveness
R = c/C = fluid 1 heat capacity rate ratio
R = C/c = fluid 2 heat capacity rate ratio
t, t' = fluid 1 inlet and outlet temperatures, °C
T, T' = fluid 2 inlet and outlet temperatures, °C
U = overall heat transfer coefficient, W/°C m^2

The symbol ^ on P, **P**, M, or H denotes the same quantities for a configuration in which the direction of flow of one of the fluids has been reversed.

Table 1 Examples of overall parallel-flow and counterflow configurations, for which the effectiveness satisfies equation (1)

Overall parallel flow		Overall counterflow	
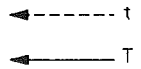	Parallel flow $P = \frac{1 - \exp[-NTU\,(1+R)]}{1+R}$	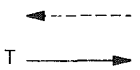	Counterflow $\hat{P} = \frac{1 - \exp[-NTU\,(1-R)]}{1 - R\exp[-NTU\,(1-R)]}$
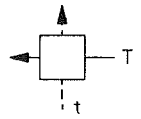	Mixed-mixed single-pass crossflow $P = 1/\left[\frac{1}{K_1} + \frac{R}{K_2} - \frac{1}{NTU}\right]$ $K_1 = 1 - \exp(-NTU)$ $K_2 = 1 - \exp(-R\,NTU)$ (Stevens et al. (1957))	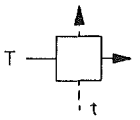	$\hat{P} = P$
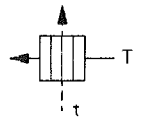	Unmixed-mixed single-pass crossflow $P = [1 - \exp(-KR)]/R$ $K = 1 - \exp(-NTU)$ (Stevens et al. (1957))	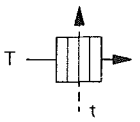	$\hat{P} = P$
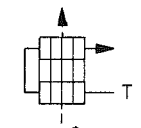	Two-pass cocrossflow, fluid 1 unmixed, inverted order, fluid 2 mixed $P = (1 - \frac{K}{2})[1 - \exp(-2KR)]/R$ $K = 1 - \exp(-NTU/2)$ (Stevens et al. (1957))	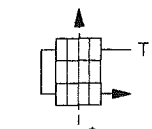	Two-pass countercrossflow, fluid 1 unmixed, inverted order, fluid 2 mixed $\hat{P} = \left[1 - \frac{1}{\frac{K}{2} + (1 - \frac{K}{2})\exp(2KR)}\right]/R$ $K = 1 - \exp(-NTU/2)$ (Stevens et al. (1957))
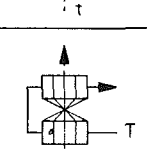	Two-pass cocrossflow, fluid 1 unmixed, identical order, fluid 2 mixed $P = \{1 - \exp(-KR)[\exp(-KR) + K^2 R]\}/R$ $K = 1 - \exp(-NTU/2)$ (Stevens et al. (1957))	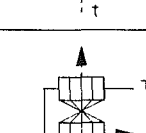	Two-pass countercrossflow, fluid 2 unmixed, identical order, fluid 2 mixed $\hat{P} = \left[1 - \frac{\exp(-KR)}{\exp(KR) - K^2 R}\right]/R$ $K = 1 - \exp(-NTU/2)$ (Stevens et al. (1957))
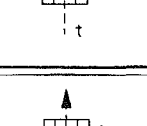	Three-pass cocrossflow, fluid 1 unmixed, inverted order, fluid 2 mixed $P = [1 - (1 - \frac{K}{2})^2 \exp(-3KR) - A\exp(-KR)]/R$ $K = 1 - \exp(-NTU/3)$ $A = K(1 - \frac{K}{4}) + K^2 R\,(1 - \frac{K}{2})$ (Stevens et al. (1957))	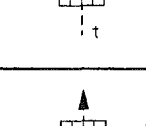	Three-pass countercrossflow, fluid 1 unmixed, inverted order, fluid 2 mixed $\hat{P} = \left[1 - \frac{1}{(1 - \frac{K}{2})^2 \exp(3KR) + A\exp(KR)}\right]/R$ $K = 1 - \exp(-NTU/3)$ $A = K(1 - \frac{K}{4}) - K^2 R\,(1 - \frac{K}{2})$ (Stevens et al. (1957))
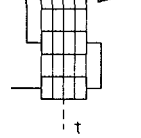	Three-pass cocrossflow, fluid 1 unmixed, identical order, fluid 2 mixed $P = [1 - X^3 - 2K^2 R X^2 - AX]/R$ $K = 1 - \exp(-NTU/3)$ $X = \exp(-KR)$ $A = K^2 R\,(1 - K + \frac{K^2}{2} R)$ (Stevens et al. (1957))	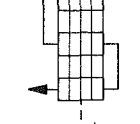	Three-pass countercrossflow, fluid 1 unmixed, identical order, fluid 2 mixed $\hat{P} = \left[1 - \frac{1}{X^3 - 2K^2 R X^2 + AX}\right]/R$ $K = 1 - \exp(-NTU/3)$ $X = \exp(KR)$ $A = -K^2 R(1 - K - \frac{K^2}{2} R)$ (Stevens et al. (1957))
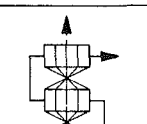	Overall parallel-flow 1-2 TEMA G shell-and-tube exchanger $P = (B - \alpha^2)/(A - R\alpha^2 + 2)$ $A = R(1 - \alpha)^2/(1 - R/2)$ $B = [4 - \beta(2 - R)]/(2 + R)$ $\alpha = \exp[-NTU(2 - R)/4]$ $\beta = \exp[-NTU(2 + R)/2]$ (Pignotti (1984b))	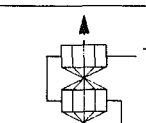	Overall counterflow 1-2 TEMA G shell-and-tube exchanger $\hat{P} = (B - \alpha^2)/(A + 2 + RB)$ $A = -R(1 - \alpha)^2/(1 + R/2)$ $B = [4 - \beta(2 + R)]/(2 - R)$ $\alpha = \exp[-NTU(2 + R)/4]$ $\beta = \exp[-NTU(2 - R)/2]$ (Schindler and Bates (1960))
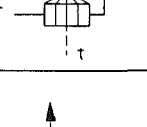	1-2 TEMA J shell-and-tube exchanger $P = 2/(R + 2\phi')$ $\phi' = 1 + \gamma\frac{1+\phi}{1-\phi} - 2\gamma\frac{\gamma\phi + (1-\phi)\psi}{(1-\phi)^2 + \gamma(1-\phi^2)}$ $\phi = \exp(-NTU\gamma)$ $\psi = \exp[-NTU(\gamma - 1)/2]$ $\gamma = (1 + R^2/4)^{1/2}$ (Jaw (1964))	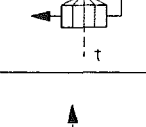	$\hat{P} = P$

fluids, is then described by the matrix M given by the matrix product

$$M(R, \mathrm{NTU}) = M^B(R, \mathrm{NTU}^B)\, M^A(R, \mathrm{NTU}^A) \qquad (15)$$

whereas for the corresponding countercurrent assembly, obtained after inversion of one fluid, such as shown in Fig. 1 (b), we can write

$$\hat{H}(R, \mathrm{NTU}) = \hat{H}^B(R, \mathrm{NTU}^B)\, \hat{H}^A(R, \mathrm{NTU}^A) \qquad (16)$$

Derivation

The derivation of equation (1) is achieved by proving the validity of equation (11) for an arbitrary configuration in which one of the fluids is mixed throughout. This requires the following stages:

Table 1 (continued)

Overall parallel flow		Overall counterflow	
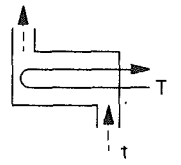	1-2 TEMA E shell-and-tube exchanger $P = \dfrac{2}{1 + R + A \coth(A\ NTU/2)}$ $A = (1 + R^2)^{1/2}$ (Nagle (1933))	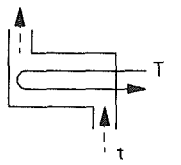	$\hat{P} = P$
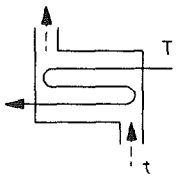	1-3 TEMA E shell-and-tube exchanger, same end $P = [1 - (AC + B^2)/C]/R$ $\lambda_{1,2} = (-3 \pm \delta)/2 \qquad \delta = [9 + 4R(R+1)]^{1/2}$ $X_{1,2} = \exp(\lambda_{1,2}\, NTU/3)/2\delta$ $A = X_1 (R - \lambda_1)(R + \lambda_2)/2\lambda_1 - E +$ $+ X_2 (R - \lambda_2)(R + \lambda_1)/2\lambda_2 + 1/(1+R)$ $B = X_2(R + \lambda_1) - X_1(R + \lambda_2) + E$ $C = X_1(3R - \lambda_2) - X_2(3R - \lambda_1) + E$ $E = \exp(-R\ NTU/3)/2$ (Pignotti (1986))	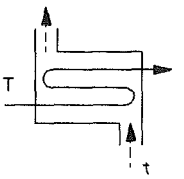	1-3 TEMA E shell-and-tube exchanger, opposite end $\hat{P} = [1 - C/(AC + B^2)]/R$ $\lambda_{1,2} = (-3 \pm \delta)/2 \qquad \delta = [9 + 4R(R-1)]^{1/2}$ $X_{1,2} = \exp(\lambda_{1,2}\, NTU/3)/2\delta$ $A = X_1 (R + \lambda_1)(R - \lambda_2)/2\lambda_1 - E +$ $+ X_2 (R + \lambda_2)(R - \lambda_1)/2\lambda_2 + 1/(1-R)$ $B = X_1(R - \lambda_2) - X_2(R - \lambda_1) + E$ $C = -X_1(3R + \lambda_2) + X_2(3R + \lambda_1) + E$ $E = \exp(R\ NTU/3)/2$ (Pignotti (1986))
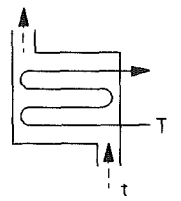	1-4 TEMA E shell-and-tube exchanger $P = 4\,[2(1+R) + \delta \coth \frac{NTU\ \delta}{4} +$ $+ R \tanh(NTU\ R/4)]^{-1}$ $\delta = (4 + R^2)^{1/2}$ (Nagle (1933))	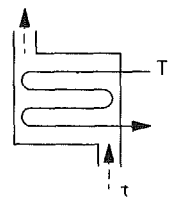	$\hat{P} = P$

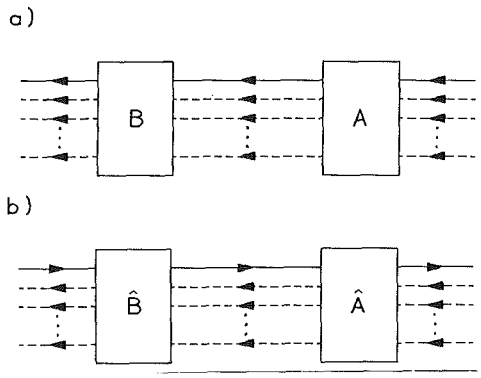

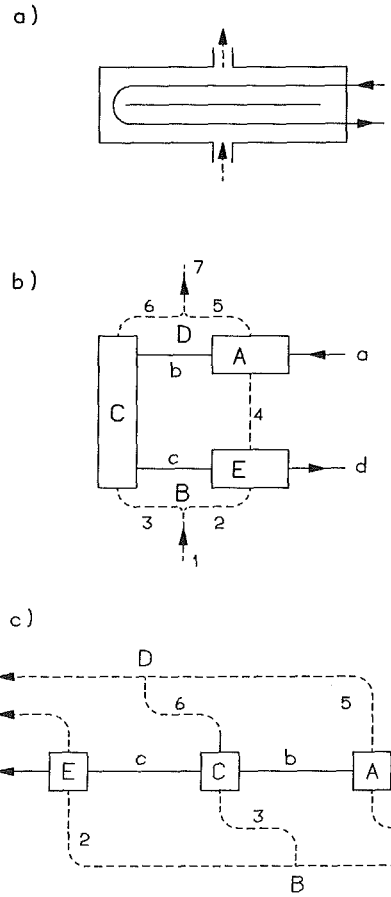

Fig. 1 *(a)* **Overall parallel current assembly of two exchangers A and B, with one fluid mixed throughout. *(b)* Overall countercurrent assembly obtained from *(a)* after inversion of one fluid.**

1 Establishing that the most general configuration of the type considered can be approximated to any desired degree of accuracy by an assembly of component units, each of which satisfies equation (11).

2 Proving that the property of equation (11) is preserved by the process of assembling these components together.

First Stage

We illustrate the first stage with the example of the TEMA G exchanger sketched in Fig. 2(*a*). This exchanger can be broken into three parts, labeled A, C, and E, and two nodes, B and D, shown in Fig. 2(*b*). A and E are parallel-flow type exchangers, while C is a countercurrent one. The streams involved are labeled "*a*" through "*d*" for the mixed (tube) fluid, whereas the split (shell) fluid streams are numbered from 1 to 7.

Figure 2(*c*) shows how the arrangement of Fig. 2(*b*) can be displayed, with all streams proceeding from right to left, except for stream 4. In order to have stream 4 also proceed in the same direction, it is divided into two parts, 4 and 4′, as shown

Fig. 2 *(a)* **Overall countercurrent G-shell exchanger. *(b)* Same exchanger, constructed from two parallel-current exchangers A and E, one counterflow exchanger C, and two nodes B and D. *(c)* Same as *(b)*, after stream 4 is cut, and all streams are shown flowing from right to left.**

in Fig. 2(*c*). Stream 4 enters the diagram from the right, while stream 4′ exits at the left end. At a later stage we show how to attach these loose ends to each other and reconstruct the original topology of Fig. 2(*b*).

The thermal matrix for the assembly of Fig. 2(*c*) can now be obtained as the product of matrices M^E through M^A, each one corresponding to a portion of the diagram in which either an exchanger unit or a node operates

$$M = M^E\, M^D\, M^C\, M^B\, M^A \tag{17}$$

In the above expression, M^E relates the outlet temperatures T_d, t_4', and t_7, to the "inlet" ones for the last stage of the diagram, namely, T_c, t_2, and t_7. The fact that t_7 is unchanged in this last stage, which only involves the E exchanger, is reflected by the presence of two zeroes and a one in the third row of M^E. In the same fashion, M^D only includes the effect of the node D, which merges streams 5 and 6 into stream 7, and therefore relates T_c, t_2, and t_7, to T_c, t_2, t_5, and t_6. Thus, we can write

$$\begin{vmatrix} T_d \\ t_4' \\ t_7 \end{vmatrix} = M^E \begin{vmatrix} T_c \\ t_2 \\ t_7 \end{vmatrix} = \begin{bmatrix} \begin{bmatrix} & M_{pc} & \end{bmatrix} & \begin{matrix} 0 \\ 0 \end{matrix} \\ \begin{matrix} 0 & 0 \end{matrix} & 1 \end{bmatrix} \begin{vmatrix} T_c \\ t_2 \\ t_7 \end{vmatrix} \tag{18}$$

and

$$\begin{vmatrix} T_c \\ t_2 \\ t_7 \end{vmatrix} = M^D \begin{vmatrix} T_c \\ t_2 \\ t_5 \\ t_6 \end{vmatrix} = \begin{bmatrix} 1 & 0 & 0 & 0 \\ 0 & 1 & 0 & 0 \\ 0 & 0 & 1/2 & 1/2 \end{bmatrix} \begin{vmatrix} T_c \\ t_2 \\ t_5 \\ t_6 \end{vmatrix} \tag{19}$$

where M_{pc} is a 2×2 submatrix that describes the parallel current E exchanger. Similar expressions are written for the remaining matrix factors in equation (17), and for the corresponding H matrices. From the fact that M_{pc}, and the analogous expression for countercurrent exchange, satisfy equation (11), it follows that M^A through M^E also do.

The only additional operation to be performed to reproduce the configuration of Fig. 2(*b*) is to tie together the loose ends of streams 4 and 4′. This "reduction" process is described by Pignotti (1984a), and is achieved by setting $t_4' = t_4$ in the expression

$$\begin{vmatrix} T_d \\ t_4' \\ t_7 \end{vmatrix} = M \begin{vmatrix} T_a \\ t_4 \\ t_1 \end{vmatrix} \tag{20}$$

and eliminating t_4 from this set of linear equations. This leads to

$$\begin{vmatrix} T_d \\ t_7 \end{vmatrix} = M_R \begin{vmatrix} T_a \\ t_1 \end{vmatrix} \tag{21}$$

The reduced 2×2 matrix M_R thus obtained is the thermal matrix for the overall countercurrent G-shell exchanger, and from it the corresponding entry for the effectiveness in Table 1 can be found. In order to prove that the overall parrallel current effectiveness can be obtained from that expression and equation (1), we still have to prove that the matrix multiplication and reduction operations performed preserve the validity of equation (11). This is discussed in the next section.

Second Stage

Figure 1(*a*) shows an exchanger obtained by series coupling of two components, A and B, with overall parallel current

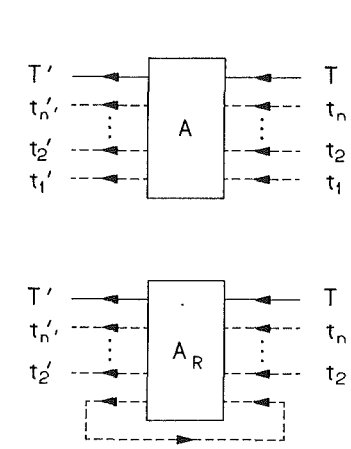

Fig. 3 (*a*) Exchanger with n inlet and n' outlet streams for the unmixed fluid. (*b*) Same exchanger as in (*a*), after a reduction has been performed in the 1-1′ stream pair.

connection. We assume that A and B satisfy equation (11), namely,

$$\begin{aligned} \hat{M}^A(R, \text{NTU}^A) &= H^A(-R, \text{NTU}^A) \\ \hat{M}^B(R, \text{NTU}^B) &= H^B(-R, \text{NTU}^B) \end{aligned} \tag{22}$$

and show that the combined exchanger also satisfies equation (11).

We readily establish from Fig. 1(*b*) that the configuration obtained after inverting one fluid in the combined exchanger can also be reached by countercurrent coupling of two components, labeled $\hat{\text{A}}$ and $\hat{\text{B}}$, which are just equal to A and B with one fluid inverted. Hence, equations (15) and (16) apply. In addition, because inverting one fluid twice amounts to not changing anything, it is trivially true that $\hat{\hat{M}} = M$. Therefore, from equation (22), we can write

$$\begin{aligned} \hat{H}^A(-R, \text{NTU}^A) &= M^A(R, \text{NTU}^A) \\ \hat{H}^B(-R, \text{NTU}^B) &= M^B(R, \text{NTU}^B) \end{aligned} \tag{23}$$

and, using equations (15) and (16), with R replaced by $-R$

$$\begin{aligned} \hat{H}(-R, \text{NTU}) &= \hat{H}^B(-R, \text{NTU}^B)\hat{H}^A(-R, \text{NTU}^A) \\ &= M^B(R, \text{NTU}^B)M^A(R, \text{NTU}^A) = M(R, \text{NTU}) \end{aligned} \tag{24}$$

from which equation (11) follows.

The remaining relation to be proved is that if M satisfies equation (11), so does the reduced matrix M_R, an example of which has been shown at the end of the previous section. Figure 3(*a*) shows a generic exchanger, in which the heat capacity rates of one of the inlet and outlet streams of the unmixed fluid, labeled 1 and 1′, are assumed to be equal. The corresponding temperatures are labeled t_1 and t_1', respectively. The $(n'+1)\times(n+1)$ thermal matrix M is such that

$$\begin{vmatrix} T' \\ t_1' \\ t_2' \\ \cdot \\ \cdot \\ \cdot \\ t'_{n'} \end{vmatrix} = M \begin{vmatrix} T \\ t_1 \\ t_2 \\ \cdot \\ \cdot \\ \cdot \\ t_n \end{vmatrix} \tag{25}$$

Figure 3(*b*) shows the reduced exchanger, in which a bypass is established between streams 1 and 1′. The reduced $n'\times n$ matrix M_R is such that

$$\begin{vmatrix} T' \\ t_2' \\ \cdot \\ \cdot \\ \cdot \\ t'_{n'} \end{vmatrix} = M_R \begin{vmatrix} T \\ t_2 \\ \cdot \\ \cdot \\ \cdot \\ t_n \end{vmatrix} \tag{26}$$

Setting $t_1' = t_1$ in equation (25), and solving for t_1, we obtain

$$t_1 = [M_{10}\ T + M_{12}\ t_2 + \ \ldots\ + M_{1n}\ t_n]/(1 - M_{11}) \qquad (27)$$

Replacing this in equation (25) we find

$$[M_R]_{ji} = M_{ji} + M_{j1}\ M_{1i}/(1 - M_{11}) \qquad (28)$$

Similar expressions can be obtained for $[H_R]_{ji}$ and $[\hat{M}_R]_{ji}$. Therefore,

$$[\hat{M}_R(R, \text{NTU})]_{ji} = [\hat{M}(R, \text{NTU})]_{ji}$$
$$+ [\hat{M}(R, \text{NTU})]_{j1}[\hat{M}(R, \text{NTU})]_{1i}/\{1 - [\hat{M}(R, \text{NTU})]_{11}\}$$
$$= [H(-R, \text{NTU})]_{ji} + [H(-R, \text{NTU})]_{j1}[H(-R, \text{NTU})]_{1i}/$$
$$\{1 - [H(-R, \text{NTU})]_{11}\} = [H_R(-R, \text{NTU})]_{ji} \qquad (29)$$

which completes the proof.

Discussion

Whereas the above proofs, which show that the matrix multiplication and reduction preserve equation (11), are quite general, we have not proved that these operations suffice to construct the thermal matrix for an arbitrary geometry. The example of the G-shell exchanger, however, shows all the needed ingredients. It may be argued that it is a particularly simple example, in which only three exchangers and two nodes, denoted A through E in Fig. 2, are required to represent exactly the idealized geometry of the exchanger. This is of course true, and decompositions of this degree of simplicity cannot be expected to be found for arbitrary configurations. It should be noted, however, that there are other elements that satisfy equation (1), such as mixed-mixed and unmixed-mixed crossflow geometries, that can be used to construct a complex assembly. In addition, it is not imperative to match exactly a given geometry, but rather to be able to approximate it with any prescribed degree of accuracy, by a sufficiently large number of adequately coupled constitutive elements. We can therefore safely conclude that equation (1) is valid, no matter how complex the exchanger is, provided one fluid is mixed throughout the exchanger. This conclusion is born out by the list of solved examples in Table 1.

The relation derived can be used in two ways. The first is to obtain new P-R-NTU relations. Consider, for instance, a countercrossflow exchanger, with six passes and one row per pass, with mixed tube fluid, and unmixed out-of-tube fluid. An expression for the effectiveness, too long to be reproduced here, was derived by Nicole (1972). However, the corresponding one for the co-crossflow case is not available in the open literature, and is quite cumbersome to derive. Using equation (1), however, the correct formula is immediately obtained.

Equation (1) can also be used if a computer program is available for the numerical calculation of the effectiveness of either an overall parallel current, or an overall countercurrent geometry, but not for both. The missing case is easily solved running the computer program for negative values of R, and using equation (1) to obtain the desired result. As an example of this type of application, consider the six-plate exchanger of Fig. 4, with three single-stream passes for fluid 1, and two double-stream passes for fluid 2. Figures 4(a) and 4(b) correspond to the overall parallel and counterflow connections, respectively. A numerical computer calculation for the former gives $P = 0.4923$ for $R = 1$ and NTU $= 5$. When we run the program for $R = -1$ and NTU $= 5$, we obtain $P = 2.3784$, an obviously physically meaningless value. When, however, this value is used in equation (1), we obtain, for the effectiveness of the configuration of Fig. 4(b), with $R = 1$ and NTU $= 5$

$$P = 2.3784/(1 + 2.3784) = 0.7040$$

A computer program also available for the calculation of the effectiveness of the arrangement of Fig. 4(b), confirms that this is the correct value.

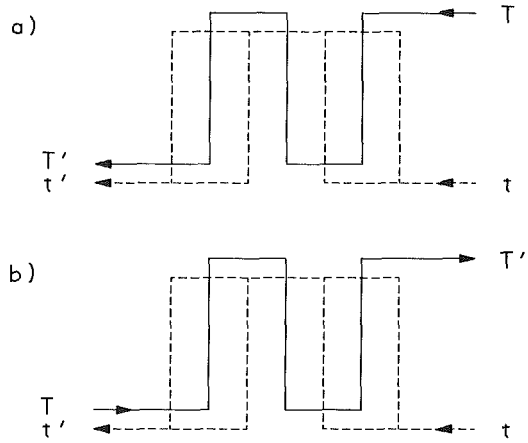

Fig. 4 Six-plate exchanger, with two passes for fluid 1 and three passes for fluid 2, with (a) overall parallel-flow connection and (b) overall counterflow connection

In summary, equation (1) is applicable whenever an algorithm, be it a formula, collection of formulas, or computer program, is available for the calculation of the effectiveness of a configuration. It provides the means of obtaining, through the use of the same algorithm for negative values of R, the effectiveness of a different configuration, related to the previous one in a precise way. The only restriction, apart from the usual assumptions in this type of calculations, is that, for equation (1) to be valid, one of the fluids has to be perfectly mixed throughout the exchanger.

Acknowledgments

This work was sponsored by a CONICET-NSF Cooperative Research Program.

The author is indebted to Mr. Pablo I. Tamborenea, who wrote the computer program for the numerical calculation of the effectiveness of the plate exchanger geometry.

The author also wishes to express his gratitude to Professor Geoffrey Chew, from whom, in a rather different context, he learned the basic ideas that gave rise to the present work.

References

Domingos, J. D., 1969, "Analysis of Complex Assemblies of Heat Exchangers," *Int. J. Heat Mass Transfer*, Vol. 12, pp. 537–548.

Jaw, L., 1964, "Temperature Relations in Shell and Tube Exchangers Having One Pass Split-Flow Shells," ASME JOURNAL OF HEAT TRANSFER, Vol. 86, pp. 408–416.

Nagle, W. M., 1933, "Mean Temperature Difference in Multipass Heat Exchanger," *Ind. Eng. Chem.*, Vol. 25, pp. 604–609.

Nicole, F. J. L., 1972, "Mean Temperature Difference in Cross-Flow Heat Exchange," M. Sc. Thesis, University of Pretoria, Pretoria, South Africa, p. 53.

Pignotti, A., 1984a, "Matrix Formalism for Complex Heat Exchangers," ASME JOURNAL OF HEAT TRANSFER, Vol. 106, pp. 352–360.

Pignotti, A., 1984b, "Flow-Reversibility of Heat Exchangers," ASME JOURNAL OF HEAT TRANSFER, Vol. 106, pp. 361–368.

Pignotti, A., 1986, "Analytical Solution for the Thermal Effectiveness of a 1-3 TEMA E Shell-and-Tube Heat Exchanger," *Proceedings of the 2nd Latin American Congress on Heat and Mass Transfer*, Sao Paulo, Brazil, 1986, pp. 254–265.

Schindler, D. L., and Bates, H. T., 1960, "True Temperature Difference in a 1-2 Divided-Flow Heat Exchanger," Chemical Engineering Progress Symposium Series No. 30, Vol. 56, pp. 203–206.

Shah, R. K., and Mueller, A. C., 1985, "Heat Exchanger Basic Thermal Design Methods," *Handbook of Heat Transfer Applications*, 2nd ed., W. M. Rohsenow, J. P. Hartnett, and E. N. Ganic, eds., McGraw-Hill, New York, Chap. 4, Part I, pp. 4-1 to 4-77.

Stevens, R. A., Fernandez, J., and Woolf, J. R., 1957, "Mean Temperature Difference in One, Two, and Three-Pass Crossflow Heat Exchangers," *Trans. ASME*, Vol. 79, pp. 287–297.

Multipass Plate Heat Exchangers—Effectiveness-NTU Results and Guidelines for Selecting Pass Arrangements

S. G. Kandlikar
Mechanical Engineering Department,
Rochester Institute of Technology,
Rochester, NY 14623-0887
Mem. ASME

R. K. Shah
Harrison Radiator Division,
General Motors Corporation,
Lockport, NY 14094-1896
Fellow ASME

Plate heat exchangers are classified on the basis of number of passes on each side and the flow arrangement in each channel, taking into account the end plate effects. This results in four configurations each for the 1-1 (1 Pass-1 Pass), 2-1, 2-2, 3-3, 4-1, 4-2, and 4-4 arrangements, and six configurations for the 3-1 arrangement. These arrangements are analyzed using the Gauss-Seidel iterative finite difference method; the plate arrangement that yields the highest effectiveness in each pass configuration is identified. Comprehensive results are presented in tabular form for the temperature effectiveness P_1 and log-mean temperature difference correction factor F as functions of the number of transfer units NTU_1, the heat capacity rate ratio R_1, and the total number of thermal plates. On the basis of these results, specific guidelines are outlined for the selection of appropriate plate heat exchanger configurations.

Introduction

Plate heat exchangers (PHE) originally received particular attention from the dairy industry due to their suitability in hygienic applications. Soon their use became widespread in the food, juice, beverage, and pharmaceutical industries due to the ease of cleaning and the thermal control required for sterilization and pasteurization. They are currently used in diverse industries such as the synthetic rubber industry, paper mills, petrochemical plants, and in process heaters, coolers, and closed-circuit cooling systems. In process industry, PHEs are used when special materials (such as stainless steel, titanium, Inconel, and Hastelloy) are required for heat exchanger construction in specific applications; this is where the PHEs are probably most cost competitive with shell-and-tube heat exchangers.

Plate heat exchangers are mostly used in liquid-to-liquid heat transfer applications, in condensing high-density vapors with specially designed plates, and as evaporators. They are generally not suited for gas-to-gas heat transfer applications because of high pressure drops. The maximum operating pressure is limited to about 2.5 MPa (350 psig) and the operating temperature to about 150°C (300°F) with elastomer gaskets.

Extensive literature is available on various design aspects of the PHEs. The more comprehensive recent literature is summarized by Focke (1983), Cooper and Usher (1983), Raju and Bansal (1983a, 1983b), and Shah and Focke (1988).

Literature Review

The ϵ-NTU results or the LMTD correction factors F have been obtained by previous investigators for a number of plate heat exchanger arrangements. A detailed literature review has been provided by Shah and Kandlikar (1988), and hence only a brief review is presented here.

Jackson and Troupe (1966) analyzed the 1-1 and 2-2 arrangements with overall counterflow and parallel flow, and 4-4 arrangements with overall counterflow. They obtained limited results for $0.3 \le NTU_1 \le 12$, $C_{min}/C_{max} = 0.25, 0.5, 0.75$, and 1, and the number of thermal plates[1] N up to 5. Since N is greater than 40 in most PHEs, their results for $N < 5$ have a very limited utility. Foote (1967) obtained F factors as a function of $P_1R_1/(1-P_1R_1)$ with R_1 as a parameter for 2-1, 3-1, and 4-1 pass arrangements for $N \to \infty$ and $N \le 11$. Again her results have a limited use since the effect of N is not clearly shown in the application range of N = 40-100.

Marriott (1971) presented empirical F factors for 1-1, 2-1, 2-2, and 3-1 flow arrangements, as a function of $NTU_1 \le 11$ and $0.7 \le R_1 \le 1.4$. However, no details were given regarding how the empirical F factors were obtained and what the number of plates investigated was. The number of thermal plates cannot be very large for these results since $F = 1$ for $N \to \infty$ for 1-1, 2-2, 3-3, and 4-4 overall counterflow arrangements.

Kandlikar (1984) numerically analyzed 1-1, 2-1, 2-2, and 3-1 counterflow arrangements, and 1-1 and 2-2 parallel flow arrangements. Most of the results were presented for $N = 3$ and 5. His results were extended by Shah and Kandlikar (1988) for 1-1, 2-1, and 3-1 flow arrangements where N was systematically varied from 3 to ∞, NTU_1 from 0.2 to 5.0, and R_1 from 1 to 6 depending upon the pass arrangement, and detailed tabular results were provided for P_1 and F. It was shown that the "end effect" due to a small number of thermal plates is important only for $N < 40$ for 1-1, 2-1, and 3-1 arrangements. Also, design guidelines were presented for the selection of 1-1, 2-1, or 3-1 pass exchanger for $R_1 \le 2$.

The present work is an extension of the work by Shah and Kandlikar (1988): (1) A detailed classification is made for various flow arrangements, (2) detailed results for P_1 and F are presented as functions of NTU_1, R_1, and N for the best configurations of 1-1, 2-1, 2-2, 3-1, 3-3, 4-1, 4-2, and 4-4 arrangements, and (3) design guidelines are presented for selecting a suitable multipass plate arrangement. The results for 3-2 and 4-3 pass arrangements for $N < \infty$ are not presented here due to space constraints. However, effectiveness formulas for these arrangements with $N \to \infty$ are given in Kandlikar and Shah (1989).

Contributed by the Heat Transfer Division and presented at the ASME Winter Annual Meeting, Boston, Massachusetts, December 13-18, 1987. Manuscript received by the Heat Transfer Division July 17, 1987. Keywords: Heat Exchangers, Modeling and Scaling.

[1] In a plate heat exchanger, two outer plates serve as end plates and ideally do not transfer heat, while the remaining plates, known as thermal plates, transfer heat.

Analysis

The analysis of different plate heat exchangers was carried out using the numerical scheme and computer program developed by Kandlikar (1984). In this section, only a few relevant details are provided to show how the temperature effectiveness P_1 and the LMTD correction factor F are computed for various plate heat exchanger configurations.

The plate exchanger is analyzed under the following idealizations: The heat exchanger operates under steady-state conditions; heat losses to surroundings are negligible—this idealization is reasonable since there are dead spaces between the cover and end plates, a situation that closely resembles an adiabatic wall; the overall heat transfer coefficient is constant and uniform throughout the heat exchanger; the specific heat and other fluid properties are constant throughout the heat exchanger so that the heat capacity rate R and NTU are treated as constants; temperature and fluid velocities are uniform across the channel width and at the inlet of the channel for each fluid stream; the fluid flow rate is uniformly distributed among the channels in each pass, and the fluid is perfectly mixed across a flow channel and between two passes; heat transfer across thermal plates is one-dimensional only and no heat is conducted either in the fluid or within the plates in the direction of fluid flow; in case of a phase change, the effective specific heat is either infinite, or is constant by virtue of a linear variation in the fluid saturation temperature.

Each channel is divided into n steps of equal area starting with $i=1$ at the inlet to $i = n$ at the outlet of the fluid stream in each channel. Thus $i=1$ always refers to the first section at the inlet end for each channel irrespective of the flow direction as shown in Fig. 1. All temperatures were nondimensionalized as follows:

$$\theta = (T - T_{c,\text{in}}) / (T_{h,in} - T_{c,in}) \tag{1}$$

For any element in a given channel, the heat transferred to the fluid from the adjacent channels is equated to the change in the enthalpy of the fluid. The temperature change is expressed in terms of the first-order backward-difference equation for the first step, and the second-order backward-difference equation for all subsequent steps. Developing such equations for each step in every channel resulted in a set of simultaneous equations which are solved using the Gauss-Seidel iterative technique. The resulting outlet temperatures from each channel in the last pass for each stream are averaged to obtain the respective stream outlet temperatures from the heat exchanger. The temperature effectivenesses for the two streams are then calculated as follows:

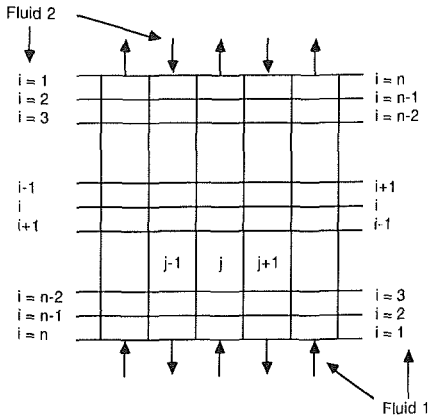

Fig. 1 The grid structure employed in the finite difference analysis of a PHE

$$P_1 = \begin{cases} \theta_{1,out} & \text{for Fluid 1 cold} \\ 1-\theta_{1,out} & \text{for Fluid 1 hot} \end{cases} \tag{2}$$

$$P_2 = \begin{cases} \theta_{2,out} & \text{for Fluid 2 cold} \\ 1-\theta_{2,out} & \text{for Fluid 2 hot} \end{cases} \tag{3}$$

where P_1 and P_2 are defined as

$$P_1 = \frac{T_{1,in} - T_{1,out}}{T_{1,in} - T_{2,in}}; \qquad P_2 = \frac{T_{2,out} - T_{2,in}}{T_{1,in} - T_{2,in}} \tag{4}$$

The number of steps used in the program were varied from 20 to 1000, and it was found that 100 steps were adequate to obtain ϵ within an accuracy of 0.0001. The computer ϵ were also found to be quite insensitive to the initial guesses supplied. Hence, the initial temperature variation was assumed to be linear along each flow channel with a temperature effectiveness of 80 percent for each fluid. In the subsequent iterations, the previous set of temperatures was used even though recent values of temperature were available at some of the steps. The total number of iterations varied from 15 to 50 depending upon the pass arrangement and the number of plates.

The LMTD correction factor F was calculated from individual stream temperature effectiveness P_1, NTU_1, and R_1 as follows:

$$F = \frac{1}{\text{NTU}_1(1-R_1)} \ln \frac{(1-P_1R_1)}{(1-P_1)} = \frac{1}{\text{NTU}_2(1-R_2)} \ln \frac{(1-P_2R_2)}{(1-P_2)} \tag{5}$$

Nomenclature

A = heat transfer area on one side of an exchanger, m^2
C = flow stream heat capacity rate = Wc_p, W/°C
c_p = specific heat of fluid at constant pressure, J/kg°C
F = log-mean temperature difference correction factor
h = heat transfer coefficient, $W/m^2°C$
m = number of passes on a given fluid stream side
N = total number of thermal plates in a single-pass or multipass plate heat exchanger
n = number of passes on a given fluid stream side
NTU = number of heat transfer units for the entire heat exchanger; $\text{NTU} = UA/C_{\min}$, $\text{NTU}_1 = UA/C_1$, $\text{NTU}_2 = UA/C_2$
P = temperature effectiveness of a given fluid stream; see equations (2)–(4) for definitions of P_1 and P_2
R = heat capacity rate ratio; $R_1 = C_1/C_2$, $R_2 = C_2/C_1$
U = overall heat transfer coefficient, $W/m^2°C$
W = mass flow rate, kg/s
ϵ = heat exchanger effectiveness, larger of P_1 and P_2
θ = temperature defined by equation (1)

Subscripts

i = node number along the flow length, see Fig. 1
in = inlet
min = minimum
max = maximum
out = outlet
1 = fluid stream with lower number of passes through the heat exchanger
2 = fluid stream with higher number of passes through the heat exchanger

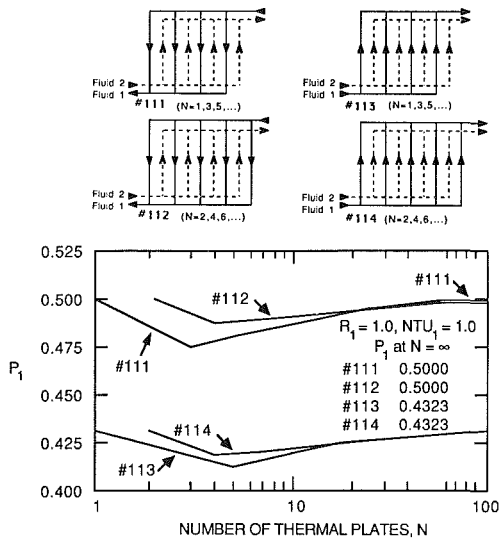

Fig. 2 Four possible 1-1 arrangements and their performance comparison at $R_1 = 1$ and $NTU_1 = 1$

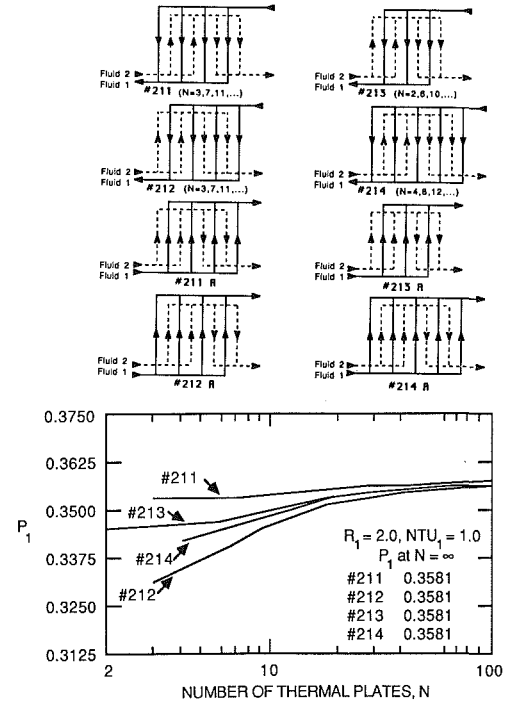

Fig. 3 Four possible 2-1 arrangements with four additional equivalent arrangements, and their performance comparison at $R_1 = 2$ and $NTU_1 = 1$

Equation (5) is valid for $R_1, R_2 \neq 1$. For $R_1 = R_2 = 1$

$$F = \frac{P_1}{NTU_1(1-P_1)} = \frac{P_2}{NTU_2(1-P_2)} \tag{6}$$

where NTU_1, NTU_2, R_1, and R_2 are defined as

$$NTU_1 = UA/C_1; \qquad NTU_2 = UA/C_2 \tag{7}$$

$$R_1 = C_1/C_2; \qquad R_2 = C_2/C_1 \tag{8}$$

For further details on the numerical scheme, refer to Kandlikar (1984) and Shah and Kandlikar (1988).

Classification

Based on the gasketing of the plates, many combinations of passes are possible on each fluid side in a plate exchanger. One of the common ways of classifying two-fluid plate heat ex-

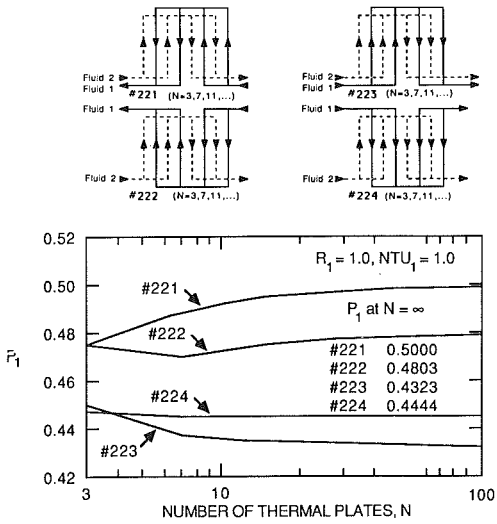

Fig. 4 Four possible 2-2 arrangements and their performance comparison at $R_1 = 1$ and $NTU_1 = 1$

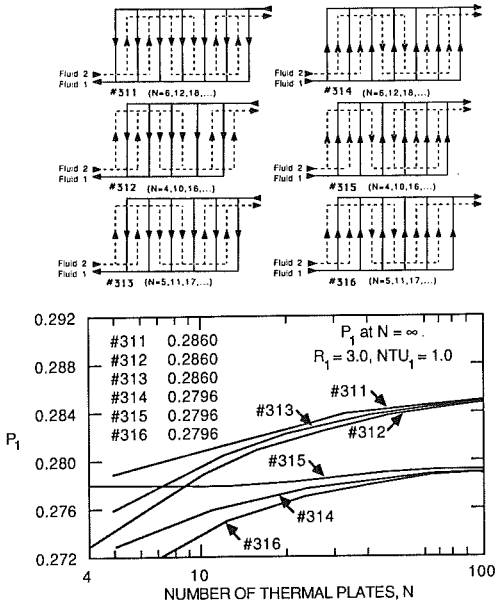

Fig. 5 Six possible 3-1 arrangements and their performance comparison at $R_1 = 3$ and $NTU_1 = 1$

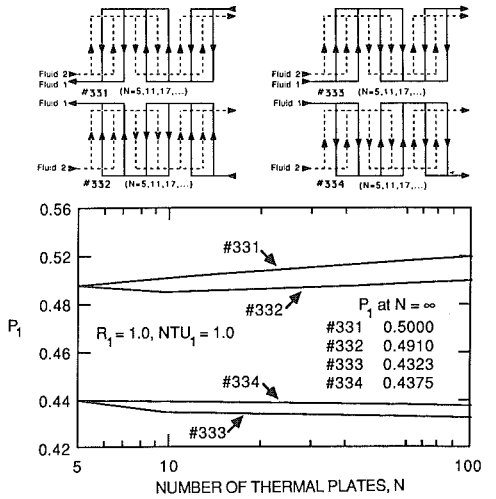

Fig. 6 Four possible 3-3 arrangements and their performance comparison at $R_1 = 1$ and $NTU_1 = 1$

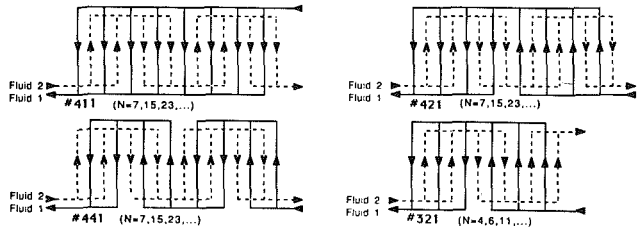

Fig. 7 The best configurations for 4-1, 4-2, and 4-4 arrangements, and the best 3-2 arrangement

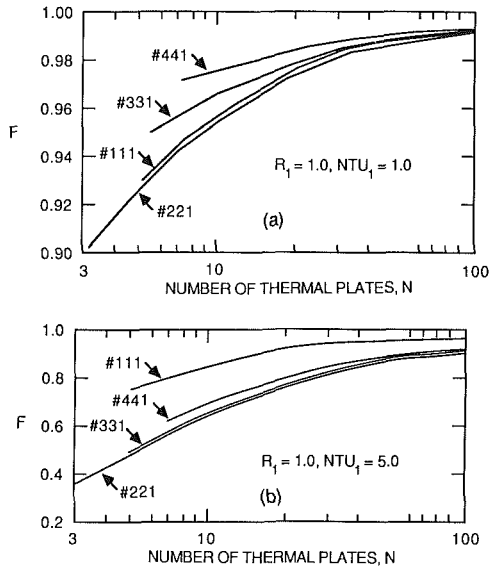

Fig. 8 Influence of number of plates on performance of 1-1, 2-2, 3-3, and 4-4 arrangements: (*a*) $R_1 = 1$ and $NTU_1 = 1$; (*b*) $R_1 = 1$ and $NTU_1 = 5$

changers is on the basis of the number of passes for each fluid stream. Possible arrangements are 1-1 single pass, and 2-1, 2-2, etc., multipass arrangements. Here 2 in 2-1 refers to 2 passes on Fluid 1 side and 1 refers to 1 pass on the Fluid 2 side. In this paper, the plate heat exchangers are further classified according to the flow directions of each stream in the channels resulting in counterflow or parallel flow across any thermal plate, and across the overall heat exchanger, taking into account the end effects.

Such a classification results in four configurations each for 1-1 (Nos. 111-114 in Fig. 2), 2-1 (Nos. 211-214 in Fig. 3), 2-2 (Nos. 221-224 in Fig. 4), and 3-3 (Nos. 331-334 in Fig. 6), and six configurations for the 3-1 arrangement (Nos. 311-316 in Fig. 5). Similar classification results in four configurations each for 4-1, 4-2, and 4-4 arrangements, which are also analyzed in this paper.

Using the principle of flow reversibility by Pignotti (1984), it can be shown that any other flow arrangements for these multiplass cases can be reduced to one of the arrangements shown here in Figs. 2-6. This will be illustrated later for a 2-1 exchanger.

The arrangements can be basically classified as overall counterflow (Nos. 111, 112, 211, 212, 311, 312, 221, 222, 331, and 332), and overall parallel flow (Nos. 113, 114, 213, 214, 313, 314, 223, 224, 333, and 334). In all these arrangements, the number of channels in each pass of a given fluid side of a multipass arrangement is assumed to be the same.

To illustrate that all the possible flow arrangements are included here, let us consider the case of 2-1 arrangements. Figure 3 shows four basic and four additional arrangements (Nos. 211A, 212A, 213A, and 214A). At first glance, the latter

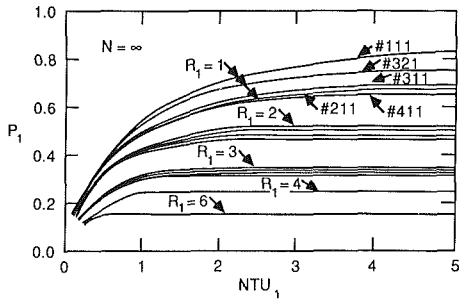

Fig. 9 Performance comparison of four multipass arrangements 1-1, 2-1, 3-1, and 4-1 arrangements at $R_1 = 1, 2, 3, 4$, and 6; $N = \infty$

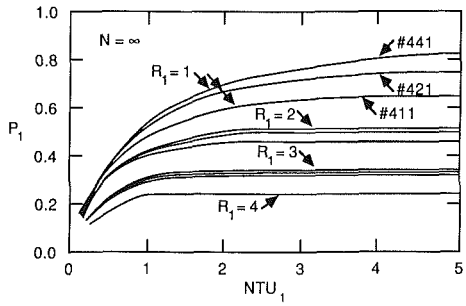

Fig. 10 Performance comparison of three four-pass arrangements 4-1, 4-2, and 4-4 at $R_1 = 1, 2, 3$, and 4; $N = \infty$

arrangements seem to be quite different from Nos. 211-214, which are shown. According to the flow reversibility principle shown by Pignotti (1984), when the two fluid streams in any heat exchanger are reversed simultaneously, the ϵ-NTU relationship remains the same. Consider Nos. 211 and 211A. Reversing the flow directions of both streams in No. 211A will not change the ϵ-NTU relationship from that of the original No. 211A configuration. In the reversed 211A (not shown by a schematic in Fig. 3), streams 1 and 2 would enter from the right side and the flow directions in all channels would be reversed. A mirror image of this reversed 211A is the 211 arrangement. Alternatively, comparing each channel from the right side of the reversed 211A with the channels starting from the left side in 211, it can be seen that the same parallel flow and counterflow orders are obtained between the adjacent channels as well as for each fluid passes. This clearly demonstrates the equivalence between configurations Nos. 211 and 211A. Similarly, it can be seen that Nos. 212A, 213A, and 214A are respectively equivalent to Nos. 212, 213, and 214. This principle of flow reversibility can be extended to other pass arrangements to show the equivalence between any additional configurations and the ones shown here.

Results

The results generated in this work were compared with the available results from literature. Jackson and Troupe (1966) presented their results in graphic form for No. 111 with $N =$ 3, 5, 7, and 9, and for Nos. 112, 113, and 114 with a maximum of eight thermal plates. Results for Nos. 221, 222, with $N =$ 3 and for 331 with $N = 7$ were also presented. Foote (1967) presented results in graphic form for No. 211 with $N = 3$, 7, 11, ∞ and $R_1 = 2$, 3, 4, 5, 7, and 10; and for No. 314 with $N = 5$ and ∞, and $R_1 = 2$, 3, and 4. The results of both these works were compared with the present work, and for every case the agreement was within the error of reading the values from the chart.

Tables 1-8 provide detailed temperature effectiveness P_1 for the Fluid 1 side (the side with a minimum number of passes), and the log-mean temperature difference correction factor F for the 1-1, 2-1, 2-2, 3-1, 3-3, 4-1, 4-2, and 4-4 arrangements. The capacity rate ratio R_1 is varied from 0.5 to 2.0 for the

Table 1 P_1 and F as functions of NTU_1 and R_1 for 1-1 arrangement No. 111

R_1	NTU_1	N= 5		N= 7		N= 11		N= 23		N= 47		N= 71		N= 95		N= ∞	
		P_1	F	P_1	F	P_1	F	P_1	F	P_1	F	P_1	F	P_1	F	P_1	F
0.50	0.20	0.1720	0.9882	0.1724	0.9910	0.1729	0.9939	0.1733	0.9969	0.1736	0.9984	0.1736	0.9989	0.1737	0.9992	0.1738	1.0000
	0.40	0.3015	0.9770	0.3027	0.9823	0.3041	0.9880	0.3055	0.9939	0.3062	0.9970	0.3064	0.9980	0.3065	0.9985	0.3069	1.0000
	0.60	0.4020	0.9660	0.4043	0.9739	0.4067	0.9823	0.4091	0.9910	0.4104	0.9955	0.4108	0.9969	0.4110	0.9977	0.4117	1.0000
	0.80	0.4821	0.9553	0.4853	0.9656	0.4887	0.9766	0.4922	0.9881	0.4940	0.9940	0.4946	0.9959	0.4950	0.9969	0.4959	1.0000
	1.00	0.5471	0.9449	0.5512	0.9575	0.5555	0.9710	0.5601	0.9852	0.5624	0.9925	0.5632	0.9950	0.5635	0.9962	0.5647	1.0000
	1.50	0.6652	0.9199	0.6711	0.9376	0.6774	0.9571	0.6840	0.9778	0.6873	0.9887	0.6885	0.9924	0.6890	0.9943	0.6908	1.0000
	2.00	0.7436	0.8962	0.7506	0.9183	0.7582	0.9432	0.7662	0.9704	0.7704	0.9849	0.7718	0.9898	0.7725	0.9923	0.7746	1.0000
	3.00	0.8386	0.8535	0.8462	0.8814	0.8550	0.9155	0.8644	0.9548	0.8694	0.9766	0.8710	0.9842	0.8719	0.9880	0.8744	1.0000
	4.00	0.8920	0.8174	0.8989	0.8475	0.9075	0.8880	0.9171	0.9383	0.9222	0.9675	0.9239	0.9779	0.9248	0.9832	0.9274	1.0000
	5.00	0.9250	0.7875	0.9307	0.8171	0.9384	0.8614	0.9473	0.9207	0.9521	0.9573	0.9538	0.9708	0.9546	0.9777	0.9572	1.0000
	7.00	0.9615	0.7435	0.9647	0.7676	0.9700	0.8125	0.9768	0.8838	0.9806	0.9339	0.9819	0.9537	0.9826	0.9644	0.9847	1.0000
	10.0	0.9849	0.7034	0.9859	0.7170	0.9883	0.7540	0.9920	0.8282	0.9942	0.8919	0.9950	0.9208	0.9954	0.9374	0.9966	1.0000
0.80	0.20	0.1675	0.9860	0.1679	0.9893	0.1684	0.9928	0.1689	0.9963	0.1692	0.9982	0.1693	0.9987	0.1693	0.9991	0.1695	1.0000
	0.40	0.2881	0.9728	0.2895	0.9792	0.2910	0.9859	0.2925	0.9929	0.2932	0.9964	0.2935	0.9976	0.2936	0.9982	0.2940	1.0000
	0.60	0.3791	0.9602	0.3815	0.9695	0.3841	0.9793	0.3866	0.9895	0.3880	0.9947	0.3884	0.9965	0.3886	0.9973	0.3893	1.0000
	0.80	0.4502	0.9480	0.4536	0.9601	0.4572	0.9729	0.4608	0.9862	0.4627	0.9931	0.4633	0.9953	0.4636	0.9965	0.4645	1.0000
	1.00	0.5073	0.9362	0.5116	0.9510	0.5161	0.9667	0.5207	0.9830	0.5230	0.9914	0.5238	0.9943	0.5242	0.9957	0.5254	1.0000
	1.50	0.6103	0.9082	0.6164	0.9290	0.6229	0.9515	0.6295	0.9751	0.6329	0.9874	0.6340	0.9915	0.6346	0.9936	0.6363	1.0000
	2.00	0.6791	0.8823	0.6865	0.9080	0.6944	0.9367	0.7026	0.9674	0.7067	0.9834	0.7081	0.9889	0.7088	0.9916	0.7109	1.0000
	3.00	0.7654	0.8371	0.7739	0.8691	0.7837	0.9082	0.7939	0.9520	0.7991	0.9754	0.8008	0.9834	0.8017	0.9875	0.8043	1.0000
	4.00	0.8177	0.8003	0.8260	0.8343	0.8366	0.8811	0.8480	0.9367	0.8538	0.9673	0.8558	0.9779	0.8567	0.9833	0.8597	1.0000
	5.00	0.8531	0.7710	0.8606	0.8040	0.8712	0.8555	0.8833	0.9216	0.8895	0.9590	0.8915	0.9722	0.8926	0.9790	0.8957	1.0000
	7.00	0.8988	0.7293	0.9039	0.7559	0.9133	0.8097	0.9255	0.8919	0.9320	0.9422	0.9341	0.9605	0.9352	0.9699	0.9386	1.0000
	10.0	0.9374	0.6925	0.9398	0.7080	0.9464	0.7552	0.9572	0.8495	0.9633	0.9163	0.9654	0.9419	0.9664	0.9554	0.9696	1.0000
1.00	0.20	0.1645	0.9846	0.1650	0.9882	0.1656	0.9920	0.1661	0.9959	0.1664	0.9979	0.1665	0.9986	0.1665	0.9990	0.1667	1.0000
	0.40	0.2795	0.9700	0.2810	0.9771	0.2825	0.9845	0.2841	0.9921	0.2849	0.9961	0.2852	0.9974	0.2853	0.9980	0.2857	1.0000
	0.60	0.3646	0.9562	0.3670	0.9665	0.3696	0.9773	0.3723	0.9885	0.3736	0.9942	0.3741	0.9961	0.3743	0.9971	0.3750	1.0000
	0.80	0.4300	0.9429	0.4334	0.9562	0.4370	0.9703	0.4407	0.9849	0.4426	0.9924	0.4432	0.9949	0.4435	0.9962	0.4444	1.0000
	1.00	0.4819	0.9300	0.4862	0.9463	0.4907	0.9634	0.4953	0.9814	0.4976	0.9906	0.4984	0.9937	0.4988	0.9953	0.5000	1.0000
	1.50	0.5744	0.8998	0.5805	0.9224	0.5869	0.9470	0.5934	0.9728	0.5967	0.9862	0.5978	0.9908	0.5983	0.9931	0.6000	1.0000
	2.00	0.6356	0.8722	0.6428	0.8998	0.6506	0.9310	0.6586	0.9645	0.6626	0.9820	0.6640	0.9879	0.6646	0.9909	0.6667	1.0000
	3.00	0.7122	0.8249	0.7203	0.8583	0.7299	0.9006	0.7399	0.9481	0.7449	0.9735	0.7466	0.9822	0.7475	0.9866	0.7500	1.0000
	4.00	0.7591	0.7876	0.7668	0.8221	0.7772	0.8720	0.7885	0.9321	0.7943	0.9651	0.7962	0.9765	0.7971	0.9823	0.8000	1.0000
	5.00	0.7914	0.7587	0.7982	0.7912	0.8087	0.8453	0.8209	0.9166	0.8271	0.9567	0.8292	0.9708	0.8302	0.9780	0.8333	1.0000
	7.00	0.8342	0.7189	0.8389	0.7437	0.8483	0.7987	0.8613	0.8868	0.8681	0.9404	0.8704	0.9595	0.8716	0.9694	0.8750	1.0000
	10.0	0.8726	0.6850	0.8747	0.6981	0.8816	0.7448	0.8942	0.8456	0.9016	0.9168	0.9041	0.9430	0.9054	0.9567	0.9091	1.0000
1.25	0.20	0.1609	0.9827	0.1615	0.9868	0.1620	0.9910	0.1626	0.9955	0.1629	0.9977	0.1630	0.9985	0.1631	0.9989	0.1632	1.0000
	0.40	0.2693	0.9665	0.2708	0.9743	0.2724	0.9826	0.2740	0.9912	0.2749	0.9956	0.2751	0.9970	0.2753	0.9978	0.2757	1.0000
	0.60	0.3472	0.9510	0.3497	0.9625	0.3523	0.9745	0.3550	0.9871	0.3564	0.9935	0.3569	0.9956	0.3571	0.9967	0.3578	1.0000
	0.80	0.4058	0.9362	0.4093	0.9510	0.4129	0.9667	0.4166	0.9830	0.4184	0.9914	0.4191	0.9943	0.4194	0.9957	0.4203	1.0000
	1.00	0.4516	0.9219	0.4558	0.9399	0.4602	0.9590	0.4648	0.9791	0.4671	0.9894	0.4679	0.9929	0.4683	0.9947	0.4694	1.0000
	1.50	0.5313	0.8886	0.5370	0.9132	0.5431	0.9404	0.5493	0.9693	0.5525	0.9844	0.5536	0.9895	0.5541	0.9921	0.5557	1.0000
	2.00	0.5827	0.8586	0.5892	0.8881	0.5964	0.9223	0.6039	0.9597	0.6077	0.9794	0.6089	0.9862	0.6096	0.9896	0.6115	1.0000
	3.00	0.6453	0.8088	0.6520	0.8426	0.6604	0.8878	0.6694	0.9405	0.6739	0.9693	0.6754	0.9793	0.6762	0.9844	0.6785	1.0000
	4.00	0.6825	0.7710	0.6885	0.8040	0.6970	0.8556	0.7066	0.9216	0.7116	0.9591	0.7132	0.9722	0.7141	0.9790	0.7166	1.0000
	5.00	0.7075	0.7427	0.7123	0.7721	0.7203	0.8260	0.7302	0.9029	0.7353	0.9486	0.7370	0.9650	0.7379	0.9734	0.7405	1.0000
	7.00	0.7393	0.7052	0.7420	0.7252	0.7482	0.7759	0.7574	0.8668	0.7625	0.9272	0.7642	0.9498	0.7651	0.9616	0.7677	1.0000
	10.0	0.7652	0.6743	0.7660	0.6823	0.7696	0.7212	0.7768	0.8169	0.7813	0.8940	0.7828	0.9252	0.7836	0.9420	0.7859	1.0000
1.50	0.20	0.1574	0.9808	0.1580	0.9853	0.1586	0.9901	0.1593	0.9950	0.1596	0.9975	0.1597	0.9983	0.1597	0.9987	0.1599	1.0000
	0.40	0.2594	0.9628	0.2610	0.9715	0.2626	0.9807	0.2643	0.9902	0.2652	0.9951	0.2655	0.9967	0.2656	0.9975	0.2661	1.0000
	0.60	0.3307	0.9457	0.3332	0.9583	0.3359	0.9716	0.3386	0.9856	0.3400	0.9927	0.3405	0.9951	0.3407	0.9963	0.3414	1.0000
	0.80	0.3831	0.9293	0.3864	0.9455	0.3900	0.9628	0.3936	0.9810	0.3955	0.9904	0.3961	0.9936	0.3964	0.9952	0.3974	1.0000
	1.00	0.4231	0.9136	0.4271	0.9331	0.4314	0.9541	0.4358	0.9765	0.4381	0.9881	0.4389	0.9920	0.4392	0.9940	0.4404	1.0000
	1.50	0.4908	0.8771	0.4960	0.9032	0.5016	0.9329	0.5074	0.9651	0.5104	0.9822	0.5114	0.9880	0.5119	0.9910	0.5134	1.0000
	2.00	0.5329	0.8448	0.5384	0.8752	0.5448	0.9121	0.5514	0.9537	0.5549	0.9762	0.5560	0.9839	0.5566	0.9879	0.5584	1.0000
	3.00	0.5818	0.7928	0.5868	0.8254	0.5934	0.8723	0.6007	0.9304	0.6045	0.9635	0.6058	0.9752	0.6065	0.9812	0.6084	1.0000
	4.00	0.6091	0.7551	0.6130	0.7848	0.6189	0.8355	0.6260	0.9065	0.6297	0.9498	0.6310	0.9657	0.6316	0.9739	0.6336	1.0000
	5.00	0.6263	0.7279	0.6290	0.7525	0.6339	0.8027	0.6403	0.8825	0.6437	0.9351	0.6449	0.9551	0.6455	0.9656	0.6474	1.0000
	7.00	0.6458	0.6931	0.6468	0.7071	0.6497	0.7495	0.6543	0.8359	0.6570	0.9031	0.6579	0.9311	0.6584	0.9465	0.6598	1.0000
	10.0	0.6585	0.6654	0.6586	0.6679	0.6597	0.6960	0.6620	0.7749	0.6635	0.8515	0.6640	0.8885	0.6643	0.9103	0.6652	1.0000
2.00	0.20	0.1507	0.9770	0.1514	0.9823	0.1520	0.9880	0.1527	0.9939	0.1531	0.9969	0.1532	0.9980	0.1533	0.9985	0.1535	1.0000
	0.40	0.2410	0.9553	0.2427	0.9656	0.2444	0.9766	0.2461	0.9881	0.2470	0.9940	0.2473	0.9960	0.2475	0.9970	0.2479	1.0000
	0.60	0.3003	0.9347	0.3028	0.9495	0.3054	0.9654	0.3081	0.9823	0.3095	0.9910	0.3100	0.9940	0.3102	0.9955	0.3109	1.0000
	0.80	0.3417	0.9150	0.3448	0.9337	0.3481	0.9543	0.3515	0.9764	0.3533	0.9880	0.3539	0.9919	0.3542	0.9939	0.3551	1.0000
	1.00	0.3718	0.8962	0.3753	0.9183	0.3791	0.9432	0.3831	0.9704	0.3852	0.9849	0.3859	0.9898	0.3862	0.9923	0.3873	1.0000
	1.50	0.4193	0.8535	0.4231	0.8815	0.4275	0.9155	0.4322	0.9549	0.4347	0.9766	0.4355	0.9842	0.4359	0.9880	0.4372	1.0000
	2.00	0.4460	0.8174	0.4495	0.8475	0.4538	0.8880	0. 585	0.9383	0.4611	0.9675	0.4619	0.9779	0.4624	0.9832	0.4637	1.0000
	3.00	0.4733	0.7632	0.4755	0.7905	0.4788	0.8361	0.4827	0.9025	0.4849	0.9461	0.4857	0.9627	0.4861	0.9715	0.4872	1.0000
	4.00	0.4860	0.7275	0.4871	0.7480	0.4892	0.7909	0.4920	0.8649	0.4936	0.9207	0.4942	0.9437	0.4945	0.9564	0.4954	1.0000
	5.00	0.4925	0.7034	0.4930	0.7170	0.4942	0.7540	0.4960	0.8282	0.4971	0.8919	0.4975	0.9209	0.4977	0.9374	0.4983	1.0000
	7.00	0.4978	0.6744	0.4978	0.6774	0.4982	0.7015	0.4988	0.7646	0.4993	0.8311	0.4994	0.8667	0.4995	0.8894	0.4998	1.0000
	10.0	0.4996	0.6524	0.4996	0.6460	0.4996	0.6562	0.4998	0.6993	0.4999	0.7538	0.4999	0.7874	0.4999	0.8103	0.5000	1.0000

1-1, 2-2, 3-3, and 4-4 arrangements. The R_1 range is from 1.0 to 4.0 for 2-1 and 4-2 arrangements, 1.5 to 6.0 for 3-1, and 2.0 to 8.0 for the 4-1 arrangement. These ranges correspond to the same flow rate ratios in individual channels for different multipass arrangements. The NTU_1 values are varied from 0.2 to 10.0. The number of plates is varied between 3 and 95.

It is noted that although the P_1 values are accurate to the fourth digit, the associated F values may not be so accurate especially at higher NTUs where P_1 or P_2 approaches unity and F becomes very sensitive to P values, as seen from equation (5). For example, as seen from Table 4, for $R_1 = 6.0$ and $NTU_1 = 5$, $P_1 = 0.1667$ for $N = 48$, 72, and 92, but the corresponding F values are 0.3738, 0.3877, and 0.3999. In fact at $NTU_1 = 10$, this error becomes so large that the computed F values were beyond the limiting values of 0 and 1; an asterisk is shown for F values under such conditions. For these cases, a small error even in the fifth digit of P_1 is greatly amplified.

Table 2 P_1 and F as functions of NTU_1 and R_1 for 2-1 arrangement No. 211

R_1	NTU_1	N= 3		N= 7		N= 11		N= 23		N= 47		N= 71		N= 95		N=∞	
		P_1	F	P_1	F	P_1	F	P_1	F	P_1	F	P_1	F	P_1	F	P_1	F
1.00	0.20	0.1645	0.9845	0.1647	0.9861	0.1650	0.9882	0.1654	0.9907	0.1656	0.9921	0.1656	0.9926	0.1657	0.9929	0.1658	0.9936
	0.40	0.2777	0.9613	0.2780	0.9624	0.2787	0.9660	0.2797	0.9705	0.2802	0.9732	0.2804	0.9741	0.2805	0.9745	0.2808	0.9759
	0.60	0.3587	0.9324	0.3586	0.9318	0.3597	0.9362	0.3611	0.9421	0.3620	0.9457	0.3623	0.9469	0.3624	0.9475	0.3629	0.9495
	0.80	0.4185	0.8996	0.4177	0.8966	0.4190	0.9013	0.4208	0.9082	0.4219	0.9123	0.4223	0.9137	0.4225	0.9145	0.4231	0.9168
	1.00	0.4637	0.8646	0.4621	0.8591	0.4634	0.8637	0.4655	0.8710	0.4668	0.8754	0.4672	0.8770	0.4675	0.8778	0.4682	0.8804
	1.50	0.5374	0.7744	0.5344	0.7652	0.5354	0.7684	0.5375	0.7749	0.5390	0.7793	0.5395	0.7810	0.5397	0.7818	0.5406	0.7845
	2.00	0.5797	0.6896	0.5765	0.6806	0.5768	0.6815	0.5785	0.6862	0.5798	0.6899	0.5803	0.6913	0.5805	0.6920	0.5814	0.6944
	3.00	0.6225	0.5497	0.6222	0.5489	0.6208	0.5458	0.6210	0.5461	0.6217	0.5477	0.6220	0.5484	0.6221	0.5488	0.6227	0.5502
	4.00	0.6414	0.4471	0.6462	0.4566	0.6435	0.4512	0.6418	0.4479	0.6417	0.4477	0.6417	0.4478	0.6418	0.4479	0.6420	0.4484
	5.00	0.6504	0.3720	0.6607	0.3895	0.6572	0.3834	0.6537	0.3775	0.6527	0.3759	0.6525	0.3756	0.6524	0.3754	0.6523	0.3752
	7.00	0.6570	0.2737	0.6765	0.2987	0.6725	0.2934	0.6661	0.2849	0.6635	0.2816	0.6627	0.2807	0.6624	0.2803	0.6616	0.2792
	10.0	0.6590	0.1933	0.6859	0.2183	0.6829	0.2154	0.6738	0.2065	0.6692	0.2023	0.6679	0.2011	0.6673	0.2006	0.6655	0.1990
1.60	0.20	0.1563	0.9818	0.1563	0.9817	0.1565	0.9839	0.1569	0.9867	0.1571	0.9883	0.1572	0.9889	0.1572	0.9892	0.1573	0.9901
	0.40	0.2539	0.9516	0.2535	0.9494	0.2541	0.9528	0.2550	0.9577	0.2555	0.9606	0.2557	0.9616	0.2558	0.9621	0.2560	0.9637
	0.60	0.3182	0.9128	0.3173	0.9082	0.3181	0.9123	0.3194	0.9185	0.3201	0.9223	0.3204	0.9236	0.3205	0.9243	0.3210	0.9265
	0.80	0.3623	0.8686	0.3611	0.8629	0.3620	0.8672	0.3635	0.8741	0.3644	0.8785	0.3648	0.8800	0.3649	0.8808	0.3655	0.8833
	1.00	0.3935	0.8219	0.3923	0.8168	0.3933	0.8210	0.3949	0.8283	0.3960	0.8329	0.3963	0.8346	0.3965	0.8354	0.3971	0.8381
	1.50	0.4395	0.7063	0.4402	0.7094	0.4412	0.7132	0.4429	0.7203	0.4441	0.7250	0.4445	0.7267	0.4447	0.7276	0.4454	0.7304
	2.00	0.4623	0.6044	0.4667	0.6206	0.4677	0.6243	0.4695	0.6309	0.4706	0.6353	0.4711	0.6370	0.4713	0.6378	0.4720	0.6405
	3.00	0.4815	0.4524	0.4948	0.4920	0.4963	0.4968	0.4981	0.5029	0.4994	0.5069	0.4998	0.5084	0.5000	0.5092	0.5008	0.5116
	4.00	0.4879	0.3533	0.5090	0.4053	0.5115	0.4124	0.5137	0.4186	0.5150	0.4224	0.5155	0.4239	0.5158	0.4246	0.5165	0.4268
	5.00	0.4903	0.2869	0.5171	0.3429	0.5210	0.3525	0.5236	0.3591	0.5250	0.3627	0.5255	0.3641	0.5258	0.3648	0.5266	0.3669
	7.00	0.4917	0.2068	0.5249	0.2589	0.5317	0.2723	0.5354	0.2799	0.5368	0.2831	0.5374	0.2843	0.5377	0.2849	0.5385	0.2867
	10.0	0.4924	0.1454	0.5288	0.1864	0.5388	0.2012	0.5443	0.2102	0.5457	0.2126	0.5462	0.2134	0.5464	0.2139	0.5471	0.2151
2.00	0.20	0.1511	0.9801	0.1510	0.9789	0.1512	0.9811	0.1516	0.9841	0.1518	0.9859	0.1519	0.9865	0.1519	0.9868	0.1520	0.9878
	0.40	0.2394	0.9452	0.2388	0.9412	0.2393	0.9446	0.2402	0.9498	0.2407	0.9528	0.2408	0.9540	0.2409	0.9545	0.2412	0.9563
	0.60	0.2944	0.8997	0.2934	0.8941	0.2941	0.8982	0.2952	0.9047	0.2959	0.9087	0.2962	0.9101	0.2963	0.9109	0.2967	0.9132
	0.80	0.3300	0.8481	0.3292	0.8434	0.3300	0.8479	0.3313	0.8552	0.3321	0.8598	0.3324	0.8614	0.3326	0.8623	0.3331	0.8650
	1.00	0.3540	0.7939	0.3538	0.7930	0.3547	0.7977	0.3561	0.8055	0.3571	0.8105	0.3574	0.8122	0.3576	0.8132	0.3581	0.8161
	1.50	0.3866	0.6632	0.3899	0.6796	0.3911	0.6853	0.3928	0.6940	0.3939	0.6994	0.3942	0.7014	0.3944	0.7024	0.3950	0.7055
	2.00	0.4009	0.5533	0.4090	0.5891	0.4106	0.5965	0.4126	0.6063	0.4138	0.6121	0.4143	0.6142	0.4145	0.6153	0.4151	0.6186
	3.00	0.4113	0.3997	0.4281	0.4603	0.4311	0.4726	0.4341	0.4856	0.4357	0.4928	0.4362	0.4953	0.4365	0.4966	0.4373	0.5006
	4.00	0.4140	0.3066	0.4369	0.3740	0.4416	0.3910	0.4457	0.4075	0.4478	0.4165	0.4485	0.4197	0.4489	0.4213	0.4500	0.4261
	5.00	0.4149	0.2470	0.4414	0.3122	0.4476	0.3326	0.4530	0.3523	0.4557	0.3629	0.4566	0.3667	0.4570	0.3685	0.4583	0.3744
	7.00	0.4154	0.1771	0.4449	0.2311	0.4537	0.2536	0.4614	0.2776	0.4651	0.2910	0.4663	0.2957	0.4669	0.2982	0.4688	0.3057
	10.0	0.4158	0.1244	0.4463	0.1640	0.4570	0.1842	0.4674	0.2100	0.4724	0.2257	0.4740	0.2315	0.4748	0.2345	0.4773	0.2442
2.50	0.20	0.1449	0.9779	0.1447	0.9754	0.1449	0.9777	0.1453	0.9810	0.1455	0.9829	0.1456	0.9836	0.1456	0.9840	0.1457	0.9851
	0.40	0.2228	0.9370	0.2221	0.9315	0.2225	0.9350	0.2233	0.9405	0.2238	0.9439	0.2239	0.9451	0.2240	0.9457	0.2243	0.9477
	0.60	0.2677	0.8833	0.2669	0.8777	0.2675	0.8821	0.2686	0.8890	0.2692	0.8934	0.2694	0.8950	0.2695	0.8958	0.2699	0.8984
	0.80	0.2948	0.8222	0.2947	0.8213	0.2955	0.8264	0.2966	0.8344	0.2974	0.8395	0.2976	0.8413	0.2978	0.8423	0.2982	0.8452
	1.00	0.3118	0.7589	0.3130	0.7664	0.3138	0.7724	0.3152	0.7814	0.3160	0.7870	0.3162	0.7890	0.3164	0.7900	0.3169	0.7933
	1.50	0.3326	0.6116	0.3382	0.6468	0.3396	0.6560	0.3413	0.6677	0.3423	0.6745	0.3427	0.6769	0.3428	0.6782	0.3434	0.6821
	2.00	0.3403	0.4956	0.3506	0.5536	0.3527	0.5670	0.3550	0.5823	0.3562	0.5908	0.3567	0.5938	0.3569	0.5954	0.3575	0.6000
	3.00	0.3449	0.3465	0.3618	0.4223	0.3656	0.4441	0.3693	0.4679	0.3711	0.4810	0.3717	0.4855	0.3720	0.4879	0.3730	0.4950
	4.00	0.3458	0.2624	0.3661	0.3355	0.3714	0.3623	0.3765	0.3934	0.3790	0.4116	0.3798	0.4181	0.3802	0.4214	0.3815	0.4319
	5.00	0.3461	0.2105	0.3679	0.2752	0.3743	0.3034	0.3805	0.3393	0.3837	0.3621	0.3847	0.3707	0.3852	0.3751	0.3868	0.3895
	7.00	0.3463	0.1507	0.3690	0.1997	0.3766	0.2252	0.3845	0.2636	0.3887	0.2929	0.3901	0.3051	0.3908	0.3118	0.3928	0.3354
	10.0	0.3466	0.1059	0.3694	0.1405	0.3774	0.1600	0.3866	0.1937	0.3917	0.2252	0.3934	0.2406	0.3943	0.2499	0.3969	0.2898
3.00	0.20	0.1391	0.9756	0.1387	0.9721	0.1390	0.9744	0.1393	0.9779	0.1395	0.9801	0.1396	0.9808	0.1396	0.9812	0.1398	0.9824
	0.40	0.2077	0.9288	0.2069	0.9222	0.2074	0.9259	0.2081	0.9318	0.2085	0.9355	0.2087	0.9369	0.2088	0.9375	0.2090	0.9397
	0.60	0.2443	0.8664	0.2438	0.8625	0.2444	0.8672	0.2453	0.8749	0.2459	0.8797	0.2461	0.8814	0.2462	0.8823	0.2465	0.8852
	0.80	0.2647	0.7958	0.2654	0.8010	0.2661	0.8070	0.2671	0.8161	0.2678	0.8218	0.2680	0.8239	0.2682	0.8249	0.2685	0.8282
	1.00	0.2766	0.7237	0.2789	0.7422	0.2798	0.7499	0.2810	0.7606	0.2817	0.7671	0.2820	0.7694	0.2821	0.7706	0.2825	0.7743
	1.50	0.2896	0.5632	0.2964	0.6165	0.2980	0.6300	0.2997	0.6458	0.3006	0.6547	0.3010	0.6578	0.3011	0.6594	0.3016	0.6644
	2.00	0.2937	0.4455	0.3043	0.5198	0.3067	0.5398	0.3090	0.5622	0.3102	0.5744	0.3106	0.5787	0.3108	0.5809	0.3115	0.5876
	3.00	0.2957	0.3050	0.3106	0.3855	0.3143	0.4147	0.3180	0.4498	0.3199	0.4706	0.3205	0.4781	0.3208	0.4820	0.3217	0.4941
	4.00	0.2960	0.2297	0.3125	0.2998	0.3172	0.3311	0.3220	0.3741	0.3244	0.4032	0.3252	0.4145	0.3256	0.4205	0.3267	0.4406
	5.00	0.2961	0.1840	0.3131	0.2429	0.3184	0.2723	0.3239	0.3173	0.3267	0.3523	0.3276	0.3672	0.3281	0.3756	0.3295	0.4059
	7.00	0.2963	0.1318	0.3135	0.1746	0.3191	0.1979	0.3253	0.2383	0.3287	0.2763	0.3298	0.2955	0.3303	0.3074	0.3320	0.3637
	10.0	0.2966	0.0927	0.3136	0.1226	0.3193	0.1393	0.3258	0.1699	0.3294	0.2020	0.3306	0.2204	0.3312	0.2329	0.3330	0.3303
4.00	0.20	0.1283	0.9711	0.1278	0.9655	0.1281	0.9681	0.1284	0.9721	0.1286	0.9746	0.1287	0.9755	0.1287	0.9760	0.1288	0.9774
	0.40	0.1815	0.9117	0.1809	0.9049	0.1812	0.9090	0.1819	0.9159	0.1822	0.9203	0.1824	0.9219	0.1825	0.9227	0.1827	0.9253
	0.60	0.2055	0.8310	0.2058	0.8343	0.2063	0.8404	0.2071	0.8497	0.2075	0.8556	0.2077	0.8577	0.2078	0.8588	0.2081	0.8623
	0.80	0.2169	0.7412	0.2187	0.7635	0.2194	0.7725	0.2203	0.7846	0.2209	0.7919	0.2211	0.7945	0.2212	0.7959	0.2215	0.8001
	1.00	0.2226	0.6535	0.2261	0.6973	0.2270	0.7100	0.2281	0.7255	0.2287	0.7344	0.2289	0.7376	0.2290	0.7393	0.2293	0.7444
	1.50	0.2276	0.4787	0.2345	0.5589	0.2361	0.5820	0.2377	0.6086	0.2385	0.6234	0.2388	0.6286	0.2389	0.6313	0.2393	0.6395
	2.00	0.2287	0.3672	0.2376	0.4553	0.2397	0.4863	0.2418	0.5242	0.2429	0.5468	0.2432	0.5551	0.2434	0.5593	0.2439	0.5729
	3.00	0.2291	0.2467	0.2394	0.3205	0.2422	0.3544	0.2451	0.4046	0.2465	0.4420	0.2469	0.4577	0.2472	0.4665	0.2479	0.4979
	4.00	0.2291	0.1853	0.2397	0.2431	0.2428	0.2724	0.2460	0.3210	0.2476	0.3642	0.2482	0.3855	0.2484	0.3986	0.2492	0.4580
	5.00	0.2292	0.1484	0.2398	0.1950	0.2430	0.2194	0.2463	0.2618	0.2480	0.3031	0.2486	0.3256	0.2489	0.3405	0.2497	0.4334
	7.00	0.2293	0.1063	0.2399	0.1396	0.2430	0.1573	0.2464	0.1888	0.2482	0.2211	0.2488	0.2399	0.2491	0.2531	0.2500	0.4049
	10.0	0.2296	0.0748	0.2400	0.0981	0.2431	0.1104	0.2465	0.1325	0.2482	0.1555	0.2488	0.1690	0.2491	0.1785	0.2500	0.3835

It is not possible to reduce this error any further in the present scheme since the numerical method is accurate only to the fourth digit in P_1 values, which is more than adequate for engineering calculations.

Figures 2–6 show the different multipass arrangements for 1-1, 2-1, 2-2, 3-1, and 3-3 exchangers along with their performance comparison as a function of number of thermal plates up to $N = 100$ at specific R_1 and NTU_1 values. Figure 7 shows the best configurations for each of the multipass arrangements 4-1, 4-2 and 4-4, for which the results are provided in Tables 6-8. Also, the best configuration for a 3-2 arrangement is shown in Fig. 7.

A few comparative results are shown in graphic form for different multipass arrangements. Figures 8, 9, and 10 show the effects of N, NTU_1, and the pass arrangement on P_1 and F.

Table 3 P_1 and F as functions of NTU_1 and R_1 for 2-2 arrangement No. 221

R_1	NTU_1	N= 3		N= 7		N= 11		N= 23		N= 47		N= 71		N= 95		N=∞	
		P_1	F	P_1	F	P_1	F	P_1	F	P_1	F	P_1	F	P_1	F	P_1	F
0.50	0.20	0.1735	0.9978	0.1732	0.9961	0.1733	0.9970	0.1735	0.9983	0.1737	0.9991	0.1737	0.9994	0.1737	0.9996	0.1738	1.0000
	0.40	0.3048	0.9912	0.3047	0.9905	0.3052	0.9929	0.3060	0.9961	0.3064	0.9980	0.3066	0.9986	0.3067	0.9990	0.3069	1.0000
	0.60	0.4061	0.9804	0.4070	0.9835	0.4083	0.9879	0.4098	0.9934	0.4107	0.9966	0.4110	0.9977	0.4112	0.9983	0.4117	1.0000
	0.80	0.4853	0.9656	0.4882	0.9750	0.4904	0.9820	0.4929	0.9904	0.4944	0.9950	0.4949	0.9967	0.4951	0.9975	0.4959	1.0000
	1.00	0.5479	0.9473	0.5537	0.9654	0.5569	0.9752	0.5606	0.9869	0.5626	0.9932	0.5633	0.9954	0.5637	0.9966	0.5647	1.0000
	1.50	0.6547	0.8889	0.6707	0.9364	0.6768	0.9552	0.6835	0.9765	0.6871	0.9879	0.6883	0.9919	0.6889	0.9939	0.6908	1.0000
	2.00	0.7172	0.8190	0.7455	0.9021	0.7547	0.9314	0.7644	0.9639	0.7694	0.9815	0.7711	0.9876	0.7720	0.9906	0.7746	1.0000
	3.00	0.7775	0.6737	0.8300	0.8239	0.8447	0.8756	0.8594	0.9335	0.8669	0.9655	0.8694	0.9767	0.8706	0.9824	0.8744	1.0000
	4.00	0.8000	0.5493	0.8720	0.7416	0.8910	0.8134	0.9093	0.8969	0.9184	0.9454	0.9214	0.9629	0.9229	0.9718	0.9274	1.0000
	5.00	0.8085	0.4540	0.8946	0.6629	0.9168	0.7495	0.9374	0.8552	0.9474	0.9210	0.9507	0.9456	0.9523	0.9584	0.9572	1.0000
	7.00	0.8130	0.3300	0.9151	0.5300	0.9415	0.6292	0.9640	0.7620	0.9745	0.8580	0.9780	0.8983	0.9797	0.9206	0.9847	1.0000
	10.0	0.8138	0.2317	0.9248	0.3934	0.9543	0.4874	0.9772	0.6222	0.9873	0.7364	0.9905	0.7936	0.9920	0.8292	0.9966	1.0000
0.80	0.20	0.1690	0.9965	0.1687	0.9950	0.1689	0.9962	0.1692	0.9979	0.1693	0.9989	0.1694	0.9993	0.1694	0.9995	0.1695	1.0000
	0.40	0.2910	0.9860	0.2913	0.9874	0.2920	0.9907	0.2929	0.9949	0.2934	0.9974	0.2936	0.9982	0.2937	0.9987	0.2940	1.0000
	0.60	0.3814	0.9691	0.3836	0.9775	0.3852	0.9838	0.3871	0.9913	0.3882	0.9956	0.3886	0.9970	0.3887	0.9978	0.3893	1.0000
	0.80	0.4499	0.9467	0.4551	0.9656	0.4579	0.9756	0.4610	0.9871	0.4628	0.9934	0.4633	0.9956	0.4636	0.9966	0.4645	1.0000
	1.00	0.5024	0.9195	0.5119	0.9520	0.5159	0.9662	0.5205	0.9823	0.5229	0.9909	0.5237	0.9939	0.5241	0.9954	0.5254	1.0000
	1.50	0.5884	0.8381	0.6114	0.9121	0.6193	0.9387	0.6276	0.9681	0.6319	0.9837	0.6333	0.9890	0.6341	0.9918	0.6363	1.0000
	2.00	0.6361	0.7494	0.6745	0.8667	0.6863	0.9072	0.6984	0.9514	0.7046	0.9751	0.7067	0.9833	0.7077	0.9874	0.7109	1.0000
	3.00	0.6790	0.5879	0.7462	0.7708	0.7657	0.8382	0.7849	0.9135	0.7946	0.9552	0.7978	0.9697	0.7995	0.9771	0.8043	1.0000
	4.00	0.6935	0.4667	0.7831	0.6795	0.8093	0.7682	0.8346	0.8722	0.8472	0.9326	0.8513	0.9542	0.8534	0.9653	0.8597	1.0000
	5.00	0.6986	0.3808	0.8039	0.5989	0.8358	0.7020	0.8660	0.8299	0.8809	0.9082	0.8859	0.9371	0.8883	0.9521	0.8957	1.0000
	7.00	0.7009	0.2746	0.8239	0.4719	0.8644	0.5872	0.9022	0.7470	0.9205	0.8564	0.9266	0.8996	0.9296	0.9228	0.9386	1.0000
	10.0	0.7012	0.1924	0.8340	0.3477	0.8824	0.4582	0.9276	0.6355	0.9490	0.7757	0.9559	0.8373	0.9594	0.8721	0.9696	1.0000
1.00	0.20	0.1661	0.9956	0.1659	0.9942	0.1661	0.9956	0.1663	0.9976	0.1665	0.9988	0.1666	0.9992	0.1666	0.9994	0.1667	1.0000
	0.40	0.2821	0.9826	0.2827	0.9853	0.2835	0.9892	0.2845	0.9942	0.2851	0.9970	0.2853	0.9979	0.2854	0.9985	0.2857	1.0000
	0.60	0.3659	0.9618	0.3687	0.9736	0.3705	0.9811	0.3726	0.9900	0.3738	0.9949	0.3742	0.9965	0.3744	0.9974	0.3750	1.0000
	0.80	0.4278	0.9345	0.4343	0.9595	0.4373	0.9714	0.4407	0.9850	0.4425	0.9923	0.4432	0.9949	0.4435	0.9961	0.4444	1.0000
	1.00	0.4742	0.9019	0.4854	0.9434	0.4899	0.9603	0.4948	0.9793	0.4973	0.9894	0.4982	0.9929	0.4987	0.9947	0.5000	1.0000
	1.50	0.5478	0.8075	0.5736	0.8969	0.5820	0.9283	0.5908	0.9627	0.5954	0.9810	0.5969	0.9872	0.5977	0.9904	0.6000	1.0000
	2.00	0.5866	0.7096	0.6283	0.8450	0.6408	0.8920	0.6536	0.9434	0.6601	0.9710	0.6623	0.9806	0.6634	0.9853	0.6667	1.0000
	3.00	0.6193	0.5423	0.6893	0.7394	0.7097	0.8150	0.7298	0.9005	0.7399	0.9483	0.7433	0.9651	0.7450	0.9737	0.7500	1.0000
	4.00	0.6294	0.4246	0.7200	0.6430	0.7474	0.7397	0.7738	0.8553	0.7869	0.9234	0.7913	0.9479	0.7935	0.9605	0.8000	1.0000
	5.00	0.6326	0.3443	0.7371	0.5607	0.7703	0.6706	0.8021	0.8104	0.8177	0.8973	0.8229	0.9296	0.8255	0.9464	0.8333	1.0000
	7.00	0.6338	0.2473	0.7531	0.4358	0.7951	0.5545	0.8356	0.7258	0.8554	0.8448	0.8619	0.8918	0.8652	0.9170	0.8750	1.0000
	10.0	0.6340	0.1732	0.7607	0.3179	0.8108	0.4285	0.8606	0.6174	0.8850	0.7693	0.8930	0.8349	0.8971	0.8715	0.9091	1.0000
1.25	0.20	0.1625	0.9945	0.1623	0.9933	0.1626	0.9949	0.1629	0.9972	0.1630	0.9986	0.1631	0.9990	0.1631	0.9993	0.1632	1.0000
	0.40	0.2716	0.9783	0.2724	0.9827	0.2733	0.9874	0.2744	0.9933	0.2750	0.9965	0.2753	0.9977	0.2754	0.9983	0.2757	1.0000
	0.60	0.3475	0.9528	0.3511	0.9688	0.3530	0.9777	0.3553	0.9882	0.3565	0.9940	0.3569	0.9959	0.3572	0.9969	0.3578	1.0000
	0.80	0.4019	0.9195	0.4095	0.9520	0.4128	0.9662	0.4164	0.9823	0.4183	0.9910	0.4190	0.9939	0.4193	0.9954	0.4203	1.0000
	1.00	0.4415	0.8806	0.4542	0.9329	0.4589	0.9531	0.4640	0.9755	0.4667	0.9875	0.4676	0.9916	0.4680	0.9937	0.4694	1.0000
	1.50	0.5012	0.7716	0.5289	0.8784	0.5375	0.9154	0.5465	0.9558	0.5511	0.9774	0.5526	0.9848	0.5534	0.9886	0.5557	1.0000
	2.00	0.5306	0.6642	0.5734	0.8189	0.5859	0.8732	0.5986	0.9331	0.6050	0.9656	0.6072	0.9768	0.6082	0.9825	0.6115	1.0000
	3.00	0.5530	0.4933	0.6207	0.7015	0.6404	0.7855	0.6595	0.8827	0.6690	0.9384	0.6722	0.9582	0.6738	0.9684	0.6785	1.0000
	4.00	0.5589	0.3808	0.6432	0.5989	0.6686	0.7021	0.6928	0.8299	0.7048	0.9082	0.7087	0.9371	0.7107	0.9521	0.7166	1.0000
	5.00	0.5604	0.3070	0.6549	0.5145	0.6849	0.6274	0.7132	0.7775	0.7269	0.8762	0.7315	0.9142	0.7337	0.9343	0.7405	1.0000
	7.00	0.5610	0.2199	0.6650	0.3918	0.7016	0.5062	0.7356	0.6798	0.7519	0.8095	0.7572	0.8640	0.7598	0.8942	0.7677	1.0000
	10.0	0.5610	0.1540	0.6692	0.2819	0.7109	0.3815	0.7504	0.5568	0.7685	0.7086	0.7744	0.7808	0.7773	0.8236	0.7859	1.0000
1.50	0.20	0.1590	0.9934	0.1589	0.9924	0.1592	0.9943	0.1595	0.9969	0.1597	0.9984	0.1598	0.9989	0.1598	0.9992	0.1599	1.0000
	0.40	0.2615	0.9741	0.2625	0.9801	0.2635	0.9856	0.2647	0.9923	0.2654	0.9960	0.2656	0.9973	0.2657	0.9980	0.2661	1.0000
	0.60	0.3303	0.9438	0.3343	0.9640	0.3364	0.9744	0.3388	0.9865	0.3401	0.9931	0.3405	0.9953	0.3407	0.9965	0.3414	1.0000
	0.80	0.3778	0.9048	0.3862	0.9446	0.3896	0.9610	0.3933	0.9796	0.3953	0.9896	0.3960	0.9930	0.3963	0.9947	0.3974	1.0000
	1.00	0.4114	0.8599	0.4250	0.9226	0.4298	0.9460	0.4349	0.9718	0.4376	0.9856	0.4385	0.9903	0.4390	0.9927	0.4404	1.0000
	1.50	0.4594	0.7376	0.4874	0.8602	0.4959	0.9025	0.5045	0.9488	0.5090	0.9737	0.5104	0.9823	0.5112	0.9867	0.5134	1.0000
	2.00	0.4811	0.6228	0.5227	0.7932	0.5346	0.8542	0.5464	0.9222	0.5524	0.9597	0.5544	0.9728	0.5554	0.9795	0.5584	1.0000
	3.00	0.4958	0.4511	0.5579	0.6644	0.5754	0.7546	0.5921	0.8623	0.6003	0.9264	0.6030	0.9498	0.6043	0.9618	0.6084	1.0000
	4.00	0.4991	0.3447	0.5731	0.5561	0.5947	0.6617	0.6146	0.7983	0.6242	0.8874	0.6273	0.9218	0.6289	0.9400	0.6336	1.0000
	5.00	0.4998	0.2769	0.5804	0.4705	0.6050	0.5807	0.6270	0.7340	0.6373	0.8437	0.6407	0.8889	0.6424	0.9138	0.6474	1.0000
	7.00	0.5000	0.1980	0.5861	0.3516	0.6144	0.4551	0.6387	0.6152	0.6496	0.7471	0.6531	0.8093	0.6548	0.8464	0.6598	1.0000
	10.0	0.4999	0.1386	0.5881	0.2502	0.6189	0.3341	0.6448	0.4762	0.6554	0.6037	0.6588	0.6724	0.6604	0.7177	0.6652	1.0000
2.00	0.20	0.1524	0.9912	0.1523	0.9905	0.1526	0.9929	0.1530	0.9961	0.1532	0.9980	0.1533	0.9986	0.1533	0.9990	0.1535	1.0000
	0.40	0.2427	0.9656	0.2441	0.9751	0.2452	0.9820	0.2465	0.9904	0.2472	0.9950	0.2474	0.9967	0.2476	0.9975	0.2479	1.0000
	0.60	0.2989	0.9259	0.3036	0.9546	0.3058	0.9677	0.3082	0.9830	0.3095	0.9913	0.3100	0.9941	0.3102	0.9956	0.3109	1.0000
	0.80	0.3350	0.8756	0.3442	0.9299	0.3475	0.9507	0.3512	0.9741	0.3531	0.9867	0.3538	0.9911	0.3541	0.9933	0.3551	1.0000
	1.00	0.3586	0.8191	0.3728	0.9022	0.3773	0.9314	0.3822	0.9640	0.3847	0.9815	0.3856	0.9876	0.3860	0.9906	0.3873	1.0000
	1.50	0.3888	0.6738	0.4150	0.8239	0.4223	0.8756	0.4297	0.9335	0.4334	0.9656	0.4347	0.9768	0.4353	0.9824	0.4372	1.0000
	2.00	0.4000	0.5493	0.4360	0.7417	0.4455	0.8135	0.4546	0.8969	0.4592	0.9455	0.4607	0.9629	0.4614	0.9719	0.4637	1.0000
	3.00	0.4059	0.3832	0.4537	0.5919	0.4660	0.6873	0.4770	0.8097	0.4822	0.8918	0.4839	0.9242	0.4847	0.9416	0.4872	1.0000
	4.00	0.4068	0.2893	0.4599	0.4770	0.4738	0.5764	0.4852	0.7138	0.4904	0.8200	0.4921	0.8676	0.4929	0.8949	0.4954	1.0000
	5.00	0.4069	0.2317	0.4624	0.3935	0.4771	0.4874	0.4886	0.6222	0.4936	0.7364	0.4952	0.7936	0.4960	0.8292	0.4983	1.0000
	7.00	0.4069	0.1655	0.4640	0.2868	0.4796	0.3640	0.4910	0.4769	0.4956	0.5768	0.4970	0.6326	0.4977	0.6709	0.4998	1.0000
	10.0	0.4068	0.1158	0.4644	0.2018	0.4806	0.2592	0.4918	0.3435	0.4961	0.4156	0.4974	0.4568	0.4981	0.4858	0.5000	1.0000

Discussion

The tabular results presented here provide detailed values of P_1 and F for a large number of pass arrangements. In selecting a particular pass arrangement, it is necessary to compare the performance of various arrangements from heat transfer as well as pressure drop viewpoints. Due to space limitations, such a comparison is presented in the following sections for a few typical cases only.

Influences of Pass Arrangements and Flow Directions. The numerical scheme described earlier was employed to evaluate the performance of different configurations in order to determine the best one for each multipass arrangement.

As mentioned earlier, the flow arrangements can be basically classified as overall counterflow and overall parallel flow. In PHEs, the overall counterflow arrangement is used exclusively since it yields higher effectiveness and heat transfer performance than that obtained by the overall parallel flow arrange-

Table 4 P_1 and F as functions of NTU_1 and R_1 for 3-1 arrangement No. 311

R_1	NTU_1	N= 6		N= 12		N= 18		N= 24		N= 48		N= 72		N= 96		N= ∞	
		P_1	F	P_1	F	P_1	F	P_1	F	P_1	F	P_1	F	P_1	F	P_1	F
1.50	0.20	0.1574	0.9805	0.1579	0.9847	0.1582	0.9868	0.1583	0.9879	0.1586	0.9898	0.1587	0.9904	0.1587	0.9908	0.1588	0.9918
	0.40	0.2567	0.9478	0.2582	0.9561	0.2589	0.9601	0.2594	0.9624	0.2600	0.9661	0.2603	0.9674	0.2604	0.9681	0.2608	0.9702
	0.60	0.3227	0.9070	0.3252	0.9188	0.3264	0.9246	0.3270	0.9279	0.3282	0.9333	0.3285	0.9353	0.3288	0.9363	0.3294	0.9393
	0.80	0.3684	0.8621	0.3717	0.8768	0.3734	0.8842	0.3743	0.8884	0.3758	0.8953	0.3763	0.8977	0.3766	0.8990	0.3774	0.9029
	1.00	0.4012	0.8161	0.4052	0.8331	0.4072	0.8416	0.4083	0.8465	0.4102	0.8546	0.4109	0.8576	0.4112	0.8591	0.4122	0.8637
	1.50	0.4517	0.7080	0.4568	0.7276	0.4594	0.7377	0.4609	0.7437	0.4634	0.7537	0.4643	0.7574	0.4648	0.7593	0.4662	0.7651
	2.00	0.4796	0.6176	0.4851	0.6368	0.4879	0.6470	0.4896	0.6531	0.4924	0.6638	0.4935	0.6677	0.4940	0.6698	0.4957	0.6761
	3.00	0.5093	0.4879	0.5143	0.5025	0.5168	0.5102	0.5185	0.5153	0.5215	0.5248	0.5226	0.5285	0.5232	0.5305	0.5251	0.5366
	4.00	0.5261	0.4049	0.5294	0.4134	0.5311	0.4178	0.5324	0.4212	0.5351	0.4284	0.5362	0.4315	0.5368	0.4331	0.5387	0.4384
	5.00	0.5381	0.3493	0.5391	0.3517	0.5397	0.3530	0.5405	0.3548	0.5425	0.3596	0.5435	0.3619	0.5441	0.3632	0.5458	0.3674
	7.00	0.5566	0.2822	0.5517	0.2730	0.5499	0.2696	0.5494	0.2688	0.5499	0.2697	0.5505	0.2708	0.5509	0.2715	0.5521	0.2737
	10.0	0.5788	0.2323	0.5644	0.2087	0.5585	0.2002	0.5562	0.1970	0.5544	0.1946	0.5544	0.1946	0.5545	0.1947	0.5548	0.1952
2.40	0.20	0.1459	0.9759	0.1464	0.9803	0.1466	0.9824	0.1467	0.9836	0.1469	0.9854	0.1470	0.9861	0.1470	0.9865	0.1472	0.9875
	0.40	0.2252	0.9327	0.2265	0.9419	0.2271	0.9462	0.2274	0.9486	0.2280	0.9524	0.2281	0.9538	0.2282	0.9545	0.2285	0.9566
	0.60	0.2717	0.8795	0.2739	0.8937	0.2748	0.9002	0.2753	0.9038	0.2762	0.9095	0.2765	0.9116	0.2766	0.9126	0.2771	0.9158
	0.80	0.3008	0.8232	0.3037	0.8419	0.3049	0.8504	0.3056	0.8551	0.3067	0.8627	0.3071	0.8653	0.3073	0.8667	0.3079	0.8709
	1.00	0.3200	0.7679	0.3234	0.7904	0.3250	0.8007	0.3258	0.8063	0.3272	0.8155	0.3276	0.8188	0.3279	0.8204	0.3286	0.8255
	1.50	0.3468	0.6477	0.3512	0.6754	0.3532	0.6884	0.3543	0.6958	0.3560	0.7080	0.3566	0.7123	0.3569	0.7146	0.3579	0.7215
	2.00	0.3607	0.5572	0.3653	0.5851	0.3674	0.5987	0.3686	0.6068	0.3705	0.6206	0.3712	0.6256	0.3716	0.6283	0.3727	0.6364
	3.00	0.3760	0.4419	0.3797	0.4629	0.3815	0.4741	0.3826	0.4815	0.3847	0.4957	0.3855	0.5013	0.3859	0.5042	0.3871	0.5136
	4.00	0.3855	0.3760	0.3875	0.3875	0.3887	0.3947	0.3896	0.4004	0.3916	0.4129	0.3923	0.4183	0.3928	0.4213	0.3941	0.4311
	5.00	0.3924	0.3350	0.3928	0.3374	0.3933	0.3404	0.3939	0.3440	0.3956	0.3542	0.3963	0.3592	0.3967	0.3620	0.3981	0.3717
	7.00	0.4019	0.2886	0.3999	0.2757	0.3992	0.2715	0.3991	0.2712	0.4000	0.2762	0.4006	0.2800	0.4010	0.2823	0.4023	0.2911
	10.0	0.4098	0.2560	0.4064	0.2272	0.4044	0.2149	0.4035	0.2100	0.4032	0.2083	0.4035	0.2101	0.4038	0.2116	0.4050	0.2184
3.00	0.20	0.1388	0.9729	0.1393	0.9775	0.1395	0.9796	0.1396	0.9808	0.1398	0.9827	0.1399	0.9834	0.1399	0.9838	0.1400	0.9849
	0.40	0.2071	0.9234	0.2083	0.9336	0.2088	0.9381	0.2091	0.9406	0.2096	0.9446	0.2097	0.9460	0.2098	0.9467	0.2101	0.9489
	0.60	0.2439	0.8632	0.2458	0.8795	0.2467	0.8866	0.2471	0.8905	0.2479	0.8967	0.2481	0.8989	0.2482	0.9000	0.2486	0.9034
	0.80	0.2653	0.8006	0.2679	0.8229	0.2690	0.8325	0.2696	0.8377	0.2705	0.8461	0.2708	0.8490	0.2710	0.8505	0.2715	0.8550
	1.00	0.2787	0.7410	0.2818	0.7680	0.2831	0.7798	0.2838	0.7863	0.2849	0.7967	0.2853	0.8003	0.2854	0.8021	0.2860	0.8078
	1.50	0.2965	0.6169	0.3001	0.6501	0.3017	0.6654	0.3026	0.6741	0.3039	0.6884	0.3044	0.6935	0.3046	0.6962	0.3053	0.7043
	2.00	0.3055	0.5293	0.3090	0.5617	0.3106	0.5779	0.3115	0.5876	0.3129	0.6043	0.3134	0.6105	0.3137	0.6137	0.3145	0.6237
	3.00	0.3155	0.4245	0.3178	0.4476	0.3190	0.4609	0.3198	0.4702	0.3213	0.4883	0.3218	0.4956	0.3220	0.4995	0.3229	0.5122
	4.00	0.3214	0.3678	0.3225	0.3799	0.3233	0.3886	0.3238	0.3959	0.3251	0.4130	0.3256	0.4207	0.3258	0.4249	0.3267	0.4395
	5.00	0.3253	0.3336	0.3255	0.3361	0.3258	0.3400	0.3262	0.3450	0.3272	0.3599	0.3277	0.3675	0.3279	0.3719	0.3287	0.3878
	7.00	0.3298	0.2956	0.3291	0.2835	0.3289	0.2795	0.3289	0.2800	0.3294	0.2892	0.3298	0.2960	0.3300	0.3003	0.3307	0.3179
	10.0	0.3323	0.2692	0.3316	0.2431	0.3311	0.2311	0.3309	0.2264	0.3310	0.2272	0.3312	0.2318	0.3313	0.2353	0.3320	0.2543
3.75	0.20	0.1306	0.9693	0.1311	0.9742	0.1313	0.9764	0.1314	0.9777	0.1315	0.9796	0.1316	0.9803	0.1316	0.9807	0.1317	0.9818
	0.40	0.1872	0.9123	0.1883	0.9240	0.1888	0.9289	0.1891	0.9316	0.1895	0.9359	0.1896	0.9374	0.1897	0.9381	0.1899	0.9405
	0.60	0.2146	0.8441	0.2164	0.8637	0.2171	0.8718	0.2175	0.8762	0.2181	0.8831	0.2183	0.8855	0.2184	0.8867	0.2187	0.8904
	0.80	0.2293	0.7750	0.2316	0.8021	0.2325	0.8135	0.2330	0.8195	0.2337	0.8291	0.2339	0.8325	0.2341	0.8342	0.2345	0.8393
	1.00	0.2379	0.7110	0.2405	0.7440	0.2415	0.7581	0.2421	0.7658	0.2429	0.7780	0.2432	0.7823	0.2433	0.7844	0.2438	0.7911
	1.50	0.2488	0.5855	0.2515	0.6242	0.2526	0.6426	0.2532	0.6531	0.2542	0.6706	0.2545	0.6769	0.2546	0.6802	0.2551	0.6902
	2.00	0.2542	0.5031	0.2564	0.5391	0.2575	0.5581	0.2581	0.5699	0.2590	0.5908	0.2593	0.5986	0.2595	0.6027	0.2600	0.6158
	3.00	0.2600	0.4106	0.2612	0.4344	0.2618	0.4496	0.2623	0.4608	0.2630	0.4842	0.2633	0.4941	0.2635	0.4995	0.2639	0.5179
	4.00	0.2630	0.3628	0.2635	0.3749	0.2638	0.3846	0.2641	0.3935	0.2647	0.4161	0.2649	0.4271	0.2650	0.4334	0.2654	0.4567
	5.00	0.2647	0.3345	0.2648	0.3374	0.2649	0.3419	0.2650	0.3481	0.2654	0.3683	0.2656	0.3796	0.2657	0.3866	0.2660	0.4145
	7.00	0.2661	0.3035	0.2660	0.2936	0.2659	0.2903	0.2660	0.2916	0.2661	0.3052	0.2662	0.3158	0.2663	0.3231	0.2665	0.3595
	10.0	0.2666	0.2819	0.2665	0.2605	0.2665	0.2503	0.2664	0.2465	0.2665	0.2501	0.2665	0.2573	0.2665	0.2630	0.2666	0.3121
4.50	0.20	0.1231	0.9659	0.1235	0.9711	0.1237	0.9734	0.1238	0.9747	0.1240	0.9767	0.1240	0.9774	0.1240	0.9778	0.1241	0.9789
	0.40	0.1700	0.9018	0.1711	0.9152	0.1715	0.9207	0.1717	0.9236	0.1721	0.9282	0.1722	0.9298	0.1722	0.9306	0.1724	0.9331
	0.60	0.1905	0.8261	0.1921	0.8494	0.1927	0.8588	0.1930	0.8637	0.1935	0.8715	0.1936	0.8741	0.1937	0.8755	0.1940	0.8796
	0.80	0.2005	0.7514	0.2025	0.7836	0.2032	0.7969	0.2036	0.8040	0.2042	0.8151	0.2044	0.8190	0.2045	0.8209	0.2048	0.8269
	1.00	0.2061	0.6843	0.2082	0.7229	0.2090	0.7396	0.2094	0.7486	0.2101	0.7630	0.2103	0.7681	0.2104	0.7706	0.2107	0.7784
	1.50	0.2130	0.5600	0.2148	0.6027	0.2156	0.6238	0.2160	0.6362	0.2167	0.6572	0.2169	0.6649	0.2170	0.6689	0.2174	0.6814
	2.00	0.2163	0.4835	0.2177	0.5212	0.2183	0.5423	0.2187	0.5559	0.2193	0.5811	0.2195	0.5910	0.2196	0.5962	0.2199	0.6132
	3.00	0.2197	0.4016	0.2202	0.4250	0.2205	0.4409	0.2207	0.4533	0.2211	0.4814	0.2213	0.4942	0.2213	0.5014	0.2215	0.5276
	4.00	0.2211	0.3604	0.2213	0.3722	0.2214	0.3819	0.2215	0.3914	0.2217	0.4178	0.2218	0.4318	0.2219	0.4405	0.2220	0.4767
	5.00	0.2217	0.3362	0.2218	0.3396	0.2218	0.3442	0.2218	0.3506	0.2220	0.3734	0.2220	0.3875	0.2221	0.3968	0.2221	0.4429
	7.00	0.2221	0.3097	0.2221	0.3020	0.2221	0.2995	0.2221	0.3010	0.2221	0.3156	0.2222	0.3277	0.2222	0.3364	0.2222	0.4009
	10.0	0.2222	0.2923	0.2222	0.2749	0.2222	0.2661	0.2222	0.2631	0.2222	0.2679	0.2222	0.2761	0.2222	0.2822	0.2222	0.3674
6.00	0.20	0.1098	0.9592	0.1102	0.9653	0.1103	0.9678	0.1104	0.9692	0.1105	0.9714	0.1106	0.9721	0.1106	0.9725	0.1107	0.9737
	0.40	0.1421	0.8816	0.1430	0.8991	0.1433	0.9059	0.1435	0.9095	0.1438	0.9150	0.1439	0.9169	0.1439	0.9178	0.1440	0.9207
	0.60	0.1536	0.7922	0.1548	0.8236	0.1552	0.8359	0.1554	0.8424	0.1558	0.8523	0.1559	0.8557	0.1559	0.8575	0.1561	0.8627
	0.80	0.1584	0.7085	0.1597	0.7507	0.1602	0.7683	0.1604	0.7777	0.1608	0.7927	0.1609	0.7978	0.1610	0.8004	0.1612	0.8084
	1.00	0.1609	0.6386	0.1621	0.6862	0.1626	0.7079	0.1629	0.7199	0.1632	0.7394	0.1633	0.7464	0.1634	0.7499	0.1636	0.7610
	1.50	0.1639	0.5221	0.1647	0.5677	0.1650	0.5927	0.1652	0.6082	0.1655	0.6366	0.1656	0.6476	0.1656	0.6535	0.1658	0.6727
	2.00	0.1652	0.4570	0.1657	0.4937	0.1659	0.5165	0.1660	0.5324	0.1662	0.5651	0.1662	0.5793	0.1663	0.5873	0.1664	0.6158
	3.00	0.1663	0.3908	0.1664	0.4119	0.1664	0.4268	0.1665	0.4394	0.1665	0.4717	0.1666	0.4890	0.1666	0.4996	0.1666	0.5501
	4.00	0.1666	0.3583	0.1666	0.3693	0.1666	0.3778	0.1666	0.3866	0.1666	0.4134	0.1666	0.4295	0.1666	0.4410	0.1667	0.5142
	5.00	0.1666	0.3395	0.1666	0.3437	0.1666	0.3475	0.1666	0.3529	0.1667	0.3738	0.1667	0.3877	0.1667	0.3999	0.1667	0.4918
	7.00	0.1667	0.3184	0.1667	0.3126	0.1667	0.3117	0.1667	0.3129	0.1667	0.3251	0.1667	0.3350	0.1667	0.3412	0.1667	0.4701
	10.0	0.1667	*	0.1667	*	0.1667	*	0.1667	*	0.1667	*	0.1667	*	0.1667	*	0.1667	*

ment. In order to show some trends, the temperature effectiveness P_1 is plotted as a function of the number of thermal plates N for various 1, 2, and 3 pass arrangements in Figs. 2-6. These figures are plotted for $NTU_1 = 1$, and for R_1 values such that equal heat capacity rates are obtained in each channel for the two fluids.

Figure 2 shows the temperature effectiveness P_1 for each 1-1 arrangement, plotted as a function of number of thermal plates for $R_1 = 1$ and $NTU_1 = 1$. As expected, the effectiveness values for counterflow arrangements Nos. 111 and 112 are higher than the parallel flow arrangements Nos. 113 and 114. The difference between Nos. 111 and 112 is due to an unequal number of passages on the two sides resulting in different end effects. This difference decreases rapidly with increasing number of thermal plates. Arrangement No. 111 is slightly superior to No. 112 for $N > 15$ due to equal number of flow channels on each side.

Figure 3 shows effectiveness values for four 2-1 arrange-

Table 5 P_1 and F as functions of NTU_1 and R_1 for 3-3 arrangement No. 331

R_1	NTU_1	N= 5		N= 11		N= 17		N= 23		N= 47		N= 71		N= 95		N=∞	
		P_1	F	P_1	F	P_1	F	P_1	F	P_1	F	P_1	F	P_1	F	P_1	F
0.50	0.20	0.1736	0.9990	0.1735	0.9982	0.1736	0.9986	0.1736	0.9988	0.1737	0.9994	0.1737	0.9995	0.1737	0.9996	0.1738	1.0000
	0.40	0.3059	0.9959	0.3059	0.9956	0.3061	0.9966	0.3063	0.9973	0.3066	0.9985	0.3067	0.9990	0.3067	0.9993	0.3069	1.0000
	0.60	0.4091	0.9909	0.4094	0.9921	0.4100	0.9941	0.4104	0.9953	0.4110	0.9975	0.4112	0.9983	0.4113	0.9987	0.4117	1.0000
	0.80	0.4910	0.9840	0.4921	0.9877	0.4931	0.9910	0.4937	0.9929	0.4947	0.9962	0.4951	0.9975	0.4953	0.9980	0.4959	1.0000
	1.00	0.5569	0.9752	0.5592	0.9825	0.5608	0.9873	0.5616	0.9901	0.5631	0.9948	0.5636	0.9965	0.5639	0.9973	0.5647	1.0000
	1.50	0.6738	0.9459	0.6804	0.9663	0.6834	0.9761	0.6851	0.9815	0.6878	0.9904	0.6888	0.9935	0.6893	0.9951	0.6908	1.0000
	2.00	0.7473	0.9076	0.7591	0.9462	0.7638	0.9621	0.7664	0.9708	0.7704	0.9848	0.7718	0.9898	0.7725	0.9923	0.7746	1.0000
	3.00	0.8271	0.8142	0.8503	0.8969	0.8580	0.9276	0.8619	0.9442	0.8681	0.9709	0.8702	0.9803	0.8712	0.9851	0.8744	1.0000
	4.00	0.8639	0.7143	0.8973	0.8401	0.9072	0.8866	0.9122	0.9120	0.9198	0.9536	0.9223	0.9685	0.9236	0.9761	0.9274	1.0000
	5.00	0.8817	0.6214	0.9236	0.7807	0.9351	0.8419	0.9407	0.8760	0.9490	0.9333	0.9518	0.9543	0.9531	0.9653	0.9572	1.0000
	7.00	0.8952	0.4749	0.9491	0.6672	0.9624	0.7499	0.9684	0.7982	0.9769	0.8851	0.9796	0.9195	0.9809	0.9380	0.9847	1.0000
	10.0	0.8995	0.3400	0.9634	0.5303	0.9776	0.6259	0.9834	0.6846	0.9908	0.8005	0.9929	0.8524	0.9939	0.8825	0.9966	1.0000
0.80	0.20	0.1692	0.9984	0.1691	0.9977	0.1692	0.9982	0.1693	0.9985	0.1694	0.9992	0.1694	0.9994	0.1694	0.9995	0.1695	1.0000
	0.40	0.2926	0.9935	0.2927	0.9940	0.2930	0.9955	0.2932	0.9964	0.2936	0.9981	0.2937	0.9987	0.2938	0.9990	0.2940	1.0000
	0.60	0.3857	0.9856	0.3865	0.9889	0.3873	0.9919	0.3877	0.9936	0.3885	0.9966	0.3887	0.9977	0.3889	0.9983	0.3893	1.0000
	0.80	0.4577	0.9748	0.4598	0.9825	0.4611	0.9874	0.4619	0.9902	0.4631	0.9948	0.4636	0.9965	0.4638	0.9973	0.4645	1.0000
	1.00	0.5145	0.9612	0.5184	0.9749	0.5204	0.9821	0.5216	0.9861	0.5234	0.9928	0.5240	0.9951	0.5244	0.9963	0.5254	1.0000
	1.50	0.6130	0.9173	0.6229	0.9515	0.6270	0.9660	0.6292	0.9738	0.6326	0.9864	0.6338	0.9908	0.6344	0.9931	0.6363	1.0000
	2.00	0.6733	0.8630	0.6907	0.9231	0.6970	0.9462	0.7003	0.9587	0.7055	0.9786	0.7073	0.9856	0.7082	0.9891	0.7109	1.0000
	3.00	0.7371	0.7421	0.7708	0.8571	0.7816	0.8996	0.7871	0.9226	0.7956	0.9596	0.7985	0.9727	0.7999	0.9793	0.8043	1.0000
	4.00	0.7651	0.6269	0.8142	0.7868	0.8292	0.8481	0.8367	0.8818	0.8481	0.9374	0.8519	0.9573	0.8539	0.9677	0.8597	1.0000
	5.00	0.7774	0.5298	0.8401	0.7183	0.8588	0.7957	0.8679	0.8392	0.8818	0.9130	0.8864	0.9403	0.8887	0.9546	0.8957	1.0000
	7.00	0.7849	0.3915	0.8674	0.5976	0.8920	0.6967	0.9038	0.7554	0.9213	0.8615	0.9270	0.9032	0.9299	0.9256	0.9386	1.0000
	10.0	0.7870	0.2767	0.8840	0.4630	0.9149	0.5736	0.9293	0.6444	0.9499	0.7835	0.9566	0.8437	0.9599	0.8775	0.9696	1.0000
1.00	0.20	0.1664	0.9980	0.1663	0.9973	0.1664	0.9979	0.1664	0.9983	0.1665	0.9991	0.1666	0.9993	0.1666	0.9995	0.1667	1.0000
	0.40	0.2841	0.9919	0.2843	0.9929	0.2846	0.9947	0.2849	0.9959	0.2853	0.9978	0.2854	0.9985	0.2855	0.9989	0.2857	1.0000
	0.60	0.3708	0.9821	0.3719	0.9868	0.3728	0.9905	0.3732	0.9925	0.3741	0.9960	0.3744	0.9973	0.3745	0.9980	0.3750	1.0000
	0.80	0.4366	0.9687	0.4392	0.9792	0.4407	0.9851	0.4416	0.9884	0.4429	0.9939	0.4434	0.9959	0.4437	0.9969	0.4444	1.0000
	1.00	0.4877	0.9521	0.4924	0.9700	0.4946	0.9788	0.4959	0.9836	0.4979	0.9915	0.4986	0.9942	0.4989	0.9957	0.5000	1.0000
	1.50	0.5743	0.8992	0.5856	0.9422	0.5900	0.9595	0.5924	0.9689	0.5961	0.9839	0.5974	0.9891	0.5980	0.9919	0.6000	1.0000
	2.00	0.6256	0.8356	0.6451	0.9087	0.6519	0.9363	0.6554	0.9511	0.6609	0.9747	0.6628	0.9830	0.6638	0.9872	0.6667	1.0000
	3.00	0.6777	0.7008	0.7142	0.8332	0.7258	0.8825	0.7317	0.9091	0.7408	0.9525	0.7438	0.9679	0.7454	0.9757	0.7500	1.0000
	4.00	0.6988	0.5800	0.7514	0.7555	0.7674	0.8248	0.7754	0.8631	0.7876	0.9271	0.7917	0.9503	0.7938	0.9623	0.8000	1.0000
	5.00	0.7073	0.4832	0.7733	0.6822	0.7933	0.7677	0.8032	0.8163	0.8182	0.8999	0.8232	0.9312	0.8257	0.9476	0.8333	1.0000
	7.00	0.7116	0.3525	0.7962	0.5580	0.8228	0.6634	0.8358	0.7272	0.8553	0.8442	0.8618	0.8910	0.8651	0.9161	0.8750	1.0000
	10.0	0.7138	0.2494	0.8097	0.4256	0.8435	0.5389	0.8599	0.6137	0.8843	0.7641	0.8925	0.8301	0.8966	0.8673	0.9091	1.0000
1.25	0.20	0.1629	0.9975	0.1628	0.9970	0.1629	0.9977	0.1630	0.9982	0.1631	0.9990	0.1631	0.9993	0.1632	0.9995	0.1632	1.0000
	0.40	0.2738	0.9900	0.2741	0.9916	0.2745	0.9938	0.2748	0.9952	0.2752	0.9974	0.2754	0.9982	0.2754	0.9987	0.2757	1.0000
	0.60	0.3530	0.9778	0.3544	0.9842	0.3554	0.9886	0.3559	0.9912	0.3568	0.9954	0.3571	0.9969	0.3573	0.9976	0.3578	1.0000
	0.80	0.4116	0.9612	0.4147	0.9749	0.4163	0.9821	0.4173	0.9862	0.4187	0.9928	0.4192	0.9951	0.4195	0.9963	0.4203	1.0000
	1.00	0.4560	0.9409	0.4614	0.9640	0.4638	0.9746	0.4651	0.9804	0.4672	0.9898	0.4679	0.9931	0.4683	0.9948	0.4694	1.0000
	1.50	0.5286	0.8773	0.5409	0.9306	0.5455	0.9515	0.5480	0.9627	0.5518	0.9807	0.5531	0.9870	0.5537	0.9902	0.5557	1.0000
	2.00	0.5695	0.8032	0.5899	0.8913	0.5967	0.9239	0.6003	0.9415	0.6058	0.9696	0.6077	0.9795	0.6086	0.9845	0.6115	1.0000
	3.00	0.6080	0.6543	0.6444	0.8045	0.6556	0.8612	0.6612	0.8923	0.6698	0.9432	0.6727	0.9614	0.6741	0.9708	0.6785	1.0000
	4.00	0.6220	0.5299	0.6721	0.7183	0.6870	0.7957	0.6944	0.8392	0.7054	0.9131	0.7091	0.9404	0.7110	0.9546	0.7166	1.0000
	5.00	0.6268	0.4356	0.6877	0.6399	0.7058	0.7324	0.7145	0.7863	0.7275	0.8811	0.7319	0.9176	0.7340	0.9369	0.7405	1.0000
	7.00	0.6290	0.3151	0.7032	0.5128	0.7261	0.6210	0.7369	0.6881	0.7525	0.8158	0.7576	0.8690	0.7602	0.8982	0.7677	1.0000
	10.0	0.6320	0.2244	0.7119	0.3847	0.7393	0.4939	0.7520	0.5678	0.7696	0.7214	0.7752	0.7923	0.7779	0.8338	0.7859	1.0000
1.50	0.20	0.1595	0.9970	0.1594	0.9965	0.1596	0.9973	0.1596	0.9979	0.1597	0.9989	0.1598	0.9992	0.1598	0.9994	0.1599	1.0000
	0.40	0.2639	0.9880	0.2644	0.9903	0.2648	0.9929	0.2651	0.9944	0.2656	0.9971	0.2657	0.9980	0.2658	0.9985	0.2661	1.0000
	0.60	0.3362	0.9734	0.3378	0.9817	0.3388	0.9868	0.3394	0.9898	0.3404	0.9946	0.3407	0.9964	0.3409	0.9972	0.3414	1.0000
	0.80	0.3881	0.9538	0.3916	0.9708	0.3933	0.9793	0.3942	0.9840	0.3957	0.9916	0.3963	0.9944	0.3965	0.9958	0.3974	1.0000
	1.00	0.4265	0.9298	0.4322	0.9580	0.4347	0.9704	0.4360	0.9772	0.4381	0.9882	0.4389	0.9920	0.4392	0.9940	0.4404	1.0000
	1.50	0.4865	0.8559	0.4991	0.9194	0.5036	0.9436	0.5059	0.9566	0.5096	0.9775	0.5109	0.9849	0.5115	0.9885	0.5134	1.0000
	2.00	0.5183	0.7723	0.5382	0.8742	0.5447	0.9116	0.5480	0.9320	0.5531	0.9645	0.5548	0.9760	0.5557	0.9819	0.5584	1.0000
	3.00	0.5459	0.6126	0.5791	0.7766	0.5889	0.8400	0.5938	0.8751	0.6011	0.9334	0.6035	0.9545	0.6047	0.9655	0.6084	1.0000
	4.00	0.5547	0.4875	0.5983	0.6829	0.6106	0.7664	0.6165	0.8142	0.6251	0.8974	0.6280	0.9291	0.6294	0.9458	0.6336	1.0000
	5.00	0.5574	0.3973	0.6085	0.6005	0.6226	0.6969	0.6291	0.7542	0.6385	0.8588	0.6415	0.9008	0.6430	0.9234	0.6474	1.0000
	7.00	0.5588	0.2866	0.6180	0.4727	0.6345	0.5789	0.6418	0.6460	0.6515	0.7790	0.6544	0.8381	0.6558	0.8719	0.6598	1.0000
	10.0	0.5624	0.2058	0.6231	0.3505	0.6417	0.4514	0.6493	0.5201	0.6585	0.6661	0.6610	0.7383	0.6622	0.7829	0.6652	1.0000
2.00	0.20	0.1530	0.9960	0.1529	0.9956	0.1531	0.9967	0.1531	0.9974	0.1533	0.9986	0.1533	0.9990	0.1534	0.9993	0.1535	1.0000
	0.40	0.2455	0.9840	0.2461	0.9877	0.2466	0.9910	0.2469	0.9930	0.2474	0.9963	0.2476	0.9975	0.2476	0.9981	0.2479	1.0000
	0.60	0.3053	0.9647	0.3072	0.9766	0.3083	0.9832	0.3089	0.9870	0.3098	0.9932	0.3102	0.9954	0.3104	0.9965	0.3109	1.0000
	0.80	0.3456	0.9389	0.3494	0.9626	0.3511	0.9735	0.3520	0.9796	0.3535	0.9894	0.3540	0.9928	0.3543	0.9946	0.3551	1.0000
	1.00	0.3736	0.9076	0.3796	0.9462	0.3819	0.9621	0.3832	0.9709	0.3852	0.9849	0.3859	0.9898	0.3862	0.9922	0.3873	1.0000
	1.50	0.4136	0.8143	0.4251	0.8969	0.4290	0.9276	0.4310	0.9442	0.4340	0.9710	0.4351	0.9804	0.4356	0.9851	0.4372	1.0000
	2.00	0.4319	0.7144	0.4486	0.8401	0.4536	0.8866	0.4561	0.9121	0.4599	0.9536	0.4612	0.9685	0.4618	0.9761	0.4637	1.0000
	3.00	0.4453	0.5413	0.4696	0.7223	0.4759	0.7958	0.4789	0.8376	0.4832	0.9104	0.4845	0.9380	0.4852	0.9526	0.4872	1.0000
	4.00	0.4488	0.4206	0.4778	0.6167	0.4847	0.7059	0.4877	0.7590	0.4918	0.8581	0.4930	0.8990	0.4937	0.9215	0.4954	1.0000
	5.00	0.4497	0.3400	0.4817	0.5303	0.4888	0.6260	0.4917	0.6846	0.4954	0.8006	0.4965	0.8525	0.4970	0.8825	0.4983	1.0000
	7.00	0.4509	0.2460	0.4851	0.4069	0.4924	0.5015	0.4950	0.5614	0.4979	0.6866	0.4987	0.7492	0.4990	0.7889	0.4998	1.0000
	10.0	0.4544	0.1789	0.4869	0.2977	0.4944	0.3803	0.4967	0.4348	0.4990	0.5503	0.4994	0.6106	0.4996	0.6508	0.5000	1.0000

ments. Arrangement No. 211, with counterflow at the inlet of the two-pass stream, is the best arrangement. Note that it has one more pair of counterflow passages than No. 212; the latter has one more pair of parallel flow passages. Numbers 213 and 214 have an unequal number of total flow channels on the two fluid sides of the heat exchanger.

The effectiveness values for six different 3–1 arrangements are illustrated in Fig. 5. As expected, the counterflow arrangements Nos. 311–313 are superior to the parallel flow arrangements, Nos. 314–316. Number 311 gives the best performance since it has two counterflow passes with an overall counterflow arrangement. The additional flow passage on one pass side for No. 311, as compared to No. 313, affects the performance in two ways: (*i*) It provides an additional counterflow plate, and (*ii*) the end effects are entirely shifted to the one-pass fluid side. Both these effects improve the performance of No. 311 over No. 313, although the improvement is quite small (less than 0.3 percent in P_1 values for $N > 10$).

A similar comparison for the 2–2 and 3–3 arrangements is shown in Figs. 4 and 6, and it can be seen that Nos. 221 and

Table 6 P_1 and F as functions of NTU_1 and R_1 for 4-1 arrangement No. 411

R_1	NTU_1	N= 7		N= 15		N= 23		N= 47		N= 71		N= 95		N= ∞	
		P_1	F	P_1	F	P_1	F	P_1	F	P_1	F	P_1	F	P_1	F
2.00	0.20	0.1514	0.9823	0.1516	0.9842	0.1517	0.9853	0.1519	0.9865	0.1519	0.9870	0.1520	0.9872	0.1520	0.9880
	0.40	0.2397	0.9467	0.2402	0.9503	0.2406	0.9523	0.2409	0.9546	0.2411	0.9555	0.2411	0.9559	0.2414	0.9573
	0.60	0.2944	0.9001	0.2954	0.9055	0.2959	0.9084	0.2964	0.9117	0.2966	0.9129	0.2967	0.9135	0.2971	0.9154
	0.80	0.3301	0.8483	0.3314	0.8556	0.3320	0.8592	0.3328	0.8633	0.3330	0.8648	0.3332	0.8656	0.3336	0.8680
	1.00	0.3542	0.7951	0.3560	0.8045	0.3567	0.8088	0.3576	0.8136	0.3579	0.8153	0.3581	0.8162	0.3586	0.8189
	1.50	0.3881	0.6706	0.3910	0.6848	0.3920	0.6902	0.3932	0.6961	0.3936	0.6983	0.3938	0.6993	0.3945	0.7027
	2.00	0.4045	0.5684	0.4083	0.5856	0.4095	0.5914	0.4109	0.5978	0.4114	0.6001	0.4116	0.6013	0.4124	0.6049
	3.00	0.4192	0.4263	0.4243	0.4451	0.4256	0.4502	0.4271	0.4562	0.4277	0.4584	0.4280	0.4596	0.4288	0.4632
	4.00	0.4259	0.3386	0.4316	0.3561	0.4328	0.3599	0.4342	0.3645	0.4347	0.3664	0.4350	0.3674	0.4359	0.3705
	5.00	0.4300	0.2807	0.4360	0.2966	0.4369	0.2990	0.4379	0.3020	0.4384	0.3034	0.4387	0.3042	0.4396	0.3068
	7.00	0.4347	0.2094	0.4413	0.2228	0.4415	0.2232	0.4416	0.2236	0.4419	0.2242	0.4421	0.2246	0.4427	0.2260
	10.0	0.4380	0.1512	0.4458	0.1632	0.4453	0.1623	0.4440	0.1603	0.4439	0.1601	0.4439	0.1601	0.4441	0.1603
3.20	0.20	0.1370	0.9763	0.1371	0.9776	0.1372	0.9788	0.1374	0.9802	0.1374	0.9807	0.1374	0.9810	0.1375	0.9819
	0.40	0.2023	0.9277	0.2027	0.9311	0.2029	0.9333	0.2032	0.9360	0.2034	0.9370	0.2034	0.9375	0.2036	0.9392
	0.60	0.2365	0.8668	0.2372	0.8734	0.2376	0.8768	0.2381	0.8808	0.2382	0.8823	0.2383	0.8830	0.2386	0.8854
	0.80	0.2558	0.8018	0.2570	0.8128	0.2575	0.8175	0.2580	0.8228	0.2582	0.8247	0.2583	0.8257	0.2586	0.8287
	1.00	0.2674	0.7381	0.2690	0.7538	0.2696	0.7598	0.2702	0.7663	0.2705	0.7687	0.2706	0.7698	0.2710	0.7735
	1.50	0.2815	0.5996	0.2841	0.6254	0.2849	0.6340	0.2858	0.6432	0.2861	0.6465	0.2862	0.6482	0.2867	0.6532
	2.00	0.2874	0.4961	0.2907	0.5274	0.2917	0.5375	0.2927	0.5484	0.2931	0.5524	0.2932	0.5544	0.2938	0.5606
	3.00	0.2925	0.3643	0.2966	0.3984	0.2977	0.4089	0.2989	0.4209	0.2993	0.4255	0.2995	0.4279	0.3002	0.4355
	4.00	0.2949	0.2871	0.2994	0.3204	0.3005	0.3301	0.3017	0.3416	0.3021	0.3462	0.3024	0.3487	0.3031	0.3570
	5.00	0.2962	0.2364	0.3011	0.2687	0.3022	0.2775	0.3033	0.2878	0.3038	0.2922	0.3040	0.2947	0.3048	0.3031
	7.00	0.2973	0.1736	0.3031	0.2038	0.3041	0.2115	0.3051	0.2194	0.3055	0.2230	0.3057	0.2251	0.3065	0.2330
	10.0	0.2978	0.1228	0.3044	0.1495	0.3056	0.1568	0.3064	0.1623	0.3067	0.1646	0.3069	0.1661	0.3076	0.1726
4.00	0.20	0.1284	0.9725	0.1285	0.9736	0.1286	0.9748	0.1288	0.9763	0.1288	0.9769	0.1288	0.9772	0.1289	0.9782
	0.40	0.1819	0.9164	0.1822	0.9200	0.1824	0.9225	0.1827	0.9255	0.1828	0.9266	0.1829	0.9272	0.1830	0.9291
	0.60	0.2069	0.8473	0.2076	0.8558	0.2079	0.8599	0.2082	0.8645	0.2084	0.8662	0.2084	0.8671	0.2087	0.8698
	0.80	0.2197	0.7753	0.2208	0.7901	0.2212	0.7960	0.2216	0.8024	0.2218	0.8047	0.2219	0.8059	0.2221	0.8095
	1.00	0.2268	0.7062	0.2283	0.7277	0.2288	0.7353	0.2293	0.7436	0.2295	0.7465	0.2296	0.7480	0.2299	0.7525
	1.50	0.2348	0.5622	0.2370	0.5964	0.2376	0.6076	0.2383	0.6198	0.2385	0.6241	0.2386	0.6262	0.2390	0.6330
	2.00	0.2379	0.4599	0.2405	0.4999	0.2413	0.5132	0.2420	0.5279	0.2423	0.5333	0.2424	0.5361	0.2428	0.5448
	3.00	0.2406	0.3339	0.2436	0.3766	0.2444	0.3910	0.2452	0.4081	0.2455	0.4148	0.2456	0.4184	0.2461	0.4302
	4.00	0.2417	0.2610	0.2450	0.3029	0.2458	0.3171	0.2466	0.3347	0.2469	0.3420	0.2470	0.3460	0.2475	0.3600
	5.00	0.2423	0.2132	0.2458	0.2535	0.2466	0.2675	0.2474	0.2848	0.2477	0.2923	0.2478	0.2965	0.2483	0.3123
	7.00	0.2426	0.1545	0.2466	0.1907	0.2474	0.2043	0.2482	0.2207	0.2484	0.2281	0.2486	0.2326	0.2490	0.2504
	10.0	0.2427	0.1085	0.2470	0.1375	0.2479	0.1503	0.2487	0.1659	0.2489	0.1727	0.2491	0.1766	0.2495	0.1965
5.00	0.20	0.1188	0.9680	0.1188	0.9689	0.1189	0.9702	0.1190	0.9718	0.1191	0.9725	0.1191	0.9728	0.1192	0.9739
	0.40	0.1604	0.9032	0.1607	0.9077	0.1609	0.9105	0.1611	0.9140	0.1612	0.9154	0.1613	0.9160	0.1614	0.9182
	0.60	0.1773	0.8249	0.1779	0.8367	0.1782	0.8417	0.1785	0.8474	0.1786	0.8494	0.1787	0.8505	0.1788	0.8538
	0.80	0.1850	0.7449	0.1860	0.7658	0.1863	0.7733	0.1867	0.7815	0.1868	0.7844	0.1868	0.7859	0.1870	0.7905
	1.00	0.1889	0.6703	0.1901	0.6999	0.1905	0.7099	0.1909	0.7207	0.1911	0.7245	0.1911	0.7264	0.1914	0.7324
	1.50	0.1930	0.5222	0.1946	0.5660	0.1951	0.5808	0.1955	0.5972	0.1957	0.6030	0.1958	0.6059	0.1960	0.6154
	2.00	0.1945	0.4222	0.1963	0.4714	0.1968	0.4887	0.1973	0.5087	0.1974	0.5163	0.1975	0.5203	0.1977	0.5331
	3.00	0.1957	0.3022	0.1977	0.3530	0.1982	0.3722	0.1986	0.3961	0.1988	0.4059	0.1989	0.4114	0.1991	0.4305
	4.00	0.1962	0.2333	0.1982	0.2820	0.1987	0.3015	0.1991	0.3273	0.1993	0.3387	0.1994	0.3451	0.1996	0.3700
	5.00	0.1963	0.1888	0.1985	0.2338	0.1990	0.2533	0.1994	0.2800	0.1995	0.2922	0.1996	0.2994	0.1998	0.3299
	7.00	0.1964	0.1356	0.1987	0.1723	0.1992	0.1903	0.1996	0.2174	0.1997	0.2306	0.1998	0.2388	0.1999	0.2792
	10.0	0.1964	0.0948	0.1988	0.1219	0.1993	0.1365	0.1997	0.1610	0.1999	0.1744	0.1999	0.1824	0.2000	0.2370
6.00	0.20	0.1101	0.9638	0.1101	0.9645	0.1102	0.9658	0.1103	0.9677	0.1104	0.9684	0.1104	0.9688	0.1105	0.9700
	0.40	0.1426	0.8909	0.1429	0.8966	0.1431	0.8999	0.1432	0.9040	0.1433	0.9055	0.1434	0.9063	0.1435	0.9088
	0.60	0.1540	0.8038	0.1546	0.8196	0.1548	0.8258	0.1551	0.8327	0.1552	0.8352	0.1552	0.8365	0.1554	0.8405
	0.80	0.1587	0.7166	0.1595	0.7441	0.1598	0.7537	0.1601	0.7640	0.1602	0.7677	0.1602	0.7695	0.1604	0.7753
	1.00	0.1609	0.6377	0.1619	0.6753	0.1622	0.6881	0.1625	0.7018	0.1626	0.7066	0.1626	0.7091	0.1628	0.7167
	1.50	0.1631	0.4878	0.1642	0.5397	0.1645	0.5579	0.1649	0.5786	0.1650	0.5864	0.1650	0.5903	0.1652	0.6031
	2.00	0.1639	0.3904	0.1651	0.4466	0.1654	0.4677	0.1657	0.4929	0.1658	0.5029	0.1658	0.5084	0.1659	0.5266
	3.00	0.1644	0.2752	0.1657	0.3311	0.1660	0.3541	0.1662	0.3847	0.1663	0.3979	0.1664	0.4057	0.1665	0.4349
	4.00	0.1646	0.2102	0.1659	0.2610	0.1662	0.2842	0.1664	0.3173	0.1665	0.3330	0.1665	0.3423	0.1666	0.3829
	5.00	0.1646	0.1690	0.1660	0.2136	0.1663	0.2357	0.1665	0.2699	0.1666	0.2868	0.1666	0.2968	0.1666	0.3494
	7.00	0.1646	0.1208	0.1660	0.1547	0.1663	0.1730	0.1666	0.2045	0.1666	0.2220	0.1666	0.2339	0.1667	0.3088
	10.0	0.1646	0.0844	0.1661	0.1085	0.1664	0.1219	0.1666	0.1466	0.1666	0.1618	0.1666	0.1720	0.1667	0.2763
8.00	0.20	0.0953	0.9558	0.0954	0.9564	0.0954	0.9580	0.0955	0.9602	0.0956	0.9611	0.0956	0.9616	0.0956	0.9630
	0.40	0.1152	0.8672	0.1155	0.8768	0.1156	0.8814	0.1158	0.8868	0.1158	0.8888	0.1159	0.8899	0.1159	0.8932
	0.60	0.1205	0.7633	0.1210	0.7890	0.1212	0.7982	0.1213	0.8081	0.1214	0.8118	0.1214	0.8137	0.1215	0.8193
	0.80	0.1223	0.6642	0.1229	0.7053	0.1230	0.7194	0.1232	0.7347	0.1233	0.7402	0.1233	0.7430	0.1234	0.7517
	1.00	0.1231	0.5798	0.1237	0.6317	0.1238	0.6499	0.1240	0.6701	0.1240	0.6775	0.1241	0.6814	0.1241	0.6935
	1.50	0.1238	0.4305	0.1244	0.4938	0.1245	0.5180	0.1247	0.5475	0.1247	0.5592	0.1247	0.5657	0.1248	0.5876
	2.00	0.1240	0.3380	0.1246	0.4022	0.1247	0.4291	0.1248	0.4641	0.1249	0.4795	0.1249	0.4882	0.1249	0.5214
	3.00	0.1242	0.2320	0.1247	0.2885	0.1249	0.3161	0.1249	0.3563	0.1250	0.3758	0.1250	0.3885	0.1250	0.4476
	4.00	0.1242	0.1749	0.1248	0.2211	0.1249	0.2454	0.1250	0.2858	0.1250	0.3073	0.1250	0.3215	0.1250	0.4083
	5.00	0.1242	0.1400	0.1248	0.1778	0.1249	0.1985	0.1250	0.2347	0.1250	0.2557	0.1250	0.2682	0.1250	0.3845
	7.00	0.1242	0.0998	0.1248	0.1272	0.1249	0.1423	0.1250	0.1694	0.1250	0.1860	0.1250	0.1981	0.1250	0.3865
	10.0	0.1242	0.0696	0.1250	0.0875	0.1249	0.0994	0.1250	0.1187	0.1250	0.1304	0.1250	0.1384	0.1250	0.3424

Table 7 P_1 and F as functions of NTU_1 and R_1 for 4-2 arrangement No. 421

R_1	NTU_1	N= 7		N= 15		N= 23		N= 47		N= 71		N= 95		N= ∞	
		P_1	F	P_1	F	P_1	F	P_1	F	P_1	F	P_1	F	P_1	F
1.00	0.20	0.1661	0.9958	0.1661	0.9962	0.1662	0.9969	0.1663	0.9976	0.1664	0.9978	0.1664	0.9980	0.1664	0.9984
	0.40	0.2832	0.9876	0.2834	0.9889	0.2837	0.9902	0.2840	0.9917	0.2841	0.9923	0.2842	0.9926	0.2844	0.9936
	0.60	0.3692	0.9755	0.3699	0.9784	0.3704	0.9804	0.3710	0.9830	0.3712	0.9840	0.3713	0.9845	0.3717	0.9860
	0.80	0.4345	0.9603	0.4357	0.9650	0.4364	0.9680	0.4374	0.9717	0.4377	0.9730	0.4379	0.9737	0.4384	0.9759
	1.00	0.4851	0.9422	0.4870	0.9492	0.4880	0.9532	0.4893	0.9580	0.4897	0.9598	0.4900	0.9607	0.4907	0.9636
	1.50	0.5712	0.8881	0.5750	0.9019	0.5768	0.9086	0.5789	0.9164	0.5796	0.9193	0.5800	0.9208	0.5813	0.9254
	2.00	0.6232	0.8269	0.6291	0.8481	0.6317	0.8574	0.6345	0.8682	0.6356	0.8721	0.6361	0.8741	0.6378	0.8804
	3.00	0.6786	0.7039	0.6890	0.7385	0.6928	0.7519	0.6971	0.7671	0.6986	0.7726	0.6994	0.7755	0.7018	0.7845
	4.00	0.7049	0.5971	0.7192	0.6404	0.7241	0.6560	0.7294	0.6739	0.7313	0.6804	0.7323	0.6837	0.7353	0.6944
	5.00	0.7187	0.5111	0.7364	0.5588	0.7420	0.5752	0.7481	0.5941	0.7503	0.6011	0.7515	0.6047	0.7549	0.6161
	7.00	0.7315	0.3891	0.7544	0.4388	0.7608	0.4544	0.7679	0.4727	0.7705	0.4796	0.7718	0.4832	0.7760	0.4949
	10.0	0.7377	0.2813	0.7663	0.3278	0.7731	0.3407	0.7806	0.3557	0.7833	0.3615	0.7848	0.3647	0.7896	0.3752
1.60	0.20	0.1579	0.9946	0.1579	0.9949	0.1580	0.9956	0.1581	0.9964	0.1582	0.9967	0.1582	0.9969	0.1583	0.9974
	0.40	0.2594	0.9828	0.2596	0.9843	0.2599	0.9858	0.2602	0.9877	0.2604	0.9885	0.2604	0.9889	0.2606	0.9901
	0.60	0.3285	0.9654	0.3292	0.9689	0.3297	0.9715	0.3303	0.9748	0.3306	0.9760	0.3307	0.9766	0.3311	0.9786
	0.80	0.3777	0.9434	0.3789	0.9497	0.3797	0.9535	0.3806	0.9582	0.3809	0.9600	0.3811	0.9609	0.3817	0.9637
	1.00	0.4137	0.9177	0.4156	0.9274	0.4167	0.9326	0.4179	0.9389	0.4183	0.9412	0.4185	0.9424	0.4193	0.9461
	1.50	0.4700	0.8436	0.4739	0.8638	0.4755	0.8726	0.4774	0.8828	0.4781	0.8865	0.4785	0.8884	0.4796	0.8944
	2.00	0.5003	0.7651	0.5063	0.7962	0.5086	0.8084	0.5111	0.8223	0.5120	0.8274	0.5124	0.8300	0.5139	0.8381
	3.00	0.5290	0.6224	0.5389	0.6710	0.5421	0.6883	0.5456	0.7079	0.5468	0.7151	0.5474	0.7188	0.5494	0.7304
	4.00	0.5410	0.5118	0.5541	0.5702	0.5580	0.5904	0.5622	0.6135	0.5637	0.6220	0.5645	0.6264	0.5668	0.6405
	5.00	0.5470	0.4296	0.5626	0.4925	0.5671	0.5140	0.5719	0.5389	0.5735	0.5483	0.5744	0.5532	0.5770	0.5688
	7.00	0.5522	0.3207	0.5718	0.3847	0.5771	0.4066	0.5826	0.4325	0.5845	0.4426	0.5855	0.4479	0.5886	0.4652
	10.0	0.5549	0.2297	0.5782	0.2881	0.5843	0.3090	0.5905	0.3338	0.5926	0.3437	0.5937	0.3490	0.5971	0.3669
2.00	0.20	0.1527	0.9937	0.1528	0.9941	0.1528	0.9947	0.1529	0.9956	0.1530	0.9960	0.1530	0.9962	0.1531	0.9968
	0.40	0.2448	0.9796	0.2451	0.9813	0.2453	0.9830	0.2457	0.9852	0.2458	0.9860	0.2459	0.9864	0.2461	0.9878
	0.60	0.3043	0.9588	0.3050	0.9629	0.3055	0.9659	0.3061	0.9696	0.3063	0.9709	0.3064	0.9716	0.3068	0.9740
	0.80	0.3446	0.9325	0.3458	0.9401	0.3465	0.9446	0.3474	0.9499	0.3477	0.9519	0.3479	0.9530	0.3484	0.9563
	1.00	0.3728	0.9021	0.3747	0.9141	0.3756	0.9202	0.3767	0.9274	0.3771	0.9301	0.3773	0.9314	0.3780	0.9357
	1.50	0.4139	0.8164	0.4176	0.8415	0.4190	0.8518	0.4207	0.8637	0.4213	0.8680	0.4216	0.8702	0.4225	0.8772
	2.00	0.4341	0.7289	0.4396	0.7672	0.4415	0.7814	0.4436	0.7976	0.4443	0.8035	0.4447	0.8065	0.4458	0.8161
	3.00	0.4516	0.5782	0.4599	0.6359	0.4624	0.6560	0.4651	0.6789	0.4660	0.6873	0.4665	0.6917	0.4680	0.7055
	4.00	0.4583	0.4679	0.4688	0.5355	0.4718	0.5589	0.4748	0.5860	0.4759	0.5962	0.4764	0.6015	0.4780	0.6186
	5.00	0.4615	0.3889	0.4736	0.4602	0.4769	0.4855	0.4802	0.5153	0.4814	0.5267	0.4819	0.5327	0.4837	0.5522
	7.00	0.4641	0.2871	0.4787	0.3575	0.4824	0.3844	0.4861	0.4168	0.4873	0.4296	0.4879	0.4365	0.4898	0.4596
	10.0	0.4652	0.2040	0.4818	0.2657	0.4862	0.2926	0.4902	0.3261	0.4915	0.3399	0.4921	0.3475	0.4940	0.3744
2.50	0.20	0.1465	0.9927	0.1466	0.9929	0.1466	0.9937	0.1468	0.9947	0.1468	0.9951	0.1468	0.9953	0.1469	0.9960
	0.40	0.2281	0.9757	0.2283	0.9775	0.2286	0.9795	0.2289	0.9820	0.2290	0.9830	0.2291	0.9835	0.2293	0.9851
	0.60	0.2771	0.9507	0.2778	0.9556	0.2782	0.9590	0.2788	0.9633	0.2790	0.9649	0.2791	0.9658	0.2794	0.9685
	0.80	0.3082	0.9193	0.3094	0.9288	0.3100	0.9340	0.3108	0.9403	0.3111	0.9426	0.3112	0.9438	0.3117	0.9477
	1.00	0.3286	0.8833	0.3304	0.8985	0.3312	0.9056	0.3322	0.9141	0.3326	0.9172	0.3327	0.9188	0.3333	0.9239
	1.50	0.3559	0.7844	0.3591	0.8161	0.3603	0.8284	0.3616	0.8424	0.3621	0.8476	0.3623	0.8502	0.3631	0.8586
	2.00	0.3679	0.6875	0.3723	0.7349	0.3737	0.7518	0.3753	0.7711	0.3758	0.7781	0.3761	0.7817	0.3769	0.7933
	3.00	0.3771	0.5305	0.3833	0.5986	0.3850	0.6223	0.3868	0.6495	0.3874	0.6597	0.3877	0.6650	0.3886	0.6821
	4.00	0.3803	0.4223	0.3877	0.4991	0.3896	0.5268	0.3915	0.5592	0.3921	0.5717	0.3924	0.5783	0.3934	0.6000
	5.00	0.3817	0.3473	0.3900	0.4262	0.3921	0.4563	0.3940	0.4924	0.3946	0.5067	0.3949	0.5144	0.3958	0.5401
	7.00	0.3827	0.2534	0.3922	0.3274	0.3945	0.3598	0.3964	0.4006	0.3970	0.4175	0.3973	0.4268	0.3981	0.4600
	10.0	0.3831	0.1787	0.3933	0.2394	0.3959	0.2712	0.3979	0.3151	0.3984	0.3345	0.3987	0.3458	0.3993	0.3895
3.00	0.20	0.1407	0.9917	0.1407	0.9918	0.1408	0.9926	0.1409	0.9938	0.1409	0.9943	0.1410	0.9945	0.1410	0.9953
	0.40	0.2127	0.9719	0.2130	0.9740	0.2132	0.9761	0.2135	0.9790	0.2137	0.9800	0.2137	0.9806	0.2139	0.9824
	0.60	0.2530	0.9427	0.2536	0.9486	0.2541	0.9526	0.2546	0.9574	0.2548	0.9593	0.2549	0.9602	0.2552	0.9633
	0.80	0.2768	0.9063	0.2779	0.9180	0.2785	0.9240	0.2792	0.9311	0.2794	0.9339	0.2796	0.9353	0.2800	0.9397
	1.00	0.2915	0.8650	0.2931	0.8838	0.2938	0.8920	0.2946	0.9018	0.2949	0.9054	0.2951	0.9073	0.2955	0.9132
	1.50	0.3094	0.7539	0.3121	0.7927	0.3130	0.8069	0.3140	0.8234	0.3143	0.8294	0.3145	0.8325	0.3151	0.8423
	2.00	0.3164	0.6496	0.3199	0.7059	0.3209	0.7255	0.3220	0.7480	0.3224	0.7563	0.3226	0.7606	0.3231	0.7743
	3.00	0.3213	0.4894	0.3258	0.5662	0.3270	0.5933	0.3281	0.6250	0.3284	0.6371	0.3286	0.6435	0.3292	0.6644
	4.00	0.3229	0.3841	0.3280	0.4676	0.3292	0.4992	0.3303	0.5370	0.3306	0.5520	0.3308	0.5602	0.3313	0.5876
	5.00	0.3235	0.3132	0.3291	0.3961	0.3303	0.4303	0.3314	0.4728	0.3317	0.4902	0.3318	0.4999	0.3323	0.5336
	7.00	0.3239	0.2266	0.3300	0.2998	0.3313	0.3358	0.3323	0.3838	0.3326	0.4049	0.3327	0.4171	0.3330	0.4642
	10.0	0.3240	0.1592	0.3304	0.2159	0.3318	0.2490	0.3328	0.2984	0.3330	0.3225	0.3331	0.3371	0.3333	0.4059
4.00	0.20	0.1299	0.9896	0.1299	0.9896	0.1300	0.9906	0.1301	0.9920	0.1301	0.9926	0.1301	0.9929	0.1302	0.9938
	0.40	0.1860	0.9643	0.1863	0.9670	0.1865	0.9696	0.1868	0.9731	0.1869	0.9745	0.1869	0.9752	0.1871	0.9774
	0.60	0.2129	0.9269	0.2135	0.9353	0.2138	0.9402	0.2142	0.9463	0.2144	0.9487	0.2145	0.9499	0.2147	0.9537
	0.80	0.2266	0.8805	0.2276	0.8974	0.2280	0.9051	0.2285	0.9143	0.2287	0.9178	0.2288	0.9196	0.2291	0.9253
	1.00	0.2341	0.8288	0.2353	0.8560	0.2358	0.8667	0.2364	0.8794	0.2365	0.8841	0.2366	0.8865	0.2370	0.8942
	1.50	0.2417	0.6965	0.2435	0.7497	0.2440	0.7683	0.2446	0.7898	0.2448	0.7978	0.2449	0.8019	0.2452	0.8152
	2.00	0.2443	0.5820	0.2463	0.6543	0.2468	0.6793	0.2473	0.7084	0.2475	0.7194	0.2476	0.7253	0.2478	0.7444
	3.00	0.2458	0.4215	0.2481	0.5103	0.2486	0.5436	0.2490	0.5840	0.2492	0.6002	0.2492	0.6091	0.2494	0.6395
	4.00	0.2461	0.3240	0.2487	0.4126	0.2492	0.4502	0.2495	0.4979	0.2496	0.5185	0.2497	0.5301	0.2498	0.5729
	5.00	0.2463	0.2614	0.2489	0.3432	0.2494	0.3822	0.2497	0.4344	0.2498	0.4583	0.2498	0.4722	0.2499	0.5288
	7.00	0.2463	0.1875	0.2491	0.2531	0.2496	0.2895	0.2499	0.3425	0.2499	0.3693	0.2499	0.3866	0.2500	0.4753
	10.0	0.2463	0.1313	0.2491	0.1791	0.2496	0.2085	0.2499	0.2543	0.2500	0.2792	0.2500	0.2950	0.2500	0.4339

Table 8 P_1 and F as functions of NTU_1 and R_1 for 4–4 arrangement No. 441

R_1	NTU_1	N= 7		N= 15		N= 23		N= 47		N= 71		N= 95		N= ∞	
		P_1	F	P_1	F	P_1	F	P_1	F	P_1	F	P_1	F	P_1	F
0.50	0.20	0.1737	0.9994	0.1736	0.9990	0.1737	0.9992	0.1737	0.9996	0.1737	0.9996	0.1737	0.9997	0.1738	1.0000
	0.40	0.3064	0.9977	0.3063	0.9975	0.3065	0.9981	0.3067	0.9990	0.3067	0.9993	0.3068	0.9995	0.3069	1.0000
	0.60	0.4102	0.9949	0.4104	0.9954	0.4107	0.9966	0.4111	0.9980	0.4113	0.9987	0.4114	0.9990	0.4117	1.0000
	0.80	0.4932	0.9910	0.4937	0.9927	0.4942	0.9946	0.4950	0.9970	0.4953	0.9980	0.4954	0.9985	0.4959	1.0000
	1.00	0.5604	0.9861	0.5615	0.9897	0.5624	0.9924	0.5634	0.9959	0.5639	0.9972	0.5641	0.9978	0.5647	1.0000
	1.50	0.6812	0.9691	0.6845	0.9797	0.6863	0.9855	0.6884	0.9922	0.6892	0.9947	0.6896	0.9960	0.6908	1.0000
	2.00	0.7592	0.9464	0.7653	0.9670	0.7680	0.9766	0.7711	0.9876	0.7722	0.9915	0.7728	0.9936	0.7746	1.0000
	3.00	0.8476	0.8867	0.8597	0.9347	0.8642	0.9540	0.8691	0.9757	0.8709	0.9835	0.8717	0.9875	0.8744	1.0000
	4.00	0.8914	0.8150	0.9090	0.8953	0.9149	0.9261	0.9210	0.9608	0.9231	0.9733	0.9242	0.9797	0.9274	1.0000
	5.00	0.9145	0.7393	0.9367	0.8515	0.9435	0.8944	0.9504	0.9432	0.9526	0.9612	0.9538	0.9705	0.9572	1.0000
	7.00	0.9342	0.5977	0.9637	0.7593	0.9713	0.8241	0.9783	0.9019	0.9805	0.9319	0.9815	0.9478	0.9847	1.0000
	10.0	0.9406	0.4377	0.9781	0.6303	0.9859	0.7169	0.9920	0.8293	0.9937	0.8770	0.9945	0.9037	0.9966	1.0000
0.80	0.20	0.1693	0.9991	0.1693	0.9987	0.1693	0.9990	0.1694	0.9994	0.1694	0.9995	0.1694	0.9996	0.1695	1.0000
	0.40	0.2932	0.9964	0.2932	0.9965	0.2934	0.9974	0.2937	0.9986	0.2938	0.9990	0.2938	0.9993	0.2940	1.0000
	0.60	0.3873	0.9919	0.3877	0.9935	0.3881	0.9952	0.3886	0.9973	0.3888	0.9982	0.3890	0.9986	0.3893	1.0000
	0.80	0.4607	0.9858	0.4617	0.9896	0.4625	0.9924	0.4634	0.9959	0.4638	0.9972	0.4640	0.9979	0.4645	1.0000
	1.00	0.5193	0.9780	0.5212	0.9850	0.5224	0.9891	0.5238	0.9942	0.5243	0.9960	0.5246	0.9970	0.5254	1.0000
	1.50	0.6230	0.9519	0.6282	0.9702	0.6306	0.9789	0.6333	0.9888	0.6342	0.9924	0.6347	0.9943	0.6363	1.0000
	2.00	0.6893	0.9179	0.6985	0.9517	0.7022	0.9660	0.7064	0.9821	0.7078	0.9878	0.7086	0.9908	0.7109	1.0000
	3.00	0.7646	0.8341	0.7832	0.9061	0.7898	0.9340	0.7968	0.9652	0.7993	0.9763	0.8005	0.9821	0.8043	1.0000
	4.00	0.8021	0.7420	0.8305	0.8538	0.8398	0.8965	0.8496	0.9448	0.8529	0.9624	0.8546	0.9714	0.8597	1.0000
	5.00	0.8216	0.6528	0.8595	0.7989	0.8713	0.8561	0.8833	0.9220	0.8874	0.9466	0.8895	0.9593	0.8957	1.0000
	7.00	0.8363	0.5029	0.8911	0.6925	0.9072	0.7737	0.9229	0.8726	0.9281	0.9113	0.9307	0.9319	0.9386	1.0000
	10.0	0.8371	0.3535	0.9111	0.5575	0.9321	0.6600	0.9514	0.7958	0.9575	0.8533	0.9606	0.8852	0.9696	1.0000
1.00	0.20	0.1665	0.9988	0.1665	0.9985	0.1665	0.9989	0.1666	0.9994	0.1666	0.9994	0.1666	0.9996	0.1667	1.0000
	0.40	0.2848	0.9955	0.2849	0.9959	0.2851	0.9970	0.2854	0.9983	0.2855	0.9989	0.2855	0.9992	0.2857	1.0000
	0.60	0.3726	0.9900	0.3732	0.9922	0.3737	0.9943	0.3743	0.9968	0.3745	0.9979	0.3746	0.9984	0.3750	1.0000
	0.80	0.4400	0.9823	0.4413	0.9875	0.4422	0.9909	0.4432	0.9951	0.4436	0.9966	0.4438	0.9975	0.4444	1.0000
	1.00	0.4931	0.9727	0.4955	0.9820	0.4967	0.9870	0.4983	0.9931	0.4988	0.9953	0.4991	0.9964	0.5000	1.0000
	1.50	0.5853	0.9408	0.5912	0.9642	0.5938	0.9747	0.5968	0.9867	0.5978	0.9910	0.5984	0.9932	0.6000	1.0000
	2.00	0.6428	0.8999	0.6533	0.9420	0.6574	0.9593	0.6618	0.9786	0.6634	0.9855	0.6642	0.9891	0.6667	1.0000
	3.00	0.7065	0.8025	0.7272	0.8886	0.7344	0.9216	0.7420	0.9586	0.7446	0.9719	0.7459	0.9787	0.7500	1.0000
	4.00	0.7369	0.7001	0.7683	0.8289	0.7785	0.8784	0.7890	0.9349	0.7926	0.9556	0.7945	0.9663	0.8000	1.0000
	5.00	0.7517	0.6055	0.7934	0.7680	0.8064	0.8330	0.8196	0.9089	0.8242	0.9375	0.8264	0.9524	0.8333	1.0000
	7.00	0.7610	0.4549	0.8208	0.6542	0.8388	0.7434	0.8567	0.8540	0.8627	0.8980	0.8658	0.9215	0.8750	1.0000
	10.0	0.7586	0.3143	0.8378	0.5167	0.8621	0.6251	0.8854	0.7729	0.8932	0.8367	0.8972	0.8725	0.9091	1.0000
1.25	0.20	0.1631	0.9986	0.1630	0.9983	0.1631	0.9987	0.1631	0.9992	0.1632	0.9995	0.1632	0.9996	0.1632	1.0000
	0.40	0.2746	0.9944	0.2748	0.9951	0.2750	0.9964	0.2753	0.9980	0.2754	0.9986	0.2755	0.9990	0.2757	1.0000
	0.60	0.3551	0.9875	0.3558	0.9907	0.3564	0.9932	0.3570	0.9963	0.3573	0.9975	0.3574	0.9981	0.3578	1.0000
	0.80	0.4154	0.9779	0.4170	0.9850	0.4179	0.9892	0.4190	0.9942	0.4194	0.9961	0.4197	0.9970	0.4203	1.0000
	1.00	0.4619	0.9660	0.4646	0.9782	0.4660	0.9844	0.4676	0.9917	0.4682	0.9944	0.4685	0.9957	0.4694	1.0000
	1.50	0.5401	0.9271	0.5467	0.9567	0.5494	0.9694	0.5524	0.9839	0.5535	0.9891	0.5540	0.9917	0.5557	1.0000
	2.00	0.5870	0.8780	0.5980	0.9301	0.6022	0.9509	0.6067	0.9742	0.6082	0.9825	0.6090	0.9867	0.6115	1.0000
	3.00	0.6359	0.7651	0.6567	0.8673	0.6636	0.9063	0.6709	0.9502	0.6734	0.9661	0.6747	0.9743	0.6785	1.0000
	4.00	0.6573	0.6528	0.6876	0.7990	0.6970	0.8561	0.7067	0.9222	0.7099	0.9465	0.7116	0.9594	0.7166	1.0000
	5.00	0.6665	0.5540	0.7056	0.7313	0.7172	0.8044	0.7288	0.8916	0.7327	0.9249	0.7347	0.9425	0.7405	1.0000
	7.00	0.6705	0.4063	0.7240	0.6097	0.7393	0.7054	0.7537	0.8279	0.7584	0.8781	0.7608	0.9056	0.7677	1.0000
	10.0	0.6664	0.2769	0.7344	0.4701	0.7537	0.5794	0.7707	0.7333	0.7759	0.8025	0.7784	0.8422	0.7859	1.0000
1.50	0.20	0.1597	0.9983	0.1596	0.9980	0.1597	0.9985	0.1598	0.9991	0.1598	0.9994	0.1598	0.9996	0.1599	1.0000
	0.40	0.2649	0.9933	0.2651	0.9944	0.2653	0.9958	0.2657	0.9977	0.2658	0.9984	0.2659	0.9988	0.2661	1.0000
	0.60	0.3385	0.9850	0.3393	0.9891	0.3399	0.9921	0.3406	0.9957	0.3408	0.9971	0.3410	0.9978	0.3414	1.0000
	0.80	0.3922	0.9737	0.3939	0.9825	0.3949	0.9874	0.3960	0.9933	0.3965	0.9954	0.3967	0.9965	0.3974	1.0000
	1.00	0.4325	0.9595	0.4355	0.9744	0.4369	0.9818	0.4385	0.9903	0.4391	0.9934	0.4394	0.9950	0.4404	1.0000
	1.50	0.4980	0.9136	0.5046	0.9493	0.5073	0.9643	0.5102	0.9812	0.5113	0.9872	0.5118	0.9903	0.5134	1.0000
	2.00	0.5351	0.8566	0.5458	0.9185	0.5497	0.9427	0.5539	0.9698	0.5554	0.9795	0.5561	0.9844	0.5584	1.0000
	3.00	0.5710	0.7302	0.5899	0.8466	0.5959	0.8911	0.6021	0.9418	0.6042	0.9602	0.6052	0.9698	0.6084	1.0000
	4.00	0.5850	0.6103	0.6111	0.7702	0.6187	0.8340	0.6262	0.9089	0.6287	0.9372	0.6299	0.9521	0.6336	1.0000
	5.00	0.5903	0.5097	0.6225	0.6963	0.6313	0.7758	0.6396	0.8731	0.6422	0.9112	0.6435	0.9317	0.6474	1.0000
	7.00	0.5912	0.3670	0.6332	0.5685	0.6437	0.6673	0.6525	0.7983	0.6551	0.8544	0.6564	0.8858	0.6598	1.0000
	10.0	0.5870	0.2480	0.6385	0.4292	0.6506	0.5353	0.6594	0.6891	0.6617	0.7622	0.6627	0.8063	0.6652	1.0000
2.00	0.20	0.1532	0.9977	0.1532	0.9975	0.1532	0.9981	0.1533	0.9989	0.1534	0.9993	0.1534	0.9994	0.1535	1.0000
	0.40	0.2466	0.9910	0.2468	0.9928	0.2471	0.9947	0.2475	0.9971	0.2476	0.9980	0.2477	0.9985	0.2479	1.0000
	0.60	0.3078	0.9800	0.3087	0.9860	0.3093	0.9899	0.3101	0.9946	0.3103	0.9963	0.3105	0.9972	0.3109	1.0000
	0.80	0.3498	0.9650	0.3517	0.9774	0.3527	0.9838	0.3538	0.9914	0.3542	0.9941	0.3545	0.9956	0.3551	1.0000
	1.00	0.3796	0.9464	0.3826	0.9670	0.3840	0.9766	0.3856	0.9876	0.3861	0.9916	0.3864	0.9936	0.3873	1.0000
	1.50	0.4238	0.8867	0.4298	0.9347	0.4321	0.9540	0.4346	0.9757	0.4354	0.9835	0.4359	0.9875	0.4372	1.0000
	2.00	0.4457	0.8151	0.4545	0.8954	0.4574	0.9262	0.4605	0.9608	0.4616	0.9733	0.4621	0.9798	0.4637	1.0000
	3.00	0.4636	0.6657	0.4767	0.8056	0.4803	0.8600	0.4838	0.9236	0.4850	0.9474	0.4856	0.9599	0.4872	1.0000
	4.00	0.4690	0.5371	0.4852	0.7142	0.4891	0.7880	0.4925	0.8788	0.4935	0.9149	0.4940	0.9345	0.4954	1.0000
	5.00	0.4703	0.4377	0.4891	0.6303	0.4930	0.7169	0.4960	0.8294	0.4969	0.8771	0.4973	0.9039	0.4983	1.0000
	7.00	0.4692	0.3078	0.4921	0.4956	0.4960	0.5921	0.4985	0.7273	0.4990	0.7913	0.4993	0.8302	0.4998	1.0000
	10.0	0.4662	0.2066	0.4932	0.3620	0.4973	0.4545	0.4993	0.5901	0.4997	0.6604	0.4998	0.7062	0.5000	1.0000

331 yield the best performance. A similar comparison was carried out for 4-1, 4-2, and 4-4 arrangements. The best configurations for these arrangements are shown in Fig. 7. In the above classification, the best performing configuration for a given arrangement is listed as the first one in each figure (Figs. 2-6). For convenience, these configurations are abbreviated as 1-1 for No. 111, 2-2 for No. 221, and so on in the following discussion. These arrangements are further analyzed and the results are presented in the following sections.

Effect of Number of Thermal Plates. Influence of number of plates on the LMTD correction factor F for the 1-1, 2-2, 3-3, and 4-4 arrangements is shown in Figs. 8(*a*) and 8(*b*). Figure 8(*a*) corresponds to $R_1 = 1$, and $NTU_1 = 1$; Fig. 8(*b*) corresponds to $R_1 = 1$ and $NTU_1 = 5$. It can be seen that for each arrangement, F_1 approaches asymptotic values as $N \to \infty$. The arrangement yielding the best performance in each figure is different, and it can be seen that it is a function of NTU_1 and R_1. This shows that a detailed analysis is needed at any given set of operating variables for comparing the performance of different multipass arrangements.

P_1 for $N \to \infty$ can be computed using closed-form formulas for each arrangement. These formulas are derived by Kandlikar and Shah (1989) for the plate arrangements discussed here. The temperature effectiveness values P_1 for $N \to \infty$ using these formulas are generated for each arrangement and are included in Tables 1-8 in the last column.

Design Guidelines. The 1-1 counterflow PHE is used when the flow rates (heat capacity rates) are approximately equal. For a finite number of thermal plates, the effectiveness for this arrangement (No. 111) is lower than that for a pure counterflow arrangement due to the end effects. However, if there are a large number of thermal plates (e.g., $N > 100$), two problems may occur: (1) Flow velocity may be low in each pass resulting in a lower heat transfer coefficient, and (2) Flow maldistribution may result within the plate pack. A common remedy is to employ two passes on one or both fluid sides. For the same number of thermal plates (and hence surface area), a 2-2 PHE will have a higher heat transfer coefficient on each side and hence a higher NTU than the 1-1 unit. Of course, the pressure drop on each side of the 2-2 PHE will be approximately eight times higher than that for the 1-1 unit at the same flow rates. Thus the 2-2 PHE will have a better utilization of the pressure drop if it is within the allowed limit. If the pressure drop is of no major concern, sometimes 3-3, 4-4, or even higher equal numbers of passes are used in specific applications to yield high NTU and effectiveness, and close temperature approaches.

Figure 8 is a plot of the influence of the number of thermal plates on F for 1-1, 2-2, 3-3, and 4-4 arrangements at $NTU_1 = 1$ and 5. All PHEs suffer from the end effects, which become less significant with increasing values of N, and also with increasing numbers of passes on the fluid side flowing in the end channels. However, an additional influence is introduced in multipass arrangements due to the presence of parallel flow passages across a thermal plate between two passes. This influence reduces the performance, with 2-2 affected most, followed by 3-3, 4-4, etc., in that order. This is clearly seen from Fig. 8(*a*) for $R_1 = 1$ and $NTU_1 = 1$, and Fig. 8(*b*) for $R_1 = 1$ and $NTU_1 = 5$. The 1-1 arrangement suffers from the end effect at lower values of NTU_1 and its performance is below the 4-4 and 3-3 arrangements. At higher values of NTU_1, the end effects become less significant as compared to the penalty due to parallel passages in multipass arrangements, and 1-1 yields the best performance as seen from Fig. 8(*b*).

A careful review of P_1 for 3-3 (Table 5) versus 4-4 (Table 8) at same values of NTU_1, R_1, and N indicates differences less than 2 percent for $N > 23$. It may be inferred from this trend that the P_1-NTU_1 or F-NTU_1 relationship for n pass-n pass with $n > 4$ can be conservatively determined from the 4-4 arrangement (Table 8).

When there is a significant imbalance in the flow rate of the two fluids, the fluid having the lower flow rate is generally channeled through multiple passes and the other fluid through either a lower number of passes or one pass, such as 2-1, 3-1, 3-2, 4-1, 4-2, or 4-3 arrangements. This results in approximately the same flow through individual flow passages. Such an arrangement would yield a higher heat transfer coefficient for the fluid having multiple passes and minimize the flow maldistribution, if any. The other reason for the fluid flowing through a lower number of passes could be that its allowed pressure drop is limited. The P_1 versus NTU_1 comparison is shown in Fig. 9 for 1-1, 2-1, 3-1, 3-2, and 4-1 arrangements and in Fig. 10 for 4-1, 4-2, and 4-4 arrangements for various values of R_1. The following observations may be made from these figures:

- For engineering purposes, different pass arrangements influence P_1 only for $R_1 = 1$ and 2 because one pass (in 2-1, 3-1, 3-2, 4-3) or two passes (in 4-1) in parallel flow reduce the effectiveness compared to that for all passes in counterflow (as in 1-1, 2-2, 3-3, or 4-4). However, the influence of the parallel flow passes becomes negligible for $R_1 > 3$ as found from Fig. 9, although it is not clear to the authors why. In reality for a given number and type of thermal plates, the heat transfer coefficient for the multipass fluid side is higher with an increasing number of passes on that side because of the increased flow velocity. This will result in higher NTU_1 and subsequently higher P_1, and partially or totally compensate for the reduction in P_1 due to parallel flow passes, if any. Of course, the pressure drop on the multipass fluid side will increase sharply as the number of passes increases, and it is the pressure drop that will dictate how many passes are reasonable on the low fluid flow rate side.
- For $R_1 \geq 3$, the number of passes on each side has a negligible influence on P_1 as found from Figs. 9 and 10 and the detailed tabular results. Hence, for a significant difference in the heat capacity rates, it is the pressure drop, flow maldistribution, and other design criteria that are more important for the selection of passes on each side.
- For $R_1 = 1$, the 1-1 arrangement would be the preferable to 2-1, 3-1, or 4-1 because of the significantly higher P_1 compared to the other arrangements.
- For $R_1 = 1$, P_1 at a given NTU_1 decreases as the number of passes on the Fluid 2 side are increased. As seen from Fig. 9 for $NTU_1 > 1.5$, the arrangements in decreasing order of the effectiveness are 1-1, 3-2, 3-1, 2-1, and 4-1. Note that the 3-1 arrangement is more effective than the 2-1 arrangement since 2/3 of the passages in 3-1 are in counterflow, as compared to only 1/2 in 2-1. At NTU_1 values below 1.5, P_1 values for 2-1, 3-1, and 4-1 are very close to each other, and a crossover among these graphs is observed.
- For $R_1 = 2$, P_1 for the 2-1 PHE is lower than that for the 1-1 PHE because of parallel flow of fluids in one pass. However, this will be partially compensated for by the increased heat transfer coefficient for the two-pass side, which will result in higher NTU_1, and subsequently P_1. Hence, if the pressure drop is within permissible limits on the two-pass side, design calculations should be carried out using appropriate heat transfer coefficients to decide 2-1 versus 1-1 pass arrangement.

A review of the results in Tables 2 and 7 for 2-1 versus 4-2 arrangements indicates the effectiveness P_1 for 4-2 is slightly higher than that for 2-1 as expected for increasing number of passes for an overall counterflow arrangement. However, the final choice of 4-2 versus 2-1 will be dependent upon the allowed pressure drops.

Summary and Conclusion

Starting with a detailed classification for plate heat exchangers, comprehensive numerical results are generated for 1-1, 2-1, 2-2, 3-1, 3-3, 4-1, 4-2, and 4-4 overall counterflow arrangements; such numerical results are not presented here for 3-2 and 4-3 arrangements due to space constraints. These results are presented in terms of the temperature effectiveness P_1 and log-mean temperature difference correction factor F for a wide range of NTU_1, R_1, and N. In most operating ranges, the influence of the number of thermal plates can be neglected for $N > 40$. The following are the specific conclusions of the study:

- For approximately equal flow rates on each fluid side, the 1-1 arrangement yields the highest effectiveness for $NTU_1 > 5$. However, if the number of thermal plates is large, such as $N > 100$, either the resultant heat transfer coefficient may be too low or flow maldistribution may occur. In this case, the choice may be to go to an n-n pass arrangement with $n > 1$ depending upon the allowed pressure drops.
- For a 2-1 exchanger, while the effectiveness is low at a given NTU_1, the heat transfer coefficient is high compared to the 1-1 exchanger, resulting in higher NTU_1, and hence P_1 may be higher or lower than that for 1-1 at the same fluid flow rates. Detailed design calculations should therefore be made to decide 2-1 versus 1-1 arrangement depending upon the allowed pressure drops.
- For n-n pass exchangers with $n > 4$, use the results for 4-4 given in Table 8 as a conservative estimate.
- When there is a significant difference in the flow rates of the two fluid streams, the preferred pass arrangement is m-n ($m > n$) with the lower flow rate fluid flowing through m passes. This yields approximately the same flow rate through individual channels.

For $R_1 = 1$ and 2, P_1 decreases in order for 1-1, 3-2, 3-1, 2-1, 4-1, etc., arrangements. Since the heat transfer coefficient increases with increasing number of passes on a given side, the detailed design calculations are necessary to determine which is the best pass arrangement for the allowed pressure drop. For $R_1 \geq 3$, there is essentially no difference in P_1 at given NTU_1, R_1, and $N > 95$ for the foregoing pass arrangements. In this case, choose the highest number of passes that the pressure drop on each side can allow.

- As expected, P_1 values will be slightly higher for 4-2 compared to that for 2-1 for specified NTU_1 and R_1. Hence, use 4-2 if the pressure drops can be tolerated. A similar conclusion may be inferred for pass arrangements with relationships similar to 4-2 versus 2-1.

References

Cooper, A., and Usher, J. D., 1983, "Plate Heat Exchangers," in: *Heat Exchanger Design Handbook*, E. U. Schlünder, Editor-in-Chief, Vol.3, Section 3.7, Hemisphere Publishing Corp., Washington, DC.

Focke, W. W., 1983, "Plate Heat Exchanger: Review of Transport Phenomena and Design Procedures," CSIR Report CENG 445, CSIR, Pretoria, South Africa.

Foote, M. R., 1967, "Effective Mean Temperature Differences in Multipass Heat Exchangers," NEL Report No. 303, National Engineering Lab, Glasgow, United Kingdom.

Jackson, B. W., and Troupe, R. A., 1966, "Plate Exchanger Design by ϵ-NTU Method," *Chemical Engineering Progress Symposium Series*, No. 64, Vol. 62, p. 185-190.

Kandlikar, S. G., 1984, "Performance Curves for Different Plate Heat Exchanger Configurations," ASME Paper No. 84-HT-26.

Kandlikar, S. G., and Shah, R. K., 1989, "Asymptotic Effectiveness-NTU Formulas for Multipass Plate Heat Exchangers," ASME JOURNAL OF HEAT TRANSFER, Vol. 111, this issue.

Marriott, J., 1971, "Where and How to Use Plate Heat Exchangers," *Chemical Engineering*, Vol. 78, No. 8, pp. 127-133.

Pignotti, A., 1984, "Flow Reversibility of Heat Exchangers," ASME JOURNAL OF HEAT TRANSFER, Vol. 106, pp. 361-368.

Raju, K. S. N., and Bansal, J. C., 1983a, "Plate Heat Exchangers and Their Performance," in: *Low Reynolds Number Flow Heat Exchangers*, S. Kakaç, R. K. Shah, and A. E. Bergles, eds., pp. 899-912, Hemisphere Publishing Corp., Washington, DC.

Raju, K. S. N., and Bansal, J. C., 1983b, "Design of Plate Heat Exchangers," in: *Low Reynolds Number Flow Heat Exchangers*, S. Kakac, R. K. Shah, and A. E. Bergles, eds., pp. 913-932, Hemisphere Publishing Corp., Washington, DC.

Shah, R. K., and Focke, W. W., 1988, "Plate Heat Exchangers and Their Design Theory," in: *Heat Transfer Equipment Design*, R. K. Shah, E. C. Subbarao, and R. A. Mashelkar, eds., Hemisphere Publishing Corp., Washington, DC.

Shah, R. K., and Kandlikar, S. G., 1988, "The Influence of the Number of Thermal Plates on Plate Heat Exchanger Performance," in: *Current Researches in Heat and Mass Transfer*, A Compendium and a Festchrift for Professor Arcot Ramachandran, pp. 267-288, Hemisphere Publishing Corp., Washington, DC.

Asymptotic Effectiveness-NTU Formulas for Multipass Plate Heat Exchangers

S. G. Kandlikar
Mechanical Engineering Department,
Rochester Institute of Technology,
Rochester, NY 14623-0887
Mem. ASME

R. K. Shah
Harrison Radiator Division,
General Motors Corporation,
Lockport, NY 14094-1896
Fellow ASME

The effectiveness of a plate heat exchanger with a finite number of plates is affected by the end channels, and the channels between two adjacent passes. These effects become less significant as the number of thermal plates becomes large, N > 40, as shown by Kandlikar and Shah (1989). In the present paper, closed-form equations are derived for plate heat exchangers with N = ∞ in terms of temperature effectiveness P_1 as a function of the capacity rate ratio R_1 and the number of transfer units NTU_1 for the following pass arrangements: 1-1, 2-1, 2-2, 3-1, 3-2, 3-3, 4-1, 4-2, 4-3, and 4-4.

Introduction

Plate heat exchangers (PHEs) offer a simple arrangement in which the heat transfer surface area and heat transfer duty can be readily changed by adding or removing a few plates. Also the flexibility in the flow channeling could be utilized in deciding pass arrangements for each stream going through the plate heat exchanger. This decision is generally based on the required heat transfer duty, individual plate characteristics, and available pressure drops.

A detailed classification of different plate heat exchanger configurations on the basis of the number of thermal plates and passes is presented by Kandlikar and Shah (1989). A computer program was developed to calculate P_1 as a function of R_1, NTU_1, and N for all possible 1-1 (1 pass-1 pass), 2-1, 2-2, 3-1, and 3-3 arrangements, and one each for 4-1, 4-2, and 4-4 arrangements. Tabular results were presented for the commonly employed overall counterflow arrangements. Guidelines were also presented for selecting a particular pass arrangement.

The end channels differ from the interior channels in a plate heat exchanger due to adiabatic wall conditions on the ends resulting in heat transfer from one side only. Similarly, the plates between two passes have different flow configuration, parallel flow or counterflow, as compared to the plates within the two adjacent passes. The influence of end effects and interpass plates become significant only when the number of thermal plates is small. As seen from the results presented by Kandlikar and Shah (1989), these effects become less significant with increasing number of thermal plates. For $N > 40$, P_1 values closely approach those for $N \to \infty$. These effects are not present for $N = \infty$, and hence are not considered in the analysis to follow.

The objectives of this paper are:

- to show that different plate heat exchanger arrangements with an infinite number of thermal plates reduce to assemblies of individual parallel and counterflow heat exchangers.
- to derive the temperature effectiveness formulas for a few typical plate arrangements with an infinite number of thermal plates, and present the effectiveness formulas for all plate arrangements up to 4-4 PHE in tabular form.

Analysis

The effectiveness of complex assemblies of heat exchangers was analyzed by Domingos (1969). He presented closed-form expressions for effectivenesses for the assemblies by applying matrix transformation rules using individual heat exchanger effectivenesses as building blocks. Domingos' method is restricted to those complex assemblies for which: (1) there are only two inlet and two outlet streams from each individual exchanger, and (2) the building blocks of heat exchangers are connected by the fluid streams only in certain ways. For example, as seen later in Fig. 2, both outlet streams from exchanger A do not go to any single heat exchanger, B, C, or D, and Domingos' method cannot work for the complex assembly of heat exchangers of Fig. 2.

Pignotti (1984, 1986) presented a generalized matrix formalism to handle heat exchanger assemblies with more than two inlet or outlet streams, and with arbitrary fluid paths connecting different heat exchangers. These methods are able to offer closed-form expressions for highly complicated heat exchanger assemblies; however, the algebra involved is sometimes still quite complex, but not impossible. In this paper, two approaches are presented for obtaining closed-form expressions. The first one utilizes the basic definitions and heat balances in deriving the effectiveness formulas. It is used in deriving P_1-NTU_1 formulas for a majority of the configurations. The method is illustrated in this paper for arrangement #321 (#321 refers to 3 pass-2 pass plate heat exchanger configuration #1 as shown in the schematic included in Table 1). However, Pignotti (1984, 1986) offers shortcuts to this method to make it straightforward with fewer algebraic manipulations; hence his method is used to derive the results reported in Table 1 for the 3-2, 3-3, 4-3, and 4-4 arrangements.

Idealizations. Some of the basic idealizations made in the analysis of plate heat exchangers are listed below.

- Heat exchanger is operating under steady-state conditions.
- The fluid properties are constant throughout the heat exchanger.
- The fluid velocities are uniform across individual plate heat exchanger channels.
- The fluid flow is uniformly distributed among parallel flow channels.
- Heat losses to surroundings are negligible.
- The heat transfer coefficient is uniform across plate heat exchanger channels.

Basic Combining Rules for Assemblies of Heat Exchangers. The three arrangements shown in Figs. 1(*a*), 1(*b*), and 1(*c*) are the basic building blocks for analyzing many plate heat exchanger configurations with an infinite number of thermal plates. In the present work, these basic blocks are employed

Contributed by the Heat Transfer Division for publication in the JOURNAL OF HEAT TRANSFER. Manuscript received by the Heat Transfer Division December 4, 1987. Keywords: Heat Exchangers, Modeling and Scaling.

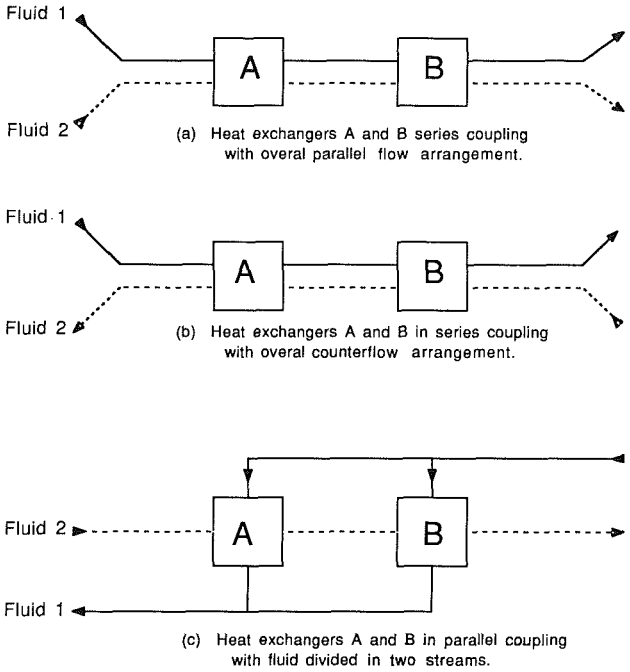

Fig. 1(*a–c*) Three basic heat exchanger assemblies analyzed by Domingos (1969)

along with the basic definitions and subsequent algebraic manipulations to obtain the effectivenesses of multipass plate exchangers. As will be shown later, any multiplass plate exchanger with $N = \infty$ can be reduced to an arrangement consisting of assemblies of heat exchangers. The temperature effectiveness P_1 for the three basic arrangements is given by the following equations derived by Domingos (1969) under the idealizations listed above:

Series coupling of two heat exchangers with overall parallel flow arrangement (Fig. 1*a*)

$$P_1 = P_{A,1} + P_{B,1} - P_{A,1}P_{B,1}(1 + R_1) \tag{1}$$

where $P_{A,1}$ and $P_{B,1}$ are temperature effectivenesses of fluid 1 for heat exchangers A and B respectively.

Series coupling of two heat exchangers with overall counterflow arrangement (Fig. 1*b*)

$$P_1 = \frac{P_{A,1} + P_{B,1} - P_{A,1}P_{B,1}(1 + R_1)}{1 - R_1 P_{A,1} P_{B,1}} \tag{2}$$

Parallel coupling of two exchangers with fluid 1 divided in two streams (Fig. 1*c*)

$$P_2 = P_{A,2} + P_{B,2} - P_{A,2}P_{B,2} \tag{3}$$

Expression for P_1 can be obtained from equation (3) by utilizing the following relations in Fig. 1(*c*):

$$P_2 = R_1 P_1 \tag{4}$$

$$P_{A,2} = R_{A,1} P_{A,1} \tag{5}$$

$$P_{B,2} = R_{B,1} P_{B,1} \tag{6}$$

Combining equations (3)–(6), P_1 can be expressed as

$$P_1 = \frac{1}{R_1}(R_{A,1}P_{A,1} + R_{B,1}P_{B,1} - R_{A,1}R_{B,1}P_{A,1}P_{B,1}) \tag{7}$$

where, in equations (1)–(7), P_1 and P_2 are the overall temperature effectivenesses of fluids 1 and 2, respectively; $P_{A,1}$, $P_{A,2}$, $P_{B,1}$, and $P_{B,2}$ are the corresponding individual temperature effectivenesses of fluids 1 and 2 in heat exchangers A and B; R_1 and R_2 are the overall capacity rate ratios for fluids 1 and 2, respectively. Note that $R_1 = 1/R_2$; $R_{A,1}$, $R_{A,2}$, $R_{B,1}$, and $R_{B,2}$ are the corresponding capacity rate ratios for fluids 1 and 2 in heat exchangers A and B.

Equation (7) can be extended to arrangements with more than two dividing paths for fluid 1 by successfully applying equation (7) to one pair of heat exchangers at a time. Consider, for example, the arrangement shown in Fig. 1(*c*) with an additional heat exchanger C (not shown) connected in series with A and B for fluid 2, and in parallel with A and B for fluid 1. P_2 for this arrangement is obtained as

$$P_2 = P_{A,2} + P_{B,2} + P_{C,2} - P_{A,2}P_{B,2} - P_{B,2}P_{C,2} - P_{C,2}P_{A,2} + P_{A,2}P_{B,2}P_{C,2} \tag{8}$$

Introducing equations (4)–(6), and the following equation:

$$P_{C,2} = R_{C,1} P_{C,1} \tag{9}$$

in equation (8), an expression for P_1 with three parallel paths in Fig. 1(*c*) can be obtained.

Derivation of P_1-NTU_1 Formulas for Different Plate Heat Exchangers With an Infinite Number of Plates

The P_1-NTU_1 formulas are derived now for different mul-

Nomenclature

A = heat transfer surface area on one fluid side of the heat exchanger, m^2
C = capacity rate of individual fluid streams, W/°C
F = log-mean temperature difference correction factor
N = number of thermal plates in a plate heat exchanger
NTU = number of transfer units of individual fluid streams; $NTU_1 = UA/C_1$ and $NTU_2 = UA/C_2$
P = temperature effectiveness of individual fluid stream
R = capacity rate ratio; $R_1 = C_1/C_2$ and $R_2 = C_2/C_1$
r = capacity rate ratio (fluid 1 capacity rate/fluid 2 capacity rate) for individual heat exchangers in an assembly of heat exchangers
T = temperature of a fluid stream, °C
θ = nondimensional fluid stream temperature defined by equation (18)
$\Delta\theta$ = absolute value of nondimensional temperature change of a fluid stream through a heat exchanger

Subscripts

A, B, C, D = parallel or counterflow heat exchangers representing parts of a multipass plate heat exchanger
c = counterflow heat exchanger arrangement
cold = cold fluid stream
hot = hot fluid stream
I = fluid stream state at an intermediate location in the heat exchanger
in = fluid stream state at the inlet to heat exchanger
out = fluid stream state at the outlet from heat exchanger
p = parallel flow heat exchanger arrangement
1, 2 = fluid streams

Table 1 Temperature effectiveness formulas for different plate arrangements with an infinite number of plates

Arrangement	Formula for P_1^*, N=∞
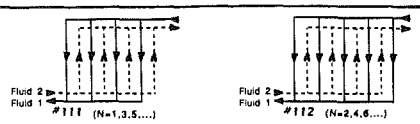	$P_1 = P_c$; with $P_c = P_c(NTU_1, R_1)$.
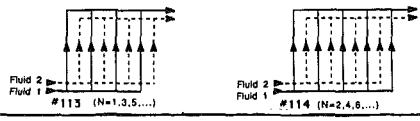	$P_1 = P_p$; with $P_p = P_p(NTU_1, R_1)$.
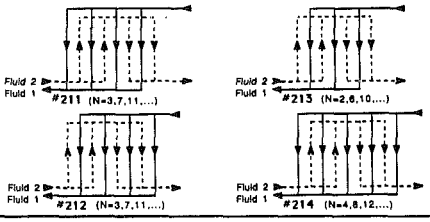	$P_1 = \frac{1}{2}(P_c + P_p - \frac{1}{2} P_c P_p R_1)$ with $P_c = P_c(NTU_1, R_1/2)$, $P_p = P_p(NTU_1, R_1/2)$
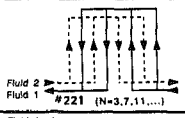	same as 111.
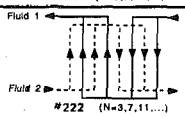	$P_1 = \frac{2P_p - P_p^2(1+R_1)}{1 - R_1 P_p^2}$; with $P_p = P_p(NTU_1/2, R_1)$
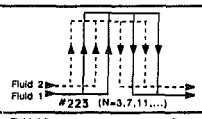	same as 113
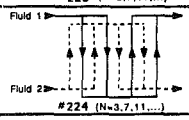	$P_1 = P_c[2 - P_c(1 + R_1)]$; with $P_c = P_c(NTU_1/2, R_1)$
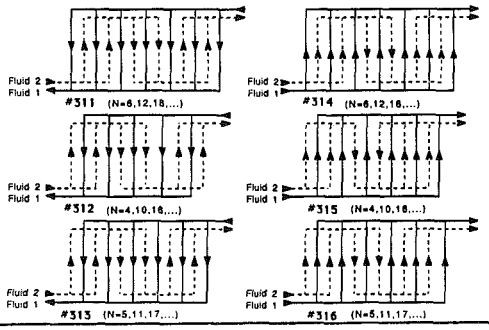	$P_1 = \frac{1}{3}[P_{B,1} + P_{A,1}(1 - P_{B,1} R_1/3) \times (2 - P_{A,1} R_1/3)]$; where for #311, 312 and 313, $P_{A,1} = P_c$ and $P_{B,1} = P_p$ and for #314, 315, and 316, $P_{A,1} = P_p$ and $P_{B,1} = P_c$ and for all #311 through 316, $P_c = P_c(NTU_1, R_1/3)$ and $P_p = P_p(NTU_1, R_1/3)$

*See the footnote at the end of Table 1.

tipass plate heat exchanger configurations described by Kandlikar and Shah (1989). Most plate heat exchanger configurations with an infinite number of plates are reduced to an assembly of basic parallel flow or counterflow heat exchangers shown in Figs. 1(*a*)–1(*c*). Some arrangements such as 3-2 and 4-3 result in more complex fluid flow paths among the individual heat exchangers; these are analyzed by Pignotti's method (1984, 1986). Temperature effectiveness formulas for the assemblies of basic parallel flow and counterflow heat exchangers of Figs. 1(*a*)–1(*c*) are obtained by using the combining rules described in the preceding section, or by using a basic approach as described later for configuration #321.

In the following sections, the numbering for plate exchanger configurations (schematics in Table 1) used is the same as that by Kandlikar and Shah (1989). The different configurations for a given pass arrangement are due to the end effects and the relative directions of the two fluids. For example, #111 and #112 both have a single pass on each fluid side with the fluids flowing in the opposite directions. In #111, each fluid has the same number of fluid streams through the plate exchanger, while in #112 fluid 1 has one more stream than fluid 2. However, when $N \rightarrow \infty$, the difference between the two arrangements becomes negligible and both configurations reduce to a pure counterflow exchanger, and hence P_1 for #111 and #112 is same as for the pure counterflow exchanger. The same thinking applies to other single-pass or multipass configurations for which the formulas for P_1 are summarized next.

#111 and #112. P_1 is same as that for a counterflow arrangement.

#113 and #114. P_1 is same as that for a parallel flow arrangement.

Table 1 (continued)

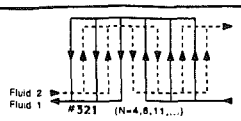	$P_1 = \frac{1}{R_1}(a + 0.5\,b + 0.5\,c + d)$; where $a = \frac{2R_1 e f^2 - 2ef + f - f^2}{2R_1 e^2 f^2 - e^2 - f^2 - 2ef + e + f}$ $b = a(e-1)/f$, $c = (1-a)/e$, $d = R_1 e^2 c - R_1 e + R_1 - c/2$, and $e = 1/(2R_1 P_c/3)$, $f = 1/(2R_1 P_p/3)$ with $P_c = P_c(NTU_1/2, 2R_1/3)$ $P_p = P_p(NTU_1/2, 2R_1/3)$
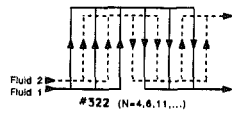	$P_1 = P_c + P_p - (2/9 + r/3)(P_c^2 + P_p^2) - (5/9 + 4r/3) P_c P_p + r(1+r) P_c P_p (P_c + P_p)/3 - r^2 P_c^2 P_p^2/9$; where $r = 2R_1/3$, $P_p = P_p(NTU_1/2, r)$ and $P_c = P_c(NTU_1/2, r)$
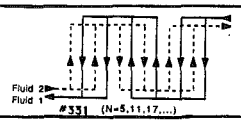	same as 111
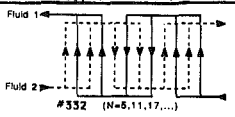	$P_1 = \frac{1}{R_1}(a + b + c)$; where $a = \frac{(d-e)^2}{d^3 + e^2 - 3de + e}$, $b = \frac{a(d-1)}{d-e}$, $c = (1 - a - b)/d$, and $d = \frac{1}{P_p R_1}$, $e = \frac{1}{R_1}$, with $P_p = P_p(NTU_1/3, R_1)$
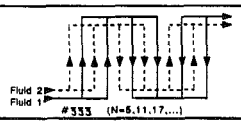	same as 113
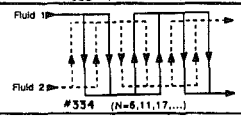	$P_1 = 3P_c - 3(1+r)P_c^2 + (1+r)^2 P_c^3$; where $r = R_1$ and $P_c = P_c(NTU_1/3, r)$
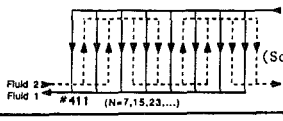	$P_1 = P_I - P_I^2 R_1/4$; where $P_I = (P_c + P_p - R_1 P_c P_p/4)/2$, with $P_c = P_c(NTU_1, R_1/4)$ and $P_p = P_p(NTU_1, R_1/4)$
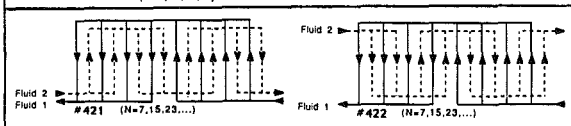	$P_1 = P_I + \frac{P_I(1-P_I)(1-P_I R_1)}{1 - P_I^2 R_1}$; where $P_I = (P_c + P_p - P_c P_p R_1/2)/2$, with $P_c = P_c(NTU_1/2, R_1/2)$ and $P_p = P_p(NTU_1/2, R_1/2)$
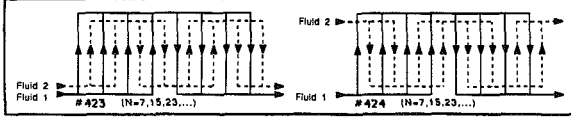	$P_1 = 2P_I - (1+R_1)P_I^2$; where $P_I = (P_c + P_p - P_c P_p R_1/2)/2$, with $P_c = P_c(NTU_1/2, R_1/2)$, and $P_p = P_p(NTU_1/2, R_1/2)$

#211–#214, #311–#316, and #411–#414. #211 reduces to the assembly shown in Fig. 1(*c*) with divided flow in fluid 1. P_1 for this arrangement is given by equation (7) with A as a counterflow heat exchanger, and B as a parallel flow heat exchanger. The effectivenesses of A and B are given by the respective counterflow and parallel flow equations. Thus

$$P_{A,1} = P_c(\text{NTU}_{A,1}, \quad R_{A,1}) \tag{10}$$

and

$$P_{B,1} = P_p(\text{NTU}_{B,1}, \quad R_{B,1}) \tag{11}$$

where P_c (NTU_1, R_1) is the temperature effectiveness of fluid 1 in counterflow arrangement with NTU_1 as the number of transfer units and R_1 as the capacity rate ratio; P_p (NTU_1, R_1) is defined similarly to P_c, but for a parallel flow arrangement.

Since fluid 1 is divided into two equal streams, $R_{A,1}$ and $R_{B,1}$ are given by

$$R_{A,1} = \frac{C_{A,1}}{C_{A,2}} = \frac{C_1/2}{C_2} = R_1/2 \tag{12}$$

Similarly,

$$R_{B,1} = R_1/2 \tag{13}$$

$\text{NTU}_{A,1}$ and $\text{NTU}_{A,2}$ are given by

$$\text{NTU}_{A,1} = \frac{U A_A}{C_{A,1}} = \frac{U A/2}{C_1/2} = \text{NTU}_1 \tag{14}$$

$$\text{NTU}_{B,1} = \frac{U A_B}{C_{B,1}} = \frac{U A/2}{C_1/2} = \text{NTU}_1 \tag{15}$$

Table 1 (continued)

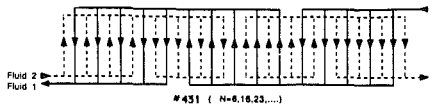	$P_1 = A + [B\,D\,(1-G) + B\,Q\,E]/[(1-G)\,(1-H) - Q\,S]$ where $A = (3\,P_c + P_p - r\,P_c\,P_p)/4$, $B = 1 - A$, $D = (1 - r\,P_c)\,(3\,P_c + 3\,P_p - 2\,r\,P_c\,P_p - r\,P_p^2)/6$, $E = (1 - r\,P_c)\,(3 - 2\,r\,P_c - r\,P_p)\,(P_c + 3\,P_p - r\,P_c\,P_p - 2\,r\,P_p^2)/12$, $G = r\,[(P_c^2 + 3\,P_p^2) + P_c\,P_p\,(3 - r\,P_c - 2\,r\,P_p)]/6$, $H = r\,[3\,P_c^2 + P_p^2 + P_c\,P_p\,(3 - 2\,r\,P_c - r\,P_p)]/6$, $Q = 1 - (P_c + P_p)/2 + r\,P_c\,P_p/3$, $S = E\,r\,P_c/(1 - r\,P_c) + r\,P_p\,(P_c + 3\,P_p - r\,P_p\,(P_c + 2\,P_p))/12$, and $r = 3\,R_1/4$, $P_c = P_c(NTU_1/3, r)$ and $P_p = P_p(NTU_1/3, r)$
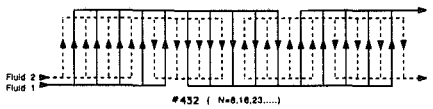	$P_1 = P_p\,(1 - r\,P_p)\,A/2 + (1 - r\,P_p)\,(3 - r\,P_c - 2\,r\,P_p)\,B/3 + (P_c + 3\,P_p - r\,P_c\,P_p)\,D/4$; where $A = 1 - (3\,P_c + P_p - r\,P_c\,P_p)/4$, $B = (3\,P_c + P_p - r\,P_c\,P_p - 2\,r\,P_c^2 + 2\,A\,P_c)/4$, $D = r\,P_c^2/2 + A\,(2 - P_c - P_p)/2 + 2\,B\,r\,P_p/3$, and $r = 3\,R_1/4$, $P_c = P_c(NTU_1/3, r)$ and $P_p = P_p(NTU_1/3, r)$
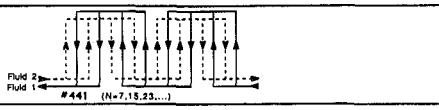	same as 111
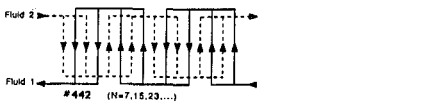	$P_1 = A\,[1 + B\,D/(1 - r\,A^2)]$; where $A = P_p\,[1 + (1 - P_p)\,(1 - r\,P_p)/(1 - r\,P_p^2)]$ $B = (1 - P_p)^2\,[1 + r\,P_p^2/(1 - r\,P_p^2)]$ $D = (1 - r\,P_p)^2/(1 - r\,P_p^2)$, and $r = R_1$, and $P_p = P_p(NTU_1/4, r)$
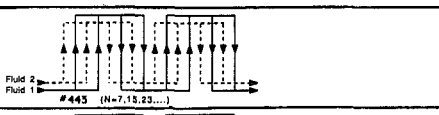	same as 113
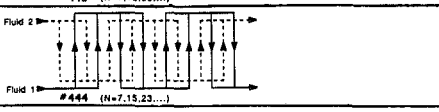	$P_1 = 4\,P_c - 6\,(1 + r)\,P_c^2 + 4\,(1 + r)^2\,P_c^3 - (1 + r)^3\,P_c^4$; with $r = R_1$, $P_c = P_c(NTU_1/4, r)$

* In the above formulas, P_c and P_p are counterflow and parallel flow temperature effectiveness given by

$$P_c(NTU, R_1) = \begin{cases} \dfrac{1 - \exp[-NTU_1(1 - R_1)]}{1 - R_1 \exp[-NTU_1(1 - R_1)]} & \text{for } R_1 \neq 1 \\ NTU_1/(1 + NTU_1) & \text{for } R_1 = 1 \end{cases} \quad \text{and} \quad P_p(NTU_1, R_1) = \frac{1 - \exp[-NTU_1(1 + R_1)]}{1 + R_1}$$

The final expression for P_1 for #211 is obtained by incorporating equations (10)–(15) into equation (7) and is presented in Table 1. Arrangements #212–#214 are equivalent to #211. In a manner analogous to #211, expressions for #311–#316, #411 and #412 can be obtained by including additional heat exchangers along fluid 2 stream, and with a further splitting of fluid 1 stream through three heat exchangers for #311, and through four heat exchangers for #411. Three additional arrangements #412–#414 for 4–1 PHEs are possible similar to 2–1 PHEs due to the end and interpass effects. Since for $N = \infty$ they are all equivalent to #411, schematics of #412–#414 are not included in Table 1 for space considerations.

#221–#224, #331–#334, and #441–#444. #221 with $N = \infty$ may be considered as two counterflow heat exchangers combined in overall counterflow, similar to Fig. 1(*a*). P_1 is given by equation (1) with

$$P_{A,1} = P_{B,1} = P_c(\text{NTU}_{A,1}, \quad R_{A,1}) \tag{16}$$

where P_c is the temperature effectiveness of a counterflow heat exchanger with

$$R_{A,1} = R_1, \text{ and } \text{NTU}_{A,1} = \text{NTU}_1/2 \tag{17}$$

The resulting assembly represents a pure counterflow heat exchanger, as confirmed by the effectiveness expression for #221 in Table 1.

Similarly, formulas for #222–#224 can be obtained by combining appropriate counterflow and parallel flow basic heat exchangers in overall counterflow (#222), or overall parallel flow (#223 and #224). The resulting equations are given in Table 1.

#331–#334 may be analyzed by successively combining heat exchangers according to Fig. 1(*a*) or Fig. 1(*b*). #331 and #333 are identical to pure counterflow and pure parallel flow exchangers, respectively. #332 is analyzed by representing it in terms of the basic blocks of Figs. 1(*a*)–1(*c*). #334 is analyzed by employing the Pignotti's method (1984, 1986). The effectiveness expressions for these arrangements are presented in Table 1.

#441 and #443 are identical to pure counterflow and pure parallel flow exchangers, respectively. #442 and #444 result in complex coupling of fluid streams. Pignotti's method is em-

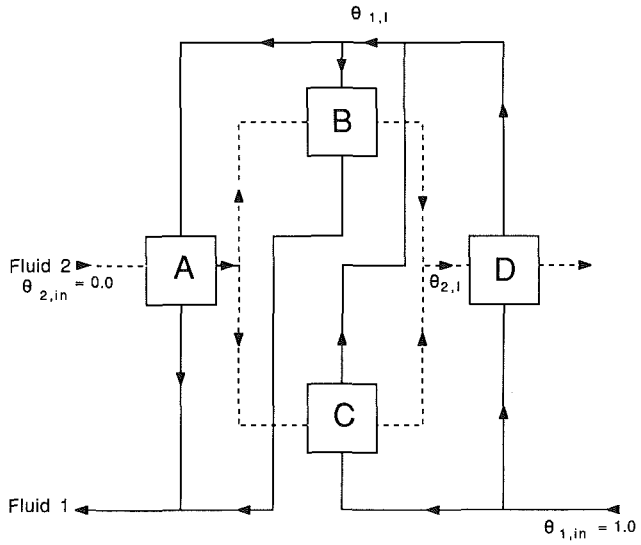

Fig. 2 Plate heat exchanger arrangement #321 represented by an assembly of four heat exchangers: A, B, C, and D

ployed for these arrangements and the resulting closed-form formulas are given in Table 1.

#321. #321 is equivalent to the assembly of heat exchangers shown in Fig. 2. Note that the middle pass on fluid 2 is shared equally by the two passes on the fluid 1 side. It is also possible to apply the matrix methods developed by Pignotti (1984, 1986) to this arrangement. Pignotti and Tamborenea (1988) present a detailed description of this method for various arrangements including #321. Although Pignotti's method is simpler algebraically, the method presented here provides a physical insight into the derivation. Pignotti's method is an ingenious shortcut of this method.

The temperatures at various locations in the heat exchanger assembly are made nondimensional by introducing θ, defined as

$$\theta = \frac{T - T_{\text{cold},in}}{T_{\text{hot},in} - T_{\text{cold},in}} \tag{18}$$

Without loss of generality, let us assume that fluid 1 is hot and fluid 2 is cold. The nondimensional temperatures at the inlet of the two streams are then

$$\theta_{1,in} = 1.0 \tag{19}$$

and

$$\theta_{2,in} = 0.0 \tag{20}$$

It can be readily seen that the outlet temperatures and the corresponding temperature effectivenesses of the two streams are related by

$$P_1 = 1 - \theta_{1,out} \tag{21}$$

and

$$P_2 = \theta_{2,out} \tag{22}$$

Using the definitions of the temperature effectiveness of a fluid as a ratio of its temperature change across the heat exchanger divided by the inlet temperature difference between the two fluids, the temperature change of fluid 2 through heat exchangers A through D may be expressed as follows:

$$\Delta\theta_{A,2} = P_{A,2}\theta_{1,I} \tag{23}$$

$$\Delta\theta_{B,2} = P_{B,2}(\theta_{1,I} - \Delta\theta_{A,2}) \tag{24}$$

$$\Delta\theta_{C,2} = P_{C,2}(1 - \Delta\theta_{A,2}) \tag{25}$$

$$\Delta\theta_{D,2} = P_{D,2}(1 - \theta_{2,I}) \tag{26}$$

Fluid 1 is divided into two streams at the inlet, 2/3 of the flow

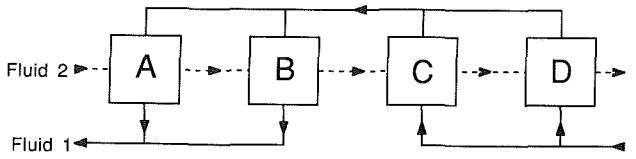

Fig. 3 Arrangement #421 represented by an assembly of two counterflow heat exchangers

going through D, and 1/3 going through C. Thus the intermediate temperature $\theta_{1,I}$ can be expressed as the flow rate averaged mean temperature of the two outlet streams of fluid 1 coming out of C and D, and is given by

$$\theta_{1,I} = \frac{1}{3}(1 - \Delta\theta_{C,1}) + \frac{2}{3}(1 - \Delta\theta_{D,1}) \tag{27}$$

From an energy balance

$$\Delta\theta_{C,1} = \Delta\theta_{C,2}/R_{C,1} \tag{28}$$

$$\Delta\theta_{D,1} = \Delta\theta_{D,2}/R_{D,1} \tag{29}$$

Substituting equations (28) and (29) into equation (27) and simplifying yields

$$\theta_{1,I} = 1 - \frac{1}{3}\frac{\Delta\theta_{C,2}}{R_{C,1}} - \frac{2}{3}\frac{\Delta\theta_{D,2}}{R_{D,1}} \tag{30}$$

Similarly, fluid 2 after going through A is divided equally in B and C. The intermediate temperature $\theta_{2,I}$ is given by

$$\theta_{2,I} = \Delta\theta_{A,2} + \frac{1}{2}(\Delta\theta_{B,2} + \Delta\theta_{C,2}) \tag{31}$$

Using the values of $\theta_{1,I}$ and $\theta_{2,I}$ from equations (30) and (31), equations (23)–(26) have four unknown temperature changes. They can be solved either algebraically or by the following matrix:

$$\begin{bmatrix} \frac{1}{P_{A,2}} & 0 & \frac{1}{3R_{C,1}} & \frac{2}{3R_{D,1}} \\ 1 & \frac{1}{P_{B,2}} & \frac{1}{3R_{C,1}} & \frac{2}{3R_{D,1}} \\ 1 & 0 & \frac{1}{P_{C,2}} & 0 \\ 1 & 0.5 & 0.5 & \frac{1}{P_{D,2}} \end{bmatrix} \begin{bmatrix} \Delta\theta_{A,2} \\ \Delta\theta_{B,2} \\ \Delta\theta_{C,2} \\ \Delta\theta_{D,2} \end{bmatrix} = \begin{bmatrix} 1 \\ 1 \\ 1 \\ 1 \end{bmatrix} \tag{32}$$

The matrix given by equation (32) can be solved to yield the unknown $\Delta\theta$'s. The total temperature change (rise) for fluid 2 is also identical to the overall temperature effectiveness (since $\theta_{1,in} = 1$ and $\theta_{2,in} = 0$), and is given by

$$P_2 = \Delta\theta_{A,2} + 0.5(\Delta\theta_{B,2} + \Delta\theta_{C,2}) + \Delta\theta_{D,2} \tag{33}$$

Subsequently, P_1 is given by

$$P_1 = P_2/R_1 \tag{34}$$

In the above derivation, the individual heat exchanger effectivenesses are calculated using the appropriate parallel or counterflow formulas with respective capacity rate ratios and NTU's. The final formula for P_1 is given in Table 1.

#322. #322 is analyzed by Pignotti's method (1984, 1986). The resulting formula is given in Table 1.

#421–#424. #421 may be represented by four counterflow heat exchangers as shown in Fig. 3. First, the heat exchangers A and B, and heat exchangers C and D, are combined together according to Fig. 1(*c*), and the two resulting assemblies are then combined according to Fig. 1(*b*). The resulting formulas are given in Table 1.

#431 and #432. #431 and #432 are very complex arrangements with splits in fluid streams. These arrangements are analyzed

Table 2 P_1 and F as functions of NTU_1 and R_1 for $N = \infty$ for four PHE arrangements: #321, #332, #431, and #442 (refer to Table 1 for schematics)

	PHE #321			PHE #332			PHE #431			PHE #442		
NTU_1	R_1	P_1	F	R_1	P_1	F	R_1	P_1	F	R_1	P_1	F
0.2		0.1699	0.9984		0.1737	0.9993		0.1713	0.9993		0.1737	0.9996
0.4		0.2947	0.9937		0.3062	0.9970		0.2990	0.9972		0.3065	0.9983
0.6		0.3894	0.9864		0.4098	0.9934		0.3974	0.9938		0.4106	0.9963
0.8		0.4632	0.9766		0.4923	0.9883		0.4752	0.9892		0.4939	0.9934
1.0		0.5218	0.9648		0.5590	0.9819		0.5378	0.9835		0.5615	0.9897
1.5		0.6249	0.9284		0.6784	0.9602		0.6504	0.9652		0.6838	0.9772
	0.750			0.500			0.667			0.500		
2.0		0.6902	0.8856		0.7547	0.9317		0.7239	0.9422		0.7633	0.9602
3.0		0.7651	0.7942		0.8404	0.8599		0.8107	0.8874		0.8549	0.9152
4.0		0.8045	0.7075		0.8822	0.7786		0.8579	0.8275		0.9016	0.8599
5.0		0.8279	0.6316		0.9042	0.6976		0.8862	0.7683		0.9273	0.7992
7.0		0.8531	0.5124		0.9233	0.5567		0.9169	0.6616		0.9512	0.6782
10.0		0.8695	0.3923		0.9312	0.4099		0.9374	0.5375		0.9628	0.5271
0.2		0.1636	0.9974		0.1693	0.9988		0.1656	0.9989		0.1694	0.9993
0.4		0.2758	0.9902		0.2930	0.9953		0.2821	0.9955		0.2934	0.9973
0.6		0.3566	0.9790		0.3866	0.9895		0.3681	0.9902		0.3878	0.9940
0.8		0.4169	0.9645		0.4595	0.9815		0.4338	0.9832		0.4617	0.9895
1.0		0.4633	0.9474		0.5174	0.9714		0.4855	0.9746		0.5209	0.9837
1.5		0.5413	0.8972		0.6191	0.9382		0.5756	0.9478		0.6264	0.9641
	1.200			0.800			1.067			0.800		
2.0		0.5885	0.8425		0.6831	0.8961		0.6328	0.9155		0.6949	0.9382
3.0		0.6412	0.7371		0.7542	0.7976		0.6995	0.8438		0.7748	0.8727
4.0		0.6693	0.6486		0.7886	0.6967		0.7363	0.7727		0.8170	0.7976
5.0		0.6869	0.5777		0.8062	0.6055		0.7591	0.7080		0.8409	0.7213
7.0		0.7083	0.4748		0.8206	0.4639		0.7861	0.6029		0.8637	0.5848
10.0		0.7257	0.3766		0.8256	0.3330		0.8077	0.4933		0.8745	0.4364
0.2		0.1595	0.9968		0.1665	0.9985		0.1620	0.9992		0.1666	0.9992
0.4		0.2639	0.9879		0.2845	0.9941		0.2714	0.9942		0.2850	0.9967
0.6		0.3364	0.9744		0.3719	0.9869		0.3498	0.9880		0.3733	0.9926
0.8		0.3888	0.9570		0.4387	0.9770		0.4082	0.9796		0.4412	0.9869
1.0		0.4279	0.9369		0.4910	0.9645		0.4530	0.9690		0.4949	0.9797
1.5		0.4913	0.8795		0.5810	0.9242		0.5289	0.9372		0.5891	0.9556
	1.500			1.000			1.333			1.000		
2.0		0.5280	0.8193		0.6361	0.8742		0.5752	0.8999		0.6489	0.9242
3.0		0.5671	0.7095		0.6956	0.7616		0.6268	0.8201		0.7176	0.8469
4.0		0.5875	0.6224		0.7230	0.6525		0.6539	0.7447		0.7529	0.7616
5.0		0.6002	0.5555		0.7364	0.5587		0.6703	0.6790		0.7724	0.6786
7.0		0.6158	0.4621		0.7465	0.4206		0.6895	0.5769		0.7902	0.5379
10.0		0.6289	0.3759		0.7495	0.2992		0.7047	0.4757		0.7978	0.3946
0.2		0.1546	0.9961		0.1630	0.9982		0.1575	0.9982		0.1631	0.9990
0.4		0.2500	0.9852		0.2743	0.9927		0.2587	0.9932		0.2749	0.9959
0.6		0.3130	0.9688		0.3543	0.9837		0.3282	0.9852		0.3558	0.9907
0.8		0.3567	0.9483		0.4139	0.9714		0.3781	0.9749		0.4167	0.9837
1.0		0.3880	0.9248		0.4596	0.9561		0.4153	0.9625		0.4638	0.9747
1.5		0.4360	0.8599		0.5357	0.9073		0.4751	0.9250		0.5442	0.9452
	1.875			1.250			1.667			1.250		
2.0		0.4619	0.7946		0.5803	0.8483		0.5091	0.8822		0.5933	0.9073
3.0		0.4877	0.6819		0.6257	0.7213		0.5441	0.7946		0.6469	0.8168
4.0		0.5004	0.5976		0.6450	0.6055		0.5608	0.7157		0.6727	0.7213
5.0		0.5081	0.5353		0.6537	0.5107		0.5704	0.6497		0.6861	0.6326
7.0		0.5171	0.4515		0.6596	0.3785		0.5807	0.5515		0.6974	0.4904
10.0		0.5240	0.3773		0.6611	0.2675		0.5883	0.4583		0.7016	0.3544
0.2		0.1498	0.9953		0.1596	0.9978		0.1532	0.9979		0.1597	0.9988
0.4		0.2369	0.9825		0.2645	0.9912		0.2467	0.9919		0.2652	0.9950
0.6		0.2916	0.9636		0.3376	0.9805		0.3082	0.9826		0.3392	0.9889
0.8		0.3277	0.9401		0.3906	0.9659		0.3506	0.9705		0.3935	0.9805
1.0		0.3526	0.9137		0.4302	0.9479		0.3811	0.9562		0.4346	0.9699
1.5		0.3884	0.8425		0.4936	0.8910		0.4273	0.9137		0.5020	0.9351
	2.250			1.500			2.000			1.500		
2.0		0.4063	0.7733		0.5289	0.8239		0.4515	0.8662		0.5412	0.8910
3.0		0.4228	0.6594		0.5623	0.6853		0.4741	0.7723		0.5811	0.7887
4.0		0.4304	0.5780		0.5752	0.5653		0.4837	0.6912		0.5987	0.6853
5.0		0.4347	0.5197		0.5806	0.4713		0.4888	0.6255		0.6072	0.5928
7.0		0.4393	0.4434		0.5839	0.3455		0.4938	0.5306		0.6136	0.4516
10.0		0.4423	0.3782		0.5846	0.2432		0.4970	0.4429		0.6157	0.3231
0.2		0.1409	0.9939		0.1531	0.9970		0.1451	0.9972		0.1533	0.9983
0.4		0.2134	0.9775		0.2462	0.9883		0.2247	0.9894		0.2469	0.9934
0.6		0.2542	0.9537		0.3068	0.9741		0.2723	0.9774		0.3086	0.9852
0.8		0.2786	0.9251		0.3482	0.9550		0.3025	0.9622		0.3512	0.9741
1.0		0.2939	0.8936		0.3774	0.9317		0.3223	0.9444		0.3816	0.9602
1.5		0.3133	0.8123		0.4202	0.8599		0.3488	0.8930		0.4275	0.9152
	3.000			2.000			2.667			2.000		
2.0		0.3215	0.7378		0.4411	0.7786		0.3603	0.8379		0.4508	0.8599
3.0		0.3280	0.6237		0.4582	0.6228		0.3689	0.7344		0.4711	0.7376
4.0		0.3305	0.5477		0.4637	0.4997		0.3719	0.6504		0.4784	0.6228
5.0		0.3318	0.4957		0.4656	0.4099		0.3732	0.5855		0.4814	0.5271
7.0		0.3328	0.4304		0.4665	0.2965		0.3742	0.4955		0.4833	0.3916
10.0		0.3332	0.3778		0.4667	0.2079		0.3747	0.4158		0.4838	0.2769

using Pignotti's method (1984, 1986). The effectiveness expressions are given in Table 1.

Asymptotic tabular results for the arrangements 321, 332, 431, and 442 are given in Table 2 as functions of NTU_1 and R_1. For all other pass arrangements of Table 1, the asymptotic tabular results are given by Kandlikar and Shah (1989). These tables may be used in deciding the more effective pass arrangement while selecting a PHE. However, additional factors

such as the allowable pressure drops and the flow maldistribution strongly influence the final selection of a PHE arrangement.

Conclusions

Multipass plate heat exchangers with an infinite number of plates are represented by assemblies of basic parallel and counterflow heat exchangers. Temperature effectivenesses of these plate heat exchangers are derived using basic definitions and a method developed by Pignotti (1984, 1986). Formulas for all plate heat exchanger combinations with 1 through 4 passes on each fluid side (36 multipasses in total) are presented in Table 1.

References

Domingos, J. D., 1969, "Analysis of Complex Assemblies of Heat Exchangers," *Int. J. Heat Mass Trans.*, Vol. 12, pp. 537–548.

Kandlikar, S. G., and Shah, R. K., 1989, "Multipass Plate Heat Exchangers—Effectiveness-NTU Results and Guidelines for Selecting Pass Arrangements," ASME JOURNAL OF HEAT TRANSFER, Vol. 111, this issue.

Pignotti, A., 1984, "Matrix Formalism for Complex Heat Exchangers," ASME JOURNAL OF HEAT TRANSFER, Vol. 106, pp. 352–360.

Pignotti, A., 1986, "Analytical Techniques for Basic Thermal Design of Complex Heat Exchanger Configurations," *Heat Transfer 1986*, Hemisphere Publishing Corporation, Washington, DC, Vol. 1, pp. 249–256.

Pignotti, A., and Tamborenea, P., 1988, "Thermal Effectiveness of Multipass Plate Heat Exchangers," *Int. J. Heat Mass Trans.*, Vol. 31, pp. 1983–1991.

Cost-Optimal Design of Dry Cooling Towers Through Mathematical Programming Techniques

J. D. Buys
Senior Lecturer,
Department of Mathematics.

D. G. Kröger
Professor,
Department of Mechanical Engineering.
Mem. ASME

University of Stellenbosch,
Stellenbosch, South Africa

The Constrained Variable Metric Algorithm is chosen to minimize the objective function (cost) in the design of a natural draft dry cooling tower. An existing cooling system design that has specific performance characteristics under prescribed operating conditions is selected as a reference unit. By changing design variables, but not exceeding prescribed constraints, a more cost-effective design is achieved. The influence of various parameters, and the sensitivity of the objective function to these parameters, are evaluated.

Introduction

In this study the application of modern minimization techniques to obtain cost-optimal designs of large natural draft dry cooling towers and systems incorporating these towers is illustrated. Various optimization methods applied to the design of air-cooled heat exchangers have been summarized by Hedderich et al. (1982). We have chosen the Constrained Variable Metric Algorithm (Powell, 1978) (also known as the Sequential Quadratic Programming Method, or Han's Method), to solve the problem of minimizing the objective function (cost), subject to prescribed constraints. A comparative study of 27 computer codes for constrained minimization by Hock and Schittkowski (1983), has rated codes based on this method as the best currently available. The method is relatively complicated and requires a substantial amount of computation, as a quadratic minimization problem has to be solved at each iteration of the minimization process. However, we have found that the FORTRAN routine VMCWD (Powell, 1983) solves our problem reliably and efficiently. The computational overhead of the numerical algorithm is compensated for by fewer iterations and hence fewer evaluations of the problem functions. This is important in our problem, since each computation of the cost and the constraint equations involves a relatively large number of numerical operations.

Optimizing the Cost

Suppose that a dry cooling tower with circular finned tube heat exchangers, of the type referred to in Appendix A, is to be designed, for a specified cooling rate Q_{ct}, when coupled to a condenser having a specified thermal conductance UA_{con}. For a minimum-cost design, values have to be assigned to all design variables in order to solve the following minimization problem:

Minimize C (Appendix C, equation (C1)) subject to the constraints:

(*a*) Heat balance equations (A1) and (A2).
(*b*) Draft equation (A39).
(*c*) Constant condenser thermal conductance UA_{con} (Appendix B).
(*d*) Geometric constraints, for example $P_t \geq d_f$. For practical reasons, further constraints such as $P_f \geq P_{fL}$ (avoid fouling) and $W_b \leq W_{bU}$ (limit bundle width for transportation) may be required.

The minimization problem as formulated above is an example of the general nonlinear constrained mathematical programming problem, which may be written as follows (see Luenberger, 1984, for example):

Minimize $F(X)$ subject to the constraints:

$$g_i(X) = 0, \quad i = 1, \ldots, m_e,$$

$$g_i(X) \geq 0, \quad i = m_e + 1, \ldots, m$$

where $X = (x_1, x_2, \ldots, x_n)$ is a vector of variables. A number of numerical techniques for solving problems of this type have been developed and are finding their way into engineering design. See Hedderich et al. (1982) for a discussion of some applications of minimization in heat exchanger design and also for additional references.

The Constrained Variable Metric Method does not require a feasible starting point and in general no feasible point is available before the iteration has converged to the minimum value of the cost function. During each iteration the partial derivatives of the cost function and all constraint functions are required; in this case the derivatives are calculated numerically with a finite difference approximation. Variables and constraints of the minimization problem should be carefully scaled to ensure that all quantities used by the minimization algorithm have approximately equal magnitudes. See Gill et al. (1981) for a discussion of the importance and technique of proper scaling.

In addition to the design variables that are to be chosen to minimize the total annual cost C, the minimization problem contains parameters such as T_{a1}, T_s, L_t, C_{wf}, and others, which are fixed at prescribed values due to physical constraints or practical considerations. It is of some interest to investigate the "sensitivity" of the optimal value of C with respect to these parameters, since this gives an indication of the relative importance of the parameters and may help in deciding which of the parameters have to be specified accurately and those for which a rough estimate will suffice. The sensitivity of C is determined as follows:

Suppose α is a parameter of the model, then the mimimum value of C, say C^*, is a function of α:

$$C^* = C^*(\alpha)$$

By the sensitivity of C with respect to α, we mean the derivative $\partial C^*/\partial\alpha$, evaluated at the prescribed value of α.

If the Lagrangian function of the general optimization problem is defined as

Contributed by the Heat Transfer Division for publication in the JOURNAL OF HEAT TRANSFER. Manuscript received by the Heat Transfer Division March 2, 1988. Keywords: Environmental Heat Transfer, Finned Surfaces, Heat Exchangers.

$$L(X, \Lambda) = F(X) - \sum_{i=1}^{m} \lambda_i g_i(X)$$

where $\Lambda = (\lambda_1, \ldots, \lambda_m)$ is the vector of Lagrangian multipliers, and the minimum value of F as a function of a parameter α is denoted by $F^*(\alpha)$, then it is shown by Fiacco (1983) that

$$\frac{\partial F^*}{\partial \alpha} = \frac{\partial L}{\partial \alpha}(X^*, \Lambda^*)$$

where X^* is the optimal solution and Λ^* the associated Lagrange multipliers. Since the Constrained Variable Metric Method computes the Lagrange multipliers λ_i in the course of solving the constrained minimization problem, it is a simple matter to compute $\partial F^*/\partial \alpha$ once the optimal solution is known. A convenient scale-invariant measure of the sensitivity of the optimal value with respect to α may then be written as

$$\frac{\Delta F^*}{F^*} \div \frac{\Delta \alpha}{\alpha} \approx \alpha \frac{\partial F^*}{\partial \alpha} \div F^*$$

A Case Study

In order to illustrate the application of minimization techniques to the cooling tower design, an existing dry cooling system design is considered (details are listed in Appendix B), and the possibility of an improved design is investigated. Using existing and estimated values for all variables and parameters, the work point of the cooling tower is determined by solving the heat balance equations (A1) and (A2) and the draft equation (A39) by varying $\dot{m}_a$, T_{ao}, and T_{wo}. The resulting value of $Q_{ct} = 329.06$ MW is then assumed as the target cooling rate of the tower, and the computed value of $UA_{con} = 3.30 \times 10^7$ W/K, as the prescribed condenser thermal conductance. The minimization problem is then solved as described previously, in order to investigate whether the design of this cooling tower and the heat exchangers might be improved, i.e., whether a tower with the same cooling rate but with a lower annual cost can be designed. The following are used as design variables, which can be varied, subject to the constraints, to minimize C: t_f, d_f, d_i, θ, P_t, H_5, H_3, d_5 and $\dot{m}_w$. In order not to exceed the limitations of the finned tube correlations, an equilateral tube layout is chosen ($P_l = 0.866\, P_t$). Both the values of the tube wall thickness $(d_o - d_i)/2 = 1.655$ mm and the fin root thickness $(d_r - d_o)/2 = 1.10$ mm are retained.

Since the variation of d_3 results in a tower of unacceptably low height, its original design value of 82.958 m is retained. Because of geometric considerations, it is only possible to cover effectively 52.4 percent of the cooling tower inlet cross-sectional area with heat exchanger bundles, as is the case in the original design. The optimum number of bundles is thus a function of this area and the bundle dimensions.

Although P_f is a variable, it is not listed since its optimum value is always found to be equal to its lower bound value $P_{fL} = 2.35$ mm, except when the fin thickness is required to be 0.5 mm, in which case the optimum fin pitch is 3.22 mm. Similarly the optimum value of W_b is always found to be equal to its upper bound value, which is chosen as $W_{bU} = 3$ m in this case.

The results of the calculations are presented in Tables 1, 2, and 3. The first line of Table 1 shows the values of the design variables for the existing tower design, and the second line the optimal values. Subsequent lines show the values obtained when one of the design variables is regarded as a fixed parameter and the cost is optimized with respect to the other variables.

The cost of the "optimum" tower is found to be very much less than that based on the original design. It is however noted that the aluminum fin would have to be only 0.078 mm thick, which is impractical considering the large fin diameter. By increasing the fin thickness to a more practical value, the cost of the tower increases correspondingly. Changes in other parameters within practical limits have only a very small influence on the cost of the tower.

Table 2 shows the sensitivity of the optimal cost with respect to some prescribed parameters. For example, if the cost of the fin material C_{fm} is increased by 1 percent, the optimal cost will increase by approximately 0.318 percent.

Nomenclature

A = area, m^2
C = cost, \$/annum
C_D = drag coefficient
c_p = specific heat, J/kg K
d = diameter, m
Eu = Euler number
e = effectiveness
F_D = drag force, N
F_t = LMTD correction factor
f = friction factor
G = mass velocity, kg/s m^2
g = gravitational acceleration, m/s^2
H = height, m
h = heat transfer coefficient, W/m^2 K
i = interest rate on capital
K = loss coefficient
k = thermal conductivity, W/m K
L = length, m
m = number of constraints
$\dot{m}$ = flow rate, kg/s
n = number of design variables or number of years or number
P = pitch, m or power, W
Pr = Prandtl number
p = pressure, N/m^2
Q = heat transfer rate, W
R = gas (air) constant, J/kg K
Re = Reynolds number
T = temperature, °C or K
t = thickness, m
U = overall heat transfer coefficient, W/m^2 K
v = velocity, m/s
W = width, m
x = variable
z = height
α = parameter of model
ϵ = surface roughness
η = efficiency
θ = semi-apex angle, deg
ρ = density, kg/m^3
σ = contraction ratio
τ = annual operating hours

Subscripts

a = air
b = bundle
c = contraction
con = condenser
ct = cooling tower
ctc = cooling tower contraction
cte = cooling tower expansion
d = downstream or diagonal
e = effective or electricity or equality
f = fin
fr = frontal
he = heat exchanger
i = inlet or inside
L = lower bound
l = longitudinal
m = material
o = outlet or outside
p = pump
r = root
s = stream or shell
t = tube or total or transversal
tb = tubes per bundle
tr = tube rows
ts = tower supports
U = upper bound
w = water
wf = weighting factor
wp = water passes

Table 1 Dimensions of optimized cooling system

Parameter	t_f (mm)	d_f (mm)	d_i (mm)	θ (°)	P_t (mm)	H_5 (m)	H_3 (m)	d_5 (m)	$\dot{m}_w$ (kg/s)	C ($/annum)
Existing tower design	0.5	57.2	22.09	30.75	58.0	120.0	13.67	58.0	4 390	863 022
Optimum tower	0.078	75.4	33.0	24.5	77.0	101.0	25.1	66.9	5 274	548 793
t_f	0.1	76.4	33.5	25.7	79.8	101.7	25.1	66.8	5 203	552 363
	0.3	75.2	33.9	31.3	86.6	118.1	25.0	64.2	5 029	674 646
	0.5	72.9	31.3	30.6	78.1	135.3	24.8	61.9	5 031	811 463
d_f	.076	70	30.4	24.3	71.8	99.8	25.0	67.2	4 954	550 076
	.079	80	35.3	24.6	81.3	102.1	25.0	66.6	5 567	549 580
	.081	90	40.8	24.7	90.9	105.1	24.9	65.7	6 284	555 750
d_i	.077	64.7	25	23.9	64.7	96.7	25.4	68.7	4 220	557 691
	.077	72.0	30	24.5	72.2	98.9	25.1	67.6	4 866	549 727
	.078	77.7	35	24.5	80.0	102.4	25.0	66.5	5 552	549 138
θ	.067	74.4	33.0	20	78.5	95.2	25.2	68.5	5 439	557 577
	.079	75.6	33.0	25	76.8	101.9	25.0	66.7	5 257	548 899
	.095	77.3	33.5	30	77.3	112.7	24.8	64.1	5 208	558 683
P_t	.075	70.0	29.6	24.5	70	98.8	25.1	66.9	5 274	548 793
	.079	77.5	34.5	24.4	80	102.2	25.1	67.3	4 838	550 408
	.084	84.5	39.7	24.2	90	106.5	25.0	65.8	6 193	552 956
H_5	.080	72.4	30.2	22.2	72.4	80	16.0	73.0	5 232	558 196
	.078	74.9	32.4	24.1	75.9	95	21.7	68.0	5 243	549 252
	.078	75.7	33.4	24.8	77.7	110	31.6	65.9	5 289	549 449
H_3	.078	75.6	33.2	24.5	75.9	91.3	10	64.7	5 372	566 272
	.078	75.5	33.1	24.5	77.0	96.2	20	66.8	5 293	549 389
	.078	75.4	33.0	24.5	77.0	106.0	30	66.9	5 276	549 101
d_5	.078	75.8	33.6	24.8	77.5	104.9	24.9	60	5 333	550 584
	.078	75.3	32.8	24.3	76.8	99.6	25.1	70	5 262	549 105
	.078	74.8	32.1	24.0	75.8	96.0	25.2	80	5 198	553 932
$\dot{m}_w$	.082	67.9	26.9	24.4	67.9	102.0	25.3	67.6	4 000	557 162
	.078	74.1	31.7	24.5	75.0	100.8	25.2	67.1	5 000	549 044
	.077	78.7	36.2	24.3	81.7	101.9	24.8	66.4	6 000	550 109
P_f=2.0mm	.069	75.1	33.9	25.1	80.4	98.3	25.1	67.5	5 257	525 667
P_f=2.5mm	.081	75.5	32.6	24.2	75.7	102.0	25.0	66.7	5 280	557 924
P_f=3.0mm	.096	75.4	33.1	23.1	75.4	108.5	25.1	65.7	5 577	587 188

Table 3 shows the sensitivity of the optimal cost with respect to some of the empirical correlations which were employed in the calculations. These were calculated as follows. To investigate the sensitivity with respect to K_{he}, for example, K_{he} was replaced by αK_{he}, where the value of α was equated to unity and the sensitivity of the cost was calculated with respect to α. From Table 3 it may be deduced, for example, that the tower support loss coefficient K_{ts} has a negligible effect on the optimal value of C and may well have been deleted from the calculations.

Table 2 Sensitivity of parameters

Parameter	Sensitivity	Parameter	Sensitivity
T_s	-12.3	C_{tm}	0.135
C_s	0.371	L_t	0.085
C_{fm}	0.318	τ	0.058
P_{fL}	0.267	ϵ	-0.0005

Table 3 Sensitivity of correlations

Correlation	Sensitivity	Correlation	Sensitivity
h_a (A.5)	-0.383	K_{cte} (A.28)	0.0171
$K_{he\theta}$ (A.31)	0.284	K_{ctc} (A.27)	0.0167
K_{he} (A.29)	0.181	K_{ct} (A.23)	0.0128
E_u (A.30)	0.177	K_{ts} (A.22)	0.0009

Conclusions

In a multidimensional design space, an intuitive approach to optimizing a system becomes a futile exercise. For a limited number of variables, analytic approaches may indicate certain trends (Moore, 1972, 1973), but these methods are inadequate in the case of more detailed system optimizations. An effective procedure for achieving a cost-optimized design for a dry cooling system is demonstrated.

The resultant finned tube has dimensions corresponding closely to commercially available tubes with d_o = 38.1 mm (1.5 in.) and d_f = 76.2 mm (3 in.). The optimum fin thickness is however impractically thin and a more costly thicker fin would have to be specified.

Although it may be argued that the optimum finned tube need not always necessarily be one that is commercially available, or may be difficult to manufacture with existing equipment, the geometry proposed does pose a challenge and gives direction to manufacturers of finned tubes. Furthermore, in the case of large towers, significant lengths of tubes are required (up to 2000 km per tower), justifying the setting up of suitable machinery for the manufacture thereof.

The optimum cooling tower is considerably lower than the tower proposed in the existing design, while the inlet is considerably higher. It should however be noted that the optimum tower height increases as the fin thickness increases. For a fixed fin pitch, an increase in fin thickness causes the flow resistance to increase and this requires a greater draft effect to achieve the same cooling rate.

References

Briggs, D. E., and Young, E. H., 1963, "Convection Heat Transfer and Pressure Drop of Air Flowing Across Triangular Pitch Banks of Finned Tubes," *Chem. Eng. Prog. Symp. Ser.*, Vol. 59, No. 41, pp. 1–10.

Fiacco, A. V., 1983, *Introduction to Sensitivity and Stability Analysis in Nonlinear Programming*, Academic Press, New York.

Geldenhuys, J. D., and Kröger, D. G., 1986, "Aerodynamic Inlet Losses in Natural Draft Cooling Towers," *Proc., 5th IAHR Cooling Tower Workshop*, Monterey.

Gill, P. E., Murray, W., and Wright, M. H., 1981, *Practical Optimization*, Academic Press, New York.

Gnielinski, V., 1975, *Forsch. Ing.-Wes.*, Vol. 41, No. 1.

Haaland, S. E., 1983, "Simple and Explicit Formulas for the Friction Factor in Turbulent Pipe Flow," ASME *Journal of Fluids Engineering*, Vol. 105, No. 3, pp. 89–90.

Hedderich, C. P., Kelleher, M. D., and Vanderplaats, G. N., 1982, "Design and Optimization of Air-Cooled Heat Exchangers," ASME JOURNAL OF HEAT TRANSFER, Vol. 104, pp. 683–690.

Hock, W., and Schittkowski, K., 1983, "A Comparative Peformance Evaluation of 27 Nonlinear Programming Codes," *Computing*, Vol. 30, pp. 335–358.

Kays, W. M., 1950, "Loss Coefficients for Abrupt Changes in Flow Cross Section With Low Reynolds Number Flow in Single and Multiple Tube Systems," *Trans. ASME*, Vol. 72, No. 8, pp. 1067–1074.

Kotzé, J. C. B., Bellstedt, M. O., and Kröger, D. G., 1986, "Pressure Drop and Heat Transfer Characteristics of Inclined Finned Tube Heat Exchanger Bundles," *Proc. 8th Int. Heat Transfer Conf.*, San Francisco, CA.

Luenberger, D. G., 1984, *Linear and Nonlinear Programming*, Addison-Wesley, New York.

Moore, F. K., 1972, "On the Minimum Size of Natural-Draft Dry Cooling Towers for Large Power Plant," ASME Paper No. 72-WA/HT-60.

Moore, F. K., 1973, "The Minimization of Air Heat-Exchange Surface Areas of Dry Cooling Towers for Large Power Plants," *Heat Transfer Digest*, Vol. 6, pp. 13–23.

Powell, M. J. D., 1978, "A Fast Algorithm for Nonlinearly Constrained Optimization Calculations," *Proceedings of the Dundee Conference, 1977*, Lecture Notes in Mathematics, Vol. 630, G. A. Watson, ed., Springer-Verlag, Berlin, pp. 144–157.

Powell, M. J. D., 1983, "VMCWD: A Fortran Subroutine for Constrained Optimization," *SIGMAP Bulletin*, No. 32.

Robinson, K. K., and Briggs, D. E., 1965, "Pressure Drop of Air Flowing Across Triangular Pitch Banks of Finned Tubes," *AIChE Eighth National Heat Transfer Conference*, pp. 177–184.

Schmidt, T. E., 1945, "La Production Calorifique des Surfaces Munies Dailettes," *Annexe du Bulletin de l'Institut International du Froid*, Annex G-5.

APPENDIX A

Consider the example of a hyperbolic natural draft dry cooling tower as shown in Fig. A1.

The heat exchanger bundles assembled in the form of **A** frames or **V** arrays, as shown in Fig. A2(*b*), are located horizontally at the inlet cross section to the tower. The density of the heated air inside the tower is less than that of the atmosphere outside the tower, with the result that the pressure inside the tower at H_3 is less than the external pressure at the same elevation. This pressure differential causes air to flow through the tower at a rate that is dependent on the various flow resistances encountered, the cooling tower dimensions, and the heat exchanger characteristics.

The heat transfer characteristics of the latter are expressed by the following equations:

$$Q_{ct} = \dot{m}_a c_{pa} (T_{a4} - T_{a3}) = \dot{m}_w c_{pw} (T_{wi} - T_{wo}) \quad \text{(A1)}$$

and

$$Q_{ct} = \frac{UA\, F_t [(T_{wi} - T_{a4}) - (T_{wo} - T_{a3})]}{\ln[(T_{wi} - T_{a4})/(T_{wo} - T_{a3})]} \quad \text{(A2)}$$

where

$$UA = (1/h_{ae} A_a + 1/h_w A_w)^{-1} \quad \text{(A3)}$$

For round bimetallic, extruded finned tubes, as shown in Fig. A2(*a*), the effective air-side thermal conductance may be expressed as

$$h_{ae}A_a = \left[\frac{1}{h_a e_f A_a} + \frac{\ln(d_o/d_i)}{2\pi k_t L_{tt}} + \frac{\ln(d_r/d_o)}{2\pi k_f L_{tt}} \right]^{-1} \quad \text{(A4)}$$

According to Briggs and Young (1963) the air-side heat transfer coefficient for such tubes may be approximated by

$$h_a = \frac{0.134}{d_r} k_a \, \mathrm{Re}_a^{0.681} \, \mathrm{Pr}_a^{0.33} \left[\frac{2(P_f - t_f)}{d_f - d_r} \right]^{0.2} \left[\frac{P_f - t_f}{t_f} \right]^{0.1134} \quad \text{(A5)}$$

in the case of a staggered arrangement, while the effectiveness of the extended surface is defined as

$$e_f = 1 - A_f (1 - \eta_f)/A_a \quad \text{(A6)}$$

According to Schmidt (1945), the fin efficiency may be approximated by

$$\eta_f = \tanh \phi / \phi \quad \text{(A7)}$$

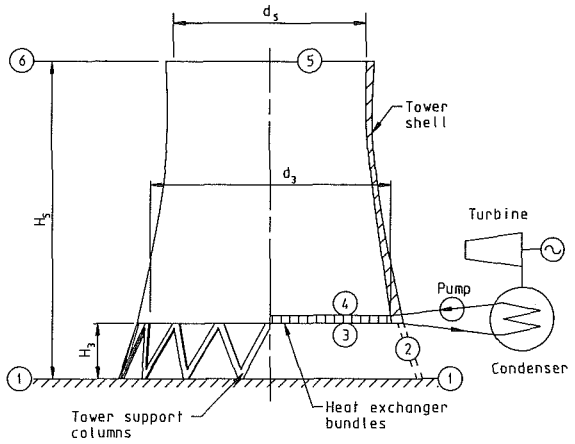

Fig. A1 Natural draft dry cooling tower

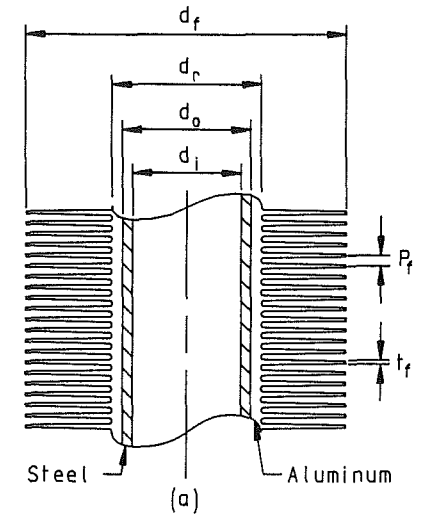

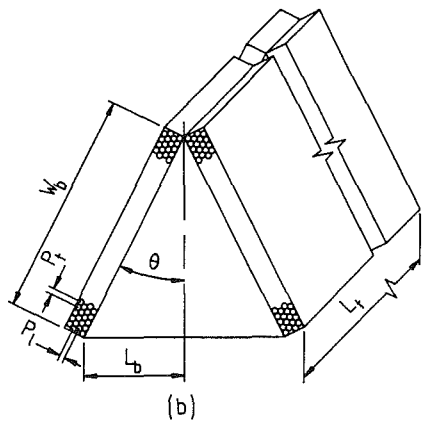

Fig. A2 Finned tube and A-frame heat exchanger

where

$$\phi = \frac{d_f - d_r}{\sqrt{2}} \sqrt{\frac{h_a}{k_f t_f}} \left[1 + 0.35 \ln \left(\frac{d_f}{d_r} \right) \right]$$

The water-side heat transfer coefficient is (Gnielinski, 1975)

$$h_w = \frac{k_w f_w (\mathrm{Re}_w - 1000)\mathrm{Pr}_w [1 + (d_i/L_t)^{0.67}]}{8 d_i [1 + 12.7 (f_w/8)^{0.5} (\mathrm{Pr}_w^{0.67} - 1)]} \quad \text{(A8)}$$

where the pipe friction factor is, according to Haaland (1983), given by

$$f_w = 0.3086 \left[\log_{10} \frac{6.9}{\mathrm{Re}_w} + \left(\frac{\epsilon}{3.7\, d_i} \right)^{1.11} \right]^{-2} \quad \text{(A9)}$$

The power required to pump water through the heat exchanger tubes is

$$P_w = \pi d_i^2\, \Delta p_w\, G_w\, L_t\, n_{tb}\, n_b / 4\rho_w \quad \text{(A10)}$$

where

$$\Delta p_w = \frac{f_w G_w^2}{2\rho_w d_i} \text{ and } G_w = \frac{4\dot{m}_w n_{wp}}{\pi d_i^2\, n_{tb} n_b}$$

The air flow rate through the tower is determined by the draft equation, which is derived as follows:

In the atmosphere external to the tower the variation of pressure with elevation in a gravity field is given by

$$dp_a = -\rho_a g dz \quad \text{(A11)}$$

For a perfect gas the following relation holds:

$$\rho_a = p_a / RT_a \quad \text{(A12)}$$

Since the temperature distribution in the atmosphere near ground level changes continuously, an arbitrary reference condition is selected for this analysis. According to the International Standard Atmosphere (ISA), the mean temperature lapse rate in the troposphere is 0.0065 K/m, resulting in the following temperature distribution in the atmosphere:

$$T_a = T_{a1} - 0.0065z \quad \text{(A13)}$$

Substitute equations (A12) and (A13) into equation (A11) and integrate from 1 to 6:

$$p_{a1} - p_{a6} = p_{a1} \left[1 - (1 - 0.0065 H_5 / T_{a1})^{153.85 g/R} \right] \quad \text{(A14)}$$

where $H_6 = H_5$ is the tower height, $g = 9.8$ m/s^2, and $R = 287.04$ J/kg K.

The air accelerates from stagnant ambient conditions at 1 and enters through the tower supports at 2 to section 3 before flowing through the heat exchanger bundles. A total pressure balance between 1 and 4 yields

$$p_{a1} - \left(p_{a4} + \frac{\rho_{a4} v_{a4}^2}{2} \right) = (K_{ts} + K_{ct} + K_{ctc} + K_{he\theta} + K_{cte})_{he} \left(\frac{1}{2\rho_{a34}} \right) \left(\frac{\dot{m}_a}{A_{fr}} \right)^2 + \rho_{a1} g H_3 \quad \text{(A15)}$$

where $\dot{m}_a$ is the air mass flow rate through the tower and all loss coefficients are based on the frontal area of the heat exchanger and the mean density through it.

In determining the density after the heat exchanger, the specified pressure at ground level is employed in the perfect gas relation, i.e.,

$$\rho_{a4} = p_{a1} / RT_{a4} \quad \text{(A16)}$$

Furthermore, for all practical purposes

$$\rho_{a3} = \rho_{a1} = p_{a1} / RT_{a1} \quad \text{(A17)}$$

The mean density of the air flowing through the heat exchanger follows from

$$1/\rho_{a34} = 0.5\, (1/\rho_{a1} + 1/\rho_{a4}) = 0.5R(T_{a1} + T_{a4})/p_{a1} \quad \text{(A18)}$$

The loss coefficient through the tower supports K_{ts} is based on the drag coefficient for such bodies, i.e.,

$$C_{Dts} = 2F_{Dts} / \rho_{a1} v_{a2}^2 A_{ts} \quad \text{(A19)}$$

With equation (A19), the effective pressure drop across the tower supports is given by

$$\Delta p_{ats} = n_{ts} F_{Dts} / \pi\, d_3\, H_3 = 0.5\, \rho_{a1} v_{a2}^2\, C_{Dts}\, L_{ts} d_{ts} n_{ts} / \pi\, d_3 H_3 \quad \text{(A20)}$$

where L_{ts} is the support length and d_{ts} is its effective diameter or width, and n_{ts} is the number of tower supports. The corresponding loss coefficient based on the conditions at the tower supports 2 is

$$K_{ts} = 2\Delta p_{ats} / \rho_{a1} v_{a2}^2 = C_{dts}\, L_{ts}\, d_{ts}\, n_{ts} / \pi\, d_3\, H_3 \quad \text{(A21)}$$

For substitution in equation (A15), this loss coefficient is required to be based on conditions at the heat exchanger, i.e.,

$$K_{ts} = 2\Delta p_{ats} / \rho_{a34}\, (\dot{m}_a / A_{fr})^2 = \frac{C_{Dts}\, L_{ts}\, d_{ts}\, n_{ts}\, A_{fr}^2}{(\pi\, d_3\, H_3)^3} \left(\frac{\rho_{a34}}{\rho_{a1}} \right) \quad \text{(A22)}$$

It is assumed that the air density and velocity distribution through the supports are uniform.

Due to separation at the lower edge of the cooling tower shell and distorted inlet flow patterns, a cooling tower loss coefficient K_{ct3} based on the tower cross-sectional area 3 can be defined to take these effects into consideration. The cooling tower loss coefficient based on conditions at the heat exchanger is

$$K_{ct} = K_{ct3} \frac{\rho_{a34}}{\rho_{a1}} \left(\frac{A_{fr}}{A_3} \right)^2 \quad \text{(A23)}$$

where K_{ct3} may be approximated by (Geldenhuys and Kröger, 1986)

$$K_{ct3} = 0.072\, (d_3/H_3)^2 - 0.34\, d_3/H_3 + 1.7 \quad \text{(A24)}$$

Depending on the heat exchanger bundle arrangement in the cooling tower base, only a portion of the available area is effectively covered due to the rectangular shape of the bundles. This reduction in effective flow area results in contraction and subsequent expansion losses. These losses may be approximated by corresponding loss coefficients based on the effective reduced flow area A_{e3} (Kays, 1950)

$$K_{ctc3} = 1 - 2/\sigma_c + 1/\sigma_c^2 \quad \text{(A25)}$$

where σ_c is the jet contraction ratio and

$$K_{cte3} = (1 - A_{e3}/A_3)^2 \quad \text{(A26)}$$

The effective area A_{e3} corresponds to the frontal area of the heat exchanger bundles if they are installed horizontally. In the case of V arrays, A_{e3} corresponds to the projected frontal area of the bundles.

Based on the conditions at the heat exchanger, the above expressions become

$$K_{ctc} = (1 - 2/\sigma_c + 1/\sigma_c^2)\, (\rho_{a34}/\rho_{a1})\, (A_{fr}/A_{e3})^2 \quad \text{(A27)}$$

and

$$K_{cte} = (1 - A_{e3}/A_3)^2\, (\rho_{a34}/\rho_{a4})\, (A_{fr}/A_{e3})^2 \quad \text{(A28)}$$

Where the cooling air flows normally through a heat exchanger, the loss coefficient is readily expressed in terms of the Euler number, i.e.,

$$K_{he} = \frac{2}{\sigma^2} \left[\mathrm{Eu} + \frac{\rho_{a1} - \rho_{a4}}{\rho_{a1} + \rho_{a4}} \right] \quad \text{(A29)}$$

where according to Robinson and Briggs (1965)

$$\mathrm{Eu} = \frac{18.93\, n_{tr}}{\mathrm{Re}_a^{0.316}} \left(\frac{d_r}{P_l} \right)^{0.927} \left(\frac{P_t}{P_d} \right)^{0.515} \quad \text{(A30)}$$

If the flow approaches and leaves the heat exchanger obliquely, as is the case for an array of V bundles, the following relation holds (Kotzé et al., 1986):

$$K_{he\theta} = K_{he} + \frac{\rho_{a34}}{\rho_{a1}} \left(\frac{1}{\sin \theta_m} - 1 \right) \left[\left(\frac{1}{\sin \theta_m} - 1 \right) + 2\, K_c^{0.5} \right] + \frac{\rho_{a34}}{\rho_{a4}} K_d \quad \text{(A31)}$$

where

$$\theta_m = 0.0019\theta^2 + 0.9133\theta - 3.1558$$

$$K_d = \exp (5.488405 - 0.2131209\theta + 3.533265 \times 10^{-3}\theta^2 - 0.2901016 \times 10^{-4}\, \theta^3)$$

and

$$K_c = 0.05$$

After the heat exchanger, the flow through the tower is essentially isentropic. The change in total pressure between sections 4 and 5 in the tower is thus

$$(p_{a4} + 0.5\rho_{a4} v_{a4}^2) - (p_{a5} + 0.5\rho_{a5} v_{a5}^2) = \rho_{a45} g(H_5 - H_3) \quad \text{(A32)}$$

where it is assumed that $H_4 \approx H_3$ for a relatively thin heat exchanger. The temperature at the tower outlet is

$$T_{a5} = T_{a4} + [0.5(v_{a4}^2 - v_{a5}^2) + g(H_3 - H_5)]/c_{pa} \quad \text{(A33)}$$

From the perfect gas relation it thus follows that for $p_{a5} = p_{a6}$ the density at the outlet of the tower is

$$\rho_{a5} = p_{a6}/R[T_{a4} + 0.5(v_{a4}^2 - v_{a5}^2)/c_{pa} + g(H_3 - H_5)/c_{pa}] \quad \text{(A34)}$$

where p_{a6} is obtained from equation (A14).

In most practical towers, the change in kinetic energy between sections 4 and 5 is normally approximately an order of magnitude smaller than the corresponding change in potential energy. Equation (A34) may thus be simplified:

$$\rho_{a5} \approx p_{a6}/R[T_{a4} + g(H_3 - H_5)/c_{pa}] = p_{a6}/R\,[T_{a4} - 0.00975\,(H_5 - H_3)] \quad \text{(A35)}$$

The mean density in the tower between 4 and 5 is

$$\rho_{a45} \approx 0.5(\rho_{a4} + \rho_{a5}) \quad \text{(A36)}$$

The change in pressure through the cooling tower is obtained by adding equations (A15) and (A32):

$$p_{a1} - p_{a5} = (K_{ts} + K_{ct} + K_{ctc} + K_{heo} + K_{cte})_{he} \frac{1}{2\rho_{a34}} \left(\frac{\dot{m}_a}{A_{fr}}\right)^2 + \rho_{a1} gH_3 + \rho_{a45} g(H_5 - H_3) + \rho_{a5} v_{a5}^2/2 \quad \text{(A37)}$$

From continuity it follows that

$$v_{a5} = \dot{m}_a/\rho_{a5} A_5 \quad \text{(A38)}$$

Since $p_{a1} - p_{a6} = p_{a1} - p_{a5}$, equations (A14) and (A37) can be equated to give with equation (A38)

$$p_{a1}\,[1 - (1 - 0.0065\,H_5/T_{a1})^{5.25}] = (K_{ts} + K_{ct} + K_{ctc} + K_{heo} + K_{cte})_{he} \frac{1}{2\rho_{a34}} \left(\frac{\dot{m}_a}{A_{fr}}\right)^2 + 9.8[\rho_{a1} H_3 + \rho_{a45}\,(H_5 - H_3)] + \frac{1}{2\rho_{a5}} \left(\frac{\dot{m}_a}{A_5}\right)^2 \quad \text{(A39)}$$

This expression is known as the draft equation for natural draft cooling towers.

APPENDIX B

A cooling system, as shown schematically in Fig. A1 is designed to reject $Q_{ct} = 329.06$ MW heat at an ambient air pressure of $p_a = 84{,}600$ N/m^2 and a temperature of $T_{a1} = 15.6$°C. The cooling tower inlet water temperature is $T_{wi} = 61.45$°C and the flow rate is $\dot{m}_w = 4390$ kg/s.

The proposed cooling tower is $H_5 = 120$ m high and has an inlet height of $H_3 = 13.67$ m. Its outlet diameter is $d_5 = 58$ m and the inlet diameter is $d_3 = 82.958$ m. There are a total of $n_{ts} = 60$ tower supports, each $L_{ts} = 15.78$ m long with an effective diameter of $d_{ts} = 0.5$ m. The drag coefficient of each support is $C_{Dts} = 2$.

Extruded bimetallic finned tubes as shown in Fig. A2(a) are employed. The steel core tube has an inside diameter of $d_i = 22.09$ mm and an outside diameter of $d_o = 25.4$ mm. The aluminum fins have a diameter of $d_f = 57.2$ mm with a root diameter of $d_r = 27.6$ mm, a mean thickness of $t_f = 0.5$ mm and a pitch of $P_f = 2.8$ mm. The density of the steel core tube is $\rho_t = 7850$ kg/m^3 and its thermal conductivity is $k_t = 50$ W/m K. The aluminum fins have a density of $\rho_f = 2707$ kg/m^3 and a thermal conductivity of $k_f = 204$ W/m K.

The finned tubes are assembled in the form of heat exchanger bundles, each $L_t = 15$ m long and $W_b = 2.262$ m wide. Each bundle contains $n_{tb} = 154$ finned tubes arranged on a triangular pitch with $P_t = 58$ mm and $P_l = 50.2$ mm. There are $n_{tr} = 4$ tube rows with $n_{t/r} = 39$ tubes per row and $n_{wp} = 2$ water passes. The bundles are arranged in the form of A frames or V arrays as shown in Fig. A2(b). The semi-apex angle of each A frame is $\theta = 30.75$ deg and there are a total of $n_b = 142$ bundles arranged in this manner.

For this particular design the overall thermal conductance of the surface steam condenser is given as $UA_{con} = 3.30 \times 10^7$ W/K. This value is retained as a constant in the optimization process. In view of the fact that the cost of the condenser is usually small when compared to that of the dry cooling tower, this assumption is not unreasonable.

APPENDIX C

The annual operating cost of a natural draft cooling tower may be approximated by the equation

$$C = C_{\text{pump}} + \frac{i(1+i)^n}{(1+i)^n - 1}\,[C_{ct} + C_{he} + C_p]\ \$/\text{annum} \quad \text{(C1)}$$

where the first term represents annual pumping costs and the second term the annual capital repayment over n years at an interest rate i.

The annual cost of the water pumping power is

$$C_{\text{pump}} = 4.33\ C_e\ \tau\ P_w \quad \text{(C2)}$$

where P_w is given by equation (A10) and the constant 4.33 is a factor to account for additional circuit pressure drops and pump and motor efficiencies.

If the cooling tower shell is approximated by a conical frustrum, its construction cost may be expressed as

$$C_{ct} = \frac{\pi}{2} C_s\,(d_3 + d_5)\,[(H_5 - H_3)^2 + (d_3 - d_5)^2]^{0.5} \quad \text{(C3)}$$

The cost of the heat exchangers is modeled by

$$C_{he} = n_{tb}\, n_b\, L_t\,[C_{wf}\,(C_t + C_f) + C_{\text{fix}}] \quad \text{(C4)}$$

where the cost of the tubes and the fins per unit length of tube are, respectively,

$$C_t = \pi\,\rho_t\,C_{tm}\,(d_o^2 - d_i^2)/4 \quad \text{(C5)}$$

and

$$C_f = \pi\,\rho_f C_{fm}\,[(d_f^2 - d_r^2)t_f + (d_r^2 - d_o^2)\,(P_f - t_f)]/4P_f \quad \text{(C6)}$$

A weighting factor C_{wf} and fixed cost factor C_{fix} take into consideration labor and related costs.

The capitalized cost of the water pump and piping is approximated by

$$C_p = 0.02\,(C_{ct} + C_{he}) \quad \text{(C7)}$$

It is emphasized that the cost equations given above are an attempt to model the annual cost of a specific cooling tower and are not meant to be generally applicable. For the case study discussed in the main body of the paper, the following values were assumed:

Interest on capital $i = 0.1$, repayment period $n = 30$ years, electricity cost $C_e = 5$ c/kWh, tower shell construction cost $C_s = \$100/\text{m}^2$, weighting factor $C_{wf} = 2$ and $C_{\text{fix}} = \$2$/m, price of steel for tubes $C_{tm} = \$0.8$/kg, and price of aluminum for fins $C_{fm} = \$4.2$/kg. The tower is operational for $\tau = 6570$ hours/annum and to simplify the analysis it is assumed that steam and ambient air temperatures remain unchanged.

Two-Dimensional Effects on the Response of Packed Bed Regenerators

J. A. Khan

D. E. Beasley

Thermal-Fluid Sciences Research Laboratory,
Department of Mechanical Engineering,
Clemson University,
Clemson, SC 29634

Packed beds have a wide range of applications as heat transfer and energy storage devices. Employed as a regenerator, a packed bed is subject to the flow of a heat transfer fluid, which alternately stores and recovers energy from a packing of discrete particles. The flow direction reverses during the addition and removal of energy. The nature of a packing of discrete particles in a container is such that variations in the resistance to flow and in the void fraction occur across the cross section of the packing. Particularly, the region of the bed near the boundary of the container has a markedly reduced resistance to flow. In addition, the wall effect on the packing geometry changes the void fraction in the near-wall region. The purpose of the present study is to quantify the two-dimensional effects of nonuniform void fraction, velocity, and temperature distributions in a packed bed regenerator on the dynamic and steady periodic behavior. A two-dimensional numerical model of the transient response of a packed bed subject to the flow of a heat transfer fluid has been developed and verified through comparison with measured responses. The model includes the effects of nonuniform velocity and porosity in the bed, and the effects of axial and radial thermal dispersion. The results of the present computations are compared with one-dimensional transient periodic results to demonstrate the two-dimensional effects on the transient response of a packed bed regenerator to a step change in fluid temperature. The classical dimensionless parameters, such as reduced length and reduced time, are not sufficient to characterize the two-dimensional transient nature of a packed bed regenerator. This study identifies the range of bed-to-particle-diameter ratios over which the transient response is significantly influenced by the wall effect on void fraction and flow.

Introduction

A thermal regenerator is an energy recovery heat exchanger used to transfer energy between two fluid streams by temporarily storing energy from the high-temperature fluid stream in a permeable packing, and subsequently recovering this stored energy. The two primary forms of regenerators are the rotary regenerator and the packed bed regenerator. The focus of this study will be the packed bed regenerator. Packed beds have a wide variety of applications as heat transfer and energy storage devices. Packed bed regenerators are primarily employed for high-temperature applications or in cases where there are significant pressure differences between the hot and cold fluid streams. The geometry considered in this study is a cylindrical container randomly packed with uniform, spherical particles. The cycle of operation consists of a heating period and a cooling period. During the heating period, the cycle time and the energy storage capacity of the permeable packing are chosen to optimize the total energy recovery, or to meet a specific process demand. During the cooling period, cool fluid recovers the energy that was stored in the matrix during the heating period; the flow during the cooling period is in the opposite direction to that during the heating period. The operation is cyclic, between the heating and cooling periods, with accompanying flow reversals.

The purpose of the present study is to quantify the two-dimensional effects due to nonuniform velocity and void fraction distributions in a packed bed regenerator, and to describe the effect of container-to-particle-diameter ratio on the average void fraction and the void fraction distribution and velocity distribution within the packed bed. In applications where there exist variations in the thermal loads, the transient response characteristics of a regenerator become important to its design and to the control of the process. A two-dimensional numerical model of the transient response of a packed bed subject to the flow of a heat transfer fluid has been previously developed for the purpose of describing the dynamic response of a packed bed for thermal energy storage during both charging and recovery modes of operation (Beasley and Clark, 1984). The primary emphasis was for solar thermal system applications. The present study applies an extended modeling effort to the case of the packed bed regenerator. The model proposed in this study is not limited to any particular set of flow conditions, or boundary conditions. However, to provide a reasonable scope for the present study, the case of a symmetric, balanced regenerator is considered. The objectives of the present study were to determine the range of bed-to-particle-diameter ratios for which two-dimensional effects are important, to quantify these two-dimensional effects on the transient and steady periodic response, and to examine the effect of the thermal capacitance and longitudinal conduction effects of the wall of the regenerator.

Background

Regenerators. Numerous previous studies have yielded both analytical and numerical solutions for the steady periodic and transient responses of regenerators. London et al. (1964) examined the dynamic characteristics of a counterflow gas turbine regenerator subject to a step change in one of the inlet fluid temperatures. A dimensional analysis for the general one-dimensional case is presented; the study includes both direct transfer and periodic flow regenerators. Resulting from this study is a set of nondimensional parameters, which provide

Contributed by the Heat Transfer Division and presented at the 24th National Heat Transfer Conference, Pittsburgh, Pennsylvania, August 9–12, 1987. Manuscript received by the Heat Transfer Division June 26, 1987. Keywords: Heat Exchangers, Heat Recovery, Packed and Fluidized Beds.

for a generalized one-dimensional description of a regenerator. Dunkle and Ellul (1972) applied relationships for heat transfer and fluid flow to regenerators, thermal storage beds, and evaporative coolers. Computational solutions are presented for the design of these devices in the steady periodic regime. Wilmott (1964) and Wilmott and Burns (1977) employed a computational method to derive the transient response of a periodic-flow regenerator. The study presents the responses of a regenerator to a step change in one of the fluid temperatures from a steady-periodic condition to a new steady-periodic condition. The results are presented in a nondimensional form, as derived by London et al. (1964).

Recent studies have addressed several particular aspects of the steady periodic regenerator problem. Heggs and Mitchell (1983) presented a method for predicting the effectiveness of asymmetric-unbalanced regenerators. Baclic (1983) uses the Galerkin method to solve the case of a symmetric and balanced counterflow regenerator. The method leads to an explicit statement for the regenerator effectiveness. Recently, Connor and Chiang (1986) presented results for a periodic storage heat exchanger that consisted of a series of flow channels separated by the energy storage material. The steady fluid outlet temperatures and heat transfer rates are presented.

Radial Variations in Packed Beds. Previous models of the dynamic response of packed bed regenerators have assumed the void, velocity, and transport coefficients to be uniform across the cross section of the packing. However, measurements indicate that the void fraction ϵ and the azimuthally averaged fluid velocity have significant radial variations. Cylindrical and rectangular beds randomly packed with uniform spheres display damped oscillatory variations of ϵ with radius

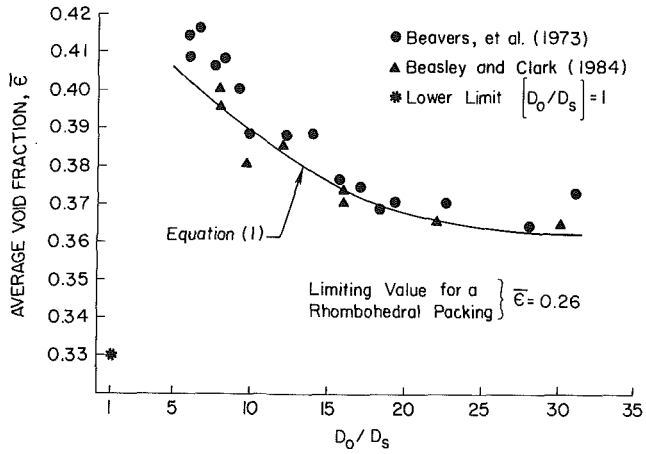

Fig. 1 Average void fraction as a function of bed-to-particle-diameter ratio for a randomly packed bed of uniform spheres

for approximately five particle diameters from a wall (Benenati and Brosilow, 1962). The difference in the radius of curvature of the wall and of the spheres that form the packing causes the void fraction to be 1.0 at the wall, and introduces local order into the otherwise random packing.

The mean void fraction $\bar{\epsilon}$ for a packed bed is a function of the bed-to-particle-diameter ratio, D_o/D_s, as shown in Fig. 1. The variation of $\bar{\epsilon}$ with D_o/D_s for a randomly packed bed of uniform spheres is derived from the data of Beavers et al. (1973) and Beasley and Clark (1984), and may be described by the following equation for $D_o/D_s < 28$:

Nomenclature

a = interphase surface area per unit volume = $6(1-\epsilon)/D_s$
A = $u\Delta t/(2\,\Delta x)$
A_b = interphase surface area of the bed = $A_c L_b a$
A_c = cross-sectional area of the bed
A_w^i = inner wall surface area
A_w^o = outer wall surface area
B = $\kappa\,\Delta t$
c = fluid heat capacity
c_s = solid heat capacity
C = $\Delta t\kappa/[(1 + \gamma\Delta t)\Delta x]$
C_o = proportionality constant, turbulent dispersion contribution to effective conductivity
D = $\kappa\gamma(\Delta t)^2/(1 + \gamma\,\Delta t)$
D_s = particle diameter
E = $1.0 + B - D + 2L + 2N$
h = interphase heat transfer coefficient
h = interphase heat transfer coefficient
h_w = wall heat transfer coefficient
$\bar{h}$ = bulk heat transfer coefficient
k_w = wall thermal conductivity
k_e^R = radial effective thermal conductivity
k_e^x = axial effective thermal conductivity
L = $k_e^R\,\Delta t/[\rho c\ (\Delta R_i)^2]$
L_b = bed length
m = mass of gas resident in the regenerator
$\dot{m}_f$ = flow rate of fluid
M = $k_e^R\,\Delta t/(2\rho c R_i^* \Delta R_i)$
n = number of axial nodes
N = $k_e^x\,\Delta t/[\rho c(\Delta x)^2]$
Nu = Nusselt number = hD_s/k
P = pressure
Pe_o = superficial Peclet number = $\rho c u_o L/k_f$
Pe_i = $\rho c u_o L/k_e^i$
R = radial direction coordinate
R_i^* = radius of node i
ΔR_i = radial increment i
Re_o = superficial Reynolds number = $u_o\,D_s/\nu$
t = time
t_o = period
Δt = time step size
T = fluid temperature
T_∞ = ambient temperature
u = interstitial fluid velocity = u_o/ϵ
u_o = superficial velocity
U_∞ = overall loss coefficient for the wall
x = axial direction coordinate
Δx = axial spatial increment
γ = $6h/\rho_s c_s D_s$
ϵ = local void fraction
$\bar{\epsilon}$ = average void fraction
$\epsilon_{g1}, \epsilon_{g2}$ = dimensionless measure of transient response-fixed bed regenerator, defined by equations (14) and (15)
η = dimensionless time, defined by equation (11)
κ = $ha/\rho c\epsilon$
λ = reduced length, defined by equation (12)
μ = dynamic viscosity
ν = kinematic viscosity
ξ = dimensionless length, defined by equation (10)
ρ = fluid density
ρ_s = solid density
ρ_w = wall density
π = reduced period, defined by equation (13)
χ = solid temperature
ψ = wall temperature

Subscripts

out = outlet

Superscripts

$'$ = refers to hot period
$''$ = refers to cold period
(n) = refers to cycle number n
(o) = refers to cyclic equilibrium prior to step change
(∞) = refers to cyclic equilibrium after step change

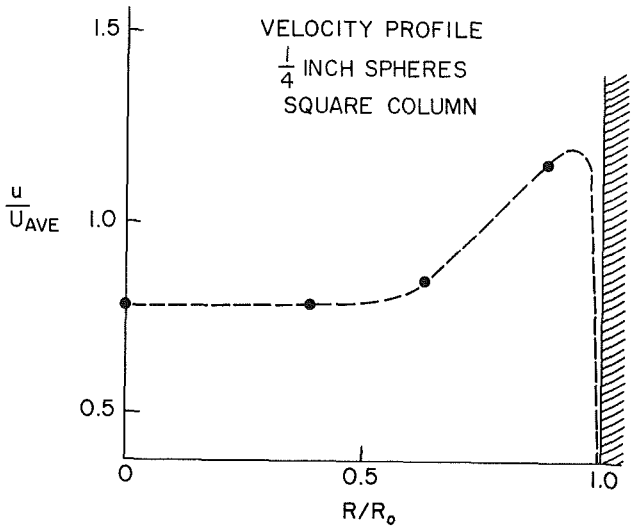

Fig. 2 Velocity profile for a randomly packed bed of uniform spheres

$$\epsilon = 0.4272 - 4.516 \times 10^{-3}(D_o/D_s) + 7.881 \times 10^{-5}(D_o/D_s)^2 \quad (1)$$

For values of $D_o/D_s > 28$ the void fraction is 0.3625.

Measurements of velocity profiles in randomly packed beds of uniform spheres by Schwartz and Smith (1953) and other researchers show preferential flow in the near-wall region. Observations of the velocity profile at the exit of a 10.2 cm (4 in.) square column packed with 0.635 cm (0.25 in.) diameter uniform spheres by Newell and Standish (1973) demonstrate the variations of velocity with radial location, as shown in Fig. 2. In addition, the momentum transfer associated with wall-fluid interaction is different from that associated with the matrix of spheres in the interior of the bed. Mickley et al. (1965) have shown that even if a constant void fraction exists across the cross section there is still less resistance to flow in the near-wall region. These effects indicate that at least a two-dimensional model of the temperature distribution in a packed bed is necessary for a complete description of the dynamic thermal response of the bed.

Thermal Dispersion. Thermal dispersion is a term used to describe the transport of energy in a porous medium due to conduction through the matrix of solid and fluid, finite interphase heat transfer rates, turbulent dispersion in the fluid phase, and temperature gradients within the particles themselves. Consider a step change in inlet temperature for a one-dimensional flow through a porous medium at a uniform initial temperature. With no thermal dispersion, the thermal wave would progress through the medium as a square wave. Thermal dispersion causes a broadening of the thermocline in any real system as the thermal wave progresses. For the present case of an axisymmetric geometry, the thermal dispersion is quantitatively described by the axial and radial effective thermal conductivities, and the solid to fluid (interphase) heat transfer coefficient. The appropriate description of both axial and radial thermal dispersion has been the subject of much previous research, primarily in association with packed bed chemical reactors (Green et al., 1964; Chandresakara et al., 1980). The primary controlling factor for gas/solid systems at typical gas flow rates is the interphase heat transfer coefficient; however, at low Peclet numbers and for systems where the ratio of the solid to fluid heat capacity is small, the effects of axial conduction and turbulent dispersion through the porous matrix may become significant. Recently, a model of the transient response of a randomly packed bed of uniform spheres was developed that included the effects of both axial and radial thermal dispersion (Beasley and Clark, 1984).

In cases where the intraparticle temperature distribution effects are significant, Bradshaw et al. (1970) demonstrated that the rate of heat transfer from the solid to the fluid could be properly described by modifying the magnitude of the interphase heat transfer coefficient. The heat transfer coefficient is determined as a function of the particle Biot number, providing a correction for the deviation of the surface temperature away from the lumped thermal capacitance value for the particle. Clearly, intraparticle temperature gradients result in elevated particle surface temperatures and therefore reduce the effective heat transfer coefficient. For the present study, particle sizes and fluid flow rates were chosen so that no correction to the heat transfer coefficient was necessary.

Analysis and Modeling

To determine the two-dimensional effects on regenerator response, an accurate model of the transient temperature variations in the axial and radial directions during charging and recovery is required. The two-dimensional computational model of a regenerator used in this study is an extension of an existing heat transfer model, as developed by Beasley and Clark (1984). The model employs appropriately averaged governing equations for the fluid and solid phases, and the wall of the container; these equations and a brief mathematical description of the model are provided in the Appendix. The effects of axial and radial thermal dispersion, and energy losses at the wall are included in the model. Provisions for flow reversal at the end of each regenerator cycle are provided by a change in the origin of the axial coordinate, and restructuring of the coefficient matrix resulting from the finite-difference equations. These equations are solved using a fully implicit scheme. The integral form of the governing equations requires empirical inputs in the form of the heat transfer coefficient and the effective thermal conductivities of the porous matrix.

The validity of the model and the computational routine was demonstrated by comparison with other models in one dimension, through computational experiment, including energy balances, and through comparison with comprehensive experimental measurements in packed beds. This computational model has previously been demonstrated to compare favorably with measured data documenting the two-dimensional aspects of cylindrical beds randomly packed with uniform spheres, subject to a time varying inlet fluid temperature. Examples of measured and computed temperature distributions will be presented that clearly demonstrate the two-dimensional aspects of packed bed response.

Results

Two-dimensional effects on the dynamic response of packed beds are the result of the nonuniformity of flow across the cross section, combined with the increased average void fraction in the near wall region and the wall effect, including energy losses. To demonstrate these effects, results from previous comparisons between the present model and experimental results will be presented. Figure 3 is the transient response of a packed bed subject to a step change in inlet fluid temperature as measured by Vanden Broek and Clark (1980–1982). This bed was comprised of steel spheres having a diameter of 5.6 mm. The bed diameter was 80 mm, and the heat transfer fluid was air. The bed had an extremely thin PVC wall, which was insulated so that the thermal wall effect was very small, as evidenced by the rapid rise in the solid temperatures at the wall. The increased flow in the near wall region causes the solid temperature in this region to rise more quickly than the solid temperature in the central region of the bed. As a steady condition is approached, the temperatures of the particles at the wall become lower than those at the center due to energy

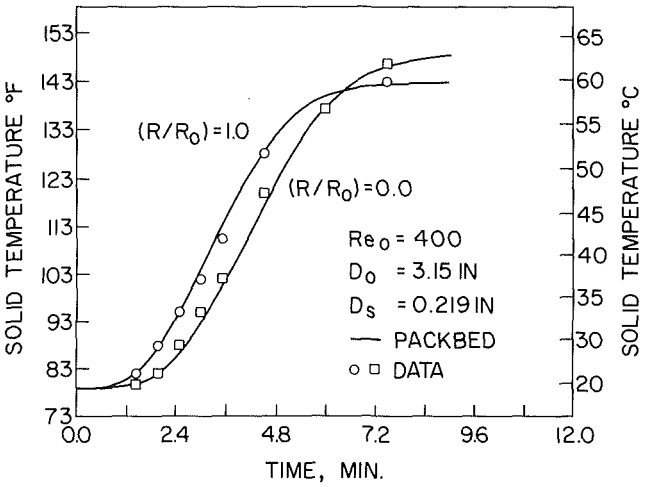

Fig. 3 Measured and computed solid temperature response for the bed of Vanden Broek and Clark, $\epsilon = 0.368$; void fraction variation: $(R/R_o) < 0.86$, $\epsilon = 0.35$; $0.86 < (R/R_o) < 1.0$, $\epsilon = 0.42$

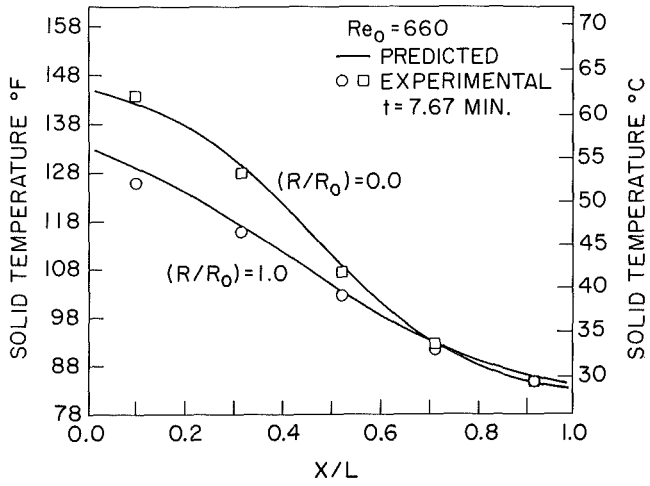

Fig. 4 Measured and computed solid temperature dynamic response for a randomly packed bed of uniform spheres having significant thermal wall effects

losses through the wall. The form of the present model employed to predict the temperature distributions in packed beds incorporates the effects of losses through the wall and the wall thermal capacitance. Figure 4 shows the transient response of a packed bed of uniform spheres where the wall has a significant effect due to its heat capacity, and due to the longitudinal conduction of energy in the wall. This bed was 38.1 cm in diameter, with a steel wall of thickness 0.3175 cm. It is evident from a comparison of Figs. 3 and 4 that the thermal capacitance, longitudinal conduction, and energy losses associated with the wall can significantly affect the dynamic thermal response in the near wall region. However, the predictions of the present computational model compare favorably with these experimental results. Further comparisons between the model predictions and measured temperature distributions from a number of packed beds may be found in Beasley and Clark (1984) and Beasley (1983).

The transient response of the packed bed regenerator can be characterized using the nondimensional measures of length and time, ξ and η, respectively. The dimensionless length is defined as

$$\xi = \frac{\bar{h}A_b x}{\dot{m}_f c L_b} \tag{2}$$

and the dimensionless time is defined by

$$\eta = \frac{\bar{h}A_b\left[t - \dfrac{mx}{\dot{m}_f L_b}\right]}{A_c(1-\epsilon)\rho_s c_s L_b} \tag{3}$$

From these dimensionless independent variables, parameters describing the heating and cooling periods can be derived. The reduced length is defined as

$$\lambda = \frac{\bar{h}A_b}{\dot{m}_f c} \tag{4}$$

and the reduced period as

$$\Pi = \frac{\bar{h}A_b\left(t_o - \dfrac{m}{\dot{m}_f}\right)}{A_c(1-\epsilon)\rho_s c_s L_b} \tag{5}$$

A parameter describing the transient response must also be defined; Willmott and Burns (1977) discuss the nature of the averaging process necessary to describe the transient response of a packed bed regenerator. The response of the regenerator is measured in terms of the chronologically and spatially averaged exit fluid temperature. For the period in which the step

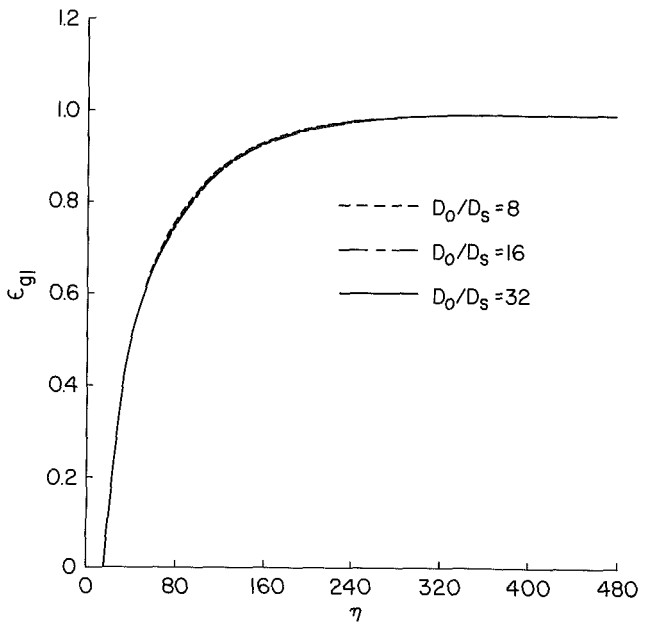

Fig. 5 One-dimensional model predictions for the transient response of a packed bed regenerator with $\lambda = 28$ and $\pi = 16$

change occurs, in this case the heating period, the parameter is $\epsilon_{gl}^{(n)}$, defined as

$$\epsilon_{gl}^{(n)} = \frac{T'^{(n)}_{out} - T'^{(o)}_{out}}{T'^{(\infty)}_{out} - T'^{(o)}_{out}} \tag{6}$$

For the cooling period, or the period for which no change in boundary condition occurs, the parameter is denoted as $\epsilon_{g2}^{(n)}$, defined as

$$\epsilon_{g2}^{(n)} = \frac{T''^{(n)}_{out} - T''^{(o)}_{out}}{T''^{(\infty)}_{out} - T''^{(o)}_{out}} \tag{7}$$

For this study, the regenerator is assumed to be constructed by randomly packing uniform spheres into a container. As previously stated, the value of D_o/D_s determines the average void fraction in the packing. The computational scheme is employed to determine the transient response of a particular packed bed regenerator, and the results nondimensionalized as described above. The working fluid had the properties of air, and the solid matrix properties were varied to achieve the

Table 1 Input parameters for the computational model

	D_o/D_s		
	8	16	32
Bed length, cm	60.96	60.96	60.96
Particle diameter, mm	12.7	12.7	12.7
Particle density, kg/m³	5899.4	6307.9	6550.0
Particle specific heat, kJ/kg°C	1.047	1.047	1.047
Fluid flow rate, $m^3/s \times 10^3$	6.19	27.4	115.8
Fluid density, kg/m³	1.18	1.18	1.18
Fluid viscosity, $kg/ms \times 10^5$	1.952	1.952	1.952
Fluid thermal conductivity, W/m°C	0.028	0.028	0.028
Fluid specific heat, kJ/kg°C	1.009	1.009	1.009
Fluid Prandtl number	0.7	0.7	0.7
Period, min	24.0	24.0	24.0
Average void fraction	0.396	0.375	0.636
Void fraction (central region)	0.3775	0.3634	0.3561
Void fraction (wall region)	0.46	0.46	0.46

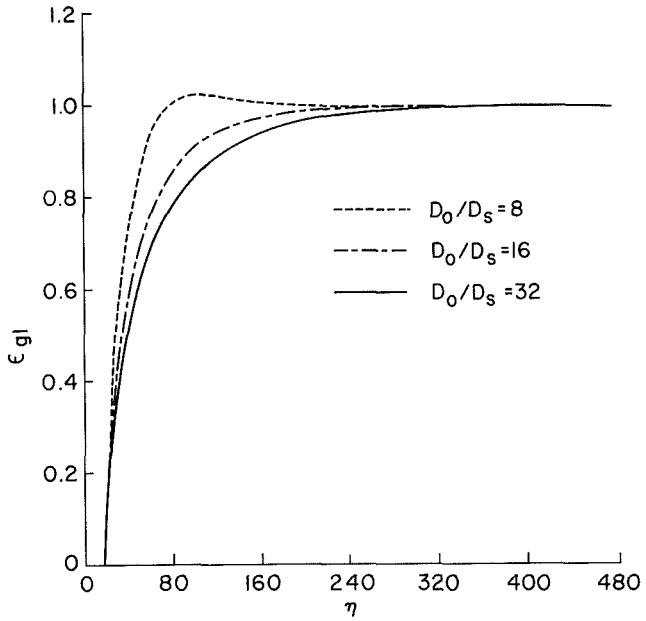

Fig. 6 Two-dimensional model predictions for the transient response of a packed bed regenerator with $\lambda = 28$ and $\pi = 16$

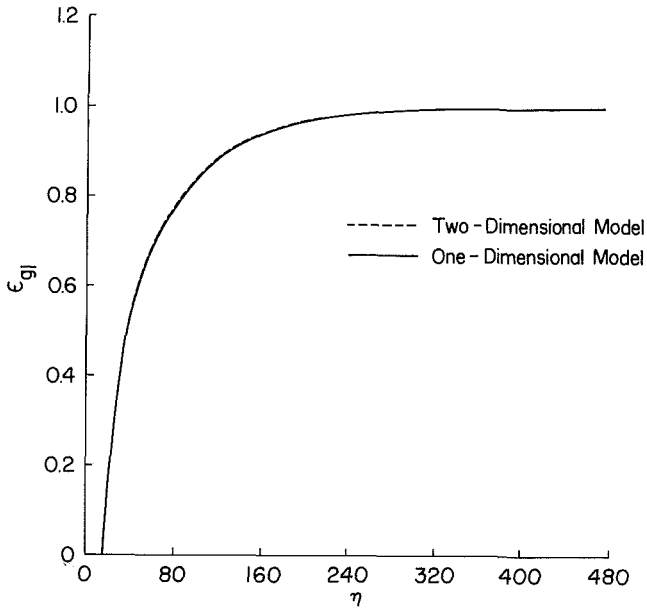

Fig. 7 Comparison of one-dimensional and two-dimensional response of a packed bed regenerator with $D_o/D_s = 32$, $\lambda = 28$, and $\pi = 16$

desired nondimensional parameters. The computational model can be reduced to a one-dimensional form having a uniform void fraction and velocity distribution. Figure 5 is a plot of the transient response of a regenerator as computed using a one-dimensional model of the transient response, for a reduced period of 16 and a reduced length of 28. The effect of D_o/D_s in the one-dimensional case is to change the value of the average void fraction in the bed. It is clear that the nondimensional parameters as used by Willmott and Burns (1977) are appropriate for the description of the one-dimensional transient response, even in cases where the average void fraction varies with D_o/D_s.

Figure 6 is a plot of the response for the same reduced length, reduced period, and average void fractions as in Fig. 5, but employing the two-dimensional model of the regenerator. The input parameters for this physical system are provided in Table 1. A two-region model is adopted for the void fraction variation in a cylindrical bed packed with uniform spheres. Such a model has previously been successfully employed to predict temperature distributions in packed beds. For this case a region extending inward from the wall to $D_s/2$ has an elevated void fraction, while the remainder of the bed has a uniform void fraction. The wall region void fraction is held constant, and the void fraction in the central region varied to yield the appropriate average value, given by equation (1). Here, the effect of the flow maldistribution, with flow bypassing in the near wall region, is evident at the bed-to-particle diameter ratio is reduced. Typically, the two-dimensional effects in packed beds are considered negligible for $D_o/D_s > 30$. The plot shows values of the response parameter greater than 1 for $D_o/D_s = 8$ at early times. This behavior is a result of the flow's bypassing the central region of the bed immediately after the step change is applied. Clearly, the effect of the two-dimensional nature of the bed is to increase the rate at which the bed responds. It is expected that the two-dimensional effects on the response of the bed would be very small as D_o/D_s is increased to values greater than 30. Figure 7 confirms that the one-dimensional and two-dimensional solutions collapse to the same result at a value of $D_o/D_s = 32$.

The steady-periodic response of a packed bed regenerator by definition reaches a value of $\epsilon_{g1} = 1.0$. Therefore, other variables must be examined to determine the results of radial variations in flow and void fraction. During charging of the regenerator, flow by passing in the near-wall region causes a different response in this region of the bed. Figures 3 and 4, for a step-change inlet fluid temperature and a uniform initial condition, show quite different response characteristics in the central and near-wall regions, demonstrating that temperatures are not uniform radially. If no rise in the exit fluid temperature occurs during charging, the only two-dimensional effect would be the radial variation in temperature; the total energy storage would not be affected. These radial temperature variations in

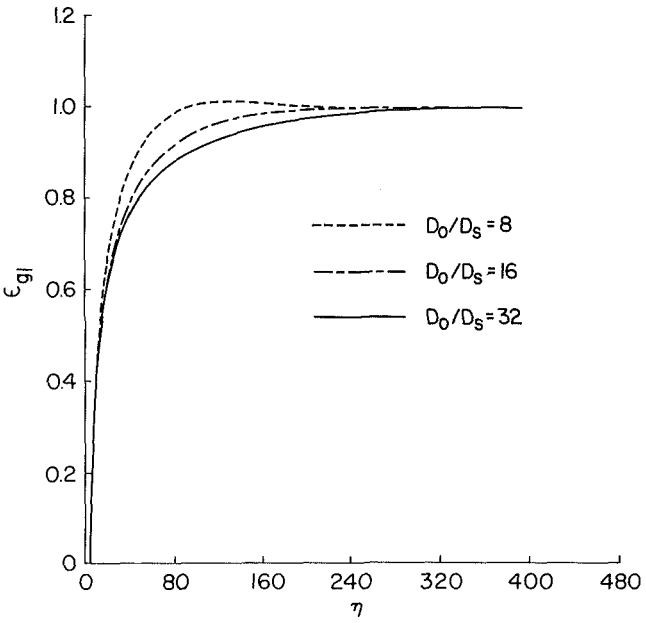

Fig. 8 Two-dimensional model predictions for the transient response of a packed bed regenerator with $\lambda = 28$ and $\pi = 4$

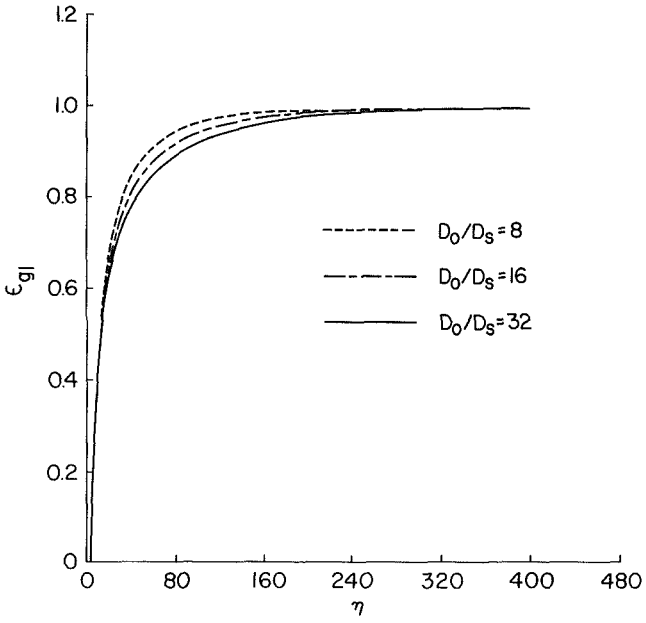

Fig. 10 One-Dimensional transient response of a packed bed regenerator with a 3.2-mm-thick steel wall, $\lambda = 28$ and $\pi = 4$

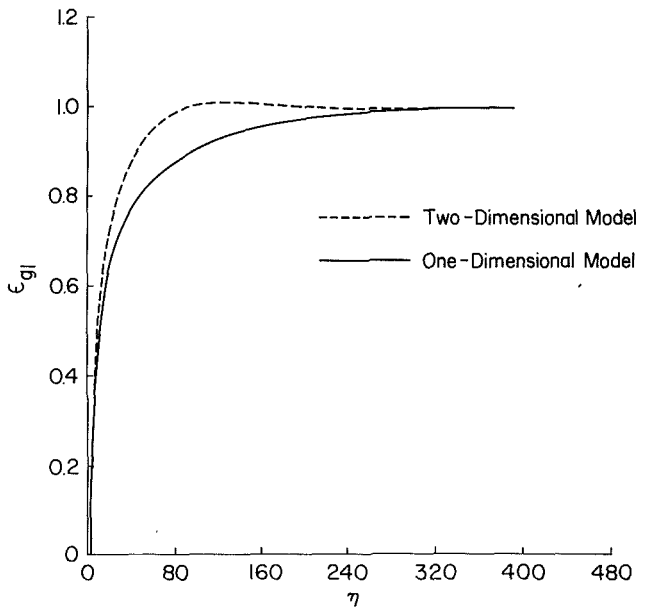

Fig. 9 Comparison of one-dimensional and two-dimensional response of a packed bed with $D_o/D_s = 8$, $\lambda = 28$, and $\pi = 4$

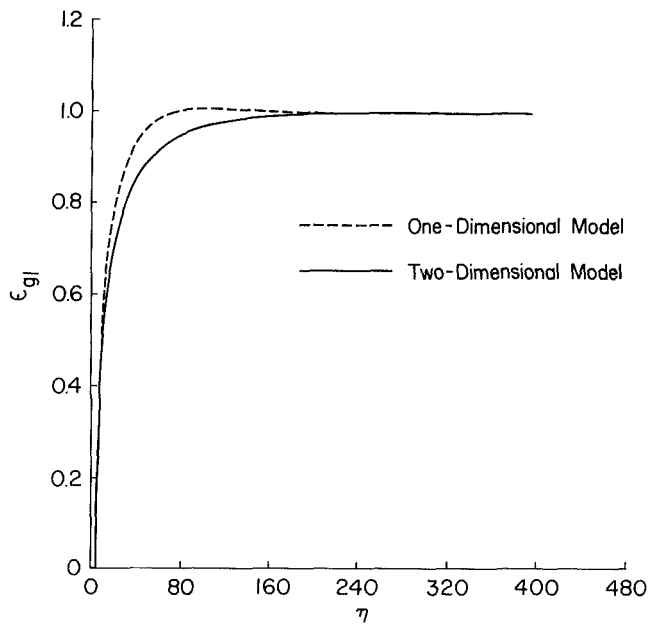

Fig. 11 Comparison of one-dimensional and two-dimensional response of a packed bed regenerator with a 3.2-mm-thick steel wall, $D_o/D_s = 8$, $\lambda = 28$, and $\pi = 4$

the bed would not affect the mixed mean exit temperatures of the regenerator during recovery, but may cause a radial variation in exit fluid temperature. It should be noted that the thermal capacitance of the wall may offset some of the effects of increased flow in the near-wall region. In Fig. 4, the thermal effects of the wall cause the temperature to be lower at the wall, even though there is a significantly higher flow rate of fluid in this region.

Figure 8 is a plot of the response for the two-dimensional case with a reduced period of 4 and a reduced length of 28. For comparison with Fig. 6, smaller values of reduced period may be interpreted as a reduction in the cycle time for a given regenerator. For reduced heating times, the thermal wave created at the inlet does not penetrate as far through the bed, and the flow bypassing is of less consequence. For example, if there were no rise in exit fluid temperature during the heating period, there could be no two-dimensional effect. This might correspond to a very short cycle time, or a very long regenerator.

Figure 9 is a comparison of the one-dimensional and two-dimensional response of a particular regenerator for $D_o/D_s = 8$. Again the effect of flow bypassing is to increase the response rate for a particular bed-to-particle-diameter ratio. The magnitude of the difference between the two cases will decrease with increasing D_o/D_s.

An additional effect on regenerator response results from the thermal capacitance and the longitudinal conduction in a bounding wall. A complete model of the coupled heat transfer between a packed bed and the wall of the container is described in Beasley and Clark (1984). Figure 10 is a plot of the one-dimensional response for a regenerator having a steel wall 3.2

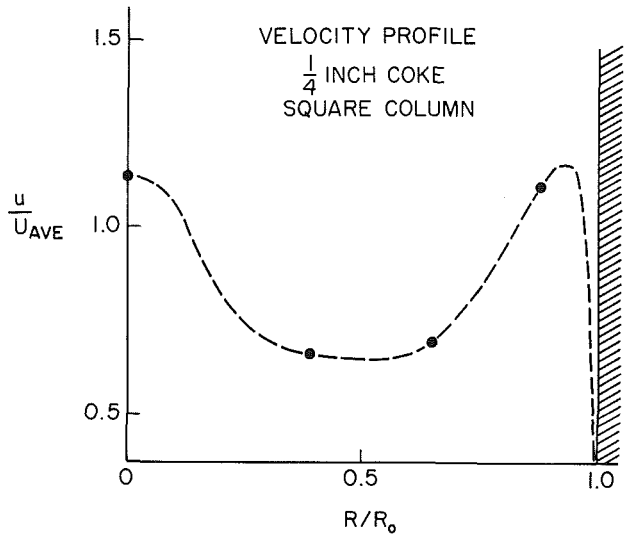

Fig. 12 Velocity profile for randomly shaped and sized particles in a square container

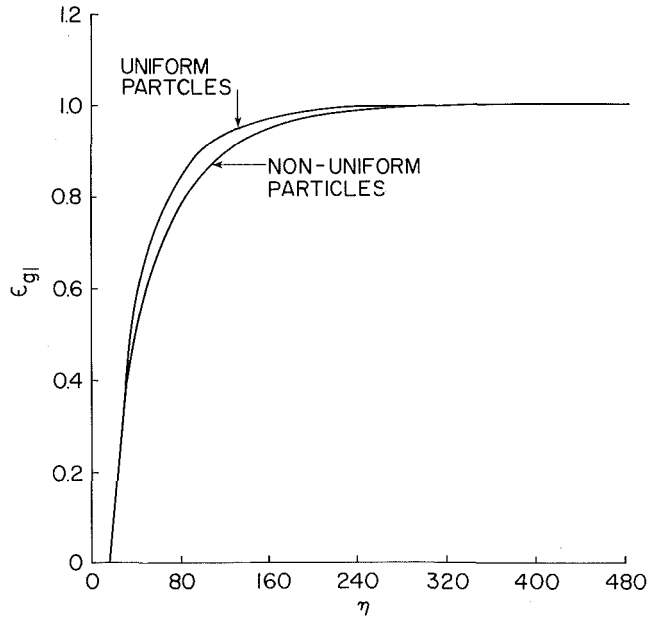

Fig. 13 Comparison of regenerator response for uniform spherical particles and nonuniform particles, D_o/D_s = 16, λ = 28, and π = 16

mm thick, and an overall loss coefficient of 5.68 W/m°C, where the loss coefficient is defined per unit length along the bed. The wall thermal capacitance and longitudinal conduction effects increase as the bed-to-particle-diameter ratio is reduced by reducing the bed size. The particle size for this plot is constant at 12.7 mm. The presence of the wall of the regenerator reduces the effect of flow bypassing through its coupled thermal capacitance with the near wall region of the bed. Figure 11 compares the one-dimensional and two-dimensional solutions for the regenerator described above, with a 3.2-mm-thick steel wall. The difference between the one and two-dimensional solutions is reduced by the presence of the wall of the container.

Many regenerators are constructed using irregular particles packed in a rectangular container; however only an extremely limited amount of information on velocity distribution in such a geometry exists, and no measurements of void fraction that extend across the entire cross section of the bed have been performed. Newell and Standish (1973) measured the velocity distribution for irregular coke particles in a square container. The measured velocity profile is shown in Fig. 12. The measured velocity profile indicates a more complex variation of void fraction in such a container than in a packing of uniform spheres. The implications of these measurements are discussed in detail by Beasley and Clark (1984).

A void fraction variation may be derived from this measured velocity distribution, by using equation (A6). The resulting void fraction and flow distribution are then used to predict the transient response of a regenerator, and the results compared with the packing of uniform spheres in Fig. 13. A nonuniform packing clearly may respond differently than a packing of uniform spheres; however the trends with D_o/D_s will be consistent. Further study is necessary to quantify the void fraction distribution in beds of nonuniform particles.

Conclusions

A two-dimensional model of the transient response of a packed bed regenerator is proposed, including the effects of axial and radial thermal dispersion, and nonuniformities in the void fraction and velocity within the packing. The model is employed to examine the effects of nonuniform void fraction and velocity on the transient response of regenerators. The results of the study indicate that flow bypassing in the near wall region of a packed bed of uniform spheres increases the response rate of the regenerator to a step change in the temperature of one of the fluid streams. Thus, for the complete description of the transient response of a packed bed regenerator, the bed-to-particle-diameter ratio must be included along with the classical dimensionless parameters, reduced length and reduced period. The two-dimensional aspects of the response decrease with increasing bed-to-particle-diameter ratio, and become negligible for values greater than 30. The presence of a container wall for a packed bed can significantly influence the temperature distribution in the near-wall region, and thus the transient response. Further study is necessary to describe the effects of container geometry and particle shape and size distribution on void fraction.

References

Baclic, B. S., 1983, "A Closed-Form Solution for the Symmetric and Balanced Counterflow Regenerator: Application of the Galerkin Method," ASME Paper No. 83-WA/HT-89.

Baddour, R. F., and Yoon, C. Y., 1960, "Local Radial Effective Conductivity and Wall Effect in Packed Beds," *Chem. Engng. Prog. Symp. Series*, Vol. 57, No. 32, pp. 35-50.

Beasley, D. E., 1983, "Dynamic Response of a Packed Bed for Thermal Energy Storage," Ph.D. Thesis, University of Michigan, Ann Arbor, MI.

Beasley, D. E., and Clark, J. A., 1984, "Transient Response of a Packed Bed for Thermal Energy Storage," *Int. J. Heat Mass Transfer*, Vol. 27, No. 9, pp. 1659-1669.

Beavers, G. J., Sparrow, E. M., and Rondenz, D. E., 1973, "Influence of Bed Size on the Flow Characteristics and Porosity of Randomly Packed Beds of Spheres," ASME *Journal of Applied Mechanics*, Vol. 40, pp. 655-660.

Benenati, R. F., and Brosilow, C. B., 1962, "Void Fraction Distribution in Beds of Spheres," *AIChE Journal*, Vol. 8, No. 3, pp. 359-361.

Bradshaw, A. V., Johnson, A., McLachlan, N. H., and Chiu, Y. T., 1970, "Heat Transfer Between Air and Nitrogen and Packed Beds of Non-reacting Solids," *Trans. Inst. Chem. Engng.*, Vol. 48, pp. T77-T84.

Chandresakara, B. C., Rudraiah, N., and Nagaraj, S. T., 1980, "Velocity and Dispersion in Porous Media," *Int. J. Engng. Science*, Vol. 18, pp. 921-929.

Connor, L. N., and Chiang, Kuo-Ning, 1986, "Heat Transfer Characteristics of a Periodic Storage Heat Exchanger," ASME Paper No. 86-WA/HT-76.

Dunkle, R. V., and Ellul, W. M. J., 1972, "Randomly-Packed Particulate Bed Regenerators and Evaporative Coolers," *Mech. Chem. Engng. Trans. I. E. Aust.* V.1.MC8, No. 2, pp. 117-121.

Ergun, S., 1952, "Fluid Flow through Packed Columns," *Chem. Engng. Prog.*, Vol. 48, No. 2, pp. 89-94.

Galloway, T. R., and Sage, B. H., 1970, "A Model of the Mechanism of Transport in Packed, Distended and Fluidized Beds," *Chem. Engng. Science*, Vol. 25, pp. 495-516.

Green, D. W., Perry, R. H., and Babcock, R. E., 1964, "Longitudinal Dispersion of Thermal Energy Through a Porous Media With a Flowing Fluid," *AIChE Journal*, Vol. 10, pp. 645-651.

Gunn, D. J., and Vortmeyer, D., 1982, "Heat Transfer in Fixed Bed Chemical Reactors," *Proceedings of the Seventh International Heat Transfer Conference*, Munich, Vol. 6, Paper No. CP3, pp. 13-18.

Gunn, D. J., 1978, "Transfer of Heat or Mass to Particles in Fixed and Fluidized Beds," *Int. J. Heat Mass Transfer*, Vol. 21, pp. 467-476.

Heggs, P. J., and Mitchell, S., 1983, "Prediction of the Performance of Asymmetric-Unbalanced Regenerators," ASME Paper No. 83-WA/HT-88.

Jaguaribe, E. F., and Beasley, D. E., 1984, "Modeling of Effective Thermal Conductivity and Diffusivity of a Packed Bed With Stagnant Fluid," *Int. J. Heat Mass Transfer*, Vol. 27, No. 3, pp. 399-407.

London, A. L., Sampsell, P. F., and McGowan, J. G., 1964, "The Transient Response of Gas Turbine Plant Heat Exchangers—Additional Solutions for Regenerators of the Periodic-Flow and Direct-Transfer Types," ASME *Journal of Engineering for Power*, Vol. 86, pp. 127-135.

McDonald, I. F., El-Sayed, M. S., and Dullien, F. A. L., 1979, "Flow Through Porous Media—The Ergun Equation Revisited," *Ind. Engng. Chem. Fundam.*, Vol. 18, No. 3, pp. 199-207.

Mickley, H. S., Smith, K. A., and Korchak, E. I., 1965, "Fluid Flow in Packed Beds," *Chemical Engng. Science*, Vol. 20, pp. 237-246.

Newell, R., and Standish, N., 1973, "Velocity Distribution in Rectangular Packed Beds and Non-ferrous Blast Furnaces," *Metall. Trans.*, Vol. 4, pp. 1851-1857.

Schwartz, C. E., and Smith, J. M., 1953, "Flow Distribution in Packed Beds," *Ind. Engng. Chemistry*, Vol. 45, No. 6, pp. 1209-1218.

Stanek, V., and Szekely, J., 1974, "Three Dimensional Flow of Fluids Through Nonuniform Packed Beds," *AIChE Journal*, Vol. 20, No. 5, pp. 974-980.

Szekely, J., and Poveromo, J. J., 1975, "Flow Maldistribution in Packed Beds: A Comparison of Measurements With Predictions," *AIChE Journal*, Vol. 21, No. 4, pp. 769-775.

Vanden Broek, C., and Clark, J. A., 1980-1982, "Heat Transfer in a Column Packed With Spheres," Von Karman Institute Lecture Series.

Willmott, A. J., 1964, "Digital Computer Simulation of a Thermal Regenerator," *Int. J. Heat Mass Transfer*, Vol. 7, pp. 1291-1302.

Willmott, A. J., and Burns, A., 1977, "Transient Response of Periodic-Flow Regenerators," *Int. J. Heat Mass Transfer*, Vol. 20, pp. 753-761.

Yagi, S., and Kunii, D., 1957, "Studies on Effective Thermal Conductivities in Packed Beds," *AIChE Journal*, Vol. 3, No. 3, pp. 373-381.

APPENDIX

The following axisymmetric equations govern the temperature distribution in two-dimensional packed beds, where the void fraction ϵ and velocity u vary with radial location:

Fluid Phase

$$\frac{\partial T}{\partial t} + u\frac{\partial T}{\partial x} = \frac{k_e^x}{\rho c}\frac{\partial^2 T}{\partial x^2} + \frac{k_e^R}{\rho c}\left[\frac{1}{R}\frac{\partial T}{\partial R} + \frac{\partial^2 T}{\partial R^2}\right] + \frac{ha}{\rho c\epsilon}(\chi - T) \tag{A1}$$

Solid Phase

$$\rho_s c_s(1-\epsilon)\frac{\partial \chi}{\partial t} = ha(T-\chi) \tag{A2}$$

Wall

$$\rho_w c_w \frac{\partial \psi}{\partial t} = k_w \frac{\partial^2 \psi}{\partial x^2} + h_w A_w^i (T-\psi) + U_\infty A_w^o (T_\infty - \psi) \tag{A3}$$

These equations include the effects of radial and axial thermal dispersion and the effects of the wall heat capacity, longitudinal conduction, and losses to the environment. A discussion of the inclusion of the axial dispersion term in the solid or the fluid equation is provided by Gunn and Vortmeyer (1982).

The governing equations are approximated by fully implicit finite difference equations. The simplicity of the solid equation allows an explicit statement for the solid temperature at the future time step $n + 1$

$$\chi_{i,j}^{n+1} = (1+\gamma\Delta t)^{-1}(\chi_{i,j}^n + \gamma\Delta t T_{i,j}^{n+1}) \tag{A4}$$

where i and j denote the radial and axial locations of the appropriate node, and n indicates the present time step. Substituting this expression for the solid temperature at the future time step, $n + 1$, into the finite difference form of equation (A1), yields the following form for the governing equation for the temperature at the general node:

$$E\cdot T_{i,j}^{n+1} + (A-N)\cdot T_{i,j+1}^{n+1} - (A+N)\cdot T_{i,j-1}^{n+1} - (L+M)\cdot T_{i+1,j}^{n+1} - (L-M)T_{i-1,j}^{n+1} = T_{i,j}^n + C\cdot\chi_{i,j}^n \tag{A5}$$

The boundary conditions at the inlet and outlet must be specified for the computational scheme. Most previous models have simply assigned the fluid temperature at the first node to be equal to the forcing inlet fluid temperature. However, since the first node has associated with it a mass of solid, this is not physically correct. The formulation used here utilizes a central difference approximation for both $\partial T/\partial x$ and $\partial^2 T/\partial x^2$. Thus, at the inlet node the difference approximation contains a temperature that is physically outside the packing; this temperature is assigned the value of the forcing inlet fluid temperature, an approach that seems in better accord with the physical circumstances.

The velocity distribution in the bed as a function of radial position is derived from a modified form of the Ergun equation (Ergun, 1952). Stanek and Szekely (1974) and Szekely and Poveromo (1975) have successfully used a vectorized form of the Ergun equation to predict three-dimensional flow in packed beds. Thus, the following equation is used to establish the pressure gradient, which then governs the radial variations in axial velocity for one-dimensional flow through a packed bed

$$-\frac{\partial p}{\partial x} = \frac{150\mu(1-\epsilon)^2}{D_s^2\epsilon^3}u_o + 1.75\frac{\rho(1-\epsilon)}{D_s\epsilon^3}u_o^2 \tag{A6}$$

where ϵ is a function of R. A recent review of the variability in the geometry-dependent constants, 150 and 1.75, is given by MacDonald et al. (1979). The appropriate boundary condition for equation (A6) is a constant pressure difference across the bed.

Once the velocity distribution in the bed is established, the difference equations yield a set of simultaneous linear equations for the fluid and the wall temperatures at each time step. The coefficient matrix is updated after each time step. The solution of the linear equations is accomplished utilizing a matrix decomposition method for banded matrices, which reduces storage requirements and computing times.

The integral nature of the governing equations requires empirical input for the heat transfer coefficient and the effective thermal conductivity. A complete review of the background necessary to establish the transport coefficients for the present model is not possible within the limitations of the current paper. However, the developments may be found in Beasley and Clark (1984), and further details in Beasley (1983). The correlation used to predict the heat transfer coefficient was developed by Galloway and Sage (1970), with constants from measured data (Beasley and Clark, 1984) as

$$\mathrm{Nu} = 2.0 + 1.354\ \mathrm{Re}_o^{1/2}\mathrm{Pr}^{1/3} + 0.0326\ \mathrm{Re}_o\mathrm{Pr}^{1/2} \tag{A7}$$

The fluid phase effective thermal conductivities, k_e^x and k_e^R, embody the convective transport due to turbulent dispersion in the fluid phase, and pure conduction in the matrix of both phases. To illustrate, the energy equation for the fluid phase may be written

$$\rho c\frac{\partial T}{\partial t} + \rho c\,\mathbf{u}\cdot\nabla T = -\nabla\cdot[k_e^o\nabla T] - \nabla\cdot[E_{ij}\nabla T] + \frac{ha}{\epsilon}(\chi - T) \tag{A8}$$

where

E_{ij} = fluid dispersion coefficient

k_e^o = stagnant bed effective thermal conductivity

Here $\mathbf{u}$ is the mean interstitial velocity, averaged over an area large relative to the pore diameter, and thus does not contain local fluctuations; the energy transport due to these fluctuations is embodied in E_{ij}. Typically k_e^o and E_{ij} are combined to produce k_e, the net effective thermal conductivity. Since the fluid phase is continuous in a packed bed of discrete particles, but the solid phase is not, an independent effective conductivity for the solid phase is not necessary, and would be, at best, partially redundant (see Gunn, 1978). For an axisymmetric,

two-dimensional case, it is assumed that the transport of energy both radially and axially is the superposition of a diffusional process upon the volume averaged convective transport. Thus two effective thermal conductivities are required, k_e^x and k_e^R, to characterize the transport in the two direction. Much effort has been directed toward defining and predicting the behavior of effective conductivities in both stagnant beds, and beds with flowing fluids.

Some insight may be gained into the nature of the effective conductivity if we allow, as is typical,

$$k_e = k_e^o + k_e^t \tag{A9}$$

where k_e^o = stagnant bed conductivity and k_e^t = contribution due to turbulent dispersion. From this definition, and the diffusion equation for the steady-state condition in nondimensional form, the following relation is derived:

$$\mathrm{Pe}_i = \frac{\mathrm{Pe}_o}{f(\mathrm{Pe}_o) + \dfrac{k_e^o}{k}} \tag{A10}$$

Yagi and Kunii (1957) assigned

$$\frac{k_e^t}{k} = C \cdot \mathrm{Pe}_o \tag{A11}$$

yielding

$$\mathrm{Pe}_i = \frac{\mathrm{Pe}_o}{C \cdot \mathrm{Pe}_o + \dfrac{k_e^o}{k_f}} \tag{A12}$$

Values of C in the radial case used in this study are given by Baddour and Yoon (1960). Numerous other theoretical and experimental studies are reviewed by Beasley (1983). In the axial case, measured values of C range from 0.2 to 1.0; an intermediate value of 0.5 is chosen for this study. For systems where $\rho_s c_s \gg \rho c$ and high Peclet numbers the influence of diffusion in the matrix and turbulent dispersion in the fluid phase on axial thermal dispersion is small, and the results are not significantly affected by k_e^x. For liquid systems the value of C must be chosen with greater care. Finally a value of k_e^o/k_f must be determined. The stagnant bed thermal conductivity is a function of the fluid and solid phase conductivity, as well as the bed geometry (Jaguaribe and Beasley, 1984). For air–glass or other similar systems, k_e^o/k_f is approximately 10. The stagnant bed thermal conductivity has been widely measured, and these measurements lend confidence to predicted values (Jaguaribe and Beasley, 1984).

Friction and Heat Transfer Characteristics of Helical Turbulent Air Flow in Annuli

N. S. Gupte
Senior Research Assistant.

A. W. Date
Professor of Mechanical Engineering.

Indian Institute of Technology,
Bombay, India

Friction and Nusselt number data have been measured and semi-empirically evaluated for twisted tape generated helical flow in annuli. Results have been obtained for radius ratios of 0.41 and 0.61 and twist ratios of ∞, 5.302, 5.038, and 2.659. The increase in pressure drop and heat transfer rates obtained are comparable to those reported for twisted tape generated swirl flow in tubes. Also, for the same heat transfer rates the pumping power requirements compare favorably with those for empty annuli. The analytical predictions based on the principle of superposition of pressure drops and analogy between heat and momentum transfer have yielded excellent predictions for $y = \infty$ *and 5.302 but somewhat poor agreement at* $y = 2.659$.

Introduction

That considerable augmentation in heat transfer is obtainable in turbulent flows through circular tubes by means of twisted tapes was recognized first by Royds (1921). Subsequently a large number of papers brought out the precise extent of augmentation in twisted tape generated turbulent flow through extensive experiments and semi-empirical analysis. Most of the single-phase turbulent flow data available through 1973 have been reviewed by Date (1973). The review showed that the heat transfer rate is significantly influenced by the Reynolds number, the Prandtl number, the twist ratio of the tape, the fin effect of the tape, and the wall to bulk temperature ratio (i.e., heating and cooling effect). Semi-empirical analyses from Smithberg and Landis (1964), Thorsen and Landis (1968), Lopina and Bergles (1969), and Migay (1969) were able to predict the augmentation within 20 percent of the experimental data. The overall conclusion is that while tape generated helical turbulent flow achieves heat transfer augmentation up to 250 percent, the increase in friction factor may in fact be of the order of 400 percent. As such, tape generated helical flow appears attractive over a straight turbulent flow in empty tubes only when comparisons are made on the basis of total pumping power required to achieve a given heat flux.

Following the numerical work of Date (1974), who predicted friction and heat transfer characteristics of laminar and turbulent twisted tape flow in tubes, considerable interest has been evinced in measurements of laminar flow characteristics, e.g., Hong and Bergles (1976), du Plessis (1982), Sukhatme et al. (1987), etc. The predictions showed that nearly a 10 to 50-fold increase in heat transfer is obtainable for only 2 to 2.5-fold increases in pressure drop, particularly for laminar flow of high Prandtl number fluids. The experimental works cited above have used fluid with Prandtl number ranging from 10 to 700 and have confirmed the augmentations in friction factor and Nusselt number predicted by Date (1974). More recently, MacArthur and Patankar (1985) have extended Date's analytical framework to compute friction factor and Nusselt number augmentation numerically in annuli fitted with a helical tape for Prandtl numbers of 0.7 and 5.0.

This paper deals with turbulent flow in annuli fitted with a helical tape, where besides the parameters affecting the tube flow characteristics, the radius rato is an additional parameter. Figure 1 explains the geometry of the annulus fitted with a helical tape. The purpose of this paper is to present experimentally determined friction factor and Nusselt number data for turbulent air flow through annuli with radius ratios of 0.41 and 0.61 and twist ratios of 2.659, 5.302, 5.038, and ∞. Also presented is a semi-empirical analysis for prediction of the characteristics.

No previous work is known to the present authors dealing with tape generated turbulent helical flow in annuli. However, data on empty annuli have been published in the literature, e.g. Kays and Leung (1963).

Analytical Predictions

By defining a coordinate system that rotates with the orientation of the twisted tape, Date (1974) derived differential equations governing mass, momentum, and energy transfer for twisted tape generated helical flow in a circular tube. The same equations are applicable to the tape generated helical flow in an annulus.

Friction Factor

By retaining the most significant terms in the axial momentum equation, it can be shown that for fully developed flow the axial pressure gradient is given by

$$\partial \bar{p}/\partial z = -[r^{-1}\partial(r\tau_{rz})/\partial r + r^{-1}\partial(\tau_{\theta z})/\partial\theta] \quad (1)$$
$$-[\pi H^{-1}\partial p'/\partial\theta] \quad (2)$$
$$-[\rho\pi H^{-1}\partial u^2/\partial\theta] \quad (3) \qquad (1)$$

where $\partial p'/\partial\theta$, from the tangential momentum equation, is given by

$$\partial p'/\partial\theta = -[r^{-1}\,\partial(r^2\tau_{r_\theta})/\partial r + \pi r H^{-1}\,\partial\tau_{\theta z}/\partial\theta] \qquad (2)$$

Term (1) in equation (1) represents the contribution of the axial shear stresses; term (2) represents the axial component of the tangential pressure gradient; and term (3) represents the momentum loss largely experienced as a result of the continuous withdrawal of the low-momentum boundary layer fluid into the core even when the flow is fully developed. Smithberg and Landis (1964) interpreted term (3) as the "vortex mixing" term and confined its contribution to the near wall regions inside the "buffer layers."

To make further progress toward development of an expression for the friction factor, we integrate equation (1) over the cross-sectional area within the limits $r_i \le r \le r_o$ and $0 \le \theta \le \theta_o$. Thus, term (1) then becomes

$$\text{Term (1)} = \theta_o\,(r_o\tau_{rz_o} + r_i\,\tau_{rz_i}) + (\tau_{rz_i} + \tau_{rz_o})\,(r_o - r_i) \qquad (3)$$

where τ_{rz_o} and τ_{rz_i} are assumed to be uniform at the outer and

Contributed by the Heat Transfer Division for publication in the JOURNAL OF HEAT TRANSFER. Manuscript received by the Heat Transfer Division August 18, 1987. Keywords: Augmentation and Enhancement, Finned Surfaces, Forced Convection.

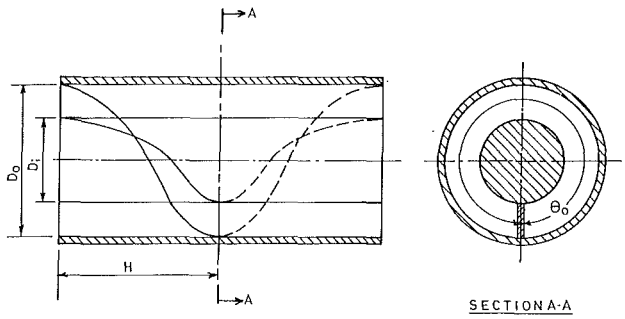

Fig. 1 Geometry of an annulus with helical tape

inner radii, and $\tau_{\theta z}$ at $\theta=0$ and $\theta=\theta_o$ is assumed uniform and equal to $(\tau_{rz_i}+\tau_{rz_o})/2$.

The contribution of Term (2) is evaluated via equation (2) to yield

$$\text{Term (2)} = (\pi/H)\ (r_i^2\,\tau_{r\theta_i} + r_o^2\tau_{r\theta_o})\ \theta_o + (1/3)(\pi/H)^2(\tau_{rz_i}+\tau_{rz_o})(r_o^3-r_i^3) \tag{4}$$

Backshall (1967) has however shown that the boundary layer shear near the walls can be resolved, so that

$$\tau_{r\theta_i} = (\pi r_i/H)\tau_{rz_i}$$

and

$$\tau_{r\theta_o} = (\pi r_o/H)\ \tau_{rz_o} \tag{5}$$

Equation (4) then becomes

$$\text{Term (2)} = (\pi/H)^2\ [\tau_{rz_i}\ (r_i^3\theta_o + (r_o^3-r_i^3)/3 + \tau_{rz_o}\ (r_o^3\theta_o + (r_o^3-r_i^3)/3)] \tag{6}$$

Finally the vortex mixing term is integrated as

$$\text{Term (3)} = -(\pi\rho/H)\int_{r_i}^{r_o}\int_0^{\theta_o}(\partial u^2/\partial\theta)\ r\ dr\ d\theta$$

$$= (\rho\pi\ \bar{u}/H)\int_{r_i}^{r_o}(u_{\max}-u)\ r\ dr$$

$$= (\rho\pi\ \bar{u}/H)\left[\int_{r_i}^{r_i+\delta_i}(u_{\max}-u)\ r\ dr + \int_{r_i+\delta_i}^{r_o-\delta_o}\times(u_{\max}-u)\ r\ dr + \int_{r_o-\delta_o}^{r_o}(u_{\max}-u)\ r\ dr\right]$$

where δ_i and δ_o are the buffer layer thicknesses near the inner and outer walls, respectively. If it is assumed that the contribution of the second integral, which represents the "core" region of the flow, is negligible compared to other two terms, then

$$\text{Term (3)} = (\rho\pi\bar{u}\nu^2/H)\left[\int_0^{\delta_i^+}\left(\frac{u_{\max_i}-u^+}{u_{\tau_i}}\right)\right)(y^+ + r_i^+)\ dy^+ + \int_0^{\theta_0^+}\left(\frac{u_{\max_o}-u^+}{u_{\tau_o}}\right)(y^+ - r_o^+)\ dy^+\Big]$$

Assuming $\delta_i^+ = \delta_o^+ = 30$ and using universal velocity profiles given by

$$u^+ = y^+;\quad 0\le y^+\le 5$$
$$u^+ = 5\ \ln\ (0.543\ y^+);\quad 5\le y^+\le 30. \tag{7}$$

we get

$$\text{Term (3)} = (\rho\pi\ \bar{u}\nu^2/H)\ [(1/u\tau_i) \times \{u^+_{\max_i}\ (890.15+30r_i^+) - 5179.85 - 281.4r_i^+\} - \{1/u_{\tau_o}\}\ \{u^+_{\max_o}\ (890.15-30r_o^+) - 5179.85 + 281.4r_o^+\}] \tag{8}$$

In the absence of detailed information on axial velocity profiles, $u_{\max}$ is evaluated at $D_h/2$. In passing we note that the left-hand side of equation (1), when integrated, yields $(\partial\bar{p}/\partial z)\ (r_o^2-r_i^2)\ \theta_o/2$ since $\partial\bar{p}/\partial z$ is constant over the cross section.

We now introduce the following dimensionless quantities:

$$r^* = r_i/r_o \tag{9}$$
$$y = (H/2)/(r_o-r_i) \tag{10}$$
$$\tau^* = \tau_{rz_i}/\tau_{rz_o} = (r^{*0.686}-r^{*2})/(r^*(1-r^{*0.686})) \tag{11}$$
$$f_y = (1/2)(d\bar{p}/dz)\ D_h/(\rho\bar{u}^2) \tag{12}$$
$$f_\infty = \bar{\tau}/(\rho\bar{u}^2) = 0.046\ \mathrm{Re}^{-0.2} \tag{13}$$
$$\mathrm{Re} = \bar{u}\ D_h/\nu \tag{14}$$
$$D_h^* = D_h/r_o = 2\theta_o\ (1-r^{*2})/(\theta_o(1+r^*)+2(1-r^*)) \tag{15}$$
$$K_1 = \tau_{rz_o}/\bar{\tau} = [(1+r^*)\ \theta_o + 2(1-r^*)]/[(1+r^*\tau^*)\theta_o + (1+\tau^*)(1-r^*)] \tag{16}$$
$$K_2 = \theta_o\ (1+r^*\tau^*) + (1-r^*)(1+\tau^*) \tag{17}$$
$$K_3 = [\pi^2/(4y^2(1-r^*)^2)]/[\theta_o(1+r^2\tau^*) + (1-r^{*3})(1+\tau^*)/3] \tag{18}$$
$$K_4 = K_5\ [K_6\ \{890\ (\tau^{*-1}-1) + 30\ K_7\ (r^*\tau^{*-0.5}+1)\} + 5180\ (1-\tau^{*-0.5}) - 281.4\ K_7\ (r^*-1)] \tag{19}$$

Nomenclature

C_p = specific heat at constant pressure, J/K kg
D = diameter, m
D_h = hydraulic diameter, m
H = half-pitch of helix, m
h = heat transfer coefficient, W/(m²K)
$\bar{p}$ = average pressure, N/m²
p' = variable pressure, N/m²
q = heat flux density, W/m²
r = radius, m
T = temperature, K
u = axial velocity, m/s
u_τ = shear velocity, m/s
Y = distance from wall, m
α = helix angle, rad
δ = buffer layer thickness, m
ν = kinematic viscosity, m²/s
ρ = mass density, kg/m³
τ = shear stress, N/m²

Dimensionless Groups

D_h^* = hydraulic diameter $= D_h/r_o$
f = friction factor $= (\Delta P\ D_h)/(2\rho\ Lu^{-2})$
Nu = Nusselt number $= h\ D_h/K$
Pr = Prandtl number $= \mu\ C_p/K$
Re = Reynolds number $= Dh\ \bar{u}/\nu$
St = Stanton number $= h/\rho\ \bar{u}\ C_p$
ΔT^+ = dimensionless temperature difference, defined by equation (31)
y = twist ratio $= H/(2(r_o-r_i))$
y^+ = dimensionless distance from wall $= Y\ u_\tau/\nu$

Subscripts

b = bulk
empty = annulus without tape
i = referring to inner wall
ii = only inner wall heated
o = referring to outer wall
oo = only outer wall heated
w = referring to wall
y = referring to twist ratio of y
∞ = referring to twist ratio of $y=\infty$
r, θ, z = cylindrical polar coordinates

$$K_5 = (\sqrt{K_1}/(2y(1-r^*))\sqrt{2/f_\infty}\ \mathrm{Re}^{-2} \quad (20)$$

$$K_6 = [5.5 + 2.5\ \ln\ (\mathrm{Re}\sqrt{f_\infty/2}/2)]/\sqrt{K_1} = u^+_{\max}/\sqrt{K_1} \quad (21)$$

and

$$K_7 = (1/D^*_h)\sqrt{f_\infty/2}\ \mathrm{Re}/\sqrt{K_1} \quad (22)$$

where $\bar{\tau}$ is the average axial shear stress and the expression for τ^* in equation (11) is the same as that used by Kays and Leung (1963) for turbulent flow in an empty annulus.

Combining equation (3), (6), and (8) and using definitions (9)–(22) it can be shown that

$$f_y = D^*_h[(0.5\ K_1(K_2+K_3)\ f_\infty + \pi D^{*2}_h\ K_4)/(\theta_o(1-r^{*2}))] \quad (23)$$

This then is the required expression for the friction factor in twisted tape generated helical flow in an annulus. It should be noted that K_3 and K_4 depend on the twist ratio y. Thus, when $y=\infty$ (or a straight tape), $K_3 = K_4 = 0$ and $f_{y=\infty} = f_\infty$.

Modification for Low Reynolds Numbers

Equation (23), when used for low turbulent Reynolds numbers, was found to overpredict the experimental data. The source of overprediction was traced to the total neglect of the "core" region in the estimate of vortex mixing loss. As such, it was proposed to partially include the core region by extending the integration from δ^+ up to to y^+_m, where

$$u/u_{\max} = (y/D_h/2))^{1/7} \text{ for } 30 < y^+ < y^+_m.$$

The result of the integration yields an additional term in the numerator of equation (23). This additional term is

$$K'_4 = K_5K_6[((y^{+2}_m/2) - 450)(1+\tau^{*-0.5})$$
$$+ (\sqrt{K_1}\ D^+_h)(r^*-1)/D^*_h)(y^+_m - 30) - (D^+_h/2)^{-0.1428}$$
$$\{0.4666(1+\tau^{*-0.5})(y^{+2.413}_m - 1463.8)$$
$$+ (0.875\ \sqrt{K_1}\ D^*_h\ (r^*-1)/D^*_h)\ (y^{+1.143}_m - 48.79)\}] \quad (24)$$

where $D^+_h = \mathrm{Re}\sqrt{f_\infty/2}$.

and

$$y^+_m = \begin{cases} 200 & \text{for } \mathrm{Re} < 10{,}000 \\ 100 & \text{for } 10{,}000 \le \mathrm{Re} \le 16{,}000 \\ 30 & \text{for } \mathrm{Re} > 16{,}000 \end{cases}$$

Thus

$$f_y = D^*_h\ [\{0.5K_1(K_2+K_3)\ f_\infty + \pi\ D^{*2}_h\ (K_4+K'_4)\}$$
$$/(\theta_o(1-r^{*2}))] \quad (25)$$

where $K'_4 = 0$ for $\mathrm{Re} > 16{,}000$.

Nusselt Number

Following Date (1974) again, the energy equation for fully developed turbulent flow can be written as

$$\rho C_p \partial(uT)/\partial z = -[r^{-1}\partial(rq_r)/\partial r + r^{-1}\partial q_\theta/\partial\theta]$$
$$\text{(1)}$$
$$-(\pi/H)\rho C_p \partial(uT)/\partial\theta \quad (26)$$
$$\text{(2)}$$

where the left-hand side represents the axial convection heat transfer; Term (1) represents the turbulent diffusive heat transfer attributed to shear effects and Term (2) represents the "vortex mixing" effect. Upon integration, the left-hand side of equation (26) is simply

$$\theta_o(q_{w_o}r_o + q_{w_i}r_i) \quad (27)$$

Now if we assume that the fin effect of the tape is negligible, then

$$\text{Term (1)} = \theta_o\ (q_{r_o}r_o + q_{r_i}r_i) \quad (28)$$

Finally Term (2) is written as

$$\text{Term (2)} = -(\rho C_p\ \pi/H)\int_{r_i}^{r_o}\int_0^{\theta_o} \partial(uT)/\partial\theta\ r\ dr\ d\theta$$

$$= (\rho C_p \pi\bar{u}/H)\int_{r_i}^{r_o}(T - T_{\min})\ r\ dr$$

Again assuming that the integration is significant only in the region close to the inner and outer walls, we have

$$\text{Term (2)} = (\rho\ C_p\bar{u}\pi\nu^2/H)\left[\int_0^{\delta^+_i}((T-T_{\min})(y^+ + r^+_i)/u^2_{\tau_i})\ dy^+ \right.$$
$$\left. - \int_0^{\delta^+_o}((T-T_{\min})(y^+ - r^+_o)/u^2_{\tau_o})dy^+\right] \quad (29)$$

Now letting

$$T - T_{\min} = (T_w - T_{\min}) - \Delta T^+\ q_w/(\rho C_p u_\tau); \quad (30)$$

$$\Delta T^+ = \mathrm{Pr}\ y^+ \text{ for } 0 \le y^+ \le 5 \quad (31a)$$

$$\Delta T^+ = 5[\mathrm{Pr} + \ln\ [(1-\mathrm{Pr}) + (\mathrm{Pr}\ y^+/5]] \text{ for } 5 < y^+ < 30 \quad (31b)$$

and substituting with appropriate suffices, we get

$$\text{Term (2)} = -(\rho C_p\bar{u}\nu^2/(Hu^2_{\tau_o})(i_1 + i_2 - i_3)\pi \quad (32)$$

where

$$i_1 = (T_{w_o} - T_{\min})(450 - 30r^+_o)$$
$$- (T_{w_i} - T_{\min})(450 + r^+_i)(u^2_{\tau_o}/u^2_{\tau_i})$$

$$i_2 = (q_{w_i}/(\rho C_p u_{\tau_i}))\ [(137.5\ \mathrm{Pr} + A)\ r^+_i + 5250\ \mathrm{Pr}^{0.731}]$$

and

$$i_3 = (q_{w_o}/(\rho C_p u_{\tau_o}))\ [5250\ \mathrm{Pr}^{0.731} - (137.5\ \mathrm{Pr} + A)r^+_o].$$

In the above derivation

$$A = (25/\mathrm{Pr})\ [((1+5\ \mathrm{Pr})/\mathrm{Pr})\ \{\ln\ (1+5\ \mathrm{Pr}) - 1\} + 1] \quad (33)$$

and following Smithberg and Landis (1964)

$$\int_0^{\delta^+} \Delta T^+ y^+ dy^+ \simeq 5250\ \mathrm{Pr}^{0.731} \quad (34)$$

In order to derive an expression for Nusselt number we define the following quantities:

$$q^*_w = q_{w_i}/q_{w_o} \quad (35)$$

$$q^*_r = q_{r_i}/q_{r_o} \text{ (to be evaluated shortly)} \quad (36)$$

$$\mathrm{St}_{w_o} = h_{w_o}/(\rho C_p\bar{u}) = q_{w_o}/(\rho C_p\bar{u}(T_{w_o} - T_b))$$
$$= \mathrm{Nu}_{w_o}/(\mathrm{Re}\ \mathrm{Pr}) \quad (37)$$

$$\mathrm{St}_{r_o} = q_{r_o}/(\rho C_p\bar{u}(T_{w_o} - T_b))$$
$$= \sqrt{K_{1f\infty}/(2\ \cos\ \alpha_o)}/(0.9\ (PF + \sqrt{2\ \cos\ \alpha_0/(K_1 f_\infty)}\ )) \quad (38a)$$

$$\mathrm{St}_{r_i} = \sqrt{K_1\tau^* f_\infty/(2\ \cos\ \alpha_i)}/$$
$$(0.9(PF + \sqrt{2\ \cos\ \alpha_i/(\tau^*\ K_1)})\ f_\infty)\ ) \quad (38b)$$

$$K_8 = \pi\nu^2/(Hr_o\ \theta_o\ (1+r^*)u^2_{\tau_o})$$
$$= \pi D^{*2}_h/(y(1-r^{*2})\ \theta_o\ K_1\ f_\infty\ \mathrm{Re}^2) \quad (39)$$

$$K_9 = (1 + r^*q^*_r)/(1+r^*) \quad (40)$$

$$K_{10} = (1 + r^*q^*_w)/(1+r^*) \quad (41)$$

$$K_1 = ((137.5\ \mathrm{Pr} + A)\ r^+_i + 5250\ \mathrm{Pr}^{0.731})/\sqrt{\tau^*} \quad (42)$$

$$K_{12} = 5250\ Pr^{0.731} - (137.5\ \mathrm{Pr} + A)\ r^+_o \quad (43)$$

$$r^+_o = (\mathrm{Re}/D^*_h)\sqrt{f_\infty\ K_1/2} \quad (44)$$

$$r^+_i = (\mathrm{Re}\ r^*K_1/D^*_h)\sqrt{f_\infty\tau^*/2} \quad (45)$$

Equation (38) above assumes analogy between wall friction and diffusion heat transfer and is modeled following the formula given by Jayatillaka and Spalding (1966) where the

resistance of sublayers is represented by the p function approximately given by

$$PF = 9.24\ [(\Pr/0.9)^{0.75} - 1] \tag{46}$$

Note that equation (38) for St_{r_o} is based on total shear, i.e., $\sqrt{\tau_{rz_o}^2 + \tau_{r\theta_o}^2}$ or $\tau_{rz_o}/\cos\alpha_o$. Similarly, St_{r_i} can be defined based on q_{r_i}, which in turn is based on the total shear at the inner wall, i.e., τ_{rz_i}, $/\cos\alpha_i$. Thus

$$q_r^* = q_{r_i}/q_{r_o} = \mathrm{St}_{r_i}/\mathrm{St}_{r_o}$$

$$= \sqrt{\tau^*\cos\alpha_o/\cos\alpha_i}\left[\frac{PF + \dfrac{\sqrt{2\cos\alpha_o}}{\sqrt{K_1 f_\infty}}}{PF + \dfrac{\sqrt{2\cos\alpha_i}}{\sqrt{K_1 \tau^* f_\infty}}}\right]\left(\frac{T_{w_i} - T_b}{T_{w_o} - T_b}\right) \tag{47}$$

where

$$\alpha_i = \tan^{-1}(\pi r_i/H) \tag{48}$$

$$\alpha_o = \tan^{-1}(\pi r_o/H) \tag{49}$$

Combining equations (27), (28), (32), and (33) and using definitions (35) to (49), we can write

$$\mathrm{Nu}_{w_o}/(\mathrm{Re}\ \Pr) = K_{13}/K_{14} \tag{50a}$$

where

$$K_{13} = \mathrm{St}_{r_o} K_9 - K_8\ \{((T_{w_o} - T_{\min})/(T_{w_o} - T_b))(450 - 30\ r_o^+) - ((T_{w_i} - T_{\min})/(T_{w_o} - T_b))\ K_1 f_\infty\ (450 + 30\ r_i^+)/2\} \tag{50b}$$

and

$$K_{14} = K_{10} + K_8\sqrt{2/(K_1 f_\infty)}\ (q_w^*\ K_{11} - K_{12}) \tag{50c}$$

It is clear then that evaluation of Nu_{w_o} is possible only when the temperature ratios $(T_{w_o} - T_{\min})/(T_{w_o} - T_b)$, $(T_{w_i} - T_{\min})/(T_{w_o} - T_{\min})$ and $(T_{w_i} - T_b)\ /\ (T_{w_o} - T_b)$ are defined. Their values are governed by Re, Pr, the nature of the boundary conditions, and the geometry (i.e., r^* and θ_o). Incidentally it is easy to discern that the Nusselt number based on heat transfer coefficient at the inner tube is given by

$$\mathrm{Nu}_{w_i} = \mathrm{Nu}_{w_o}\ q_w^*\ (T_{w_o} - T_b)/(T_{w_i} - T_b)$$

or

$$\mathrm{Nu}_{w_i}/(\mathrm{Re}\ \Pr) = K_{15}/K_{16} \tag{51a}$$

where

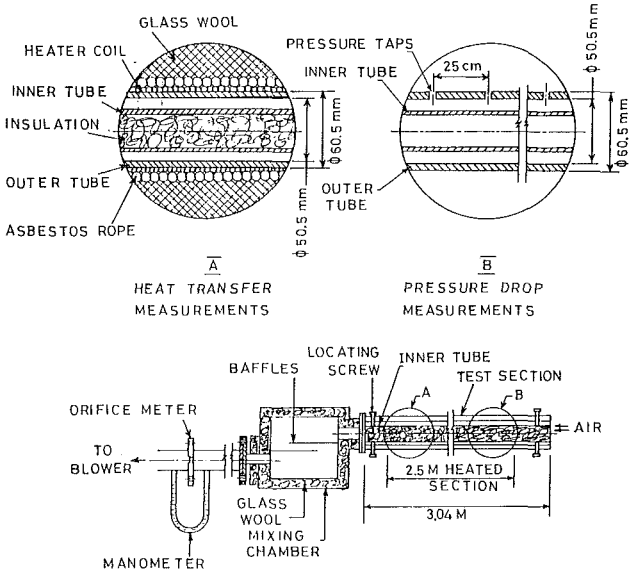

Fig. 2 Experimental setup

$$K_{15} = \mathrm{St}_{r_i} K_9/q_r^* - (K_8/(T_{w_i} - T_b))\ \{(T_{w_o} - T_{\min})\ (450 - 30 r_o^+) - (T_{w_i} - T_{\min})\ K_1 f_\infty\ (450 + 30 r_i^+)/2\} \tag{51b}$$

and

$$K_{16} = (K_{10}/q_w^*) + K_8\sqrt{2/(K_1 f_\infty)}\ (K_{11} - K_{12}/q_w^*) \tag{51c}$$

Case of Only Outer Wall Heated ($q_{w_i} = 0$). For this case it may be resonable to assume that $T_{w_i} \simeq T_{\min} \simeq T_b$ which yields $q_r^* = 0$. Now since $q_w^* = 0$, equation (50) reduces to

$$\mathrm{Nu}_{oo}/(\mathrm{Re}\ \Pr) = [\mathrm{St}_{r_{oo}}\ (1 + r^*)^{-1.0} - K_8\ (450 - 30\ r_o^+)]/[(1 + r^*)^{-1.0} - K_8 K_{12}\sqrt{2/(K_1 f_\infty)}] \tag{52}$$

where the subscript ∞ is a reminder that only the outer wall is heated.

Case of Only Inner Wall Heated ($q_{w_o} = 0$). For this case again if it is assumed that $T_{w_o} \simeq T_{\min} \simeq T_b$, which yields $q_r^* = \infty$ and also $q_w^* = \infty$, equation (51) reduces to

$$\frac{\mathrm{Nu}_{ii}}{\mathrm{Re}\ \Pr} = \frac{\mathrm{St}_{r_{ii}}\ r^*(1 + r^*)^{-1.0} + 0.5\ K_8\ K_1\ f_\infty\ (450 + 30\ r_i^+)}{r^*\ (1 + r^*)^{-1.0} + K_8 K_{11}\sqrt{2/(f_\infty\ K_1)}} \tag{53}$$

where the subscript ii denotes that only the inner wall is heated.

In the present work, experiments have been performed with $q_{w_i} = 0$ and a finite q_{w_o}. As such, equation (52) will be used for comparison with experimental results. Also only one value of θ_o i.e., 2π) and two values of r^* are considered in the experiments, whereas equations (50) to (53) are general and applicable to any θ_o, r^*, y, and q_w^*, provided the assumptions made are valid.

Experimental Setup

The pressure drop and heat transfer tests were performed in a horizontal experimental setup, which consisted of the test section, the mixing chamber, the orifice meter, and a centrifugal blower used in a suction mode (see Fig. 2).

The test section was 2.5 m long and consisted of an MS seamless pipe (50.5 mm i.d., 60.5 mm o.d.) inside which a hollow GI tube was inserted. Outer diameters of the inner tubes were 20.7 mm and 30.7 mm, respectively, yielding radius ratios of 0.41 and 0.61.

The heat transfer tests were performed with the outer tube heated. The inner tube, which is hollow, is insulated by packing it with glass wool insulation from inside. The outer tube was covered with the fiberglass tape (0.1 mm thick) to provide adequate electrical insulation. Over the tape, eight coils of SWG No. 25 Nichrome heater wire sleeved in fiberglass were wound. The Nichrome heater wire was subsequently wrapped around with asbestos rope of 1.2 cm diameter. Further insulation was provided by wrapping an 8.1-cm-thick glass wool blanket.

Mounting of helical tapes on the inner tube required considerable care. Helical grooves were cut on the outside of the inner tube on a Universal horizontal milling machine. However, as the test section was 2.5 m long, grooves could not be cut on the entire length at once. As such, the inner tube was cut into five pieces 50 cm long, which could be accommodated on the available milling machine. The pieces were subsequently joined by means of press-fit bushes with proper alignment of helical grooves between successive pieces. The helical tape, which was made out of 0.8-mm-thick GI sheet, also could not be soldered in the grooves over the entire length of the tube. As such, small pieces of typically 7 to 10 cm were soldered in the grooves in succession. This prevented distortion of the tape. The tape was subsequently covered with cotton adhesive tape over which black steel-grip tape was put. This provided a

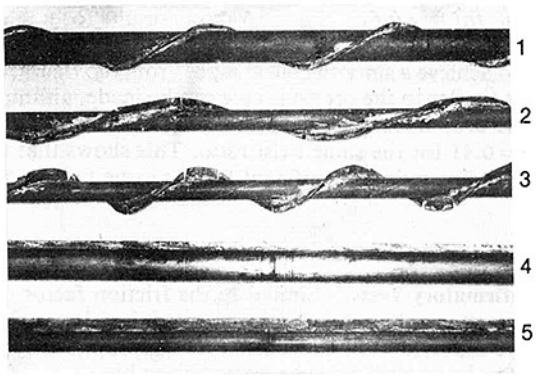

INNER TUBES (FROM TOP TO BOTTOM):

1) $r^* = 0.61$; $y = 5.038$

2) $r^* = 0.41$; $y = 5.302$

3) $r^* = 0.41$; $y = 2.659$

4) $r^* = 0.61$; $y = \infty$

5) $r^* = 0.41$; $y = \infty$

Fig. 3 Photograph of inner tubes with helical tapes

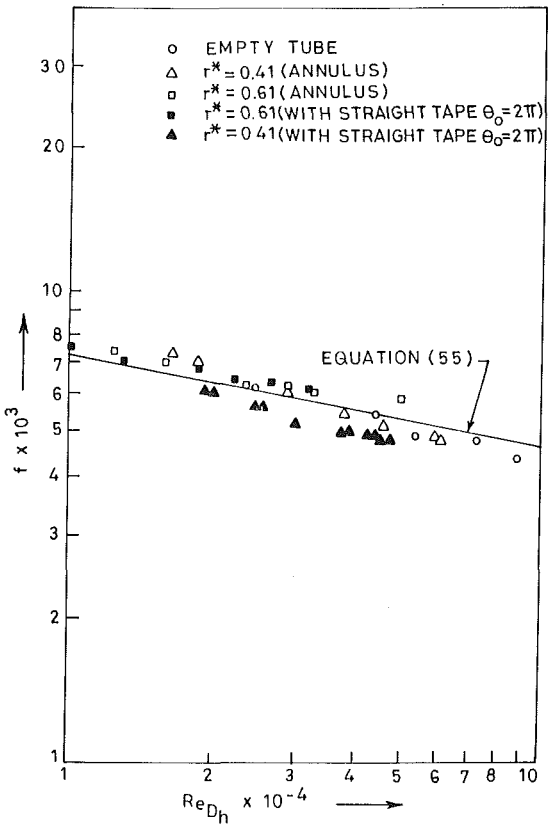

Fig. 4 Confirmatory tests for friction factor

smooth surface on the entire tape and prevented fin effects of the tape. The width of the tape was chosen according to the radius ratio considered, with proper allowance made for thickness of the adhesive and steel-grip tapes. As such, the inner tubes with helical tape mounting, when inserted, provided good snug fit and ensured concentricity of the inner tubes with respect to outer tube. Figure 3 shows the photographs of the inner tubes mounted with straight and helical tapes.

In the empty annulus experiments, however, concentricity had to be ensured by means of three radial set screws at each end of the test section (see Fig. 2).

The entry of air to the test section was directly from the ambient air with a short hydrodynamic development length of 27 cm. At the end of the test section a mixing chamber with two baffles was provided. Between the mixing chamber and the blower a calibrated orifice meter (radius ratio = 0.7, discharge coefficient = 0.59) was provided for measurement of air flow. A vertical **U**-tube manometer with water as the working fluid was used for this purpose. Finally, to prevent vibrations from being transmitted to the test section, the blower was connected by a rubber bellow.

Measurements

Pressure taps of 4 mm diameter were provided 25 cm apart on the entire test section. A multitube water manometer was used for pressure measurements. For all Reynolds numbers and radius ratios tested, constant axial pressure gradient was observed for $z/(D_o - D_i)$ greater than 20.

In the heat transfer experiments all temperatures were measured by means of SWG No. 30 copper-constantan thermocouples. The standard calibration charts were corrected for the ice point and the boiling point (Gupte, 1986) and the error was evenly distributed between these points. Nine themocouples (31.25 cm apart) were silver soldered on the outer tube. The inlet and exit (in the mixing chamber) temperatures were measured by five thermocouples each and average value was noted. The Nichrome heater wire was connected to a stabilized 230 V a-c supply through a voltage regulator (0 to 230 V). The emf of the thermocouples, the supply voltage, and the resistance of Nichrome heater wire (29.6 ohm) were measured by means of digital multimeter model No. hp 3465 A. The power supplied was calculated from measured supply voltage and resistance.

In order to estimate the heat losses the test setup was calibrated under "no-flow" conditions. The calibration curve was approximated by

$$Q_{\text{Loss}} = 0.4059\, L\, (\bar{T}_w - T_{\text{amb}}) \text{ Watts} \qquad (54)$$

where L is the length of pipe in m over which T_w is averaged.

It took, typically, 2 to 2½ h to obtain a steady state for each run. Experiments were conducted with three different values of heat input (570 W, 350 W, and 250 W) to check the reproducibility of the results. The difference between wall and bulk temperatures varied from 10°C to 30°C at different heat inputs.

The maximum estimated error in the measurement of friction factor was 2 percent, whereas in case of Nusselt number it was 10 percent (Gupte, 1986).

Friction Factor Results

Confirmatory Tests. It is well known that using hydraulic diameter as the characteristic dimension, the friction factor for noncircular ducts can be correlated by

$$f = 0.046\, \text{Re}_{D_h}^{-0.2} \qquad (55)$$

which is applicable to empty tube turbulent flows. Experiments were conducted for the following cases to validate the test setup:

1 Empty tube, 50.5 mm i.d.

2 Empty annulus, $r_i = 10.35$ mm, $r_o = 25.25$ mm, $r^* = 0.41$

3 Empty annulus, $r_i = 15.4$ mm, $r_o = 25.25$ mm, $r^* = 0.61$

4 Straight tape annulus, $r_i = 10.35$ mm, $r_o = 25.25$ mm, $r^* = 0.41$, $\theta_o = 2\pi$

5 Straight tape annulus, $r_i = 15.4$ mm, $r_o = 25.25$ mm, $r^* = 0.61$, $\theta_o = 2\pi$

Fig. 4 shows the comparison of the above five cases with the correlation where agreement within 12 percent is observed.

Helical Flow Results

Results for $r^* = 0.41$. Figure 5 shows friction factor data for helical turbulent flow with $y = \infty$, 5.302, and 2.659. Plotted in the figure is equation (25). The experimental results show a pressure drop increase of 120 percent for $y = 5.302$ and 300 percent for $y = 2.659$ over the value for $y = \infty$. It will be recognized through that the pressure drops for $y = \infty$ exceed the pressure drop for empty annulus by $(D_{h,\,\text{empty}}/D_{h,\,y=\infty})^{1.2}$ or by 16 percent. It will be noticed that for finite values of y the experimental friction factor essentially varies as $\text{Re}^{-0.2}$. The predictions however show a somewhat steeper slope. The data for Re > 16,000, however, appear to be well predicted by equation (25). The near constancy of f at low Reynolds numbers for $y = 2.659$ is somewhat surprising. Unfortunately data for higher values of y in this range of Re were not taken. The only plausible reason for the near constancy is that in helical flows the laminar-to-turbulent transition does not show a very sharp departure from the fully turbulent friction factor curve. Secondly, the velocity profile at $y = 2.659$ can be expected to be qualitatively different from those at $y \geq 5.3$ as has been experienced in the twisted tape in a tube (Smithberg and Landis, 1964). More data for higher twists are needed to confirm the trend observed here.

Result for $r^* = 0.61$. Figure 6 shows results for $y = \infty$ and 5.033. The tighter twist ratio was not considered as it was difficult to achieve a smooth helical tape. From the figure, observations similar to the previous case can be made, although the pressure drop increase is 200 percent higher for $r^* = 0.61$ than for $r^* = 0.41$ for the same twist ratio. This shows that the effect of radius ratio is significant for the same twist ratio.

Heat Transfer Results

Confirmatory Tests. Similar to the friction factor results, the Nusselt numbers for the empty annuli and straight tape duct are expected to be correlated (with appropriate hydraulic diameter) by an empirical correlation given by

$$\text{Nu} = 0.021\ \text{Pr}^{0.4}\text{Re}^{0.8}\ (T_w/T_b)^{-0.32} \qquad (56)$$

In all our experiments the value of T_w/T_b was between 1.047 and 1.049 and the Prandtl number varied between 0.696 and 0.702. Figure 7 shows the comparison of the present experiment with equations (52) and (56) (equation (52) is plotted for $y = \infty$). Equation (56) overpredicts the experimental results by a maximum of 16 percent, whereas equation (52) underpredicts by a maximum of 15 percent.

Helical Flow Results

Results for $r^* = 0.41$. Figure 8 shows experimental results for $y = \infty$, 5.302, and 2.659, where equation (52) is also plotted. It is seen that the heat transfer coefficients for $y = 5.302$ and $y = 2.659$ exceed the values for $y = \infty$ by 25 percent and 75 percent. For the straight tape annulus, i.e., for $y = \infty$, on the other hand, the heat transfer coefficient exceeds the empty annulus values by $(D_{h,\text{empty}}/D_{h,y=\infty})^{0.2}$ or for $r^* = 0.41$ by 3 percent.

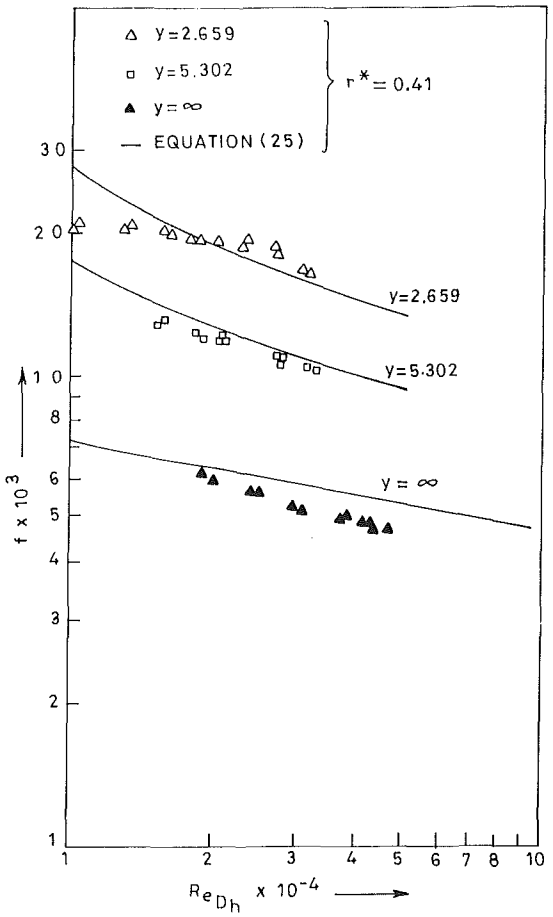

Fig. 5 Friction factor data for helical flow ($r^* = 0.41$, $\theta_o = 2\pi$)

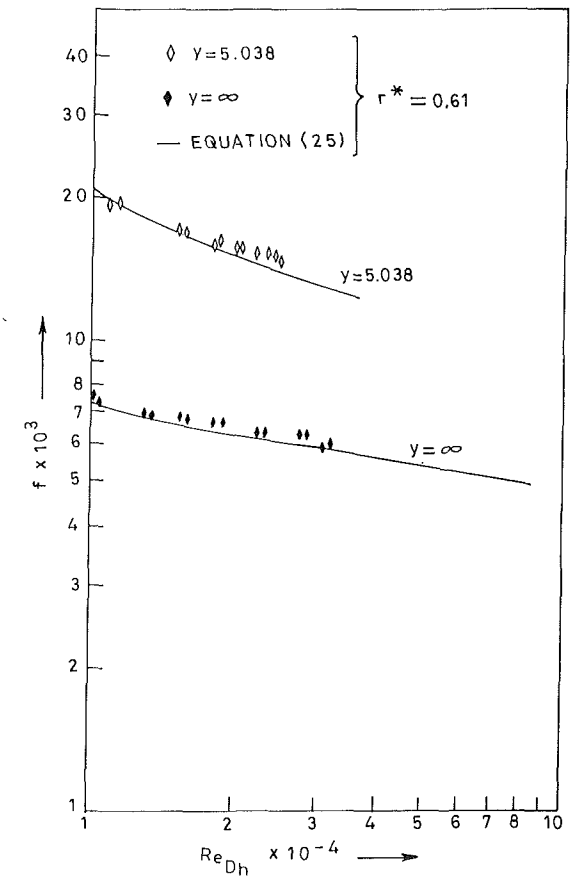

Fig. 6 Friction factor data for helical flow ($r^* = 0.61$, $\theta_o = 2\pi$)

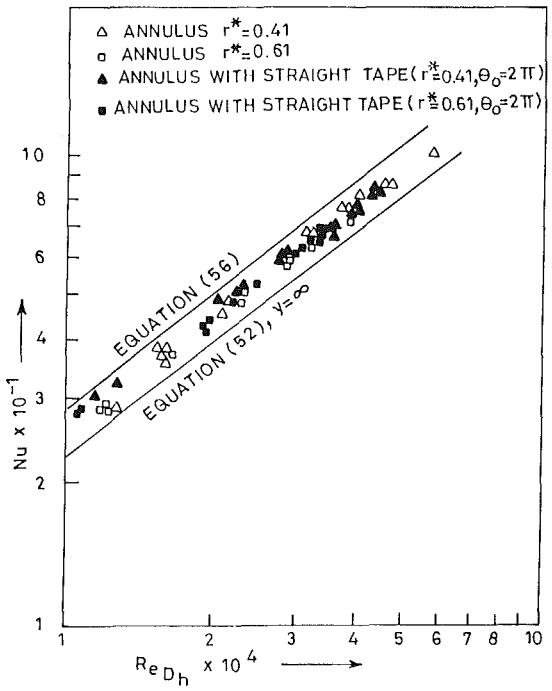

Fig. 7 Confirmatory tests for Nusselt number

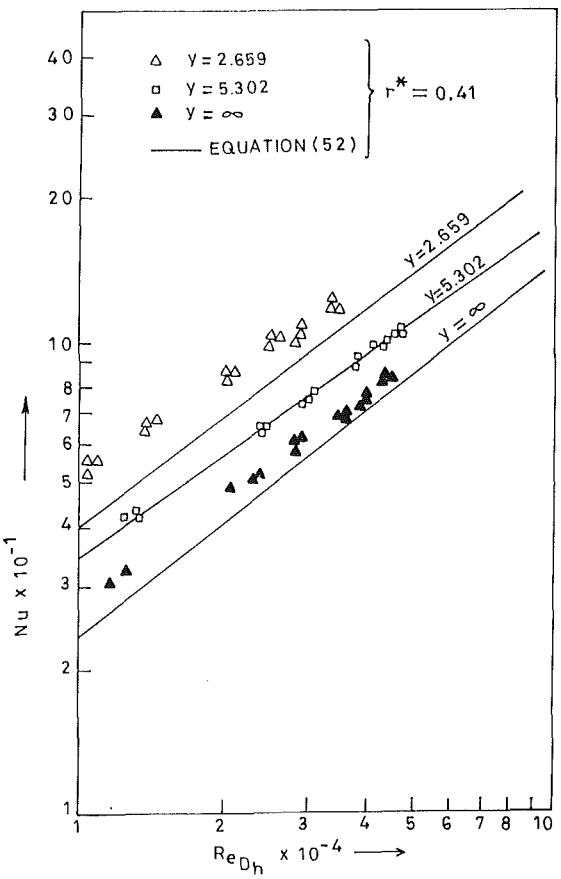

Fig. 8 Nusselt number data for helical flow ($r^* = 0.41$, $\theta_0 = 2\pi$)

Results for $r^* = 0.61$. Figure 9 shows the results for $y = \infty$ and 5.038. Also plotted in the figure is equation (52). Like the friction factor results the augmentation in heat transfer is again higher for $r^* = 0.61$ than for $r^* = 0.41$ by 50 percent.

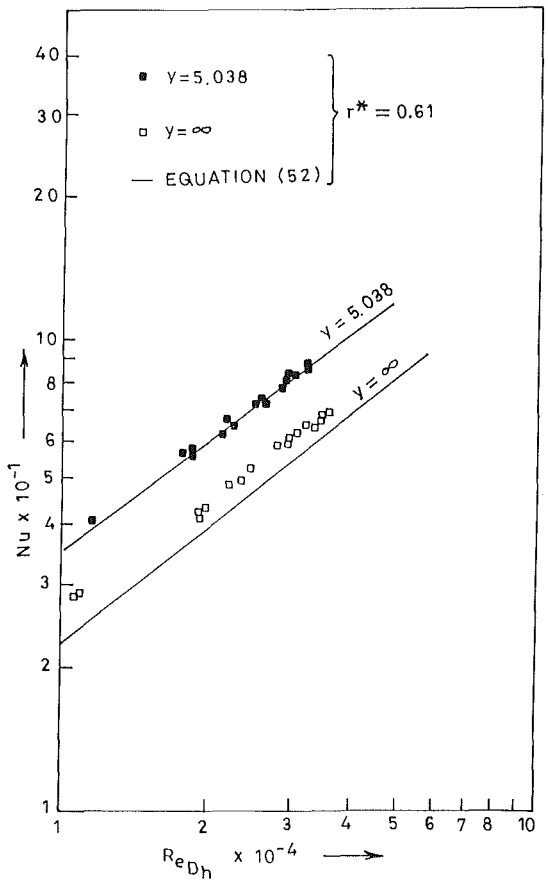

Fig. 9 Nusselt number data for helical flow ($r^* = 0.61$, $\theta_0 = 2\pi$)

For the present radius ratio ($D_{h,\text{empty}}/D_{h,y=\infty}$) = 1.08, the straight tape heat transfer coefficient exceeds the empty annulus value by 1.5 percent for the same mass flow rate.

Conclusions

1 For nonhelical flows, both the pressure drop and heat transfer measurements have agreed with the well-accepted correlations for noncircular ducts within 15 percent.

2 The experimental results for helical flow have shown that for the same twist ratio the increase in pressure drop exceeds the increase in heat transfer irrespective of the radius ratios. For $y = 5.302$, for example, at the same Reynolds number based on hydraulic diameter, the increases in pressure drop and heat transfer coefficient over an empty annulus are 90 percent and 60 percent, respectively, at $r^* = 0.41$. At $r^* = 0.61$ and $y = 5.033$ the respective figures are 200 percent and 70 percent. At tighter twist ratios both the percentages are even greater. These findings are similar to those observed for twisted tape generated swirl flow in tubes.

3 The semi-analytical expressions developed have predicted the Nusselt numbers with good agreement for $y = \infty$ and $y = 5.302$ and 5.038. However, at extremely tight ratios of $y = 2.659$ the experimental data are underpredicted by 25 percent. Since velocity and temperature profiles are not available, further improvements cannot be brought about. Also, the assumption of uniform shear stress at the walls is particularly questionable for tighter twist. It may be noted however that the correlations developed are general and may be applied to other values of r^*, θ_0 (more helical tapes), and y, to guide further experimentation.

4 For the same heat transfer rates, the pumping power ($\dot{P}$) required is given by

Table 1 $\dot{P}_y/\dot{P}_{empty}$ for various Re_{empty} and y

$\frac{Re_{empty}}{y}$	$r^*=0.41$			$r^*=0.61$		
	25,000	40,000	50,000	25,000	40,000	50,000
∞	1.539	1.665	1.574	2.490	2.520	2.280
5.302	1.230	1.423	1.461	–	–	–
5.038	–	–	–	1.393	1.336	1.235
2.659	0.352	0.519	0.560	–	–	–

Table 2 $\dot{h}_y/\dot{h}_{empty}$ for various Re_{empty} and y

$\frac{Re_{empty}}{y}$	$r^*=0.41$			$r^*=0.61$		
	25,000	40,000	50,000	25,000	40,000	50,000
∞	0.944	0.837	0.947	0.861	0.845	0.831
5.302	0.944	0.901	0.946	–	–	–
5.038	–	–	–	0.897	0.930	0.923
2.659	1.284	1.159	1.212	–	–	–

$$\dot{P}_y/\dot{P}_{empty} = (f_y/f_{empty})(D_{h,\,empty}/D_{h,\,y})^4\ (Re_y/Re_{empty})^3 \quad (57)$$

where Re_y and Re_{empty} are Reynolds numbers giving the same heat transfer coefficients for the annulus with tape and the empty annulus, respectively. The values of $\dot{P}_y/\dot{P}_{empty}$ for $r^* = 0.41$ and for $r^* = 0.61$ for various Re_{empty} and twist ratios are given in Table 1.

Similarly, for the same pumping power, the heat transfer rate is given by

$$h_y/h_{empty} = (Nu_y/Nu_{empty})(D_{h,empty}/D_{h,y}) \quad (58)$$

where Nu_y and Nu_{empty} are Nusselt numbers obtained for the same pumping power. The values of h_y/h_{empty} for $r^* = 0.41$ and $r^* = 0.61$ for various Re_{empty} and twist ratios are given in Table 2, where Re_{empty} corresponds to the Reynolds number obtained by a fixed pumping power.

As such, under certain circumstances helical flow may be considered favorably in the design of heat exchangers operating under turbulent flow conditions.

5 It is desirable to carry out experiments with more tapes with $\theta_o = \pi$, $\pi/2$, etc., and to improve the predictive capability of the analysis through thorough probing of velocity and temperature fields.

References

Backshall, R. G., 1967, "An Investigation of the Boundary Layer in Turbulent Swirling Pipe Flow," M.S. Thesis, New York University, New York.

Date, A. W., 1973, "Flow in Tubes Containing Twisted Tapes," *Heating and Ventilation Engineer*, Vol. 47, pp. 240–249.

Date, A. W., 1974, "Predictions of Fully Developed Flow in a Tube Containing a Twisted Tape," *International Journal of Heat and Mass Transfer*, Vol. 17, pp. 845–859.

du Plessis, J. P., 1982, "Laminar Flow and Heat Transfer in a Smooth Tube With a Twisted Tape Insert," Ph. D. Thesis, University of Stellenbosch, South Africa.

Gupte, N. S., 1986, "Friction and Heat Transfer Characteristics of Helical Turbulent Air Flow in Ducts," M. S. Tech. Thesis, Department of Mechanical Engineering, Indian Institute of Technology, Bombay.

Hong, S. W., and Bergles, A. E., 1976, "Augmentation of Laminar Flow Heat Transfer in Tubes by Means of Twisted Tape Inserts," ASME JOURNAL OF HEAT TRANSFER, Vol. 98, p. 251.

Jayatillaka, C. L. V., and Spalding, D. B., 1966, "A Survey of the Theoretical and Experimental Information on the Resistance of the Laminar Sub-layer to Heat and Mass Transfer," *Proceedings, 2nd All Soviet Union Conference on Heat and Mass Transfer*, Minsk, USSR.

Kays, W. M., and Leung, E. Y., 1963, "Heat Transfer in Annular Passages – Hydrodynamically Developed Turbulent Flow With Arbitrarily Prescribed Heat Flux," *International Journal of Heat and Mass Transfer*, Vol. 6, pp. 537–557.

Lopina, R. F., and Bergles, A. E., 1969, "Heat Transfer and Pressure Drop in Tape Generated Swirl Flow," ASME JOURNAL OF HEAT TRANSFER, Vol. 91, p. 434.

MacArthur, J. W., and Patankar, S. V., 1985, "Effects of Swirling Laminar Flow on Heat Transfer Augmentation in Annular Passages with Twisted Radial Fins," *Advances in Enhanced Heat Transfer* – 1985, HTD-Vol. 43, pp. 73–80.

Migay, V. K., 1969, "Friction and Heat Transfer in Twisted Flow Inside a Pipe," English translation FTD-HT-23-1258-68.

Royds, R., 1921, *Heat Transmission by Radiation, Conduction and Convection*, Constable and Camp Ltd., London, pp. 190–201.

Smithberg, E., and Landis, F., 1964, "Friction and Forced Convection Heat Transfer Characteristics in Tubes With Twisted Tape Swirl Generators," ASME JOURNAL OF HEAT TRANSFER, Vol. 86, pp. 39–49.

Sukhatme, S. P., Gaitonde, U. N., Shidoire, C. S., and Kuncolienkar, R. S., 1987, Department of Mechanical Engineering, Indian Institute of Technology, Bombay, Private Communication.

Thorsen, R, and Landis, F., 1968, "Friction and Heat Transfer Characteristics in Turbulent Swirl Flow Subject to Large Transverse Temperature Gradients," ASME JOURNAL OF HEAT TRANSFER, Vol. 90, pp. 87–97.

Augmentation of Laminar Forced-Convective Heat Transfer by the Application of a Transverse Electric Field

T. Fujino[1]
Graduate Student.

Y. Yokoyama
Graduate Student.

Y. H. Mori
Associate Professor.
Mem. ASME

Department of Mechanical Engineering,
Keio University,
Yokohama 223, Japan

The effect of a uniform d-c electric field on laminar forced-convective heat transfer has been studied experimentally with a weakly conducting fluorocarbon refrigerant in the liquid state that is flowing in a channel confined by parallel-plate electrodes, one of which serves as a heat transfer surface of uniform heat flux. The dependencies of the heat transfer coefficient and the pressure drop on the sign and the magnitude of an applied voltage, the heat flux at the heat transfer surface, the electrical conductivity of the test fluid, etc. are presented, and the structure and the mechanism of the electroconvection causing the heat transfer enhancement are considered.

Introduction

An externally applied d-c electric field across a plane layer of a dielectric liquid is known to cause an instability in the layer that is sometimes called "electroconvection." Electroconvection seems to be an attractive tool for enhancing convective heat transfer, particularly in the low Reynolds number flow of a weakly conducting liquid through a narrow space where the application of any of conventional passive enhancement methods (Bergles, 1978) is neither easy nor effective.

In the case of a uniform d-c electric field applied to a dielectric liquid, the dominant destabilization force causing the electroconvection is the Coulomb force resulting from the interaction of the electric field with free space-charge, which is nonuniformly distributed in the liquid. There are two generally accepted versions about the origin of the distribution of net space-charge: One assumes that the distribution results from the thermally induced variation in electrical conductivity of the liquid, and the other assumes injection of charge from either or both electrodes as the cause of the distribution. Martin and Richardson (1984) called the existing theoretical models of electroconvection employing the former version "conductivity models," and those employing the latter version "mobility models." According to the conductivity models, a temperature gradient in the liquid is an indispensable condition for the convection to occur, and the intensity of the convection must be dependent on the magnitude of the temperature gradient. According to the mobility models, the electroconvection can occur irrespective of the presence or absence of a temperature gradient in the liquid. The convection may be dependent, however, on the temperature gradient, if one is present, since the mobility of charge carriers is dependent on the temperature. The extent of the dependency of the convection on the temperature gradient is presumably dependent on the relation between the charge injection strength and the temperature dependency of the mobility (Worraker and Richardson, 1979).

Turnbull (1968) was the first to establish a theoretical model of electroconvection, which is classified in the category of the conductivity models. He dealt with a thermally stabilized plane layer of a weakly conducting liquid, and presented the threshold condition for the instability. He also showed experimentally that as the convection is induced in an otherwise stagnant layer of castor oil or corn oil, the heat transfer across the layer is enhanced. Later Porter and Smith (1974) and Kikuchi and Taketani (1979) studied the effect of uniform d-c fields on forced convective heat transfer to transformer oil or kerosene in a horizontally oriented rectangular channel. The upper and lower walls of the channel, made of brass or copper plates, served as the electrodes. The upper wall also served as the heat transfer surface of constant heat flux. Both of their results show a significant increase in the heat transfer coefficient with an increase in the magnitude of the voltage applied to the lower wall while the upper wall is grounded. Of particular interest in the results shown by Porter and Smith is the fact that the increase in heat transfer coefficient with an increase in the applied voltage is more significant at the higher one of the two levels of heat flux selected in their experiments. This fact is consistent with the conductivity models. Porter and Smith pointed out that the threshold condition for the electroconvection observed in their experiments is in good agreement with that predicted by Turnbull's theory.

More recently Fujino and Mori (1987) dealt with an upward flow of R 113 (trichlorotrifluoroethane) in a vertically oriented parallel-plate channel equipped with a pair of semi-silvered glass-plate electrodes imbedded in the channel walls. Either electrode provided the heat transfer surface, while a positive or negative voltage was imposed on the other electrode. Fujino and Mori observed, in the flow field confined by the electrodes, electrically induced longitudinal rolls that presumably played the primary role in increasing the heat transfer coefficient with an increase in the magnitude of the applied voltage. The variation of heat transfer coefficient with the voltage showed, in contrast to that shown by Porter and Smith (1974), almost no dependency on the heat flux at the heated electrode surface. This fact indicates the dominancy of space charge generated by some mechanism practically independent of the temperature gradient in the flow field of R 113, and hence is more consistent with the mobility models than with the conductivity models.

The present paper reports on our study performed as an extension to the preliminary work of Fujino and Mori (1987). The dependencies of heat transfer coefficient and pressure drop on the sign and magnitude of applied voltage and on the heat flux at the heated electrode surface are presented. Also shown is the effect of addition of an electrolyte to the test fluid causing a significant change in its electrical conductivity. Based on the obtained knowledge on these matters, the struc-

[1]Present address: Kanagawa Works, Hitachi Ltd., Hadano 259-13, Japan.

Contributed by the Heat Transfer Division for publication in the JOURNAL OF HEAT TRANSFER. Manuscript received by the Heat Transfer Division November 3, 1987. Keywords: Augmentation and Enhancement, Forced Convection.

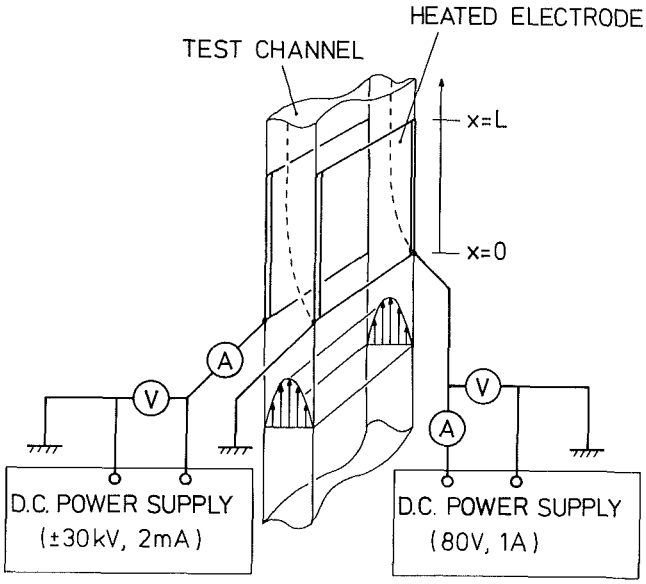

Fig. 1 Main portion of experimental apparatus (schematic)

ture and the mechanism of electroconvection and its possible utility as a means for enhancing heat transfer are considered.

Experimental

The experimental setup used in the present work was essentially the same as the one used in the preceding work of Fujino and Mori (1987). The test channel was made of polymethyl methacrylate (PMMA) plates, and was 2×120 mm in cross section. The channel was set vertically, and the test liquid, trichlorotrifluoroethane, known as R 113, was forced to flow upward in it. It was equipped with a pair of electrode plates, each extending over the full width of the channel (120 mm) and 200 mm in length along the flow direction, as illustrated in Fig. 1. Each electrode plate was so imbedded in the channel wall—a PMMA substrate plate—that its surface was just flush with that of the wall and hence the electrode spacing was equal to 2 mm. The part of the channel confined by the electrodes is called the test section hereafter. The channel extended over another 200 mm upstream from the test section. Thus, the liquid flow was likely to be fully developed in the direction normal to the electrode surfaces at the inlet of the test section. The electrode plate to provide the heat transfer surface was either a Pyrex-glass plate semi-silvered with lead oxide or a nickel-plated Bakelite plate. It was always grounded and held approximately at earth potential, while a small voltage difference was applied across its width to provide uniform heat flux at its metallized surface, which was in contact with the flowing liquid. The other electrode plate to provide an adiabatic wall was a Pyrex-glass plate semi-silvered with lead oxide. Positive or negative voltage was applied to this plate by use of a Spellman RHR 30PN30 high-voltage power supply. The local temperatures on each electrode plate were measured with thermocouples attached to the rear of the plate. Five thermocouples were simply glued onto the rear surface of the glass electrode plate, while twenty thermocouples were fixed to the rear surface of the Bakelite electrode plate in such a way that the junction of each thermocouple was buried in a hole that had been drilled on the surface almost piercing the plate. The temperatures measured by these thermocouples were regarded as the local temperatures on the frontal surfaces of the plates. Possible errors due to this assumption were analytically evaluated to be insignificant as exemplified later.

Pressure taps connected to manometers were installed at the inlet and the outlet of the test section. The difference in static pressure between these two positions was found by photographing the menisci in the manometers and by analyzing the developed films on an analysis projector.

The test liquid, R 113, was circulated in a closed loop consisting of the test channel and other auxiliary components such as reservoirs, a heat exchanger, a filter, a pump, etc. Except for the electrode surfaces in the test channel, no metal was exposed to the liquid in the loop. Thus, possible ion injection into the liquid was limited to that from the electrode surfaces. The flow rate of the liquid was always controlled so as to maintain the Reynolds number, defined as $\mathrm{Re} = u_m d/\nu$, at 191, where d is the channel thickness (2 mm), u_m the average velocity given as the quotient of the volume flow rate of the liquid

Nomenclature

C_i = $q_i d^2/(\epsilon|\phi|)$
C_o = $q_o d^2/(\epsilon|\phi|)$
d = electrode spacing
h_m = average heat transfer coefficient
K = charge carrier mobility
L = longitudinal length of test section
M = $\sqrt{\epsilon/\rho/K}$
Δp_e, Δp_0 = static pressure drop in the test section under an electric field and that under no electric field
q_i = charge density at injecting electrode
q_o = charge density in liquid due to dissociation of dissolved electrolyte
q_w = heat flux at the heated electrode surface
Re = Reynolds number $= u_m d/\nu$
Re* = Re that would be available when W_E is converted into the pumping power
R_T = critical electric Reynolds number $= K|\phi_T|/\nu$ for laminar-to-turbulent transition of electroconvection
T_b = bulk temperature of liquid
T_C = critical electric Rayleigh number $= \epsilon|\phi_C|/(\mu K)$ for the inception of electroconvection
T_w = temperature at the surface of heated electrode
u_m = average flow velocity
W_E = electric power consumption caused by the voltage difference across the electrodes
W_P = pumping power
x = longitudinal distance measured from the leading edge of the test section
Γ = volume flow rate per unit width of the test section
ϵ, ϵ_0 = electrical permittivities of liquid and of free space
μ = dynamic viscosity
ν = kinematic viscosity
ρ = mass density
σ = electrical conductivity
ϕ_C, ϕ_T = voltage applied to the electrode opposite to the heated electrode; its critical value for the onset of electroconvection and that for laminar-to-turbulent transition of electroconvection

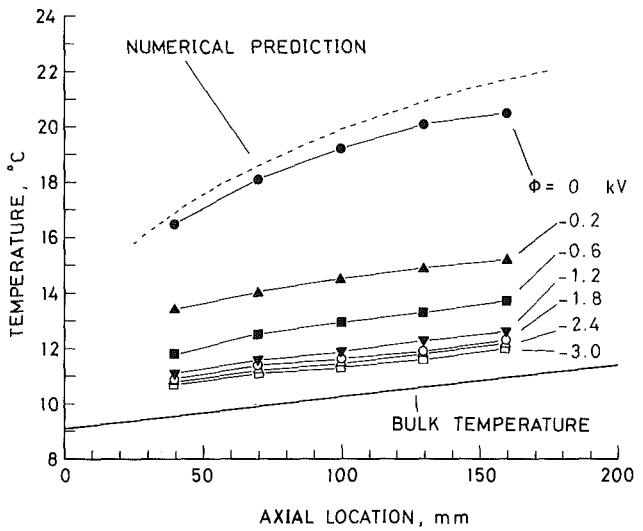

Fig. 2 Temperature distributions on heated glass-plate electrode: a trace amount of ASA-3 was added to the test liquid, R 113, increasing its conductivity to the order of 1 nS/m; Re = 191, q_w = 1.6 kW/m^2

by the cross-sectional area os the channel, and ν the kinematic viscosity of the liquid.

In some of the experiments we added a trace amount of an electrolyte solution ASA-3 (Shell Oil Co.), whose principal ingredient is xylene, to the test liquid to increase its conductivity from the order of 0.1 nS/m to that of 1 nS/m.

Results and Discussion

Heat Transfer and Pressure Drop. Figure 2 exemplifies a typical set of data on temperature distributions on the surface of a heated electrode in the absence and presence of electric fields. The data were obtained with the glass plate used as the heated electrode and with R 113 dissolving some amount of ASA-3 solution. The uncertainties of the temperature data are estimated to be within $+0.4/-0.2$ K, due to a finite heat loss to the rear side of the plate and a possible error in an electronic data acquisition system we used. Also shown for comparison in Fig. 2 is the numerical prediction of the temperature distribution for simple convective heat transfer to a plane Poiseuille flow of R 113 from either wall having uniform heat flux. (This calculation was repeated using several different grids, and no appreciable difference in the solution depending on the grid fineness was found.) A generally good agreement is found between the prediction and the experimental data obtained in the absence of electric field, indicating that the expected condition of uniform heat flux on the heated electrode surface was satisfied with a reasonable accuracy in the experiments. Strictly speaking, however, the deviation of the experimental data from the prediction exceeds, particularly in a downstream part of the test section, the possible temperature measurement error stated above; this is presumably ascribable, for the most part, to a heat loss from the trailing edge of the heated electrode plate that we have not evaluated.

As a measure for evaluating the extents of heat transfer enhancement due to the applied fields, we employ the average heat transfer coefficient defined as

$$h_m = q_w / \left\{ \int_0^L [T_w(x) - T_b(x)] dx / L \right\} \tag{1}$$

where $T_w(x)$ is the local temperature at the heated electrode surface, which is determined by interpolating or extrapolating such data as those exemplified in Fig. 2, and $T_b(x)$ is the local bulk temperature of a liquid simply calculated from the liquid temperature at the entrance of the test section, T_{in}, and from the value of q_w as

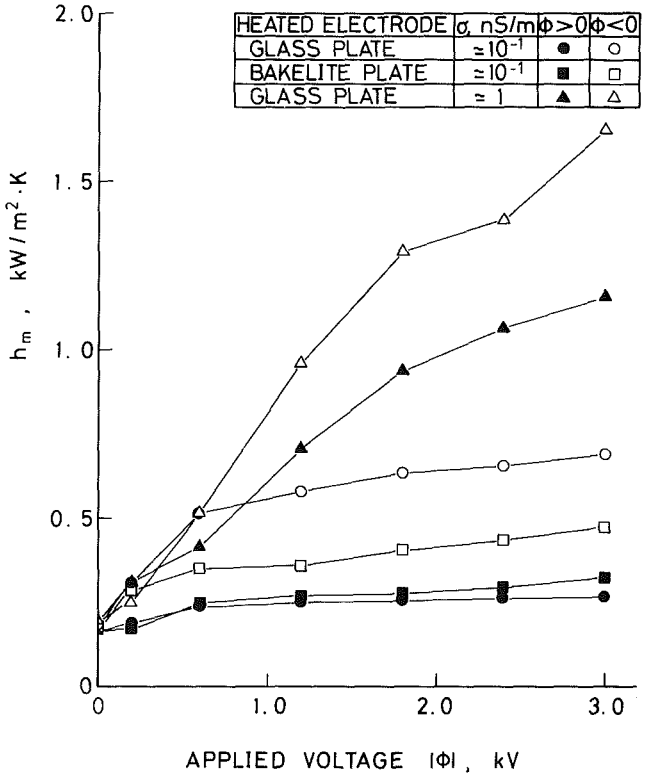

Fig. 3 Dependencies of average heat transfer coefficient on the magnitude of applied voltage: Re = 191, q_w = 1.6 kW/m^2

$$T_b(x) = T_{in} + q_w x / (\rho c_p \Gamma) \tag{2}$$

(Note that Fujino and Mori (1987) defined h_m by equation (1) but with T_{in} substituting for $T_b(x)$.) Figure 3 shows the dependency of h_m on the magnitude of voltage ϕ applied to the electrode opposite to the heated electrode under each of the six representative conditions characterized by the heated-electrode material, the sign of ϕ, and the order of electrical conductivity of the liquid. Each data point represents the mean of a few h_m values, obtained in different runs, whose uncertainties are estimated, based on the root-sum-square method (ASME, 1986), to be $+5/-6$ percent (for the lowest h_m values) to $+20/-24$ percent (for the highest h_m values). The scatter of the h_m values represented by each point was within ± 10 percent around the mean value indicated by the point. The uncertainty in ϕ was estimated to be as small as ± 5 V. In general, the application of negative voltages yielded larger enhancements. The heat transfer from the glass-plate electrode was enhanced to larger extents than that from the Bakelite-plate electrode when negative voltages were applied, and this was reversed when positive voltages were applied. The addition of a trace amount of the electrolyte solution, ASA-3, to R 113, causing an increase in its electrical conductivity, resulted in a drastic increase in the extents of enhancement at higher levels of voltages of either sign.

The values of h_m obtained with the heated glass-plate electrode are plotted in Fig. 4 against the heat flux at its surface, q_w. Each data point shown there has an uncertainty of $+5/-6$ to $+11/-13$ percent in h_m—the larger the h_m value, the larger the relative uncertainty—and one of ± 5 percent in q_w. It is evident that the extents of increases in h_m due to the applied fields were almost independent of the heat flux. This was just the same irrespective of the sign of ϕ, the material of the heated electrode, and the conductivity σ of the liquid. Figure 5 shows fractional increases in the static pressure drop over the test section caused by the application of voltages. The vertical bar on each data point indicates the range of variation

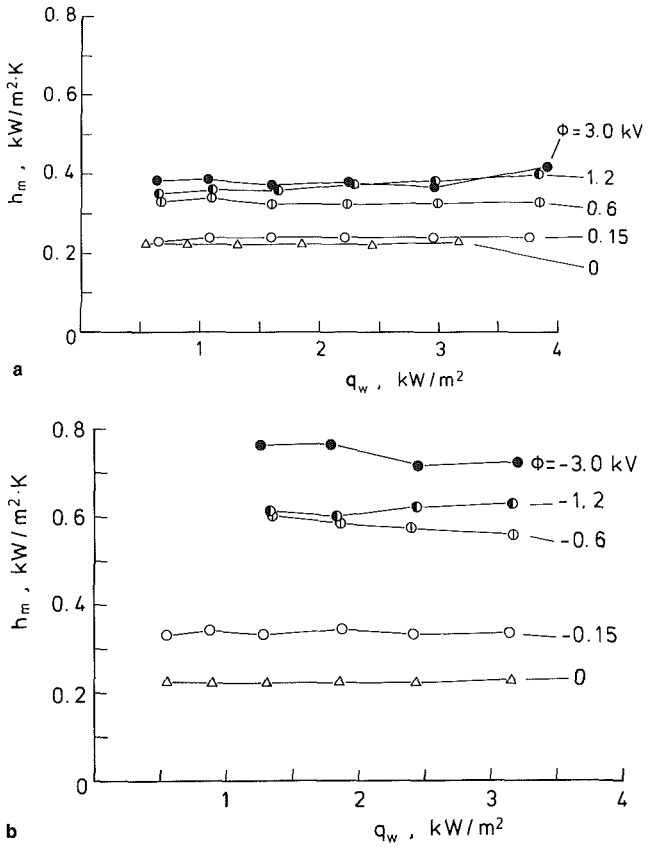

Fig. 4 Average heat transfer coefficient versus heat flux at the surface of glass-plate electrode: Re = 191; no addition of ASA-3 to R 113

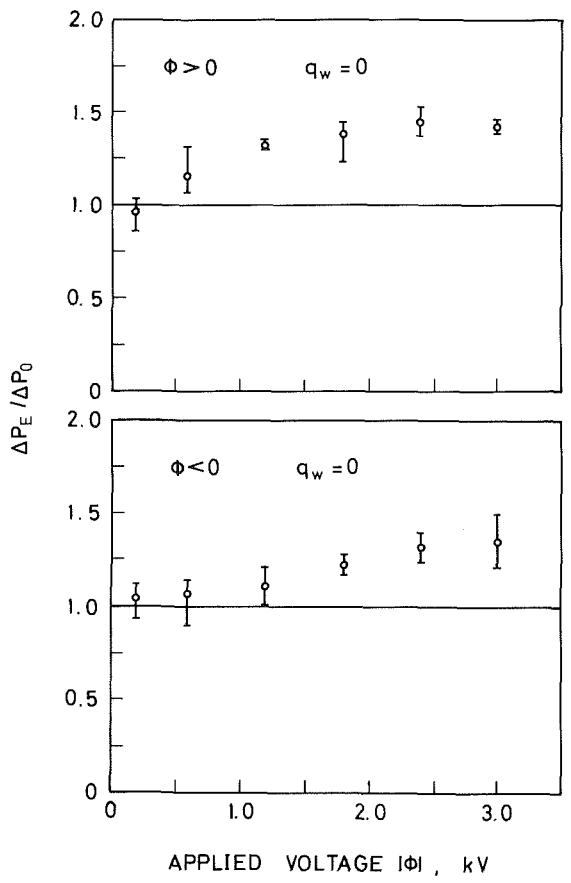

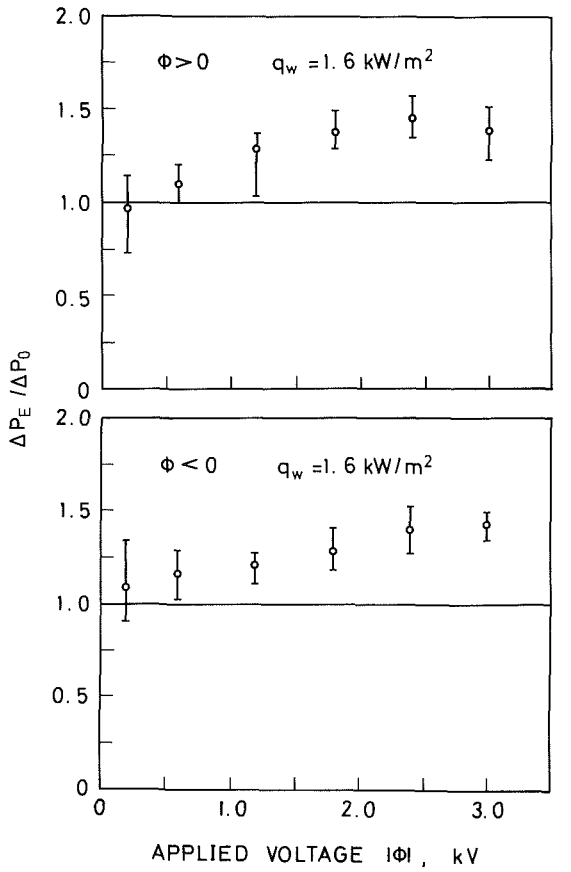

Fig. 5 Fractional increases, caused by applying voltages, in pressure drop over the test section plotted against the magnitude of applied voltages: Re = 191; no addition of ASA-3 to R 113

of $\Delta p_E/\Delta p_0$, which reflected a fluctuation of Δp_E during its measurement. The increase in the pressure drop with an increase of $|\phi|$ is ascribed to an electrically induced secondary flow (Fujino and Mori, 1987), which must be the cause of such increase in h_m as shown in Fig. 3. Consistent with the independency of h_m on the heat flux q_w, little dependency of the pressure drop on q_w is recognized in Fig. 5. Another finding that should be noted is the little dependency of the pressure drop on the sign of ϕ, which is in contrast with the heavy dependency of h_m on the sign of ϕ. These findings are interpreted below.

Structure of the Flow Field. The shadowgraphic observation through the glass-plate electrodes (Fujino and Mori, 1987) showed that the electroconvection taking the form of the secondary flow in the system of present interest is characterized by longitudinal rolls and, at higher levels of $|\phi|$, some turbulent motion superimposed on the rolls. It was also noted that the shadowgraphic images of the secondary flow hardly changed with q_w. The practical independencies on q_w of the shadowgraphic images, h_m (Fig. 4) and the pressure drop (Fig. 5) indicate that the secondary flow was little affected by the temperature field in the liquid. The fact that the pressure drop was little altered by the change in sign of ϕ suggests that the pattern, scale, and strength of the secondary flow in the test section were little altered as a whole by the change of the sign of ϕ. Meanwhile the dependency of h_m on the sign of ϕ (Fig. 4) shows that in the liquid layer adjacent to the heated electrode surface the secondary flow was more intensely induced, when negative voltages were applied to the nonheated electrode and hence the heated electrode served as the positive electrode. The only version that can consistently explain all of the findings and consequences described above is as follows: The secondary flow was not symmetrically located in each cross section of the channel but was concentrated on the positive electrode side

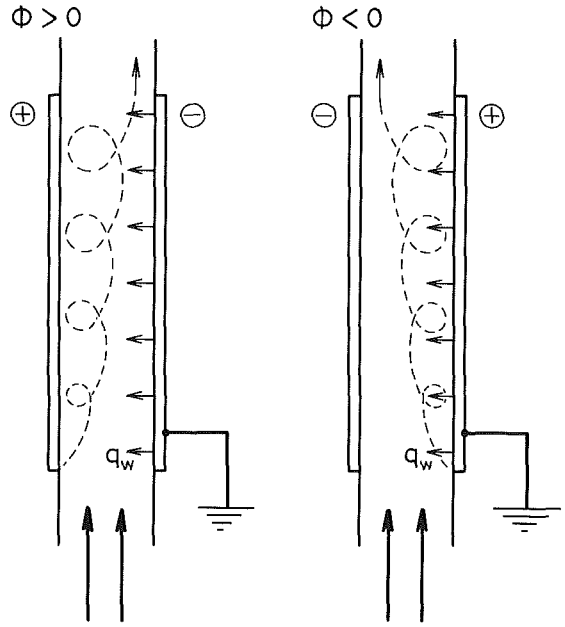

Fig. 6 Schematic illustration of electrically induced secondary flow assumed to be concentrated on the positive electrode side, whichever electrode is releasing the heat

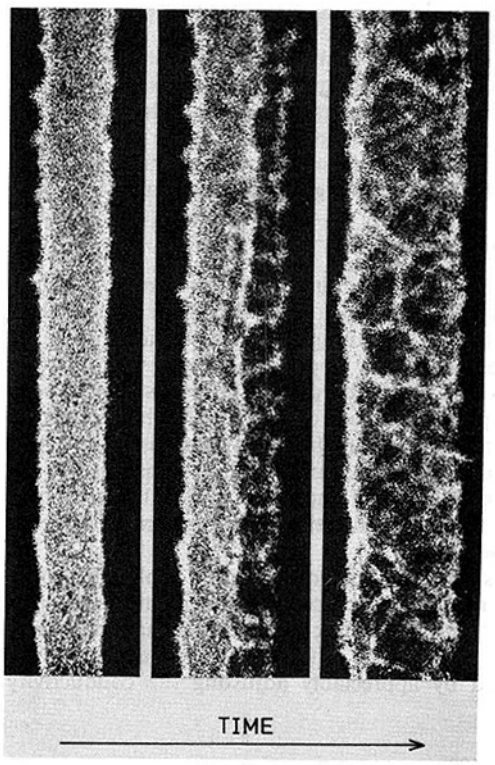

Fig. 7 Shadowgraphs showing a disturbed region developing from the earthed electrode side (right) to the opposite electrode (left) after imposing a voltage, 0.6 kV: time interval between neighboring shadowgraphs is 0.2 s

whether it was heated or not. Figure 6 is an illustration of the version. If this version were true, the secondary flow could interact more effectively with the otherwise stable thermal boundary layer on the heated electrode, when it served as the positive electrode, and hence would yield higher values of h_m; while the asymmetry of the secondary flow would be little reflected in the pressure drop.

The above version was originally presented in the preceding paper by Fujino and Mori (1987). Since we have obtained, in the present work, the pressure-drop data that support this version, we have discussed the version again in this subsection incorporating the pressure-drop data into the other results on heat transfer and flow observation.

Table 1 Critical voltages for electroconvection

	Criteria for the case of unipolar charge injection	Present experiments
Onset of convection	$T_C \equiv \frac{\epsilon\lvert\phi_C\rvert}{\mu K} \sim 100^{*} \rightarrow \lvert\phi_C\rvert \sim 57\ V^{\dagger}$	$\lvert\phi_C\rvert = 55 \pm 5$ V
Laminar-to-turbulent transition	$R_T \equiv \frac{K\lvert\phi_T\rvert}{\nu} \sim \frac{30}{M}^{**} \rightarrow \lvert\phi_T\rvert \sim 133\ V^{\dagger}$	$\lvert\phi_T\rvert = 130 \pm 30$ V

* Atten and Lacroix, 1979

** Lacroix, Atten and Hopfinger, 1975

† Following properties were used: $K = 1.7 \times 10^{-8}$ m^2/V-s, $\epsilon/\epsilon_0 = 2.4$, $\mu = 0.73$ mPa·s, $\rho = 1575$ kg/m^3

The Mechanism of Electroconvection. The independence of h_m and the pressure drop on the heat flux shows that the space charge that gives rise to electroconvection via Coulombic forces was generated by some mechanism that is intrinsically independent of the temperature field in the liquid. The most probable mechanism is injection of charge from either or both electrodes.

We conducted an additional experiment expecting to have some evidence for the charge injection in the system of present interest. The test section that we prepared for this purpose consisted of a pair of glass-plate electrodes, each 20 mm in width and 2 mm apart from each other, and side walls made of transparent polymethyl methacrylate plates. The test section was filled with a stagnant liquid R 113. A voltage difference was generated in one step across the electrodes, and the development of convection induced in the liquid was observed through the side walls of the channel with the aid of laser shadowgraphy, while a minimum heating was applied from the rear of each electrode to enable the shadowgraphic observation. Figure 7 gives a set of shadowgraphs showing the disturbed region developing from the earthed electrode side after a voltage of 0.6 kV was applied to the opposite electrode. These shadowgraphs indicate that the charge carriers playing a primary role in destabilizing the liquid were negative ions injected from the negative electrode.[2] Assuming that the advancing speed of the front of the disturbed layer represents the mobility K of the ions, we estimated K to be 1.7×10^{-8} m^2/V-s with an uncertainty of ± 20 percent. If we substitute this value of mobility into expressions for critical conditions for the onset of electroconvection (Atten and Lacroix, 1979) and for the laminar-to-turbulent transition of the convection (Lacroix et al., 1975), which were experimentally determined under the condition of a purely unipolar charge injection, we can predict the magnitudes of the voltage $|\phi|$ corresponding to those critical conditions as shown in Table 1. Also shown for comparison in Table 1 are the values of $|\phi|$ determined by use of such shadowgraphic observations as those described in the preceding paper (Fujino and Mori, 1987). A reasonably good agreement is found between predicted and experimental values for either critical condition. Thus, we can consistently explain all of our experimental results by assuming the charge injection from the negative electrode as the dominant mechanism for electroconvection.

A question arising from the above consideration is whether the electroconvection originating from the charge injection from one electrode (say, negative electrode) provides, under a steady state, more intensive agitation at the charge-injecting electrode side or at the other electrode side. No definite answer

[2] The electrochemical mechanism of the ion injection from the eletrode is not discussed in this paper. A discussion in this aspect is given, for example, by Denat et al. (1979).

to the question is available for the present. Here we refer only to two numerical analyses of electroconvection induced in an insulating liquid layer subject to unipolar charge injection, which seem relevant to the present question. One by Hopfinger and Gosse (1971) dealing with a transient process shows that as a steady state is achieved, the rate of production of turbulent energy is higher at the side of electrode opposite to the charge-injecting electrode. The other by Suzuki and Sawada (1983) shows that the electroconvection can have a pattern of stable rolls whose centers have some offsets toward the electrode opposite to the charge-injecting electrode. These results of numerical analyses suggest that the liquid is agitated more intensely at the positive-electrode side, if the charge is injected from the negative electrode, and hence they are consistent with the interpretation of our experimental results stated above. In order to settle the problem, however, it is necessary to examine in detail the structure of electroconvection using a relevant turbulence model.

Effects of Addition of Electrolyte. As shown in Fig. 3, the addition of an electrolyte solution, ASA-3, to R 113 caused significantly larger enhancements of heat transfer, particularly at higher levels of $|\phi|$. Evidently this fact shows that stronger convections were induced when the electrolyte solution was added to R 113. A brief discussion on the cause of the convection enhancement is given in Appendix.

The electroconvection intensified by the addition of ASA-3 must increase both h_m and the frictional drag in the test section. Nevertheless the apparent loss of static pressure, Δp_E, was reduced by the addition of ASA-3. As a matter of fact, $\Delta p_E/\Delta p_0$ was nearly unity, almost independent of the sign and magnitude of ϕ and of the heat flux q_w when ASA-3 was added so as to increase σ to the order of 1 nS/m. Further addition of ASA-3 causing a higher value of σ even resulted in a decrease of $\Delta p_E/\Delta p_0$ below unity with an increase in $|\phi|$. Thus, it seems that when σ is increased to a certain extent by the addition of electrolyte, an anomalous mechanism arises that can reduce the apparent pressure loss despite an increase in the frictional drag, due to the electroconvection, with an increase in $|\phi|$. The most probable mechanism is the one conceived by Honda and Atten (1978) to explain the negative electroviscous effect: The dissociation of the electrolyte causes a thin axially developing heterocharge layer on either electrode, which in turn induces such a nonuniform electric field as to stress the liquid in the direction of the primary flow.[3]

Evaluation of Heat Transfer Augmentation. Here we regard the test section used in the present experiments as a module of heat transfer device, and attempt to assess its performance. In doing this we follow the method that Takimoto et al. (1988) employed in evaluating the heat transfer enhancement obtained by the application of corona discharge to an air flow in a channel. For this purpose we have calculated the power W_P required to make the liquid flow in the test section against the pressure difference Δp_E, and have determined the electric power consumption W_E based on the data on ϕ and the electric current across the test section. In Fig. 8 the data on h_m are plotted against the sum of W_P and W_E in the whole range of the present experiments. The uncertainties of the values of $W_P + W_E$ indicated by the data points are estimated, based on the root-sum-square method, to be within ± 11 percent. Also shown in Fig. 8 for comparison are the values of Reynolds number Re* that could be available if W_E were converted with 100 percent efficiency into the pumping power to cause the liquid to flow at a higher rate through the test section, and a numerical prediction of h_m that would be available in a plane Poiseuille flow at each level of Re*. (The

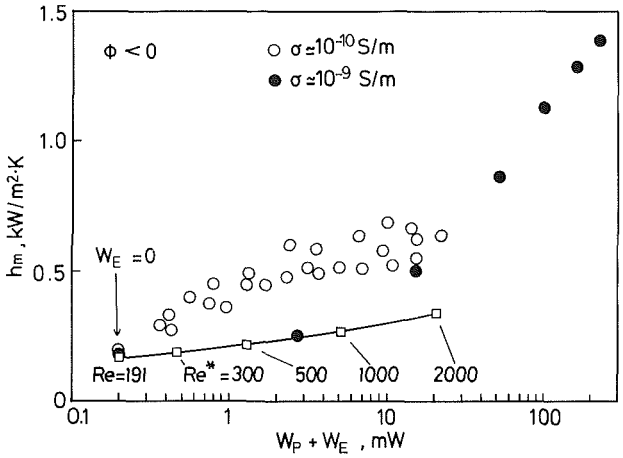

Fig. 8 Average heat transfer coefficient versus the sum of pumping power W_P and electric power W_E consumed in the test section: the open rectangles represent the numerical predictions of h_m that would be available if W_E were converted into the pumping power to attain higher flow rates of liquid

calculation to predict h_m at each level of Re* was repeated using several different grids, and no appreciable difference in the solution depending on the fineness of grids was found.) It should be noted that in calculating the pumping power presented here we have not taken into account any drag other than that in the test section. An increase in the total pumping power required to obtain a higher level of Re* in a practical system is therefore much larger than that read on the graph in Fig. 8. The results compiled in the graph suggest that the application of electricity to induce a secondary flow can be an efficient means for enhancing heat transfer in some practical applications wherein the use of a high Reynolds number turbulent flow of a cooling liquid is difficult.

Concluding Remarks

This study has demonstrated a particular system in which the charge injection at either electrode presumably plays a dominant role in causing electroconvection in a liquid even in the presence of an appreciable temperature gradient. The dominancy of the charge injection must be related to some system parameters, one of which is the channel thickness (i.e., the electrode spacing) being as small as 2 mm. With much larger channel thicknesses, such as those used by Turnbull (1968) and by Porter and Smith (1974), the dominancy of the role of the charge injection may be suppressed, as mentioned in Appendix.

The study has also shown that the application of an electric field across a low Reynolds number channel flow of a weakly conducting liquid can be an efficient means for enhancing heat transfer. The degree of the enhancement may be significantly extended by appreciably adjusting the conductivity of the liquid.

References

ASME, 1986, "Measurement Uncertainty—ANSI/ASME PTC 19.1-1985," *ASME Performance Test Codes, Supplement on Instruments and Apparatus*, Part 1.

Atten, P., and Lacroix, J. C., 1979, "Non-Linear Hydrodynamic Stability of Liquids Subjected to Unipolar Injection," *Journal de Mechanique*, Vol. 18, pp. 469-510.

Bergles, A. E., 1978, "Enhancement of Heat Transfer," *Proceedings of the 6th International Heat Transfer Conference*, Hemisphere Publishing Corp., Washington, DC, Vol. 6, pp. 89-108.

Denat, A., Gosse, B., and Gosse, J. P., 1979, "Ion Injections in Hydrocarbons," *Journal of Electrostatics*, Vol. 7, pp. 205-225.

Fujino, T., and Mori, Y. H., 1987, "The Effect of a Transverse Electric Field on Laminar Channel Flow With a Constant Heat Rate," *Flow Visualization IV*, C. Veret, ed., Hemisphere Publishing Corp., Washington, DC, pp. 643-648.

Honda, T., and Atten, P., 1978, "Electroviscous Effect in Poiseuille Flow

[3] This mechanism is distinct from well-known electro-osmosis in that the axial stress results from a thin but macroscopic heterocharge layer instead of an electric double layer on either electrode.

Under Electrolysis Condition," *Proceedings of the 6th International Conference on Conduction and Breakdown in Dielectric Liquids*, pp. 315–320.

Hopfinger, E. J., and Gosse, J. P., 1971, "Charge Transport by Self-Generated Turbulence in Insulating Liquids Submitted to Unipolar Injection," *The Physics of Fluids*, Vol. 14, pp. 1671–1682.

Kikuchi, K., and Taketani, T., 1979, "Enhancement of Forced Convection Heat Transfer by the Effect of Direct Current High Voltage Electric Field" (in Japanese), *Journal of Mechanical Engineering Laboratory*, Mechanical Engineering Laboratory, Ibaraki, Japan, Vol. 33, pp. 53–68.

Lacroix, J. C., Atten, P., and Hopfinger, E. J., 1975, "Electro-Convection in a Dielectric Liquid Layer Subjected to Unipolar Injection," *Journal of Fluid Mechanics*, Vol. 69, pp. 539–563.

Martin, P. J., and Richardson, A. T., 1984, "Conductivity Models of Electrothermal Convection in a Plane Layer of Dielectric Liquid," ASME JOURNAL OF HEAT TRANSFER, Vol. 106, pp. 131–136.

Porter, J. E., and Smith, R. B., 1974, "The Effect of a Transverse Electrostatic Field on Laminar Flow Heat Transfer in a Rectangular Channel," *Proceedings of the 5th International Heat Transfer Conference*, JSME/SCEJ, Tokyo, Vol. 2, pp. 198–202.

Suzuki, M., and Sawada, Y., 1983, "Relative Stabilities of Metastable States of Convecting Charged-Fluid Systems by Computer Simulation," *Physical Review A*, Vol. 27, pp. 478–489.

Takimoto, A., Tada, Y., Yamada, K., and Hayashi, Y., 1988, "Heat Transfer Enhancement in a Convective Field With Corona Discharge" (in Japanese), *Transactions of the JSME*, Ser. B, Vol. 54, pp. 695–703.

Turnbull, R., 1968, "Electroconvective Instability With a Stabilizing Temperature Gradient. I. Theory, II. Experimental Results," *The Physics of Fluids*, Vol. 11, pp. 2588–2603.

Worraker, W. J., and Richardson, A. T., 1981, "The Effect of Temperature-Induced Variations in Charge Carrier Mobility on a Stationary Electrohydrodynamic Instability," *Journal of Fluid Mechanics*, Vol. 93, pp. 29–45.

APPENDIX

Addition of Electrolyte as an Electroconvection Promotor

Addition of an electrolyte to a nonpolar liquid causes an increase in the charge density in the liquid due to the dissociation of the electrolyte, q_o, or a dimensionless parameter defined as $C_o = q_o d^2/(\epsilon|\phi|) = \sigma d^2/(2\epsilon K|\phi|)$ (Denat et al., 1979), where ϵ and σ are the permittivity and the conductivity of the liquid, respectively, d is the electrode spacing, and C_o represents the ratio of the conduction current to the injection current. A fact to be stressed here is that the charge density at the injecting electrode, q_i, can increase with an increase in q_o or σ. Denat et al. (1979) experimentally showed that the dimensionless injection parameter defined as $C_i = q_i d^2/(\epsilon|\phi|)$ is uniquely dependent on C_o with a constant proportional factor irrespective of the liquid used. Therefore, the addition of ASA-3 to R 113 in the present experiments, causing an increase in σ from the order of 0.1 nS/m to 1 nS/m and hence an increase in C_o by one order, presumably resulted in a rise of q_i and C_i by one order as well, and thereby intensified the electroconvection.

Effect of Channel Thickness

The dimensionless parameter C_o can also be increased with an increase in the channel thickness d instead of an increase in the charge density in the liquid q_o. Martin and Richardson (1984) suggested that as C_o increases with an increase in d, the charge generation due to the thermally induced gradients in conductivity can become more prominent. This is possibly the reason why the experimental results obtained by Turnbull (1968) and by Porter and Smith (1974) with much larger electrode spacings can be explained well by exclusively assuming this mechanism of charge generation instead of the injection. In general, both mechanisms can share the role for inducing electroconvection depending on the magnitude of C_o, as long as the liquid used is rather pure and hence an increase in C_o does not result in a promotion of charge injection.

Kelvin-Helmholtz Instability and Cooling Limitations of a Vertical Molten Sheet Confined by Alternating Magnetic Fields

J. R. Hull
Argonne National Laboratory,
Argonne, IL 60439
Mem. ASME

Limitations imposed by a Kelvin-Helmholtz-type instability on the cooling of a vertical molten sheet that is confined by magnetic fields alternating in time are calculated. The molten sheet is cooled by a gas stream flowing on both sides of the sheet. The Kelvin-Helmholtz instability imposes a maximum velocity on the cooling gas, which limits the cooling rate. The maximum cooling rate is calculated with respect to the maximum velocity, gas physical properties, flow channel geometry, surface tension, and magnetic field properties.

Introduction

Production of metal plates and sheets of steel, aluminum, and copper accounts for a significant fraction of the energy consumption of many industrialized nations. A large reduction in the energy requirement could be achieved if the plates could be continuously cast in near-net shape. The use of magnetic levitation in induction melting (Peifer, 1965) and continuous casting of aluminum (Getselev, 1971) has led to the suggestion that magnetic levitation of molten steel can achieve a continuous casting of near-net shape while maintaining or possibly improving the metallurgical properties of the steel (Hull et al., 1987). One option for electromagnetic casting is the suspension of a vertical, molten metal sheet in a high-frequency, alternating magnetic field. The frequency is high enough so that the electromagnetic skin depth is a small fraction of the sheet thickness, and the magnetic field is configured so that the pressure of the magnetic field applied to the sheet surface exactly balances the metallostatic pressure of the molten metal. The metallostatic pressure may be substantially reduced by application of a traveling magnetic field. The field parameters are chosen to avoid magnetically induced instability in the sheets, e.g., as discussed by McHale and Melcher (1982). When the metal sheet leaves the electromagnetic caster, the surface of the sheet, together with a sufficiently large fraction of the interior, has solidified to the point that mechanical support of the sheet is possible.

To minimize the size of the magnet and maximize material throughput, the molten sheet must be cooled quickly. In order to augment radiation cooling, a fast-flowing vertical stream of inert cooling gas is introduced on both sides of the molten sheet. This hydrodynamic configuration introduces the possibility of a Kelvin-Helmholtz-type instability (Chandrasekhar, 1961). The instability arises because the pressure perturbation exerted by the gas can do work on the interface, and at a sufficiently large gas velocity the instability can tear apart the molten sheet. In this paper the maximum velocity of the cooling gas is calculated, as indicated by the onset of the Kelvin-Helmholtz-type instability. This velocity limit is then used to calculate the maximum cooling of the sheet by the gas stream.

A number of authors have examined the Kelvin-Helmholtz problem with constant magnetic fields (e.g., Chandrasekhar, 1961; Gerwin, 1968), and Garnier and Moreau (1983) have solved for the instability conditions in the presence of alternating magnetic fields. The latter solution is not applicable in the present problem, however, because the uniform and constant magnetic field strengths assumed by Garnier and Moreau to be present at the surface of the molten metal provide a stabilizing influence when magnetic tension arises from the distortion of the field lines as the surface of the molten metal deforms. In the present case the stabilization occurs because the field strength changes as the surface deforms. The details of the magentic field configuration for this type of problem can be evaluated numerically (Lavers, 1986; Meyer et al., 1987), but such calculations are not yet accurate enough to predict instability conditions.

While no previous work has addressed the present problem directly, several studies give insight into the analysis. Miles (1962) indicated that the resonance between Tollmien-Schlichting waves and free surface waves occurs well below the Kelvin-Helmholtz limit for water, but that agreement is good between experiments and Kelvin-Helmholtz instability predictions for oils with the higher viscosity associated with molten metals. Chang and Russell (1965) showed that at low Mach numbers the stability conditions between a compressible gas stream and an adjacent liquid layer do not differ significantly from those of incompressible gas flows. They also showed that at sonic and supersonic gas velocities the system is always unstable, despite the stabilizing influence of surface tension. Nayfeh and Saric (1971) concluded that at low liquid Reynolds number and subsonic gas flow, stability conditions are independent of viscosity in linear analysis, the nonlinear motion of the gas has no effect, and the nonlinear motion of the viscous liquid is stabilizing. Drazin's finite amplitude analysis (1970) and Thorpe's experiments (1968, 1969) indicated that idealizations of the linear stability analysis to the Kelvin-Helmholtz problem lead to results that are applicable to real flows.

Basic Analysis

The initial stationary state is indicated in Fig. 1, with a molten slab denoted by subscript 2 between two slabs of coolant gas denoted by subscripts 1 and 3. The confinement magnets are located outside this system. Both the molten metal and coolant gas are approximated by incompressible, inviscid fluids, with the mean stream flow in the z direction with velocity W. We are concerned only with the purely molten state and assume that the densities of the liquid and gas are homogeneous in the y and z directions.

Contributed by the Heat Transfer Division for publication in the JOURNAL OF HEAT TRANSFER. Manuscript received by the Heat Transfer Division February 8, 1988. Keywords: Flow Instability, Liquid Metals, Materials Processing and Manufacturing Processes.

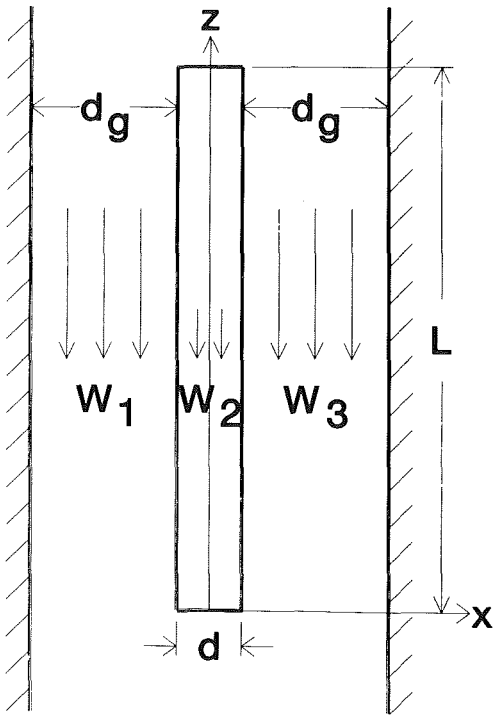

Fig. 1 Schematic diagram of vertical molten slab between two gas-filled cooling channels

The magnetic field generates a pressure P_m in the x direction that acts at the surface of the molten metal. In the stationary state this pressure exactly cancels the metallostatic pressure P_o along the two interfaces between the liquid metal and the gas. In addition, conservation of magnetic flux between the molten slab and the magnet requires the pressure to change as

$$P_m = P_o - \gamma(x_s - x_{so}) \tag{1}$$

where x_s is the position of the free surface and x_{so} is the surface position at equilibrium. If the free surface of the molten slab moves toward the magnet, the flux between the magnet and the slab compresses, and the magnetic pressure increases. A corresponding pressure decrease occurs for movement of the surface away from the magnet.

The calculation follows along the lines of Chandrasekhar (1961). The basic hydrodynamic equations governing the perturbation are

$$\rho\frac{\partial u}{\partial t} + \rho W\frac{\partial u}{\partial z} = -\frac{\partial}{\partial x}(\delta P) + T\left[\left(\frac{\partial^2}{\partial y^2} + \frac{\partial^2}{\partial z^2}\right)(\delta x_s)\right]\delta(x-x_s) - \gamma\delta x_s\delta(x-x_s) \tag{2}$$

$$\rho\frac{\partial v}{\partial t} + \rho W\frac{\partial v}{\partial z} = -\frac{\partial}{\partial y}(\delta P) \tag{3}$$

$$\rho\frac{\partial w}{\partial t} + \rho W\frac{\partial w}{\partial z} + \rho u\frac{\partial W}{\partial x} = -\frac{\partial}{\partial x}(\delta P) - g\delta\rho \tag{4}$$

$$\frac{\partial u}{\partial x} + \frac{\partial v}{\partial y} + \frac{\partial w}{\partial z} = 0 \tag{5}$$

$$\frac{\partial}{\partial t}(\delta x_s) + W_s\frac{\partial}{\partial z}(\delta x_s) = u(x_s) \tag{6}$$

$$\frac{\partial}{\partial t}(\delta\rho) + W\frac{\partial}{\partial z}(\delta\rho) = -u\frac{\partial\rho}{\partial x} \tag{7}$$

representing, respectively, conservation of momentum in each coordinate direction; incompressibility; the continuity of the free surface from one medium to the next; and the equation of state after homogeneity in the y and z directions has been considered. Adopting a normal mode analysis, the perturbed variables are assumed to have the form

$$u,\ v,\ w,\ \delta\rho,\ \delta P,\ \delta x_s \sim \exp[nt + ik_y y + ik_z z] \tag{8}$$

After we substitute into equations (2)–(7) and take derivatives, we solve the resulting set of equations for u. At a free surface

$$\Delta_s[\rho(n+ik_z W)Du - ik_z\rho u(DW)] = [-ik_z g\Delta_s(D\rho) + k^2(\gamma + k^2 T)]\left(\frac{u}{n+ik_z W}\right)_s \tag{9}$$

where

$$k^2 = k_y^2 + k_z^2$$

Nomenclature

A, a, A_1, A_2 = coefficients
B, b = coefficients
c = coefficient
c_g = specific heat of gas
D = $\partial/\partial x$
d = thickness of slab
g = acceleration of gravity
h = heat transfer coefficient
K = thermal conductivity
k = wave number
L = length of molten slab
n = time constant
Nu = Nusselt number
P = pressure
Pr = Prandtl number
Q = cooling rate
Re = Reynolds number
T = surface tension
T_g = initial gas temperature
T_s = temperature of molten metal
t = time
u, v, w = perturbed fluid velocities in the x, y, z directions, respectively
W = main fluid flow velocity in the z direction
x = coordinate direction perpendicular to slab
y = coordinate direction parallel to slab and perpendicular to mean flow
z = coordinate direction parallel to slab and parallel to mean flow
α = coefficient
β = exponential factor = $kd/2$
γ = restoring pressure of magnetic field = $\partial P_m/\partial x$
$\Delta_s(f)$ = $f_{x=x_s+0} - f_{x=x_s-0}$
δ = perturbed quantity
$\delta(x)$ = Dirac delta function
μ = gas viscosity
ρ = density

Subscripts

c = critical
D = hydraulic diameter
g = gas
m = magnetic
o = equilibrium
s = free surface
1, 2, 3 = fluid type

and Δ_s represents a jump that a quantity experiences at an interface. Away from a surface

$$(n+ik_zW)(D^2-k^2)u-ik_zu(D^2W)+\frac{(D\rho)}{\rho}[(n+ik_zW)(Du)-ik_zu(DW)] \quad (10)$$

$$-\frac{ik_zg}{\rho}\left(\frac{ik_zu(DW)(D\rho)}{(n+ik_zW)^2}-\frac{uD^2\rho+(Du)(D\rho)}{n+ik_zW}\right)=0$$

At this stage of the analysis, both W and ρ may have an x dependence.

Two Fluid Half-Planes With Vertical Boundary

Consider the case of two uniform fluid half-planes in relative vertical motion, separated by a vertical boundary at $x=0$, and subject to equations (1)–(10). Let the stream velocities W_1 and W_2 be constant, and let densities ρ_1 and ρ_2 be constant, i.e.,

$$DW_1=DW_2=0$$
$$D\rho_1=D\rho_2=0$$

Away from the boundaries, equation (10) reduces to

$$(D^2-k^2)u_1=0 \qquad (x<0) \quad (11)$$
$$(D^2-k^2)u_2=0 \qquad (x>0) \quad (12)$$

with solutions

$$u_1=A(n+ik_zW_1)\exp(k_xx) \qquad (x<0) \quad (13)$$
$$u_2=A(n+ik_zW_2)\exp(-k_xx) \qquad (x>0) \quad (14)$$

For the solutions to satisfy equations (11) and (12), $k_x=k$. At $x=0$, equation (9) reduces to

$$\Delta_s[\rho(n+ik_zW)Du]=k^2(\gamma+k^2T)\left(\frac{u}{n+ik_zW}\right)_s \quad (15)$$

$$\rho_2(n+ik_zW_2)^2+\rho_1(n+ik_zW_1)^2+(\gamma+k^2T)k^2/k_x=0 \quad (16)$$

The characteristic equation is

$$n^2(\rho_1+\rho_2)+n[2ik_z(\rho_1W_1+\rho_2W_2)]-k_z^2(\rho_1W_1^2+\rho_2W_2^2)+k(\gamma+k^2T)=0 \quad (17)$$

a quadratic equation for the time constant n. In order for the solution to be stable, the discriminant of equation (17) must be negative, resulting in the stability condition

$$(W_1-W_2)^2<\frac{(\rho_1+\rho_2)k(\gamma+k^2T)}{\rho_1\rho_2k_z^2} \quad (18)$$

Minimizing the right-hand side of equation (18) with respect to k_z results in

$$k=k_z$$

Further minimization with respect to k results in

$$k_c=(\gamma/T)^{1/2} \quad (19)$$

and substituting this into equation (18) results in

$$(W_1-W_2)^2<2(\rho_1+\rho_2)(\gamma T)^{1/2}/(\rho_1\rho_2) \quad (20)$$

Unless this condition is met, the interface will be unstable in the Kelvin–Helmholtz sense.

Molten Slab Between Two Gas Streams

Consider now the case indicated in Fig. 1, where a molten metal slab of thickness d and vertical velocity W_2 is sandwiched between two gas streams with vertical stream velocities W_1 and W_3, respectively. The y–z plane is centered in the molten slab, and a magnetic restoring force acts at both free surfaces of the molten metal, as discussed above. The density is homogeneous within each of the fluid slabs. Further, assume $d_g \gg 1/k_c$. The solution follows arguments similar to those in the previous section. A normal mode analysis gives the perturbed fluid velocities

$$u_1=A_1(n+ik_zW_1)\exp(kx) \qquad (x<-d/2) \quad (21)$$

$$u_2=(n+ik_zW_2)[A_2\exp(kx)+A_3\exp(-kx)] \qquad (-d/2<x<d/2) \quad (22)$$

$$u_3=A_4(n+ik_zW_3)\exp(-kx) \qquad (d/2<x) \quad (23)$$

Continuity at the free surface requires

$$A_1e^{-\beta}=A_2e^{-\beta}+A_3e^{\beta} \quad (24)$$
$$A_4e^{-\beta}=A_2e^{\beta}+A_3e^{-\beta} \quad (25)$$

and application of equation (15) at each surface results in

$$\rho_2(n+ik_zW_2)^2(A_2e^{-\beta}-A_3e^{\beta})-\rho_1(n+ik_zW_1)^2A_1e^{-\beta}=k(\gamma+k^2T)A_1e^{-\beta} \quad (26)$$

$$-\rho_2(n+ik_zW_2)^2(A_2e^{\beta}-A_3e^{-\beta})-\rho_3(n+ik_zW_3)^2A_4e^{-\beta}=k(\gamma+k^2T)A_4e^{-\beta} \quad (27)$$

Equations (24)–(27) may be solved for the case when the gas streams on both sides of the molten slab are identical, i.e., $W_1=W_3$, and $\rho_1=\rho_3$. There are two roots to the characteristic equation, which yield the stability criteria

$$(W_1-W_2)^2<\frac{[\rho_2+\rho_1\coth(\beta)]k(\gamma+k^2T)}{\rho_1\rho_2k_z^2} \quad (28)$$

$$(W_1-W_2)^2<\frac{[\rho_2+\rho_1\tanh(\beta)]k(\gamma+k^2T)}{\rho_1\rho_2k_z^2} \quad (29)$$

For a given k_z and k, the right-hand side of equation (29) is always less than the right-hand side of equation (28). Equation (29) should then always be taken as the stability criterion for the problem. The right-hand side of equation (29) is always less than the right-hand side of equation (18). However, because $\rho_1 \ll \rho_2$ for the problem at hand, equation (18) should be sufficiently accurate, in view of the other approximations made in the analysis.

Imposed Cooling Limits

For the system illustrated in Fig. 1, we ignore radiative cooling and assume that the superheat in the molten metal is negligible so that the slab surface is at a uniform temperature. We assume that the molten metal and gas physical properties are independent of temperature and that the magnetic field properties are constant with height. In practice the latter assumption would be implemented by using the values for the point where the magnetic restoring pressure was weakest. The rate of heat removal from one side of the molten slab, per unit width of the slab, is given by

$$Q=\rho_gc_gWd_g(T_s-T_g)\left[1-\exp\left(\frac{-hL}{\rho_gc_gWd_g}\right)\right] \quad (30)$$

$$h=\mathrm{Nu}_DK_g/(2d_g) \quad (31)$$

For normal turbulent flow in a channel, the correlation for Nusselt number is usually given in the form

$$\mathrm{Nu}_D=a\,\mathrm{Pr}^b\,\mathrm{Re}_D^c$$
$$\mathrm{Re}_D=2\,\rho_g\,d_g\,W_g/\mu_g \quad (32)$$

If we assume that the molten slab is stationary compared to the gas stream and also assume that the gas density is much less than the density of the molten metal, then from previous sections, we know that the Kelvin–Helmholtz-type instability places a limit on W_g, given by

$$W_g=(2/\rho_g)^{1/2}(\gamma T)^{1/4} \quad (33)$$

Using equations (31)–(33) in equation (30) gives

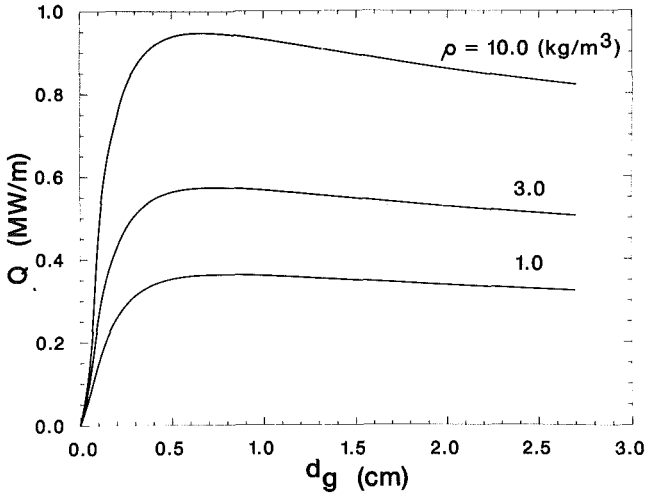

Fig. 2 Calculated heat removal rate versus thickness of gas channel

$$Q = A\, d_g\, \rho_g^{1/2}\left[1-\exp\left(\frac{-B}{d_g^{2-c}\rho_g^{(1-c)/2}}\right)\right] \tag{34}$$

$$A = 2^{1/2} c_g (\gamma T)^{1/4} (T_s - T_g)$$

$$B = \frac{aK_g L\ \mathrm{Pr}^b}{8^{(1-c)/2} c_g \mu_g^c (\gamma T)^{(1-c)/4}}$$

For a given channel width, Q increases with increasing gas density. If we optimize Q with respect to the channel width, we find an optimum width as given by

$$d_g = \left[\frac{B}{\alpha\, \rho_g^{(1-c)/2}}\right]^{1/(2-c)} \tag{35}$$

where α is a solution of the equation

$$1 + (2-c)\alpha - \exp(\alpha) = 0 \tag{36}$$

A maximum heat removal rate is given by

$$Q = A\ (B/\alpha)^{2-c}(1-e^{-\alpha})\ \rho_g^{1/(4-2c)} \tag{37}$$

Physically, a maximum heat removal rate must occur as a compromise between the tendency for a decrease in $(T_s - T_g)$ with decreasing d_g because of a smaller heat capacity of the gas, and a decrease in temperature gradient as d_g increases because of an increase in boundary layer thickness.

The heat removal rate on one side of the molten slab as a function of gas channel width is shown in Fig. 2 for several gas densities and for the parameters indicated in Table 1. Economics dictate that the gas channel should be as small as possible to minimize the amount of cooling gas used. On the other hand, the cooling rate must be large enough to compensate for the eddy current heating from the magnetic field and still solidify the liquid metal quickly. The trends shown in Fig. 2 indicate that the channel width can be approximately one-half the optimum, as calculated by equation (35), without sacrificing too much cooling power. In practice, the minimum channel width is likely to be determined by the space needed by bulk oscillations of the molten sheet within the magnetic field. In addition, if the channel width is too small, then the proximity of the solid channel wall will enhance the pressure variations of the gas flow and decrease the critical gas velocity, as was indicated by Kordyban (1977) for the nonmagnetic case.

For the parameters in Table 1, $k_c = 2310\ \mathrm{m}^{-1}$, corresponding to a critical wavelength of 2.7 mm, approximately the channel width beyond which the cooling rate is relatively level. For this wavelength the fluid surface tension and magnetic restoring force are equally effective in preventing wave disturbances. For smaller wavelengths than this, surface tension dominates, and for larger wavelengths, the magnetic force is the most significant effect. In this example it does not appear feasible to increase the maximum gas velocity by reducing the channel width below the critical wavelength, because the decrease in channel width reduces the cooling rate more than the corresponding increase in velocity raises it.

Table 1 Numerical values for parameters used in example calculations

$a = 0.023$	$b = 0.4$
$C = 0.8$	$\alpha = 0.354$
$T = 1.872$ N/m	$\gamma = 1.0\times10^7$ N/m^3
$T_s = 1540$°C	$T_g = 40$°C
$L = 1.33$ m	$K_g = 0.052$ W/(m•K)
$\mu_g = 1.0\times10^{-4}$ kg/(m•s)	$c_g = 1086$ J/(kg•K)
$A = 1.52\times10^8$ W/(m$^{1/2}$•kg$^{1/2}$)	$B = 1.09\times10^{-3}$ m$^{3/2}$/kg$^{1/10}$

Discussion and Concluding Remarks

The critical gas velocity has been calculated by linear stability analysis for the case in which a vertical molten sheet is constrained by magnetic fields that provide a surface restoring force on the sheet and a cooling gas is directed parallel to the sheet surface. The critical velocity to the fourth power is proportional to the product of the liquid surface tension and the restoring pressure gradient exerted by the magnetic field. The value for the critical velocity has been used to predict the maximum cooling rate for the sheet.

Gravity does not play a role in the stability calculations of the previous sections. For the small-amplitude linear analysis, the surface is not perturbed enough for gravity to have a first-order effect. Once the disturbance of the free surface is large enough, however, gravity should have a further destabilizing effect. Thus, the calculated limit for the velocity should be a very real limit for the cooling process.

The Nusselt number of equation (32) can be increased somewhat by the use of turbulence enhancement methods in the gas channel. The effect of these enhancement methods on the hydrodynamic instability is unknown, but for some methods there might be no detrimental effect, because the Kelvin–Helmholtz-type instability was calculated in the previous sections with the assumption that the velocity was constant in the gas channel. In reality, the mean velocity profile near the surface of the slab goes as $x^{1/n}$, where x is distance from the slab and n is an integer that increases with Re. One effect of turbulence enhancement is to increase n, i.e., to make the profile more like that used in the stability calculations of the previous sections. Thus, while a maximum gas velocity has been calculated, it seems reasonable to expect that the heat transfer coefficient may be increased somewhat without initiating hydrodynamic instability, if the velocity limitation is maintained.

Acknowledgments

This work was sponsored by the U.S. Department of Energy, Office of Industrial Programs, under Contract W-31-109-Eng-38. The author is indebted to J. Battles, B. Misra, D. Rote, and L. Turner for helpful discussions, and especially to V. Shah for critically reviewing an early version of the manuscript.

References

Chandrasekhar, S., 1961, *Hydrodynamic and Hydromagnetic Stability*, Oxford University Press, London, Chap. XI.

Chang, I. D., and Russell, P. E., 1965, "Stability of a Liquid Layer Adjacent to a High-Speed Gas Stream," *Phys. Fluids*, Vol. 8, pp. 1018–1026.

Drazin, P. G., 1970, "Kelvin–Helmholtz Instability of Finite Amplitude," *J. Fluid Mech.*, Vol. 42, pp. 321–335.

Garnier, M., and Moreau, R., 1983, "Effect of Finite Conductivity on the Inviscid Stability of an Interface Submitted to a High-Frequency Magnetic Field," *J. Fluid Mech.*, Vol. 127, pp. 365–377.

Gerwin, R. A., 1968, "Hydromagnetic Surface Waves in a Conducting Liquid Surrounded by a Flowing Gas," *Phys. Fluids*, Vol. 11, pp. 1699–1708.

Getselev, Z. N., 1971, "Casting in an Electromagnetic Field," *J. Metals*, Vol. 23, No. 10, pp. 38–39.

Hull, J. R., Lari, R. J., Praeg, W. F., and Turner, L. R., 1987, "Horizontal Electromagnetic Casting of Thin Metal Sheets," U.S. Patent No. 4,678,024.

Kordyban, E., 1977, "Some Characteristics of High Waves in Closed Channels Approaching Kelvin–Helmholtz Instability," ASME *Journal of Fluids Engineering*, Vol. 99, pp. 339–346.

Lavers, J. D., 1986, "Force Distributions Produced by an Electromagnetic Mold," *IEEE Trans. Indus. Appl.*, Vol. IA-22, pp. 586–593.

McHale, E. J., and Melcher, J. R., 1982, "Instability of a Planar Liquid Layer in an Alternating Magnetic Field," *J. Fluid Mech.*, Vol. 114, pp. 27–40.

Meyer, J. L., Szekeley, J., El-Kaddah, N., Vives, C., and Ricou, R., 1987, "Electromagnetic and Fluid Flow Phenomena in a Mercury Model System of the Electromagnetic Casting of Aluminum," *Met Trans. B.*, Vol. 18B, pp. 529–548.

Miles, J. W., 1962, "On the Generation of Surface Waves by Shear Flows, Part 4," *J. Fluid Mech.*, Vol. 13, pp. 433–448.

Nayfeh, A. H., and Saric, W. S., 1971, "Non-linear Kelvin–Helmholtz Instability," *J. Fluid Mech.*, Vol. 46, pp. 209–231.

Peifer, W. A., 1965, "Levitation Melting—a Survey of the State-of-the-Art," *J. Metals*, Vol. 17, pp. 487–493.

Thorpe, S. A., 1968, "A Method of Producing a Shear Flow in a Stratified Fluid," *J. Fluid Mech.*, Vol. 32, pp. 693–704.

Thorpe, S. A., 1969, "Experiments on the Instability of Stratified Shear Flows: Immiscible Fluids," *J. Fluid Mech.*, Vol. 39, pp. 25–48.

Thermal Stability of Horizontally Superposed Porous and Fluid Layers

M. E. Taslim
Assoc. Mem. ASME

U. Narusawa
Mem. ASME

Department of Mechanical Engineering,
Northeastern University,
Boston, MA 02115

The results of stability analyses for the onset of convective motion are reported for the following three horizontally superposed systems of porous and fluid layers: (a) a porous layer sandwiched between two fluid layers with rigid top and bottom boundaries, (b) a fluid layer overlying a layer of porous medium, and (c) a fluid layer sandwiched between two porous layers. By changing the depth ratio $\hat{d}$ from zero to infinity, a set of stability criteria (i.e., the critical Rayleigh number Ra_c and the critical wave number a_c) is obtained, ranging from the case of a fluid layer between two rigid boundaries to the case of a porous layer between two impermeable boundaries. The effects of k/k_m (the thermal conductivity ratio), δ (the square root of the Darcy number), and α (the nondimensional proportionality constant in the slip condition) on Ra_c and a_c are also examined in detail. The results in this paper, combined with those reported previously for Case (a) (Pillatsis et al., 1987), will provide a comprehensive picture of the interaction between a porous and a fluid layer.

Introduction

The linear stability of horizontally superposed porous and fluid layers has been studied previously by the authors (Pillatsis et al., 1987). This paper reports an extension of the previous work.

When a layer of porous medium is present adjacent to a fluid layer, the heat and mass transfer in one layer is affected by the presence of the other. In the natural environment, for example, seasonal and catastrophic changes in the hydrothermal structure of oceans, lakes, and ponds can be affected by the exchange of heat and solutes between the fluid layer and rocks/sediments. There are also numerous industrial situations that require analyses of the interaction between a fluid layer and a fluid-saturated porous medium, such as porous bed thermal storage systems and porous heat pipes. In relation to metal processing technology, the melting and solidification of alloys can occur over a wide temperature range, resulting in a porous (mushy) zone between solid and liquid regions (Glicksman et al., 1986).

There are two approaches to formulating a problem of superposed porous and fluid layers. One is to use the Brinkman equation for the porous layer with the continuity of velocity and shear as interfacial conditions. This approach was used by Somerton and Catton (1982) for the study of the stability of a fluid-saturated porous medium with internal heat generation overlaid with a fluid layer, and by Beckermann et al. (1986) for the analysis of natural convection heat transfer in a vertically superposed system of porous and fluid layers. The other approach is to employ Darcy's equation for the porous layer with the slip conditions, proposed by Beavers and Joseph (1967), as one of the interfacial conditions. Nield (1977, 1983) applied this method to the stability analyses of (*a*) a fluid layer on top of a porous layer and (*b*) a porous layer sandwiched between two fluid layers. Nield was able to obtain exact solutions for the case in which constant heat flux is applied at the bottom (i.e., the case in which the horizontal wave number is zero). Poulikakos et al. (1986) also reported a numerical analysis of high Rayleigh number convection for the case of a fluid layer on top of a porous layer, using the slip condition.

Figure 1 shows the three geometric configurations investigated in this paper. The case depicted in Fig. 1(*a*) (Case (*a*)), a porous layer sandwiched between two fluid layers, was reported in the previous work when the top and bottom boundaries are hydrodynamically free. The case of rigid top and bottom boundaries is examined in the present analysis. The case of a fluid layer overlying a layer of porous medium, Fig. 1(*b*) (Case (*b*)), is also analyzed for a rigid top and an impermeable bottom boundary. Finally, linear stability is studied for the case of a fluid layer sandwiched between two porous layers, Fig. 1(*c*) (Case (*c*)). All three cases are relevant to practical applications, and the results presented here may be used as criteria for the study of convective heat transfer in superposed systems of porous and fluid layers.

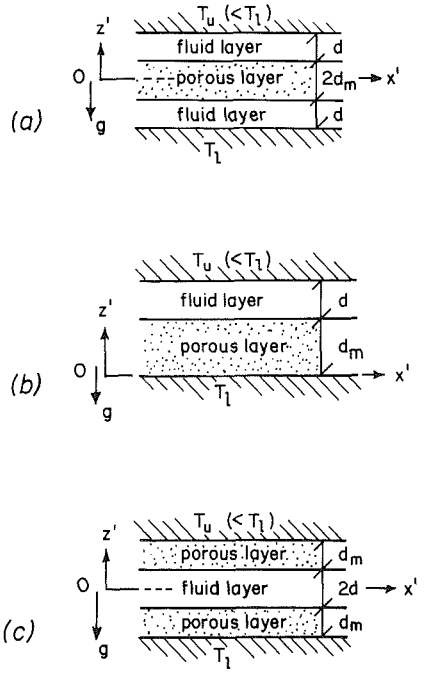

Fig. 1 Geometric configuration studied in the present analyses: (*a*) a porous layer sandwiched between two fluid layers; (*b*) a fluid layer overlying a layer of porous medium; (c) a fluid layer sandwiched between two porous layers

Contributed by the Heat Transfer Division for publication in the JOURNAL OF HEAT TRANSFER. Manuscript received by the Heat Transfer Division June 3, 1987. Keywords: National Convection, Porous Media.

Analyses

Since the formulation and the method of solution were given in detail in the previous paper (Pillatsis et al., 1987), only an outline of the analyses is given here. Under the assumptions of a two-dimensional, incompressible flow, the Boussinesq approximation and a linearized equation of state, the governing equations can be linearized with respect to the steady conduction state. They are:

For the fluid layer

$$\nabla^4 w + \mathrm{Ra}\partial^2 T_p/\partial x^2 = 0 \tag{1}$$

$$w + \nabla^2 T_p = 0 \tag{2}$$

For the porous layer

$$-\nabla_m^2 w_m + \mathrm{Ra_m}\partial^2 T_{mp}/\partial x_m^2 = 0 \tag{3}$$

$$w_m + \nabla_m^2 T_{mp} = 0 \tag{4}$$

where w and w_m are vertical velocities, and T_p and T_{mp} are the nondimensional temperature deviations from the steady conduction state. The nondimensional space coordinates, x, x_m, z, and z_m are defined as

$$z = (z' - d_m)/d, \quad z_m = z'/d_m$$

for Cases (a) and (b) in Fig. 1 and

$$z = z'/d, \quad z_m = (z' - d)/d_m$$

for Case (c) in Fig. 1 with

$x = x'/d$ and $x_m = x'/d_m$ for all cases.

It should be noted that Cases (a) and (c) can be solved for the upper half-region of the geometric configurations because of the symmetry with respect to $z' = 0$. Boundary and interfacial conditions are:

1 Thermal conditions at the interface between a solid boundary and a fluid (or a porous) layer

$$T_p = 0 \tag{5}$$

$$T_{mp} = 0 \tag{6}$$

2 Thermal conditions at the interface between a fluid layer and a porous layer

Temperature continuity:

$$T_p = \epsilon_T T_{mp} \tag{7}$$

Heat flux continuity:

$$\partial T_p/\partial z = \partial T_{mp}/\partial z_m \tag{8}$$

3 Hydrodynamic conditions at the interface between a solid boundary and a fluid layer

Nonslip condition:

$$w = \partial w/\partial z = 0 \tag{9, 10}$$

4 Hydrodynamic conditions at the interface between a solid boundary and a porous layer

Impermeability condition:

$$w_m = 0 \tag{11}$$

5 Hydrodynamic conditions at the interface between a fluid layer and a porous layer

Vertical velocity continuity:

$$\epsilon_T w = w_m \tag{12}$$

Normal stress continuity:

$$\delta^2 \epsilon_T \hat{d}^3 (3\partial^3 w/\partial x^2 \partial z + \partial^3 w/\partial z^3) = -\partial w_m/\partial z_m \tag{13}$$

Slip conditions:

Nomenclature

a = nondimensional wave number in the fluid layer
a_m = nondimensional wave number in the porous layer
d = depth of the fluid layer for Cases (a) and (b), half-depth of the fluid layer for Case (c)
d_m = depth of the porous layer for Cases (b) and (c), half-depth of the porous layer for Case (a)
$\hat{d}$ = depth ratio $= d_m/d$
D_T, D_{Tm} = thermal diffusivities
g = gravitational acceleration
h, h_m = see equation (20)
k, k_m = thermal conductivities
K = permeability
Ra = Rayleigh number for the fluid layer $= \alpha_T g\beta d^4/\nu D_T$
$\mathrm{Ra_m}$ = Rayleigh number for the porous layer $= \alpha_T g\beta_m K d_m^2/\nu D_{Tm}$
T_1 = temperature at the bottom boundary
T_u = temperature at the top boundary
T_p', T_{mp}' = temperature deviations from the steady conduction state
$T_p = T_p'/(\beta d)$
$T_{mp} = T_{mp}'/(\beta_m d_m)$
u' = horizontal velocity in the fluid layer
u_m' = horizontal velocity in the porous layer
$u = (d/D_T)u'$
$u_m = (d_m/D_{Tm})u_m'$
w' = vertical velocity in the fluid layer
w_m' = vertical velocity in the porous layer
$w = (d/D_T)w'$
$w_m = (d_m/D_{Tm})w_m'$
W, W_m = see equation (20)
$x = x'/d$
x' = horizontal coordinate (see Fig. 1)
$x_m = x'/d_m$
$z = (z' - d_m)/d$ for Cases (a) and (b); z'/d for Case (c)
z' = vertical coordinate (see Fig. 1)
$z_m = z'/d_m$ for Cases (a) and (b); $(z' - d)/d_m$ for Case (c)
α = constant of proportionality in the slip condition
α_T = thermal expansion coefficient
$\beta = k_m(T_1 - T_u)/(k_m d + k d_m)$
$\beta_m = k(T_1 - T_u)/(k_m d + k d_m)$
$\delta = \sqrt{K}/d_m$
$\Delta = \delta\hat{d}/\alpha$
$\epsilon_T = k d_m/k_m d$
θ, θ_m = see equation (20)
ν = kinematic viscosity

Subscripts

m = porous layer
p = perturbed quantity

$$\epsilon_T \hat{d}(\partial w/\partial z \pm \Delta \partial^2 w/\partial z^2) = \partial w_m/\partial z_m \quad (14a)$$

$$\epsilon_T \hat{d}(\partial w/\partial z \pm \Delta(\partial^2 w/\partial z^2 + \partial^2 w/\partial x^2) = \partial w_m/\partial z_m \quad (14b)$$

6 Symmetry conditions at the midplane for Cases (*a*) and (*c*):

$$\partial T_p/\partial z = 0 \quad (15)$$

$$\partial T_{mp}/\partial z_m = 0 \quad (16)$$

$$\partial w_m/\partial z_m = 0 \quad (17)$$

$$\partial w/\partial z = \partial^3 w/\partial z^3 = 0 \quad (18,19)$$

In equations (14*a*) and (14*b*), the minus sign holds for Cases (*a*) and (*b*), while the plus sign has to be used for Case (*c*). The slip condition, originally proposed by Beavers and Joseph (1967), has been proven valid experimentally for a unidirectional flow (Beavers and Joseph, 1967; Beavers et al., 1970). Equation (14*a*) is the original slip condition, written in terms of w and w_m. Jones (1973) also proposed a generalized slip condition for a multidirectional flow as the relationship between the slip velocity and the shear stress. Equation (14*b*) corresponds to the generalized slip condition proposed by Jones. These two different forms of the slip condition are used alternately in this study to examine the effect of differences in the form of the slip condition on stability criteria. The proper choice among the boundary and interfacial conditions given above depends on geometric configurations: i.e., equations (5), (7)–(10), (12)–(14), (16) and (17) are used for Case (*a*), equations (5)–(14) are used for Case (*b*), and equations (6)–(8), (11)–(15), (18), and (19) are used for Case (*c*).

The solution to the problem may be sought in the form

$$\begin{Bmatrix} w \\ T_p \end{Bmatrix} = \begin{Bmatrix} W(z) \\ \theta(z) \end{Bmatrix} \cdot h(x)$$

$$\begin{Bmatrix} w_m \\ T_{mp} \end{Bmatrix} = \begin{Bmatrix} W_m(z_m) \\ \theta_m(z_m) \end{Bmatrix} \cdot h_m(x_m) \quad (20)$$

where $d^2h/dx^2 + a^2h = 0$ and $d^2h_m/dx_m^2 + a_m^2 h_m = 0$ with a and a_m being the nondimensional horizontal wave numbers. Upon the substitution of equation (20) into equations (1)–(4), and the elimination of θ and θ_m, we obtain

$$D^6 W - 3a^2 D^4 W + 3a^4 D^2 W + (\mathrm{Ra} \cdot a^2 - a^6) W = 0$$

$$D_m^4 W_m - 2a_m^2 D_m^2 W_m + (a_m^4 - \mathrm{Ra}_m \cdot a_m^4) W_m = 0 \quad (21)$$

The general solutions to equations (21) are presented by two convergent power series (Sparrow et al., 1964). Then equations (21) yield two recursion formulae for the coefficients of the power series with the boundary and interfacial conditions providing the characteristic equation for the determination of the critical conditions for the onset of convective motion. The reader is referred to our previous work (Pillatsis et al., 1987) for more details on the power series solutions. The characteristic equation contains the following four nondimensional parameters: $\hat{d}$, δ, ϵ_T, and Δ, the magnitudes of which depend on the geometry and physical properties of the fluid and the porous matrices, and have to be specified for our numerical study. For a given set of these parameters, the characteristic equation may be solved for Ra (or $\mathrm{Ra_m}$) for a given value of a (or a_m). For a particular value of a, the corresponding Rayleigh number has a value that is smaller than that for any other a, and this is the critical condition, ($\mathrm{Ra_c}$, a_c) or ($\mathrm{Ra_{mc}}$, a_{mc}), at which instability sets in. Ra and $\mathrm{Ra_m}$, and a and a_m are related to each other through the relations

$$\mathrm{Ra_m} = \delta^2 \hat{d}^2 \epsilon_T^2 \cdot \mathrm{Ra} \quad (22)$$

$$a_m^2 = \hat{d}^2 a^2. \quad (23)$$

Table 1 Comparison between the original and the generalized slip conditions

	δ	$\epsilon_T = \hat{d}$	α	Original slip condition	Generalized slip condition
Case (a) with rigid boundaries	5×10^{-2}	10	10	$\mathrm{Ra_{mc}}$=8.272 a_{mc}=1.437	8.271 1.437
Case (b)	10^{-2}	1	1	$\mathrm{Ra_c}$=1421.039 a_c=2.776	1420.918 2.776
Case (c)	10^{-2}	1	1	$\mathrm{Ra_c}$=78.097 a_c=1.269	78.096 1.269

Results and Discussion

The ratio of the layer thicknesses, $\hat{d} = d_m/d$, ranges from zero (a fluid layer between two horizontal boundaries) to ∞ (a porous layer between two horizontal boundaries). For a given value of $\hat{d}$, ϵ_T is proportional to the conductivity ratio k/k_m. In this investigation, the effect of ϵ_T was studied for the range of $0.001\hat{d} \le \epsilon_T \le 10\hat{d}$; while the range of δ (= square root of the Darcy number) was selected to be 10^{-2} to 10^{-5}. According to previous experimental studies, the magnitude of the slip coefficient α depends on the porosity and the structure of the porous medium, varying from 0.1 to 4.0 (Beavers and Joseph, 1967; Beavers et al., 1970). Therefore, the effect of α was examined over a range of $10^{-1} \le \alpha \le 10$ (i.e., $\delta\hat{d}/10 \le \Delta \le 10\delta\hat{d}$). The number of terms utilized in the power series solutions n was set to $n = 30$ for the numerical analysis of Cases (*a*) and (*b*), and $n = 45$ for Case (*c*). Any further increase in n did not affect the computed critical Rayleigh number up to the third digit after the decimal point. In our previous work (Pillatsis et al., 1987), it was confirmed that the selection between the original and the generalized slip condition did not affect the results significantly for Case (*a*) with *free* top and bottom boundaries, showing that $\partial w/\partial x$ is very small compared to $\partial u/\partial z$ at the interface. The same conclusion is drawn from our numerical results for all three cases examined in the present study. Table 1 compares typical critical values for the onset of convection, using the original and the generalized slip conditions. It should also be mentioned here that as δ decreases, the difference between the critical values obtained from the two forms of the slip condition becomes smaller.

The critical conditions are [$\mathrm{Ra_c}$, a_c] = [1707.765, 3.12] and [1707.765/2^4(= 106.735), 3.12/2(= 1.56)] for a fluid layer of thickness d and $2d$, respectively, between two horizontal rigid boundaries at specified temperatures (Nield, 1967). On the other hand, for a layer of porous medium of thickness d_m and $2d_m$ between two impermeable boundaries at specified temperatures, the critical conditions for the onset of convection are [$\mathrm{Ra_{mc}}$, a_{mc}] = [$4\pi^2$(= 39.4784), π] and [$4\pi^2/2^2$(= 9.8696), $\pi/2$(= 1.5708)], respectively (Lapwood, 1948). Table 2 is presented to show that our solutions correctly approach these two limits as $\hat{d} \to 0$ or ∞. In our previous work (Pillatsis et al., 1987), the critical values of the limiting cases were shown to be reached for Case (*a*) with free top and bottom boundaries. Therefore, we may conclude that the slip condition can successfully reduce itself to the limiting boundary conditions (i.e., free and rigid boundaries at the solid–fluid interface as well as an impermeable boundary at the solid–porous medium interface).

A further examination of limiting cases is made through a comparison between the present study and the work by Catton and Lienhard (1984) and Lienhard (1987). Catton and

Table 2 Approaches to the fluid limit ($\hat{d} \to 0$) and the porous layer limit ($\hat{d} \to \infty$); $\delta = 10^{-2}$, $\alpha = 1$, $\epsilon_T = \hat{d}$, with the original slip condition of Beavers and Joseph

$\hat{d}$	Case (b)	Case (c)	$\hat{d}$	Case (b)	Case (c)
0	Ra_c=1707.765 a_c=3.120	Ra_c=106.735 a_c=1.560	∞	Ra_{mc}=39.478 a_{mc}=3.141	Ra_{mc}=9.870 a_{mc}=1.571
10^{-3}	1706.345 3.115	106.646 1.558	10^{3}	39.433 3.139	9.840 1.571
10^{-2}	1694.025 3.105	105.863 1.553	10^{2}	38.912 3.119	9.579 1.563
10^{-1}	1603.631 3.026	99.318 1.510	50	37.947 3.079	9.298 1.556
1	1421.039 2.776	78.097 1.269	10	24.274 2.418	7.210 1.526

Table 3 Comparison of results from this study (Case (*a*) with $\alpha = 1$, $\delta = 10^{-5}$) with those of Catton and Lienhard: Ra_{ac}

		k/k_m			
		0.2	1.0	5.0	100.
$\hat{d}$ = 0.01	Catton-Lienhard	1345.3	1312.6	1305.4	1299.8
	This study	1338.4	1304.9	1297.6	1295.9
$\hat{d}$ = 0.1	Catton-Lienhard	1527.9	1378.5	1318.4	1297.5
	This study	1525.7	1372.9	1313.4	1296.7
$\hat{d}$ = 0.3	Catton-Lienhard	1612.7	1454.7	1340.7	1298.5
	This study	1612.0	1452.5	1338.8	1298.1
$\hat{d}$ = 1.0	Catton-Lienhard	1634.9	1492.2	1358.2	1299.6
	This study	1634.6	1491.8	1357.8	1299.3

Table 4 Effect of δ on the critical conditions, Ra_{mc} [a_{mc}], [$\hat{d} = \epsilon_T (k/k_m = 1)$, $\Delta = 0.05$ with the original slip condition] for Case (*a*) with rigid boundaries and Case (*b*)

$\hat{d}$	δ	Case (a)	Case (b)
10	5×10^{-2}	8.271 [1.437]	33.160 [2.874]
	2.5×10^{-2}	7.527 [1.370]	30.320 [2.752]
	10^{-2}	5.439 [1.114]	24.521 [2.432]
	5×10^{-3}	3.965 [0.843]	21.993 [2.254]
100	10^{-2}	9.717 [1.559]	38.876 [3.117]
	5×10^{-3}	9.689 [1.556]	38.756 [3.113]
	10^{-3}	8.946 [1.491]	36.044 [2.990]
	10^{-4}	4.124 [0.715]	26.789 [2.347]
500	5×10^{-3}	9.840 [1.569]	39.369 [3.137]
	5×10^{-4}	9.811 [1.566]	39.243 [3.132]
	10^{-4}	9.192 [1.531]	36.974 [3.030]
	10^{-5}	4.352 [0.759]	27.499 [2.373]

Table 5 Critical conditions, Ra_c[a_c], for Case (*b*), a fluid layer overlying a layer of porous medium ($\hat{d} = 1$ with the original slip condition)

α [ϵ_T]	$\delta = 10^{-2}$	$\delta = 10^{-3}$	$\delta = 10^{-4}$
0.1 [1.0]	1173.892 [2.621]	1438.721 [2.792]	1487.491 [2.816]
1.0 [0.1]	1606.179 [3.036]	1662.479 [3.060]	1667.564 [3.062]
1.0 [1.0]	1421.039 [2.776]	1487.302 [2.815]	1492.804 [2.819]
1.0 [10.]	1149.892 [2.300]	1323.041 [2.592]	1329.287 [2.596]
10. [1.0]	1468.445 [2.799]	1492.614 [2.819]	1493.340 [2.819]

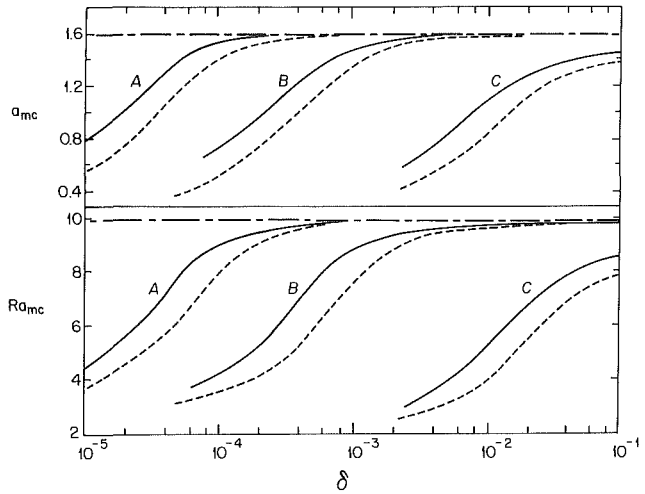

Fig. 2 Variation of the critical condition (Ra_{mc} and a_{mc}) with δ for Case (*a*), a porous layer sandwiched between two fluid layers; ——: porous layer limit of Ra_{mc} = 9.8696 and a_{mc} = 1.5708; ——: rigid top and bottom boundaries; — — — —: free top and bottom boundaries; (A) $\hat{d} = 5 \times 10^2$, (B) $\hat{d} = 10^2$, (C) $\hat{d} = 10$ [$\epsilon_T = \hat{d}$ ($k/k_m = 1$), $\Delta = 5 \times 10^{-2}$ for all curves]

Lienhard performed a linear stability analysis of a solid plate separating two fluid layers: i.e., Case (*a*) in Fig. 1 with the porous layer replaced by a solid layer. In their analysis the thickness of the upper fluid layer is generally different from that of the lower fluid layer. Their reported critical Rayleigh numbers for the case of an identical thickness for the upper and lower fluid layers (given in Table 2 of their paper) are compared with our results when δ is very small (10^{-5}). The comparison is given in Table 3, which confirms that the critical Rayleigh number of the superposed porous/fluid layers correctly converges to that of the superposed solid/fluid layers when δ is made sufficiently small.

The rigid boundary at the solid–fluid interface suppresses the onset of convective motion, while the slipping at the interface between the fluid layer and the porous layer has a freeing effect compared to the case of impermeable boundaries. Figure 2, which shows a summary of our numerical results for Case (*a*), a layer of porous medium bounded by thin fluid layers (i.e., $\hat{d} >> 1$), confirms the general effect of the boundary condition described above. In other words, for a fixed value of $\hat{d}$, a curve for the case of rigid boundaries is always located above the corresponding curve for the case of free boundaries. As δ decreases, the critical conditions deviate from the values for a porous layer between two impermeable boundaries, indicating that the presence of fluid layers and the interfacial slip effect become increasingly important. Some representative values are also listed in Table 4 for both Case (*a*) with the rigid top/bottom boundaries and Case (*b*). These resutls, given in Fig. 2 and Table 4, are obtained for a fixed value of $\Delta = \delta\hat{d}/\alpha$ with $\hat{d} >> 1$. A higher value of Δ indicates more interfacial slip, which lowers the critical Rayleigh number. In the previous paper (Pillatsis et al., 1987), it was shown for Case (*a*) with $\hat{d} >> 1$ (i.e., a porous layer sandwiched between two thin fluid layers) that the effect of Δ on the critical condition becomes important only for high-permeability porous media ($\delta = \sqrt{\mathrm{Da}} = 10^{-3}$–$10^{-2}$). Therefore, as $\hat{d}$ becomes smaller, it may be expected that the effect of Δ on the critical conditions would become smaller. This is shown in Fig. 4 and Table 5. Table 5 indicates that a high value of δ ($= 10^{-2}$) combined with a low value of α ($= 0.1$) affects the critical conditions most, whereas, in Fig. 4 with $\delta = 10^{-3}$, variation of α from 0.1 to 10 does not affect the critical conditions significantly.

The effects of different magnitudes of ϵ_T and α on the

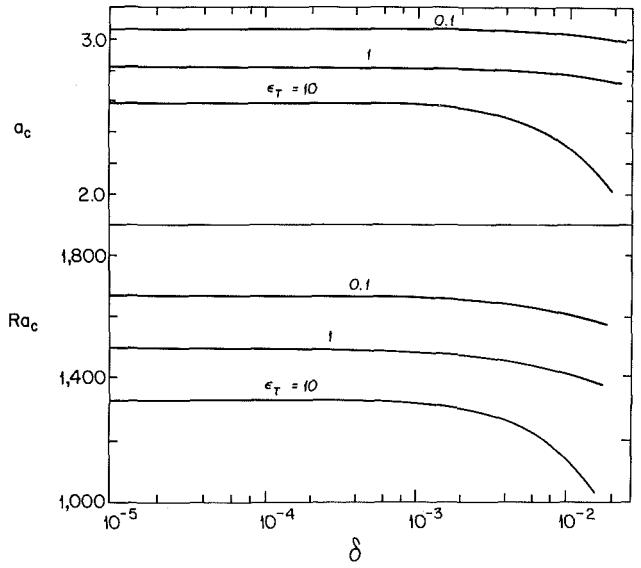

Fig. 3 Effect of δ and ϵ_T on Ra_c and a_c for Case (*b*), a fluid layer overlying a layer of porous medium ($\hat{d}=1$, $\epsilon_T = k/k_m$, $\alpha=1$)

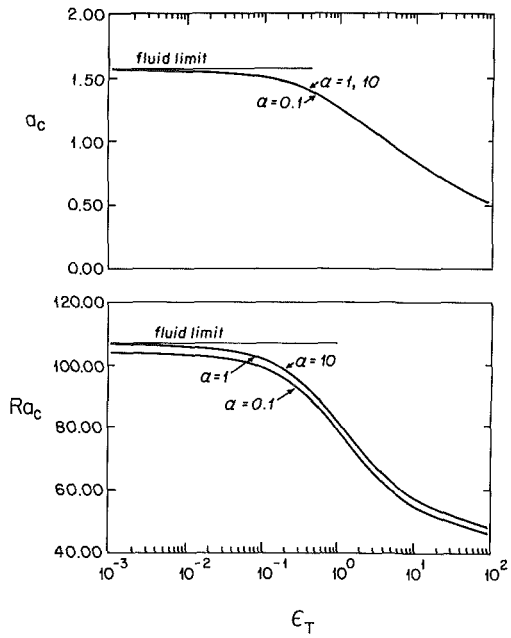

Fig. 4 Effect of ϵ_T and α on Ra_c and a_c for Case (*c*), a fluid layer sandwiched between two porous layers ($\hat{d}=1$, $\epsilon_T = k/k_m$, $\delta = 10^{-3}$)

critical condition are plotted in Fig. 3 for Case (*b*), in which the depth ratio $\hat{d}$ is set to unity with $\alpha=1$, and in Fig. 4 for Case (*c*), in which $\hat{d}$ and δ are fixed to 1 and 10^{-3}, respectively. More numerical values, relevant to Figs. 3 and 4, are tabulated in Tables 5 and 6. In Fig. 3 both Ra_c and a_c are fairly insensitive to decreases in δ below $\sim 10^{-3}$, although there is a slight increase in Ra_c and a_c as the permeability of the porous medium decreases. Both Figs. 3 and 4 indicate that the reduction in ϵ_T (or the conductivity ratio k/k_m) from 1.0 to 0.1 affects the magnitude of both Ra_c and a_c as significantly as its increase from 1.0 to 10. Furthermore, according to Fig. 4, the critical condition is not greatly affected by the magnitude of α, although a larger value of α has a stabilizing effect.

Figure 5 summarizes the variation of the critical condition with $\hat{d}$ for Case (*c*). The corresponding list of numerical values, as well as that for Case (*b*), is given in Tables 7 and 8, respectively. For $\hat{d}<1/10$, the presence of a porous layer is destabilizing; however, the critical condition remains relative-

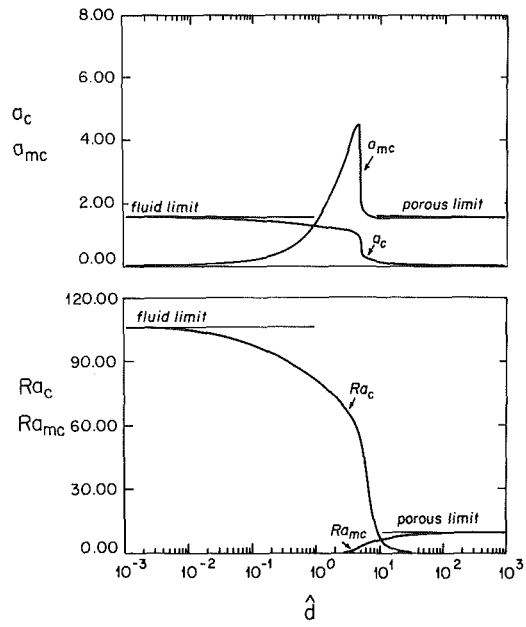

Fig. 5 Effect of $\hat{d}$ on the critical conditions for Case (*c*), a fluid layer sandwiched between two porous layers [$\epsilon_T = \hat{d}(k/k_m = 1)$, $\alpha=1$, $\delta = 10^{-2}$]

Table 6 Effect of δ on the critical conditions, Ra_c [a_c], for Case (*c*), a fluid layer sandwiched between two porous layers ($\hat{d}=1$, $\alpha=1$)

δ	ϵ_T = 0.1	ϵ_T = 1	ϵ_T = 10
10^{-2}	98.655 [1.503]	78.0972 [1.269]	53.7778 [0.830]
10^{-3}	101.835 [1.513]	81.1472 [1.279]	57.0442 [0.843]
10^{-4}	102.142 [1.514]	81.4334 [1.280]	57.2901 [0.844]
10^{-5}	102.172 [1.514]	81.4619 [1.280]	57.3138 [0.844]

Table 7 Effect of $\hat{d}$ on the critical conditions for Case (*c*) [$\delta = 10^{-2}$, $\alpha=1$, $\epsilon_T = \hat{d}(k/k_m = 1)$]

$\hat{d}$	Ra_c [a_c]	$\hat{d}$	Ra_{mc} [a_{mc}]
5	56.343 [.8992]	5	3.521 [4.496]
2	71.917 [1.172]	10	7.209 [1.526]
1	78.097 [1.269]	20	8.504 [1.537]
10^{-1}	99.318 [1.510]	40	9.160 [1.552]
10^{-2}	105.863 [1.553]	10^{2}	9.578 [1.563]
10^{-3}	106.646 [1.558]	10^{3}	9.840 [1.572]

Table 8 Effect of $\hat{d}$ on the critical conditions for Case (*b*), a fluid layer overlying a layer of porous medium [$\epsilon_T = \hat{d}(k/k_m = 1)$, $\alpha=1$, and $\delta = 10^{-2}$]

$\hat{d}$	Ra_c [a_c]	$\hat{d}$	Ra_{mc} [a_{mc}]
3.3	1080.139 [0.642]	3.3	12.810 [2.120]
3.2	1181.073 [2.503]	3.5	13.551 [2.090]
3.0	1206.772 [2.541]	5.0	17.187 [2.110]
1.0	1421.039 [2.776]	10.	24.274 [2.418]
10^{-2}	1694.025 [3.105]	10^{2}	38.912 [3.119]

ly close to that for a fluid layer between two rigid boundaries. Similarly, for $\hat{d} > 10$, the fluid layer has a destabilizing effect, compared with the case of a porous layer between two impermeable boundaries. For the intermediate region of $1/10 < \hat{d} < 10$, our linear stability analysis indicates a strong dependence of the critical condition on $\hat{d}$. The change of a_{mc} with $\hat{d}$ in this region experiences a maximum point, compared with the smooth variation of a_c. It should be noted that a and a_c are related through equation (23).

Conclusions

The stability criteria for the onset of thermal convection are studied for horizontally superposed systems of porous and fluid layers. The major conclusions of this study are:

1 The utilization of the slip condition correctly predicts the critical conditions for various limiting cases as the parameters such as $\hat{d}$, δ, and ϵ_T take extreme values.

2 The selection between the slip condition in its original form and that in a generalized form does not affect the results significantly.

3 For intermediate values of $\hat{d}$, the critical conditions depend strongly on the thickness ratio $\hat{d}$.

4 The critical conditions are fairly insensitive to a decrease in δ $(=\sqrt{\mathrm{Da}})$ below 10^{-3} for fixed values of $\hat{d}$, ϵ_T (or k/k_m), and α.

5 As Δ $(=\delta\hat{d}/\alpha) \to 0$, the slip condition approaches the nonslip condition. Therefore, generally for fixed values of $\hat{d}$ and α, the slip effect becomes smaller as δ $(=\sqrt{\mathrm{Da}})$ decreases.

6 The critical conditions are significantly affected by a magnitude of ϵ_T (or the conductivity ratio) greater than ~ 0.1.

References

Beavers, G. S., and Joseph, D. D., 1967, "Boundary Conditions at a Naturally Permeable Wall," *J. Fluid Mech.*, Vol. 30, pp. 197–207.

Beavers, G. S., Sparrow, E. M., and Magnuson, R. A., 1970, "Experiments on Coupled Parallel Flows in a Channel and a Bounding Porous Medium," ASME *Journal Basic Engineering*, Vol. 92, pp. 843–848.

Beckermann, C., Ramadhyani, S., and Viskanta, R., 1986, "Natural Convection Flow and Heat Transfer Between a Fluid Layer and a Porous Layer Inside a Rectangular Enclosure," *AIAA/ASME 4th Thermophysics and Heat Transfer Conference*, Boston, MA, ASME HTD-Vol. 56, pp. 1–12.

Catton, I., and Lienhard, J. H. V., 1984, "Thermal Stability of Two Fluid Layers Separated by a Solid Interlayer of Finite Thickness and Thermal Conductivity," ASME JOURNAL OF HEAT TRANSFER, Vol. 106, pp. 605–612.

Glicksman, M. E., Coriell, S. R., and McFadden, G. B., 1986, "Interaction of Flows With the Crystal-Melt Interface," *Ann. Rev. Fluid Mech.*, Vol. 18.

Jones, I. P., 1973, "Low Reynolds Number Flow Past a Porous Spherical Shell," *Proc. Camb. Phil. Soc.*, Vol. 73, pp. 231–238.

Lapwood, E. R., 1948, "Convection of a Fluid in a Porous Medium," *Proc. Camb. Phil. Soc.*, Vol. 44, pp. 508–521.

Lienhard, J. H. V., 1987, "An Improved Approach to Conduction Boundary Conditions for the Rayleigh-Bénard Instability," ASME JOURNAL OF HEAT TRANSFER, Vol. 109, pp. 378–387.

Nield, D. A., 1967, "The Thermohaline Rayleigh-Jeffreys Problem," *J. Fluid Mech.*, Vol. 29, pp. 545–553.

Nield, D. A., 1967, "Onset of Convection in a Fluid Layer Overlying a Layer of Porous Medium," *J. Fluid Mech.*, Vol. 81, pp. 513–522.

Nield, D. A., 1983, "Boundary Correction for the Rayleigh–Darcy Problem: Limitations of the Brinkman Equation," *J. Fluid Mech.*, Vol. 128, pp. 37–46.

Pillatsis, G., Taslim, M. E., and Narusawa, U., 1987, "Thermal Instability of a Fluid-Saturated Porous Medium Bounded by Thin Fluid Layers," ASME *Journal of Heat Transfer*, Vol. 109, pp. 677–682.

Poulikakos, D., Bejan, A., Selimos, B., and Blake, K. R., 1986, "High Rayleigh Number Convection in a Fluid Overlying a Porous Bed," *Int. J. Heat Fluid Flow*, Vol. 7, pp. 109–114.

Somerton, C. W., and Catton, I., 1982, "On the Thermal Instability of Superposed Porous and Fluid Layers," ASME JOURNAL OF HEAT TRANSFER, Vol. 104, pp. 160–165.

Sparrow, E. M., Goldstein, R. J., and Jonsson, V. K., 1964, "Thermal Instability in a Horizontal Fluid Layer: Effect of Boundary Conditions and Nonlinear Temperature Profile," *J. Fluid Mech.*, Vol. 18, pp. 513–528.

On Natural Convection Heat Transfer From Three-Dimensional Bodies of Arbitrary Shape

A. V. Hassani

K. G. T. Hollands

Department of Mechanical Engineering,
University of Waterloo,
Waterloo, Ontario, Canada, N2L 3G1

A simple expression is developed for the natural convection heat transfer from three-dimensional bodies of arbitrary shape immersed in an extensive fluid. The expression applies to both laminar and turbulent regimes and requires the calculation of purely geometric properties of the bodies. Experiments were performed with air, covering a Rayleigh number (Ra) *range of from 10 to* 10^8*, on different body shapes oriented in various directions: for example, circular or square disks, a short circular cylinder of height equal to diameter and a similar cylinder but with hemispherical ends, prolate and oblate spheroids of various aspect ratio, and an "apple core" shape. Comparison between the predictions of the expression and the experimental results of this work and those gathered from several other sources ranging up to* $\mathrm{Ra} = 10^{14}$ *showed very good agreement, with an average rms difference of 3.5 percent for* $\mathrm{Ra} < 10^8$ *and 22 percent for* $10^8 < \mathrm{Ra} < 10^{14}$.

Introduction

Natural convection heat transfer from isothermal, nonspherical bodies immersed in an extensive fluid at different temperature has formed the subject of several recent publications. Experiments on various spheroids (Raithby et al., 1976), on a "stubby" cylinder (Sparrow and Ansari, 1983), on cubes (Sparrow and Stretton, 1985) and on cubes and a bisphere (Chamberlain et al., 1985) have been reported. Sparrow and Ansari (1983) and Sparrow and Stretton (1985) demonstrated that both the King and Lienhard methods were incapable of predicting their experimental results with better than 25 percent accuracy. Sparrow and Stretton (1985) gave a correlation for bodies of unity aspect ratio, which fitted their data closely. Raithby et al. (1976) and Chamberlain et al. (1985) compared their results to the predictions of the method introduced by Raithby and Hollands (1975) and found good ageement. Some workers have tried to reduce the problem of predicting the heat transfer to the finding, by trial and error, of a characteristic length scale for Nusselt and Rayleigh numbers so that data for all shapes are correlated by a single Nu–Ra relation. But for a wide Rayleigh number range and for bodies with aspect ratio distinctly different from unity, the chances of finding the right length scale (if indeed it exists) appears remote. A better approach is to develop an equation from simplified theoretical arguments, such as those presented by Raithby and Hollands (1975, 1985).

Their method, which comprises a two-step process, first calculates the local thickness Δ_x of a hypothetical stationary fluid layer (called the conduction layer) surrounding the body. Then (in the second step) it solves for the conduction heat transfer through this layer, this heat transfer then being assumed to be identical to the sought natural convection heat transfer. Although the method requires considerably less effort to use than, say, solving the full set of equations of motion and energy, it can still require substantial effort and skill for complex bodies. Thus there is a need for simplifying both steps in the two-step process without sacrificing the method's overall accuracy.

The second step, which reduces to finding the conduction shape factor of a conduction layer, was recently simplified somewhat by Hassani and Hollands (1986). Following Chamberlain et al. (1985), they replaced the boundary layer of variable thickness by a layer of uniform thickness $\bar{\Delta}$ equal to the area-weighted harmonic mean of the local thickness Δ_x. Then, using the Churchill–Usagi (1972) interpolation technique between conduction shape factors S_∞ and S_o (corresponding to asymptotically large and small values of $\bar{\Delta}$, respectively), they obtained for the conduction shape factor $S(\bar{\Delta})$ at mean thickness $\bar{\Delta}$

$$S(\bar{\Delta}) = (S_o^n\ (\bar{\Delta}) + S_\infty^n)^{1/n} \tag{1}$$

where n is a specified function of the shape of the body.

The first step—determining the local thickness Δ_x and the average thickness $\bar{\Delta}$—calls for what can be a complicated calculational procedure requiring the evaluation of integral relations for the local laminar thickness Δ_{lx}, and the local turbulent thickness Δ_{tx}. The actual thickness of the local boundary layer is then decided using a certain selection criterion (if $\Delta_{lx} < 4/3\ \Delta_{tx}$, $\Delta_x = \Delta_{lx}$; otherwise $\Delta_x = \Delta_{tx}$). Integration around the body then gives the mean thickness $\bar{\Delta}$. The present paper simplifies this first step, replacing this rather cumbersome procedure with a new method that blends laminar and turbulent solutions for $\bar{\Delta}$, using a Churchill–Usagi interpolation. Combining the resulting expressions for $\bar{\Delta}$ with equation (1) will yield a general-purpose, easily calculated expression for Nu as a function of Ra.

Since both methods—the original Raithby–Hollands method and the simplification described herein—are approximate, they can benefit from testing against new experimental data, as can the correlation equations of other workers. In this paper new experimental data are presented on several body shapes. These new data are used to help set the second Churchill–Usagi index in the new formulation, and to test the various methods. These experiments are described first.

Experiments

The purpose of the experiments was to produce plots of Nu versus Ra covering a wide range of Rayleigh number (10^1 to 10^8) for external natural convection from a range of shapes of isothermal bodies immersed in air ($\mathrm{Pr} \approx 0.71$). The experimental method and the apparatus were the same as those used by Chamberlain et al. (1985). Briefly described, the method involves raising the temperature of the body, using an imbedded electric heater, to about 30 K above ambient, turning the heater off, then following the transient decay of the

Contributed by the Heat Transfer Division and presented at the ASME/AIChE National Heat Transfer Conference, Pittsburgh, Pennsylvania, August 9–12, 1987. Manuscript received by the Heat Transfer Division October 10, 1987. Keywords: Measurement Techniques, Natural Convection.

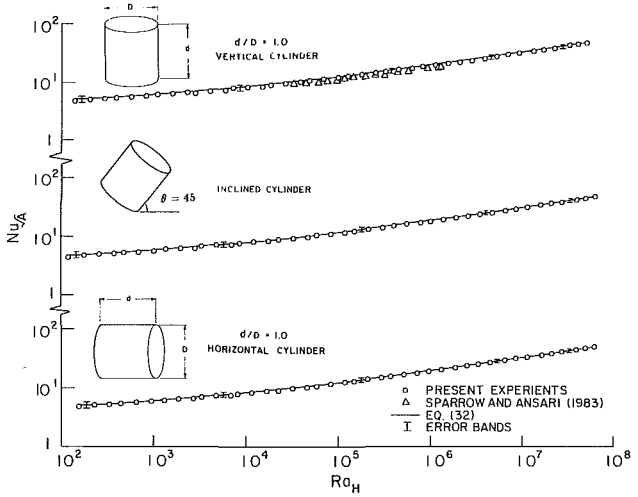

Fig. 1 Experimental results and predictions for cylinder in various orientations

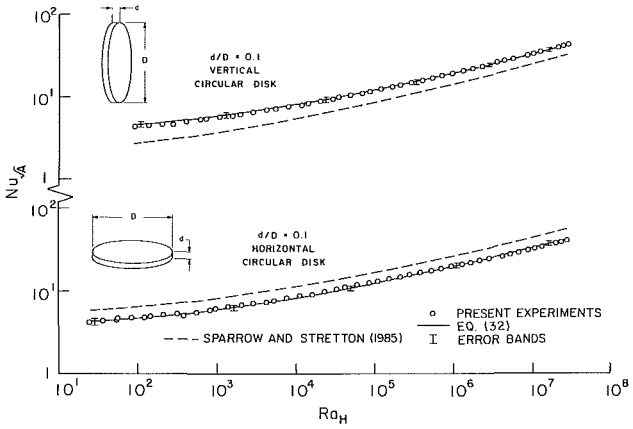

Fig. 2 Experimental results and predictions for circular disk

body temperature. From this decay curve (not assumed to be exponential), and the heat capacity of the body, the heat transfer coefficient for the body at each of three times in the decay process is calculated. After correction for radiation, this yields the corresponding values of the convection coefficient h_c. The experiments were carried out with the body suspended inside a pressure vessel and repeated at fixed values of the air pressure ranging from 0.5 kPa to 700 kPa. This wide pressure range enabled the experiments to cover a wide range of Rayleigh number.

Illustrated (for the various orientations tested) in the insets of Fig. 1-6, the bodies tested comprised the following: a cylinder of aspect ratio $\gamma = d/D = 1.0$; a similar cylinder but with hemispherical ends; a circular and a square disk of aspect ratio $\gamma = d/D = 0.1$; two oblate spheroids of aspect ratios $\gamma = C/B = 0.1$ and 0.5, respectively; a prolate spheroid of aspect ratio $\gamma = C/B = 0.52$; and the "apple core" shape shown in the inset of Fig. 6. Each body was machined from aluminum alloy to a tolerance of 0.1 mm and an electrical heater was embedded inside the body. Thermocouples of 0.075 mm diameter were embedded inside holes of 1 mm diameter drilled into the body. Details on the method of embedding the electric heaters and the thermocouples and the check for body temperature uniformity are given by Hasssani (1987). The spheroids (oblate and prolate) were the same as those used by Raithby et al. (1976) but modified by replacing the electric heater and by replacing the thick thermocouples and electric lead wires with ones of much smaller gage. After this modification the conduction losses along the thin wires were small enough that they could be neglected, as they were for the other bodies tested here (see Chamberlain et al., 1985, for a discussion on wire losses).

To obtain the body's heat capacity C^* and effective surface emissivity $\bar{\epsilon}$ (both are needed for data reduction) Chamberlain et al. (1985) relied on property values of the aluminum and

Nomenclature

A = heat transfer surface area of the body, m^2
A_h = horizontal downward-facing surface of a heated body, or horizontal upward-facing surface of a cooled body, m^2
A_l = nonhorizontal downward (upward) facing surface of a heated (cooled) body, m^2
A_u = upward (downward) facing surface of a heated (cooled) body, m^2
B = major axis of spheroid, m
C = minor axis of spheroid, m
C^* = heat capacity of the body, J/K
$\bar{C}_l$ = $0.671(1+(0.492/\mathrm{Pr})^{9/16})^{-4/9}$, or 0.515 for Pr = 0.71
C_l = function of Pr and ϕ given by equations (17) and (18)
$\bar{C}_l$ = average value of C_l over a body to be approximated by equation (22)
$\hat{C}_l$ = $\hat{C}_l\sqrt{A}/H$
d = the thickness of disks or the height of cylinders, m
G = quantity given by equation (8) and approximated by equation (16)
H = characteristic length defined by equation (31), m
h_C = average convection heat transfer coefficient, W/m^{2}K
h_z = length scale along surface streamline
h_χ = length scale on the surface of a body in the direction orthogonal to the streamline
$\bar{h}_\chi$ = length scale defined by equation (11)
I = current passing through the electrical heater of the body, A
k = thermal conductivity of fluid, W/mK
L_m = longest straight line passing through the body, m
L = characteristic dimension, m
m = exponent used in Churchill-Usagi fit, given by equation (34)
n = exponent of Churchill-Usagi fit, given by equation (33)
Nu = Nusselt number = $QL/A\Delta Tk$
$Nu_{c,}\sqrt{A}$ = conduction Nusselt number based on $\sqrt{A}$, approximately equal to 3.51
$Nu\sqrt{A}$ = Nusselt number based on $\sqrt{A}$, $Q\sqrt{A}/A\Delta Tk$
$P(z)$ = local perimeter at height z, m
$\bar{P}$ = perimeter averaged over the total height of the body, m
Pr = Prandtl number = $\mu C_p/k$
Q = convective heat transfer from body, W

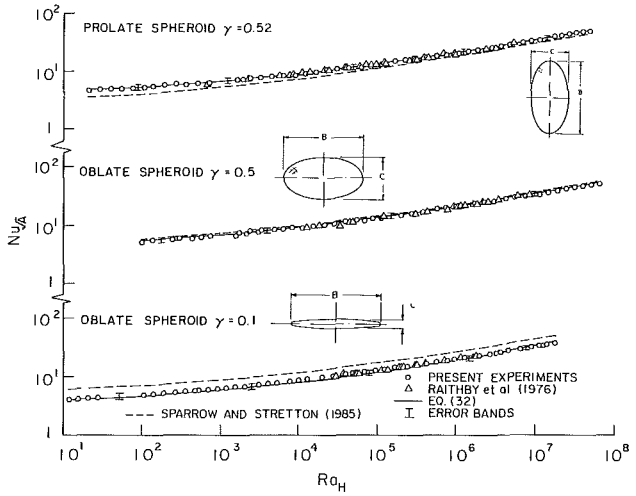

Fig. 3 Experimental results and predictions for prolate and oblate spheroids

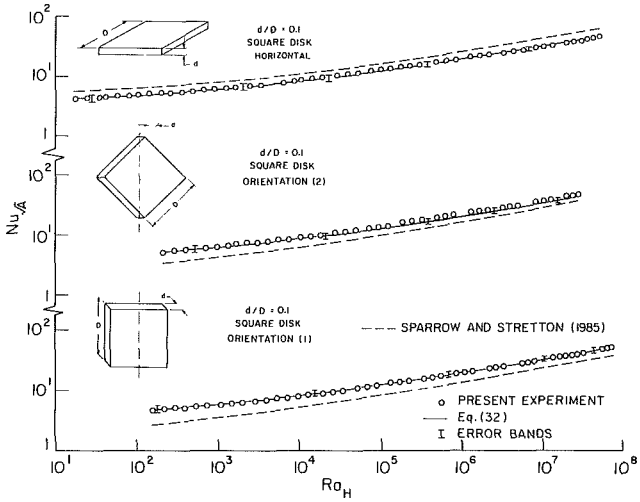

Fig. 4 Experimental results and predictions for square disk in different orientations

separate emissivity measurements using a reflectometer. The possible errors in these quantities contributed important uncertainties in their experimental results. The present set of experiments reduced this uncertainty by carrying out a separate set of measurements in which the bodies were suspended in a bell jar vacuum chamber whose pressure was kept below 10^{-4} Pa, effectively eliminating gaseous conduction. (The Knudsen number for these experiments was approximately 100, indicating a free molecule regime. Calculated according to Kennard, 1938, the gaseous conduction was less than 1 percent of the radiation). A constant d-c voltage was suddenly applied across the body's electric heater and the resulting transient heating was observed until steady state was established (about 30 h). The body temperature T_b, the chamber wall temperature T_v, the heater voltage V, and the current I passing through the heater were measured at preset times during the transient heating process. An energy balance on the body gives

$$\frac{dT_b}{dt} = \frac{VI}{C^*} - \frac{\bar{\epsilon}\sigma A}{C^*}\left(T_b^4 - T_v^4\right) \tag{2}$$

in which t is time and A is the surface area of the body. The quantity dT_b/dt was estimated at each preset time, using Lagrange's four-point differentiation formula, and plotted against the corresponding values of $T_b^4 - T_v^4$. Using regression analysis, a straight line was fit to this plot, and the slope and the intercept of this line were used to obtain VI/C^* and $\bar{\epsilon}\sigma A/C^*$, in equation (2), from which C^* and $\bar{\epsilon}$ were determined (see Hassani, 1987, for more details). An error analysis revealed that the resulting errors in C and $\bar{\epsilon}$ were less than 1.8 and 4 percent, respectively, the dominant error in these quantities being the uncertainties in the slope and the intercept of

Nomenclature (cont.)

Q_R = radiative heat transfer from body, W
R = radius of the sphere or cylinder, m
Ra_H = Rayleigh number based on H, $g\beta\Delta TH^3/\nu\alpha$
Ra_L = Rayleigh number based on L, $g\beta\Delta TL^3/\nu\alpha$
S = conduction shape factor, m
$S_o(\bar{\Delta})$ = conduction shape factor for a region of very small thickness, m
S_∞ = conduction shape factor for a region of very large thickness, m
$S_{f,x}$ = streamline length for given χ, m
$\bar{S}_f$ = average streamline length defined by equation (12), m
t = time, S
T_a = ambient temperature, K
T_b = body temperature, K
T_v = pressure vessel or vacuum chamber wall temperature, K
ΔT = temperature difference between the body and the fluid far from the body, K
V = d-c voltage supplied across the electrical heater of the body, volt
v = volume of the body, m^3
z = elevation of a point above bottom point of the body, m
z_f = total height of the body, m
α = thermal diffusivity of fluid, m^2/s
β = volumetric coefficient of thermal expansion, 1/K
γ = aspect ratio, d/D, C/B, B/C
Δ_{lx} = local conduction layer thickness for laminar boundary layer, m
Δ_x = local conduction layer thickness for a laminar or turbulent boundary layer, m
Δ_{tx} = local conduction layer thickness for turbulent boundary layer, m
$\bar{\Delta}$ = area-weighted harmonic mean of the local thickness, m
$\bar{\Delta}_l$ = mean conduction layer thickness when the flow around body is completely laminar, m
$\bar{\Delta}_t$ = mean conduction layer thickness when the flow around body is completely turbulent, m
$\bar{\epsilon}$ = effective surface emissivity $= Q_R/\sigma A_b(T_b^4 - T_v^4)$
μ = dynamic viscosity, kg/ms
ν = kinematic viscosity, m^2/s
ρ = density, kg/m^3
ϕ = angle measured between vertical direction and surface (see Fig. 8)
χ = circumferential coordinate around a three-dimensional body, Fig. 8, m

Table 1 Properties and dimensions of the tested bodies

Body Shape	D or B mm	d or C mm	Effective Surface Emissivity, $\bar{\epsilon}$	Heat capacity J/K
Circular Cylinder, $\gamma = 1.0$	43.0	43.0	0.062 ± 0.002	152.9 ± 2.7
Cylinder with Hemispherical Ends	35.0	70.0	0.063 ± 0.002	137.7 ± 2.5
Circular Disk, $\gamma = 0.1$	82.0	8.2	0.059 ± 0.002	104.8 ± 1.8
Square Disk, $\gamma = 0.1$	81.0	8.1	0.090 ± 0.003	132.8 ± 2.1
Oblate Spheroid, $\gamma = 0.1$	80.0	8.0	0.074 ± 0.003	67.1 ± 1.2
Oblate Spheroid, $\gamma = 0.5$	78.6	39.2	0.085 ± 0.003	313.0 ± 4.8
Prolate Spheroid, $\gamma = 0.52$	77.1	40.0	0.082 ± 0.003	158.7 ± 2.7
Apple Core	Fig.(6)	Fig.(6)	0.044 ± 0.002	77.1 ± 1.3

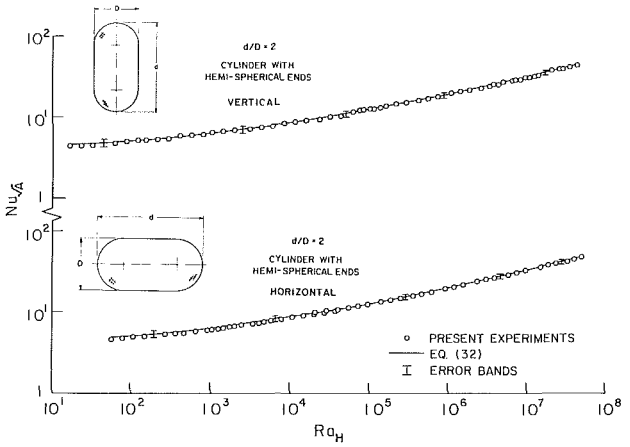

Fig. 5 Experimental results and predictions for cylinder with hemispherical ends

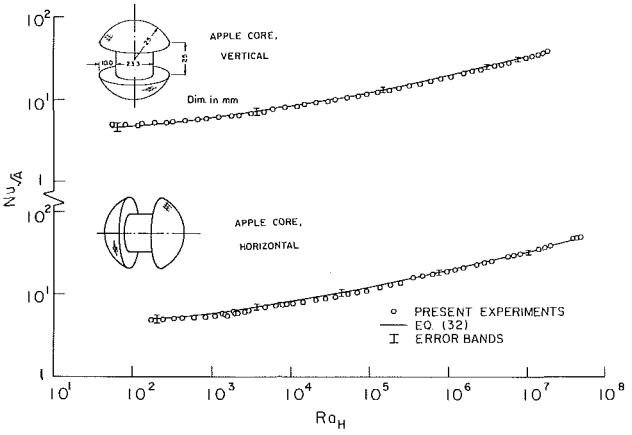

Fig. 6 Experimental results and predictions for "apple core" shape

the fit. The calculated values of $\bar{\epsilon}$ and C^* for each body are given in Table 1. It is important to note that the areas of the presssure vessel and the vacuum chamber are both much larger (almost 140 times) than the surface area of the bodies tested. Therefore the calculated $\bar{\epsilon}$ is independent of the enclosure geometry.

The data for each run were processed to yield Nusselt and Rayleigh numbers, as described by Chamberlain et al. (1985), except that the length scale used in the Nusselt number was chosen as $\sqrt{A}$ and that in the Rayleigh number was the group $H = (z_f \tilde{P}^2)^{1/3}$ (the reasons for these choices of length scales are explained in the next section). The results are shown in Figs. 1–6 and 10–12. The solid lines are predicted results, which will be discussed later.

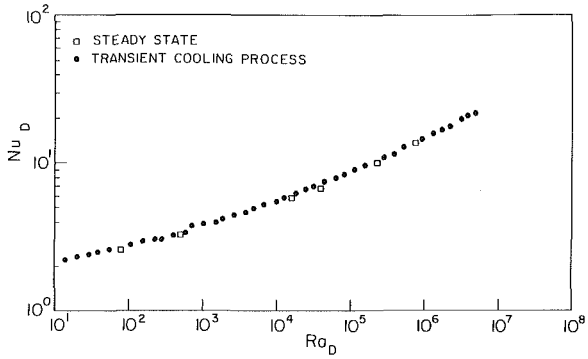

Fig. 7 Experimental results of steady state and transient cooling process for vertical cylinder with $d/D = 1.0$.

An implicit assumption in the transient cooling method is that the decay process is slow enough that the measured (transient) convection coefficients are near enough to the steady-state ones, so that what is being reported is indeed steady-state data. To test this hypothesis for one of the bodies, a set of steady-state measurements at different pressure levels (covering $80 < \mathrm{Ra}_D < 8 \times 10^5$) was carried out, by applying a constant d-c voltage across the body's heater and allowing the body to reach to steady-state temperature in the pressure vessel. The convective heat transfer coefficient was then estimated from an energy balance on the body

$$VI = h_c A(T_b - T_a) + \sigma A \bar{\epsilon}(T_b^4 - T_v^4) \tag{3}$$

The resulting Nusselt number, plotted in Fig. 7, showed that within experimental error the same Nusselt versus Rayleigh number curve was produced as for the transient measurements. It was therefore concluded that the quasi-steady-state assumption was valid. Further details are given by Hassani (1987).

A detailed error analysis (see Hassani, 1987) showed that the uncertainty $d\mathrm{Ra}$ in Rayleigh number is dominated by the uncertainty in pressure measurements, and is given by

$$\frac{d\mathrm{Ra}}{\mathrm{Ra}} = \frac{0.27}{\sqrt{\mathrm{Ra}}} + 0.024 \tag{4}$$

At a low pressure, such as 0.8 kPa corresponding to $\mathrm{Ra} \approx 10$, the relative uncertainty in Ra is about 10 percent, but this reduces to 2.5 percent at $P = 680$ kPa, corresponding to $\mathrm{Ra} = 10^7$. The uncertainty $d\mathrm{Nu}$ in Nusselt number was found to given by

$$\frac{d\mathrm{Nu}}{\mathrm{Nu}} = 0.038 + \frac{0.11}{\mathrm{Nu}} \tag{5}$$

which indicates an uncertainty of less than 10 percent for Nu = 2.0 and an uncertainty of less than 4 percent for Nu = 30. The dominant uncertainties in Nu were in the temperature–time curve fit and in the emissivity. The Nusselt number uncertainty bands are shown in Figs. 1–6 and 10–12.

The measurements reported by Sparrow and Ansari (1983) for a vertical cylinder of the same height-to-diameter ratio ($\gamma = d/D = 1.0$) as tested here are shown in Fig. 1. Very good agreement with the present measurements is observed. The measurements of Raithby et al. (1976) for the spheroids are presented in Fig. 3 along with the present results on modified versions of the same spheroids. In basic agreement with the earlier data, the present data show less scatter and cover a wider Rayleigh number range.

Simplification to the Raithby-Hollands Method

Evaluating the Integrals. Raithby and Hollands (1975, 1985) showed that if the boundary layer is everywhere laminar

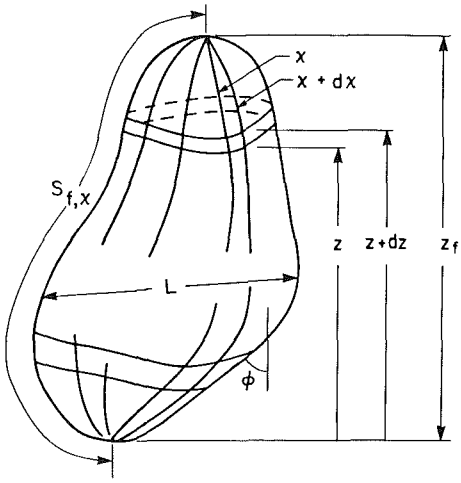

Fig. 8 Surface coordinate system for three-dimensional convection

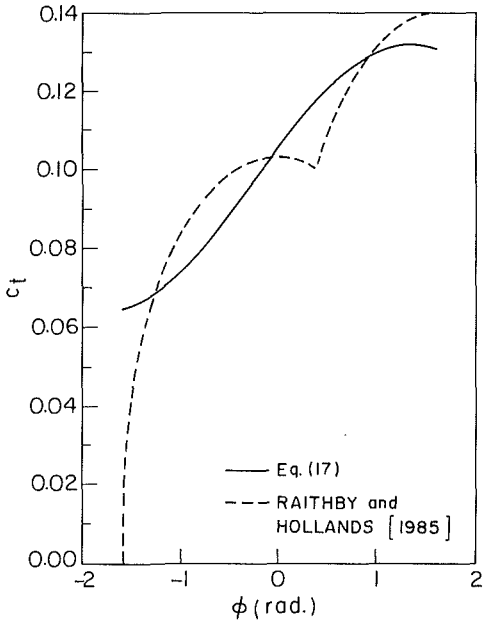

Fig. 9 Curve fit to C_t

$$\bar{\Delta} = \bar{\Delta}_l = \frac{L}{G\,\bar{C}_l\,Ra_L^{1/4}} \tag{6}$$

and if it is everywhere turbulent

$$\bar{\Delta} = \bar{\Delta}_t = \frac{L}{\bar{C}_t\,Ra_L^{1/3}} \tag{7}$$

where $\bar{C}_l$ in equation (6) is a function only of Prandtl number ($\bar{C}_l = 0.515$ for air), and Ra_L is the Rayleigh number based on (arbitrary) characteristic scale L. The quantities G and $\bar{C}_t$ are given by two integral expressions as follows:

$$G = \frac{L^{1/4}}{A}\int_{\chi_i}^{\chi_f}\left(\int_0^{z_f}\frac{h_\chi^{4/3}}{\cos^{2/3}\phi}\,dz\right)^{3/4} d\chi \tag{8}$$

and

$$\bar{C}_t = \frac{1}{A}\int_A C_t\,dA \tag{9}$$

The coordinates χ and z are the surface coordinate system illustrated in Fig. 8. χ denotes the circumferential position of a point on the surface and is constant along a streamline and z is the elevation of a point above the lowest point on a hot body

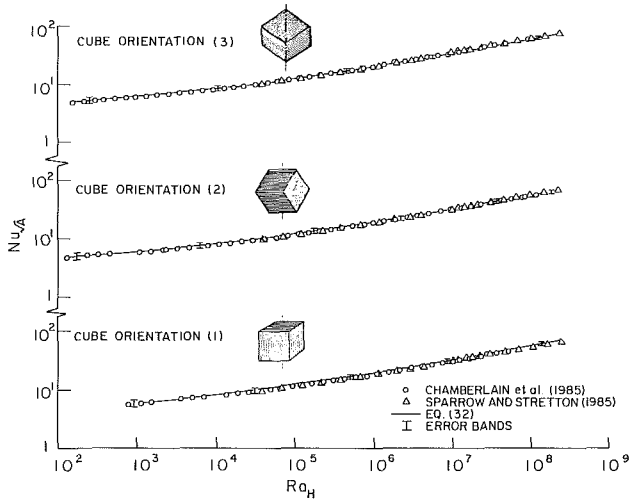

Fig. 10 Experimental results and predictions for cube in different orientations

or the highest point on a cold body. The metrics for this system are h_χ and h_z. The angle ϕ, measured between the vertical direction and surface of the body, varies between $-\pi/2 < \phi < \pi/2$, being positive if the buoyancy force pulls the fluid away from the surface and negative if it presses the fluid onto the surface. The quantity C_t is a function of Pr and ϕ given by Raithby and Hollands (1985) and plotted for Pr = 0.71 as the dashed line in Fig. 9.

Performing the integrations indicated by equations (8) and (9) is sometimes very difficult. This section provides some approximations, which lead to simple expressions for G and $\bar{C}_t$. Equation (8) is simplified by three assumptions: first

$$\cos\phi \approx \bar{\cos}\,\phi = \frac{1}{S_{f,x}}\int_0^{S_{f,x}}\cos\phi\,dS = \frac{z_f}{S_{f,x}} \tag{10}$$

where $S_{f,\chi}$ is the streamline length for a given χ, and z_f is the total height of the body; second

$$h_\chi \approx \bar{h}_\chi = \frac{1}{z_f}\int_0^{z_f} h_\chi dz \tag{11}$$

and third

$$S_{f,\chi} \approx \bar{S}_f = \frac{\int_{\chi_i}^{\chi_f} S_{f,\chi}\bar{h}_\chi d_\chi}{\int_{\chi_i}^{\chi_f}\bar{h}_\chi\,d_\chi} \tag{12}$$

Now it can be shown that the perimeter $\bar{P}$ averaged over the total height of the body is given by

$$\bar{P} = \frac{1}{z_f}\int_0^{z_f} P(z)dz = \frac{1}{z_f}\int_{\chi_i}^{\chi_f}\int_0^{z_f} h_\chi dz\,d\chi \tag{13}$$

where $P(z)$ is the local perimeter at height z. Also the area of the body can be expressed as

$$A = \int_{\chi_i}^{\chi_f} S_{f,\chi}\,\bar{h}_\chi d\chi \tag{14}$$

Thus the denominator of equation (12) is $\bar{P}$ and the numerator is A, so that

$$\bar{S}_f = \frac{A}{\bar{P}} \tag{15}$$

Now by substituting equations (10)–(15) in equation (8) and

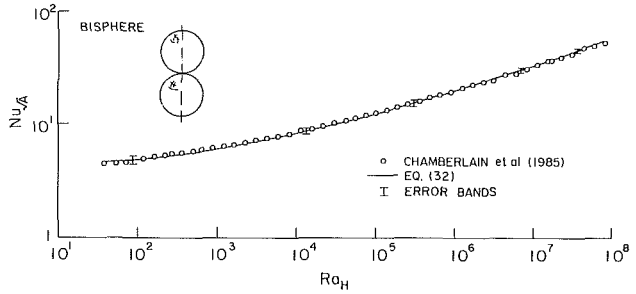

Fig. 11 Experimental results and predictions for bisphere

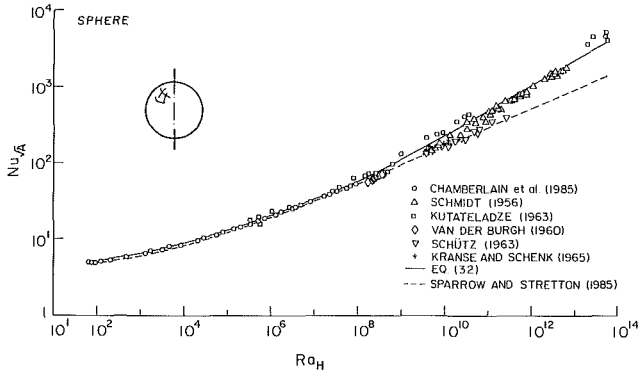

Fig. 12 Experimental results and predictions for sphere

performing the integrations, a simple expression for G is obtained

$$G=\left(\frac{z_f L\ \bar{P}^2}{A^2}\right)^{1/4} \tag{16}$$

For calculating $\bar{C}_t$, given by equation (9), a function was developed to approximate the Raithby–Hollands (1985) expression for C_t as a function of ϕ. The form of the function was judiciously chosen so that the integrals required for the evaluation of $\bar{C}_t$ would be tractable and yield simple results, the parameters of the fit being chosen to fit the Raithby–Hollands curve. The first attempt satisfied the model closely except for a very narrow range close to $\phi=-\pi/2$; it was decided to make the approximate function discontinuous at $\phi=-\pi/2$ to handle this difficult point. This process resulted in the following function for C_t:

$$C_t=a+b\ sin\ (\phi)+e\ \cos\ (\phi),\quad \text{for}-\frac{\pi}{2}<\phi\le\frac{\pi}{2} \tag{17}$$

$$C_t=0,\quad \text{for}\ \phi=-\frac{\pi}{2} \tag{18}$$

where (for air) $a=0.098$, $b=0.033$, and $e=0.008$. To perform the integration of equation (9) for a heated body ($T_b > T_a$), the surface area of the body must be divided into three sections: the lower nonhorizontal surface A_l where $-\pi/2<\phi\le 0$, the upper surface A_u where $0<\phi\le\pi/2$, and finally all horizontal downward-facing surfaces A_h for which $\phi=-\pi/2$ (for a cooled body ($T_b < T_a$), the surface area of the body must be divided into the following three sections: the upper nonhorizontal surface A_u where $-\pi/2<\phi\le 0$, the lower surface A_l where $0<\phi\le\pi/2$, and all horizontal upward-facing surfaces A_h for which $\phi=-\pi/2$). Clearly $A=A_h+A_l+A_u$. Since C_t is equal to zero over A_h, this surface does not contribute to $\bar{C}_t$. Performing the integration by parts gives

$$\bar{C}_t=a-a\frac{A_h}{A}+\frac{b}{A}\int_{A_l}\sin\phi\ dA+\frac{b}{A}\int_{A_u}\sin\phi\ dA+\frac{e}{A}\int_{A_l+A_u}\cos\phi\ dA \tag{19}$$

which can be rewritten as

$$\bar{C}_t=a-a\frac{A_h}{A}+b\frac{A_h}{A}+\frac{b}{A}\int_{A_l+A_h}\sin\phi\ dA+\frac{b}{A}\int_{A_u}\sin\phi\ dA+\frac{e}{A}\int_{A_l+A_u}\cos\phi\ dA \tag{20}$$

The fourth and fifth terms in equation (20) are both equal in magnitude to the projected area over a horizontal surface but they are of opposite sign, so they cancel. The last term can be written in terms of $\bar{P}$ by noting that

$$\int_A\cos(\phi)\ dA=\int_z\int_\chi h_\chi d\chi dz=\int_z P(z)dz=z_f\bar{P} \tag{21}$$

Thus $\bar{C}_t$ for air can be expressed in terms of quantities that have already been used to calculate G

$$\bar{C}_t=0.098-(0.065)\frac{A_h}{A}+0.008\frac{z_f\bar{P}}{A} \tag{22}$$

Comparison between $\bar{C}_t$ values obtained from equation (22) and from the expression given by Raithby and Hollands (1985) for different geometries showed a maximum difference of 5.3 percent, which occurred for the oblate spheroid with $\gamma=0.1$. Horizontal orientation of square and circular disks showed deviations of 4.0 percent and the rest of the shapes (including various orientation of each shape) showed differences of less than 2 percent. Figure 9 shows that the maximum difference between C_t of equations (17) and (18) and that of Raithby–Hollands occurs at angles close to $-\pi/2$, which corresponds to bodies with horizontal downward-facing surfaces (for the case of heated bodies) or to bodies with horizontal upward-facing surfaces (for the case of cooled bodies). Therefore larger errors in $\bar{C}_t$ are expected for bodies with a higher A_h/A ratio.

Derivation of Expression for Nu. The thickness of the uniform conduction layer $\bar{\Delta}$ can be estimated by positing that $\bar{\Delta}$ can be obtained by taking a (second) Churchill–Usagi (1972) interpolation of two values of $\bar{\Delta}$; the value $\bar{\Delta}_l$ when the flow around the body is completely laminar, and the value $\bar{\Delta}_t$ when the flow is completely turbulent. Thus

$$\frac{1}{\bar{\Delta}}=\left(\left(\frac{1}{\bar{\Delta}_l}\right)^m+\left(\frac{1}{\bar{\Delta}_t}\right)^m\right)^{1/m} \tag{23}$$

where m is the exponent of the Churchill–Usagi fit (different from n in equation (1)). Substituting for $\bar{\Delta}_l$ and $\bar{\Delta}_t$ from equations (6) and (7) results in an expression for the uniform conduction layer surrounding the body

$$\frac{1}{\bar{\Delta}}=\frac{1}{L}\left((G\ \bar{C}_l\ \mathrm{Ra}_L^{1/4})^m+(\bar{C}_t\ \mathrm{Ra}_L^{1/3})^m\right)^{1/m} \tag{24}$$

where G and $\bar{C}_t$ are given by equations (16) and (22). The next step is to obtain the heat conducted through this uniform layer. To solve this conduction problem, Hassani and Hollands (1986) suggested a solution of the form given by equation (1) and approximated the asymptotic solution of the conduction shape factor S_o for a thin layer by

$$S_o=\frac{A}{\bar{\Delta}} \tag{25}$$

Substituting from equations (16) and (24), the asymptotic

solution of the conduction shape factor $S_o(\bar{\Delta})$ for a thin uniform layer becomes

$$S_o(\bar{\Delta})=\frac{A}{L}\left[\left[\left(\frac{Lz_f\bar{P}^2}{A^2}\right)^{1/4}\bar{C}_l Ra_L^{1/4}\right]^m+(\bar{C}_l Ra_L^{1/3})^m\right]^{1/m} \tag{26}$$

The other asymptote S_∞ of equation (1) can be closely estimated by the approximate method suggested by Chow and Yovanovich (1982). They showed that S_∞ for a body of fixed area is a slowly changing function of its shape and therefore can be expressed by

$$S_\infty = \mathrm{Nu}_{c,\sqrt{A}}\sqrt{A} \tag{27}$$

where $Nu_{c,\sqrt{A}}$, the conduction Nusselt of the body based on $\sqrt{A}$, is approximately constant and equal to 3.51.

Equations (26) and (27) are then substituted into equation (1), which becomes

$$S(\bar{\Delta})=\left[\frac{A^n}{L^n}\left[\left(\left(\frac{Lz_f\bar{P}^2}{A^2}\right)^{1/4}\bar{C}_l Ra_L^{1/4}\right)^m+(\bar{C}_l\, Ra_L^{1/3})^m\right]^{n/m}+\left(\frac{\mathrm{Nu}_{c,L}A}{L}\right)^n\right]^{1/n} \tag{28}$$

The conduction shape factor in terms of heat loss and Nusselt number is given by

$$S=\frac{Q}{k\Delta T}=\frac{Nu_L A}{L} \tag{29}$$

where Nu_L is based on the characteristic length L. Thus equation (28) can be rewritten in terms of Nu_L

$$\mathrm{Nu}_L=\left[\left[\left(\left(\frac{Lz_f\bar{P}^2}{A^2}\right)^{1/4}\bar{C}_l \mathrm{Ra}_L^{1/4}\right)^m+(\bar{C}_l \mathrm{Ra}_L^{1/3})^m\right]^{n/m}+\left(\frac{\mathrm{Nu}_{c,\sqrt{A}}L}{\sqrt{A}}\right)^n\right]^{1/n} \tag{30}$$

where $\bar{C}_t$ is given by equation (22) and $\bar{C}_l$ is a constant equal to 0.515 for $Pr = 0.71$. This expression is applicable to three-dimensional bodies of complex shape. It is of interest to define a new characteristic length for Ra

$$H=(z_f\,\bar{P}^2)^{1/3} \tag{31}$$

and to base Nu on $\sqrt{A}$. This reduces equation (30) to the more compact form

$$\mathrm{Nu}_{\sqrt{A}}=[[(\bar{C}_l\, Ra_H^{1/4})^m+(\hat{C}_t\, Ra_H^{1/3})^m]^{n/m}+(\mathrm{Nu}_{c\sqrt{A}})^n]^{1/n} \tag{32}$$

where $\hat{C}_t=\bar{C}_t\sqrt{A}/H$. Equation (32) is easy to use; its coefficients depend only on simple geometric properties of the body and the Prandtl number.

Estimation of the Exponents n and m. Hassani and Hollands (1986) presented a graph for determining exponent n from two dimensionless "shape factors" of the body: $\sqrt{A}/L_m$ and $v^{2/3}/A$, where L_m is the length of the longest straight line passing through the body and v is the body volume. An empirical formula fitting this graph has been found to be

$$n=\left[1.26-\frac{(2-\sqrt{A}/L_m)}{9\sqrt{1.-4.79v^{2/3}/A}},\ 1.0\right]_{\max} \tag{33}$$

For example, for a sphere $\sqrt{A}/L_m=\sqrt{\pi}$, $v^{2/3}/A=(36\pi)^{-1}$, and $n=1$. The formula covers the range for n: $1\le n\le 1.2$, which includes a very wide range of body shapes. Using a constant value of n of 1.07 will produce a maximum difference of six percent between the calculated Nusselt number and the Nusselt number determined using the value of n given by equation (33).

The second exponent m, will be first obtained for each shape by finding the best fit to the available experimental data. Since m relates to the relative importance of the laminar and turbulent terms, its value should be related to that fraction of the body covered with turbulence. We therefore tried to relate m to the ratio of heat transfer by totally turbulent flow to that of laminar flow, which for a given Pr is proportional to $\hat{C}_t \mathrm{Ra}_H^{1/12}$. To find a relationship between the m and $\hat{C}_t Ra_H^{1/12}$, a total of almost 400 experimental data points of different geometries was used. The data of the cylinder with aspect ratio one, the square disk, and the apple core shape in different orientations were kept aside for later examination of the resulting expression.

Unfortunately, the present experiments did not cover a Rayleigh range beyond 10^8, even though this range is vital for the close determination of m. However a few workers such as Schmidt (1956), Van der Burgh (1960), Kutateladze (1963), Schutz (1963), and Kranse and Schenk (1965) have measured heat transfer from a sphere for $\mathrm{Ra} > 10^9$, so their measurements for the sphere were used to extend the expression for m to higher Rayleigh number. Kutateladze (1963) carried out his measurements in air ($Pr = 0.71$), but Van der Burgh (1960) and Kranse and Schenk (1965) used liquid benzene ($\mathrm{Pr} = 8.3$). Schmidt (1956) used alcohols and water ($\mathrm{Pr} \approx 5$ to 14) and Schutz (1963) measured the mass transfer by electrolysis of copper sulfate with a spherical electrode ($\mathrm{Pr} = 1800$). To convert the data of the above workers (except Kutateladze) to an equivalent set of data for air, their Rayleigh number values were scaled using an equation of Churchill (1983).

For each data point, through a trail and error procedure, an m value, which resulted in a minimum difference between the experimental and the predicted results (using equatiion (32)), was found. The m values so found were then plotted versus $\hat{C}_t Ra_H^{1/12}$. This plot showed a peak at $\hat{C}_t Ra_H^{1/12}=0.5$ where $m = 14.5$ and reached asymptotically to $m = 2.5$ when $\hat{C}_t Ra_H^{1/12}$ approached zero or infinity. This suggested a regression analysis giving the following expression for m:

$$m=2.5+12.0e^{-13|\hat{C}_t Ra_H^{1/12}-0.5|} \tag{34}$$

Equation (34) should be verified for geometries other than spheres whenever the experimental data for $Ra > 10^9$ become available for other shapes. However it should give reasonable results for bodies of various shape.

In summary, equations (22), and (32)-(34) constitute the simplified form of the Raithby-Hollands equations for the external natural convection heat transfer from three-dimensional bodies. The use of these equations consists of the following steps, which highlight the method. Determine the following geometric properties of the body: surface areas A and A_h, volume v, longest linear dimension L_m, and height z_f. Express the body's local perimeter $P(z)$ as a function of the vertical height z above the lowest point on the body; then determine the mean perimeter $\bar{P}$ from

$$\bar{P}=\frac{1}{z_f}\int_0^{z_f}P(z)\,dz \tag{35}$$

(for example, for a sphere of radius R, $\mathrm{P}(z) = 2\pi\sqrt{R^2-(R^2-z^2)}$, and $\bar{P}=\pi^2R/2$). Calculate H from equation (31): $H=(z_f\bar{P}^2)^{1/3}$. Determine $\bar{C}_t$ from equation (22), $\hat{C}_t$ from $\hat{C}_t = \bar{C}_t\sqrt{A}/H$, n from equation (33), $\bar{C}_l$ from knowledge of the Prandtl number: $\bar{C}_l = 0.671\,(1+(0.492/\mathrm{Pr}^{9/16}))^{-4/9}$. Determine the conduction Nusselt number $\mathrm{Nu}_{c,\sqrt{A}}$ based on $\sqrt{A}$, either by simply assuming that $\mathrm{Nu}_{c,\sqrt{A}} = 3.51$ or from a solution to the conduction problem in which the body is immersed in a stationary medium of conductivity k. All parameters have now been determined, and $\mathrm{Nu}_{\sqrt{A}}$ can be determined as a function of Ra_H from equations (32) and (34). Provided $\mathrm{Ra}_H < (\bar{C}_l/\hat{C}_t)^{12}$, the turbulent term does not contribute more than a few percent to the calculated

Nusselt number, so that equation (32) can be closely approximated by the simpler equation

$$\mathrm{Nu}_{\sqrt{A}} = [(\bar{C}_l \mathrm{Ra}_H^{1/4})^n + (\mathrm{Nu}_{c,\sqrt{A}})^n]^{1/n} \quad (36)$$

In the development of these equations, no assumption was made about the Prandtl number, with one major exception: The equation for $\bar{C}_l$ assumes Pr = 0.71. The working out of a simple equation for $\bar{C}_l$ for other Prandtl numbers will be the subject of a separate paper. Except for the evaluation of m, the Churchill–Usagi exponent used to blend the turbulent and laminar regions, all the coefficients in these equations are derived from first principle arguments and were not adjusted to fit the data.

Comparisons with Experimental Results

Comparison of Simplified Method With the Data of the Bodies Used to Develop Equation (34). The predictions of equations (22) and (32)–(34) were compared to the experimental results of this work and to the data gathered from several sources such as the data of spheres, bispheres, and cubes from Chamberlain et al. (1985), the data of cubes from Sparrow and Stretton (1985), the data of short circular cylinders from Sparrow and Ansari (1983), and the data of spheres at high Rayleigh numbers from Kutateladze (1956), Van der Burgh (1960), Schutz (1963), Kranse and Schenk (1965) and Schmidt (1968). The predicted results are plotted as solid lines in Figs. 1–6, and 10–12. The shape of the body, the coefficients of equation (32), the n-value, the rms, and the maximum differences for each shape are listed in Table 2. The data for the sphere show the highest rms difference, 22 percent, between the experimental data and the predictions of equation (32). This difference is mainly due to the large scatter in the data of Schutz (1963), Kranse and Schenk (1965), and Kutateladze (1956); the sphere data of Chamberlain et al. (1985) show only 3.3 percent rms difference from the predicted results. Another shape with high rms difference is the cube (Fig. 1) in orientation (1) with an rms difference of 5.4 percent. In this case, 67 percent of the experimental data lie within 6 percent of the predicted results and all are within 10.0 percent. For the horizontal circular disk, 75 percent of the experimental data fall within 5 percent of the predictions and all are within 9.0 percent (Fig. 2). For the circular disk in vertical position, 89 percent of the data are within 5 percent of the predicted results and all are within 9.0 percent (Fig. 2). The cylinder with hemispherical ends showed rms differences of 2.9 percent and 5.2 percent in vertical and horizontal orientations, respectively; see Fig. 5. For the oblate spheroid of C/B = 0.5, 91 percent of the date lie within 5.0 percent of the predictions (Fig. 3). The oblate spheroid of C/B = 0.1 showed a maximum difference of 13.0 percent and an rms difference of 5.9 percent. This shape shows higher deviations from the predicted results over $8 \times 10^3 < \mathrm{Ra}_H < 10^5$; see Fig. 3. This behavior was also noticed in the case of a circular disk in a horizontal orientation. Some of the differences between the equations and the plots shown in figures can be attributed to experimental error: For a Nusselt number error of 3 percent and a Rayleigh number error of 7 percent, the expected rms error in the plots is approximately 4 percent.

Comparison of Simplified Method With Other Data. The experimental data of the cylinder with aspect ratio one, the square disk, and the apple core shape in different orientations were used to examine the applicability of equation (34) to geometries other than those used in its development. The predicted results for these geometries were obtained from equations (22) and (32)–(34). The $\hat{C}_l$, $\mathrm{Nu}_{c,\sqrt{A}}$, the n value, and the rms and maximum differences for each orientation are listed in Table 2. The comparison between the experimental data and the predictions showed very good agreement in all cases. Figures 1 and 4 show the results for the short cylinder and the square disk, respectively. A square disk in a horizontal orientation showed an rms difference of 4.9 percent with a maximum difference of 8.4 percent. Similar to the horizontal orientation of the circular disk and to the oblate spheroid with C/B = 0.1, the data for this case also showed larger deviation from the predicted results over $8 \times 10^3 < \mathrm{Ra}_H < 10^5$. Presented in Fig. 6, the data of the apple core shape in vertical orientation showed an rms difference of 3.5 percent from the predicted results with a maximum difference of 11.0 percent. The horizontal orientation of this shape showed an rms difference of 3.8 percent and a maximum difference of 9.7 percent.

Table 2 Coefficients of equation (32) and the deviation of its predictions from the experimental results

Body Shape	$\sqrt{A}/H$	$\hat{C}_l$	$Nu_{C,\sqrt{A}}$	n	%RMS Diff.	% Max. Diff.
Sphere	0.971	0.101	3.545	1.00	22.0	75.0
Bi-Sphere	1.090	0.114	3.475	1.07	2.1	5.8
Oblate Spheroid, $\gamma = 0.10$	1.500	0.148	3.342	1.14	5.9	13.0
Oblate Spheroid, $\gamma = 0.50$	1.014	0.104	3.525	1.06	2.7	6.6
Prolate Spheroid, $\gamma = 0.52$	1.006	0.106	3.566	1.00	2.8	6.3
Circular Disk, Vertical	0.940	0.101	3.353	1.15	2.8	8.9
Circular Disk, Horizontal	1.390	0.099	3.353	1.15	4.2	8.7
Square Disk, Vertical (1)	0.915	0.094	3.334	1.11	3.4	7.5
Square Disk, Vertical (2)	1.003	0.105	3.334	1.11	5.3	9.7
Square Disk, Horizontal	1.333	0.096	3.334	1.11	4.9	8.4
Cube Orientation (1)	0.972	0.090	3.388	1.1	5.4	9.8
Cube Orientation (2)	0.962	0.100	3.388	1.1	2.9	6.1
Cube Orientation (3)	0.961	0.102	3.388	1.1	2.3	4.7
Vertical Cylinder, $\gamma = 1.0$	1.012	0.094	3.444	1.11	1.7	5.0
Horizontal Cylinder, $\gamma = 1.0$	0.930	0.097	3.444	1.11	1.9	4.1
Inclined Cylinder, $\theta = 45$	0.935	0.098	3.444	1.11	3.0	6.9
Cylinder with Hemispherical Ends, Vertical	1.000	0.105	3.527	1.00	2.9	6.1
Cylinder with Hemispherical Ends, Horizontal	0.924	0.096	3.527	1.00	5.2	8.9
Apple Core, Vertical	1.246	0.116	3.450	1.20	3.5	11.0
Apple Core, Horizontal	0.871	0.092	3.450	1.20	3.8	9.7

The satisfactory agreement between the experimental data of the above (test) shapes and the predicted results indicates that equation (34) gives a reasonable m value for bodies of various configuration.

Comparison of Data With Previous Correlations. The data are now compared to the equations suggested by other workers, namely Sparrow and Stretton (1985) and Yovanovich (1987).

Sparrow and Stretton (1985) suggested an equation for predicting heat transfer from bodies of various shape. Although they restrict the applicability of their equation to bodies with "aspect ratio close to unity," we feel it useful to compare their equation to the results of wide range of bodies tested in the present work. The results are compared in Table 3 and shown only (for the sake of clarity) for some of the bodies in Figs. 2–4 and 12. As expected their correlation shows high differences (up to 41 percent) for bodies with aspect ratio not close to unity. Large differences are also noted for the sphere at high Rayleigh number; see Fig. 12. As the data and the equation depart with increasing Ra, the difference noted cannot be put down simply to scatter in the data.

The equation suggested by Yovanovich (1987) is an empirical correlation in which the key coefficient was estimated by fitting curves to part of the experimental data of this paper and also to that of Chamberlain et al. (1985). Specifically Yovanovich used the data for spheres, the bisphere, and three orientations of the cube from Chamberlain et al.'s work and for the prolate spheroid, the two oblate spheroids and the cylinder in three directions from the present. Therefore for a fair comparison, we will compare the predictions of

Table 3 Comparison of data with Yovanovich and Sparrow-Stretton correlations

Body Shape	Yovanovich		Sparrow-Stretton	
	%RMS Diff.	%max. Diff.	%RMS Diff.	%max. Diff
Bi-Sphere			13.7	21.9
Oblate Spheroid, $\gamma = 0.10$			41.7	49.5
Oblate Spheroid, $\gamma = 0.50$			7.7	15.7
Prolate Spheroid, $\gamma = 0.52$			15.1	22.9
Circular Disk, Vertical	14.4	23.9	29.0	36.6
Circular Disk, Horizontal	5.0	14.4	35.2	45.4
Square Disk, Vertical (1)	18.1	27.7	32.2	41.4
Square Disk, Vertical (2)	19.3	28.9	29.0	34.0
Square Disk, Horizontal	4.8	8.8	29.3	36.3
Cube Orientation (1)			5.2	9.4
Cube Orientation (2)			2.5	5.2
Cube Orientation (3)			5.3	8.6
Vertical Cylinder, $\gamma = 1.0$			7.4	12.6
Horizontal Cylinder, $\gamma = 1.0$			5.4	7.6
Cylinder with Hemispherical Ends, Vertical	2.5	6.2	18.3	27.1
Cylinder with Hemispherical *Ends, Horizontal*	3.1	6.7	3.5	6.9
Apple Core, Vertical	8.2	11.3	11.2	16.5
Apple Core, Horizontal	11.3	24.0	10.3	18.

Yovanovich's equation for present experimental results for geometries not used by him, namely the circular and square disks in vertical and horizontal orientations, cylinder with hemispherical ends, and apple core shape. Table 3 shows the rms and maximum error for each case.

There are two important differences between equation (32) and the correlation equation suggested by Yovanovich. One is that equation (32) is comprised of two parts, namely, laminar and turbulent terms, which enables it to predict heat transfer at Rayleigh numbers as high as 10^{14}, as shown in Fig. 12, while Yovanovich has restricted his correlation to $Ra \leq 10^8$. The other is that equation (32) takes into account the orientation of the body whereas Yovanovich's equation does not. It is possible to construct a curve through any one of the bodies that follows the experimental data slightly more exactly than equation (32). But the purpose of this exercise is to give the user a general purpose equation suitable for any body shape, not specifically the bodies discussed in this study.

It is clear from these comparisons that equations (32) can predict heat transfer over a wide range of body types and of Ra (up to 10^{14}) with good accuracy, whereas other correlations are restricted to a more limited range of Ra and to certain body shapes and orientations.

Conclusions

Heat transfer from bodies of arbitrary shape can be closely predicted over a wide range of Rayleigh number using equations (22) and (32)–(34). The predictions of these equations for a wide variety of three-dimensional bodies immersed in air were compared to the experimental data of this work and other studies. In general, the experimental data compared very well to the predictions. The maximum rms difference in Nu or $Ra_H < 10^8$ is 5.9 percent, of which about 4 percent can be attributed to experimental error. The rms difference for $10^8 < Ra_H < 10^{14}$ is 22 percent, but most of this is attributed to the large scatter in the data. The predicted results for bodies with smaller aspect ratio such as disks showed larger deviation from the experimental data (the maximum difference was 13 percent), and as the aspect ratio increased, this deviation decreased. Unfortunately, the available experimental data for $Ra_H > 10^9$ are restricted to the spherical shape. It is recommended that experimental data for $Ra_H > 10^9$ be obtained for other geometries, so that the equations can be verified for these geometries as well.

Comparison of the data of this paper with the equation of Sparrow and Stretton shows rms deviations of up to 7.4 percent for bodies having aspect ratio unity and $Ra < 10^8$, but for bodies of more irregular shape or at higher Rayleigh numbers, rms differences ranging up to 41 percent are observed. The empirical equation suggested by Yovanovich, which is restricted to $Ra < 10^8$, deviates from experimental data by rms differences ranging up to 19.3 percent.

Acknowledgments

This work was supported through an operating grant from the Natural Sciences and Engineering Research Council of Canada (NSERC). This support and the advice and encouragement received from Prof. G. D. Raithby are gratefully acknowledged. We also thank Prof. M. M. Yovanovich for making his bell jar available.

References

Chamberlain, M. J., Hollands, K. G. T., and Raithby, G. D., 1985, "Experiments and Theory on Natural Convection Heat Transfer From Bodies of Complex Shape," ASME JOURNAL OF HEAT TRANSFER, Vol. 107, pp. 624–629.

Chow, Y. L., and Yovanovich, M. M., 1982, "The Space Factor of the Capacitance of a Conductor," *Journal of Applied Physics*, Vol. 53, No. 12, pp. 8470–8475.

Churchill, S. W., 1983, "Comprehensive, Theoretically Based, Correlating Equations for Free Convection From Isothermal Spheres," *Chem. Eng. Commun.*, Vol. 24, pp. 339–352.

Churchill, S. W., and Usagi, R., 1972, "A General Expression for the Correlation of Rates of Transfer and Other Phenomena," *AICHE J.*, Vol. 18, pp. 1121–1128.

Hassani, A. V., and Hollands, K. G. T., 1986, "Shape Factor for the Conduction Layer Arising in Natural Convection Problems," presented at the ASME Winter Annual Meeting, Anaheim, CA, Dec. 7–12.

Hassani, A. V., 1987, "An Investigation of Free Convection Heat Transfer From Bodies of Arbitrary Shape," Ph.D. Thesis, Mechanical Engineering Department, University of Waterloo, Waterloo, Ontario, Canada.

Kennard, E. H., 1938, *Kinetic Theory of Gases*, McGraw-Hill, New York, pp. 315–320.

Kranse, A. A., and Schenk, J. 1965, "Thermal Free Convection From a Solid Sphere," *Appl. Sci. Res.*., Sect. A, Vol. 15, pp. 397.

Kutateladze, S. S., 1963, *Fundamentals of Heat Transfer,* Academic Press, New York, pp. 288–297.

Raithby, G. D., and Hollands, K. G. T., 1975, "A General Method of Obtaining Approximate Solutions to Laminar and Turbulent Free Convection Problems," *Advances in Heat Transfer*, Academic Press, Vol. 11, see also *Int. J. Heat Mass Transfer*, Vol. 17, pp. 1620–1622.

Raithby, G. D., Pollard, A., Hollands, K. G. T., and Yovanovich, M. M., 1976, "Free Convective Heat Transfer From Spheroids," ASME JOURNAL OF HEAT TRANSFER, Vol. 98, pp. 452–458.

Raithby, G. D., and Hollands, K. G. T., 1985, *Handbook of Heat Transfer Fundamentals*, 2nd ed., W. M. Rohsenow, J. P. Hartnett, and E. N. Ganic, eds., McGraw-Hill, New York, Chap. 6

Schmidt, E., 1956, "Versuche zum Warmeubergang bei naturlicher Konvection," *Chem. Ing. Tech.*, Vol. 28, pp. 175.

Shutz, G., 1963, "Natural Convection Mass-Transfer Measurements on Spheres and Horizontal Cylinders by an Electrochemical Method," *Int. Journal of Heat Mass Transfer*, Vol. 6, pp. 873.

Sparrow, E. M., and Ansari, M. A., 1983, "A Refutation of King's Rule for Multi-Dimensional External Natural Convection," *Int. J. Heat Mass Transfer*, Vol. 26, pp. 1357–1364.

Sparrow, E. M., and Stretton, A. J., 1985, "Natural Convection From Variously Oriented Cubes and from Other Bodies of Unity Aspect Ratio," *Int. J. Heat Mass Transfer*, Vol. 28, No. 4, pp. 741–752.

Van der Burgh, J., 1960, "Thermal Convection at a Melting Benzene Surface," *Appl. Sci. Res.*, Sect. A., Vol. 9, p. 293.

Yovanovich, M. M., 1987, "On the Effect of Shape, Aspect Ratio and Orientation Upon Natural Convection From Isothermal Bodies of Complex Shape," presented at the ASME Winter Annual Meeting, Boston, MA, Dec. 13–18.

Experimental and Numerical Studies of Natural Convection in Trapezoidal Cavities

S. W. Lam

R. Gani

Department of Mechanical Engineering,
Monash University,
Clayton, Victoria 3168, Australia

J. G. Symons

Division of Construction and Engineering,
Commonwealth Scientific and Industrial
Research Organisation,
Highett, Victoria 3190, Australia

Natural convection heat transfer has been studied experimentally and numerically for horizontal prismatic cavities of trapezoidal section having a hot horizontal base, a cool inclined top, and insulated vertical walls. Experimental results are presented for a cavity with width-to-mean height ratio of 4, Rayleigh numbers (based on the mean cavity height) from 10^3 to 10^7, and top surface inclinations from 0 to 25 deg to the horizontal. For a given top surface inclination, the Nusselt-Rayleigh relationship follows the usual trend, but with an interesting anomaly, in which higher Nusselt numbers than expected are obtained in the range $8 \times 10^3 < Ra < 2 \times 10^5$ for inclinations of 0 and 5 deg. Overall, as the inclination of the top surface is increased, the Nusselt number decreases, an effect that becomes greater at higher angles. The proportions of convective heat flow rate into the high side and low side of the cavity were measured and show distinct maxima at particular Rayleigh numbers (which are independent of the top surface inclination angle). The equation $Nu = 0.168\,[Ra\,(1 + \cos\theta)/2]^{0.278}\,[(1 - \cos\theta_{max})/(\cos\theta - \cos\theta_{max})]^{-0.199}$ correlates the experimental results to within 6.9 percent for the ranges $4 \times 10^3 < Ra < 10^7$ and $0 \text{ deg} \le \theta \le 25$ deg, apart from the anomalous region previously indicated. It is suggested that this correlation applies for $A \ge 4$. The numerical model uses a false transient ADI finite difference scheme to solve the governing two-dimensional vorticity and energy transport equations. Nusselt numbers computed by the model are in good agreement with the experimental values. The convective flow patterns generated by the model exhibit changes in number and in size of cells for different Rayleigh numbers and different top surface inclinations.

Introduction

Natural convection in cavities has received increasing attention over the last two decades. Rectangular cavities, in particular, have been prime targets of many previous studies, as reviewed by Catton (1978). However, many important building spaces, such as attics, industrial buildings, and electronic equipment packages are nonrectangular. This paper, therefore, aims at improving the understanding of natural convective heat transfer in these types of cavity, specifically in horizontal prismatic cavities of trapezoidal section heated from below. The cavity of interest in this study is shown in Fig. 1, and comprises a trapezoidal prism with hot isothermal bottom, cold isothermal sloping top, and adiabatic side vertical walls.

Iyican et al. (1980a, 1980b) and Lee (1984) have investigated natural convection in trapezoidal cavities numerically and experimentally. The geometry of the cavities, however, is of parallel top and bottom surfaces and sloping side walls. Poulikakos and Bejan (1983a) describe the transient behavior of a fluid within a shallow triangular attic space having a cold roof top and a hot bottom surface. The vertical boundary, acting as a plane of symmetry to a full isosceles triangular attic space, has zero shear stress and therefore presents a different situation to the problem discussed here. The same authors (1983b) have obtained both water and air data for natural convection heat transfer in one triangular enclosure heated from below. Their air data are for the Rayleigh range of 2×10^5 to 10^6 and their water data are for the range of 3×10^7 to 8×10^7 (using the notation of this paper). The results for the two fluids do not compare well with each other. Other studies on nonrectangular cavities include the work of Van Doormaal et al. (1981) on an air layer bounded above by a cooled plate and below by a heated vee-corrugated surface, the experiments of Thirst and Probert (1978), on isosceles triangular cavities, and the numerical study of Akinsete and Coleman (1982), on right-angled triangular enclosures. Be-

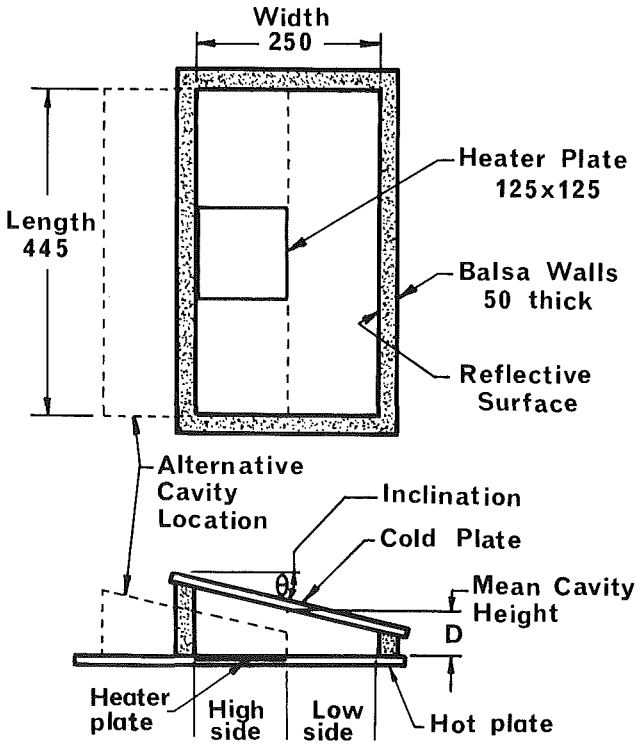

Fig. 1 Sectional plan and elevation of the experimental apparatus

Contributed by the Heat Transfer Division and presented at the 2nd ASME/JSME Thermal Engineering Conference, Honolulu, Hawaii, March 22-27, 1987. Manuscript received by the Heat Transfer Division August 24, 1987. Keywords: Natural Convection, Solar Energy.

cause of the differences in geometry of the cavities and the orientations of the hot and cold surfaces, the results of the above studies have not lent themselves to useful interpretation for the situation presented in this paper.

Experimental Apparatus and Procedures

The experimental cavity was bounded top and bottom by two copper plates acting as cold and hot isothermal surfaces, respectively (Fig. 1). The hot lower plate was horizontal and was maintained at 60°C. The cold upper plate was at 30°C and could be inclined from 0 to 25 deg to the horizontal. The four vertical side walls were made from 50-mm-thick low-density balsa wood ($k \sim 0.04$ W m^{-1} K^{-1}) forming a 250 × 445 mm rectangular plan-form cavity. The inner surfaces of the side walls were lined with aluminized polyester film (having an emittance of 0.02) to minimize their radiative heat transfer.

The apparatus was covered with fiberglass insulation and was placed in a pressure chamber filled with dry air. For a given geometry of the cavity and fixed hot and cold-plate temperatures, the Rayleigh number was varied by changing the pressure of the dry air in the chamber. The whole system was allowed to settle for at least 45 min after the pressure had been adjusted, then data were collected and averaged for test periods of 45 to 90 min. Final data for the experiment were obtained by time averaging the values measured at each interval over the whole test period.

The heat flux from the hot surface into the cavity was measured by the guarded heater plate technique. A 125 × 125 mm copper test plate was inserted into a recess machined out of the hot plate, and a highly sensitive heat flux meter was sandwiched between the test plate and the hot plate. The test plate was electrically heated and computer controlled so that the heat flux between the test plate and the hot plate was close to zero. The electrical power supplied to the test plate was therefore a measure of the total heat transfer rate from this surface into the cavity. Since the width of the test plate was only half the width of the test region, the heat transfer rates at the low side and the high side of the cavity were measured separately; some measurements were also made with the test plate placed centrally. A more detailed description of the apparatus and its operation is given by Peck (1984).

The measured total heat transfer rate consists of a convective component Q_c, and a radiative and boundary loss component Q_{r+b}. In these experiments, Q_{r+b} is unaffected by variations in gas pressure, and so is constant for each experimental model. If Ra is less than the value required for the onset of convection (when Nu < 1.05), then the total heat transfer rate equals $Q_k + Q_{r+b}$. As Q_k can be estimated numerically, then Q_{r+b} can be found, by difference. This value is valid for all Ra.

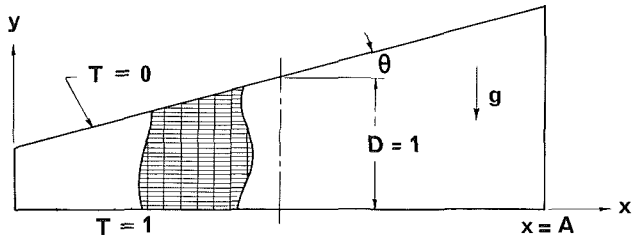

NUMERICAL MODEL

Fig. 2 Schematic of the coordinates and grid used in the numerical solution for a trapezoidal cavity

The overall Nusselt number is defined by the equation

$$\mathrm{Nu} = (Q_{c,L} + Q_{c,H})/(Q_{k,L} + Q_{k,H}) \tag{1}$$

where $Q_{c,L}$ and $Q_{c,H}$ were the convective heat transfer rates for the low side and the high side, respectively, and $Q_{k,L}$ and $Q_{k,H}$ were the corresponding conductive heat transfer rates, evaluated numerically using the two-dimensional heat conduction equation for the particular cavity shape. The overall uncertainties from these experiments were estimated to be less than ±7 percent for both Nu and Ra, as indicated in the appendix.

Governing Equations for the Numerical Analysis

In order to provide an initial insight into the heat transfer and fluid flow mechanisms, a two-dimensional numerical analysis was attempted. Using the Boussinesq approximation, the two-dimensional vorticity and energy transport equations governing the motion of a fluid and heat transfer within the cavity of Fig. 2 may be written in the following nondimensional form:

$$\frac{1}{\mathrm{Pr}}\left(\frac{\partial \zeta}{\partial t} + u\frac{\partial \zeta}{\partial x} + v\frac{\partial \zeta}{\partial y}\right) = \nabla^2\zeta + \mathrm{Ra}\frac{\partial T}{\partial x} \tag{2}$$

and

$$\frac{\partial T}{\partial t} + u\frac{\partial T}{\partial x} + v\frac{\partial T}{\partial y} = \nabla^2 T \tag{3}$$

where

$$\zeta = -\nabla^2\psi \tag{4}$$

The horizontal and vertical components of velocity are given by

Nomenclature

A = cavity width/mean height aspect ratio
c_p = specific heat capacity at constant pressure, J kg^{-1} K^{-1}
D = mean cavity height, m
g = acceleration due to gravity, m s^{-2}
h = overall nondimensional vertical temperature gradient at the hot surface
k = thermal conductivity, W m^{-1} K^{-1}
Nu = overall Nusselt number (see equation (1))
Nu* = modified Nusselt number (see equation (9))
Pr = Prandtl number
Q = heat transfer rate from test plate, W
Ra = Rayleigh number (based on mean cavity height) $= g\beta(T_1' - T_2')\rho^2 D^3 c_p/\mu k$
t' = time, s
T' = temperature, K
u' = horizontal component of velocity, m s^{-1}
v' = vertical component of velocity, m s^{-1}
x' = horizontal dimension, m
y' = vertical dimension, m
α = false transient factor
β = coefficient of volumetric expansion, K^{-1}
ζ' = vorticity, m^{-2}
θ = inclination of the cold plate to the horizontal, deg
κ = thermal diffusivity = $k/\rho c_p$, m^2 s^{-1}
μ = dynamic viscosity, Pa s
ρ = density, kg m^{-3}
ψ' = stream function

Subscripts

c = convective
H = high side of the cavity
k = conductive
L = low side of the cavity
max = maximum value
$r+b$ = radiative and boundary loss
0 = overall for the cavity
1 = hot surface
2 = cold surface

$$u = \frac{\partial \psi}{\partial y} \text{ and } v = -\frac{\partial \psi}{\partial x} \tag{5}$$

The nondimensional quantities are defined in terms of the dimensional ones as $x = x'/D$, $y = y'/D$, $t = t'\kappa/D^2$, $u = u'D/\kappa$, $v = v'D/\kappa$, $T = (T_1' - T')/(T_1' - T_2')$, $\zeta = \zeta' D^2$, and $\psi = \psi'$.

To speed up the convergence to steady-state solutions, false transient factors α_ζ and α_T, as in Mallinson and de Vahl Davis (1973), were introduced to equations (2) and (3), while equation (4) was modified by the addition of a false transient term $(1/\alpha_\psi)\,(\partial\psi/\partial t)$. The values of α_ζ used ranged from 1 to 0.01, α_T ranged from 10 to 1, while α_ψ ranged from 100 to 10. The choice of the values of these transient factors does not affect the final steady-state solution but the computer time required to obtain a converged solution may vary significantly. The modified set of false transient equations to be solved, together with (5), were

$$\frac{1}{\mathrm{Pr}}\left(\frac{1}{\alpha_\zeta}\frac{\partial \zeta}{\partial t} + u\frac{\partial \zeta}{\partial x} + v\frac{\partial \zeta}{\partial y}\right) = \nabla^2\zeta + \mathrm{Ra}\frac{\partial T}{\partial x} \tag{6}$$

$$\frac{1}{\alpha_T}\frac{\partial T}{\partial t} + u\frac{\partial T}{\partial x} + v\frac{\partial T}{\partial y} = \nabla^2 T \tag{7}$$

$$\frac{1}{\alpha_\psi}\frac{\partial \psi}{\partial t} = \nabla^2\psi + \zeta \tag{8}$$

The boundary conditions used were $T = 0$ on the upper sloping surface, and $T = 1$ on the lower horizontal surface. The vertical walls were taken to be adiabatic, i.e., $\partial T/\partial x = 0$.

At the boundaries, since all were stationary, nonslip, and impermeable, $u = v = 0$ while ψ was constant and was conveniently assumed to be zero.

Boundary vorticity was evaluated by the formula

$$\zeta = \left(\frac{\partial u}{\partial y} - \frac{\partial v}{\partial x}\right)$$

suitably discretized at the boundary.

A uniform rectangular mesh was superimposed on the solution region. The aspect ratio of the grid spacings was adjusted so that the upper sloping boundary passed through grid intersections as shown in Fig. 2. Equations (5) to (8) were discretized at each mesh point using forward differences in time and central differences in space. The resulting finite difference equations were solved by a Peaceman–Rachford (1955) alternating direction implicit (ADI) scheme (see, for example, de Vahl Davis, 1976).

The convective heat transfer rate into the cavity from the hot surface was expressed in terms of the overall Nusselt number, which can be rewritten as

$$\mathrm{Nu} = h_c/h_k$$

where $h_c = (1/A)\int_0^A \partial T/\partial y|_{y=0}\, dx$, and $h_k = h_c$ evaluated at Ra = 0.

Discussion of Experimental Results

Tests were conducted with a mean cavity height of 63 mm and θ = 0, 5, 15, and 25 deg. Ra ranged from 10^3 to 10^7. Results are presented in Fig. 3 as Nu versus Ra for various θ. As a basis for the following discussions, the Ra for the onset of convection was taken to be the Ra at which Q_c departed from the Q_k value by 5 percent.

For θ = 0 deg, the onset of convection occurred at Ra = 2340. As Ra was increased Nu increased smoothly, except that when Ra $\sim 10^4$, Nu increased sharply and when Ra $\sim 2 \times 10^5$, Nu decreased. This anomalous result had been reproduced experimentally several times, both while increasing and decreasing Ra, and the sudden change in Nu was of the order of 14 percent, which is higher than the uncertainties of the experimental procedure.

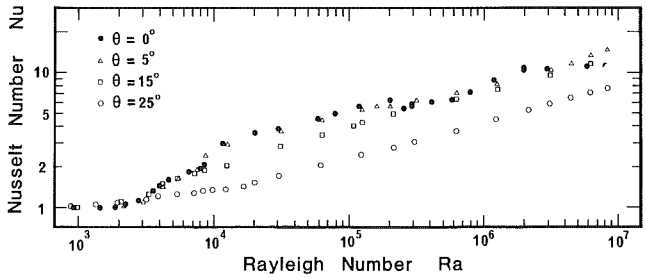

Fig. 3 Experimental results for trapezoidal cavities of 63 mm mean height at various upper surface inclinations

In a previous study, Lam et al. (1985) used the same experimental equipment and trapezoidal cavity but with a mean height of only 25 mm. For that geometry it was shown that the measurements were in very good agreement with accepted results for the classic Rayleigh–Benard problem; however, no anomalous region was found. To the authors' knowledge, this present study is the first to consider this particular cavity geometry, and is the first reported observation of the anomalous results.

When θ = 5 deg similar trends were observed as for the θ = 0 case, except that convection started at Ra = 2270. The sudden changes in Nu at Ra $\sim 10^4$ and Ra $\sim 2 \times 10^5$ were not as obvious as for the θ = 0 deg case but were still discernible.

In the case of θ = 15 deg, the onset of convection was at Ra = 1300 and from then on Nu increased smoothly with Ra. When θ = 25 deg, Ra for the onset of convection was 1100 and again Nu increased smoothly and gradually with Ra.

Apart from the anomalous results already noted for θ = 0 and 5 deg, the effect on Nu of increasing θ from 0 to 15 deg seemed to be insignificant in the ranges $10^3 < \mathrm{Ra} < 10^4$ and $4 \times 10^5 < \mathrm{Ra} < 10^7$. A further increase of θ to 25 deg raised Nu slightly above those of the other angles in the range $10^3 < \mathrm{Ra} < 3 \times 10^3$. For $\mathrm{Ra} > 3 \times 10^3$ the values of Nu were significantly lower than those for the other angles.

It should be noted that while in general Nu decreases with an increase in θ, there is a trend for Q_c to increase with θ, but this becomes uncertain above Ra = 10^6.

An attempt was made to find a single equation correlating Nu with Ra and θ for the whole range of tests. However, this was found to be unsatisfactory because of the different trends in the variations of Nu and θ for different ranges of Ra. For the purpose of general engineering applications a correlation equation was therefore sought for $\mathrm{Ra} > 4 \times 10^3$ only, and omitting the anomalous results for 0 and 5 deg.

A least-squares fit of the form

$$\mathrm{Nu} = a\left[\mathrm{Ra}\left(\frac{1+\cos\theta}{2}\right)\right]^b\left[\frac{1-\cos\theta_{\max}}{\cos\theta - \cos\theta_{\max}}\right]^c$$

was used, where $\theta_{\max}$ is the maximum angle of inclination of the top surface for a given width-to-mean height aspect ratio. The term $\mathrm{Ra}\,(1+\cos\theta)/2$ accounts for the inclination of the top surface. The term $(1-\cos\theta_{\max})/(\cos\theta - \cos\theta_{\max})$, which is a geometric factor, accounts for the changes in relative conducted heat flow through the different shaped cavities as θ changes. For θ = 0 deg, the baseline conducted heat is that for parallel plates, and for $\theta = \theta_{\max}$, the gap between the top and bottom plate at the lower end is zero, giving rise to an infinite value of conducted heat.

The values of best fit for a, b, and c were found to be 0.168, 0.278, and −0.199, respectively, with a standard error of ±6.9 percent, defined as the standard deviation of the ratio of the difference between the predicted and measured Nu to the measured value. The experimental data are shown, together with the correlation equation, in Fig. 4. For $A > 4$, the available

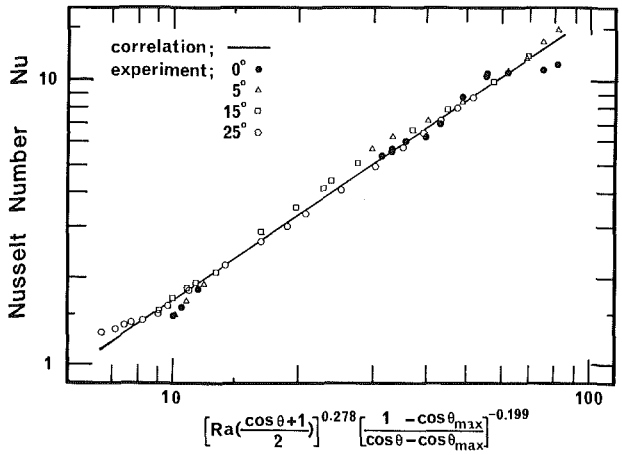

Fig. 4 Graph of the correlation equation superimposed onto the experimental data

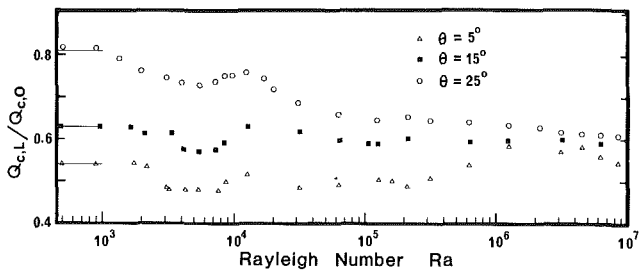

Fig. 5 Ratio of experimentally measured local to overall heat transfer rate versus Ra for θ = 5, 15, and 25 deg

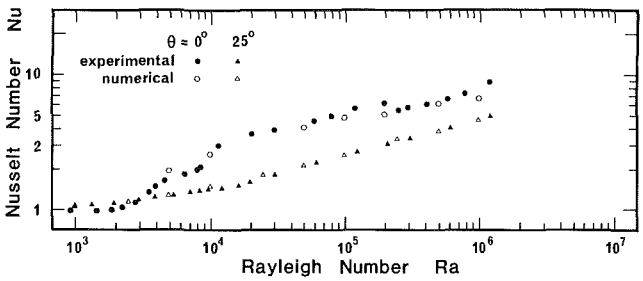

Fig. 6 Comparisons of experimental and numerical results for θ = 0 and 25 deg

range of tilt angles is low and therefore the correlation tends towards Nu = 0.168 $Ra^{0.278}$, which agrees within 5 percent with the two region correlation for rectangular cavities: Nu = 0.157 $Ra^{0.285}$ given in Buchberg et al. (1976). Therefore it is suggested that the correlation is applicable for all $A \geq 4$.

In comparison with the correlation equation obtained here, that of Poulikakos and Bejan (1983b) for air yields convective heat flow rates that are twice as large, after correcting for the different notations; while their correlation for water has an uncharacteristically large index on the Rayleigh number.

For greater simplicity in calculating Q_c, a modified Nusselt number Nu* can be used, so that for any given cavity only $Q_{k,\theta=0}$ needs to be estimated

$$\mathrm{Nu}^* = \mathrm{Nu}(Q_{k,\theta}/Q_{k,\theta=0}) \tag{9}$$

For $A \geq 4$

$$\frac{\mathrm{Nu}^*}{\mathrm{Nu}} = 0.995\left(\frac{1-\cos\theta_{\max}}{\cos\theta-\cos\theta_{\max}}\right)^{0.382}$$

with a standard error of ±0.7 percent.

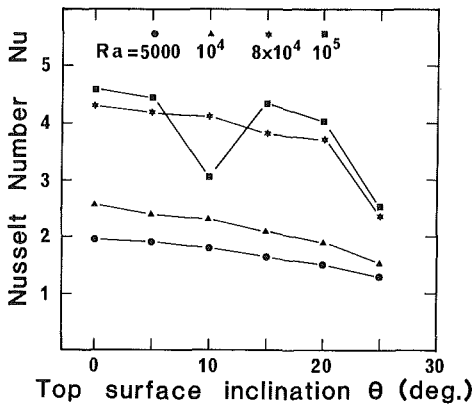

Fig. 7 Numerically evaluated Nu versus θ at Ra = 5000, 10^4, 8×10^4, and 10^5

The heat transfer rate for each side of the cavity is shown in Fig. 5 for three angles of θ. The results indicate very similar trends for all three angles. In the region up to the onset of convection, the low side always contributes more than half of the total heat flow, as is expected from the two-dimensional conduction analysis. At the onset of convection this proportion decreases, which indicates greater involvement of the high side in transporting heat away from the hot surface. The ratio $Q_{c,L}/Q_{c,0}$, however, increases again to a local maximum at Ra ~ 10^4. Another, smaller, local maximum is similarly observed at Ra ~ 2×10^5. Incidentally, the values of Ra ~ 10^4 and 2×10^5 correspond to the abrupt changes in Nu already noted in Fig. 3. For Ra > 10^6, the values of $Q_{c,L}/Q_{c,0}$ for all the three cases tend to converge to a common value, which should become 0.5 for very high Ra.

Discussion of Numerical Results

The numerical results presented here are for Ra up to 10^6, Pr = 0.71, A = 4, and θ from 0 to 25 deg. For the θ = 0 deg case, mesh sizes (relative to the mean height) of from 0.1 to 0.4 in the x direction and 0.025 to 0.1 in the y direction were tried and showed less than 5 percent variation in the calculated heat transfer values. Therefore the remainder of the numerical studies were conducted with mesh sizes of 0.1 to 0.125 in the x direction and 0.01 to 0.047 in the y direction as a compromise between limited computer memory and reasonable accuracy.

A comparison of the numerically computed heat transfer results with the experimental values is shown in Fig. 6. For the sake of clarity, only those values for θ = 0 and θ = 25 deg are presented. Results of other θ also exhibit good agreement between the numerical and experimental values. The discrepancy is typically 3 to 5 percent. The anomaly of a decrease in Nu with an increase in Ra at θ = 0 deg and Ra ~ 2×10^5, observed in the experiment, was not detected by the numerical solution. However, a similar effect was observed in the numerical results for θ = 10 deg at Ra = 10^5.

The variations of Nu with θ for various Ra from the numerical results are shown in Fig. 7. At Ra < 10^4, the effect of θ on Nu is small, there being a gradual decrease in Nu as θ increases. This effect becomes more obvious at higher values of θ and Ra. At Ra = 10^5, there is an anomalous reduction in Nu at θ = 10 deg. This anomaly can be related to the flow patterns within the cavity as described below.

While the authors acknowledge that a two-dimensional numerical analysis cannot adequately describe the three-dimensional flows that occur in a trapezoidal cavity, the simple two-dimensional model can predict heat transfer rates to an acceptable accuracy.

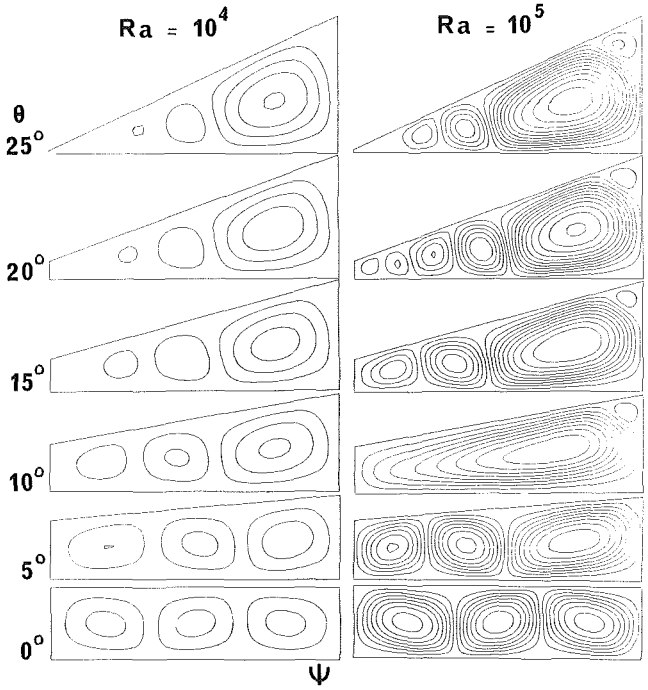

Fig. 8(*a*) Numerically computed streamlines, increment = 5

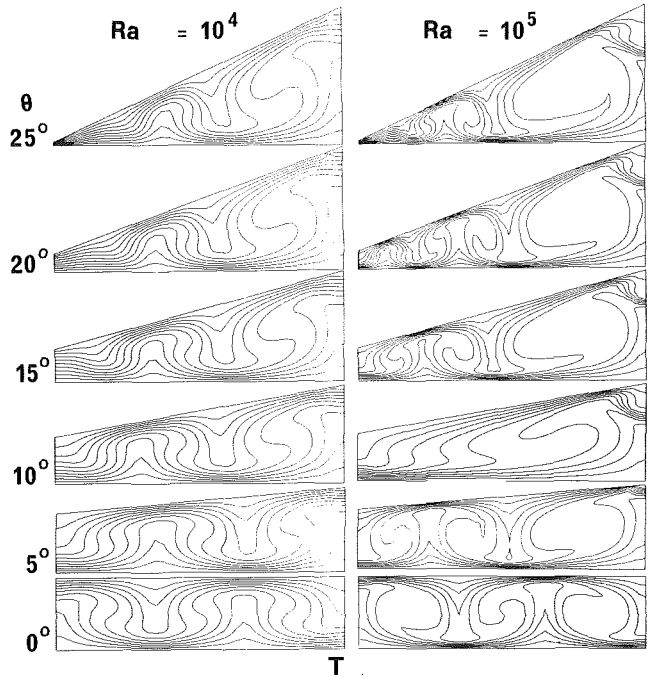

Fig. 8(*b*) Numerically computed isotherms, increment = 0.1

A study of the numerically evaluated streamlines and isotherms of Figs. 8(*a*) and 8(*b*) indicates that for Ra = 10^4 the number of convective cells is three for each value of θ. Except in the case of θ = 0 deg, the cell on the high side of the cavity is the largest, particularly when θ is large. The cell on the lower end diminishes in size as θ increases from 5 to 25 deg. At $\theta >$ 15 deg, the low side cell shifts away from the lower end-wall toward the center of the cavity. This creates a relatively stagnant zone at the lower end where conduction is still the dominant mode of heat transfer, as indicated by the near parallel isotherms. Poulikakos and Bejan (1983a) obtained only a single cell circulation at Ra = 9000 and A = 10, 5, and 2 (defined according to the nomenclature of this paper). The difference may be due to the absence of a vertical shear boundary in their model.

As Ra is increased to 10^5, various patterns develop for different values of θ. At θ = 0 and 5 deg the three-cell circulation still exists. For θ = 5 deg, the cell on the high side becomes bigger, pushing the other two toward the low side of the cavity. At θ = 10 deg the streamlines show a single large cell occupying nearly the whole of the cavity. The merging of the cells into a single cell results in a much lower Nu, as mentioned in the discussion of the Nu versus θ graph above. A small cell has formed at the top corner of the high side of the cavity; however, it contributes little to the overall heat transfer rate since it does not contact the hot surface and it does not distort the large cell. In the case of θ = 15 deg, the streamlines reveal three cells with a rather small one just appearing at the top corner of the high side of the cavity. The larger cell has expanded to occupy more than half of the width of the cavity. The other two cells have been pushed toward the lower end, eliminating the stagnant region, which existed at Ra = 10^4.

At θ = 20 deg, the cell on the low end has divided itself into three smaller ones pushing the circulation further into the low end corner. A small cell again appears at the top corner of the high side for both θ = 20 and 25 deg. However, in the θ = 25 deg case the three main cell pattern is re-established and the higher end one has increased its size to cover more than half of the width of the cavity. The sudden drop in Nu at Ra = 10^5 and θ = 10 deg associated with the reduction of the number of convective cells lends qualitative support that the experimental anomaly at Ra ~ 2×10^5 and θ = 0 and 5 deg is due to a change in the flow pattern.

Conclusions

(*a*) The onset of convection in a trapezoidal cavity occurs at progressively lower Ra as θ is increased from 0 deg.

(*b*) While Nu decreases with an increase of θ, the actual heat transfer rates indicate a complex relationship with Ra and θ. A correlation of the experimental results in the range $4 \times 10^3 <$ Ra $< 10^7$ and 0 deg $\leq \theta \leq$ 25 deg yields:

$$\mathrm{Nu} = 0.168 \left[\mathrm{Ra} \left(\frac{1+\cos\theta}{2} \right) \right]^{0.278} \left[\frac{1-\cos\theta_{\max}}{\cos\theta - \cos\theta_{\max}} \right]^{-0.199}$$

with a standard error of 6.9 percent. It is suggested that this equation may be used for $A \geq 4$.

(*c*) Generally, there is a much greater convective flow on the high side than on the low side of the cavity. However, the low side still contributes more than half of the convective (or conductive) heat flow rate.

(*d*) The numerical results indicated that at Ra = 10^4 the number of convective cells is three for each of θ studied. At Ra = 10^5, cavities with higher θ generally have a greater number of cells, which in turn have higher convective heat transfer rates.

(*e*) The experimental heat transfer results are, in general, in close agreement with those computed numerically using the two-dimensional form of the governing equations. In most cases the errors between the two results are of the order of 3 to 5 percent. It is therefore concluded that the two-dimensional numerical model is adequate in the evaluation of heat transfer rates within the cavities described in this paper.

References

Akinsete, V. A., and Coleman, T. A., 1982, "Heat Transfer by Steady Laminar Free Convection in Triangular Enclosures," *Int. J. Heat Mass Transfer*, Vol. 25, 1982, pp. 991–998.

Buchberg, H., Catton, I., and Edwards, D. K., 1976, "Natural Convection in Enclosed Spaces—A Review of Application to Solar Energy Collection," ASME JOURNAL OF HEAT TRANSFER, Vol. 98, pp. 182–188.

Catton, I., 1978, "Natural Convection in Enclosures," *Proc. 6th International*

Heat Transfer Conference, Toronto, Vol. 6, Hemisphere Press, Washington, DC, pp. 13–31.

de Vahl Davis, G., 1976, "Program FRECON for the Numerical Solution of Free Convection in a Rectangular Cavity," Report No. 1976/FMT/1, School of Mechanical and Industrial Engineering, The University of New South Wales.

Iyican,L., Bayazitoglu, Y., and Witte, L. C., 1980a,"An Analytical Study of Natural Convective Heat Transfer Within a Trapezoidal Enclosure," ASME JOURNAL OF HEAT TRANSFER, Vol. 102, pp. 640–647.

Iyican, L., Witte, L. C., and Bayazitoglu, Y., 1980b, "An Experimental Study of Natural Convection in Trapezoidal Enclosures," ASME JOURNAL OF HEAT TRANSFER, Vol. 102, pp. 648–653.

Kline, S. J., and McClintock, F. A., 1953, "Describing Uncertainties in Single-Sample Experiments," *Mech. Eng.*, pp. 3–8.

Lam, S. W., Gani, R., and Symons, J. G., 1985, "Natural Convection in Trapezoidal Cavities," Third Australasian Conference on Heat and Mass Transfer, University of Melbourne, Australia, May.

Lee, T. S., 1984, "Computational and Experimental Studies of Convective Fluid Motion and Heat Transfer in Inclined Non-rectangular Enclosures," *Int. J. Heat and Fluid Flow*, Vol. 5, Butterworth and Co. (Publishers) Limited, pp. 29–36.

Mallinson, G. D., and de Vahl Davis, G., 1973, "The Method of the False Transient for the Solution of Coupled Elliptic Equations," *J. Comp. Phys.*, Vol. 12, 1973, pp. 435–461.

Peaceman, D. W., and Rachford Jr., H. H., 1955, "The Numerical Solution of Parabolic and Elliptic Differential Equations," *J. Soc. Indus. Appl. Math.*, No. 3, pp. 38–41.

Peck, M. K., 1984, "An Apparatus for the Measurement of Natural Convection Heat Transfer in Enclosures," CSIRO Division of Energy Technology Technical Report TR4, Commonwealth Scientific and Industrial Research Organisation.

Poulikakos, D., and Bejan, A., 1983a, "The Fluid Dynamics of an Attic Space," *J. Fluid Mech.*, Vol. 131, pp. 251–269.

Poulikakos, D., and Bejan, A., 1983b, "Natural Convection Experiments in a Triangular Enclosure," ASME JOURNAL OF HEAT TRANSFER, Vol. 105, pp. 652–655.

Thirst, T. J., and Probert, S. D., 1978, "Heat Transfer Versus Pitch Angle for Nonventilated, Triangular-Sectioned, Apex-Upward Air-Filled Spaces," *Thermal Transmission Measurements of Insulation*, ASTM STP 660, R. P. Tye, ed., American Society for Testing and Materials, pp. 203–210.

Van Doormaal, J. P., Raithby, G. D., and Strong, A. B., 1981, "Prediction of Natural Convection in Non-rectangular Enclosures Using Orthogonal Curvilinear Coordinates," *Numerical Heat Transfer*, Vol. 4, pp. 21–38.

APPENDIX

Experimental Uncertainty

The method of Kline and McClintock (1953) was used in the analysis of the experimental uncertainties on Ra and Nu. In the experiment, Ra was evaluated from the equation

$$\mathrm{Ra} = \frac{g\Delta T D^3 p^2 c_p}{\mu k R^2 T_m^3 Z^2}$$

where p is the pressure of dry air in the pressure vessel, R is the specific gas constant, $\Delta T = T_h' - T_c'$, $T_m = (T_h' + T_c')/2$, and Z is the compressibility of dry air. The uncertainties on g and R were considered negligible and the uncertainty on Ra is then given by

$$\frac{\delta \mathrm{Ra}}{\mathrm{Ra}} = \left\{ \left(\frac{\delta \Delta T}{\Delta T}\right)^2 + \left(3\frac{\delta D}{D}\right)^2 + \left(2\frac{\delta p}{p}\right)^2 + \left(-3\frac{\delta T_m}{T_m}\right)^2 + \left(-\frac{\delta \mu}{\mu}\right)^2 + \left(\frac{\delta c_p}{c_p}\right)^2 + \left(-\frac{\delta k}{k}\right)^2 + \left(-2\frac{\delta Z}{Z}\right)^2 \right\}^{1/2}$$

The uncertainty estimate of all variables was based on 20:1 odds. Typical values used in the above analysis were $\delta\Delta T/\Delta T = 0.6$ percent, $\delta D/D = 0.8$ percent, $\delta p/p = 0.1$ percent, $\delta T_m/T_m = 0.5$ percent, $\delta\mu/\mu = 1.5$ percent, $\delta c_p/c_p = 2$ percent, $\delta k/k = 2$ percent, and $\delta Z/Z = 0.2$ percent. A minimum of 250 data points were collected for each run and the standard deviation, σ_{Ra}, of Ra was evaluated. The uncertainty on the scattering of the data was estimated at a 95 percent confidence interval, given by $1.96\ \sigma_{\mathrm{Ra}}/\sqrt{N}$, where N is the number of data points. The total uncertainty on Ra is then given by

$$u_{\mathrm{Ra}} = \delta \mathrm{Ra} + 1.96\ \sigma_{Ra}/\sqrt{N}$$

The uncertainty of Nu was similarly evaluated; thus

$$\frac{\delta \mathrm{Nu}}{\mathrm{Nu}} = \left[\left(\frac{\delta h_c}{h_c}\right)^2 + \left(\frac{\delta h_k}{h_k}\right)^2 \right]^{1/2}$$

where δh_c and δh_k were in turn estimated with the uncertainties of the measured, raw data using the same method. The values of the uncertainties of the associated variables used in the calculations are: those of the power input to the heater test plate, estimated to be ± 0.2 percent, and those of the outputs of the heat flux meter, estimated to be ± 1.5 percent. The total uncertainty on Nu is evaluated as

$$u_{\mathrm{Nu}} = \delta \mathrm{Nu} + 1.96\ \sigma_{\mathrm{Nu}}/\sqrt{N}$$

Turbulent Natural Convection Flow on a Heated Vertical Wall Immersed in a Stratified Atmosphere

A. K. Kulkarni
Associate Professor.
Mem. ASME

S. L. Chou
Former graduate student.

Department of Mechanical Engineering,
The Pennsylvania State University,
University Park, PA 16802

This paper presents a comprehensive mathematical model and numerical solutions for a natural convection flow over an isothermal, heated, vertical wall immersed in an ambient atmosphere that is thermally stratified. The model assumes a laminar flow near the leading edge, which then becomes a transitional flow, and finally becomes fully turbulent away from the leading edge. Effects of several typical cases of ambient stratification on heat transfer to the wall, peak velocity, and temperature are examined. It is found that the velocity field is affected more significantly by the "memory" of upstream ambient conditions than the temperature field.

Introduction

Natural convection flow over an isothermal vertical surface suspended in an infinite quiescent atmosphere having uniform temperature has been studied by several investigators. However, there are many situations in which the quiescent media may not be isothermal. Flow over the wall of a cryogenic tank, a burning vertical wall in a room with an open door, and heat rejection from a power plant to a lake, are but a few examples where there is a natural convection flow in a stratified ambient atmosphere. A rectangular enclosure having one vertical wall heated and the other cooled with the top and bottom panels insulated presents a well-studied situation in which the core of the enclosure is stratified and a boundary layer-type natural convection flow is set up on the walls (Eichhorn, 1969; Giel and Schmidt, 1986). An excellent review on this general subject has recently been presented by Jaluria (1985). Careful examination of the existing literature, however, reveals that the problem of turbulent natural convection over an isothermal vertical surface immersed in a stratified atmosphere has never been investigated analytically; this problem is the focus of the present paper. The primary objective is to understand the changes caused by the atmospheric stratification in the fluid flow and heat transfer characteristics of a natural convection flow, as compared to flow in a uniform atmosphere.

A laminar natural convection flow on an isothermal vertical surface in a uniform-temperature atmosphere forms a classical textbook solution. Similar types of flow, but in a stratified ambient atmosphere, have also been studied for many specific cases by several investigators using various analytical methods such as similar solutions (Cheesewright, 1967; Yang et al., 1972; Kulkarni et al. 1987), the local nonsimilarity approach (Chen and Eichhorn, 1976), a finite difference technique (Venkatachala and Nath, 1981), a perturbation method (Fujii et al., 1974), and other approximate methods (Raithby and Hollands, 1978). Results for velocity profiles, temperature profiles, and heat transfer have been presented by these investigators. All the analytical results predict inversion of temperature and reversal of flow under certain conditions of stratification; however, very few experimental data are available to validate the models. Heat transfer measurements and plume height observations made by Chen and Eichhorn (1976) for a natural convection flow over an isothermal cylinder in a thermally stratified water tank were generally found to agree with their own predictions under laminar flow conditions.

Turbulent natural convection flow over an isothermal wall immersed in a uniform temperature atmosphere has been studied extensively (see, for example, Plumb and Kennedy, 1977, and Cheesewright and Dastbaz, 1983). Buoyant plumes and jets in stratified media have also been of considerable interest. Most of the investigations have considered linearly stratified, stable media, and the most sought-after parameter was maximum upward penetration of the jet or the height of plume. The density variation at the center of the plume was also reported in some studies. Correlations have been proposed relating these parameters to the density gradient and local weight deficit. An excellent discussion on this topic, with extensive bibliography, is presented by Chen and Rodi (1980).

Mathematical Model

Physical Description. The mathematical model attempts to predict fluid flow and heat transfer characteristics of a natural convection flow over an isothermal vertical surface immersed in a quiescient ambient atmosphere having a vertical stable thermal gradient. The practical situation that motivated this study was fire in a compartment, such as a room or an aircraft cabin. Under these circumstances, the atmosphere in the compartment becomes thermally stratified wherein a hot layer of gases floats on the top of a layer of relatively fresh, cold air. Figure 1 shows a schematic of this situation. The actual vertical thermal gradient may be steep at the interface or nearly linear from the bottom to the top depending on ventilation ports, origin of fire, etc. Natural convection flow over the heated vertical walls of the compartment is influenced by the ambient stratification in mainly two ways. First, the upward buoyancy force, which is the major driving force behind the entire flow, depends on the local temperature of the ambient atmosphere at any vertical location. Second, the temperature boundary condition at the outer edge of the boundary layer becomes height dependent. A strong stratification may also cause a flow reversal and a temperature inversion near the outer edge of the boundary, according to predictions of most of the previous studies mentioned earlier.

In order to study the fluid flow and thermal changes caused by the stratification, results for two typical forms of ambient temperature distribution are compared with those for uniform atmosphere in this paper. The vertical wall is considered to be isothermal and at a higher temperature than the entire at-

Contributed by the Heat Transfer Division and presented at the ASME/AIChE National Heat Transfer Conference, Pittsburgh, Pennsylvania, August 9–12, 1987. Manuscript received by the Heat Transfer Division May 4, 1987. Keywords: Natural Convection, Stratified Flows, Turbulence.

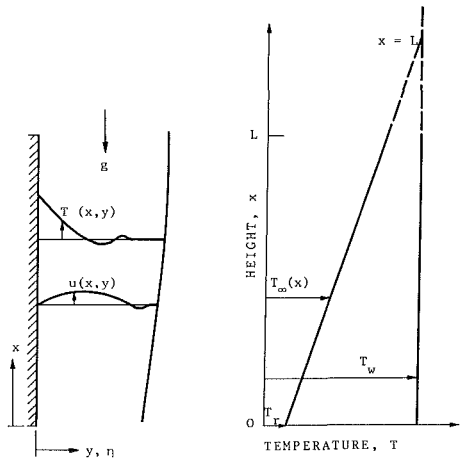

Fig. 1 A schematic of the flow and linearly stratified ambient temperature

mosphere in order to avoid a strong, negatively buoyant flow, which would break down the boundary layer nature of the flow. The ambient atmosphere is assumed to be quiescent. Although the natural convection and the thermal diffusion process will eventually mix the stratified atmosphere and make it uniform, the characteristic flow time is typically much shorter than the characteristic time required to mix the stably stratified atmosphere. Therefore, a steady-state flow approximation appears to be reasonable, which has also been employed in most previous stratified flow studies. Temperature-dependent transport properties of air are evaluated at the local mean film temperature, which is a function of the height.

Transition-to-Turbulence Model. A simple calculation based on a typical length scale (say, height of a wall in a room) and the buoyancy forces (created by hot gases resulting from a fire) showed that a Grashof number is on the order of 10^{11}. The measurements of Cheesewright (1968) revealed that, for a natural convection flow over an isothermal vertical plate immersed in a uniform temperature atmosphere, transition begins somewhere near $\mathrm{Gr} \cong 1 \times 10^{10}$. The experimental data of Warner and Arpaci (1968) also support these findings. Since this range of Grashof numbers can cover a significant portion of the flow field in the present problem, a model that accounts for laminar-transitional-turbulent flow regimes has been incorporated in the present study.

As noted at the outset, the primary objective of the present work is to understand the effect of stratification of the ambient atmosphere on the overall velocity field, the temperature distribution, and heat transfer characteristics, rather than to make a detailed study of turbulence quantities. Moreover, the present status of understanding of turbulent natural convection flows in a stratified atmosphere is not sufficiently advanced to require complex models to study the first-order effects of stratification in the natural convection flows. Consequently, the turbulence model is kept relatively simple for ease in numerical solution while retaining important physical aspects of turbulence. The present study is based on solutions of the boundary layer equations in their partial differential form, with an eddy-viscosity model used for transitional and turbulent regimes. The model for fully turbulent flow is primarily based on that of Cebeci and Khattab (1975), who studied turbulent, natural convection heat transfer from a vertical wall. No new empirical constants are introduced; all the constants are the same as those available in literature for forced convection flows. The transitional flow model is primarily based on the model of Price and Harris (1972), who solved a problem involving forced convection of a perfect gas undergoing laminar-transitional-turbulent flow.

Governing Equations. Equations governing the natural convection, laminar-transitional-turbulent boundary layer flow of air over a vertical wall take the following form, using the Boussinesq approximation (i.e., the density variation is only considered in the buoyancy term)

$$\frac{\partial u}{\partial x} + \frac{\partial v}{\partial y} = 0 \tag{1}$$

$$u\frac{\partial u}{\partial x} + v\frac{\partial u}{\partial y} = \beta g\,[T - T_\infty(x)] + \frac{\partial}{\partial y}\left[(\nu + \Gamma\,\epsilon_m)\frac{\partial u}{\partial y}\right] \tag{2}$$

$$u\frac{\partial T}{\partial x} + v\frac{\partial T}{\partial y} = \frac{\partial}{\partial y}\left[\left(\alpha + \Gamma\frac{\epsilon_m}{\mathrm{Pr}_t}\right)\frac{\partial T}{\partial y}\right] \tag{3}$$

The thermally stratified, quiescent atmosphere imposes the following boundary conditions:

$$y = 0: \quad u = v = 0, \quad T = T_W \tag{4}$$

$$y \to \infty; \quad u \to 0, \quad T \to T_\infty(x) \tag{5}$$

Here, the ambient temperature $T_\infty(x)$ is prescribed according to the problem to be solved and T_w is a known constant.

The contribution of turbulence to the effective viscosity is considered separately for inner and outer regions of the boundary layer (Cebeci and Smith, 1974)

$$\epsilon_m = \epsilon_{m,i} = [0.4\,y\,(1 - e^{-y/A})]^2\left|\frac{\partial u}{\partial y}\right|, \quad \epsilon_{m,i} < \epsilon_{m,o}$$

$$\epsilon_{m,o} = (0.075\,\delta)^2\left|\frac{\partial u}{\partial y}\right|, \quad \epsilon_{m,i} > \epsilon_{m,o} \tag{6}$$

where $A = 26\,\nu\,(\tau_w/\rho)^{-1/2}$ and $(\tau_w/\rho) = \nu\,|\partial u/\partial y|_{y=0}$.

The contribution of turbulence to the thermal diffusivity is

Nomenclature

A = a parameter, equation (6)
F = dimensionless stream function
g = acceleration due to gravity
Gr = Grashof number, equation (8)
k = thermal conductivity
L = height of wall
Nu = Nusselt number
Pr = Prandtl number
Pr_t = turbulent Prandtl number, equation (7)
q_w = convective local heat flux at wall
Q_w = cumulative heat transfer from leading edge
Ra = Rayleigh number
T = temperature
v = velocity in horizontal direction
x = vertical coordinate
$\bar{x}$ = dimensionless distance along wall = x/L
y = horizontal coordinate
α = thermal diffusivity
β = coefficient of thermal expansion
Γ = intermittency coefficient
δ = boundary layer thickness
ϵ_m = eddy viscosity
η = dimensionless distance, equation (8)
θ = dimensionless temperature, equation (9)
ν = kinematic viscosity
ρ = density
τ_w = shear stress at wall
ψ = stream function

Subscripts

i = inner region
o = outer region
max = maximum value
w = wall
∞ = ambient atmosphere

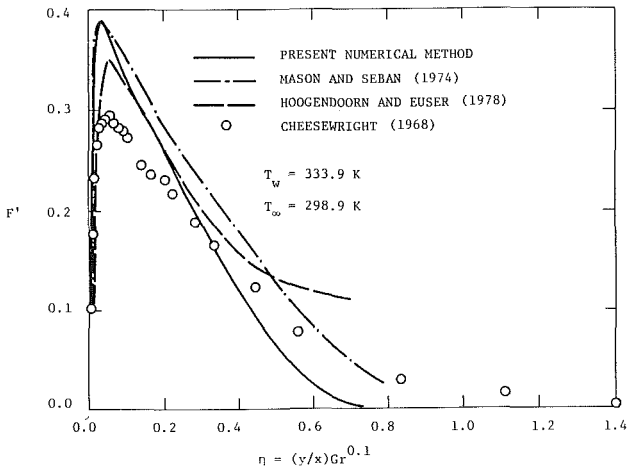

Fig. 2(*a*) Comparison of results for dimensionless upward velocity at x = 2.0 m

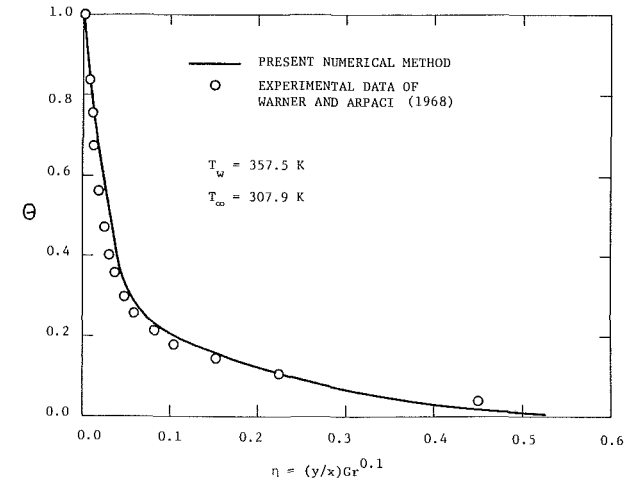

Fig. 2(*b*) Comparison of results for dimensionless temperature at x = 2.0 m

related to ϵ_m via the turbulence Prandtl number Pr_t. Cebeci and Smith (1974) first proposed a complex expression for Pr_t involving five constants determined from experiments. However, they discovered that the predictions were not sensitive to the turbulent Prandtl number assumption over a significant range of Prandtl number, including Pr = 0.72, which they studied in detail. We adapted a simpler expression for turbulent Prandtl number suggested by Price and Harris (1972)

$$Pr_t = 0.45\ [2 - (y/\delta)^2] \tag{7}$$

The transition from laminar to fully turbulent flow is governed by the parameter Γ, which appears in equations (2) and (3). It represents the steamwise intermittency distribution of turbulent spots in the transitional regime. It may be noted that the intermittency-distribution factor Γ is 0.0 for laminar flow, 1.0 for fully turbulent flow, and ranges between 0.0 and 1.0 for the transitional regime of the flow. In general, it is assumed to be a function of x only. Price and Harris (1972) suggested a complex exponential functional form for $\Gamma(x)$ for a forced convection flow. In the absence of data in the transitional regime of buoyancy dominated flows, we assume a linear variation of $\Gamma(x)$ between 0.0 and 1.0 in the transitional regime, which happens to be a reasonably good approximation to the complex form suggested by Price and Harris (1972).

The boundary layer grows from zero thickness at the leading edge to its maximum thickness at the top of the wall. In order to reduce the loss of accuracy due to the growing boundary layer thickness and to remove the singularity at $x = 0$, the y coordinate is "stretched" using a transformation that is commonly employed to obtain similarity variables.

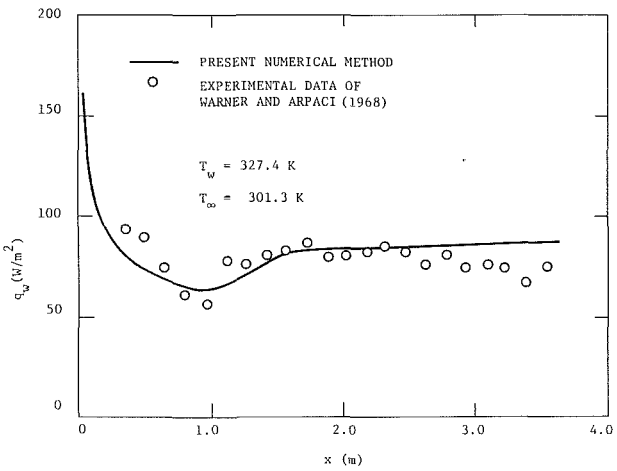

Fig. 2(*c*) Comparison of results for heat flux at wall

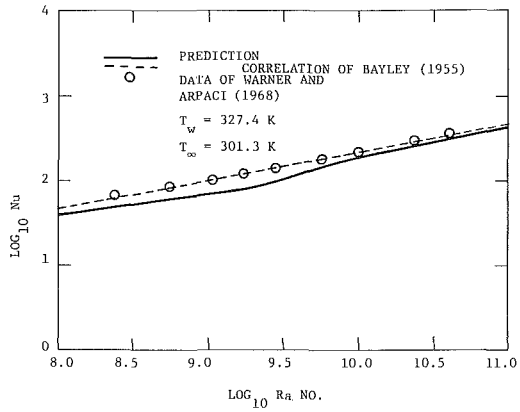

Fig. 2(*d*) Comparison of predicted Nusselt number variation with experimental data

$$y = \eta \left\{ \frac{g\beta[T_w - T_\infty(x)]}{\nu^2 x} \right\}^{-1/4} = \eta\ Gr^{-1/4} x \tag{8}$$

where β, the coefficient of volumetric thermal expansion, is assumed to be the reciprocal of the local mean film temperature, i.e., $\beta = 2/[T_w + T_\infty(x)]$.

Dimensionless forms of temperature and stream function are introduced as follows:

$$\theta(x, \eta) = \frac{T - T_\infty(x)}{T_w - T_\infty(x)} \tag{9}$$

$$F(x, \eta) = \{\beta g\ [T_w - T_\infty(x)]\ \nu^2\ x^3\}^{-1/4}\ \psi(x, y) \tag{10}$$

where $u = \partial\psi/\partial y$; $v = -\partial\psi/\partial x$.

Using the above transformation, the continuity equation is automatically satisfied and equations (2) and (3) reduce to

$$\left[\left(1 + \frac{\epsilon_m}{\nu}\right) F''\right]' + \frac{3}{4} FF'' - \frac{1}{2}(F')^2 + \theta - \frac{x}{2[T_w - T_\infty(x)]} \frac{dT_\infty(x)}{dx} \left[\frac{1}{2} FF'' - (F')^2\right] = x\left(F' \frac{\partial F'}{\partial x} - F'' \frac{\partial F}{\partial x}\right) \tag{11}$$

$$\left[\left(\frac{1}{Pr} + \frac{\epsilon_m}{\nu\ Pr_t}\right) \theta'\right]' + \frac{3}{4} F\theta'$$

$$+ \frac{x}{[T_w - T_\infty(x)]} \frac{dT_\infty(x)}{dx} \left(F'\theta - F' - \frac{1}{4} F\theta'\right)$$

$$= x\left(F' \frac{\partial\theta}{\partial x} - \theta' \frac{\partial F}{\partial x}\right) \tag{12}$$

where the prime denotes partial differentiation with respect to η. The boundary conditions become

$$\eta = 0: \quad F = F' = 0, \quad \theta = 1 \tag{13}$$
$$\eta \to \infty: \quad F' = 0, \quad \theta = 0$$

Results and Discussion

The above set of governing equations was solved numerically using a modified Keller Box finite difference method (Cebeci and Bradshaw, 1984). The equations were first transformed by defining three new variables for F', F'', and θ'. This resulted in a set of five, first-order, coupled, partial differential equations. The equations were then converted into a finite difference form using a central difference scheme. Nonlinear terms were quasilinearized based on Taylor's series expansion, and finally, the block-tridiagonal-elimination procedure was used to obtain the solution.

The surrounding medium was assumed to be air, behaving like a perfect gas, and its properties were evaluated at the mean film temperature at a given x location. Flow was assumed to be laminar for $Gr_x < 2 \times 10^9$, turbulent for $Gr_x > 10^{10}$, and transitional within this range of local Grashof number, based on experimental data from literature (Cheesewright, 1968).

Comparisons for Uniform Atmosphere Results. In addition to the standard numerical checks (such as energy and momentum balance at randomly selected locations inside the boundary layer, variation of step size, etc.), the computer code was tested for accuracy by first setting $\Gamma = 0$. This makes the flow field laminar, results for which are well known. Results from the present model for a turbulent flow over an isothermal vertical wall immersed in a uniform, quiescent, ambient atmosphere are compared with experimental and analytical results from literature in Fig. 2. Normalized velocity profiles at $x = 2$ m shown in Fig. 2(*a*) were obtained from experimental data of Cheesewright (1968) and Hoogendoorn and Euser (1978) as well as predictions of Mason and Seban (1974) and our model. Our predictions somewhat underestimate the velocity near the edge of the boundary layer; otherwise the agreement is good. Data of Cheesewright (1968) are low near the peak compared to other results; however, some reservations have been raised about this velocity data set in the literature (Hoogendoorn and Euser, 1978). Figure 2(*b*) shows comparison of temperature data by Warner and Arpaci (1968) with our calculations for heat transfer results. The calculations were performed assuming laminar-transitional-turbulent flow at preset values of local Grashof numbers for transition, as mentioned earlier. Figure 2(*c*) shows the local heat transfer variation with x and shows a clear laminar-to-turbulent transition, with a good agreement between our predictions and data. Figure 2(*d*) shows comparison of the overall trend of the Nusselt number variation with Rayleigh number with the data of Warner and Arpaci (1968) and the correlation of Bayley (1955), again with good agreement.

It should be noted that in all of the above comparisons, the empirical constants used in the laminar-transitional-turbulent flow model were taken directly from the literature; absolutely no matching was made between the data and calculations at any of the data points. No suitable data were found in the literature for comparison of results for natural convection in a stratified atmosphere.

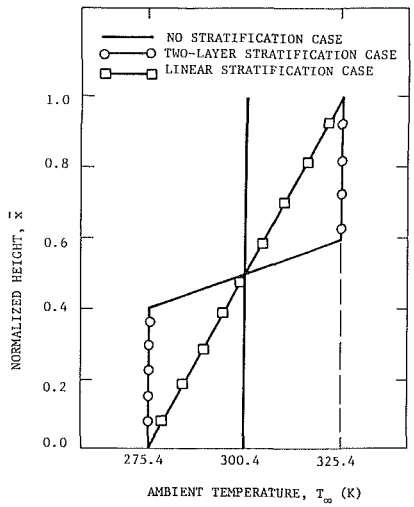

Fig. 3 Ambient temperature profiles of the three stratification cases

Stratified Atmosphere Results

Three Cases to Be Studied. In order to study the effect of ambient stratification on natural convection, a comparison must be made for results from stratified and nonstratified cases on an equivalent basis. Therefore, we have presented results for three different types of ambient temperature variation as shown in Fig. 3. The base case is that of uniform ambient temperature equal to 300.4 K and the wall temperature of 358.3 K. The reason for selecting these values is the availability of a significant amount of data at this condition on various parameters of importance, such as velocity, temperature, and heat transfer (Cheesewright, 1968). All the results are presented assuming that the total height of the vertical surface, L, is equal to 2.6 m. The height is typical for interior of a room and it has been used in experimental investigations.

For stratified cases, we present calculations for two specific forms of ambient temperature variation with respect to the height, although any form of stratification can be handled by the mathematical model. One form is a linear temperature variation from the bottom to the top, with temperature increasing with height (see Fig. 3). The other form is a two-layer stratification with a finite gradient of temperature separating the two layers. In particular, for the second case we have selected a uniform temperature from the bottom to 40 percent of the wall height, i.e., T_∞ = constant for $0 < \bar{x} < 0.4$; linearly increasing temperature up to 60 percent of wall height; and then a higher uniform temperature up to the top. These two forms of stratification are not unusual in case of a room fire (see for example, data of Quintiere et al., 1981). The important common factor among the three cases is that the mean value of the ambient temperature weighted by the height is the same (300.4 K).

The difference between the ambient temperature at the top and bottom of the wall is somewhat arbitrarily selected to be 50 deg. Because of the above condition, the ambient temperature at the center wall height is the same for all the cases. The entire ambient temperature range is deliberately kept below that of the wall temperature to avoid a dominant negatively buoyant flow and a severe breakdown of the boundary layer structure. Even in the present cases there is a region, especially where the stratification is severe, in which the boundary layer flow assumption may be questionable. However, this region is very small compared to the overall flow field and it is confined only to the outer edge of the boundary layer. For the cases of uniform atmosphere, linearly stratified atmosphere, and two-layer atmosphere, the locations of the end of the laminar regime are found to be $\bar{x} = 0.28$, 0.26, and 0.28,

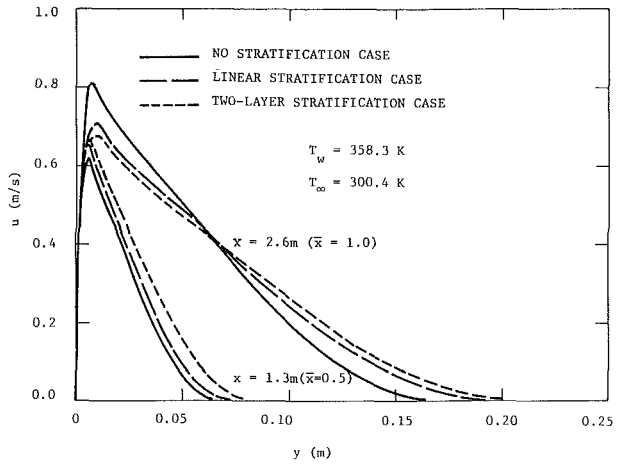

Fig. 4 Profiles of vertical velocity in the boundary layer for the three stratification cases

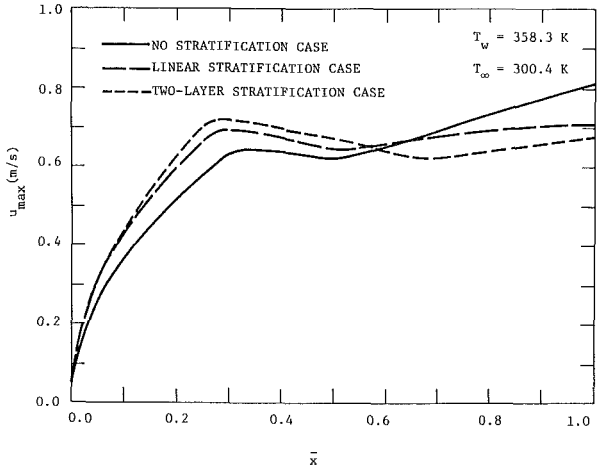

Fig. 5 Profiles of maximum vertical velocity along the *x* direction for the three stratification cases (height of the wall *L* = 2.6 m)

respectively, and the onset of fully turbulent regime is at $\bar{x}$ = 0.48, 0.48, and 0.41, respectively.

Velocity Profiles. Predicted values of the upward velocity as a function of the perpendicular distance from the wall are presented in Fig. 4 at the midheight and full height of the wall, i.e., $\bar{x}$ = 0.5 and 1.0 (based on L = 2.6 m) for the three cases. It may be noted that the results are presented for dimensional parameters, despite the convention of presenting velocity results in the form of u/u_{max} or $u/(g\beta\Delta Tx)^{1/2}$ and the convention of using η for the distance from the leading edge. This is done intentionally, in order to facilitate the comparison of results for various stratification cases. Factors used for nondimensionalizing the parameters in problems involving natural convection contain T_∞ and β, which depend upon the specific type of stratification under consideration in the present problem.

Velocity profiles at $\bar{x}$ = 0.5 in Fig. 4 show that the upward velocity is the largest for the two-layer stratification case and smallest for the uniform atmosphere case everywhere in the boundary layer. This may be explained on the basis of buoyancy, which is the main force driving the flow. The velocity at any x location is the cumulative effect of the buoyancy force from the leading edge to that location (or the flow "memory"). The mean buoyancy force between $o < \bar{x} < 0.5$ is the maximum for the two-layer case since $T_\infty(x)$ for this case is always less than $T_\infty(x)$ for the other two cases. The mean buoyancy force is the minimum for the uniform temperature case.

The variation of the maximum upward velocity u_{max} with

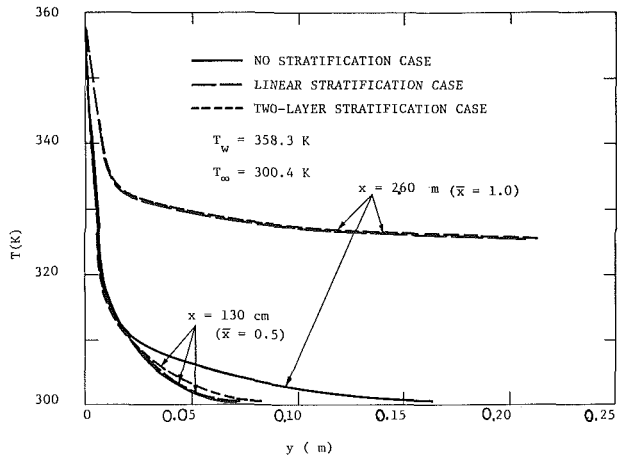

Fig. 6 Profiles of temperature in the boundary layer for the three cases

the height shown in Fig. 5 reveals interesting effects of stratification. For the uniform temperature case, u_{max} first rises quickly in the laminar region, remains approximately constant in the transitional region, and then rises slowly in the fully turbulent boundary layer. For the two-layer case, u_{max} rises much more quickly initially because of the higher buoyancy, and then it slightly slows down in the transition and stratification region until it reaches its lowest value at $\bar{x}$ = 0.65. The momentum in the upstream flow increases rapidly and is significantly higher at the end of the strongly buoyant region ($\bar{x}$ = 0.4). Then it suddenly encounters a relatively low buoyancy region, which can no longer support the momentum and the high shear rate in the boundary layer. The velocity therefore begins to adjust to the local buoyancy force, which is related to $[T(x, y) - T_\infty(x)]$. Eventually the flow starts to pick up the momentum in the uniform buoyancy region of $\bar{x} > 0.6$. However, the growth rate of u_{max} is sufficiently slow above $\bar{x}$ = 0.6 and u_{max} is the lowest at $\bar{x}$ = 1.0 for the two-layer case as compared to the other two cases. The maximum vertical velocity for the linear stratification case generally remains between that for the uniform temperature and two-layer stratification cases, because the local buoyancy force for the linear case is always between that of the other two cases.

Temperature Profiles. Figure 6 shows the temperature variation inside the buoyancy layer for the three cases at midheight and full height of the wall. The effect of stratification on temperature variation in the boundary layer at $\bar{x}$ = 0.5 is practically negligible. Note that the ambient temperature is identical for all three cases at $\bar{x}$ = 0.5. At $\bar{x}$ = 1.0, temperature profiles for the linear and two-layer stratified atmosphere cases are close, but temperature for the uniform temperature case is well below the other two. This observation is consistent with the fact that the ambient temperature is the same for the linear and two-layer cases, and lower for the uniform temperature case. Thus it appears that the temperature inside the boundary layer is strongly tied to the local ambient temperature, rather that the memory of the flow, or "history" (upstream variation) of $T_\infty(x)$. As shown later, this has a significant influence on the local heat transfer.

The difference in the behavior of momentum and energy transport may be explained by the following argument. The momentum transport is a predominantly cumulative effect starting from the leading edge. Even in the case of nonstratified atmosphere, the momentum in the boundary layer continues to grow and the maximum velocity increases "without limit" (from the theoretical point of view); i.e., the higher the wall, the greater is u_{max}. On the other hand, the growth of the energy transport is more severely restricted because the maximum possible temperature in the flow is the wall temperature, which

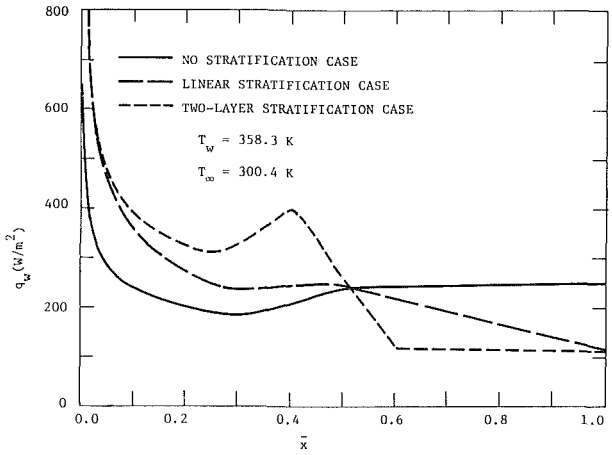

Fig. 7 Profiles of heat flux at wall for the three stratification cases (height of the wall L = 2.6 m)

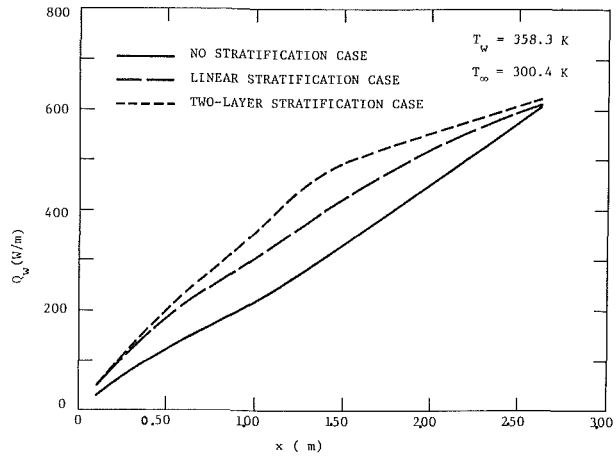

Fig. 8 Profiles of cumulative heat transfer from the leading edge for the three stratification cases

is a constant. In all the cases of stratified atmosphere, the boundary condition on temperature changes, but the boundary condition on velocity remains unchanged. The velocity distribution is changed through the buoyancy force (i.e., via the ambient temperature). Thus the temperature profiles are immediately affected by the externally applied conditions, whereas the velocity profiles lag behind the temperature.

Heat Transfer. Figure 7 shows the local heat transfer rate as a function of the distance from the leading edge for the three cases of stratification. Again, we preferred to present the results in dimensional quantities for the heat transfer because of the nonconstant $T_\infty(x)$, which is normally used in nondimensionalization. Use of a heat transfer coefficient is also inconvenient for the same reason. The local heat transfer rates differ significantly for the three cases and they appear to respond strongly to the variation of $T_\infty(x)$. In other words, the effect of upstream flow conditions in terms of the temperature gradient at the wall is not carried into the downstream significantly, unlike momentum. Consequently the heat transfer rate changes suddenly for the two-layer stratification case, and it varies relatively smoothly for the linear stratification case.

The peculiar trend of local heat transfer for the two-layer case showing a clear maximum is not entirely unexpected. Even for the nonstratified case, the local heat transfer coefficient h, and therefore the local heat flux, $q_w = h(T_w - T_\infty)$, both decrease in the laminar region, then increase in the transitional region until the flow becomes fully turbulent, and then slowly decrease in the turbulent region. In the two-layer case, the latter two trends for the local heat flux are accentuated by the fact that $(T_w - T_\infty)$ decreases sharply.

The difference in the behavior of thermal- and momentum-related parameters in this problem is analogous to the situation of a burning vertical wall with a laminar fire immersed in a stratified atmosphere. It has been shown analytically and experimentally that the heat transfer rate to the wall is relatively insensitive to the upstream memory of the flow, but the gas velocity and shear stress at the wall are sensitive to the upstream memory (Kulkarni and Hwang, 1986a, 1986b).

Predictions for the cumulative heat transfer from the leading edge are shown in Fig. 8 for the three cases of stratification. Heat transfer is the greatest for the two-layer case at any given $\dot{x}$, until $\bar{x} = 1$. However, the total heat transferred from the wall does not differ significantly for the three cases.

Overall, the atmospheric stratification appears to affect the fluid flow and thermal characteristics of the natural convection flow in an interesting manner. The relationship between the stratification and the velocity field is strongly nonlinear due to the upstream memory. In other words, a simple linear combination of results from the corresponding nonstratified cases will not accurately predict results for a stratified case. Conversely, the interaction of stratification and the temperature as well as the heat transfer appears to be approximately linear (less effect of upstream history of $T_\infty(x)$ compared to the velocity field). Indeed there is a strong need for experimental verification of these analytical results.

Summary and Conclusion

The problem of laminar-transitional-turbulent natural convection over an isothermal, hot wall immersed in a stratified, quiescent atmosphere has been solved numerically. Results for velocity and temperature profiles in the boundary layer and heat transfer to the wall are presented and studied in detail for three different cases of ambient thermal stratification. The velocity field is found to be significantly affected by the upstream "memory" of the flow. The temperature profiles are less affected by the upstream conditions; they are mainly dependent on local boundary conditions.

Acknowledgments

This work was partially supported by a grant from the Center for Fire Research, National Institute of Standards and Technology, Gaithersburg, MD.

References

Bayley, F. J., 1955, "An Analysis of Turbulent Free Convection Heat Transfer," *Proc. Inst. Mech. Engineers*, Vol. 169, No. 20, p. 361.

Cebeci, T., and Bradshaw, P., 1965, *Physical and Computational Aspects of Convective Heat Transfer*, Springer-Verlag, New York.

Cebeci, T., and Khattab, A., 1975, "Prediction of Turbulent Free Convective Heat Transfer From a Vertical Flat Plate," ASME JOURNAL OF HEAT TRANSFER, Vol. 97, pp. 469-471.

Cebeci, T., and Smith, A. M. O., 1974, *Analysis of Turbulent Boundary Layers*, Academic Press, New York.

Cheesewright, R., 1967, "Natural Convection From a Plane Vertical Surface in Nonisothermal Surroundings," *International Journal of Heat and Mass Transfer*, Vol. 10, pp. 1847-1859.

Cheesewright, R., 1968, "Turbulent Natural Convection From a Vertical Plane Surface," ASME JOURNAL OF HEAT TRANSFER, Vol. 99, pp. 1-8.

Cheesewright, R., and Dastbaz, A., 1983, "The Structure of Turbulence in a Natural Convection Boundary Layer," *9th Symposium on Turbulent Shear Flows*, Federal Republic of Germany, p. 17.25.

Chen, C. C., and Eichhorn, R., 1976, "Natural Convection From a Vertical Surface to a Thermally Stratified Fluid," ASME JOURNAL OF HEAT TRANSFER, Vol. 98, pp. 446.

Chen, C. J., and Rodi, W., 1980, *Vertical Turbulent Buoyant Jets—A Review of Experimental Data*, Pergamon Press, New York.

Eichhorn, R., 1969, "Natural Convection in a Thermally Stratified Fluid," *Progress in Heat and Mass Transfer*, Vol. 2, Pergamon Press, New York, pp. 41-53.

Fujii, T., Takeuchi, M., and Morioka, I., 1974, "Laminar Boundary Layer of Free Convection in a Temperature Stratified Environment," *Proceedings, Fifth International Heat Transfer Conference*, Tokyo, NC2.2, pp. 44-48.

Giel, P., and Schmidt, F. W., 1986, "An Experiment Study of High Rayleigh Number Natural Convection in an Enclosure," *Proceedings of the Eighth International Heat Transfer Conference*, San Francisco, CA.

Hoogendoorn, C. J., and Euser, H., 1978, "Velocity Profiles in the Turbulent Free Convection," *Proceedings, Sixth International Heat Transfer Conference*, Toronto, NC-2, pp. 193–197.

Jaluria, Y., 1985, in: *Natural Convection Fundamentals and Applications*, S. Kakac, W. Aung, and R. Viskanta, eds., Hemisphere Pub. Corp., Washington, DC, pp. 51–74.

Kulkarni, A. K., and Hwang, J. J., 1986a, "Vertical Wall Fire in a Stratified Ambient Atmosphere," *Twenty-first International Symposium on Combustion*, The Combustion Institute, Pittsburgh, PA, pp. 45–51.

Kulkarni, A. K., and Hwang, J. J., 1986b, "An Experimental Study of Vertical Wall Fire in a Stratified Ambient Atmosphere," 1986 Technical Meeting, The Eastern Section of the Combustion Institute, Puerto Rico.

Kulkarni, A. K., Jacobs, H. R., and Hwang, J. J., 1987, "Similarity Solution for Natural Convection Flow Over an Isothermal Vertical Wall Immersed in Thermally Stratified Medium," *International Journal of Heat and Mass Transfer*, Vol. 30, pp. 691–698.

Mason, H. B., and Seban, R. A., 1974, "Numerical Predictions for Turbulent Free Convection From Vertical Surfaces," *International Journal of Heat and Mass Transfer*, Vol. 17, pp. 1329–1336.

Plumb, O. A., and Kennedy, L. A., 1977, "Application of a K–ϵ Turbulence Model to Natural Convection From a Vertical Isothermal Surface," ASME JOURNAL OF HEAT TRANSFER, Vol. 99, pp. 79–85.

Price, J. M., and Harris, J. E., 1972, "Computer Program for Solving Compressible Nonsimilar-Boundary-Layer Equations for Laminar, Transitional or Turbulent Flows of a Perfect Gas," NASA-Langley Report L-8037.

Quintiere, J. G., Rinkinen, W. J., and Jones, W. W., 1981, "The Effect of Room Openings on Fire Plume Experiment," *Combustion Science and Technology*, Vol. 26, pp. 193.

Raithby, G. D., and Hollands, K. G. T., 1978, "Heat Transfer by Natural Convection Between a Vertical Surface and a Stably Stratified Fluid," ASME JOURNAL OF HEAT TRANSFER, Vol. 100, pp. 378–381.

Venkatachala, B. J., and Nath, G., 1981, "Nonsimilar Laminar Natural Convection in a Thermally Stratified Fluid," *International Journal of Heat and Mass Transfer*, Vol. 24, p. 1848.

Warner, C. Y., and Arpaci, V. S., 1968, "An Experimental Investigation of Turbulent Natural Convection in Air Along a Vertical Heated Flat Plate," *International Journal of Heat and Mass Transfer*, Vol. 11, pp. 397–403.

Yang, K. T., Novotny, J. L., and Cheng, Y. S., 1972, "Laminar Free Convection From a Nonisothermal Plate Immersed in a Temperature Stratified Medium," *International Journal of Heat and Mass Transfer*, Vol. 15, pp. 1097–1109.

Numerical Investigation of Near-Wall Turbulent Heat Transfer Taking Into Account the Unsteady Heat Conduction in the Solid Wall

N. Kasagi
Associate Professor.
Mem. ASME

A. Kuroda
Graduate Student.

M. Hirata
Professor.

Department of Mechanical Engineering,
The University of Tokyo,
Tokyo 113, Japan

The deterministic near-wall turbulence model developed by Kasagi et al. (1984b) is used in a numerical analysis of turbulent heat transfer, in which the unsteady heat conduction inside the wall associated with the turbulent flow unsteadiness is taken into account. Unlike the typical methodology based on Reynolds decomposition, the algebraic expressions for the three fluctuating velocities given by the model are directly introduced into the governing energy equation. From the numerical results of the unsteady conjugate heat transfer, the statistical quantities, such as temperature variance, turbulent heat flux, and turbulent Prandtl number, are obtained for fluids of various Prandtl numbers. It is demonstrated that the near-wall behavior of these quantities is strongly influenced by the thermal properties and thickness of the wall. In addition, the budget of the temperature variance associated with coherent turbulence structure is calculated and, except for dissipation, each budget term is in qualitative agreement with the experiment.

Introduction

Analyses and predictions of turbulent transport phenomena are in most cases based upon the phenomenological turbulence models for the Reynolds stress and the turbulent heat flux in the Reynolds-averaged momentum and energy equations (see, e.g., Launder, 1978, and Hirata et al., 1982). It is well known that the success of such analyses hinges on the validity of the near-wall turbulence model and the wall boundary conditions (see Patel et al., 1985). In the calculation of a flow field, the nonslip boundary condition is imposed to represent the existence of a solid wall. However, it is not straightforward to give a unique thermal boundary condition on the wall surface, which is in contact with a turbulent flow, because of the wall-side unsteady heat conduction associated with the intrinsic unsteadiness of turbulence, as pointed out by Iritani et al. (1980), Kasagi et al. (1984a), and Khabakhpasheva (1986).

There are circumstances in which the temperature fluctuation on the wall surface should be evaluated to avoid thermal fatigue failure of solid structures. This problem, however, cannot be handled by the aforementioned turbulence models, which are all based on Reynolds averaging, and thus, new turbulence models must be developed. The development of such turbulence models would improve the accuracy of the evaluation of the mechanical integrity of heat transfer components, particularly in extremely high-heat-flux devices such as atomic power plants and advanced micro-electronic equipment.

Coherent structures in wall-bounded turbulent shear flows have been studied experimentally in detail (Cantwell, 1981), and the streamwise vortical motions are suggested as a primary turbulence mechanism for the production of Reynolds stress and turbulence energy in the near-wall region (see, e.g., Blackwelder and Eckelmann, 1979, and Kasagi et al., 1984b). These structures of near-wall turbulence have also been the subject of theoretical and numerical works, such as Einstein and Li (1956), Thomas (1978), Hatziavramidis and Hanratty (1979), Kasagi et al. (1984b, 1986a), and Chapman and Kuhn (1986), among which only a one-dimensional surface renewal model has been used in the coupled problem of turbulent heat transfer and unsteady wall-side heat conduction (e.g., Sinai, 1987). This conjugate heat transfer has been extensively studied by Russian researchers, e.g., Polyakov (1974), Geshev (1978), and Khabakhpasheva (1986). They demonstrated both analytically and experimentally that the temperature fluctuation in the close proximity of a wall differs for different fluid–solid combinations.

Recently, Kasagi et al. (1984b) developed a structural turbulence model for the region close to the wall. This unsteady two-dimensional model, termed the streamwise pseudo-vortical motion (SPVM) model, predicts the near-wall statistical quantities and the dynamic behavior of turbulence in good agreement with the experimental observations. Kasagi et al. (1986b) used the simplified steady SPVM model in their preliminary numerical investigation of turbulent heat transfer near the wall; the results are quite promising.

In the present work, the original unsteady model of Kasagi et al. (1984b) is used in order to begin to understand the near-wall behavior of the statistical quantities of temperature fluctuations for various Prandtl-number fluids. The effect of the wall-side unsteady heat conduction associated with the flow unsteadiness is also studied.

Unsteady Streamwise Pseudo-Vortical Motion (SPVM) Model

Kasagi et al. (1984b) observed unsteady longitudinal vortical motions near the wall in a fully developed two-dimensional turbulent channel flow with the hydrogen bubble flow visualization technique. The centers of these motions are located mostly in the region of $y^+ = 20 \sim 50$, and the diameter is typically about $40\ \nu/u_\tau$. Assuming that the vortical motions primarily contribute to the momentum transport in the near-wall region, they proposed the SPVM model, which assumes secondary flow patterns periodic in time as well as in the spanwise direction, as shown in Fig. 1. Although the vortical

Contributed by the Heat Transfer Division and presented at the 2nd ASME/JSME Joint Thermal Engineering Conference, Honolulu, Hawaii, March 22–27, 1987. Manuscript received by the Heat Transfer Division February 16, 1988.
Keywords: Conjugate Heat Transfer, Forced Convection, Turbulence.

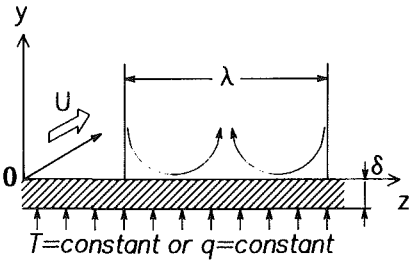

Fig. 1 Streamwise pseudo-vortical motion model

motions appeared as either solitary or a pair of counter-rotating vortices in the experiment, the regular spanwise periodicity was assumed because of equal probabilities of positive and negative signs in vorticity. Since the turbulence structures, e.g., streaky structures, near the wall have a streamwise length scale, which is an order of magnitude larger than those in the y and z directions, homogeneity in the x direction is assumed. Thus, the three fluctuating velocity components are given as follows:

$$u'^{+} = C_1(y^+ + c_1 y^{+2})\sin(2\pi z^+/\lambda^+)\sin(2\pi t^+/T^+) \quad (1)$$

$$v'^{+} = C_2(y^{+2} + c_2 y^{+3})\sin(2\pi z^+/\lambda^+)\sin(2\pi t^+/T^+ + \phi) \quad (2)$$

$$w'^{+} = C_3(y^+ + c_3 y^{+2})\cos(2\pi z^+/\lambda^+)\sin(2\pi t^+/T^+ + \phi) \quad (3)$$

where $C_1 = -0.72$, $C_2 = 0.0082$, $C_3 = 0.26$, $c_1 = -0.033$, $c_2 = -0.017$, $c_3 = -0.025$, $\cos(\phi) = 0.4$. The values of constants have been determined so as to reproduce some important features of the near-wall turbulent field, such as the wall-limiting value of the ratio $\tilde{w}'/\tilde{u}'$, the relative correlation coefficient between u' and v', and the near-wall maximum values of turbulence intensities, under the continuity condition. This model is found to predict well the near-wall turbulence statistics (i.e., mean velocity profiles, three rms velocity fluctuations, and Reynolds stresses), which are experimentally observed in various flow geometries such as pipe, channel, and boundary layer flows.

The spanwise wavelength is taken to be the experimentally measured mean streak spacing (see the reviews by Cantwell, 1981, and Hirata et al., 1982), $\lambda^+ = 100$. The time scale of the coherent fluid motion T^+ is considered to be on the order of the bursting period, but the values measured experimentally show a considerable scatter, and even the proper scaling remains an open question, as discussed by Hirata et al. (1982). Hence, the effect of the model's time scale is examined preliminarily by varying the value of T^+ in the present work. The representation of the flow field by equations (1) ~ (3) satisfies the continuity equation, but not the instantaneous momentum equations. However, as mentioned above, it reproduces the turbulence statistics well at least in the region of $y^+ \lesssim 20$.

Numerical Computation of the Unsteady Thermal Field

The thermal field under consideration is assumed to be fully developed. The structure of the near-wall thermal field is also elongated in the streamwise direction; for example, the length scale is more than 1000 viscous wall units, as pointed by Iritani et al. (1985). Thus, the dimensionless energy equations for the region near the solid-fluid interface reduce to the following expressions:

$$\frac{\partial\theta}{\partial t^+} + v'^{+}\frac{\partial\theta}{\partial y^+} + w'^{+}\frac{\partial\theta}{\partial z^+} = \frac{1}{\mathrm{Pr}}\left(\frac{\partial^2}{\partial y^{+2}} + \frac{\partial^2}{\partial z^{+2}}\right)\theta,$$

in the fluid (4)

$$\frac{\partial\theta}{\partial t^+} = \frac{1}{\mathrm{Pr}}\left(\frac{\partial^2}{\partial y^{++2}} + \frac{\partial^2}{\partial z^{++2}}\right)\theta,$$

in the solid (5)

The convection and diffusion terms in the x direction are neglected; this is equivalent to the assumption of a constant flux layer. The velocity components v'^{+} and w'^{+} are given by equations (2) and (3). At the solid-fluid interface, the boundary conditions for temperature and heat flux are imposed as follows:

$$\theta\Big|_{y^+ \to +0} = \theta\Big|_{y^{++} \to -0} \quad (6a)$$

$$K\frac{\partial\theta}{\partial y^+}\Big|_{y^+ \to +0} = \frac{\partial\theta}{\partial y^{++}}\Big|_{y^{++} \to -0} \quad (6a)$$

where K denotes the thermal activity ratio of fluid and solid (Luikov, 1968). The Prandtl number of the fluid is varied from 0.02 to 70. The two major parameters for the conjugate heat transfer system, K and δ^{++}, are varied from 0.01 to 100 and from 0 to 50, respectively. The statistical mean is defined as the integral mean over the wavelength λ^+ and the period T^+ as follows:

$$\bar{a}(y^+) = \frac{1}{T^+\lambda^+}\int_0^{T^+}\int_0^{\lambda^+} a(y^+, z^+, t^+)\, dz^+ dt^+ \quad (7)$$

The thermal wall boundary condition is given as either iso-

Nomenclature

c_p = specific heat at constant temperature
K = thermal activity ratio $= \sqrt{\rho_f c_{pf}\lambda_f/\rho_w c_{pw}\lambda_w}$
Pr = Prandtl number
Pr_t = turbulent Prandtl number $= \epsilon_m/\epsilon_h$
q = heat flux
R = ratio of the wall-surface temperature fluctuation to that on the isoflux wall
$R_{v\theta}$ = correlation coefficient between v' and θ' $= \overline{v'\theta'}/(\tilde{v}'\tilde{\theta}')$
T = time scale
t = time
u, v, w = velocity components in the x, y, and z directions
u_τ = friction velocity $= \sqrt{\tau_w/\rho}$
x = streamwise distance
y = distance from the wall
z = spanwise distance
δ = wall thickness
ϵ_h = thermal eddy diffusivity $= -\overline{v'\theta'}/(\partial\theta/\partial y)$
ϵ_m = eddy diffusivity $= -\overline{u'v'}/(\partial\bar{u}/\partial y)$
θ = temperature
θ_τ = friction temperature $= \bar{q}_w/(\rho c_p u_\tau)$
κ = thermal diffusivity
λ = thermal conductivity, or mean low-speed streak spacing
ν = kinematic viscosity
ρ = density
τ = shear stress
ϕ = phase angle in the SPVM model; $\cos\phi = 0.4$
ψ = phase angle $= 2\pi t^+/T^+ + \phi$

Subscripts

$(\ )_w$ = wall
$(\ )_f$ = fluid

Superscripts

$(\ )'$ = fluctuating quantity
$(\ )^+$ = normalized by the wall-layer parameters u_τ, θ_τ, and ν
$(\ )^{++}$ = dimensionless length $= (\ )^+\sqrt{\kappa_f/\kappa_w}$
$(\tilde{\ })$ = root-mean-square value
$(\bar{\ })$ = statistical average

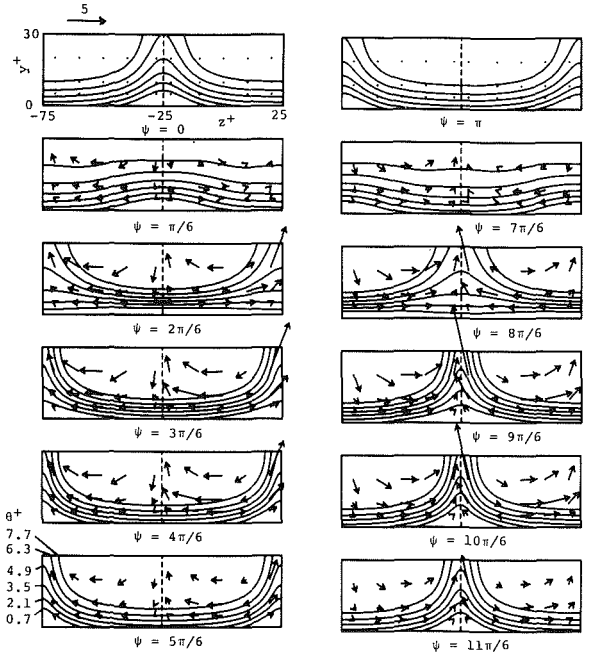

Fig. 2 Phase change of isothermal contours of the unsteady thermal field; Pr = 0.7, T^+ = 200, isoflux wall, δ^{++} = 0; velocity vectors and turbulent heat flux vectors are indicated in the left- and right-hand halves of each diagram, respectively

thermal or constant heat flux (isoflux) on the backside surface of the solid wall (i.e., at $y = -\delta$) as shown in Fig. 1. The particular case of $\delta = 0$ corresponds to either ideally isothermal or isoflux wall with infinitesimally small wall thickness. At a position far away from the wall, an isothermal boundary condition is always assumed because the turbulence mixing is considered to be vigorous in that region. The position at which this outer boundary condition is imposed is varied as y^+ = 39, 49, and 59. As a result, it is confirmed that the difference between the numerical results for Pr $\geq$ 0.7 with the outer boundary located at y^+ = 39 and 49 is negligible in the region of $y^+ \leq 20$. For Pr $\leq$ 0.07, the mean temperature distributions do not depend upon the outer boundary position, but the rms temperature fluctuations at $y^+ \leq 20$ increase by about 12 and 3 percent for Pr = 0.02 and 0.07, respectively, when the boundary position is moved from y^+ = 49 to y^+ = 59. The present results are obtained with the boundary positions at y^+ = 39 for Pr $\geq$ 0.7 and y^+ = 59 for Pr $\leq$ 0.07.

For the numerical integration, the central difference scheme is used with a uniform grid in the y direction, while the Fourier spectral method of Gottlieb and Orszag (1977) is used in the z direction. The Adams-Bashforth and Adams-Bashforth Crank-Nicolson schemes (Peyret and Taylor, 1983) are adopted for the time integration; the results obtained by these methods are in close agreement with each other. In order to maintain numerical accuracy as the Prandtl number is increased, it is necessary to decrease both the grid space and time increment and increase the number of polynomials in the Fourier expansion series. For instance, a grid space of $\delta y^+ = 0.5$ and 10 polynomials are used with a time increment of $\delta t^+ \simeq 0.14$ for Pr = 0.7, while $\delta y^+ = 0.25$, 34 polynomials and $\delta t^+ = 0.035$ for Pr = 7.

In order to assess the numerical accuracy, numerical errors have been evaluated by systematically changing the computational conditions; for example, the change in the numerical results of statistical quantities described in this paper is confirmed to be negligible for each Pr, even when the grid space in the y direction is doubled. The numerical computation is started with a linear temperature distribution with y^+ and is continued until a solution periodic in time is obtained.

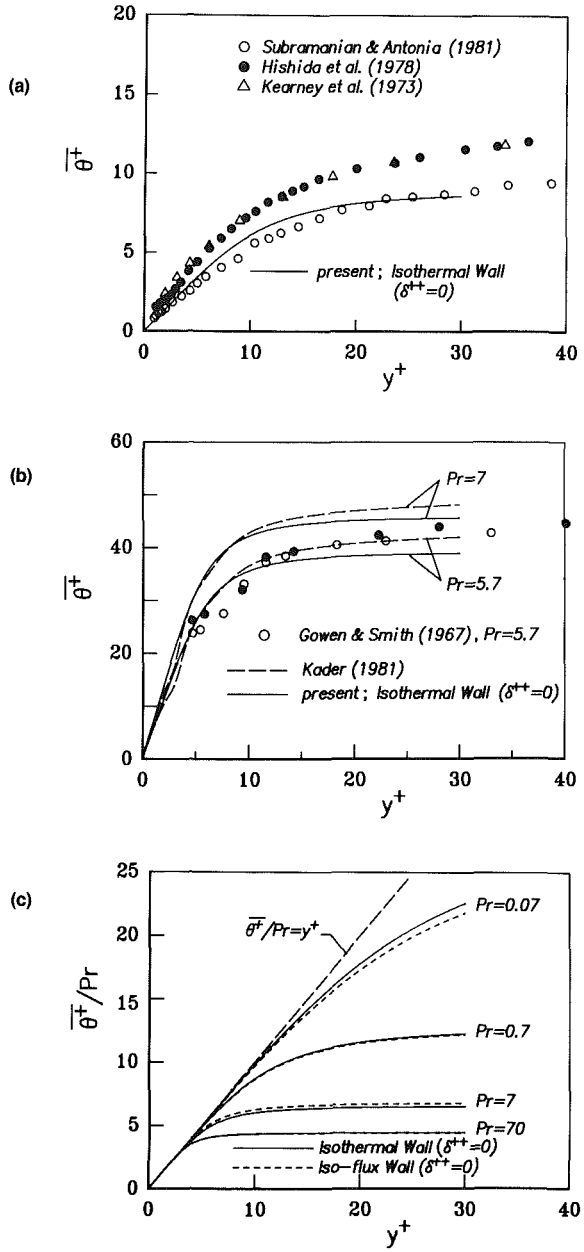

Fig. 3 Mean temperature distributions near the wall with δ^{++} = 0: (*a*) Pr = 0.7, (*b*) Pr = 5.7, 7, (*c*) Pr = 0.07 ~ 70

Results and Discussion

In the preliminary computations with $\delta = 0$, the model's time scale T^+ is varied because its value has not been well established experimentally (Hirata et al., 1982). With T^+ = 100 ~ 300, which is a typical experimental data range, it is found that the value of T^+ has an appreciable effect on the numerical results. The calculated turbulent heat flux tends to decrease slightly with decreasing T^+; as a result, the mean temperature $\bar{\theta}^+$ increases for both isothermal and isoflux walls. Presently, the time scale of T^+ = 200 was selected after reviewing the mean temperature profile for Pr = 7 given by the empirical formula of Kader (1981). It is noted that the numerical results for ideally isothermal and isoflux walls (δ = 0) will be mainly shown hereafter unless otherwise described, since the results for the solid-fluid conjugate system generally fall between those of the two ideal cases.

A typical example of a predicted two-dimensional thermal field for Pr = 0.7 is shown in Fig. 2; an isoflux condition is

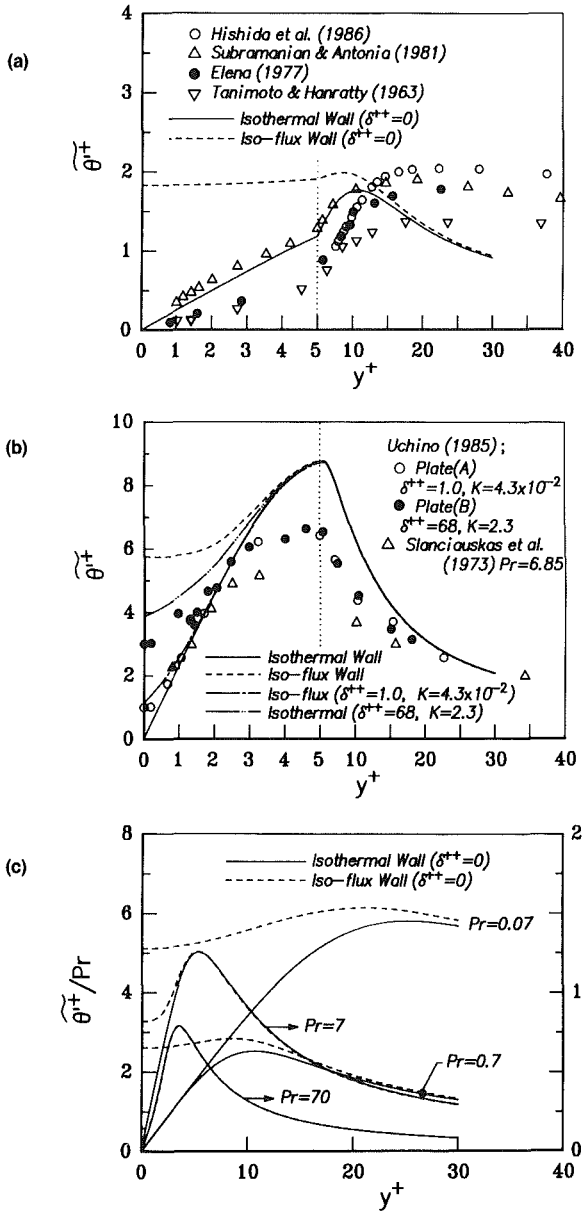

Fig. 4 Near-wall distributions of rms temperature fluctuations: (*a*) Pr = 0.7, (*b*) Pr = 7, (*c*) Pr = 0.07 ~ 70

applied at the wall. Velocity vectors and turbulent heat flux vectors are represented in the left- and right-hand halves of each diagram, respectively. An appreciable phase lag between the unsteady development of thermal sublayer and the velocity fluctuations is observed: e.g., at the phases of $\psi = 0$ and π, all the velocity vectors are equal to zero but the isotherms are not parallel to the wall. It is also seen that the turbulent heat transfer primarily occurs in the regions where the upward and wall-ward fluid motions take place and that the turbulent heat flux of large magnitude appears intermittently in space and time. In the case of the isothermal wall, results similar to those in Fig. 2 are obtained, except that the isotherms near the wall always remain parallel to the wall.

In Figs. 3(*a*) and 3(*b*), the mean temperature profiles for the isothermal wall case are shown along with the available experimental data and the empirical formula by Kader (1981). Although there are noticeable differences between the predictions and the experimental data, the present results lie well within the experimental uncertainty. Figure 3(*c*) shows a comparison between the temperature profiles under the isothermal and isoflux wall conditions. The difference is generally small,

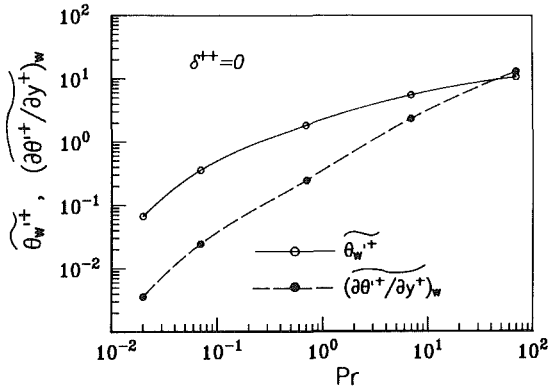

Fig. 5 The rms fluctuations of temperature on the isoflux wall and of temperature gradient on the isothermal wall

even when the wall-side heat conduction is taken into account; this behavior is generally accepted as characteristic of turbulent heat transfer. For Pr = 70, the calculated result in the logarithmic region is about 35 percent higher than that predicted by Kader's formula. This might be due to the fact that the present model takes into account only the large-scale coherent turbulent motions and ignores the residual random components in smaller scales. In addition, presently the turbulent heat transfer processes for various Prandtl-number fluids are represented by the fluid motion of a fixed wave number component. The latter effect cannot be neglected particularly for high-Prandtl-number fluids.

The root-mean-square temperature fluctuations for Pr = 0.7 and 7 are shown in Figs. 4(*a*) and 4(*b*), respectively, and their dependence upon the Prandtl number in Fig. 4(*c*). In the experiments referred to in Fig. 4(*a*), it is estimated that the wall temperature was held essentially constant (i.e., isothermal wall boundary condition). For example, Subramanian and Antonia (1981) used an electrically heated stainless-steel foil as a wall surface in a turbulent boundary layer of air. However, the prediction with $K \simeq 10^{-4}$ and $\delta^{++} \simeq 5$, which have been evaluated from their experimental conditions, suggests that the temperature fluctuation on the wall surface should be negligibly small, as discussed later. For Pr = 0.7, however, the present result gives smaller values than the experimental ones at $y^{+} \gtrsim 15$, because of the isothermal boundary condition imposed at the outer boundary.

In Fig. 4(*b*), the measurements by Uchino (1985) were made in a two-dimensional water channel flow with two different wall materials; a 6.8-mm-thick copper plate heated from the backside (Plate A) and a 30-μm-thick stainless-steel foil attached to a 15-mm-thick bakelite board and heated directly by an electric current (Plate B). Figure 4(*b*) also includes the predictions for these two conjugate cases. Since the measurements in the vicinity of the wall are associated with considerably large uncertainty, it can be said that overall agreement between the calculated and experimental results is reasonably good. As shown in Figs. 4(*a*) and 4(*b*), the difference between the numerical results under the ideally isothermal and isoflux wall conditions is seen in the region of $y^{+} \lesssim 20$ for Pr = 0.7 and $y^{+} \lesssim 4$ for Pr = 7, respectively. This effect of the wall thermal condition becomes limited to a shorter distance from the wall as Pr is increased, as shown in Fig. 4(*c*).

Figure 5 shows the temperature fluctuation and the fluctuating temperature gradient on the ideally isoflux and isothermal wall surfaces, respectively. Both of these increase monotonically with increasing Pr. When the fluctuating temperature gradient is divided by Pr, it becomes the ratio of the rms fluctuation to the mean of heat transfer coefficient. For high Schmidt numbers, Shaw and Hanratty (1977) have ob-

Table 1 Thermal activity ratio for various fluid/solid combinations (20°C, 1 atm); data from Holman (1976)

Fluid	Mercury	Air	Water	Glycerin
Pr	0.0249	0.708	6.78	12.5
	$\times 10^{-1}$	$\times 10^{-4}$	$\times 10^{-2}$	$\times 10^{-2}$
Aluminum	1.82	2.51	7.13	4.18
Lead	5.64	7.75	22.1	12.9
18-8 Cr-Ni	5.30	7.28	20.7	12.1
Copper	1.12	1.53	4.36	2.55
Glass	30.5	41.9	119.	69.8
Plexiglas	68.6	94.2	268.	157.

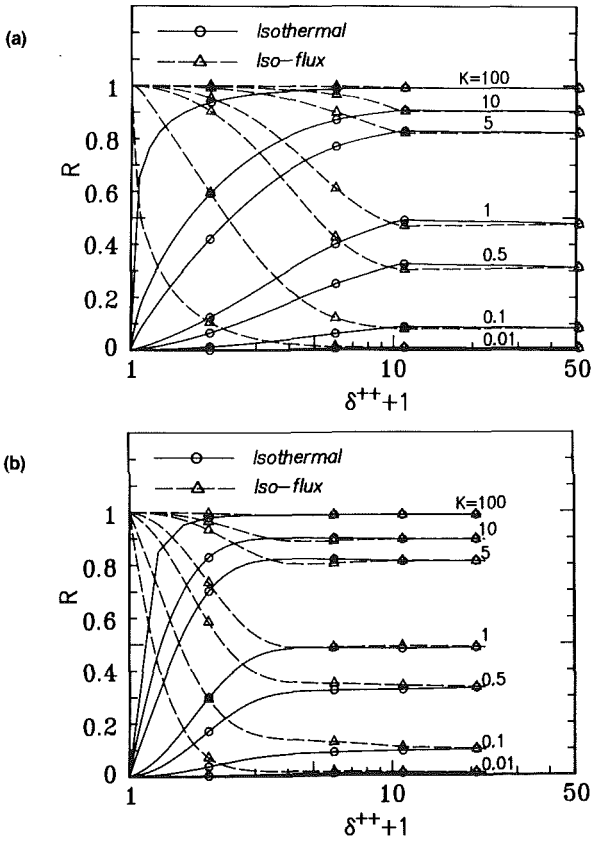

Fig. 6 Ratio of the rms wall temperature fluctuation to that on the isoflux wall of $\delta^{++} = 0$: (*a*) Pr = 0.7, (*b*) Pr = 7

tained the values of 0.2 ~ 0.3, which are in good agreement with the present results.

The ratio of the wall-surface temperature fluctuation in the conjugate case to that of the ideally isoflux wall, R, is shown for two Prandtl numbers in Figs. 6(*a*) and 6(*b*). As δ^{++} is increased, these ratios under the isothermal and isoflux heating conditions collapse and approach an asymptotic value that depends only on the thermal activity ratio K. The value of K for combinations of air and practical structural materials, such as metals, glass, and plastics, is on the order of $10^{-4} \sim 10^{-3}$, as shown in Table 1. Hence, the wall temperature fluctuation in an air flow should be negligibly small so that the wall can be regarded as ideally isothermal, unless the wall thickness δ is extremely small. This is not the case for liquids listed in Table 1, because the value of K reaches the order of 1. This difference appears in Fig. 4(*b*), where there is an appreciable

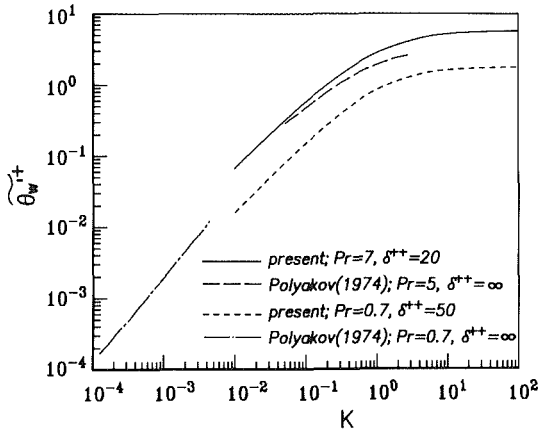

Fig. 7 The rms wall-surface temperature fluctuations on an infinitely thick wall

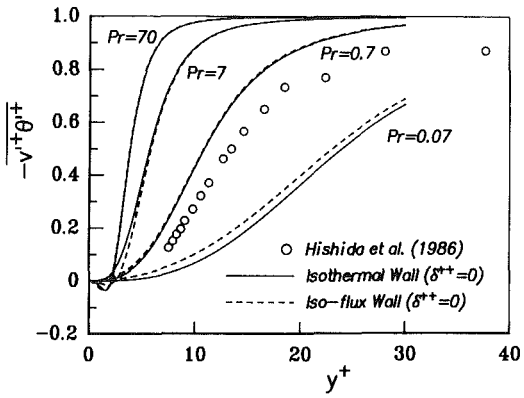

Fig. 8 Distributions of turbulent heat flux for Pr = 0.07 ~ 70

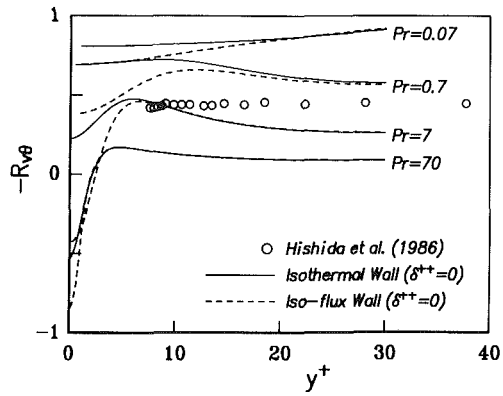

Fig. 9 Relative correlation coefficient between the velocity and temperature fluctuations for Pr = 0.07 ~ 70

difference between the wall temperature fluctuations on the two different wall materials in a turbulent water flow.

The rms wall-surface temperature fluctuations for two Prandtl numbers are represented in Fig. 7. Note that, referring to Figs. 6(*a*) and 6(*b*), both the results of $\delta^{++} = 20$ for Pr = 7 and $\delta^{++} = 50$ for Pr = 0.7 can be interpreted as those obtained when the wall is infinitely thick. Also included in Fig. 7 are the results of Polyakov (1974), who has made a mathematical analysis of the coupled heat transfer on an infinitely thick wall using a linearized energy equation in the viscous sublayer. Although these two studies have used very different analytical methods, the agreement is fairly good. It is seen that the wall temperature fluctuations increase as the thermal activity ratio is increased, but they eventually reach constant values beyond $K \simeq 10$.

In Figs. 8 and 9, the turbulent heat flux and the correlation coefficient between v' and θ' are presented. For larger Prandtl numbers, the turbulent heat flux approaches the asymptotic value of 1 at a smaller distance from the wall, and this results in a decrease in thickness of the conductive linear layer, as shown in Fig. 3(*c*). The turbulent heat flux has negative values very close to the wall ($y^+ \lesssim 3$) for Pr = 70 with the isothermal wall and for Pr = 7 and 70 with the isoflux wall. This phenomenon is caused by the large phase lag between the unsteady development of thermal sublayer and the vortical fluid motions. Thus, the negative heat flux is likely to occur for larger Prandtl number fluids with the isoflux wall rather than the isothermal wall. This problem, however, will be addressed in future investigations taking into account smaller scale turbulence. The correlation coefficient tends to decrease as Pr is increased, showing maximum values near the wall for Pr $\geq$ 0.7. For Pr = 0.7, the present results of both $-\overline{v'^+\theta'^+}$ and $-R_{v\theta}$ are larger than those measured by Hishida et al. (1986). This is because the present model is comprised of only coherent fluid motions and ignores random ones.

Figures 10(*a*) and 10(*b*) show the thermal eddy diffusivities under the two wall conditions. Negative values are obtained because of the negative turbulent heat flux mentioned above. Regardless of sign, ϵ_h/ν is found to be proportional to y^{+2} and y^{+3} as $y^+ \to 0$ for the isoflux wall and the isothermal wall, respectively. This wall limiting behavior agrees with the theoretical consideration of Kasagi et al. (1986*b*). In addition, the value of ϵ_h/ν is dependent on Pr near the wall; this effect is more enhanced in the case of the isoflux wall. In the region away from the wall where the Prandtl number's effect is rather weak, ϵ_h/ν becomes asymptotically proportional to y^{+3}, independent of the wall thermal boundary condition. This is qualitatively in agreement with Mizushina et al. (1970), although the numerical results show slightly larger values than their experimental data for Pr = 6 ~ 40.

Figures 11(*a*) and 11(*b*) summarize the turbulent Prandtl numbers calculated for various Prandtl numbers. For both wall conditions, the turbulent Prandtl number increases rapidly beyond $y^+ = 15$, because the eddy diffusivity given by the present model is no longer valid in that region. Hence, it is reasonable to assume that the turbulent Prandtl numbers should remain constant away from the wall. The asymptotic values in Figs. 11(*a*) and 11(*b*) are somewhat smaller than the value of $\mathrm{Pr}_t = 0.8 \sim 0.9$, which is often assumed for the fluids of Pr ~ 1. In the result for Pr = 0.02 under the isothermal wall condition, the values of $\mathrm{Pr}_t = 0.75 \sim 0.85$ are obtained for $0 \leq y^+ \leq 10$. This suggests that the turbulent Prandtl number increases as Pr is decreased below 0.07 in accordance with the prediction by Jischa and Rieke (1979). For larger Prandtl numbers, Pr_t becomes much larger in the vicinity of the wall and even infinite in some cases. The same tendency can also be observed in the results of the surface renewal model by Thomas (1978) and the profile analysis by Hammond (1985), although their results do not show negative values.

The budget equation of temperature variance, $\overline{\theta'^{+2}}$, is derived for a fully developed thermal field as follows:

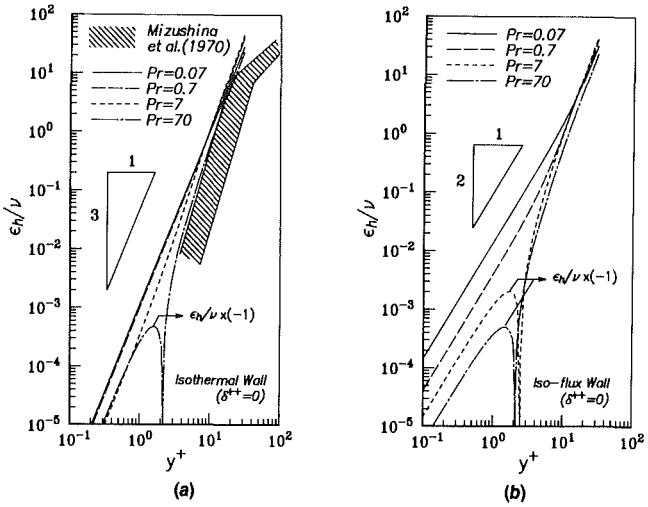

Fig. 10 Near-wall distributions of thermal eddy diffusivity: (*a*) isothermal wall, (*b*) isoflux wall

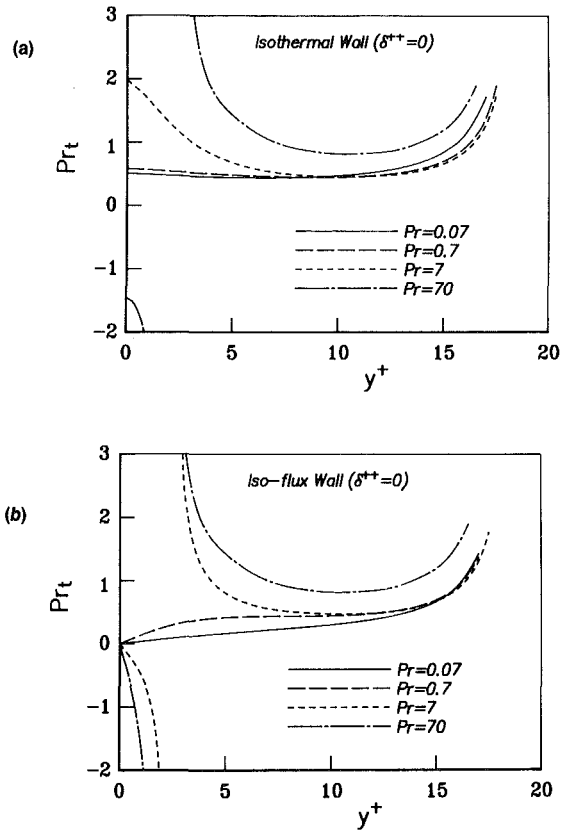

Fig. 11 Turbulent Prandtl number near the wall: (*a*) isothermal wall, (*b*) isoflux wall

$$-2\overline{v'^+\theta'^+}\frac{\partial\overline{\theta^+}}{\partial y^+} + \frac{1}{\mathrm{Pr}}\frac{\partial^2}{\partial y^{+2}}(\overline{\theta'^{+2}}) + \frac{\partial}{\partial y^+}(-\overline{v'^+\theta'^{+2}}) - \frac{2}{\mathrm{Pr}}\overline{\frac{\partial\theta'^+}{\partial x_j^+}\frac{\partial\theta'^+}{\partial x_j^+}} = 0 \qquad (8)$$

Production | Molecular diffusion | Turbulent diffusion | Dissipation

where the last term indicates the sum for $x_j = x$, y, and z. In Figs. 12(*a*) and 12(*b*), each term appearing in the above equation under the isothermal wall condition is shown for Pr = 0.7 and 0.07, respectively. The production and two diffusion terms agree qualitatively with the experimental results of Krishnamoorthy and Antonia (1987). In particular, the production predicted at $y^+ \leq 10$ is in good quantitative agreement. These results suggest that, in the near-wall region, the coherent fluid

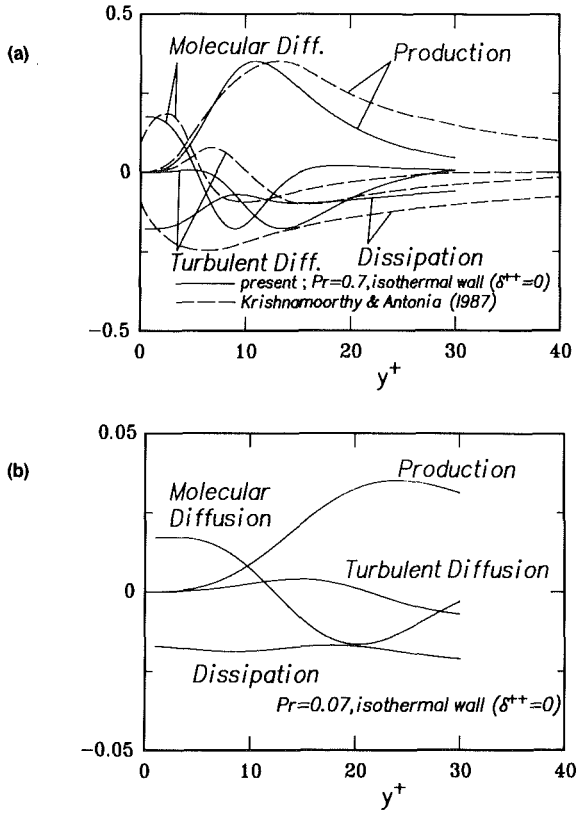

Fig. 12 Budget of the temperature variance: (*a*) Pr = 0.7, isothermal wall, (*b*) Pr = 0.07, isothermal wall

motions presently modeled play a predominant role in the production and diffusion processes of temperature fluctuations. The profile of the turbulent diffusion in Fig. 12(*a*) shows a nonzero value at $y^+ = 10$, where the rms temperature fluctuation reaches a maximum as shown in Fig. 4(*a*). This result indicates that the gradient-type modeling of this term in the transport equation of temperature variance is not adequate, as has been pointed out by Nagano and Hishida (1985). There is a large discrepancy in the dissipation term, since the present model does not include the smaller scale components that are dominant in the dissipation process for Pr $\gtrsim$ 1. For Pr = 0.7 under the isoflux wall condition, a similar result has been obtained except for the molecular diffusion and dissipation terms, which become about 1/2 ~ 1/3 of those in Fig. 12(*a*) in the region of $y^+ \lesssim 15$. In Fig. 12(*b*), it is seen that when Pr is decreased to 0.07 the turbulent diffusion becomes relatively small in the region close to the wall.

Conclusions

The turbulent heat transfer near the wall is investigated for Pr = 0.02 ~ 70 using the streamwise pseudo-vortical motion model. The unsteady heat conduction inside the wall is also taken into account. As a result, the statistical quantities of the thermal field are predicted. The results are qualitatively and quantitatively in reasonable agreement with available experimental data. Thus, it is confirmed that the coherent turbulent structures also play primary role in the scalar transport near the wall.

The following conclusions can also be derived:

1 The near-wall statistical quantities, including the mean and fluctuating temperature, the turbulent heat flux, the turbulent Prandtl number, and the budget of temperature variance, are affected appreciably by the thermal wall condition, i.e., isothermal or isoflux. When the wall-side heat conduction is taken into account, the statistical values fall between those in the two extreme cases of ideally isothermal and isoflux walls.

2 The rms wall temperature fluctuation depends upon solid-fluid combination and wall thickness. For air, however, the wall made of practical structural materials can be regarded as isothermal, unless the wall is extremely thin.

3 The turbulent heat flux increases monotonically in the near-wall region as Pr is increased. In the region closer to the wall ($y^+ \lesssim 3$), it becomes smaller and may even take a negative value. The relative correlation coefficient between v' and θ' decreases with increasing Pr.

4 The thermal eddy diffusivity is proportional to about the third power of y^+ in the region of $y^+ \gtrsim 5$, while toward the wall it shows asymptotic behavior, which depends upon Pr as well as the wall thermal condition.

5 The turbulent Prandtl number has a constant value, which depends on Pr, away from the wall, but it shows an extremely large value in the vicinity of the wall for high Prandtl numbers.

6 The budget of the temperature variance is predicted reasonably well, but the dissipation process cannot be reproduced well for Pr $\gtrsim$ 1. For lower Prandtl numbers, the turbulent diffusion becomes relatively small near the wall.

Acknowledgments

The authors are grateful to Mr. E. Takahashi for reviewing the manuscript. This work was supported through the Grant-in-Aid for General Scientific Research (No. 61460103) by the Japanese Ministry of Education, Science, and Culture.

References

Blackwelder, R. F., and Eckelmann, H., 1979, "Streamwise Vortices Associated With the Bursting Phenomenon," *Journal of Fluid Mechanics*, Vol. 94, pp. 577–594.

Cantwell, B. J., 1981, "Organized Motion in Turbulent Flow," *Annual Review of Fluid Mechanics*, M. Van Dyke et al., eds., Annual Review Inc., Palo Alto, Vol. 13, pp. 457–515.

Chapman, D. R., and Kuhn, G. D., 1986, "The Limiting Behavior of Turbulence Near a Wall," *Journal of Fluid Mechanics*, Vol. 170, pp. 265–292.

Einstein, H. A., and Li, H., 1956, "The Viscous Sublayer Along a Smooth Boundary," *Proceedings of the American Society of Civil Engineers*, Vol. 82, pp. 293–319.

Elana, M., 1977, "Etude Experimentale de la Turbulence au Voisinage de la Paroi d'un Tube Legerement Chauffe," *International Journal of Heat and Mass Transfer*, Vol. 20, pp. 935–944.

Geshev, P. I., 1978, "The Influence of Thermal Conductivity of the Wall on the Value of the Turbulent Prandtl Number in a Viscous Sublayer" (in Russian), *Journal of Engineering Physics*, Vol. 35, pp. 292–296.

Gottlieb, D., and Orszag, S. A., 1977, "Numerical Analysis of Spectral Methods: Theory and Applications," *CBMS-NSF Regional Conference Series in Applied Mathematics*, Society for Industrial and Applied Mathematics, Philadelphia, Vol. 26, pp. 1–170.

Gowen, R. A., and Smith, J. W., 1967, "The Effect of the Prandtl Number on Temperature Profiles for Heat Transfer in Turbulent Pipe Flow," *Chemical Engineering Science*, Vol. 22, pp. 1707–1711.

Hammond, G. P., 1985, "Turbulent Prandtl Number Within a Near-Wall Flow," *AIAA Journal*, Vol. 23, pp. 1668–1669.

Hatziavramidis, D. T., and Hanratty, T. J., 1979, "The Representation of the Viscous Wall Region by a Regular Eddy Pattern," *Journal of Fluid Mechanics*, Vol. 95, pp. 655–679.

Hirata, M., Tanaka, H., Kawamura, H., and Kasagi, N., 1982, "Heat Transfer in Turbulent Flows," *Proceedings of the 7th International Heat Transfer Conference*, U. Grigull et al., eds., Hemisphere Publishing Corp., Washington, DC, Vol. 1, pp. 31–57.

Hishida, M., Nagano, Y., and Shiraki, T., 1978, "Structure of Turbulent Velocity and Temperature Fluctuations in Fully Developed Pipe Flow" (in Japanese), *Transactions of JSME*, Vol. 44B, pp. 126–134.

Hishida, M., Nagano, Y., and Tagawa, M., 1986, "Transport Processes of Heat and Momentum in the Wall Region of Turbulent Pipe Flow," *Proceedings of the 8th International Heat Transfer Conference*, C. L. Tien et al., eds., Hemisphere Publishing Corp., Washington, DC, Vol. 3, pp. 925–930.

Holman, J. P., 1976, *Heat Transfer*, 4th ed., McGraw-Hill, New York.

Iritani, Y., Kasagi, N., and Hirata, M., 1980, "Turbulent Heat Transfer Taking Into Account the Thermal Capacity of the Wall: A Comparison Between Isothermal and Constant Heat-Flux Walls" (in Japanese), *Reprint of JSME*, No. 800-18, pp. 249–251.

Iritani, Y., Kasagi, N., and Hirata, M., 1985, "Heat Transfer Mechanism and Associated Turbulence Structure in the Near-Wall Region of a Turbulent

Boundary Layer," *Turbulent Shear Flows IV*, L. Bradbury et al., eds., Springer-Verlag, Berlin, pp. 223–234.

Jischa, M., and Rieke, H. B., 1979, "About the Prediction of Turbulent Prandtl and Schmidt Numbers From Modeled Transport Equations," *International Journal of Heat and Mass Transfer*, Vol. 22, pp. 1547–1555.

Kader, B. A., 1981, "Temperature and Concentration Profiles in Fully Turbulent Boundary Layers," *International Journal of Heat and Mass Transfer*, Vol. 24, pp. 1541–1544.

Kasagi, N., Suzuki, M., and Hirata, M., 1984a, "Turbulent Convective Heat Transfer Taking Into Account the Wall-Side Unsteady Heat Conduction Associated With the Bursting" (in Japanese), *Proceedings of the 21st National Heat Transfer Symposium of Japan*, Heat Transfer Society of Japan, Tokyo, pp. 10–12.

Kasagi, N., Hirata, M., and Nishino, K., 1984b, "Streamwise Pseudo-Vortical Structures and Associated Vorticity in the Near-Wall Region of a Wall-Bounded Shear Flow," *Proceedings of the 9th Symposium on Turbulence*, X. B. Reed, Jr., et al., eds., University of Missouri—Rolla, pp. 24.1–24.10; also in *Experiments in Fluids*, 1986, Vol. 4, pp. 309–318.

Kasagi, N., Nishino, K., and Hirata, M., 1986a, "Toward Structural Modeling of the Wall-Bounded Turbulent Shear Flow," *Proceedings of the 3rd Asian Congress of Fluid Mechanics*, Tokyo, pp. 549–552.

Kasagi, N., Harumi, K., and Hirata, M., 1986b, "An Analysis of the Turbulent Transport Mechanism Near the Wall by Streamwise Pseudo-Vortical Motion Model," *Proceedings of the 8th International Heat Transfer Conference*, C. L. Tien et al., eds., Hemisphere Publishing Corp., Washington, DC, Vol. 3, pp. 1103–1108.

Kearney, D. W., Kays, W. M., and Moffat, R. J., 1973, "Heat Transfer to a Strongly Accelerated Turbulent Boundary Layer; Some Experimental Results, Including Transpiration," *International Journal of Heat and Mass Transfer*, Vol. 16, pp. 1289–1305.

Khabakhpasheva, Y. M., 1986, "Experimental Investigation of Turbulent Momentum and Heat Transfer in the Proximity of the Wall," *Proceedings of the 8th International Heat Transfer Conference*, C. L. Tien et al., eds., Hemisphere Publishing Corp., Washington, DC, Vol. 1, pp. 79–90.

Krishnamoorthy, L. V., and Antonia, R. A., 1987, "Temperature-Dissipation Measurements in a Turbulent Boundary Layer," *Journal of Fluid Mechanics*, Vol. 176, pp. 265–281.

Launder, B. E., 1978, "Heat and Mass Transport," *Topics in Applied Physics*, P. Bradshaw, ed., Springer-Verlag, Berlin, pp. 232–287.

Luikov, A. V., 1968, *Analytical Heat Diffusion Theory*, J. P. Hartnett, ed., Academic Press, New York.

Mizushina, T., Ito, R., and Ogino, F., 1970, "Eddy Diffusivity Distribution Near the Wall," *Preprints of the 4th International Heat Transfer Conference*, U. Grigull et al., eds., VDI, Düsseldorf, Vol. 2, FC 2.8.

Nagano, Y., and Hishida, M., 1985, "Production and Dissipation of Turbulent Velocity and Temperature Fluctuations in Fully Developed Pipe Flow," *Proceedings of the 5th Symposium on Turbulent Shear Flows*, Cornell University, Ithaca, NY, pp. 14.19–14.24.

Patel, V. C., Rodi, W., and Scheuerer, G., 1985, "Turbulence Models for Near-Wall and Low Reynolds Number Flows: A Review," *AIAA Journal*, Vol. 23, pp. 1308–1319.

Peyret, R., and Taylor, T. D., 1983, *Computational Methods for Full Flow*, Springer-Verlag, Berlin.

Polyakov, A. F., 1974, "Wall Effect of Temperature Fluctuations in the Viscous Sublayer," *Teplofizika Vysokikh Temperatur*, Vol. 12, pp. 328–337.

Shaw, D. A., and Hanratty, T. J., 1977, "Turbulent Mass Transfer Rates to a Wall for Large Schmidt Numbers," *AIChE Journal*, Vol. 23, pp. 28–37.

Sinai, Y. L., 1987, "A Wall Function for the Temperature Variance in Turbulent Flow Adjacent to a Diabatic Wall," ASME JOURNAL OF HEAT TRANSFER, Vol. 109, pp. 861–865.

Slanciauskas, A., Drizius, M. R., and Zukauskas, A., 1973, "Temperature Fluctuations in the Wall Region During Turbulent Flow of a Viscous Liquid Along a Plate," *Heat Transfer—Soviet Research*, Vol. 5, pp. 74–83.

Subramanian, C. S., and Antonia, R. A., 1981, "Effect of Reynolds Number on a Slightly Heated Turbulent Boundary Layer," *International Journal of Heat and Mass Transfer*, Vol. 24, pp. 1833–1846.

Tanimoto, S., and Hanratty, T. J., 1963, "Fluid Temperature Fluctuation Accompanying Turbulent Heat Transfer in a Pipe," *Chemical Engineering Science*, Vol. 18, pp. 307–311.

Thomas, L. C., 1978, "A Formulation for ϵ_M and ϵ_H Based on the Surface Renewal Principle," *AIChE Journal*, Vol. 24, pp. 101–106.

Uchino, K., 1985, "Effect of Wall Thermal Boundary Condition on the Turbulent Heat Transport in the Near-Wall Region" (in Japanese), MS Thesis, Department of Mechanical Engineering, University of Tokyo, Tokyo, Japan.

General Analysis of Steady Laminar Mixed Convection Heat Transfer on Vertical Slender Cylinders

T.-Y. Wang

C. Kleinstreuer
Mem. ASME

Department of Mechanical and Aerospace Engineering,
North Carolina State University,
Raleigh, NC 27695-7910

A general analysis has been developed to study fluid flow and heat transfer characteristics for steady laminar mixed convection on vertical slender cylinders covering the entire range from pure forced to pure natural convection. Two uniquely transformed sets of axisymmetric boundary-layer equations for the constant wall heat flux case and the isothermal surface case are solved using a two-point finite difference method with Newton linearization. Of interest are the effects of the new mixed convection parameter, the cylinder heating/cooling mode, the transverse curvature parameter, and the Prandtl number on the velocity/temperature profiles and on the local skin friction parameter and the heat transfer parameter. The results of the validated computer simulation model are as follows. Depending upon the magnitude and direction of the buoyancy force, i.e., the value of the mixed convection parameter and the heating or cooling mode applied, natural convection can have a significant effect on the thermal flow field around vertical cylinders. Specifically, strong variations of the local skin friction parameter and reversing trends in the heat transfer parameter are produced as the buoyancy force becomes stronger in aiding flow. The skin friction parameter increases with higher curvature parameters and Prandtl numbers. Similarly, the modified Nusselt number is larger for higher transverse curvature parameters; however, this parameter may reverse the impact of the Prandtl number on the Nusselt number for predominantly forced convection.

1 Introduction

Numerous industrial applications involve both forced and natural convection along vertical slender cylinders where transverse curvature effects, the heating/cooling mode, and the type of thermal boundary condition are important. With the exception of the papers by Lee et al. (1986, 1987) and by Lin and Chen (1988), previous studies considered pure forced convection, pure free convection, or mixed convection for only a limited range of Richardson numbers. Lee et al. (1986, 1987) analyzed mixed convection along vertical slender cylinders with transformation parameters covering the entire range of thermal convection. However, a number of shortcomings are indicated in their papers. Extra measures were needed to avoid numerical instability. Their code is limited to Prandtl number fluids of $Pr \leq 100$. Fluid mechanics properties and variable mesh designs are not discussed and model-accuracy checks are too few. Lin and Chen (1988) proposed a new mixed convection parameter for steady laminar flow past a vertical isothermal plate, also allowing a simulation of the entire range of convection heat transfer. In extending their analysis, we concentrate on axisymmetric boundary-layer flow past a vertical slender cylinder with constant wall heat flux or isothermal surface where the surface temperature is either greater or less than the free-stream temperature. The two sets of uniquely transformed differential equations are solved using an implicit finite difference technique. The computer simulation model is validated with accepted special-case data published by Wilks (1973) for forced convection on a flat plate with constant wall heat flux, Cebeci (1974) for natural convection on a vertical slender cylinder using a finite difference solution method, and Aziz and Na (1982) for free convection on a vertical cylinder using a perturbation solution. Recent papers in which mixed thermal convection on a vertical slender cylinder is treated include studies by Bui and Cebeci (1985) for Newtonian fluids and by Wang and Kleinstreuer (1988) for power-law fluids. Both investigations are, however, limited to a restrictive range of Richardson numbers as mentioned above.

The general analysis developed and discussed in this paper contains the contributions by Lin and Chen (1988), Kleinstreuer and Wang (1988), and Wang and Kleinstreuer (1988) as distinct special cases. This model is more powerful, more flexible, and yet simpler than the analyses proposed by Lee et al. (1986, 1987).

2 Analysis

Consider steady laminar axisymmetric boundary-layer flow of a Newtonian fluid with constant properties except for temperature-dependent density variations, which may influence the buoyancy force. When the wall temperature is higher than the ambient temperature, i.e., $T_w > T_\infty$ or $Z = 1$, the buoyancy force will aid the upwardly directed uniform stream, and when $T_w < T_\infty$, or $Z = -1$, the resulting buoyancy force will retard the forced flow. Neglecting near-wake effects, the governing equations with the Boussinesq assumption read (Fig. 1)

$$\frac{\partial}{\partial x}(ru) + \frac{\partial}{\partial r}(rv) = 0 \tag{1}$$

$$u\frac{\partial u}{\partial x} + v\frac{\partial u}{\partial r} = Zg\beta\,|T - T_\infty| + \frac{\nu}{r}\frac{\partial}{\partial r}\left(r\frac{\partial u}{\partial r}\right) \tag{2}$$

and

$$u\frac{\partial T}{\partial x} + v\frac{\partial T}{\partial r} = \frac{\alpha}{r}\frac{\partial}{\partial r}\left(r\frac{\partial T}{\partial r}\right) \tag{3}$$

The boundary conditions are:

Contributed by the Heat Transfer Division and presented at the 25th National Heat Transfer Conference, Houston, Texas, July 24–27, 1988. Manuscript received by the Heat Transfer Division March 11, 1988. Keywords: Mixed Convection, Modeling and Scaling.

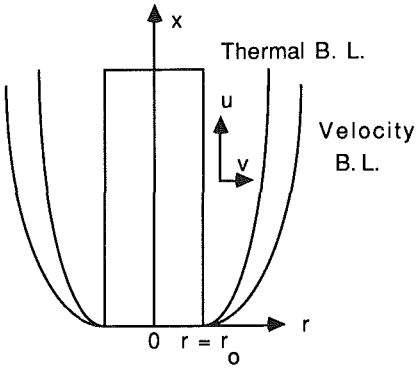

Fig. 1 System schematics with coordinates

(*i*) for the constant wall heat flux case at $r = r_o$,

$$u = v = 0 \text{ and } q_w = -k(\partial T/\partial r);$$

(*ii*) for the constant wall temperature case at $r = r_o$,

$$u = v = 0 \text{ and } T = T_w. \tag{4a-c}$$

For both cases, $u = u_\infty$ and $T = T_\infty$ when $r \to \infty$. With respect to the mathematical singularity at the leading edge, we assume $u = 0$ and $T = T_\infty$ for both cases, i.e., the heated cylinder ($Z = 1.0$) and the cooled cylinder ($Z = -1.0$).

Instead of solving equations (1) through (4*a-c*) directly, a new coordinate transformation is employed for each thermal boundary condition case, in order to reduce the numerical work required for the solution.

2.1 Transformed Equations for Constant Wall Heat Flux Case. Using scale analysis (cf. Bejan, 1984), it can be shown that for fluids with large Prandtl numbers, the transition from natural to forced convection can be expressed as (Kleinstreuer, 1989)

$$\frac{\left(\frac{\delta_{th}}{x}\right)^{FC}}{\left(\frac{\delta_{th}}{x}\right)^{NC}} = \frac{\mathrm{Ra}^{1/5}}{\mathrm{Pr}^{1/3}\mathrm{Re}^{1/2}} \begin{cases} > 0(1) \text{ for natural convection} \\ < 0(1) \text{ for forced convection} \end{cases}$$

Similarly, for $\mathrm{Pr} << 1$ fluids

$$\frac{\left(\frac{\delta_{th}}{x}\right)^{FC}}{\left(\frac{\delta_{th}}{x}\right)^{NC}} = \frac{\mathrm{Ra}^{1/5}}{\mathrm{Pr}^{1/2}\mathrm{Re}^{1/2}} \begin{cases} > 0(1) \text{ for natural convection} \\ < 0(1) \text{ for forced convection} \end{cases}$$

Here

$$\mathrm{Ra} = \frac{g\beta\,|q_w|\,x^4}{\alpha\nu k} \tag{5a}$$

$$\mathrm{Re} = \frac{u_\infty x}{\nu} \tag{5b}$$

Hence, a dimensionless coordinate

$$\zeta \sim \frac{\mathrm{Ra}^{1/5}}{\mathrm{Re}^{1/2}} \sim x^{3/10}$$

or mixed convection parameter can be constructed similar to the one proposed independently by Lin and Chen (1988) as

Nomenclature

c_f = local skin friction coefficient
F = dimensionless stream function
G = dimensionless stream function
g = gravitational acceleration
h = local heat transfer coefficient
k = thermal conductivity
Nu = local Nusselt number
Pr = Prandtl number
q = local heat flux rate
Ra = Rayleigh number (constant wall heat flux case)
Ra* = Rayleigh number (isothermal wall case)
Re = Reynolds number
r = radial coordinate
r_o = radius of cylinder
T = temperature
U = reference velocity for c_f
u_∞ = free-stream velocity
u = velocity component in x direction
v = velocity component in y direction
x = longitudinal coordinate
Z = dimensionless parameter; $Z = 1$ for heated cylinders and $Z = -1$ for cooled cylinders
α = thermal diffusivity
β = thermal expansion coefficient
δ = boundary-layer thickness
ϵ = transverse curvature parameter
ϵ^* = transformed curvature parameter
ζ = mixed convection parameter (for constant wall heat flux case)
ζ^* = mixed convection parameter (constant wall temperature case)
η = dimensionless parameter
η^* = reduced dimensionless parameter
θ = dimensionless temperature (constant wall heat flux case)
θ^* = transformed dimensionless temperature
λ = dimensionless parameter (constant wall heat flux case)
λ^* = dimensionless parameter (constant wall temperature case)
ν = kinematic viscosity
ξ = dimensionless parameter
ρ = density of fluid
σ = dimensionless parameter
τ = shear stress
ϕ = dimensionless temperature (isothermal wall case)
ψ = stream function
ω = dimensionless parameter

Subscripts

∞ = ambient condition
cyl = cylinder
fp = flat plate
q = constant wall heat flux
th = thermal
T = isothermal wall
w = wall condition

Superscripts

NC = natural convection
FC = forced convection

$$\zeta = \frac{(\sigma \mathrm{Ra})^{1/5}}{(\omega \mathrm{Re})^{1/2}} \tag{6a}$$

where

$$\sigma = \frac{\mathrm{Pr}}{1+\mathrm{Pr}} \tag{6a}$$

$$\omega = \frac{\mathrm{Pr}}{(1+\mathrm{Pr})^{1/3}} \tag{6b}$$

Clearly, for $\mathrm{Pr} >> 1$, $\zeta \to (\delta_{th})FC/(\delta_{th})NC$ and for $\mathrm{Pr} << 1$, $\zeta \to (\delta_{th})FC/(\delta_{th})NC$.

Introducing the following variables (Wang and Kleinstreuer, 1988):

$$\xi = \frac{\zeta}{1+\zeta} \tag{7a}$$

$$\eta = \frac{r^2 - r_o^2}{2r_o x}\lambda \tag{7b}$$

with

$$\lambda = (\omega \mathrm{Re})^{1/2} + (\sigma \mathrm{Ra})^{1/5} \tag{7c}$$

$$\psi = r_o \alpha \lambda F(\xi, \eta) \tag{7d}$$

$$\theta = \frac{T - T_\infty}{\dfrac{q_w x}{k\lambda}} \tag{7e}$$

and employing the stream function approach, equations (2) and (3) are transformed to

$$\mathrm{Pr}[(1+\epsilon_q \eta)F'']' + \frac{1}{2}\left(1 + \frac{3}{5}\xi\right)FF'' - \frac{3}{5}\xi F'^2 + Z(1+\mathrm{Pr})\xi^5\theta = \frac{3}{10}\xi(1-\xi)\left[F'\frac{\partial F'}{\partial \xi} - F''\frac{\partial F}{\partial \xi}\right] \tag{8}$$

and

$$[(1+\epsilon_q \eta)\theta']' + \frac{1}{2}\left(1 + \frac{3}{5}\xi\right)F\theta' - \frac{1}{2}\left(1 - \frac{3}{5}\xi\right)F'\theta = \frac{3}{10}\xi(1-\xi)\left[F'\frac{\partial \theta}{\partial \xi} - \theta'\frac{\partial F}{\partial \xi}\right] \tag{9}$$

The associated boundary conditions are

$$F(\xi, 0) = 0 \tag{10a}$$

$$F'(\xi, 0) = 0 \tag{10b}$$

$$\theta'(\xi, 0) = -1 \tag{10c}$$

$$F'(\xi, \infty) = (1+\mathrm{Pr})^{1/3}(1-\xi)^2 \tag{10d}$$

$$\theta(\xi, \infty) = 0 \tag{10e}$$

The transverse curvature parameter is defined as

$$\epsilon_q = \frac{2x}{r_o \lambda} \tag{11}$$

and the primes denote differentiation with respect to η.

Of special interest are the skin friction coefficient, $c_f = \tau_w/(1/2\rho U^2)$, where a pseudo-velocity U replaces the traditional reference velocity u_∞, and the local Nusselt number, $\mathrm{Nu} = hx/k$. Selecting for the constant wall heat flux case

$$U_q = u_\infty + [g\beta |q_w| x^{3/2} \nu^{1/2}/k]^{2/5} \tag{12a}$$

a dimensionless skin friction parameter can be formed as

$$\mathrm{SFP}_q \equiv 1/2 c_f \lambda = \frac{F''(\xi,0)}{\mathrm{Pr}}[(1-\xi)^2/\omega + \xi^2/(\sigma \mathrm{Pr})^{2/5}]^{-2} \tag{12b}$$

The dimensionless heat transfer parameter is defined as

$$\mathrm{HTP}_q \equiv \mathrm{Nu}/\lambda = 1/\theta(\xi,0) \tag{13}$$

2.2 Transformed Equations for Isothermal Wall Case. The parameters introduced by Lin and Chen (1988) are extended to describe mixed convection on a vertical isothermal cylinder with curvature effects. The following variables and dimensionless groups are defined as

$$\zeta^* = (\sigma \mathrm{Ra}^*)^{1/4}/(\omega \mathrm{Re})^{1/2} \tag{14a}$$

where

$$\mathrm{Ra}^* = \frac{g\beta |T_w - T_\infty| x^3}{\alpha \nu} \tag{14b}$$

and

$$\xi = \frac{\zeta^*}{1+\zeta^*} \tag{15a}$$

$$\eta = \frac{r^2 - r_o}{2r_o x}\lambda^* \tag{15b}$$

$$\psi = r_o \alpha \lambda^* G(\xi, \eta) \tag{15c}$$

$$\phi = \frac{T - T_\infty}{T_w - T_\infty} \tag{15d}$$

where

$$\lambda^* = (\omega \mathrm{Re})^{1/2} + (\sigma \mathrm{Ra}^*)^{1/4} \tag{15e}$$

The mixed convection parameter λ^* can be reduced to $\mathrm{Ra}^{*1/4}/(\mathrm{Re}^{1/2}\mathrm{Pr}^{1/3})$ for large Prandtl numbers and to $(\mathrm{Ra}^*\mathrm{Pr})^{1/4}/(\mathrm{RePr})^{1/2}$ for small Prandtl numbers (Bejan, 1984).

Equations (2) and (3) can be transformed to

$$\mathrm{Pr}[(1+\epsilon_T \eta)G'']' + \frac{(2+\xi)}{4}GG'' - \frac{1}{2}\xi G'^2 + Z(1+\mathrm{Pr})\xi^4\phi = \frac{\xi(1-\xi)}{4}\left[G'\frac{\partial G'}{\partial \xi} - G''\frac{\partial G}{\partial \xi}\right] \tag{16}$$

and

$$[(1+\epsilon_T \eta)\phi']' + \frac{(2+\xi)}{4}G\phi' = \frac{\xi(1-\xi)}{4}\left[G'\frac{\partial \phi}{\partial \xi} - \phi'\frac{\partial G}{\partial \xi}\right] \tag{17}$$

subject to the boundary conditions

$$G(\xi, 0) = 0 \tag{18a}$$

$$G'(\xi, 0) = 0 \tag{18b}$$

$$\phi(\xi, 0) = 1 \tag{18c}$$

$$G'(\xi, \infty) = (1+\mathrm{Pr})^{1/3}(1-\xi)^2 \tag{18d}$$

$$\phi(\xi, \infty) = 0. \tag{18e}$$

The transverse curvature parameter is defined as

$$\epsilon_T = \frac{2x}{r_o \lambda^*} \tag{19}$$

Table 1 Data comparison of forced convection for a flat plate with constant wall heat flux thermal boundary condition ($\epsilon = 0$)

Pr	$f''(\xi,0)$		$\theta^*(\xi,0)$	
	Wilks (1973)	Present Method	Wilks (1973)	Present Method
0.1	0.33257	0.3320	4.93984	4.9481
0.72	0.3326	0.3320	2.4375	2.4400
1	0.3326	0.3320	2.1775	2.1790
10	0.3326	0.3320	1.0016	1.0022
100	0.3326	0.3320	0.4644	0.4647

Table 2 Data comparison of ratio of local Nusselt numbers, $(Nu)_{cyl}/(Nu)_{fp}$, for natural convection (isothermal wall case)

ϵ^*	Pr = 0.72			Pr = 1.0		
	Present Method	Cebeci (1974)	Aziz & Na (1982)	Present Method	Cebeci (1974)	Aziz & Na (1982)
0	1.0	1.0	1.0	1.0	1.0	1.0
0.503	1.205	1.210	1.219	1.183	1.188	1.197
1.064	1.418	1.422	1.445	1.373	1.380	1.399
2.093	1.763	1.778	1.821	1.690	1.704	1.736
3.364	2.157	2.177	2.232	2.049	2.068	2.106
4.000	2.343	2.366	2.419	2.219	2.240	2.274
5.030	2.633	2.660	2.700	2.484	2.508	2.527

ϵ^*	Pr = 10			Pr = 100		
	Present Method	Cebeci (1974)	Aziz & Na (1982)	Present Method	Cebeci (1974)	Aziz & Na (1982)
0	1.0	1.0	1.0	1.0	1.0	1.0
0.503	1.095	1.096	1.096	1.050	1.051	1.051
1.064	1.195	1.196	1.196	1.104	1.107	1.107
2.093	1.368	1.373	1.367	1.203	1.204	1.207
3.364	1.567	1.575	1.560	1.322	1.318	1.327
4.000	1.663	1.672	1.650	1.377	1.373	1.385
5.030	1.812	1.823	1.788	1.467	1.460	1.478

The heat transfer parameter is now defined as

$$\mathrm{HTP}_T \equiv \mathrm{Nu}/\lambda^* = -\phi'(\xi, 0) \tag{20}$$

With the new pseudo-velocity for the isothermal wall case

$$U_T = u_\infty + [g\beta\,|T_w - T_\infty|\,x]^{1/2} \tag{21a}$$

the dimensionless skin friction parameter reads

$$\mathrm{SFP}_T \equiv 1/2c_f\lambda^* = \frac{G''(\xi,0)}{\mathrm{Pr}}[(1-\xi)^2/\omega + \xi^2/(\sigma\mathrm{Pr})^{1/2}]^{-2} \tag{21b}$$

3 Solution Method

A two-point finite difference technique with Newton's linearization method (Cebeci and Bradshaw, 1977) has been used to solve the reduced equations and somewhat simplified boundary conditions (8) to (10*a–e*) or (16) to (18*a–e*). A uniform grid in the ξ direction was used with a total of 101 grid points but a variable mesh density was needed to accommodate steep gradients near the cylinder surface. The location of the boundary-layer edge η_∞ is strongly dependent upon the transverse curvature parameter and the Prandtl number. For example $\eta_\infty(\epsilon = 0.0$ and $\mathrm{Pr} = 0.7) \approx 6$ but $\eta_\infty(\epsilon = 2.0$ and $\mathrm{Pr} = 100) \approx 500$.

Numerical error testing has been accomplished by straightforward repeat calculations with finer meshes to check grid independence of the results and by local mesh refinement in the η-direction with smooth transition to the coarser region.

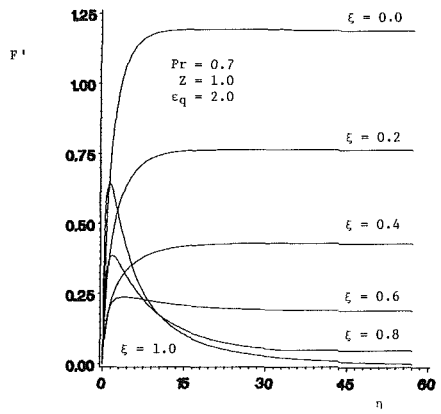

Fig. 2(*a*) Profiles of $F'(\xi, \eta)$ for heated cylinder ($q_w = \mathrm{const}$)

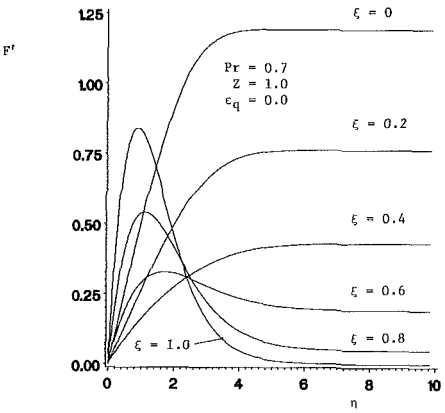

Fig. 2(*b*) Profiles of $F'(\xi, \eta)$ for heated vertical flat plate ($q_w = \mathrm{const}$)

4 Results and Discussion

The accuracy of the computer simulation model is documented in Tables 1 and 2. In addition, predictive results of the general analysis matched exactly the simulation results of special case studies published by Lin and Chen (1988) and by Wang and Kleinstreuer (1988) for $n = 1$ (Newtonian fluids). Table 1 indicates good agreement with data from Wilks (1973) for forced convection past a vertical flat plate. The variables used in Table 1 relate to the definitions in equations (7*d*) and (7*e*) as follows:

$$f''(\xi, 0) \equiv [(1+\mathrm{Pr})/\mathrm{Pr}]^{-1/2}F''(\xi, 0) \text{ and } \theta^*(\xi, 0) \equiv \omega^{-1/2}\theta(\xi, 0)$$

In Table 2, the local Nusselt number ratio $(Nu)_{cyl}/(Nu)_{fp}$ is compared with data from Cebeci (1974) and Aziz and Na (1982) for natural convection on a vertical slender cylinder. The agreement is within one percent for Cebeci's finite difference solution, while the perturbation method of Aziz and Na generated higher values for low Prandtl numbers. In Table 2, the relation between ϵ_T and ϵ^* is (equation (19))

$$\epsilon^* = (2\mathrm{Pr})^{1/2}/(1+\mathrm{Pr})^{1/4}\epsilon_T$$

The evolution of the profiles $F' \sim [u(r, x)/u_\infty]$ from pure forced convection ($\xi = 0$ or $\zeta = 0$, i.e., $\beta \equiv 0$) to the natural convection limit ($\xi = 1$ or $\zeta \to \infty$) is shown in Fig. 2(*a*) for a heated vertical cylinder ($\epsilon \neq 0$) and in Fig. 2(*b*) for a vertical flat plate ($\epsilon = 0$). The change in η scale reflecting the thick boundary layer due to transverse curvature effects (Fig. 2*a*) has to be noted (cf. Kleinstreuer and Eghlima, 1985).

To examine the effect of a cooled cylinder ($Z = -1$)

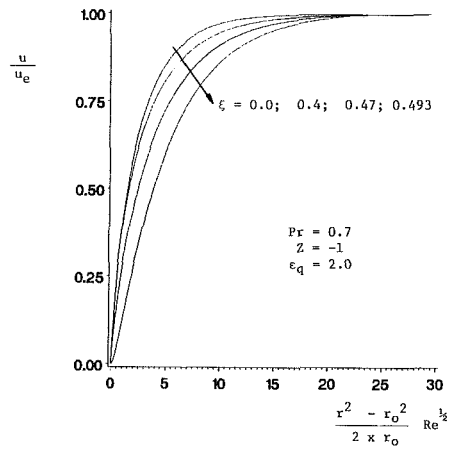

Fig. 3(*a*) Velocity profiles for cooled cylinder (q_w = const)

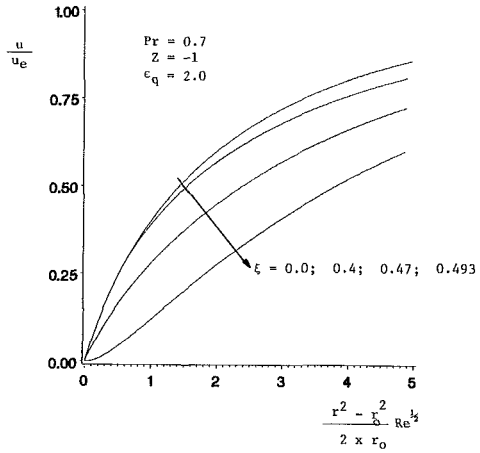

Fig. 3(*b*) Axial velocity profiles of Fig. 3(*a*) near the wall

generating a buoyancy force that opposes the free stream, the dimensionless axial velocity

$$u/u_\infty = F'(\xi,\eta)/[(1+\mathrm{Pr})^{1/3}(1-\xi)^2]$$

is plotted in Fig. 3(*a*) versus

$$\eta^* = \frac{r^2 - r_o^2}{2xr_o}\mathrm{Re}^{1/2} = \eta(1-\xi)/\omega^{1/2}$$

When compared to Fig. 2(*a*), it is evident that the (negative) buoyancy force tends to retard the convective upward flow. Furthermore, for $\xi > 0.493$, flow separation may occur (cf. Fig. 3*b*).

The dimensionless temperature profiles $\theta(\xi, \eta)$ for a vertical cylinder and a flat plate are given in Figs. 4(*a*) and 4(*b*), showing the smooth transition from forced to free convection. Largely determined by the velocity field (cf. Figs. 2(*a*) and 2(*b*)), the dimensionless temperature gradient is significantly steeper at the cylinder surface (Fig. 4(*a*)) than at the flat wall (Fig. 4(*b*)). While moving from forced to free convection, the emerging buoyancy effect reverses the trend of decreasing velocity F' and temperature θ in the region $0 < \eta \leq 10$ for vertical cylinders (cf. Figs. 2*a* and 4*a*) and in the region $0 < \eta \leq 3$ for vertical flat plates (cf. Figs. 2*b* and 4*b*).

The variations of the skin friction parameters, $\mathrm{SFP_q}$ and $\mathrm{SFT_T}$, for air and water as a function of ξ are shown in Figs. 5(*a*) and 5(*b*) for different transverse curvature parameters. The graphs for the constant wall heat flux case (Fig. 5*a*) are quite similar to the isothermal surface case (Fig. 5*b*) as long as $\xi \leq 0.3$. The vertical flat plate ($\epsilon = 0$ appears as a special case reflecting the established values for pure forced convection

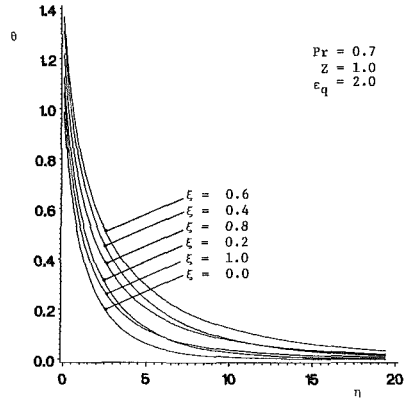

Fig. 4(*a*) Temperature profiles $\theta(\xi, \eta)$ for heated cylinder (q_w = const)

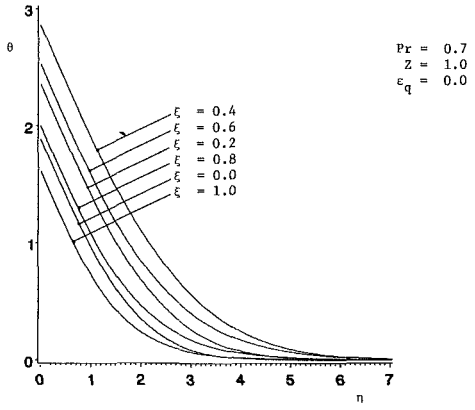

Fig. 4(*b*) Temperature profiles $\theta(\xi, \eta)$ for vertical flat plate (q_w = const)

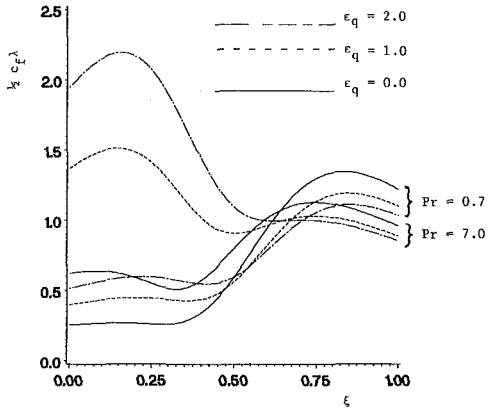

Fig. 5(*a*) Local skin friction parameter $\mathrm{SFP_q}(\xi)$ for different transverse curvature parameters and Prandtl numbers

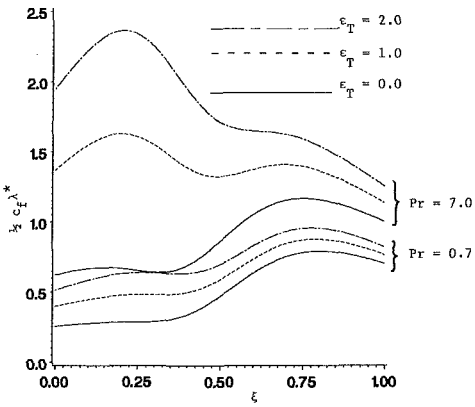

Fig. 5(*b*) Local skin friction parameter $\mathrm{SFP_T}(\xi)$ for different transverse curvature parameters and Prandtl numbers

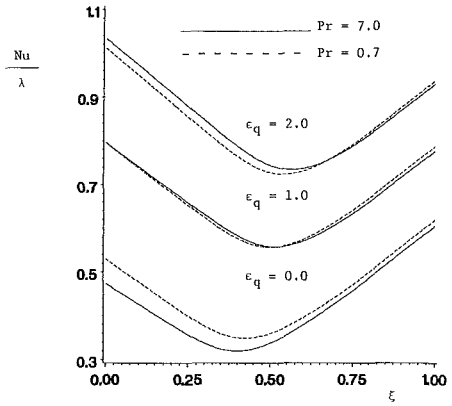

Fig. 6(a) Local heat transfer parameter $HTP_q(\xi)$ for different transverse curvature parameters and Prandtl numbers

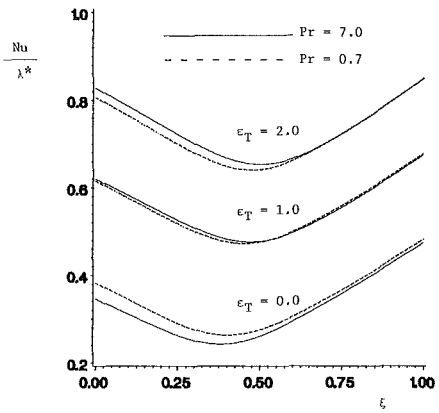

Fig. 6(b) Local heat transfer parameter $HTP_T(\xi)$ for different transverse curvature parameters and Prandtl numbers

(e.g., $1/2c_f\mathrm{Re}^{1/2}=0.332$ for $\mathrm{Pr}=0.7$; $\xi=0$, $T_w=\text{const}$) and for pure free convection (e.g., $1/2c_f\lambda^*=0.7083$ for $\mathrm{Pr}=0.72$; $\xi=1$, $T_w=\text{const}$). Both the Prandtl number and the transverse curvature parameters have profound effects on SFP = SFP(ξ). For the constant wall heat flux case (Fig. 5*a*), $\mathrm{SFP_q}$ increases in the predominantly forced convection regime, $\xi<5.0$, when ξ, ϵ, or Pr increases. This trend is basically reversed in the free convection regime where the buoyancy force dominates and largely determines the velocity gradient at the cylinder surface and hence the wall shear stress $\tau_w\sim c_f\sim\mathrm{SFP}$. As shown in Fig. 5(*b*), the buoyancy effect on $\mathrm{SFP_T}$ is not as strong; $\mathrm{SFP_T}$ increases with larger ϵ and Pr throughout the mixed parameter range $0\le\xi\le1$.

The heat transfer parameter HTP is given for the entire range of mixed thermal convection for different Prandtl numbers and transverse curvature parameters (Figs. 6*a* and 6*b*). Based on a computer experiment, it was found that for $\mathrm{HTP_q}=\mathrm{HTP_q}(\mathrm{Pr}\text{ and }\xi;\ \epsilon=2.0)$, where $0.01\le\mathrm{Pr}\le100$ and $0\le\xi\le1.0$, the minimum value for $\mathrm{HTP_q}$ exhibits also a shifting minimum with different ϵ values in the range $0.4\le\xi\le0.6$ (cf. Fig. 6*a*). Recalling that $\mathrm{HTP_q}=1/\theta(\xi,0)$, the trend of HTP_q (ξ,ϵ_q) can be explained by examining the wall temperatures in Fig. 4(*b*) for $\epsilon_q=0$ and in Fig. 4(*a*) for $\epsilon_q=2.0$. The situation is quite similar for the isothermal wall case (Fig. 6*b*) except that $\mathrm{HTP_q}(\xi,\epsilon_q)>\mathrm{HTP_T}(\xi,\epsilon_T)$. Figures 6(*a*) and 6(*b*) also indicate that transverse curvature may reverse the effect of the Prandtl number on the heat transfer parameter for predominantly forced convection, say, $\xi<0.5$.

5 Conclusions

A new analysis of steady laminar thermal flow along vertical slender cylinders has been presented, unifying and improving existing studies of pure forced, mixed, and pure free convection heat transfer. Two uniquely transformed sets of axisymmetric boundary-layer equations for the constant wall heat flux case and the isothermal surface case have been solved using Keller's box method on a variable-density mesh. The effects of the Prandtl number, the transverse curvature parameter, and the cylinder heating/cooling mode on fluid mechanics and heat transfer parameters are illustrated for a smooth transition of the entire range of thermal convection.

Starting with the forced-convection regime, $\xi<0.5$, the transverse curvature parameter, ϵ, the fluid Prandtl number Pr, and the thermal wall conditions (i.e., $q_w=\text{const}$ or $T_w=\text{const}$) influence the local skin friction parameter SFP and the local heat transfer parameter HTP, as expected. SFP and HTP increase with increasing ϵ or Pr and do not differ significantly with the type of thermal boundary condition. An exception is ϵ, which may reverse the impact of Pr on HTP for $\xi<0.5$.

Moving into the free-convection regime, $\xi>0.5$, the increasing buoyancy force reverses the trends for SFP and HTP, especially for $\mathrm{SFP_q}=\mathrm{SFP_q}(\mathrm{Pr},\epsilon_q)$. The strong changes in SFP (ξ; ϵ, Pr) and HTP (ξ; ϵ, Pr) around $\xi=0.5$ can be directly interpreted from the near-wall behavior of the velocity $u=u$ (η; ξ, ϵ, Pr) and the temperature $\theta=\theta(\eta;\ \xi,\ \epsilon,\ \mathrm{Pr})$, respectively.

In summary, the validated computer simulation model is an accurate, flexible and predictive tool for the basic analyses and design applications of an important group of convection heat transfer problems.

References

Aziz, A., and Na, T. Y., 1982, "Improved Perturbation Solutions for Laminar Natural Convection on a Vertical Cylinder," *Wärme- und Stoffübertragung*, Vol. 16, pp. 83-87.

Bejan, A., 1984, *Convection Heat Transfer*, Wiley, New York.

Bui, M. N., and Cebeci, T., 1985, "Combined Free and Forced Convection on Vertical Slender Cylinders," ASME JOURNAL OF HEAT TRANSFER, Vol. 107, pp. 476-478.

Cebeci, T., 1974, "Laminar Free Convection Heat Transfer From the Outer Surface of a Vertical Slender Circulation Cylinder," *Proc. Int. Heat Transf. Conf.*, NC 1.4, pp. 15-19.

Cebeci, T., and Bradshaw, P., 1977, *Momentum Transfer in Boundary Layers*, Hemisphere Publishing Corp., Washington, D.C.

Kleinstreuer, C., and Eghlima, A., 1985, "Analysis and Simulation of New Approximation Equations for Boundary-Layer Flow on Curved Surfaces," *Math. and Comp. in Simul.*, Vol. 27, pp. 308-325.

Kleinstreuer, C., and Wang, T.-Y., 1989, "Convection Heat Transfer in Water at 4°C Past Vertical Slender Cylinders," *Journal Thermophysics and Heat Transfer*, Vol. 3, No. 1.

Kleinstreuer, C., 1989, *Engineering Fluid Dynamics—An Interdisciplinary Systems Approach*, Springer-Verlag, New York, in press.

Lee, S. L., Chen, T. S., and Armaly, B. F., 1986, "Mixed Convection Along Isothermal Vertical Cylinders and Needles," *Proceedings of the Eighth International Heat Transfer Conference*, Vol. 3, pp. 1425-1432.

Lee, S. L., Chen, T. S., and Armaly, B. F., 1987, "Mixed Convection Along Vertical Cylinders and Needles With Uniform Heat Flux," ASME JOURNAL OF HEAT TRANSFER, Vol. 109, pp. 711-716.

Lin, H. T., and Chen, C. C., 1988, "Mixed Convection on Vertical Plate for Fluids of any Prandltl Number," *Wärme- und Stoffübertragung*, Vol. 22, pp. 159-168.

Wang, T. Y., and Kleinstreuer, C., 1988, "Combined Free-Forced Convection Heat Transfer Between Vertical Slender Cylinders and Power-Law Fluids," *International Journal of Heat and Mass Transfer*, Vol. 31, pp. 91-98.

Wilks, G., 1973, "Combined Forced and Free Convection Flow on Vertical Surfaces," *International Journal of Heat and Mass Transfer*, Vol. 16, pp. 1958-1964.

Mixed Convection Heat Transfer to Power Law Fluids in Arbitrary Cross-Sectional Ducts

A. Lawal
Department of Chemical Engineering,
University of Port Harcourt,
Port Harcourt, Nigeria

An analytical investigation of three-dimensional mixed convection flow and heat transfer to power-law fluids in horizontal arbitrary cross-sectional ducts is undertaken. The continuity equation and parabolic forms of the energy and momentum equations in rectangular coordinates are transformed into new orthogonal coordinates with the boundaries of the duct coinciding with the coordinate surfaces. The transformed equations are solved by the finite difference technique. The fluid enters the duct with constant velocity and temperature profiles with the wall of the duct subjected to constant temperature. Local heat transfer coefficients and pressure drop for several values of Gr/Re and power-law index n *are computed for the triangular, square, trapezoidal, pentagonal, and circular ducts. The buoyancy force is found to increase both the Nusselt number and the pressure drop.*

Introduction

Laminar flow and heat transfer processes play a key role in such vital industries as foods, polymer, and petrochemical, where heat exchangers constitute an integral part of the processing equipment. In the design of industrial heat exchangers several techniques have been proposed for heat transfer enhancement. One method that is attracting increasing attention suggests the use of noncircular arbitrarily shaped but axially uniform cross-sectional ducts to exploit the economic benefit that may arise from greater compactness. Compact heat exchangers such as rotary regenerators are made up of noncircular passages, which can be simulated by rectangular, triangular, pentagonal, etc., shapes. The study of noncircular duct shapes is also of relevance in the design of automobile radiators (triangular shape) and the simulation of internal convection cooling of turbine blades and nozzle guide vanes (rectangular and equilateral triangular shapes).

Most fluids of industrial interest are adequately characterized rheologically by the purely viscous power-law behavior and because of their highly viscous nature, processing conditions are often within the laminar flow regime. In addition, the fluid density sometimes exhibits strong temperature dependence, making it necessary to incorporate buoyancy effects into the flow analysis. The effect of natural convection is generally an increase of the heat transfer coefficient over that for purely forced convection in the region where it exists.

Mixed convection heat transfer to circular tubes has been extensively investigated both theoretically and experimentally. The presence of gravitational effects in the momentum equations introduces a mathematical complexity that, even for a simple geometry like the circular pipe, precludes closed-form solutions. When the cross-sectional shape of the tube is allowed to be arbitrary, the complexity is further accentuated. The limited, almost nonexistent research effort on arbitrarily shaped ducts is therefore not unexpected.

Newell and Bergles (1970) presented a detailed numerical study of mixed convection heat transfer in a horizontal circular tube with fully developed flow and thermally developing heat transfer. Their thermal boundary condition in the axial direction was that of uniform heat flux, while peripherally the wall temperature was either kept constant or the variation was allowed to be dictated by the thermal conductance of the fluid system. Correlations for Nusselt number and friction factor for water were developed based on the numerical results and fair agreement was obtained between literature data and analytical predictions. Zeldin and Smith (1972) considered a vertical tube with the wall and entering fluid at constant but different temperatures. An experimental program was also executed by Zeldin and Smith. For pure forced convection, the agreement between predictions and data was satisfactory, but it was not particularly so for the mixed convection data.

In a series of articles (Cheng and Hwang, 1969; Cheng et al., 1972; Ou et al., 1974), the horizontal rectangular channel with varying aspect ratio was treated. The flow was taken to be fully developed in all the studies. In Cheng and Hwang (1969), the thermal boundary conditions of axially uniform wall heat flux and peripherally constant wall temperature were imposed. Numerical results on friction factor and Nusselt number were presented for different flow, thermal, and geometric parameters. The numerical technique, based on the point relaxation method, experienced convergence difficulties for high Rayleigh numbers. The restriction of infinite Prandtl number was imposed in Cheng et al. (1972) with the constant heat flux condition while the companion work, Ou et al. (1974), assumed constant wall temperature. Through numerical experimentation, it was shown that the infinite Prandtl number condition is practically equivalent to $Pr > 10$. The work of Nakamura et al. (1980) was very similar to that of Ou et al. (1974) except that attention was focused on triangular ducts. A previous study by Nakamura et al. (1977) had considered inclined triangular ducts with axially uniform wall heat flux and peripherally uniform wall temperature.

All of the foregoing studies were concerned with Newtonian fluids. There are few studies documenting the enhancement of heat transfer to non-Newtonian fluids by buoyancy effects. Of these, mention should be made of the works of Gori (1978a, 1978b), Marner and McMillan (1972), and Oliver and Jenson (1964). They all assumed fully developed flow condition at the entrance and a power-law rheological behavior. Although buoyancy effects generally augment heat transfer, a dilatant power-law fluid exerts an opposing effect, which sometimes could be so dominant as to completely annul the heat transfer enhancement (Marner and McMillan, 1972). Oliver and Jenson (1964) investigated experimentally the effects of natural convection on heat transfer to pseudoplastic fluids in horizontal tubes subjected to the constant wall temperature condition. Correlating equations were developed for the mean heat transfer coefficient.

Contributed by the Heat Transfer Division for publication in the JOURNAL OF HEAT TRANSFER. Manuscript received by the Heat Transfer Division May 20, 1987. Keywords: Materials Processing and Manufacturing Processes, Mixed Convection.

In the present work, we shall present results of theoretical investigation of mixed convection heat transfer to power-law fluids in horizontal ducts with arbitrarily shaped but axially uniform cross section. To our knowledge, there is no documented attempt to address this problem despite its obvious industrial relevance. Pressure drop and local heat transfer coefficients as functions of pertinent thermal and hydrodynamic parameters will be presented and discussed.

Analysis

The problem to be investigated is that of steady mixed convection flow and heat transfer to power-law fluids in horizontal ducts of arbitrary cross section (Fig. 1). Both the velocity and temperature profiles are uniform at the entrance and subsequently develop simultaneously in the duct, the walls of which are maintained at a constant temperature different from the entrance value. In its most general form, the power-law model can be written as

$$\tau_{ij} = \mu_o \, |\tfrac{1}{2}\Delta_{ij}:\Delta_{ij}|^{\frac{n-1}{2}} \, \Delta_{ij} \tag{1}$$

where n is the power-law index and μ_o the consistency index. The variation of density in the buoyancy term will be accounted for using the classical Boussinesq approximation

$$\rho = \rho_w (1 + \beta(T - T_w)) \tag{2}$$

With the neglect of viscous dissipation and expansion/cooling effects, the problem is completely described, although a solution to the appropriate form of the equations of conservation of mass, momentum, and energy may not be feasible. This is in part due to the elliptic nature of the equations, which, for an acceptable degree of numerical accuracy, would place excessive demands on both storage and computing time.

Our numerical solution technique takes advantage of the marginal ellipticity of the physical problem by neglecting the axial diffusion terms in the equations of conservation of momentum and energy. The resulting equations are parabolic; therefore a two-dimensional computational mesh can be constructed at each cross section and stacked together to form the three-dimensional domain. A considerable reduction in both storage and computing time requirements is thus achieved. The strategy for dealing with the arbitrary shape of the duct cross section consists of transforming the physical domain into a rectangular duct using a coordinate transformation technique. The conservation equations are similarly transformed and due to space limitations, the governing equations will only be presented in transformed coordinates.

The parabolized conservation equations have been successfully used in predicting experimental data on mixed convection heat transfer in ducts (Newell and Bergles, 1970; Greif, 1978; Gori, 1978a).

The assumption of negligible longitudinal diffusion ceases to hold as soon as backflow generated in the case under consideration by intense secondary flow sets in. In practice, backflows, even though they cannot be discounted, are not a common occurrence in straight, uniform cross-sectional ducts, the flows of which are normally characterized by moderate Gr/Re values.

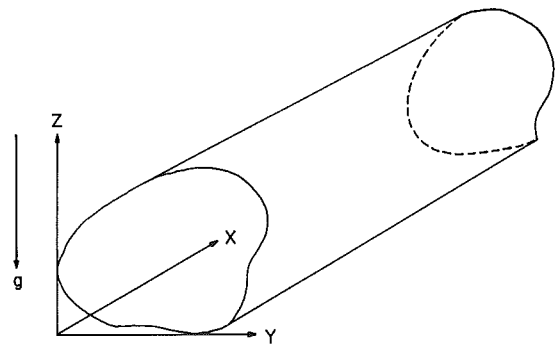

Fig. 1 Geometry of arbitrary cross-sectional duct in Cartesian coordinates

Nomenclature

C_p = heat capacity
C_7 = temperature–viscosity coefficient
D_h = hydraulic diameter
f = dependent variable at a grid point
g = acceleration due to gravity
Gr = Grashof number $= (\rho^2 g\beta(T_e - T_w) D_h^{2n+1}/\mu^2)$
Gr′ = Grashof number $= u_e^{2-2n}\rho^2 g\beta(q'/k) D_h^{2n+1}/\mu^2$
J = Jacobian $= Y_\xi Z_\eta - Y_\eta Z_\xi$
k = thermal conductivity
n = power law index
$\mathbf{n}$ = unit normal vector
Nu_{X^*} = local Nusselt number $= D_h[(\partial T/\partial \mathbf{n})_{w,m}]_{X^*}/(T_w - T_b)$
p = transverse pressure
$\bar{p}$ = mean axial pressure
P = dimensionless transverse pressure $= (p_e - p)/\rho u_e^2$
$\bar{P}$ = dimensionless mean axial pressure $= (p_e - \bar{p})/\rho u_e^2$
Pe = Peclet number $= (\rho C_p)\, u_e D_h/k$
Pr = Prandtl number $= (\rho C_p)\, \mu u_e^{n-1}/(k\rho_m D_h^{n-1})$
q' = total heat input per unit axial length
q'' = wall heat flux
R_{mass} = residual mass
Re = Reynolds number $(= D_h^n \rho_m u_e^{2-n}/\mu_e)$
T = temperature
u = axial velocity
U = dimensionless axial velocity $= u/u_e$
v = velocity in Y direction
V = dimensionless velocity in Y direction $= v/u_e$
w = velocity in z direction
W = dimensionless velocity in Z direction $= w/u_e$
x = axial distance
X = dimensionless axial distance $= x/D_h$
$\bar{X}_i$ = Cartesian coordinates
X^* = dimensionless axial coordinate $= x/D_h P_e$
ΔX = axial step size $= \Delta(x/D_h)$
y = transverse coordinate
Y = dimensionless transverse coordinate $= y/D_h$
z = transverse coordinate
Z = dimensionless transverse coordinate $= z/D_h$
α = $Z_\eta^2 + Y_\eta^2$
β = coefficient of volume expansion or grid control function
γ = $Y_\xi^2 + Z_\xi^2$
Δ_{ij} = rate of deformation tensor
ϵ = prescribed error
ζ = curvilinear coordinate
η = curvilinear coordinate
θ = dimensionless temperature $= T - T_w/T_e - T_w$
μ = consistency index
ξ = curvilinear coordinate
ξ^i = generalized curvilinear coordinates
ρ = density
τ_{ij} = stress tensor

Subscripts

b = bulk
e = entrance
i, j = space subscripts denoting grid points
m = mean
max = maximum
w = wall condition

Coordinate Transformation Equations. Essentially, the coordinate transformation technique relies on finding a unique, orthogonal transformation of the arbitrary cross section of the duct into one of the canonical domains, here the rectangle. Let the orthogonal curvilinear coordinates be related to the Cartesian coordinates by the transformation

$$\xi^i = \xi^i(\bar{X}_1, \bar{X}_2, \bar{X}_3) \tag{3a}$$

The inverse of this transformation is then given by

$$\bar{X}_i = \bar{X}_i(\xi^1, \xi^2, \xi^3) \tag{3b}$$

Apart from the use of elliptic partial differential equations, a procedure adopted in this study, there are other popular but less versatile methods of achieving the desired transformation.

If we make the following association:

$$Y = \bar{X}_1 \qquad Z = \bar{X}_2 \qquad X = \bar{X}_3 \tag{4a}$$

$$\xi^1 = \xi \qquad \xi^2 = \eta \qquad \xi^3 = \zeta \tag{4b}$$

for a three-dimensional system with an arbitrary but axially uniform shape, the required partial differential equations are (Lawal and Mujumdar, 1985)

$$\frac{\partial^2 Y}{\partial \xi^2} + \beta^2 \frac{\partial^2 Y}{\partial \eta^2} - H\frac{\partial Y}{\partial \xi} - \beta^2 Q \frac{\partial Y}{\partial \eta} = 0 \tag{5a}$$

$$\frac{\partial^2 Z}{\partial \xi^2} + \beta^2 \frac{\partial^2 Z}{\partial \eta^2} - H\frac{\partial Z}{\partial \xi} - \beta^2 Q \frac{\partial Z}{\partial \eta} = 0 \tag{5b}$$

where

$$\beta = \frac{h'(\xi)}{aq'(\eta)}\ ;\ H = \frac{h''(\xi)}{h'(\xi)};\ Q = \frac{q''(\eta)}{q'(\eta)}$$

The functions h and q above are used in exercising control on the grid spacing and for uniform grids; $h(\xi) = \xi$ and $q(\eta) = \eta$. The shape factor a is obtained from:

$$Z_n = \frac{aq' Y_\xi}{h'} \tag{6}$$

Associated with the transformation is the Jacobian given by

$$\mathrm{J} = Y_\xi Z_\eta - Y_\eta Z_\xi \tag{7}$$

and when coupled with equations (3*a*) and (3*b*) produces the relations

$$\xi_Y = \frac{Z_\eta}{\mathrm{J}} \qquad \xi_Z = -\frac{Y_\eta}{\mathrm{J}} \tag{8a}$$

$$\eta_Y = \frac{-Z_\xi}{\mathrm{J}} \qquad \eta_Z = \frac{Y_\xi}{\mathrm{J}} \tag{8b}$$

The numerical solution of the coordinate transformation equations is straightforward and since the procedure is detailed well in Mobley and Stewart (1980), it will not be described here. An example of a uniform grid induced in a pentagonal duct is shown in Fig. 2.

Conservation Equations in Transformed Coordinates. The equations of conservation need to be transformed with the unavoidable consequence of greater complexity. With equations (8*a*) and (8*b*) and other relations (Lawal and Mujumdar, 1985), the partial derivatives in Cartesian coordinates can be related to their counterparts in the new curvilinear coordinates. The scale factors that appear in the transformed conservation equations are readily provided by the solution to the coordinate transformation equations.

With all the foregoing assumptions, the conservation equations are:

Integral Mass Constraint:

$$\iint U\mathrm{J}\,d\xi\,d\eta - \iint \mathrm{J}\,d\xi\,d\eta = R_{\text{mass}} \tag{9a}$$

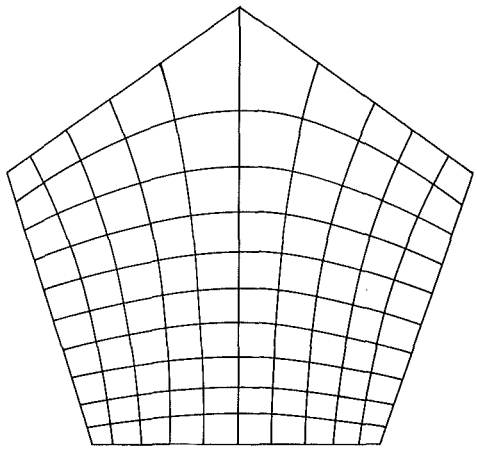

Fig. 2 Curvilinear coordinates induced in a pentagonal duct

Continuity:

$$\frac{\partial U}{\partial X} + \frac{Z_\eta}{\mathrm{J}}\frac{\partial V}{\partial \xi} - \frac{Z_\xi}{\mathrm{J}}\frac{\partial V}{\partial \eta} - \frac{Y_\eta}{\mathrm{J}}\frac{\partial W}{\partial \xi} + \frac{Y_\xi}{\mathrm{J}}\frac{\partial W}{\partial \eta} = 0 \tag{9b}$$

X-Momentum:

$$\begin{aligned} U\frac{\partial U}{\partial X} &+ \frac{(Z_\eta V - Y_\eta W)}{\mathrm{J}}\frac{\partial U}{\partial \xi} + \frac{(Y_\xi W - Z_\xi V)}{\mathrm{J}}\frac{\partial U}{\partial \eta} = \frac{d\bar{P}}{dX} \\ &+ \frac{1}{2\mathrm{Re}}\left\{\frac{M}{\mathrm{J}}\left[\left(\frac{\alpha U_\xi}{\mathrm{J}}\right)_\xi + \left(\frac{\gamma U_\eta}{\mathrm{J}}\right)_\eta\right]\right. \\ &+ \frac{1}{\mathrm{J}}\left[\left(\frac{\alpha (MU)_\xi}{\mathrm{J}}\right)_\xi + \left(\frac{\gamma (MU)_\eta}{\mathrm{J}}\right)_\eta\right] \\ &\left. - \frac{U}{\mathrm{J}}\left[\left(\frac{\alpha M_\xi}{\mathrm{J}}\right)_\xi + \left(\frac{\gamma M_\eta}{\mathrm{J}}\right)_\eta\right]\right\} \\ &+ \frac{1}{\mathrm{Re}}\left\{\left(\frac{Z_\eta}{\mathrm{J}}\frac{\partial M}{\partial \xi} - \frac{Z_\xi}{\mathrm{J}}\frac{\partial M}{\partial \eta}\right)\frac{\partial V}{\partial X}\right. \\ &\left. + 2\frac{\partial M}{\partial X}\frac{\partial U}{\partial X} + \left(\frac{Y_\xi}{\mathrm{J}}\frac{\partial M}{\partial \eta} - \frac{Y_\eta}{\mathrm{J}}\frac{\partial M}{\partial \xi}\right)\frac{\partial W}{\partial X}\right\} \end{aligned} \tag{10}$$

Y-Momentum:

$$\begin{aligned} U\frac{\partial V}{\partial X} &+ \frac{(Z_\eta V - Y_\eta W)}{\mathrm{J}}\frac{\partial V}{\partial \xi} \\ &+ \frac{(Y_\xi W - Z_\xi V)}{\mathrm{J}}\frac{\partial V}{\partial \eta} = \frac{Z_\eta}{\mathrm{J}}\frac{\partial P}{\partial \xi} - \frac{Z_\xi}{\mathrm{J}}\frac{\partial P}{\partial \eta} \\ &+ \frac{1}{2\mathrm{Re}}\left\{\frac{M}{\mathrm{J}}\left[\left(\frac{\alpha V_\xi}{\mathrm{J}}\right)_\xi + \left(\frac{\gamma V_\eta}{\mathrm{J}}\right)_\eta\right] + \frac{1}{\mathrm{J}}\left[\left(\frac{\alpha (MV)_\xi}{\mathrm{J}}\right)_\xi\right.\right. \\ &\left.\left. + \left(\frac{\gamma (MV)_\eta}{\mathrm{J}}\right)_\eta\right] - \frac{V}{\mathrm{J}}\left[\left(\frac{\alpha M_\xi}{\mathrm{J}}\right)_\xi + \left(\frac{\gamma M_\eta}{\mathrm{J}}\right)_\eta\right]\right\} \\ &+ \frac{1}{R_e}\left\{\frac{1}{\mathrm{J}^2}\left(Z_\eta^2\frac{\partial M}{\partial \xi} - Z_\eta Z_\xi\frac{\partial M}{\partial \eta}\right)\frac{\partial V}{\partial \xi}\right. \\ &+ \frac{1}{\mathrm{J}^2}\left(Z_\xi^2\frac{\partial M}{\partial \eta} - Z_\eta Z_\xi\frac{\partial M}{\partial \xi}\right)\frac{\partial V}{\partial \eta} \\ &+ \frac{\partial M}{\partial X}\frac{\partial V}{\partial X} + \frac{\partial M}{\mathrm{J}\partial X}\left[Z_\eta\frac{\partial U}{\partial \xi} - Z_\xi\frac{\partial U}{\partial \eta}\right] \\ &+ \frac{1}{\mathrm{J}^2}\left(Z_\eta Y_\xi\frac{\partial M}{\partial \eta} - Y_\eta Z_\eta\frac{\partial M}{\partial \xi}\right)\frac{\partial W}{\partial \xi} \\ &\left. + \frac{1}{\mathrm{J}^2}\left(Y_\eta Z_\xi\frac{\partial M}{\partial \xi} - Y_\xi Z_\xi\frac{\partial M}{\partial \eta}\right)\frac{\partial W}{\partial \eta}\right\} \end{aligned}$$

Z-Momentum:

$$U\frac{\partial W}{\partial X}+\frac{(Z_\eta V-Y_\eta W)}{J}\frac{\partial W}{\partial \xi}+\frac{(Y_\xi W-Z_\xi V)}{J}\frac{\partial W}{\partial \eta}=\frac{Y_\xi}{J}\frac{\partial P}{\partial \eta}-\frac{Y_\eta}{J}\frac{\partial P}{\partial \xi}+\frac{\mathrm{Gr}\theta}{\mathrm{Re}^2}+\frac{1}{2\mathrm{Re}}\left\{\frac{M}{J}\left[\left(\frac{\alpha W_\xi}{J}\right)_\xi+\left(\frac{\gamma W_\eta}{J}\right)_\eta\right]+\frac{1}{J}\left[\left(\frac{\alpha(MW)_\xi}{J}\right)_\xi+\left(\frac{\gamma(MW)_\eta}{J}\right)_\eta\right]-\frac{W}{J}\left[\left(\frac{\alpha M_\xi}{J}\right)_\xi+\left(\frac{\gamma M_\eta}{J}\right)_\eta\right]\right\}+\frac{1}{\mathrm{Re}}\left\{\frac{1}{J^2}\left(Y_\eta^2\frac{\partial M}{\partial \xi}-Y_\eta Y_\xi\frac{\partial M}{\partial \eta}\right)\frac{\partial W}{\partial \xi}+\frac{1}{J^2}\left(Y_\xi^2\frac{\partial M}{\partial \eta}-\frac{Y_\eta Y_\xi}{J^2}\frac{\partial M}{\partial \xi}\right)\frac{\partial W}{\partial \eta}+\frac{\partial M}{\partial X}\frac{\partial W}{\partial X}+\frac{\partial M}{J\partial X}\left[Y_\xi\frac{\partial U}{\partial \eta}-Y_\eta\frac{\partial U}{\partial \xi}\right]+\frac{1}{J^2}\left(Y_\eta Z_\xi\frac{\partial M}{\partial \eta}-Z_\eta Y_\eta\frac{\partial M}{\partial \xi}\right)\frac{\partial V}{\partial \xi}+\frac{1}{J^2}\left(Z_\eta Y_\xi\frac{\partial M}{\partial \xi}-Y_\xi Z_\xi\frac{\partial M}{\partial \eta}\right)\frac{\partial V}{\partial \eta}\right\} \tag{12}$$

Energy

$$U\frac{\partial \theta}{\partial X}+\frac{(Z_\eta V-Y_\eta W)}{J}\frac{\partial \theta}{\partial \xi}+\frac{(Y_\xi W-Z_\xi V)}{J}\frac{\partial \theta}{\partial \eta}=\frac{1}{2\mathrm{Pe}}\left\{\frac{1}{J}\left[\left(\frac{\alpha\theta_\xi}{J}\right)_\xi+\left(\frac{\gamma\theta_\eta}{J}\right)_\eta\right]+\frac{1}{J}\left[\left(\frac{\alpha}{J}(\theta)_\xi\right)_\xi+\left(\frac{Y}{J}(\theta)_\eta\right)_\eta\right]\right\} \tag{13}$$

where M is given by

$$M=\left\{2\left(\left(\frac{\partial U}{\partial X}\right)^2+\left(\frac{Z_\eta}{J}\frac{\partial V}{\partial \xi}-\frac{Z_\xi}{J}\frac{\partial V}{\partial \eta}\right)^2+\left(\frac{Y_\xi}{J}\frac{\partial W}{\partial \eta}-\frac{Y_\eta}{J}\frac{\partial W}{\partial \xi}\right)^2+\left(\frac{\partial V}{\partial X}+\frac{Z_\eta}{J}\frac{\partial U}{\partial \xi}-\frac{Z_\xi}{J}\frac{\partial U}{\partial \eta}\right)^2+\left(\frac{\partial W}{\partial X}-\frac{Y_\eta}{J}\frac{\partial U}{\partial \xi}+\frac{Y_\xi}{J}\frac{\partial U}{\partial \eta}\right)^2+\left(\frac{Z_\eta}{J}\frac{\partial W}{\partial \xi}-\frac{Z_\xi}{J}\frac{\partial W}{\partial \eta}-\frac{Y_\eta}{J}\frac{\partial V}{\partial \xi}+\frac{Y_\xi}{J}\frac{\partial V}{\partial \eta}\right)^2\right\}^{\frac{n-1}{2}} \tag{14}$$

The flow and heat transfer variables have been suitably nondimensionalized and their definitions relegated to the nomenclature. For a given geometry, the flow and heat transfer parameters are n, x/D_h, Re, Pr, and Gr/Re.

Boundary Conditions. With the transformation to the curvilinear coordinate system, the boundaries of the duct now coincide with coordinate surfaces; hence boundary conditions can be specified along constant coordinate lines. Since the transformed equations retain their parabolicity, downstream boundary conditions are not needed.

The required boundary conditions are:

$$U=1.0;\quad V=0;\quad W=0;\quad \tilde{P}=0;\quad X=0 \tag{15a}$$

$$\theta=1.0 \qquad X=0 \tag{15b}$$

$$U=0;\quad V=0;\quad W=0;\quad \theta=0;\quad \xi=1,\ I \text{ for all } \eta \tag{15c}$$

$$U=0;\quad V=0;\quad W=0;\quad \theta=0;\quad \eta=1,\ K \text{ for all } \xi \tag{15d}$$

Solution of Conservation Equations. The transformed conservation equations are solved on a rectangular domain using the finite-difference method. The product (nonlinear) terms of the momentum equations are linearized by setting the unknown to its value at the previous axial step. The axial momentum equation is treated separately from the transverse momentum equations, which are decoupled by assuming a pressure field. The transverse velocities and the pressure distribution are then corrected by solving the appropriate correction equations. Further details are available in Lawal and Mujumdar (1984).

A standard grid network with the dependent variables stored at each grid point is laid out on the computational domain having a spacing of $\Delta\xi=\Delta\eta=1$ in the ξ and η directions, respectively.

Uniform grids were used throughout. Second-order central difference scheme is employed in approximating all partial derivatives in the transverse directions and the upwind scheme for the first-order derivatives in the axial direction. All the finite-difference equations are cast in a form suitable for the line SOR technique, which is the solution method employed.

Results and Discussion

The accuracy of the finite difference code has been verified by checking the results against those of previous researchers in Lawal and Mujumdar (1985) and Lawal (1985). For example, natural convection effects were included in the analysis of Briley (1974) for flow of a Newtonian fluid in a square duct heated at constant heat input per unit axial length. Briley's results compared very favorably with those of Cheng and Hwang (1969) for the fully developed condition. His velocity distribution (extracted from a plot) is shown in Fig. 3, which also includes the predictions of the present work. The differences are insignificant and are within the inherent uncertainty of reading a graph. The code has also been tested against experimental data on the heat transfer coefficient for a power-law fluid flowing in a circular pipe subjected to the constant heat input per unit axial length and peripherally constant wall temperature (Lawal and Mujumdar, 1987). The relevant parameters for the selected run are as indicated in Fig. 4. It is clearly evident that the numerical code successfully predicts the data.

All the foregoing results and those to be presented were generated from a 21×21 uniform grid at each axial location and the results obtained on a finer grid (41×41) were only marginally different. The axial step size was very small at the entrance ($\Delta X/\mathrm{Re}=2.5\times10^{-5}$) and it became progressively coarser ($\Delta X/\mathrm{Re}=1.25\times10^{-3}$ at $X=2.5$). In general, the computation was terminated at $X\cong0.3$ by which point the flow, for the values of Gr/Re, had become hydrodynamically developed as indicated by the numerically constant slope of the pressure profile. Thermally, the changes in Nu_{X^*} were insignificant (≤1 percent). About 100 steps were required to attain these conditions. As a convergence criterion, we adopted

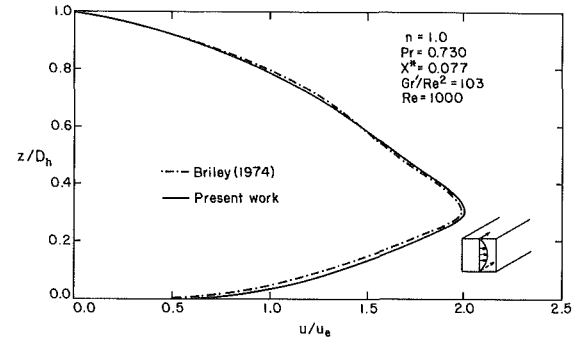

Fig. 3 Centerplane velocity profiles for flow of a Newtonian fluid in mixed convection in a square duct

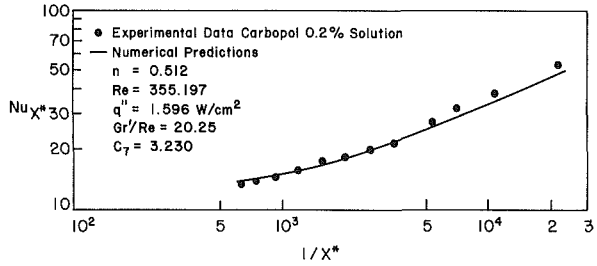

Fig. 4 Comparison of experimental data with numerical predictions for mixed convection, fully developed flow of a power-law fluid in a circular pipe

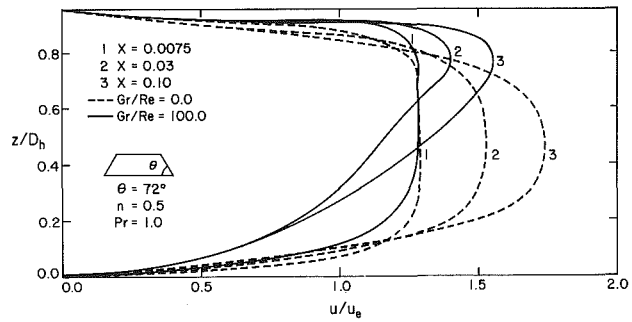

Fig. 5 Axial development of axial velocity through centerplane for a pseudoplastic fluid ($n = 0.5$) in a trapezoidal duct

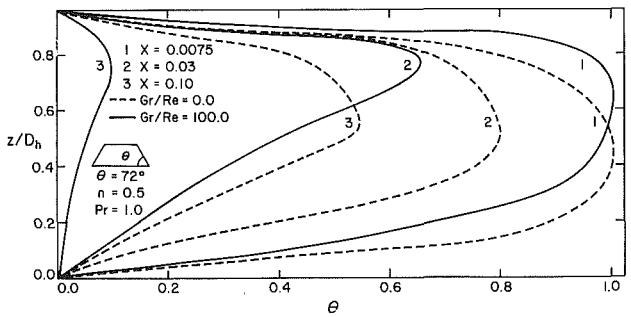

Fig. 6 Axial development of temperature through centerplane for a pseudoplastic fluid ($n = 0.5$) in a trapezoidal duct

$$\epsilon = |f_{i,j}^{(n+1)} - f_{i,j}^{(n)}| / |f_{i,j}^{(n+1)}| < 10^{-5} \tag{16}$$

where $f_{i,j}^{(n)}$ is the value of a dependent variable at the nth iteration level.

The Prandtl number of this work is a generalized Pr, which arises naturally for flow of power-law fluids in arbitrary cross-sectional ducts. Unlike the conventional Prandtl number, it is not a fluid property alone because of its dependence on n, D_h, and u_e, but it reduces to the conventional Pr for a Newtonian fluid ($n = 1$). In the development of the code, cognizance was taken of the fact that a widely applicable code would be preferable. Newtonian gases and liquids are power-law fluids with $\mathrm{Pr} \cong 1$ and a code based on the assumption of infinite Pr will not and has been shown not to be applicable. A generalized code on power-law fluids (Newtonian inclusive) undergoing simultaneous development of both flow and heat transfer is better tested with low Pr. Such a code can be used in studying infinite Pr flows by simply setting Pr equal to a large number.

The temperature dependence of viscosity has been ignored since its superposition will make it difficult to quantify the effect of natural convection (reflected in the value of Gr/Re), the prime objective of this study. Negligible variations of viscosity with temperature and high Gr/Re values are not mutually exclusive, even in practice. The code developed is capable of and in fact has been used in predicting experimental data with variable viscosity (Filkova et al., 1987; Lawal and Mujumdar, 1987).

The importance of natural convection is reflected in the magnitude of the dimensionless group Gr/Re. Since in this parameter the buoyancy force is calculated with respect to $T_e - T_w$ and since for liquids β is positive, $\mathrm{Gr/Re} > 0$ indicates cooling. It can however be easily established that the analysis is equally applicable to heating with the exception of a sign change.

The axial development of the velocity profile for a power-law fluid of $n = 0.5$ and $\mathrm{Gr/Re} = 100$ is shown in Fig. 5, while the corresponding temperature profiles are as indicated on Fig. 6. The qualitative similarity is remarkable but not unexpected. Very close to the entrance ($X = 0.0075$) the effect of natural convection can be perceived already as evidenced by the distortion of the velocity and temperature profiles from their usual parabolic shape.

As we proceed downstream the position of maximum velocity or temperature shifts from the core toward the upper wall under the influence of gravity. The fluid in the core of the duct with higher temperature and lower density rises to replace the heavier fluid in the wall region. But because the wall region is associated with a higher thermal gradient the secondary flow so generated is more intense. Farther downstream ($X = 0.1$) the effects are accentuated as the maximum shifts closer to the wall.

The distribution of the local heat transfer coefficient can now be examined in light of the temperature and velocity profiles development. Depicted in Figs. 7 (*a*, *b*) respectively is the effect of Gr/Re on Nu_{X^*} for a pseudoplastic fluid ($n = 0.5$) and a dilatant fluid ($n = 1.25$). As Gr/Re increases, the location where natural convection becomes important shifts closer to the entrance. Beyond this point, Nu_{X^*} is increased primarily due to the decrease of the bulk temperature brought about by the secondary flow. At a certain axial location, which is Gr/Re dependent, a maximum is reached. At this point, the driving force for buoyancy, which is the difference in temperature between the wall and the fluid, attains an asymptotic value. Thereafter forced convection, which has the effect of reducing Nu_{X^*}, becomes dominant and the Nusselt number therefore approaches the forced convection value from above. Theoretically, the two profiles should merge at infinity, but in practice they become almost indistinguishable at a very large value of X^*. This is in general the qualitative behavior and is more pronounced for the pseudoplastic ($n < 1$) fluids. This can be attributed to the fact that the pseudoplastics are characterized by steeper velocity gradients near the wall (Lawal and Mujumdar, 1984), which expectedly lead to steeper temperature gradients for this mixed convection case. The influence of the power-law index on Nu_{X^*} is more clearly seen from Fig. 8. In the region where natural convection is significant, as Gr/Re increases, the increase in Nu_{X^*} due to pseudoplastic behavior is accentuated. Whereas for pseudoplastic fluids both the non-Newtonian and buoyancy effects augment heat transfer, for shear-thickening fluids, they oppose each other.

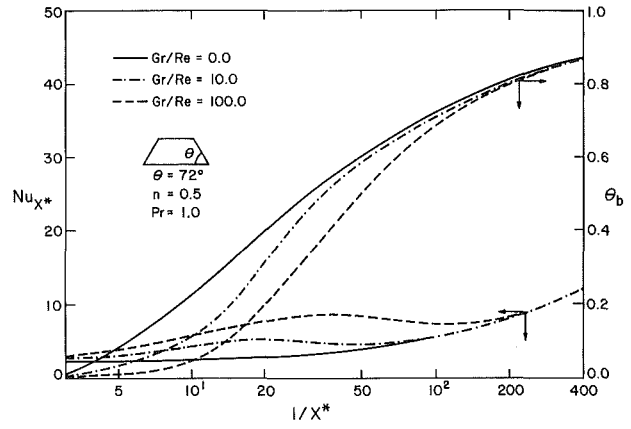

Fig. 7(a)

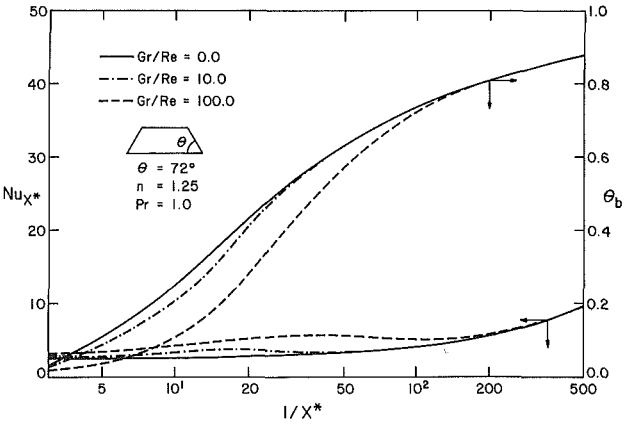

Fig. 7(b)

Fig. 7 Nu_{X^*} and θ_b versus axial coordinate for power-law fluids in a trapezoidal duct

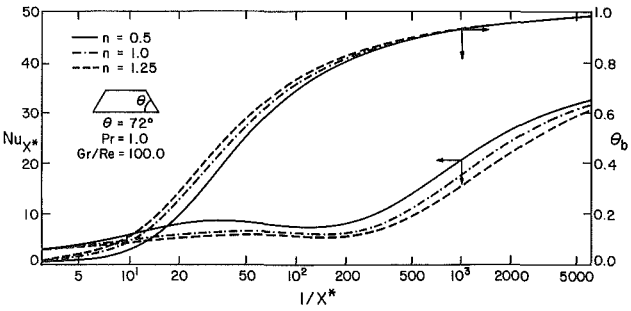

Fig. 8 The effect of power-law index on Nu_{X^*} and θ_b for mixed convection heat transfer in a trapezoidal duct

The dimensionless mean axial pressure ($\bar{P}$) and the maximum axial velocity are plotted in Figs. 9(*a*, *b*) against the axial coordinate. As Gr/Re increases, so does the pressure drop regardless of the value of n. However the increase is more noticeable as the fluid becomes less pseudoplastic. This increase that has been widely observed in horizontal combined convection flows is attributed principally to the increased velocity gradients at the wall. For pure forced convection, u_{max}/u_e increases with axial distance but in mixed convection flows depending on the value of Gr/Re, it is possible for a minimum to appear somewhere along the duct. However, once the buoyancy driving force attains its asymptotic value this effect disappears and forced convection accelerates the flow. Vector plots of secondary flow at a selected axial location are depicted in Fig. 10.

The results for pentagonal, circular, triangular, and square ducts were qualitatively similar to those of the trapezoidal

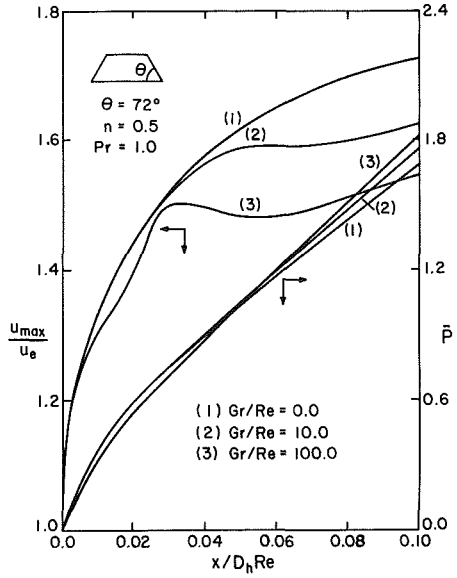

Fig. 9(a)

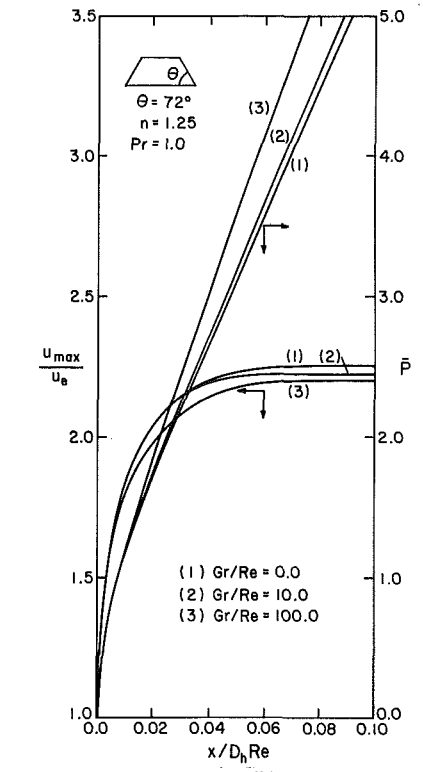

Fig. 9(b)

Fig. 9 u_{max}/u_e and $\bar{P}$ versus axial coordinate for power-law fluids in a trapezoidal duct

ducts; however for high Gr/Re values the triangular duct exhibits a differing behavior.

As was the case for the other geometries the axial development of the velocity profile for the triangular duct bears a striking resemblance to that of the temperature profile. However for Gr/Re = 100.0, the secondary flow due to the natural convection is so intense that local maxima develop near the walls and a minimum in the core. Moreover at $X \simeq 0.04375$, a flow reversal exhibited by negative values of axial velocity occurs. As the parabolic flow assumption does not hold for this situation, any computational effort beyond this point is wasteful. The Nu_{X^*} and θ_b are plotted against axial coordinate in Fig. 11. Again the qualitative behavior of their distribution is similar to that of other geometries except

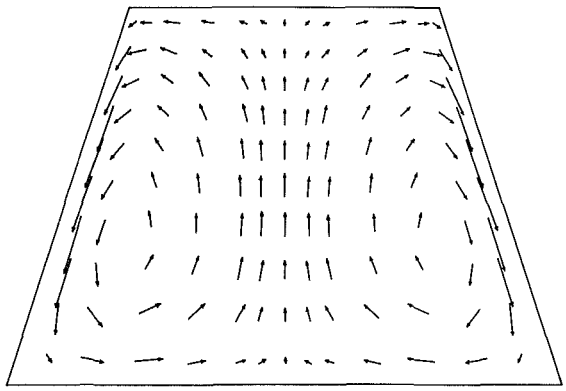

Fig. 10 Vector plots of secondary flow in a trapezoidal duct

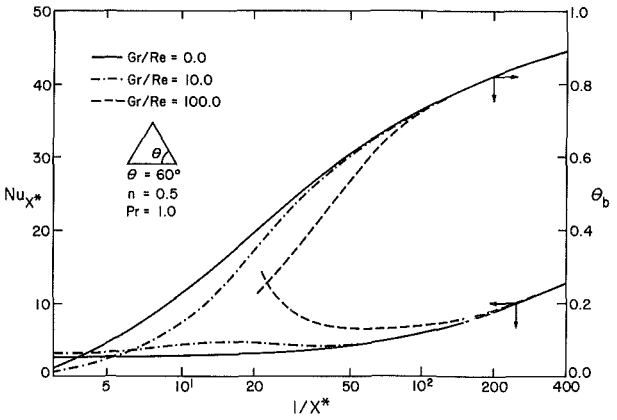

Fig. 11 Nu_X^* and θ_b versus axial coordinate for a pseudoplastic fluid in a triangular duct

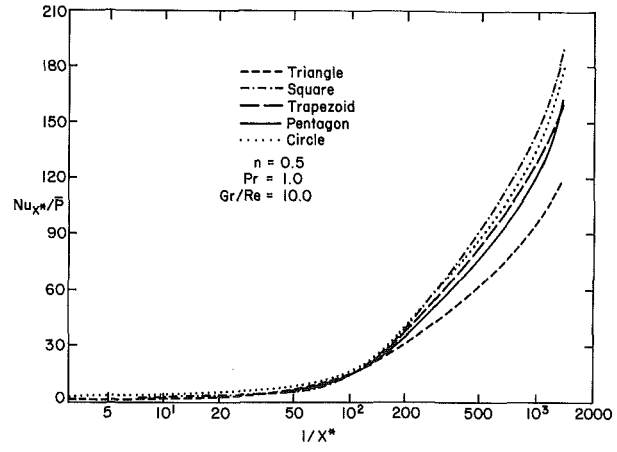

Fig. 12 $Nu_X^*/\bar{P}$ versus axial coordinate for a pseudoplastic fluid ($n = 0.5$) in triangular, square, trapezoidal, pentagonal, and circular ducts

that for $Gr/Re = 100.0$, flow reversal precluded computation beyond $X = 0.04375$.

The Nusselt number and $\bar{P}$, being dimensionless, are independent of the scale of the geometry (e.g., D_h). Hence for the same values of parameters (i.e., Pr, n, Gr/Re) for all the geometries any difference in values of Nu_X^* (or $\bar{P}$) is indicative of the effect of the duct cross-sectional shape regardless of the value of D_h.

Table 1(a) Pressure drop of a pseudoplastic fluid ($n = 0.5$) in mixed convection heat transfer

Axial Location X/Re	Triangle $\bar{P}$	Square $\bar{P}$	Trapezoid $\bar{P}$	Pentagon $\bar{P}$	Circle $\bar{P}$
.00075	0.1959	0.1294	0.1456	0.1427	0.1314
.00150	0.2139	0.1505	0.1663	0.1651	0.1540
.00750	0.3521	0.3145	0.3237	0.3326	0.3156
.03000	0.7765	0.7433	0.7520	0.7700	0.7559
.04875	1.0540	1.0295	1.0345	1.0690	1.0606
.08625	1.5576	1.5703	1.5686	1.6248	1.6402
.10	1.7427	1.7632	1.7622	1.8222	1.8456

Table 1(b) Pressure drop of a Newtonian fluid in mixed convection heat transfer

Axial Location X/Re	Triangle $\bar{P}$	Square $\bar{P}$	Trapezoid $\bar{P}$	Pentagon $\bar{P}$	Circle $\bar{P}$
.00075	0.2463	0.1959	0.2102	0.2179	0.2068
.00150	0.3101	0.2810	0.2896	0.3022	0.2884
.00750	0.6995	0.6913	0.6963	0.6936	0.6943
.03000	1.5883	1.5665	1.5838	1.5843	1.6195
.04875	2.1947	2.1916	2.2108	2.2230	2.3020
.08625	3.3506	3.4051	3.4237	3.4724	3.6222
.10	3.7644	3.8362	3.8548	3.9125	4.0905

Table 1(c) Pressure drop of a shear-thickening fluid ($n = 1.25$) in mixed convection heat transfer

Axial Location X/Re	Triangle $\bar{P}$	Square $\bar{P}$	Trapezoid $\bar{P}$	Pentagon $\bar{P}$	Circle $\bar{P}$
.00075	0.3046	0.2787	0.2874	0.3029	0.2880
.00150	0.4115	0.4081	0.4094	0.4218	0.4110
.00750	0.9665	0.9457	0.9579	0.9490	0.9595
.03000	2.2068	2.1793	2.2024	2.2077	2.2822
.04875	3.0859	3.0867	3.1120	3.1437	3.2863
.08625	4.7883	4.8658	4.8934	4.9731	5.2564
.10	5.4028	5.5062	5.5347	5.6318	5.9675

The ratio $Nu_X^*/\bar{P}$ for each of the five geometries is plotted against axial distance in Fig. 12 for the indicated hydrodynamic and thermal parameters. Very close to the entrance ($1/X^* > 3 \times 10^2$) the square duct seems to be superior to other geometries and as natural convection becomes more pronounced ($1/X^* \simeq 2 \times 10^2$) the circular geometry begins to exhibit better heat transfer characteristics until far downstream, the differences between the geometries become imperceptible.

Of all the geometries considered, the triangular duct appears to be the worst based on criterion adopted and the chosen hydrodynamic and thermal parameters. Actual values of $\bar{P}$ and Nu_X^* at selected axial locations for different values of the power-law index are presented in Tables 1(a–c) and 2(a–c).

Conclusions

The equations governing mixed convection flow and heat transfer to power-law fluids in horizontal arbitrary cross-sectional ducts have been solved using the finite difference technique. The variation of Nu_X^* along the duct indicates that the buoyancy effect can be considered negligible up to a certain axial location, which is dependent on the values of Gr/Re and the power-law index n. Beyond this point, buoyancy force increases Nu_X^* with this effect being more pronounced with the pseudoplastic fluids than the shear-thickening fluids. The pressure drop is also significantly increased by natural convection with the pseudoplastic fluids experiencing less increase than either the Newtonian or the shear-thickening fluids.

For each geometry, there is a critical value of Gr/Re above which flow reversal would occur. The results of this study showed that the critical value for the triangular duct is lower than that of the other geometries considered in this work. It is also expected that this value would be dependent on the

Table 2(*a*) Nu_{X^*} for a pseudoplastic fluid ($n = 0.5$) in mixed convection heat transfer

Axial Location X^*	Triangle Nu_{X^*}	Square Nu_{X^*}	Trapezoid Nu_{X^*}	Pentagon Nu_{X^*}	Circle Nu_{X^*}
.00075	23.3830	24.6699	23.1372	23.2887	23.4882
.00150	16.1957	17.0826	16.7629	16.0036	16.6749
.00750	7.0729	6.2721	6.5019	6.7416	6.8954
.03000	3.9667	4.8272	4.7882	4.8341	5.8847
.04875	4.3288	5.4743	5.3908	5.5378	6.3674
.08625	4.1753	4.7150	4.6330	4.9147	5.2322
.10	4.0146	4.4209	4.3501	4.6118	4.9163
.20	3.5670	3.9191	3.8629	4.0907	4.3755

Table 2(*b*) Nu_{X^*} for a Newtonian fluid in mixed convection heat transfer

Axial Location X^*	Triangle Nu_{X^*}	Square Nu_{X^*}	Trapezoid Nu_{X^*}	Pentagon Nu_{X^*}	Circle Nu_{X^*}
.00075	18.6934	21.6561	20.4389	19.4359	20.3844
.00150	14.6235	13.1817	13.7278	12.4737	13.5074
.00750	5.5506	5.0604	5.1437	5.6593	5.6243
.03000	3.3075	3.8114	3.7323	3.9165	4.4714
.04875	3.3590	4.0724	3.9559	4.0891	4.6730
.08625	3.3355	3.8398	3.7397	3.9040	4.2991
.10	3.2524	3.6856	3.5947	3.7807	4.1463
.20	2.8784	3.2632	3.1820	3.3482	3.6739

Table 2(c) Nu_{X^*} for a shear-thickening fluid ($n = 1.25$) in mixed convection heat transfer

Axial Location X^*	Triangle Nu_{X^*}	Square Nu_{X^*}	Trapezoid Nu_{X^*}	Pentagon Nu_{X^*}	Circle Nu_{X^*}
.00075	17.6337	18.7241	18.1807	16.6315	18.0431
.00150	13.3535	10.7443	11.7872	10.7682	11.5787
.00750	4.9775	4.7815	4.7798	5.3171	5.3099
.03000	3.0853	3.4923	3.4211	3.6440	4.0833
.04875	3.0123	3.5570	3.4604	3.6730	4.1302
.08625	2.9886	3.4700	3.3769	3.5901	3.9494
.10	2.9416	3.3845	3.2952	3.5202	3.8610
.20	2.5960	2.9899	2.9097	3.1104	3.4131

power-law index. Further numerical experimentation involving wider parameter ranges is required to investigate this in detail.

Acknowledgments

The author wishes to express his gratitude to the McGill University Computing Centre, Montreal, Canada and Shell Petroleum Development Company Limited, Port Harcourt, Nigeria for making available the computing time required for the completion of the work reported in this paper. The line drawings were skillfully prepared by Mrs. C. Braide while the typing of the manuscript was excellently done by Mr. A. Anele. The continued encouragement provided by Ms. Yinka Princewill during the preparation of this paper is gratefully acknowledged.

References

Briley, W. R., 1974, "Numerical Method for Predicting Three-Dimensional Steady Viscous Flow In Ducts," *J. Comp. Phys.*, Vol. 14, pp. 8–28.

Cheng, K. C., and Hwang, G., 1969, "Numerical Solution for Combined Free and Forced Laminar Convection in Horizontal Rectangular Channels," ASME JOURNAL OF HEAT TRANSFER, Vol. 91, pp. 59–66.

Cheng, K. C., Hong, S. W., and Hwang, G. J., 1972, "Buoyancy Effects on Laminar Heat Transfer in the Thermal Entrance Region of Horizontal Rectangular Channels With Uniform Wall Heat Flux for Large Prandtl Number Fluid," *Int. J. Heat Mass Transfer*, Vol. 15, pp. 1819–1836.

Filkova, I., Lawal, A., Koziskova, B., and Mujumdar, A. S., 1987, "Heat Transfer to a Power-Law Fluid in Tube Flow: Numerical and Experimental Studies," *Journal of Food Engineering*, Vol. 6, pp. 143–151.

Gori, F., 1978a, "Variable Physical Properties in Laminar Heating of Pseudoplastic Fluid with Constant Wall Heat Flux," ASME JOURNAL OF HEAT TRANSFER, Vol. 110, pp. 220–223.

Gori, F., 1978b, "Effects of Variable Physical Properties in Laminar Flow of Pseudoplastic Fluids," *Int. J. Heat Mass Transfer*, Vol. 21, pp. 247–250.

Greif, R., 1978, "An Experimental and Theoretical Study of Heat Transfer in Vertical Tube Flows," ASME JOURNAL OF HEAT TRANSFER, Vol. 100, pp. 86–91.

Lawal, A., 1985, "Laminar Flow and Heat Transfer To Variable Property Power-Law Fluids in Arbitrary Cross-Sectional Ducts," Ph.D. Thesis, McGill University, Montreal, Canada.

Lawal, A., and Mujumdar, A. S., 1984, "Forced Convection Heat Transfer to a Power-Law Fluid in Arbitrary Cross-Section Ducts," *Can. J. Chem. Eng.*, Vol.. 62, pp. 326–333.

Lawal, A., and Mujumdar, A. S., 1985, "Laminar Flow and Heat Transfer in Power-Law Fluids Flowing in Arbitrary Cross-Sectional Ducts," *Numerical Heat Transfer*, Vol. 8, pp. 217–244.

Lawal, A., and Mujumdar, A. S., 1988, "Experimental Study of Heat Transfer to Pseudoplastic Fluids in Square and Circular Tubes," *Chem. Eng. Comm.*, in press.

Marner, W. J., and McMillan, H. K., 1972, "Combined Free and Forced Laminar Non-Newtonian Convection in a Vertical Tube with Constant Wall Temperature," *Chem. Eng. Sci.*, Vol. 27, pp. 473–488.

Mobley, C. D., and Stewart, R. J., 1980, "On the Numerical Generation of Boundary-Fitted Orthogonal Curvilinear Coordinate Systems," *J. Comp. Phys.*, Vol. 34, pp. 124–135.

Nakamura, H., Matsuura, A., Kiwaki, J., Hiraoka, S., and Yamada, I., 1977, "Combined Free and Forced Laminar Convection in Triangular Ducts," *Journal of Chemical Engineering of Japan*, Vol. 10, pp. 109–116.

Nakamura, H., Matsuura, A., Kiwaki, J., Hiraoka, S., and Yamada, I., 1980, "Combined Free and Forced Laminar Convection in Thermal Entrance Region of Horizontal Triangular Ducts," *Journal of Chemical Engineering of Japan*, Vol. 13, pp. 110–116.

Newell, P. H., and Bergles, A. E., 1970, "Analysis of Combined Free and Forced Convection for Fully Developed Laminar Flow in Horizontal Tubes," ASME JOURNAL OF HEAT TRANSFER, Vol. 92, pp. 83–93.

Oliver, D. R., and Jenson, V. G., 1964, "Heat Transfer to Pseudoplastic Fluids in Laminar Flow in Horizontal Tubes," *Chem. Eng. Sci.*, Vol. 19, pp. 115–129.

Ou, J., Cheng, K. C., and Lin, R., 1974, "Natural Convection Effects on Graetz Problem in Horizontal Rectangular Channels With Uniform Wall Temperature For Large Pr," *Int. J. Heat Mass Transfer*, Vol. 17, pp. 835–843.

Zeldin, B., and Schmidt, F. W., 1972, "Developing Flow With Combined Forced-Free Convection in an Isothermal Vertical Tube," ASME JOURNAL OF HEAT TRANSFER, Vol. 94, pp. 211–223.

Theory of Melting With Natural Convection in an Enclosed Porous Medium

A. Bejan
Department of Mechanical Engineering and Materials Science, Duke University, Durham, NC 27706
Fellow ASME

This paper reports a complete theory of the melting that occurs in a confined porous medium saturated with phase-change material and heated from the side. Darcy flow characteristics are assumed for the liquid phase. The solid phase is isothermal and at the melting point. The first part of the paper reports a matched boundary layer solution for natural convection dominated melting in the quasi-steady regime. The second part reports a solution for the heat transfer during the two earlier regimes, pure conduction followed by mixed conduction and convection. Together, the two solutions cover the entire history of transient heating administered from the side. This theory shows that the liquid-side Stefan number has a profound effect on the heat transfer and melting rates.

1 Background

The objective of this paper is to report a theoretical solution to the problem of melting in the presence of natural convection in a porous medium saturated with a phase-change material. The porous medium is held in a rectangular enclosure, which is being heated from the side. The porous medium is initially saturated with solid phase-change material; its initial temperature is uniform and equal to the melting point of the phase-change material. The heating from the side consists of suddenly raising the side wall temperature and maintaining it at a constant level above the melting point.

The general subject of melting in a porous medium saturated with phase-change material has received increasing attention during the past decade (see, for example, Epstein and Cho, 1976; Reid, 1978; Okada and Fukumoto, 1982; Weaver, 1985; Weaver and Viskanta, 1985, 1986a, 1986b; Chellaiah and Viskanta, 1987a, 1987b, Kazmierczak et al., 1987). Most closely related to the problem stated in the first paragraph are the studies of Kazmierczak et al. (1986) and Jany and Bejan (1988). Kazmierczak et al. (1986) have reported the similarity solution for the natural convection boundary layer near the solid–liquid interface in a porous medium whose liquid-saturated zone is infinitely large and isothermal. They showed that the Stefan number (the degree of superheat of the liquid) has a profound effect on the heat transfer and melting rates. Jany and Bejan (1988) considered the confined porous medium melting problem stated in the first paragraph. Relying on scale analysis and numerical experiments in the limit of vanishing Stefan numbers, they showed that the melting process follows a sequence of characteristic "regimes," namely, (*i*) conduction, (*ii*) mixed conduction and convection, and (*iii*) convection.

Worth noting is that the present porous medium problem has a very important counterpart in the field of melting with natural convection in fluids (i.e., in the absence of a porous matrix). The voluminous literature that has been devoted to the fluid problem was reviewed not long ago by Viskanta (1985). Finite-difference analyses of the fluid version of the problem have been reported by Sparrow et al. (1977), Ho and Viskanta (1984), Gadgil and Gobin (1984), Okada (1984), and Webb and Viskanta (1986). The ultimate objective of the work described in this paper is to demonstrate that it is possible to construct a purely analytical treatment that covers the entire three-regime sequence of the transient heating and melting phenomenon.

2 The Cold Boundary Layer

We begin with the analysis of the "convection dominated regime" (Jany and Bejan, 1988), whose equivalent in an enclosed phase-change material without a porous matrix is better known as the "quasi-steady regime" (e.g., Viskanta, 1985; Webb and Viskanta, 1985). The main features of the temperature distribution in the liquid space are the two distinct boundary layers that line the heated wall and the solid–liquid interface (Fig. 1). The core region of the liquid space is thermally stratified: Its temperature is represented by the unknown function $T_c(y)$. The horizontal boundary layers that line the top and bottom walls and the details of the flow in the four corners are being neglected.

The analysis consists of first obtaining temperature and flow field solutions for the two vertical boundary layer regions, and then meshing these solutions with a third (unique) solution for the core region. This approach is the same as the one used by Weber (1975) and Simpkins and Blythe (1980) in the theoretical study of pure natural convection (without melting) in a rectangular porous medium heated fron the side.

Consider first the cold boundary layer shown on the left side of Fig. 1. The Cartesian system of coordinates x–y is attached to the solid–liquid interface. In this system, the melting that occurs at the interface sustains a finite flow of liquid across the $x = 0$ surface, into the cold boundary layer. The horizontal velocity of the liquid flow through the $x = 0$ surface, $u_0(y)$, is one of the important unknowns of the problem, as it represents the rate of steady erosion of the solid–liquid interface.

The boundary layer-simplified equations for momentum and energy in the cold layer are well known (see, for example, Bejan, 1984)

$$\frac{\partial v}{\partial x} = \frac{Kg\beta}{\nu}\frac{\partial T}{\partial x} \tag{1}$$

$$u\frac{\partial T}{\partial x} + v\frac{\partial T}{\partial y} = \alpha\frac{\partial^2 T}{\partial x^2} \tag{2}$$

They hold for a homogeneous and isotropic porous medium saturated with a liquid whose flow is slow enough to conform to the Darcy regime. The velocity components (u, v) are volume-averaged quantities. The temperature (T) is the local temperature of both the liquid and the solid matrix, which are

Contributed by the Heat Transfer Division for publication in the JOURNAL OF HEAT TRANSFER. Manuscript received by the Heat Transfer Division January 29, 1988. Keywords: Natural Convection, Phase-Change Phenomena, Porous Media.

locally in thermal equilibrium. The thermal diffusivity (α) is defined as the ratio between the effective thermal conductivity of the porous matrix saturated with liquid, divided by the heat capacity (ρc) of the liquid alone.

The liquid is being treated as incompressible everywhere except in the buoyancy term (the right side) of the momentum equation (1), in which the density gradient $\partial\rho/\partial x$ has been replaced by $-\rho\beta\partial T/\partial x$. This substitution is appropriate when $\beta\Delta T \ll 1$, where β and ΔT are the coefficient of thermal expansion and the temperature difference maintained between the heated wall and the solid. The latter is isothermal and at the melting point T_m. The physical properties K, β, ν, and α are assumed constant; their definitions can be found in the Nomenclature.

It was shown by Weber (1975) that the Oseen-linearized version of the boundary layer energy equation (2) admits an analytical solution for temperature in terms of exponentials in x. Fitting Weber's exponential profiles to the present problem, we write immediately

$$T = T_c(1 - e^{-x/\delta}) \tag{3}$$

where T_c is the temperature difference between the core and the solid–liquid interface. Likewise, T is the temperature excess above the melting point of the phase-change material (note that $T = 0$ along the $y = 0$ interface). The unknown function $\delta(y)$ is the thickness of the cold boundary layer. The assumption that the core is thermally stratified (T_c) is supported by the high-Ra isotherm patterns obtained in a numerical simulation of the same phenomenon by Jany and Bejan (1987). The assumption of exponential temperature profile, equation (3), is not mandatory: Other profile shapes can be used in this type of analysis, as was demonstrated by Simpkins and Blythe (1980).

The corresponding vertical velocity profile is obtained by substituting equation (3) into equation (1), integrating once in x, and imposing the far-field condition $v \to 0$ as $x/\delta \to \infty$. The result is

$$v = -\frac{Kg\beta}{\nu} T_c\, e^{-x/\delta} \tag{4}$$

The T and v profiles presented above do not satisfy the energy equation (2) exactly. In accordance with Weber's (1975) method, we force these profiles to satisfy the integral form of the energy equation, that is, the result of integrating equation (2) from $x = 0$ to $x = \infty$:

$$u_\infty T_c - u_0 T_0 + \frac{d}{dy}\int_0^\infty vT dx = -\alpha\left(\frac{\partial T}{\partial x}\right)_{x=0} \tag{5}$$

The second term on the left side vanishes because T_0 (i.e., the value of T on the solid–liquid interface) is zero. The unknown horizontal velocity far from the phase-change interface $u_\infty(y)$ follows from the integral of the mass conservation equation

$$\frac{\partial u}{\partial x} + \frac{\partial v}{\partial y} = 0 \tag{6}$$

which is

$$u_\infty - u_0 + \frac{d}{dy}\int_0^\infty v dx = 0 \tag{7}$$

Finally, the velocity through the $x = 0$ interface u_0 is related to the heat flux impinging on the interface

$$k\left(\frac{\partial T}{\partial x}\right)_{x=0} = \rho h_{sf} u_0 \tag{8}$$

In other words, after using equation (3)

$$u_0 = \frac{kT_c}{\rho h_{sf}\delta} \tag{9}$$

It is worth noting that the porosity of the medium does not appear as a factor on the right side of equation (8), because u_0 is a volume-averaged velocity. The factor h_{sf} is the product of the latent heat times the porosity of the medium. It is assumed further that the solid and liquid phases of the phase-change material have the same density (ρ).

At this point we can skip the algebra and report the result of combining equations (5), (7), and (9), i.e., the energy integral condition

$$\mathrm{Ste}\,\tau + \frac{1}{2}\tau\tilde{\delta}\frac{d\tilde{\delta}}{d\tilde{y}} = -1 \tag{10}$$

This dimensionless form is based on the following definitions:

$$\tilde{y} = \frac{y}{H} \tag{11}$$

$$\tilde{\delta} = \frac{\delta}{H}\mathrm{Ra}^{1/2} \tag{12}$$

Nomenclature

A = function, equation (34)
c = specific heat of liquid
C = constant, equation (29)
C_1 = constant, equation (53)
F = function of Stefan number, equation (42)
F_r = function of Stefan number, equation (38)
g = gravitational acceleration
G_c = function of Stefan number, equation (62)
G_0 = function of Stefan number, equation (61)
h_{sf} = latent heat of fusion, multiplied by the porosity
H = height
I = integral, equation (57)
k = thermal conductivity of liquid-saturated porous medium
K = permeability
m, n = dummy variables
Nu = overall Nusselt number for the cold side, equation (40)
Nu_r = overall Nusselt number for the warm (right) side, equation (36)
Q = overall heat transfer rate into the solid–liquid interface, equation (39)
Q_c = convective contribution during the mixed regime, equation (56)
Q_r = overall heat transfer rate through the heated (right) wall, equation (35)
Ra = Darcy-modified Rayleigh number, equation (15)
s = deflection of the solid–liquid interface
Ste = Stefan number, equation (14)
t = time
T = excess temperature of the cold boundary layer (the difference between the actual temperature and the melting point T_m)
ΔT = temperature difference between the heated wall and the solid–liquid interface (T_m)
T_c = excess temperature of the core region
T_r = excess temperature of the warm boundary layer
u, v = volume-averaged velocity components in the cold boundary layer
u_c = horizontal velocity in the core region

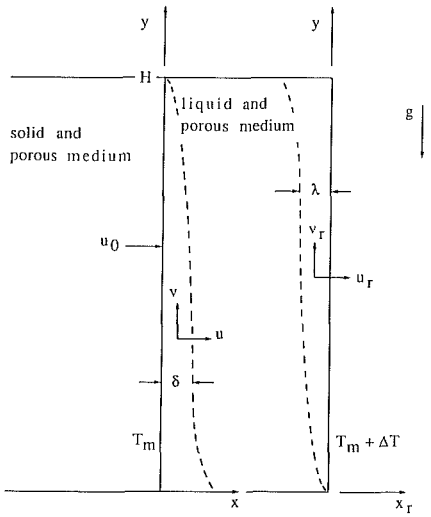

Fig. 1 Confined porous medium saturated with phase-change material, being heated from the right

$$\tau = \frac{T_c}{\Delta T} \tag{13}$$

$$\mathrm{Ste} = \frac{c\Delta T}{h_{sf}} \tag{14}$$

The Stefan number Ste measures the degree of superheat experienced by the liquid phase (note that c is the lone specific heat of the liquid). The Rayleigh number appearing in equation (12) is the classical Darcy-modified group,

$$\mathrm{Ra} = \frac{Kg\beta H\Delta T}{\alpha\nu} \tag{15}$$

The analysis of the cold boundary ends with the observation that the mass conservation integral (7) yields the following dimensionless equation:

$$\tilde{u}_\infty = \frac{\tau}{\tilde{\delta}}\,\mathrm{Ste} + \frac{d}{d\tilde{y}}(\tau\tilde{\delta}) \tag{16}$$

The dimensionless far-field velocity $\tilde{u}_\infty$ is defined as

$$\tilde{u}_\infty = \frac{u_\infty}{\alpha/H}\,\mathrm{Ra}^{-1/2} \tag{17}$$

In summary, the analysis concludes with two differential equations [namely (10) and (16)] that relate three unknown functions (τ, $\tilde{\delta}$, and $\tilde{u}_\infty$). In order to close the problem we turn our attention to the boundary layer that coats the heated wall of the enclosure.

3 The Warm Boundary Layer

Consider now the Cartesian frame x_r–y attached to the right wall, whose temperature is $T = \Delta T$. The equations for momentum and energy conservation are the same as equations (1) and (2), in which x is now replaced by x_r and (T, u, v) by (T_r, u_r, v_r). The warm boundary layer (thickness λ) extends toward negative x_r values. The analysis of this layer follows the steps outlined in the preceding section; therefore, in the interest of conciseness, we review only the main results.

The exponential profiles for excess temperature and vertical velocity are

$$T_r = T_c + (\Delta T - T_c)e^{x_r/\lambda} \tag{18}$$

$$v_r = \frac{Kg\beta}{\nu}(\Delta T - T_c)e^{x_r/\lambda} \tag{19}$$

The energy integral condition is obtained by integrating equation (2) from $x_r = 0$ to $x_r = -\infty$

$$(u_r)_{-\infty}T_c - u_{r,0}\Delta T + \frac{d}{dy}\int_0^{-\infty} v_r T_r\,dx_r = -\alpha\left(\frac{\partial T_r}{\partial x_r}\right)_{x_r=0} \tag{20}$$

The mass conservation integral is obtained similarly

$$(u_r)_{-\infty} - u_{r,0} + \frac{d}{dy}\int_0^{-\infty} v_r\,dx_r = 0 \tag{21}$$

In both integral conditions the impermeable wall description requires $u_{r,0} = 0$. The far-field horizontal velocity is the actual velocity in the core region, $u_c(y)$, unknown,

$$(u_r)_{-\infty} = u_c \tag{22}$$

Finally, the dimensionless counterparts of equations (20) and (21) are

$$\tau\frac{d}{d\tilde{y}}\left[\tilde{\lambda}(1-\tau)\right] - \frac{1}{2}\frac{d}{d\tilde{y}}\left[\tilde{\lambda}(1-\tau^2)\right] = -\frac{1-\tau}{\tilde{\lambda}} \tag{23}$$

$$\tilde{u}_c = \frac{d}{d\tilde{y}}\left[\tilde{\lambda}(1-\tau)\right] \tag{24}$$

in which the new dimensionless variables are

Nomenclature (cont.)

$\tilde{u}_c$ = dimensionless horizontal velocity in the core region, equation (26)
u_r, v_r = volume-averaged velocity components in the warm boundary layer
u_0 = melting velocity, equation (9)
$\tilde{u}_0$ = dimensionless melting velocity, equation (43)
u_∞ = horizontal velocity outside the cold boundary layer
$\tilde{u}_\infty$ = dimensionless velocity outside the cold boundary layer, equation (17)
$u_{0,\mathrm{avg}}$ = average melting rate, equation (44)
$\tilde{u}_{0,\mathrm{avg}}$ = dimensionless average melting rate, equation (45)
x, y = system of coordinates attached to the solid–liquid interface, Fig. 1
x_r, y = system of coordinates attached to the heated wall, Fig. 1
x_1, y = system of coordinates attached to the heated wall, Fig. 7
X = thickness of the liquid-saturated zone during the mixed conduction and convection regime, equation (40)
$\tilde{y}$ = dimensionless vertical position, equation (11)
α = thermal diffusivity of liquid-saturated porous medium
β = coefficient of thermal expansion
δ = thickness of the cold boundary layer
$\tilde{\delta}$ = dimensionless cold boundary layer thickness, equation (12)
θ = dimensionless time, equation (52)
λ = thickness of the warm boundary layer
$\tilde{\lambda}$ = dimensionless warm boundary layer thickness, equation (25)
Λ = function of Stefan number, equation (49)
ν = kinematic viscosity
ρ = density
τ = dimensionless core temperature, equation (13)

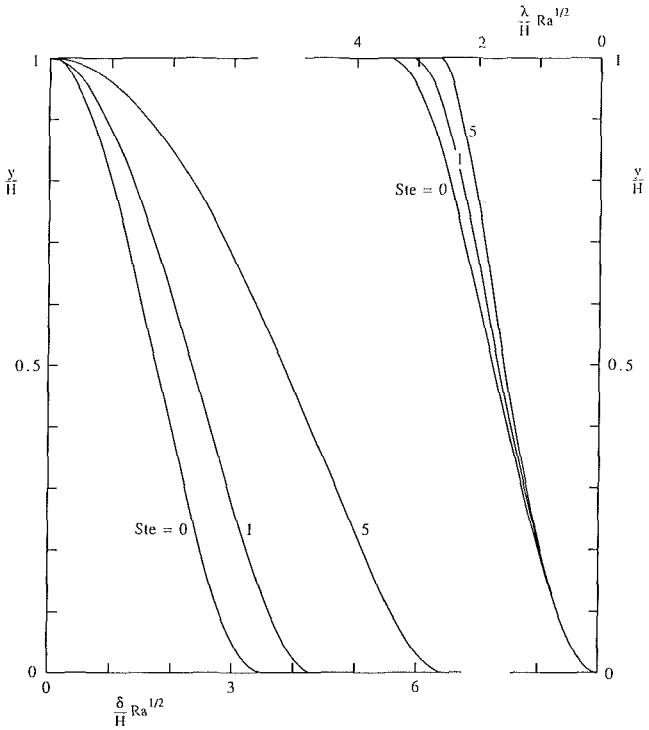

Fig. 2 The thicknesses of the cold boundary layer (left side) and warm boundary layer (right side)

$$\tilde{\lambda} = \frac{\lambda}{H}\,\mathrm{Ra}^{1/2} \tag{25}$$

$$\tilde{u}_c = \frac{u_c}{\alpha/H}\,\mathrm{Ra}^{-1/2} \tag{26}$$

In summary, the analysis of the warm boundary layers produces two additional equations, (23) and (24), involving two additional unknowns, $\tilde{\lambda}$ and $\tilde{u}_c$. The closure problem recognized in the last paragraph of section 2 persists, which is why we consider next the task of matching the cold and warm boundary layer solutions to a unique core region solution.

4 Matched Boundary Layer Solution

The core region is characterized by thermal stratification, $T_o(y)$, zero vertical velocity, and horizontal flow, $u_c(y)$. The latter completes the loop started by the two vertical boundary layer flows.

The existence of a unique core temperature distribution was recognized already in sections 2 and 3, where a unique T_c (or τ) appears in the analysis. In the case of the far-field horizontal velocity, however, a distinction had to be made because the $u_\infty(y)$ of section 2 is not the same as the $u_c(y)$ of section 3. The difference between u_∞ and u_c stems from the fact that the x-y frame of the cold boundary layer moves to the left (i.e., away from the stationary core) with the melting speed $u_0(y)$. The relationship between the two is purely kinematic

$$u_\infty - u_0 = u_c \tag{27}$$

Substituting into this last equation the u_∞, u_0, and u_c estimates provided, respectively, by equations (16), (9), and (24), we obtain finally the relation needed for closing the problem

$$\frac{d}{d\tilde{y}}(\tau\tilde{\delta}) = \frac{d}{d\tilde{y}}\left[(1-\tau)\tilde{\lambda}\right] \tag{28}$$

The problem reduces to solving equations (10), (23), and (28) for only three unknowns, τ, $\tilde{\delta}$, and $\tilde{\lambda}$. The integration of equation (28) leads to

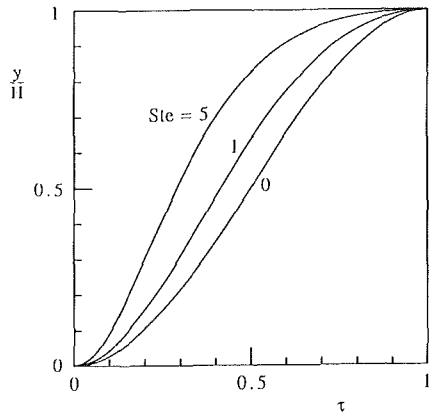

Fig. 3 Temperature distribution in the core region

$$\tau\tilde{\delta} = (1-\tau)\tilde{\lambda} + C \tag{29}$$

in which the constant C is zero because the starting thickness of the warm layer ($\tilde{\lambda}$) is zero at $\tilde{y} = 0$, where the core region also reaches its lowest temperature, $\tau = 0$. Conversely, C must be zero so that $\tilde{\delta} = 0$ at the top of the enclosure, where $\tau = 1$. Either of these arguments is equivalent to claiming that the top and bottom walls of the liquid-saturated zone are impermeable. This claim means that $\tau(0) = 0$ and $\tilde{\delta}(1) = 0$ [see equation (4)] and that $\tau(1) = 1$ and $\tilde{\lambda}(0) = 0$ [cf. equation (19)]. Finally, the elimination of $\tilde{\lambda}$ between equations (29) and (23) yields

$$\frac{d}{d\tilde{y}}\left(\frac{\tau\tilde{\delta}}{1-\tau}\right) = \frac{2}{\tau\tilde{\delta}} \tag{30}$$

Equations (10) and (30) can be integrated analytically by first eliminating $\tilde{y}$ between them. The key results of the analytical solution are

$$\tilde{\delta} = A(1-\tau)(1+\tau^2\mathrm{Ste})^{-1/2} \tag{31}$$

$$\tilde{\lambda} = A\tau(1+\tau^2\mathrm{Ste})^{-1/2} \tag{32}$$

$$\tilde{y} = \frac{A^2}{4\,\mathrm{Ste}}\left[\frac{\tau(1+\tau\,\mathrm{Ste})}{1+\tau^2\mathrm{Ste}} - \frac{\tan^{-1}(\tau\,\mathrm{Ste}^{1/2})}{\mathrm{Ste}^{1/2}}\right] \tag{33}$$

where A depends only on the Stefan number

$$A = 2\,\mathrm{Ste}^{1/2}\left[1 - \frac{\tan^{-1}(\mathrm{Ste}^{1/2})}{\mathrm{Ste}^{1/2}}\right]^{-1/2} \tag{34}$$

The left side of Fig. 2 shows the solution obtained for the cold boundary layer thickness. The function $\tilde{\delta}(\tilde{y})$ increases monotonically in the flow direction (downward); its bottom value $\tilde{\delta}(0)$ is finite. The contribution of the present solution over Weber's is that its documents the Stefan number effect. The cold boundary layer thickness increases substantially as the Stefan number increases.

Figure 3 illustrates the manner in which the core temperature distribution responds to changes in the Stefan number. The core temperature distribution is symmetric about the midheight level only when Ste = 0. The core temperature decreases at all levels as Ste increases above zero. Said another way, the average core temperature in the melting and natural convection problem (finite Ste) is always lower than the average core temperature in the pure natural convection problem (Ste = 0).

The thickness of the warm boundary layer has been plotted on the right side of Fig. 2. We learn in this way that the warm boundary layer becomes thinner as the Stefan number increases. The Ste effect on the warm layer, however, is less pronounced than on the boundary layer that descends along the solid-liquid interface.

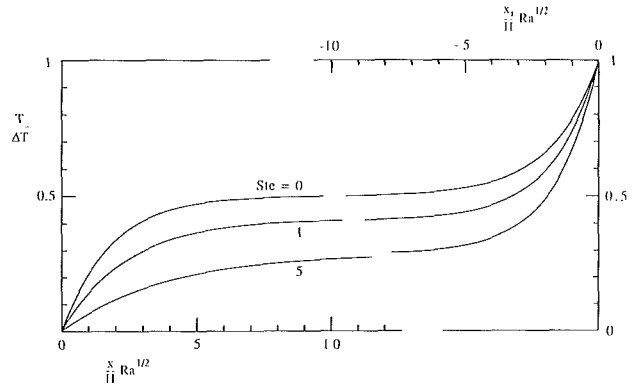

Fig. 4 Temperature distribution across the liquid-saturated region ($\tilde{y} = 0.5$)

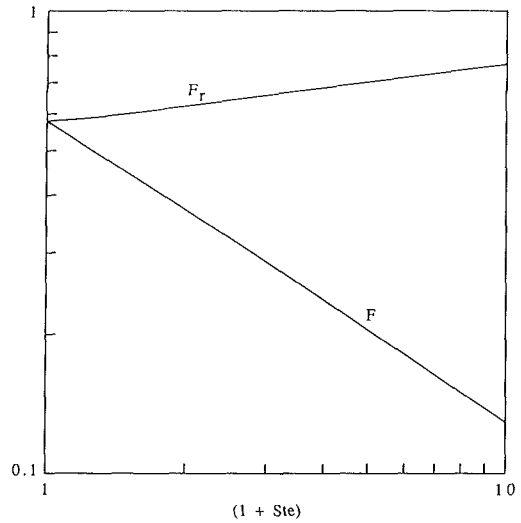

Fig. 5 Stefan number effect on the chief results of the matched boundary layer solution

All these features are evident in Fig. 4, which shows the distribution of temperature across the liquid zone at midheight. The curves have been drawn by combining the $\tau(0.5)$, $\tilde{\delta}(0.5)$, and $\tilde{\lambda}(0.5)$ values with the temperature profile expressions (3) and (18). This figure shows how the two boundary layer solutions mesh in the core region, that is, sufficiently far from both vertical surfaces. Regardless of horizontal location, the temperature decreases steadily as the Stefan number increases. These changes are accompanied also by the thickening of the cold boundary layer and the thinning of the warm layer.

5 The Heat Transfer and Melting Rates

The more useful result of the preceding theory is the ability to predict the rate at which the melting and natural convection process draws heat from the right wall of the system. This heat transfer rate is

$$Q_r = k \int_0^H \left(\frac{\partial T_r}{\partial x_r}\right)_{x_r=0} dy \tag{35}$$

or, as an overall Nusselt number

$$\mathrm{Nu}_r = \frac{Q_r}{k\Delta T} = \mathrm{Ra}^{1/2} F_r\,(\mathrm{Ste}) \tag{36}$$

where

$$F_r(\mathrm{Ste}) = \int_0^1 \frac{1-\tau}{\tilde{\lambda}}\, d\tilde{y} \tag{37}$$

and, after using equations (32) and (33)

Table 1 Stefan number effect on the solution for the quasi-steady convection regime

Ste	$\tilde{\delta}(0)$	$\tilde{\lambda}(1)$	F	F_r
0	3.464	3.464	0.577	0.577
0.2	3.662	3.343	0.517	0.593
0.5	3.929	3.208	0.451	0.613
0.8	4.169	3.107	0.402	0.629
1	4.317	3.053	0.376	0.638
2	4.965	2.867	0.289	0.673
5	6.418	2.620	0.181	0.732
10	8.164	2.462	0.118	0.779

$$F_r = \frac{\mathrm{Ste}^{3/4}}{[\mathrm{Ste}^{1/2} - \tan^{-1}(\mathrm{Ste}^{1/2})]^{1/2}} \left\{ \frac{(\mathrm{Ste}-1)(\mathrm{Ste}+1)^{1/2} - 2\,\mathrm{Ste}}{\mathrm{Ste}(\mathrm{Ste}+1)} + \mathrm{Ste}^{-3/2} \ln[\mathrm{Ste}^{1/2} + (\mathrm{Ste}+1)^{1/2}] \right\} \tag{38}$$

The approximate proportionality $\mathrm{Nu}_r \sim \mathrm{Ra}^{1/2}$ revealed by equation (36) is expected from the scale analysis of the same problem (Jany and Bejan, 1988). The new aspect unveiled by the present solution is the effect of the Stefan number. Representative F_r values are presented in Table 1 and as the top curve in Fig. 5. These values show that the heat transfer rate in the quasi-steady regime increases gradually as the Stefan number increases.

One quantity of interest on the cold side of the liquid-saturated region is the overall heat transfer rate into the solid-liquid interface,

$$Q = k \int_0^H \left(\frac{\partial T}{\partial x}\right)_{x=0} dy \tag{39}$$

or the left-side Nusselt number

$$\mathrm{Nu} = \frac{Q}{k\Delta T} = \mathrm{Ra}^{1/2} F(\mathrm{Ste}) \tag{40}$$

in which F is shorthand for the integral

$$F(\mathrm{Ste}) = \int_0^1 \frac{\tau}{\tilde{\delta}}\, d\tilde{y} \tag{41}$$

This integral can be evaluated using equations (31) and (33)

$$F = \frac{\mathrm{Ste}^{-3/4}}{[\mathrm{Ste}^{1/2} - \tan^{-1}(\mathrm{Ste}^{1/2})]^{1/2}} \times \left\{ \ln[\mathrm{Ste}^{1/2} + (\mathrm{Ste}+1)^{1/2}] - \left(\frac{\mathrm{Ste}}{\mathrm{Ste}+1}\right)^{1/2} \right\} \tag{42}$$

and its behavior is illustrated in Table 1 and Fig. 5. We see that the left-side Nusselt number decreases dramatically as the Stefan number decreases.

In summary, the effect of increasing the Stefan number is to accentuate the difference between the heat transfer administered to the right wall (Nu_r) and the heat transfer absorbed by the solid-liquid interface (Nu). The difference between the two heat transfer rates is steadily being spent on raising the temperature of the newly created liquid up to the average temperature of the liquid-saturated zone.

Another quantity that can be anticipated based on this theory is the average melting rate. Note that in equation (9) we have the means with which to calculate the rate at which the solid-liquid interface migrates toward the left. The dimensionless counterpart of this local melting rate is

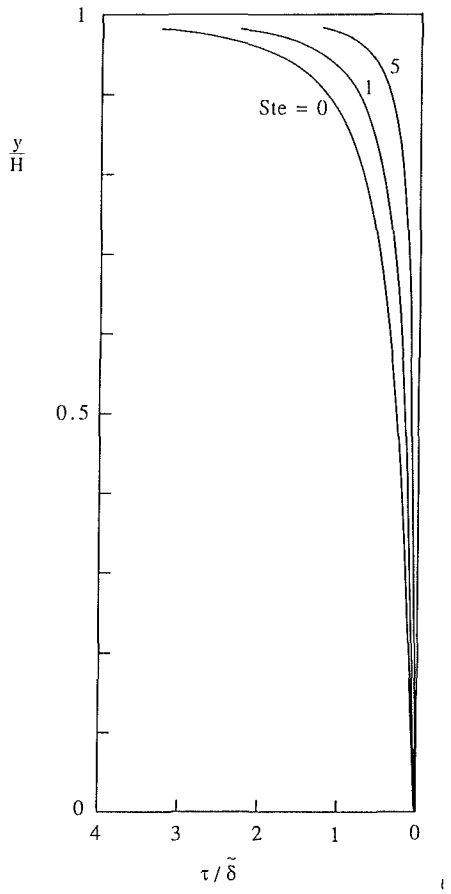

Fig. 6 The shape of the solid-liquid interface

$$\tilde{u}_0 = \frac{u_0}{\alpha/H}\,\mathrm{Ra}^{-1/2} = \mathrm{Ste}\,\frac{\tau}{\tilde{\delta}} \tag{43}$$

The $\tilde{u}_0$ function depends on y in the same way as the ratio $\tau/\tilde{\delta}$, which has been plotted in Fig. 6. The melting rate is noticeably higher near the top of the solid–liquid interface, where the solid phase-change material comes in contact with the warm liquid discharged from the upper portion of the warm boundary layer. Since the melting process is steady, the shape of the $\tau/\tilde{\delta}$ function is also the shape of the eroded solid–liquid interface. The ratio $\tau/\tilde{\delta}$ blows up at $\tilde{y} = 1$; however, at this level as well as at $\tilde{y} = 0$ all the matched boundary layer solutions of the type constructed in sections 2–4 break down (Weber, 1975; Bejan, 1979b; Simpkins and Blythe, 1980).

By integrating equation (43) we obtain the overall melting rate. This can be expressed as an average melting speed

$$u_{0,\mathrm{avg}} = \frac{1}{H}\int_0^H u_0 dy \tag{44}$$

which in dimensionless form reads

$$\tilde{u}_{0,\mathrm{avg}} = \mathrm{Ste}\int_0^1 \frac{\tau}{\tilde{\delta}}\,d\tilde{y} = \mathrm{Ste}\,F \tag{45}$$

The function $\tilde{u}_{0,\mathrm{avg}}$ depends only on the Stefan number, as is shown in Table 1 and Fig. 5.

In closing, it is worth commenting on the use of (1 + Ste) as abscissa in Fig. 5. This choise has the effect of making the F and F_r curves appear nearly straight in the double-logarithmic plane, improving in this way the accuracy associated with reading numerical values directly off Fig. 5. This observation leads to two very simple formulas

$$F_r \cong 3^{-1/2}(1 + 1.563\ \mathrm{Ste})^{0.107} \tag{46}$$

$$F \cong 3^{-1/2}(1 + 0.822\ \mathrm{Ste})^{-0.715} \tag{47}$$

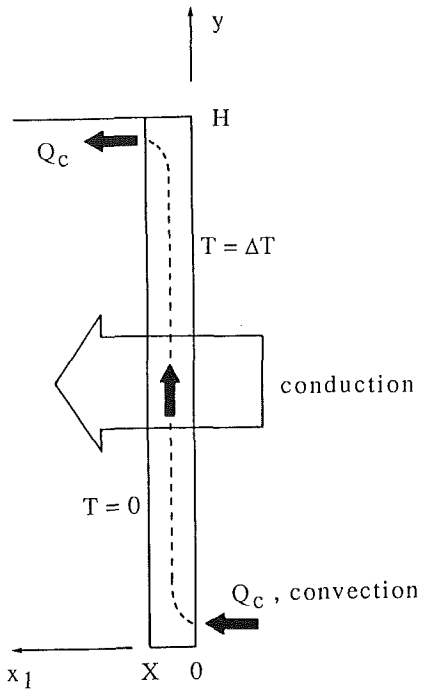

Fig. 7 Combined conduction and convection during the early stages of the natural convection melting process

which approach within 0.5 percent the values calculated based on equations (38) and (42).

6 The Nusselt Number History: Theory of Conduction Mixed With Convection

So far we have considered only the quasi-steady regime, in which the heat transfer mechanism is dominated by boundary layer convection. This is the regime that sets in at relatively late stages in the melting process, when the liquid-saturated zone has had time to grow to a width that exceeds the boundary layer thickness scale.

In the very beginning of the melting process the liquid-saturated region is infinitely slender and the heat transfer mechanism is that of pure conduction. With reference to the slender liquid zone sketched in Fig. 7, the history of the thickness X is described by the well-known Neumann solution (Carslaw and Jaeger, 1959)

$$X = 2\Lambda(\alpha t)^{1/2} \tag{48}$$

in which Λ is a dimensionless function of Ste

$$\frac{\exp(-\Lambda^2)}{\mathrm{erf}\,\Lambda} = \pi^{1/2}\,\frac{\Lambda}{\mathrm{Ste}} \tag{49}$$

According to the same solution, the excess temperature of the liquid-saturated porous medium depends on t and x_1 (and not on y), where x_1 is chosen such that it increases toward the left in Fig. 7

$$T = \Delta T\left[1 - \frac{1}{\mathrm{erf}\,\Lambda}\,\mathrm{erf}\,\frac{x_1}{2(\alpha t)^{1/2}}\right] \tag{50}$$

The overall heat transfer rate delivered through the heated wall (Q_r, or Nu_r in the preceding section) is also well known. For example, in the limit Ste = 0 the overall Nusselt number decays as

$$\mathrm{Nu}_r = 2^{-1/2}\theta^{-1/2} \tag{51}$$

in which θ is the dimensionless time encountered in this class of problems (e.g., Webb and Viskanta, 1985)

Table 2 Stefan number effect on the solution for the regime of conduction mixed with convection

Λ	Ste	G_0	G_c
0	0	$2^{-1/2}$	$2^{1/2}/12$
0.5	0.5923	0.8342	0.1097
0.7	1.373	0.9753	0.1021
0.8	1.996	1.074	0.0974
1	4.060	1.349	0.0865
1.1	5.755	1.538	0.0804
1.2	8.172	1.772	0.0740
1.3	11.66	2.063	0.0673

$$\theta = \frac{\alpha t}{H^2}\,\mathrm{Ste} \tag{52}$$

The objective of this section is to develop an analytical transition from the short-time Nusselt number (51) to the long-time expression of the quasi-steady regime, equation (36). In other words, the objective is to develop a heat transfer theory that holds starting with $\theta = 0$ and covers the entire period during which the heat transfer mechanism is, in order, pure conduction, conduction and convection, and finally convection.

The new theory is based on the observation that even in the limit $\theta \to 0$ when the liquid region approaches zero thickness, there is liquid motion in the liquid saturated region. This observation is backed by the momentum equation (1), in which x is now replaced by $(-x_1)$, and where the right side is finite [recall the conduction temperature profile (50)]. Integating the momentum equation in x_1 we obtain

$$v = \frac{Kg\beta\Delta T}{\nu}\left\{1 - \frac{1}{\mathrm{erf}\Lambda}\,\mathrm{erf}\left[\frac{x_1}{2H}\left(\frac{\mathrm{Ste}}{\theta}\right)^{1/2}\right] + C_1\right\} \tag{53}$$

The constant C_1 follows from the condition that the net vertical flow through the gap of width X must be zero. In the end, the v expression reads

$$v = \frac{Kg\beta\Delta T}{\nu}\left[\frac{\int_0^{\Lambda}\mathrm{erf}m\,dm}{\Lambda\mathrm{erf}\Lambda} - \frac{\mathrm{erf}\left(\frac{x_1}{X}\Lambda\right)}{\mathrm{erf}\,\Lambda}\right] \tag{54}$$

It is easy to verify that this vertical profile represents a counterflow whose warm branch rises along the right (heated) wall. Using the calculus of limits one can show further that the T and v profiles are linear in the limit $\mathrm{Ste} \to 0$, in which equation (49) reduces to

$$\Lambda = \left(\frac{\mathrm{Ste}}{2}\right)^{1/2} \tag{55}$$

Any counterflow in which a temperature difference exists between the two branches serves as conduit for heat convection in the longitudinal direction of the arrangement (Bejan, 1979a). In our case the convective heat transfer Q_c travels upward through the slender liquid-saturated zone and lands on the uppermost portion of the solid–liquid interface (Fig. 7). It is due to Q_c that the interface starts to deviate from the perfect vertical and flat shape as early as in the conduction regime, when the value of Q_c is actually small relative to the overall heat transfer rate.

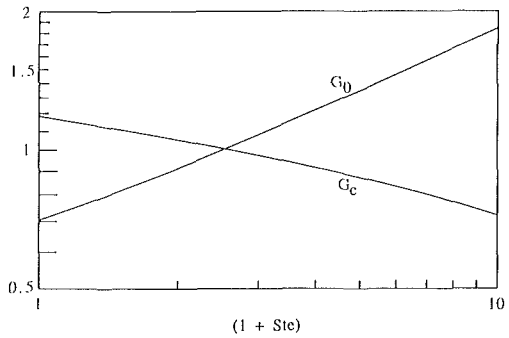

Fig. 8 Stefan number effect on the heat transfer solution for the mixed conduction and convection regime

The incipient convective heat transfer contribution is

$$Q_c = \int_0^X \rho c v\, T\, dx = \rho c\,\frac{Kg\beta\Delta T}{\nu}\,\Delta T\, X\, I \tag{56}$$

where the function I(Ste) is the integral

$$I(\mathrm{Ste}) = \int_0^1 \left[\frac{\int_0^{\Lambda}\mathrm{erf}m\,dm}{\Lambda\mathrm{erf}\Lambda} - \frac{\mathrm{erf}(n\Lambda)}{\mathrm{erf}\Lambda}\right]\left[1 - \frac{\mathrm{erf}(n\Lambda)}{\mathrm{erf}\Lambda}\right] dn \tag{57}$$

This function was evaluated numerically [see equation (62), below, and Table 2]. The numerical work was made somewhat simpler by the observation that the integral that appears in the integrand can be calculated with the formula

$$\int_0^{\Lambda}\mathrm{erf}\; m\; dm = \mathrm{ierfc}\;\Lambda - \pi^{-1/2} + \Lambda \tag{58}$$

In the conduction regime the effect of Q_c on the overall heat transfer rate is purely additive, because the top and bottom ends of the liquid-zone temperature field (the only patches affected by the flow of Q_c) are negligible in height when compared with the rest of the system (height H). It is as if the conduction heat transfer that proceeds horizontally through a cross section of height H is unaware of the convective heat transfer that travels in the perpendicular direction, up the chimney (Fig. 7). The instantaneous total heat transfer rate through the right wall is therefore

$$Q_r = kH\left(-\frac{\partial T}{\partial x_1}\right)_{x_1=0} + Q_c \tag{59}$$

where the first term on the right side accounts for the dominant conduction contribution. Employing the Nu_r notation defined in equation (36), the Q_r expression (59) translates into

$$\mathrm{Nu}_r = G_0\theta^{-1/2} + G_c\mathrm{Ra}\;\theta^{1/2} \tag{60}$$

where G_0 and G_c depend only on the Stefan number

$$G_0 = \frac{\mathrm{Ste}^{1/2}}{\pi^{1/2}\mathrm{erf}\;\Lambda} \tag{61}$$

$$G_c = 2\Lambda I\;\mathrm{Ste}^{-1/2} \tag{62}$$

The functions G_0(Ste) and G_c(Ste) are presented in Table 2 and Fig. 8. Reading the table from left to right we see that the numerical procedure that delivers the G_0 and G_c values begins with first selecting a value for the dimensionless parameter Λ. The Stefan number has a sizable effect on both G_0 and G_c. For fixed values of θ and Ra, the effect of increasing the Stefan number is to diminish the relative importance of the convection contribution to the overall Nusselt number (60).

In view of the reasoning on which equation (60) is based, we must keep in mind that this Nu_r expression cannot be used

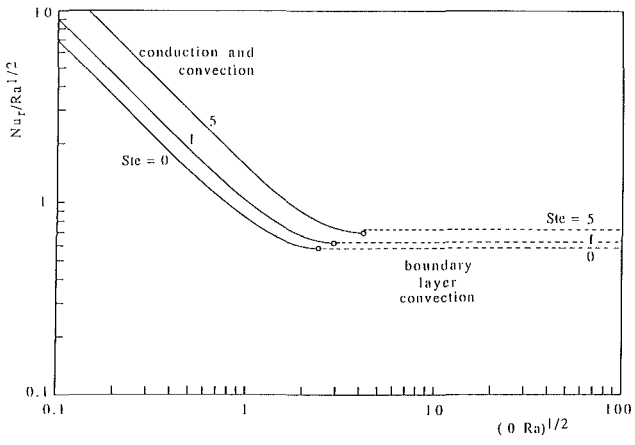

Fig. 9 Time variation of the Nusselt number during the conduction, mixed, and convection regimes, and the smooth connection between the two theories advanced in this paper

beyond the moment θ when the second (convection) term begins to outweigh the first (conduction) term. This condition, i.e.,

$$G_0\theta^{-1/2} > G_c \mathrm{Ra}\ \theta^{1/2} \tag{63}$$

yields the following time criterion for the domain of validity of equation (60):

$$\theta \mathrm{Ra} < \frac{G_0}{G_c} \tag{64}$$

The G_0 and G_c curves of Fig. 8 show that the ratio G_0/G_c increases noticeably as the Stefan number increases. This ratio is summarized with an accuracy better than 0.6 percent, by the simple formula

$$\frac{G_0}{G_c} \cong 6(1+0.568\ \mathrm{Ste})^{0.803}, \qquad 0 \le \mathrm{Ste} \le 11.66 \tag{65}$$

The solid lines of Fig. 9 show the Nusselt number history predicted by equation (60) all the way up to the time limit (64). That limit, or the point of expiration of each solid curve, is indicated by a circle. The abscissa of Fig. 9 shows the value of the group θRa, which came to light in equation (64). Plotted on the ordinate is the group $\mathrm{Nu_r Ra^{-1/2}}$: This group was chosen in order to achieve an Ra correlation of the Nusselt number in the convection limit [see equation (36)].

The horizontal dash lines of Fig. 9 represent the Nusselt number values that prevail at long times in the boundary layer regime of sections 2–5. It is truly remarkable that two different and admittedly approximate theories [equations (36) and (60)] provide a practically continuous description for the time variation of the overall Nusselt number. Only when Ste increases above 5, a mismatch of a few percentage points develops between $\mathrm{Nu_r/Ra^{1/2}}$ values predicted by the two theories at the transition time (64).

7 Concluding Remarks

The preceding theory has been constructed in two parts. In the first part, a matched boundary layer solution was constructed for the convection or quasi-steady regime, when the liquid region is wide enough to house distinct boundary layers. The second part (section 6) has been devoted to the heat transfer regimes that, in time, precede the convection-dominated regime. Together, the two parts provide a surprisingly simple theoretical means of anticipating the overall thermal behavior of the porous medium during the transient heating process.

The quantitative predictions made possible by the present theory can be compared directly with the numerical results published recently by Jany and Bejan (1987, 1988) for the Ste $\to$ 0 limit. The numerical study shows that in the convection (quasi-steady) regime the Nusselt number reaches the maximum plateau value of $\mathrm{Nu\ Ra^{-1/2}} = 0.54$ when Ra = 200, and $\mathrm{Nu\ Ra^{-1/2}} = 0.62$ when Ra = 800 (see Fig. 2 of Jany and Bejan, 1988). These numerical results agree very well with the theoretical value of $\mathrm{Nu/Ra^{1/2}} = 0.577$, which is listed as F (Ste = 0) in Table 1.

Regarding the accuracy of the finite-Ste effect predicted by this theory, a qualitative comparison can be made with Kazmierczak et al.'s (1986) study of melting from a vertical flat plate. Using the same observation that in the present study led to the simple formulas (46) and (47), I was able to correlate within 1 percent Kazmierczak et al.'s tabulated results for overall heat transfer into the two-phase interface, with the formula

$$\frac{\mathrm{Nu}}{\mathrm{Ra}^{1/2}} \cong 0.444(1+0.776\ \mathrm{Ste})^{-0.735} \tag{66}$$

The right side of this formula is nearly the same as that of equation (47) of the present study. This finding lends confidence in the finite Stefan number effect anticipated by the present theory.

The simplicity of the analytical work described in this paper is due in part to the assumptions on which it was based. Key among these is the assumption that the two-phase interface remains nearly plane and vertical during the convection regime of sections 2–5. This assumption breaks down eventually, because as the time passes the uneven melting rate u_0 leads to a curved interface whose *shape*, only, resembles that of the curves shown in Fig. 6. The shape illustrated in Fig. 6 should not be confused with the actual displacement (deflection) of the solid–liquid interface. The displacement is described by the function $s(y, t)$, which is defined next.

The question of when (beyond what time scale θ Ra, Fig. 9) the convectin regime theory breaks down can be answered by reasoning that the curvature of the interface plays an important role when its slope ds/dy is no longer negligible when compared with 1. In this argument, $s(y, t)$ is the function describing the instantaneous shape of the interface, i.e., the travel and deformation of the interface, toward the left in Fig. 1. In the quasi-steady regime s is proportional to both u_0 and t

$$s = u_0 t \tag{67}$$

Therefore, in view of equations (43) and (52), the "small curvature" criterion $ds/dy < 1$ becomes

$$\theta\ Ra^{1/2} \frac{d}{d\tilde{y}} \left(\frac{\tau}{\tilde{\delta}}\right) < 1 \tag{68}$$

Combining the above result with the time of the beginning of convection-dominated melting, equation (64), we conclude that the quasi-steady regime analysis of sections 2–5 is valid in the time interval

$$\frac{G_0}{G_c} < \theta\ \mathrm{Ra} < \mathrm{Ra}^{1/2}\left[\frac{d}{d\tilde{y}} \left(\frac{\tau}{\tilde{\delta}}\right)\right] \tag{69}$$

Employing the calculus of limits, we find that in the limit Ste $\to$ 0 this double inequality reduces to

$$6 < \theta\ \mathrm{Ra} < 4(1-\tilde{y})^{3/2}\mathrm{Ra}^{1/2} \tag{70}$$

In the opposite extreme, Ste $\gg$ 1, the curvature of the interface is negligible in the θ Ra interval

$$\frac{G_0}{G_c} < \theta\ \mathrm{Ra} < 2\ \mathrm{Ste}(1-\tilde{y})^2\mathrm{Ra}^{1/2} \tag{71}$$

where, according to equation (65), the ratio G_0/G_c scales roughly as $\mathrm{Ste}^{0.803}$.

The convection time criteria (69)–(71) demonstrate, first,

that the small-curvature assumption always breaks down in a certain region near the top of the interface ($\tilde{y} = 1$). The $Ra^{1/2}$ factor appearing on the right side of these time criteria shows that this top region (in which the interface curvature is important) becomes shorter as Ra increases. Therefore, the small-curvature assumption of sections 2–5 is compatible with the high Rayleigh number limit, that is, with the limit of distinct vertical boundary layers invoked at the start of the quasi-steady regime analysis (section 2).

Second, the large-Stefan number limit presented in equation (71) demonstrates that the act of increasing Ste does not threaten in any way the validity of the analysis of sections 2–5. Along the θ Ra time scale, *both* the start of the convection-dominated regime and the breakdown of the small-curvature assumption are delayed as Ste increases.

Looking ahead, the boundary layer treatment of the quasi-steady regime can be refined by focusing in detail on the flow and temperature field near the corners and in the horizontal layers near the top and bottom walls. This work may proceed along the path traced in the study of the corresponding pure convection problem (Blythe et al., 1982; Daniels et al., 1982). Similarly, the treatment of the mixed regime (section 6) may be advanced by considering the corner flow where the convection rate Q_c begins to erode the upper end of the solid–liquid interface (Fig. 7).

In the meantime, I used the analytical method of this paper to solve the related problem of melting in an enclosure without porous matrix (Began, 1989).

Acknowledgments

This work was sponsored by the Electric Power Research Institute through contract No. RP 8006-4 under the management of Dr. Jong H. Kim.

References

Bejan, A., 1979a, "A General Variational Principle for Thermal Insulation System Design," *Int. J. Heat Mass Transfer*, Vol. 22, pp. 219–228.

Bejan, A., 1979b, "On the Boundary Layer Regime in a Vertical Enclosure Filled With Porous Medium," *Lett. Heat Mass Transfer*, Vol. 6, pp. 93–102.

Bejan, A., 1984, *Convection Heat Transfer*, Wiley, New York, p. 361.

Bejan, A., 1989, "Analysis of Melting by Natural Convection in an Enclosure," *Int. J. Heat Fluid Flow*, Vol. 10, in press.

Blythe, P. A., Daniels, P. G., and Simpkins, P. G., 1982, "Thermally Driven Cavity Flows in Porous Media. I. The Vertical Boundary Layer Structure Near the Corners," *Proc. R. Soc. Lond.*, Vol. A380, pp. 119–136.

Blythe, P. A., Simpkins, P. G., and Daniels, P. G., 1983, "Thermal Convection in a Cavity Filled With a Porous Medium: A Classification of Limiting Behaviours," *Int. J. Heat Mass Transfer*, Vol. 26, pp. 701–708.

Carslaw, H. S., and Jaeger, J. C., 1959, *Conduction of Heat in Solids*, 2nd ed., Oxford University Press, Oxford, p. 287.

Chellaiah, S., and Viskanta, R., 1987a, "Freezing of Water and Water-Salt Solutions Around Aluminum Spheres," *Int. Comm. Heat Mass Transfer*, Vol. 14, pp. 437–446.

Chellaiah, S., and Viskanta, R., 1987b, "Natural Convection Flow Visualization in Porous Media," *Int. Comm. Heat Mass Transfer*, Vol. 14, pp. 607–616.

Daniels, P. G., Blythe, P. A., and Simpkins, P. G., 1982, "Thermally Driven Cavity Flows in Porous Media. II. The Horizontal Boundary Layer Structure," *Proc. R. Soc. Lond.*, Vol. A382, pp. 135–154.

Epstein, M., and Cho, D. H., 1976, "Melting Heat Transfer in Steady Laminar Flow Over a Flat Plate," ASME JOURNAL OF HEAT TRANSFER, Vol. 98, pp. 531–533.

Gadgil, A., and Gobin, D., 1984, "Analysis of Two-Dimensional Melting in Rectangular Enclosures in the Presence of Convection," ASME JOURNAL OF HEAT TRANSFER, Vol. 106, pp. 20–26.

Ho, C.-J., and Viskanta, R., 1984, "Heat Transfer During Melting From an Isothermal Vertical Wall," ASME JOURNAL OF HEAT TRANSFER, Vol. 106, pp. 12–19.

Jany, P., and Bejan, A., 1987, "Melting in the Presence of Natural Convection in a Rectangular Cavity Filled with Porous Medium," Report DU-AB-4, Department of Mechanical Engineering and Materials Science, Duke University, Durham, NC.

Jany, P., and Bejan, A., 1988, "The Scales of Melting in the Presence of Natural Convection in a Rectangular Cavity Filled with Porous Medium," ASME JOURNAL OF HEAT TRANSFER, Vol. 110, pp. 526–529.

Kazmierczak, M., Poulikakos, D., and Pop, I., 1986, "Melting From a Flat Plate Embedded in a Porous Medium in the Presence of Steady Natural Convection," *Numerical Heat Transfer*, Vol. 10, pp. 571–581.

Kazmierczak, M., Poulikakos, D., and Sadowski, D., 1987, "Melting of a Vertical Plate in Porous Medium Controlled by Forced Convection of a Dissimilar Fluid," *Int. Comm. Heat Mass Transfer*, Vol. 14, pp. 507–518.

Okada, M., 1984, "Analysis of Heat Transfer During Melting From a Vertical Wall," *Int. J. Heat Mass Transfer*, Vol. 27, pp. 2057–2066.

Okada, M., and Fukumoto, R., 1982, "Melting Around a Horizontal Pipe Embedded in a Frozen Porous Medium," *Trans. Japan Soc. Mech. Engrs.*, Vol. 48B, pp. 2041–2049 (in Japanese).

Reid, R. L., 1978, "Integral Methods for the Melting of Permafrost by Groundwater Flow," *AIChE Symposium Series*, pp. 265–270.

Simpkins, P. G., and Blythe, P. A., 1980, "Convection in a Porous Layer," *Int. J. Heat Mass Transfer*, Vol. 23, pp. 881–887.

Sparrow, E. M., Patankar, S. V., and Ramadhyani, S., 1977, "Analysis of Melting in the Presence of Natural Convection in the Melt Region," ASME JOURNAL OF HEAT TRANSFER, Vol. 99, pp. 520–526.

Viskanta, R., 1985, "Natural Convection in Melting and Solidification," *Natural Convection: Fundamentals and Applications*, S. Kakac, W. Aung, and R. Viskanta, eds., Hemisphere, Washington, DC, pp. 845–877.

Weaver, J. A., 1985, "Solid–Liquid Phase Change Heat Transfer in Porous Media," MSME Thesis, Purdue University, West Lafayette, IN.

Weaver, J. A., and Viskanta, R., 1985, "Freezing of Liquid Saturated Porous Media," *Heat Transfer in Porous Media and Particulate Flows*, L. S. Yao et al., eds., ASME, HTD-Vol. 46, pp. 1–8.

Weaver, J. A., and Viskanta, R., 1986a, "Freezing of Water Saturated Porous Media in a Rectangular Cavity," *Int. Comm. Heat Mass Transfer*, Vol. 13, pp. 245–252.

Weaver, J. A., and Viskanta, R., 1986b, "Melting of Frozen, Porous Media Contained in a Horizontal or a Vertical, Cylindrical Capsule," *Int. J. Heat Mass Transfer*, Vol. 29, pp. 1943–1951.

Webb, B. W., and Viskanta, R., 1985, "On the Characteristic Length Scale for Correlating Melting Heat Transfer Data," *Int. Comm. Heat Mass Transfer*, Vol. 12, pp. 637–646.

Webb, B. W., and Viskanta, R., 1986, "Analysis of Heat Transfer During Melting of a Pure Metal From an Isothermal Vertical Wall," *Numerical Heat Transfer*, Vol. 9, pp. 539–558.

Weber, J. E., 1975, "The Boundary Layer Regime for Convection in a Vertical Porous Layer," *Int. J. Heat Mass Transfer*, Vol. 18, pp. 569–573.

Effect of Solid Subcooling on Natural Convection Melting of a Pure Metal

C. Beckermann
Department of Mechanical Engineering,
The University of Iowa,
Iowa City, IA 52242

R. Viskanta
Heat Transfer Laboratory,
School of Mechanical Engineering,
Purdue University,
West Lafayette, IN 47907

A combined experimental and numerical study is reported of melting of a pure metal inside a vertical rectangular enclosure with natural convection in the liquid and conduction in the solid. The numerical model is successfully verified by conducting a series of experiments covering a wide range of hot and cold wall temperatures. It is found that solid subcooling significantly reduces the melting rate when compared to melting with the solid at the fusion temperature. Because the cooled wall is held below the fusion temperature of the metal, the solid/liquid interface eventually reaches a stationary position. For moderate values of the subcooling parameter the steady-state interface is almost vertical and parallel to the cold wall. Strong subcooling results in an early termination of the melting process, such that natural convection in the relatively small liquid region cannot fully develop. For moderate subcooling, correlations have been derived for the steady-state volume and heat transfer rates. While many aspects of melting with solid subcooling appear to be similar to ordinary nonmetallic solids, important differences in the local flow structures and heat transfer mechanisms are observed.

Introduction

Solid/liquid phase change in enclosures with natural convection in the liquid phase has recently received considerable research attention (Viskanta, 1985) due to its large number of applications, including latent heat storage, materials processing, crystal growth, casting of metals, purification of materials, and others. The effects of natural convection in the melt on the phase-change process are now well understood for certain geometries and medium to high Prandtl number fluids (Viskanta, 1985). Despite its importance in many industrial applications, melting or solidification of metals with natural convection in the liquid phase has received only little research attention. Experiments with lead (Szekely and Chhabra, 1970), mercury (Chiesa and Guthrie, 1974), gallium (Gau and Viskanta, 1986), and tin (Wolff and Viskanta, 1987) have demonstrated, however, that natural convection can considerably affect the solid/liquid interface shape and motion during phase change of low Prandtl number fluids. This has also been confirmed by numerical studies of melting of pure metals from a vertical wall (Webb and Viskanta, 1986; Wolff and Viskanta, 1987).

In all previous studies of melting of metals in enclosures, heat conduction in the solid phase is not considered. While natural convection in the melt increases the melting rate, subcooling of the solid acts to decrease the melting rate because of heat extraction through the solid away from the solid/liquid interface. If the cooled wall is held below the fusion temperature of the metal, the melting process can be completely terminated and the system will reach a steady state where the convective heat transfer from the melt to the interface is balanced by the heat conduction through the solid. The combined effects of natural convection in the liquid and heat conduction in the solid have been studied for melting of ordinary nonmetallic solids in rectangular enclosures (Benard et al., 1986; Kassinos and Prusa, 1986). While Benard and coworkers report the results of only one test case, Kassinos and Prusa present numerical results for the interface positions and/or melt volumes of two cases with solid subcooling. Because of the high thermal conductivity of metals, heat conduction in the solid can, however, be expected to exert an even stronger influence on melting of metals.

The purpose of the present study is to examine the influence of heat conduction in the solid phase of a pure metal during melting driven by natural convection in the melt. A series of experiments is performed in a rectangular enclosure heated and cooled at two opposite vertical side walls using gallium as the phase-change material. Measurements of the temperature distributions and interface positions are utilized to infer the heat transfer and melting phenomena for a variety of hot and cold wall temperature combinations. The experiments are supplemented by numerical simulations of the various test cases. The numerical results are validated through comparisons with the experimental data.

Analysis

Model Equations. The physical system considered in the present study is shown in Fig. 1. The vertical side walls of the enclosure are of height H and maintained at uniform temperatures, while the connecting horizontal walls of length L are considered adiabatic. Initially, the solid metal and the vertical sidewalls are at a uniform temperature, T_C, that is below the fusion temperature, i.e., $T_C < T_f$. At time $t=0$, the melting process is initiated by raising impulsively the left vertical sidewall temperature to T_H, where $T_H > T_f$.

In the present model, the flow is assumed to be laminar, incompressible, and two-dimensional, and the Boussinesq approximation is invoked. The thermophysical properties are assumed constant, but may be different for the liquid and solid phases. Because of the small Stefan numbers encountered in the present study (see Experiments), normal velocities at the solid/liquid interface due to density change upon melting can be neglected (Prusa and Yao, 1985; Kassinos and Prusa, 1986). With the foregoing assumptions, the mass, momentum, and energy conservation equations for the liquid and solid phases can be written in dimensionless form (see Nomenclature) as

Liquid:

$$\nabla \cdot \mathbf{u} = 0 \tag{1}$$

$$\frac{\partial \mathbf{u}}{\partial \mathrm{Fo}} + (\mathbf{u} \cdot \nabla)\mathbf{u} = -\nabla p + \mathrm{Pr}\ \nabla^2 \mathbf{u} + \mathrm{Ra}\ \mathrm{Pr}\ \Theta_l \mathbf{e}_\eta \tag{2}$$

Contributed by the Heat Transfer Division for publication in the JOURNAL OF HEAT TRANSFER. Manuscript received by the Heat Transfer Division May 24, 1988. Keywords: Liquid Metals, Natural Convection, Phase-Change Phenomena.

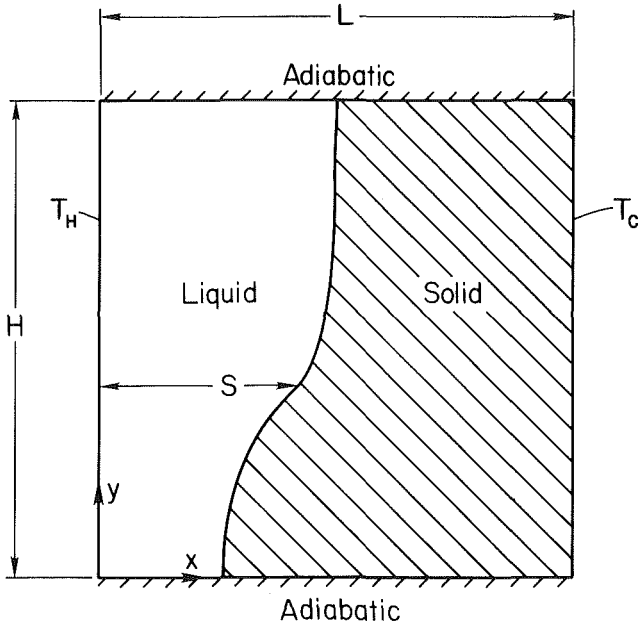

Fig. 1 Schematic of the physical model and coordinate system

$$\frac{\partial \Theta_l}{\partial \mathrm{Fo}} + \mathbf{u} \cdot \nabla \Theta_l = \nabla^2 \Theta_l \tag{3}$$

Solid:

$$\frac{\partial \Theta_s}{\partial \mathrm{Fo}} = \alpha^* \nabla^2 \Theta_s \tag{4}$$

The initial and boundary conditions for the present system may be stated as

Initial Conditions ($Fo < 0$):

$$s = 0, \quad \Theta_s = -1 \tag{5}$$

Boundary Conditions ($Fo \geq 0$):

$$\begin{aligned} &\mathbf{u} = 0, \quad \Theta_l = 1 && \text{at } \xi = 0, \quad 0 \leq \eta \leq A \\ &\mathbf{u} = 0, \quad \Theta_s = -1 && \text{at } \xi = 1, \quad 0 \leq \eta \leq A \\ &\mathbf{u} = 0, \quad \frac{\partial \Theta_{l \text{ or } s}}{\partial \eta} = 0 && \text{at } \eta = 0 \text{ or } A, \quad 0 \leq \xi \leq 1 \end{aligned} \tag{6}$$

In addition, the conditions at the solid/liquid interface, $\xi = s(\eta, \mathrm{Fo})$, are given by

$$\begin{aligned} &\mathbf{u} = 0 \\ &\Theta_s = \Theta_l = 0 \\ &k^* S_T (\nabla \Theta_s \cdot \mathbf{n}) - (\nabla \Theta_l \cdot \mathbf{n}) = \frac{\rho^*}{\mathrm{Ste}} V_n \end{aligned} \tag{7}$$

The dimensionless equations (1) to (7) show that the present problem is governed by eight dimensionless parameters, namely, the Rayleigh (Ra), Prandtl (Pr), and Stefan (Ste) numbers, the aspect ratio A, the subcooling parameter S_T, as well as the property ratios k^*, ρ^*, and α^*. However, equations (7) indicate that $k^* S_T$ and ρ^*/Ste can, theoretically, be combined into single parameters, thereby reducing the number of dimensionless parameters to six. As is commonly done in the solid/liquid phase-change literature, all results in the present study will be presented as functions of a dimensionless time τ, defined as

$$\tau = \mathrm{Fo}\,\mathrm{Ste} \tag{8}$$

With the above scaling of the Fourier number and in the limit of small Stefan numbers ($\mathrm{Ste} \to 0$) the solution does not depend explicitly on the Stefan number. For the range of Stefan numbers considered in this study ($\mathrm{Ste} < 0.08$), the above statement represents a good approximation. Consequently, the user of the dimensionless time τ will aid in the presentation of the results, although the present calculations are performed for finite Stefan numbers (see also the next section).

Note that the temperatures in the liquid and solid are nondimensionalized using the temperature differences $\Delta T_l = T_H - T_f$ and $\Delta T_s = T_f - T_C$, respectively. Consequently, the dimensionless temperatures are limited to values between 0 and 1 in the liquid and 0 and -1 in the solid. With $S_T = \Delta T_s / \Delta T_l$, the subcooling parameter is equal to zero for no subcooling of the solid ($T_C = T_f$), and is limited to values greater than zero.

The results for the average heat transfer rates at the vertical side walls bounding the liquid and solid will be presented in terms of average Nusselt numbers defined as

$$\overline{\mathrm{Nu}}_l = -\frac{1}{A} \int_0^A \frac{\partial \Theta_l}{\partial \xi} \, d\eta \qquad \text{at } \xi = 0$$

Nomenclature

A = aspect ratio = H/L
c = specific heat, J/kg K
Fo = Fourier number = $t\alpha_l/L^2$
g = gravitational acceleration, m/s^2
h = convective heat transfer coefficient, W/m^{2}K
h_f = latent heat of fusion, J/kg
H = height of enclosure, m
k = thermal conductivity, W/mK
k^* = thermal conductivity ratio = k_s/k_l
L = length of enclosure, m
$\mathbf{n}$ = normal unit vector
Nu = Nusselt number = hL/k_l
P = pressure, Pa
p = dimensionless pressure = $PL/\rho_l \alpha_l^2$
Pr = Prandtl number = ν_l/α_l
Ra = Rayleigh number = $g\beta\Delta T_l L^3/\nu_l \alpha_l$
s = dimensionless interface position = S/L
S = interface position, m
S_T = subcooling parameter = $\Delta T_s/\Delta T_l$
Ste = Stefan number = $c_l \Delta T_l / h_f$
t = time, s
T = temperature, K
ΔT_l = temperature difference across liquid = $T_H - T_f$, K
ΔT_s = temperature difference across solid = $T_f - T_C$, K
$\mathbf{u}$ = dimensionless velocity = UL/α_l
$\mathbf{U}$ = velocity, m/s
v_n = dimensionless normal interface velocity = $V_n L/\alpha_l$
V = dimensionless melt volume, see equation (10)
V_n = normal interface velocity, m/s
x = horizontal coordinate, m
y = vertical coordinate, m
α = thermal diffusivity, m^2/s
α^* = thermal diffusivity ratio = α_s/α_l
β = coefficient of thermal expansion, 1/K
η = dimensionless vertical coordinate = y/L
Θ_l = dimensionless liquid temperature = $(T_l - T_f)/\Delta T_l$
Θ_s = dimensionless solid temperature = $(T_s - T_f)/\Delta T_s$
ν = kinematic viscosity, m^2/s
ξ = dimensionless horizontal coordinate = x/L
ρ = density, kg/m^3
ρ^* = density ratio = ρ_s/ρ_l
τ = dimensionless time = FoSte

Subscripts

C = cold wall
f = fusion
H = hot wall
l = liquid
s = solid

$$\overline{\mathrm{Nu}}_s = -\frac{k^* S_T}{A}\int_0^A \frac{\partial \Theta_s}{\partial \xi}\, d\eta \quad \text{at } \xi = 1 \tag{9}$$

According to the above equations, the heat transfer rates at both sidewalls ($\xi = 0$ and 1) are referenced to the heat transfer by conduction across the liquid region. At steady state (i.e., for a stationary solid/liquid interface), this will result in equal values of the Nusselt numbers at both side walls.

The temporal variation of the average solid/liquid interface location will be presented in terms of a dimensionless melt (liquid) volume defined as

$$V = \frac{1}{A}\int_0^A s\, d\eta \tag{10}$$

Solution Procedure. The movement and the irregular shape of the solid/liquid interface considerably complicate the numerical solution of the coupled equations (1) to (7). In the present study, a modified form of the implicit/explicit approach proposed by Sparrow and co-workers (Sparrow and Chuck, 1984; Sparrow and Ohkubo, 1986) is adopted for the treatment of the interface movement. The numerical solution proceeds through a series of small time intervals during which the solid/liquid interface is assumed to be fixed. For each such time interval, the field equations are solved by a fully *implicit* solution scheme (without neglecting the unsteady terms) in the now fixed liquid and solid domains. The solution of the field equations provides the energy fluxes at the interface after that time interval. The displacement of the interface can then be calculated *explicitly* (i.e., without iterations) from the interfacial energy balance, equation (7), and new solution domains are generated for the next time step. Since the interface displacement is performed at the end of the time interval, the present approach avoids complications in the formulation of the numerical solution scheme for the field equations due to a moving grid system (Sparrow and Ohkubo, 1986), as well as the iterative interaction of the temperature and velocity fields with the interface displacement (Sparrow and Chuck, 1984). The accuracy of this approach is demonstrated in the literature (Sparrow and Chuck, 1984; Sparrow and Ohkubo, 1986). It has been shown that for small Stefan numbers, the temperature and velocity fields are not strongly influenced by the movement of the interface (Prusa and Yao, 1985; Benard et al., 1986; Kassinos and Prusa, 1986). For the small Stefan numbers encountered in the present study (see Experiments), this effect is negligible. In the following, the numerical procedures for solving the field equations during each time interval are outlined.

The field equations (1) to (4), together with the boundary and initial conditions, equations (5) to (7), were solved utilizing a modified form of the control-volume-based discretization scheme described in detail elsewhere (Hsu, 1982; Webb and Viskanta, 1986). In this scheme, the field equations are integrated over discrete nonorthogonal control volumes. The additional terms due to the nonorthogonality of the grid are fully retained in the discretized equations. This is particularly important in view of the fact that for the conditions of the present study, the tilt ($\partial s/\partial \eta$) and curvature ($\partial^2 s/\partial \eta^2$) of the solid/liquid interface can be relatively large (see Results and Discussion and Yao, 1980). As mentioned previously, the present algorithm is based on an implicit discretization scheme for the unsteady terms in the field equations, without invoking the quasi-steady convection approximation (Benard et al., 1986; Webb and Viskanta, 1986). Other details of the computational sequence are essentially the same as in Hsu (1982) and do not need to be repeated here. The algorithm was considerably modified to facilitate the calculations to be performed simultaneously in the two domains (i.e., liquid and solid).

The highly irregular shapes of the liquid and solid domains were accommodated in the calculations by using a nonorthogonal curvilinear grid. After each movement of the interface new grids were algebraically generated utilizing a power-law clustering scheme (Webb and Viskanta, 1986). This procedure provides a high concentration of nodal points near the vertical boundaries and the solid/liquid interface where velocity and thermal boundary layers need to be accurately resolved. The nodal points were only slightly skewed in the η direction. In the calculations reported in the present study, grids of 26×26 nodal points were selected for the liquid and solid domains. It is realized that this relatively coarse grid might not be adequate to resolve all details of the flow structures in the liquid domain. The selected mesh size should only be viewed as a compromise between accuracy and computational cost. Additional tests of the accuracy of the numerical algorithm were performed for the limiting cases of melting of a pure substance without solid subcooling (Webb and Viskanta, 1986) and thermal natural convection in a square enclosure (DeVahl Davis and Jones, 1983) and good agreement with results reported in the literature was found.

The calculations were initialized by assuming the presence of a liquid layer of negligibly small thickness (i.e., $s < 0.01$). During the initial period of the simulation, a dimensionless time step of $\Delta \mathrm{Fo} = 10^{-3}$ (~ 0.16 s) was utilized to assure a very small interface displacement. The time step was continually increased. Close to steady state, the time step was approximately equal to $\Delta \mathrm{Fo} = 0.1$ (16 s). For each time step, the iterations were terminated when the dependent variables agreed to four significant figures at each nodal point and the residual source of mass was less than 1×10^{-5}. The numerical algorithm was partially vectorized and the calculations were performed on a CYBER 205 computer. A typical simulation of a melting process required a CPU time of about 1500 s in order to reach steady state.

Experiments

Experiments were performed in a well-insulated test cell of square cross section. The test cell had inside dimensions of 4.76 cm in height and width and 3.81 cm in depth. The relatively small size of the test cell was mainly dictated by the high price of the phase-change material (gallium). The horizontal bottom wall was constructed of a phenolic plate, while the top wall and the vertical front and back walls were made of Lexan. Both the phenolic plate and the Lexan have low thermal conductivities when compared to gallium. The two vertical side walls, which served as the heat source/sink, were multipass heat exchangers machined out of a copper plate. The heat exchangers were connected through a valve system to two constant-temperature baths (Haake A82). Each heat exchanger contained three loops through which the flow rate could be controlled independently. The temperatures of each heat exchanger were measured with three thermocouples epoxied separately into small-diameter holes, which were drilled close to the surface of the copper plate facing the fluid. In all experiments, the temperatures of each heat exchanger were uniform to within ± 0.2°C of the desired temperature.

Measurement of the temperature distribution inside the test cell was made with 33 thermocouples with a wire diameter of 0.127 mm. They were placed in three different stainless steel rakes located at heights of 0.635, 2.38, and 4.125 cm measured from the bottom of the test cell. The rakes were positioned such that the temperatures were measured along the vertical centerplane of the test cell. The rake arms were oriented perpendicular to the flow direction (i.e., normal to the x–y plane) to minimize their influence on the flow field. Since the temperatures were essentially uniform over the depth of the

Table 1 Summary of experimental conditions ($A = 1.0$ Pr $= 0.0208$, $\alpha^* = 1.105$, $k^* = 1.0$, $\rho^* = 0.969$)

Experiment	ΔT_l, °C	ΔT_s, °C	S_T	Ra	Ste
1	10.2	4.8	0.468	3.275×10^5	5.074×10^{-2}
2	10.2	9.8	0.957	3.275×10^5	5.074×10^{-2}
3	10.2	19.8	1.935	3.275×10^5	5.074×10^{-2}
4	5.2	14.8	2.831	1.673×10^5	2.592×10^{-2}
5	15.2	14.8	0.971	4.877×10^5	7.557×10^{-2}

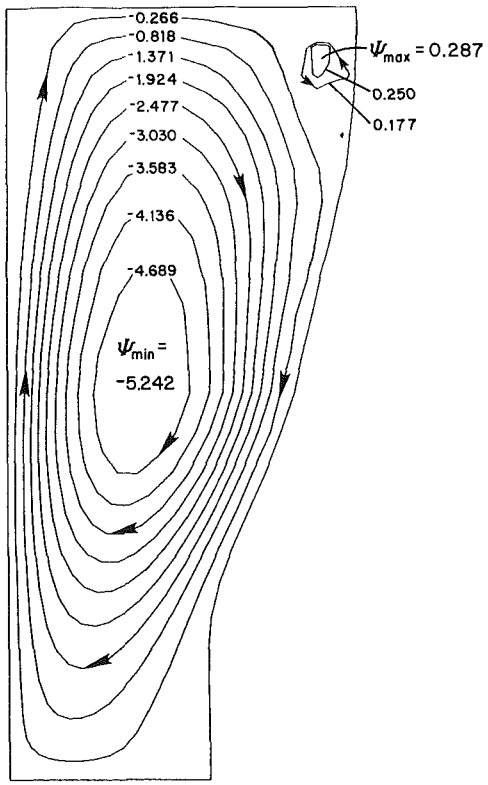

Fig. 2(a) Predicted streamlines

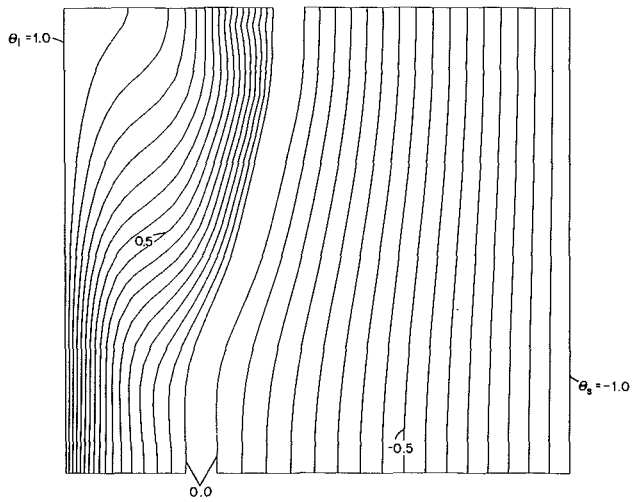

Fig. 2(b) Predicted isotherms (equal increments)

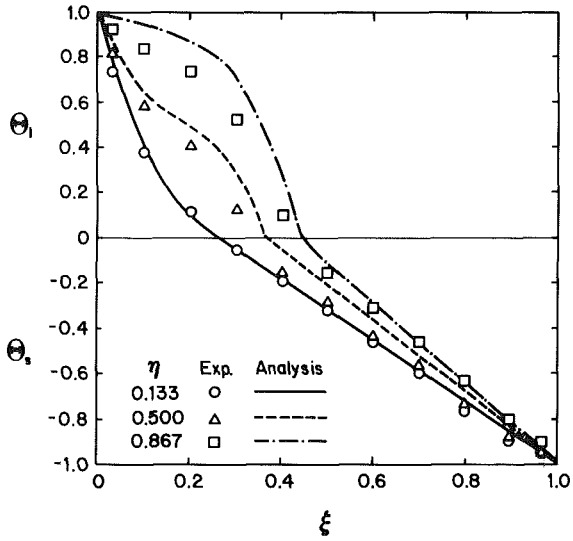

Fig. 2(c) Comparison of measured and predicted temperature profiles

Fig. 2 Results for Experiment 1 at $\tau = 0.0558$ ($t = 3$ min)

test cell, heat conduction along the rake arms can be expected to be negligibly small. The uncertainty in the location of each thermocouple bead was approximately ±0.2 mm. All thermocouples were calibrated with an accuracy of ±0.1°C. The thermocouples were connected to an HP-85 data-logger and computer through which the temperatures could be measured and stored at preselected time intervals. The copper heat exchangers as well as the thermocouple rakes were protected from the liquid metal used as the phase-change material by a very thin coat of spray paint.

The phase-change material utilized in the experiments was 99.99 percent pure gallium. This metal is desirable as a test material mainly because of its low fusion temperature ($T_f = 29.78$°C), enabling the experiments to be conducted close to ambient temperature, thereby reducing undesirable heat exchange with the surrounding through the Lexan and phenolic walls. In addition, the thermophysical properties of solid and liquid gallium are well documented (Cubberly, 1979). The highly anisotropic nature of the solid gallium crystals as well as the high cost of gallium of this purity are the two major disadvantages of using gallium as the phase-change material.

A total of five melting experiments was performed, covering a wide range of hot and cold wall temperatuers (and, hence, a wide range of S_T and Ra). The experimental conditions together with the values of the dimensionless parameters are summarized in Table 1. All properties were evaluated at the mean temperatures of the liquid and the solid. The thermal conductivity of the solid gallium was obtained by taking an average of the values for the three crystal axes (Gau and Viskanta, 1986).

In preparing for each experiment, the test cell was filled with successive layers of liquid gallium, which were slowly solidified before more liquid was added. This was done to ensure a homogeneous structure of the solid in the test cell. Volume change during phase-change (gallium contracts by about 3 percent upon melting) was accommodated by allowing liquid gallium to enter the test cell through a small hole drilled

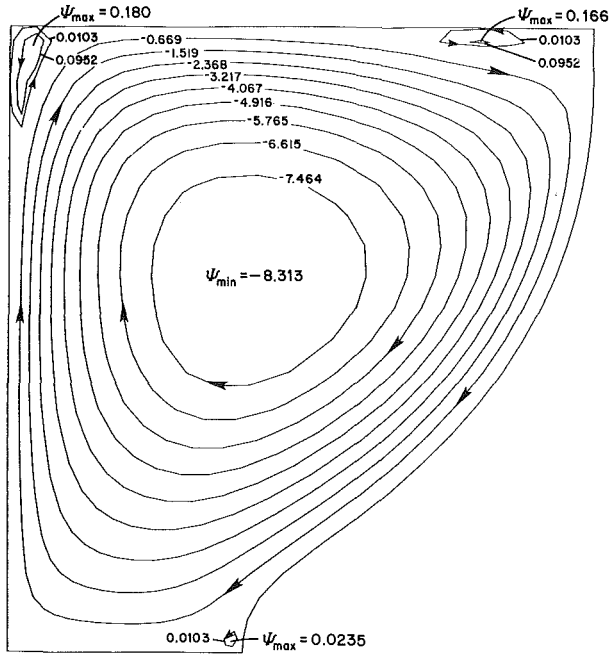

Fig. 3(*a*) Predicted streamlines

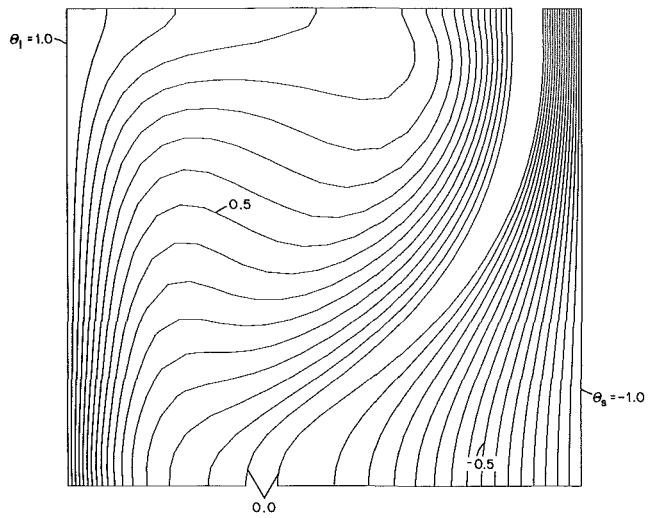

Fig. 3(*b*) Predicted isotherms (equal increments)

in the top plate. In order to obtain uniform initial temperature of the solid, the water from the cold constant temperature bath was circulated through both heat exchangers for at least 5 h. In the meantime, the temperature of the hot constant temperature bath was maintained at T_H. The experiment was initiated by switching the left heat exchanger from the cold to the hot constant temperature bath. Due to the thermal inertia of the system and the large heat flux at the hot wall during the initial period of the melting experiment, it took approximately 20 s for the left heat exchanger to reach the temperature desired as the boundary condition.

The solid/liquid interface positions during the melting experiments were determined by interpolating the fusion temperature from the thermocouple readings. Since the horizontal distance between two thermocouple junctions was 4.75 mm, the error in the calculated interface location was estimated to be less than 2 mm. The accuracy of this method was also tested using a dip-stick to measure the solid/liquid interface positions. For this purpose, an L-shaped glass rod with a pointed tip was connected to an x–y measurement system.

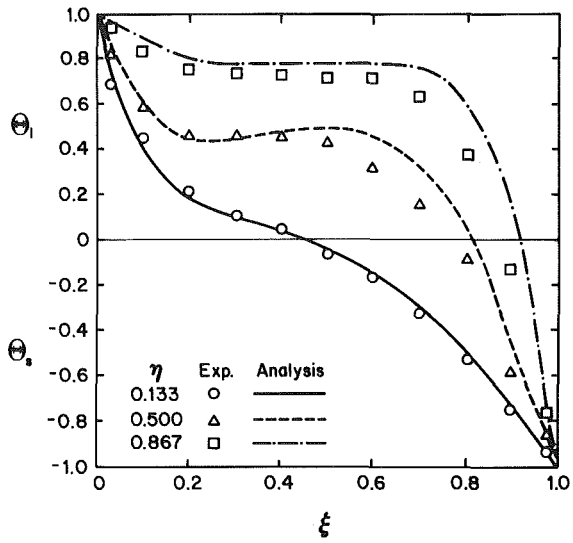

Fig. 3(c) Comparison of measured and predicted temperature profiles

Fig. 3 Results for Experiment 1 at $\tau = 0.1857$ ($t = 10$ min)

Good agreement with values interpolated from simultaneous temperature measurements was found.

Results and Discussion

Experiment 1. The numerical and experimental results for Experiment 1 are presented in detail in this section, which is followed by a discussion and comparison of the other experiments. The streamlines, isotherms, and temperature profiles at $\tau = 0.0558$ ($t = 3$ min), 0.1857 (10 min), and 0.9275 (50 min) are shown in Figs. 2, 3, and 4, respectively. In order to illustrate small recirculations in the corners of the melt region, two additional streamlines with values close to zero were plotted in Figs. 2(*a*), 3)*a*), and 4(*a*). Because the increments between these two streamlines are not the same as the constant increment for the other streamlines in the boundary layer and core regions, the spacings of the streamlines in the corners represent different mass flow rates. The time evolutions of the Nusselt numbers and the dimensions melt volume are presented in Figs. 5 and 6, respectively. Also shown in Figs. 5 and 6 are the corresponding curves for the limiting case of no fluid flow (i.e., Ra = 0) and zero solid subcooling (i.e., $S_T = 0$).

In Experiment 1, the melting process can be divided into four successive regimes:

- an initial pure conduction regime, during which the solid/liquid interface moves parallel to the hot wall;
- a regime characterized by developing convection in the upper portion of the liquid region and pure conduction in the lower portion; consequently, the interface exhibits a strong curvature in the upper portion and remains vertical in the lower portion;
- a convection-dominated regime, during which the entire interface is curved and moves faster in the upper than in the lower portion;
- and, finally, a regime during which the melting process is significantly influenced by heat extraction from the cold wall; melting takes place primarily in the lower portion of the enclosure and the interface reaches, eventually, a stationary position almost parallel to the cold wall.

The first two regimes are very similar to what has been observed in melting of a pure metal without solid subcooling (Webb and Viskanta, 1986) and of an ordinary nonmetallic solid with solid subcooling (Bernard et al., 1986). As can be seen from Figs. 5 and 6, the melting and heat transfer processes during the initial conduction regime follow very closely

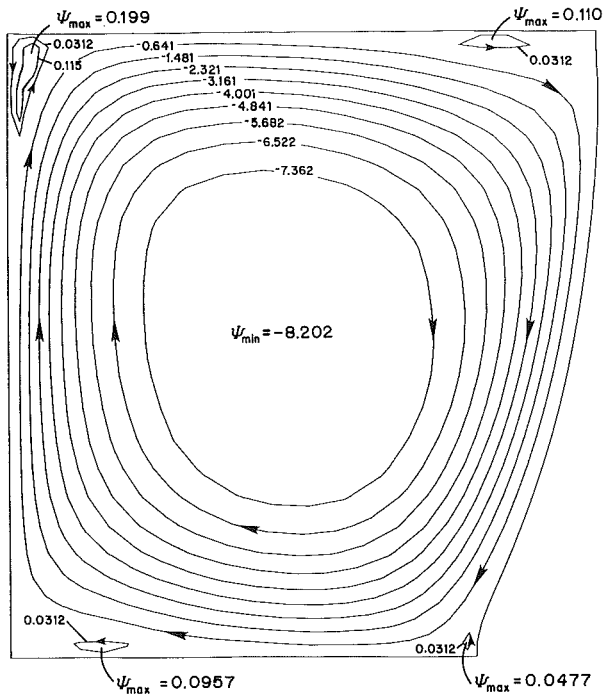

Fig. 4(*a*) Predicted streamlines

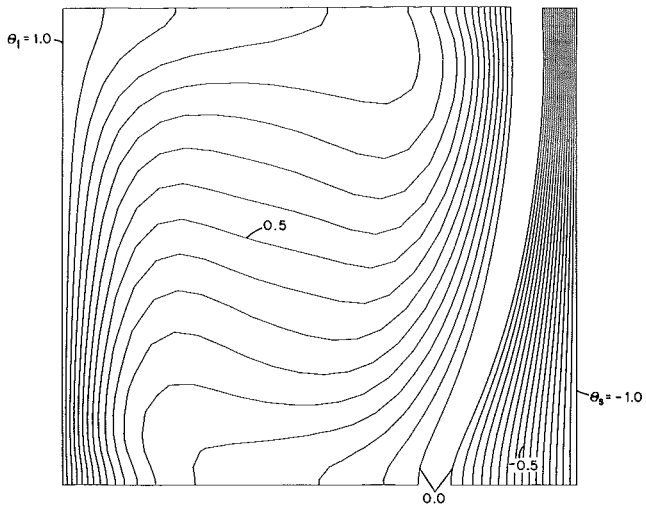

Fig. 4(*b*) Predicted isotherms (equal increments)

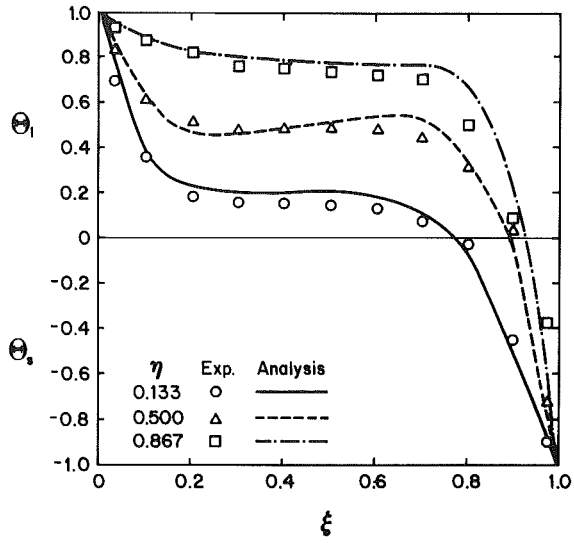

Fig. 4(*c*) Comparison of measured and predicted temperature profiles

Fig. 4 Results of Experiment 1 at $\tau = 0.9275$ ($t = 50$ min)

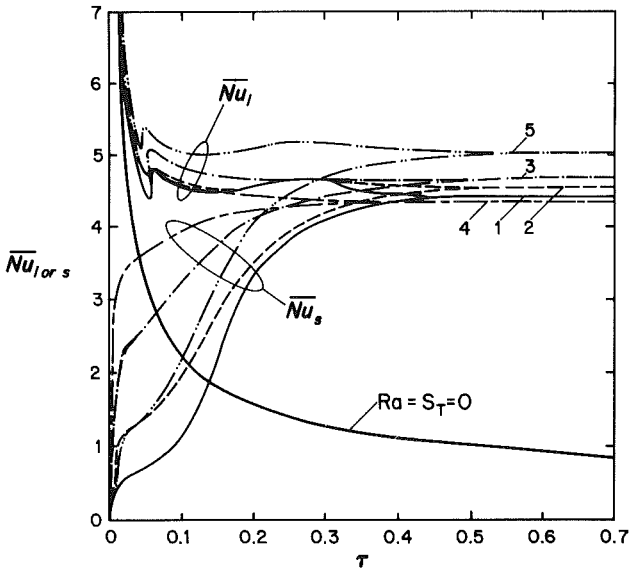

Fig. 5 Predicted time evolution of the average Nusselt numbers at the hot and cold walls

the analytical solution for the limiting case of $\mathrm{Ra} = S_T = 0$. Figures 2(*a*) and 2(*b*) show typical streamlines and isotherms, respectively, for the second regime at $\tau = 0.0558$ ($t = 3$ min). Natural convection encompasses the upper three quarters of the melt region, with thermal boundary layers present along the hot wall and the (now) curved solid/liquid interface. In the lower quarter, however, the isotherms as well as the interface are almost vertical, indicating conduction-dominated heat transfer. Note the presence of a weak secondary recirculation cell in the upper right corner of the melt region. Such recirculation cells (see also Figs. 3*a* and 4*a*) are typical for natural convection of low Prandtl number fluids (i.e., liquid metals) and have been observed in other studies (Webb and Viskanta, 1986; Wolff and Viskanta, 1987; Wolff et al., 1988).

The second regime ends shortly after $\tau = 0.558$ (Fig. 2) when the convection region has expanded all the way to the bottom of the enclosure. Figure 5 shows that at this time, the average Nusselt number at the hot wall reaches a local minimum. The relatively small values of the Nusselt number at the cold wall

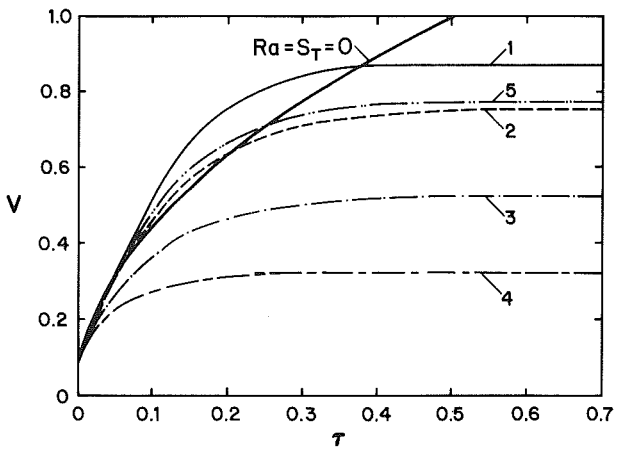

Fig. 6 Predicted time evolution of the melt volume

indicate that heat extraction from the cold wall and, hence, solid subcooling has only little influence on the melting process during the first two regimes in Experiment 1. Despite the presence of natural convection during the second regime, an examination of Fig. 6 reveals that the melt volume at the end of the second regime ($\tau = 0.06$) is almost identical to the one for the case of $\mathrm{Ra} = S_T = 0$. Again, similar observations have been made in studies of melting of metals without solid subcooling (Webb and Viskanta, 1986, Wolff and Viskanta, 1987).

During the third regime, natural convection takes place in the entire melt region. Because the temperature of the liquid metal decreases as it flows down the solid/liquid interface, the temperature gradients and, hence, the melting rates are larger in the upper than in the lower portion of the enclosure. This results in a smoothly curved interface, intersecting the adiabatic top and bottom walls at right angles.

Figures 3(*a*) and 3(*b*) show the predicted steamlines and isotherms, respectively, at $\tau = 0.1857$ ($t = 10$ min), close to the end of the third regime. Thermal boundary layers are present along the hot wall and the interface, while weak recirculation cells can be observed in both the upper and the lower right corners of the melt region. The interface in the upper right third of the enclosure is now very close to the cold wall, resulting in large temperature gradients in the solid in this region. Due to the strong curvature of the interface, the horizontal extent of the solid region at the bottom of the enclosure is still large ($s(\eta = 0) \approx 0.36$) and the temperature gradients in the solid are relatively small. The Nusselt number at the hot wall (Fig. 5) decreases slightly from a value of 4.8 at the beginning ($\tau = 0.06$) to 4.5 at the end ($\tau = 0.18$) of the third regime. On the other hand, the Nusselt number at the cold wall increases sharply (from 0.75 to 2.6), indicating that the melting process is increasingly influenced by heat conduction through the solid. Figure 6 shows that in the third regime, the dimensionless melt volume increases at a higher rate than for the limiting case of $\mathrm{Ra} = S_T = 0$. It is well known (Webb and Viskanta, 1986) that in convection-dominated melting without solid subcooling, the melt volume increases almost linearly with time. However, for the present case ($S_T = 0.468$), the melt volume (V) versus time (τ) curve increasingly departs from an initially linear behavior. At the end of the third regime ($\tau = 0.18$), the average melting rate (i.e., $dV/d\tau$) has decreased again to almost the same value as for $\mathrm{Ra} = S_T = 0$. In other words, the effect of solid subcooling on the melting process in Experiment 1 is significant during the later stages of the third regime. However, the general natures of the convection and melting processes remain similar to the ones without solid subcooling until the end of the third regime. As will be discussed in the next section, the above observations are only true for Experiment 1 and, hence, relatively small values of the subcooling parameter ($S_T < 0.5$).

On the other hand, the fourth regime is unique to melting with solid subcooling. Due to the small extent of the solid in the upper portion of the cavity, the heat transfer rates through the liquid and solid are now balanced, so that the solid/liquid interface does not move. In the lower portion, however, the interface continues to move, because the horizontal extent of the solid is larger, while the temperature gradients in the solid are smaller than in the upper region. Consequently, the interface becomes increasingly vertical and parallel to the cold isothermal wall, as the system approaches steady state. The streamlines and isotherms at $\tau = 0.9275$ ($t = 50$ min) are shown in Figs. 4(*a*) and 4(*b*), respectively. At this time, the interface has reached a stationary position and the heat transfer rates through the liquid and solid are equal. The natural convection patterns in the liquid region are very similar to the ones for a vertical square cavity (Wolff et al., 1988). The interface still exhibits a slight curvature, because the natural convection flow downward along the interface causes a variation in the

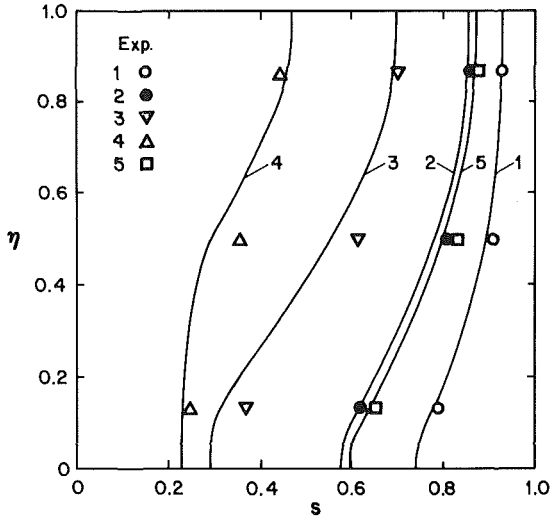

Fig. 7 Comparison of measured and predicted steady-state interface positions

local heat transfer rates. Figure 5 shows that the Nusselt number at the hot wall stays approximately constant throughout the third and fourth regimes (there is a slight maximum at about $\tau = 0.3$), while the Nusselt number at the cold wall continues to increase until it approaches the same value as Nu_l (at approximately $\tau = 0.45$). Similarly, the melt volume (Fig. 6) slowly approaches its steady-state value.

Comparison of Predictions With Experiments. As a representative example, comparisons between the predicted and measured temperatures are presented for Experiment 1 at $\tau = 0.0558$, 0.1857, and 0.9275 in Figs. 2(*c*), 3(*c*), and 4(*c*), respectively. Comparisons between predicted and measured solid/liquid interface positions at steady state are shown for all experiments in Fig. 7. In general, the experimental data agree with the predicted temperatures to within about 5 percent of the total temperature difference across the test cell. It is believed that most of the discrepancies can be attributed to experimental uncertainties, including inaccuracies in the thermocouple locations and readings as well as imperfect boundary conditions (isothermal and adiabatic). It can be observed that at all times the measurements indicate a lower intensity of natural convection in the melt region than predicted, which can be attributed to the presence of the thermocouple rake in the test cell. The discrepancies in the steady-state interface positions (Fig. 7) are well within the experimental uncertainties associated with the present measurement technique (see Experiments). It can be said that more accurate measurement techniques are needed to validate the predictions fully. In particular, measurements of the velocities in the liquid metal would be highly desirable for verifying the predicted flow patterns.

Uncertainties in the numerical predictions are primarily due to an insufficiently fine grid and the neglect of three-dimensional natural convection structures. Minor inaccuracies may be due to the neglect of density change upon melting and of thermophysical property variations with temperature. However, the good agreement between the measured and predicted melting rates and temperature distributions established some confidence in the numerical results.

Effects of Rayleigh Number and Solid Subcooling. Comparisons of the predicted average Nusselt numbers, dimensionless melt volume, and steady-state interface positions in Experiments 1 to 5 are shown in Figs. 5, 6, and 7, respectively. An examination of the results for Experiments 1, 2, and 3 reveals the effect of different subcooling parameters (S_T) on the melting process at the same Rayleigh number. The time

evolution of the Nusselt number at the hot wall ($\overline{Nu}_l$) in Experiments 2 and 3 follows quite closely the one for Experiment 1 (see Fig. 5). On the other hand, with increasing S_T, the Nusselt number at the cold wall ($\overline{Nu}_s$) increases at a much faster rate, indicating that for large S_T ($S_T \geq 2$), the influence of solid subcooling on the melting process is important almost from the beginning during all melting regimes. As expected, the melting rates decrease drastically with increasing S_T. In Experiment 2, the melting rate for the first three regimes is almost the same as for $Ra = S_T = 0$, while in Experiment 3, the melting rate is, except for the first conduction regime, smaller than for $Ra = S_T = 0$ (see Fig. 6). It should be noted that for the three experiments, the first two melting regimes (see Experiment 1) are of approximately the same duration. However, for large S_T (e.g., Experiment 3) a distinction between the third and fourth regime cannot be made, because of the strong influence of solid subcooling in both of these regimes. As in Experiment 1, the average Nusselt numbers at the hot wall ($\overline{Nu}_l$) stay approximately constant during the third and fourth regimes of Experiments 2 and 3, indicating that natural convection is quasi-steady. Steady-state is in all three experiments at approximately the same time ($\tau = 0.45$). With increasing S_T, the final melt volume decreases, while the steady-state interface (Fig. 7) becomes more curved. The latter is due to the fact that for large subcooling the steady-state interface is at a relatively large distance from the isothermal cold wall and, hence, its shape is more influenced by the natural convection in the liquid. It is also interesting to note the slight increase of the steady-state Nusselt number with increasing S_T and, hence, decreasing steady-state melt volume. This indicates that for natural convection in liquid metals, the Nusselt number increases only slightly with increasing "aspect ratio" (of the melt volume) (see also Wolff et al., 1988). The steady-state characteristics of the melting experiments are discussed in more detail in the next section.

A comparison of Experiments 2 and 5 shows the effect of increasing Rayleigh number (Ra) on the melting process at approximately the same value of the subcooling parameter ($S_T \approx 0.96$). Because it was impossible to vary the Rayleigh number in the present experiments by more than a factor of about three, the results for the two experiments are quite similar. However, it can be observed that both the melt volume and the Nusselt number at the cold wall increase at a faster rate for a higher Rayleigh number (see Figs. 5 and 6). As expected, the Nusselt number at the hot wall is at all times higher for a higher Rayleigh number.

The results of Experiments 4 reveal the effects of a very large value of the subcooling parameter ($S_T = 2.831$). The shape of the interface in steady-state (Fig. 7) suggest that for such large subcooling of the solid, the melting process never goes through the third and fourth (convection dominated) regimes. The melt volume stays small so that natural convection can develop only in the upper portion of the melt region, and the interface in the upper portion remains practically vertical throughout the experiment. In other words, Experiment 4 reaches a steady state approximately in the middle of the second regime. Because natural convection does not develop fully, Experiment 4 also has the smallest Nusselt number at steady state.

The above discussion shows that the melting process in the present experiments consists of a number of distinct regimes. However, the physical nature of each regime varies considerably for different amounts of solid subcooling. Although attempts have been made to identify the various regimes, it has not been possible to correlate the present results (i.e., $\overline{Nu}$ and V) as functions of the relevant dimensionless parameters. Such correlations would involve consideration of each regime separately and matching of the functional relationships between the regimes. It cannot be expected that a single relation can be obtained for the entire melting process and reasonable ranges of S_T and Ra. While for small solid subcooling, some of the results obtained for $S_T = 0$ (Webb and Viskanta, 1986) can be applied to the first three regimes (see Experiment 1), correlations for the steady-state behavior are presented in the following section.

Steady-State Characteristics. Assuming that at steady state the solid/liquid interface is (almost) vertical, integration of the interfacial energy balance, equation (7), over the height of the cavity (with $v_n = 0$) results in

$$V|_{\text{final}} = 1 - \frac{c_1 k^* S_T}{\overline{Nu}_l|_{\text{final}}} \tag{11}$$

The factor c_1 has been added in equation (11) in order to correct for the curvature of the steady-state interface (see Fig. 7). With $c_1 = 1.19$, equation (1) correlates the final melt volumes for Experiments 1, 2, and 5 to within 0.5 percent. For Experiment 3 ($S_T = 1.935$), the relative error increases to about 3 percent, while equation (11) is not applicable to Experiment 4. The large increase in the error for $S_T > 2$ can be attributed to the strong curvature of the interface as well as to the small value of $V|_{\text{final}}$, both of which cause a large departure from the assumption of one-dimensional conduction in the solid. According to equation (11), the subcooling parameters S_T must be less than $\overline{Nu}_l/k^*$ for melting to take place (i.e., for the final melt volume to be greater than zero). It is also interesting to note that equation (11) can be utilized to estimate the average Nusselt number at steady-state, if the final melt volume is known (e.g., through measurements).

An attempt has been made to correlate the steady-state average Nusselt number ($\overline{Nu}_l|_{\text{final}}$) as a function of the dimensionless parameters that govern the natural convection heat transfer in the liquid region. According to Bejan (1984), in the boundary layer regime the Nusselt number for $Pr < 1$ scales such that the following correlation can be written:

$$\overline{Nu}_l|_{\text{final}} = c_2(RaPr)^{1/4} \tag{12}$$

With $c_2 = 0.5$, equation (12) correlates the results for Experiments 1, 2, 3, and 5 to within 3 percent. Equation (12) is not applicable to Experiment 4, because natural convection is not in the boundary layer regime. The good fit of the present data with the above correlation indicates that the average Nusselt number is not strongly influenced by the curvature of the interface as well as by the different "aspect ratios" of the liquid regions at steady state. As can be seen from Fig. 5, equation (12) should also provide a good estimate of $\overline{Nu}_l$ throughout the third and fourth regimes in Experiments 1, 2, 3, and 5, because natural convection during these regimes is quasi-steady. The Prandtl number dependence has been checked with data obtained for natural convection of tin ($Pr = 0.011$) in a vertical square enclosure (Wolff et al., 1988) and excellent agreeement with the above correlation has been found. Good agreement has also been found with quasi-steady Nusslet numbers obtained for natural convection melting of gallium without solid subcooling (Webb and Viskanta, 1986). Note that substitution of equation (12) into (11) results in a correlation for the final melt volume that is a function of known parameters only.

Conclusions

A study has been performed of natural convection melting of a pure metal with subcooling of the solid. The numerical predictions are verified through a number of experiments, covering a range of Rayleigh numbers and subcooling parameters. It is found that the melting process consists of a sequence of four regimes and eventually approaches a steady state. For small solid subcooling, the first three regimes are found to be similar to the ones observed in melting without subcooling, while for moderate subcooling ($S_T \approx 1$) significant

differences can already be observed after the first two regimes. Large values of the subcooling parameter ($S_T > 2$) result in an early termination of the melting process and the last two regimes may never take place. It is shown that natural convection and solid subcooling have a considerable influence on melting of a metal. While many aspects of natural convection melting with solid subcooling appear to be similar for high and low Prandtl number fluids, important differences in the local flow structures and heat transfer mechanisms have been identified. It is concluded that additional research is necessary to arrive at general correlations for the dependence of the average Nusselt numbers and the melting rate on the governing dimensionless parameters. For moderate values of the subcooling parameter ($S_T < 2$), equations have been derived that accurately correlate the steady-state melt volume and heat transfer rates in the present system. Additional analyses and experiments are also needed to investigate the effects of different aspect ratios and a wider Rayleigh number range on melting of metals in enclosures.

Acknowledgments

The work reported in this paper was supported, in part, by the National Science Foundation under Grant No. CBT-8313573. Computer facilities were made available by Purdue University Computing Center.

References

Bejan, A., 1984, *Convection Heat Transfer*, Wiley, New York.

Benard, C., Gobin, D., and Zanoli, A., 1986, "Moving Boundary Problem: Heat Conduction in the Solid Phase of a Phase-Change Material During Melting Driven by Natural Convection in the Liquid," *International Journal of Heat and Mass Transfer*, Vol. 29, pp. 1669–1681.

Chiesa, F. M., and Guthrie, R. I. L., 1974, "Natural Convection Heat Transfer Rates During Solidification and Melting of Metals and Alloy Systems," ASME JOURNAL OF HEAT TRANSFER, Vol. 95, pp. 377–390.

Cubberly, W. H., 1979, *Metal Handbook-Properties and Selection: Nonferrous Alloys and Pure Metals*, 9th ed., ASM, Metals Park, OH, pp. 811–814.

DeVahl Davis, G., and Jones, I. P., 1983, "Natural Convection in a Square Cavity: a Comparison Exercise," *International Journal of Numerical Methods in Fluids*, Vol. 3, pp. 227–248.

Gau, C., and Viskanta, R., 1986, "Melting and Solidification of a Pure Metal on a Vertical Wall," ASME JOURNAL OF HEAT TRANSFER, Vol. 108, pp. 174–181.

Hsu, C. F., 1982, "A Curvilinear-Coordinate Method for Momentum, Heat, and Mass Transfer in Domains of Irregular Geometry," Ph.D. Thesis, University of Minnesota, Minneapolis, MN.

Kassinos, A., and Prusa, J., 1986, "Effects of Density Change and Subcooling on the Melting of a Solid in a Rectangular Enclosure," *Proceedings, 8th International Heat Transfer Conference*, U. Grigull et al., eds., Hemisphere, Washinhton, DC, pp. 1787–1792.

Prusa, J., and Yao, L. S., 1985, "Effects of Density Change and Subcooling on the Melting of a Solid Around a Horizontal Heated Cylinder," *Journal of Fluid Mechanics*, Vol. 155, pp. 193–212.

Sparrow, E. M., and Chuck, W., 1984, "An Implicit/Explicit Numerical Solution Scheme for Phase-Change Problems," *Numerical Heat Transfer*, Vol. 7, pp. 1–15.

Sparrow, E. M., and Ohkubo, Y., 1986, "Numerical Analysis of Two-Dimensional Transient Freezing Including Solid-Phase and Tube-Wall Conduction and Liquid-Phase Natural Convection," *Numerical Heat Transfer*, Vol. 9, pp. 59–77.

Szekely, J., and Chhabra, P. S., 1970, "The Effect of Natural Convection on the Shape and Movement of the Melt-Solid Interface in the Controlled Solidification of Lead," *Metallurgical Transactions B*, Vol. 1B, pp. 1195–1203.

Viskanta, R., 1985, "Natural Convection in Melting and Soldification," in: *Natural Convection: Fundamentals and Applications*, S. Kakac et al., eds. Hemisphere, Washington, DC, pp. 845–877.

Webb, B. W., and Viskanta, R., 1986, "Analysis of Heat Transfer During Melting of a Pure Metal From an Isothermal Vertical Wall," *Numerical Heat Transfer*, Vol. 5, pp. 539–558.

Wolff, F., and Viskanta, R., 1987, "Melting of a Pure Metal From a Vertical Wall," *Experimental Heat Transfer*, Vol. 1, pp. 17–30.

Wolff, F., Beckermann, C., and Viskanta, R., 1988, "Natural Convection of Liquid Metals in Vertical Cavities," *Experimental Thermal and Fluid Science*, Vol. 1, pp. 83–91.

Yao, L. S., 1980, "Analysis of Heat Transfer in Slightly Eccentric Annuli," ASME JOURNAL OF HEAT TRANSFER, Vol. 102, pp. 279–284.

Freezing of Water-Saturated Porous Media in the Presence of Natural Convection: Experiments and Analysis

S. Chellaiah

R. Viskanta

Heat Transfer Laboratory,
School of Mechanical Engineering,
Purdue University,
West Lafayette, IN 47907

Freezing of superheated water-porous media (glass beads) contained in a rectangular test cell has been studied both experimentally and numerically. The effects of liquid superheat and imposed temperature difference were investigated. When the superheat across the liquid region was small the flow in the porous media was weak, and the interface was almost planar. For larger superheats, natural convection flow and the solidification front shape and velocity were found to depend on the imposed temperature and the permeability of the porous medium. Due to the density inversion of water, the rate of freezing was higher, either at the top or at the bottom of the cell, depending on the amount of superheat. The measured temperature distributions were compared with predictions of numerical model that considered both conduction in the solid and natural convection in the liquid region. This model is based on volumetric averaging of the macroscopic transport equations, with phase change assumed to occur volumetrically over a small temperature range. Both Brinkman and Forchheimer extensions were added to the Darcy equations. The effect of density inversion of water on the fluid flow and heat transfer has been modeled. Good agreement has been found between the experimental data and numerical predictions.

Introduction

There are many engineering systems and processes occurring in nature that involve the freezing of liquid-saturated porous media. Some examples are the freezing of soil (Lunardini, 1981), freeze drying of foodstuffs (Albin et al., 1982), latent heat-of-fusion energy storage (ME staff, 1983), and artificial freezing of ground as a structural support and as a water barrier for construction and mining purposes (Sanger, 1968). The design and evaluation of ground-based heat pumps that use heat exchanger pipes buried underground (Metz, 1983; Svec et al., 1983) depend on understanding of the freezing and thawing of the soil. Despite these varied and many applications, relatively little attention has been given to the study of solid/liquid phase change of liquid-saturated porous media (Aung and Yener, 1985). The related problem of natural convection in porous media in the absence of phase change has been investigated both experimentally and numerically by many researchers, and reviews are available (Combarnous and Bories, 1975; Cheng, 1978).

There have been a number of theoretical studies concerned with freezing of water-saturated porous media in the absence (Weaver and Viskanta, 1986) and in the presence (Sliepcevich and Hashemi, 1973; Goldstein and Reid, 1978; Frivik and Comini, 1982) of seepage or ground water flow. For example, Sliepcevich and Hashemi used a finite element method to study the freezing around a row of pipes in the presence of ground water flow normal to the pipe centerline. They employed the same energy equation for the solid and the liquid regions and accounted for latent heat effects by the temperature dependent specific heat over a suitable temperature range. O'Neill and Albert (1984) have investigated numerically solidification of porous media in the presence of natural convection using a finite element method, but were not specifically concerned with the freezing of water.

Several combined experimental and theoretical studies were concerned with freezing of water-saturated porous media (Frivak and Comini, 1982; Weaver and Viskanta, 1986; Chellaiah and Viskanta, 1988). Frivak and Comini (1982) modeled the freezing and thawing of soils in the presence of seepage using a finite element method. The predicted temperatures were compared with experimental data obtained on a laboratory model of a soil freezing system. Weaver and Viskanta (1986) investigated the freezing of a water-saturated porous medium in a cylindrical capsule. The agreement between numerical model predictions considering conduction only and experimental data was good for a water-glass-bead system; however, for a water-aluminum ball system there were significant discrepancies between data and predictions due to an unreliable effective thermal conductivity model of the porous media. Chellaiah and Viskanta (1988) studied the freezing of saturated and superheated water in porous media in a rectangular enclosure cooled from a vertical wall. For freezing of saturated water, good agreement was found between the one-dimensional heat conduction model and the experimental temperature distributions, frozen volume fractions, and solid/liquid interface locations.

This paper reports on the combined experimental and numerical investigation of freezing of a porous medium saturated with superheated liquid. Water and glass beads constitute the liquid and porous medium, respectively. The macroscopic transport equations are volumetrically averaged, with phase change assumed to occur volumetrically over a small temperature range. In the liquid region, both the Brinkman and Forchheimer extensions were included in the Darcy's equation. The effect of density inversion of water on the fluid flow and heat transfer has been modeled. The experimental temperatures and the deduced solid/liquid interface positions were compared with the predictions of the numerical model.

Experiments

Test Cell. Solidification experiments were performed in a

Contributed by the Heat Transfer Division for publication in the JOURNAL OF HEAT TRANSFER. Manuscript received by the Heat Transfer Division March 16, 1988. Keywords: Moving Boundaries, Natural Convection, Phase-Change Phenomena.

rectangular test cell with inner dimensions of 205 mm in length, 203 mm in height and 127 mm in width. The top, bottom, front, and back sides were made of Plexiglas (12.5 mm thick). Two Plexiglas plates separated by a 6-mm air gap were used on the front and back of the test cell to minimize the effect of heat gains and condensation of moisture. A 7.5-mm-wide and 172-mm-long slot was cut in the top plate. The test cell was filled with water and glass beads through this opening. A lid fit snugly into this slot. Two 11-mm-dia holes were cut on this lid to bring out the thermocouple wires.

Two copper heat exchangers with milled passages for flow of coolant constituted the left and right endwalls of the test cell. The flow passages inside the heat exchanger were milled in such a way that the maximum temperature variation along the surface of the heat exchanger was within ±0.2°C. Six thermocouples were placed along the surface of the heat exchanger to check the uniformity of the temperature along the faces. The entire test cell was covered with 50-mm-thick Styrofoam on all sides. The test cell was placed on an iron plate fitted with leveling screws.

Two thermocouple rakes with 21 copper-constantan thermocouples in each and supported on two half rings epoxied onto the surface of the heat exchangers were located at 1/3 and 2/3 height from the bottom and along the center plane of the test cell. This was a compromise between the resolution desired and the disturbance of the system by additional rakes. The temperature readings were automatically recorded, at preset intervals, using a data logger connected to a VAX microcomputer.

Test Materials and Procedure. Spherical soda-lime glass beads of average diameters 2.85 mm, 6 mm, and 12 mm constituted the porous media. The properties used for the numerical study were for a soda-lime glass with a chemical composition as close as could be obtained to the chemical composition of the beads used in this study. The test cell was filled with glass beads with rakes kept in position. Once distilled and degasified water was carefully siphoned into the test cell without introducing air bubbles into the system. A mixture of ethyl alcohol and water was circulated through the heat exchangers from two constant-temperature baths and the porous matrix and water were allowed to cool to the desired initial temperature.

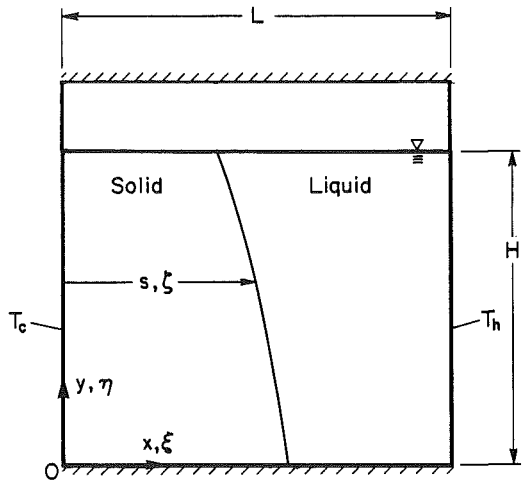

Fig. 1 Schematic of the test cell

The freezing was initiated by switching one of the constant temperature baths to a third one that was already precooled separately to the desired temperature. The natural convection flow in the unfrozen porous media and the flow structure were observed in parallel flow visualization experiments.

Analysis

The physical system modeled consists of a rectangular cavity with two vertical walls maintained at two different temperatures and the top and bottom surfaces insulated. The cavity is filled with a mixture of water and uniform size glass spheres (porous matrix). At $t = 0$, the system is at a uniform temperature greater than or equal to the fusion temperature, $T_i > T_f$ of the liquid. At time $t > 0$, a uniform temperature less than the fusion temperature is imposed on the left wall. Freezing is initiated at this wall and the interface moves from left to right (Fig. 1). The following simplifying assumptions are made in the analysis: (1) The porous medium is isotropic, homogeneous, and has uniform porosity; (2) the porous matrix and the phase change material (PCM) are in local thermal equilibrium; (3) the flow is two dimensional, laminar, and

Nomenclature

A = aspect ratio = H/L
C = Forchheimer's constant = 0.55
c = specific heat, J•kg^{-1}K^{-1}
Da = Darcy number = K/L^2
d = mean bead diameter, mm
$\mathbf{g}$ = gravitational acceleration, ms^{-2}
Δh_f = latent heat of fusion, J kg^{-1}
H = height of liquid level, m
K = permeability, m^2
k = thermal conductivity, Wm^{-1}K^{-1}
L = length of cavity, m
Ra* = Rayleigh number for porous medium = $g\rho\omega KL(T_h - T_f)^q/\mu\alpha$ = RaDa
S = superheating parameter = $c_l(T_h - T_f)/\Delta h_f$
s = interface position from cold wall, m
Ste = Stefan number = $c_s(T_f - T_c)/\Delta h_f$
T = temperature, K
t = time, s
$\mathbf{u}$ = velocity vector $\mathbf{i}u + \mathbf{j}v$
u = velocity component in the x direction, m/s
V = volume, m^3
v = velocity component in the y direction, m/s
x = horizontal distance from cold wall, m, see Fig. 1
y = vertical coordinate, m, see Fig. 1
α = thermal diffusivity = $k/\rho c$, m^{2}s^{-1}
γ = volume fraction of liquid phase change material (PCM) in V_f, V_l/V_f
δ = volume fraction of liquid PCM in the volume element, $V_l/V = \phi\gamma$
ζ = dimensionless interface position = s/L
η = dimensionless vertical coordinate = y/L
θ = dimensionless temperature = $(T - T_c)/(T_h - T_c)$
μ = dynamic viscosity, N•s/m^2
ξ = dimensionless horizontal coordinate = x/L
τ = dimensionless time = $t\alpha_1/L^2$
ϕ = porosity or volume fraction of PCM in the volume element = V_f/V

Subscripts

eff = effective
f = fluid
c = cold
h = hot
l = liquid
m = maximum
p = porous matrix
ref = reference
s = solid

incompressible; (4) the volume change due to freezing is negligible; (5) the phase change medium has a definite fusion temperature; (6) the porous matrix and the solid are stationary; (7) all thermophysical properties are independent of temperature; and (8) the momentum flux due to the interface motion is negligible.

The complicated geometry, heat transfer, and flow pattern in the system prohibit the solution of the governing equations at the microscopic level. Hence, the equations are averaged over a small volume element. In general, in such a volume element, there can be both solid and liquid PCM along with the porous matrix. In the melt region, the PCM is entirely liquid and $\gamma = 1$, $\delta = \phi$; in the solid region, $\gamma = \delta = 0$. Fuller details of the development of the volume-averaged governing equations can be found (Combarnous and Bories, 1976; Cheng, 1978) and hence are not repeated here. Even though the phase change is assumed to occur at a discrete temperature, in a volume element containing both the porous matrix and the solid and liquid, the average temperature may be slightly higher or lower than T_f. Hence, it is assumed that both solid and liquid may exist simultaneously in a volume element, if its temperature lies within a small temperature difference ΔT on either side of the fusion temperature. A more detailed discussion of the model is available (Beckermann and Viskanta, 1988). The two-dimensional conservation of mass, momentum, and energy equations for freezing of liquid saturated porous media are, respectively.

$$\nabla \cdot \mathbf{u} = 0 \tag{1}$$

$$\frac{\rho_l}{\delta}\frac{\partial \mathbf{u}}{\partial t} + \frac{\rho_l}{\delta^2}(\mathbf{u}\cdot\nabla)\mathbf{u} = -\nabla p + \frac{\mu_l}{\delta}\nabla^2\mathbf{u} - \left[\frac{\mu_l}{K} + \frac{\rho_l C}{K^{1/2}}|\mathbf{u}|\right]\mathbf{u} - \rho\mathbf{g} \tag{2}$$

$$\overline{\rho c}\frac{\partial T}{\partial t} + \rho_l c_l(\mathbf{u}\cdot\nabla T) = \nabla\cdot(k_{eff}\nabla T) - \phi\rho_l\Delta h_f\frac{\partial \gamma}{\partial t} \tag{3}$$

The momentum balance takes into account the unsteady term, Forchheimer's extension, and Brinkman's extensions to the Darcy equations. Equation (3) is the volume-averaged energy equation for the general control volume containing the porous medium solid-liquid mixture. With the velocity set to zero ($\mathbf{u} = 0$), equation (3) is also appropriate for the frozen region.

The boundary conditions for temperature are

$$T = T_c \quad \text{at} \quad x = 0 \quad \text{for all } y$$
$$T = T_h \quad \text{at} \quad x = L \quad \text{for all } y \tag{5}$$
$$\frac{\partial T}{\partial y} = 0 \text{ at } y \quad = 0 \text{ and } y = H \quad \text{for all } x$$

There is no slip at the walls. At the free surface the boundary conditions for the velocity are

$$\frac{\partial u}{\partial y} = v = 0 \quad \text{at} \quad y = H \quad \text{for } s < x < H \tag{6}$$

For $t<0$, $u = v = 0$ and $T = T_h$.

The buoyancy force is $\rho\mathbf{g}$, with ρ denoting the local density corresponding to the local temperature. For fluids having a linear density–temperature relationship the usual simplification of the buoyancy term can be done. But the density–temperature relationship for water is nonlinear and it attains a maximum value at 3.98°C. Several equations of state (second, third, and fourth-degree polynomials) (Gebhart and Mollendorf, 1978; Nguyen et al., 1982; Gebhart et al., 1987) have been proposed for the density of water as a function of temperature. In this study we use the approximation for density of water suggested by Gebhart and Mollendorf (1978)

$$\rho = \rho_m(1-\omega|(T-T_m|^q) \tag{7}$$

where $\omega = 9 \cdot 2972 \times 10^{-6}\ (°C)^{-q}$, and the exponent q has the value $q = 1.8948$.

The definition of the mean thermal capacitance of the mixture ($\overline{\rho c}$) is given by

$$\overline{\rho c} = \left[\phi\rho_l c_l + (1-\phi)\rho_s c_s\right] + (1-\phi)\rho_p c_p \tag{8}$$

In the volume element containing the frozen and the unfrozen PCM and the porous matrix, the effective thermal conductivities of the frozen and the unfrozen PCM are not very much different. Therefore, a series model (Combarnous and Bories, 1975) is used to calculate the effective thermal conductivity of the frozen and unfrozen PCM mixture alone. Then, the effective thermal conductivity of the combination of the frozen and unfrozen PCM mixture and the porous matrix is calculated using the Veinberg (1967) model. The model has been found to give reliable predictions of the effective thermal conductivity when the ratio of the thermal conductivity of the porous matrix to that of the PCM is not too large (Weaver and Viskanta, 1986). It should be stressed that the effective thermal conductivity of liquid-saturated porous media under static conditions was assumed to be the same as that for a transient system with a flowing fluid in which dispersion effects may be present.

The permeability was calculated from the Kozeny–Carman equation

$$K = \frac{d^2\phi^3}{175\ (1-d)^2} \tag{9}$$

Although it is generally accepted that the inertia coefficient C in Forchheimer's extension depends on the microstructure of the porous medium, a constant value $C = 0.55$ (Beckermann and Viskanta, 1988) was used in the calculations.

The model equations are solved using the SIMPLER algorithm (Patankar, 1980). Computational details are given by Beckermann and Viskanta (1988) and need not be repeated here. After conducting numerical sensitivity studies with different grids and time steps, a uniform grid of 26 × 26 nodal points was chosen as a compromise between cost and accuracy. A dimensionless time step of $\tau = 3.13\times10^{-5}$ ($t = 10$ s) and $\Delta\theta = 0.037$ were utilized.

Results and Discussion

Experimental Results. A number of experiments with several different size beads and several different superheats were conducted. Owing to space limitations, only a few of them are discussed here. The experimental conditions are summarized in Table 1. All the properties of ice, water, and glass beads were taken at the fusion temperature of 0°C. Since water undergoes a density inversion, the Rayleigh number was calculated as suggested by Gebhart et al. (1987).

From Table 1, it is seen that the porosity ϕ varies with bead size. For a system of infinite volume, randomly packed with uniform size spheres, the porosity is constant and is independent of the bead size (Benenati and Brosilow, 1962). Since the test cell used in experiments is finite in size, there is a considerable variation of porosity near the walls, especially with the larger size beads. With 2.85 mm beads, the porosity is close to the theoretically expected value of 0.39 for randomly packed beads.

There are a large number of parameters that affect the transport processes during freezing of water saturated porous media. The parameters include the Stefan number (Ste), the Darcy number (Da), the Rayleigh number for a porous medium (Ra*), the superheating parameter (S), and the aspect ratio (A). Some of these parameters are not independent of each other. For example, the temperature difference ($T_h - T_f$) appears in both the definitions of the superheating parameter and the Rayleigh number. As a consequence, it is difficult to be comprehensive.

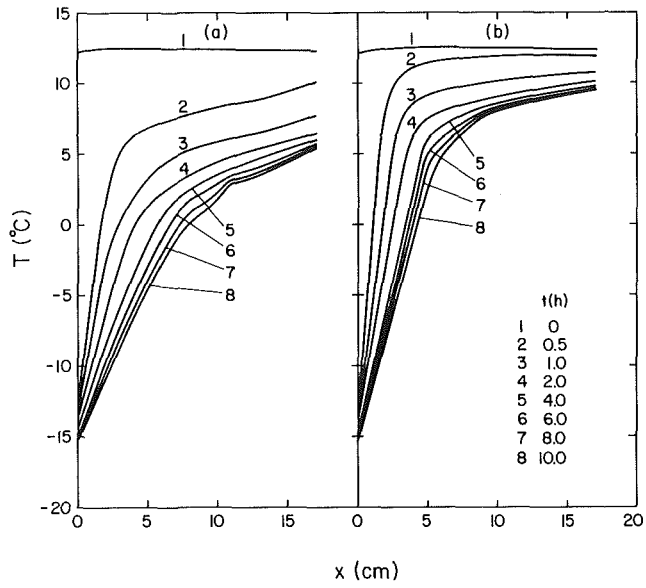

Fig. 2 Time-temperature traces at different locations for experiment 2 (Ste = 0.110, Da = 42.9 × 10^{-7}): (*a*) bottom rake (η = 0.333), and (*b*) top rake (η = 0.667)

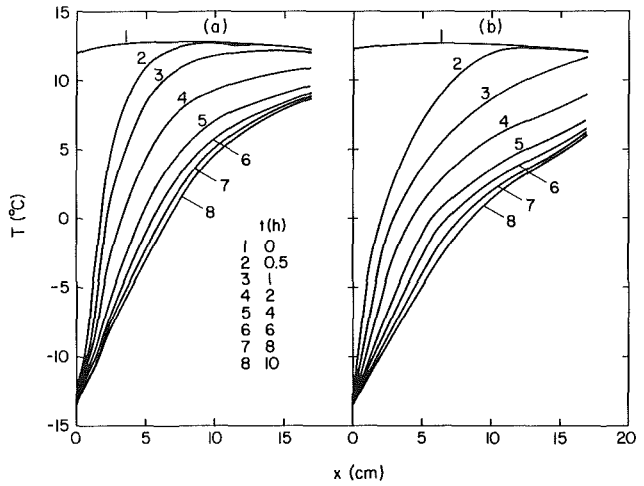

Fig. 3 Temperature distribution at different times for experiment 5 (Ste = 0.085, Da = 8.32 × 10^{-7}): (*a*) bottom rake (η = 0.333), and (*b*) top rake (η = 0.667)

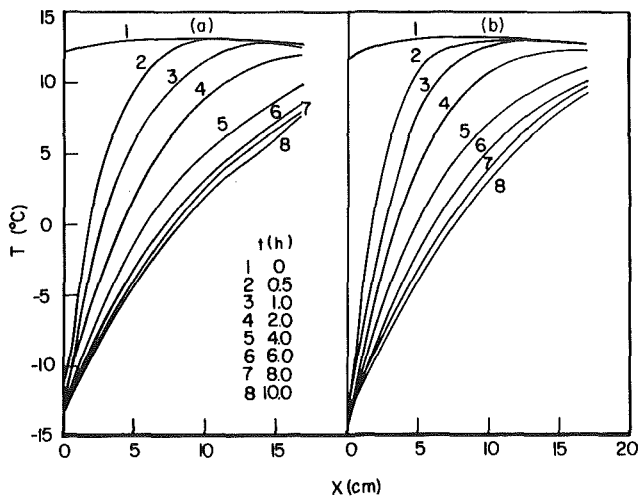

Fig. 4 Time-temperatures traces at different locations for experiment 8 (Ste = 0.164, Da = 1.52 × 10^{-7}): (*a*) bottom rake (η = 0.333), and (*b*) top rake (η = 0.667)

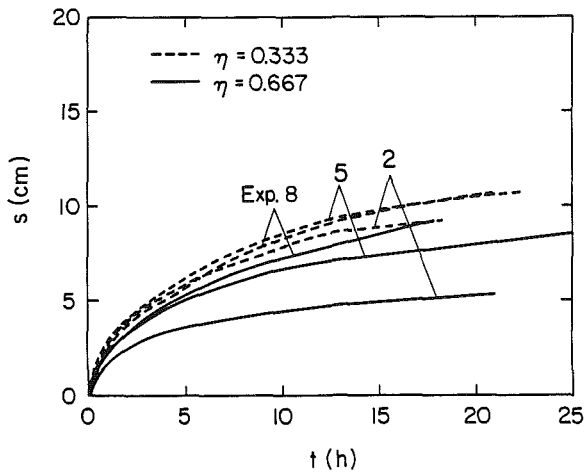

Fig. 5 Effect of bead size on the rate of freezing for experiments 2 (Da = 42.9 × 10^{-7}), 5 (Da = 8.32 × 10^{-7}), and 8 (Da = 1.52 × 10^{-7})

Some typical results are presented in the paper, and additional results are available elsewhere (Chellaiah, 1988).

Temperature Distribution. The experimentally measured temperature distributions at different times for experiments 2, 5, and 8, with about the same Stafan number and nearly equal superheating parameter but having different Darcy numbers, are presented in Figs. 2, 3, and 4, respectively. The Darcy number (Da) accounts primarily for the difference in the Rayleigh number (Ra*) in the three experiments. As will be demonstrated later, the superheating parameter is of second-order importance in comparison to the Stefan (Ste) and Rayleigh (Ra*) numbers in controlling the freezing front motion and shape.

Figure 2 shows the temperature distributions at different times for experiment 2. The temperature difference between the solidification front and the hot wall drives the natural convection flow in the liquid. The superheating parameter S = 0.157 (average initial superheat is 12.4° C), and the Rayleigh number for the porous medium is 1691. The results show that the freezing at the bottom is faster than at the top. This is similar to that observed during the freezing of pure PCM in the absence of porous matrix (Viskanta, 1985). The water near the hot wall rises and turns toward the interface. As it is cooled to 4° C, the point of maximum density, it descends along the 4° C isotherm and reaches the bottom of the cell, causing more freezing at the bottom. The water in the region bounded by the fusion front and 4° C isotherm has only a small potential to drive the flow. This flow pattern was observed in flow visualization studies under thermal conditions similar to those in this experiment (Chellaiah and Viskanta, 1987). The temperature distributions for experiments 5 and 8 are presented in Figs. 3 and 4, respectively. Compared to experiment 2, for about identical thermal conditions but smaller Darcy number, the freezing rate for experiment 5 is faster due to weaker convective flow.

Solid/Liquid Interface Position. All three (2, 5, and 8) experiments have about the same Stefan number and superheating parameter, but the difference in the rates of freezing between the top and bottom rakes decreases in the order of experiments 2, 5, and 8. For experiment 2 the times taken to freeze 1.5 cm at the top and bottom are 47.5 and 22.5 min, respectively, indicating the influence of natural convection at very early times in the experiment. For experiment 5, the corresponding times are 26 and 25 min, respectively. For exper-

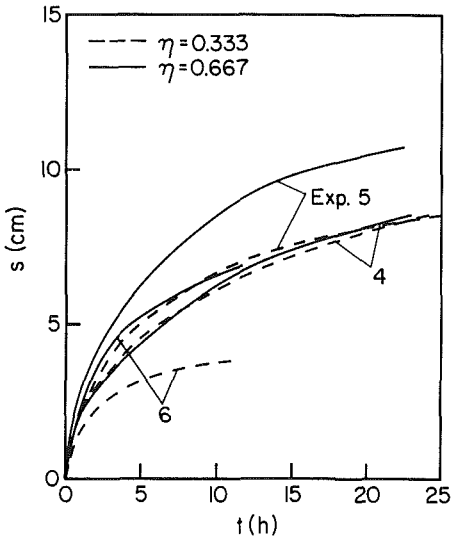

Fig. 6 Effect of Stefan and Rayleigh numbers on the rate of freezing for experiments 4 (Ste = 0.046, Ra* = 99), 5 (Ste = 0.085, Ra* = 333), and 6 (Ste = 0.076 and Ra* = 699)

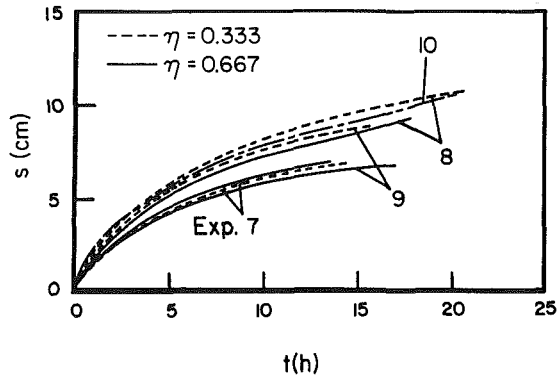

Fig. 7 Effect of superheating parameter on the rate of freezing for experiments 7, 8, and 9 (Da = 1.52 × 10^7)

iment 8, the respective times are 22 min and 21 min. These times are indicative of the strength of the convective flow present and its influence on the local freezing rate. Natural convection is strongest for experiment 2 (Ra* = 1691) and is weakest for experiment 8 (Ra* = 16.6). This is a consequence of the Darcy number, which is smallest for experiment 8 because of the low permeability of the medium.

Figure 5 shows the influence of bead size (permeability or Darcy number) on the rate of freezing for experiments 2, 5, and 8. The average superheat was about 12.5°C for experiments 2, 5, 8; therefore, the superheat parameter S was about the same, but the modified Rayleigh number (Ra*) was smallest for experiment 8. In all the experiments, the freezing at the bottom rake was faster than at the top. The influence of convection increases with time, as evidenced by the widening gap between the two curves for any experiment. The possible convective flow in the 0 to 4°C region is practically overpowered by the flow in the 4 to 12.5°C region. Hence, freezing proceeds faster at the bottom as in ordinary liquids (Viskanta, 1985; Oosthuizen, 1988). For experiment 8 the influence of convection is not as prominent as in other experiments, and the duration of the conduction-dominated freezing regime is the longest. As mentioned earlier, this is expected due to the small Darcy number (low permeability) and high resistance offered by the porous matrix to buoyancy-driven convection.

The temperature difference ($T_f - T_c$) in the Stefan number is the driving potential for heat transfer across the frozen region, while the superheat parameter is related to the Rayleigh number through the common temperature difference ($T_h - T_f$). The freezing process is influenced by all three parameters. Figure 6 shows the combined effect of the Stefan and Rayleigh numbers for the 6-mm-dia glass beads. The Stefan numbers for experiments 4, 5, and 6 are 0.046, 0.085, and 0.076, respectively. The corresponding Rayleigh numbers are 99.2, 332.7, and 699.4, respectively. In experiment 5, due to a power failure, the data acquisition was interrupted. The calculation of interface position at later times requires interpolations over long time intervals (possibly introducing big errors), and hence are not plotted. The rates of freezing decrease in order of experiments 5, 4, and 6. In experiment 4, the convection currents are weak, as revealed by the nearly equal rates of freezing along the two thermocouple rakes. The effect of convection was predominant in experiment 6. After about 10 h the experiment reached steady state and no further motion of the interface was observed. The Stefan number for experiment 5 is only about 10 percent higher that for experiment 6, but the Rayleigh number is double that of experiment 6.

Figure 7 shows the effect of initial superheating parameter, which is related to the Rayleigh number, on the rate of freezing for experiments 7, 8, and 9. Each of these experiments lasted 24 h. Near the end of this period the freezing process was very slow. Hence, to avoid large interpolation errors, only the exact times at which each thermocouple recorded 0°C were used for plotting the curves. This is the reason for the curves ending at different times. For experiment 7, there is practically no difference in the rates of freezing along the two rakes, indicating the presence of very weak convection. This is understandable, because the Rayleigh number for the porous medium is quite small (Ra* = 16.6). Between experiments 8 and 9, which have about the same Stefan number, the Rayleigh number for experiment 9 was about twice as high (i.e., higher superheat); therefore, convection sets in early and its influence is greater at later times as seen by the difference in the rates of freezing along the two rakes. The rate of freezing for an experiment with zero superheat and about the same Stefan number as for experiment 7 is also shown as experiment 10 in Fig. 7. This curve clearly reveals the extent to which natural convection flow (however weak it is) can influence and retard the freezing process.

Theoretical Predictions for Flow and Temperature Fields. The freezing process in experiment 8 was numerically simulated for 10 h of real time. The results of the simulation are presented in this section. The conditions of experiment 8 were considered to be more critical than those of experiment 1, even though the Rayleigh number for the latter was much higher, for validating the model. This is because both the Stefan number and the superheating parameter were larger for experiment 8. The predicted temperature distributions are compared (in the following section) with those measured. In this comparison the variation of cold wall temperature with time must be taken into consideration. Also, since the test cell was very wide, it was not possible to cool the entire PCM-porous matrix mixture to the desired uniform initial temperature from the ambient room conditions. The numerical model used the measured cold wall temperatures as a function of time and the average initial temperature as input data.

The streamlines and isotherms at $\tau = 0.00564$ ($t = 0.5$ h) are presented in Figs. 8(a) and 8(b), respectively. The influence of convection is revealed very clearly by the isotherms. The major portion of liquid near the hot wall has not cooled, but the interface is almost planar. The streamlines (Fig. 8a) show the strong downward flow near the interface. Compared to the upward velocity near the hot wall, the velocities in this region are about 15 times higher. The warm water on approaching the interface is cooled, becomes heavier, and flows downward. As the influence of the interface has not been felt

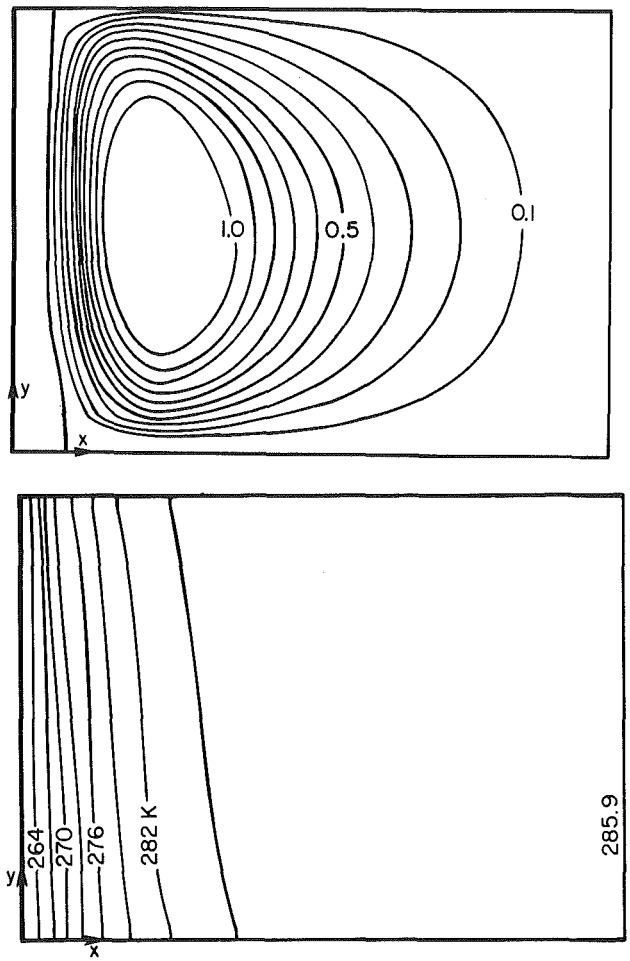

Fig. 8 Streamlines and isotherms for experiment 8 (Da = 1.52 × 10^{-7}, Ra* = 65, S = 0.164) at τ = 0.00564 (t = 0.5 h): (*a*) streamlines, and (*b*) isotherms

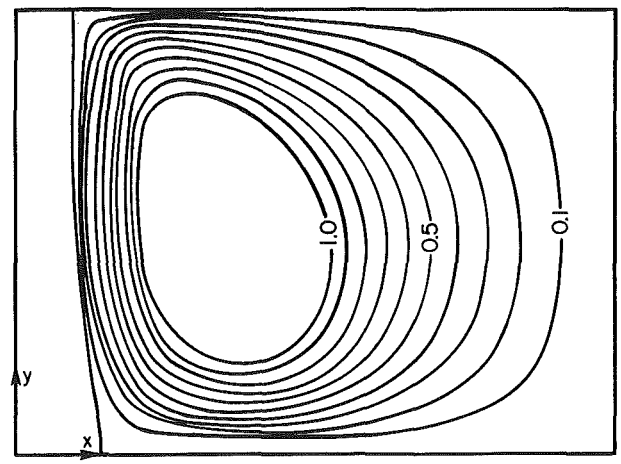

Fig. 9 Streamlines for experiment 8 at τ = 0.011 (t = 1 h)

in the regions away from it, the water in these regions rises upward. To preserve mass balance, the downward velocity must be high in the small region near the interface. Thus, only one counterclockwise cell is predicted even though water undergoes a density inversion. Flow visualization experiments (Chellaiah and Viskanta, 1987) confirmed this predicted flow pattern.

Figure 9 shows the streamlines at τ = 0.011 (t = 1 h). The region of downward flow has increased in size and the core of the cell has moved away from the solidification front. The

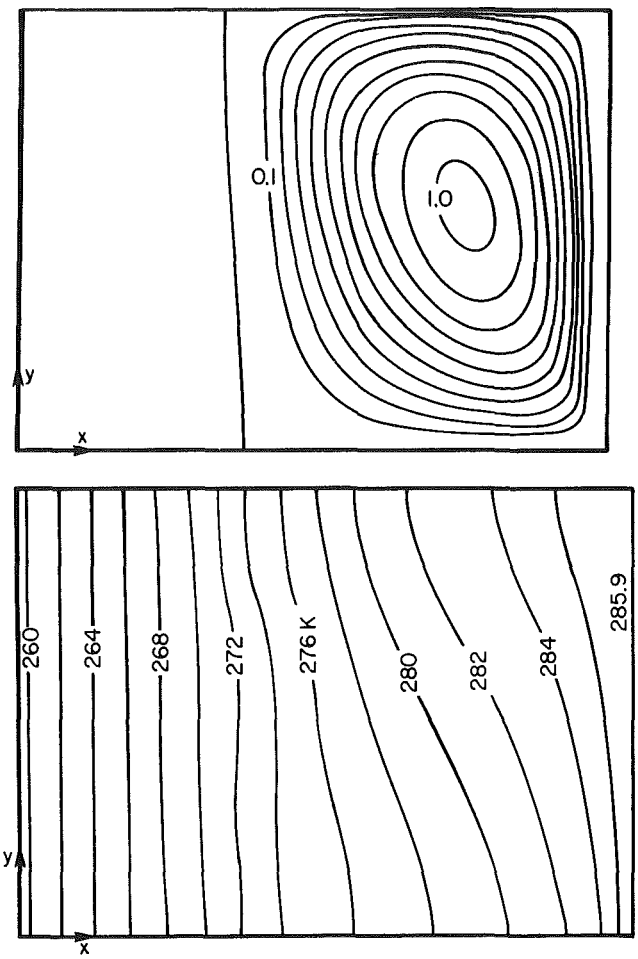

Fig. 10 Streamlines and isotherms for experiment 8 at τ = 0.113 (t = 10 h): (*a*) streamlines, and (*b*) isotherms

water near the hot wall has gained momentum and is moving upward at higher velocity. By τ = 0.056 (t = 5 h) (not shown), the influence of the cold interface has been felt in all regions and stronger convection currents are noted. The core of the cell has moved closer to the hot wall, and the flow pattern is similar, though weaker, to that observed in the case of solidification of ordinary liquids (Viskanta, 1985; Oosthuizen, 1988). The isotherms reveal the influence of natural convection and hence are inclined to the left, indicating a higher rate of freezing at the bottom than at the top.

The streamlines and isotherms at τ = 0.113 (t = 10 h) are presented in Fig. 10. The predicted upward velocity near the hot wall was found to be larger than the downward velocity near the interface. This is just opposite to that observed at t = 0.5 h (not shown). The region of downward flow has grown larger than that of upward flow. Hence, a higher upward velocity is needed to maintain mass conservation of water in the flow. The plot also shows a smaller rate of freezing near the top than at the bottom. The isotherms are smooth and well spaced, revealing stronger convection currents.

The streamlines are also smooth and crowded near the hot wall, unlike those in Fig. 8 (which were crowded near the interface). The reason for this is the same as mentioned above. The absolute values of stream function has decreased with time, indicating smaller velocity gradients or a smoother flow encompassing the entire liquid region. Again, even though the density inversion of temperature of water lies in this region, the possible flow in the region bounded by the cold wall and this isotherm is overpowered by the stronger counterclockwise flow in the remaining liquid zone.

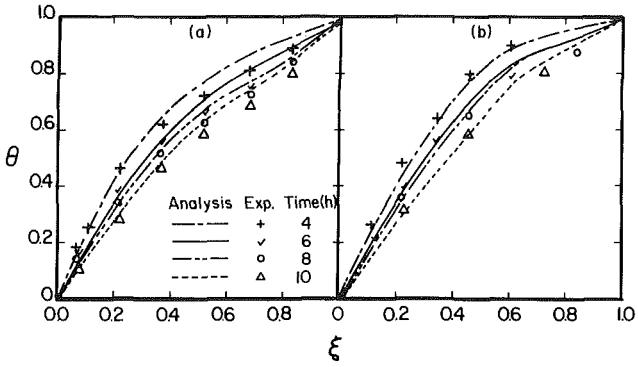

Fig. 11 Comparison of experimental and predicted temperatures for experiment 8: (*a*) bottom rake (η = 0.333) and (*b*) top rake (η = 0.667)

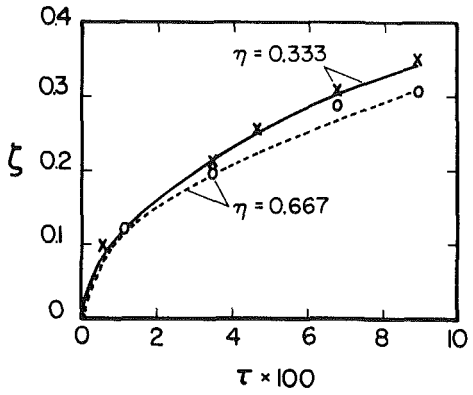

Fig. 12 Comparison of experimental and predicted interface locations for experiment 8: (*a*) bottom rake (η = 0.333), and (*b*) top rake (η = 0.667)

For experiment 1 the model predicted the presence of two cells in the liquid (Chellaiah, 1988). The water is bounded by the interface and the hot wall at an average temperature difference of 6°C. Along the interface, colder water rises and moves toward the hot wall. As it is heated, it becomes heavier and descends along the 4°C isotherm, thereby forming a clockwise-rotating cell. The water near the hot wall also rises and moves toward the interface. After cooling, the water becomes heavier and descends along the 4°C isotherm, thereby forming a counterclockwise-rotating cell. This cell flow structure was observed in the flow visualization experiments (Chellaiah and Viskanta, 1987).

Comparison of Predicted Results With Experimental Data. A comparison between the predicted and the measured temperature distributions for experiment 8 at different times and along the two different vertical locations is presented in Fig. 11. In general, the agreement between the two results is good, but the temperatures in the liquid region are always overpredicted. The discrepancy is less than 5 percent of the total temperature difference across the test cell and is within the experimental uncertainty. Any heat gains from the ambient to the test cell would tend to increase the temperatures, not lower them; therefore, the gains can be dismissed as the reason for the discrepancy. Certainly, the porosity and permeability are not uniform within distances of a few bead diameters from the solidification front and the hot wall (Chandrasekara and Vortmeyer, 1979). The effect of wall channeling due to the porosity variation near the wall is believed to be an important reason for increasing the temperature gradients near the hot boundary. The predicted temperature gradients based on uniform porosity and permeability are smaller than the measured ones, particularly at later times in the freezing process.

Figure 12 shows a comparison of the predicted and measured dimensionless interface positions. Good agreement is noted between the two results. The model predicts higher rates of freezing along the bottom rake than the top rake as observed in the experiment, but the model underpredicts the interface locations at later times. The simulation was terminated at 10 h of real time experiment, for no new additional information would have been revealed. An understanding of the flow pattern and temperature fields has already been provided by this long simulation.

There are a number of factors that may contribute to the discrepancy between data and predictions and include the following: (1) expansion of the liquid during freezing of water, (2) inappropriate permeability and effective thermal conductivity models for the porous media, (3) precise location of the interface in the region where both the liquid and solid phases exist simultaneously, and (4) numerical errors due to insufficiently fine grid. For example, the control volumes are relatively larger (8.5 mm) to be represented by a node and assigned a single temperature. All of these factors can affect the flow structure and temperature distributions in the solid and liquid regions and alter the solidification front shape and motion.

Concluding Remarks

An experimental and numerical study of freezing of liquid-saturated porous media utilizing glass beads and water has been performed. A number of different experiments using three different size glass beads and different superheats have been conducted. The experiments performed have provided conclusive evidence that natural convection in the liquid region causes the solidification front to become nonplanar and reduces the rate of freezing of water-saturated porous media. The intensity of natural convection in the unfrozen region depends on the Rayleigh number of the porous medium Ra*. Even for a Rayleigh number as low as 16.6, the effects of natural convection on the local rate of freezing are clearly evident. The larger Ra*, the more intense is the natural convection in the liquid and the more nonuniform is the solidification front. For superheats smaller than 6°C, due to the density inversion of water, natural convection caused more freezing in the upper than in the lower part of the test cell.

An enthalpy-based numerical model that considers both diffusion in the solid and liquid regions and buoyancy-driven convection in the liquid has been used to simulate freezing of liquid-saturated porous media. The numerical predictions were compared with measured temperatures and interface positions, and good correspondence has been found. The possible reasons for the discrepancy between model predictions and the data have been discussed. The computational resources needed to obtain solutions were excessive.

There is a need for flow visualization and nonintrusive diagnostics for temperature and solidification front position measurement in porous media, both in the absence and in the presence of phase change. There is also a need for developing efficient, accurate, cost-effective numerical algorithms for solving the model equations for two- and three-dimensional solid/liquid phase change of porous media in the presence of natural convection.

Acknowledgments

The work reported in this paper was supported, in part, by the Heat Transfer Program of the National Science Foundation under Grant No. CBT-8313573.

References

Albin, F. V., Srinivasamurthy, S., and Krishnamurthy, M. V., 1982, "Analysis of the Food Freeze Drying Process With Predetermined Surface Temperature Variation," in: *Drying '82*, A. S. Mazumdar, ed., Hemisphere Publishing Corp., Washington, DC, pp. 151-156.

Aung, W., and Yener, Y., 1985, "Research Directions in Natural Convec-

tion," in: *Natural Convection Fundamentals and Applications*, S. Kakac, W. Aung, and R. Viskanta, eds., Hemisphere Publishing Corp., Washington, DC, pp. 1155–1171.

Beckermann, C., and Viskanta, R., 1988, "Natural Convection, Solid/Liquid Phase Change in Saturated Porous Media," *International Journal of Heat and Mass Transfer*, Vol. 31, pp. 35–46.

Benenati, R. F., and Brosilow, C. B., 1962, "Void Fraction Distribution in Beds of Spheres," *AIChE Journal*, Vol. 8, pp. 359–361.

Chandresekara, B. C., and Vortmeyer, D., 1979, "Flow Model for Velocity Distribution in Fired Porous Beds Under Isothermal Conditions," *Wärme- und Stoffübertragung*, Vol. 12, pp. 105–111.

Chellaiah, S., and Viskanta, R., 1987, "Natural Convection Flow Visualization in Porous Media," *International Communications in Heat and Mass Transfer*, Vol. 14, pp. 607–616.

Chellaiah, S., and Viskanta, R., 1988, "Freezing of Saturated and Superheated Liquid in Porous Media," *International Journal of Heat and Mass Transfer*, Vol. 31, pp. 321–330.

Chellaiah, S., 1988, "An Experimental and Numerical Study of Solid/Liquid Phase Change of Water Saturated Porous Media in the Presence of Natural Convection," Ph.D. Thesis, Purdue University, W. Lafayette, IN.

Cheng, P., 1978, "Heat Transfer in Geothermal Systems," in: *Advances in Heat Transfer*, T. F. Irvine, Jr. and J. P. Hartnett, eds., Academic Press, New York, Vol. 14, pp. 1–106.

Combarnous, M. A., and Bories, S. A., 1976, "Hydrothermal Convection in Saturated Porous Media," in: *Advances in Hydroscience*, Academic Press, New York, Vol. 10, pp. 231–307.

Frivik, P. E., and Comini, G., 1982, "Seepage and Heat Flow in Soil Freezing," ASME JOURNAL OF HEAT TRANSFER, Vol. 104, pp. 323–328.

Gebhart, B., and Mollendorf, J. C., 1978, "Buoyancy-Induced Flows in Water Under Conditions in Which Density Extrema May Arise," *Journal of Fluid Mechanics*, Vol. 89, pp. 673–707.

Gebhart, B., Jaluria, Y., Mohafan, R. L., and Sammakia, B., 1987, *Buoyancy-Induced Flows and Transport*, Hemisphere Publishing Corp., Washington, DC.

Goldstein, M. E., and Reid, R. L., 1978, "Effect of Fluid Flow on Freezing and Thawing of Saturated Porous Media," *Proceedings of the Royal Society of London*, Series A, Vol. 365, pp. 45–73.

Hashemi, H. T., and Sliepcevich, C. M., 1973, "Effect of Seepage Stream on Artificial Soil Freezing," *ASCE Mechanics and Foundation Division*, Vol. 99, pp. 267–289.

Lunardini, V. J., 1981, *Heat Transfer in Cold Climates*, Van Nostrand Reinhold Co., New York.

ME Staff, 1983, "Seasonal Thermal Energy Storage," *Mechanical Engineering*, Vol. 105, No. 3, pp. 28–34.

Metz, P. D., 1983, "A Simple Computer Program to Model Three-Dimensional Underground Heat Flow With Realistic Boundary Condition," ASME *Journal of Solar Energy Engineering*, Vol. 105, pp. 42–49.

Nguyen, T. H., Vasseur, P., and Robillard, L., 1982, "Natural Convection Between Horizontal Concentric Cylinders With Density Inversion of Water for Low Rayleigh Numbers," *International Journal Heat and Mass Transfer*, Vol. 25, pp. 1559–1568.

O'Neill, K., and Albert, M. R., 1984, "Computation of Porous Media Natural Convection Flow and Phase Change," in: *Finite Elements in Water Resources*, J. P. Laible, C. A. Brebbia, W. Gray, and G. Pinder, eds., Springer-Verlag, Berlin, pp. 213–229.

Oosthuizen, P. H., 1988, "The Effects of Free Convection on Steady Freezing in a Porous Medium-Filled Cavity," in: *ASME Proceedings of the 1988 National Heat Transfer Conference*, H. R. Jacobs, ed., ASME, New York, Vol. 2, pp. 321–327.

Patankar, S. V., 1980, *Numerical Heat Transfer and Fluid Flow*, McGraw-Hill, New York.

Sanger, F. J., 1968, "Ground Freezing in Construction," *ASCE Mechanics and Foundations Division*, Vol. 94, pp. 131–158.

Svec, O., Goodrich, L. E., and Planar, J. H. L., 1983, "Heat Transfer Characteristics of Inground Heat Exchangers," *Journal of Energy Research*, Vol. 7, pp. 263–278.

Veinberg, A. K., 1967, "Permeability, Electrical Conductivity, Dielectric Constant and Thermal Conductivity of a Medium With Spherical and Ellipsoidal Inclusions," *Soviet Physics Doklady*, Vol. 11, pp. 593–595.

Viskanta, R., 1985, "Natural Convection in Melting and Solidification," in: *Natural Convection Fundamentals and Applications*, S. Kakac, W. Aung, and R. Viskanta, eds., Hemisphere Publishing Corp., Washington, DC, pp. 845–877.

Weaver, J. A., and Viskanta, R., 1986, "Freezing of Liquid-Saturated Porous Media," ASME JOURNAL OF HEAT TRANSFER, Vol. 108, pp. 654–659.

Combined Convection-Conduction-Radiation Boundary Layer Flows Using Optimal Control Penalty Finite Elements

L. R. Utreja
The BDM Corporation
Huntsville, AL 35806

T. J. Chung
The Department of Mechanical Engineering
The University of Alabama in Huntsville
Huntsville, AL 35899

Numerical solutions for combined convection and radiation in a laminar boundary layer on an isothermal wall are obtained using optimal control penalty (OCP) finite elements. The integro-differential energy equation is solved without any limitation of optical thickness. The expression for the divergence of radiation flux containing integral terms is written in terms of a one-dimensional radiation field for a flat plate geometry. The radiation interaction effect on the temperature distribution in the boundary layer is described. The solution of the integro-differential energy equation is then compared with known solutions in the limits of optical thickness.

1 Introduction

In the boundary layer flow of a radiating fluid, the thermal radiation alters the temperature distribution, which, in turn, affects the heat transfer at the wall. The earlier work in this area is that of Goulard and Goulard (1959) who investigated the interaction of radiation and convection for one-dimensional Couette flow. Simple approximate models have often been used in order to circumvent the computational difficulties involved in the exact formulations. In this regard, the integral terms in the expression for the radiant flux have been eliminated in the limiting cases of optical thickness. Koh and DeSilva (1962) made the approximation of an optically thin gas to study the radiation interaction effects on the boundary layer flow past a flat plate with a cold hypersonic stream. Cess (1964) came up with a better model for an optically thin gas, including effects of absorption, and evaluated first-order interaction effects upon the boundary layer heat transfer. Several other authors have studied the optically thick case for intense absorption. Viskanta and Grosh (1962) investigated laminar flow across a wedge using the Rosseland approximation. For flows with radiation alone, or with radiation and conduction, the optically thick case was shown to be a correct limit by Sparrow and Cess (1966) and Wang (1965), respectively. However, the role of the optically thick limit in the convection-radiation interaction was studied by Novotny and Yang (1967). Cess (1966) formulated the problem using the method of singular perturbations in terms of a parameter characterizing the importance of conduction versus radiation. Pai and Tsao (1966) used exponential Kernel approximation, and Oliver and McFadden (1966) used a series solution with an interactive approach to approximate the effect of radiative interaction in boundary layer flows on an isothermal flat plate. Taitel and Hartnett (1966), on the other hand, used an iterative approach to study radiation interaction with an adiabatic flat plate.

While many investigators have used a one-dimensional model of radiation flux with exponential integral terms, a simultaneous solution of the energy equation including integral terms has not been carried out for a viscous, conducting, absorbing, and emitting fluid. Taitel (1969) has derived an exact solution for the radiation layer over a flat plate for a nonviscous, nonconducting, radiation participating fluid. However, as the medium becomes dominated by convection, the numerical solutions encounter formidable difficulties using standard Galerkin finite elements. The main source of difficulty is the convection term, which renders the differential equation non-self-adjoint and the corresponding Galerkin finite element equation asymmetric and ill-conditioned.

To overcome the difficulty of the convection term, the optimal control penalty finite elements have been used by Chung (1980, 1982) for several heat transfer and fluid flow problems. More recently, Utreja and Chung (1982) have used a method of solving the compressible boundary layer equations in which the pressure gradient and heat transfer are cast in a similar form. Utreja (1982) has studied the interaction of radiation with the compressible boundary layer flow of a participating medium.

This study is concerned with the application of optimal control penalty finite elements to the solution of compressible boundary layer flow in a radiation participating medium using various approximations for the radiation flux (Chung, 1984).

2 Laminar Boundary Layer Flow of a Radiation Participating Medium

Here, we consider the steady, two-dimensional flow of a viscous, radiation absorbing, emitting, and thermally conducting fluid. The flow is considered parallel to the flat surface in the free stream. The geometry of the physical model and the coordinate system are illustrated in Fig. 1. The surface is assumed to be black and at a uniform temperature. Additional assumptions are:

- The fluid is assumed to be nonscattering (i.e., the absence of droplets and suspended particles. In general, the wavelength for the thermal radiation is sufficiently large, so that the Rayleigh scattering, which is inversely proportional to the fourth power of the wavelength, is negligible).
- The fluid has an absorption coefficient independent of wavelength.
- The heat transfer by conduction and radiation is considered to be one dimensional.

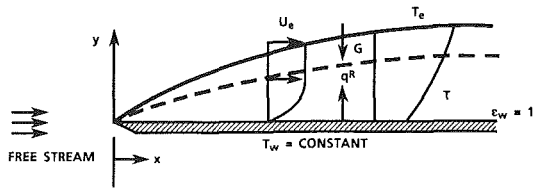

Fig. 1 Sketch of the physical model and coordinate system

Contributed by the Heat Transfer Division for publication in the JOURNAL OF HEAT TRANSFER. Manuscript received by the Heat Transfer Division February 23, 1988. Keywords: Numerical Methods, Radiation, Radiation Interactions.

The governing equations representing the physical system described above for the boundary layer flow of a radiating gas are written in the form

$$\frac{\partial}{\partial x}(\rho u)+\frac{\partial}{\partial y}(\rho v)=0 \tag{1}$$

$$\rho\left(u\frac{\partial u}{\partial x}+v\frac{\partial u}{\partial y}\right)=-\frac{\partial p}{\partial x}+\frac{\partial}{\partial y}\left(\mu\frac{\partial u}{\partial y}\right) \tag{2}$$

$$\rho c_p\left(u\frac{\partial T}{\partial x}+v\frac{\partial T}{\partial y}\right)=\frac{\partial}{\partial y}\left(k\frac{\partial T}{\partial y}\right)+\mu\left(\frac{\partial u}{\partial y}\right)^2-\frac{\partial q^R}{\partial y} \tag{3}$$

The expression for the gray wall radiative flux $\partial q^R/\partial y$ in terms of the optical length τ and integro-exponential functions $E_n(\tau)$ is given as

$$\frac{\partial q^R}{\partial \tau}(0,\,x)=4\sigma T^4(\tau,\,x)-2\epsilon_w E_2(\tau)\sigma T_w^4$$

$$-4(1-\epsilon_w)E_2(\tau)\int_0^\infty \sigma T^4(\tau',\,x)E_2(\tau')d\tau'$$

$$-2\int_0^\infty \sigma T^4(\tau',\,x)E_1(|\tau-\tau'|)d\tau' \tag{4}$$

For the problem under consideration, $\epsilon_w=1$, and the wall temperature T_w is constant. The exponential integral function $E_n(\tau)$ is given by the expression

$$E_n(\tau)=\int_0^1 \tau'^{(n-2)}\exp(-\tau/\tau')d\tau' \tag{5}$$

Since the pressure remains constant across the boundary layer in the boundary layer simplifications, the equation of state for a perfect fluid becomes

$$\rho T=\rho_e T_e \tag{6}$$

The specific heat c_p and the Prandtl number Pr are assumed to be constant. The thermal conductivity and the viscosity are assumed to be linear functions of temperature

$$\frac{\mu}{\mu_e}=\frac{K}{K_e}=C\frac{T}{T_e} \tag{7}$$

where C is the Chapman-Rubesin factor (Chapman and Rubesin, 1949) and is taken to be unity in the present case.

The equations are nondimensionalized and transformed from (x, y) coordinates into a new system (ξ, η). The resulting equations taken from Utreja (1982) are

$$ff''+f'''=0 \tag{8}$$

and

$$\frac{\partial^2\theta}{\partial\eta^2}+\mathrm{Pr}f\frac{\partial\theta}{\partial\eta}-\mathrm{Pr}f'\xi\frac{\partial\theta}{\partial\xi}=$$

$$-\frac{(\gamma-1)}{4}\mathrm{PrM}^2(f'')^2+N_{R-C}\zeta\frac{\partial Q^R}{\partial\eta} \tag{9}$$

where

$$\eta=\frac{1}{2x^{1/2}}\int_0^y \rho/\rho_e dy \tag{10}$$

$$\xi=x^{1/2} \tag{11}$$

$$\zeta=2\mathrm{Bu}\xi \tag{12}$$

$$N_{R-C}=\mathrm{RePr}/B_0\tau_L \tag{13}$$

$$\frac{\partial Q^R}{\partial\eta}=4\theta^4(\xi,\,\eta)-2\zeta^2\int_0^\infty \theta^4(\xi,\,\tau')E_1(\zeta|\eta-\tau'|)d\tau'$$

$$-2\theta_w^4\zeta E_2(\zeta\eta) \tag{14}$$

$$\tau=\frac{\rho_e\kappa}{\sqrt{R_e}}\int_0^y \rho/\rho_e dy \tag{15}$$

Defining nondimensional optical depth results in

$$\tau_L=\rho_e\kappa L \tag{16}$$

$$\mathrm{Bu}=\frac{\rho_e\kappa L}{\sqrt{R_e}}=\frac{\tau_L}{\sqrt{R_e}} \tag{17}$$

in which θ is the nondimensional temperature T/T_e, and the primes denote differentiation with respect to the coordinate η. The boundary conditions are

$$f(0)=f'(0),\quad f'(\infty)=2 \tag{18}$$

Nomenclature

B_0 = Boltzmann number $=\rho_e u_e C_p T_e/\sigma T_e^4$
Bu = Bouger number $=\rho_e\kappa L/\sqrt{\mathrm{Re}}$
c_p = specific heat at constant pressure
C = Chapman-Rubesin factor
E = $(\gamma-1)\mathrm{M}_e^2$
E_n = exponential integral function $=\int_0^1 \mu^{n-2}\exp(-\tau/\mu)d\mu$
f = velocity function $=\psi/\sqrt{x}$
G = incident radiative flux
K = thermal conductivity
L = plate length
M = Mach number
n = index of refraction
N = dimensionless conduction-radiation parameter $=k\kappa/4n^2\sigma T^{*3}$
N_{R-C} = extrinsic radiation parameter $=\mathrm{RePr}/B_0\tau_L$
p = pressure
Pr = Prandtl number $=c_p\mu/k$
Q^R = nondimensional radiative flux $=q^R/\sigma T_e^4$
Re = Reynolds number $=\rho_e u_e L/\mu_e C$
T = temperature
u, v = components of velocity in the orthogonal x and y directions
x, y = Cartesian orthogonal coordinates
γ = specific heat ratio
ϵ = emissivity
ζ = intrinsic radiation parameter $=2\mathrm{Bu}\xi$
η = independent variable $=1/(2\sqrt{x})\int_0^y \rho^* dy$
θ = dimensionless temperature T/T_e
κ = mass absorption coefficient
λ = penalty constant
ρ = density of the fluid
σ = Stefan-Boltzmann constant
Ω = volume space

Subscripts

e = boundary layer edge property
w = wall property
∞ = free-stream property

Superscripts

$*$ = reference value

$$\left.\begin{aligned}\theta(\xi, 0)=\theta_w, \quad \theta(0, \eta)=1\\ \theta(\xi, \eta_\infty)=1\end{aligned}\right\} \tag{19}$$

3 The Optimal Control Penalty Finite Elements (OCP)

In the OCP method, higher order differential equations are reduced to a system of lower order equations (Utreja, 1982). A cost function is then developed as a sum of the squares of the residual errors. The auxiliary constraint equations are added to the original transformed lower order equation via penalty constants. The objective is to seek an extremum of the cost function with respect to the dependent variables. The advantage of the method lies in the fact that the resulting matrix is symmetric and positive definite, and both the essential and natural boundary conditions can be prescribed at the boundary nodes. In addition, the introduction of a penalty constant on the square of residual errors places emphasis on the approximation used in the auxiliary constraint equations. The use of a penalty constant generally improves the accuracy of the approximation and enhances rate of convergence.

The OCP finite element equations for each element are obtained using isoparametric elements and the numerical integration will be performed using Gaussian quadrature. The Blasius equation was solved separately and the results are presented by Utreja (1982). Considering f, f', and f'', therefore, to be known functions, the OCP analog of the energy equation (9) in terms of residuals R_1 and R_2 becomes

$$R_1=\frac{\partial H}{\partial \eta}+\mathrm{Pr}\, f\frac{\partial \theta}{\partial \eta}-\mathrm{Pr}f'\xi\frac{\partial \theta}{\partial \xi}+\frac{\gamma-1}{4}\mathrm{PrM}^2(f'')^2-N_{R-C}\zeta\frac{\partial Q^R}{\partial \eta}=0 \tag{20}$$

$$R_2=H-\frac{\partial \theta}{\partial \eta}=0 \tag{21}$$

We construct the cost function J such that

$$J=\int_\Omega R_1^2 d\Omega+\lambda\int R_2^2 d\Omega \tag{22}$$

We minimize the cost function and obtain

$$\delta J=\frac{\partial J}{\partial \theta\alpha}\delta\theta_\alpha+\lambda\frac{\partial J}{\partial H_\alpha}\delta H_\alpha=0 \tag{23}$$

Since $\delta\theta_\alpha$ and δH_α are arbitrary, we must have

$$\int_\Omega\left(R_1\frac{\partial R_1}{\partial \theta_\alpha}+\lambda R_2\frac{\partial R_2}{\partial H_\alpha}\right)d\Omega=0 \tag{24}$$

These operations result in algebraic equations of the form

$$A_{ij}(X)X_j=f_i \tag{25}$$

Here, X_j are the unknown quantities to be solved and A_{ij} is the positive definite and symmetric matrix for a set of finite element equations. Equation (25) represents a system of nonlinear algebraic equations, which are best solved using the Newton–Raphson method

$$J_{ij}\Delta X_j^{(n+1)}=-f_i^{(n)} \tag{26}$$

where

$$J_{ij}=\frac{\partial f_i^{(n)}}{\partial X_j} \tag{27}$$

$$\Delta X_j^{(n+1)}=X_j^{(n+1)}-X_j^{(n)} \tag{28}$$

in which J_{ij} is the Jacobian matrix whose inversion is avoided in the calculation of $\Delta X_j^{(n+1)}$. The value of the quantities at a new iteration step is determined by equation (28). It should be noted that the elements of the J_{ij} matrix contain the penalty constant. The rate of convergence depends greatly on the choice of penalty constants, which was investigated numerically. It is emphasized here that the advantage of the optimal control finite element method is the well-conditioned matrix equations, which provide stability and accuracy.

4 Treatment of Radiative Flux Term

The radiative flux term (14) can be written in terms of the coordinate η as

$$\frac{\partial Q^R}{\partial \eta}=\zeta\left[4\theta^4(\xi,\eta)-2\zeta\int_0^\infty\theta^4(\xi,\eta')E_1(\zeta|\eta-\eta'|)d\eta'-\theta_w^4E_2(\eta)-2\bar{G}E_2(\zeta[\eta_d-\eta])\right] \tag{29}$$

In the OCP equations, the first term on the right-hand side is retained as the nonlinear term so that an iterative approach can be used for the Newton–Raphson technique. The third and fourth terms are treated as constants since the wall temperature θ_w and the incident flux $\bar{G}$ are prescribed. However, a special technique is needed to handle the second term. It involves an integral of a quantity containing the unknown θ. Consider the integral

$$\int_0^\infty\theta^4(\xi,\eta')E_1(\zeta|\eta-\eta'|)d\eta'=F(\xi,\eta) \tag{30}$$

As shown in equation (30), the desired integral is a function of ξ and η and is represented as $F(\xi, \eta)$. The temperature $\theta(\xi, \eta)$ is considered to be a known value from the previous iteration. The values of $\theta(\xi, \eta)$ for η greater than the physical domain are taken to be the free-stream values. The product (θ^4E_1) is obtained for each nodal point represented by $\zeta\,(=2\mathrm{Bu}\xi)$ and η. The exponential integral E_1 is calculated using its series approximation

$$E_1(z)=-a-\ln(z)+z-z^2/4!+z^3/18!-z^4/96!+\ldots \tag{31}$$

where a is the Euler constant.

The integral in equation (30) is then performed using Simpson's Rule for each nodal point. A finite element analog of the quantity $F(\xi, \eta)$ is written as

$$F(\xi,\eta)=\Phi_\alpha F_\alpha \tag{32}$$

where θ_α are the interpolation functions for the global nodes and α and F_α are the corresponding nodal values of the functions $F(\xi, \eta)$.

5 Discussions and Results

The accuracy of the OCP method was first determined by comparing computed results against the Blasius solution and the Stewartson solution for the compressible boundary layer. However, for the case of a radiation boundary layer where the exact solution is not available, an acceptable solution was considered to have been obtained when the convergence criteria were met. That is, a pointwise root mean square error between the previous and current iterative cycles less than 10^{-5} was taken as the converged solution.

Here, we assume that the fluid has a Prandtl number $\mathrm{Pr}=1.0$ and the extrinsic radiation parameter $N_{R-C}=10^5$, where N_{R-C} is a measure of the radiation heat flux to the convective heat flux, and the case considered corresponds to a strong radiative interaction. The noninteraction temperature profile is used as an initial iterate for the radiation interaction case. The value of the penalty constant that yields a maximum value of the temperature gradient at the wall is selected as an optimal value of λ. The optimal value of λ is found to be 10^5. It is pointed out that convergence is very slow in the radiation interaction case. The computational results presented here are obtained after six iterations, using 550 nodes. It should be mentioned, however, that the solution stability and accuracy

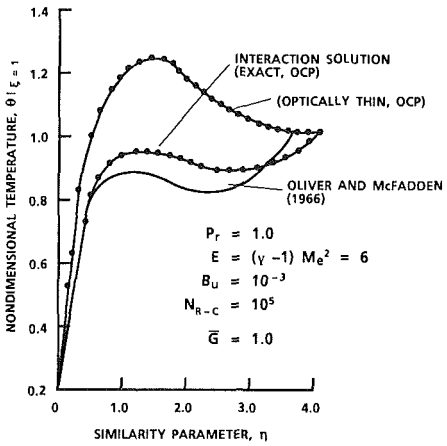

Fig. 2 Radiation interaction temperature profiles (no incident flux, $\bar{G}=0$)

achieved by the optimal control penalty far outweigh the slow convergence. This is particularly important because the solution cannot even be obtained without the special numerical scheme, such as the OCP method employed in the present study, due to excessively ill-conditioned matrix equations arising from the convective terms.

Figure 2 shows the temperature distribution in the thermal boundary layer at $\xi=1.0$. Also plotted are temperature profiles for the optically thin case (Cess, 1964) and the results of Oliver and McFadden (1966). It is seen that the peak temperature in the thermal boundary layer for the exact case is at the outer edge of the thermal layer, whereas the optically thin case yields a higher peak. That is, the effect of the exact description of radiation flux is to decrease the peak temperature and flatten out the temperature profile. In the optically thin case, however, the temperature profile asymptotically approaches the free-stream temperature. Another effect of radiation is to decrease the temperature gradient $\partial\theta/\partial\eta$ at the wall. It is also observed that the radiation penetration distance is larger than the thermal layer thickness. The comparison with Oliver and McFadden (1966) shows that even though the peak temperature occurs at about the same η location, the present results show a higher peak and more flattening of the temperature profile. A finite conduction is observed at the edge of the thermal layer.

The radiation interaction temperature profiles with an incident radiant flux at the outer edge of the thermal layer considered are shown in Fig. 3. The peak temperature in the thermal layer in this case is higher than the free-stream temperature. Also, the temperature gradient at the wall is larger than the case of a zero radiant flux. Once again, the radiation penetration distance is much larger than the thermal layer thickness. The results are in agreement with those of Oliver and McFadden (1966). The peak temperature is shown to be at the same η location in the two cases and the present results indicate more flattening of the boundary layer temperature profile.

An OCP solution is obtained for the optically thick limit using the Rosseland approximation described by Viskanta and Grosh (1962). The governing equation solved is

$$\left(\left(1+\frac{4\theta^3}{3N}\right)\theta'\right)' + \mathrm{Pr} f\theta' = 0$$

subjected to boundary conditions

$$f = f' = 0 \qquad \theta = \theta_w \text{ at } \eta = 0$$

$$f' = 1 \qquad \theta = \theta_\infty \text{ at } \eta \to \infty$$

The dimensionless parameter N determines the role of conduction versus radiation. The results are computed for two values of N and are presented in Fig. 4. For the case of $N=1$, the

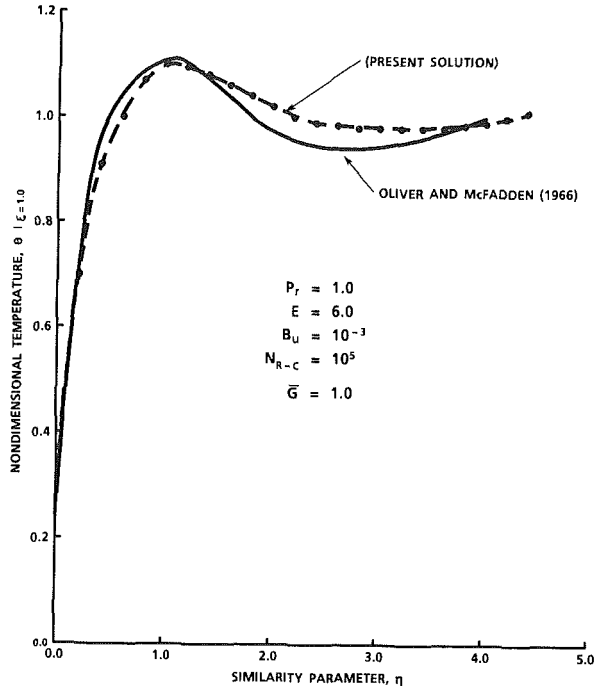

Fig. 3 Radiation interaction profiles with incident flux ($E=6.0$, $\theta_w=0.2$)

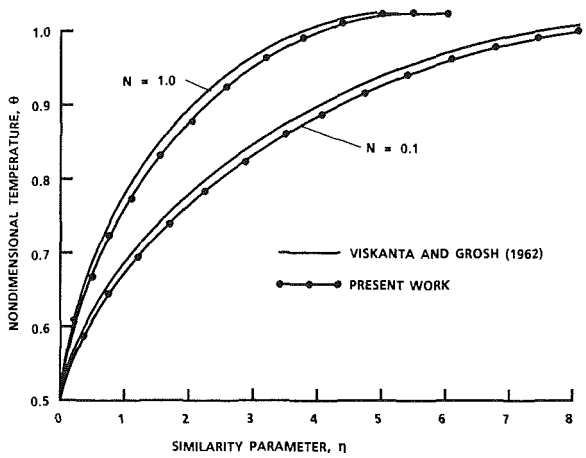

Fig. 4 Temperature profiles as functions of the similarity variable η for Pr = 1.0, $\theta_w=0.5$, and $\theta_0=1.0$

energy transport by molecular conduction is of the same order of magnitude as radiation, and in the $N=0.1$ case, the radiation dominates. It is observed that the effect of radiation (lower value of N) is to thicken the thermal boundary layer. For the $N=1$ case, the thermal boundary layer thickness matches that of Viskanta and Grosh (1964). For the radiation dominant case, the OCP method yields a thicker thermal boundary layer. It is attributed to a higher value of wall temperature.

6 Conclusions

The application of a novel finite element method for the solution of combined conduction, convection, and radiation has been successfully attempted. The advantage of the method is that the solution matrix is symmetric and positive definite, and both the essential and natural boundary conditions can be prescribed at the boundary. The solution stability and accuracy achieved by the optimal control penalty finite elements far outweigh the slow convergence. This is particularly impor-

tant because the solution cannot even be obtained without such a special numerical scheme due to excessively ill-conditioned matrix equations arising from the convective terms.

It has been shown that the effect radiation is to thicken the thermal boundary layer. In the absence of incident radiation flux, the peak temperature occurs at the edge of the thermal boundary layer. With incident radiation flux, on the other hand, the peak temperature occurs within the thermal boundary layer.

References

Cess, R. D., 1964a, "The Interaction of Thermal Radiation With Conduction and Convection Heat Transfer," *Advances in Heat Transfer*, T. F. Irvine and J. P. Hartnett, eds., Vol. I, Academic Press, New York, pp. 1-50.

Cess, R. D., 1964b, "Radiation Effects Upon Boundary Layer Flow of an Absorbing Gas," ASME JOURNAL OF HEAT TRANSFER, Vol. 86, pp. 469-475.

Cess, R. D., 1966, "The Interaction of Thermal Radiation in Boundary Layer Heat Transfer," 3rd International Heat Transfer Conference, US-ASME-No. 167, Chicago, IL.

Chapman, D. R., and Rubesin, M. W., 1949, "Temperature and Velocity Profiles in the Laminar Boundary Layer With Arbitrary Distribution to Surface Temperature," *J. Aerospace Sciences*, Vol. 16, pp. 547-565.

Chung, T. J., and Karr, G. R., 1980, "Finite Element Analysis in Convective Heat Transfer," *Numerical Heat Transfer*, Vol. 3, pp. 35-46.

Chung, T. J., Karr, G. R., and Kim, J. Y., 1982, "Optimal Control Penalty Finite Elements in Fluid Dynamics," in: *Finite Elements in Fluids*, Vol. 5, Wiley, New York.

Chung, T. J., and Kim, J. Y. 1984, "Two-Dimensional Combined Mode Heat Transfer by Conduction, Convection, and Radiation in Emitting, Absorbing, and Scattering Media—Solution by Finite Elements," ASME JOURNAL OF HEAT TRANSFER, Vol. 106, No. 2, pp. 448-452.

Goulard, R., and Goulard, M., 1959, "Energy Transfer in the Couette Flow of a Radiant and Chemically Reacting Gas," *Proceedings*, The Heat Transfer and Fluid Mechanics Institute, Stanford University Press, Palo Alto, CA, pp. 126-139.

Koh, J. Y. C., and DeSilva, C. N., 1962, "Interaction Between Radiation and Convection in the Hypersonic Boundary Layer on a Flat Plate," *J. of American Rocket Society*, Vol. 32, pp. 739-743.

Novotny, J. L., and Yang, K., 1967, "The Interaction of Thermal Radiation in Optically Thick Boundary Layers," ASME Paper No. 67-HT-9.

Oliver, C. C., and McFadden, P. W., 1966, "The Interaction of Radiation and Convection in the Laminar Boundary Layer," ASME JOURNAL OF HEAT TRANSFER, Vol. 88, pp. 205-213.

Pai, S. I., and Tsao, C. K., 1966, "A Uniform Flow of a Radiating Gas Over a Flat Plate," *Proceedings, 3rd International Heat Transfer Conference*, Chicago, Vol. 5, pp. 129-137.

Sparrow, E. M., and Cess, R. D., 1966, *Radiation Heat Tranfser*, Wadsworth Publishing Co., Belmont, CA.

Taitel, Y., and Hartnett, J. D., 1966, "Equilibrium Temperatures in a Boundary Layer Flow Over a Flat Plate of Absorbing-Emitting Gas," ASME Paper No. 66-WA/HT-48.

Taitel, Y., 1969, "Exact Solution for the Radiation Layer Over a Flat Plate," ASME JOURNAL OF HEAT TRANSFER, Vol. 91, pp. 188-189.

Utreja, L. R., 1982, "Radiative-Convective Heat Transfer in Compressible Boundary Layers by Optimal Control Penalty Finite Elements," Ph.D. Dissertation, University of Alabama in Huntsville.

Utreja, L. R., and Chung, T. J., 1982, "Similar Solutions of Compressible Boundary Layer Equations Using Optimal Control Penalty Finite Elements," Paper A4-6, 11th SECTAM Conference, Huntsville, AL.

Viskanta, R., and Grosh, R. J., 1962, "Boundary Layer in Thermal Radiation Absorbing and Emitting Media," *Int. J. Heat Mass Transfer*, Vol. 5, pp. 795-806.

Wang, L. S., 1965, "Differential Methods for Combined Radiation and Conduction," Ph.D. Thesis, University of California, Berkeley.

K. Saito[1]

F. A. Williams

Department of Mechanical and Aerospace Engineering,
Princeton University,
Princeton, NJ 08544

I. S. Wichman[2]

J. G. Quintiere

Center for Fire Research,
National Bureau of Standards,
Gaithersburg, MD 20899

Upward Turbulent Flame Spread on Wood Under External Radiation

Experiments were performed to obtain histories of surface temperatures and rates of upward flame spread for vertically oriented, thermally thick wood slabs exposed to surface fluxes of thermal radiation up to 2.6 W/cm². Above a critical irradiance sustained upward flame spread occurred for Douglas-fir particle board with pilot initiation at the base of the fuel face. Data obtained included temperatures, flame heights, pyrolysis-front heights, combustion duration, and char-layer thickness for various irradiances and preheat times. The measurements were compared with theory.

Introduction

Upward turbulent flame spread over vertically oriented fuel surfaces is known to pose one of the most severe problems in accidental fires because of the associated rapid rates of fire spread. Many flammability tests have been designed to assess hazards of upward spread for different construction materials. Since wood is used widely in residential housing, it is important for these tests to apply readily and accurately to wood-based materials. Unfortunately existing test methods are insufficient to allow prediction of upward spread for wood in residential environments, and consequent deficiencies in fire-safety standards persist in present fire codes (Alpert et al., 1986). The work reported here represents an attempt to gain improved understanding of the characteristics of upward flame spread on wooden materials, for use in developing better test methods and fire codes.

Several investigators (Kashiwagi et al., 1987; Parker, 1985; Atreya et al., 1986) have pointed out that the nonhomogeneity of natural woods complicates the task of obtaining reliable and reproducible flammability data for these materials. A manufactured product, Douglas-fir particle board, retains the general combustion characteristics of natural woods but exhibits more uniform physical and thermal properties. Its basic flammability properties therefore are more reproducible and have been measured with accuracy in earlier studies (Kashiwagi et al., 1987; Harkleroad et al., 1983). This same fuel was employed in the earlier research that led to the present work (Saito et al., 1986).

In our previous study (Saito et al., 1986) upward turbulent flame spread was investigated experimentally for polymethylmethacrylate and particle board by use of an apparatus in which initiation of spread was achieved by a line-source gas burner, with various rates of heat release, positioned at the bottom of the fuel surface. The configuration did not involve external radiant energy input, and it was observed that sustained upward flame spread occurred for polymethyl methacrylate but not for wood. Even with the burner left on for more than ten minutes at its highest heat-release rate, so that steady state had practically been approached, flames did not spread to the top of the large wood sample. This behavior is associated with the formation of a char layer on the wood surface, which retards the temperature rise of the virgin fuel and eventually becomes thick enough to prevent further gasification of the wood. It is therefore likely that upward flame spread observed in real-world scenarios is associated with external energy input to the surface from adjacent burning fuels. Consequently, the present experiments were designed to investigate the level of external energy flux needed to achieve upward spread and the dependence of the spread rate on the flux level above this critical value.

The radiation-panel apparatus at NBS was used to supply the external energy flux. This apparatus was designed to achieve nearly uniform exposure of the vertical fuel surface. The experiment is illustrated in Fig. 1. The size of the apparatus necessitated use of smaller fuel samples than those employed in our earlier work (Saito et al., 1986). However, the samples were large enough for the spread process to be turbulent, and they were larger than those employed in earlier studies (Kashiwagi et al., 1987; Parker, 1985).

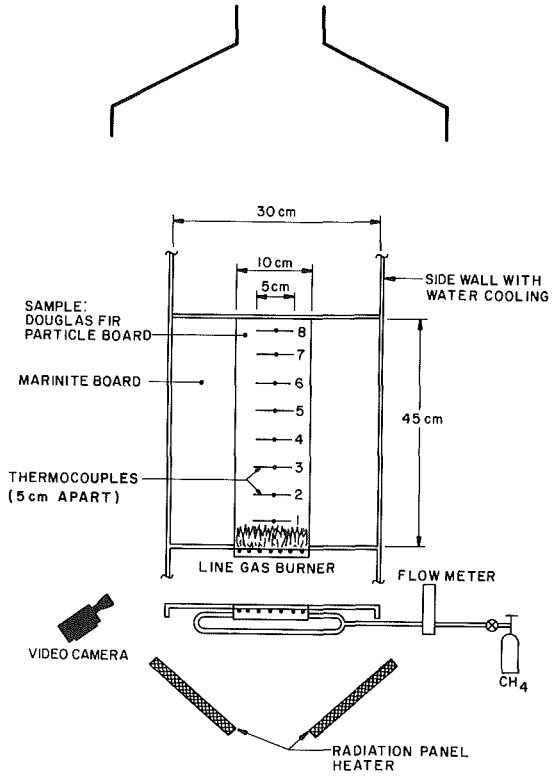

Fig. 1 Schematic diagram of the experimental apparatus; distance between thermocouples 5 cm

[1]Present address: Department of Mechanical Engineering, University of Kentucky, Lexington, KY 40506.

[2]Present address: Department of Mechanical Engineering, Michigan State University, East Lansing, MI 48824.

Contributed by the Heat Transfer Divison and presented at the National Heat Transfer Conference, Pittsburgh, Pennsylvania, August 9-12, 1987. Manuscript received by the Heat Transfer Division October 5, 1987. Paper No. 87-HT-56. Keywords: Combustion, Fire/Flames, Radiation.

Several attempts have been made recently at modeling various components of ignition, combustion, and flame-spread processes for char-forming materials (Saito et al., 1986; Hasemi, 1986; Miller and Ramohalli, 1986; Wichman and Atreya, 1987; Delichatsios, 1986; Atreya and Wichman, 1987). Reference may be made to our earlier paper (Saito et al., 1986) for a more thorough review of the literature. A comprehensive physical theory that encompasses processes occurring in both the gas and the reacting solid under transient spreading conditions remains unavailable. Nevertheless, theoretical concepts from the literature can be employed for seeking an understanding of the results of the present experiments. Despite the complexity of the ignition and combustion behavior, a reasonable degree of understanding of the observations can be obtained.

Experimental Method

Douglas-fir particle boards of 1.3 cm thickness, 45 cm height, and 10 cm width were used for the upward flame-spread tests. The samples were flush-mounted and fixed to a vertical Marinite board and a steel frame sized to fit into a radiation-panel apparatus that has previously been described fully by Harkleroad et al. (1983). The sample surface was exposed to incident radiant heat flux as shown in Fig. 1; the fluxes measured at several different points at the sample surface differed by less than ± 7.5 percent. Prior to the experiment, all samples were stored in a conditioning room, having a temperature maintained at $23 \pm 3°C$ with a relative humidity of 50 ± 5 percent, for a long enough period to equilibrate moisture. The samples were then quickly removed and mounted on the apparatus, in which a steady-state radiation condition had previously been established at one of the selected flux levels E between 0.42 W/cm^2 and 2.15 W/cm^2. The selected radiant flux level was then re-established, and after a fixed preheat time t_p a methane burner, described previously (Saito et al., 1986), was turned on at the bottom of the sample. Once ignition of the sample was established the burner was turned off, but the radiant heater was kept on through the entire experiment; exploratory tests indicated that after ignition the burner had little influence on the combustion history at the burner setting employed (giving an average energy flux of about 0.3 W/cm^2 above the flame, whose height was about 5 cm), and the results would be unchanged, within experimental error, had the burner been left on. Therefore, the burner served only as a pilot for initiating flame spread.

Combustion histories were recorded by thermocouples and by a color video camera. Temperature histories were measured by 0.1 mm diameter chromel-alumel thermocouples fixed just underneath the sample surface and arrayed equidistantly, 5 cm apart along the center line, as illustrated in Fig. 1. The method is the same as described in the previous work (Saito et al., 1986). Tests performed at different preheat times provided the time t_p needed to reach a specified surface temperature T_p as a function of the radiant flux E. A constant preheat time of $t_p = 2$ min was selected for the most detailed analysis of flame-spread data because combustion observations indicated poorer reproducibility and greater pilot-burner influences at shorter t_p, as well as poorer reproducibility and greater difficulty in achieving ignition at longer t_p. An average velocity V_F of upward flame-tip motion during the spread period was defined from the video record as the sample height plus 10 cm divided by the time interval between ignition and the time of first arrival of the averaged flame tip at this position. The color video also exhibits the onset of pyrolysis as a dark-brown front, and the upward velocity V_P of this pyrolysis front provides a measure of the upward spread rate. The averages V_{PA} over the total extent of spread, V_{PL} over the first 5 cm of spread, and V_{PU} over the last 5 cm of spread were calculated from the video records. In addition, V_{PA} was evaluated from experiments in which t_p differed from 2 min (ranging from 1 min to 40 min at different fluxes).

After spread was complete the combustion of the sample lasted only a brief time, after which the flames disappeared. Thus, the samples were never completely consumed in these experiments. The total amount of time t_s that flames existed on the sample surface was measured from the video records. In addition, the vertically averaged final thickness h_c of the char layer that formed on the sample surface was measured from samples that had been cut in half along their center lines.

Experimental Results

Representative measured temperature–time histories at eight different locations on the particle-board surface are shown in Fig. 2 for two different values of E. The numbering in Fig. 2 corresponds to the thermocouple heights shown in Fig. 1. The initial period of essentially identical readings at the lower flux occurs during preheating prior to pilot activation; at the higher flux the temperature readings of the highest thermocouples are lower, possibly because of enhanced convective cooling at these locations associated with transition to turbulence in the natural-convective boundary-layer flow. When the pilot is activated a sharp increase in the rate of increase of surface temperature occurs at essentially all locations for the

Nomenclature

c = specific heat of solid
E = externally applied radiant energy flux at the sample surface
F = energy released per unit length by the pilot flame
g = gravitational constant 9.8 m/s^2
h_c = average final char-layer thickness
K = constant prefactor in flame-height correlation
M = rate of mass loss per unit area for the burning fuel
n = constant exponent in flame-height correlation
Q = total energy flux delivered to the surface adjacent to the flame
q = heat released per unit mass of fuel consumed during flame spread
T = temperature
T_p = surface temperature at time t_p
T_S = simultaneous ignition temperature
T_s = surface temperature of pyrolyzing fuel during flame spread
t = time
t_c = characteristic combustion time of charring fuel
t_p = preheat time
t_s = total duration of flames on the sample surface
V_F = average flame-tip velocity during spread
V_P = pyrolysis-front velocity
V_{PA} = average pyrolysis-front velocity during spread
V_{PL} = average pyrolysis-front velocity during the first 5 cm of spread
V_{PU} = average pyrolysis-front velocity during the last 5 cm of spread
x_F = flame height measured from bottom of sample
x_P = pyrolysis height measured from bottom of sample
α = thermal diffusivity of solid $= \lambda/\rho c$
λ = thermal conductivity of solid
ρ = density of solid
τ = characteristic flame-spread time defined in equation (2)

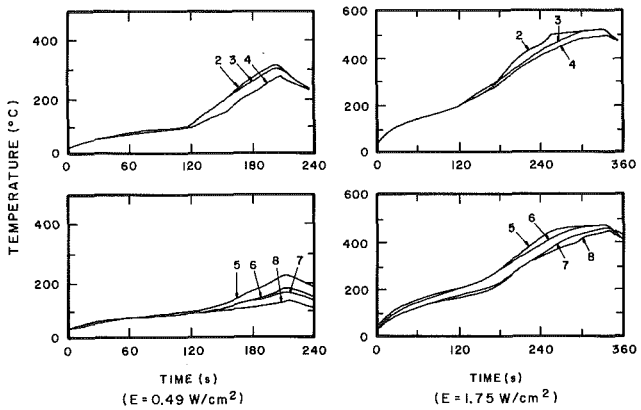

Fig. 2 Measured surface temperature histories of Douglas-fir particle board with a preheat time of 2 min at an external radiant flux of $E = 0.49$ W/cm^2 (left-hand figures) and $E = 1.75$ W/cm^2 (right-hand figures)

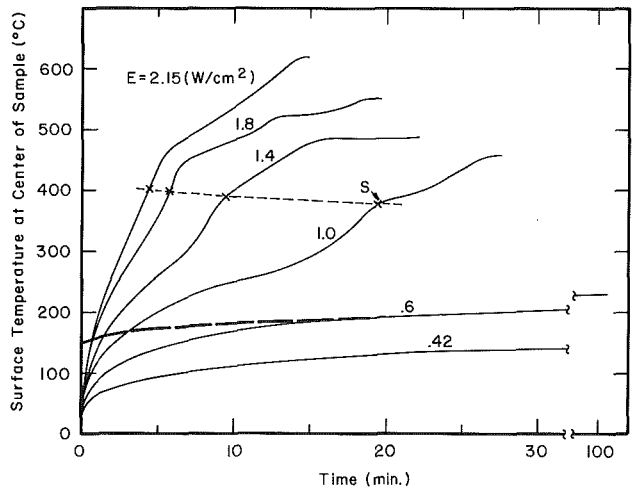

Fig. 3 Measured surface temperature at the center of the sample as a function of time at six different values of the external radiant energy flux without pilot, showing conditions for simultaneous piloted ignition (— — — —) and conditions for prompt piloted ignition (————)

higher flux and at the lower locations for the lower flux. This discontinuity in slope is caused by establishment of the flame in the boundary layer at the surface adjacent to the thermocouple. During the period of flame spread the thermocouple readings differ, and the thermocouples at the lower elevations usually exhibit the higher temperatures. After the flames are extinguished, the temperatures recorded by the thermocouples begin to decrease, all approximately at the same time.

In earlier experiments with polymethylmethacrylate (Saito et al., 1986) it was possible to extract a spread rate from the thermocouple traces by specifying a fixed pyrolysis temperature that marked the onset of vigorous gasification. This procedure was found to be inapplicable in these particleboard experiments. For char-forming materials surface temperatures at the onset of flaming exhibit greater variations with experimental conditions (Kashiwagi et al., 1987). Also, in the presence of char, surface temperatures exhibit enhanced sensitivity to ambient factors, and the turbulence was observed easily to produce surface-temperature fluctuations on the order of 10°C. The resulting scatter precluded the use of the thermocouple traces for obtaining spread rates.

Temperature-time histories recorded at the center of the sample surface are shown in Fig. 3 for six different heat fluxes. The pilot was not activated in any of these tests, and ignition did not occur. The resulting traces are in qualitative agreement with related data reported earlier (e.g., Harkleroad

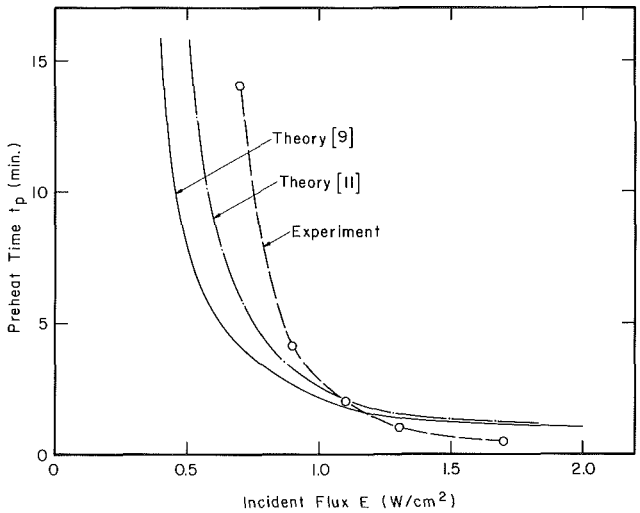

Fig. 4 Preheat time needed for prompt piloted initiation of spread as a function of the incident radiant energy flux, and the theoretically calculated preheat time to reach two different specified surface temperatures

et al., 1983). The tests were repeated with the pilot activated after various preheat times. At the lowest flux shown this did not result in flame spread. At any flux high enough for flame spread to occur, early application of the pilot resulted in spread after a measurable time delay. In these tests later application of the pilot reduced the time delay prior to spread, and at a critical preheat time prior to pilot initiation the delay became too short to measure, i.e., spread appeared to begin nearly instantaneously when the pilot was activated. However, at this critical preheat time, the velocity of upward propagation of the pyrolysis front still was measurable. As the preheat time prior to pilot application was increased still further, the propagation velocity of the pyrolysis front increased, and at a second critical preheat time, the propagation velocity appeared to approach infinity, i.e., simultaneous ignition of the entire surface was found to occur as soon as the pilot was activated. The minimum preheat time for this simultaneous ignition to occur is marked by crosses on the curves in Fig. 3. The corresponding surface temperature T_S, called here the simultaneous ignition temperature, is seen from Fig. 3 to remain approximately constant at 390°C over the range of E tested, although it increases slightly with increasing flux.

The minimum critical preheat time for spread to begin nearly instantaneously (i.e., within about 30 s) upon pilot application (the first of the two critical preheat times described above) was measured in a separate set of experiments in which t_p was fixed and E was sequentially increased until prompt (nearly delay-free) initiation of spread was observed. The results of these tests are shown by the points in Fig. 4. The approximate locus of these points is indicated by a broken line in Fig. 3 with temperatures below 200°C.

As indicated in the previous section, measurements of propagation velocities were performed with t_p fixed at 2 min. Results are shown in Fig. 5. As stated there, upward spread did not occur at this t_p when $E < 0.5$ W/cm^2. For 0.5 W/cm^2 $< E <$ 0.7 W/cm^2, an interesting phenomenon was observed: The pilot initiated a small yellow flame that soon died, then ignited a transient blue flame that traveled to the top of the sample with very little effect on its surface. Five or six repetitions of this blue-flame initiation and propagation were observed before the external flux had increased the char-layer thickness to such an extent that gasification rates were insufficient to provide concentrations of gaseous combustibles high enough for reignition. This general type of periodic premixed-flame propagation has been previously observed in piloted-ignition experiments with wood over roughly this same

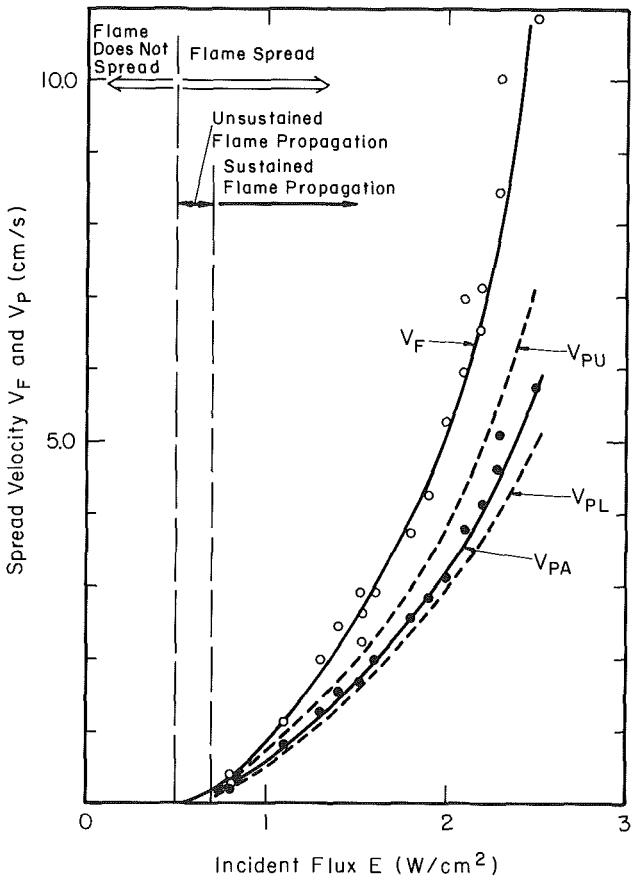

Fig. 5 Pyrolysis-front propagation velocities V_{PU}, V_{PA}, and V_{PL}, and flame-tip propagation velocity V_F, as functions of the incident radiant energy flux, for a preheat time t_p of 2 min

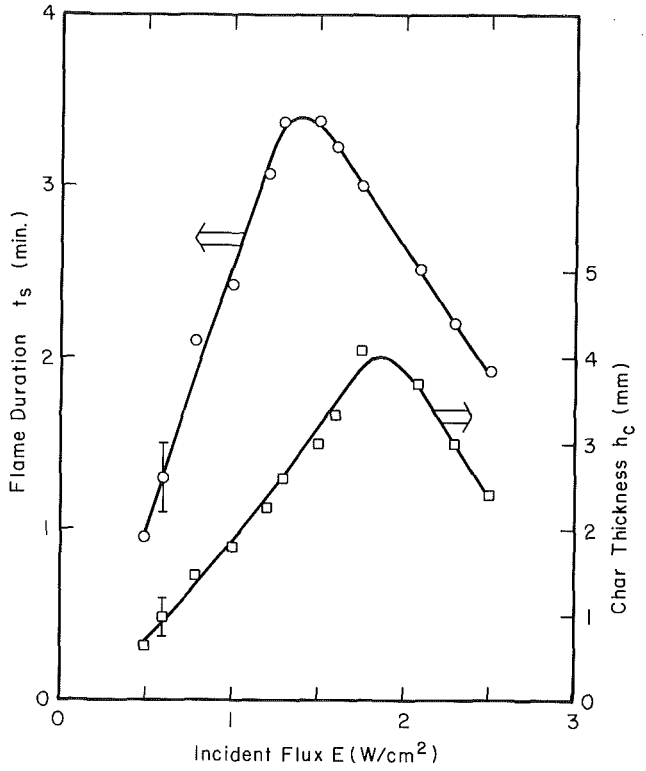

Fig. 6 Total flame duration and average final char-layer thickness as functions of the incident radiant energy flux, for a preheat time t_p of 2 min

flux range (e.g., Bushman, 1961) and is not indicative of sustained spread. Therefore no further analyses of observations in this range were performed.

In the experiments with $E>0.7$ W/cm^2, sustained upward spread to the top of the sample occurred at a velocity that increased with increasing E, as seen in Fig. 5. The solid points show the overall average spread velocity V_{PA}, and the fact that V_{PL} is less than V_{PU} suggests an acceleratory spread behavior, an inference that is also consistent with the observation that the flame-tip velocity V_F exceeds V_P. Over the range of E where data are obtained, $V_{PU}\approx 1.3\ V_{PL}$ and $V_F\approx 1.7\ V_{PA}$, roughly independent of E. Because of the limited sample height it is unclear whether acceleration would persist, or a constant velocity would be approached, or even whether deceleration would occur.

Extrapolation of the dashed line in Fig. 3 to $t_p=2$ min indicates that simultaneous ignition would occur for Fig. 5 at $E\approx 2.6$ W/cm^2. This in fact was observed in these experiments. It implies that the results shown in Fig. 5 cannot be extrapolated to higher values of E because V_P rapidly approaches infinity.

To obtain further tests of flame-spread theories, V_{PA} was measured in a series of experiments having $t_p\neq 2$ min. In these experiments, various values of t_p were employed at each value of E. Spread was achieved at $E=0.42$ W/cm^2 with $t_p=40$ min and exhibited a relatively low value of V_{PA}. At the other three values of E employed in this series (0.6 W/cm^2, 1.0 W/cm^2, and 1.8 W/cm^2), spread was achieved with measurable V_{PA} over a range of t_p that extended down to 1 min at the highest E. Results of these tests at different values of t_p conform qualitatively with the data shown in Fig. 5 and will be shown later, in connection with the discussion of spread-rate results.

Figure 6 shows the total flame duration t_S and the final average char-layer thickness h_c as functions of E for $t_p=2$ min. Both of these curves exhibit maxima, but the maxima occur at different values of E. Their existence suggests the presence of competing effects, as discussed later.

Discussion of Results on Ignition

The descriptions that have been given indicate that these experiments exhibit aspects of piloted radiant ignition, flame spread, and flame extinction. The ignition aspects can be addressed by first making reference to Fig. 3. While the curves at low fluxes show no indication of chemical activity, those for $E\geq 1$ W/cm^2 have inflections produced by chemical heat release (even though the pilot is not activated). The exothermicity results from the well-known char-formation chemistry (Williams, 1982) and is seen to begin to produce observable thermal effects for surface temperatures of about 250°C, in agreement with related observations (e.g., Harkleroad et al., 1983).

The surface temperatures corresponding to the points in Fig. 4 are seen from Fig. 3 to lie in the range of inert heating, well below 250°C. Therefore, the observed temperatures at these points (approximately 175°C) can be compared with theoretical calculations for inert heating (e.g., Harkleroad et al., 1983; Wichman and Atreya, 1987; Atreya and Wichman, 1987). The results are shown in Fig. 4. For a preheat time of two minutes, piloted ignition is predicted from the theories of Wichman and Atreya (1987) and Atreya and Wichman (1987) to occur for 1.0 W/cm$^2\lesssim E\lesssim$ 1.2 W/cm^2; the experimental result falls between these two values, giving $E\simeq 1.1$ W/cm^2. In view of the crudeness of the theoretical calculations, the agreement with the measurements is reasonable. It is found that radiative, natural-convective, and forced-convective losses from the surface all must be taken into account since they produce contributions roughly comparable in magnitude at the lower temperatures. At the higher temperatures the radiative contribution is the larger.

The temperatures along the lower broken line in Fig. 3

decrease with increasing flux, contrary to the normal behavior of ignition temperatures; moreover, they lie well below ignition temperatures of cellulosic materials. These peculiarities are associated with the character of the experiment. The heat flux from the pilot burner is not negligible in comparison with E, and burner activation eliminates convective loss. Sharp local increases in surface temperature therefore occur after the pilot is lit, bringing the surface temperature up to the pyrolysis temperature for cellulose depolymerization to volatile, combustible "tar" ($\sim 320°C$, see Williams, 1982) during the period (~ 30 s) preceding flame spread. The rate of increase of surface temperature during this initiation period is greater at higher external fluxes, probably reversing the trend suggested by the result in Fig. 3.

Unlike the temperature at which pilot application produced fairly prompt spread, the simultaneous ignition temperatures T_s shown by the crosses in Fig. 3 fall within the range of piloted ignition temperatures for wood samples reported in the literature (Simms, 1963; Kanury, 1972), 300°C to 410°C, and exhibit the expected increase with increasing flux. In view of our definition of simultaneous ignition, it is understandable that T_S falls near the upper limit of reported piloted-ignition temperatures; the samples tested here are larger than those tested previously, and a combustible mixture must exist in the gas adjacent to the entire sample surface prior to pilot activation if the burner is to produce simultaneous ignition. In contrast to the conditions of Fig. 4, the heat supplied to the solid by the pilot burner is insignificant with respect to the T_S data. "Simultaneous" ignition still necessarily involves a delay associated with gas-phase flame propagation up the sample surface, but this delay (<1s) is too short to measure by the techniques employed and much shorter than the upward spread times discussed below, which involve a gradual upward motion of the pyrolysis front.

The slight increase in T_S with increasing E, seen in Fig. 3, can be discussed in greater detail in reference to existing ignition theories. Although the exothermic char process is proceeding vigorously at T_S and contributing appreciably to dT/dt, rapid changes in this process are not responsible for ignition. Figure 3 shows that, at a temperature of T_S or somewhat above, there is a rather sharp decrease in dT/dt that must be associated with the endothermic tar process overpowering the char process. It is the tar process that produces gaseous combustibles and in that sense is responsible for ignition (Williams, 1982). Classical ignition theory predicts $T_S \sim [\ln (\text{const}/E)]^{-1}$ in a first approximation (Linan and Williams, 1971), consistent with Fig. 3, but such a theory involves exothermic condensed-phase chemistry. However, the same kind of result is obtained from gas-phase ignition theory with endothermic condensed-phase pyrolysis, provided that ignition occurs during the stage of transition from inert heating to gasification (Kindelan and Williams, 1975a, 1975b, 1977). Therefore it may be assumed that in the present experiments the gas-phase chemistry is rapid once initiated, and the variation of T_S with E is a consequence of the kinetics of the (endothermic) tar process.

The wide range of temperatures shown in Fig. 3 over which different types of ignition events may occur is remarkable. Even though the concentrations of combustible gases produced are insufficient to support flaming for $T \lesssim 320°C$, initiation of spread with the pilot burner is achievable at least over $200°C < T < 400°C$. Since even the simplest scientific ignition criteria are not satisfied in the lower portion of this range, there are practical conditions under which additional energy inputs from initiation flames must be considered in assessing flammability hazards. Thus it is expected from these experiments that if T is allowed to increase to too high a value before application of the pilot, flaming ignition and spread again will not occur because the gaseous combustible will have been depleted from the fuel surface (i.e., the tar process will have gone to completion). Glowing combustion (Williams, 1982) plays no role in these experiments because temperatures are too low.

Discussion of Results on Spread

The external radiation performs a dual function with respect to flame spread in these experiments. It preheats the sample prior to pilot initiation so that the spread occurs along a surface initially at an elevated temperature T_p. In addition, it augments the energy flux received by the sample surface during spread, above the value of the flux provided by the flame alone. Both of these effects increase the spread rate.

It is of interest to compare the present experimental results on spread with our approximate theory (Saito et al., 1986), which gives, for the spread rate,

$$dx_P/dt \equiv V_P = (x_F - x_P)/\tau \tag{1}$$

where

$$\tau = (\pi/4)\lambda\rho c(T_s - T_p)^2/Q^2 \tag{2}$$

and

$$x_F = K\left(F + q\int_0^{x_P} M dx\right)^n \tag{3}$$

The symbols here are defined in the nomenclature. Although studies of stationary wall fires have given $n = 2/3$, $K \approx 1$ cm/(W/cm)$^{2/3}$, for spread experiments it is easier and essentially as accurate to employ $n = 1$, $K = 0.1$ cm^2/W (Saito et al., 1986). The latter values will be used here for simplicity. Differentiation of equation (3) then gives

$$dx_F/dt \equiv V_F = KqM_oV_P + Kq\int_0^{x_P} (dM/dt)dx \tag{4}$$

where M_o is the value of M at the beginning of pyrolysis, typically the maximum value (Saito et al., 1986).

Within the context of this theory, preheating by the external radiation serves to increase T_p, thereby decreasing τ according to equation (2) and increasing the spread rate V_P according to equation (1). The value of T_p is readily obtained from Fig. 3, given E and t_p. The augmentation of V_P by this effect can be quite large, e.g., more than an order of magnitude.

The flame contributes about 2.5 W/cm^2 to Q (Saito et al., 1986), and the external flux may be added to this to give

$$Q = E + 2.5 \text{ W/cm}^2 \tag{5}$$

It is appreciated that the flame heat flux value is 2.5 W/cm^2, which actually varies with position and would increase due to radiation for thick flames and certain fuels. Furthermore, since spread depends on Q^2 by equation (2), variations in flame heat flux can become significant variations in the results. This augmentation of Q by E also decreases τ in equation (2), thereby increasing V_P further. The magnitude of this last increase is seen to be rather small at the smallest E's that give sustained spread but to approach a factor of nearly four at the highest E's employed.

An alternative view that should be equivalent but more complicated to apply is to allow T_p to vary during spread to include the effect of E. Then E does not appear in equation (5), and Q is constant.

The theory neglects influences of heat addition above the flame height x_F; this approximation has reasonable justification for $E = 0$ (Saito et al., 1986) but becomes increasingly poor as E increases. In the limit in which $E \gg 2.5$ W/cm^2, a modified theory is readily constructed by putting $Q = E$ and taking x_F in equation (1) to be the height of the sample. This is a significant simplification, removing the coupling with the flame height, but clearly it always predicts deceleratory spread, and it cannot be applied to the present spread experiments, all of which have $E < 2.5$ W/cm^2. Detailed estimates indicate that neglecting heat addition above the

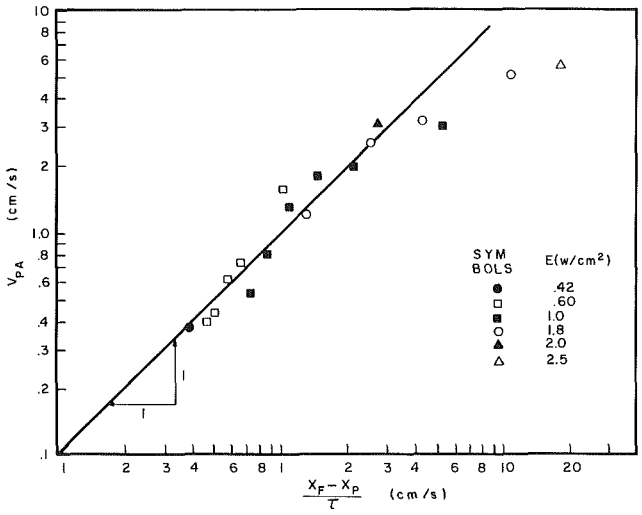

Fig. 7 Average measured spread rate V_{PA} as a function of that calculated from equation (1) for various incident radiant energy fluxes and preheat times

flame during spread is in fact a reasonable approximation for the present experiments (since, in the tests with the higher E's, x_F rapidly approaches and exceeds the sample height). Therefore, no modifications to equations (1), (2), and (3) will be made here.

A rough criterion for acceleratory upward spread over charring fuels, obtained from the theory (Saito et al., 1986), is

$$KqM_o\sqrt{t_c/\tau} > 2/\sqrt{\pi} \tag{6}$$

where t_c is a characteristic combustion time of the fuel. Our earlier estimates for wood without external radiant energy flux gave (Saito et al., 1986) $q \approx 10$ kJ/g, $M_o \approx 10^{-3}$ g/cm^{2}s (so $KqM_o \approx 1$), 150 s $\lesssim t_c \lesssim$ 400 s and 170 s $\lesssim \tau \lesssim$ 350 s. The inequality in equation (6) therefore was not satisfied, and acceleratory spread was not detected experimentally. The principal influence of application of external radiation in the present experiments was to decrease τ, which causes the inequality in equation (6) to be satisfied. Influences of E on $M_0\sqrt{t_c}$ are smaller.

A reasonable value of T_s for cellulosic materials is about 370°C (Williams, 1982), close to the value $T_S = 390$°C measured for simultaneous ignition and near the value of 395°C adopted earlier (Harkleroad et al., 1983) for particleboard ignition. Use of $T_s = 370$°C, of equation (5), and of the data in Fig. 3 may be made in equation (2) to show that for the lowest flux in Fig. 5 at which sustained flame propagation occurs the value of τ is about 0.2 times that without external radiation (i.e., 35 s $\lesssim \tau \lesssim$ 70 s). At the highest value of E for which data are shown in Fig. 5, the ratio of τ to that without radiation has decreased to a value on the order of 10^{-2}. Thus for the spread data in Fig. 5 the left-hand side of equation (6) is more than twice the value without radiation, and the inequality is satisfied. Acceleratory spread therefore is predicted to occur theoretically. Since the data show that $V_{PL} < V_{PA} < V_{PU}$, it is seen experimentally that the upward spread is acceleratory over the entire height of the sample, in agreement with the prediction. Achievement of sustained propagation in these experiments thus is equivalent to achievement of acceleratory spread.

Because of experimental inaccuracies and the primitive state of development of the theory, comparisons of observed differences between V_{PU}, V_{PA}, and V_{PL} in Fig. 5 and theoretical predictions of these differences were not made. The theory with $n = 1$ predicts that acceleration would continue no matter how tall the sample is. The result that $V_F \approx 1.7 V_{PA}$ in Fig. 5 can be compared with the prediction in equation (4) but requires an estimate of the integral appearing therein, which accounts for the influence that the burning history of the ignited portion of the surface exerts on the flame height. However, even the sign of the integral is uncertain; from representative mass-flux histories of charring fuels (Saito et al., 1986) dM/dt is negative for most of the burning history, so that the integral is negative at least for the latter part of the spread history if V_P is small enough, although it may be positive at the higher values of V_P. On the average it may be reasonable to neglect the contribution of the integral, in which case the data of Fig. 5 suggest that $KqM_o \approx 1.7$, a value 70 percent above that estimated for experiments without external radiation. Therefore, radiant fluxes on the order of 2 W/cm^2 may modify the combustion history so as to increase M_o by about 70 percent.

Observed average spread rates V_{PA} can be compared with the prediction in equation (1) by using Fig. 3 to obtain T_p and equation (5) to calculate Q in evaluating τ from equation (2) (with $T_s = 370$°C) if an average value of $x_F - x_P$ can be estimated. The representative value $x_F - x_P \approx 10$ cm may be used as a rough approximation in equation (1). When this is done, the results shown in Fig. 7 are obtained. This figure includes data over a wide range of values of t_p in addition to some of the data of Fig. 5. The product $\lambda\rho c$ was calculated from the data of Parker (1985) at a temperature given by the average of T_s and T_p in preparing Fig. 7. It is seen from Fig. 7 that the observed V_{PA} agrees quite well with the theoretical estimates. The departure is greatest for the two points at the highest values of T_p (315°C and 320°C), under which conditions the calculation becomes very sensitive to the selected value of T_s; it is to be expected that T_s will be somewhat greater at such high T_p, thereby improving agreement. The general agreement lends additional support to the qualitative correctness of the theory proposed by Saito et al. (1986).

Discussion of Results on Extinction

The results shown in Fig. 6 can be discussed on the basis of information available on combustion histories of charring fuels. Since the data correspond to $t_p = 2$ min, the preheat depth may be estimated as $\sqrt{\alpha t_p} \approx 0.5$ cm. From Fig. 3 it is seen that at the lower fluxes, T_p is too low for the charring reaction to have begun appreciably during preheating, and the preheat is inert. In this range of low fluxes, the external radiation deposits an energy per unit area in the fuel that is proportional to E, and if this energy is considered to be redistributed during combustion to heat a layer of the fuel to a specified elevated temperature (e.g., about 100°C), then the thickness of the heated layer also will be proportioned to E. If it is assumed that after pilot application the average pyrolysis rate per unit surface area for the tar-producing reaction is independent of E at these low values of E and that because of char buildup during combustion the pyrolysis front propagates only through the heated layer prior to extinction, then it is found that the flame duration is proportioned to E. In additon, if the charring during combustion is assumed to prevent surface regression, then the final char-layer thickness also will be proportioned to E. These functional behaviors for t_s and h_c are consistent with those found in Fig. 6 in the essentially linear range where $E \lesssim 1.3$ W/cm^2.

This explanation of the linearity for 0.5 W/cm^2 $< E <$ 1.3 W/cm^2 in Fig. 6 is based on the idea of a relatively thin tar-forming pyrolysis front propagating through a heated, charring layer with a ratio of total wood conversion by tar and char processes that is independent of E. As the pyrolysis front penetrates deeper into cooler fuel, its temperature and hence its velocity decrease, until eventually it produces combustible gas at a rate insufficient to support the gas-phase flame. The abrupt extinction of the gas-phase flame removes the dominant source of energy flux that supports the endothermic tar-

forming pyrolysis and thereby causes gasification to cease. Since the explanation is based on considerations of normal regression, it neglects contributions of the spread time to t_s. The total spread time is estimated from Fig. 5 to decrease roughly linearly with increasing E to about 30 s at $E = 1.3$ W/cm^2 so that the spread contribution becomes significant only at the lowest E's and can be neglected for most of the data shown. For $E \leq 0.5$ W/cm^2, Fig. 3 gives $T_p \lesssim 80°$C, and the preheating ceases to dominate the combustion time and the char-layer thickness; the char-layer thickness begins to vary appreciably with height, being ~ 1 mm (the value for $E = 0$) adjacent to the pilot and zero at heights to which the flame does not spread, so that h_c becomes uninformative.

Two different phenomena may contribute to the decrease in t_s that is observed in Fig. 6 to occur for $E \gtrsim 1.3$ W/cm^2. One would be an increase in the average pyrolysis rate per unit surface area for the tar-producing reaction, mainly through an increase in the value of this rate during the early part of the combustion history. Such an increase would be anticipated, for example, if the endothermic pyrolysis front is driven by the external flux Q, because E contributes appreciably to Q in this higher-flux range. This phenomenon thus may cause t_s to depart from the linear increase with E, but it would seem unlikely to produce the observed decrease in t_s with increasing E. A more significant phenomenon affecting Fig. 6 for $E \gtrsim 1.3$ W/cm^2 may be the char-forming reaction.

From Fig. 3 for $E \gtrsim 1.3$ W/cm^2, the preheating at $t_p = 2$ min brings the surface temperature above 170°C, where the rate of the char-forming reaction becomes nonnegligible. With this early initiation of charring, the temperature levels spend relatively more time in the range of the char reaction before climbing into the range of the tar reaction, thereby upsetting the char–tar balance, so that a greater fraction of the fuel is consumed by charring. This reduces the fuel mass available to the tar-producing reaction in the heated layer and, therefore, at a fixed average rate of consumption of fuel mass per unit area by the tar-producing reaction, decreases the combustion duration. This decrease in t_s would not bring about a corresponding change in h_c but instead would increase the final char density, according to this reasoning. For $E \gtrsim 1.8$ W/cm^2, where $T_p \gtrsim 230°$C according to Fig. 3, extensive charring is expected prior to pilot application. This must result in char-layer shrinkage, i.e., surface regression, to an extent that increases with increasing E, for agreement with the high-E data for h_c in Fig. 6. The shrinkage could occur so as to maintain a constant final char-layer density, thereby producing no break in the t_s curve at $E = 1.8$ W/cm^2.

This explanation of the observations in Fig. 6 could be tested if the average final density of the char layer could be measured. According to the explanation, this density should remain approximately constant for $E < 1.3$ W/cm^2, should increase roughly linearly with E for 1.3 W/cm$^2 < E < 1.8$ W/cm^2, and should again remain constant for $E > 1.8$ W/cm^2.

Many alternative explanations for aspects of Fig. 6 have failied. At the higher E, because of surface losses the energy deposited in the fuel by the preheat flux no longer is proportional to E, so that the heated fuel mass per unit surface area increases with E more slowly than linearly, but this gradual effect is unlikely to produce the sharp changes seen in Fig. 6. The particle board has density variation across its thickness. We measured the density variation by slicing the sample and found about 20 percent lower density over the middle third (Venkatesh et al., 1989). This small density variation is not likely to cause anomalous behavior in Fig. 6. The abruptness of the transitions in Fig. 6 seems to need sensitive processes like chemical kinetics for explanation. The suggestion that the decrease in h_c with increasing E at the higher values of E is attributable to surface regression caused by the surface reaction of glowing combustion, either before, during or after flaming, is dismissed because the measured surface temperatures always are too low for this reaction to be significant, and glowing combustion was not seen in any of these experiments. Glowing could become important for $E \gtrsim 3$ W/cm^2, but at 2.2 W/cm^2 it would require preheat times greater than 10 min before it could begin. If the explanation that has been offered here is correct then the interplay between the char and tar kinetics can cause unanticipated maxima of flame duration and char-layer thickness.

Conclusions

These experiments have shown that, in agreement with our earlier suggestion (Saito, 1986), application of modest levels of external radiant energy fluxes enables vertically oriented, thermally thick wood surfaces to support sustained upward flame spread. The radiation has a dual effect: preheating the fuel prior to pilot activation and augmenting the energy flux to the surface adjacent to the flames. The sustained upward spread is observed to be acceleratory, in agreement with estimates made from an upward-spread theory (Saito et al., 1986). Measured surface-temperature histories without a pilot flame can be used in evaluating the parameters that occur in the flame-spread theory, and when this is done the predicted and measured average velocities of upward spread agree remarkably well. Therefore, despite the complexity of combustion of char-forming materials, our understanding of their processes of upward turbulent flame spread has progressed considerably.

The ignition and combustion behaviors of wood can be affected intricately by the interplay between the char-formation and tar-formation chemical-kinetic processes. Appeal can be made to this interplay for interpreting observed temperature histories during ignition and the local maxima of the combustion duration and char-layer thickness.

Further research is needed in a number of areas. These include measurements of mass-loss rates and of char densities and spread experiments with taller samples to test continued acceleration. The theory also needs to be made more precise.

Acknowledgments

We would like to express our thanks to D. Gross, T. Kashiwagi, and W. Parker of NBS for useful discussions during the experimental work. Technical assistance by M. Harkleroad and W. Rinkinen was also greatly appreciated. One author (FAW) wishes to acknowledge partial support from National Science Foundation Grant No. INT-8403848.

References

Alpert, R. L., Delichatsios, M. A., and de Ris, J., 1986, Annual Report to NBS on Flammability Testing, Factory Mutual Research Corporation, Norwood, MA.

Atreya, A., Carpentier, C., and Harkleroad, M., 1986, "Effect of Sample Orientation on Piloted Ignition and Flame Spread," *Proceedings, The First International Symposium on Fire Safety Science*, Hemisphere Publishing Corp., pp. 97–109.

Atreya, A., and Wichman, I. S., 1987, "Heat and Mass Transfer During Piloted Ignition," *2nd ASME/JSME Conference on Heat and Mass Transfer*, Vol. 1, pp. 433–440.

Bushman, A. J., 1961, "Ignition of Some Woods Exposed to Low Level Thermal Radiation," Report No. 7306, National Bureau of Standards, Washington, DC.

Delichatsios, M. A., 1986, "A Simplified Algebraic Model for Turbulent Wall Fires," Technical Report No. FMRC J. I. ONOJ1.BU, Factory Mutual Research Corporation, Norwood, MA.

Harkleroad, M., Quintiere, J., and Walton, W., 1983, "Radiative Ignition and Opposed Flow Flame Spread Measurements on Materials," Final Report No. DOT/FAA/CT-83/28, Federal Aviation Administration, Technical Center, Atlantic City, NJ.

Hasemi, Y., 1986, "Thermal Modeling of Upward Wall Flame Spread," *Proceedings, The First International Symposium on Fire Safety Science*, Hemisphere Publishing Corp., pp. 87–96.

Kanury, A. M., 1972, "Ignition of Cellulosic Solids—A Review," *Fire Research Abstracts and Reviews*, Vol. 14, pp. 24–52.

Kashiwagi, T., Ohlemiller, T. J., and Werner, K., 1987, "Effects of External Radiant Flux and Ambient Oxygen Concentration on Nonflaming Gasification Rates and Evolved Products of White Pine," *Comb. Flame*, Vol. 69, pp. 331–345.

Kindelan, M., and Williams, F. A., 1975a, "Theory for Endothermic Gasification of a Solid by a Constant Energy Flux," *Comb. Sci. Tech.*, Vol. 10, pp. 1–19.

Kindelan, M., and Williams, F. A., 1975b, "Radiant Ignition of a Combustible Solid With Gas-Phase Exothermicity," *Acta Astronautica*, Vol. 2, pp. 955–979.

Kindelan, M., and Williams, F. A., 1977, "Gas-Phase Ignition of a Solid With In-Depth Absorption of Radiation," *Comb. Sci. Tech.*, Vol. 16, pp. 47–58.

Liñán, A., and Williams, F. A., 1971, "Theory of Ignition of a Reactive Solid by Constant Energy Flux," *Comb. Sci. Tech.*, Vol. 3, pp. 91–98.

Millar, C. A., and Ramohalli, K. N. R., 1986, "A Theoretical Heterogeneous Model of Wood Pyrolysis," *Comb. Sci. Tech.*, Vol. 46, pp. 249–265.

Parker, W., 1985, "Development of a Model for the Heat Release Rate of Wood—A Status Report," No. NBSIR85-3163, National Bureau of Standards, Gaithersburg, MD.

Saito, K., Quintiere, J. G., and Williams, F. A., 1986, "Upward Turbulent Flame Spread," *Proceedings, The First International Symposium on Fire Safety Science*, Hemisphere Publishing Corp., pp. 75–86.

Simms, D. L., 1963, "On the Pilot Ignition of Wood by Radiation," *Comb. Flame*, Vol. 7, pp. 253–261.

Venkatesh, S., Saito, K., Delichatsios, M. A., and Alpert, R. L., 1989, "Pynolysis of Charring and Non-charring Materials Using a Newly Developed FMRC Apparatus," 26th National Heat Transfer Conference, Philadelphia, PA, Aug. 6–9 (submitted).

Wichman, I. S., and Aterya, A., 1987, "A Simplifed Model for the Pyrolysis of Charring Materials," *Comb. Flame*, Vol. 86, pp. 231–247.

Williams, F. A., 1982, "Urban and Wildland Fire Phenomenology," *Prog. Energy Comb. Sci.*, Vol. 8, pp. 317–354.

Thermal Measurements in Large Pool Fires

J. J. Gregory

N. R. Keltner

R. Mata, Jr.

Thermal Test and Analysis Division,
Sandia National Laboratories,
Albuquerque, NM 87185

During the summer of 1983, a series of pool fire tests was conducted in which the test item was a 1.4-m-dia, 6.4-m-long, mild steel calorimeter with a mass of approximately 10,000 kg. The purpose of these tests was to study the thermal response of a large test item in a specified fire configuration, to define thermal boundary conditions, and to assess the repeatability of the fire environment. While the calorimeter used in the tests simulated a nuclear waste transportation cask, the results of the study have broader application to the truck and rail transport of hydrocarbon fuels and hazardous chemicals.

Introduction

There is an interest in determining the response and survivability of a variety of items when subjected to large fires, which might occur in a transportation accident or petrochemical industry accident. Specifications for conducting simulated transportation accident tests are given by the International Atomic Energy Agency (IAEA, 1985) and the U.S. Nuclear Regulatory Commission (NRC, 1983).

The thermal environment in a large open pool fire is not well defined. The highly turbulent nature of a large open pool fire and its susceptibility to winds produces temperature and flow fields that are very nonuniform in both space and time. Complete and representative theoretical models that describe the environment are not available.

The tests described in this paper involved a large cylindrical test item in a hydrocarbon pool fire configured along the guidelines of the IAEA and NRC specifications. To address the question of the repeatability of the pool fire environment and provide empirical information that could aid in modeling it, three tests were performed using identical instrumentation. A large calorimeter was used to represent a physically large, thermally massive shipping cask. Complete details of this test program are given by Gregory et al. (1987).

Test Description

The series of three half-hour tests was conducted in a 9.1 m by 18.3 m by 0.9 m deep concrete pool. The test item was a large calorimeter supported by a steel stand such that the bottom was 0.9 m above the initial level of the fuel in accordance with NRC guidelines (NRC, 1983); it was centered within the pool boundaries with the central axis aligned with the long side of the pool.

Each calorimeter was a 6.4-m-long, 1.4-m-o.d., A517 steel pipe with 3.2-cm-thick walls. The calorimeters were fabricated from surplus pipe, which already had 5-cm-thick by 15-cm-wide reinforcing ribs fillet welded to the outside of the pipe on 61-cm centers. At the ends of the pipe, 1.3-cm-thick steel plates, referred to as the end caps, were bolted on to seal the interior of the pipe. Three layers of 2.5-cm-thick Cerablanket insulation were installed against the inner wall of the pipe and against the inside of the end caps.

The east end of the calorimeter was 5.9 m from the east edge of the pool. Instrumentation was located at three axial stations in the calorimeter. Starting from the east end of the calorimeter, Station 1 was 0.46 m away, Station 2 was 2.82 m away, and Station 3 was 5.94 m away. Each station was centered between a pair of exterior ribs. At each axial station, there were four sensor locations on the interior of the pipe. Angular location 000 was on the underside of the calorimeter, then viewing from the east and moving clockwise, angular location 090 faced south, angular location 180 was at the top, and angular location 270 faced north. There was an instrumentation station located at the center of each end cap.

At each location, type K thermocouple wires were spot-welded to the inner surface of the pipe, forming an intrinsic junction. A beaded thermocouple was placed between the first and second layers of insulation. At some stations, multiple thermocouples were used in case of failure. Also, the use of multiple temperature measurements increases the stability and reliability of the estimates of the heat flux from an inverse heat conduction procedure by reducing the effects of random errors from the temperature readings.

To measure flame temperatures, 1.6-mm stainless steel sheathed, ungrounded junction, type K thermocouples were placed at various heights on water-cooled towers arranged about the large calorimeter and 5 cm from the exterior surface at each measurement station on the calorimeter. Three of the towers, named A, B, and C, were 6.1 m high and had thermocouples at 142 cm and 262 cm above the initial fuel level. Five other towers, named *2*, *3*, *4*, *6*, and *7*, were 12.2 m high and had thermocouples at 142 cm, 262 cm, 549 cm, and 1118 cm above the initial fuel surface. Figure 1 shows the placement of the calorimeter and the towers within the pool.

Four small calorimeters, constructed of 1018 mild steel, were installed on tower *3*, which was located to the west of the large calorimeter. Two of these calorimeters were 10.2-cm-dia cylinders and the other two were 20.3-cm-dia cylinders (from this point on referred to as the 10-cm or 20-cm calorimeters). These

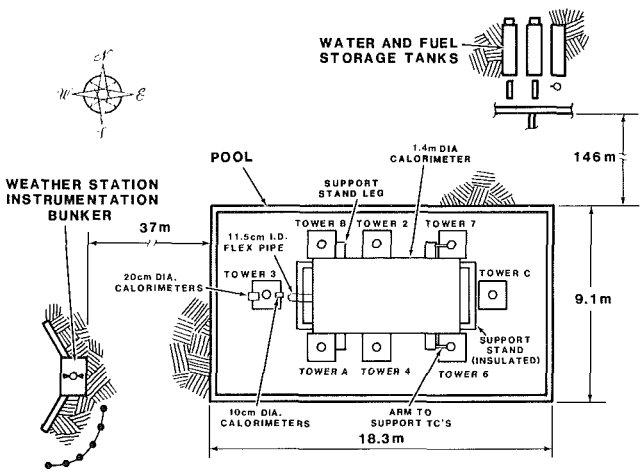

Fig. 1 Plan view of the test facility

Contributed by the Heat Transfer Division and presented at the 24th AIChE/ASME National Heat Transfer Conference, Pittsburgh, Pennsylvania, August 9–12, 1987. Manuscript received by the Heat Transfer Division October 5, 1987. Keywords: Combustion, Fire/Flames.

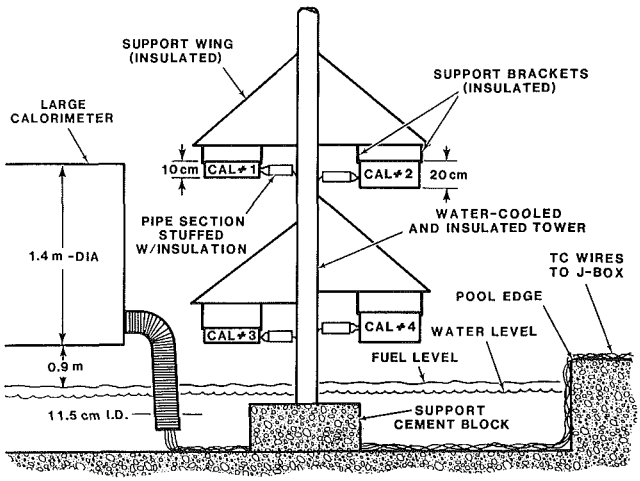

Fig. 2 Placement of small calorimeters in relation to the large calorimeter

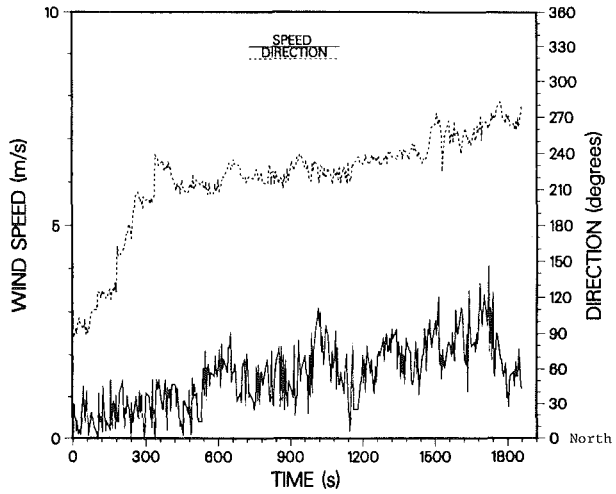

Fig. 3 Wind history for Test C

calorimeters had 3.2-cm-thick walls, were 20.3 cm long, and were cut into four quadrants.

The wall thickness of these calorimeters was the same as that of the large calorimeter. The mild steel was also chosen such that the thermal properties would be similar to those of the larger calorimeter. To reduce circumferential heat conduction between the calorimeter quadrants, a felt insulating strip was placed between them. The interior of each calorimeter was filled with Cerablanket insulation. The whole assembly was held together by 2.5-cm-thick steel caps bolted on both ends of a calorimeter.

Thermocouples were located at the center of each quadrant; these correspond to the angular stations on the large calorimeter. Type K thermocouples were spot-welded (intrinsic junctions) to the inside surface of the cylinder at each station. A beaded thermocouple was placed within the insulating material in the center of the calorimeter, in order to give an internal boundary condition.

The four smaller calorimeters were installed on tower *3* such that their axes were aligned in the same vertical plane as the axis of the large calorimeter. These calorimeters were placed on the tower such that the upper stations of a 10-cm and 20-cm calorimeter lined up with the upper station of the large calorimeter and the lower stations of the other two calorimeters lined up with the lower station of the large calorimeter, as shown in Fig. 2.

Because the wind can drastically change the flow patterns of the fire, an average wind speed of 2 m/s is the upper limit prescribed in the IAEA test specifications. An anemometer, which was located atop the bunker that housed the data logger, served as the instrument for monitoring wind speed and direction.

Test Duration and Fuel Consumption

For the tests, JP-4 aviation fuel was added to 66 cm of water in the pool, where one centimeter depth corresponds to 1670 liters. The depth of fuel added for the first and second tests, tests A and B, was 22 cm, and for the final test, test C, it was 19 cm. Tests A and B were 35 minutes long, while test C was 29 minutes long. The average fuel recession rate for tests A and B was 6.3 mm/min (17.5 liters per second) while that for test C was 6.6 mm/min (18.2 liters per second). These values are in agreement with a nominal fuel recession rate of 6.3 mm/min observed in a number of large pool fires using JP-4 fuel that have been conducted at Sandia.

In comparison, Babrauskas (1983) reports burn rates for gasoline and liquified natural gas pool fires; the values extracted from his plots are 4.3 mm/min for gasoline and 5.8 mm/min for LNG for pools of equivalent diameter, i.e., 14.6 m. Blinov and Khudiakov (1957) give experimental burning rates for gasoline and tractor kerosene; for pool diameters of 9 m and 23 m, the value as reported by Hottel (1959) for both fuels and pool sizes is about 3.8 mm/min.

After the test item and instrumentation were installed and the pool filled, the fuel was ignited by a hand-held torch. The time for the flame front to travel across the surface of the pool along the long axis and fully engulf the large calorimeter was ~ 8 s.

Wind Effects

Large-scale turbulence contributes to the large temporal and spatial fluctuations that characterize the test medium of a large open pool fire. The variable most affecting the conditions in an open pool fire is the ambient wind. The average values and standard deviations of wind speed for each test in this series were 2.0 ± 0.9 m/s, 1.2 ± 0.8 m/s, and 1.5 ± 0.8 m/s for tests A, B, and C, respectively. The prevailing wind direction for test A was from the east by southeast. For test B, the wind prevailed from the southeast, while for test C, the prevailing wind direction was from the southwest. The wind history for Test C is given in Fig. 3.

Wind influences the entrainment patterns in an open pool fire, enhancing air entrainment in some areas. As a result, the temperatures are elevated or depressed depending on local air-to-fuel ratios and efficiency of mixing. Instabilities are enhanced and turbulent flow patterns of the flame are affected. Wake regions are formed downstream of the plume and at times, spiralling vortex flows are seen in the plume at the leeward edges of the pool. Another wind effect is the tilting of the plume such that there were times when the calorimeter, towers and other instrumentation were not fully engulfed by the flames. These wind effects are erratic in nature and contribute to the large spatial and temporal varitaions that were noted within and between tests.

Flame (Gas) Temperature Data

A typical flame temperature history from a tower is shown in Fig. 4 (tower *2*, test C). The data from a single elevation possess large fluctuations, demonstrating the effects of both the characteristic turbulence of a large open pool fire and the wind. The erratic nature of the fire plume is evident from temperature histories. There are variations from tower to tower within a test and variations from test to test.

The mean temperatures were computed for all four measurement locations on each of the five 12.2-m-high towers in

Table 1 Average temperatures from the towers

	Test A				Test B				Test C			
	Test avg, K	Test st dev, K	Low avg, K	High avg, K	Test avg, K	Test st dev, K	Low avg, K	High avg, K	Test avg, K	Test st dev, K	Low avg, K	High avg, K
Twr 2												
e1	1232	107	1212	1254	1264	93	1248	1276	1292	90	1299	1286
e2	1110	121	1061	1163	1089	242	873	1241	1076	213	946	1206
e3	897	215	724	1088	929	265	644	1131	960	265	455	1187
e4	628	232	532	735	811	304	552	995	834	234	694	973
Twr 3												
e1	1065	220	948	1222	****	****	****	****	1204	147	1186	1342
e2	907	353	674	1220	1080	276	909	1391	1020	230	976	1355
e3	856	413	531	1291	812	366	568	1252	611	236	540	1156
e4	904	352	435	1160	693	283	537	974	472	155	426	828
Twr 4												
e1	1189	220	1151	1298	1145	190	1083	1297	1093	168	1078	1159
e2	1084	315	992	1353	997	205	905	1220	****	****	****	****
e3	836	208	731	1147	839	223	713	1147	777	175	704	1094
e4	584	248	470	917	623	244	508	902	569	167	515	804
Twr 6												
e1	1205	167	1194	1257	1102	181	1062	1263	1078	116	1056	1197
e2	1043	196	1002	1250	922	301	832	1288	825	212	758	1193
e3	697	225	606	1162	745	243	641	1165	710	240	620	1210
e4	550	297	439	1120	571	244	473	968	615	235	548	979
Twr 7												
e1	1278	101	1277	1284	1320	106	1317	1323	1252	123	1208	1275
e2	1062	227	1015	1286	1271	193	1160	1443	1269	154	1169	1320
e3	726	248	633	1171	948	268	447	1184	1050	225	794	1181
e4	****	****	****	****	****	****	****	****	****	****	****	****

Notes: **** = no data available; low average = flame "absent"; high average = flame "present"; e1 = elevation 142 cm; e2 = elevation 262 cm; e3 = elevation 549 cm; e4 = elevation 1118 cm

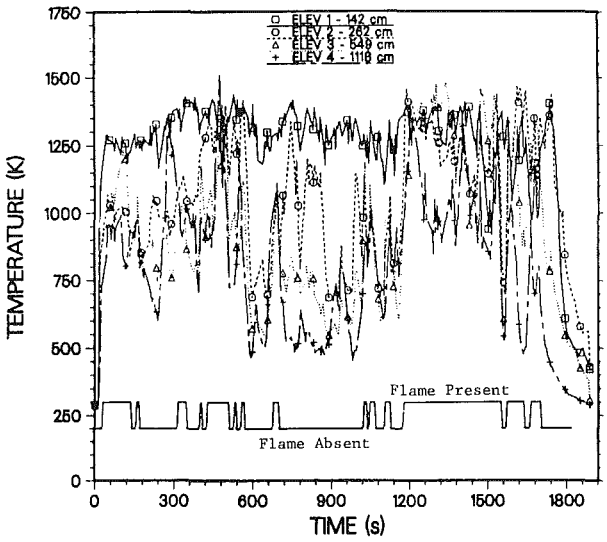

Fig. 4 Flame temperature history: Tower 2, Test C

each test. Table 1 presents these mean temperatures. The average values for elevation 1 range from 1065 to 1320 K, from 810 to 1270 K for elevation 2, from 610 to 1050 K for elevation 3, and from 470 to 905 K at elevation 4. The trend is for the mean temperature to be highest at the lowest elevation and to decrease as the elevation increases. Emphasizing the fact that the dominant wind direction was from the south for all the tests, the towers on the south side of the pool experienced lower mean temperatures. The north towers indicate higher mean values since they may be more centrally located in the plume as a result of the wind-induced tilt.

The standard deviations from the means are also given in Table 1. The trend is for the standard deviations to be smaller at the lowest elevation and to increase as the elevation increases. This is demonstrated by the fact that standard deviations average 12 percent of the mean temperature readings at elevation 1, 23 percent at elevation 2, 31 percent at elevation 3, and 38 percent at elevation 4. The larger spread in temperatures at the upper elevations is expected because at these heights, the wind effects are greater. The average of the mean temperature values obtained at a single elevation from all of the towers in a test agrees with the average values from the other two tests to within 8 percent. This agreement is very good considering the differing ambient wind conditions for each test.

In an attempt to account for wind effects, conditional sampling was used to examine the temperature data. All the data from elevation 4 on the five 12.2-m-high towers for all the tests were gathered. The probability density function of these temperature measurements was found to be bimodal in shape. One mode, at low temperatures, roughly corresponds to data taken when the wind effects were strong. The other mode, at higher temperatures, corresponds to times when the flames engulfed the towers. A setpoint temperature, which corresponded to the local minimum between the peaks of the probability density function, was chosen. This temperature was 935 K. A signal was generated that was high when the temperature was above the setpoint and low when the temperature was below the setpoint. This corresponds to a signal representing the "presence" or "absence" of flames about the towers, as shown in the conditioning signal in Fig. 4. This correspondence is not exact; however, this is a simple starting place to help in examining the fire data.

Statistics were obtained from the conditioned temperature data. The tower temperatures at each elevation were averaged during the flame present and absent periods based on the conditioning signal described above; the results are shown in Table 1. The general trends for these conditional averages are the same as the trends in the total test averages, with the mean temperatures decreasing with elevation. As can be expected, the mean flame present temperature at each elevation is higher than the mean temperature over the entire test at the corresponding elevation. The mean temperatures for the flame present condition are very consistent at the two lower elevations for all of the towers in all of the tests.

The readings obtained for the flame temperature thermocouples are lower than the true flame temperatures. The main

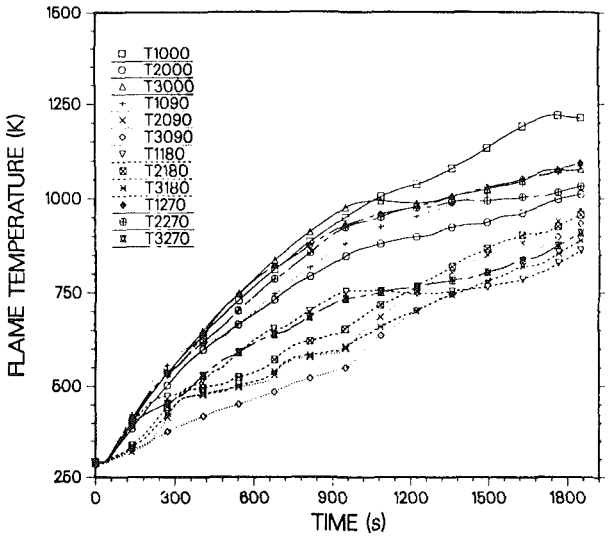

Fig. 5 Steel backface temperature history—Test A

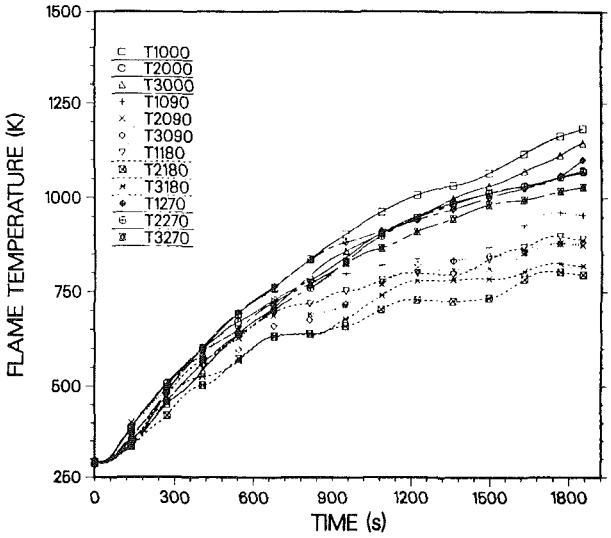

Fig. 6 Steel backface temperature history—Test B

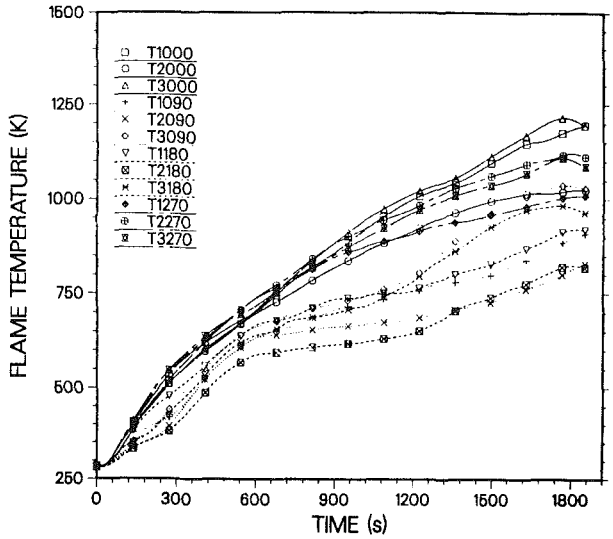

Fig. 7 Steel backface temperature history—Test C

source of error in the readings is believed to be due to radiative heat loss from the thermocopules. The error is probably the greatest for the flame thermocouples that are near the large calorimeter. This occurs because the extinction coefficient in the flames is on the order of 1/m (Longenbaugh, 1988) and these thermocouples are only 5 cm from a large, relatively cool surface. For the thermocouples mounted on the towers, the errors are believed to be small during the flame present condition and will increase during the flame absent condition. Other sources of error include transient effects, soot buildup on the thermocouples, thermocouple calibration, and data system inaccuracies; these errors were not considered in this analysis.

For the thermocouples near the calorimeter, this error is a maximum at the early times in the test and decreases as the calorimeter heats up. The error was estimated from a simplified one-parameter radiative model. The radiative view factors between the thermocouple and both the flames and the large calorimeter were found using the cross-string method with the thermocouple at the cross point. Other assumptions are a nonparticipating gas medium and blackbody radiative exchange between the thermocouple, calorimeter, and fire. Then, by performing a heat balance on a thermocouple assumed to be in radiative equilibrium with the fire at 1255 K and the calorimeter surface, this error is estimated to be approximately 12 percent of the assumed fire temperature when the calorimeter surface is cold (365 K) and 4 percent when the surface is hot (1090 K). This error estimate does not encompass all factors affecting the thermocouple readings.

Method of Obtaining Heat Flux Data

For these tests, the calorimeter backface temperatures were measured; however, the net heat flux at the outer surface is desired. To determine the net heat flux, the temperature data becomes the "boundary condition" in the inverse problem of heat conduction. This problem was solved by a numerical technique presented by Beck et al. (1985). The numerical technique was utilized by Blackwell et al. (1985) to develop a computer code, known as the Sandia One-Dimensional Direct and Inverse Thermal (SODDIT) Code, to generate net heat flux and surface temperature information given interior temperature data.

The calorimeter design was checked in several ways. The use of backface measurements was evaluated in a series of experiments in which a wall section, with multiple frontface and backface thermocouples, was exposed to known radiative heat fluxes in Sandia's Radiant Heat Facility. A thermal model was used to show that the local heat conduction was effectively one dimensional.

Because noisy data can promote instabilities in any inverse calculation, a series of simple numerical studies was used to evaluate potential errors. As a result, two approaches were used to reduce the effects of noise in the data analysis procedure. A light smoothing of the actual temperature data was introduced by fitting the data with a smoothing spline with an allowed standard deviation of 0.5 K (a fairly tight fit). An additional smoothing feature in SODDIT is the use of what is termed "future temperature" information, a concept developed by Beck et al. (1985). The future temperature approach allows the use of smaller computational time steps and increases stability. After an extensive review of the data from test A, four future times were chosen to provide calculational stability over the temperature ranges expected in the test series without eliminating the ability to resolve specific thermal events in the tests.

A study of the sensitivity of this inverse procedure to noise in the data was made by analyzing "exact" data to which varying amounts of random noise had been added. The exact temperature data were generated for a triangular heat flux pulse into a planar section of the calorimeter material that had

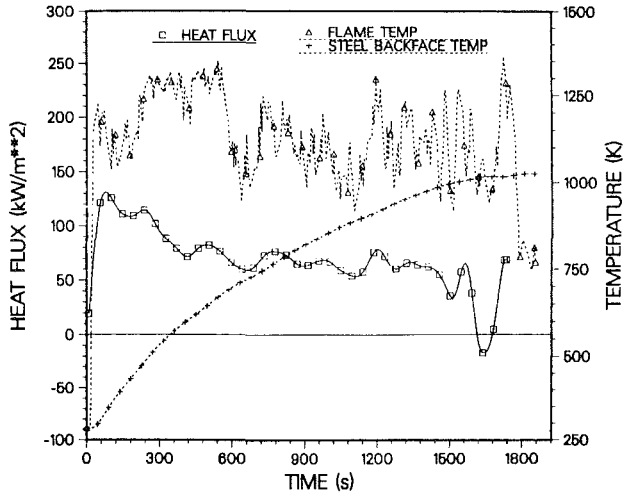

Fig. 8 Net heat flux, steel backface temperature and external flame temperature histories—bottom station

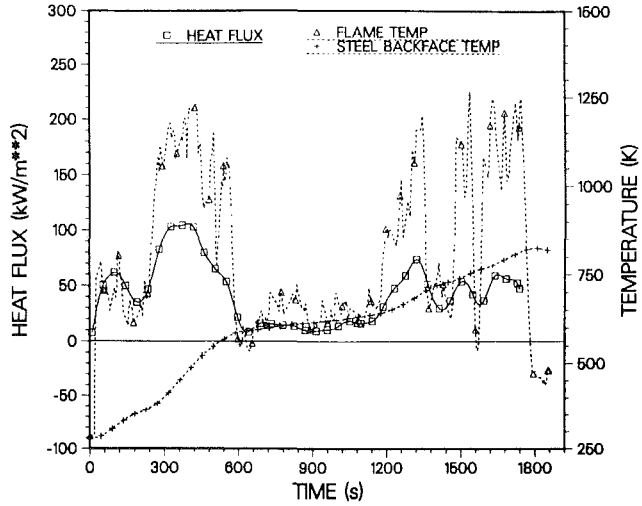

Fig. 10 Net heat flux, steel backface temperature and external flame temperature histories—top station

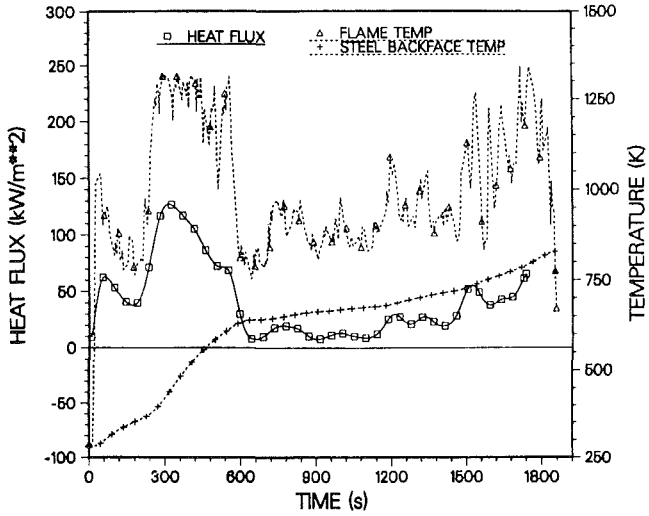

Fig. 9 Net heat flux, steel backface temperature and external flame temperature histories—south station

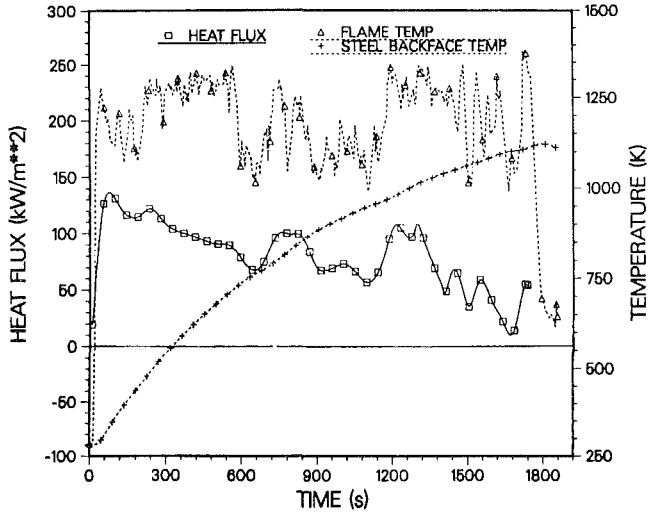

Fig. 11 Net heat flux, steel backface temperature and external flame temperature histories—north station

an insulated backface. Random noise with a standard deviation of 0.05 K to 1.1 K was added to these data. To evaluate any differences in stability as a function of the temperature, the thermophysical properties of the material were evaluated at 530 K or 895 K.

The heat flux profiles calculated from the noisy data sets were compared to the heat flux profile used to generate the exact temperture data. The maximum errors at the lower temperature ranged from 7 percent for the highest noise level to a minimum of 2 percent and then up to 4 percent at the lower noise level. At higher temperature, the values were 17, 4, and 5 percent, respectively. For reference, the random noise in the temperature data taken during the lead-in periods before the tests had a standard deviation of less than 0.03 K.

In spite of the smoothing effects, the heat flux calculations still exhibited oscillations at later times in the tests. This occurs because mild steel experiences a Curie point transition centered at ~ 1035 K. From measurements made on samples taken from the calorimeter wall, this transition is characterized by a sharp spike in specific heat capacity between 975 and 1090 K. Such an abrupt change in thermal properties causes instabilities in the inverse code; the natural fluctuations in the fire temperatures compound the instability problem. As a result, the heat flux calculations at temperatures above the transition temperature are not as reliable. Therefore, when heat flux is presented as a function of surface temperature, data are reported for values less than 1035 K.

Large Calorimeter Heat Flux Data

Temperature histories for all twelve stations are presented in Figs. 5, 6, and 7 for the three tests. These "temperature envelopes" can be used to examine the uniformity in a fire, the integrated heat flux, which is directly related to the total temperature rise, and the repeatability from fire to fire by overlaying the envelopes. A narrower envelope indicates a more uniform thermal exposure over the surface of the calorimeter. This method of comparison is limited to test items with the same thermal properties, wall thickness, and geometry.

For the four stations at the axial center of the large calorimeter, the net heat flux, the steel backface temperature, and the external flame temperature histories from Test C are given in Figs. 8 through 11. Typically, the net heat flux to the calorimeter peaked at test startup, to values between 100 and 160 kW/sq.m, and diminished as the calorimeter surface heated up. The heat flux values naturally tracked the external flame temperature values, but there was a significant amount of filtering. Some of this filtering was due to the natural damping effects of the calorimeter; note the smooth rise of the steel backface temperature curve (thermal response time is on the

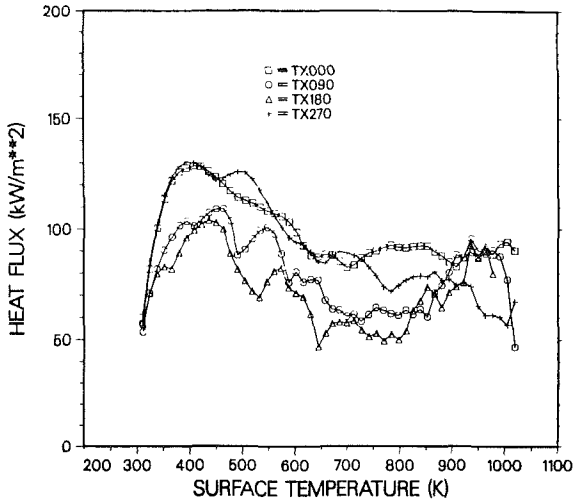

Fig. 12 Average heat fluxes for the test series

order of 9 s). There was additional filtering due to the slight smoothing introduced in preprocessing the data and to the use of future temperature information in the actual data analysis.

The trends in the flame temperatures adjacent to the calorimeter are similar to the trends for the tower flame temperature data. For the southern or 090 station, there were periods of lower values due to wind effects. This also applies to the upper, or 180 station. Videotapes of the test show times when the southern and upper parts of the calorimeter were not fully engulfed in flame; these times correlate with times of low heat flux on the plots. Even though the winds are within the prescribed limits, changes in the winds produce fluctuating, nonuniform temperature fields in the regions around the top and windward side of the large calorimeter.

Temporal data are important in the presentation of the heat flux information, because changes in the heat flux can be correlated with events in the fire, such as fluctuating flame temperatures. From the heat flux histories, total thermal input can be studied and trends within a test defined. Another useful means of data presentation is to plot heat flux as a function of surface temperature. Because the NRC and IAEA test specifications use this format, presentation of the data in this manner facilitates a direct comparison. In this form, thermal transport mechanisms in the fire can also be studied. The SODDIT code provides the estimated surface temperatures for these plots as well as the heat fluxes.

The heat fluxes with respect to angular station, i.e., all the heat flux values from three stations in each of the three tests, were averaged together at specific surface temperature values (note that the time at which a specific temperature is reached is different for each station in a test and from test to test). The mean values are plotted against surface temperature in Fig. 12. The average of the peak fluxes for the lower stations (TX000) and the north stations (TX270) was about 130 kW/sq.m. For the southern stations (TX090), the average of the peak fluxes was 110 kW/sq.m. For the upper stations (TX180), it was 100 kW/sq.m. In general, TX000 exhibited the highest, most uniform peak heat fluxes and TX180, the lowest. Stations TX270, which were on the leeward side of the calorimeter, showed much higher peak heat fluxes than TX090, which were windward during the tests.

Standard deviations from the mean values were computed; they are relatively large for all stations, demonstrating the effects of the wind and the random nature of the fire. Stations TX000 exhibited the smallest values, on the order of 15 percent of the mean. For stations TX270, the standard deviations are on the order of 25 percent, for stations TX090 and TX180, on the order of 35 percent. The stations that had greater exposure to the wind (stations TX090 and TX180) experienced larger fluctuations than the stations that were sheltered from wind effects (stations TX000 and TX270). From the visual data, the south side of the calorimeter could actually be seen at times during all three tests. Even when the plume engulfed the test item, the flame thickness was not as great on the windward and upper stations of the calorimeter; this lowers the radiative transport to these portions of the calorimeter.

Table 2 Integrated heat flux at 30 min* (kw-hr/sq. m)

Test	Angle, deg	Station 1 (East)	Station 2 (Middle)	Station 3 (West)
A	0	43.8	32.0	37.5
	90	38.2	28.8	26.4
	180	22.5	28.1	24.0
	270	38.5	34.5	25.0
	End Cap	18.3	*****	19.6
B	0	42.3	37.3	41.0
	90	28.2	23.6	23.6
	180	24.3	19.8	20.7
	270	38.5	37.3	33.9
	End Cap	19.6	*****	20.6
C	0	42.8	33.3	43.4
	90	25.7	21.4	33.5
	180	26.1	20.8	29.6
	270	33.7	39.1	38.3
	End Cap	21.6	*****	18.8

*Test C was only 29 min, so values were extrapolated to 30 min.

Table 3 Statistics for the integrated heat flux at 30 min* (kw-hr/sq. m)

Cylindrical surface	Low	Mean	High	Standard deviation, percent
Test A—All	22.5	31.6	43.8	6.8 (21.5)
Test B—All	19.8	30.9	42.3	8.3 (26.9)
Test C—All	20.8	32.3	43.4	7.7 (23.8)
Station 1—All	22.5	33.7	43.8	7.9 (23.4)
Station 2—All	19.8	30.0	39.1	6.9 (23.0)
Station 3—All	20.7	31.4	43.4	7.6 (24.2)
0 deg—All	32.0	39.3	43.8	4.4 (11.2)
90 deg—All	21.4	27.7	38.2	5.3 (19.1)
180 deg—All	19.8	24.0	29.6	3.4 (14.2)
270 deg—All	25.0	35.4	39.1	4.5 (12.7)
End Caps—All	18.3	19.8	21.6	1.2 (6.1)

*Test C was only 29 min, so values were extrapolated to 30 min.

Integrated heat flux values at 30 min are presented for the test series in Table 2. Statistics for these values are presented in Table 3. High, low, and mean values, as well as standard deviations from the mean, are provided for various groups of data. The data are grouped as follows: all cylindrical surface data with respect to test, all data for the series with respect to axial station, all data for the series with respect to angular station, and all end cap data for the test series. Note that there is approximately a two-to-one ratio between the high and low values for the first and second groupings and the standard deviations are about 25 percent. When grouped with respect to angular station, however, the spread and the standard deviations are smaller.

Small Calorimeter Heat Flux Data

Heat flux histories for the 10-cm and 20-cm calorimeters from Test C are presented in Figs. 13 through 16 along with the closest flame temperatures located above each calorimeter. For the lower calorimeters, these flame temperatures were measured ~50 cm above the upper stations and for the upper calorimeters, ~25 cm above the upper stations. The fluctuations in heat flux for the smaller calorimeters were generally greater than for the large calorimeter. This phenomenon is believed to be due to the fact that the large calorimeter damps

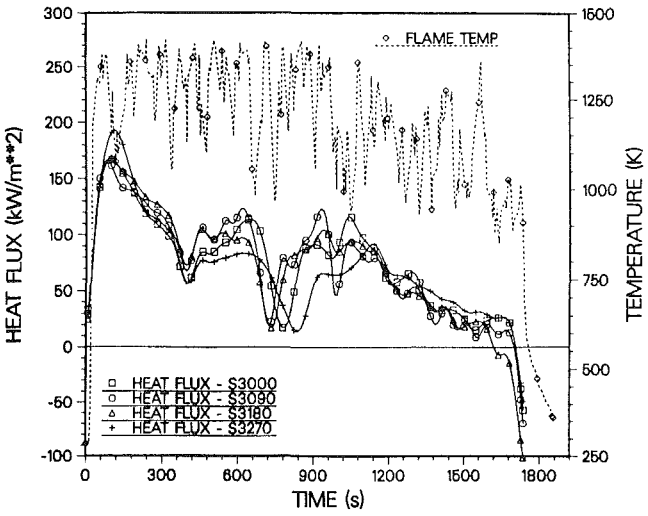

Fig. 13 Heat flux and flame temperature histories: lower 10-cm calorimeter

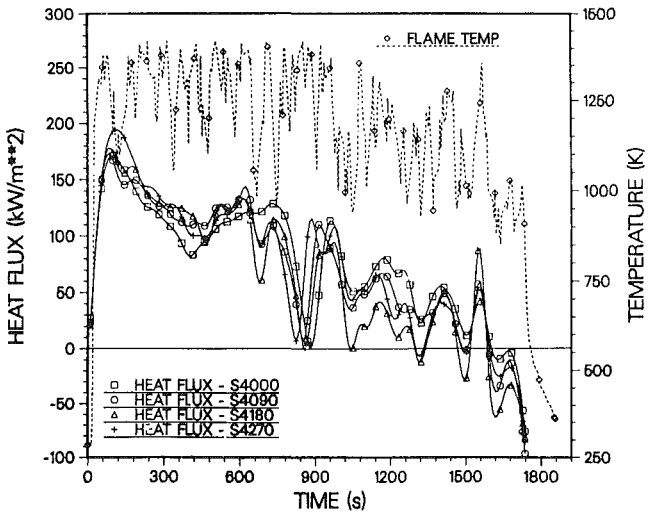

Fig. 14 Heat flux and flame temperature histories: lower 20-cm calorimeter

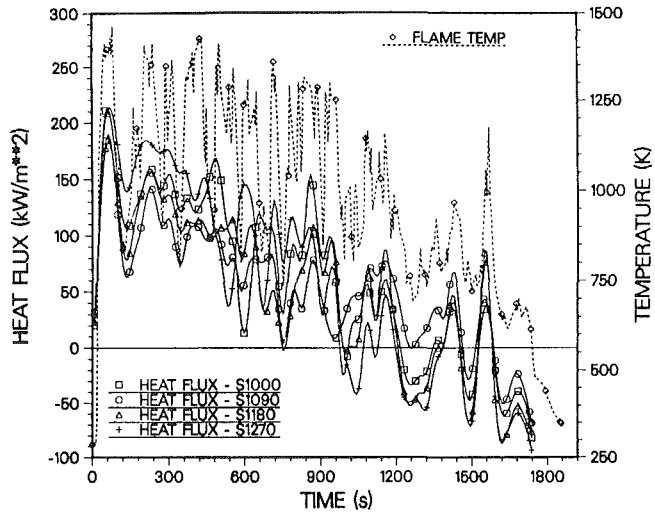

Fig. 15 Heat flux and flame temperature histories: upper 10-cm calorimeter

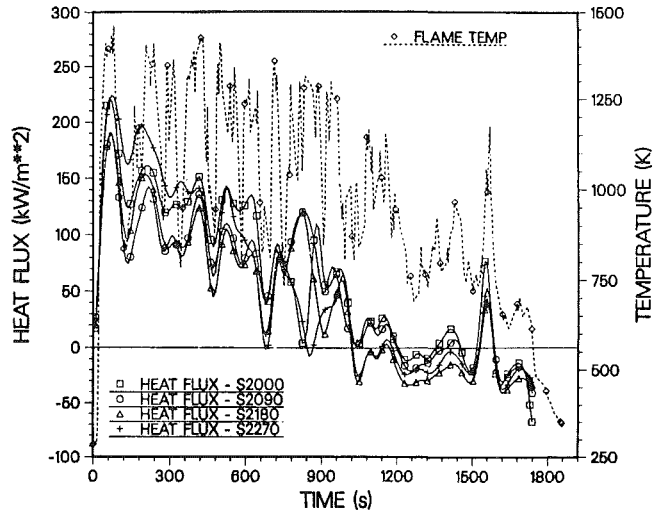

Fig. 16 Heat flux and flame temperature histories: upper 20-cm calorimeter

out the local temperature variations in the flame to a greater degree. Peak fluxes for the smaller calorimeters were generally between 160 and 200 kW/sq.m, with the exception of the upper calorimeters in test A. These calorimeters experienced relatively low fluxes for the first half of the test.

Typically, the trends in the heat flux histories from all angular stations for a single calorimeter track each other. For the upper calorimeters, however, the heat flux values differ by as much as a factor of two from one station to the next on a single calorimeter.

There are general trends for the angular variation in heat fluxes; station 270, on the leeward side, demonstrates the highest heat fluxes. The bottom station 000 follows closely, and as on the larger calorimeter, the upper and windward stations (180 and 090) demonstrate lower fluxes. The heat flux values for the small calorimeters in test A are in general lower than those in the other tests, a result of the generally lower local flame temperatures at the west end of the pool.

Discussion of Results

Heat Flux Data. On the large calorimeter, the circumferential variations in the heat flux and the integrated heat flux are probably the result of several phenomena. Fluctuating, nonuniform temperature fields due to the wind effects have been previously noted; there is a steady decrease in the average temperature with increasing elevation. Wind effects on the heat fluxes at the top and windward stations are readily apparent. Even with no wind, the variations in the convective heat transfer are significant; for a cylinder in crossflow, the local heat transfer coefficients are highest at the lower stagnation point, decrease appreciably at the sides, and then increase up to the top of the cylinder. Because the calorimeter is a massive heat sink (the maximum absorption rate was approximately 5 MW), a cooler, soot-laden boundary layer probably exists around the calorimeter; this boundary layer is believed to act as a radiation shield.

There is evidence of domelike fuel-rich vapor regions above the fuel surface in small pool fires. Corlett (1974) described pool fires of more than 1 m diameter as being "unstructured" flames with no large, cold, fuel-rich vapor dome. If the vapor dome was present in the fires in this test series, then the lowest heat flux levels would be at the 000 stations on the underside of the large calorimeters, due to a decrease in the radiant field intensity. The fact that the heat flux values are highest at the 000 stations indicates that no large vapor dome is present.

There have been studies that predict the radiant heat transfer to a horizontal cylinder engulfed in luminous flames (Birk and

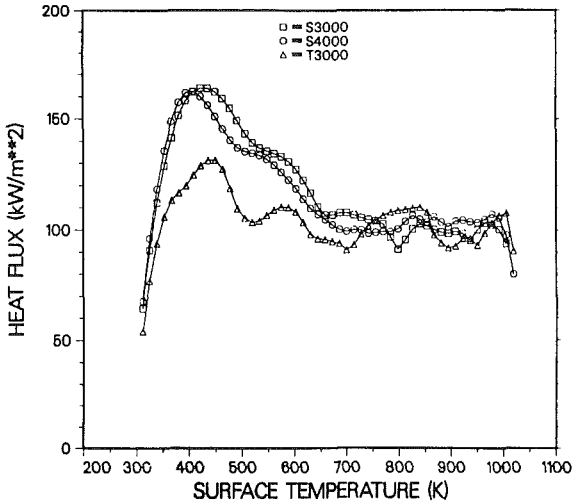

Fig. 17 Average heat flux versus surface temperature: lower stations, large and small calorimeters

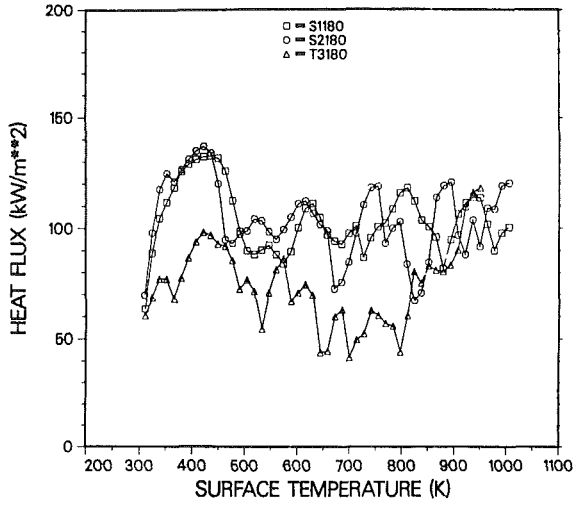

Fig. 18 Average heat flux versus surface temperature: upper stations, large and small calorimeters

Oosthuizen, 1982; Tunc and Karakas, 1985). Because there are insufficient data to define the temperature field in the flame volume, the flame is considered as a participating medium with a uniform temperature and extinction coefficient. The size of the fire and the positioning of the cylinder in the fire will strongly affect the predicted heat flux distribution. Formulations were done for cases in which the bottom of the cylinder was 0.3 m and 1 m above the pool and the width of the pool perpendicular to the cylinder axis was between 2.4 m and 7.6 m. Probably as a result of the assumption of a uniform flame temperature, these analyses predict that the highest heat fluxes will be at the top and the values will decrease along the periphery to the underside of the cylinder. The data in Table 1 show that the average temperature decreases with increasing elevation. The lowest net fluxes are measured at the top of the calorimeter (stations 180) and the highest fluxes are measured on the underside of the calorimeter (stations 000).

Because only total heat flux measurements were made in these tests, an attempt was made to estimate the radiative/convective partitioning of heat transfer to the calorimeters during the periods of low winds. Using data from Schneider and Kent (1987) for measurements made in the same pool but in a different test, the average velocity was 4.8 m/s at an elevation of 1.4 m above the initial fuel surface. This was slightly above the location of the bottom stations on the large calorimeter and the lower 10-cm and 20-cm calorimeters. Using this velocity, the convective heat transfer coefficients at the stagnation point were calculated for the three cylinders in cross-flow. The coefficients were computed for surface temperatures of 420 K, the temperature at which the peak flux occurs in Fig. 17, and a flame temperature of 1200 K, which is approximately the average temperature from Table 1 at this elevation. For these conditions, the Grashof number for the large calorimeter is 3.8×10^9 and the Reynolds number is 80,500. Assuming that the gas is air, the average Nusselt number is 120 for natural convection and 213 for forced convection. Kreith (1963) indicates that turbulent, forced convection should be assumed for these conditions.

Using correlations for forced convection from Kreith (1963), the stagnation point convective fluxes were 8.5, 22, and 32 kW/sq.m. for the 1.4-m, 20-cm, and 10-cm calorimeters, respectively. For the test series, the average total heat fluxes estimated by SODDIT at these stations, for surface temperatures of 420 K, were 130, 170, and 170 kW/sq.m. Thus, the convective flux was estimated to be 6.5, 13, and 19 percent of the total cold wall flux for the calorimeters.

The variation in the forced convection heat transfer coefficient around the large calorimeter was calculated for the conditions listed above. The approximate values of the local Nusselt number are 280 at station 000, 130 at stations 090 and 270, and 210 at station 180.

The velocity field is strongly correlated with the temperature field (McCaffrey, 1979; Schneider and Kent, 1987; Weckman, 1987). Because the flow is buoyancy dominated, the velocity will drop when the temperature drops. However, the heat transfer coefficient remains approximately constant because temperature-dependent changes in the gas properties roughly offset the effects of the changes in the gas velocity. Using the temperature and velocity measurements in Schneider and Kent (1987), the calculated heat transfer coefficient varied by less than 15 percent over a temperature range of 775 to 1275 K using the assumption of turbulent flow over a cylindrical body.

The convective heat transfer to a flat plate in parallel flow was also calculated. The analysis used the same conditions as above. The elevation of 1.4 m is slightly below the instrumentation stations on the end plates of the large calorimeter. For these conditions, the local Reynolds number is 39,300. Although the Reynolds number is below the level where the flow over a flat plate is normally considered to be turbulent, a turbulent flow correlation was used to estimate the heat transfer coefficient because the incoming or free-stream flow is believed to be turbulent.The convective flux estimate was 7 kW/sq.m. The average total heat flux estimated by SODDIT on the end plates for a surface temperature of 420 K was 108 kW/sq.m; thus, of the total cold wall heat flux to the end plates, ~7 percent is convective, and the balance radiative.

Large Versus Small Calorimeters. As shown in Fig. 2, the small calorimeters were placed with either top or bottom stations at the same elevation as the corresponding stations on the large calorimeter. Three sizes were used in an attempt to compare the heat transfer to objects of different size and total thermal capacity. The stations of interest on the large calorimeter are the bottom west station, T3000, and also the top west station, T3180. The stations from the 10-cm and 20-cm calorimeters are the bottom stations of the lower calorimeters, stations S3000 and S4000, and the top stations of the upper calorimeters, S1180 and S2180. The heat flux was averaged for each station for all three tests with the results plotted for the lower stations in Fig. 17 and for the upper stations in Fig. 18.

The average heat flux curves for the lower stations in Fig. 17 are relatively smooth. The peak flux of 130 kW/sq.m to the 1.4-m calorimeter is about 80 percent that of the peak

fluxes of 164 kW/sq.m to the 10-cm and 20-cm calorimeters. The magnitudes of the fluxes to the 10-cm and 20-cm calorimeters are roughly equivalent throughout the temperature range, and above approximately 700 K, all three curves converge to the same values.

The average heat flux curves for the upper stations in Fig. 18 fluctuate a great deal more than for the lower stations, and the magnitudes of the fluxes are noticeably smaller. The lower heat fluxes and large fluctuations probably result from wind effects. The peak flux of 90 kW/sq.m to the large calorimeter is two thirds that of the peak fluxes of 135 kW/sq.m to the smaller calorimeters. The peak fluxes to the 10 cm and 20 cm calorimeters are almost equal in magnitude but 18 percent below the fluxes to the lower calorimeters reported above.

A conditional analysis of the heat flux data from the large calorimeter was reported by Bainbridge and Keltner (1987). In this type of analysis, a subset of the data is obtained in which the wind effects are minimal; this allows estimates of the heat transfer when the calorimeter is fully engulfed by the flames. The analysis shows the same type of heat flux distribution: maximum on the bottom and minimum on the top.

The phenomena noted here support the postulation of an interaction between an object and the fire that surrounds it. The large calorimeter appears to alter this interaction because it is physically large and thermally massive. This indicates that the heat transfer to an object engulfed in a fire can be highly dependent on the properties of the item.

Summary

A series of large fire tests was conducted to supply information about the thermal exposure of a large object immersed in a fire and the repeatability of the thermal environment. Thermal measurements have been presented from three large open pool fire tests run with duplicate instrumentation. Heat flux and temperature data within the lower part of the fire have been studied in a variety of ways and the strong influence of the wind has been noted. Statistics have been developed to evaluate the test-to-test repeatability of the fire environment.The largest factor affecting the reproducibility of the environment in a large open pool fire is the wind.

Average flame temperatures at eight locations around the test item ranged from 1065–1320 K at a height of 142 cm and from 810–1270 K at a height of 262 cm above the initial pool surface. The spread in these values is quite large. When the temperatures are averaged for all eight locations in each test (a larger sample size), however, the spread in values decreases. For elevation 142 cm, averages for tests A, B, and C, respectively, were 1195, 1210, and 1185 K; these values are within 2 percent of each other. For elevation 262 cm, the average values were 1040, 1070, and 1050 K; these values are within 3 percent of each other.

The peak heat fluxes to the large test item for various locations on the item ranged from 100–160 kW/sq.m. The fluxes to the underside of the calorimeter were highest and those at the top were the lowest; this distribution is counter to the heat flux distributions predicted with simplified radiation modeling that assumes uniform flame temperatures. When averaged for all locations, the peak flux for each test was between 115 and 120 kW/sq.m.

The partitioning of the peak heat flux to the bottom location of the cylinders in crossflow was estimated to range from 6.5 to 19 percent convective with the balance radiative. The magnitude of the convective contribution is size dependent; the larger the radius of the cylinder, the lower the convective contribution to the total flux. For flat plates in parallel flow, the partitioning of the heat transport was estimated to be 6 percent convective with the balance radiative.

The total heat input or the time-integrated heat flux values for the test item were determined. The values for a single test varied with respect to location by as much as a factor of two; again, the highest values were on the bottom and lowest on the top. When all stations were averaged for a single test, the values of 31.6, 30.9, and 32.3 kW-hr/sq.m for tests A, B, and C, respectively, were within 5 percent of each other.

The physical size and thermal capacitance of a test item affect the level of thermal exposure in a fire. The effects are demonstrated when heat fluxes to the large test item are compared with the heat fluxes to smaller items in the fire. The average peak fluxes to a large calorimeter are about 75 percent of those to much smaller calorimeters.

Acknowledgments

The test program was funded by the Federal Rail Administration of the U.S. Department of Transportation (DOT). Sandia National Laboratories is operated by AT&T Technologies for the U.S. Department of Energy (DOE) under Contract No. DE-AC04-76DP00789.

References

Babrauskas, V., 1983, "Estimating Large Pool Fire Burning Rates," *Fire Technology*, Vol. 19, No. 4, pp. 251–261.

Bainbridge, B. L., and Keltner, N. R., 1987, "Heat Transfer to Large Objects in Large Pool Fires," International Conference on Major Hazards in the Transport and Storage of Pressure Liquified Gases, University of New Brunswick, Aug.; proceedings to be published in the *Journal of Hazardous Materials*.

Beck, J. V., Blackwell, B. F., and St. Clair, C. R., Jr., 1985, *Inverse Heat Conduction, Ill-Posed Problems*, Wiley, New York.

Birk, A. M., and Oosthuizen, P. H., 1982, "Model for the Prediction of Radiant Heat Transfer to a Horizontal Cylinder Engulfed in Flames," ASME Paper No. 82-WA/HT-52.

Blackwell, B. F., Douglass, R. W., and Wolf, H., 1985, "A User's Manual for the Sandia One-Dimensional Direct and Inverse Thermal (SODDIT) Code," SAND 85-2478, Sandia National Laboratories, Albuquerque, NM.

Blinov, V. I., and Khudiakov, G. N., 1957, "Certain Laws Governing Diffusion Burning of Liquids," *Doklady Akademii Nauk SSSR*, Vol. 113, pp. 1094–1098.

Corlett, R. C., 1974, "Velocity Distributions in Fires," *Heat Transfer in Fires*, Wiley, New York, pp. 239–255.

Gregory, J. J., Mata, R., Jr., and Keltner, N. R., 1987, "Thermal Measurements in a Series of Large Pool Fires," SAND 85-0196, Sandia National Laboratories, Albuquerque, NM.

Hottel, H. C., 1959, "Review: Certain Laws Governing the Diffusive Burning of Liquids," *Fire Research Abstracts and Reviews*, Vol. 1, pp. 41–43 (translated from Blinor, X. X., and Khudiakor, Y. Y., 1957, *Dokl. Akad. Nauk SSR*, Vol. 113, p. 1096).

IAEA, 1985, "Regulations for the Safe Transport of Radioactive Materials," Safety Series No. 6 of the International Atomic Energy Agency Safety Standards, Paragraph A628.11 "Fire Conditions," Advisory Material on Paragraph 628—"The Thermal Test," rev. ed., Vienna, STI/PUB/323.

Kreith, F., 1963, *Principles of Heat Transfer*, International Textbook Co., Scranton, PA.

Logenbaugh, R. S., 1985, "Experimental and Theoretical Analysis of the Radiative Transfer Inside of a Sooty Pool Fire," Master's Thesis, New Mexico State University; SAND 86-0083, Sandia National Laboratories, Albuquerque, NM, 1988.

McCaffrey, B. J., 1979, "Purely Buoyant Diffusion Flames: Some Experimental Results," NBSIR 79-1910, National Bureau of Standards, Washington, DC.

NRC, 1983, "Packaging of Radioactive Material for Transport and Transportation of Radioactive Material Under Certain Conditions," U.S. Nuclear Regulatory Commission, Title 10, Code of Federal Regulations, Part 71.

Schneider, M. E., and Kent, L. A., 1987, "Measurements of Gas Velocities and Temperatures in a Large Open Pool Fire," *Heat and Mass Transfer in Fires*, ASME-HTD-Vol. 73; to be published in *Fire Technology*.

Tunc, M. M., and Karakas, A., 1985, "Three-Dimensional Formulation of the Radiant Heat Flux Variation on a Cylinder Engulfed in Flames," ASME JOURNAL OF HEAT TRANSFER, Vol. 107, pp. 949–952.

Weckman, E. J., 1987, "The Structure of the Flowfield Near the Base of a Medium-Scale Pool Fire," Ph.D. Dissertation, University of Waterloo, Waterloo, Ontario, Canada.

Heat Transfer in Compartment Fires Near Regions of Ceiling-Jet Impingement on a Wall

L. Y. Cooper

Head, Building Fire Modeling,
Center for Fire Research,
US National Bureau of Standards,
Gaithersburg, MD 20854
Mem. ASME

The problem of heat transfer to walls from fire-plume-driven ceiling jets during compartment fires is introduced. Estimates are obtained for the mass, momentum, and enthalpy flux of the ceiling jet immediately upstream of the ceiling–wall junction. An analogy is drawn between the flow dynamics and heat transfer at ceiling-jet/wall impingement and at the line impingement of a wall and a two-dimensional, plane, free jet. Using the analogy, results from the literature on plane, free-jet flows and corresponding wall-stagnation heat transfer rates are recast into a ceiling-jet/wall-impingement-problem formulation. This leads to a readily usable estimate for the heat transfer from the ceiling jet as it turns downward and begins its initial descent as a negatively buoyant flow along the compartment walls. Available data from a reduced-scale experiment provide some limited verification of the heat transfer estimate. Depending on the proximity of a wall to the point of plume-ceiling impingement, the result indicates that for typical full-scale compartment fires with energy release rates in the range 200–2000 kW and fire-to-ceiling distances of 2–3 m, the rate of heat transfer to walls can be enhanced by a factor of 1.1–2.3 over the heat transfer to ceilings immediately upstream of ceiling-jet impingement.

Introduction

In potentially hazardous compartment fires, the total heat transfer from fire-plume-driven ceiling and wall flows to enclosure-ceiling and -wall surfaces can be a significant fraction of the fire's total energy release rate Q (Cooper et al., 1982; Cooper, 1987a). This is especially true during the critical early times of such fires when events that relate strongly to the ultimate safety of people and property are taking place. Such events would include: times of significant fire-detector and/or sprinkler-link response; times when fire-compartment environments hazardous to people are developing, and up to times when such hazardous environments are approached; and all times prior to the time when temperatures of combustible ceiling and wall surfaces reach ignition temperatures. Successful simulations of these critical events must involve reasonably accurate mathematical models of the above-mentioned heat transfer and related flow phenomena.

Algorithms to estimate heat transfer to smooth ceilings during compartment fires that are concise enough to translate into subroutines for use in practical zone-type compartment-fire-model computer programs are now available (Cooper, 1982a, 1982b, 1987a; Cooper and Woodhouse, 1986). Such is not the case for the potentially significant heat transfer to the compartment walls. It is the purpose of this paper to develop a means of estimating peak heat transfer rates from ceiling-jet-driven wall flows to wall surfaces near lines of ceiling–wall junctions. This requires predictions of the properties of ceiling jets immediately upstream of wall impingement. It is also an objective of this work to obtain the latter predictions.

The Basic Phenomena

As a fire grows in an enclosure, the hot air and products of combustion, which leave the zone of the burning object, form a plume and are convected upward by buoyancy. When the upward movement of the plume constituents is blocked by the ceiling (a distance H above the fire), they spread radially outward, forming a relatively thin turbulent ceiling jet. Depending on the proximity r_j of vertical surfaces, this ceiling jet either loses most of its momentum far out on its trajectory (in the case of an expansive ceiling with large r_j/H surfaces), or can be expected to interact vigorously with these bounding surfaces (in the case of lower aspect ratio spaces with r_j/H of the order of 1) by forming a downward wall-jet flow, which is eventually turned back upward by its own buoyancy. The flow scenario for the latter case is depicted in Fig. 1.

Once the ceiling-jet gases are blocked by bounding vertical surfaces, they begin to redistribute themselves across the entire ceiling area of the enclosure. Eventually, a relatively quiescent, stably stratified, upper-gas layer is formed below the continuing ceiling-jet activity. The bottom of this layer is defined by a distinctive material interface, which separates the lower ambient air from the upper, heated, product-of-combustion-contaminated gases. With increased time, the level of the interface continues to drop, and the average absolute temperature T_{up} of the upper-layer gases continues to rise. As depicted in Fig. 2, for small to moderate r_j/H, vigorous ceiling jet–wall flow interaction can still occur. Two cases can be distinguished. In the first, depicted in Fig. 2(*a*), the downward wall jet penetrates the interface, continues its downward flow in the lower layer, and is eventually buoyed back upward to interact with the upper layer. In the second, depicted in Fig. 2(*b*), the downward-flowing wall jet loses its downward momentum, and is turned back upward prior to penetrating the two-layer interface.

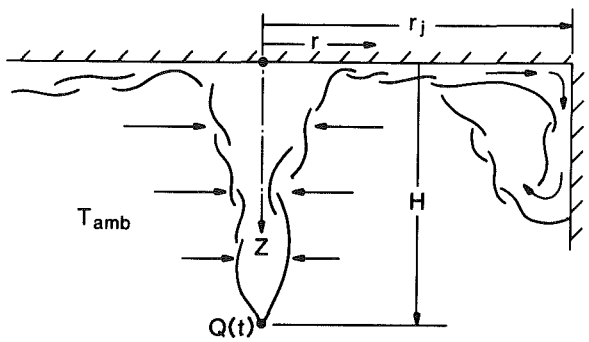

Fig. 1 Early time ceiling jet-wall interaction

Contributed by the Heat Transfer Division and presented at the 24th National Heat Transfer Conference, Pittsburgh, Pennsylvania, August 9–12, 1987. Manuscript received by the Heat Transfer Division November 23, 1987. Keywords: Fire/Flames, Natural Convection.

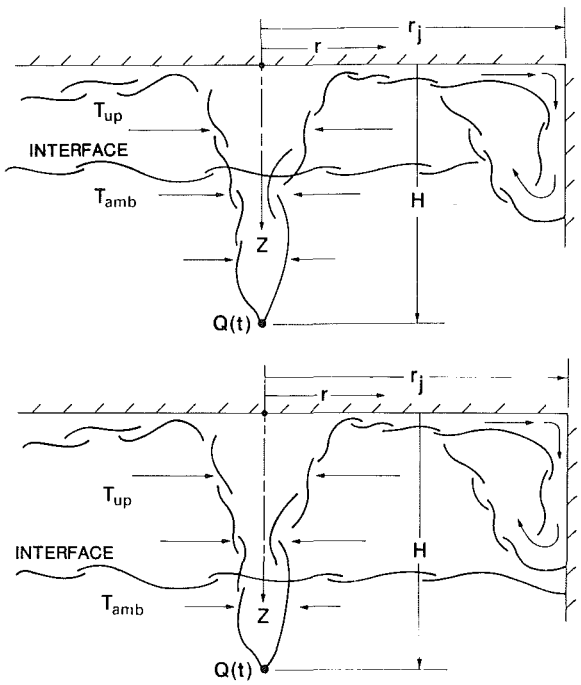

Fig. 2 Ceiling jet-wall interaction with upper layer: (*a*) penetration of interface; (*b*) no penetration of interface

An experimental program to isolate and study the type of wall flows depicted in Figs. 1 and 2 is in progress, and the first stage of this, which provides results for the flows of Figs. 1 and 2(*b*), has been completed (Jaluria and Goldman, 1986). To use these and anticipated future results on wall flows requires an understanding, not now available, of the ceiling-jet turning region near locations of ceiling jet–wall impingement. It is the objective of the present work to study the heat transfer processes at these locations.

The ceiling-jet flow and heat transfer phenomena of Fig. 2(*b*), which takes place in the relatively quiescent environment of temperature T_{up}, are similar to those of Fig. 1. Following the arguments of Cooper (1987a), where the upper layer is treated as an expansive environment with ambient temperature T_{up}, quantitative descriptions of the phenomena in Fig. 1 would also be usable in predicting those in Fig. 2(*b*). For this reason it is sufficient to focus attention here on the relatively simple configuration in Fig. 1.

Heat Transfer From Impinging Two-Dimensional Plane Air Jets

Gardon and Akfirat (1966) present data from an experimental study of heat transfer from an ambient-temperature plane jet to an isothermal wall (temperature, T_w) (Fig. 3). Data for the stagnation-line heat transfer coefficient h_s, plotted in Fig. 2 of their work, are reproduced here in Fig. 4. As will be seen below, these will be useful in the context of the Fig. 1 scenario of present interest. For $X_n/B > 14$ and Reynolds number $\mathrm{Re}_e > 2000$, a correlation for h_s was found by Gardon and Akfirat (1966) to be

$$\mathrm{Nu}_o \equiv h_s B/k = 1.2\mathrm{Re}_e^{0.58}(X_n/B)^{-0.62}; \quad \mathrm{Re}_e = \rho V_e B/\mu \qquad (1)$$

where h_s is based on the $(T_{amb} - T_w)$ temperature difference, X_n is the distance from the jet nozzle of width B, V_e is the uniform nozzle exit velocity, and μ and k are the gas viscosity and thermal conductivity, respectively.

It is conjectured that for limiting large X_n/B (i.e, a fully developed jet, relatively far downstream from the jet source), h_s should depend explicitly on the length X, the distance from

Nomenclature

B = nozzle width
b = length of a free jet
C_p = specific heat at constant pressure
f = function in equation (16)
g = acceleration of gravity
H = ceiling-to-fire distance
H'_{cj} = ceiling jet enthalpy flow per unit width, equation (18)
$H'_{cj(max)}$, $H'_{cj(min)}$ = max, min possible values of H'_{cj}
h = heat transfer coefficient, equation (4)
$\mathbf{h}$ = characteristic heat transfer coefficient, equation (15)
h_s, h_{ceiling} = h at wall stagnation, ceiling
I = an integral, equation (25)
k = thermal conductivity
M'_{cj} = ceiling jet momentum flow per unit width, equation (7)
M'_o = half of free plane jet momentum flow per unit width
$M'_{o,eq}$ = value of equivalent $M'_o = M'_{cj}(r = r_j)$, equation (14)
m'_{cj} = ceiling jet mass flow per unit width, equation (8)
m'_o = half of free plane jet mass flow rate per unit width, equation (12)
Nu_o, Nu_s = Nusselt numbers, equations (3)
Pr = Prandtl number
Q = fire's energy release rate
Q_{loss} = rate of heat loss to ceiling, equation (20)
Q^* = dimensionless Q, equation (6)
q, q_{ceiling}, q_s = convective heat transfer rate to wall, ceiling, near wall stagnation
Re_e, Re_s, Re_H = Reynolds numbers, equations (1), (3), and (15)
Ri, $\mathrm{Ri}_{\max}$ = Richardson number, equation (27), maximum possible Ri
r, r_j = distance from plume–ceiling impingement point, r at ceiling–wall junction
T = temperature in ceiling jet
T_{ch} = characteristic T, equation (26)
T_{ceiling} = T at ceiling surface
T_{up}, T_{amb}, T_w, T_{ad} = upper layer, ambient, wall, and adiabatic temperatures
V, V_{max} = plane- or ceiling-jet velocity, maximum of V
V_e = nozzle exit velocity
$\mathbf{V}$ = characteristic velocity, equation (6)
X = distance from free jet's virtual origin, equation (2)
X_{eq} = X for half plane jet, which is equivalent to ceiling jet at $r = r_j$, equation (13)
X_n = distance from nozzle
Z = distance below ceiling
α, β = constants, equations (11)
ΔT_{ch} = equation (26)
δ = Z below ceiling where $V/V_{\max} = 1/2$
η = argument of I in equation (25)
λ_r = fraction of Q radiated from combustion zone
μ = viscosity
ρ = density

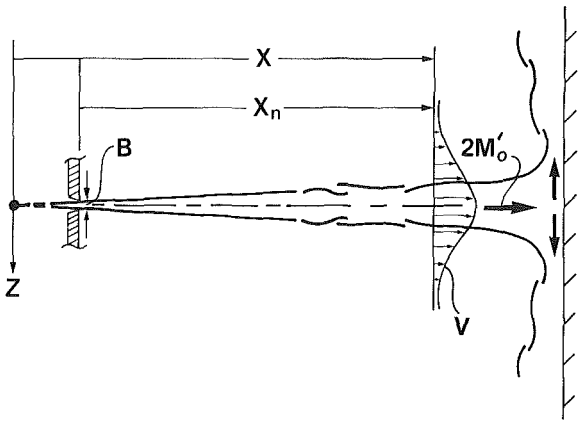

Fig. 3 Plane jet-wall impingement

the virtual origin of the jet, and not on X_n or B. Based on this conjecture, the Fig. 4 data were re-analyzed here. In this, X was taken to be

$$X = X_n + 1.95B \tag{2}$$

This is based on a review of the literature by Abramovich (1963).

The analysis leads to the following new correlation of the Gardon and Akfirat (1966) data:

$$\lim_{X/B\to\infty} \mathrm{Nu}_s = 1.74\mathrm{Re}_s^{0.58} \tag{3}$$

$$\mathrm{Nu}_s = h_s X/k = (X/B)\mathrm{Nu}_o;$$

$$\mathrm{Re}_s = (2M_o'\rho X)^{1/2}/\mu = (X/B)^{1/2}\mathrm{Re}_e$$

where $2M_o'$ is the conserved momentum flux per unit width of the jet (e.g., $2M_o' = \rho B V_e^2$). Results from the equation (3) correlation are plotted in Fig. 4 along with the original data of Gardon and Akfirat (1966). For $\mathrm{Re}_e \geq 2750$ and $X_n/B \geq 15$, equation (3) estimates all h_s data in the figure to within approximately 5 percent.

It is of interest here to extend the results of Gardon and Akfirat (1966) in order to estimate heat-transfer rates q from elevated-temperature jets to nonuniform-temperature walls. In a manner analogous to analyses by Cooper (1982a, 1982b, 1987a), Cooper and Woodhouse (1986), Veldman et al. (1975), and Zukoski and Kubota (1975), the adiabatic wall temperature T_{ad} is introduced as a characteristic temperature and it is assumed that an estimate for q can be obtained from

$$q = h(T_{ad} - T_w) \tag{4}$$

where T_w would generally vary with position from the stagnation point. Here, T_{ad} is the temperature distribution adjacent to an adiabatic wall, on which a plane jet from an elevated-temperature source is impinging. $T_{ad} = T_{amb}$ in the work of Gardon and Akfirat (1966) and for this reason the assumed formulation of equation (4) is equivalent to the assumption that its h is identical to their h. This is of particular interest here near the stagnation point where $h = h_s$.

Ceiling-Jet Properties Upstream of Jet-Wall Impingement

The purpose of this section is to develop estimates for ceiling-jet properties immediately upstream of the ceiling-wall line of intersection of Fig. 1, where the radius vector r_j is normal to the wall. These estimates will be used to obtain the desired heat transfer.

Alpert (1975) has shown that for small-to-moderate values of r/H, inertial forces are generally large compared to buoyancy forces (i.e., characteristic Richardson numbers, Ri, are small) in buoyant-plume-driven ceiling jets. This fact was used by Cooper (1982a) to argue that the flow and heat transfer characteristics of the buoyant-plume-driven ceiling jets depicted in Figs. 1 and 2 could be directly related to the analogous characteristics of wall or ceiling jets driven by heated or unheated free turbulent jets (i.e., flows with the same configurations of Fig. 1, but with a turbulent jet replacing the fire and its buoyant plume). Presumably, a ceiling jet driven by a plume would have approximately identical flow properties as that driven by an equivalent free jet, at least up to r/H (in the case of a plume) of the order of 1. The criterion of equivalence proposed by Cooper (1982a) was that the mass and momentum of the plume and of the free jet be identical at their respective points of impingement. Applying this criterion, it has been possible to recorrelate results from the literature on free-jet-driven wall flows, to use them with results from buoyant-plume-driven ceiling-jet experiments, and to obtain estimates for ceiling-jet flow and heat transfer characteristics of interest in compartment fires (Cooper, 1982a, 1982b, 1987a; Cooper and Woodhouse, 1986).

Applying the analogy between free-jet-driven wall flows and buoyant-plume-driven ceiling jets, the wall-flow results of Bakke (1957), Glauert (1956), and Poreh (1957) can be used to deduce that outside of a plume/ceiling impingement stagnation zone, defined approximately by $r/H < 0.2$, the radial velocity distribution $V(Z)$ is essentially self-similar and rises very rapidly from zero at the ceiling to a maximum V_{max} at a distance $Z = 0.23\delta$, δ being the distance below the ceiling where $V/V_{max} = 1/2$. Further, a detailed estimate for the velocity distribution of free-jet-driven wall jets can be used directly to predict the analogous velocity distribution of the plume-driven ceiling jet

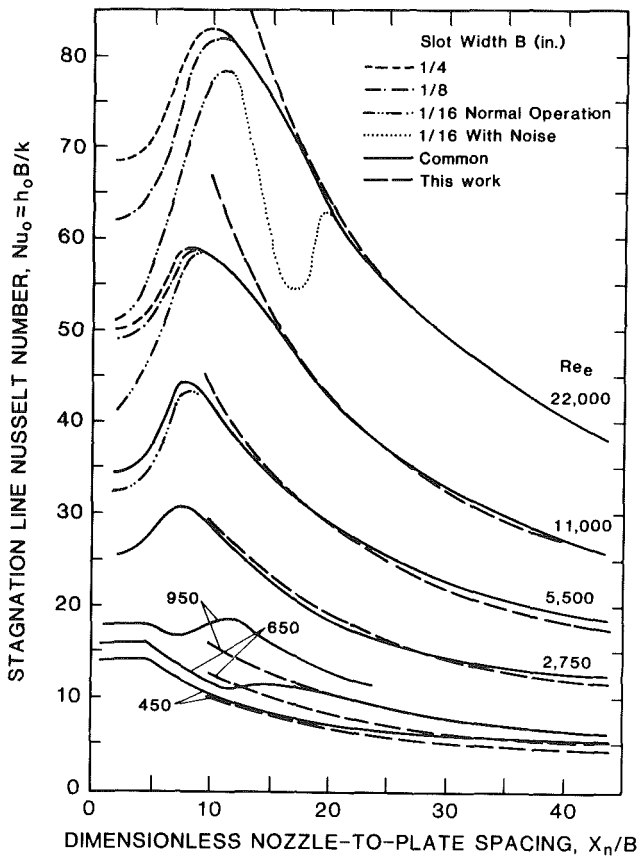

Fig. 4 Plot of stagnation-line Nusselt number from Fig. 2 of Gardon and Akfirat (1966) and from equation (3) of this work

$$V/V_{max} = \begin{cases} (8/7)[Z/(0.23\delta)]^{1/7}\{1-[Z/(0.23\delta)]/8\}, \\ \qquad 0 \le Z/(0.23\delta) \le 1 \\ \cosh^{-2}\{(0.23/0.77)\text{arccosh}(2^{1/2})[Z/(0.23\delta)-1]\}, \\ \qquad 1 \le Z/(0.23\delta) \end{cases} \tag{5}$$

The above result for the outer portion of the jet, $1 \le Z(0.23\delta)$, is obtained from Glauert (1956), and the inner-jet velocity distribution is chosen simply to satisfy $V \sim Z^{1/7}$ at $Z=0$ and $dV/dZ=0$ at $V=V_{max}$.

In equation (5), V_{max} and δ can be estimated from

$$V_{max}/\mathbf{V} = 0.85(r/H)^{-1.1}; \quad \delta/H = 0.10(r/H)^{0.9}$$
$$\mathbf{V} = g^{1/2}H^{1/2}Q^{*1/3}; \qquad Q^* = (1-\lambda_r)Q/(\rho C_p T_{amb} g^{1/2} H^{5/2}) \tag{6}$$

In equation (6), the result for V_{max} is from Cooper (1982b). The result for δ was derived using the δ wall-jet correlation of Poreh et al. (1957) and the free-jet/buoyant-plume equivalence criterion (between the plume length, H, and the free-jet length, b), as presented in equation (A6) of Cooper (1982b). Finally, g is the acceleration of gravity, C_p is the specific heat, and λ_r is the fraction of Q radiated from the fire's combustion zone.

Cooper (1987b) has shown that the estimate of equation (5) compares favorably with ceiling-jet velocity data of Alpert (1971).

In the next section the integrated mass and momentum flow per unit width of the ceiling jet, m'_{cj} and M'_{cj}, respectively, will be required. These are defined and obtained with the use of equations (5) and (6)

$$M'_{cj} \equiv \rho V_{max}^2 \delta \int_0^\infty (V/V_{max})^2 d(Z/\delta) = 0.59\rho H \mathbf{V}^2 (r/H)^{-1.3} \tag{7}$$

$$m'_{cj} \equiv \rho V_{max} \delta \int_0^\infty (V/V_{max}) d(Z/\delta) = 0.093\rho H \mathbf{V} (r/H)^{-0.2} \tag{8}$$

Equivalence Between the Half-Plane Jet and the Ceiling Jet at the Line of Wall Impingement

For the purpose of estimating the desired wall heat transfer, a new analogy is now drawn between the properties of the radially symmetric ceiling jet (Fig. 1), and half of a plane free jet (Fig. 3), immediately upstream of their respective impingement with a wall surface. Upstream of the plane-jet-turning region at the wall, which has the jet thickness as its characteristic dimension, it is noted that the two profiles are similar in shape except for a relatively thin near-surface layer where the ceiling-jet flow velocity goes from zero to its maximum value V_{max}. While the no-slip condition at the ceiling will lead to ceiling-jet stagnation corner flows that are significantly different from the flows in the immediate vicinity of plane-jet/wall impingement, it is speculated that these corner flows will likely be confined to a relatively small region with characteristic dimension 0.23δ. As can be seen in equation (5), the latter dimension is the thickness of the inner, near-surface layer of the ceiling jet. With regard to wall heat transfer, it is reasonable to expect that these corner flows will have an effect primarily on a similar-size uppermost segment of the wall. Stagnation heat transfer results to be developed here are expected to be valid for the upper part of the wall, which excludes such segments.

In the sense that they are expected to yield approximately identical stagnation wall heat transfer, it is assumed that a ceiling jet and half of a plane free jet are equivalent immediately upstream of their respective lines of wall impingement if their mass and momentum flow rates there are identical. To invoke this equivalence criterion and use the heat transfer estimate of equation (3), a representation for the mass flow rate per unit width of half of a plane free jet, m'_o, is required in addition to the equation (7) and (8) results for m'_{cj} and M'_{cj}.

Van der Hegge Zijnen (1958) proposes the following expression for the plane jet velocity distribution:

$$V/V_{max} = \exp[-\alpha(Z/X)^2]; \qquad V_{max} = \beta[2M'_o/(\rho X)]^{1/2} \tag{9}$$

where it can be shown that conservation of momentum along the X axis requires

$$\beta^2 = (2\alpha/\pi)^{1/2} \tag{10}$$

Taking α in equation (9) to be the average of the two values, 75.0 and 70.7, found for the two experiments of Van der Hegge Zijnen (1958), and using this in equation (10) leads to

$$\alpha = 72.8; \quad \beta = 2.61 \tag{11}$$

where the above value of β compares favorably with values of β that are consistent with three other plane-jet models reviewed by Abramovich (1963), i.e., $\beta = 2.56$, 2.45, and 2.83. Equations (9) and (11) are used to obtain

$$m'_o \equiv \rho V_{max} X \int_0^\infty (V/V_{max}) d(Z/X) = (M'_o \rho X)^{1/2}/\beta = 0.383(M'_o \rho X)^{1/2} \tag{12}$$

The equivalence criterion is now invoked by equating m'_o of equation (12) and $m'_{cj}(r=r_j)$ of equation (8) and then substituting M'_o with $M'_{cj}(r=r_j)$ of equation (7). This leads to the following values, X_{eq} and $M'_{o,eq}$, for X and M'_o, respectively, of a half-plane jet, which is equivalent to the ceiling jet at $r=r_j$

$$X_{eq}/H = 1.0(r_j/H)^{0.9} \tag{13}$$

$$M'_{o,eq} = M'_{cj}(r=r_j) = 0.59\rho H \mathbf{V}^2 (r_j/H)^{-1.3} \tag{14}$$

Stagnation-Point Heat Transfer

Substituting X_{eq} and $M'_{o,eq}$ of equations (13) and (14) for X and M'_o, respectively, in equation (3) yields the following relationship for h_s in terms of compartment-fire parameters

$$h_s/\mathbf{h} = 0.94 \mathrm{Re}_{\bar{H}}^{0.42} \mathrm{Pr}^{-1} (r_j/H)^{-1.0}$$
$$\mathbf{h} = \rho C_p g^{1/2} H^{1/2} Q^{*1/3}; \qquad \mathrm{Re}_H = \rho g^{1/2} H^{3/2} Q^{*1/3}/\mu \tag{15}$$

where $\mathbf{h}$ and Re_H are a normalizing heat transfer coefficient and the characteristic impingement-point Reynolds number, respectively, and where Pr is the Prandtl number.

To use equation (15) in equation (4) requires T_{ad}. This would be identical to $T_{ad}(r=r_j)$ for the ceiling jet, predicted by Cooper and Woodhouse (1986) to be

$$\frac{[T_{ad}(r/H) - T_{amb}]}{T_{amb} Q^{*2/3}} = f(r/H) = \begin{cases} 10.22 - 14.9(r/H), & 0 \le r/H \le 0.2; \\ \dfrac{8.39[1 - 1.10(r/H)^{0.8} + 0.808(r/H)^{1.6}]}{[1 - 1.10(r/H)^{0.8} + 2.20(r/H)^{1.6} + 0.690(r/H)^{2.4}]}, & r/H > 0.2 \end{cases} \tag{16}$$

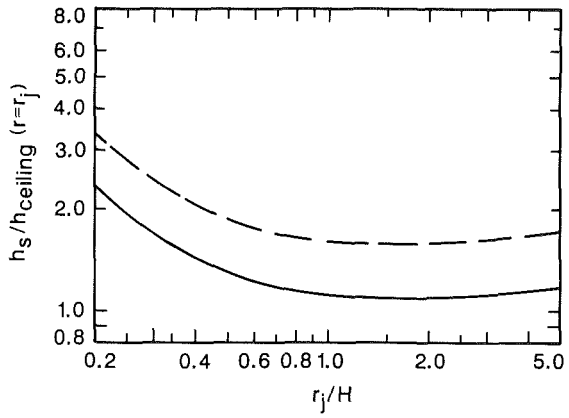

Fig. 5 Stagnation point heat transfer amplification from equation (9): —— typical full-scale; ··· reduced-scale

Considering times of identical wall and ceiling temperatures near the ceiling–wall junction, it is of interest to compare $q = q_s$, the heat transfer rate to the wall near the line of impingement, to $q_{ceiling}$, the heat transfer rate to the ceiling immediately upstream of impingement. This would provide insight into the characteristic level of heat transfer enhancement due to stagnation-line flow conditions. Taking Pr = 0.7, and using equation (4) for both wall and ceiling, equation (6) of Cooper and Woodhouse (1986) for $h_{ceiling}$, and equation (15), leads to

$$q_s/q_{ceiling}(r=r_j) = h_s/h_{ceiling}(r=r_j) = 3.5\mathrm{Re}_{\bar{H}}^{0.12}(r_j/H)^{0.2}(r_j/H+0.279)/(r_j/H-0.0771); \quad r_j/H \geq 0.2 \tag{17}$$

for a radial, plume-driven ceiling jet impinging normally on a vertical wall. In equation (17), $h_{ceiling}$ is the ceiling heat transfer coefficient.

Typical full-scale compartment fires with $(1-\lambda_r)Q$ in the range 200–2000 kW and H in the range 2–3 m are in the Re_H range $2(10^5)$–$5(10^5)$, i.e., $\mathrm{Re}_{\bar{H}}^{0.12} \approx 0.2$. The reduced-scale fires of Veldman et al. (1975), Zukoski and Kubota (1975), and You and Faeth (1979) [$Q = O(1\text{ kW})$, $H = O(1\text{ m})$] were in the Re_H range $7(10^3)$–$2(10^4)$, i.e., $\mathrm{Re}_{\bar{H}}^{0.12} \approx 0.3$. For identical r_j/H, equation (17) therefore predicts that the magnitude of heat transfer amplification near the stagnation point is approximately 1.5 greater in the reduced-scale compartment fires than in a typical full-scale compartment fire.

Results of equation (17) are plotted in Fig. 5 for the two classes of fire. These predict that in typical full-scale fires significant heat transfer amplification in the range $1.1 \leq q_s/q_{ceiling}\ (r=r_j) \leq 2.3$ will only occur in the limited range $r_j/H \leq 1.0$. For the reduced-scale fires, amplification in the range $1.4 \leq q_s/q_{ceiling}(r=r_j) \leq 3.2$ will always occur in the small-to-moderate r_j/H range for which the present estimates are valid. In Fig. 5, the prediction of locations of minimum amplification, and the actual r_j/H values of these locations, are not significant. The existence of these points of minimum amplification, i.e., minimum $h_s/h_{ceiling}$, is a result of the different predicted variations of h_s and $h_{ceiling}$, both of which decrease monotonically with increasing r_j/H.

Comparison With Experimental Data

An experiment was carried out by Mulholland (1986) with a convective buoyant plume of strength $Q = 0.117$ kW whose source was centrally located $H = 1.22$ m below the ceiling of a tightly sealed, rectangular-plan enclosure (2.13 m × 2.44 m) with controlled leakage from below. For the experiment, $Q^* = 0.657\ (10^{-4})$ and $\mathrm{Re}_H = 0.123\ (10^5)$. Data acquired included time-temperature measurements of the insulated, $0.79(10^{-3})$-m-thick, galvanized steel walls and ceiling on a line from the plume-impingement point and normal to the $r_j = 1.22$ m ceiling–wall junction. Data near this junction led to the estimated experimental fluxes $q_s = 8.\ \mathrm{W/m^2}$, $q_{ceiling}(r=r_j) = 4.\ \mathrm{W/m^2}$. This is to be compared to the equations (15)–(17) theoretical estimates $q_s = 5.57\ \mathrm{W/m^2}$ and $q_{ceiling}(r=r_j) = 3.34\ \mathrm{W/m^2}$, respectively. It is evident that more data, especially from buoyant sources with stronger Q^* and Re_H, are required to validate the utility of equations (15)–(17).

The Enthalpy Flow Rate in the Ceiling Jet

A determination of M'_{cj} and m'_{cj} per equations (7) and (8) was key to an estimate of the ceiling-jet stagnation heat transfer. They will also be useful for future reference in characterizing the initial properties of the ceiling-jet-driven wall flows of Fig. 1, e.g., for use in applying the results of Goldman and Jaluria (1986) as in Cooper (1989). The ceiling-jet enthalpy flow rate per unit width or circumference, H'_{cj}, would also be useful in this regard. This is defined by

$$H'_{cj} = \rho C_p T_{amb} V_{max}\delta \cdot \int_0^\infty (V/V_{max})\,(T/T_{amb}-1)d(Z/\delta) \tag{18}$$

where T is the temperature distribution in the ceiling jet, and where V, V_{max}, and δ can be estimated from equations (5) and (6).

Beside depending on $\lambda_r Q$, the T distribution on which H'_{cj} is dependent will vary during the course of a given fire according to the heat transfer losses from the ceiling jet between $r = 0$ and $r = r_j$. This can be estimated with use of

$$q_{ceiling} = h_{ceiling}\ (T_{ad} - T_{ceiling}) \tag{19}$$

where $T_{ceiling}$ is the local ceiling surface temperature, and where $h_{ceiling}$ and T_{ad} can be estimated from equation (6) of Cooper and Woodhouse (1986) and from the present equation (16), respectively. Assuming the ceiling jet to be thin enough and/or the jet gases to be transparent enough as to not play a significant role in radiative transfer, bounds for H'_{cj} are easy to estimate. Thus, from $r = 0$ to r_j the total rate of heat transfer from the ceiling jet Q_{loss}, and then H'_{cj}, can be obtained from

$$Q_{loss} = 2\pi \int_0^{r_j} q_{ceiling} r dr \tag{20}$$

$$H'_{cj} = [(1-\lambda_r)Q - Q_{loss}]/(2\pi r_j) \tag{21}$$

The maximum possible value for H'_{cj}, $H'_{cj(max)}$, would be for ceilings that behaved in an approximately adiabatic manner, i.e., negligible conduction into the surface, with limiting low effective surface emissivity, and, therefore, with $T_{ceiling} \approx T_{ad}$. Under such conditions all enthalpy convected from the fire's combustion zone would reach the $r = r_j$ wall location with $Q_{loss} = 0$, and

$$H'_{cj(max)} = (1-\lambda_r)Q/(2\pi r_j) \tag{22}$$

The minimum value for H'_{cj}, $H'_{cj(min)}$, would be for a ceiling that, from the initiation of the fire, had not yet been heated to temperatures significantly above its initial T_{amb} temperature. Under such circumstances, Q_{loss} can be estimated from equations (19) and (20). The result of the indicated integration leads to

$$H'_{cj(min)} = H'_{cj(max)}\{1 - Q_{loss}/[(1-\lambda_r)Q]\} \tag{23}$$

where, for the applicable r_j/H range of interest

$$Q_{loss}/[(1-\lambda_r)Q] = 2\pi[0.513\mathrm{Re}_{\bar{H}}^{1/2}\mathrm{Pr}^{-2/3} + \mathrm{Re}_{\bar{H}}^{0.3}\mathrm{Pr}^{-2/3}I(r_j/H)]; \quad 0.2 < r_j/H \tag{24}$$

$$I(\eta) = 0.0533 + \int_{0.2}^{\eta}[(\xi - 0.0771)/(\xi + 0.279)][f(\xi)/\xi^{0.2}]d\xi \tag{25}$$

and f is given in equation (16). $I(\eta)$ has been computed, and

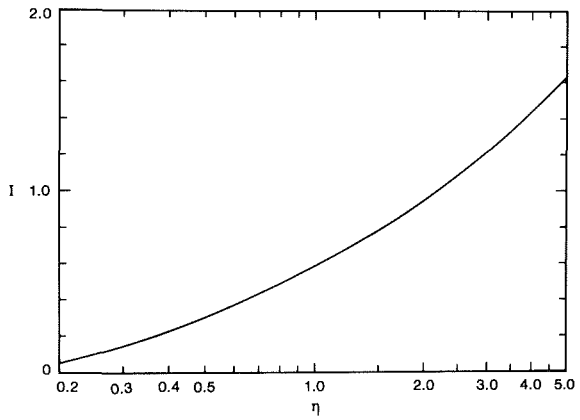

Fig. 6 Plot of the integral I defined in equation (25)

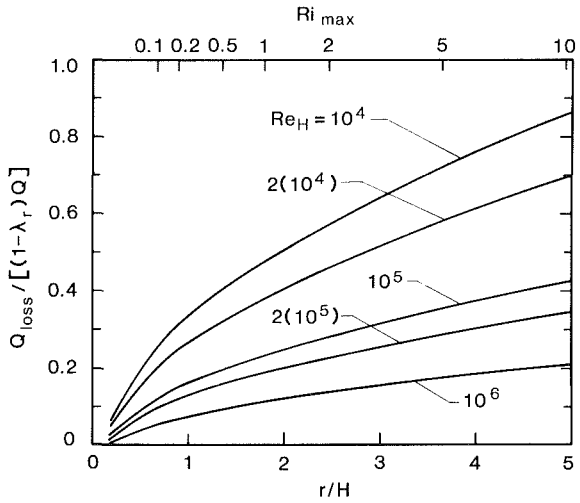

Fig. 7 Plot of $Q_{loss}/[(1-\lambda_r)Q]$ per equations (24) and (29)

is plotted in Fig. 6. Also, taking Pr = 0.7, $Q_{loss}/[(1-\lambda_r)Q]$ is plotted in Fig. 7 for different values of Re_H. As can be seen, this figure indicates that out to any particular r_j/H the relative rate of integrated ceiling heat transfer is significantly larger in reduced-scale fires than in typical full-scale fires. This result, as well as the result of equation (15) for h_s, highlights the important effect of Reynolds number on convective heat transfer in compartment fires.

An Estimate of the Range of Utility of the Results

The results developed here are based on the analogy drawn between free-jet and buoyant-plume-driven ceiling flows. While the analogy is strong for ceiling-jet flow locations where Ri, the ratio of buoyancy-to-inertial forces, is small, the analogy and corresponding results are unreliable for moderate-to-large Ri. Such regions of unreliability can be established from an estimate of $\mathrm{Ri}(r_j/H)$. Ri can be defined and obtained with the use of a characteristic temperature T_{ch} of the ceiling jet. This is taken here to be

$$\Delta T_{ch} = T_{ch} - T_{amb} = H'_{cj}/(C_p m'_{cj}) \tag{26}$$

and Ri is defined as

$$\mathrm{Ri} = g(\Delta T_{ch}/T_{amb})\delta/V^2_{max} \tag{27}$$

Using equations (6), (8), (21), (24), and (26) in equation (27) leads to

$$\mathrm{Ri} = \mathrm{Ri}_{max}\{1 - Q_{loss}/[(1-\lambda_r)Q]\} \tag{28}$$

$$\mathrm{Ri}_{max} = 1.5(r_j/H)^{2.3}/(2\pi) \tag{29}$$

where Ri_{max} is the maximum possible value for Ri, corresponding to the adiabatic ceiling, i.e., $Q_{loss} = 0$.

The upper abscissa of Fig. 7 is given as Ri_{max}. Based on the above observations it is therefore evident from this figure that in the approximate range r_j/H of 2.–5. and larger, corresponding to Ri_{max} of 2.–10. and larger, the reliability of the Q_{loss} results, and, indeed, of all the results of this work must be brought into equation on theoretical grounds. Finally, even for smaller r_j/H, experimental validation is required before the results presented here can be applied with confidence.

References

Abramovich, G. N., 1963, *The Theory of Turbulent Jets*, MIT Press, Cambridge, MA, p. 75.

Alpert, R. L., 1971, "Fire Induced Turbulent Jet," Report No.19722-2, Factory Mutual Research Corporation, Norwood, MA.

Alpert, R. L., 1975, "Turbulent Ceiling-Jet Induced by Large-Scale Fires," *Combustion Science and Technology*, Vol. 11, pp. 197–213.

Bakke, P., 1957, "An Experimental Investigation of a Wall Jet," *Journal of Fluid Mechanics*, Vol. 2, pp. 467–471.

Cooper, L. Y., 1982a, "Convective Heat Transfer to Ceilings Above Enclosure Fires," *19th International Symposium on Combustion*, Combustion Institute, Pittsburgh, PA, pp. 933–939.

Cooper, L. Y., 1982b, "Heat Transfer From a Buoyant Plume to an Unconfined Ceiling," ASME JOURNAL OF HEAT TRANSFER, Vol. 104, pp. 446–451.

Cooper, L. Y., 1987a, "Thermal Response of Unconfined Ceilings Above Growing Fires and the Importance of Convective Heat Transfer," ASME JOURNAL OF HEAT TRANSFER, Vol. 109, pp. 172–178.

Cooper, L. Y., 1989, "Ceiling Jet-Driven Wall Flows in Compartment Fires," *Combustion Science and Technology*, Vol. 62, pp. 285–296.

Cooper, L. Y., Harkleroad, M., Quintiere, J., and Rinkinen, W., 1982, "An Experimental Study of Upper Hot Layer Stratification in Full-Scale Multiroom Fire Scenarios," ASME JOURNAL OF HEAT TRANSFER, Vol. 104, pp. 741–749.

Cooper, L. Y., and Woodhouse, A., 1986, "The Buoyant Plume-Driven Adiabatic Ceiling Temperature Revisited," ASME JOURNAL OF HEAT TRANSFER, Vol. 108, pp. 822–826.

Gardon, R., and Akfirat, J. C., 1966, "Heat Transfer Characteristics of Impinging Two-Dimensional Air Jets," ASME JOURNAL OF HEAT TRANSFER, pp. 101–108.

Glauert, M. B., 1956, "The Wall Jet," *Journal of Fluid Mechanics*, Vol. 1, pp. 625–643.

Goldman, D., and Jaluria, Y., 1986, "An Experimental Study of Negatively Buoyant Flows Generated in Enclosure Fires," *Journal of Fluid Mechanics*, Vol. 166, pp. 41–56.

Mulholland, G., 1986, Private Communication, US National Bureau of Standards, Gaithersburg, MD.

Poreh, M., Tsuei, Y. G., and Cermak, J. E., 1957, "Investigation of a Turbulent Radial Wall Jet," ASME *Journal of Applied Mechanics*, pp. 457–463.

Van der Hegge Zijnen, B. G., 1958, "Measurements of the Velocity Distribution in a Plane Turbulent Jet of Air," *Applied Science Research*, Sec. A, Vol. 7, pp. 256–276.

Veldman, C. C., Kubota, T., and Zukoski, E. E., 1975, "An Experimental Investigation of the Heat Transfer From a Buoyant Gas Plume to a Horizontal Ceiling—Part 1. Unobstructed Ceiling," California Institute of Technology, NBS-GCR-77-97, US National Bureau of Standards, Gaithersburg, MD.

You, H.-Z., and Faeth, G. M., 1979, "Ceiling Heat Transfer During Fire Plume and Ceiling Impingement," *Fire and Materials*, Vol. 103, pp. 140–147.

Zukoski, E. E., and Kubota, T., 1975, "An Experimental Investigation of the Heat Transfer From a Buoyant Gas Plume to a Horizontal Ceiling—Part 2. Effects of Ceiling Layer," California Institute of Technology, NBS-GCR-77-98, US National Bureau of Standards, Gaithersburg, MD.

S. P. Venkateshan
Consultant.

P. Shakkottai
Member of Technical Staff.

E. Y. Kwack
Member of Technical Staff.
Assoc. Mem. ASME

L. H. Back
Group Supervisor.
Fellow ASME

Jet Propulsion Laboratory,
California Institute of Technology,
Pasadena, CA 91109

Acoustic Temperature Profile Measurement Technique for Large Combustion Chambers

Measurement of times of flight of sound waves can be used to determine temperatures in a gas. This paper describes a system, based on this principle, that is capable of giving the temperature profile in a nonisothermal gas volume, for example, prevalent in a large furnace. The apparatus is simple, rugged, accurate, and capable of being automated for process control applications. It is basically an acoustic waveguide where the outside temperature profile is transferred to a chosen gas contained inside the guide.

Introduction

There exists a need for developing sensors for temperature measurement for industrial applications, especially for temperature profiling in a hostile environment. An example of such an application is that of a lime kiln in the paper industry. The requirements of the sensor for this application are: (*i*) The sensor should measure temperatures varying from room temperature to 1000°C (1800°F); (*ii*) the sensor should survive the hostile environment.

In view of the above requirements, commonly employed thermocouple sensors are ruled out since they do not survive well in a hostile chemical environment, and also since long lead wires with proper insulation capable of withstanding high temperatures are needed. Thermocouple failure is fairly common and replacement is difficult and expensive in terms of down time. Often they are not replaced after failure. Radiation pyrometers have the disadvantage that they are incapable of providing information on temperature variations within their field of view. Pyrometers are restricted to the measurement of an average temperature.

We have developed an acoustic temperature profile measurement system (ATPMS) that is capable of meeting the requirements mentioned above (Shakkottai and Venkateshan, 1988). In addition, ATPMS is capable of automatic operation and hence can be used as a control element in process control applications. It is semi-intrusive, does not involve any moving parts, is simple to install, and is capable of adequate accuracy for the intended applications in lime kilns, recovery furnaces, and other such applications. It functions in any orientation and is insensitive to gently curving paths (over which the temperature profile is needed.)

Basis of the Acoustic Temperature Profile Measuring System (ATPMS)

The ATPMS is based on the fact that the speed of sound in a gas is a unique function of temperature. Even though the relation between the speed of sound and temperature has been known for a long time, and has been suggested as a means of temperature measurement (Mayer, 1873) it is only recently that the method has seen some development (Hedrich and Pardue, 1955; Plumb and Cataland, 1966; Lynnworth and Patch, 1970; Gopalsami and Raptis, 1984; O'Fallon, 1984; Wadley et al., 1986; Green, 1986). Whereas most investigations (Lynnworth and Patch, 1970; Gopalsami and Raptis, 1984; Wadley et al., 1986) dwell on the method as applied to the measurement of temperatures in a soild using the sonic method, Green (1986) deals with the measurement of temperature field in a flowing gas medium using acoustic tomography. O'Fallon (1984) gives a review of the state of the art as applicable to the measurement of temperature in coal gasification systems.

A novel feature of the present method consists in confining relatively low-frequency sound waves (in the audio range) to propagate through a chosen gas contained in a tubular sensor. Because of the low frequencies involved, there are no dispersion effects characteristic of high-frequency sound wave (ultrasound) propagation in gases. In addition, because the range of frequencies used in the sound pulses is such that the wavelengths exceed the diameter of the pipe, only the plane wave mode of propagation occurs. This eliminates dispersion effects associated with the propagation of higher modes because these modes do not propagate but are cut off. Experimental data show that the sound pulses preserve their shape upon reflection from discontinuities in the pipe. The diameter of the sensor tube can range from about 1 to 5 cm in practical situations.

The times of flight (TOF) are relatively long and are in the millisecond range, since the speeds of sound in gases are much slower than those in liquids and solids. The method is very sensitive since the TOF variations are up to 100 percent larger than a base value at room temperature, as opposed to a mere 10–20 percent larger in the case of metallic solids used by Lynnworth and Patch (1970), Gopalsami and Raptis (1984), and Wadley et al. (1986). Also, the speed of sound–temperature relationship is well known and well documented for a large temperature range in the case of gases.

The speed of sound can be accurately determined by the measurement of a distance and the corresponding time of flight (TOF). A schematic of the ATPMS is shown in Fig. 1. The system consists of a sensor tube of desired length, immersed in the gaseous environment whose temperature profile is desired. In the single ended TOF system shown, a transmitter (speaker), which doubles as a receiver (TR/RE), is fitted to one end of the sensor tube. The other end of the sensor tube is closed. The sensor tube contains a gas of known composition. The sensor is arranged to have a required number of reflectors (R_1, R_2, . . . , etc.), which may take the form of diametrically placed rods or may be obstructions of any other type. The

Contributed by the Heat Transfer Division and presented at the ASME Winter Annual Meeting, Boston, Massachusetts, December 13–18, 1987. Manuscript received by the Heat Transfer Division May 1, 1988. Keywords: Furnaces and Combustors, Measurement Techniques.

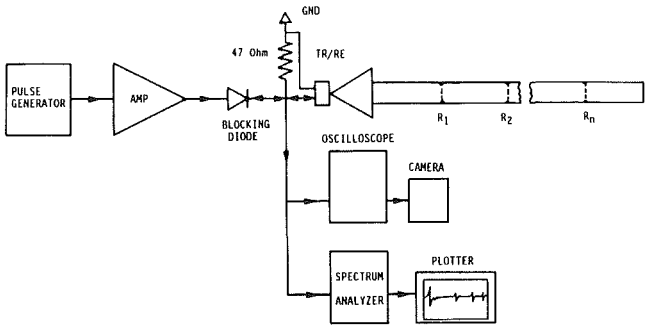

Fig. 1 Schematic of the acoustic temperature profile measuring system. The loudspeaker acts as both the transmitter and receiver of sound pulses. The spectrum analyzer is also a transient signal recorder. The blocking diode prevents reflected pulses from getting shorted out by the output stage of the amplifer.

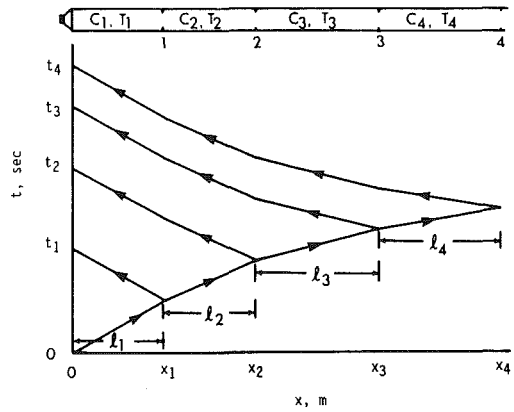

Fig. 2 Sketch of the x–t diagram for the single ended TR/RE acoustic system. Stubs at x_1, x_2, ... reflect sound pulses, which arrive at t_1, t_2, ... at the source $x = 0$. In the figure the temperature and the speed of sound are assumed to increase with x.

TR/RE is driven by a pulse generator through an amplifier. The TR/RE is also connected to either an oscilloscope or a digital waveform analyzer for time measurement.

The blocking diode isolates the amplifier from the return signal (reflected from R_1, R_2, . . . , etc.; Fig 1). A train of pulses from the signal generator results in a train of sound pulses confined to move down the sensor tube. At each one of the constrictions a part of the sound pulse is returned to the TR/RE. These return pulses produce an electrical signal across the TR/RE that is displaced temporally from the main pulse by an amount equal to the time it takes sound to travel twice the distance between the TR/RE and the appropriate reflector. The ratio of this distance to the time of flight gives the average speed of sound over the path.

An x–t diagram appropriate to the situation is shown in Fig. 2. The sensor tube is divided, as shown, into segments, l_1, l_2, . . . , etc. by the reflectors positioned along the tube. Multiple reflections caused by any two internal reflectors are typically 1/100 of the main reflections and are not shown in the figure. Assuming that the speed of sound varies because of the temperature variation along path x, the signals are received (with $t = 0$ corresponding to the transmitted pulse (or main pulse MP) at t_1, t_2, . . . , etc.). Typically, a reflected pulse has 1/10 the intensity of the main pulse. It is easy to see from the x–t plot that the speed of sound c_n in the segment l_n is given by the formula

$$c_n = 2l_n/(t_n - t_{n-1}). \tag{1}$$

The corresponding temperature T_n is deduced from the formula

$$T_n = c_n^2/(\gamma R)\text{K} \tag{2}$$

where γ is the ratio of specific heats and R is the gas constant for the gas contained in the sensor tube. In the case of air, the speed of sound at 0°C (273 K) is 331.3 m/s and hence the temperature can be deduced from the formula

$$T_n = 273\left(\frac{c_n}{331.3}\right)^2 \text{ K}. \tag{3}$$

Experiments

Before describing the ATPMS in its final form, we present below the way the final version evolved during our investigation. As is clear from Section 2, many things were taken for granted in arriving at equations (1) and (3). The basis for some of these assumptions (specifically involving equilibration, heat transfer, etc.) are given in the description of the results later on. Purely electronic and measurements aspects are discussed first.

Characteristics of the Transmitted Pulse Train. In our experiments we tried three different kinds of speakers for the production and detection of sound pulses. These were a 5×15 cm wide dispersion horn, a 9 cm piezo super horn, and a 2 cm hard dome tweeter. The wide dispersion horn had the following specifications: (1)5×15 cm solid state piezo, wide dispersion horn, 30 W continuous power, 75 W music program power, less than 1 percent total harmonic distortion, frequency 2000 to 40,000 Hz.

In the final version of the ATPMS we used the 5×15 cm wide dispersion horn because of its high sensitivity. The largest period between transmitted pulses was 0.123 s, which was due to a limitation of the signal generator that was available. It is clear that all the reflections must be received within this period and hence the round trip path length would be limited to about 40 m (or 135 ft) in room temperature air. Figure 3 shows the transmitted pulse under two vertical magnifications. It is clear that the transmitter is prone to a ringing that lasts about 1.5 msec. This means that no return signal should be received within this period (about 0.5 m round trip path length). This is not a significant limitation for the ATPMS in that a lead length of this magnitude is necessary to locate the TR/RE away from the hot gas region in which the sensor tube is to be located.

Nomenclature

c = speed of sound, m/s
l = length of a segment
R = gas constant
t = time, s
T = temperature, K
x = axial coordinate, m
α = thermal expansion coefficient, K^{-1}
γ = ratio of specific heats
λ = dimensionless thermal expansion coefficient
θ = dimensionless temperature = T_h/T_c
τ = dimensionless time = $\Delta t_c/\Delta t_h$
τ_c = time constant in Fig. 12

Subscripts

c = cold or reference
cor = correction
h = hot
i = initial
n = corresponding to nth segment
u = uncorrected
∞ = ambient or reference condition

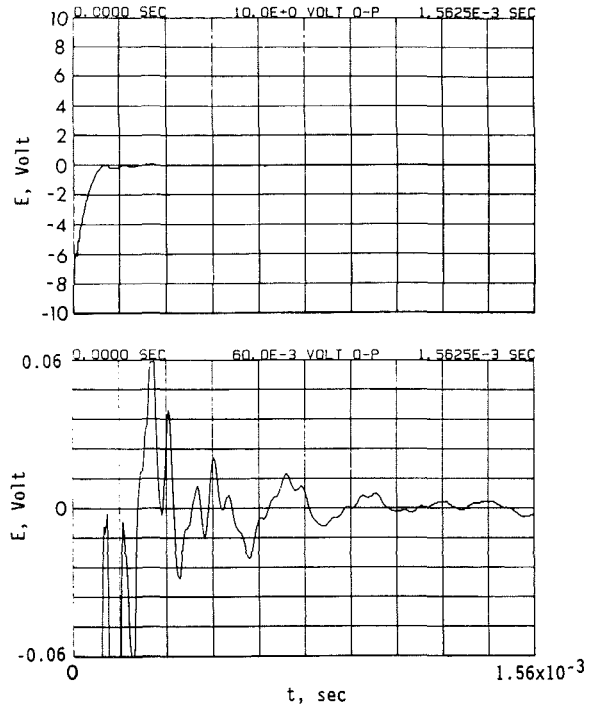

Fig. 3 The transmitted signal shown progressively enlarged in amplitude from 10 V zero to peak to 60 mV zero to peak. The signals are a-c coupled to the spectrum analyzer/wave analyzer. Ringing from 1.5 ms following the input requires the first reflection to occur beyond 1.5 ms. This corresponds to an interval of 26 cm in air.

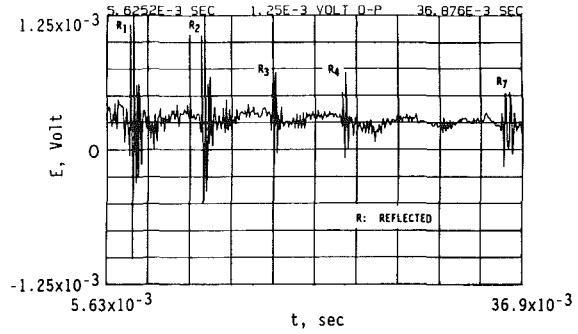

Fig. 4 Seven reflections shown on the Wavetek analyzer during an interval equal to 31.25 ms. The vertical scale is 1.25 mV from zero (middle of plot) to peak.

Time of Flight Signals. The first experiments were done with a sensor comprised of short segments having a small axial mismatch by approximately 1 mm in radius that provided the sound reflections. The sensor was placed on a long optical bench and was about 12 m long (round trip path of ≈ 24 m). For accurate time measurement, a Wavetek Signal Analyzer, capable of time accuracy of one microsecond, was used. The reflected pulses are all shown in Fig. 4. It is clear that the return pulses have a sharp structure and hence are easily separated from the background. The sharp peaks were located and measured by using a digital cursor available in the signal analyzer. The signal shown in Fig. 4 repeats extremely well from one shot to another. The background rumble also repeats in a similar fashion. This coherent noise is due to the reverberation of sound waves running inside the sensor tube. The corresponding TOF versus round trip path length plot of Fig. 5 shows excellent linearity at a measured temperature of 25.5 °C.

Heat Transfer Considerations and Options. Having thus

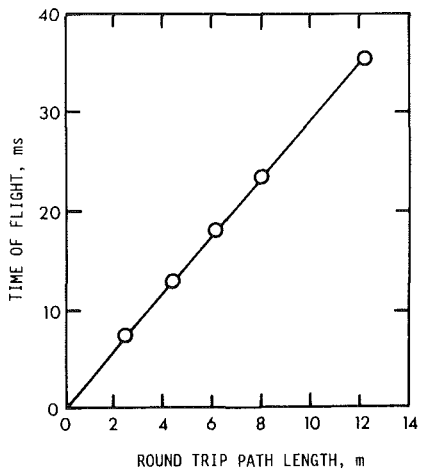

Fig. 5 Plot showing time of flight proportional to round trip path length. The calculated and observed sound speed are identical: sound speed = 346.7 m/s; derived room temperature = 25.5°C (77.9°F); room temperature = 25.55°C (78°F)

ascertained that the method is viable for measurements over relatively large path lengths, we directed our attention to some heat transfer aspects that have a bearing on the design of ATPMS. The basic requirement of the ATPMS is that the sensor be in equilibrium with the surrounding gas and *preserve* the axial variation that would have existed were the sensor absent. This requires that the following conditions be satisfied: (*i*) Heat transfer to the hot gas in the sensor should be radial; (*ii*) axial conduction in the sensor tube wall should be small; (*iii*) convection and axial diffusion in the gas in the sensor tube should be small.

These criteria require the following: (*i*) Heat transfer from the surrounding hot gases to the tube should be relatively large; (*ii*) the sensor tube wall should be relatively thin (commensurate with structural requirements) and have as low a thermal conductivity as possible; (*iii*) the diameter of sensor should be as small as possible so that large-scale convective motions do not occur.

In light of these requirements, various sensor concepts utilizing heat transfer enhancement schemes were considered. With the obvious advantages in using a chosen gas rather than the combustion gases of variable/unknown composition (note that γ will be known accurately for a chosen gas) we chose the so-called noncontact option for further study. Even though some type of heat transfer augmentation can be employed, it was found that the plain tube version was adequate. If it is desired to reduce gas convection and diffusion effects within the sensor, one could use the chosen gas under reduced pressure. Although this would require longer equilibration time and also increase the time constant of the system, it may not be a disadvantage for an industrial application.

Sensor Thermal Test System. With the requirements of both heat transfer and ruggedness, the sensor material was chosen to be stainless steel for the current tests. SS 310 has the following relevant properties: maximum temperature without excessive scaling = 1100°C (2000°F); melting range = 1400–1450°C (2550–2650°F); thermal conductivity is 13 W/mK at 100°C (212°F) and 17.3 W/m K at 500°C (932°F).

For the low-temperature tests, the setup is shown schematically in Fig 6. For the high-temperature tests the outer aluminum tube was replaced by a tubular furnace. The plastic lead tube was approximately 1 m long and the 2.54 cm o.d. stainless steel sensor tube was approximately 3 m long. Brass rods of 6 mm diameter were welded in place diametrically at approximately 25 cm intervals to provide the sound reflection sites. The other aluminum tube was approximately 2.25 m

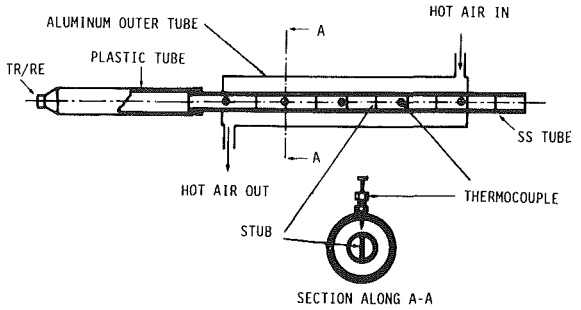

Fig. 6 Schematic view of the test setup for moderate temperature tests using a hot air gun to supply the outer hot gas in the annulus. The stainless steel tube of 2.5 cm o.d. x 1.2 mm wall thickness has the specification MIL-T8808B/8606C. The aluminum duct of 5 cm o.d. x 1.6 mm wall thickness is of specification 6061 T6 WWT 8700 6E.

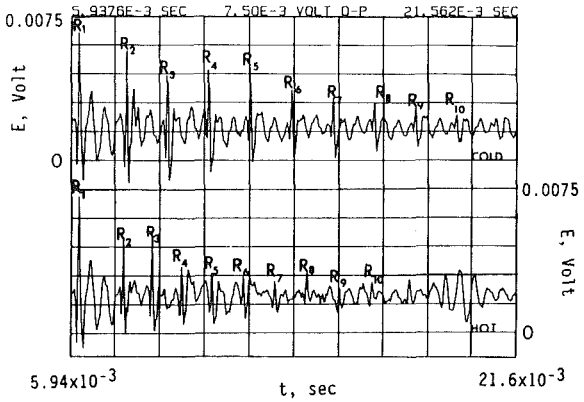

Fig. 7 Comparison of cold and hot time of flight data in the vertical pipe configuration with the hotter end below. Compression of times is clearly seen.

long. A hot air blower with 1250 W rating was used for heating and 5 chromel-alumel thermocouples immersed to a depth of 10 mm in the hot air flowing in the sensor-outer tube annulus were used to measure the air temperature.

Low-Temperature Tests

The low-temperature tests were conducted in both the horizontal and the vertical sensor configurations. In the latter case, the hot end was below and thus free convection effects, if any, would be the largest. Since length measurement using a tape measure was not accurate enough, we always used a calibration TOF experiment with the sensor at room temperature (measured to 0.1°C resolution). From these data all the sensor section l's could be obtained to an accuracy of 0.1 mm. The hot experiment followed the calibration run and used the calibrated l's to determine the temperatures.

In Fig. 7 are shown both the calibration (cold) and the test (hot) signals for the vertical sensor case. The shorter time "compression" of the signals in the hot case is clearly evident. By expanding the time axis, the times can be measured with microsecond resolution. An x–t diagram (Fig. 8) shows the cold and hot data (compare with the idealized diagram Fig. 2). A temperature profile is shown in Fig. 9 for the vertical sensor configuration with the hotter end below. The excellent agreement between the TOF and the thermocouple values is to be noted. Small axial diffusion effects are present but do not penetrate more than about 0.25 m (which is much smaller than the 3–5 m averaging needed in lime kiln applications).

High Temperature Tests

The high-temperature tests used a "Mellen" tubular furnace. In order to reduce the axial heat diffusion through the

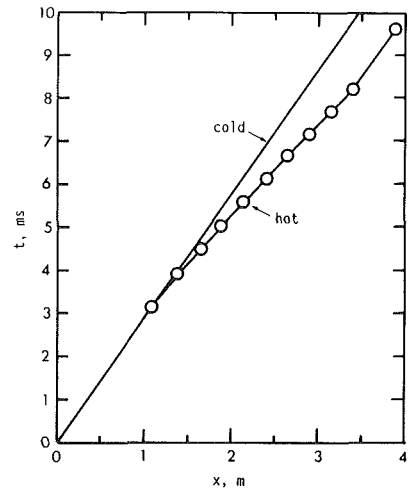

Fig. 8 x–t diagram comparing cold and hot data in the horizontal sensor configuration

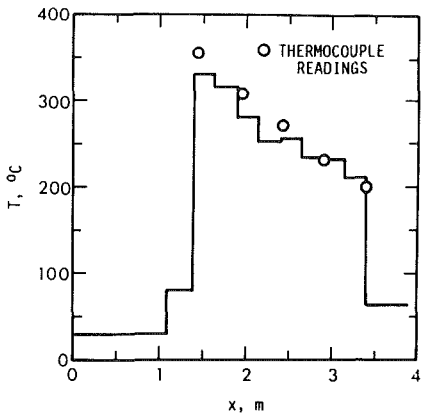

Fig. 9 Comparison of the temperature profile derived from times of flight with data from thermocouples. These data are for the vertical configuration with the hotter end below.

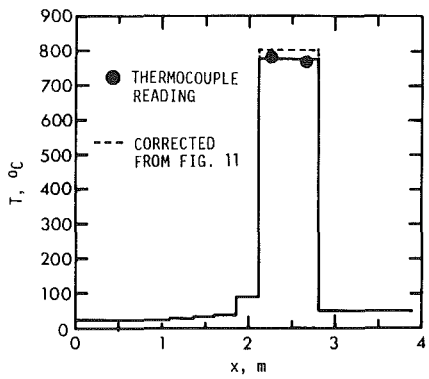

Fig. 10 Temperature profile measured in the tubular furnace for the configuration with insulating inserts compared with two thermocouple readings. The decay of temperature on either side of the hot region is extremely rapid.

sensor wall, the heated region was separated from the rest of the sensor by insulating inserts (machinable Boron Nitride), which also gave rise to the reflected signals. The temperature profile in Fig. 10 is the result from this case. The agreement with the two thermocouple readings and the excellent "edge" to the profile shows that inserts are an excellent idea. Heat transfer from the heated regions to unheated regions by conduction along the tube walls and convection in the air contained in the tube is very small.

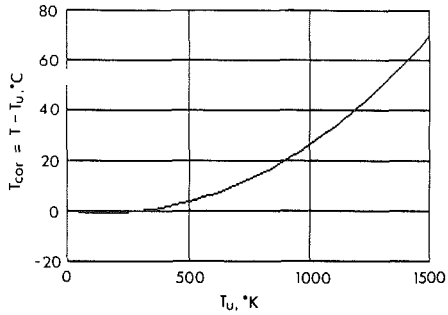

Fig. 11 Temperature correction to account for thermal expansion of stainless steel as a function of uncorrected temperature

Correction for Thermal Expansion. The quantity l_n in equation (1) increases slightly with temperature because of thermal expansion. If the spacing at cold conditions is indicated by l_c for which the time pulses are separated by interval Δt_c, we have

$$c_c = 2l_c/\Delta t_c. \tag{4}$$

Similarly under hot conditions

$$c_h = 2l_h/\Delta t_h. \tag{5}$$

Defining

$$c_h/c_c = (T_h/T_c)^{1/2} = \theta^{1/2}, \tag{6}$$

$$\tau = \Delta t_c/\Delta t_h \tag{7}$$

and

$$l_h/l_c = 1 + \alpha(T_h - T_c) = 1 + \lambda(\theta - 1) \tag{8}$$

where

$$\lambda = \alpha T_c \tag{9}$$

we get from equations (4)–(8)

$$\theta^{1/2} = (1 + \lambda(\theta - 1))\tau. \tag{10}$$

The uncorrected value of θ, corresponding to $\lambda = 0$, is given by

$$\theta_u^{1/2} = \tau. \tag{11}$$

The correction to θ is therefore given by

$$\theta_{cor} = \theta - \theta_u. \tag{12}$$

The correction to the temperature to be added to τ^2 to get the true temperature is shown in Fig. 11. A correction based on this analysis was made for the high-temperature test shown in Fig. 10 and the result is included therein.

Time Constant for the Sensor. The stainless steel tube with reflecting stubs was heated to an initial high temperature T_i by sliding a tubular furnace over it and allowed to come to equilibrium. Then the furnace was slid off, exposing the tube to the ambient. Acoustic temperatures were measured at intervals of one or two minutes. The quantity $\ln\{(T-T_\infty)/(T_i-T_\infty)\}$ was calculated from the measurements by ATPMS and plotted versus time to obtain the rate of change. Experimental data obtained for 10 min are shown in Fig. 12. The ordinate falls to -1 in 8.33 min for the stainless steel sensor tube. For comparison, tests on the same tube with breathing holes (21 holes each of 1.59 mm diameter) show a smaller time constant equal to 7.14 min. In still air, the presence of holes does not make much difference in the time constant. However, in a situation where hot gases are moving with significant velocities, the time constant would be less because of forced convection with or without holes in the tube. Note that a time constant of the order of 10 min is

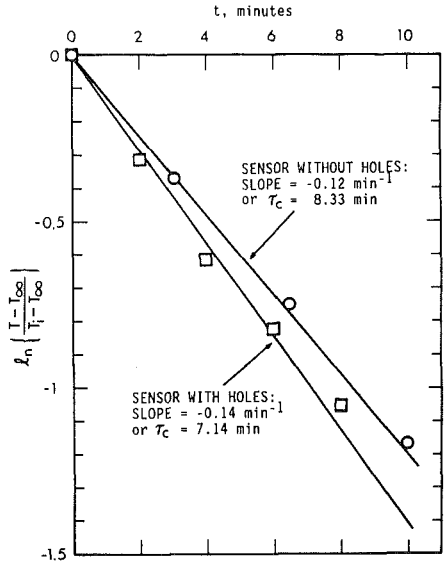

Fig. 12 Logarithmic decrement of temperatures of sensor tubes compared with and without holes

probably adequate for the control of industrial kilns and furnaces.

Accuracy of Sensor. Assuming that the temperature of the gas inside the tube is equal to the temperature of the flowing gas outside, an estimate of accuracy may be made easily. From equations (1) and (3)

$$\Delta T_n/T_n = 2\Delta c_n/c_n = -2\Delta(t_n - t_{n-1})/(t_n - t_{n-1}). \tag{13}$$

Typically, a time difference can be measured to an accuracy of 0.001 ms when the time difference has a typical value equal to 1 ms. If averages over many pulses are taken, the timing accuracy can be easily enhanced to 0.0001 ms. However, for a single shot measurement, the right-hand side of equation (13) may be taken to equal 2×10^{-3}. Therefore ΔT_n is simply equal to $2\times10^{-3}\ T_n$. For $T_n = 1000$ K, $\Delta T_n = 2$ K. Corrections for changes of tube length due to thermal expansion do not change the above estimates significantly.

Summary and Conclusions

The axial temperature profile within a tubular stainless steel sensor containing air is very close to the temperature distribution that prevails outside the tube. Small brass rods welded diametrally inside the tube are satisfactory as reflectors of sound. Pulses of sound generated by a loudspeaker mounted at one end of the tube were received by the same device after reflection from several reflectors, and the time intervals between the pulses were converted to average speeds of sound and hence to the average temperatures in the intervals between reflectors. Temperature profiles obtained by this method compared favorably with thermocouple readings. We believe the acoustic temperatures to be free of errors associated with heat conduction errors, etc., which may be present in thermocouple readings. The acoustic method was tested in both the horizontal and vertical orientations of the tube in the experiments with hot air flow outside the tube where the maximum temperatures were below 400°C. Without forced air flow, tests were also conducted in a tubular furnace up to 800°C. Corrections due to thermal expansion of the tube were also made. Satisfactory performance of the sensor was observed in all cases. The sensor tube was subjected to a hot environment and then allowed to cool down naturally in ambient air to evaluate the time constant, which was found to be approximately 10 min.

We have described an acoustic temperature profile measurement system (ATPMS) that is useful for determining temperature profiles over a wide temperature range and over large lengths. The system is simple, accurate, rugged, and insensitive to orientation. The laboratory tests presented herein have to be followed by field tests to evolve the final system useful in kiln and furnace applications.

Acknowledgments

The work described in this paper was carried out in the Applied Technologies Section of the Jet Propulsion Laboratory, California Institute of Technology, and was supported by the U.S. Department of Energy through an agreement with the National Aeronautics and Space Administration. Mr. Stanley Sobczynski is the program manager in the Industrial Programs division of the U.S. Department of Energy.

References

Gopalsami, N., and Raptis, A. C., 1984, "Acoustic Velocity and Attenuation Measurements in Thin Rods With Applications to Temperature Profiling in Coal Gasification Systems," *IEEE Trans. on Sonics and Ultrasonics*, Vol. SU-31, No. 1, pp. 32–39.

Green, S. F., 1986, "Acoustic Temperature and Velocity Measurements in Combustion Gases," *Proc. Eighth Heat Transfer Conf.*, San Francisco, CA, Vol. 2, pp. 555–560.

Hedrich, A. L., and Pardue, D. R., 1955, "Sound Velocity as a Measurement of Gas Temperature," in: *Temperature: Its Measurement and Control in Science and Industry*, H. C. Wolfe, ed., Vol. 2, Reinhold Publishing Corporation, New York, pp. 383–392.

Lynnworth, L. C., and Patch, D. R., 1970, "New Sensors for Ultrasound: Measuring Temperature Profiles," *Materials Research and Standards*, Vol. 10, pp. 6–11.

Mayer, A. M., 1873, "On an Acoustic Pyrometer," *Philosophical Magazine*, Vol. 45, p. 18.

O'Fallon, N. M., 1984, "Instrumentation and Monitoring," in: *Science and Technology of Coal and Coal Utilization*, B. R. Cooper and W. A. Ellingson, eds., Plenum Press, New York, pp. 633–634.

Plumb, H., and Cataland, G., 1966, "Acoustical Thermometer and the National Bureau of Standards Provisional Temperature Scale 2–20 (1965)," *Int. J. Scientific Metrology*, Vol. 2, No. 4, pp. 127–139.

Shakkottai, P., and Venkateshan, S. P., 1988, "System for Temperature Profile Measurement in Large Furnaces and Kilns and Method Therefor," U.S. Patent No. 4,762,425.

Wadley, H. N. G., Norton, S. J., Mauer, F., and Droney, B., 1986, "Ultrasonic Measurements of Internal Temperature Distribution," *Phil. Trans. R. Soc. London*, London, A320, pp. 341–361.

A. E. Ruggles[1]
Center for Manufacturing Productivity & Technology Transfer.

R. T. Lahey, Jr.
Department of Nuclear Engineering & Engineering Physics.
Fellow ASME

D. A. Drew
Department of Mathematical Sciences.

H. A. Scarton
Department of Mechanical, Aeronautical Engineering & Mechanics.
Mem. ASME

Rensselaer Polytechnic Institute, Troy, NY 12180-3590

The Relationship Between Standing Waves, Pressure Pulse Propagation, and Critical Flow Rate in Two-Phase Mixtures

A two-fluid model is presented that can be used to predict the celerity and attenuation of small-amplitude harmonic disturbances in bubbly two-phase flow. This frequency-dependent relationship is then used to predict the propagation of small-amplitude pressure perturbations through the use of Fourier decomposition techniques. Predictions of both standing waves and propagating pressure perturbations agree well with existing data. The low and high-frequency limits of the celerities predicted by the model are examined and their relationship to critical flow rate is demonstrated. Some limitations of the interfacial pressure model employed in conventional critical flow analysis are exposed and the implications to the prediction of critical flow rate are discussed.

Introduction

The rate at which a pressure disturbance propagates is important to the understanding and prediction of many phenomena of interest. In single-phase flows, the speed of sound (i.e., the rate at which the media can transmit small amplitude pressure perturbations) and the critical flow velocity are both functions of the local state of the media, and are essentially identical in value. In two-phase flows the speed of sound varies over a broad range of values for any given state, depending on the frequency content of the pressure perturbation. It is well known that the behavior of the speed of sound in a two-phase medium makes it difficult to determine a simple relationship between the propagation speed of small amplitude pressure disturbances and the critical flow velocity (Hsu, 1972). It is one of the purposes of this paper to establish such a relationship.

Two-Fluid Model. A general form of the one-dimensional two-fluid model is presented. The physics describing the behavior of a bubbly two-phase mixture is captured by this model.

The space-time averaged one-dimensional conservation equations for adiabatic gas/liquid flows are (Ishii, 1975)

Conservation of Mass

$$\frac{\partial}{\partial t}(\alpha_k\rho_k)+\frac{\partial}{\partial z}(\alpha_k\rho_k u_k)+\alpha_k\rho_k u_k\frac{1}{A_{xs}}\frac{dA_{xs}}{dz}=0 \tag{1}$$

Conservation of Momentum

$$\frac{\partial}{\partial t}(\alpha_k\rho_k u_k)+\frac{\partial}{\partial z}(\alpha_k\rho_k u_k^2)=-\alpha_k\frac{\partial p_k}{\partial z}+\Delta p_{ki}\frac{\partial\alpha_k}{\partial z}+\alpha_k\rho_k g_k\cos\theta+M_k-\tau_k \tag{2}$$

Conservation of Energy

$$\frac{\partial}{\partial t}(\alpha_k\rho_k h_k)+\frac{\partial}{\partial z}(\alpha_k\rho_k u_k h_k)=\alpha_k\left(\frac{\partial p_k}{\partial t}+u_k\frac{\partial p_k}{\partial z}\right)-u_k\tau_k+\frac{q''_{ki}}{L_s} \tag{3}$$

where the subscript k denotes either the gas ($k=g$) or the liquid ($k=l$) phase.

Appropriate constitutive equations must be used to model the interaction between each phase. The momentum transfer between the gas and liquid phases can be written as the sum of three forces per unit volume

$$M_l=-M_g=\alpha[F_D+F_{VM}+F_R] \tag{4}$$

where

$$\alpha\triangleq\alpha_g$$

The interfacial drag force F_D for bubbly flow can be modeled as

$$F_D=\frac{3}{8}\rho_l\frac{C_D}{R_b}(u_g-u_l)\,|u_g-u_l| \tag{5}$$

The drag coefficient C_D for the distorted bubbly flows is given by Harmathy (1960) as

$$C_D=\frac{4}{3}R_b\left[\frac{g(\rho_l-\rho_g)}{g_c\sigma(1-\alpha)}\right]^{1/2} \tag{6}$$

The virtual mass force F_{VM} is given by

$$F_{VM}=\rho_l C_{VM}a_{VM} \tag{7}$$

The virtual volume coefficient C_{VM} can be expressed as a function of the global void fraction (Ruggles et al., 1988) as

$$C_{VM}=0.5[1+12\alpha^2]\qquad(\alpha\le 20\text{ percent}) \tag{8}$$

and the virtual mass acceleration a_{VM} is given by (Drew and Lahey, 1987)

$$a_{VM}=\left[\frac{\partial u_g}{\partial t}+u_g\frac{\partial u_g}{\partial z}\right]-\left[\frac{\partial u_l}{\partial z}+u_l\frac{\partial u_l}{\partial z}\right]=\left[\frac{D_g u_g}{Dt}-\frac{D_l u_l}{Dt}\right] \tag{9}$$

The reaction force due to bubble pulsation, F_R, results from the interaction of an oscillating spherical bubble with the flow field around the bubble. This flow field is due to both bubble translation relative to the liquid phase and to radial bubble pulsations. This force is given by (Cheng et al., 1985)

$$F_R=\frac{3}{R_b}C_{VM}\rho_l(u_g-u_l)\frac{D_g R_b}{Dt} \tag{10}$$

Since the gas phase is assumed to be dispersed within the liquid phase, the wall shear stress on the gas phase is

[1]Currently at the Oak Ridge National Laboratory, Oak Ridge, TN 37831-8045.

Contributed by the Heat Transfer Division and presented at the National Heat Transfer Conference, Pittsburgh, Pennsylvania, August 9-12, 1987. Manuscript received by the Heat Transfer Division October 16, 1987. Keywords: Modeling and Scaling, Multiphase Flows.

$$\tau_g = 0 \tag{11a}$$

and the liquid phase wall shear stress is

$$\tau_l = \frac{1}{2}\frac{f}{D_H}\rho_l u_l |u_l| \tag{11b}$$

For low-pressure air/water flows, the interfacial pressure in the gas phase is related to the average pressure of the gas phase by

$$\Delta p_{gi} = p_{gi} - p_g \cong 0 \tag{12}$$

This applies when the wavelengths of the pressure variations in the gas phase, λ_g, are much greater than the bubble radius R_b.

The difference between the interfacial pressure and the mean pressure in the liquid phase is, for a nonpulsating bubble, given by (Stuhmiller, 1977)

$$p_{li} - p_l = \Delta p_{li} = -\frac{\rho_l}{4}(u_g - u_l)^2 \tag{13}$$

A relationship between the variables p_g and p_{l_∞} was used that is similar to that developed by Prosperetti (1977) and Cheng et al. (1985). A single bubble was considered to be surrounded by an infinite medium, and excited by small-amplitude sinusoidal pressure oscillations. The bubble response was assumed to be spherically symmetric and without translatory oscillations. These assumptions are valid for pressure excitations having wavelengths $\lambda_{2\phi}$, which are much greater than the bubble radius R_b. The relation is given by (Ruggles, 1987)

$$\delta p_g - \delta p_l = \rho_{l_o} R_{b_o}\left\{1 + \frac{ik_{b_o}R_{b_o}}{1 - ik_{b_o}R_{b_o}}\right\}\delta\ddot{R}_b$$

$$+\frac{4\mu_l}{R_{b_o}}\left\{1 - \left(\frac{1}{2} + \frac{1}{3\alpha_o}\right)\left[\frac{k_{b_o}^2 R_{b_o}^2}{(1 - ik_{b_o}R_{b_o})}\right]\right\}\delta\dot{R}_b - \frac{2\sigma\delta R_b}{R_{b_o}^2} \tag{14}$$

where

$$(\,) = (\,)_o + \delta(\,)$$

A departure in this paper from that of previous studies is in the definition of the wavenumber

$$k_b = \frac{\omega}{c_{2\phi}(\omega)} \tag{15}$$

Previously the wavenumber k_b was defined as ω/c_l, which assumed the surrounding media transmitted the radiated pressure disturbance at celerity c_l (the speed of sound in liquid). However, if the original sinusoidal excitation of frequency ω is propagating at celerity $c_{2\phi}(\omega)$, then it is consistent to assume that a radiated pressure disturbance of the same frequency, ω, will also be transmitted through the media at velocity $c_{2\phi}$. Hence, k_b is defined as in equation (15).

Prosperetti (1977) demonstrated that the radiated acoustic energy is negligible for frequencies below bubble resonance, where $c_{2\phi}$ is much less than c_l; thus the differences in assumed k_b are of no consequence. In contrast, the propagation speed of pressure perturbations $c_{2\phi}$ is approximately equal to c_l for frequencies above bubble resonsance; thus the old and new definitions for k_b are the same in this region. However, the definition of k_b can have an important effect near bubble resonance. It is also interesting to note that an inviscid isentropic analysis can be performed to obtain (Rschevkin, 1963)

$$\omega_r = \omega_{r_{1\phi}}\frac{\rho_l}{\rho_{2\phi}} \tag{16}$$

where $\omega_{r_{1\phi}}$ is the value for the resonant frequency if a single bubble were imbedded in single-phase liquid.

A microscopic thermodynamic analysis of a bubble suspended in a liquid medium can be used instead of the gas thermal energy equation. This type of analysis has been done previously by Prosperetti (1977), Plesset et al. (1960), and Cheng et al. (1983). The analysis of Cheng et al. (1983) involves the use of perturbations of the form

$$\delta\underline{\psi} = \underline{\psi}' e^{i(kz - \omega t)} \tag{17}$$

The results of his analysis may be summarized as

$$\delta p_g = (\rho_{g_o}\omega^2 R_{b_o})\mathrm{ZPV}\delta R_b \tag{18a}$$

and

$$\delta h_g = c_{p_{g_o}} T_{g_o}\left[\frac{\rho_{g_o}\omega^2 R_{b_o}}{\rho_{l_o}}\right]\mathrm{ZTR}\delta R_b \tag{18b}$$

where ZPV and ZTR are complex-valued functions of ω and k (Cheng et al., 1983). One can eliminate δR_b between equations (18*a*) and (18*b*) to determine the state relationship between δp_g and δh_g that is required for closure.

Dispersion Relation. Equations (1), (2), and (3) can be linearized, assuming that the spatial derivatives of the steady-state solution are of order δ or less. These equations may be

Nomenclature

A_{xs} = cross-sectional area
a = thermal diffusivity
C_{VM} = virtual mass acceleration
c = sound speed
$c_{2\phi}$ = speed of propagation (i.e., celerity) of small-amplitude pressure perturbations in a two-phase mixture
C_D = drag coefficient
C_{VM} = virtual volume coefficient
D_H = hydraulic diameter
$\frac{D_g(\,)}{Dt}$ = material derivative $= \frac{\partial(\,)}{\partial t} + u_g\frac{\partial(\,)}{\partial z}$
f = frequency; friction factor
F = force per unit volume
g = gravitational acceleration
g_c = gravitational constant
h = enthalpy
i = imaginary number $= \sqrt{-1}$
k = wavenumber $= 2\pi/\lambda$
$1/L_S$ = interfacial area density
M_k = momentum transfer term
p = pressure
q_{ki}'' = interfacial heat flux
R = radius
T = temperature
t = time
u = velocity
v = specific volume
z = axial location
α = void fraction
η = attenuation coefficient
θ = angle of inclination of flow from vertical
λ = wavelength
μ = dynamic viscosity
ρ = density
σ = surface tension
τ = wall shear
ω = angular frequency

Subscripts

b = bubble
g = gas
i = interfacial
l = liquid
o = equilibrium value
p = pressure
QS = quasi-steady
r = resonance
s = slow (low frequency)
VM = virtual mass
2ϕ = two-phase

Symbols

$\bar{(\,)}$ = effective value
$\dot{(\,)}$ = time derivative
$\langle\ \rangle$ = area averaging over the flow area
$\delta(\,)$ = perturbation
$(\,)^T$ = transpose of an array
$(\,)'$ = perturbation amplitude

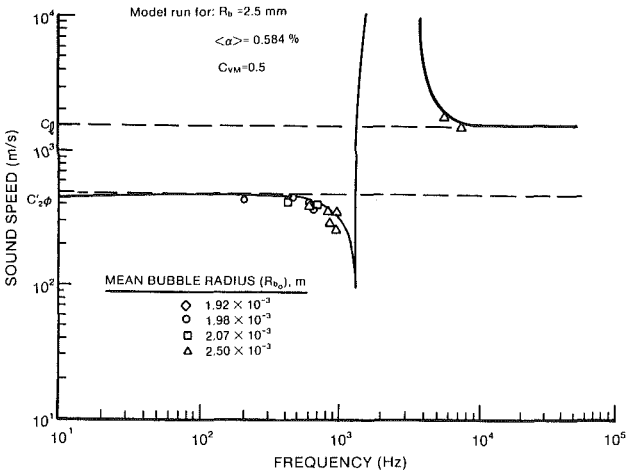

Fig. 1 Sound speed versus frequency (data from Silberman, 1957)

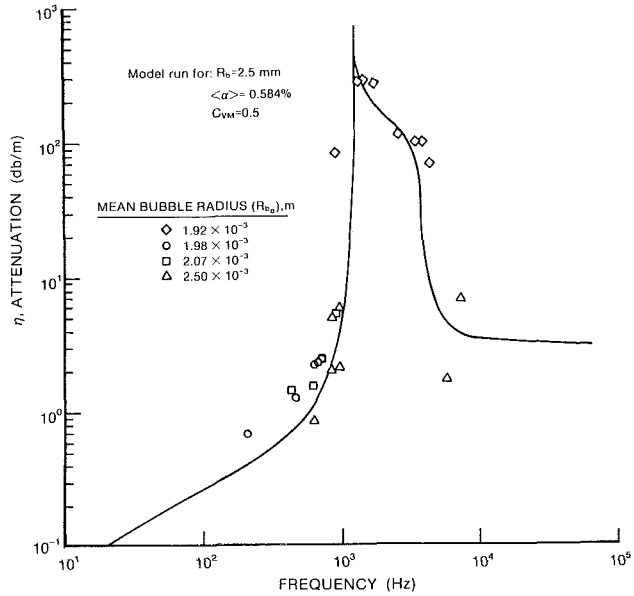

Fig. 2 Attenuation versus frequency (data from Silberman, 1957)

combined with equations (14) and (18) to form an equation set describing the response of the system to small perturbations of the form given in equation (17)

$$\underline{\underline{A}}_o \frac{\partial \delta \underline{\psi}}{\partial t} + \underline{\underline{B}}_o \frac{\partial \delta \underline{\psi}}{\partial z} = \underline{\underline{C}}'_o \delta \underline{\psi} \tag{19a}$$

where

$$\underline{\underline{C}}'_o = \underline{\underline{C}}_o + \underline{\psi}_o \frac{\partial \underline{\underline{C}}}{\partial \underline{\psi}} \bigg|_o \tag{19b}$$

and

$$\underline{\psi} = \left[\alpha,\ p_l,\ u_g,\ u_l,\ h_l,\ R_b,\ \frac{D_g R_b}{Dt}\right]^T \tag{19c}$$

Equations (17) and (19) can be written as the algebraic equation

$$\{\underline{\underline{A}}_o(\underline{\psi})[-i\omega] + \underline{\underline{B}}_o(\underline{\psi})[ik] - \underline{\underline{C}}'_o(\underline{\psi})\}\underline{\psi}' = 0 \tag{20}$$

Equation (20), in conjunction with the requirement that $\underline{\psi}'$ be finite, implies a dispersion relationship of the form

$$\det\{(\underline{\underline{A}}_o(\omega/k) - (i/k)\underline{\underline{C}}'_o) - \underline{\underline{B}}_o\} = 0 \tag{21}$$

For standing waves, equation (21) gives a relationship between

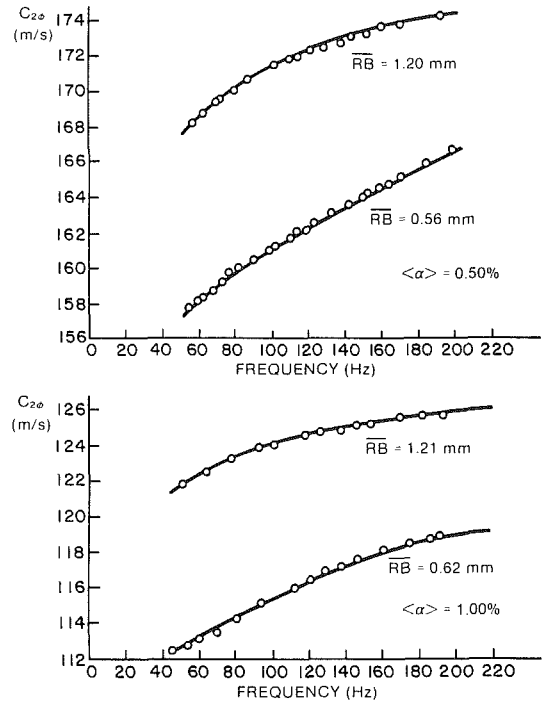

Fig. 3 Sound speed versus frequency (data from Ruggles et al., 1988)

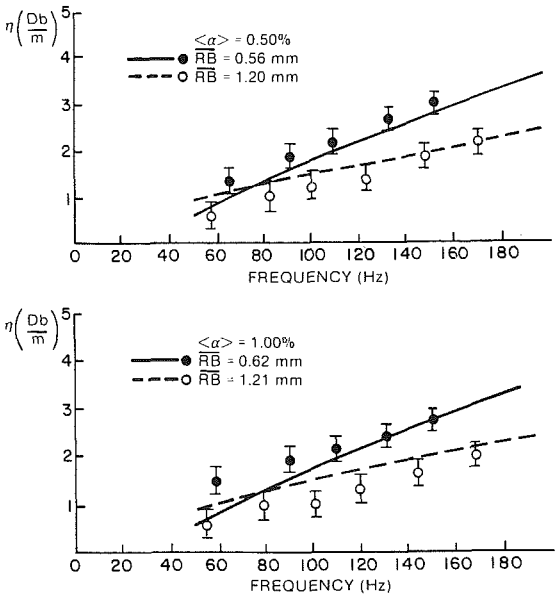

Fig. 4 Attenuation versus frequency (data from Ruggles et al., 1988)

real values of angular frequency ω and wavenumber k. The wavenumber is in general a complex number, with its real part corresponding to 2π divided by the wavelength, and its imaginary part corresponding to a spatial attenuation coefficient (η).

The dispersion relation normally gives seven roots (ω/k) for each value of angular frequency ω. Five of the seven roots yield celerities close to the convective velocities of the liquid and vapor phases, u_l and u_g. However, the wavelengths associated with these roots are too short to allow the two-fluid medium to be treated as a continuum when frequencies go above about 20 Hz. Furthermore, four of these roots are strongly attenuated. The remaining two roots travel at celerities typical of the so-called "speed of sound" in the two-phase medium. One of these roots is positive (i.e., it travels

with the flow). The other is negative and travels against the flow. These roots have velocities that vary in absolute value by a small amount associated with some two-phase convective velocity. These two roots have been used to predict the standing wave data of Silberman (1957) and Ruggles et al. (1987), where the speed of sound was taken as

$$c_{2\phi} = \frac{|[\omega/\mathrm{Re}(k)]_p^+ - [\omega/\mathrm{Re}(k)]_p^-|}{2} \tag{22}$$

It can be seen in Figs. 1-4 that this model predicts standing wave data very well. Similar agreement has been found for void fractions varying from 0.5 to 18 percent (Ruggles et al., 1988).

Prediction of Propagating Pressure Pulses. A linear perturbation of the form $\underline{\delta\Psi}$ can be represented in terms of the harmonic perturbations given in equation (17) through the superposition of Fourier integrals

$$\underline{\delta\Psi}(z, t) = \int_{\omega=-\infty}^{\infty} \sum_{j=1}^{7} g_j(\omega)\underline{\delta\psi}_j d\omega$$

$$= \int_{\omega=-\infty}^{\infty} \left[\sum_{j=1}^{7} g_j(\omega)\underline{\psi}'_j e^{i(k_j(\omega)z)}\right] e^{-i\omega t} d\omega$$

$$= \int_{\omega=-\infty}^{\infty} \left[\sum_{j=1}^{7} \underline{G}_j(\omega) e^{i(k_j(\omega)z)}\right] e^{-i\omega t} d\omega \tag{23a}$$

where

$$\sum_{j=1}^{7} \underline{G}_j(\omega) = \sum_{j=1}^{7} [g_j(\omega)\underline{\psi}'_j] = \frac{1}{2\pi}\int_{t=-\infty}^{\infty} \underline{\delta\Psi}(0, t) e^{i\omega t} dt \tag{23b}$$

and

$$\underline{g}_j(\omega) = \frac{1}{2\pi}\int_{t=-\infty}^{\infty} \underline{\delta\Psi}_j(0, t) e^{i\omega t} dt \tag{23c}$$

The $\underline{\delta\Psi}_j$ in equation (23c) is the portion of $\underline{\delta\Psi}$ due to the summation of Fourier components of eigenmode, $\underline{\delta\Psi}_j$, such that

$$\delta\Psi_j = \int_{\omega=-\infty}^{\infty} g_j(\omega)\underline{\delta\psi}_j d\omega \tag{24a}$$

and

$$\underline{\delta\Psi} = \sum_{j=1}^{7} \underline{\delta\Psi}_j \tag{24b}$$

Normally, the perturbed pressure, δp_l, is the dominant eigenmode. Equation (23*a*) can thus be simplified to give the approximate Fourier integral representation of the single state variable p_l in the propagating eigenmode associated with the traveling pressure wave

$$\delta p_l(z, t) = \int_{\omega=-\infty}^{\infty} [g_p(\omega) e^{ik_p^-(z)}] e^{i\omega t} d\omega \tag{25a}$$

where

$$g_p(\omega) = \frac{1}{2\pi}\int_{t=-\infty}^{\infty} \delta p_l(0, t) e^{i\omega t} dt \tag{25b}$$

Note that the wavenumber of the pressure perturbation traveling in the negative z direction (i.e., in the flow direction), k_p^-, has been used. This technique has been employed to predict the propagation speed and dispersion of typical pressure perturbations (Ruggles, 1987), thus relating the standing wave and propagating pressure perturbations. The time trace of a typical pressure perturbation at the lower transducer was used to generate the function $g_p(\omega)$ using a standard FFT algorithm. The time trace of the pressure pulse at the upper transducer was then constructed through a numerical evaluation of equations (25) with the values for $k_p^-(\omega)$ taken from the model's dispersion relation, equation (21). The results are shown in Fig. 5. It can be seen that the model predictions are in close agreement with the data. This further indicates that the slower eigenmodes may be omitted in the representation of δp_l, as was done in equations (25).

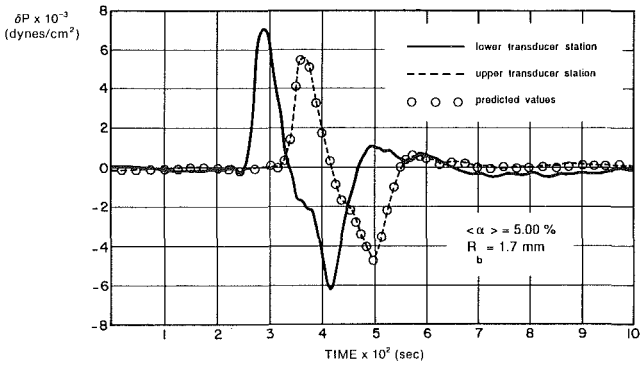

Fig. 5 Measured and predicted pressure traces

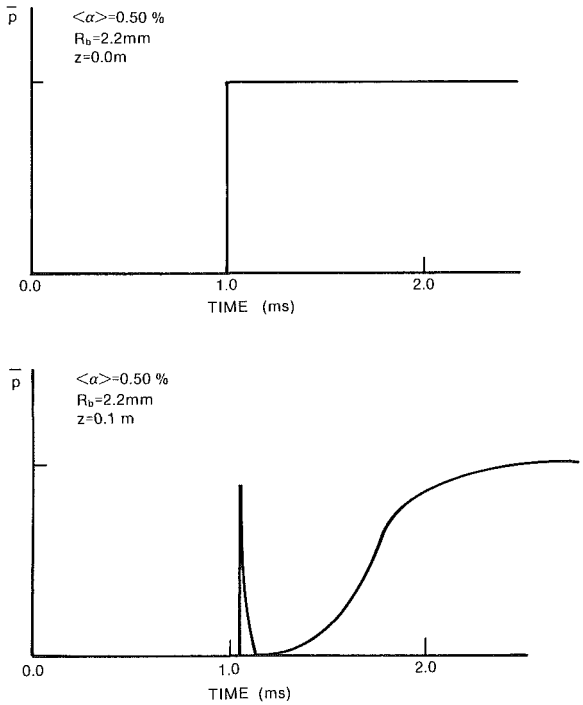

Fig. 6 Predicted dispersion of a step input

The model has also been used to predict the dispersion of a hypothetical square pulse. The results are shown in Fig. 6. Notice that the pressure pulse rapidly separates into two distinct pulses, one that is traveling relatively slowly, at the so-called two-phase speed of sound ($c_{2\phi}$), and one that is traveling much more rapidly, at the speed of sound in liquid (c_l). This is easily understood by examining the predicted values of $c_{2\phi}$ in Fig. 1. All the frequency components of the pulse having values less than bubble resonance are traveling relatively slowly, at essentially the two-phase speed of sound. In contrast, all the frequencies above bubble resonance are traveling much faster, at the speed of sound in liquid. Thus, the high-frequency components ($\omega > \omega_r$) that comprise the leading and trailing edge of a square pulse rapidly separate from the low-frequency components ($\omega < \omega_r$). All of this is accompanied by rapid attenuation of all frequency components near the bubble resonance frequency (Fig. 2).

The rapid separation of a square pulse into "slow" and "fast" portions indicates that the physical behavior that governs sound propagation for frequencies below bubble resonance is different from that which governs the propagation of sound for frequencies above bubble resonance.

The physics governing the frequencies below bubble resonance can be examined by returning to equation (14) with terms of order $k_b R_b$ neglected

$$\delta p_g(t) - \delta p_{l_\infty} = p_l R_{b_o} \delta \ddot{R}_b + \frac{4\mu_l \delta \dot{R}_b}{R_{b_o}} + \frac{2\sigma \delta R_b}{R_{b_o}^2} \tag{26}$$

This is the linearized form of the classical Rayleigh equation for a pulsating bubble. Equation (26) can be scaled by introducing the following nondimensional variables:

$$\delta R_b^* = \frac{\delta R_b}{R_b'} \tag{27a}$$

$$\delta \dot{R}_b^* = \frac{\delta \dot{R}_b}{R_b' \omega} \tag{27b}$$

and

$$\delta \ddot{R}_b^* = \frac{\delta R_b}{R_b' \omega^2} \tag{27c}$$

where R_b' is the perturbed amplitude of the bubble radius in the vector $\underline{\psi}'$.

Equation (26) can be written as

$$\delta p_g - \delta p_{l_\infty} = \rho_l R_{b_o} R_b' \omega^2 \ddot{R}_b^* + 4\mu R_b' \omega \dot{R}_b^* - \frac{R_b' \dot{R}_b^* \Delta p_{gi}}{R_{b_o}} \tag{28}$$

where

$$\Delta p_{gi} \triangleq p_{li} - p_g = -\frac{2\sigma}{R_{b_o}} \tag{29}$$

The derivative terms in equation (28) may be neglected when the following two inequalities are satisfied:

$$\frac{\rho_l R_{b_o}^2 \omega^2}{\Delta p_{gi}} \ll 1 \tag{30a}$$

$$\frac{R_{b_o} 4\mu_l \omega}{\Delta p_{gi}} \ll 1 \tag{30b}$$

Inequalities (30*a*) and (30*b*) are valid for an air/water mixture at standard temperature and pressure conditions when

$$\omega < 0.5\omega_r \tag{31}$$

Under these circumstances equation (28) reduces to

$$\delta p_g - \delta p_{l_\infty} = \frac{-R_b' \Delta p_{gi} R_b^*}{R_{b_o}} = \frac{-\Delta p_{gi} \delta R_b}{R_{b_o}} \tag{32}$$

Equation (32) indicates that the gas pressure simply follows the liquid pressure, with a correction in the gas pressure amplitude due to the perturbation in the bubble radius. In air/water mixtures at standard temperature and pressure conditions the term Δp_{gi} is of order δp_g when the equilibrium radius R_{b_o} is greater than 0.5 mm. This implies that

$$\delta p_g \cong \delta p_l \quad (\omega < 0.5\omega_r,\ R_b > 0.5 \text{ mm}) \tag{33}$$

This indicates that a quasi-static pressure relationship is sufficient for modeling the propagation of frequencies well below bubble resonance. That is

$$\Delta p_{QS} = \Delta p_{li} - \Delta p_{gi} = \frac{2\sigma}{R_{b_o}} - \frac{\rho_{l_o}}{4} (u_{g_o} - u_{l_o})^2 \tag{34}$$

It has been previously shown by Prosperetti (1977) that the bubble's thermal response is essentially adiabatic over a wide range of frequencies that satisfy equation (31). Thus the quasi-static phasic pressure relationship, equation (34), can be substituted for equations (14) and (18) in the linearized two-fluid model to obtain a low-frequency dispersion relation

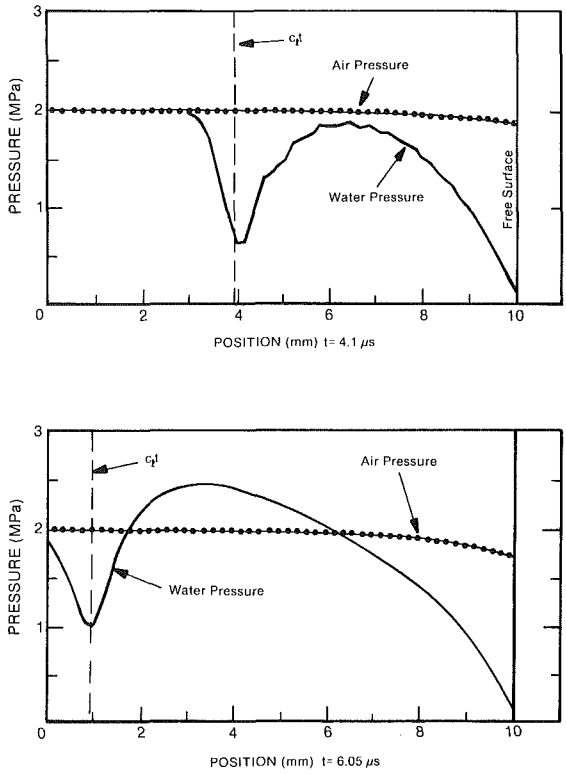

Fig. 7 Predicted propagation of a finite amplitude step change in pressure (model of Drumheller et al., 1981)

$$\det\{(\underline{\underline{A}}_s(\omega/k) - (i/k)\underline{\underline{C}}_s') - \underline{\underline{B}}_s\} = 0 \tag{35}$$

where the subscript s denotes the matrices appropriate for slow (i.e., low-frequency) disturbances.

As noted previously (Ruggles et al., 1988) two of the eigenvalues of equation (35) yield the $c_{2\phi}'$ shown in Fig. 1. The linear dispersion relation that results from equation (35) also yields $c_{2\phi}'$ (Ruggles, 1987). This is apparently because, for bubbly air/water flows, viscous effects are negligible for frequencies below bubble resonance (Prosperetti, 1977), hence, $\underline{\underline{C}}_s' \simeq 0$.

The "fast" portion of the original square wave pulse is composed of frequencies above bubble resonance. For perturbations of high frequency, $\omega \gg \omega_r$, equation (28) yields

$$R_b' \cong 0 \tag{36}$$

This implies that the bubbles are limited dynamically in their ability to follow the liquid pressure excitations; therefore, the gas phase pressure remains unperturbed. The liquid phase pressure perturbations are unable to take advantage of the gas phase compressibility since the bubbles behave as rigid spheres. Hence, when the high-frequency pressure relationship between the gas and liquid phases is introduced into the dispersion relation, the resulting prediction for the two-phase sound speed is the speed of sound in liquid, shown in Fig. 1 as c_l.

While a linear dispersion relation is only appropriate for small amplitude (i.e., acoustic) pressure disturbances, it is interesting to compare the behavior of this linear model qualitatively with a nonlinear one. Drumheller et al. (1981) have developed a model for finite amplitude waves that successfully predicts the data taken by Kuznetsov et al. (1978) and van Wijngaarden (1966). Figure 7 shows a finite amplitude pressure front propagating through a bubbly air/water mixture with an initial void fraction of 10 percent and initial bubble radii of 1.0 mm. The leading edge of the pressure front was found to travel at c_l in the liquid phase, while the leading por-

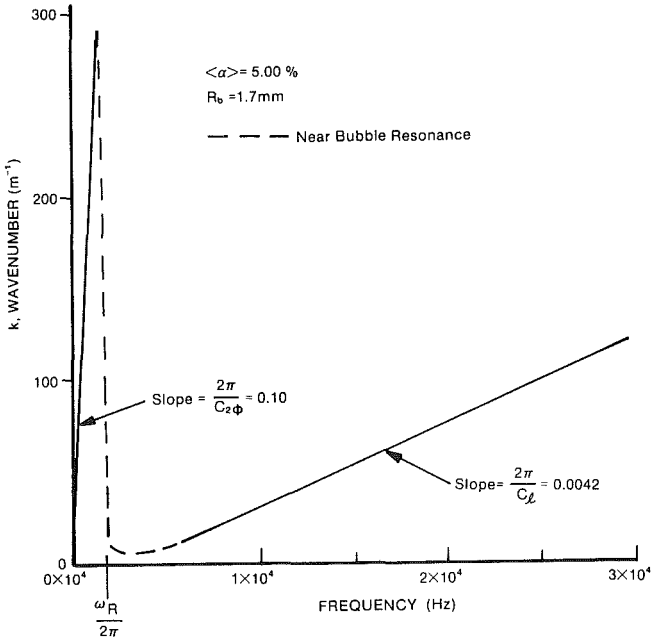

Fig. 8 Dispersion relation as predicted by a linear model (equation (21))

tion of the pressure front in the gas phase travels at a much slower velocity, $c'_{2\phi}$. The reason for this separation of the pressure front was explained by the authors as being due to the inability of the air bubbles to respond to the initial change in liquid pressure due to dynamic constraints. Thus the wave front separates in a manner consistent with that given in Fig. 6 using the linear model.

Relationship to Critical Flow. The form of the two-fluid model commonly used for critical two-phase flow analysis uses coefficient matrices that are identical to those in equation (35). In particular, for steady choked flow

$$\underline{\underline{B}}_s \frac{\partial \underline{\psi}}{\partial z} = \underline{\underline{C}}'_s \underline{\psi} \tag{37}$$

A necessary condition for choking is (Bouré et al., 1975)

$$\det[\underline{\underline{B}}_s] = 0 \tag{38}$$

The choking condition can be determined by solving equation (37) as an initial value problem, while simultaneously testing for the condition of equation (38). A detailed discussion of how this type of analysis is performed has been given by Bouré et al. (1975).

The velocity associated with the choked state (i.e., the critical flow velocity) is calculated from the characteristics (v) of the two-fluid model (Delhaye et al., 1981; Trapp and Ransom, 1982)

$$\det\{\underline{\underline{B}}_s - \underline{\underline{A}}_s v\}\Big|_{\text{choked}} = 0 \tag{39}$$

One of the eigenvalues, $v_c = 0$, determines the choking condition. This eigenvalue is the only one capable of transmitting information on pressure variation downstream of the throat to positions upstream of the throat. Once the discharge velocity at the throat reaches sonic conditions, further lowering of downstream pressure is not capable of affecting conditions upstream of the choking plane (i.e., the throat). Moreover, since equation (39) is valid for all eigenvalues, and in particular for the one that vanishes, this equation implies equation (38) when choking occurs.

Equation (39) is somewhat different from the corresponding linear dispersion relation for the "slow" pulses

$$\det\left\{\left(\underline{\underline{A}}_s v^* - \frac{i}{k}\underline{\underline{C}}'_s\right) - \underline{\underline{B}}_s\right\} = 0 \tag{40}$$

where

$$v^* = \frac{\omega}{k}$$

However, equation (40) can be put in the form of equation (39) if one takes the limit as the wave number k grows large (i.e., the high-frequency limit)

$$\det\left\{\lim_{k\to k_m}\left\{\left(\underline{\underline{A}}_s v^* - \frac{i}{k}\underline{\underline{C}}'_s\right) - \underline{\underline{B}}_s\right\}\right\} \cong \det\{\underline{\underline{A}}_s v^* - \underline{\underline{B}}_s\} \tag{41}$$

where k_m is the maximum wavenumber for which the quasi-steady pressure relationship holds. Thus we find that the wave propagation model associated with only low-frequency phenomena predicts the so-called two-phase choking velocity.

The reader is cautioned that while adiabatic models may be adequate for predictions of the two-phase sound speed $c'_{2\phi}$, they are not normally adequate for predictions of the spatial attenuation. Indeed, significant thermal attenuation can take place in the thin layer near the air/water interface that involves very little of the total gas volume, and as such does not appreciably affect the gas phase compressibility.

It is also interesting to note that the terms resident in the matrix $\underline{\underline{C}}'_o$ are due to constitutive laws often used to model phenomena such as bubble drag, wall shear, and heat transfer. These phenomena are actually based on local gradients, but for convenience they are normally modeled algebraically. Hence their appearance on the right-hand side of equation (19*a*) is a result of procedures used in averaging and modeling. Fortunately, they are not important if one is only interested in $c'_{2\phi}$.

The critical flow model just discussed was found to be consistent with the two-fluid model when the quasi-static pressure relation of equation (34) is used. This model was shown to be appropriate for pressure perturbations having frequency content well below bubble resonance, and yields the so-called two-phase sound speed $c'_{2\phi}$. However, it has been shown herein, and has been previously observed (van Wijngaarden, 1966), that a two-fluid medium is also capable of transmitting high-frequency ($\omega > \omega_r$) pressure disturbances at velocity c_l. It is significant to note that if one chose to use the dynamic pressure relationship between the gas and liquid phases appropriate for these high frequencies, then the critical flow velocity would have corresponded to c_l. It appears, however, that these modes can only be excited for situations involving rapid pressure transients.

Finally, it is interesting to note that a general spatial pressure field can be constructed either from frequencies above resonance (fast waves), or from frequencies below resonance (slow waves). This nonunique representation is possible because, as shown in Fig. 8, a significant range of frequencies above bubble resonance, and below bubble resonance, produces an identical range of wavenumbers.

Conclusions

The relationship between the linearized dispersion model for acoustic standing waves and the propagation of small amplitude pressure perturbations has been established through the use of the Fourier decomposition techniques.

Furthermore, the relationship between the celerity deduced from the linear dispersion relation and the critical flow velocity is demonstrated and shown to be unique when a simple quasi-static interfacial pressure model is used. However, the critical flow velocity predicted by these models is not the maximum velocity at which the two-phase medium can transmit information on pressure perturbations. A more exact interfacial pressure model implies higher discharge velocities for situations in which high-frequency modes are excited.

References

Bouré, J. A., Fritte, A. A., Giot, M. M., and Reocreux, M. L., 1975, "A Contribution to the Theory of Critical Two-Phase Flow: On the Links Between Maximum Flow Rates, Choking, Sonic Velocities, Propagation and Transfer Phenomena in Single and Two-Phase Flow," *Energie Primaire*, Vol. 11, pp. 1-27.

Cheng, L.-Y., Drew, D. A., and Lahey, R. T., Jr., 1983, "An Analysis of Wave Dispersion, Sonic Velocity, and Critical Flow in Two-Phase Mixtures," NUREG-CR/3372.

Cheng, L.-Y., Drew, D. A., and Lahey, R. T., Jr., 1985, "An Analysis of Wave Propagation in Bubbly Two-Component, Two-Phase Flows," ASME JOURNAL OF HEAT TRANSFER, Vol. 107, pp. 402-408.

Delhaye, J. M., Giot, M., and Riethmuller, M. L., 1981, *Thermohydraulics of Two-Phase Systems for Industrial Design and Nuclear Engineering*, McGraw-Hill, New York.

Drew, D. A., and Lahey, R. T., Jr., 1987, "The Virtual Mass and Lift Force on a Sphere in Rotating and Straining Inviscid Flow," *Int. J. Multiphase Flow*, Vol. 13, No. 1, pp. 113-121.

Drumheller, D. S., Kipp, M. E., and Bedford, A., 1981, "Transient Wave Propagation in Bubbly Liquids," *J. Fluid Mechanics*, Vol. 119, pp. 347-365.

Harmathy, T. Z., 1960, "Velocity of Large Drops and Bubbles in Media of Infinite or Restricted Extent," *AIChE Journal*, Vol. 6, No. 2.

Hsu, Y.-Y., 1972, "Review of Critical Flow Rate, Propagation of Pressure Pulse, and Sonic Velocity in Two-Phase Media," NASA Technical Note, TN D-6819.

Ishii, M., 1975, *Thermo-Fluid Dynamic Theory of Two-Phase Flow*, Eyrolles.

Kuznetsov, V. V., Nakoryakov, V. E., Pokusaev, B.G., and Screiber, I. R., 1978, "Propagation of Perturbations in a Gas-Liquid Mixture," *J. Fluid Mech.*, Vol. 85, pp. 85-96.

Landau, L. D., and Lifshitz, E. M., 1959, *Fluid Mechanics*, Pergamon Press, New York.

Plesset, M. S., and Hsieh, D. Y., 1960, "Theory of Gas Bubbly Dynamics in Oscillating Pressure Fields," *The Physics of Fluids*, Vol. 3, pp. 882-892.

Prosperetti, A., 1977, "Thermal Effects and Damping Mechanisms in the Forced Radial Oscillations of Gas Bubbles in Liquids," *J. Acoust. Soc. Am.*, Vol. 61, pp. 17-27.

Ruggles, A. E., 1987, "An Investigation of the Propagation of Pressure Perturbations in Two-Phase Flow," Ph.D. Thesis, Rensselaer Polytechnic Institute, Troy, NY.

Ruggles, A. E., Lahey, R. T., Jr., Drew, D. A., and Scarton, H. A., 1988, "An Investigation of the Propagation of Pressure Perturbations in Bubbly Air-Water Flows," ASME JOURNAL OF HEAT TRANSFER, Vol. 110, No. 2, pp. 494-499.

Rschevkin, S. N., 1963, *The Theory of Sound*, Pergamon Press, New York.

Silberman, E., 1957, "Sound Velocity and Attenuation in Bubbly Mixtures Measured in Standing Wave Tubes," *J. Acoustic Society of America*, Vol. 21, pp. 925-933.

Stuhmiller, J. H., 1977, "The Influence of Interfacial Pressure Forces on the Character of Two-Phase Flow Model Equations," *Int. J. Multiphase Flow*, Vol. 3, pp. 551-560.

Trapp, J. A., and Ransom, V. H., 1982, "A Choked Flow Calculation Criterion for Non-homogeneous, Non-equilibrium, Two-Phase Flows," *Int. J. Multiphase Flow*, Vol. 8, No. 6, pp. 669-681.

van Wijngaarden, L., 1966, "Linear and Non-linear Dispersion of Pressure Pulses in Liquid-Bubble Mixtures," *Proc. 6th Symp. on Naval Hydrodynamics*, R. D. Cooper and S. W. Doroff, eds., U.S. Govt. Printing Office, Washington, DC, pp. 129-135.

Numerical Calculation of Bubble Growth in Nucleate Boiling From Inception Through Departure

R. C. Lee
Assistant Professor of Mechanical Engineering,
Utah State University,
Logan, UT 84322-4130
Assoc. Mem. ASME

J. E. Nydahl
Professor of Mechanical Engineering,
University of Wyoming,
Laramie, WY 82071
Mem. ASME

The relative contributions of the fundamental mechanisms accounting for the enhanced heat transfer in nucleate boiling are difficult to quantify analytically or experimentally. A comprehensive model was developed that permits some accurate insights into this problem. An essential feature involved the numerical mapping of the complicated geometry to a plane where the bubble and wall boundaries lie along constant coordinate lines. The results show that microlayer evaporation accounts for 87 percent of the enhanced wall heat transfer during saturated boiling of water at 1 atm and 8.5 K wall superheat. In contrast, enhanced convective effects were essentially nonexistent during growth and minimal following departure. The analysis predicts an extremely nonuniform thermal boundary layer around the bubble, and shows that the wall thermal boundary layer regenerates almost immediately following departure.

Introduction

From a microscopic point of view, the two factors accounting for the enhanced heat transfer in nucleate boiling are forced convective effects and latent heat transport. The bubble motion produces enhanced forced convection around the site commonly termed microconvection during growth and liquid-vapor exchange following departure. The latent heat energy required to form the bubble is conducted into the bubble either directly through a liquid microlayer beneath the bubble or indirectly through the bubble cap. Following bubble departure the wall thermal boundary layer near the nucleation site is regenerated by transient conduction.

Early models for the growth of a nucleate boiling bubble (Hsu and Graham, 1961; Van Stralen, 1967; Mikic et al., 1970) neglected the microlayer and modeled the bubble cap heat transfer by assuming a thin, typically uniform, thermal boundary layer. The existence of the microlayer is now an undisputed fact, but the question of its contribution to the enhanced heat transfer in nucleate boiling is not well defined. Depending on the boiling conditions, the estimate of its contribution to the energy required for bubble growth ranges from less than 20 percent to nearly 100 percent (Voutsinos and Judd, 1975; Van Stralen et al., 1975; Judd and Hwang, 1976; Fath and Judd, 1978; Koffman and Plesset, 1983).

Several numerical models of nucleate boiling (Madhaven and Mesler, 1970; Guy and Ledwidge, 1973; Dalle Donne and Ferranti, 1975; Beer et al., 1977; Zijl et al., 1979; Fath, 1981) have been developed, but they incorporated significant simplifications and typically addressed only a portion of the bubble cycle.

Outer Flow Solution

In this paper the axisymmetric Navier-Stokes and energy equations are applied to a nucleate boiling bubble in saturated pool boiling on a horizontal surface, and are solved numerically from inception through departure. The goal was to develop a procedure that can simulate the complete nucleate boiling bubble cycle with a minimum of simplifying assumptions, and thus determine quantitatively and qualitatively the relative importance of the micromechanisms. The bubble geometry during growth and departure is shown in Fig. 1.

Contributed by the Heat Transfer Division and presented at the ASME Winter Annual Meeting, Boston, Massachusetts, December 13-18, 1987. Manuscript received by the Heat Transfer Division November 23, 1987. Keywords: Augmentation and Enhancement, Boiling, Evaporation.

The finite difference formulation uses a numerical grid generation technique that addresses the complicated geometry, time-dependent boundaries,and large grid spacing variation required to resolve both the microlayer and "infinity" boundaries. The technique employed was introduced by Thompson et al. (1974) who took the transformation to be governed by the system of elliptic partial differential equations

$$\alpha r_{\xi\xi} - 2\beta r_{\xi\eta} + \gamma r_{\eta\eta} + J^2(Pr_\xi + Qr_\eta) = 0 \quad (1)$$

$$\alpha z_{\xi\xi} - 2\beta z_{\xi\eta} + \gamma z_{\eta\eta} + J^2(Pz_\xi + Qz_\eta) = 0 \quad (2)$$

where P and Q are arbitrary weighting functions used to control grid spacing. Standard second-order finite difference approximations were used to represent these equations, and the resulting finite difference equations were solved iteratively using Newton-Raphson linearization and successive overrelaxation by lines.

The transformed Navier-Stokes and energy equations for the bulk fluid are

$$(\omega J)_t + (U_c\omega)_\xi + (V_c\omega)_\eta =$$

$$J[(\alpha\omega_{\xi\xi} - 2\beta\omega_{\xi\eta} + \gamma\omega_{\eta\eta})/J^2 + Q'\omega_\eta + P'\omega_\xi - \omega/r^2]/\mathrm{Re} \quad (3)$$

$$(\alpha\psi_{\xi\xi} - 2\beta\psi_{\xi\eta} + \gamma\psi_{\eta\eta})/J^2 + Q''\psi_\eta + P''\psi_\xi - r\omega = 0 \quad (4)$$

$$(TJ)_t + (U_cT)_\xi + (V_cT)_\eta =$$

$$J[(\alpha T_{\xi\xi} - 2\beta T_{\xi\eta} + \gamma T_{\eta\eta})/J^2 + Q'T_\eta + P'T_\xi]/\mathrm{Pe} + uTJ/r \quad (5)$$

where

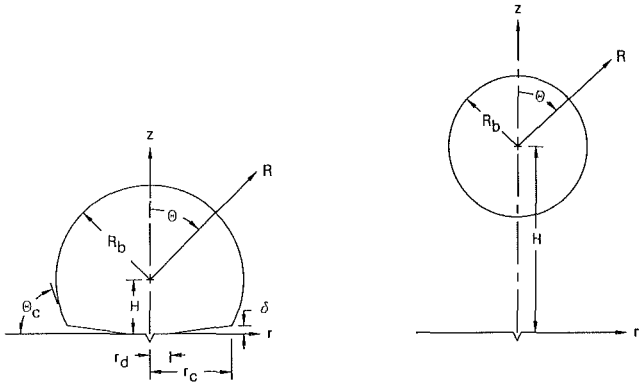

Fig. 1 Bubble geometry during growth and departure

$$P' = P + z_\eta/rJ, \qquad Q' = Q - z_\xi/rJ$$
$$P'' = P - z_\eta/rJ, \qquad Q'' = Q + z_\xi/rJ$$

The finite difference representation of equations (3)–(5) used a fully implicit forward time, central space formulation that was solved, again, using successive overrelaxation by lines.

The vorticity boundary conditions arise from the no-slip velocity condition that was imposed on both the wall and the liquid–vapor interface. A modified form of the technique of Israeli (1970) was employed where the boundary vorticity is iteratively updated according to

$$\omega_{\text{wall}}^{m+1} = \omega_{\text{wall}}^{m} + \Omega |\omega_{\max}/V_0| V_T \tag{6}$$

where Ω is an acceleration parameter, V_0 the stagnation point velocity of the bubble, and V_T the current iteration step tangential velocity. The vorticity along the line of symmetry, the outer boundary, and the dry spot contact point is taken to be zero.

The stream function along the line of symmetry above the bubble is zero, while along the bubble cap

$$\psi = -R_b^2[(H \sin^2\theta)/2 + \dot{R}_b(1-\cos\theta)] \tag{7}$$

The velocity along the microlayer–vapor interface was assumed to be zero, which makes the stream function along the microlayer and bottom wall equal to $\psi(\theta = \pi - \theta_c)$ as found from equation (7). The stream function along the outer boundary is $\psi_{\max}(1-\cos\theta)$ by assuming purely radial flow caused by bubble growth.

The temperature boundary conditions are $T=1$ along the wall, $T=T_g$ along the bubble, and zero temperature gradient along the line of symmetry. The far-field boundary condition is that provided by one-dimensional conduction into a semi-infinite medium.

The initial conditions are, physically, difficult to ascertain and explain much of the uncertainty in experimental measurements at this microscopic level. The initial velocity is taken to be everywhere zero, and the initial temperature field is assumed to be that given by one-dimensional conduction into a semi-infinite medium. The time (t_w^+) before bubble growth begins was determined using the criterion that growth occurs when the fluid temperature at the bubble height from the wall equals the bubble temperature. The resulting transcendental equation is

$$T_{\text{sat}}^+\left(1 + \frac{2\sigma v_{fg,\text{sat}} \sin\theta_c}{r_n^+ h_{fg}}\right) =$$
$$\text{erfc}\,[r_n^+(1+\cos\theta_c)/2\sin\theta_c(\alpha t_w^+)^{1/2}](T_{\text{wall}}^+ - T_\infty^+) + T_\infty^+ \tag{8}$$

The nucleation cavity radius (r_n^+) chosen for the simulations was the minimum size that would be active.

An extremely important task that must be performed throughout the development of any numerical model is comparison to experimental data, exact solutions, or previous benchmark numerical simulations. Unfortunately, the accurate experimental data associated with nucleate boiling (at the level of a nucleation site) are primarily restricted to measurements of bubble growth rate, where there is considerable scatter. While this comparison was made, an independent measure of the accuracy of the finite difference representation was required. For this reason, numerical experiments were performed based on simpler problems, but with as many of the physical characteristics of the nucleate boiling problem as possible. The three sets of tests that were performed were as follows: (*i*) Stokes' flow motion of a sphere toward a plane wall; comparison to exact solution of Brenner (1961), (*ii*) uniform, steady flow past a stationary sphere at Reynolds numbers from 0.01 to 300, including the isothermal sphere heat transfer problem; comparison to numerous benchmark numerical and experimental data, and (*iii*) impulsively started motion of a sphere in an infinite medium compared to impulsively started flow past a stationary sphere. In all cases the results were within 1 percent of the appropriate comparison solution, thus validating the fundamental accuracy of the computational code. The reader is referred to Lee (1987) for a detailed discussion of these test cases.

Nucleate Boiling Model

The significant assumptions utilized in making a simulation tractable were: (*i*) constant properties, (*ii*) bubble thermodynamic equilibrium, (*iii*) negligible evaporative resistance, (*iv*)

Nomenclature

C_D = drag coefficient = $-F_z/(\pi\rho_l U^{*2} D^{*2}/8)$
C_p = pressure coefficient
D^* = characteristic length = $[\sigma/g(\rho_l - \rho_{g,\text{sat}})]^{1/2}$
g = gravitational acceleration
h = enthalpy
H = distance from wall to center of bubble
J = Jacobian of the transformation = $r_\xi z_\eta - r_\eta z_\xi$
K = liquid thermal conductivity
$\dot{m}$ = mass transfer rate
Nu = Nussselt number = $q'' D^*/K(T_{\text{wall}}^+ - T_{\text{sat}}^+)$
p = pressure
P = transformation weighting function
Pe = Peclet number = Re • Pr
q = heat transfer rate
q'' = heat flux
Q = transformation weighting function; energy
r, z = cylindrical coordinates
R_b = bubble radius
Re = Reynolds number = $U^* D^*/\nu$
t = time
T = temperature = $(T^+ - T_{\text{sat}}^+)/(T_{\text{wall}}^+ - T_{\text{sat}}^+)$
u = radial cylindrical velocity = ψ_z/r
U^* = characteristic velocity = ν/D^*
U_c = contravariant ξ velocity = $r_\eta(z_t - v) + z_\eta(u - r_t)$
v = vertical velocity = $-\psi_r/r$; specific volume
V_c = contravariant η velocity = $r_\xi(v - z_t) + z_\xi(r_t - u)$
$\mathcal{V}$ = volume
α = transformation coefficient = $r_\eta^2 + z_\eta^2$
β = transformation coefficient = $r_\xi r_\eta + z_\xi z_\eta$
γ = transformation coefficient = $r_\xi^2 + z_\xi^2$
δ = microlayer leading edge thickness
η, ξ = transformed coordinates
θ = angular spherical coordinate
θ_c = bubble "contact" angle
ν = kinematic viscosity
ρ = density
σ = surface tension
ψ = stream function
ω = vorticity = $u_z - v_r$
Ω = relaxation parameter

Subscripts

b = bubble value
fg = change in property from liquid to vapor
g = gas value
l = liquid value
ml = microlayer value
sat = value at saturation conditions
wall = value at the wall
∞ = value at infinity

Superscripts

$+$ = dimensional variable

isothermal wall, (*v*) negligible free convection, (*vi*) no-slip velocity boundary condition around the bubble, and (*vii*) specified bubble and microlayer shape.

The energy for bubble growth is found from an integration over the bubble surface of the energy conducted from the bulk fluid

$$\dot{m}h_{fg} = K\int_A T_n^+ dA = q_b \tag{9}$$

with the energy conducted through the dry spot neglected. The volumetric change of the bubble is found through a mass balance

$$(\rho_g \forall_b)_t = \dot{m} \tag{10}$$

The remaining equations necessary to find the bubble radius (R_b^+) as a function of time are the linearized Clasius–Clapeyron equation

$$T_g^+ = T_{\text{sat}}^+ [1 + (p_g - p_{\text{sat}})v_{fg,\text{sat}}/h_{fg,\text{sat}}] \tag{11}$$

and Laplace's equation to determine the pressure increase across the liquid–vapor interface

$$p_g - \bar{p} = 2\sigma/R_b^+ \tag{12}$$

where $\bar{p}$ is the area-averaged external pressure. Equations (9)–(12) and the ideal gas equation of state represent five equations with five unknowns, coupled with the external solution.

Specification of the microlayer geometry shown in Fig. 1 requires the leading edge thickness (δ^+) and the dry spot radius (r_d^+). The leading edge thickness has been characterized both experimentally and theoretically as equal to the hydrodynamic displacement thickness immediately outside of the microlayer, which leads to the relationship

$$\delta^+ = C[\nu t^+]^{1/2} \tag{13}$$

The value of C has been reported to be from 0.3 to 1.3 (Cooper and Lloyd, 1969; Van Ouwerkerk, 1971; Dwyer and Hsu, 1975; Koffman and Plesset, 1983), but values near unity are the most accepted. δ^+ was determined for the simulations using equation (13) with the proportionality constant being parametrically varied.

The dry spot radius was found by assuming that all microlayer mass transfer into the bubble comes entirely from a change of volume of the microlayer

$$q_{ml} = -\dot{m}_{ml}h_{fg} = -h_{fg}\rho_l (\forall_{ml})_t \tag{14}$$

The energy conducted to the liquid–vapor interface is found through the bulk fluid temperature solution and Fourier's law. The quantities of interest are the overall heat transfer through the bubble cap (q_θ) and the microlayer (q_{ml}). In nondimensional form

$$\overline{\text{Nu}}_\theta = \frac{q_\theta}{K(T_{\text{wall}}^+ - T_{\text{sat}}^+)\pi D^*} = 2R_b^2 \int_0^{\pi-\theta_c} \text{Nu}_\theta \sin\theta d\theta \tag{15}$$

and

$$\overline{\text{Nu}}_{ml} = \frac{q_{ml}}{K(T_{\text{wall}}^+ - T_{\text{sat}}^+)\pi D^*} = 2\int_{r_d}^{r_c} \text{Nu}_{ml}\, rdl \tag{16}$$

where l is the coordinate along the microlayer–vapor interface and $\text{Nu}_{ml}(r = r_d)$ is set equal to 0 because it must be nearly that value inside the dry spot.

An important parameter in nucleate boiling is the departure diameter of the bubble determined by a balance of the buoyancy, drag, dry spot excess pressure, and surface tension forces. The approximation of a wedgelike microlayer is adequate for numerical calculation of the heat transfer, but at departure the actual contact angle (ϕ) must be between that shown in Fig. 1 and $\pi/2$, and was taken to be $\pi/4$. The uncertainty in the value of ϕ would be significant except that the dominant forces at departure are the buoyancy and drag forces. The resulting force balance is

$$(\rho_g \forall_b z_{c,t}^+)_t = \forall_b g(\rho_l - \rho_g) - \pi r_d^+ \sigma(2\sin\phi - 1) - \pi\rho_l U^{*2} D^{*2} C_D/8 \tag{17}$$

where z_c^+ is the center of mass of the bubble. Departure occurs when the forces balance to zero, after which the bubble position is found by a numerical integration.

The pressure distribution around the bubble is ascertained from a line integration of the primitive equations. An integration along the line of symmetry from infinity to the bubble stagnation point z_0 gives the stagnation point pressure

$$C_{p,0} = -V_0^2 + \int_{z_0}^{\infty} (4\omega_r/\text{Re} + 2v_t)_{r=0}\, dz \tag{18}$$

where V_0 is the stagnation point velocity. The pressure distribution around the bubble cap can be found most easily by using a spherical coordinate system that moves with the bubble center, resulting in

$$C_p(\theta) = C_{p,0} + 2R_b\{\ddot{H}(1 - \cos\theta) + \int_0^\theta [(\omega_R + \omega/R)/\text{Re} - \dot{R}_b\omega]_{R=R_b} d\theta\} \tag{19}$$

A boundary layer type of assumption that the pressure is only a function of r in the microlayer results in

$$C_p(r) = C_p(\theta = \pi - \theta_c) + 2/\text{Re}\int_{r_c}^{r} \omega_z \text{dr} \tag{20}$$

where $C_p(\theta = \pi - \theta_c)$ is determined from equation (19).

The drag force is determined through an integration of the pressure and viscous forces around the bubble, leaving out the buoyancy and excess pressure forces at the dry spot, which are treated as separate quantities in the force balance (equation (17)). The pressure drag coefficient for the bubble cap is

$$(C_{Dp})_\theta = 4R_b^2 \int_0^{\pi-\theta_c} C_p(\theta)\sin 2\theta d\theta \tag{21}$$

and for the microlayer is

$$(C_{Dp})_{ml} = -8\int_{r_d}^{r_c} C_p(r) r dr \tag{22}$$

where $C_p(\theta)$ and $C_p(r)$ are evaluated using equations (19) and (20), respectively. The friction drag coefficient for the bubble cap is found through an integration of the viscous stress, resulting in

$$(C_{Df})_\theta = 16R_b^2/\text{Re}\left[(1 - \cos 2(\pi - \theta_c))\dot{R}_b/R_b + \int_0^{\pi-\theta_c} \omega\Big|_{R=R_b} \sin^2\theta d\theta\right] \tag{23}$$

The total drag coefficient is then found by summing the above three components ($(C_{Dp})_\theta$, $(C_{Dp})_{ml}$, $(C_{Df})_\theta$).

Results and Discussion

The saturated nucleate boiling situation that was chosen for simulation was water at 1 atm and 8.5 K wall superheat. Water was chosen due to its obvious engineering importance, and the 8.5 K wall superheat makes available the bubble growth data of Staniszewski (1959). The "contact" angle (θ_c) was given a constant value of 60 deg, which provides the best agreement between the bubble shape shown in Fig. 1 and experimental measurements for water (cf. Han and Griffith, 1965).

Two parametric cases were investigated to quantify the impact of the assumed microlayer growth model. One case used the most widely accepted value ($C \sim 1.0$) for the growth constant in equation (13), while the other case used a reasonable lower limit ($C \sim 0.55$).

The computational grid changes dramatically during the course of the simulation, and an indication of the extreme grid spacing variation is provided in Fig. 2. Although the spacing

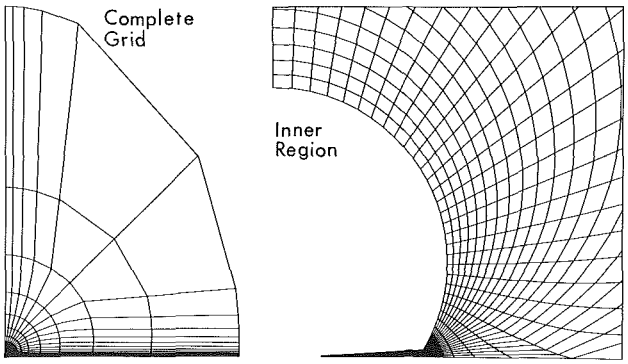

Fig. 2 Computational grid during early growth stage

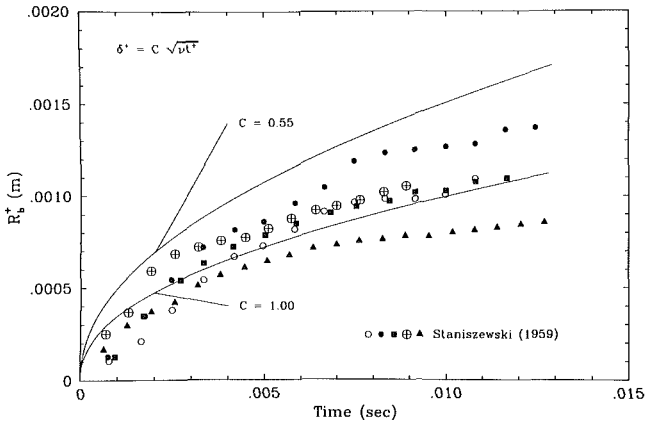

Fig. 3 Bubble growth compared to experimental data

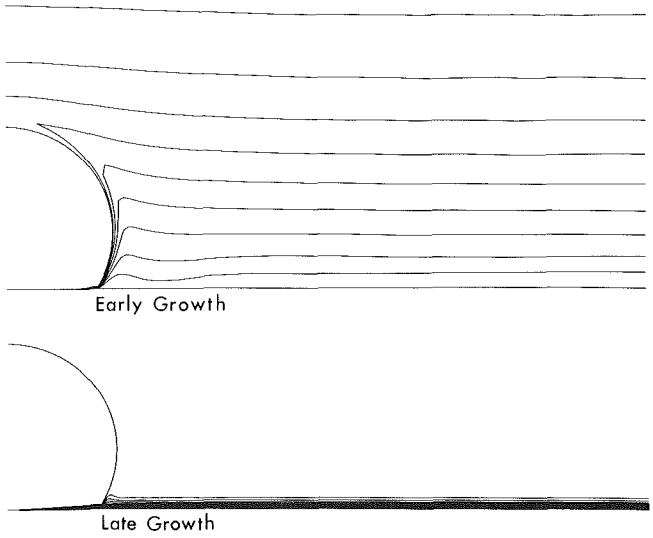

Fig. 4 Isotherms during bubble growth

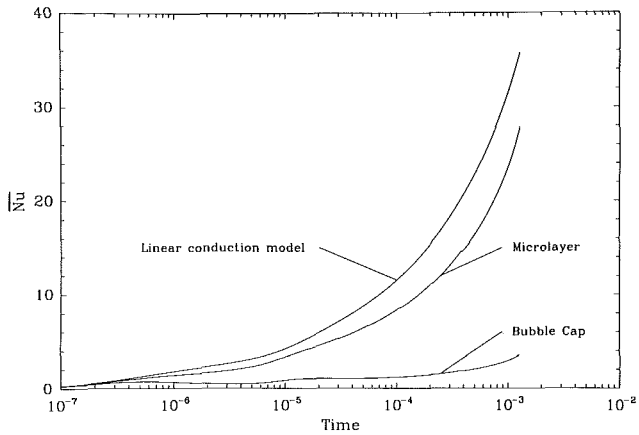

Fig. 5 Average heat transfer rates through the bubble

seems rather coarse near the outer boundary, it is appropriate because the nodes are clustered in regions with large thermal gradients.

The numerical bubble growth rates are compared to the experimental data of Staniszewski (1959) in Fig. 3. There is considerable scatter in the experimental data, although the individual growth curves are well behaved. The best agreement is where the microlayer growth constant was 1.0. For $C = 0.55$, the bubble grows significantly larger, which indicates that the microlayer provides a significant portion of the energy for bubble growth. All numerical results presented from this point are for the base parametric case ($C = 1.0$), unless otherwise indicated.

An indication of the thermal field around the bubble during growth is provided in Fig. 4. Because the bubble represents an isothermal sink in a nonuniform temperature field, the isotherms near the bubble do not uniformly surround the bubble in a boundary-layer-type manner. The folding of isotherms occurs in a thin layer near the bubble and would be very difficult to resolve experimentally, leading, perhaps, to the conclusion drawn by Beer et al. (1977) that the bubble is nonisothermal. For this boiling situation the bubble quickly grows out of the wall thermal boundary layer, with a small portion of the boundary layer wrapping around the cap. During the majority of the growth, however, there is essentially no wrapping of the wall thermal boundary layer around the bubble and the bubble cap heat transfer is essentially restricted to that portion still within the wall boundary layer. This result brings into question those growth models that assume uniform heat transfer around the bubble cap.

The overall energy for bubble growth comes from both the bubble cap and the microlayer, and the average heat transfer from these two regions is shown in Fig. 5. It is evident that the majority of the energy comes from the microlayer; in fact, it contributes nearly 90 percent of the energy for bubble growth for this boiling situation. The dominant importance of microlayer heat transfer explains the impact microlayer thickness has on bubble size. The simplest approach to microlayer heat transfer is to assume one-dimensional steady-state heat conduction and a uniform microlayer thickness of $\delta/2$, which are the assumptions made by Cooper (1969). This leads to the result

$$\overline{Nu}_{ml} \simeq 2(r_c^2 - r_d^2)(1 - T_g)/\delta \qquad (24)$$

which, using simulation values for the variables, is shown along with the numerical results in Fig. 5. The agreement is close enough to warrant the conclusion that microlayer heat capacity is not a significant variable.

Departure proved to be essentially a balance between drag and buoyancy forces, with surface tension forces being an order of magnitude smaller. The departure stage of the ebullition cycle is the most difficult period to simulate accurately because the bubble departs markedly from spherical or truncated spherical shape. The drag calculation during and following departure proved to be very unstable, and the predicted departure diameter of 3.7×10^{-3} m is outside Staniszewski's measured data range of 1.8×10^{-3} to 2.8×10^{-3} m. The ad hoc procedure that was employed during the departure stage was to limit the change in vertical velocity to stabilize the drag calculation, resulting in a slower departure than the force balance called for, but the uncertainty in the shape of the bubble makes more accurate calculation of the vertical velocity su-

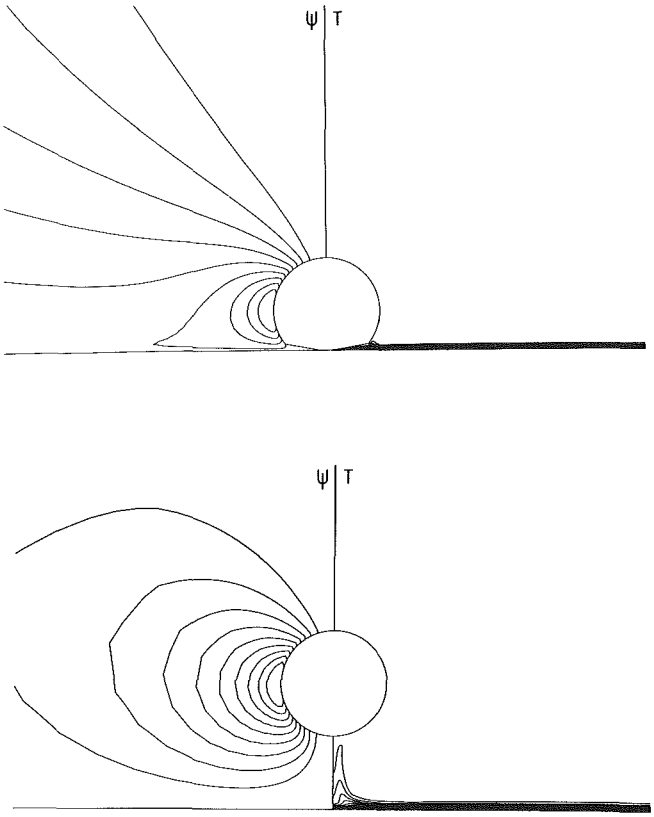

Fig. 6 ψ and T contours during and after departure

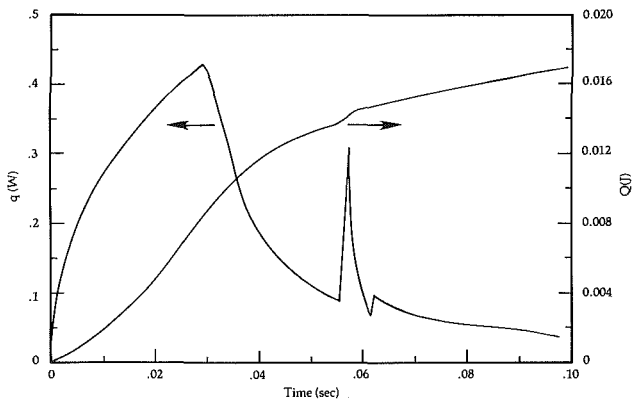

Fig. 7 Excess wall heat transfer and energy

perfluous. The shape of the bubble during departure was modified to satisfy the location of the center of mass by increasing the thickness of the microlayer until the heat transfer in that region became insignificant, and then decreasing the "contact" angle.

The flow and thermal fields during and after departure are shown in Fig. 6. An interesting feature is that the wall scavenging effect caused by departure is limited to the region immediately beneath the bubble, with the maximum effect occurring a small distance from the centerline. The simulation was terminated when the bubble was 2.4 bubble radii from the wall (3.6×10^{-2} s after the bubble had departed) at which time the Reynolds number ($2H^+R_b^+/\nu$) was 1500. An application of the nucleation criteria used to begin the simulation results in a new bubble growing almost immediately following departure when the bubble is only 1.02 bubble radii from the wall. This is not realistic, and results from uncertainty in both the actual nucleation criteria and the numerical results during departure.

Ultimately, the most important value in nucleate boiling is the wall heat transfer. The overall, excess heat transfer rate will be defined as

$$q_{\text{excess}} = 2\pi \int_0^\infty (q'' - q_0'')r^+ dr^+ \tag{25}$$

where q_0'' is the heat transfer that would exist if there were no nucleate boiling. The overall excess energy as a function of time from incipience of growth is defined as

$$Q_{\text{excess}} = \int_0^{t^+} q_{\text{excess}} dt^+ \tag{26}$$

which is a clearer measure of the enhanced heat transfer associated with the nucleate boiling bubble.

The excess heat transfer, along with the overall excess energy, for the simulation is shown in Fig. 7. Due to uncertainties about the point of departure and the subsequent bubble shape and position, the results after the start of departure should be viewed with caution, particularly with respect to the time scales. The first peak in heat transfer is due to the beginning of departure when the microlayer is destroyed, while the second sharp peak in heat transfer is due to the bubble leaving the wall. Although the magnitude of the second peak is probably too large due to numerical uncertainties, its existence is in agreement with experimental temperature measurements beneath a nucleate boiling bubble (cf. Rohsenhow, 1973) that show a small dip in wall temperature at departure. The majority of the energy (87% of the value at the end of the simulation) is provided up to the point of departure, with the remaining energy being due to enhanced convection and transient conduction. Of the energy up to departure, virtually 100 percent is transferred through that portion of the wall comprising the microlayer, pointing to the complete unimportance of microconvection. Keeping in mind that the microlayer provided nearly 90 percent of the energy for bubble growth, it is evident that the microlayer is the dominant mechanism in terms of both bubble growth and the enhanced wall heat transfer.

Concluding Remarks

The major purpose of the numerical simulations was to present a self-consistent formulation that would enable both a qualitative indication of the thermal and fluid fields during bubble growth and departure, and a quantitative comparison of the contributions of the micromechanisms to bubble growth and overall wall heat transfer.

For the conditions simulated, the microlayer proved to be the dominant micromechanism. It provided 90 percent of the energy for bubble growth, and 87 percent of the overall enhanced heat transfer. The enhanced convective heat transfer effects during growth (microconvection) proved to be essentially nonexistent, while the enhanced heat transfer following departure (a combination of enhanced convective effects and transient conduction) provided only 13 percent of the excess heat transfer. There are nucleate boiling problems where microlayer evaporation will not be the dominant mechanism, particularly at high pressures and boiling from small wires. For these cases, the picture of bubble cap heat transfer provided here is of interest. The usual model assumes that the heat transfer is uniform around the bubble cap, but the present results do not support that hypothesis and show that the portion of the bubble cap involved in heat transfer changes significantly during the growth period.

Acknowledgments

The work was performed as part of the Ph.D. dissertation of the first author while at the University of Wyoming.

References

Beer, H., Burow, P., and Best, R., 1977, "Bubble Growth, Bubble Dynamics, and Heat Transfer in Nucleate Boiling, Viewed With a Laser Interferometer," *Heat Transfer in Boiling*, E. Hahne and U. Grigull, eds., Academic Press, New York, pp. 21–52.

Brenner, H., 1961, "The Slow Motion of a Sphere Through a Viscous Fluid Toward a Plane Surface," *Chemical Engineering Science*, Vol. 16, pp. 242–251.

Cooper, M. G., and Lloyd, A. J. P., 1969, "The Microlayer in Nucleate Pool Boiling," *Int. J. Heat Mass Transfer*, Vol. 12, pp. 895–913.

Cooper, M. G., 1969, "The Microlayer and Bubble Growth in Nucleate Pool Boiling," *Int. J. Heat Mass Transfer*, Vol. 12, pp. 915–933.

Dalle Donne, M., and Ferranti, M. P., 1975, "The Growth of Vapor Bubbles in Super-heated Sodium," *Int. J. Heat Mass Transfer*, Vol. 18, pp. 477–493.

Dwyer, O. E., and Hsu, C. J., 1975, "Liquid Microlayer Thickness in Nucleate Boiling on a Heated Surface," *Letters Heat Mass Transfer*, Vol. 2, No. 2, pp. 179–187.

Fath, H. S., and Judd, R. L., 1978, "Influence of System Pressure on Microlayer Evaporation Heat Transfer," ASME JOURNAL OF HEAT TRANSFER, Vol. 100, pp. 49–55.

Fath, H.E.-B.S., 1981, "Microlayer Formation, Evaporation and Bubble Growth in Nucleate Boiling," Ph.D. Dissertation, McMaster University.

Guy, T. B., and Ledwidge, T. J., 1973, "Numerical Approach to Non-spherical Vapour Bubble Dynamics," *Int. J. Heat Mass Transfer*, Vol. 16, pp. 2393–2405.

Han, C. Y., and Griffith, P., 1965, "The Mechanism of Heat Transfer in Nucleate Pool Boiling—Part I. Bubble Initiation, Growth and Departure," *Int. J. Heat Mass Transfer*, Vol. 8, pp. 887–904.

Hsu, Y. Y., and Graham, R. W., 1961, "An Analytical and Experimental Study of the Thermal Boundary Layer and Ebullition Cycle in Nucleate Boiling," NASA TN D-594.

Israeli, M., 1970, "A Fast Implicit Numerical Method for Time Dependent Viscous Flows," *Studies in Applied Math*, Vol. 49.

Judd, R. L., and Hwang, K. S., 1976, "A Comprehensive Model for Nucleate Pool Boiling Heat Transfer Including Microlayer Evaporation," ASME JOURNAL OF HEAT TRANSFER, Vol. C98, pp. 623–629.

Koffman, L. D., and Plesset, M. S., 1983, "Experimental Observations of the Micro-layer in Vapor Bubble Growth on a Heated Surface," ASME *Journal of Heat Transfer*, Vol. 105, pp. 625–632.

Lee, R. C., 1987, "Investigation of the Mechanism of Nucleate Boiling Through Numerical Modelling," Ph.D. Dissertation, University of Wyoming.

Madhaven, S., and Mesler, R., 1970, "A Study of Vapor Bubble Growth on Surfaces," *Heat Transfer 1970*, Vol. 5, Elsevier, Amsterdam.

Mikic, B. B., Rohsenhow, W. M., and Griffith, P., 1970, "On Bubble Growth Rates," *Int. J. Heat Mass Transfer*, Vol. 13, pp. 657–666.

Rohsenow, W. M., 1973, "Boiling," *Handbook of Heat Transfer*, McGraw-Hill, New York.

Staniszewski, B. E., 1959, "Nucleate Boiling Bubble Growth and Departure," M.I.T. DSR Project No. 7-7673, Technical Report No. 16.

Thompson, J. F., Thames, F. C., and Mastin, C. W., 1974, "Automatic Numerical Generation of Body-Fitted Curvilinear Coordinate System for Field Containing Any Number of Two-Dimensional Bodies," *J. Comp. Physics*, Vol. 15, pp. 299–319.

Van Ouwerkerk, H. J., 1971, "The Rapid Growth of a Vapour Bubble at a Liquid–Solid Interface," *Int. J. Heat Mass Transfer*, Vol. 14, pp. 1415–1431.

Van Stralen, S. J. D., 1966, 1967, "The Mechanism of Nucleate Boiling in Pure Liquids and in Binary Mixtures, Parts I–IV," *Int. J. Heat Mass Transfer*, Vol. 9, pp. 995–1020, 1021–1046, Vol. 10, pp. 1469–1484, 1485–1498.

Van Stralen, S. J. D., Sohal, M. S., Cole, R., and Sluyter, W. M., 1975, "Bubble Growth Rates in Pure and Binary Systems: Combined Effect of Relaxation and Evaporation Microlayers," *Int. J. Heat Mass Transfer*, Vol. 18, pp. 453–467.

Voutsinos, C. M., and Judd, R. L., 1975, "Laser Interferometric Investigation of the Microlayer Evaporation Phenomenon," ASME JOURNAL OF HEAT TRANSFER, Vol. 97, No. 1, pp. 88–92.

Zijl, W., Ramakers, F. J. M., and Van Stralen, S. J. D., 1979, "Global Numerical Solutions of Growth and Departure of a Vapour Bubble at a Horizontal Superheated Wall in a Pure Liquid and a Binary Mixture," *Int. J. Heat Mass Transfer*, Vol. 22, pp. 401–420.

The Peak Boiling Heat Flux in Saturated Ethanol–Water Mixtures

R. P. Reddy
Graduate Assistant.
Student Mem. ASME

J. H. Lienhard
Professor.
Fellow ASME

Heat Transfer/Phase-Change Laboratory,
Mechanical Engineering Department,
University of Houston,
Houston, TX 77204-4792

The present work provides original measurements of the burnout heat flux in saturated ethanol–water mixtures, over the full range of concentrations. These data were obtained at atmospheric pressure on horizontal cylinders, ranging from 0.51 to 2.16 mm in diameter. They reveal significant improvements of the peak heat flux for mixtures, over that which would be expected from pure fluids with the properties of the mixture. This improvement is most pronounced at low ethanol mass fractions. McEligot has suggested that the improved heat flux results from a subcooling created by selective distillation at the liquid–vapor interface. Combining this idea with a recent correlation of subcooled burnout, we estimate the extent of effective subcooling qualitatively and discuss the use of this estimate to correlate burnout in binary mixtures. Two dimensionless groups are proposed to characterize this effective subcooling, both based on appropriate characterizations of the phase equilibrium diagram.

Introduction

Boiling in mixtures has been a concern for almost as long as boiling itself has been an active subject of study; the need to understand the *burnout* heat flux, q_{max}, in mixtures has been a major theme from the beginning. This need has been driven by the ubiquitous presence of mixtures in the chemical and process industries.

Reddy (1987) provides a fairly complete critical review of the literature on burnout in binary mixtures since 1941. We provide a brief summary of that review here:

Bonilla provided the first systematic study of boiling in mixtures almost a half century ago. Bonilla and Perry (1946) boiled binary mixtures of water, various alcohols, and acetone (in several combinations) on 9.1 and 6.65-cm-dia flat plate heaters. Additional mixture data by Cichelli and Bonilla (1946) and Bonilla and Eisenberg (1948) signaled to the world that such data displayed certain anomalies and were hard to reproduce.

Van Stralen produced extensive data on small horizontal cylinders in a variety of organic liquid mixtures and aqueous solutions during the 1950's (see Vos and Van Stralen, 1956; Van Wijk et al., 1956; and Van Stralen, 1956, 1959). He noted that burnout could be dramatically increased with small concentrations of alcohol in water. Van Stralen returned to the field later (see Van Stralen, 1966, 1970, and Van Stralen and Sluyter, 1969) with other suggestions for analyzing q_{max} in mixtures. These suggestions have proved to have limited value, for reasons that become apparent subsequently.

Meanwhile, many other observers (Jordan and Leppert, 1959; Dunskus and Westwater, 1961; Huber and Hoehne, 1962; Carne, 1963, 1964; Sterman et al., 1966; Grigor'ev et al., 1968; Wright and Colver, 1968; Van Stralen and Sluyter, 1969) added to the fund of burnout data using a variety of binary organic and aqueous mixtures, on a variety of heaters. Under certain conditions, many of these investigators found a phenomenon that had particularly caught Van Stralen's attention. That was the fact that, in many mixtures, q_{max} reached a local maximum at a low concentration of one component.

Unfortunately, much of the interpretation offered in these studies suffered because the influential roles of geometry and of geometric scale on burnout had not yet been identified or properly diagnosed. The work of Lienhard and several others—notably Wong, Sun, Bakhru, and Dhir (see, e.g., Lienhard and Dhir, 1973)—during the 1960s and early 1970s finally established two things about burnout in single-phase liquids:

1 The hydrodynamic processes that give rise to burnout cease to occur, and so too does the multivalued character of the boiling curve, when the Laplace number, $R' \equiv R(g[\rho_f - \rho_g]/\sigma)^{1/2}$, is reduced below a value on the order of 0.1, where R is a characteristic dimension of the heater (see, e.g., Bakhru and Lienhard, 1972).

2 When R' is greater than about 1/10, an appropriately nondimensionalized q_{max} varies systematically with R'; and does so in a different way in each of the geometric heater configurations.

There was not yet any basis for separating out the influence of geometry on q_{max} when most of the data were obtained during the 1950s and 60s; yet those influences were present, and many of the data fell in regions of low R'. Therefore, most attempts at interpreting the role of composition were muddied by the unrecognized influences of configuration and geometric scale on burnout.[1]

Two particularly important insights nevertheless did emerge during this period. First, Carne (1964) questioned the use of the equilibrium latent heat of vaporization, h_{fg}. Figure 1 shows a typical phase-equilibrium diagram for a binary azeotropic mixture. The equilibrium h_{fg} is the enthalpy difference between the liquid and vapor at the same temperature. Carne suggested that a flash evaporation process occured at constant *composition* during boiling. This being the case, the appropriate latent heat would be $h_{fg,1}$, the enthalpy difference between liquid and vapor at the same composition. This is sometimes called the "integral latent heat." While it is doubtful that pure flash evaporation occurs during boiling, Thome (1983) subsequently argued that the actual process lies somewhere *between* equilibrium and flash evaporation.

McEligot (1964) provided the second important step toward understanding binary boiling when he noted that evaporation from a liquid–vapor interface leaves the liquid phase at a higher temperature than that at which the vapor condenses.

Contributed by the Heat Transfer Division and presented at the ASME/AIChE National Heat Transfer Conference, Houston, Texas, July 24-27, 1988. Manuscript received by the Heat Transfer Division April 28, 1988. Keywords: Boiling, Phase-Change Phenomena.

[1] The burnout process in a mixture, while it differs in some features from that in a single-component fluid, still involves the same basic hydrodynamic breakdown. Our visual observation of the vapor-removal pattern supports this. We therefore assume R' still correctly compares the buoyant and surface tension forces that are the key to that breakdown; and the criterion, $R' < 0.1$, defines the breakdown in both mixtures and single-component liquids.

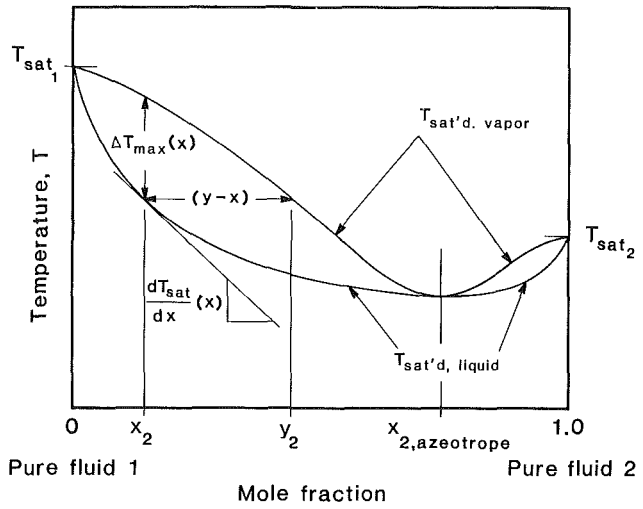

Fig. 1 Schematic phase-equilibrium diagram for a typical binary azeotropic mixture, showing nomenclature

The surrounding liquid—at the original concentration—is thus colder than the temperature at which the liquid actually evaporates. The resulting subcooling is greatest at low alcohol concentrations (owing to the shape of the ethanol-water phase-equilibrium diagram) and so too is the heat flux augmentation.

The idea of this sort of induced subcooling can only be made useful when two things are known. One is the *magnitude* of the induced subcooling and the other is its *effect* on the burnout heat flux. McEligot had access to neither. Indeed, it was not until very recently that Elkassabgi and Lienhard (1988) provided mechanistic accounts (as well as correlations based upon them) of the various influences of subcooling on burnout in pure fluids. The extent of induced subcooling in the interface remains unpredictable. A third piece of information that is also needed is the path of the evaporation process on the phase-equilibrium diagram. Thome's and Shock's (1984) study, 20 years later, provided a cogent discussion of these problems.

Kutateladze et al. (1966) pointed out another element that must be taken into account in binary boiling, namely the shape of the phase-equilibrium diagram. A glance at the diagram tells us that a variety of pairs of information will characterize the diagram completely. If we identify the liquid and vapor mole fractions of component 1 as x and y, respectively, then $T(x)$ and $T(y)$ would be such a pair, but the complete function would be unmanageable. Kutateladze correlated data with an expression of the following form, which characterizes the role of the equilibrium phase diagram:

$$\mathrm{Ku} = f([y-x]/[y-x]_{\max}) \tag{1}$$

The term $(y-x)$ is the isothermal difference between y and x and $(y-x)_{\max}$ is the maximum value that $(y-x)$ can reach on the diagram. The Kutateladze number, Ku, is defined as

$$\mathrm{Ku} \equiv \frac{q_{\max}}{h_{fg}\rho_g^{1/2}[g\sigma(\rho_f-\sigma_g)]^{1/4}} \tag{2}$$

(The denominator of equation (2) is proportional to the Zuber (1958)/Kutateladze (1950) prediction/correlation for $q_{\max}$.) Afgan (1966) also used the more limited expression, $\mathrm{Ku} = f(y-x)$, to correlate data. Of course, neither Afgan nor Kutateladze yet had any way to isolate the influence of geometry in their correlations.

Van Stralen (1970) noted that $q_{\max}$ was maximum where the quantity

$$(x-y)\frac{\Delta T_{\mathrm{sat}}}{\Delta x} \tag{3}$$

was maximum. ΔT_{sat} is the increase of the liquid saturation temperature resulting from the reduction of concentration, Δx, caused by evaporation at the interface. Since these increments are not known, we would prefer to write them as a derivative, and in so doing obtain another, albeit dimensional, characterization of the phase-equilibrium diagram

$$(x-y)\frac{dT_{\mathrm{sat}}}{dx} \tag{4}$$

After the mid-1960s, work on burnout in binary mixtures slacked off. The issue did not go away, but the flow of new ideas abated. Ishiki and Nikai (1972) provided more data, but in a range of R' less than 0.1. Matorin (1973), Gaidarov (1975), and Stephen and Preusser (1979) presented additional data and suggested empirical correlations. Frea et al. (1977)

Nomenclature

c_p = specific heat at constant pressure for the boiled liquid
g = gravitational acceleration
h_{fg}, $h_{fg,1}$ = latent heat of vaporization at constant temperature; "integral" or constant-composition latent heat of vaporization
Ja, Ja_c = volumetric Jakob number $= \rho_f c_p \Delta T_{\mathrm{sub}}/\rho_g h_{fg}$; modified volumetric Jakob number based on an effective subcooling (see equation (9))
Ku = Kutateladze number defined in equation (2)
Pe = an effective Peclet number, defined in equation (7)
$q_{\max}$, $q_{\max,\mathrm{SL}}$ = peak or "burnout" heat flux in saturated boiling; Sun and Lienhard's $q_{\max}$, equation (8)
$q_{\max,\mathrm{sub}}$ = $q_{\max}$ in subcooled boiling
R = radius of heater
R' = Laplace number $= R[g(\rho_f-\rho_g)/\sigma]^{1/2}$
T, T_{sat}, T_w = temperature, saturated liquid temperature, temperature of the wall of a heater
x = mole fraction of ethanol in the liquid phase
y = mole fraction of ethanol in the vapor phase when x is the mole fraction in the liquid phase
α = thermal diffusivity of boiled liquid
$\Delta q_{\max,\mathrm{sub}}$ = $q_{\max} - q_{\max,\mathrm{SL}}$
ΔT, $\Delta T_{\max}$, ΔT_{sub} = $T_w - T_{\mathrm{sat}}$; $T_g(x) - T_f(x)$ (see Fig. 1); $T_{\mathrm{sat}} - T_{\mathrm{bath}}$
ρ_f, ρ_g = saturated liquid and vapor densities, respectively
σ = surface tension

Subscripts

1, 2 = denoting the two components of a binary mixture
f, g = denoting the saturated liquid and vapor states

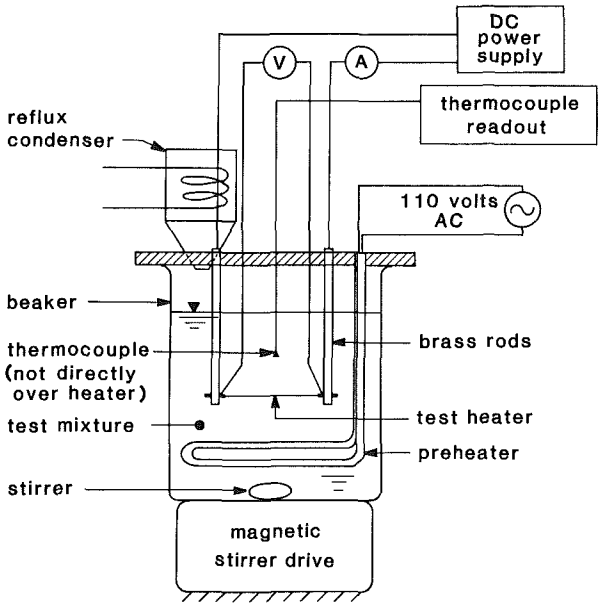

Fig. 2 Schematic diagram of the boiling apparatus

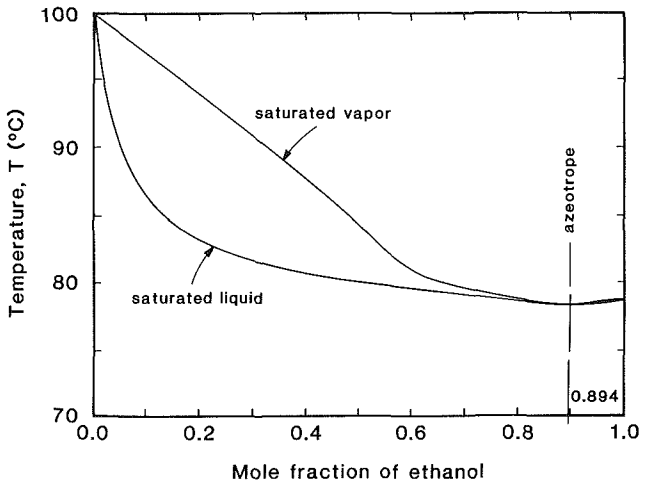

Fig. 3 The ethanol/water equilibrium phase diagram

also gave additional data, but they used a heater configuration that was subject to induced convection influences.

Thome and Shock (1984) presented a broad review of the theoretical bases of the problem, which is serving to revive interest in it. Even more recently Yang (1987) attempted to organize a new correlation of prior data that retains some of the best features of the previous ones. He nondimensionalized the characteristic temperature, equation (4), by making it into a Jakob number. He also included a Lewis number, as was suggested by Gaidarov.

The most recent contribution was Purdy and Avedisian's (1987) clean and careful experimental study of burnout in several organic mixtures. These data are important since they are the first since Cichelli and Bonilla's (1945) study on a large flat plate with vertical sidewalls. By approximating the archetypical infinite plate, Purdy and Avedisian escape geometric complications.

A close look at the accumulated literature on burnout in binary mixtures makes it clear that an accumulation of good ideas has not been fully exploited. The work of Carne, McEligot, Kutateladze, Thome, and Shock, makes it clear that:

1 Evaporation near burnout in a binary mixture is not isothermal.

2 The burnout heat flux in a binary mixture is determined in part by the shape of the equilibrium phase diagram.

3 The component process that increases the burnout heat flux in a binary mixture is subcooling of the *bulk* of the liquid *with respect to the vapor—the result of preferential evaporation* of the more volatile component at the liquid interface. (This is related to item 1.)

(The idea of an effective subcooling has also been picked up by Yue and Weber (1973, 1974) and by Marschall and Moresco (1977), who have used it to predict increased heat flux during *film* boiling in a vertical plate geometry.)

We therefore seek to obtain a well-controlled set of data that can be rationalized within these facts. We select a mixture (ethanol/water) that is well known to yield a maximum in q_{max}, and for which the best physical property information can be found. We select the geometry (a horizontal cylinder) for which behavior in single-component boiling is best documented. This gives data that stay within the size range $(0.1 \leq R' \leq 0.7)$ for which the hydrodynamic mechanisms are most clearly defined.

Experiment and Results

The experimental apparatus and procedure are straightforward, and the reader is referred to Reddy (1987) for complete details. The heater is a wire mounted in a beaker as shown in Fig. 2. The copper-plating of electrodes on the smooth wire, the inspection and cleaning procedure, and the d-c power supply are all identical to that used by Elkassabgi and Lienhard (1988) with one exception: In some cases a large d-c motor-generator set was used to reach higher currents.

The cylindrical heaters were nichrome wires with nominal diameters of 0.510, 0.767, 1.016, 1.295, and 1.626 mm; and stainless steel tubes with outer diameters of 1.803 and 2.159 mm. In all cases the active length was within a millimeter of 8 cm. The ethanol/water mixtures were premixed and the composition of the liquid bulk (away from the heater) was checked several times before and after each q_{max} observation with a GOW-MAC Gas Chromatograph. In each case, we turned the stirrer off about 30 s before making an observation. (The disappearance of significant liquid motion was affirmed by bubble movement in the tank.)

Six to eight tests were made at each condition. The probable errors in q_{max} and composition measurements were 5 percent and 1 percent, respectively. As we see in Table 1, the probable error in q_{max} compares favorably with the data scatter.

The phase equilibrium data of Chu et al. (1956), Otsuki and Williams (1956), and Hellwege (1975) for ethanol/water are represented graphically in Fig. 3. We have not plotted the data themselves, but used rational polynomial forms that fit within the accuracy of the data for use in subsequent analyses.

The 108 raw q_{max} data are reported in Table 1 and they are represented in reduced graphic form in Fig. 4 (they are also listed by Reddy (1987)). Two features of these data bear note. The smaller heaters clearly display the local maximum of q_{max} at low alcohol concentrations, while data for the larger heaters become increasingly scattered at low concentrations.

No data from previous sources could be added to this data set. In the first place, not a great deal of work has been done with the ethanol/water system. Those data that do exist represent incompletely documented experiments or R' values that are too small.

Discussion

Means for Identifying the Effective Subcooling. If, as McEligot suggested, the local maximum of q_{max} in x is caused by induced subcooling, it behooves us to evaluate that subcooling quantitatively. That can be done by comparing the in-

Table 1 A complete listing of the present burnout data

Run #	Mole Fraction Ethanol	Peak Heat Flux (MW/m^2) Mean	Std. Dev.	Mean dia. (mm)
1	0.200	1.586	0.055	0.506
2	0.195	1.238	0.028	0.797
3	0.190	1.275	0.086	1.037
4	0.258	1.548	0.056	0.502
5	0.248	1.232	0.092	0.797
6	0.238	1.241	0.044	1.034
7	0.347	1.416	0.054	0.504
8	0.343	1.228	0.041	0.799
9	0.339	1.152	0.072	1.041
10	0.461	1.176	0.030	0.504
11	0.456	1.026	0.017	0.797
12	0.452	0.990	0.043	1.036
13	0.560	1.059	0.028	0.503
14	0.559	0.927	0.031	0.790
15	0.557	0.842	0.062	1.041
16	0.660	0.939	0.013	0.502
17	0.656	0.814	0.031	0.795
18	0.651	0.753	0.025	1.026
19	0.858	0.600	0.044	0.504
20	0.856	0.564	0.014	0.793
21	0.854	0.628	0.014	1.034
22	0.750	0.693	0.021	0.501
23	0.750	0.668	0.023	0.792
24	0.750	0.666	0.015	1.036
25	1.000	0.593	0.006	0.502
26	1.000	0.550	0.013	0.790
27	1.000	0.611	0.014	1.026
28	1.000	0.544	0.022	1.265
29	1.000	0.512	0.008	1.485
30	0.936	0.586	0.032	0.502
31	0.936	0.557	0.015	0.791
32	0.936	0.616	0.007	1.017
33	0.936	0.565	0.011	1.261
34	0.936	0.541	0.008	1.484
35	0.893	0.593	0.010	0.503
36	0.893	0.583	0.016	0.791
37	0.893	0.588	0.006	1.030
38	0.893	0.587	0.008	1.264
39	0.893	0.537	0.008	1.484
40	0.000	1.532	0.105	0.502
41	0.000	1.442	0.088	1.020
42	0.000	1.643	0.165	0.787
43	0.064	1.953	0.001	0.500
44	0.058	1.535	0.086	0.792
45	0.053	1.605	0.064	1.025
46	0.133	1.691	0.054	0.500
47	0.125	1.662	0.049	0.792
48	0.118	1.614	0.048	1.027
49	0.166	1.543	0.066	0.500
50	0.161	1.418	0.081	0.792
51	0.155	1.540	0.039	1.025
52	0.028	1.794	0.251	0.501
53	0.025	1.906	0.183	0.789
54	0.022	1.879	0.257	1.026
55	1.000	0.531	0.006	1.286
56	1.000	0.509	0.014	1.622
57	1.000	0.395	0.005	2.122
58	0.799	0.566	0.015	1.286
59	0.799	0.542	0.015	1.622
60	0.799	0.402	0.003	2.122
61	0.904	0.541	0.016	1.287
62	0.904	0.526	0.011	1.618
63	0.904	0.401	0.005	2.122
64	0.657	0.688	0.015	1.287
65	0.652	0.660	0.012	1.618
66	0.648	0.654	0.003	2.122
67	0.749	0.624	0.005	1.287
68	0.749	0.585	0.004	1.617
69	0.749	0.455	0.023	2.122
70	0.527	0.861	0.017	1.285
71	0.527	0.861	0.012	1.612
72	0.526	0.880	0.037	1.821
73	0.526	0.762	0.025	2.115
74	0.465	0.926	0.028	1.286
75	0.461	0.921	0.017	1.621
76	0.458	0.990	0.038	1.821
77	0.454	0.894	0.028	2.110
78	0.319	1.065	0.027	1.267
79	0.313	1.096	0.088	1.610
80	0.307	1.295	0.022	1.820
81	0.301	1.117	0.048	2.118
82	0.141	1.278	0.034	1.289
83	0.131	1.340	0.042	1.618
84	0.122	0.943	0.026	1.821
85	0.112	0.898	0.061	2.111
86	0.252	1.165	0.026	1.261
87	0.247	1.246	0.036	1.623
88	0.242	1.267	0.044	1.822
89	0.238	1.162	0.062	2.115
90	0.000	1.411	0.264	1.287
91	0.000	1.545	0.061	1.619
92	0.000	1.349	0.036	1.819
93	0.000	1.237	0.049	2.112
94	0.184	1.306	0.022	1.286
95	0.178	1.240	0.039	1.621
96	0.172	0.964	0.121	1.821
97	0.166	0.899	0.051	2.121
98	0.092	1.333	0.063	1.286
99	0.089	1.424	0.031	1.607
100	0.086	1.176	0.030	1.821
101	0.082	1.020	0.069	2.113
102	0.035	1.070	0.077	1.288
103	0.033	1.462	0.078	1.606
104	0.032	0.734	0.042	1.821
105	0.030	0.632	0.142	2.113
106	1.000	0.390	0.015	1.821
107	0.629	0.825	0.005	1.821
108	0.364	1.189	0.020	1.821

crease of q_{max} over the conventional hydrodynamic value, with the increase of q_{max} that is predicted to occur as a consequence of subcooling.

Elkassabgi and Lienhard (1988) identified three regimes of subcooling for pure fluids: high, low and intermediate. It turns out (after the fact) that the subcoolings induced in binary boiling are all rather low. Thus the only one of their correlations of interest to us is the one for low subcooling

$$\frac{\Delta q_{max,\,sub}}{q_{max}} = 4.28\,\frac{\mathrm{Ja}}{\mathrm{Pe}^{1/4}} \tag{5}$$

where $\Delta q_{max,\,sub}$ is the increase of subcooling over the saturated value, q_{max}, and Ja is a volumetric Jakob number

$$\mathrm{Ja} \equiv \rho_f c_p \Delta T_{sub}/\rho_g h_{fg} \tag{6}$$

and Pe is an effective Peclet number,

$$\mathrm{Pe} \equiv \sigma^{3/4}/\{\alpha[g(\rho_f-\rho_g)]^{1/4}\rho_g^{1/2}\} \tag{7}$$

To find an effective ΔT_{sub} we next have to decide how much of q_{max} in a binary mixture is an excess over a "saturated" value. To obtain such an "experimental" value of $\Delta q_{max,\,sub}$, we first use the Sun–Lienhard (1970) prediction for saturated burnout

$$q_{max,\,SL} = \frac{\pi}{24}\,\rho_g^{1/2} h_{fg}[\sigma g(\rho_f-\rho_g)]^{1/4}[0.89 + 2.27\exp(-3.44R'^{1/2})] \tag{8}$$

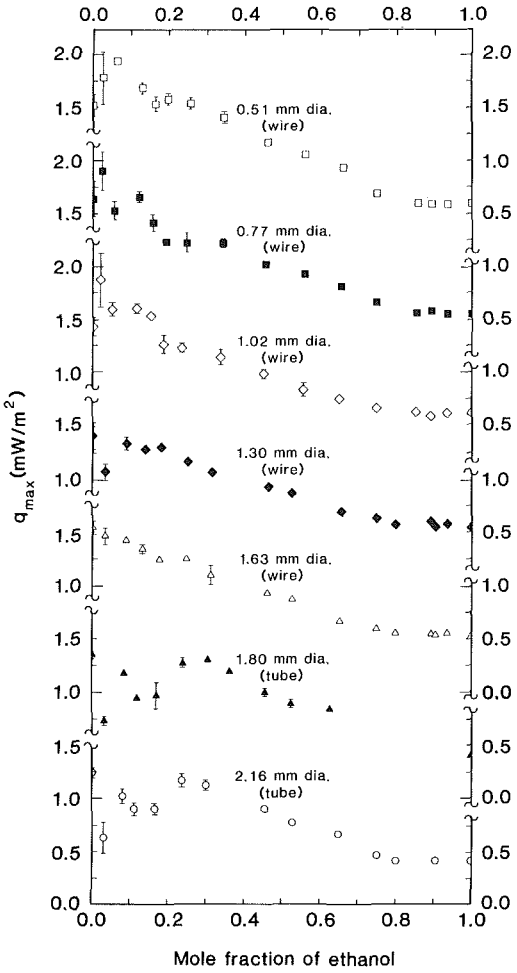

Fig. 4 The complete raw q_{max} data

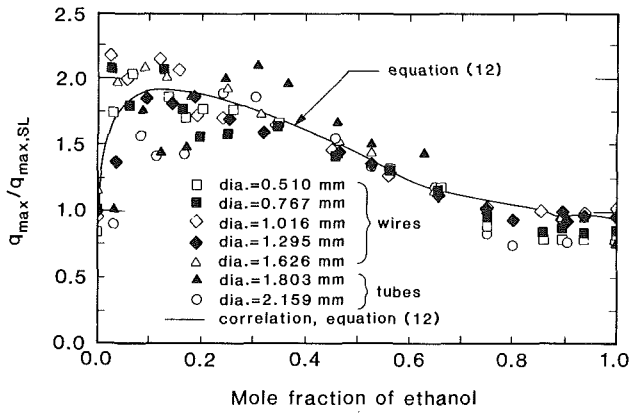

Fig. 5 The q_{max} data normalized to eliminate the role of geometric scale

(based on properties of the mixture) to obtain a value of q_{max} that would represent the mixture if effective subcooling did not take place. We subtract this $q_{max,\,SL}$ from the experimental value in each case, to get Δq_{sub}. However, there is a catch. Equation (8) reveals a small systematic error as it is applied to different liquids. It predicts our pure water burnout data very closely, but it overpredicts our burnout values in ethanol by 10 percent. We accordingly use a corrected $q_{max,\,SL}$: the value given by equation (8), divided by $(1+0.10x)$. This serves to compensate for the systematic overprediction.

Isolating the Influence of Cylinder Geometry. The present q_{max} data have been normalized by $q_{max,\,SL}$ and plotted in Fig. 5. (We defer discussion of a predictive correlation that is also included in the figure.) The data correlate rather well on these dimensionless coordinates, except at low values of x, where the scatter broadens. However, most of this scatter is introduced by the data obtained using stainless steel tubes, which are generally low. Changing from wires to tubes changes the heat transfer boundary condition from uniform-wall-temperature to uniform-heat-flux and it is clear that burnout is sensitive to this change. For the isothermal wires, however, the modified $q_{max,SL}$ normalizes the data, and therefore takes accurate account of the role of R or R' in burnout, in this case.

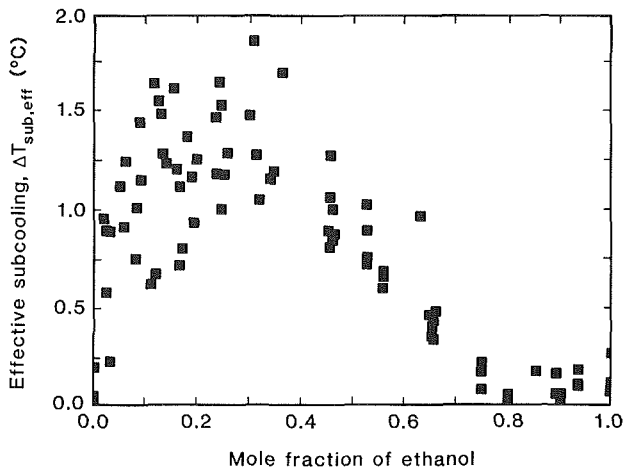

Fig. 6 Effective subcooling inferred from the present data using the low-subcooling correlation of Elkassabgi and Lienhard

An Estimation of the Effective Subcooling. The correlation given in Fig. 5 gives us greater confidence in the use of the modified $q_{max,\,SL}$ to represent q_{max} when there is no effective subcooling. We can then equate $(q_{max}-q_{max,\,SL})$ to Δq_{sub} given by equation (5) and solve the result for ΔT_{sub} using mixture properties. (These values, of course, are only inferred. However we have no means for making direct *in situ* measurements of ΔT_{sub} nor do we see such means on the horizon.)

The resulting values of ΔT_{sub}, plotted in Fig. 6, show a clear trend in x, with ΔT_{sub} vanishing at the azeotrope where effective subcooling can no longer occur. ΔT_{sub} must also remain close to zero for $x>x_{azeotrope}$, since the saturated liquid and vapor curves are very close together in that range (see Fig. 3). The numerical values of ΔT_{sub} look fairly small—all below 2 °C. These, of course, are characteristic values, not actual ones. Furthermore, it is hard to know whether 2°C should really be regarded as a small subcooling within an actual bubble.

Incorporation of Effective Subcooling Into a Burnout Correlation. What factors are missing in the correlation of burnout in a binary mixture? The obvious answer is the composition, x, of the boiled liquid; but the shape of the phase-equilibrium diagram must also be accounted in a correct correlation. The x-dependent shape of the phase equilibrium diagram can be represented using a new effective Jakob number, Ja_e, based on an effective subcooling of the liquid, which varies with x. Two candidate Jakob numbers, based on two representations of the subcooling, are

$$Ja_e \equiv \frac{\rho_f c_p (x-y)}{\rho_g h_{fg}} \frac{dT_f}{dx} \tag{9a}$$

and

$$Ja_e \equiv \frac{\rho_f c_p [T_g(x) - T_f(x)]}{\rho_g h_{fg}} \tag{9b}$$

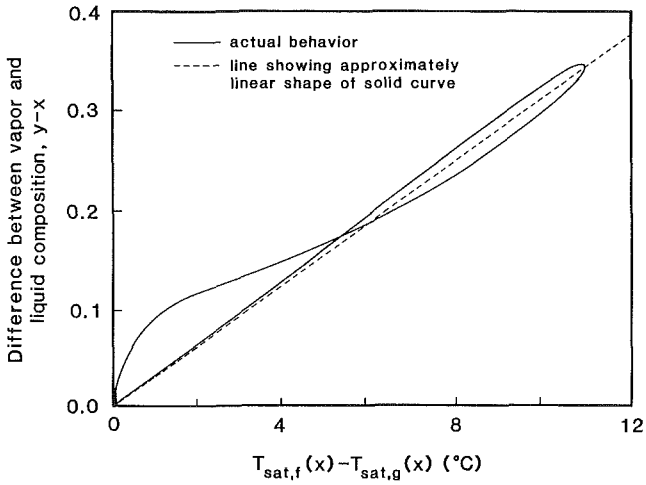

Fig. 7 The approximate linear relation between $|y-x|$ and $(T_g - T_f)$ in the ethanol/water system.

Other Ja_e's could have been created using other characterizations of the subcooling. However, equation (9*b*) proved to work better than other candidates. The effective subcoolings used here (and the other ones we tried) contain full information about the equilibrium phase diagram.

Before setting a correlation, we look at the dimensional analysis of burnout. The dimensional functional equation for q_{max} is

$q_{max} = f(h_{fg}, g(\rho_f - \rho_g), \rho_f, \rho_g, R, c_p, (T_g - T_f), \alpha,$ mass diffusivity)

These ten variables are expressible in N, m, s, °C. Hence the dimensional equation reduces to six dimensional groups

$$\text{Ku} = f(R', \text{Ja}_e, \rho_f/\rho_g, \text{Pe}, \text{Lewis No.}) \tag{10}$$

We assume two of these groups are unimportant: Mass diffusivity is normally so slow with respect to boiling processes that it should not play an important role. Hence we drop the Lewis number. Elkassabgi and Lienhard found by least-squares fitting that ρ_f/ρ_g played no role in the kindred problem of burnout in a subcooled, single-component liquids. Binary boiling appears to be sufficiently similar in its vapor removal mechanisms to warrant the use of the same assumption here.

Since Ku and R' can be combined using $q_{max,\,SL}$, we assume that binary burnout data can be correlated with an equation of the form

$$\frac{q_{max}}{q_{max,\,SL}} = \frac{1}{1 - f(\text{Ja}_e, \text{Pe})} \tag{11}$$

The range of Pe variation in these experiments was not large enough to make its general influence on q_{max} clear. It is only clear that Pe has no noticeable influence when it is varied over the small range represented by the ethanol/water system at 1 atm.

Throughout the present computations, we used actual data for physical properties wherever that was possible. In the few cases that it was not, we used standard prediction techniques of the kind described by Reid et al. (1977) (see Reddy, 1987). A simple least-squares fit of our data then yielded

$$\frac{q_{max}(1+0.10x)}{q_{max,\,SL}} = (1 - 0.170\text{Ja}_e^{0.308})^{-1} \tag{12}$$

which represents the ethanol/water data for wires alone with an rms deviation of ±8 percent. (With the tube data, the rms error increases to ±15 percent.) Equation (12) is included in Fig. 5.

A Note on the Use of (y − x) to Characterize the Phase-Equilibrium Diagram. We have noted that some authors have tried to characterize the phase-equilibrium diagram using the term $|y-x|$ evaluated at x. This term alone *ought* not be adequate to characterize the diagram fully. However, the use of $[T_g - T_f]$ has proven to be adequate in our effective subcooling model. By plotting $|y-x|$ against $[T_g - T_f]$ (see Fig. 7) for the ethanol/water system we discover a nearly linear interdependence. This is built into the nature of the phase-equilibrium diagram and may work for many other fluids as well. Thus $|y-x|$ fortuitously gives a fairly good characterization of phase-equilibrium behavior.

Accomplishments, Conclusions, and Observations

1 We have provided a carefully measured set of observations of burnout on cylinders in the ethanol/water system over a range of sizes.

2 The Sun-Lienhard burnout prediction may be used to account for size variation when $R' > 0.1$ and when its minor systematic failure for some fluids is compensated.

3 Equation (12) represents these burnout data within an rms error of ±8 percent.

4 The past success of using $|y-x|$ to characterize the phase-equilibrium diagram of ethanol/water is explainable and fortuitous.

5 Further research should be directed at:

- identifying the role of heat diffusion. This can probably be accounted in a relation of the form of equation (11), although it might be necessary to revert to equation (10).
- identifying the role of other geometries in the ethanol/water system (the flat plate would be a prime candidate).
- learning how the heater boundary condition (uniform heat flux as opposed to uniform wall temperature) influences burnout.

References

Afgan, N. H., 1966, "Boiling Heat Transfer and Burnout Heat Flux of Ethyl-Alcohol/Benzene Mixtures," *Proc. of the 3rd Int. Heat Transfer Conf.*, Chicago, Vol. 3, pp. 175–185.

Bakhru, N., and Lienhard, J. H., 1972, "Boiling From Small Cylinders," *Int. J. Heat Mass Transfer*, Vol. 15, pp. 2011–2025.

Bonilla, C. F., and Eisenberg, A. A., 1948, "Heat Transfer to Boiling Styrene and Butadiene and Their Mixtures With Water," *Ind. & Engr. Chem.*, Vol. 40, No. 6, pp. 1113–1122.

Bonilla, C. F., and Perry, C. W., 1941, "Heat Transmission to Boiling Binary Liquid Mixtures," *Trans. AIChE*, Vol. 37, pp. 269–290.

Calus, W. F., and Leonidopoulos, D. J., 1974, "Pool Boiling Binary Liquid Mixtures," *Int. J. Heat Mass Transfer*, Vol. 17, pp. 249–256.

Carne, M., 1964, "Studies of the Critical Heat Flux for Some Binary Mixtures and Their Components," *Can. J. Chem. Engr.*, Vol. 41, pp. 235–241.

Carne, M., 1964, "Some Effects of Test Section Geometry, in Saturated Pool Boiling, on the Critical Heat Flux for Some Organic Liquids and Their Mixtures," AIChE Preprint No. 6, ASME/AIChE Heat Transfer Conf., Cleveland, OH.

Chu, J. C., Wang, S. L., Levy, S. L., and Paul, R., 1956, *Vapor Liquid Equilibrium Data*, J. W. Edwards Pub. Inc., Ann Arbor.

Cichelli, M. T., and Bonilla, C. F., 1945, "Heat Transfer to Liquids Boiling Under Pressure," *Trans. AIChE*, Vol. 41, pp. 411–412..

Dunskus, T., and Westwater, J. W., 1961, "The Effect of Trace Additives on the Heat Transfer to Boiling Isopropanol," *Chem. Engr. Symp. Series*, Vol. 57, No. 32, pp. 173–181.

Elkassabgi, Y., and Lienhard, J. H., 1988, "Influences of Subcooling on Burnout of Horizontal Cylindrical Heaters," ASME JOURNAL OF HEAT TRANSFER, Vol. 110, No. 2, pp. 479–486.

Frea, W. J., Knapp, R., and Taggart, T. D., 1977, "Flow Boiling and Pool Boiling Critical Heat Flux in Water and Ethylene Glycol Mixtures," *Can. J. of Chem. Engr.*, Vol. 55, pp. 37–42.

Gaidorov, S. A., 1975, "Evaluation of the Critical Heat Flow in the Case of a Boiling Mixture of Large Volume," *J. App. Mech. and Tech. Phys.*, Vol. 16, pp. 601–603.

Grigor'ev, L. N., Khairullin, I. Kh., and Usmanov. A. G., 1968, "An Experimental Study of the Critical Heat Flux in the Boiling of Binary Mixtures," *Int. Chem Engr.*, Vol. 8, No. 1, pp. 39–42.

Happel, O., and Stephen, K., 1974, "Heat Transfer From Nucleate to the

Beginning of Film Boiling in Binary Mixtures," *Proc. 5th Int. Heat Trans. Conf.*, Tokyo, Paper B7.8, Vol. 4, pp. 340–344.

Hellwege, K. H., editor-in-chief, 1975, *Numerical Data and Functional Relationships in Science and Technology*, Group IV, Vol. 3, "Thermodynamic Equilibria of Boiling Mixtures," pp. 38–40.

Huber, D. A., and Hoehne, J. C., 1962, "Pool Boiling of Benzene, Diphenyl, and Benzene–Diphenyl Mixtures Under Pressure," ASME Paper No. 62-H-30, ASME/AIChE Heat Transfer Conf., Houston, TX.

Ishiki, N., and Nikai, I., 1972, "Boiling of Binary Mixtures," *Heat Transfer—Japanese Research*, Vol. 1, No. 4, pp. 56–66.

Jordan, D. P., and Leppert, G., 1959, "Nucleate Boiling Characteristics of Organic Reactor Coolants," *Nuc. Sci. and Engr.*, Vol. 5, pp. 349–359.

Kutateladze, S. S., 1952, *Teploperedacha pri Kondensatsii i Kipenii*, State Sci., and Tech. Pubs. of Lit. on Mach. Moscow, 1952, (also published in English *Heat Transfer in Condensation and Boiling*, 2nd ed., AEC-tr-3770, Phys. and Math., 1959).

Kutateladze, S. S., Bobrovich, G. I., Gogonin, I. I., Mamontova, N. N., and Moskvichova, V. N., 1966, "The Critical Heat Flux at the Pool Boiling of Some Binary Liquid Mixtures," *Proc. 3rd Int. Heat Transfer Conf.*, Chicago, Vol. 3, pp. 149–159.

Lienhard, J. H., and Dhir, V. K., 1973, "Extended Hydrodynamic Theory of the Peak and Minimum Pool Boiling Heat Fluxes," NASA CR-2270.

Marschall, E., and Moresco, L. L., 1977, "Analysis of Binary Film Boiling," *Int. J. Heat Mass Transfer*, Vol. 20, pp. 1013–1018.

Matorin, A. S., 1973, "Correlation of Experimental Data on Heat Transfer Crisis in Pool Boiling of Pure Liquids and Binary Mixtures," *Heat Transfer—Soviet Research*, Vol. 5, No. 1, pp. 85–89.

McEligot, D. M., 1964, "Generalized Peak Heat Flux for Dilute Binary Mixtures," *AIChE J.*, Vol. 10, No. 1, pp. 130–131.

Othmer, D. F., Moeller, W. P., Englund, S. W., and Christopher, R. G., 1951, "Composition of Vapors From Boiling Binary Solutions," *Ind. and Eng. Chem.*, Vol. 43, No. 3, pp. 707–711.

Purdy, D. J., and Avedisian, C. T., 1987, "Critical Heat Flux in Fluid Mixtures on a Large Surface With Applications to Heat Pipes and Direct Immersion Cooling of Multichip Modules," Energy Rept. No. E-87-02, Sibley School of Mech. and Aero. Engr., Cornell University.

Reddy, R., Dec. 1987, "The Critical Heat Flux in Binary Mixtures of Water and Ethanol," M. S. Thesis, Mech. Engr. Dept., University of Houston, Houston, TX.

Reid, R. C., Prausnitz, J. M., and Sherwood, T. K., 1977, *The Properties of Gases and Liquids*, McGraw-Hill, New York.

Shock, R. A. W., 1977, "Nucleate Boiling in Binary Mixtures," *Int. J. Heat Mass Transfer*, Vol. 20, pp. 701–709.

Stephen, K., and Preusser, P., 1979, "Heat Transfer and Critical Heat Flux in Pool Boiling of Binary and Ternary Mixtures," *Ger. Chem. Engr.*, Vol. 2, pp. 161–169.

Sterman, L. S., Vilemas, J. V., and Abramov, A. I., 1966, "On Heat Transfer and Critical Heat Flux in Organic Coolants and Their Mixtures," *Proc. Int. Heat Transfer Conf.*, Chicago, Vol. 4, pp. 258–270.

Sun, K.-H., and Lienhard, J. H., 1970, "The Peak Pool Boiling Heat Flux on Horizontal Cylinders," *Int. J. Heat Mass Transfer*, Vol. 13, pp. 1425–1439.

Thome, J. R., 1983, "Prediction of Binary Mixture Boiling Heat Transfer Coefficients Using Only Phase Equilibrium Data," *Int. J. Heat Mass Transfer*, Vol. 26, No. 7, pp. 965–974.

Thome, J. R., and Schock, R. A. W., 1984, "Boiling of Multicomponent Liquid Mixtures," *Adv. in Heat Transfer*, Vol. 16, pp. 59–156.

Van Stralen, S. J. D., 1956, "Heat Transfer to Boiling Binary Liquid Mixtures at Atmospheric and Subatmospheric Pressures," *Chem. Engr. Sci.*, Vol. 5, p. 290–296.

Van Stralen, S. J. D., 1959, "Heat Transfer to Boiling Liquid Mixtures," *Br. Chem. J.*, Part I, Vol. 4, pp. 8–17; Part II, Vol. 4, pp. 78–82; Part III, Vol. 6, pp. 834–840; Part IV, Vol. 7, pp. 90–97.

Van Stralen, S. J. D., 1966–7, "The Mechanism of Nucleate Boiling in Pure Liquids and Binary Mixtures," *Int, J. Heat Mass Transfer*, Part I, Vol. 9, pp. 995–1020, 1966; Part II, Vol. 9, pp. 1021–1046, 1966; Part III, Vol. 10, pp. 1469–1484, 1967; Part IV, Vol. 10, pp. 1485–1498, 1967.

Van Stralen, S. J. D., 1968, "The Boiling Paradox in Binary Liquid Mixtures," *Chem. Engr. Sci.*, Vol. 25, pp. 149–171.

Van Stralen, S. J. D., and Sluyter, W. M., 1969, "Investigations on the Critical Heat Flux of Pure Liquids and Mixtures Under Various Conditions," *Int. J. Heat Mass Transfer*, Vol. 12, pp. 1353–1384.

Van Wijk, W. R., Vos, A. S., and Van Stralen, S. J. D., 1956, "Heat Transfer to Boiling Binary Liquid Mixtures," *Chem Engr. Sci.*, Vol. 5, pp. 68–80.

Vos, A. S., and Van Stralen, S. J. D., 1956, "Heat Transfer to Boiling Water-Methylethylketone Mixtures," *Chem. Engr. Sci.*, Vol. 5, pp. 50–56.

Wright, R. D., and Colver, C. P., 1968, "Saturated Pool Boiling Burnout of Ethane-Ethylene Mixtures," *Proc. ASME/AIChE Heat Transfer Conf.*, Philadelphia, PA, Paper No. 24.

Yang, Y. M., 1987, "An Estimation of Pool Boiling Critical Heat Flux for Binary Mixtures," *Proc. 2nd ASME/JSME Joint Thermal Engr. Conf.*, Honolulu, HI, Vol. 5, pp. 439–436.

Yue, P.-L., and Weber, M. E., 1973, "Film Boiling of Saturated Binary Mixtures," *Int. J. Heat Mass Transfer*, Vol. 16, pp. 1877–1888.

Yue, P.-L., and Weber, M. E., 1974, "Minimum Film Boiling Flux of Binary Mixtures," *Trans. Inst. Chem. Engrs.*, Vol. 52, pp. 217–222.

Zuber, N., 1958, "Hydrodynamic Aspects of Boiling Heat Transfer," Ph.D. Dissertation, UCLA, Los Angeles, CA (also available as AECU-4439, Phys. and Math.).

Axisymmetric Unsteady Droplet Vaporization and Gas Temperature Distribution

S. K. Lee[1]

T. J. Chung

Department of Mechanical Engineering,
The University of Alabama in Huntsville,
Huntsville, AL 35899

Droplet vaporization and temperature distributions of axisymmetric unsteady sprays are investigated. The so-called discrete droplet model of two-phase flows, often known as the Eulerian–Lagrangian method, is used. Calculations are carried out with Eulerian coordinates using finite elements for the gas phase and the method of characteristics using the second-order Runge–Kutta scheme for the droplet liquid phase. The sensitivity of the numerical results to changes in time step, injection pulse time, grid spacing, and number of droplet characteristics is examined. Through a simple example, it is shown that applications of the finite element method to more complicated problems appear to be promising.

1 Introduction

Various approaches have been used in the literature to formulate the system of differential equations that governs the spray droplets and gas behavior. Sirignano (1986) reviews the current state of the art in computational methods of spray combustion, and describes the three different approaches:

(1) Eulerian–Eulerian method, in which both gaseous and liquid phases are treated as continuum, (2) Eulerian–Lagrangian method, in which the gas properties are formulated in Eulerian coordinates and droplet properties are described in a Lagrangian formulation (Aggarwal et al., 1983), and (3) probability density function approach (Gupta and Bracco, 1978; Westbrook, 1976).

The objective of the present paper is to investigate the feasibility of the finite element method for the solution of spray combustion problems. Although this is the first attempt toward applications of the finite element method to the droplet vaporization, it is anticipated that some of the advantages inherent in the finite element method may be exploited in resolving difficulties encountered in spray combustion in general. As an example, our task in this paper will be confined to an axisymmetric unsteady droplet vaporization and gas temperature distribution originally investigated by Aggarwal et al. (1983) using the finite difference method.

In the recent studies of finite element technologies (Chung et al., 1988; Löhner et al., 1988; Oden et al., 1988; Hughes, 1988), it has been shown that the ideas developed in the finite difference literature can be combined with finite elements in order to arrive at computational schemes quite efficient and robust. Some of the major contributions include the streamline-upwind-Petrov-Galerkin method advanced from the idea of upwinding differences useful in convective heat transfer (Hughes, 1988), and the flux-corrected-transport with finite elements (Löhner et al., 1988; Oden et al., 1988).

Due to the specific problem dealt with in the present study where there is no convective fluid motion, it is possible to work with the standard Galerkin finite elements (Chung, 1978). No special interpolation functions for the variables are required in this particular example. Specifically, the finite element analysis is performed on a system of model equations for the example reported by Aggarwal et al. (1983), in which the finite difference method was used for the gas phase with Eulerian coordinates. Four Lagrangian equations consist of liquid-phase properties, i.e., the droplet size, the droplet velocity, location of droplets, and the droplet number density. The numerical experimentation on this hybrid Eulerian–Lagrangian method shows the efficiency of utilizing finite element techniques for the gas-phase system and the second-order Runge–Kutta scheme of integration for the liquid-phase equations.

Multivaluedness of solution occurs when the initial droplet size or droplet velocity distribution is polydisperse. Multivaluedness with a monodisperse spray can also occur in the interior of the calculation domain whenever the particle paths cross each other. We shall deal with the latter case in the present study.

2 Analysis

2.1 Governing Equations. The governing partial differential equations for the gas phase and droplet liquid phase are, respectively, parabolic and hyperbolic. The hyperbolic equations are treated by the method of characteristics and are reduced to ordinary differential equations. In the present study, the model system consists of five equations: one parabolic equation for temperature θ in the gas phase and four ordinary differential equations for the four unknowns—number of droplets n associated with a given initial mass of liquid, location of a computational particle x, droplet radius R_l, and droplet velocity U_l. The gas velocity U and droplet temperature θ_l are taken to be known constants throughout the domain; moreover, the gas velocity is assumed to be uniform and oriented in the axial direction.

The nondimensionalized gas-phase and droplet liquid-phase equations are as follows (Aggarwal et al., 1983):

Gas-Phase

$$\frac{\partial\theta}{\partial t}=-\frac{\partial(U\theta)}{\partial z}+\frac{\alpha}{r}\frac{\partial\theta}{\partial r}+\alpha\left(\frac{\partial^2\theta}{\partial r^2}+\frac{\partial^2\theta}{\partial z^2}\right)-S \tag{1}$$

The nonlinear source term S is given by

$$S=\frac{k_1 n}{2\pi r\Delta r\Delta z}[1+k_2(\theta-\theta_l)]\,[1+k_3\{R_l^2[U-U_{lz})^2 + U_{lr}^2]\}^{1/4}]R_l\ln[1+k_2(\theta-\theta_l)] \tag{2}$$

where the nondimensional physical parameters are

$$k_1=\frac{1}{Z_c^2U_c\theta_c}4\pi\left(\frac{\mu'}{\rho'}\right)\left(\frac{L'}{C_p'}\right)R_c \tag{3}$$

[1]Present Address: Korea Military Academy.

Contributed by the Heat Transfer Division for publication in the JOURNAL OF HEAT TRANSFER. Manuscript received by the Heat Transfer Division November 12, 1987. Keywords: Evaporation, Multiphase Flows, Sprays/Droplets.

$$k_2 \frac{C_p' \theta_c'}{L'} \tag{4}$$

$$k_3 = \frac{0.3\sqrt{2} R_c^{1/2} U_c^{1/2}}{(\nu')^{1/2}} \tag{5}$$

$$\alpha = \frac{\lambda'}{\rho' C_p' Z_c U_c} \tag{6}$$

and the number of droplets n is related to the number density N as $N = n/2\pi r \Delta r \Delta z$. Note also that the nondimensionalization above is based on the following characteristic values: $Z_c = 10$ cm, $U_c = 100$ m/s, $\theta_c = 500$ K, and $R_c = 100$ μm.

Droplet Velocity

$$\frac{dU_l}{dt} = k_4 \frac{1}{R_l^2} (U - U_l) \tag{7}$$

with the dimensionless parameter k_4 given by

$$k_4 = \frac{4.5 Z_c}{U_c R_c^2} \frac{\mu'}{\rho_l'} \tag{8}$$

Note that the droplet velocity can be defined with respect to the location of droplets as

$$U_l = \frac{dx}{dt} \tag{9}$$

Droplet Size

$$\frac{dR_l}{dt} = -k_5 [1 + k_3 \{R_l^2 [(U - U_{lz})^2 + U_{lr}^2]\}^{1/4} \ln [1 + k_2 (\theta - \theta_l)]]/R \tag{10}$$

where the nondimensional parameter k_5 is of the form (Aggarwal and Sirignano, 1984)

$$k_5 = \frac{1}{R_c^2} \frac{Z_c}{U_c} \frac{\mu}{\rho_l} \tag{11}$$

Conservation of Number of Droplets. Assuming that the droplet does not coalesce or break up, we have

$$\frac{dn}{dt} = 0 \tag{12}$$

Here, the hyperbolic partial differential equations for the liquid phase have been converted to the equivalent system. For example, the number density of droplets N would have been described as

$$\frac{\partial N}{\partial t} + \nabla \cdot (U_l N) = 0$$

However, the form given by equation (12) is preferred to allow multivalued solutions as droplet trajectories may intersect.

The reader should refer to the justification for the use of these equations (1)–(12) in Aggarwal et al. (1983, 1984). Thus, no further elaborations are given in this paper. These governing equations for the gas phase [equation (1)] and for the droplet liquid phase [equations (7), (9), (10), and (12)] will be solved subject to the boundary and initial conditions discussed in the following section.

2.2 Boundary and Initial Conditions. At the inflow ($z = 0$), the adiabatic boundary condition for θ is prescribed as

$$-\lambda \frac{\partial \theta}{\partial z} = \bar{\alpha} (\theta - \hat{\theta}) \tag{13}$$

where $\bar{\alpha}$ is the heat transfer coefficient and $\hat{\theta}$ is the ambient temperature. Note that equation (13) is known as the Cauchy boundary condition. On the other hand, an outflow boundary, needed to make the computational domain finite, has the form

$$\frac{\partial \theta}{\partial z} = 0 \qquad \text{at } z = 1 \tag{14}$$

and the boundary conditions at the r boundary are

$$\frac{\partial \theta}{\partial r} = 0 \qquad \text{for } r = 0 \text{ and } r = 1 \tag{15}$$

Initially, θ is assumed to be the same as $\hat{\theta}$ at $t = 0$.

The droplet flow is assumed to be conical initially and flowing from a point source at a point on the axis of symmetry where $z < 0$. In the beginning, all the droplet characteristics are positioned at x ($z = 0$, r). The initial values of R_l and n are assumed to be uniform, and U_l is obtained from the assumption of a conical flow.

The boundary conditions [equations (13)–(15)] can be implemented in the process of finite element calculations. This subject will be elaborated in the following section.

3 Numerical Method and Solution Procedure

The standard Galerkin finite element formulation with linear isoparametric elements for the gas phase leads to the local form as follows (Chung, 1978):

$$\int_\Omega \left[\frac{\partial \theta}{\partial t} + U \frac{\partial \theta}{\partial z} - \frac{\alpha}{r} \frac{\partial \theta}{\partial r} - \alpha \left(\frac{\partial^2 \theta}{\partial r^2} + \frac{\partial^2 \theta}{\partial z^2} \right) + S \right] \Phi_N d\Omega = 0 \tag{16}$$

Nomenclature

C_D = drag coefficient
C_p = coefficient of specific heat at constant pressure, J/g/K
L = heat of vaporization
N = number density of droplets, 1/cm^3
n = number of droplets associated with a given initial mass of liquid
R = droplet radius, cm
Re = Reynolds number of liquid droplet
r = spatial coordinate in radial direction, cm
t = time, s
U = gas velocity, cm/s
U_l = droplet velocity, cm/s
z = spatial coordinate in axial direction, cm
α = thermal diffusivity, cm^2/s
θ = gas temperature, K
θ_l = liquid temperature, K
λ = thermal conductivity, Jcm/K/s
μ = dynamic viscosity, g/cm/s
ν = kinematic viscosity, cm^2/s
ρ = density, g/cm^3
Φ = linear element basis function used in finite element formulation

Subscripts
l = liquid property
0 = initial values
∞ = ambient values

Superscripts
( )$'$ = physical variables and parameters at dimensional coordinates

Here, the temperature is approximated in the form

$$\theta = \Phi_N \theta_N$$

where Φ_N denotes the interpolation function and θ_N represents the nodal temperature. Integrating equation (16) by parts, we obtain

$$W_{NM}\dot{\theta}_M + (A_{NM} + B_{NM} + C_{NM})\theta_M = F_N + G_N \tag{17}$$

where

$$W_{NM} = \int_\Omega \Phi_N \Phi_M \, r dr dz \tag{18}$$

$$A_{NM} = U_z \int_\Omega \Phi_N \frac{\partial \Phi_M}{\partial z} r dr dz \tag{19}$$

$$B_{NM} = \alpha \int_\Omega \left(\frac{\partial \Phi_N}{\partial r} \frac{\partial \Phi_M}{\partial r} + \frac{\partial \Phi_N}{\partial z} \frac{\partial \Phi_M}{\partial z} \right) r dr dz \tag{20}$$

$$C_{NM} = \int_\Gamma \tilde{\alpha} \overset{*}{\Phi}_N \overset{*}{\Phi}_M r d\Gamma = \int_\Gamma \tilde{\alpha} \overset{*}{\Phi}_N \overset{*}{\Phi}_M \overset{*}{\Phi}_p r_p d\Gamma \tag{21}$$

$$F_N = \int_\Gamma \tilde{\alpha} \tilde{\theta} \overset{*}{\Phi}_N r d\Gamma = \int_\Gamma \tilde{\alpha} \hat{\theta} \overset{*}{\Phi}_N \overset{*}{\Phi}_M r_M d\Gamma \tag{22}$$

$$S_{\theta_N} = -\int_\Omega \Phi_N S \, r dr dz \tag{23}$$

with $\overset{*}{\Phi}_N$ indicating the finite element interpolation along the boundary surfaces and $\dot{\theta}_M = \partial \theta_M / \partial t$. With all local elements assembled into a global form, we obtain

$$W_{ij}\dot{\theta}_j + (A_{ij} + B_{ij} + C_{ij})\theta_j = F_i + G_i \tag{24}$$

in which S_i is a nonlinear source term at the global node i. The semi-implicit form of finite element equation (23) becomes

$$\left[W_{ij} + \frac{1}{2}\Delta t (A_{ij} + B_{ij} + C_{ij}) \right] \theta_j^{n+1} = \left[W_{ij} - \frac{1}{2}\Delta t (A_{ij} + B_{ij} + C_{ij}) \right] \theta_j^n + \frac{1}{2}\Delta t \left(F_i^n + F_i^{n+1} \right) + \frac{1}{2}\Delta t \left(G_i^n + G_i^{n+1} \right) \tag{25}$$

Since the Neumann boundary condition vanishes everywhere except at the inflow region ($z = 0$), the F_i^n vector in equation (25) arises only from the Cauchy boundary condition [equations (21) and (22)]. It is seen that the Cauchy boundary condition arises naturally in the finite element formulation and, thus, is treated automatically. The solution of equation (25) has been discussed extensively in the literature. As is well known in the finite difference literature, the primary difficulty arises from the advection term A_{ij} in equation (25). For details, see the recent work by Chung et al. (1987).

The ordinary differential equations (7)–(12) are integrated over the same time step using the Runge-Kutta second-order scheme. At each point of the particle characteristics, the local values of temperature for equation (16) are calculated from linear interpolation of the four surrounding nodal values of the gas-phase equation in the computational element through which the droplet is passing. The energy exchange between phases occurs only when the particle resides in a computational element. It is evaluated by superimposing the nonlinear source term of each characteristic to the four surrounding grid points in the computational element using the concept of tributary volume-weighted linear interpolation.

The injection process may be represented by introducing the

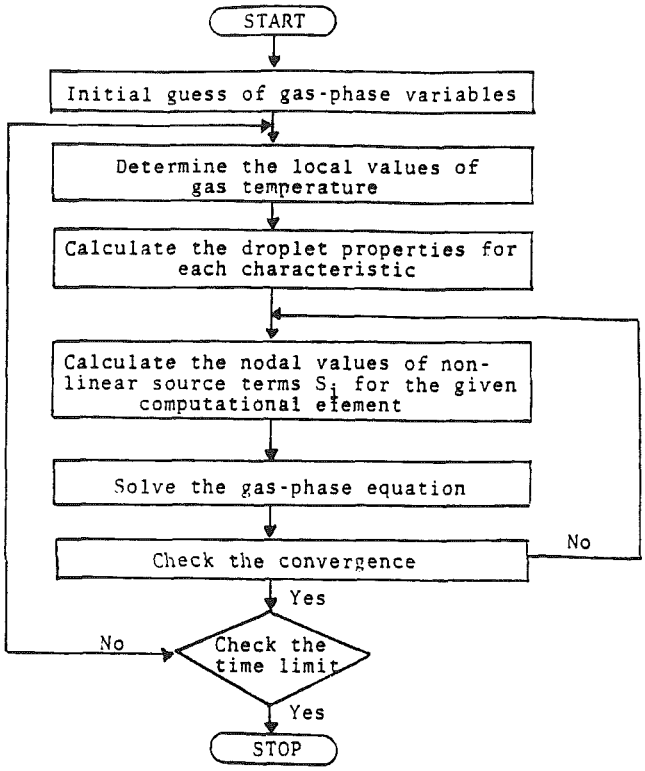

Fig. 1 Solution procedure for an Eulerian-Lagrangian formulation

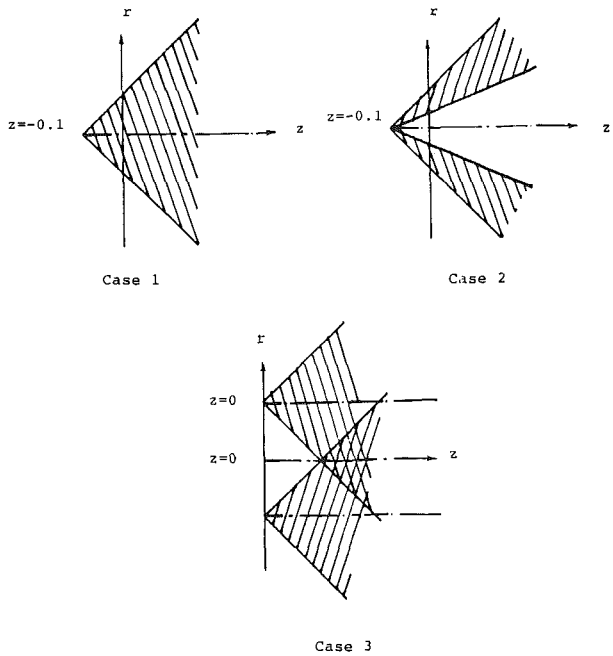

Fig. 2 Axisymmetric injector models, Case 1—regular conical spray; Case 2—hollow conical spray; Case 3—circular conical spray

injection pulse with a period τ_p. Since the total liquid mass flow rate is fixed, the number of characteristics, injection period, and the number of droplets per unit volume are related to the mass flow rate of injected liquid phase $\dot{w}_f$ as

$$\dot{w}_f = \sum_{k=1}^{E} \frac{4}{3} \pi R_l^{3(k)} \rho_l n^{(k)} / \tau_p$$

In an iteration cycle, solutions for the liquid-phase equa-

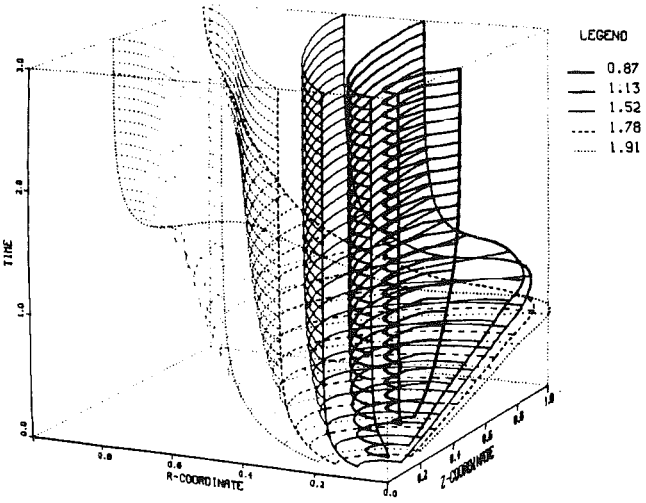

Fig. 3 Case 1, gas temperature variations with time as expressed by contour surfaces for $\theta = 0.87$, 1.13, 1.32, 1.78, and 1.91; intermediate grid, $U = U_l = 1.0$; steady state prevails as $t \to 3.0$

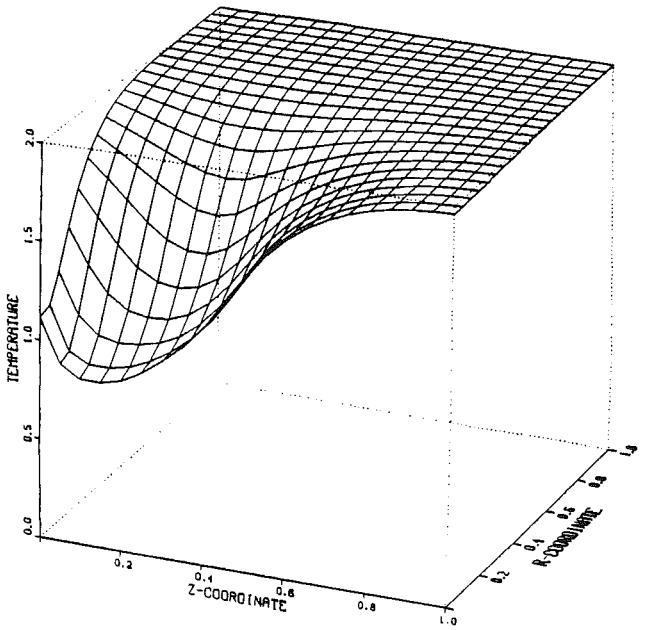

Fig. 4 Case 1, gas temperature variations at $t = 0.5$, intermediate grid, $U = U_l = 1.0$; very low temperature close to the origin

tions are first obtained at one time step; then, the θ solution is advanced in the same time step by the Crank-Nicolson finite element scheme.

Various numerical schemes can be used to integrate the ordinary differential equations (7)-(12) arising from the method of characteristics. Here, the predictor-corrector second-order Runge-Kutta method is used to integrate those characteristic equations. This approach maintains a second-order accuracy in our numerical scheme. The flow chart of the computational process is shown in Fig. 1.

In summary, it should be remarked that the finite element method has three distinct properties: (1) Complicated geometries with unstructured grids can be handled easily, (2) complicated boundary conditions can be imposed efficiently, and (3) all higher order finite difference schemes can be generated through finite elements more systematically. In the simple example problem studied in this paper, property (2) has been shown to be the distinct advantage over the finite difference method. However, if complicated geometries are

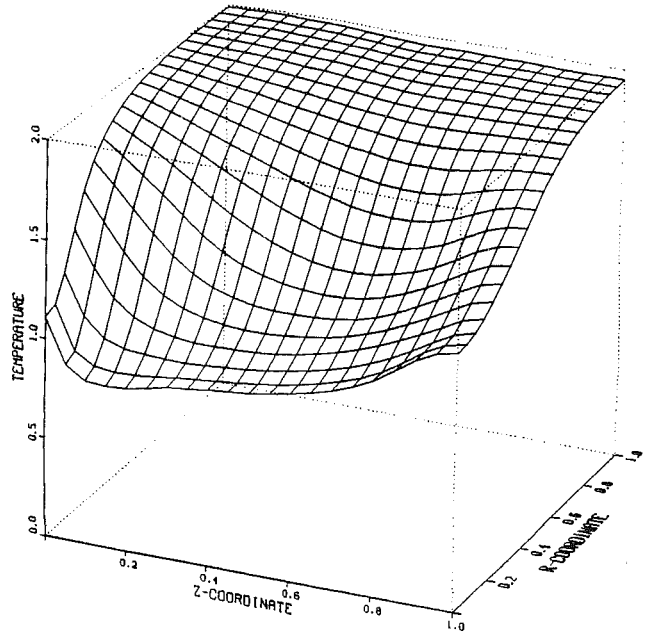

Fig. 5 Case 1, gas temperature variations at $t = 1.0$, intermediate grid, $U = U_l = 1.0$; droplets move downstream with gas temperature decreasing gradually

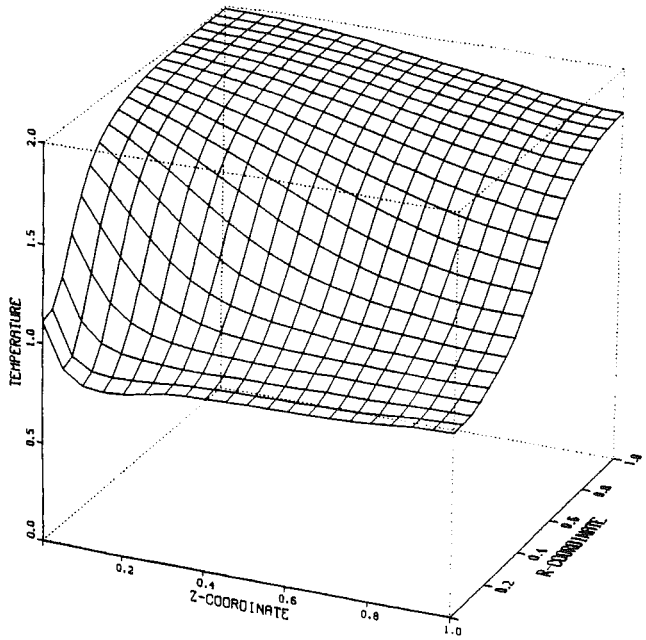

Fig. 6 Case 1, gas temperature variations at $t = 3.0$, intermediate grid, $U = U_l = 1.0$; gas temperature further decreasing downstream, but has reached the steady state

chosen and if steep gradients and disparate length and time scales are present, then some of the recent developments, such as streamline upwind/Petrov-Galerkin, Taylor-Galerkin, or Flux-Corrected Transport-Finite Elements could have been used, as mentioned in the Introduction.

4 Discussion

Three different grids were tested in the present study. The parameters varied were the number of characteristics N, the time step Δt, the grid intervals Δr and Δz, and the period of injection pulse τ_p. Data for each grid case are as follows:

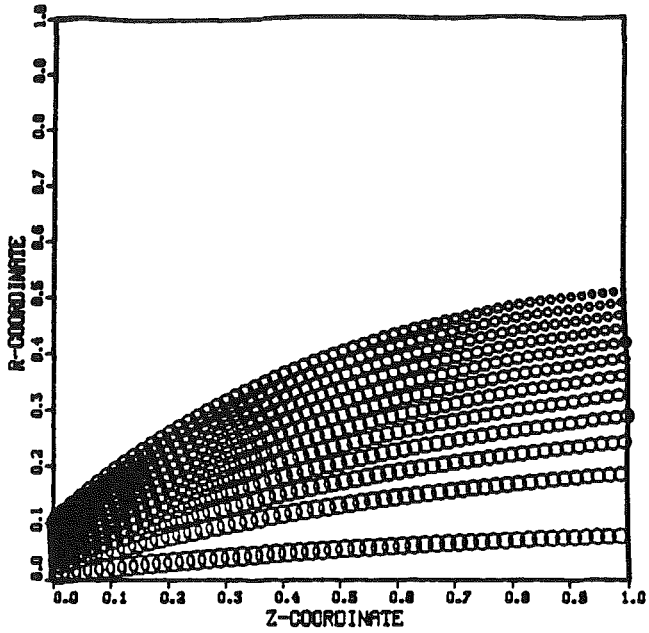

Fig. 7 Case 1, droplet volume, drop diameter amplified 300 times, fine grid, $t=3.0$, $U=U_l=1.0$, vaporization droplets significant toward downstream and toward the radial direction

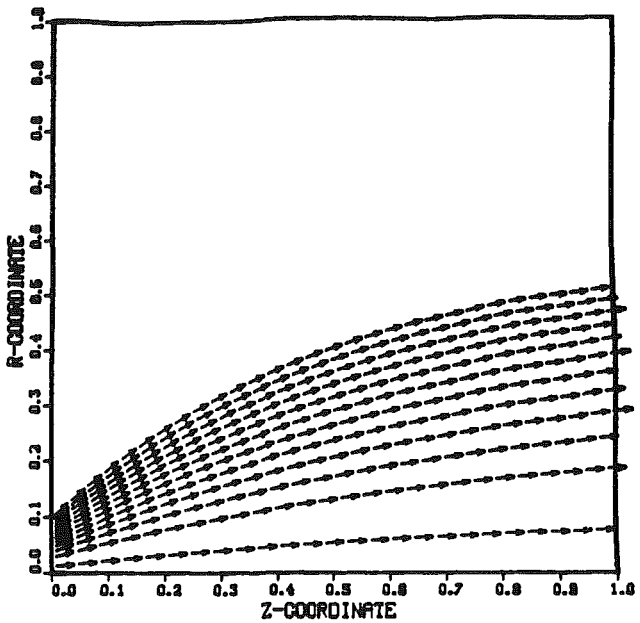

Fig. 8 Case 1, droplet velocity vector field, fine grid, $t=3.0$, $U=U_l=1.0$, plotted at every fourth particle location. Although unnoticeable on this scale, the drag causes the droplets to accelerate downstream since the gas velocity is greater than the axial component of the initial droplet velocity.

Coarse grid: $N=3$, $\Delta t=0.02$, $\Delta r=\Delta z=0.1$,

$(10\times 10$ mesh$)$ $\tau_p=0.04$

Intermediate grid: $N=6$, $\Delta t=0.01$, $\Delta r=\Delta z=0.05$,

$(20\times 20$ mesh$)$ $\tau_p=0.02$

Fine grid: $N=12$, $\Delta t=0.005$, $\Delta r=\Delta z=0.025$,

$(40\times 40$ mesh$)$ $\tau_p=0.01$

Various options of injectors used in the present study are shown schematically in Fig. 2.

The nondimensionalized physical parameters $k_1 \ldots k_5$ are calculated from the following characteristic values: $z=10$ cm,

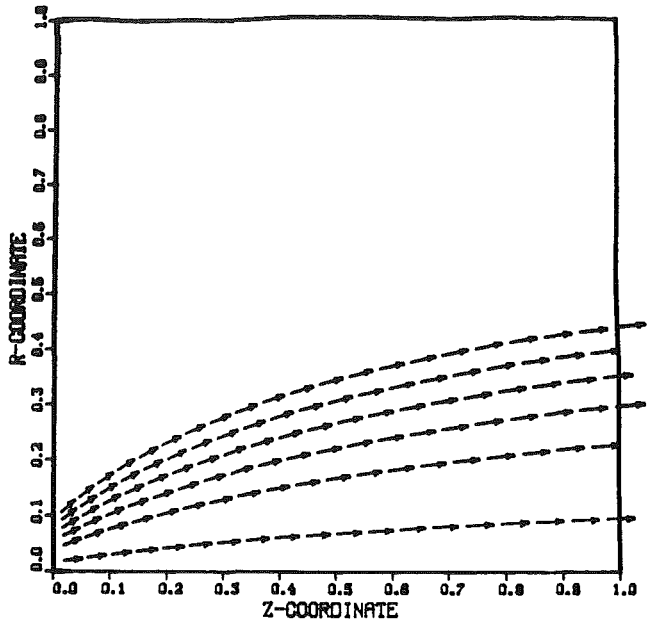

Fig. 9 Case 1, effect of gas velocity greater than the droplet velocity ($U=2.0$, $U_l=1.0$), intermediate grid, droplet trajectories are confined to a narrower band than $U=U_l=1.0$.

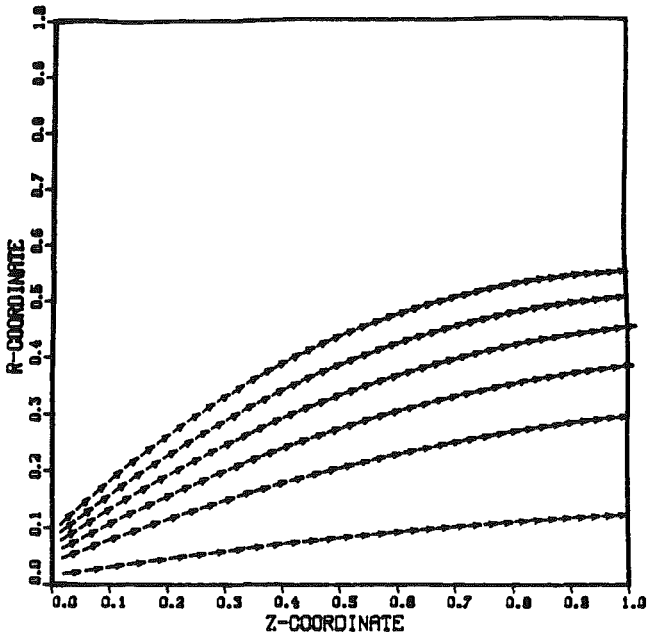

Fig. 10 Case 1, effect of gas velocity smaller than the droplet velocity ($U=0.5$, $U_l=1.0$), intermediate grid, droplet trajectories are spread in broader band

$U_c=100$ cm/s, $\theta_c=500$K, $R_c'=0.01$ cm, $\lambda'=1.38336\times 10^{-2}$ cal/cm-K-s, $\mu'=1.85283\times 10^{-4}$ g/cm-s, $\rho'=0.0003522$ g/cm^3, $L'=86.5$ cal/g, $\rho_l'=0.773$ g/cm^3, and $\alpha=0.1571$. These values lead to $k_1=0.101660\times 10^{-4}$, $k_2=1.44508$, $k_3=0.58494$, $k_4=1.07862$, and $k_5=0.239693$. These constants are for n-hexane.

Initially, convergence studies are conducted between various grids: coarse, intermediate, and fine. The L_2 norm error $\|e\|_L$ is defined as

$$\|e\|_{L_2}=\left(\int_\Omega e^2 d\Omega\right)^{1/2}=\left(\int_\Omega \Phi_\alpha \Phi_\beta d\Omega e_\alpha e_\beta\right)^{1/2}$$

where $e_\alpha=T_\alpha-\hat{T}_\alpha$, with T_α denoting the fine grid and $\hat{T}_\alpha$ the

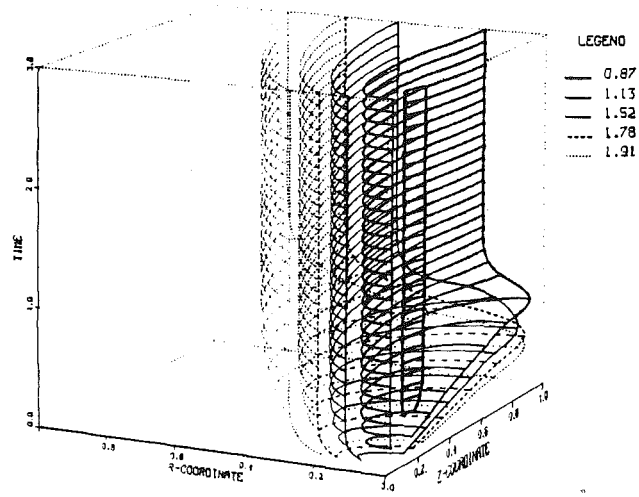

Fig. 11 Case 1, effect of gas velocity greater than the droplet velocity ($U=2.0$, $U_l=1.0$) upon gas temperature variation with time, $\theta=0.87$, 1.13, 1.52, 1.78, 1.91, intermediate grid; steady state is reached at $t=1.2$

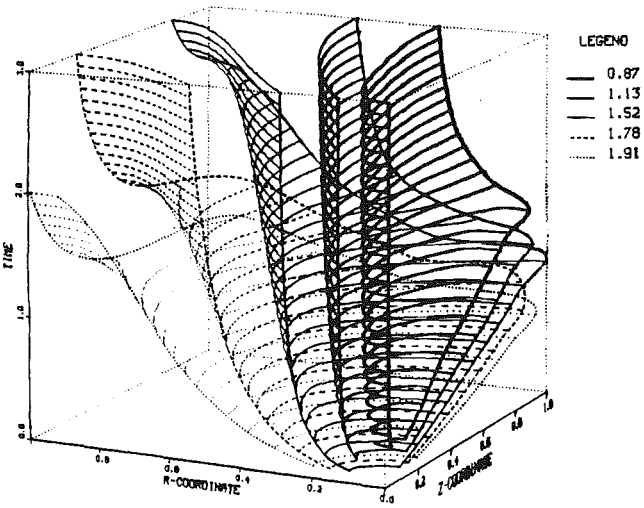

Fig. 12 Case 1, effect of gas velocity smaller than the droplet velocity ($U=0.5$, $U_l=1.0$) upon gas temperature variations with time, $\theta=0.87$, 1.13, 1.52, 1.78, 1.91, intermediate grid, steady state has not been reached even at $t=3.0$

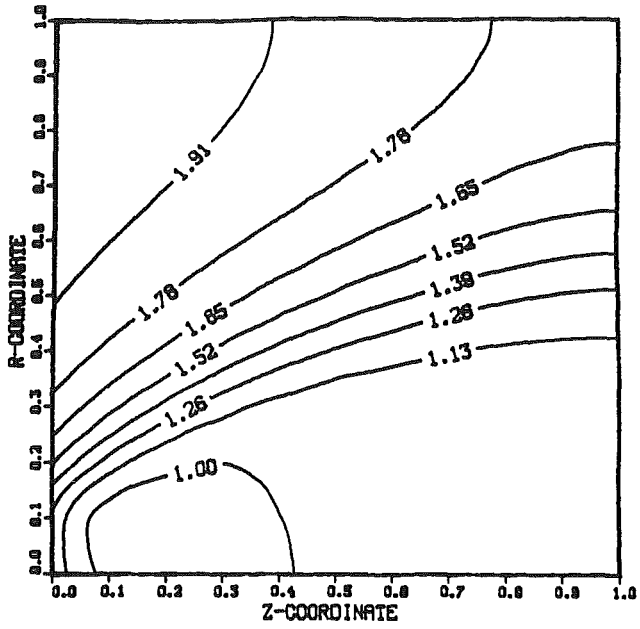

Fig. 13 Case 2, contours of gas temperature field, intermediate grid, $t=3.0$, $U=U_l=1.0$, gas temperatures along the axis are much higher than those of Case 1 since the droplets are absent in this vicinity

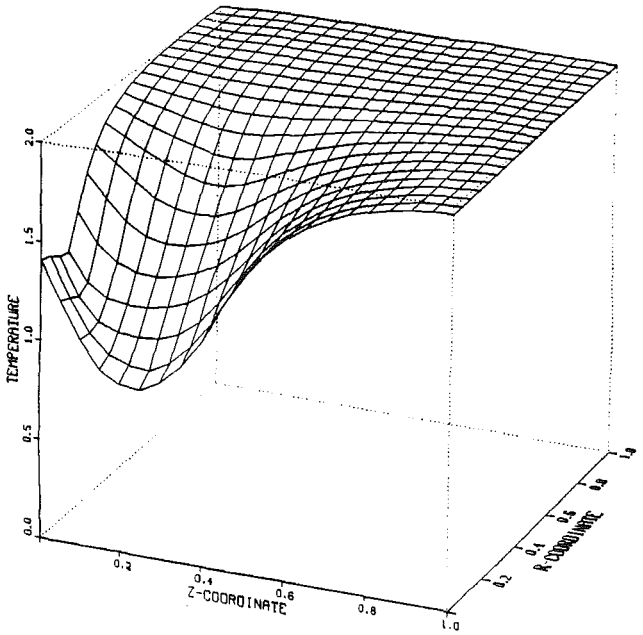

Fig. 14 Case 3, gas temperature variations at $t=0.5$, intermediate grid, $N=7$, $U=U_l=1.0$, lowest temperature occurs along the droplet trajectories

coarse or intermediate grid. Based on the L_2 norm errors, the convergence is determined to be subquadratic ($P=1.84$, where P is the slope of the logarithmic convergence curve). Parametric studies for grid sizes and the number of characteristics reveal that convergence is sensitive to the grid spacing, but insensitive to the number of characteristics. Having determined the trend of convergence, we present the results of only the fine grid in what follows.

Figure 3 shows the contours of the gas temperature field for Case 1, $U=U_l=1.0$. The initial temperature is shown to be decreasing toward $r\to 0$ and $z\to 0$ as expected. If time increases ($t\to 3.0$) for this example, note that the temperature contours spread outward, indicating convergence toward a steady-state condition. For a given time $t=0.5$, $t=1.0$, and $t=3.0$, the temperature distributions are depicted in Figs. 4, 5, and 6, respectively. It is shown that as time increases, the gas temperature decreases with droplets traveling downstream.

The droplet distributions are schematically shown in Fig. 7. Vaporization takes place as droplets move downstream, as evidenced by a decrease in sizes. It is further noted that, due to higher temperatures away from the axis of symmetry, droplets decrease in diameter with an increase in the radial coordinate. The corresponding droplet velocity vector field is shown in Fig. 8. For ease in visualization, the arrows are drawn for every fourth position of those for droplets shown in Fig. 7.

To illustrate effects of the difference between the gas velocity and initial droplet velocity, the results for $U=2.0$ and $U=0.5$ holding $U_l=1.0$ constant are presented in Figs. 9 and 10, respectively. It is seen that the magnitude of the droplet velocity increases downstream for the higher gas velocity, whereas the trend is reversed for the lower gas velocity, with the droplet velocity approaching the local gas velocity downstream. It is also evident that the lower gas velocity tends to cause the droplet spray width to be expanded downstream. Figure 11 shows that the gas velocity higher than the initial

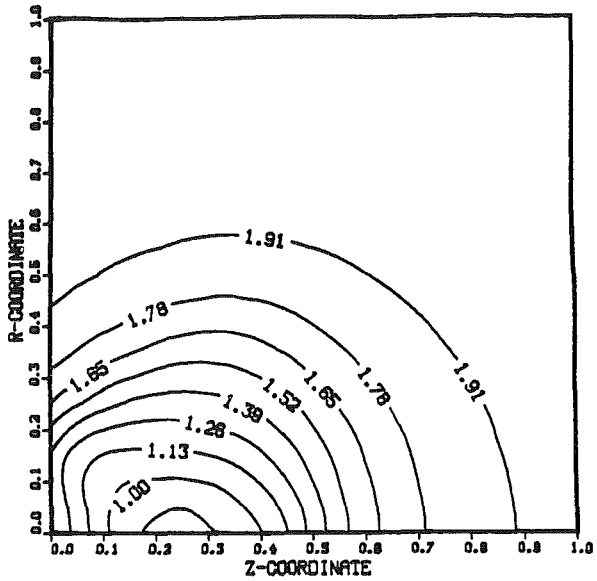

Fig. 15 Case 3, contours of gas temperature field, intermediate grid, $N=7$, $t=0.5$, $U=U_l=1.0$; extremely steep temperature gradients occurs near the injector

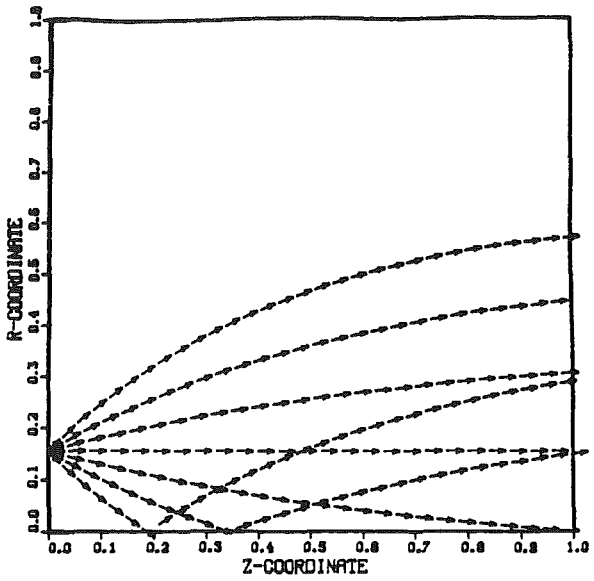

Fig. 17 Case 3, droplet velocity vector field, intermediate grid, $N=7$, $t=3.5$, $U=U_l=1.0$

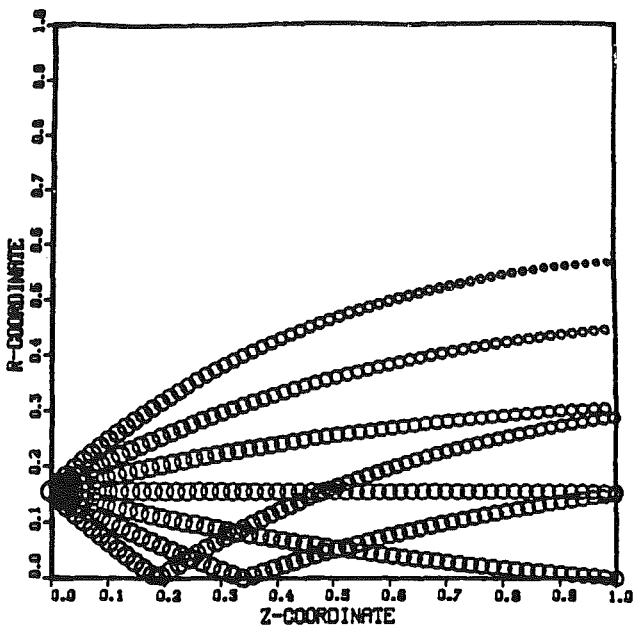

Fig. 16 Case 3, droplet volume, droplet diameters amplified 300 times, intermediate grid, $N=7$, $t=3.5$, $U=U_l=1.0$, droplets cross, leading to multivaluedness

droplet velocity causes the steady state to be reached rather quickly, whereas the trend is reversed if the gas velocity is lower than the initial droplet velocity (Fig. 12).

To investigate the effect of injection angles, the results of Case 2 are presented in Figs. 13 and 14. Notice that the gas temperature near the axis is higher than that of Case 2 since the droplets are absent along the axis (Fig. 13). Furthermore, the location of the lowest temperature moves further downstream (Fig. 14) as compared to that of Case 1.

Discussions to this point deal with injectors with angles originating from a point $z=-0.1$. To study the effects of multivaluedness with droplet trajectories crossing each other, we examine the injector with circular cavity, shown as Case 3 in Fig. 2.

Temperature distributions for Case 3 with $U=U_l=1.0$ and $N=7$ are shown in Fig. 15 for $t=0.5$. Note that the temperature gradients are rather steep in the vicinity of the injector. As seen in Figs. 16 and 17, droplets cross at various locations where droplet properties vary, thus exhibiting the multivaluedness of the solution. It should be noted that the gas temperature field is still single valued (Fig. 15). Recall that the numerical diffusion that may arise in the standard Eulerian-Eulerian formulation is absent in the present scheme.

Finally, it is remarked that the results differ as much as 20 percent from those of Aggarwal et al. (1983) in some regions of the computational domain. This is expected because the constants and parameters used in the reference were unavailable. The trend, however, is remarkably the same as those reported in the reference.

5 Conclusion

Based on the study conducted on simple examples presented in this paper, the following conclusions are drawn:

1 One of the advantages of the finite element method is the way boundary conditions are imposed. In particular, the Neumann and Cauchy boundary conditions can be implemented easily and accurately.

2 Subquadratic convergence (L_2 norm error) is obtained for grid spacing, droplet pulse time, integration time step, and number of droplet characteristics. However, convergence is insensitive to the number of droplet characteristics.

3 Extension of the present numerical scheme using finite elements to advanced topics such as interactions of droplets with turbulence, nondilute combustion, and critical point phenomena using finite elements is worthy of further research.

References

Aggarwal, S. K., Lee, D. N., Fix, G. J., and Sirignano, W. A., 1981, "Numerical Computation of Fuel-Air Mixing in a Two-Phase Axisymmetric Coaxial Free Jet Flow," *Proceedings, 4th IMACS Int. Symposium on Computer Methods for Partial Differential Equations*, IMACS.

Aggarwal, S. K., Lee, D. N., Fix, G. J., and Sirignano, W. A., 1983, "Numerical Optimization Studies of Axisymmetric Unsteady Sprays," *Journal of Computational Physics*, Vol. 50, No. 1, pp. 101-115.

Aggarwal, S. K., and Sirignano, W. A., 1984, "Numerical Modeling of One-Dimensional Enclosed Homogeneous and Heterogeneous Deflagrations," *Computers and Fluids*, Vol. 12, No. 2, pp. 145-158.

Chung, T. J., 1978, *Finite Element Analysis in Fluid Dynamics*, McGraw-Hill, New York.

Chung, T. J., Kim, Y. M., and Sohn, J. L., 1987, "Finite Element Analysis in Combustion Phenomena," *Int. J. Numerical Methods in Fluids*, Vol. 7, No. 10, pp. 989-1012.

Crowe, C. T., Sharma, M. P., and Stock, D. E., 1977, "The Particle-Source-In Cell (PSI-CELL) Model for Gas-Droplet Flows," ASME *Journal Fluids Engineering*, Vol. 99, pp. 325-332.

Dukowicz, J. K., 1980, "A Particle-Fluid Numerical Model for Liquid Sprays," *Journal of Computational Physics*, Vol. 35, pp. 229-253.

Gupta, H. C., and Bracco, F. V., 1978, "Numerical Computations of the Two-Dimensional Unsteady Sprays for Application to Engines," *AIAA J.*, Vol. 16, pp. 1053-1061.

Hughes, T. J. R., 1987, "Recent Progress in the Development and Understanding of SUPG Methods With Special Reference to the Compressible Euler and Navier-Stokes Equations," *Int. J. Numerical Methods in Fluids*, Vol. 7, No. 11, pp. 1224-1240.

Löhner, R., and Morgan, K., 1987, "Finite Element Flux-Corrected Transport (FEM-FCT) for the Euler and Navier-Stokes Equations," *Int. J. Numerical Methods in Fluids*, Vol. 7, No. 10, pp. 1093-1110.

Oden, J. T., Strouboulis, T., and Devloo, P., 1987, "Adaptive Finite Element Methods for High Speed Compressible Flows," *Int. J. Numerical Methods in Fluids*, Vol. 7, No. 11, pp. 1174-1192.

Seth, B., Aggarwal, S. K., and Sirignano, W. A., 1978, "Flame Propagation Through an Air-Fuel Spray With Transient Droplet Vaporization," *Combustion and Flame*, Vol. 32, pp. 257-270.

Sirignano, W. A., 1986, "The Formulation of Combustion Models: Resolution Compared to Droplet Spacing," ASME JOURNAL OF HEAT TRANSFER, Vol. 108, pp. 633-639.

Westbrook, C. K., 1976, "Three-Dimensional Numerical Modeling of Liquid Fuel Sprays," *16th Int. Symposium on Combustion*, Cambridge, MA, pp. 1517-1526.

R. J. Haywood
Graduate Student.

R. Nafziger
Graduate Student.

M. Renksizbulut
Associate Professor.

University of Waterloo,
Mechanical Engineering Department,
Waterloo, Ontario, Canada N2L 3G1

A Detailed Examination of Gas and Liquid Phase Transient Processes in Convective Droplet Evaporation

A finite volume numerical technique has been used to model the evaporation of an n-heptane droplet with an initial Reynolds number of 100 in air at 800 K, 1 atm. The effects of variable thermophysical properties, liquid phase motion and heating, and transient variations in droplet size and velocity are included in the analysis. With appropriate corrections for the effects of variable properties and liquid phase heating, quasi-steady correlations are shown to predict accurately the transient histories of the drag coefficient and Nusselt and Sherwood numbers. For the case investigated here, the transient effects of importance were the variation in droplet velocity, the decline in the liquid phase velocities, and the rise in the droplet surface and volume average temperatures. In spite of the transient rise in the droplet temperature, the nature of the liquid phase heating, as characterised by the liquid Nusselt number, was found to remain constant during most of the droplet lifetime.

1 Introduction

Evaporation of droplets in high-temperature convective environments is of substantial importance in a large number of practical industrial processes. Typical combustion chamber conditions and fuel spray patternation in diesel and rocket engines and gas turbines make convective evaporation at intermediate Reynolds number ($\mathrm{Re} = O(100)$) the predominant mode of droplet vaporization. Despite many years of research, further understanding of isolated droplet evaporation in the intermediate Reynolds number regime, including the effects of all gas and liquid phase transients, variable thermophysical properties, and liquid phase heat and momentum transport, is still required. In particular, the literature demonstrates a lack of consensus as to the transport processes that may be considered quasi-steady. Although most researchers acknowledge the large temperature differences intrinsic to the physical problem, few have attempted to include property variations in their models. Finally, the exact nature of liquid phase momentum and heat transfer processes for a realistic droplet are not well characterized without simplifying assumptions in either the continuous or dispersed phases. Because this work is concerned with evaporation in the intermediate Reynolds number regime, the large volume of literature dealing with droplet evaporation and combustion at very low and zero Reynolds numbers will not be discussed in the following literature review.

Using a boundary layer analysis, Prakash and Sirignano (1980) examined the convective evaporation of *n*-hexane, *n*-decane, and *n*-hexadecane droplets at 10 atm ambient pressure. Based on the observation that the gas phase residence time $2R^*/U^*_\infty$ is typically much shorter than the droplet lifetime, quasi-steadiness was assumed in all gas phase transport processes. Similarly, because the characteristic time required to establish steady liquid phase motion is much smaller than the droplet lifetime, liquid motion was assumed to behave in a quasi-steady manner. Despite finding liquid phase heating a source of unsteadiness persisting throughout most of the droplet lifetime, the quasi-steady correlations of Ranz and Marshall (1952) and Spalding (1953) were found to agree well with the results, provided an appropriate correction was made for the effects of the unsteady liquid phase heat flux. Summarizing the results of their approximate analytical solutions in a review article, Sirignano (1983) concluded that because transient heating of the droplet surface continues throughout the droplet lifetime without the surface reaching the boiling point temperature, no justification can be found for a quasi-steady assumption with respect to liquid phase heating.

Sundararajan and Ayyaswamy (1984), following similar characteristic time arguments, studied condensation on droplets at intermediate Reynolds numbers, assuming quasi-steady behavior in all processes but liquid phase heating. Because of the differences between the evaporation and condensation processes, their observations cannot readily be applied to droplet evaporation. Furthermore, because their analysis, as well as that of Prakash and Sirignano (1980), allows transient behavior only in the liquid phase heating, the importance of transient effects in the gas and liquid phases, the motion of the receding gas/liquid interface, and global transients such as droplet deceleration, are still inadequately addressed.

Dwyer and Sanders (1984a, 1984b) modeled the convective evaporation of dodecane droplets at ambient pressures of 1, 5, and 25 atm. A sophisticated numerical technique, using an adaptive grid to track the shrinking droplet, was employed. The model included the effects of transients in both phases as well as the transient deceleration of the droplet under the influence of its own drag. Variations in surface mass transfer due to droplet heating were found to be the primary cause of unsteadiness. Because drag coefficients and Nusselt numbers were found to have values lower than quasi-steady correlations would predict, it was concluded that there were large deviations from quasi-steady behavior in heat, mass, and momentum transport during the droplet lifetime. Particularly puzzling are their predictions of the drag coefficient, which not only show a decreasing trend with decreasing Reynolds number, but also indicate a very large reduction in drag due to vaporization. These trends contradict well known experimental observations (e.g., see Yuen and Chen, 1976).

In direct contrast to these conclusions, numerical studies by Renksizbulut and Haywood (1986, 1988) showed that the instantaneous drag coefficients and Nusselt numbers of droplets of *n*-heptane evaporating in their own vapor at 1 and 10 atm could be predicted using the correlations of Renksizbulut and Yuen (1983, 1983b) provided that a suitable correction is made for the effects of liquid phase heating. Further, it was demonstrated that complete droplet life histories could be

Contributed by the Heat Transfer Division for publication in the JOURNAL OF HEAT TRANSFER. Manuscript received by the Heat Transfer Division March 22, 1988. Keywords: Evaporation, Sprays/Droplets, Transient and Unsteady Heat Transfer.

predicted using a simple analytical model that utilized correlations in a quasi-steady manner together with an enhanced diffusion model for liquid heating. The liquid heating model accounted for the effects of liquid motion through the use of an effective thermal conductivity. The predictive abilities of the simple analytical model were better at lower ambient pressures. It was concluded that unsteady gas phase effects, resulting from perturbations to the velocity and temperature fields due to the higher surface regression rate at higher pressures, were responsible for the departure from quasi-steady behavior. The effects of increased surface motion and second-order drag effects, which are more pronounced at elevated pressures (Faeth, 1983), may have contributed to the observed departure because the correlations used in the model do not acknowledge these effects.

From the previous discussion it becomes clear that many of the important phenomena associated with convective droplet evaporation occur within the liquid phase. In order to assess the impact of liquid heating on droplet combustion, Law (1976) and Law and Sirignano (1977) examined the two limiting cases of; (*i*) rapid mixing in which the liquid thermal conductivity is assumed to be infinite due to the presumed intense liquid phase motion, and (*ii*) the conduction limit corresponding to a motionless liquid phase. Although useful in defining the envelope of possible liquid phase behaviors, the physical reality does not approach either of these limits. Detailed numerical results of Renksizbulut and Haywood (1986, 1988) show an initial period of rapid mixing and corresponding high rates of liquid heating associated with the establishment of a toroidal temperature field followed by a more gradual heating as the diffusion of heat proceeds normal to the established pattern of closed isotherms.

In order to understand more completely the liquid phase processes, many researchers have decoupled the problem and, while making simplifying assumptions with respect to the behavior of the continuous phase, have solved the heat, mass, and momentum transport phenomena within the liquid phase alone. Johns and Beckmann (1966) studied numerically the liquid phase mass transport, subject to the assumptions of a creeping flow velocity field in the liquid phase (the Hadamard–Rybczynski solution), and negligible continuous phase resistance to mass transfer. The observed transient liquid Nusselt number behavior consisted of a rapid initial decline followed by an oscillatory approach to an asymptotic value. For liquid Peclet numbers in excess of 60 the asymptotic Nusselt number was within 5 percent of the Kronig and Brink (1950) limit of 17.9 attained at infinite Peclet number. In terms of a general qualitative understanding of liquid phase transport phenomena, this analysis provides insight, but neglecting the transient effects of droplet deceleration and evaporation, as well as imposing a liquid phase velocity field valid only in creeping flow, limit its application in realistic cases.

Assuming an approximate surface shear stress distribution due to the relative motion of the gas with respect to the droplet, Prakash and Sirignano (1978) studied liquid droplet heating with internal circulation. The liquid motion was taken to be quasi-steady and to consist of a thin laminar boundary layer at the gas/liquid interface and an inviscid core behaving as a Hills spherical vortex. This liquid phase model was later coupled to a gas phase analysis as discussed previously. Liquid phase motion was found to reduce the time required to establish nearly uniform temperature profiles in the droplet but not toward the (instantaneous) limit suggested by a rapid mixing model. While this analysis includes many of the important gas phase phenomena that influence liquid phase motion and heating, several weaknesses still exist. The transient reduction in droplet Reynolds number and the associated reduction in liquid Peclet number may alter the nature of liquid heating during the droplet lifetime. The boundary layer analysis also neglects the wake region, making it impossible to determine the drag coefficient. Furthermore the contribution to heat and mass transfer from this region is not entirely negligible.

In this paper the evaporation of an isolated *n*-heptane

Nomenclature

B_H = heat transfer number $= c^*_{P,g}(T^*_\infty - T^*_s)/L^*_s$
B_M = mass transfer number $= (Y_{F,s} - Y_{F,\infty})/(1 - Y_{F,s})$
c_P = specific heat at constant pressure $= c^*_P/c^*_{P,\infty}$
C_D = total drag coefficient $= C_F + C_P + C_T$
C_F = friction drag coefficient $= 2F^*_F/(\rho^*_\infty v^{*2}_\infty \pi R^{*2})$
C_P = pressure drag coefficient $= 2F^*_P/(\rho^*_\infty v^{*2}_\infty \pi R^{*2})$
C_T = thrust coefficient $= 2F^*_T/(\rho^*_\infty v^{*2}_\infty \pi R^{*2})$
$\mathfrak{D}$ = species diffusion coefficient $= \mathfrak{D}^*/\mathfrak{D}^*_\infty$
F^* = force
h^*_H = heat transfer coefficient
h^*_M = mass transfer coefficient
k = thermal conductivity $= k^*/k^*_\infty$
L_s = latent heat of vaporization $= L^*_s/(c^*_{P,\infty} T^*_\infty)$
$\dot{m}^*$ = total evaporation rate
$\dot{m}''_\theta$ = local mass flux $= \dot{m}''^*_\theta/(\rho^*_\infty v^*_{\infty,o})$
M = molecular weight
Nu = Nusselt number $= 2R^* h^*_H/k^*$
p = pressure $= (p^* - p^*_\infty)/(\rho^*_\infty v^{*2}_{\infty,o})$
Pr = Prandtl number $= \mu^* c^*_P/k^*$
Q^* = heat transfer rate
r = radial coordinate $= r^*/R^*$
R = instantaneous drop radius $= R^*/R^*_o$
$\mathfrak{R}$ = universal gas constant
Re = Reynolds number $= 2R^*\rho^* v^*_\infty/\mu^*$
Re_m = Reynolds number $= 2R^*\rho^*_\infty v^*_\infty/\mu^*_f$
Sh = Sherwood number $= 2R^* h^*_M/(\rho^* \mathfrak{D}^*)$
Sc = Schmidt number $= \mu^*/(\rho^* \mathfrak{D}^*)$
t = time $= t^* v^*_{\infty,o}/R^*_o$
T = temperature $= T^*/T^*_\infty$
v^*_∞ = instantaneous free-stream velocity
V = instantaneous free-stream velocity $= v^*_\infty/v^*_{\infty,o}$
v_r = radial velocity component $= v^*_r/v^*_\infty$
v_θ = tangential velocity component $= v^*_\theta/v^*_\infty$
X = mole fraction
Y = mass fraction
θ = tangential coordinate
μ = viscosity $= \mu^*/\mu^*_\infty$
ρ = density $= \rho^*/\rho^*_\infty$
$\tau_{r\theta}$ = shear stress $= \tau^*_{r\theta}/(\mu^*_\infty v^*_\infty/R^*)$
τ_{rr} = normal shear $= \tau^*_{rr}/(\mu^*_\infty v^*_\infty/R^*)$
ϕ = generalized variable

Subscripts and Superscripts

A = air component
f = film conditions
F = fuel component
g = gas phase
H = heat transfer
l = liquid phase
M = mass transfer
o = initial conditions
r = thermal radiation
s = at the droplet surface
θ = local
∞ = free-stream conditions
* = dimensional quantity
$\hat{}$ = unit vector
$\tilde{}$ = tensor
$\bar{}$ = spatial average

Table 1 Nondimensional governing equations

THE GOVERNING EQUATIONS

$$\frac{\partial}{\partial t}(\rho V R\phi) + V^2\vec{\nabla}\cdot\left\{\rho\phi\left[\left(v_r - \frac{r}{V}\frac{dR}{dt}\right)\hat{r} + v_\theta\hat{\theta}\right]\right\} = \frac{V}{R}\vec{\nabla}\cdot\left(\Gamma_\phi\vec{\nabla}\phi\right) + S_\phi \quad (1)$$

Equation	ϕ	Γ_ϕ	S_ϕ
Continuity	1	0	S_C
Radial Momentum	v_r	$2\mu/Re_{\infty,o}$	S_{RM}
Tangential Momentum	v_θ	$2\mu/Re_{\infty,o}$	S_{TM}
Energy	T	$2k/(c_P Re_{\infty,o}Pr_\infty)$	S_E
Species	Y_F	$2\rho\mathcal{D}/(Re_{\infty,o}Sc_\infty)$	S_Y

where:

$$S_C = \rho R\frac{dR}{dt} - 2\rho V\frac{dR}{dt}$$

$$S_{RM} = V^2\left[\vec{\nabla}\cdot(\rho\vec{v}v_r) - \vec{\nabla}\cdot(\rho\vec{v}\vec{v})_r\right] - \frac{2V}{\mathrm{Re}_{\infty,o}R}\left[\vec{\nabla}\cdot\mu\vec{\nabla}v_r - \left(\vec{\nabla}\cdot\tilde{\tau}\right)_r\right] - 2\rho V v_r\frac{dR}{dt} - \frac{\partial p}{\partial r} - \rho R\cos\theta\frac{dV}{dt}$$

$$S_{TM} = V^2\left[\vec{\nabla}\cdot(\rho\vec{v}v_\theta) - \vec{\nabla}\cdot(\rho\vec{v}\vec{v})_\theta\right] - \frac{2V}{\mathrm{Re}_{\infty,o}R}\left[\vec{\nabla}\cdot\mu\vec{\nabla}v_\theta - \left(\vec{\nabla}\cdot\tilde{\tau}\right)_\theta\right] - 2\rho V v_\theta\frac{dR}{dt} - \frac{1}{r}\frac{\partial p}{\partial\theta} + \rho R\sin\theta\frac{dV}{dt}$$

$$S_E = \rho TR\frac{dV}{dt} - 2\rho TV\frac{dR}{dt} + \frac{2V}{\mathrm{Re}_{\infty,o}\mathrm{Pr}_\infty R}\frac{k}{c_P^2}\left(\vec{\nabla}T\cdot\vec{\nabla}c_P\right) + \frac{2V}{\mathrm{Re}_{\infty,o}\mathrm{Sc}_\infty R}\left(\frac{c_{P,F}-c_{P,A}}{c_P}\right)\rho\mathcal{D}\left(\vec{\nabla}T\cdot\vec{\nabla}Y_F\right)$$

$$S_Y = \rho Y_F R\frac{dV}{dt} - 2\rho Y_F V\frac{dR}{dt}$$

droplet with an initial Reynolds number of 100 at an ambient 800 K and 1 atm is examined. A numerical finite volume analysis is employed and all transients and variable property effects are included in both gas and liquid phases. An assessment will be made of the importance of all transient processes in gas and liquid phases including the shrinkage of the liquid droplet and the resulting motion of the gas/liquid interface, the deceleration of the droplet under the influence of its own drag and its effect on liquid phase motion, and the transient heating of the droplet interior. The ability of quasi-steady correlations in prediction of instantaneous drag coefficients and Nusselt and Sherwood numbers will be examined. The detailed nature of transport phenomena at the gas liquid interface as well as the liquid phase motion and heating will be presented and discussed. It is hoped that the detailed information presented in this paper will serve as benchmark data against which future analytical and numerical models may be compared.

2 Mathematical and Numerical Model

In the formulation of the problem it has been assumed that: (*i*) The droplet maintains a spherical shape, (*ii*) the flow field is laminar and axisymmetric, (*iii*) there are no external body forces, (*iv*) thermal radiative, viscous dissipation, Soret and Dufour effects and pressure diffusion are negligible, (*v*) thermodynamic equilibrium prevails at the gas/liquid interface, and (*vi*) air is insoluble in the liquid droplet. All effects due to variable thermophysical properties, liquid phase motion and heating, and transient variations in droplet size and velocity are included in the analysis. Expressions for conservation of mass, momentum, energy, and species in spherical polar coordinates, subject to the above assumptions, and nondimensionalized as outlined in the nomenclature section, are given in Table 1.

Nondimensionalizing lengths and velocities according to instantaneous values is done for convenience in the numerical modeling. In the transformed coordinates the boundary far from the droplet and the gas/liquid interface remain stationary and boundary conditions far from the droplet remain temporally constant. The penalty paid for this convenience is

Table 2 Nondimensionalized boundary conditions; for the present study $r_\infty = 40$

BOUNDARY CONDITIONS

Gas/liquid interface:	$T_{\ell,s} = T_{g,s}$,	$v_{\theta,\ell,s} = v_{\theta,g,s}$
$(r = 1, 0 \le \theta \le \pi)$	$-\left(k\frac{\partial T}{\partial r}\right)_{\ell,s} = -\left(k\frac{\partial T}{\partial r}\right)_{g,s} + \frac{1}{2}\mathrm{Re}_{\infty,o}\mathrm{Pr}_\infty R\dot{m}''_\theta L_s$	
	$\dot{m}''_\theta = \frac{2}{\mathrm{Re}_{\infty,o}\mathrm{Sc}_\infty}\left[\frac{-\rho\mathcal{D}}{R(1-Y_F)}\frac{\partial Y_F}{\partial r}\right]_{g,s}$	
	$X_{F,s} = p^*_{F,s}\left(T^*_s\right)/p^*_\infty$	
	$v_{r,\ell,s} = \frac{1}{V}\left(\frac{\dot{m}''_\theta}{\rho_{\ell,s}} + \frac{dR}{dt}\right)$;	$v_{r,g,s} = \frac{1}{V}\left(\frac{\dot{m}''_\theta}{\rho_{g,s}} + \frac{dR}{dt}\right)$
	$\mu_{\ell,s}\left(\frac{\partial v_\theta}{\partial r} - \frac{v_\theta}{r} + \frac{1}{r}\frac{\partial v_r}{\partial\theta}\right)_{\ell,s}$	$= \mu_{g,s}\left(\frac{\partial v_\theta}{\partial r} - \frac{v_\theta}{r} + \frac{1}{r}\frac{\partial v_r}{\partial\theta}\right)_{g,s}$
Free stream inlet:	$T = 1$	$Y_F = 0$
$(r = r_\infty, 0 \le \theta \le \pi/2)$	$v_r = -\cos\theta$	$v_\theta = \sin\theta$
Free stream outlet:	$\frac{\partial\phi}{\partial r} = 0$;	$\phi = v_r, v_\theta, T, Y_F$
$(r = r_\infty, \pi/2 \le \theta \le \pi)$		
Axes of symmetry:	$\frac{\partial\phi}{\partial\theta} = 0$;	$\phi = v_r, T, Y_F$
$(0 \le r \le r_\infty, \theta = 0, \pi)$	$v_\theta = 0$	
Origin:	$\frac{\partial\phi}{\partial r}\Big)_{\theta=\pi/2} = 0$;	$\phi = v_r, T, Y_F$
$(r = 0)$		

manifested in the extra terms appearing in the governing equations. The boundary conditions are given in Table 2.

Expressions for overall conservation of mass and momentum complete the mathematical model and are as follows:

Conservation of Mass:

$$\frac{dR}{dt} = -\frac{1}{2\bar{\rho}_l}\left(\int_0^\pi \dot{m}''_\theta\sin\theta\, d\theta + \frac{2}{3}R\frac{d\bar{\rho}_l}{dt}\right) \quad (2)$$

Conservation of Momentum:

$$\frac{dV}{dt} = -\frac{3}{8}\frac{C_D V^2}{\bar{\rho}_l R} \quad (3)$$

For completeness the definitions of drag coefficients, Nusselt, and Sherwood numbers are also given here

$$C_F = \frac{8}{\mathrm{Re}_{\infty,o}RV}\int_0^\pi (\tau_{r\theta}\sin\theta - \tau_{rr}\cos\theta)_s\sin\theta\, d\theta \quad (4)$$

$$C_P = \frac{4}{V^2}\int_0^\pi p_s\cos\theta\sin\theta\, d\theta \quad (5)$$

$$C_T = 2\int_0^\pi \rho_g\left(v_r^2\sin 2\theta - 2v_r v_\theta\sin^2\theta\right)_s d\theta \quad (6)$$

$$\mathrm{Nu}_\infty = \frac{1}{2}\int_0^\pi \left(\frac{2k_g}{1-T}\frac{\partial T}{\partial r}\right)_{s,\theta}\sin\theta\, d\theta \quad (7)$$

$$\mathrm{Sh}_\infty = \frac{1}{2}\int_0^\pi \left(\frac{2\rho_g\mathcal{D}}{Y_{F,\infty}-Y_F}\frac{\partial Y_F}{\partial r}\right)_{s,\theta}\sin\theta\, d\theta \quad (8)$$

Clearly the coupled, nonlinear transport equations and boundary conditions forming the mathematical model do not admit an exact analytical solution and for this reason a numerical approach was taken. Integration of the transport equations over discrete control volumes and discrete time steps led to the formation of sets of linearized equations of the form:

$$a_P\phi_P = a_N\phi_N + a_S\phi_S + a_E\phi_E + a_W\phi_W + b \quad (9)$$

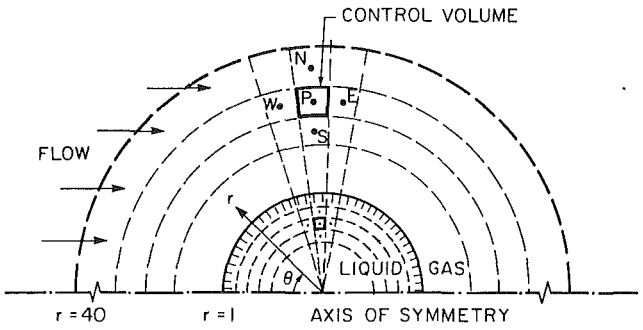

Fig. 1 The numerical solution domain and grid layout

relating the value of ϕ at any point P to the values at the neighboring points N, S, E, and W, as shown in Fig. 1. The linearized equation sets were solved using an iterative line Gauss-Seidel method with overrelaxation. Iteration at the coefficient level is also necessary due to the nonlinearity of the coefficients $a_{N,S,E,W,P}$ and b. Boundary conditions at the gas/liquid interface were implemented by discretizing the governing boundary conditions for special interface control volumes of zero thickness, leading to equations similar in form to equation (9). In this way, simultaneous solution of both phases could be accomplished, ensuring a direct and accurate coupling. Details of the lengthy derivation leading to equation (9), the thermophysical properties used, and other aspects of the numerical procedure are given in the theses by Haywood (1986) and Nafziger (1988).

The numerical grid, shown in Fig. 1, was formed of orthogonal annular control volumes bounded by lines of constant r and θ, with 45 control volumes tangentially equally spaced at 4 deg intervals and 70 control volumes radially unequally spaced. On the liquid side 20 radial control volumes with a nondimensional spacing of $\Delta r = 0.0125$ adjacent to the droplet surface flaring at a rate of 12.9 percent toward the origin were used. In the gas phase 50 radial control volumes with $\Delta r = 0.0125$ at the droplet surface and flaring at a rate of 12.7 percent were employed resulting in $r_\infty = 40$.

Because there are no known exact solutions for the problem under investigation, it was necessary to test the accuracy of the numerical predictions by comparison to existing benchmark experimental and numerical correlations for test problems that isolated relevant aspects of the complete problem. Predicted total drag values for isothermal solid spheres at Reynolds numbers between 1 and 250 were within 1 percent of the experimental correlation of Clift et al. (1978). The point of flow separation was predicted within 0.5 deg and the trailing vortex length within 3 percent of experimentally observed values. Predicted component drag values were within 1 percent of the numerical predictions of Cliffe and Lever (1984) and total drag values for isothermal liquid spheres at Reynolds numbers between 100 and 300 were within 1 percent of the numerical data of LeClair and Hamilec (1972). Total drag coefficients and Nusselt numbers agreed within 1 and 2 percent, respectively, of the correlations of Renksizbulut and Yuen (1983a, 1983b) for solid spheres with heat transfer.

Because economic constraints preclude extensive grid refinement studies for the complete transient problem, the study of solution sensitivity to the size and shape of the grid were restricted to the test problems previously mentioned. Tangential control volume spacings of 3, 4, and 5 deg, corresponding to 60, 45, and 30 tangential control volumes, respectively, affected drag values by less than 1 percent. The use of 30 rather than 20 control volumes radially in the liquid phase resulted in less than 0.1 percent change in the gas/liquid interface velocity and negligible change in the liquid vortex center location. The use of up to 80 radial control volumes in the gas phase, covering a range of r_∞ between 20 and 80, with

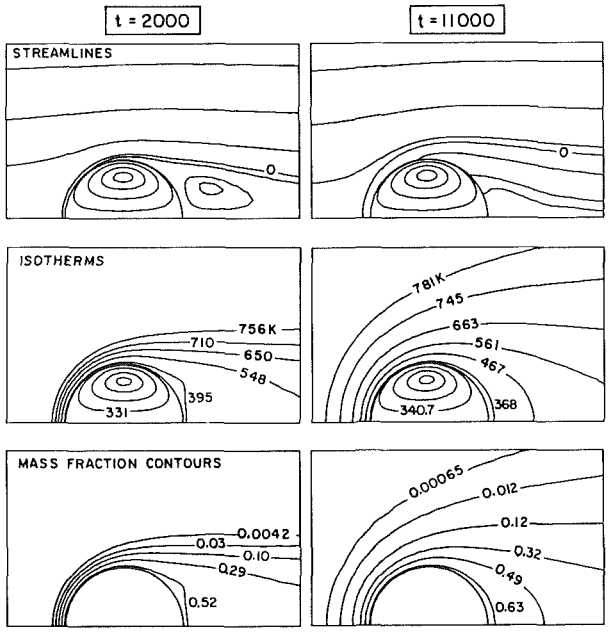

Fig. 2 Streamlines, isothermals, and mass fraction contours at $t = 2000$ and 11,000. The remaining liquid phase isothermals are 323 K, 315 K, 312 K at $t = 2000$, and 340.5 K, 340.4 K, 340.3 K at $t = 11{,}000$.

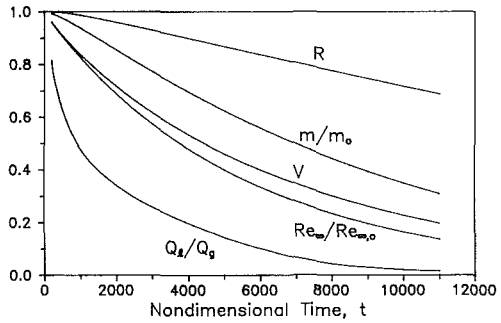

Fig. 3 Droplet radius, mass, velocity, Reynolds number, and liquid heating fraction histories

either a smaller rate of grid flare or smaller control volumes, resulted in changes of predicted drag values of less than 1 percent. The timestep sensitivity of the numerical solution was investigated through a series of trials of timestep-halving at various times throughout the transient development. For example, a test involving 100 timesteps corresponding to about 5 percent of the total droplet lifetime resulted in accumulated differences less than 0.2 percent in the key parameters of interest such as R, V, C_D, Nu, and Sh. Hence the results are believed to be reasonably grid and timestep independent.

3 Results and Discussion

The following results describe the life history of an n-heptane droplet evaporating in air at 800 K and 1 atm pressure. The droplet is initially uniform in temperature at 298 K with no internal motion and has an initial Reynolds number of 100 based on free-stream thermophysical properties.

Streamlines, isotherms, and isomass contour plots are shown in Fig. 2 at two times during the droplet lifetime. Qualitatively, the importance of convection in both the liquid and gas phases is apparent: in the gas phase by the fore-aft nonsymmetry; and in the liquid phase by the similarity between the streamlines and isotherms. The effect of surface blowing due to vaporization is also noted in the displacement of the zero streamline away from the droplet surface. The

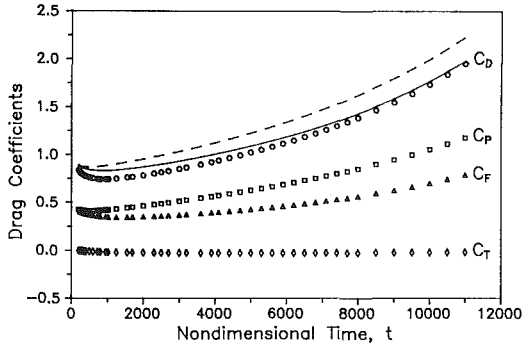

Fig. 4 Drag coefficients; ○ —fully numerical solution;—equation (10); - - - Yuen and Chen (1976) correlation; □ —C_P; Δ—C_F; ◇ —C_T

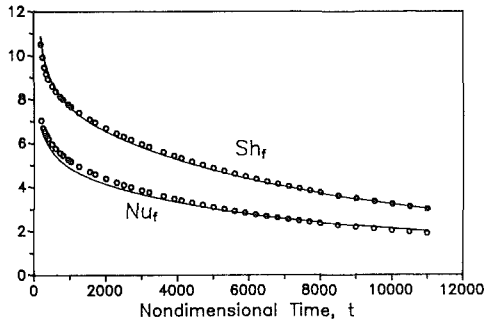

Fig. 5 Nusselt and Sherwood number histories; ○ —fully numerical solution;—equation (12) for Nu and equation (13) for Sh

transient Reynolds number, liquid heating fraction, velocity, radius, and mass histories are shown in Fig. 3. The droplet spends a significant portion of its lifetime at Reynolds numbers where convection effects are dominant, although it is arguable whether the assumption of boundary layer behavior is valid especially at later times. Liquid heating persists for about the first half of the droplet lifetime in the present case. With higher vaporization rates expected at elevated pressures, liquid heating will persist for a greater portion of the lifetime. Because the time required to heat the droplet is of the same order as the droplet lifetime, liquid heating is an important source of unsteady behavior.

Figures 4 and 5 show the transient histories of the momentum, heat, and mass transfer rates as characterized by the total drag coefficient, Nusselt, and Sherwood numbers, respectively. Except for an early rapid reduction, the total drag coefficient follows the expected increasing trend as the droplet Reynolds number decreases. The early reduction in C_D is caused by the modification of the flow field and transport properties in the vicinity of droplet surface with the onset of evaporation. Specifically, vaporization acts to decrease drag by (*i*) thickening the boundary layer and thus reducing the shear stress at the droplet surface, and (*ii*) reducing the mixture viscosity in the gas phase boundary layer by increasing the concentration of cold fuel vapor. Following the methodology of Haywood and Renksizbulut (1986) the drag history can be predicted based on the drag correlation of Renksizbulut and Yuen (1983a)

$$C_D(1+B'_{Hf})^{0.2} = \frac{24}{\mathrm{Re}_m}(1+0.2\mathrm{Re}_m^{0.63}); \quad 10 \le \mathrm{Re}_m \le 300 \tag{10}$$

where

$$B'_{Hf} = \frac{c^*_{Pf}(T^*_\infty - \tilde{T}^*_s)}{L^*_s}\left(1 - \frac{Q_l}{Q_g} + \frac{Q_r}{Q_g}\right) \tag{11}$$

The quasi-steady prediction of this correlation is in good agreement with the numerical data as seen in Fig. 4. Some departure is observed earlier in the droplet lifetime when the droplet surface mobility is strongest. This is consistent with the fact that the right-hand side of equation (10) is based on the standard drag curve for solid spheres. Although some attempts have been made (Nafziger, 1988) to modify equation (10) for the effects of surface mobility, there are insufficient data at the present time to achieve this objective.

Figure 4 also shows the component drag histories. Pressure drag is found to be the dominant drag component throughout the droplet lifetime. This is consistent with the fact that blowing due to evaporation reduces friction drag but at the same time destabilizes the boundary layer leading to early flow separation and hence higher pressure drag as compared to the solid sphere case. Thrust caused by asymmetric surface mass efflux was found to be negligible, contributing to at most 3 percent reduction in C_D. Surprisingly the major contribution to C_T comes from the second term of the integral in equation (6). Yuen and Chen (1976) have proposed using the standard drag curve with the viscosity in the Reynolds number based on the one-third reference state. As shown in Fig. 4 this approach did not produce encouraging results.

The transient heat transfer behavior in some respects parallels that of the momentum transfer. With the onset of surface blowing, the thickening boundary layer and reduced thermal conductivity in the cold, fuel-rich region near the droplet surface both act to impede the transfer of energy to the droplet surface, and a rapid initial decline in the Nusselt number is observed. Once blowing is established the slowly decreasing Reynolds number and associated reduced convective transport lead to a more gentle decreasing trend in Nu. Again, with appropriate modification for the effects of liquid phase heating, variable properties, and surface blowing, the Nusselt number history is predicted reasonably well by the Renksizbulut–Yuen (1983b) correlation

$$\mathrm{Nu}_f(1+B'_{Hf})^{0.7} = 2 + 0.57\mathrm{Re}_m^{1/2}\mathrm{Pr}_f^{1/3}; \quad 20 \le \mathrm{Re}_m \le 2000 \tag{12}$$

As expected, the transient dynamics of the mass transfer are very similar to the heat transfer. The thickened boundary layer and modified properties in the cold, fuel-rich boundary rapidly decrease the mass transfer during the initial stages of evaporation. A more gentle decrease in the Sherwood number is then observed, owing to the reduced convection effects as the Reynolds number decays. The following quasi-steady mass transfer correlation, similar in form to the Nusselt number correlation, predicts the transient Sherwood number behavior with good accuracy:

$$\mathrm{Sh}_f(1+B_M)^{0.7} = 2 + 0.87\mathrm{Re}_m^{1/2}\mathrm{Sc}_f^{1/3}; \quad 20 \le \mathrm{Re}_m \le 2000 \tag{13}$$

where

$$B_M = \frac{\tilde{Y}_{F,s} - Y_{F,\infty}}{1 - \tilde{Y}_{F,s}} \tag{14}$$

This correlation, derived by Nafziger and Renksizbulut (1988), is based on the experimental data of Renksizbulut (1981) and Downing (1960). Because significant liquid heating will reduce the surface temperature, thereby reducing the surface fuel mass fraction and consequently the mass transfer number, the correction for the effects of liquid phase heating is already implicit in the calculation of B_M.

Attention is now shifted from the overall characteristics of heat mass and momentum transport, in order to make a more detailed examination of the transport phenomena at the surface of and within the droplet. Shown in Fig. 6 is the transient development in surface velocity gradients. It is interesting to note that at all times the $\partial v_\theta/\partial r$ term is the largest of the gradients, and barring extreme liquid motion it will dominate the surface shear stress.

The magnitudes of the surface tangential velocity and sur-

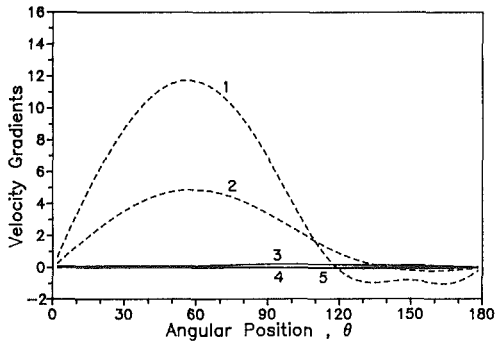

Fig. 6 Surface velocity gradients; (1) $\partial v_\theta/\partial r$ at $t=2000$; (2) $\partial v_\theta/\partial r$ at $t=11{,}000$; (3) $\partial v_r/\partial r$ at $t=2000$; (4) $\partial v_r/\partial\theta$ at $t=2000$; (5) $\partial v_\theta/\partial\theta$ at $t=2000$

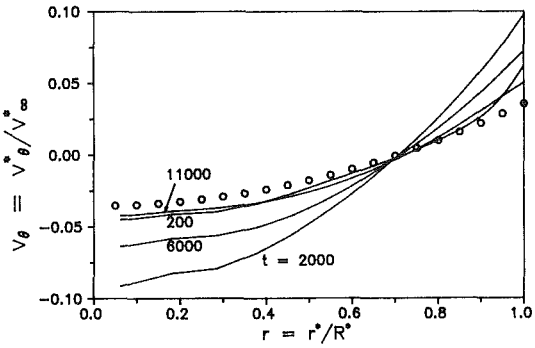

Fig. 9 Tangential liquid velocities along $\theta=90$ deg; ◯ —the Hadamard-Rybczynski solution

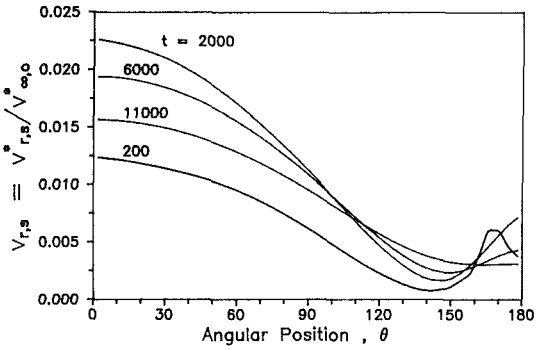

Fig. 7 Surface radial velocity history

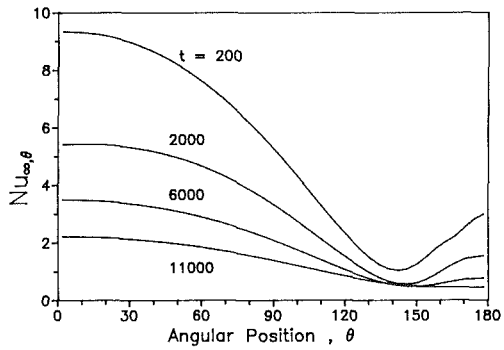

Fig. 10 Local Nusselt number history

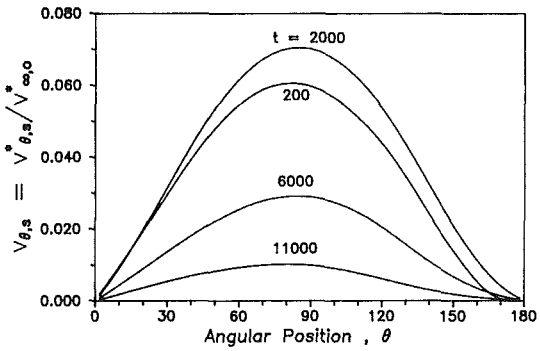

Fig. 8 Surface tangential velocity history

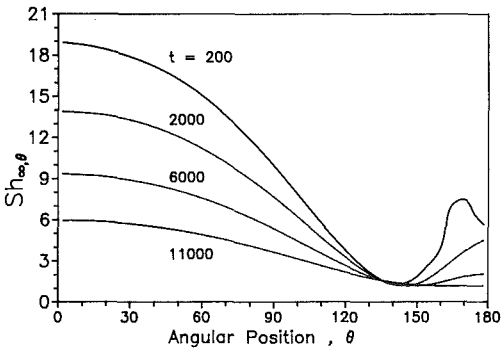

Fig. 11 Local Sherwood number history

face radial gas velocities, scaled with respect to the initial free-stream velocity, are shown in Figs. 7 and 8 for four different times during the transient development. The radial surface velocity peaks early in the lifetime when liquid heating begins to diminish, the surface fuel vapor pressure rises, and convective transport is greatest. As the droplet slows, convection of heat and mass become less effective and vaporization is reduced. The maximum and minimum radial surface velocities occur at the front stagnation point and at the point of flow separation, respectively, at all times. The tangential surface velocity peaks at a maximum of about 7 percent of the free-stream occurring at about $\theta=80$ deg, just aft of the region of maximum aerodynamic shear, early in the lifetime. The intensity of the surface motion decays beyond that time as a result of the droplet deceleration, although the azimuthal location of the maxima remains essentially temporally invariant.

The transient evolution of tangential velocities within the droplet along the plane $\theta=90$ deg is shown in Fig. 9. The liquid circulation is established quickly and a rapid rise in liquid velocities througout the droplet is observed. A gradual decline follows, caused by the transient reduction in free-stream Reynolds number. The rapid increase in the liquid phase velocities, peaking before 10 percent of the droplet lifetime has elapsed, reinforces the arguments of Prakash and Sirignano (1978) that the characteristic time to establish liquid phase motion is short and that the liquid motion can be considered quasi-steady. The results show however that the intensity of liquid phase motion does vary considerably during the droplet lifetime and that the transient effect of droplet deceleration produces profound transient variations in liquid phase motion. Also shown in Fig. 9 are the velocities predicted by the Hadamard-Rybczynski solution. Clearly, the liquid flow field is not predicted well by this creeping flow analysis, except at the lower free-stream Reynolds numbers encountered towards the end of the droplet lifetime. It would appear that the liquid phase flow model proposed by Prakash and Sirignano (1978), consisting of a core region of Hills Spherical vortex and a thin laminar boundary layer at the gas/liquid interface, is more in line with the observed high liquid Reynolds number flow but direct comparison is difficult because predicted liquid velocities are not presented in their work.

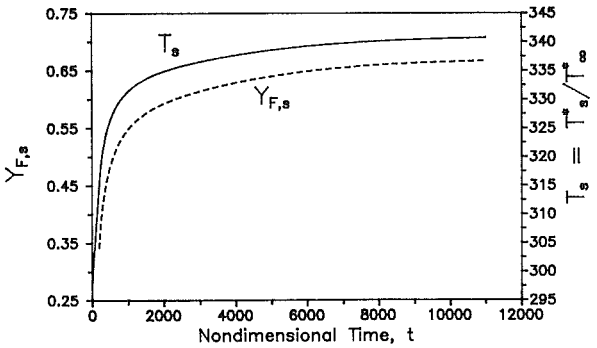

Fig. 12 Average surface temperature and fuel mass fraction histories;—T_S; - - - $Y_{F,S}$

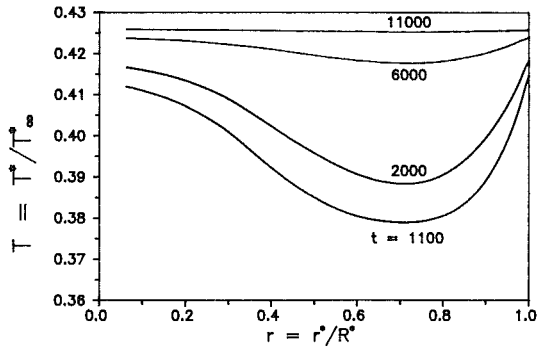

Fig. 13 Liquid temperatures along $\theta = 90$ deg

The transient evolution of the local Nusselt and Sherwood numbers are shown in Figs. 10 and 11, respectively. The reduction in convective heat and mass transport arising from the transient decay in free-stream Reynolds number is seen directly in the reduction in the Nusselt and Sherwood numbers at the stagnation point and in the wake region. As expected, the minima occur very near the point of flow separation and proceed rearward with time. From the results of the present analysis it can be shown that ignoring contributions from the wake region, defined for convenience as $\theta \geq 120$ deg, results in errors in the prediction of the average Nusselt number of 6.4, 6.1, 7.0, and 9.3 percent for $t = 200$, 2000, 6000, and 11,000, respectively. This is in agreement with the postulated error of Prakash and Sirignano (1980) of about 15 percent in boundary layer types of analyses.

The transient histories of the average surface temperature and fuel mass fraction are shown in Fig. 12. It is worth noting that angular variations in the surface temperature were most pronounced early in the droplet lifetime. For example the range in surface temperatures at $t = 200$ was between 313K and 332K about a surface area weighted average of 315K. The strong sensitivity of vapor pressure to temperature is responsible for the unusual bump in the Sh variation observed in Fig. 12 at $t = 200$ in the wake region.

As discussed previously and shown in Fig. 3, liquid phase heating absorbs a significant fraction of the energy available at the droplet surface for about half the droplet lifetime. This result is expected because, as many researchers have indicated, the diffusion of heat in the liquid phase is the slowest transport process inherent to the problem. The qualitative nature of liquid heating can be best understood by examination of the liquid phase temperature contours shown in Fig. 2 and the liquid temperature profiles along the plane ($\theta = 90$ deg) shown in Fig. 13. It is clear that the liquid temperature does not remain spatially invariant and, in spite of the intense liquid motion, the so-called rapid mixing model of liquid phase

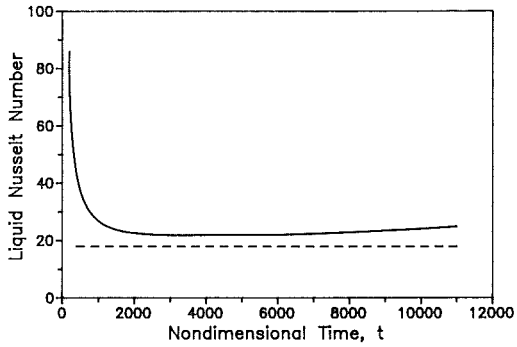

Fig. 14 Liquid Nusselt number history;—fully numerical solution; - - - asymptotic value of Johns and Beckmann (1966)

heating is not applicable. The self-similar nature of the temperature profiles as shown in Fig. 13 suggests that the liquid temperature field quickly reaches an asymptotic profile and that the liquid heating may be in some sense quasi-steady. Adopting the methodology of Johns and Beckmann (1966) a liquid Nusselt number can be defined based on the difference between the liquid surface and volume average temperatures, viz.,

$$\mathrm{Nu}_l = \frac{1}{\bar{k}_l} \int_0^\pi \frac{2k_l}{(\bar{T}_s - \bar{T}_l)} \frac{\partial T}{\partial r}\bigg)_{s,\theta,l} \sin\theta \, d\theta \qquad (15)$$

Figure 14 shows the transient evolution Nu_l. A rapid initial decrease, associated with the establishment of the liquid phase "quasi-steady" temperature field, followed by a nearly constant Nu_l of about 22 for the duration of the liquid heating period, is observed. It appears that the concept of an asymptotic Nusselt number of Johns and Beckmann is applicable in this case. For the problem investigation the liquid Peclet numbers defined analogously to Johns and Beckmann, viz.,

$$\mathrm{Pe}_l = \frac{\mathrm{Re}_{\infty,0}\mathrm{Pr}_\infty}{4}\left(\frac{1}{1+\mu_l/\mu_\infty}\right) (\rho_l^*/\rho_\infty^*)\,(c_{p,l}^*/c_{p,\infty}^*)\,(k_\infty^*/k_l^*) \qquad (16)$$

are of order 1000, hence their results would predict an asymptotic Nu_l of 17.9, which is the Kronig and Brink (1950) limit. The discrepancy is expected since the Johns–Beckmann data were based on an assumed velocity field corresponding to the Hadamard–Rybczynski solution, shown earlier not to be representative of the actual situation during most of the droplet lifetime, nor does their solution include the effects of variable properties. Because the ratios of specific heat, thermal conductivity, viscosity, and density for typical liquid hydrocarbons and air at 1 atm pressure will be of order 1, 1, 10, and 1000, respectively, the liquid Peclet number as defined by equation (16) will generally be of order 1000 for droplets initially in the intermediate Reynolds numbers range. It is hypothesized that the observed constant liquid Nusselt number behavior is typical for fuel droplets evaporating in air at intermediate Reynolds numbers and low ambient pressures. Figure 14 does not display any of the oscillations found by Johns–Beckmann attributable to the initial circulations of the liquid phase, but this is not unexpected since the boundary conditions for the present problem result in an increasing surface temperature whereas Johns–Beckmann assumed a constant surface temperature. In previous work by Renksizbulut and Haywood (1986, 1988), studying heptane droplets evaporating in their own vapor, a situation in which the surface temperature remains at the boiling point at all times, such oscillations were observed.

4 Conclusions

The transient drag coefficient and Nusselt and Sherwood number histories computed by the complete numerical model

are well predicted by the quasi-steady correlations of Renksizbulut and Yuen (1983a, 1983b) and Renksizbulut and Nafziger (1988). It is concluded therefore that transient effects in the gas phase, the recession of the gas/liquid interface, and second-order drag effects are unimportant at lower pressures ($p \leq 10$ atm). The deceleration of the droplet under the influence of its own drag has been shown to be an important transient effect and for droplets with initial Reynolds numbers of order 100, reductions in the Reynolds number of an order of magnitude can be expected over the droplet lifetime, during which about 80 percent of the original mass is vaporized.

Although the liquid phase motion has been shown to adjust very quickly in response to the shear imparted by the gas phase, the transient decline in the free-stream Reynolds number results in a slow transient decline in the liquid phase motion and in this sense the liquid motion must be considered unsteady.

Liquid phase heating has also been shown to display unsteady behavior. The transient rise in the droplet average and surface temperatures persists for a significant portion of the droplet lifetime. In spite of this unsteadiness, the nature of the liquid phase heating, as characterized by the liquid Nusselt number, has been shown to remain relatively constant. Although the observed asymptotic liquid Nusselt number did not agree with the Kronig and Brink limit, the concept of a rapid approach to a limiting liquid phase Nusselt number appears conceptually correct, and we expect this may generally be true for typical hydrocarbons evaporating in air at low ambient pressures. Departure of the observed liquid Nusselt number from the exact Kronig and Brink limit is due to the considerably higher Reynolds number flow in the present situation as well as variable property effects.

References

Cliffe, K. A., and Lever, D. A., 1984, "Isothermal Flow Past a Blowing Sphere," TP.1042, Theoretical Physics Division, AERE, Harwell, Oxfordshire, United Kingdom.

Clift, R., Grace, J. R., and Weber, M. E., 1978, *Bubbles, Drops and Particles*, Academic Press, New York.

Downing, C. G., 1960, "The Effect of Mass Transfer on Heat Transfer in the Evaporation of Drops of Pure Liquids," Ph.D. Thesis, University of Wisconsin, WI.

Dwyer, H. A., and Sanders, B. R., 1984a, "Droplet Dynamics and Vapourization With Pressure as a Parameter," ASME Paper No. 84-WA/HT-20.

Dwyer, H. A., and Sanders, B. R., 1984b, "Detailed Computation of Unsteady Droplet Dynamics," *Twentieth Symp. (Int.) in Combustion*, Ann Arbor, MI, pp. 1743-1749.

Faeth, G. M., and 1983, "Evaporation and Combustion of Sprays," *Proc. Energy Combust. Sci.*, Vol. 9, pp. 1-76.

Haywood, R. J., 1986, "Variable-Property, Blowing and Transient Effects in Convective Droplet Evaporation With Internal Circulation," M.A.Sc. Thesis, University of Waterloo, Ontario, Canada.

Haywood, R. J., and Renksizbulut, M., 1986, "On Variable-Property, Blowing and Transient Effects in Convective Droplet Evaporation With Internal Circulation," *Proceedings of the Eighth International Heat Transfer Conference*, San Francisco, CA.

Johns, L. E., Jr., and Beckmann, R. B., 1966, "Mechanism of Dispersed-Phase Mass Transfer in Viscous, Single-Drop Extraction Systems," *AIChE Journal*, Vol. 12, pp. 10-16.

Kronig, R., and Brink, J. C., 1950, "On the Theory of Extraction From Falling Droplets," *Appl. Sci. Res.*, Vol. A2, p. 142.

LeClair, B. P., Hamielec, A. E., Pruppacher, H. R., and Hall, W. D., 1972, "A Theoretical and Experimental Study of the Internal Circulation in Water Drops Falling at Terminal Velocity in Air," *Journal of the Atmospheric Sciences*, Vol. 29, pp. 728-740.

Law, C. K., 1976, "Unsteady Droplet Combustion With Droplet Heating," *Combust. Flame*, Vol. 26, pp. 17-22.

Law, C. K., and Sirignano, W. A., 1977, "Unsteady Droplet Combustion With Droplet Heating—II: Conduction Limit," *Combust. Flame*, Vol. 28, pp. 175-186.

Nafziger, R., 1988, "Convective Droplet Transport Phenomena in High-Temperature Air Streams," M.A.Sc. Thesis, University of Waterloo, Ontario, Canada.

Prakash, S., and Sirignano, W. A., 1978, "Liquid Fuel Droplet Heating With Internal Circulation," *Int. J. Heat Mass Transfer*, Vol. 21, pp. 885-895.

Prakash, S., and Sirignano, W. A., 1980, "Theory of Convective Droplet Vaporization With Unsteady Heat Transfer in the Circulating Liquid Phase," *Int. J. Heat Mass Transfer*, Vol. 23, pp. 253-268.

Ranz, W. E., and Marshall, W. R., 1952, "Evaporation From Drops—I and II," *Chemical Engineering Progress*, Vol. 48, No. 3, pp. 141-173.

Renksizbulut, M., 1981, "Energetics and Dynamics of Droplet Evaporation in High Temperature Intermediate Reynolds Number Flows," Ph.D. Thesis, Northwestern University, Evanston, IL.

Renksizbulut, M., and Haywood, R. J., 1988, "Transient Droplet Evaporation With Variable Properties and Internal Circulation at Intermediate Reynolds Numbers," *Int. J. of Multiphase Flow*, Vol. 14, pp. 189-202.

Renksizbulut, M., and Yuen, M. C., 1983a, "Numerical Study of Droplet Evaporation in a High-Temperature Air Stream," ASME JOURNAL OF HEAT TRANSFER, Vol. 105, pp. 389-397.

Renksizbulut, M., and Yuen, M. C., 1983b, "Experimental Study of Droplet Evaporation in a High-Temperature Air Stream," ASME JOURNAL OF HEAT TRANSFER, Vol. 105, pp. 384-388.

Renksizbulut, M., and Nafziger, R., 1988, paper in preparation.

Sirignano, W. A., 1983, "Fuel Droplet Vaporization and Spray Combustion Theory," *Prog. Energy and Combust. Sci.*, Vol. 9, pp. 291-322.

Spalding, D. B., 1953, "Experiments on the Burning and Extinction of Liquid Fuel Spheres," *Fuel*, Vol. 32, pp. 169-185.

Sundararajan, T., and Ayyaswamy, P. S., 1984, "Hydrodynamics and Heat Transfer Associated With Condensation on a Moving Drop: Solutions for Intermediate Reynolds Numbers," *J. Fluid Mech.*, Vol. 149, pp. 33-58.

Yuen, M. C., and Chen, L. W., 1976, "On Drag of Evaporating Liquid Droplets," *Combustion Sci. Tech.*, Vol. 14, pp. 86-91.

Axisymmetric Interfacial Condensation Model

F. M. Gerner[1]
Assoc. Mem. ASME

C. L. Tien[2]
Fellow ASME

Department of Mechanical Engineering,
University of California,
Berkeley, CA 94720

This paper employs a simple axisymmetric model to study interfacial condensation. Numerical results show the effects of interfacial forces, subcooling of the liquid, superheating of the vapor, and the presence of a noncondensable gas in the vapor. While pressure and shear stress play an important role in determining the flow fields, and hence interfacial mass and energy transport, interfacial mass fluxes do not. Subcooling of the liquid is the dominant mechanism in determining the interfacial condensation rate. While superheating of the vapor is insignificant, except near the critical point, a noncondensable gas in the vapor greatly reduces condensation.

Introduction

The purpose of this work is to analyze interfacial condensation. Specifically it examines the condensation taking place at the surface of a subcooled liquid pool, when there is subsurface liquid motion. While other investigators have examined interfacial pool condensation (Banerjee, 1985; Celata et al., 1987; Jones, 1966; Thomas, 1979), all of their results have been either purely experimental or semi-empirical. This work provides a simple, yet rigorous, model to demonstrate clearly how interfacial phenomena, such as interfacial shear stress and condensation mass flux, affect the velocity fields and hence the interfacial mass and energy transport. In addition to studying the effects of subcooling the liquid, superheating the vapor and the presence of a noncondensable gas in the vapor are also examined.

The model to be analyzed is shown in Fig. 1. A subcooled liquid flows toward a flat gas–liquid interface. In general, the gas is a mixture of a superheated vapor and a noncondensable gas. To satisfy the no-slip and force balance conditions at the interface the gas mixture must also be in motion. In order to simplify the formulation and to focus attention on the interface, steady-state axisymmetric laminar stagnation flows are assumed to exist in both the liquid and the mixture. Therefore boundary conditions are required only in the direction normal to the interface. Inviscid flow occurs in both fluids except for thin boundary layers on either side of the interface. In many actual forced-convection systems the fluids are circulating. Near the interface, however, the flow appears to be a uniform axial flow. The axisymmetric model accounts for most of the physics, using a relatively simple exact solution of the Navier–Stokes equations.

The proposed model, with minor modifications, would apply to a variety of other problems, including binary condensation and gaseous mixing. As will be seen, the solution procedure first specifies conditions at the interface and then solves for the driving potentials (which is the subcooling for pure-component condensation). Therefore complicated phase equilibria can be incorporated into the model with little effort. Of course the model is limited to laminar flow near a flat interface. Although the flat interface is a major assumption, it has been experimentally observed (Celata, 1987b). Also, since this work was completed, it has been brought to the authors' attention that a similar adiabatic solution has been performed (Wang, 1985). Aside from the adiabatic assumption, Wang's model is slightly simpler in that it does not rigorously satisfy a force balance in the normal direction.

The next section outlines the mathematical formulation. After introducing the numerical procedure used, adiabatic stagnation flows are studied. Liquid subcooling, vapor superheat, and the presence of a noncondensable gas in the vapor are then discussed.

While this work closely models the direct contact condensation above a circulating liquid pool, such as occurs in the pressurizer of a nuclear power plant, it has much wider relevance. The same interactions between interfacial forces and interfacial mass fluxes occur near all vapor-liquid condensation interfaces (of course for wavy or turbulent interfaces the relationship is quantitatively more complicated). The reason is that interfacial heat and mass transfer is a very local phenomenon. Of course for other applications, such as laminar-film condensation, the noninterface boundary conditions are different, but the relationship between the dynamic and mass and energy transfer near the interface is very similar.

Formulation

The analytical model is shown in Fig. 1. It should be noted that the subscripted z coordinate (to be explained later) is solely for numerical convenience. The following steady-state axisymmetric (assuming no swirl) equations governing conservation of mass, momentum, energy, and noncondensable gas species are for constant density and constant transport properties of the pure substances:

$$\frac{\partial u_i}{\partial r} + \frac{u_i}{r} + \frac{\partial w_i}{\partial z_i} = 0 \tag{1}$$

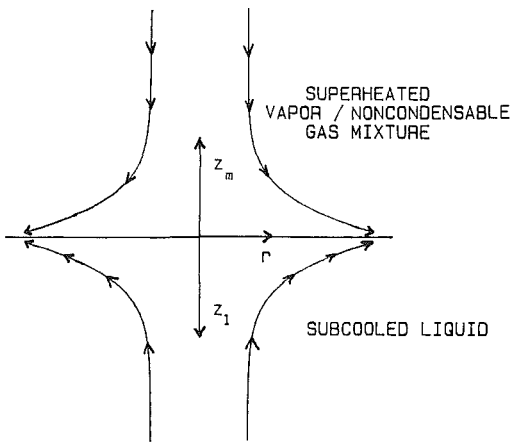

Fig. 1 Condensation model

[1]Currently Assistant Professor, University of Cincinnati, Cincinnati, OH 45221.
[2]Currently with the Department of Mechanical Engineering, University of California—Irvine, Irvine, CA 92717.

Contributed by the Heat Transfer Division and presented at the National Heat Transfer Conference, Houston, Texas, July 24-27, 1988. Manuscript received by the Heat Transfer Division April 20, 1988. Keywords: Condensation, Direct-Contact Heat Transfer, Phase-Change Phenomena.

$$u_i \frac{\partial u_i}{\partial r} + w_i \frac{\partial u_i}{\partial z_i} = \frac{-1}{\rho_i} \frac{\partial P_i}{\partial r} + \nu_i \left(\frac{\partial^2 u_i}{\partial r^2} + \frac{1}{r} \frac{\partial u_i}{\partial r} - \frac{u_i}{r^2} + \frac{\partial^2 u_i}{\partial z_i^2} \right) \quad (2)$$

$$u_i \frac{\partial w_i}{\partial r} + w_i \frac{\partial w_i}{\partial z_i} = \frac{-1}{\rho_i} \frac{\partial P_i}{\partial z_i} + \nu_i \left(\frac{\partial^2 w_i}{\partial r^2} + \frac{1}{r} \frac{\partial w_i}{\partial r} + \frac{\partial^2 w_i}{\partial z_i^2} \right) \pm g \quad (3)$$

where the + is for the liquid and − for the vapor, and

$$w_i \frac{dT_i}{dz_i} = \alpha_i \frac{d^2 T_i}{dz_i^2} \quad (4)$$

$$w_m \frac{dm_g}{dz_m} = D_m \frac{d^2 m_g}{dz_m^2} \quad (5)$$

where diffusion-thermo and thermo-diffusive effects have been neglected. Also temperature and noncondensable gas mass fraction are only functions of distance from the interface. This is a consequence of the infinite nature of the axisymmetric model and assuming that the saturation temperature is constant along the interface. The latter is thermodynamically justifiable, for most common substances, since from the Clausius–Clapeyron relation (Callen, 1985), and the known pressure gradients, thermal gradients along the interface are very small relative to the subcooling.

The far fields ($z_i \to \infty$) are assumed to be inviscid uniform flows

$$u_i = a_i r, \quad w_i = -2a_i z_i + C_i \quad (6)$$

$$T_i = T_{i\infty}, \quad m_g = m_{g\infty} \quad (7)$$

At the interface ($z_m = z_l = 0$), the conditions are

$$u_l = u_m, \quad -\rho_l w_l = \rho_m w_m \quad (8)$$

$$P_l - 2\mu_l \frac{\partial w_l}{\partial z_l} = P_m - 2\mu_m \frac{\partial w_m}{\partial z_m}$$

$$-\mu_l \left(\frac{\partial w_l}{\partial r} + \frac{\partial u_l}{\partial z_l} \right) = \mu_m \left(\frac{\partial w_m}{\partial r} + \frac{\partial u_m}{\partial z_m} \right) \quad (9)$$

$$T_l = T_m = T_s, \quad -k_l \frac{dT_l}{dz_l} = \rho_l w_l h_{vl} + k_m \frac{dT_m}{dz_m} \quad (10)$$

$$m_g w_m = D_m \frac{\partial m_g}{\partial z_m} \quad (11)$$

Equations (8) represent the no-slip and conservation of mass conditions, equations (9) force balances, equations (10) continuity of temperature (neglecting the interfacial resistance) and conservation of energy, and equation (11) conservation of species for a noncondensable gas that is insoluble in the liquid. Additionally the thermodynamic relation between the saturation temperature and the noncondensable gas fraction is required to couple the interface conditions.

Note that the following assumptions are necessary only when there is a noncondensable gas present. When the vapor is pure, these thermodynamic and ideal gas assumptions are unnecessary. In order to arrive at a relationship between the noncondensable gas fraction and the saturation temperature at the interface, saturation pressure and saturation temperature are first related using P_m and $T_s(P_m)$ as a reference. Note that for purposes of thermodynamic calculations the total pressure, P_m, is assumed constant. This neglects the radial pressure gradients that drive the flow, and are included in the momentum equations, and assumes negligible condensation-induced depressurization, which is a good assumption for the condensation rates considered in this study. The relationship between noncondensable gas fraction and partial vapor pressure allows saturation temperature to be related directly to the noncondensable gas fraction.

Under the assumption of local equilibrium, the saturation curve is assumed to obey the simple Clausius–Clapeyron relation (Callen, 1985)

$$\frac{dP_s}{dT_s} = \frac{h_{vl}}{T_s(1/\rho_v - 1/\rho_l)} \quad (12)$$

Neglecting the specific volume of the liquid ($1/\rho_l$) relative to that of the vapor ($1/\rho_v$), which is a good assumption except near the critical point, and using the ideal gas law

$$\frac{P}{\rho} = RT \quad (13)$$

yields

$$\frac{P_s}{P_m} = \exp\left[-\frac{h_{vl}}{R_v} \left(\frac{1}{T_s} - \frac{1}{T_s(P_m)} \right) \right] \quad (14)$$

To determine the partial pressure of the vapor in terms of the noncondensable gas fraction, it is necessary to invoke the ideal gas law, conservation of mass

$$m_v + m_g = 1 \quad (15)$$

and Dalton's Law

$$P_v + P_g = P_m \quad (16)$$

The partial pressure of the vapor at the interface is found to be

$$\frac{P_v}{P_m} = \left[1 + \frac{m_{go}}{1 - m_{go}} \frac{M_v}{M_g} \right]^{-1} \quad (17)$$

Nomenclature

a = stagnation parameter
C_i = constant in equation (6)
C_p = specific heat at constant pressure
D = binary diffusion coefficient
F = dimensionless similarity variable, equation (24)
h_{vl} = latent heat of vaporization
$h(z)$ = represents z dependence of pressure, equation (26)
Ja = Jakob number, equations (21) and (22)
k = thermal conductivity
m_{go} = reference noncondensable gas fraction, chosen as $m_g(0)$
m_j = mass fraction = ρ_j/ρ_m
M = molecular weight
P = pressure
Pr = Prandtl number = ν/α
r = radial coordinate
R = specific gas constant
Sc = Schmidt number = ν/D
T = temperature
u = radial velocity
w = axial velocity
z = axial coordinate
α = thermal diffusivity
μ = dynamic viscosity
ν = kinematic viscosity
ρ = density

Subscripts

g = noncondensable gas
i = dummy, represents l or m
j = dummy, represents v or g
l = liquid
m = vapor/noncondensable gas mixture
o = stagnation
s = saturation
v = vapor
∞ = infinity

Superscripts

$*$ = dimensionless, equation (19)
$+$ = alternate nondimensionalization, equation (47)

Since the partial pressure of the vapor at the interface is equal to the saturation pressure, the desired relation becomes

$$1+\frac{m_{go}}{1-m_{go}}\frac{M_v}{M_g}=\exp\left[\frac{h_{vl}}{R_vT_s(P_m)}\left(\frac{T_s(P_m)}{T_s}-1\right)\right] \quad (18)$$

Introducing the dimensionless quantities (m_g is already dimensionless)

$$u_i^*=u_i\,(\nu_i a_i)^{-1/2},\quad w_i^*=w_i(\nu_i a_i)^{-1/2}$$
$$r_i^*=r(\nu_i/a_i)^{-1/2},\quad z_i^*=z_i\,(\nu_i/a_i)^{-1/2} \quad (19)$$
$$T_i^*=\frac{T_i-T_{i\infty}}{T_s(P_m)-T_{i\infty}}$$

the following dimensionless parameters result:

Fluid Mechanical

$$\frac{\mu_v}{\mu_l},\quad \frac{\rho_v(P_m)}{\rho_l} \quad (20)$$

Subcooling

$$\mathrm{Ja}_l=\frac{C_{pl}(T_s(P_m)-T_{l\infty})}{h_{vl}},\quad \mathrm{Pr}_l=\frac{\nu_l}{\alpha_l} \quad (21)$$

Superheating

$$\mathrm{Ja}_v=\frac{C_{pv}(T_{m\infty}-T_s(P_m))}{h_{vl}},\quad \mathrm{Pr}_v=\frac{\nu_v}{\alpha_v} \quad (22)$$

Noncondensable Gas

$$\mathrm{Sc}_m,\quad m_{g\infty},\quad \frac{M_g}{M_v},\quad \frac{\mu_g}{\mu_v},\quad \frac{C_{pg}}{C_{pv}},$$
$$\frac{k_g}{k_v},\quad \frac{h_{vl}}{R_vT_s(P_m)},\quad \frac{T_{l\infty}}{T_s(P_m)},\quad \frac{T_{m\infty}}{T_s(P_m)} \quad (23)$$

The following similarity solutions, which satisfy continuity identically, exist:

$$u_i^*=r_i^*\frac{dF_i(z_i^*)}{dz_i^*},\quad w_i^*=-2F_i(z_i^*) \quad (24)$$

Substitution into the z-direction momentum equation yields

$$\frac{\partial^2 P_l}{\partial r\partial z_i}=0 \quad (25)$$

which implies that $\partial P_i/\partial r$ can be evaluated from the inviscid far field

$$P_o-P_i=1/2\;\rho_i\,(a_i^2r^2+h_i(z)) \quad (26)$$

and by equating radial pressure gradients at the interface

$$a_l/a_m=(\rho_m/\rho_l)^{1/2} \quad (27)$$

where ρ_m/ρ_l is assumed constant and equal to the interface value. It is evaluated using the ideal gas and Dalton's laws as

$$\frac{\rho_m}{\rho_l}=\frac{\rho_v(P_m)}{\rho_l}\frac{M_g}{M_v}\frac{T_s(P_m)}{T_s}\left[m_{go}+\frac{M_g}{M_v}(1-m_{go})\right]^{-1} \quad (28)$$

Then the governing equations and boundary conditions become

$$\left(\frac{dF_i}{dz_i^*}\right)^2-2F_i\frac{d^2F_i}{dz_i^{*2}}=1+\frac{d^3F_i}{dz_i^{*3}} \quad (29)$$

$$-2\mathrm{Pr}_iF_i\frac{dT_i^*}{dz_i^*}=\frac{d^2T_i^*}{dz_i^{*2}} \quad (30)$$

where for the mixture

$$\frac{\mathrm{Pr}_m}{\mathrm{Pr}_v}=\left(1-m_{go}+\frac{C_{pg}}{C_{pv}}m_{go}\right)\left(\frac{1}{1+\frac{m_{go}}{1-m_{go}}\frac{M_v}{M_g}}+\frac{\mu_g}{\mu_v}\frac{1}{1+\frac{M_g}{M_v}\frac{1-m_{go}}{m_{go}}}\right)\Bigg/\left(\frac{1}{1+\frac{m_{go}}{1-m_{go}}\frac{M_v}{M_g}}+\frac{k_g}{k_v}\frac{1}{1+\frac{M_g}{M_v}\frac{1-m_{go}}{m_{go}}}\right) \quad (31)$$

$$-2\mathrm{Sc}_m\,F_m\frac{dm_g}{dz_m^*}=\frac{d^2m_g}{dz_m^{*2}} \quad (32)$$

where Sc_m is treated as a constant.

For $z_i^*\to\infty$

$$dF_i/dz_i^*=1,\quad T_i^*=0,\quad m_g=m_{g\infty} \quad (33)$$

For $z_i^*=0$

$$\frac{dF_l}{dz_l^*}=\left(\frac{\rho_l}{\rho_m}\right)^{1/2}\frac{dF_m}{dz_m^*} \quad (34)$$

$$F_l=-\left(\frac{\rho_m}{\rho_l}\right)^{1/4}\left(\frac{\mu_m}{\mu_l}\right)^{1/2}F_m \quad (35)$$

$$-\frac{d^2F_l}{dz_l^{*2}}=\left(\frac{\mu_m}{\mu_l}\right)^{1/2}\left(\frac{\rho_l}{\rho_m}\right)^{1/4}\frac{d^2F_m}{dz_m^{*2}} \quad (36)$$

$$\frac{\mathrm{Ja}_l}{\mathrm{Pr}_l}\frac{dT_l^*}{dz_l^*}=2F_l+\left(\frac{\rho_m}{\rho_l}\right)^{1/4}\left(\frac{\mu_m}{\mu_l}\right)^{1/2}\frac{\mathrm{Ja}_m}{\mathrm{Pr}_m}\frac{dT_m^*}{dz_m^*} \quad (37)$$

$$T_i^*=\frac{T_s-T_{i\infty}}{T_s(P_m)-T_{i\infty}} \quad (38)$$

$$-2F_m\,\mathrm{Sc}_m\,m_g=\frac{dm_g}{dz_m^*} \quad (39)$$

where

$$\frac{\mu_m}{\mu_l}=\frac{\mu_v}{\mu_l}\left[\frac{1}{1+\frac{m_{go}}{1-m_{go}}\frac{M_v}{M_g}}+\frac{\mu_g}{\mu_v}\left(\frac{1}{1+\frac{M_g}{M_v}\frac{1-m_{go}}{m_{go}}}\right)\right] \quad (40)$$

and

$$\mathrm{Ja}_m=\mathrm{Ja}_v\left[(1-m_{go})+\frac{C_{pg}}{C_{pv}}m_{go}\right] \quad (41)$$

Solution

Of primary importance in this study is the interfacial condensation rate. In order to understand the mechanisms controlling the condensation rate, superheat and noncondensable gas effects are neglected and some very simple analytical results are derived that can be used to explain the basic physics. Before proceeding, it is useful to discuss the parameters that affect the solution. First, as is apparent from the nondimensionalization, there are momentum boundary layers formed in both the liquid and vapor whose thicknesses scale as $(\nu_i/a_i)^{1/2}$. In these boundary layers the velocities scale as $(\nu_i a_i)^{1/2}$. Also there exists a thermal boundary layer in the liquid that is of order $(\alpha_l/a_l)^{1/2}$, where the temperature difference $(T_l-T_{l\infty})$ scales as $(T_s(P_m)-T_{l\infty})$.

Using the thermal boundary layer scales implies

$$\frac{dT_l}{dz_l}\sim\frac{T_{l\infty}-T_s(P_m)}{(\alpha_l/a_l)^{1/2}} \quad (42)$$

This along with the interfacial energy balance (equation (37)) allows the condensation parameter to be scaled

$$-F_f(0) \sim \mathrm{Ja}_l \mathrm{Pr}_l^{-1/2} \tag{43}$$

The condensation parameter is seen to be affected by both the liquid Jakob number Ja_l and the liquid Prandtl number Pr_l. The Jakob number is the ratio of sensible to latent heat. For a given mass flow rate, the higher the Jakob number, the greater is the capacity of a fluid to transport heat, relative to the energy associated with phase change. A large Prandtl number, however, implies that the thermal diffusivity is small. Therefore for a given temperature drop, the liquid cannot transport as much heat and consequently condensation is inhibited.

While the condensation parameter depends strongly upon the Jakob and Prandtl numbers, it is also affected by the viscosity and density ratios. They do this primarily by influencing the fluid mechanics. For a low vapor-to-liquid viscosity ratio, μ_v/μ_l, interfacial shear stress has little effect upon the liquid velocity field. Also low vapor-to-liquid density ratios, ρ_v/ρ_l, imply that the ratio of liquid to vapor velocity is small. As seen from equation (27) this means that in order to have a given stagnation pressure, a fluid with a low density must have a high velocity.

Analytical Solution. Before proceeding, it is instructive to examine the case of low interfacial shear stress with low condensation rates. This would be the case for low values of μ_v/μ_l (low Ja_l and high Pr_l would also contribute to lower condensation rates). If there is very little interfacial shear stress and condensation the velocity field in the liquid is unaffected by the interface and may be approximated by the inviscid solution

$$F_l = z_l^* \tag{44}$$

Substituting this into the liquid energy equation (equation (30)) and using equation (37) yields

$$-F_f(0) = \mathrm{Ja}\,(\pi\,\mathrm{Pr}_l)^{-1/2} \tag{45}$$

which agrees with the scaling estimate to within a factor of $\pi^{-1/2} \sim 0.564$.

Numerical Solution. While the simple analytical solution, equation (45), should give the correct order of magnitude, as should the scaling approximation, equation (43), more precise numerical results require solution of equations (29), (30), and (32), along with far field conditions (33) and interface conditions (34)–(39). Additionally the thermodynamic relation, equation (18), and binary mixture property relations, equations (28), (31), (40), and (41), are required. It is now apparent why z_m and z_l were used. Since one boundary condition is at infinity for both the vapor/noncondensable gas mixture and the liquid and the mixture field equations are decoupled from the liquid field equations (except at the interface), what is physically a three-point boundary-value problem can be represented mathematically as a two-point boundary-value problem (the two boundaries, $z_m^* \to \infty$, $z_l^* \to \infty$, merge to simply $z^* \to \infty$, and the interface conditions become boundary conditions at $z^* = 0$).

The resulting system of nonlinear ordinary differential equations has no known closed-form solution; therefore it must be solved numerically. It should be noted that this is a system of five ordinary differential equations, of which two are third order and three are second order. There are five infinity conditions, seven interface conditions, and five auxiliary relations. To attempt to solve this system blindly would be extremely difficult. Clearly a more intelligent approach is necessary. Due to the nondimensionalization, velocity is not a parameter in this problem. Basically after choosing the substances and total pressure there are only three free parameters. They are the liquid free-stream temperature (or Ja_l), mixture free-stream temperature (Ja_v), and free-stream noncondensable gas fraction ($m_{g\infty}$). They act as the driving potentials and determine the conditions at the interface $F_f(0)$, $m_g(0)$, and T_s. However to solve the problem in this fashion is very difficult. Instead interface conditions $F_f(0)$ and $m_g(0)$ are chosen and the driving potentials that yield these conditions are determined. Koh (1962) used a similar procedure to determine the Jakob number for forced-convective condensation onto a flat plate.

The first step is to choose the condensable and noncondensable substances, the total pressure (P_m) and corresponding saturation temperature ($T_s(P_m)$). The dimensionless parameters given by equations (20)–(23), except for Ja_l, Ja_v, $m_{g\infty}$, $T_{l\infty}/T_s(P_m)$, and $T_{m\infty}/T_s(P_m)$, which are determined at the very end, are determined. Choosing $m_g(0)$ allows T_s and the mixture properties to be determined using equations (18), (28), (31) and (40). Next the energy equations are decoupled from the momentum equations. This is accomplished by specifying $F_f(0)$.

The momentum equations are solved first. Once $F_f(0)$ is specified, they are given by equations (29), (33), (34), (36), and

$$F_m(0) = -\left(\frac{\rho_l}{\rho_m}\right)^{1/4}\left(\frac{\mu_l}{\mu_m}\right)^{1/2} F_l(0) \tag{46}$$

In order to solve this system a shooting technique was used (Press et al., 1986). The equations were first expressed as a system of first-order ODE's. $F_l'(0)$ and $F_l''(0)$ were guessed, equations (34) and (36) used to calculate $F_m'(0)$ and $F_m''(0)$ and a fourth-order adaptive-step-size Runge–Kutta scheme was used to shoot to $z^* = 10$ (the infinity boundary condition). Finally a Newton–Raphson technique was used to match the infinity conditions, given by equation (33).

Once the $F_i(z^*)$ are known the energy equations are solved. New dimensionless temperatures are introduced

$$T_i^+ = \frac{T_i - T_{i\infty}}{T_s - T_{i\infty}} = T_i^* \frac{T_s(P_m) - T_{i\infty}}{T_s - T_{i\infty}} \tag{47}$$

and the energy equation then becomes

$$-2\,\mathrm{Pr}_i F_i T_i^{+\prime} = T_i^{+\prime\prime} \tag{48}$$

with boundary conditions

$$T_i^+(0) = 1, \quad T_i^+(\infty) = 0 \tag{49}$$

By using a shooting technique similar to that used for the momentum equations $T_i^{+\prime}(0)$ can be found. Knowing $T_i^{+\prime}(0)$ and thermophysical properties, and using equation (37), allows calculation of Ja_l and Ja_m. Actually there are many combinations of Ja_l and Ja_m that are possible for a given condensation rate. Finally $m_{go} = m_g(0)$ and equation (39) are used to calculate $m_g'(0)$. These along with equation (32) allow a shoot to determine $m_{g\infty}$.

Discussion

The model is now used to study the effects the flow field, liquid subcooling, vapor superheat, and the presence of a noncondensable gas have upon the interfacial transport near a condensation interface.

Fluid Flow. In order to gain a better understanding of the flow fields, it is instructive to examine the case of two pure fluids flowing toward each other and meeting at an interface, when there is a uniform temperature field. Since there are no temperature gradients and the vapor is pure, only two dimensionless parameters , μ_v/μ_l and $\rho_v(P_m)\,/\,\rho_l = \rho_v/\rho_l$ (or equivalently μ_m/μ_l and ρ_m/ρ_l), are important. Note also that ρ_v is a constant when there is no noncondensable gas. This no-condensation case corresponds to choosing $F_f(0) = 0$. Aside from providing a basic understanding of the fluid mechanics, there are two reasons for studying such flows. One is that for low Jakob and/or high Prandtl numbers the adiabatic velocity profiles are good approximations and using the adiabatic $F_l(z^*)$ to solve equations (30), (33), and (38) (which becomes $T_l^* = 1$ for a pure saturated vapor) for $T^{*\prime}(0)$, $F_f(0)$ can be approximated from equation (37). This is basically how the simple

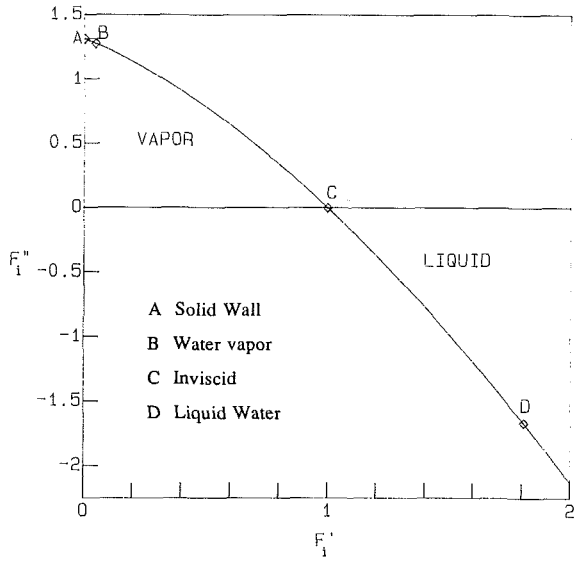

Fig. 2 Relationship between interfacial shear stress and radial velocity for adiabatic flows

analytical solution, equation (45), was derived where it was known that for $\mu_v/\mu_l = 0$, $F_l = z^*$. It is of course contradictory first to assume that $F_l(0) = 0$ and then solve the energy equation and equation (37) to determine a nonzero $F_l(0)$, but for low Ja and/or high Pr it is found to be a good approximation. The other reason to study adiabatic solutions is that they are good starting solutions for numerical schemes.

Treated individually, equations (29) are the same as the equations that describe ordinary axisymmetric stagnation-point flow into a wall (Schlichting, 1979). Also the infinity conditions, equations (33), are the same. With $F_i(0) = 0$ (the adiabatic case), the only difference is that $F_i'(0)$ is nonzero (i.e., there is a radial velocity at the interface). The reason for this velocity is that the other fluid does not exert the same shear stress at the interface as would a solid wall (i.e., $F_i''(0)$ is not equal to 1.312 as for stagnation flow into a wall). It is important to note that specifying a dimensionless shear stress at the interface ($F_i''(0)$) completely solves the fluid mechanics problem. Therefore it is possible to determine the dimensionless interfacial shear stress ($F_i''(0)$) as a function of the radial interfacial velocity ($F_i'(0)$). This is shown in Fig. 2 (it should be noted that $F_i'(0) = 2$ is a rather arbitrary stopping point).

In order to be a valid adiabatic solution, points representing the vapor and liquid must lie on this curve. Additionally the ratio of their abscissae and ordinates must obey equations (34) and (36). Thus for adiabatic flows, the flow fields are entirely determined by $(\rho_l/\rho_v)^{1/2}$ and $(\rho_l/\rho_v)^{1/4}$ $(\mu_v/\mu_l)^{1/2}$. For systems of interest $(\rho_l/\rho_v)^{1/2} \geq 1$. Also as equation (36) shows, the $F_i''(0)$ have opposite signs. This implies that the vapor lies at or to the left of Point C, while the liquid lies at or to the right of Point C. Note that a high vapor flow rate tends to accelerate the liquid at the interface, while a low liquid flow rate tends to retard the vapor.

In order to show the utility of Fig. 2, saturated water properties were used at atmospheric pressure to obtain: $\mu_v/\mu_l = 4.26 \times 10^{-2}$ and $\rho_v/\rho_l = 6.22 \times 10^{-4}$ (Collier, 1972). Iteration revealed that Points B ($F_v'(0) = 0.045$, $F_v' = 1.276$) and D ($F_l' = 1.807$, $F_l'' = -1.668$) represent saturated steam and liquid water, respectively. Note that since $(\rho_l/\rho_v)^{1/2}$ is large the steam essentially feels a wall (point A represents stagnation flow into a wall). The high vapor flow rate, however, imposes a large interfacial shear stress that greatly accelerates the liquid at the interface. It is interesting to show the effect that vapor shear stress has upon the condensation rate. Still using atmospheric water with a $Pr_l = 1.76$ (Collier, 1972) the adiabatic velocity profile can be substituted into the liquid energy equation (equation (30)) to solve for $T^{*\prime}(0) = -1.842$. For small Ja_l and/or large Pr_l equation (37) can be used (neglecting superheat) to approximate

$$F_l(0) = -0.523\ Ja_l$$

Comparing this with the inviscid approximation from equation (45)

$$F_l(0) = -0.425\ Ja_l$$

it can be seen that by accelerating the liquid near the interface, the shear stress increases convection in the liquid and increases the condensation rate by over 20 percent.

Subcooling. Condensation occurs because the subcooled liquid is able to remove the latent heat that the vapor gives up as it changes phase. In order to concentrate attention on the effects of liquid subcooling, the vapor is assumed, in this section, to be pure and saturated. In addition to the fluid mechanical parameters, Ja_l and Pr_l are also important. These can be thought of as the degree of subcooling and the ratio of momentum to thermal boundary layer thicknesses in the liquid, respectively. As alluded to earlier, it is expected that for small Jakob numbers the adiabatic and true velocity and temperature profiles are very similar. In this section this hypothesis will be tested. Saturated atmospheric water will be used to demonstrate the effect of interfacial shear stress and higher Jakob numbers (which tend to increase condensation) upon the condensation rate at the interface.

The first case examined is for $Ja_l = 1.85 \times 10^{-2}$, which corresponds to a 10.0°C subcooling. Figures 3 and 4 show the velocity profiles in both the liquid and the vapor and the temperature profile in the liquid. Shown in the left side of Fig. 3 are the dimensionless shear stress F_l'', dimensionless radial velocity F_l', and the dimensionless axial velocity F_l, versus axial distance from the interface z^*. The dot-dashed and dashed lines represent cases where no condensation is occurring, or $F_l(0) = 0$. Although they do not occur for nonadiabatic flows, the no-condensation cases are useful for comparison. The dot-dashed lines represent the case where no shear stress acts at the interface ($\mu_v/\mu_l = 0$). In this case the liquid behaves inviscidly, supports no shear stress, maintains a uniform radial velocity (for a given r), and decelerates linearly toward the interface. The dashed lines represent an impenetrable interface that supports a shear stress. The large vapor velocities, needed to maintain the stagnation pressure, impose a radially outward (negative by this sign convention) shear stress at the interface, which sweeps the liquid along and thereby increases its velocity. This diagram vividly illustrates the effect that interfacial shear stress has upon the velocity field in the liquid. The solid lines include the effects of condensation at the interface. Mass transfer at the interface appears to augment the radial sweeping action of the vapor. Essentially high momentum (large radial velocity) droplets are introduced into the liquid at the interface and increase its radial velocity. The right side of Fig. 3 shows that the increased liquid convection due to the shear stress tends to cool the boundary layer and slightly increases the heat flux at the interface. The condensation mass transfer appears to have a minimal effect upon the temperature profile. Figure 4 shows these relations for the vapor. The dot-dashed lines represent the classic stagnation flow into a wall (Schlichting, 1979). The dashed curves show that, for an impenetrable interface, the liquid affects the vapor almost as if it were a solid wall. The suction due to condensation tends to increase the interfacial shear stress very near the interface.

Although the axisymmetric interfacial transport model is valuable in providing physical insight, it does a good job of predicting the interfacial heat transfer for some realistic systems. Figure 5 shows predictions of the model compared with some experimental heat transfer data (Celata, 1987b). The heat transfer coefficient shown is defined as the interfacial heat flux

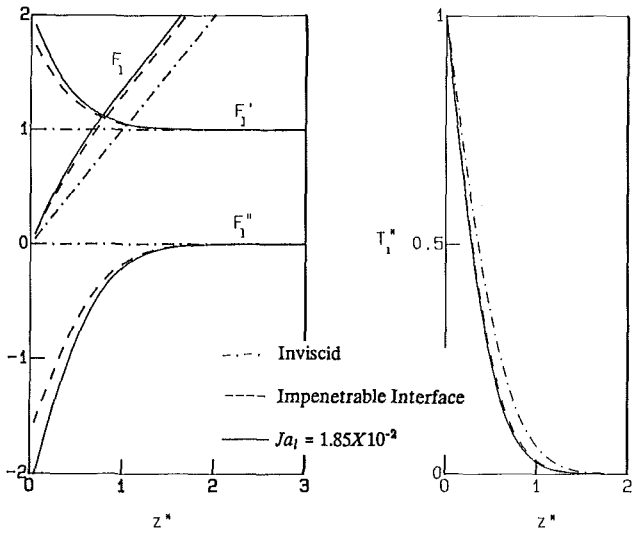

Fig. 3 Velocity and temperature profiles for atmospheric liquid water

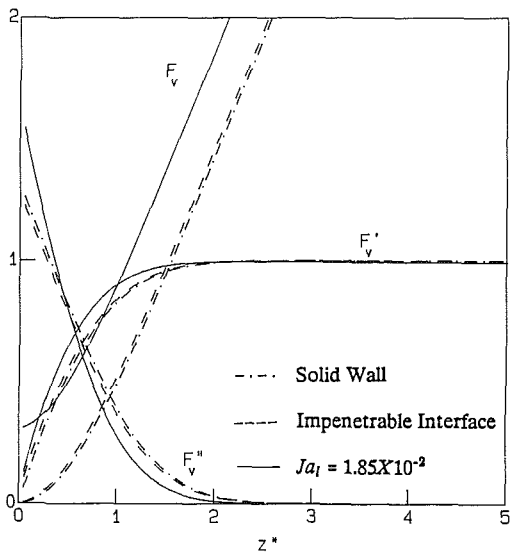

Fig. 4 Velocity profile for saturated atmospheric steam

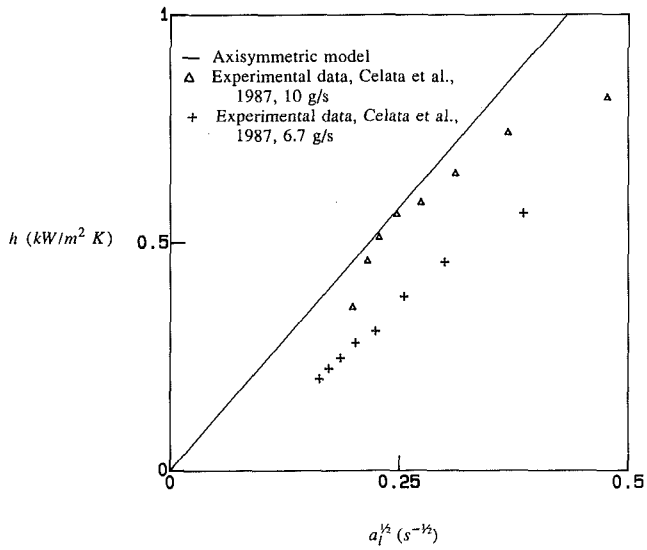

Fig. 5 Comparison of axisymmetric model with experimental data for pure-component condensation

divided by the subcooling in the liquid. It is plotted versus the square root of the stagnation parameter. Celata et al.'s experiment consisted of a cylindrical pressure vessel in which the liquid water was caused to flow in a stagnation flow. The major difference with the axisymmetric condensation model is that the experiment's finite geometry meant that there were radial temperature gradients. Their experiment closely models the pressurizer in a nuclear power plant and the direct contact condensation that occurs between saturated steam and subcooled liquid water. Celata et al. were able to predict their experimental data very well after the introduced three empirical constants. The axisymmetric condensation model, which uses no empirical constants, predicts the higher mass flow-rate data very well. The overprediction of heat transfer for the lower mass flow-rate data is believed to be due to radial temperature gradients that Celata et al. report for their experiment. At lower flow rate, the boundary layer is not as strong and radial temperature gradients occur. These radial temperature gradients heat the subcooled liquid and inhibit its ability to transfer heat from the interface and cause condensation.

Superheating. In this section the effects of superheating a pure vapor are examined (there is no noncondensable gas). A superheated vapor supplies sensible energy to the interface that must be removed by the subcooled liquid. Therefore the liquid's ability to remove latent heat is impaired and condensation is inhibited. In addition to the fluid flow and subcooling parameters, Ja_v, which represents the degree of superheat, and Pr_v, which is the ratio of momentum to thermal boundary layer thicknesses in the vapor, are also important. As expected numerical results show that large Ja_v tend to suppress condensation. Large Pr_v, however, tend to mitigate this effect, see equation (37), and therefore appear to enhance condensation.

Rather than rehash the cases examined for subcooling with a slight modification to account for superheating, it is instructive to determine if and when superheating is important. From examining the interfacial energy balance, equation (37), which relates the temperature field to the condensation rate, it is seen that when $(\rho_m/\rho_l)^{1/4}\ (\mu_m/\mu_l)^{1/2}$ is small, relative to unity, superheat is negligible relative to the subcooling. This is often the case. For example, atmospheric water has $(\rho_m/\rho_l)^{1/4}\ (\mu_m/\mu_l)^{1/2} = 3.26 \times 10^{-2}$. Numerical results verify that, for atmospheric water, superheat is not important unless it is much greater than the subcooling. A logical question is: When is superheat important?

In order to answer this question, Fig. 6 was prepared. It represents the neutral stability curve for condensation of water vapor. It shows the superheat necessary, for a given subcooling, to completely inhibit condensation as a function of total pressure. It was determined by solving the momentum and energy equations with $F_i(0) = 0$ and then using equation (37) to solve for the ratio of the vapor superheat to liquid subcooling. There are a few interesting points to this figure. First it should be noted that condensation will occur only if the corresponding point lies below this curve. That is to say, at a given pressure, if the ratio of superheat to subcooling is large enough condensation cannot occur. In fact if the superheat is large enough evaporation will occur. Also for a given superheat to subcooling ratio, if the pressure is too high, condensation is prevented. The most interesting observation, however, is that, for most pressures, the superheat is much larger than the subcooling. This implies that moderate superheats, relative to the subcooling, have little effect upon the condensation rate. As can be seen from this figure this is true for most of the pressure range. Near the critical point, however, $(\rho_m/\rho_l)^{1/4}\ (\mu_m/\mu_l)^{1/2}$ approaches one and superheat is just as significant as the subcooling.

Noncondensables. There are two primary mechanisms by

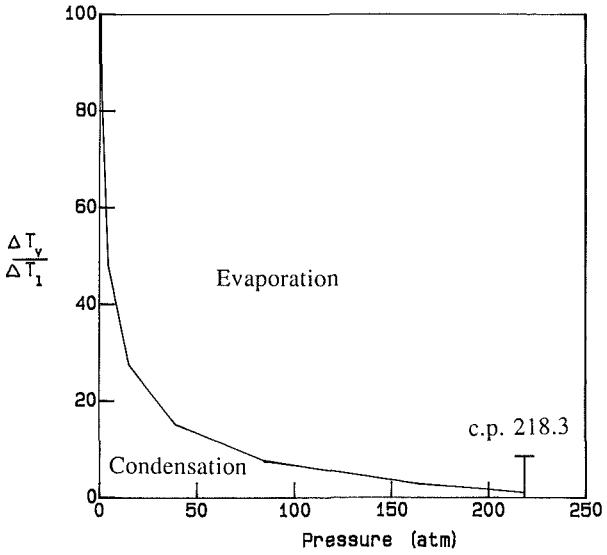

Fig. 6 Neutral stability curve for condensation of water vapor

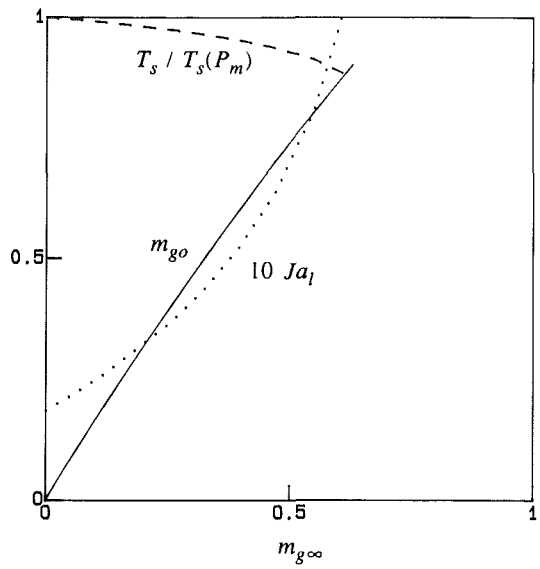

Fig. 7 Effects of mass diffusion upon condensation for atmospheric air/steam mixture, $F_l(0) = -10^{-2}$

which the presence of a noncondensable gas in the vapor affects the condensation process. One way is that it alters the thermophysical and transport properties of the mixture. The other way is that it lowers the partial pressure of the vapor at the interface, decreases the effective subcooling, and hence inhibits condensation. The only effect of the three dimensionless parameters μ_g/μ_v, k_g/k_v, and C_{pg}/C_{pv} is to alter the thermophysical and transport properties represented by equations (28), (31), (40), and (41). A large μ_g/μ_v ratio tends to increase the μ_m/μ_l ratio. A large k_g/k_v tends to decrease Pr_m. A large C_{pg}/C_{pv} tends to increase both Pr_m and Ja_m. Of course if any of these parameters is drastically different from 1, the constant property assumption breaks down. $T_{l\infty}/T_s(P_m)$ and $T_{m\infty}/T_s(P_m)$ are in a sense reduced temperatures; they relate the thermodynamics, which depend primarily upon the absolute temperature, and the heat transfer, which depends largely upon the temperature differences.

There are two parameters M_g/M_v and $h_{vl}/[R_v T_s (P_m)]$, whose primary effect is to determine the interfacial thermodynamic relation between m_{go} and T_s. Aside from altering thermophysical and transport properties, the ratio of the molecular weights, M_g/M_v, is important in determining the thermodynamic relation between m_{go} and T_s (see equation (18)). For a given mass fraction, m_{go}, a large M_g/M_v ratio implies that the mole fraction of noncondensable gas is low and consequently the saturation temperature, T_s, is very near $T_s(P_m)$. The dimensionless parameter $h_{vl}/[R_v T_s (P_m)]$ is the ratio of the latent heat of the vapor molecules as compared to their kinetic energy. The saturation temperature of substances with a high latent heat, relative to their kinetic energy, is less sensitive to changes in saturation pressure; see equations (12) and (18).

In addition to the gross thermophysical and transport properties and the interfacial thermodynamics the noncondensable gas species equation (32) is important in determining the relationship between the noncondensable mass fraction at infinity, $m_{g\infty}$, and the noncondensable gas fraction at the interface. The Schmidt number, Sc_m, is the mass transfer analog to the Prandtl number, Pr_m, for the energy transfer. It represents the ratio between the thicknesses of the momentum and mass transfer boundary layers. The other important dimensionless parameter is the noncondensable gas fraction at infinity, $m_{g\infty}$, which of course is related to m_{go} and hence the interfacial saturation temperature.

It has been shown that many parameters affect condensation under the influence of a noncondensable gas. However most applications involve condensation of an atmospheric mixture of water vapor and air. Therefore attention will be restricted to this case and the effect of $m_{g\infty}$ upon the condensation process will be determined. Figure 7 shows both the interfacial noncondensable gas fraction, m_{go}, and interfacial saturation temperature as functions of noncondensable gas fraction at infinity, $m_{g\infty}$, for $F_l(0) = -10^{-2}$. As can be seen m_{go} is a very strong function of $m_{g\infty}$. In other words a small free-stream noncondensable gas fraction produces a much larger interfacial noncondensable gas fraction. The exponential relationship, equation (18), between m_{go} and $T_s/T_s(P_m)$ somewhat dampens the effect upon the interfacial saturation temperature.

Figure 7 also shows that the subcooling necessary to maintain this condensation rate increases greatly as the free-stream noncondensable gas fraction is increased. Since the slope of the curve is rapidly increasing it is seen that for large noncondensable gas fractions, slight changes have a dramatic effect upon the subcooling required to maintain condensation.

Conclusions

In this paper a simple axisymmetric model is used to study interfacial condensation. The one-dimensional governing equations are solved numerically. Of special interest are how interfacial mass and momentum balances affect the velocity and temperature fields in the liquid, and hence the condensation rate. For common fluids, such as water, interfacial forces are very important. The low vapor-to-liquid density ratios require that, in order to maintain the proper stagnation pressure, the velocity be very high in the vapor. The large vapor velocity at the interface exerts a large interfacial shear stress upon the liquid, which increases convection, and hence condensation, in the liquid. The interfacial mass transfer, however, does not significantly affect the velocity profile except for extremely large subcoolings in the liquid. This implies that the momentum equations can be solved independently and the condensation rate determined from the resulting temperature field.

The primary mechanism causing the condensation is liquid subcooling: It removes the latent heat from the vapor and causes it to condense at the interface. Superheating induces a temperature gradient in the vapor, which causes heat to be transferred from the vapor toward the interface. This energy must be removed by the liquid, which consequently is less effective at removing latent heat and causing condensation. Small to moderate superheats in the vapor, however, do not

significantly inhibit condensation except near the critical point. The presence of a noncondensable gas in the vapor significantly lowers the interfacial saturation temperature. Consequently, there is a lower thermal driving potential and condensation is reduced.

References

Banerjee, S., 1978, "A Surface Renewal Model for Interfacial Heat and Mass Transfer in Transient Two-Phase Flow," *Int. J. Multiphase Flow*, Vol. 4, pp. 571–573.

Callen, H. B., 1985, *Thermodynamics and an Introduction to Thermostatistics*, 2nd ed., Wiley, New York, pp. 228–231.

Celata, G. P., Cumo, M., Farello, G. E., and Focardi, G., 1987a, "Direct Contact Condensation of Superheated Steam on Water," *Int. J. Heat Mass Transfer*, Vol. 30, pp. 449–458.

Celata, G. P., Gumo, M., Farello, G. E., and Focardi, G., 1987b, "A Theoretical Model of Direct Contact Condensation on a Horizontal Surface," *Int. J. Heat Mass Transfer*, Vol. 30, pp. 459–467.

Collier, J. G., 1972, *Convective Boiling and Condensation*, McGraw-Hill, New York, p. 430.

Jones, O. C., 1966, "Condensation Heat Transfer at an Agitated Steam–Water Interface," ASME Paper No. 66-WA/HT-42.

Koh, J. C. Y., 1962, "Film Condensation in a Forced-Convective Boundary-Layer Flow," *Int. J. Heat Mass Transfer*, Vol. 5, pp. 941–954.

Press, W. H., Flannery, B. P., Teukolsky, S. A., and Vetterling, W. T., 1986, *Numerical Recipes*, Cambridge University Press, Cambridge, United Kingdom, Chaps. 15, 16.

Schlichting, H., 1979, *Boundary-Layer Theory*, McGraw-Hill, New York, pp. 100–101.

Thomas, R. M., 1979, "Condensation of Steam on Water in Turbulent Motion," *Int. J. Multiphase Flow*, Vol. 5, pp. 1–15.

Wang, C. Y., 1985, "Stagnation Flow on the Surface of a Quiescent Fluid—an Exact Solution of the Navier-Stokes Equations," *Quarterly of Appl. Math.*, Vol. 43, No. 2, pp. 215–223.

An Approximate Analysis for General Film Condensation Transients

M. I. Flik
Research Assistant.

C. L. Tien
A. Martin Berlin Professor.
Fellow ASME

Department of Mechanical Engineering,
University of California,
Berkeley, CA 94720

This work presents a simple, powerful technique for analyzing a broad class of film condensation transients. The analysis shows that general film condensation transients are governed by the propagation of a kinematic wave along the film. Scaling arguments establish conditions for the use of quasi-steady profiles in the integral conservation equations. An elementary method permits simple solutions of the governing hyperbolic equation for time-step changes with arbitrary initial conditions. The application of this method yields closed-form solutions for step changes of body force, vapor shear, and wall temperature for a laminar film and for step changes of body force and wall temperature for a film within a porous medium. These approximate results agree excellently with numerical solutions of the complete boundary-layer equations. This technique has applications to a wide class of film condensation transients and to film boiling and convective vaporization transients.

Introduction

Transient film condensation is a heat transfer mode that occurs under certain conditions in the condensers of power and refrigeration systems and in two-phase thermosyphons and heat pipes. Sudden changes in the system parameters, such as the cooling heat flux or the vapor flow rate, cause transients in these systems where condensation heat transfer controls the device performance. Condensers aboard spacecraft experience transients due to abrupt alterations of the body-force acceleration at takeoff and re-entry and due to reorientation effects. Film condensation transients occur during loss-of-coolant accidents in the steam generators of pressurized water reactors. Transient condensation provides heating in soldering processes of electronic circuits. Film condensation transients also occur within porous media, such as in wicked heat pipes and steam-injection enhanced oil recovery.

Sparrow and Siegel (1959) gave an approximate analytical solution for laminar condensate flow in the degenerate case of zero initial film thickness with a time-step change of the wall temperature. Cheng and Chui (1984) analyzed the same problem for a porous medium, assuming Darcian flow of the condensate. Chung (1963) solved the laminar-flow boundary-layer equations for unsteady subcooling and body force using a perturbation method. His results only allow the prediction of trends, not of the entire transient. Wilson (1976) extended Sparrow and Siegel's treatment to two-dimensional unsteady flow of the condensate and gave a general formulation of the problem. However, his results are limited to the same degenerate case. Wallis (1969) pointed out the occurrence of kinematic waves in falling films and solved the special case of unsteadily draining films. However, he did not analyze the transient film motion due to changes in the system parameters. Reed et al. (1987) obtained a solution of the complete set of unsteady boundary-layer equations for laminar-film flow by means of numerical scheme. A modified version of this solution accounts for the presence of a porous medium. This finite-difference code, though effective in handling arbitrary transients, requires considerable computing time and cannot be incorporated easily in simulation or design programs.

There is a need for analytical solutions that account for arbitrary initial conditions. This study remedies this shortage with a general analysis based on the integral conservation equations for the condensate film. Scaling arguments establish conditions under which quasi-steady velocity and temperature profiles are applicable. The discussion of the resulting equation reveals the wave characteristics of general film condensation transients. General transients constitute a Cauchy problem for the governing equation. An elementary method obtains simple solutions for time-step changes with arbitrary initial conditions.

The study demonstrates the application of this method by examining two cases of technical importance: laminar-film condensation on a vertical plate after a time-step change of vapor shear, body-force acceleration, and wall temperature, and film condensation on a vertical plate in a porous medium with constant porosity and isotropic permeability after a time-step change of body force and wall temperature. The method yields analytical solutions for the film thickness as a function of streamwise location and time, and for the duration of the transient. Knowledge of the film thickness allows determination of the heat transfer coefficient. For both cases the approximate analytical solutions are compared to the numerical solutions given by Reed et al. (1987).

Analysis

Conservation Equations. Figure 1 shows the general physical model for transient film condensation with or

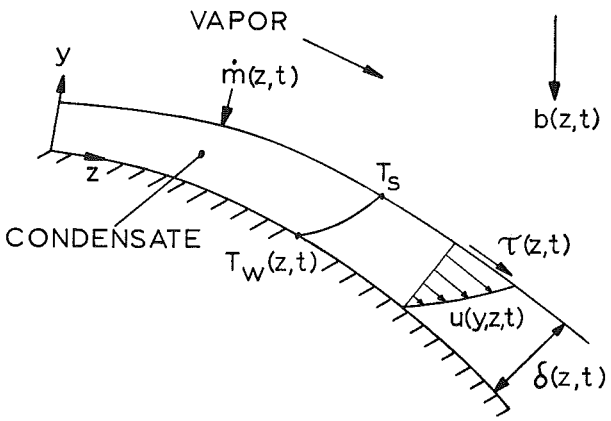

Fig. 1 Physical model of transient film condensation

Contributed by the Heat Transfer Division and presented at the National Heat Transfer Conference, Houston, Texas, July 24-27, 1988. Manuscript received by the Heat Transfer Division March 22, 1988. Keywords: Condensation, Phase-Change Phenomena, Transient and Unsteady Heat Transfer.

without the presence of a porous medium. Here the problem is analyzed in two dimensions, i.e., no gradients in the x direction are considered. Wilson (1976) gives the extension of the general formulation to three dimensions. A single-component vapor flows along a cold surface with a velocity varying in time and streamwise location. The vapor condenses at a rate $\dot{m}(z, t)$ and forms a thin condensate film. The unsteady vapor movement induces an unsteady shear stress $\tau(z, t)$ at the smooth interface. This shear stress, together with the unsteady body force, the resistance of the porous matrix, and the pressure gradient, determines the motion of the condensate film. Thus the condensate velocity is a function of cross-stream and streamwise position as well as of time. The magnitude of the body force vector, b, can vary along z, e.g., in a rotating heat pipe. The wall temperature is a function of z and t, whereas the interface is assumed to be at the saturation temperature, which remains constant for small pressure variation. Capillary effects in porous media are not considered.

If the condensate is a Newtonian fluid with constant properties, the volume-averaged boundary-layer equations for the film become (Catton, 1985)

$$\frac{\partial u}{\partial z}+\frac{\partial v}{\partial y}=0 \tag{1}$$

$$\frac{1}{\epsilon}\frac{\partial u}{\partial t}+\frac{1}{\epsilon^2}u\frac{\partial u}{\partial z}+\frac{1}{\epsilon^2}v\frac{\partial u}{\partial y}=-\frac{\nu}{\kappa}u-\frac{1}{\rho_l}\frac{\partial p(z,t)}{\partial z}+\frac{\nu}{\epsilon}\frac{\partial^2 u}{\partial y^2}+b_z(z,t) \tag{2}$$

$$(\rho c)_e\frac{\partial T}{\partial t}+(\rho c)_l u\frac{\partial T}{\partial z}+(\rho c)_l v\frac{\partial T}{\partial y}=k_e\frac{\partial^2 T}{\partial y^2} \tag{3}$$

where ϵ is the porosity of the matrix, κ its permeability, and the subscript e denotes effective properties. The quadratic inertial term is omitted in the momentum equation, since it is negligible for low-speed flow in porous media. In the absence of a porous medium, $\epsilon\to 1$ and $\kappa\to\infty$. The effects of curvature in the streamwise direction are not considered except in the body-force term, where b_z is the body-force acceleration in the streamwise direction.

An analytical or simple numerical treatment of the problem requires the integration of these equations. However, one significant simplification can be made a priori. Reed et al. (1987) substantiated that in the case of laminar-film flow the unsteady and inertia terms in the momentum equation can be neglected if Ja/Pr is smaller than the order of unity, a range encompassing all practical situations except the condensation of liquid-metal vapors. For film condensation in porous media, the study of White and Tien (1987) shows that to the first order inertia effects are negligible. Within the limit given below the unsteady term can be neglected for porous media as well. These results imply that instead of solving the complete momentum equation it is possible to integrate the continuity and energy equations using a velocity profile that satisfies the momentum equation without unsteady and inertia terms at any time t.

The integral continuity equation is

$$\dot{m}=\epsilon\rho_l\frac{\partial\delta}{\partial t}+\rho_l\frac{\partial}{\partial z}\int_0^\delta u\,dy \tag{4}$$

It should be noted that Cheng and Chui (1984) omitted the porosity multiplying the first term on the right-hand side of equation (4). Using the differential continuity equation, the energy equation (3) is integrated across the film to obtain

Nomenclature

a = convection correction factor, equation (9)

$A = \mathrm{Ja}/\left(1+\frac{3}{8}\mathrm{Ja}\right)$

b = magnitude of body-force vector, m/s^2

b_z = body force in z direction $= b(z, t)\sin\phi(z)$, m/s^2

$B = \mathrm{Ja}/\left(1+\frac{1}{2}\mathrm{Ja}\right)$

c = specific heat, J/kgK

C = wave speed, m/s

$D = \mathrm{Ja}_l/\left(1+\frac{\sigma}{2\epsilon}\mathrm{Ja}_l\right)$

E = functional, equation (18), m/s

g = dimensionless body force in z direction $= b_z/g_n$

g_n = gravity acceleration on earth $= 9.80665$ m/s^2

h = heat transfer coefficient, W/m^{2}K

i_{fg} = latent heat of vaporization, J/kg

Ja = Jakob number $= c_l\Delta T/i_{fg}$

k = thermal conductivity, W/mK

$K = \left(1+\frac{1}{3}\mathrm{Ja}\right)\Big/\left(1+\frac{3}{8}\mathrm{Ja}\right)$

$L = 2\mathrm{Ja}_l\hat{t}_{ss}$

$\dot{m}$ = Local condensation rate, kg/m^{2}s

p = pressure, N/m^2

P, Q, R = functionals, equation (12)

Pr = condensate Prandtl number $= \nu/\alpha$

$S = (\hat{\delta}^2-2\mathrm{Ja}_l\hat{t})^{1/2}$

t = time, s

T = temperature, °C

T_s = saturation temperature, °C

T_w = wall temperature, °C

$\Delta T = T_s - T_w$, K

u = streamwise velocity, m/s

u_D = Darcy velocity $= (\rho_l-\rho_v)g_n\kappa/\mu$, m/s

v = cross-stream velocity, m/s

V, W = functionals, equation (16)

y = cross-stream coordinate, m

z = streamwise coordinate, m

α = condensate thermal diffusivity, m^2/s

δ = condensate film thickness, m

ϵ = porosity

θ = dimensionless temperature $= (T-T_s)/(T_w-T_s)$

Θ = functional, equation (16)

κ = permeability, m^2

μ = condensate dynamic viscosity, kg/ms

ν = condensate kinematic viscosity, m^2/s

ρ = density, kg/m^2

$\sigma = (\rho c)_e/(\rho c)_l$

τ = interfacial shear stress, N/m^2

ϕ = angle between surface normal and body-force vector, rad

Superscripts

~ = dimensionless quantity for laminar film

^ = dimensionless quantity for film in a porous medium

Subscripts

e = effective property, $X_e = \epsilon X_l + (1-\epsilon)X_m$

l = condensate property

m = porous matrix property

ss = steady state

v = vapor property

0 = before transient

1 = after transient

$$(\rho c)_e \frac{\partial}{\partial t}\int_0^\delta (T-T_s)dy + (\rho c)_l \frac{\partial}{\partial z}\int_0^\delta u(T-T_s)dy$$

$$= k_e\left[\frac{\partial T}{\partial y}\right]_{y=0}^{y=\delta} \tag{5}$$

The energy balance at the interface is

$$\dot{m} i_{fg} = k_e\left(\frac{\partial T}{\partial y}\right)_{y=\delta} \tag{6}$$

assuming that no conduction of heat toward the interface occurs in the vapor. The integral continuity equation governs the dynamics of the film growth whereas the integral energy equation accounts for film subcooling and convection.

The time needed for the development of the profiles is of the order of the time constant for cross-stream diffusion. For film flow in a porous medium, the time constant for cross-stream diffusion of heat is of the order $\delta^2(\rho c)_e/k_e$, for cross-stream transport of momentum δ^2/ν. Combining equations (4) and (6) and balancing the condensation rate with the time derivative of the film thickness yields the order of the time constant for film growth, $\epsilon\delta^2(\rho c)_l/\mathrm{Ja}k_e$. For the quasi-steady profile assumption to be valid, the time required to develop the profiles must be significantly shorter than the time constant for film growth. This leads to the requirements that

$$\frac{\sigma}{\epsilon}\,\mathrm{Ja} << 1, \qquad \frac{k_e}{(\rho c)_l}\frac{\mathrm{Ja}}{\nu\epsilon} << 1 \tag{7}$$

for the use of quasi-steady temperature and velocity profiles, respectively. In the case of a laminar film, these requirements become $\mathrm{Ja} << 1$, $\mathrm{Ja/Pr} << 1$, which have been given by Reed et al. (1987).

A balance of the first and second terms on the right-hand side of equation (4) shows that the ratio of a velocity scale to a streamwise length scale is of the order of the porosity divided by the time constant for film growth. Substitution of this relation into the momentum equation (2) and identifying the time scale of the unsteady term with the time constant for film growth shows that the unsteady and inertia terms are of the same order. Hence the second requirement of equation (7) also is the condition for the omission of the inertia terms, which agrees with the findings of Reed et al. (1987) for laminar film flow.

If the same argument is applied to the energy equation (3), one finds that the convective terms are of the order of the unsteady term divided by σ/ϵ, which is greater than or equal to unity. If the first requirement of equation (7) is satisfied, then the convective terms can be neglected, resulting in a linear temperature profile, which is employed in the specific cases analyzed in the next section. However, Reed et al. (1987) showed that the transient film thickness can be predicted well using quasi-steady profiles for Ja and Ja/Pr up to unity. Hence equation (7) appears to be a conservative criterion for the validity of quasi-steady profiles. This suggests the retention of the convective terms in the integral energy equation that account for the film subcooling, and the consideration of nonlinear temperature profiles for general transients.

General Transients. The quasi-steady profiles are given by

$$u = u(y, \delta, \tau(z, t), b_z(z, t)) \tag{8}$$

$$\frac{T-T_s}{T_w-T_s} = \theta(y, \delta, a(z, t)) \tag{9}$$

where the function $a(z, t)$ is a correction factor for convective effects. It applies to a nonlinear temperature profile and accounts for the change of its shape in space and time. The profiles given by equations (8) and (9) satisfy the steady momentum equation without inertia terms and the steady energy equation as well as the boundary conditions

$$u(y=0)=0, \qquad \mu\left(\frac{\partial u}{\partial y}\right)_{y=\delta} = \tau(z, t) \tag{10}$$

$$T(y=0)=T_w(z, t), \qquad T(y=\delta)=T_s \tag{11}$$

The interfacial shear stress depends on the vapor free-stream velocity, the film velocity at the interface $u(\delta, z, t)$, and the condensation rate $\dot{m}(z, t)$. In this analysis, $\tau(z, t)$ is treated as a prescribed, known parameter. Blangetti and Naushahi (1980) proposed an expression derived from film theory that accounts for the augmentation of interfacial momentum exchange due to mass transfer. If $\dot{m}(z, t)$ and $u(\delta, z, t)$ can be estimated a priori, then this relation determines the interfacial shear. Otherwise, a simple friction-factor expression can be employed, a good approximation for low interface velocity and condensation rate and high vapor velocity.

Substitution of the temperature and velocity profiles into equations (4) to (6) and elimination of $\dot{m}$ and $(\partial T/\partial y)_{y=\delta}$ yields a first-order quasi-linear partial differential equation for the film thickness in z and t,

$$P(\delta, z, t)\frac{\partial \delta}{\partial t} + Q(\delta, z, t)\frac{\partial \delta}{\partial z} = R(\delta, z, t) \tag{12}$$

where P, Q, and R are as follows:

$$P = (\rho c)_e \frac{\partial \Theta}{\partial \delta}\Delta T + i_{fg}\rho_l \epsilon \tag{13}$$

$$Q = (\rho c)_l \frac{\partial W}{\partial \delta}\Delta T + i_{fg}\rho_l \frac{\partial V}{\partial \delta} \tag{14}$$

$$R = -k_e \Delta T\left(\frac{\partial \theta}{\partial y}\right)_{y=0} - i_{fg}\rho_l\left(\frac{\partial V}{\partial \tau}\frac{\partial \tau}{\partial z} + \frac{\partial V}{\partial b_z}\frac{\partial b_z}{\partial z}\right)$$
$$- (\rho c)_e\left(\Delta T \frac{\partial \Theta}{\partial a}\frac{\partial a}{\partial t} + \Theta\frac{\partial(\Delta T)}{\partial t}\right)$$
$$- (\rho c)_l\left[\Delta T\left(\frac{\partial W}{\partial \tau}\frac{\partial \tau}{\partial z} + \frac{\partial W}{\partial b_z}\frac{\partial b_z}{\partial z} + \frac{\partial W}{\partial a}\frac{\partial a}{\partial z}\right) + W\frac{\partial(\Delta T)}{\partial z}\right] \tag{15}$$

where

$$V(\delta, z, t) = \int_0^\delta u dt, \quad W(\delta, z, t) = \int_0^\delta u\theta dy,$$

$$\Theta(\delta, z, t) = \int_0^\delta \theta dy \tag{16}$$

For $P \neq 0$ this becomes

$$\frac{\partial \delta}{\partial t} + C(\delta, z, t)\frac{\partial \delta}{\partial z} = E(\delta, z, t), \tag{17}$$

where

$$C = \frac{\mathrm{Ja}\dfrac{\partial W}{\partial \delta} + \dfrac{\partial V}{\partial \delta}}{\sigma\mathrm{Ja}\dfrac{\partial \Theta}{\partial \delta} + \epsilon}, \qquad E = \frac{R}{P} \tag{18}$$

Equation (17) describes a hyperbolic wave traveling along the positive z axis. Whitham (1974) terms waves of this kind *kinematic waves* since they arise merely from continuity requirements. An equivalent form is

$$dt = \frac{dz}{C(\delta, z, t)} = \frac{d\delta}{E(\delta, z, t)} \tag{19}$$

which is a pair of ordinary differential equations. The first of them,

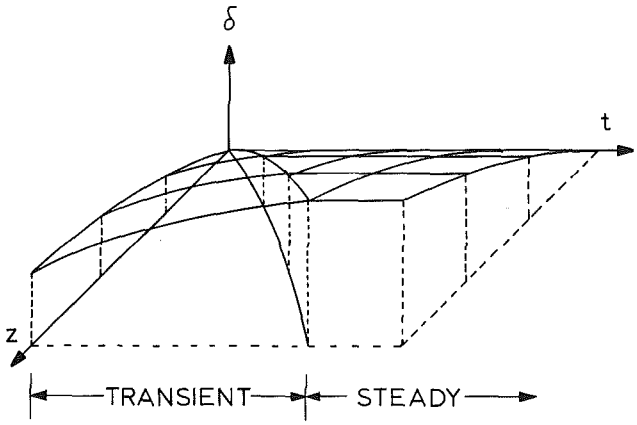

Fig. 2 Schema of particular solution satisfying initial conditions for a step change

$$\frac{dz}{dt} = C(\delta, z, t) \tag{20}$$

is the equation for the characteristics in the zt-plane, giving the slope $\tan^{-1}(1/C)$ at every point, and thus describing the propagation of a wave element along the stream with an instantaneous speed C. This can be seen by noting that equation (17) states that the total derivative of the film thickness along a characteristic is equal to E. Hence the propagation of a kinematic wave along the film governs general film condensation transients.

Transients are initiated by a change in the system parameters

$$X(z, t) = \begin{cases} X_0(z) & \text{for } t<0 \\ \bar{X}(z, t) & \text{for } 0 \le t \le t_1, \quad X = \mathrm{Ja}, \tau, b_z, a \\ X_1(z) & \text{for } t \ge t_1 \end{cases} \tag{21}$$

For the leading edge, the initial values of δ are given by the steady-state solution of

$$C_0(\delta, z)\frac{\partial \delta}{\partial z} = E_0(\delta, z), \qquad \delta(z=0) = 0 \tag{22}$$

where the subscript 0 indicates evaluation at the parameter values X_0. In the case of a blunt body, the first derivative of δ with respect to z vanishes at the vertex $z=0$ rather than δ itself. These initial data constitute a *Cauchy problem* for the governing equation (17). The particular integral surface passing through the prescribed curve in the δz plane must be found from the manifold of solutions. This solution exists for continuous C and E provided that the Jacobian satisfies the condition (John, 1982)

$$det\begin{bmatrix} 1 & 0 \\ C(\delta, z, t) & 1 \end{bmatrix} \neq 0 \tag{23}$$

which is satisfied identically for all $C(\delta, z, t)$.

Time-Step Change. A simple, special case is a time-step change of the parameters, $t_1 \to 0$. This case is particularly useful to compare the dynamic characteristics of different systems. However, there is also an anomaly associated with this case. Due to the time-step change, the wave speed C and the total derivative E change their values discontinuously. The step change in C prescribes two different slopes at any position at $t=0$. These step changes lead to a discontinuity in the first derivative of the solution $\delta(z, t)$ traveling along the limiting characteristic as shown in Fig. 2. This must be distinguished from the phenomenon of breaking when the film thickness δ becomes multivalued. A necessary condition for breaking is a negative streamwise gradient of the wave speed. In the examples of the next section the wave speed is a montonically increasing function of the film thickness. The transient film thickness is seen to increase montonically along z after a step change for all times. Hence in these cases breaking does not occur during transients.

Figure 2 shows the limiting characteristic separating the transient from the steady-state region for the case of a leading edge after a time-step change. It is found by integrating the ordinary differential equations (19) subject to the conditions $\delta(z=0)=0$ and $t_{ss}(z=0)=0$, yielding a relation of the form $G(t_{ss}, z)=0$, where t_{ss} denotes the duration of the transient at a position z. Steady state is achieved at a given position when the wave element, which started at $t=0$ at the leading edge, has passed by. Hildebrandt (1949) gives a simple method for solving the Cauchy problem resulting from arbitrary time-step changes. If

$$f_1(\delta, z, t) = d_1 \tag{24}$$

$$f_2(\delta, z, t) = d_2 \tag{25}$$

are two independent integrals of equation (19) and if the initial data are given by

$$f_3(\delta, z) = 0 \text{ at } t=0 \tag{26}$$

then the elimination of z, δ, t from equations (24) to (26) yields a functional relation $F(d_1, d_2)=0$, and the particular solution is

$$F[f_1(\delta, z, t), f_2(\delta, z, t)] = 0 \tag{27}$$

Figure 2 shows schematically that the particular solution only exists in the transient region and reaches the steady-state value on the limiting characteristic. This leads to the discontinuous first derivative of the film thickness referred to earlier.

From the solution for the film thickness the heat transfer coefficient is found by

$$h(z, t) = -k_e\left(\frac{\partial \theta(y, \delta, a(z, t))}{\partial y}\right)_{y=0} \tag{28}$$

Results and Discussion

This section analyzes two technically important cases: laminar film condensation on a vertical plate with a time-step change of wall temperature, body force, and vapor shear, and film condensation on a vertical plate within a porous medium with a time-step change of wall temperature and body force. In both cases the film starts at the leading edge with zero thickness.

Laminar Film. The wall is assumed to be isothermal, and body force and vapor shear do not vary with z. Convection of energy is neglected and the pressure gradient is given by the hydrostatic pressure in the vapor region. The substitution of the quasi-steady profiles

$$u = \frac{\tau}{\mu}y + \frac{b_z(\rho_l - \rho_v)}{\mu}\left(\delta y - \frac{1}{2}y^2\right) \tag{29}$$

$$\theta = 1 - \frac{y}{\delta} \tag{30}$$

into the integral continuity and energy equations, together with the interface balance, yields the nondimensional governing equation

$$\left(1+\frac{1}{2}Ja\right)\tilde{\delta}\frac{\partial \tilde{\delta}}{\partial \tilde{t}} + \left(1+\frac{3}{8}\mathrm{Ja}\right)(K\tilde{\tau} + \tilde{g}\tilde{\delta})\tilde{\delta}^2\frac{\partial \tilde{\delta}}{\partial \tilde{z}} = \mathrm{Ja} \tag{31}$$

where the dimensionless parameters are

$$\tilde{\delta}=\delta/(\nu^2/g_n)^{1/3}, \qquad \tilde{t}=t\alpha/(\nu^2/g_n)^{2/3}, \tag{32}$$

$$\tilde{z}=\frac{z/\mathrm{Pr}}{(\nu^2/g_n)^{1/3}(1-\rho_v/\rho_l)}, \qquad \tilde{\tau}=\frac{\tau}{(\nu g_n)^{2/3}(\rho_l-\rho_v)},$$

$$\tilde{g}=b_z/g_n, \qquad K=\frac{1+\frac{1}{3}\,\mathrm{Ja}}{1+\frac{3}{8}\,\mathrm{Ja}}$$

Within the limit for the Ja number given in the previous section the coefficient K can be set equal to unity. The wave speed in this case is

$$\tilde{C}=(\tilde{\tau}+\tilde{g}\tilde{\delta})\tilde{\delta}\,\frac{1+\frac{3}{8}\,\mathrm{Ja}}{1+\frac{1}{2}\,\mathrm{Ja}} \tag{33}$$

a result also given by Wallis (1969) for the case of no vapor shear and neglecting subcooling.

Transients are initiated by a simultaneous time-step change of body force, vapor shear, and wall temperature,

$$X(t)=\begin{cases}X_0 \text{ for } t\le 0\\ X_1 \text{ for } t>0\end{cases} \qquad X=\mathrm{Ja},\ \tilde{g},\ \tilde{\tau} \tag{34}$$

Together with the boundary condition $\tilde{\delta}(\tilde{z}=0)=0$, this corresponds to an initial condition of the form

$$\frac{1}{3}\,\tilde{\tau}_0\tilde{\delta}^3+\frac{1}{4}\,\tilde{g}_0\tilde{\delta}^4=A_0\tilde{z} \text{ at } \tilde{t}=0 \tag{35}$$

where

$$A_0=\frac{\mathrm{Ja}_0}{1+\frac{3}{8}\,\mathrm{Ja}_0} \tag{36}$$

a relation also given by Rohsenow et al. (1956). The particular solution in the transient region becomes

$$\frac{1}{3}\left(\tilde{\tau}_1-\frac{A_1}{A_0}\,\tilde{\tau}_0\right)(\tilde{\delta}^2-2B_1\tilde{t})^{3/2}+\left(\tilde{g}_1-\frac{A_1}{A_0}\,\tilde{g}_0\right)\left(\frac{1}{2}\,\tilde{\delta}^2-B_1\tilde{t}\right)^2=\frac{1}{3}\,\tau_1\tilde{\delta}^3+\frac{1}{4}\,\tilde{g}_1\tilde{\delta}^4-A_1\tilde{z} \tag{37}$$

for $\tilde{\tau}<\tilde{t}_{ss}$, where

$$A_1=\frac{\mathrm{Ja}_1}{1+\frac{3}{8}\,\mathrm{Ja}}, \qquad B_1=\frac{\mathrm{Ja}_1}{1+\frac{1}{2}\,\mathrm{Ja}_1} \tag{38}$$

This is an implicit relation for the film thickness as a function of z and t for which the Newton–Raphson iteration converges rapidly. Differentiation of this solution with respect to z shows that $\partial\delta/\partial z$ is positive and finite for all times except at the leading edge. When steady state is achieved, the right-hand side of equation (37) becomes zero which implies

$$\tilde{t}_{ss}=\frac{\tilde{\delta}_{ss}^2}{2B_1} \tag{39}$$

Hence the duration of the transient is related to the steamwise location by

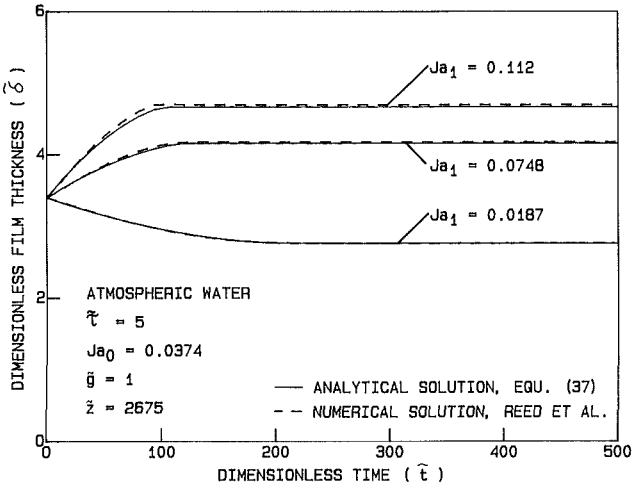

Fig. 3 Laminar film: step change of wall temperature

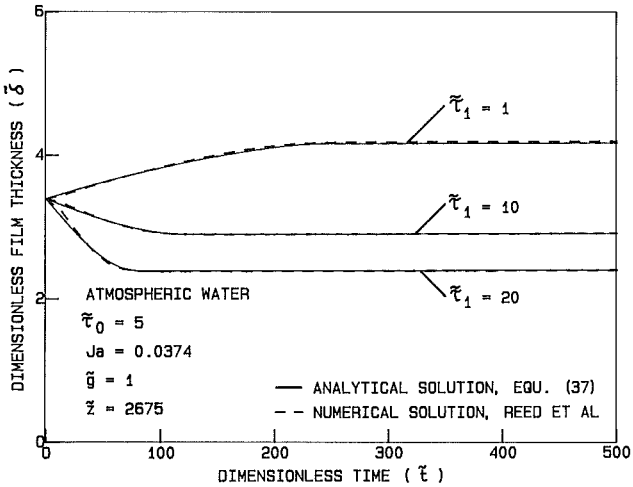

Fig. 4 Laminar film: step change of vapor shear

$$\frac{1}{3}\,\tilde{\tau}_1(2B_1\tilde{t}_{ss})^{3/2}+\tilde{g}_1(B_1\tilde{t}_{ss})^2=A_1\tilde{z} \tag{40}$$

A degenerate case is the limit $A_0\to 0$, which corresponds to the wall initially being at saturation temperature with no condensate film. The solution for this case is

$$\tilde{\delta}=\begin{cases}\sqrt{2B_1\tilde{t}} & \text{for } \tilde{t}<\tilde{t}_{ss}\\ \tilde{\delta}_{ss} & \text{for } \tilde{t}\ge\tilde{t}_{ss}\end{cases} \tag{41}$$

which corresponds to the result of Sparrow and Siegel (1959) for no vapor shear. In this case initial vapor shear and body force do not influence the film behavior. The film grows at the same rate at every streamwise location until it reaches its steady-state thickness.

For atmospheric water the approximate solution, equation (37), agrees very well with the numerical results of Reed et al. (1987). In this case, the Ja number is 0.0374, corresponding to $\Delta T=20$ K. This value of Ja is well within the limit given in the previous section for the use of quasi-steady profiles. Figure 3 presents a step change of the wall subcooling corresponding to a rapid change of the coolant-side conditions in a condenser. Enhanced subcooling augments condensate flow and film thickness. The smaller the subcooling, the longer the transient prevails and vice versa. An abrupt increase in vapor shear is seen in Fig. 4 to enhance the drag on the condensate film and

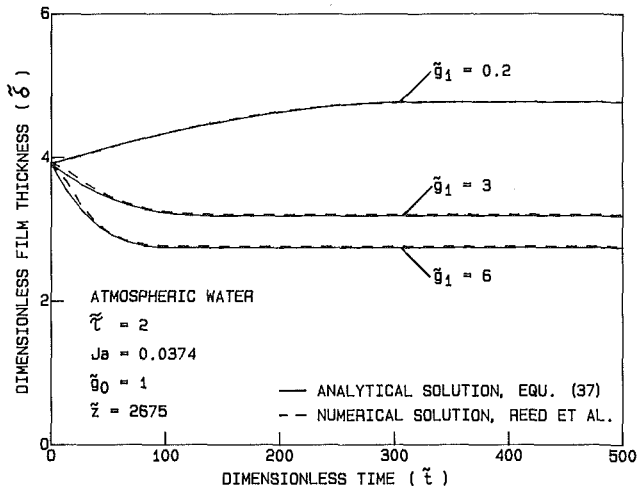

Fig. 5 Laminar film: step change of body force

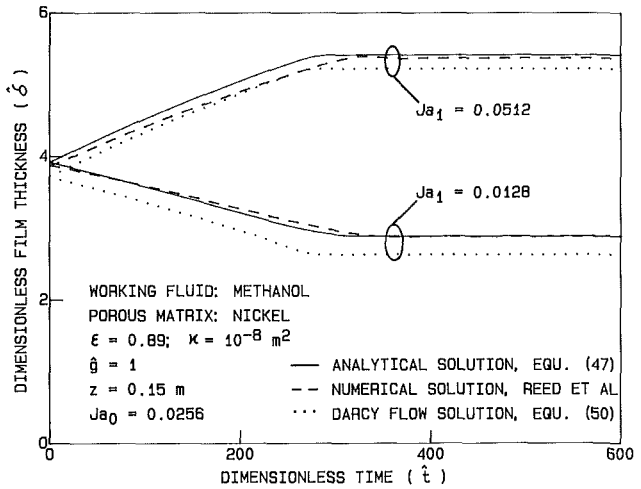

Fig. 6 Porous medium: step change of wall temperature

to make it thinner. Higher vapor shear shortens the transient. Such a situation occurs when the vapor flow rate increases suddenly in a tube-side condenser. Figure 5 shows a step change of the body force acceleration. Condensers aboard spacecraft experience this during takeoff or re-entry. An increase in body force reduces the film thickness and shortens the transient and vice versa.

Porous Medium. Typically, vapor velocities are small for film condensation in porous media. Hence, the vapor shear is negligible. The porous medium is assumed to have uniform porosity ϵ and an isotropic permeability κ. The same assumptions are made for wall temperature, pressure gradient, and body force as in the preceding section.

The exact solution to the steady momentum equation without inertia terms that satisfies the associated boundary conditions is

$$u=\frac{\kappa}{\mu}\, b_z(\rho_l-\rho_v)[1-\mathrm{sech}((\epsilon/\kappa)^{1/2}\delta)\cosh((\epsilon/\kappa)^{1/2}(\delta-y))] \tag{42}$$

which is also the first-order solution found by White and Tien (1987) employing a perturbation analysis of the complete set of steady boundary-layer equations. They also showed that to the first order the temperature profile is linear, which is used here, assuming the wall to be isothermal. In heat pipes, an important application of condensation in porous media, ΔT is desired to be small in order to achieve a small overall temperature difference between heat input and rejection. Then the film subcooling is very small and it is not necessary to consider the energy equation.

Combining equations (4) and (6) and using the specified profiles yields the governing equation

$$\hat{\delta}\frac{\partial\hat{\delta}}{\partial\hat{t}}+\hat{g}\hat{\delta}\left[1-\frac{1}{\cosh^2\hat{\delta}}\right]\frac{\partial\hat{\delta}}{\partial\hat{z}}=\mathrm{Ja} \tag{43}$$

where

$$\hat{\delta}=\delta\sqrt{\epsilon/\kappa},\quad \hat{t}=t\,\frac{k_e}{\kappa(\rho c)_l},\quad \hat{z}=z\,\frac{k_e\epsilon}{u_D\kappa(\rho c)_l},\quad \hat{g}=\frac{b_z}{g_n} \tag{44}$$

The wave speed is

$$\hat{C}=\hat{g}\left[1-\frac{1}{\cosh^2\hat{\delta}}\right] \tag{45}$$

increasing monotonically with $\hat{\delta}$.

Transients are initiated by a time-step change of body force and wall temperature leading to an initial condition that is a steady solution of equation (43),

$$\frac{1}{2}\hat{\delta}^2-\hat{\delta}\tanh\hat{\delta}+\ln(\cosh\hat{\delta})=\frac{\mathrm{Ja}_0}{\hat{g}_0}\,\hat{z}\ \text{at}\ \hat{t}=0 \tag{46}$$

satisfying $\hat{\delta}(\hat{z}=0)=0$. Equation (46) is identical with the first-order solution of White and Tien (1987) showing that it is consistent to neglect the energy equation. For $\kappa\to\infty$, $\epsilon\to1$, this result approaches asymptotically the Nusselt solution, $\hat{\delta}\sim(4\mathrm{Ja}_0\hat{z}/g_0)^{1/4}$, and for $\kappa\to0$, ϵ finite, it merges into the solution for a Darcian velocity profile, $\hat{\delta}\sim\sqrt{2\mathrm{Ja}_0\hat{z}/\hat{g}_0}$. Both limits are physically meaningful: For vanishing resistance of the porous medium the flow becomes laminar, and for very low permeability the resistance of the porous matrix dominates over the viscous effects at the wall.

The particular solution for the film thickness is the implicit relation

$$\left(\frac{1}{2}S^2-S\tanh S+\ln(\cosh S)\right)\left(1-\frac{\mathrm{Ja}_1}{\mathrm{Ja}_0}\,\frac{\hat{g}_0}{\hat{g}_1}\right)$$

$$=\frac{1}{2}\hat{\delta}^2-\hat{\delta}\tanh\hat{\delta}+\ln(\cosh\hat{\delta})-\frac{\mathrm{Ja}_1}{\hat{g}_1}\,\hat{z}\ \text{for}\ \hat{t}\le\hat{t}_{ss} \tag{47}$$

where $S^2=\hat{\delta}^2-2\mathrm{Ja}_1\hat{t}$. The streamwise gradient of the film thickness is positive and finite for all $\hat{t}$ except at $\hat{z}=0$. The time needed to achieve steady state is found from

$$\frac{1}{2}L=\sqrt{L}\tanh\sqrt{L}+\ln(\cosh\sqrt{L})=\frac{\mathrm{Ja}_1}{\hat{g}_1}\,\hat{z} \tag{48}$$

where $L=2\mathrm{Ja}_1\hat{t}_{ss}$, and the steady-state film thickness is

$$\hat{\delta}_{ss}=\sqrt{L} \tag{49}$$

The assumption of a Darcian velocity profile, $u=\hat{g}u_D$, and incorporation of the energy equation yields an explicit solution for the transient film thickness

$$\hat{\delta}=\left[2D\hat{t}\left(1-\frac{B_0\hat{g}_1}{B_1\hat{g}_0}\right)+2\,\frac{B_0\hat{z}}{\hat{g}_0}\right]^{1/2}\ \text{for}\ \hat{t}\le t_{ss} \tag{50}$$

where

$$B_0=\frac{\mathrm{Ja}_0}{1+\dfrac{1}{2}\,\mathrm{Ja}_0},\qquad D=\frac{\mathrm{Ja}_1}{\left(1+\dfrac{\sigma}{2\epsilon}\,\mathrm{Ja}_1\right)} \tag{51}$$

In this case the steady-state film thickness and the transient duration are

$$\hat{\delta}_{ss}=\left(\frac{2B_1\hat{z}}{\hat{g}_1}\right)^{1/2},\qquad \hat{t}_{ss}=\frac{B_1\hat{z}}{\hat{g}_1 D} \tag{52}$$

For Darcy flow, the wave speed, $\hat{C}=\hat{g}_1 D/B_1$, is independent of $\hat{\delta}$, which leads to the linear relation for $\hat{t}_{ss}$ in equation (52).

Figure 6 shows a comparison between these relations and the numerical result obtained by a modification of the algorithm of Reed et al. (1987). This case concerns unsteady condensation after a step change of the wall temperature. Such a transient typically occurs in the condenser sections of heat pipes due to an abrupt change of cooling conditions. The porous matrix is made of nickel and the working fluid is methanol, representing a typical heat-pipe combination. For $\epsilon=0.89$, σ/ϵ becomes 1.24, which is close to unity. With values of $i_{fg}=1.10\times 10^6$ J/kg and $c_l=2814$ J/kgK, a typical temperature difference of $\Delta T=10$ K yields $\mathrm{Ja}=0.0256$. The agreement between the analytical solution for the no-slip velocity profile and the numerical result is seen to be very good. The Darcy-flow solution consistently underpredicts the film thickness because it does not account for the velocity defect near the wall. This analysis clearly demonstrates that it is more important to employ the correct velocity profile than to consider the subcooling of the film, except for the case of very small permeabilities. However, the Darcy-flow solution has the advantage of being explicit.

Concluding Remarks

This analysis reveals that the propagation of a kinematic wave along the film governs general film condensation transients. To predict the film thickness, the details of the film dynamics are not important. It is merely necessary to satisfy the continuity requirement and the interface balance. An elementary method permits simple solutions for arbitrary time-step changes. The analytical results derived for specific cases agree very well with the numerical solutions of the complete boundary-layer equations. Breaking of the wave cannot occur in these cases. The comparison of the duration of the transient derived in this study with the time constant of a conduction transient through the wall permits an assessment of the relative importance of the film condensation and the conduction transient.

The technique presented here allows the accurate determination of the heat flux during transients and the time required to achieve steady state. The approximate solutions are particularly suitable for incorporation into design and simulation computer codes. The method can be extended to turbulent film flow since the integral mass and energy balances hold irrespective of the flow regime when the expression for the wall heat flux is consistent with the employed turbulence model. However, the time constant of the film growth must be several orders larger than the time scale of the turbulent fluctuations to ensure proper time-averaging. Furthermore, this technique has applications to problems with more complicated geometries and to film boiling and forced-convection vaporization transients.

Acknowledgments

The authors wish to thank Ms. J. M. Usher and Mr. F. M. Gerner for providing the numerical solutions.

References

Blangetti, F., and Naushahi, M. K., 1980, "Influence of Mass Transfer on the Momentum Transfer in Condensation and Evaporation Phenomena," *International Journal of Heat and Mass Transfer*, Vol. 23, pp. 1694–1695.

Catton, I., 1985, "Natural Convection Heat Transfer in Porous Media," *Natural Convection*, S. Kakac, W. Aung, and R. Viskanta, eds., Hemisphere Publishing Corporation, Washington, DC, pp. 514–547.

Cheng, P., and Chui, D. K., 1984, "Transient Film Condensation on a Vertical Surface in a Porous Medium," *International Journal of Heat and Mass Transfer*, Vol. 27, pp. 795–798.

Chung, P. M., 1963, "Unsteady Laminar Film Condensation on a Vertical Plate," ASME Journal of Heat Transfer, Vol. 85, pp. 63–70.

Hildebrand, F. B., 1949, *Advanced Calculus for Engineers*, Prentice-Hall, Inc., New York, pp. 368–378.

John, F., 1982, *Partial Differential Equations*, Springer-Verlag, New York, pp. 9–18.

Reed, J. G., Gerner, F. M., and Tien, C. L., 1987, "Transient Condensation of a Laminar Film Onto a Vertical Plate," Paper No. 87-1534, AIAA 22nd Thermophysics Conference, Honolulu, HI, June 8–10. Also *Journal of Thermophysics and Heat Transfer*, Vol. 2, pp. 257–263.

Rohsenow, W. M., Webber, J. H., and Ling, A. T., 1956, "Effect of Vapor Velocity on Laminar and Turbulent-Film Condensation," *Transactions ASME*, Vol. 78, pp. 1637–1643.

Sparrow, E. M., and Siegel, R., 1959, "Transient Film Condensation," ASME *Journal of Applied Mechanics*, Vol. 81, No. 1, pp. 120–121.

Wallis, G. B., 1969, *One-Dimensional Two-Phase Flow*, McGraw-Hill, New York, pp. 122–132.

White, S. M., and Tien, C. L., 1987, "Analysis of Laminar Film Condensation in a Porous Medium," *Proceedings, ASME-JSME Thermal Engineering Joint Conference*, P. J. Marto and I. Tanasawa, eds., Vol. 2, pp. 401–406.

Whitham, G. B., 1974, *Linear and Nonlinear Waves*, Wiley, New York, Chap. 2.

Wilson, S. D. R., 1976, "Unsteady and Two-Dimensional Flow of a Condensate Film," ASME Journal of Heat Transfer, Vol. 98, pp. 313–315.

Horizontal-Tube Falling-Film Evaporation With Structured Surfaces

M.-C. Chyu
Assistant Professor,
Department of Mechanical Engineering,
Texas Tech University,
Lubbock, TX 79409-4289
Assoc. Mem. ASME

A. E. Bergles
Professor,
Department of Mechanical Engineering,
Aeronautical Engineering, and Mechanics,
Rensselaer Polytechnic Institute,
Troy, NY 12180-3590
Fellow ASME

Extensive experimental tests for tubes with commercial structured surfaces in a horizontal single-tube falling-film evaporator were conducted. The test sections were hollow copper cylinders with GEWA-T, Thermoexcel-E, or High Flux surfaces electrically heated by inserted cartridge heaters. A smooth surface cylinder was also tested for reference. All tubes were tested in both pool boiling and falling-film evaporation with water. The results reveal that falling-film evaporation provides much higher heat transfer coefficients than pool boiling in the low heat flux, convective region. The GEWA-T surface enhances heat transfer through its increased and accessible area, while Thermoexcel-E and High Flux demonstrate high heat transfer performances because of enhanced nucleate boiling. The falling-film evaporation data for the structured surfaces either merge or show a tendency to merge with the respective pool boiling curves at high heat fluxes. Unusual incipient boiling behavior of Thermoexcel-E and the effects of factors such as surface aging, surface subcooling, film flow rate, liquid feed height, and rate of heat flux change, are described.

1 Introduction

As is the case with other industrial heat exchangers, a strong incentive exists to improve horizontal-tube falling-film (also called spray-film) evaporators. The objective may be to increase the evaporative capacity or to reduce the required overall temperature driving force by retubing a given heat exchanger. For a new heat exchanger, the size can be reduced for a specified evaporative capacity. When the falling film is heated by condensing steam, the heat transfer rate is controlled by the heat transfer coefficient on the evaporating side. Enhancement of heat transfer on the evaporating side thus increases the overall heat transfer coefficient and makes it possible to achieve the objectives.

Several special heat transfer surfaces have been used in horizontal spray-film evaporators. Grooved (e.g., Schultz et al., 1977) and knurled surfaces (e.g., Fletcher et al., 1975), featuring relatively large-scale surface structures, provide heat transfer coefficients as much as 2.5 times the plain surface values based on a fixed heat flux. The other surface type tested for horizontal tube evaporators is the porous surface, which promotes nucleate boiling by providing small-scale structures to facilitate the generation of vapor (e.g., Hillis et al., 1979; Sabin and Poppendiek, 1978). Heat transfer coefficients up to three times those of a smooth tube have been reported. A comprehensive literature survey can be found in the reference by Chyu (1984).

The present study emphasizes the application of enhanced pool boiling surfaces to horizontal-tube falling-film evaporators. A variety of special surface geometries to promote nucleate boiling have been developed based on the understanding of the character of nucleation sites, the conditions promoting the formation of stable vapor traps, and the mechanism of thin film evaporation in porous structures (Webb, 1981). Three such surface geometries have been selected for this study based on their potential to enhance falling-film evaporators.

The GEWA-T surface of Wieland-Werke AG, F. R. Germany, has circumferential re-entrant grooves that are formed by properly flattening the tips of spiral fins of an integral-fin tube to restrict the mouth of the space between two neighboring fins. Single-tube (e.g., Yilmaz and Westwater, 1981; Marto et al., 1985) and tube-bundle (e.g., Stephan and Mitrovic, 1981) pool boiling tests in different liquids have been conducted. Heat transfer coefficients were about three times those of smooth tubes. A limited number of failing-film evaporation data with a horizontal tube were reported by Chyu et al. (1982). Falling-film evaporation on the outside of a vertical tube was studied by Fagerholm et al. (1985). A heat transfer coefficient ten times that of the smooth tube was possible.

The Thermoexcel-E surface of Hitachi Wire and Cable, Ltd., Japan, has minute, parallel tunnels running underneath with very small, regularly spaced holes on the surface. Pool boiling tests have been conducted for a variety of liquids with a single tube (Yilmaz and Westwater, 1981) and with a tube bundle (Arai et al., 1977). Heat transfer coefficients five to ten times those of the plain tube were reported. Falling-film evaporation of R-11 was tested on a vertical, flat Thermoexcel-E surface (Nakayama, 1982). Heat transfer coefficients up to twelve times those of the smooth tube were reported in a test of falling-film evaporation on a vertical tube (Fagerholm et al., 1985).

Nucleate boiling enhancement can also be achieved by the use of porous metal coatings, notably the High Flux surface manufactured by the Linde Division of Union Carbide Corporation. The coating is composed of metal particles that are bonded to each other and to the substrate by brazing or sintering. The heat transfer characteristics of this surface have been considered in several studies (e.g., Yilmaz and Westwater, 1981; Nakayama et al., 1980, 1982; Bergles and Chyu, 1982). Typically, the flooded heat transfer coefficients are about ten times those of the plain surface. Coefficients five times larger were observed with a horizontal-tube falling-film evaporator (Chyu et al., 1982). The coated surface provided heat transfer coefficients eight times greater in a vertical-tube falling-film evaporation test (Fagerholm et al., 1985).

Although these structured surfaces have demonstrated remarkable enhancement in pool boiling, only the High Flux surface has actually been tested in a horizontal tube falling-film evaporator. Yet, some variables that are known to be influential in falling-film evaporation on a plain surface, such

Contributed by the Heat Transfer Division and presented at the 23rd National Heat Transfer Conference, Denver, Colorado, August 1985. Manuscript received by the Heat Transfer Division August 19, 1986. Keywords: Augmentation and Enhancement, Evaporation, Natural Convection.

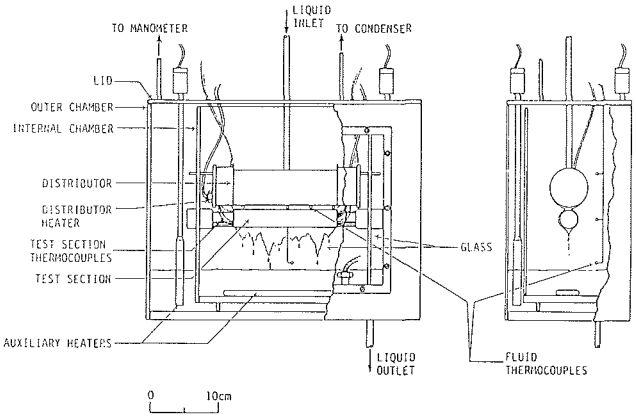

Fig. 1 Test chamber for falling-film evaporation and pool boiling tests (falling-film mode shown)

as flow rate and liquid feed height, have never been thoroughly investigated for this surface. In general, there is a need to explore the heat transfer characteristics of these structured surfaces for falling-film evaporator service and to compare these data with pool boiling data. Water was selected as the working liquid for the present tests because of the need for such data in desalination. A study of falling-film evaporation on a smooth surface cylinder was reported in a companion paper (Chyu and Bergles, 1987).

2 Experimental Facility and Procedure

Falling-film evaporation of water on a horizontal cylinder at atmospheric pressure was studied. Experiments using electrically heated test sections with smooth, GEWA-T, Thermoexcel-E, or High Flux surfaces were conducted to investigate the effects of liquid supply mode, surface structure, surface aging, surface subcooling, heat flux, film flow rate, liquid feed height, and rate of heat flux change. The test circuit included a circulation pump, a filter, a rotameter, flow adjusting valves, and a test chamber. This facility was designed to perform either falling-film evaporation or flooded boiling experiments. As shown in Fig. 1, an inner chamber holding the liquid distributor, the test section, and the auxiliary heaters was placed inside a large chamber. The double-chamber configuration was important in maintaining a saturated condition in the inner space without using heavy insulation that would have hindered visual observations. It also isolated the test section from the rather strong circulation induced by auxiliary heaters in the pool boiling tests. The pool in the inner chamber was maintained within 0.1 K of the saturation temperature. In the falling-film evaporation tests, the same subcooling limit was maintained in the vapor space. The system pressure was atmospheric for all tests, with a typical value of 0.99 bar.

The falling liquid film was formed by distributing saturated (less than 0.1 K subcooling) water in unsteady columns or drips to the horizontal test cylinder at random points along the apex line. This simulated the situation in a real falling-film evaporator where a lower tube receives runoff in a random pattern from the tube above. The detailed configuration of the distributor is given by Chyu (1984). The liquid feed height was adjusted by moving the distributor up and down along slots on the side walls of the inner chamber. The feed flow rate was measured by the rotameter in the circuit. It was observed in the present setup that liquid fed in a sheet when the gap between the distributor and the test cylinder was smaller than 3 mm.

The experimental apparatus was arranged so that the falling-film evaporation test and the pool boiling test could be conducted with one immediately following the other. For example, the system could be switched to the pool boiling mode from the falling-film evaporation mode by closing the outlet of the test chamber to raise the pool level in the chamber above the test cylinder and shutting off the feed distribution. The distributor was then elevated to avoid any interference with the boiling test cylinder.

The test cylinders were of copper, nominally 25.4 mm in diameter and 152 or 110 mm in length. A central 12.7-mm-diameter hole was provided for a cartridge heater. Six thermocouple wells of 1 mm diameter, 40 to 50 mm in depth, were drilled 60 deg apart at each end, with outer edges approximately 1.5 mm from the outer base surface. Because such a small hole that deep may not be straight, a novel method (Chyu, 1984) was developed to locate precisely the position of the thermocouple junction. This information was needed to estimate the temperature drop between the thermocouple junction and the base surface of the cylinder accurately. The cartridge heaters were soldered into the cylinders to eliminate contact resistance. Both ends of the test cylinders were insulated with silicone seal after the thermocouple installation.

The average heat flux was calculated using the base area of the structured surface and the average power over the active length of the cartridge heater. This was justified by a conduction analysis showing that, at a considerable axial distance away from the inactive zone of the cartridge heater, the heat flux in the test cylinder is essentially the average value based on the active length of the heater (Chyu and Bergles, 1988). The wall temperature was taken as the mean of the twelve wall temperatures inferred from thermocouple readings. In fact, both the experimental data and analysis showed that the test cylinders were essentially isothermal at the outer surface because of the thick wall. This closely simulates the situation in a real falling-film evaporator heated by condensing steam.

The five test sections are described as follows:

1	smooth surface, machined microroughness
GEWA-T19C	Wieland-Werke GEWA-T deformed low fin surface, 19 fins/in (748 fins/m), 0.125 mm gap width
GEWA-T26B	same as above except 26 fins/in (10.2 fins/cm), 0.15 mm gap width
TE	Hitachi Thermoexcel-E tunnel-pore surface, 0.12 mm pore diameter
HF	Union Carbide Linde High Flux metallic porous matrix surface, 0.38 mm matrix thick; about 45 percent of the copper particles constituting the matrix ranged from 200 mesh (74 μm) to 325 mesh (44 μm), with the remainder being finer

Nomenclature

D = diameter of test cylinder, diameter of the base circumference in case of structured surface
H = liquid feed height
$\bar{h}$ = average heat transfer coefficient = $\overline{q''}/\overline{\Delta T}$
k = thermal conductivity
$\overline{q''}$ = average surface heat flux, based on base area in case of structured surface
Re = film Reynolds number = $4\Gamma/\mu$
$\overline{\Delta T}$ = average wall superheat = $\overline{T_w} - T_{sat}$
T_{sat} = saturation temperature
$\overline{T_w}$ = average wall temperature
Γ = mass flow rate of film per unit length on one side of tube
μ = dynamic viscosity

All the surface treatments were provided directly by the manufacturers. The GEWA-T and TE were considered to be suitable for boiling water while the HF was suggested for boiling of refrigerants.

The experimental tests are coded for convenience as follows: Mode of flow—Test section—Surface aging—Surface subcooling—Heat flux—Film flow rate—Ratio of liquid feed height to tube diameter—Qualitative rate of heat flux change—Direction of heat flux change. The heat flux, film flow rate, and ratio of feed height to tube diameter do not apply to the pool boiling test curves.

The codes used for the above terms are defined as follows:

Mode of flow	FFE = falling film evaporation PB = pool boiling
Test section	As listed above
Surface aging	D = Surface first heated in air before the test in order to evaporate the liquid likely to be entrapped in the surface structure. B = Surface given a high heat flux (about 90,000 W/m^2) so as to trigger fully established nucleate boiling in saturated liquid for more than 30 min before the run.
Surface subcooling	The temperature difference between saturation and the temperature to which the surface was cooled before the run after predrying or preboiling, K.
Heat flux, $\overline{q''}$	Heat transfer rate per unit area (base or nominal area in case of the structured surfaces), W/m^2.
Film flow rate, Γ	Supply film flow rate per unit length on one side of tube, kg/s-m.
Ratio of liquid feed height to tube diameter, H/D	Parameter involving cylinder diameter and the distance between the liquid distributor and the top of the test cylinder, dimensionless
Qualitative rate of heat flux change	C = Power changed continuously and slowly (about 4000 W/m^2-min) to a new operation condition S = Power changed stepwise, from hundreds to thousands of W/m^2 per step
Direction of changing heat flux	INC = increasing heat flux. DEC = decreasing heat flux.

A "V" (variable) is used to code one of the quantitative variables, $\overline{q''}$, Γ, or H/D, when it is taken as the independent variable in the test run. All the surfaces were cleaned with acetone before each test. The working fluid was degassed for at least two hours before each test.

The estimated uncertainties for the data presented are as follows: ± 220 W/m^2 in heat flux, ± 0.06 K in wall superheat and surface subcooling, ± 0.004 kg/s-m in film flow rate, and ± 0.1 in ratio of feed height to diameter.

Complete details of the experimental work can be found in the work by Chyu (1984).

3 Results and Discussion

The heat transfer performances of various surfaces in the falling-film and pool boiling modes are compared in Figs. 2–5. The advantage of the falling-film evaporation at low temperature difference is quite evident; this is the result of a higher convective heat transfer coefficient in the falling-film mode. However, the advantage diminishes at high heat flux (or large superheat) when nucleate boiling is established in pool boiling.

In the present test range, the falling-film data for the plain test cylinder exhibited in Fig. 2 show no significant change in the slope of the curve that would indicate prevalent or fully established nucleate boiling. Fully established nucleate boiling is expected at a higher heat flux level; however, this would exceed the likely operating heat flux range in an actual falling-film evaporator. The data in Fig. 2 suggest that the FFE fully established nucleate boiling curve would lie to the right of the fully established pool boiling curve. Figure 2 also shows data for the plain test cylinder before and after polishing with aluminum oxide abrasive cloths (Nos. 240 and 600). After this cleaning procedure, the falling-film evaporation data followed the same curve as that before cleaning because convection was the dominant mode and the heat transfer was not influenced by the slight change of surface roughness. On the other hand, the pool boiling heat transfer coefficient showed a 20 percent improvement (evaluated at constant $\overline{q''}$) after cleaning because of the exposure of fresh nucleation sites.

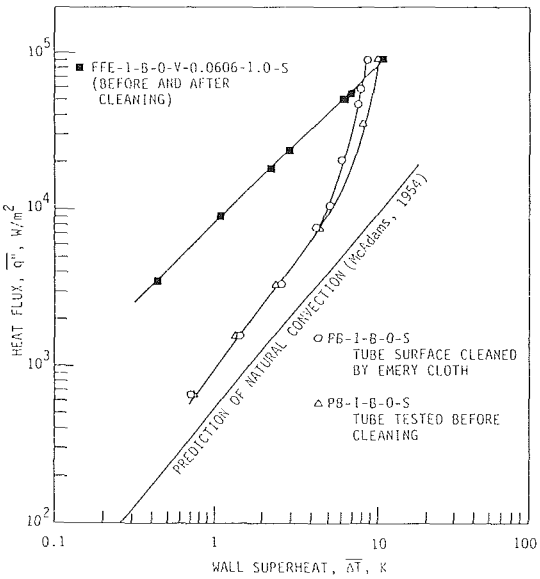

Fig. 2 Comparison of typical falling film evaporation and pool boiling data for the plain tube

Even though significant nucleate boiling in a falling liquid film was observed on a vertical wall (Kim et al., 1983), it was not observed on a horizontal cylinder in the present test. This is because nucleate boiling is more difficult to achieve on a horizontal tube than on a vertical plate or tube. Nucleate boiling will not occur before the film flow is heated to a substantial superheat after passing through a certain length of preheating zone. The maximum available preheating length on a horizontal tube is only half of the circumference, which is much shorter than the length of the vertical plate employed in the tests reported by Kim et al. As a result, it takes a higher heat flux to initiate nucleate boiling on the horizontal tube than on the vertical wall.

The falling-film evaporation and pool boiling data of the GEWA-T surface are compared in Fig. 3. The pool boiling data compared were taken by Ayub (1986) using exactly the same test section employed in the present study. The two curves in Fig. 3 are comparable even though the surface aging procedures, degrees of surface subcooling, and heat flux change rates are different, because these factors were found to be not important to the GEWA-T surface. This is based on tests run with variation of these factors using GEWA-T in the present study. The falling-film evaporation data demonstrate remarkably better heat transfer performance than pool boiling in the low superheat range. There seems to be a tendency of the falling-film evaporation and the pool boiling curves to merge at high heat flux.

A merging tendency similar to that of GEWA-T surface is also demonstrated by the FFE and PB data for the Ther-

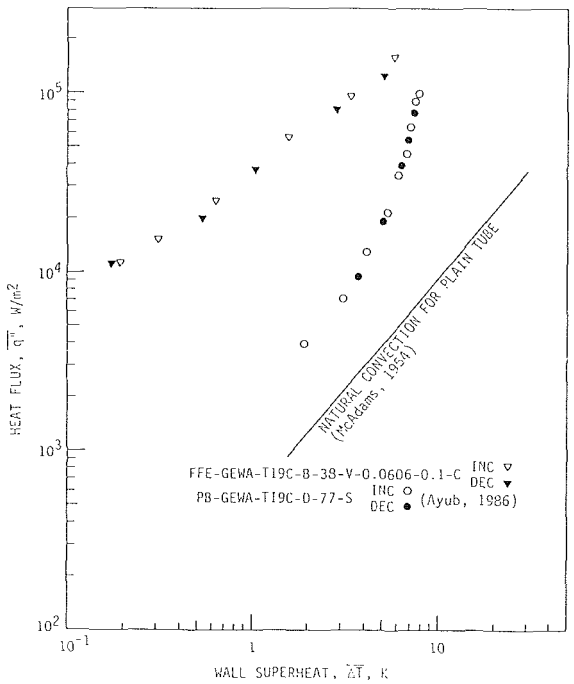

Fig. 3 Comparison of falling-film evaporation and pool boiling data for the GEWA-T tube

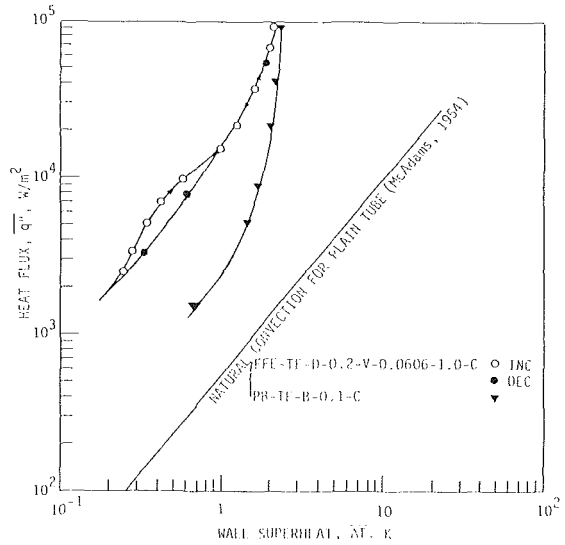

Fig. 4 Comparison of the falling film evaporation and pool boiling data for the Thermoexcel-E surface

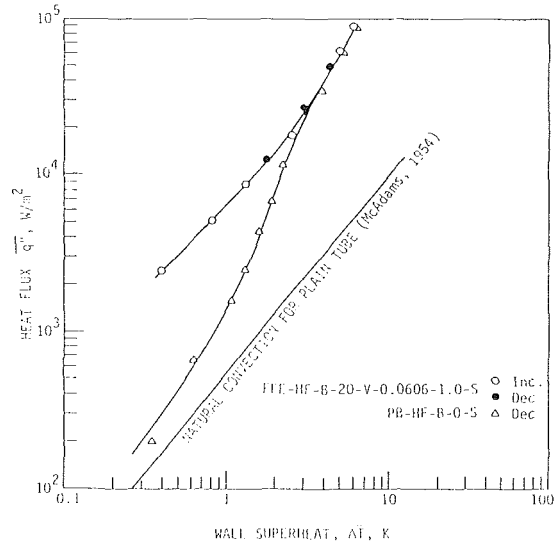

Fig. 5 Comparison of the falling-film evaporation and the pool boiling performances of the High Flux surface

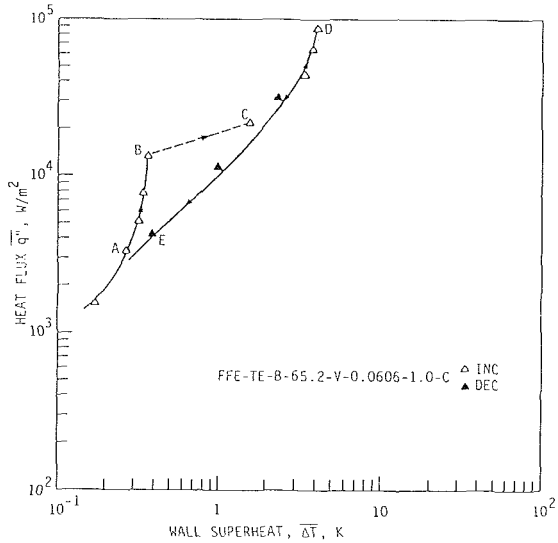

Fig. 6 $\overline{q''}$ versus $\overline{\Delta T}$ curve for the FFE-TE-B test

moexcel-E and High Flux surfaces, respectively. The data exhibited in Fig. 4 were obtained by first conducting an FFE test (FFE-TE-D-0.2-V-0.0606-1.0-C), including increasing and decreasing power, then raising the power to the limit immediately following the FFE test, shifting to the PB mode, and taking data as the power decreased. Hence the PB curve obtained (PB-TE-B-0.1-C) is characterized by a B surface aging treatment because the surface was preboiled in the preceding FFE test. The PB curve is also characterized by a 0.1 K surface subcooling because it is the maximum surface subcooling the surface experienced during the transition from falling-film evaporation to pool boiling. The FFE and PB data in Fig. 4 are basically based on the same number of nucleation sites on the surface because all active nucleation sites were preserved during the transition. The closeness of FFE and PB data at high heat flux levels suggests that there is the same mechanism of nucleate boiling heat transfer in both falling-film evaporation and pool boiling. In the lower heat flux range where convection is relatively more important, the FFE data demonstrate better heat transfer coefficients than the PB data. In fact, the PB curve preceded by a FFE test in Fig. 4 is very close to that obtained during decreasing power in a pool boiling test. Data of a similar test with the High Flux surface are exhibited in Fig. 5. The FFE and PB curves are shown to merge at a relatively low heat flux level. Merging of FFE and PB data with a Thermoexcel-E surface was also observed by Nakayama et al. (1982).

The falling-film evaporation data of Thermoexcel-E in Fig. 4 exhibit a difference between the power-increasing and the power-decreasing curves. This phenomenon was also observed in the test shown in Fig. 6. In this test, the inception of nucleate boiling was first observed at a superheat of about 0.27 K (point A). Numerous tiny bubbles were generated at high frequency from the surface. The data follow a steep curve to point B, where the heat transfer coefficient reaches an unusually high value of 3.69×10^4 W/m^2-K. Nucleate boiling then diminished before point C was reached. At this point, hardly any bubbles

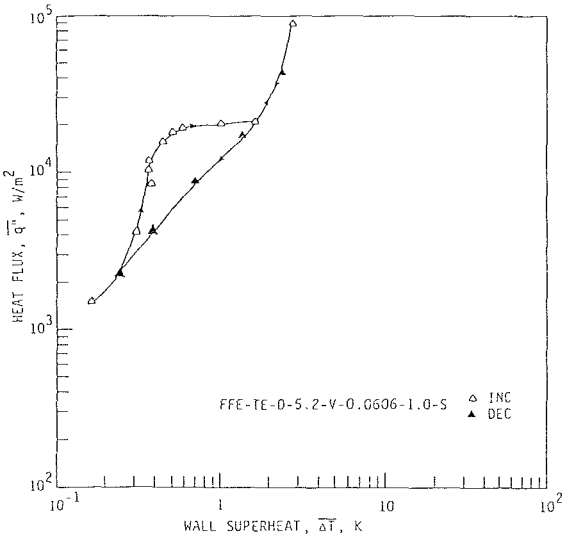

Fig. 7 $\overline{q''}$ versus $\overline{\Delta T}$ curve for the FFE-TE-B test

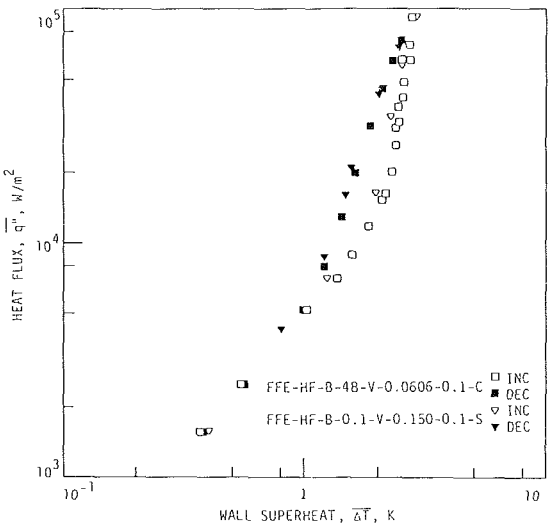

Fig. 8 $\overline{q''}$ versus $\overline{\Delta T}$ curves of FFE-HF-B tests

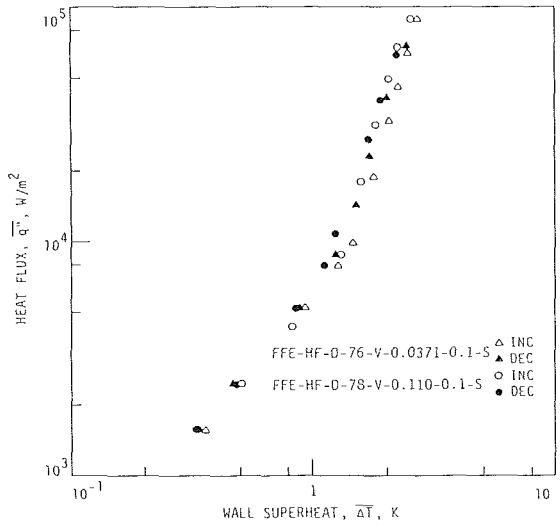

Fig. 9 $\overline{q''}$ versus $\overline{\Delta T}$ curves of FFE-HF-D tests

were observed and the liquid film appeared smooth. The heat flux was increased slowly and continuously from B to C; however, no data were recorded between the two points. Bubbling did not resume until about $\overline{q''} = 5 \times 10^4$ W/m^2. Bubbles generated this time were significantly larger in size and lower in frequency than before. After reaching the power limit at power D, power was reduced, and the data followed a different curve representing a lower heat transfer coefficient down to point E. The curve DE could be repeated to within ± 0.01 K by subsequent increase or decrease of power. The transition from the first-stage boiling to the normal boiling was more carefully traced in another test, the results of which are shown in Fig. 7.

The first-stage nucleate boiling was also evident in the pool boiling tests with the Thermoexcel-E surface (Chyu, 1984). However, this phenomenon was not observed in the pool boiling test in Fig. 4 because, in that test, pool boiling data were taken during decreasing power following the FFE test, and the normal mode of nucleate boiling had been established during the preceding falling-film evaporation tests. Hence, first-stage nucleate boiling was observed only during the increase of power in the FFE test, not in the PB test.

It is believed that the first-stage nucleate boiling is initiated from nucleation sites within the channels. The bubbles formed in the channels provide the observed vapor phase passing through selected pores. As the heat flux increases and the void fraction becomes so high that a vapor core is surrounded by a liquid film on the inside wall of the channel, the heat transfer mechanism changes, eventually reverting to a dynamic cycle involving bubble ejection through some pores and suction of liquid into the tunnels through the others (Nakayama et al., 1980).

Falling film evaporation on the High Flux porous surface features generation of numerous tiny bubbles at high frequency from the many vapor generation pores provided by the structure. The bubbles were observed moving down around the tube with the film flow. The liquid film was smooth in appearance because the small bubbles did not significantly disturb the film flow. The data of the High Flux surface exhibited boiling curve hysteresis if the surface was preboiled and followed by a substantial subcooling before the test, as shown in Fig. 8. This pretest procedure consumes the air content in the surface cavities during preboiling, and the vapor phase in the cavities is condensed during the following surface subcooling. Hence, fewer active nucleation sites are available when the test is started by increasing the heat flux. Since potential nucleation sites can be reactivated as power is increased, there is more nucleate boiling for a particular heat flux level during decreasing heat flux than increasing heat flux. Therefore, the decreasing curve falls to the left of the increasing curve.

Hysteresis was not observed if the High Flux surface was treated with the D-aging procedure. In the D-aging procedure, the surface is heated in the air to evaporate liquid likely to be entrapped in the surface structure, so that the potential nucleation sites are filled with air. Therefore, all the nucleation sites are active from the beginning of the test, and there is no significant difference between the curves of increasing and decreasing heat flux, as shown by the data in Fig. 9.

The above behavior of a High Flux surface under the influence of surface aging and surface subcooling is similar to that observed in pool boiling tests (Bergles and Chyu, 1982), and falling-film evaporation on a vertical tube (Fagerholm et al., 1985). This behavior is observed with a High Flux surface only. Surface aging and subcooling do not have any noteworthy influence on the other surfaces tested in this study.

The GEWA-T surface exhibited falling-film evaporation curves without significant slope changes or "knees," with a typical result shown in Fig. 3. This suggests that boiling was never a dominant mode of heat transfer in the heat flux range tested, even though bubbles were observed at high heat flux

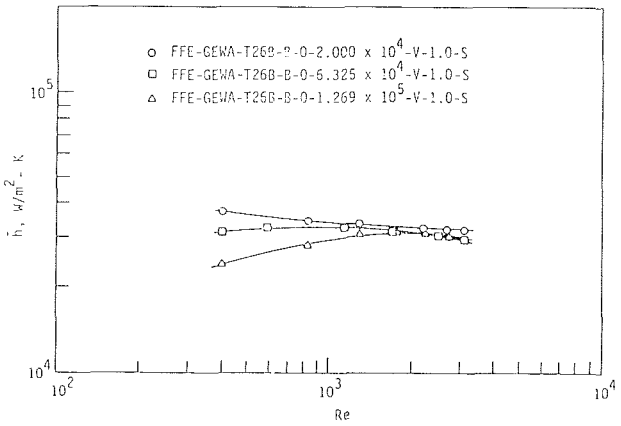

Fig. 10 Effect of film Reynolds number of the falling film evaporation heat transfer coefficient of the GEWA-T26B surface

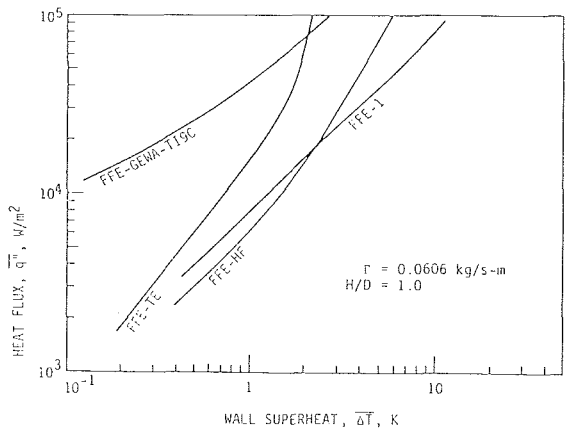

Fig. 11 Comparison of falling-film evaporation characteristics of different surfaces

levels. However, the convective heat transfer performance of this surface is much better than that of the other surfaces. This is due to the increased surface area provided by the T-shaped fins. The contribution of increased surface area is confirmed by a comparison between the FFE data in Figs. 2 and 3, which show an enhancement of GEWA-T surface about three times as high as the plain surface. This agrees approximately with the increase in the total area of GEWA-T surface, which is 0.21 m^2/m, compared with 0.0798 m^2/m for the plain tube.

It was visually observed that the circumferential grooves in the GEWA-T surface were readily flooded by the liquid. Even the small gap width of 0.15 mm (GEWA-T26B), the minimum size provided by the manufacturer, was not able to prevent water from flooding the channels. At low flow rates,the channels carried the flow and the tips of the deformed fins appeared dry. At higher heat flux levels, bubbles generated inside the channels could be seen at the bottom of the tube where flow emerged from the channels. At even higher flux levels, liquid splashed out of the openings as a result of bubbles bursting inside the channels. At higher flow rates, the fin tips were wetted; however, they dried out at high heat fluxes. The bubbles tended to remain in the channels and flowed down to the bottom of the tube. This bubble behavior is similar to that observed by Stephan and Mitrovic (1981) in flooded boiling with GEWA-T tubes, except that the direction of the channel flow is reversed. Test results (Chyu 1984) show no significant difference between the performances of GEWA-T19C and GEWA-T26B, despite the difference in the dimensions. This in fact supports the previous observation that the advantage with GEWA-T is mainly due to increased surface area. Because the total areas of the two GEWA-T surfaces are close (0.21 m^2/m for 19C and 0.27 m^2/m for 26B), their heat transfer performances are also close.

The effect of film flow rate on the falling-film evaporation coefficient of the GEWA-T surface is demonstrated in Fig. 10 by three h versus Re curves with constant heat fluxes. At the lowest heat flux (2.000×10^4 W/m^2), h decreases slightly with Re because the thickness of the film covering the surface increases with flow rate. However, contrary behavior is exhibited by the data at a higher heat flux (1.269×10^5 W/m^2), which shows h increasing with Re. At low flow rates, the heat transfer coefficient decreases as the heat flux increases. This is probably because evaporation partially dries out the surface. Such dryout would first occur at the exterior surface, or the tip of the T-fin. At high Re, there is sufficient liquid and no dryout occurs, thus all data converge to the same value of h despite the differences in q''.

Heat transfer coefficients with the Thermoexcel-E and High Flux surfaces are independent of the film flow rate in most of the range tested, except at very low heat flux levels. This was demonstrated by the invariable average wall temperatures measured when the film flow rate was changed at constant power to the test section in the present experiment. The insignificant effect of film flow rate is because boiling is the predominant mode of heat transfer on Thermoexcel-E or High Flux surface, and the overall heat transfer is not greatly affected by the change of film flow rate, which has a relatively weak influence on nucleate boiling.

The heat transfer coefficient was found to increase with liquid feed height with a plain tube (Chyu and Bergles, 1987), even though the increase is small and disappears as boiling becomes important. In the present study, the heat transfer coefficients of Thermoexcel-E and High Flux are found to be basically independent of changes in feed height, especially at high heat fluxes when nucleate boiling prevails. This was shown by the invariable average wall temperatures measured while moving the liquid distributor up and down at constant heat flux levels during the experiment. Apparently, when nucleate boiling prevails on these enhanced surfaces, the overall heat transfer is not influenced by the change of liquid feed height which has a relatively weak effect on the nucleate boiling. The effect of feed height is also insignificant with the GEWA-T surface in the present test range. This is probably because the channel flow is sheltered by the restricted geometry from the already weak influence of feed flow. Specifically, the impact of liquid feed would have little influence on the channel flow between fins if it impinges on the tops of the T-shaped fins.

The rate of heat flux change has been shown to influence the pool boiling heat transfer from a High Flux surface by motivating the metastable bubbles whose growth is limited by the cooler liquid surrounding the heating surface (Bergles and Chyu, 1982). The consequence is that the inception of boiling occurs at a lower superheat if the heat flux is changed stepwise. In the present tests, however, the rate of heat flux change has little effect on falling-film evaporation on the High Flux surface. There is also no noteworthy influence of heat flux change on the Thermoexcel-E and GEWA-T surfaces.

The heat transfer performances of all the surfaces tested are compared in Fig. 11. Among numerous test curves obtained in this study, only the curves with $\Gamma = 0.0606$ kg/s-m and $H/D = 1.0$ for different surfaces are exhibited. The start-up curves for Thermoexcel-E and High Flux surfaces are not shown in this figure. All the structured surfaces show substantial enhancement in heat transfer over the plain surface. The GEWA-T has the greatest advantage at low superheat where an enhancement of about eight times that of a plain tube based on a fixed heat flux is achieved. Thermoexcel-E provides highest heat transfer rate at high superheat, with an enhancement as high as five times, because of enhanced nucleate boiling provided by the surface structure. The High Flux surface dem-

onstrates moderate enhancement in the high heat flux range. However, it is noted that the present High Flux surface is sized for boiling refrigerant, while the GEWA-T and Thermoexcel-E surfaces tested were recommended for water service. The High Flux surface may demonstrate better heat transfer performance than the present water test result when boiling refrigerant. This may also be the reason fouling was observed on the High Flux surface in the present tests. The difference between the present results and those of Fagerholm et al. (1985) could be due to different working fluids and tube orientations.

4 Summary and Recommendations

The present tests of three commercial structured surfaces and a smooth surface show that falling-film evaporation provides much higher heat transfer coefficients than pool boiling in the low-heat-flux, convective region. The falling-film evaporation data for the structured surfaces either merge or show a tendency to merge with the respective pool boiling curves at high heat fluxes. High Flux and Thermoexcel-E surfaces are characterized by incipient boiling at low superheats and high boiling coefficients. The first-stage nucleate boiling on the Thermoexcel-E surface before normal boiling was observed for the first time in the present study. The GEWA-T surface primarily enhances the convective heat transfer through increased surface area; it yields the highest coefficient in the low superheat region. Surface aging and surface subcooling have influences only on boiling curve hysteresis for the High Flux porous surface. Film flow rate and liquid feed height have small influences on Thermoexcel-E and High Flux only in a nonboiling convection regime; the effects vanish when boiling is predominant. The GEWA-T surface demonstrates a heat transfer performance influenced by the film flow rate. The influence varies with the heat flux level.

For subsequent investigation, it is recommended that tests be conducted with other fluids of interest to the power and process industries, particularly those with high wettability. More data are needed at higher power levels. Other types of structured surfaces should be tested taking into account the variables shown to be important in the present study.

Acknowledgments

This study was carried out in the Heat Transfer Laboratory at Iowa State University and supported in part by the U.S. Department of Energy under Contract No. DC-AC22-78ET13127 and Grant No. DE-FG07-811D12222. Test sections and technical assistance were provided by Mr. C. F. Gottzmann and Mr. P. S. O'Neill of the Linde Division of Union Carbide Corporation, Mr. K. Menze of Wieland-Werke AG, and Dr. W. Nakayama of Hitachi, Ltd.

References

Arai, N., Fukushima, T., Arai, A., Nakajima, T., Fujie, K., and Nakayama, W., 1977, "Heat Transfer Tubes Enhancing Boiling and Condensation in Heat Exchangers of a Refrigerating Machine," *ASHRAE Transactions*, Vol. 83, Pt. 2, pp. 58–69.

Ayub, Z. H., 1986, "Pool Boiling From GEWA Surfaces in Water and R-113," Ph.D. Dissertation, Iowa State University, Ames, IA.

Bergles, A. E., and Chyu, M.-C., 1982, "Characteristics of Nucleate Pool Boiling From Porous Metallic Coatings," ASME JOURNAL OF HEAT TRANSFER, Vol. 104, pp. 279–285.

Chyu, M.-C., 1979, "Boiling Heat Transfer From a Structured Surface," M.S. Thesis, Iowa State University, Ames, IA.

Chyu, M.-C., 1984, "Falling Film Evaporation on Horizontal Tubes With Smooth and Structured Surfaces," Ph.D. Dissertation, Iowa State University, Ames, IA.

Chyu, M.-C., and Bergles, A. E., 1987, "An Analytical and Experimental Study of Falling-Film Evaporation on a Horizontal Tube," ASME JOURNAL OF HEAT TRANSFER, Vol. 109, pp. 983–990.

Chyu, M.-C., and Bergles, A. E., 1988, "Thermal Analysis on the Electric Cylindrical Test Heater for Heat Transfer Experiments," *Experimental Thermal and Fluid Science*, Vol. 1, No. 1, pp. 19–27.

Chyu, M.-C., Bergles, A. E. and Mayinger, F., 1982, "Enhancement of Horizontal Tube Spray Film Evaporators," *Heat Transfer 1982*, Proceedings of the 7th International Heat Transfer Conference, Munich, F. R. Germany, Vol. 6, pp. 275–280.

Fagerholm, N.-E., Kivioja, K., Ghazanfari, A.-R., and Jarvinen, E., 1985, "Using Structured Surfaces to Enhance Heat Transfer in Falling Film Flow," I. I. F. - I. I. R. - Commission E2 Trondheim (Norway), pp. 187-192.

Fletcher, L. S., Sernas, V., and Parken, W. H., 1975, "Evaporation Heat Transfer Coefficients for Thin Sea Water Films on Horizontal Tubes," *Industrial and Engineering Chemistry, Process Design and Development*, Vol. 14, pp. 411–416.

Gottzmann, C. F., O'Neill, P. S., Minton, P. E., 1973, "High Efficiency Heat Exchangers," *Chemical Engineering Progress*, Vol. 69, No. 7, pp. 69–75.

Hillis, D. L., Lorenz, J. L., Yung, D. T., and Sather, N. F., 1979, "OTEC Performance Test of the Union Carbide Sprayed-Bundle Evaporator," Department of Energy Report ANL-OTEC-PS-3.-OTEC-PS-3.

Kim, H.-K., Fakeeha, A., and Mesler, R., 1983, "Nucleate Boiling in Flowing and Horizontal Liquids Films," *Interfacial Transport Phenomena*, ASME HTD-Vol. 23, pp. 61–65.

Marto, P. J., Wanniarachchi, A. S., and Pulido, R. I., 1985, "Augmenting the Nucleate Pool-Boiling Characteristics of GEWA-T Finned Tubes in R-113," *Augmentation of Heat Transfer in Energy Systems*, ASME HTD-Vol. 52, pp. 67–73.

McAdams, W. H., 1954, *Heat Transmission*, 3rd ed., McGraw-Hill, New York.

Nakayama, W., Daikoku, T., and Nakajima, T., 1980, "Modeling of Liquid Suction Mechanism in Porous Surface Boiling," ASME Paper No. 80-HT-122.

Nakayama, W., Daikoku, T., and Nakajima, T., 1982, "Enhancement of Boiling and Evaporation on Structured Surfaces With Gravity Driven Film of R-11," *Heat Transfer 1982*, Proceedings of the 7th International Heat Transfer Conference, Munich, F. R. Germany, Vol. 4, pp. 409–414.

Sabin, C. M., and Poppendiek, H. F., 1978, "Film Evaporation of Ammonia Over Horizontal Round Tubes," *Proceedings of the Fifth Ocean Thermal Energy Conversion Conference*, Miami Beach, FL, Vol. 3, pp. V1237–V1260.

Schulz, V. N., Edwards, D. K., and Catton, I., 1977, "Experimental Determination of Evaporative Heat Transfer Coefficients on Horizontal Threaded Tubes," *AIChE Symposium Series*, Vol. 73, No. 164, pp. 223–227.

Stephan, K., and Mitrovic, J., 1981, "Heat Transfer in Natural Convective Boiling of Refrigerants and Refrigerant-Oil-Mixtures in Bundles of T-Shaped Finned Tubes," *Advances in Enhanced Heat Transfer*, ASME HTD-Vol. 18, pp. 131–146.

Webb, R. L., 1981, "The Evolution of Enhanced Surface Geometries for Nucleate Boiling," *Heat Transfer Engineering*, Vol. 2, No. 3-4, pp. 46–69.

Yilmaz, S., and Westwater, J. W., 1981, "Effects of Commercial Enhanced Surfaces on the Boiling Heat Transfer Curve," *Advances in Enhanced Heat Transfer*, ASME HTD-Vol. 18, pp. 73–91.

Yundt, B., and Rhinesmith, R., 1981, "Horizontal Spray-Film Evaporation," *Chemical Engineering Progress*, Vol. 77, Sept., pp. 69–74.

A Theoretical Model of Film Condensation in a Bundle of Horizontal Low Finned Tubes

H. Honda

S. Nozu

Y. Takeda[1]

Department of Mechanical Engineering,
Okayama University,
Okayama 700, Japan

The previous theoretical model of film condensation on a single horizontal low finned tube is extended to include the effect of condensate inundation. Based on the flow characteristics of condensate on a vertical column of horizontal low finned tubes, two major flow modes, the column mode and the sheet mode, are considered. In the column mode, the surface of the lower tubes is divided into the portion under the condensate column where the condensate flow is affected by the impinging condensate from the upper tubes, and the portion between the condensate columns where the condensate flow is not affected by the impinging condensate. In the sheet mode, the whole tube surface is assumed to be affected by the impinging condensate. Sample calculations for practical conditions show that the effects of the fin spacing and the number of vertical tube rows on the heat transfer performance is significant for R-12, while the effects are small for steam. The predicted value of the heat transfer coefficient for each tube row compares well with available experimental data, including four fluids and five tube bundles.

Introduction

Low integral finning is a highly effective means of enhancing film condensation heat transfer on a horizontal tube. Systematic experimental data on the effects of fin geometry and condensing fluid have been reported in the recent literature (Yau et al., 1985; Marto et al., 1986; Masuda and Rose, 1987a, 1987b; Wanniarachchi et al., 1985, 1986). Theoretical models that can predict the heat transfer performance of single tubes with sufficient accuracy exist in the literature (Webb et al., 1985; Adamek, 1985; Honda and Nozu, 1987; Honda et al., 1987a). A review of these results is given by Marto (1986). However, the foregoing models for a single tube are not directly applicable to actual condensers with large tube bundles, since the heat transfer performance is affected by the combined effects of vapor shear and condensate inundation.

The present paper deals with a relatively simple case of film condensation in a bundle of horizontal low finned tubes with a small to medium rate of condensate inundation and negligible vapor shear. Katz and Geist (1948) reported the earliest experimental data for film condensation on a vertical column of horizontal finned tubes. They showed that the heat transfer deterioration due to condensate inundation is much smaller than that predicted by the Nusselt theory (1916) for a smooth tube bundle. This fact was confirmed by recent experimental data by Gogonin et al. (1983) and Marto (1986). Ishihara and Palen (1983) proposed a modified Beatty and Katz equation (1948) for predicting the heat transfer coefficient in the laminar film and rippled film regions. This equation was based on the gravity-drained condensate flow model and included empirical correction factors for the rippling of condensate and the condensate retention. While their prediction method was supported by available experimental data, recent theoretical studies (Webb et al., 1985; Adamek, 1985; Honda and Nozu, 1987; Honda et al., 1987a) show that the condensate flow on the fin surface is strongly affected by the surface tension forces.

The factors leading to a relatively small heat transfer deterioration due to condensate inundation for horizontal finned tubes are: (1) nonuniform inundation along the tube length at low inundation rate; (2) the effect of surface tension, which acts to drive condensate on the fin surface into the groove between the adjacent fins. The present paper develops a theoretical model taking account of these factors. Based on the flow characteristics of condensate on a vertical column of horizontal low finned tubes revealed in a previous study (Honda et al., 1987b), the previous theoretical model for a single horizontal tube (Honda et al., 1987a) is extended to include the effect of condensate inundation.

Theoretical Analysis

We consider film condensation in a bundle of horizontal low finned tubes with negligible vapor shear. The flow pattern of falling condensate varies with the condensate flow rate. Honda et al. (1987b) classified the observed flow patterns into four major flow modes: droplet mode, column mode, column and sheet mode, and sheet mode. They also showed that the flow mode transitions are closely connected with the value of the dimensionless group $K = \Gamma(g/\rho_1)^{1/4}/\sigma^{3/4}$, where Γ is the flow rate of falling condensate per unit length for one side of a tube. In this paper, in order to simplify the analysis, only the column mode and sheet mode are considered and the other flow modes are included in the column mode.

Based on the previous experimental results (Honda et al., 1987b), the transition criterion of the flow mode is assumed as

$$\begin{matrix}\text{Column mode for } K \le 0.42 \\ \text{Sheet mode for } K > 0.42\end{matrix} \qquad (1)$$

Column Mode. The physical model of condensate flow in the column mode is shown in Fig. 1(*a*). In this flow mode the surface of a lower tube is divided into the portion between the condensate columns and the portion under the condensate column. In the former portion, the condensation phenomenon on the tube surface is not affected by the falling condensate. This portion is termed the unaffected region (*U* region). In the latter portion, on the other hand, the condensate from the upper tubes flows down the tube circumference channeling through a number of grooves between adjacent fins. This portion is termed the affected region (*A* region).

Based on the previous experimental results (Honda et al., 1987b), the proportion of surface area covered with the impinging condensate $f\,(<1)$ is assumed as

[1]Presently at Sharp Co., Ltd., 3-1-72, Kita-Kamei, Yao 581, Japan.

Contributed by the Heat Transfer Division and presented at the ASME Winter Annual Meeting, Boston, Massachusetts, December 13–18, 1987. Manuscript received by the Heat Transfer Division September 28, 1987. Keywords: Condensation, Finned Surfaces.

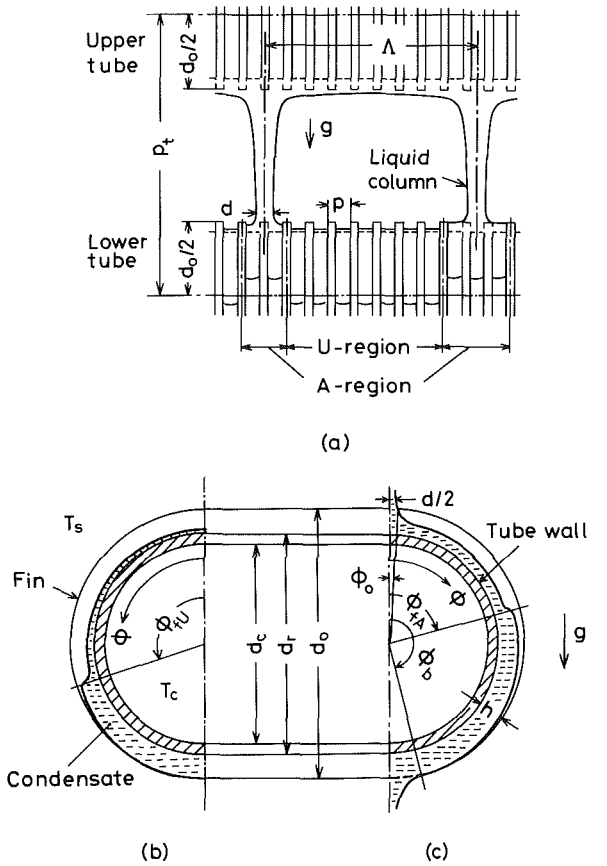

Fig. 1 Physical model of condensate flow: (*a*) column mode; (*b*) tube cross section in *U* region; (c) tube cross section in *A* region

$$f = cd/\Lambda \quad \text{for } cd \geq p \quad \text{and } K \leq 0.42$$
$$f = p/\Lambda \quad \text{for } cd < p \quad \text{and } K \leq 0.42 \tag{2}$$

where c is the proportionality constant, d is the diameter of impinging condensate column, Λ is the column distance, and p is the fin pitch. According to the experimental results, the c value was not affected by the vertical tube pitch, but was weakly dependent on the kinematic viscosity of condensate ν_1. The optimum value of c was found to be 1.5 for R-113 and methanol ($\nu_1 = 4.6 \times 10^{-7}$ and 6.9×10^{-7} m^2/s, respectively), and 2.0 for normal propanol ($\nu_1 = 2.8 \times 10^{-6}$ (m^2/s). For the experimental data cited in the next section, it is sufficiently accurate to assume $c = 1.5$. The d value is given analytically by equation (10) of the previous paper (Honda et al., 1987b), which is based on the balance of momentum, gravity, and surface tension forces acting on the falling condensate. The Λ value is determined by the most unstable Taylor wavelength for a thin film (Yung et al., 1980) as

$$\Lambda = 2\pi\sqrt{2\sigma/\rho_1 g} \tag{3}$$

The tube cross sections in the U and A regions are shown in Figs. 1(*b*) and 1(*c*), respectively. A saturated vapor with temperature T_s condenses on the tube through which a coolant with temperature T_c is flowing. The diameters at the fin tip and fit root are d_o and d_r, respectively, and the inner diameter is d_c. The ϕ_{fU} and ϕ_{fA} denote the flooding angle below which the interfin space is almost completely filled with condensate. The ϕ_{fU} value is given by equation (23) of the previous paper (Honda et al., 1987a). The ϕ_{fA} value is a function of the condensate flow rate through a groove between adjacent fins. In the A region, the fin surfaces $0 \leq \phi \leq \phi_o$ and $\phi_b \leq \phi \leq \pi$ are covered with the falling condensate and are not effective for condensation. The ϕ_o value is given by

$$\phi_o = d/d_o \tag{4}$$

Following the practice for a single finned tube (Honda and Nozu, 1987; Honda et al., 1987a), the angular portions $0 \leq \phi \leq \phi_{fU}$ and $0 \leq \phi \leq \phi_{fA}$ are termed the unflooded region, and the angular portions $\phi_{fU} \leq \phi \leq \pi$ and $\phi_{fA} \leq \phi \leq \pi$ are termed the flooded region. Thus, the tube surface in the column mode is divided into four regions with different characteristics; i.e., the unflooded region in the U and A regions, and the flooded region in the U and A regions. These are termed the U_u, A_u, U_f, and A_f regions, respectively, where the subscript u denotes the unflooded region and f the flooded region.

The tube surface in each region is further subdivided into the thin film region and the thick film region. The condensate generated in the thin film region is driven by combined gravity and surface tension forces into the thick film region, which has a concave meniscus. Then the condensate is drained circumferentially by gravity. Figure 2 shows four possible cases of condensate profile in a groove between adjacent fins. The dimensions specifying the fin geometry are: fin pitch p, fin height h, fin spacing at fin tip s (or fin thickness at fin tip t), radii of curvature at the corner of fin tip and fin root r_o and r_r, and fin half-tip angle θ. It is assumed that $h << d_o$ and r_o, $r_r << h$. The radius of curvature and the cross-sectional area (per one half of a groove) of the thick film are r and A, respectively. In Case A of Fig. 2, the thick condensate film is formed

Nomenclature

$2A$ = cross-sectional area of thick film per groove, Fig. 2
c = constant, equation (2)
d = diameter of impinging condensate column; also thickness of impinging condensate sheet
d_c = tube inside diameter
d_e = equivalent diameter of thick film = $8A/p_w$
d_o = diameter at fin tip
d_r = diameter at fin root
F = dimensionless quantity = $2Ad_e^2/p^4$
f = proportion of surface area covered with impinging condensate
g = gravitational acceleration
h = fin height
h_{fg} = specific enthalpy of evaporation
K = dimensionless quantity = $\Gamma(g/\rho_1)^{1/4}/\sigma^{3/4}$
k = thermal conductivity
$2M$ = flow rate of impinging condensate per groove
$2m$ = flow rate of condensate generated on the tube surface per fin pitch
N = total number of tubes in a vertical row
n = number of tubes in a vertical row counted from top row
P = condensate to vapor pressure difference in thick film region = $-\sigma/r$
p = fin pitch
p_t = tube pitch
p_w = wetted perimeter of thick film per groove
q = heat flux based on equivalent smooth tube area
Re = Reynolds number = $\{M + m(\phi)\}d_e/A\mu_1$
r = radius of curvature of concave meniscus in thick film region, Fig. 2

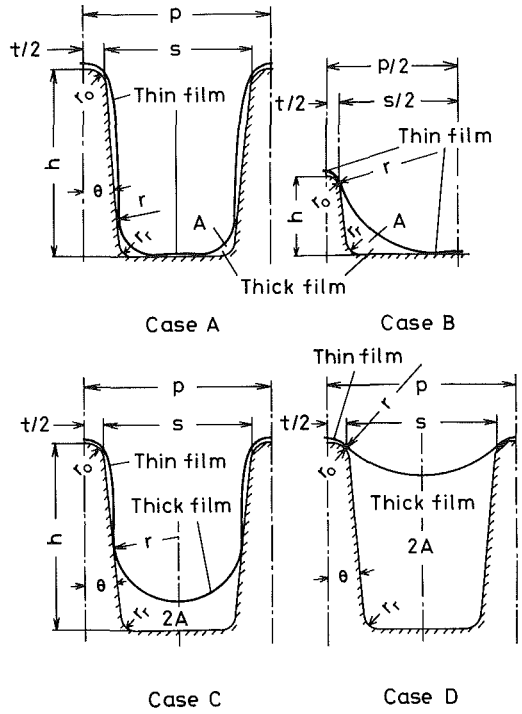

Fig. 2 Condensate profile in a groove

only at the corner of fin root and the rest of the surface is covered with the thin film. In Case B with a relatively low fin height as compared with the fin spacing, the thick film is in contact with the corner of fin tip. In Cases C and D, the whole fin root tube surface is covered with the thick film. In Case D, the thick film is in contact with the corner of fin tip. It is also possible for the whole tube surface to be completely flooded with condensate when the rate of inundation is large. However, this case will not be considered in the present paper.

In the U_u and A_u regions, one of the foregoing four cases will occur depending on the fin geometry and the condensate flow rate through a groove between adjacent fins. In the U_f and A_f regions, on the other hand, experimental results (Honda et al., 1983, 1987b) show that only Case D is possible. In the latter regions, the radius of curvature of the thick film decreases as ϕ decreases and takes a minimum value r_f at $\phi = \phi_f$. Figure 3 shows two possible cases of the thick film profile

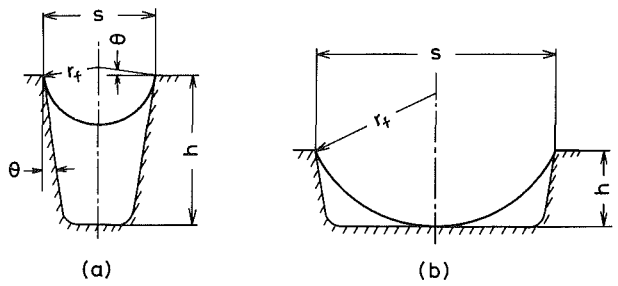

Fig. 3 Thick film profile at flooding point: (a) $s/2 \cos\theta \le h/(1-\sin\theta)$; (b) $s/2 \cos\theta > h/(1-\sin\theta)$

at $\phi = \phi_f$, where a small radius of curvature at the corner of fin tip is neglected to simplify the analysis. In Fig. 3(*a*) for $s/2 \cos\theta \le h/(1-\sin\theta)$, the thick film touches only the fin tip with a contact angle of 0 rad. In Fig. 3(*b*) for $s/2 \cos\theta > h/(1-\sin\theta)$, on the other hand, the thick film touches the root surface also. Hence, the value of r_f is determined by the geometry of the groove as

$$\begin{aligned} r_f &= s/2 \cos\theta \quad \text{for} \quad s/2 \cos\theta \le h/(1-\sin\theta) \\ r_f &= h\{1+(s/2h)^2\}/2 \quad \text{for} \quad s/2 \cos\theta > h/(1-\sin\theta) \end{aligned} \tag{5}$$

The heat transfer rates in the U_u and U_f regions are obtained by using the same calculation procedure as for a single tube (Honda et al., 1987a). This procedure is based on an approximate analytical solution of the vapor-to-coolant heat transfer problem taking account of circumferential wall conduction. According to this procedure, the local heat flux and the local average wall temperature for the U_u region, q_{Uu} and T_{wUu}, and those for the U_f region, q_{Uf} and T_{wUf}, are obtained by solving simultaneous nonlinear equations under given conditions of vapor, tube, and coolant.

For the A_u and A_f regions, the single tube theory must be modified for the effects of condensate inundation. It is assumed that the impinging condensate from the upper tube is distributed uniformly within each groove in the A region.

Neglecting the momentum change, the overall force balance for the condensate flow through a groove (assumed to be laminar) is written as

$$\frac{\lambda}{8\rho_1}\left\{\frac{M+m(\phi)}{A}\right\}^2 p_w = 2A\left(\rho_1 g \sin\phi - \frac{2}{d_m}\frac{dP}{d\phi}\right) \tag{6}$$

where λ is the perimeter average friction factor, M is the flow

Nomenclature (cont.)

r_o, r_r = radii of curvature of fin surface at corners of fin tip and fin root, respectively
s = fin spacing at fin tip
T = temperature
t = fin thickness at fin tip
u_c = coolant velocity
α_m = average heat transfer coefficient based on equivalent smooth tube area, equation (24)
α_{mo} = average heat transfer coefficient for single smooth tube
2Γ = flow rate of falling condensate per unit tube length
ϵ = actual surface area to equivalent smooth tube area ratio
θ = fin half-tip angle
Λ = most unstable Taylor wavelength for thin film, equation (3)
λ = perimeter average friction factor
μ_1 = dynamic viscosity of condensate
ν_1 = kinematic viscosity of condensate
ρ_1 = density of condensate
σ = surface tension
ϕ = angular coordinate, Fig. 1
ϕ_b = boundary of angular portion covered with falling condensate, Fig. 1
ϕ_f = flooding angle, Fig. 1
ϕ_o = boundary of angular portion covered with impinging condensate, Fig. 1

Subscripts

A = affected region
c = coolant; also coolant side
f = flooded region; also flooding point
m = average value
s = saturation
U = unaffected region
u = unflooded region
w = tube wall

rate of impinging condensate per one half of a groove, $m(\phi)$ is the flow rate of condensate generated on the tube surface per one half of a fin pitch, p_w is the wetted perimeter of the thick film per groove, $d_m = (d_o + d_r)/2$, and $P = -\sigma/r$ is the condensate-to-vapor pressure difference. The M value is related to Γ for the upper tube and the heat transfer rates on the upper tubes as

$$M = \frac{\Gamma p}{2f} = \frac{\pi d_o p}{4 h_{fg} f} \sum_{j=1}^{n-1} (q_m)_j \tag{7}$$

where n is the number of tubes in a vertical row counted from the top row and $(q_m)_j$ is the average heat flux for the jth tube. Neglecting the circumferential flow of condensate in the thin film region, $m(\phi)$ is related to the local heat flux $q(\phi)$ as

$$m(\phi) = \int_0^{\phi} p d_o q(\phi) d\phi / 4 h_{fg} \tag{8}$$

Equation (6) can be written in nondimensional form as

$$\frac{\{M + m(\phi)\}\nu_1}{\rho_1 g p^4} = \frac{F}{\lambda \mathrm{Re}} \left(\sin \phi - \frac{2}{\rho_1 g d_m} \frac{dP}{d\phi} \right) \tag{9}$$

where $F = 2A d_e^2 / p^4$, $d_e = 8A/p_w$ is the equivalent diameter of the thick film, and $\mathrm{Re} = \{M + m(\phi)\} d_e / A \mu_1$. The $\lambda\mathrm{Re}$ factor is a function of the thick film geometry. The approximate expression for $\lambda\mathrm{Re}$ for Cases A, B, and C in Fig. 2 is given by equation (29) and Table 1 of the previous paper (Honda et al., 1987a), and that for Case D is given by equation (19) of another previous paper (Honda et al., 1987b). Since the geometric parameters of the thick film, r, p_w, A, d_e, and F are interrelated, $F/\lambda\mathrm{Re}$ in equation (9) can be expressed as a function of either A or r.

Equation (9) is solved to obtain the thick film profiles for the A_u and A_f regions using different procedures. For the A_u region, the heat transfer rate in the region $0 \le \phi \le \phi_o$ is neglected and $q(\phi)$ in the region $\phi_o \le \phi \le \phi_{fA}$ is approximated by the local heat flux at $\phi = \phi_1$, q_{Au}, where ϕ_1 is defined as

$$\sin \phi_1 = \int_{\phi_o}^{\phi_{fA}} \sin \phi d\phi / (\phi_{fA} - \phi_o) \tag{10}$$

Thus, the expression for $m(\phi)$ is simplified as

$$m(\phi) = p d_o q_{Au} (\phi - \phi_o) / 4 h_{fg} \quad \text{for } \phi_o \le \phi \le \phi_{fA} \tag{11}$$

The ϕ_{fA} value is obtained from the solution of equation (9) for the A_f region. The P value in the A_u region changes from $2\sigma/d$ at $\phi = \phi_o$ to $-\sigma/r_f$ at $\phi = \phi_{fA}$. Thus, the pressure gradient term in equation (9) may be approximated by the average value defined as

$$dP/d\phi = -\sigma(2/d + 1/r_f)/(\phi_{fA} - \phi_o) \tag{12}$$

By substituting equations (7), (11), and (12) and the expression for $\lambda\mathrm{Re}$ into equation (9), the resulting nonlinear equation was solved iteratively, with a convergence criterion of 10^{-4}, to obtain the A value at $\phi = \phi_1$.

For the A_f region, the heat transfer rate in the region $\phi_b \le \phi \le \pi$ is neglected and $q(\phi)$ in the region $\phi_{fA} \le \phi \le \phi_b$ is approximated by the local heat flux at $\phi = \phi_2$, q_{Af}, where ϕ_2 is defined as the angle at which the local P value is equal to the average pressure of this region, i.e.,

$$P(\phi_2) = \int_{\phi_{fA}}^{\phi_b} P(\phi) d\phi / (\phi_b - \phi_{fA}) \tag{13}$$

Thus, it follows from equations (8) and (11) that

$$m(\phi) = p d_o \{ q_{Au}(\phi_{fA} - \phi_o) + q_{Af}(\phi - \phi_{fA}) \} / 4 h_{fg} \quad \text{for } \phi_{fA} \le \phi \le \phi_b \tag{14}$$

It is relevant to note that equation (13) can be written in terms of r as

$$r(\phi_2) = (\phi_b - \phi_{fA}) \left\{ \int_{\phi_{fA}}^{\phi_b} \frac{d\phi}{r(\phi)} \right\}^{-1} \tag{15}$$

Substitution of the expression for P into equation (9) yields the following ordinary differential equation for the curvature of the thick film:

$$\frac{d}{d\phi}\left(\frac{1}{r}\right) = -\frac{\rho_1 g d_m}{2\sigma} \left\{ \sin \phi - \frac{\lambda\mathrm{Re}\{M + m(\phi)\}\nu_1}{F \rho_1 g p^4} \right\} \tag{16}$$

The boundary conditions for equation (16) are assumed as

$$d(1/r)/d\phi = 0 \text{ and } r = \infty \text{ at } \phi = \phi_b \tag{17}$$

Equation (17) indicates that the groove is completely flooded below $\phi = \phi_b$. Substitution of equation (17) into equation (16) yields

$$\sin \phi_b = \left(\frac{\lambda\mathrm{Re}}{F}\right)_b \frac{\{M + m(\phi_b)\}\nu_1}{\rho_1 g p^4} \tag{18}$$

where $(\lambda\mathrm{Re}/F)_b$ denotes the $\lambda\mathrm{Re}/F$ value at $\phi = \phi_b$. Equation (18) is solved iteratively to obtain ϕ_b.

Equation (18) does not have a solution when M is greater than a critical value M_c. A reasonably good approximation to M_c is obtained by putting $\phi_b = \pi/2$, $M = M_c$, and $m = 0$ in equation (18) as

$$M_c = \left(\frac{F}{\lambda\mathrm{Re}}\right)_b \frac{\rho_1 g p^4}{\lambda_1} \tag{19}$$

Accordingly, the present theoretical model is not applicable to the case of $M > M_c$. In the case of $M < M_c$, equation (16) was integrated numerically in the $-\phi$ direction, starting with $1/r(\phi_b) = 0$. The Hamming's method (variable step size) was adopted for the numerical calculation with the convergence criterion of 10^{-6}. The calculated value of r first decreased as ϕ increased. When M was small, $r = r_f$ was reached at some ϕ. The numerical calculation was terminated there and the ϕ value at this point was assumed as ϕ_{fA}. When M was large, r took a minimum that was greater than r_f and increased again with further decreasing ϕ. For the latter case, ϕ_{fA} was assumed to be equal to ϕ_o.

Once the thick film profiles at $\phi = \phi_1$ and ϕ_2 are determined, the local heat flux q_{Ai} and the local average wall temperature T_{wAi} $(i = u, f)$ are obtained by using the same procedure as for a single tube. However, since the heat transfer rate and condensate flow rate are interrelated, an iterative calculation is required to obtain a converged solution. It should be mentioned here that the existence of angular portions that are not effective for condensation heat transfer ($0 \le \phi \le \phi_o$ and $\phi_b \le \phi \le \pi$) was neglected in the calculation of T_{wAi}. This simplification is sufficiently accurate for the numerical results presented in Figs. 5–8, because ϕ_o, $(\pi - \phi_b) << \pi$.

Sheet Mode. The condensate flow through the groove in the sheet mode is basically the same as that for the A region in the column mode, except that the impinging condensate is distributed uniformly along the tube length. The theoretical model developed for the A region can be applied to the sheet mode with the following modifications:

1 The d value in equation (4) is replaced by the thickness of impinging condensate sheet. Assuming free fall of condensate, this value is expressed in terms of Γ for the upper tube as

$$d = \frac{2\Gamma}{\rho_1 \{2g(p_t - d_o)\}^{1/2}} \tag{20}$$

(2) The f value is given by

$$f = 1 \tag{21}$$

(3) Following the previous paper (Honda et al., 1987b), the boundary condition for equation (13) is assumed as

$$d(1/r)/d\phi = 0 \text{ and } r = 1.2s \text{ at } \phi = \phi_b \tag{22}$$

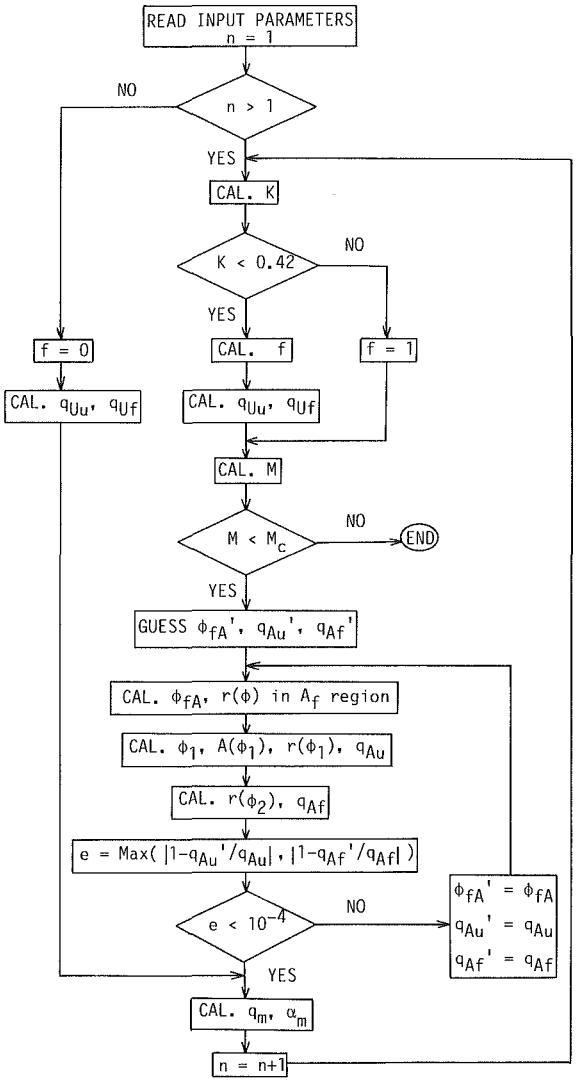

Fig. 4 Flow chart of numerical calculation

Average Heat Transfer. The average heat flux for a tube q_m is given by the area average of the local heat fluxes as

$$q_m = \{q_{Au}(\tilde{\phi}_{fA} - \tilde{\phi}_o) + q_{Af}(\tilde{\phi}_b - \tilde{\phi}_{fA})\}f + \{q_{Uu}\tilde{\phi}_{fU} + q_{Uf}(1 - \tilde{\phi}_{fU})\}(1-f) \quad (23)$$

where $\tilde{\phi} = \phi/\pi$. In general, q_{Au} and q_{Uu} are considerably greater than q_{Af} and q_{Uf}. The average heat transfer coefficient α_m is defined as

$$\alpha_m = \left\{\frac{T_s - T_c}{q_m} - \frac{d_o}{2k_w}\ln\left(\frac{d_r}{d_c}\right) - \frac{d_o}{d_c}\frac{1}{\alpha_c}\right\}^{-1} \quad (24)$$

where α_c is the coolant-side heat transfer coefficient.

In the previous paper for a single tube (Honda and Nozu, 1987; Honda et al., 1987a), α_m was defined as the ratio of q_m to the area average condensation temperature difference at the fin root. Numerical results show that the difference in the α_m values between the two definitions is within 1 percent for practical cases.

Calculation Procedure. For given conditions of vapor, tube bundle, and coolant, the q_m and α_m values for each tube row are obtained by executing the following procedure (see Fig. 4):

1 For the top tube row, apply the calculation procedure for a single tube, terminate the iteration when the q_{Uu} and q_{Uf} values converged to within 0.01 percent, and calculate the q_m and α_m from equations (23) and (24), respectively.

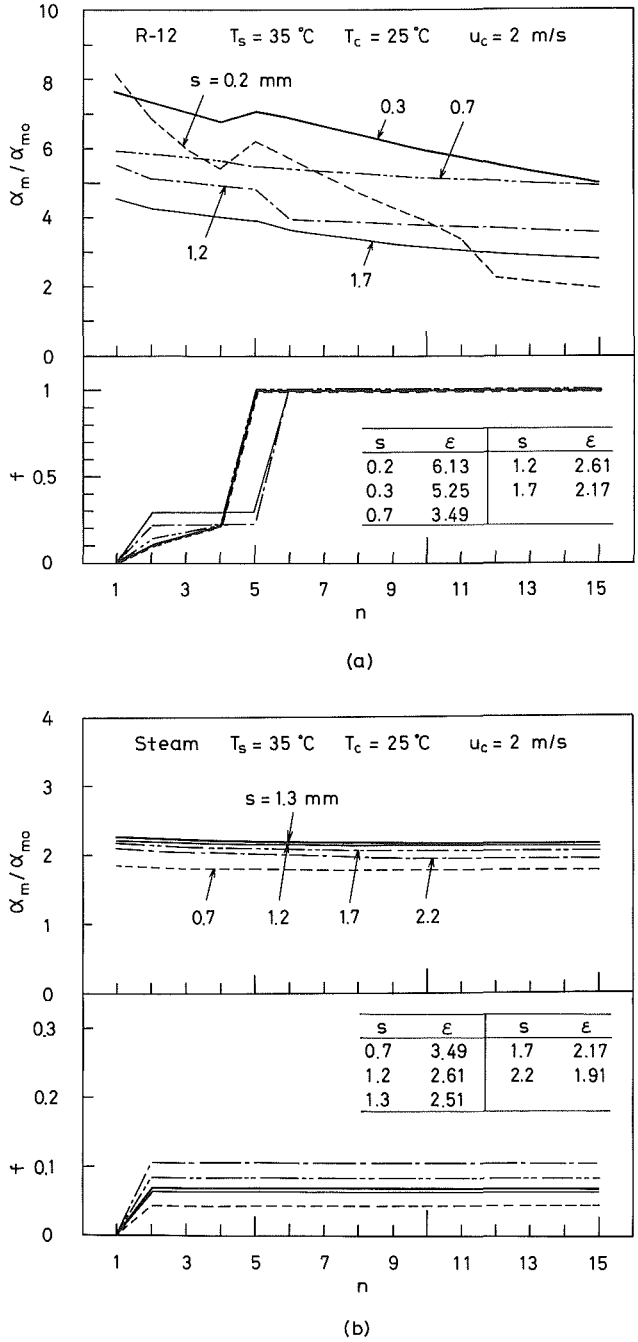

Fig. 5 Effects of fin spacing and number of vertical tube row on α_m/α_{mo} and f; T_s = 35 deg C, T_c = 25 deg C, u_c = 2 m/s, copper tube, d_o = 19.1 mm, d_c = 14.5 mm, h = 1.4 mm, t = 0.3 mm, $r_o = r_r = 0$, $\theta = 0$, and p_t = 31 mm: (*a*) R-12; (*b*) steam

2 For the second and subsequent rows, distinguish the flow mode of impinging condensate using the criteria given by equation (1), and calculate f from equation (2) or (21).

3-1 For the U region, calculate q_{Uu} and q_{Uf} using the same procedure as that for a single tube.

3-2 For the A region, calculate M from equation (7), assume ϕ_{fA}, q_{Au}, and q_{Af} values, solve equation (16) to obtain ϕ_{fA} and $r(\phi)$ in the A_f region, calculate ϕ_1 from equation (10), solve equation (9) to obtain A at $\phi = \phi_1$, calculate r (ϕ_2) from equation (15), calculate q_{Au} and q_{Af} using the same procedure as that for a single tube, and repeat the procedure until old and new values of q_{Au} and q_{Af} agree to within 0.01 percent.

3-3 Calculate q_m and α_m from equations (23) and (24), respectively.

Table 1 Variation of dimensionless parameters with number of vertical tube row

n	f	$Mv_1/\rho_1 gp^4$	ϕ_{fU}/π	ϕ_{fA}/π	F_{Uu}	F_{Au}
R-12, s = 0.2 mm						
1	0	---	0.635	---	1.29×10^{-2} C	---
4	0.206	6.90×10^{-3}	0.635	0.016*	1.29×10^{-2} C	---
5	1.0	1.84×10^{-3}	---	0.611	---	0.135 C
11	1.0	4.33×10^{-3}	---	0.402	---	0.321 C
12	1.0	5.03×10^{-3}	---	0.023*	---	---
15	1.0	5.53×10^{-3}	---	0.026*	---	---
R-12, s = 1.2 mm						
1	0	---	0.854	---	4.29×10^{-4} A	---
5	0.223	2.93×10^{-4}	0.854	0.843	4.29×10^{-4} A	2.42×10^{-2} C
6	1.0	8.13×10^{-5}	---	0.884	---	8.20×10^{-3} C
15	1.0	2.06×10^{-4}	---	0.881	---	1.85×10^{-2} C
Steam, s = 1.3 mm						
1	0	---	0.445	---	1.11×10^{-4} A	---
5	0.067	3.72×10^{-4}	0.445	0.399	1.11×10^{-4} A	1.21×10^{-2} C
15	0.067	1.30×10^{-3}	0.445	0.348	1.11×10^{-4} A	3.52×10^{-2} C

* $\phi_{fA} = \phi_o$
A Case A in Fig.2
C Case C in Fig.2

4 Proceed to the next row, repeat (2) and (3) when $M < M_c$, stop the calculation when $M > M_c$.

Results and Discussion

Effects of Fin Spacing and Number of Vertical Tube Row. Figures 5(*a*) and 5(*b*) present illustrative examples showing the effects of s and n on the α_m/α_{mo} and f values for condensation of R-12 and steam, respectively. The α_{mo} denotes the Nusselt solution (1916) for a smooth tube with the same values of d_o and $(T_s - T_{wm})$ as the finned tube. The conditions for the numerical calculation are: $T_s = 35°C$, $T_c = 25°C$, $u_c = 2$ m/s, copper tube, $d_o = 19.1$ mm, $d_c = 14.5$ mm, $h = 1.4$ mm, $t = 0.3$ mm, $r_o = r_r = 0$, $\theta = 0$, and $p_t = 31$ mm. The α_c was estimated by using the Dittus and Boelter equation (1930) for fully developed turbulent heat transfer in a smooth tube.

Figure 5(*a*) shows the case of R-12 with relatively small values of σ and h_{fg}. The α_m/α_{mo} value is strongly influenced by s and decreases sharply with increasing n for $s = 0.2$ mm, which is the optimum fin spacing for the top tube. On the other hand, α_m/α_{mo} decreases gradually with increasing n for $s \geq 0.3$ mm. The optimum s value for $2 \leq n \leq 15$ exists near 0.3 mm. It is also seen that α_m/α_{mo} increases at transition from the column mode to the sheet mode for $s \leq 0.3$ mm, while it decreases for $s \geq 0.7$ mm. Figure 5(*b*) shows the case of steam with relatively large values of σ and h_{fg}. The α_m/α_{mo} value is considerably smaller than that for R-12 and is weakly dependent on s and n. The optimum s value exists near 1.3 mm.

The actual surface area to equivalent smooth tube area ratio ϵ for each tube is also shown in Fig. 5. A comparison of the α_m/α_m and ϵ values for each tube reveals that $\alpha_m/\alpha_{mo} > \epsilon$ for R-12 excepting the case of $s = 0.2$ mm and $n \geq 3$, while $\alpha_m/\alpha_{mo} < \epsilon$ for steam excepting the case of $s = 2.2$ mm and $n \leq 8$. This difference is due to relatively large values of ϕ_{fU}, ϕ_{fA} (see Table 1) and the fin efficiency for R-12 as compared with those for steam. It is relevant to note here that the calculated value of the fin efficiency was from 0.92 to 0.97 for R-12 and from 0.42 to 0.63 for steam. This indicates that the optimum fin thickness for R-12 is smaller than 0.3 mm, because the effect of increasing ϵ as a result of decreasing the fin thickness is expected to be greater than that of decreasing the fin efficiency. On the other hand, the optimum fin thickness for steam is found to be around 0.75 to 1.0 mm (Wanniarachchi et al., 1985).

The foregoing results for R-12 and steam are related to the behavior of condensate in the U and A regions. Table 1 shows the variation of dimensionless parameters f, $Mv_1/\rho_1 gp^4$, ϕ_{fU}/π, ϕ_{fA}/π, F_{Uu}, and F_{Au} with n, where F_{Uu} and F_{Au} denote the F value at $\phi = \phi_{fu}/2$ and ϕ_1, respectively. The numerical results are presented only for specific values of s and n, which are necessary to explain the α_m/α_{mo} results in Fig. 5. In Table 1, the ϕ_{fA}/π values corresponding to the case of $\phi_{fA} = \phi_o$ are denote with asterisk. The classification of the condensate profile in the groove (see Fig. 2) is also shown by symbols A and C at the upper right corner of the F_{Uu} and F_{Au} values. The F_{Uf} and F_{Af} values ($= 0.65 \sim 1.0$) are not listed in Table 1, because $F_{Uf} \simeq F_{Af}$ and the variation of F_{Af} with n is small.

The upper portion of Table 1 shows the case of R-12 and $s = 0.2$ mm. This case is characterized by relatively large values of $Mv_1/\rho_1 gp^4$ and F_{Au}. The ϕ_{fA} decreases as $Mv_1/\rho_1 gp^4$ increases and reaches ϕ_o when $Mv_1/\rho_1 gp^4 \gtrsim 5\times10^{-3}$. At $n = 4$, the flow mode of impinging condensate is the column mode. Since $\phi_{fA} = \phi_o$ for this row, the average heat flux for the A region is only 24.5 percent as large as that for the U region. At $n = 5$, the flow mode of impinging condensate is the sheet mode. For this row, ϕ_{fA} is close to ϕ_{fU} for $n \leq 4$, and the classification of the condensate profile for the A_u region is the same as that for the U_u region for $n \leq 4$ (i.e., Case C), although F_{Au} is about ten times as large as F_{Uu}. Consequently, q_m for $n = 5$ is only 9 percent smaller than the average heat flux for the U region for $n \leq 4$. As a result, α_m/α_{mo} increases at the column mode to sheet mode transition. The α_m/α_{mo} decreases with further increasing n and decreases rather sharply at $n = 12$. This is due to the sudden decrease of ϕ_{fA}/π from 0.402 at $n = 11$ to 0.023 at $n = 12$.

The middle portion of Table 1 shows the case of R-12 and $s = 1.2$ mm. This case is characterized by small values of $Mv_1/\rho_1 gp^4$ and F_{Au}. Consequently, the variation of ϕ_{fA}/π with n is very small. At $n = 5$, the flow mode of impinging condensate is the column mode. For this row, ϕ_{fA} is close to ϕ_{fU}, but the classification of the condensate profile for the A_u region (Case C) is different from that for the U_u region (Case A). In general, the heat transfer coefficient for Case C is smaller than that for Case A. Thus, the average heat flux for the A region is about 22 percent smaller than that for the U region. At $n = 6$, the flow mode of impinging condensate is the sheet mode. For this row, ϕ_{fA} is about 5 percent greater than that for $n = 5$ and the classification of the condensate profile for the A_u region is the same as that for $n = 5$ (i.e., Case C). Consequently, q_m for $n = 6$ is about 7 percent greater than the average heat flux for the A region for $n = 5$, but is about 16 percent smaller than the average heat flux for the U region for $n \leq 5$. As a result, α_m/α_{mo} decreases at the column mode to sheet mode transition.

The lower portion of Table 1 shows the case of steam and $s = 1.3$ mm. In general, the steam results are characterized by a small value of f (see Fig. 5*b*). As a result, α_m/α_{mo} is affected only slightly by the condensate inundation.

Table 2 Summary of experimental data used for comparison with theoretical predictions

Bundle	Fluid	Dimensions of tube and bundle										Reference
		N	p_t mm	d_o mm	d_c mm	p mm	h mm	t_m mm	r_o mm	r_r mm	θ rad	ε	
1[b]	R-12 n-butane Acetone	6	33.3	18.95	13.97	1.69	1.58	0.51	0.11[a]	0.40[a]	0.106	2.42	Katz and Geist (1948)
2[b]	R-12	10	31.0	20.6	15.8[a]	2.00	1.41	1.01	0.34[a]	0.33[a]	0.363	1.84	Gogonin et al. (1983)
3[b]		10	31.0	16.74	12.3[a]	1.32	1.23	0.67	0.26[a]	0.25[a]	0.185	2.36	
4[b]		10	31.0	16.64	12.9[a]	1.24	0.87	0.62	0.25[a]	0.25[a]	0.269	1.96	
5[c]	Steam	12	23.9	17.9	12.7	2.5	1.0	1.0	0.0	0.0	0.0	1.69	Marto (1986)

a Estimated value
b Vertical column of horizontal low finned tubes
c Simulated tube bundle using an inundation tube

Comparison With Experimental Data. The predictions of the present theoretical model are compared with available experimental data. There is a small amount of experimental data on the heat transfer for each tube row. A summary of the experimental data is presented in Table 2. The experimental data by Katz and Geist (1948) and Gogonin et al. (1983) are for

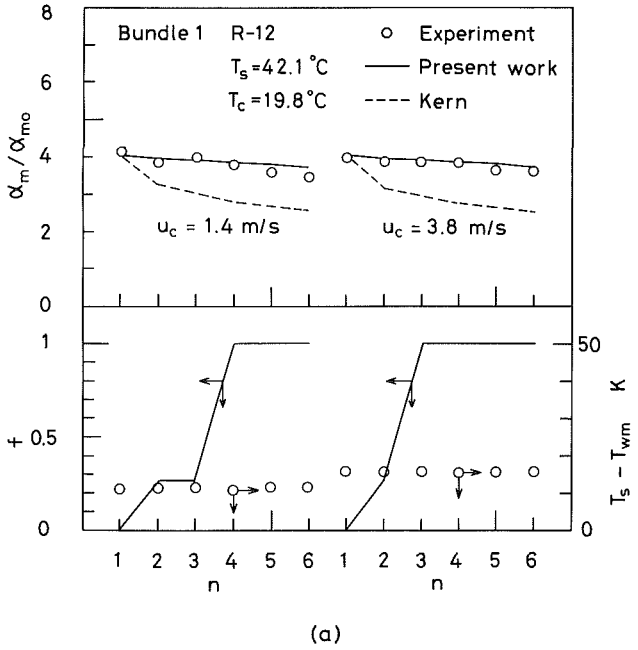

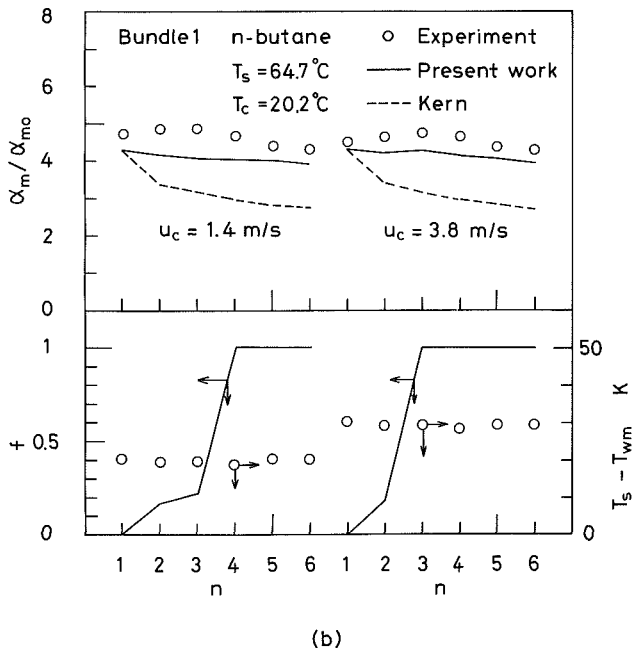

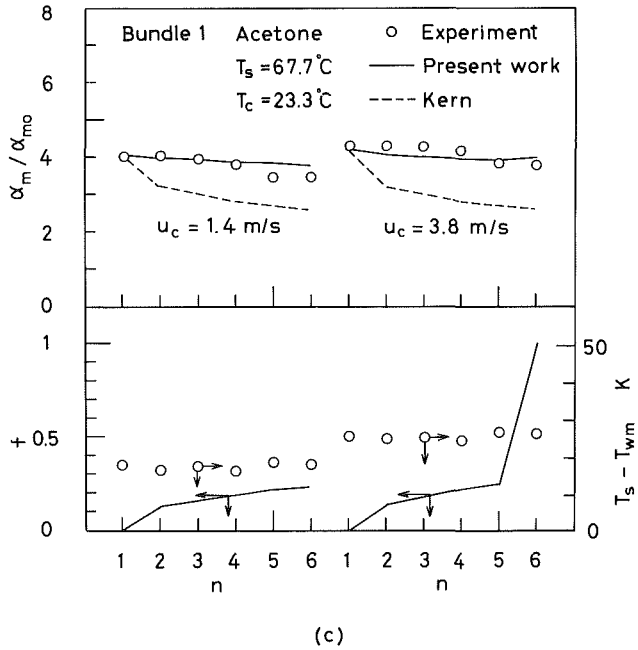

Fig. 6 Comparison of measured and predicted α_m/α_{mo} values, Bundle 1: (*a*) R-12; (*b*) *n*-butane; (*c*) acetone

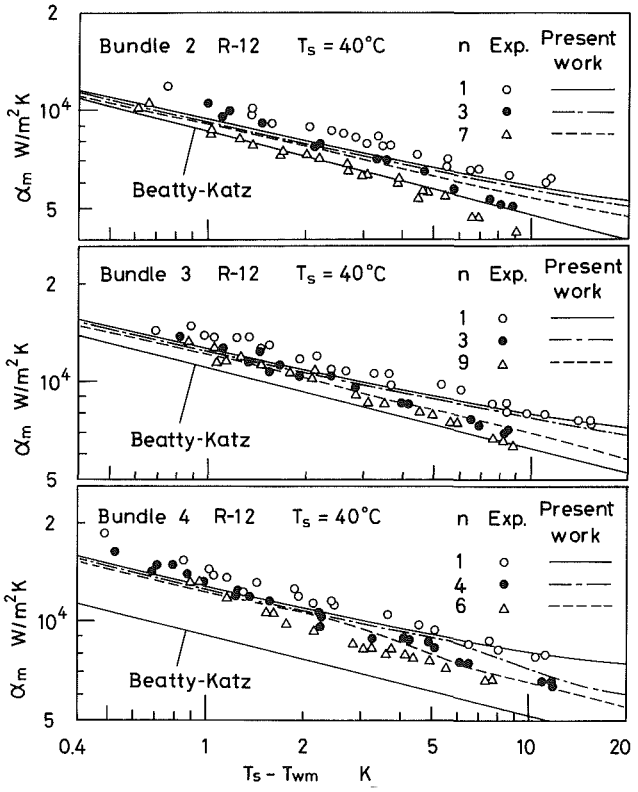

Fig. 7 Comparison of measured and predicted α_m values; R-12, Bundles 2, 3, and 4

nearly stagnant vapor, while those by Marto (1986) are for downward flowing vapor with a velocity of about 1 m/s.

Figures 6(*a*), 6(*b*), and 6(*c*) show comparisons with the R-12, *n*-butane and acetone data of Katz and Geist (1948), respectively. In the upper portion of Fig. 6, the measured and predicted values of the enhancement ratio α_m/α_{mo} at two u_c values are plotted as a function of n. The measured value of $(T_s - T_{wm})$ and the predicted value of f are also shown in the lower portion of Fig. 6. The measured values of α_m and $(T_s - T_{wm})$ in Fig. 6 were calculated from the overall heat transfer data in the literature by using the modified Wilson plot method. It is seen that the predicted value of α_m/α_{mo} decreases gradually with increasing n except that the *n*-butane and acetone results show a small increase in α_m/α_{mo} at transition from the column mode ($f<1$) to the sheet mode ($f=1$). The latter result is due to a relatively large increase in ϕ_{fA} at the column mode to sheet mode transition (about 0.20 rad for *n*-butane and 0.29 rad for acetone) as compared to the case of R-12 (about 0.10 rad). The agreement between the measured and predicted values is very good for R-12 and acetone, and is within 15 percent for *n*-butane. This difference is partly due to the error in the determination of α_m by using the modified Wilson plot method. Also included in Fig. 6 is the prediction where the effect of condensate inundation is accounted for by the correction factor $n^{5/6} - (n-1)^{5/6}$, which is derived from the Kern equation (1958) for a bundle of smooth tubes. It is

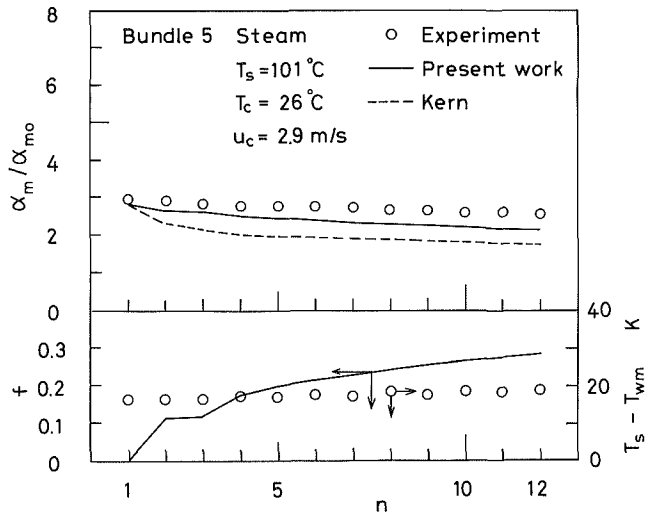

Fig. 8 Comparison of measured and predicted α_m/α_{mo} values; steam, Bundle 5

seen that the Kern equation overpredicts the effect of condensate inundation for the Katz and Geist data.

Figure 7 shows the comparison with the R-12 data of Gogonin et al. (1983), where the α_m values for three tube bundles are plotted as a function of $(T_s - T_{wm})$. The prediction of the Beatty and Katz equation (1948) for a single tube is also shown for comparison. Gogonin et al. reported the heat transfer coefficient for the lateral fin surface, which was obtained by subtracting the heat transfer rates at the fin tip and fin root (calculated from the Nusselt equation for a horizontal cylinder) from the measured heat transfer rate. The measured α_m value in Fig. 7 was obtained by reversing this procedure. The agreement between the measurement and the prediction is within 12 percent for most of the data points.

Figure 8 shows the comparison with the steam data of Marto (1986), where the α_m/α_{mo}, $(T_s - T_{wm})$ and f values are plotted as a function of n. As seen from the variation of f, the predicted flow mode is the column mode for all tube rows. This is in contrast to the case of organic fluids shown in Fig. 6, where the column mode to sheet mode transition occurs at relatively small values of n. The predicted α_m/α_{mo} value is 5 to 20 percent lower than the measured value. This difference is partly due to the existence of downward vapor velocity of about 1 m/s in the experiments.

Concluding Remarks

A prediction method for heat transfer during film condensation in a bundle of horizontal low finned tubes with negligible vapor shear was presented. The method is based on the previously proposed prediction method for a single tube and takes account of the flow characteristics of condensate on a vertical column of horizontal low finned tubes. For given conditions of vapor, tube bundle, and coolant, the heat transfer rate for each tube row is obtained by solving a set of simultaneous nonlinear equations describing the vapor to coolant conjugate heat transfer.

Sample calculations for a set of practical conditions were made to study the effects of fin spacing and the number of vertical tube row. In the case of R-12 with relatively small values of σ and h_{fg}, the α_m value is strongly influenced by s and decreases sharply with increase of n at small s. The optimum s value exists near 0.3 mm. In the case of steam with relatively large values of σ and h_{fg}, on the other hand, the α_m value is weakly dependent on s and n, and the optimum s value exists near 1.3 mm.

The prediction of the average heat transfer coefficient for each tube row was compared with available experimental data including four fluids and five tube bundles. The agreement was satisfactory for the R-12 and acetone data, and was fairly good for the n-butane and steam data.

Acknowledgments

We wish to thank Professor Marto for informing us of the details of his experimental data.

References

Adamek, T., 1985, "Rechenmodell der Filmkondensation an engberippten Kondensatorrohren," *Wärme- und Stoffübertragung*, Vol. 19, pp. 145–157.

Beatty, K. O., Jr., and Katz, D. L., 1948, "Condensation of Vapors on Outside of Finned Tubes," *Chemical Engineering Progress*, Vol. 44, pp. 55–70.

Dittus, F. W., and Boelter, L. M., 1930, "Heat Transfer in Automobile Radiators of the Tubular Type," *Univ. Calif. Pub. Eng.*, Vol. 2, pp. 443–461.

Gogonin, I. I., Kabov, O. A., and Sosunov, V. I., 1983, "Heat Transfer in Condensation of R-12 Vapor on Bundles of Finned Tubes," *Kholodil'naya Tekhnika*, No. 1, pp. 26–29.

Honda, H., and Nozu, S., 1987, "A Prediction Method for Heat Transfer During Film Condensation on Horizontal Low Integral-Fin Tubes," ASME JOURNAL OF HEAT TRANSFER, Vol. 109, pp. 218–225.

Honda, H., Nozu, S., and Mitsumori, K., 1983, "Augmentation of Condensation on Horizontal Finned Tubes by Attaching a Porous Drainage Plate," *Proceedings, ASME-JSME Thermal Engineering Joint Conference*, Y. Mori and W-J. Wang, eds., Vol. 3, pp. 289–295.

Honda, H., Nozu, S., and Uchima, B., 1987a, "A Generalized Prediction Method for Heat Transfer During Film Condensation on a Horizontal Low Finned Tube," *Proceedings, 2nd ASME-JSME Thermal Engineering Joint Conference*, P. J. Marto and I. Tanasawa, ed., JSME, Vol. 4, pp. 385–392.

Honda, H., Nozu, S., and Takeda, Y., 1987b, "Flow Characteristics of Condensate on a Vertical Column of Horizontal Low Finned Tubes," *Proceedings, 2nd ASME-JSME Thermal Engineering Joint Conference*, P. J. Marto and I. Tanasawa, eds., ASME, Vol. 1, pp. 517–524.

Ishihara, K., and Palen, J. W., 1983, "Condensation of Pure Fluids on Horizontal Finned Tube Bundles," *Institution of Chemical Engineers Symposium Series*, No. 5, pp. 429–446.

Katz, D. L., and Geist, J. M., 1948, "Condensation on Six Finned Tubes in a Vertical Row," *Trans. ASME*, Vol. 70, pp. 907–914.

Kern, D. Q., 1958, "Mathematical Development of Loading in Horizontal Condensers," *AIChE Journal*, Vol. 4, No. 2, pp. 157–160.

Marto, P. J., 1986, "Recent Progress in Enhancing Film Condensation Heat Transfer on Horizontal Tubes," *Proceedings, 8th International Heat Transfer Conference*, C. L. Tien et al., eds., Hemisphere Publishing Corp., Washington, DC, Vol. 1, pp. 161–170; private communication.

Marto, P. J., Mitrou, A. S., Wanniarachchi, A. S., and Rose, J. W., 1986, "Film Condensation of Steam on Horizontal Finned Tubes: Effect of Fin Shape," *Proceedings, 8th International Heat Transfer Conference*, C. L. Tien et al., eds., Hemisphere Publishing Corp., Washington, DC, Vol. 4, pp. 1695–1700.

Masuda, H., and Rose, J. W., 1987a, "Condensation of Ethylene Glycol on Horizontal Integral-Fin Tubes," *Proceedings, 2nd ASME-JSME Thermal Engineering Joint Conference*, P. J. Marto and I. Tanasawa, eds., ASME, Vol. 1, pp. 525–530.

Masuda, H., and Rose, J. W., 1987b, "An Experimental Study of Condensation of Refrigerant R-113 on Low Integral-Fin Tubes," *Heat Transfer Science and Technology*, B. X. Wang, ed., Hemisphere Publishing Corp., Washington, DC, pp. 480–487.

Nusselt, W., 1916, "Die Oberflächenkondensation des Wasserdampfes," *Zeit. Ver. Deut. Ing.*, Vol. 60, pp. 541–546, 569–575.

Wanniarachchi, A. S., Marto, P. J., and Rose, J. W., 1985, "Film Condensation of Steam on Horizontal Finned Tubes: Effect of Fin Spacing, Thickness and Height," *Multiphase Flow and Heat Transfer*, V. K. Dhir et al., eds., ASME HTD-Vol. 47, pp. 93–99.

Wanniarachchi, A. S., Marto, P. J., and Rose, J. W., 1986, "Film Condensation of Steam on Horizontal Finned Tubes: Effect of Fin Spacing," ASME JOURNAL OF HEAT TRANSFER, Vol. 108, pp. 960–966.

Webb, R. L., Rudy, T. M., and Kedzierski, M. A., 1985, "Prediction of the Condensation Coefficient on Horizontal Integral-Fin Tubes," ASME JOURNAL OF HEAT TRANSFER, Vol. 107, pp. 369–376.

Yau, K. K., Cooper, J. R., and Rose, J. W., 1985, "Effect of Fin Spacing on the Performance of Horizontal Integral-Fin Condenser Tubes," ASME JOURNAL OF HEAT TRANSFER, Vol. 107, pp. 377–383.

Yung, D., Lorenz, J. J., and Ganic, E. N., 1980, "Vapor/Liquid Interaction and Entrainment in Falling Film Evaporators," ASME JOURNAL OF HEAT TRANSFER, Vol. 102, pp. 20–25.

C. A. Busse
Process Engineering Division Head,
Professor,
Commission of the European Communities,
Joint Research Centre—Ispra Establishment,
21020 Ispra (VA), Italy

R. I. Loehrke
Professor,
Mechanical Engineering Department,
Colorado State University,
Fort Collins, CO 80523

Subsonic Pressure Recovery in Cylindrical Condensers

A method is presented for predicting laminar, subsonic flow in axisymmetric cylindrical heat pipe condensers. The method involves the use of the boundary layer approximation and a noncontinuous power series to describe the velocity profile under conditions including strong axial flow reversal. A comparison between laminar predictions and measurements indicates that transition to turbulent flow in the condenser begins when the absolute value of the radial Reynolds number exceeds 6. The condenser pressure recovery in the turbulent regime can be calculated from the momentum flow at the condenser inlet and an empirical wall-friction parameter.

1 Introduction

Large pressure variations can occur in the vapor along the length of a heat pipe at high Mach numbers (see Fig. 1). These variations, due to frictional and inertial effects, have a significant influence on the heat transfer limits of the heat pipe (Dunn and Reay, 1982). Even at low Mach numbers, the vapor phase pressure profile determines, in part, the dry-out characteristics of a heat pipe. It also strongly influences the distribution of surplus liquid outside the capillary structure (Busse and Kemme, 1980) and, therefore, the thermal resistance of a heat pipe. Consequently, it is important to be able to predict the vapor flow characteristics accurately.

A method for analyzing subsonic vapor flow and an associated computer code are described by Busse and Prenger (1984). The method is based on a two-dimensional, boundary-layer model of the flow and was used in the mentioned reference to predict the pressure drop in heat pipe evaporators over a range of operating conditions. A laminar-flow analysis was considered appropriate for the evaporator, since previous research has shown that axial duct flow is stabilized by mass injection so that transition to turbulent flow is delayed until high Reynolds numbers are reached (Huesmann and Eckert, 1968).

This paper is concerned with the prediction of the pressure distribution in heat pipe condensers. The problem was studied first by Cotter (1965) for incompressible flow and the limiting cases $|\mathrm{Re}_r| \ll 1$ and $|\mathrm{Re}_r| \gg 1$. He concluded that for $|\mathrm{Re}_r| \ll 1$ the viscous effects dominate and the pressure gradient is the same as in a Poiseuille flow, while for $|\mathrm{Re}_r| \gg 1$ the flow is inertia-dominated and the deceleration of the condensing vapor results in a recovery of $4/\pi^2 \approx 40$ percent of the pressure drop occurring in the evaporator. Recent measurements of Haug, however, have shown that for $|\mathrm{Re}_r| \gg 1$ pressure recoveries of about 90 percent occur (Haug, 1984; Haug and Busse, 1985). Therefore, a revision of Cotter's model is necessary, along with an extension to intermediate radial Reynolds numbers and to compressible flow, which often occurs in heat pipes during startup.

Cotter used a fairly simple model. For $|\mathrm{Re}_r| \gg 1$ it is based on the assumptions of (1) laminar flow, and (2) velocity profiles that remain geometrically similar in the evaporator (cosine profile) and in the condenser (rectangular profile). Furthermore, it is tacitly assumed (3) that the transition between these profiles, which requires a decrease of the momentum flow, occurs without pressure recovery. This assumption seems to be the weakest point of the model, because it is not clear how the momentum is destroyed in a laminar inertia-dominated flow. Making instead the assumption that the decrease of the momentum flow is fully transformed into a pressure rise, the pressure recovery would increase to 100 percent, which is much closer to the experimental values.

Additionally, assumptions (1) and (2) are not appropriate for a realistic condenser model. A number of studies have shown that the assumption of similarity profiles is, in fact, valid in the evaporator for incompressible flow at all $\mathrm{Re}_{r,e}$ but in the condenser only for $|\mathrm{Re}_{r,c}| \ll 1$, and that for $|\mathrm{Re}_{r,c}| \gg 1$ strong profile variations occur along the entire condenser (Weissberg, 1959; Hornbeck, 1963; Busse, 1967). The reason for this is that, for internal flows, both the viscous force and mass injection tend to establish an equilibrium profile, while mass extraction is an inherently unstable process, which promotes movement away from the equilibrium condition (Busse, 1987). Figure 2 gives a quantitative example of the development of the laminar velocity profile in a cylindrical condenser.

Furthermore, the flow will generally not be laminar for $|\mathrm{Re}_{r,c}| \gg 1$. The positive axial pressure gradient in the condenser leads to flows with inflectional velocity profiles and even to reverse flow at the wall (see Fig. 2). This causes the appearance of turbulence at very low axial Reynolds number Re. Berman (1958), Bourgarel (1966), and Quaile and Levy (1975) have investigated incompressible flow in cylindrical tubes with porous walls. They found that suction can induce turbulence at axial Reynolds numbers much below those needed for the same transition at zero suction. Quaile and Levy have observed fluctuations characteristic of transition from laminar to

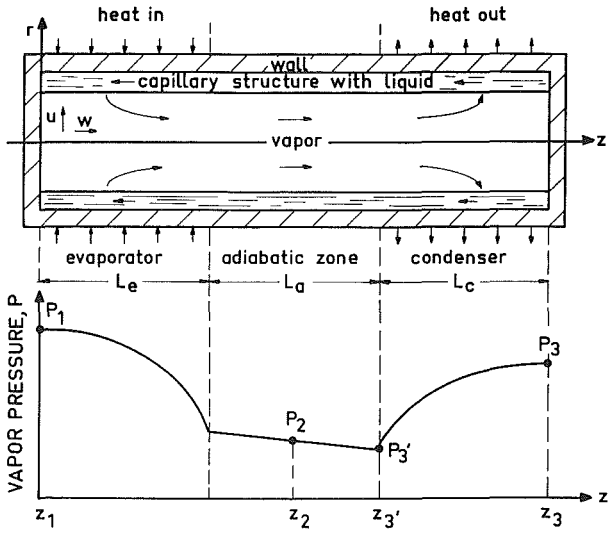

Fig. 1 Flow pattern and vapor pressure distribution in a cylindrical heat pipe (schematically, for subsonic flow and $|\mathrm{Re}_r| \gg 1$)

Contributed by the Heat Transfer Division and presented at the 8th International Heat Transfer Conference, San Francisco, California, August 1986. Manuscript received by the Heat Transfer Division August 27, 1987. Keywords: Condensation, Heat Pipes and Thermosyphons.

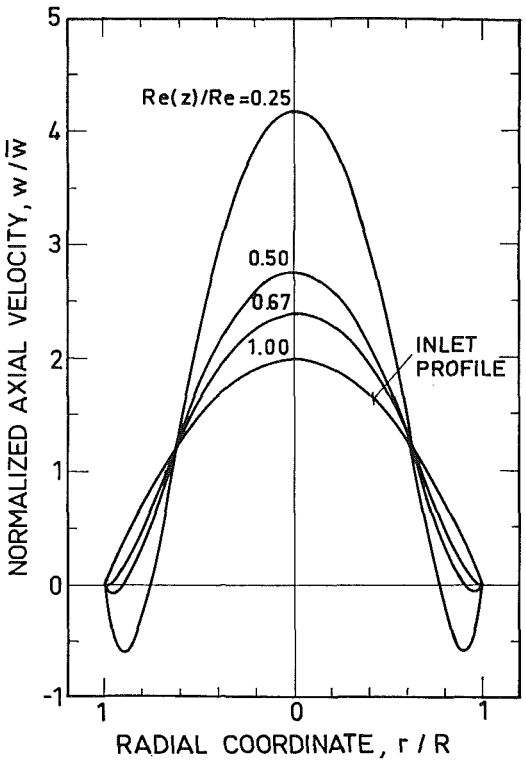

Fig. 2 Development of the laminar velocity profile in a cylindrical condenser, for $Re_{r,c} = -10$, $\bar{M} \ll 1$ and a parabolic inlet profile. Curve parameter Re(z)/Re = ratio of axial mass flow to axial mass flow at condenser inlet.

turbulent flow at axial Reynolds numbers as low as a few hundred. The fluctuations appeared as soon as the radial Reynolds number was smaller than -6. This destabilizing influence of mass removal or wall suction on internal flows contrasts the external-flow rule "suction stabilizes the flow" (Schlichting, 1979; Busse, 1987).

The objective of the present paper is to present methods for predicting subsonic pressure recovery in cylindrical condensers. In the first part it is shown how the analytical method of Busse and Prenger (1984) can be extended to laminar-flow predictions in condensers under conditions including strong flow reversal. The second part deals with the use of the laminar-flow analysis to interpret the results of pressure recovery measurements in the condenser of a heat pipe. The emphasis is on identifying the influence of transition to turbulence on integral condenser pressure recovery.

2 Method of Laminar Flow Analysis

This section of the paper contains a summary of the analytical model and solution procedure described by Busse and Prenger (1984). The description of the solution procedure is expanded to include a discussion of the use of noncontinuous power series to describe the vapor velocity profile.

2.1 Laminar Vapor Flow Model. The laminar, steady, compressible vapor flow in a heat pipe is calculated using the computer code AGATHE, which is based on a two-dimensional flow model. The vapor is described as an isothermal perfect gas so

$$\frac{P}{\rho} = c^2 = \text{const} \tag{1}$$

This model was primarily chosen for the purpose of analyzing heat pipes that use organic working fluids of high molecular weight. Such vapors have a very high molar heat capacity, which keeps them nearly isothermal during expansion or compression. As a result such vapors get superheated on expansion and not supersaturated like a vapor with molecules composed of only a few atoms. However, the isothermal perfect gas seems also to be a reasonable approximation for this latter case (Busse, 1973). The temperature of the gas is approximated by the average temperature of the liquid-vapor interface in the evaporator. The vapor flow is described by the conservation of mass

$$\frac{\partial}{\partial r}(r\rho u) + r\frac{\partial}{\partial z}(\rho w) = 0 \tag{2}$$

and the conservation of momentum using Prandtl's boundary layer approximation (Schlichting, 1979)

$$\frac{\partial P}{\partial z} = -\rho\left(u\frac{\partial w}{\partial r} + w\frac{\partial w}{\partial z}\right) + \frac{\mu}{r}\frac{\partial}{\partial r}\left(r\frac{\partial w}{\partial r}\right) \tag{3}$$

$$\frac{\partial P}{\partial r} = 0 \tag{4}$$

Equations (4) and (1) imply that the density is not a function of r.

The boundary layer approximation is based on the assumption that the radial velocity component u is small with respect to the average axial velocity component $\bar{w}$. This implies specifically that $u_R \ll \bar{w}$. With the global mass conservation

Nomenclature

a_i = velocity profile coefficient
A = cross-sectional area of vapor channel = πR^2
c = speed of sound in the vapor
f = Fanning friction factor, equation (17)
h_{fg} = specific heat of vaporization
i = number of typical term in series of velocity profile coefficients
L = length of heat pipe section
m = number of last term in continuous part of series of velocity profile coefficients
$\bar{M}$ = average Mach number, equation (18)
n = number of last term in series of velocity profile coefficients
P = vapor pressure
r = radial coordinate
R = radius of vapor channel
$\mathrm{Re}(z)$ = local axial Reynolds number = $2R\rho\bar{w}/\mu$
Re = axial Reynolds number at the entrance to the condenser
Re_r = radial Reynolds number = $-R\rho u_R/\mu$
u = radial component of vapor velocity
w = axial component of vapor velocity
$\bar{w}$ = axial component of vapor velocity averaged over the cross section
z = axial coordinate
β = momentum factor, equation (16)
η = dimensionless radial coordinate, equation (9)
μ = viscosity of vapor
ρ = vapor density
φ = wall friction parameter, equation (20)

Subscripts

a = adiabatic section
c = condenser section
e = evaporator section
R = liquid-vapor interface, $r = R$
1 = location of upstream end of evaporator, $z = z_1$
2 = location of midpoint of adiabatic section, $z = z_2$
3 = location of downstream end of condenser, $z = z_3$
3′ = location of upstream end of condenser, $z = z_{3'}$

$$\frac{d(\rho \bar{w} A)}{dz} = -2\pi R \rho u_R \tag{5}$$

this condition becomes $L_c/D \gg 1$, provided that u_R varies relatively little along the condenser.

The validity of the boundary layer approximation was examined by Busse and Prenger (1984). Good agreement was obtained between the prediction obtained for the pressure distribution along the axis of a cylindrical condenser using the boundary layer equations and those obtained using the Navier-Stokes equations for L_c/D as small as 2.5. A recent comparison of numerical solutions of the complete Navier-Stokes equations with the boundary layer analysis for an annular heat pipe also came to the conclusion that the boundary layer presentation provides a sufficiently accurate picture of the vapor pressure variation in the evaporator and the condenser both for low and high values of $|\mathrm{Re}_r|$ (Faghri, 1987). The boundary layer approximation permits a considerable reduction in the computation effort for solving the flow problem; therefore, AGATHE runs quickly on a minicomputer.

The following boundary conditions are used:

$$w_R = 0 \tag{6}$$

$$\bar{w}_3 = 0 \tag{7}$$

The interfacial mass flux ρu_R, which is determined by the heat delivered to the liquid-vapor interface, and the pressure P_3' and the axial velocity $w_3'(r)$ at the condenser inlet, are considered as given. In practice these quantities have to be determined by modeling the vapor flow upstream of the condenser inlet (Busse and Prenger, 1984) and the heat transfer between heat source or sink and the liquid-vapor interface. It should be noted that, with specified R, ρu_R, and $(\rho \bar{w})_3'$, the condenser length L_c cannot also be chosen as it is determined by the mass conservation (5) and the boundary condition (7). The analysis of a condenser of given length, therefore, requires an iterative procedure.

2.2 Solution Procedure. The velocity profile is approximated by a power series

$$w = \bar{w}(z) \sum_{i=1}^{n} a_i(z) \eta^{i-1} \tag{8}$$

with

$$\eta = \left(\frac{r}{R}\right)^2 \tag{9}$$

For symmetry reasons, equation (8) contains only even powers of r. The main task is to determine the n velocity profile coefficients a_i, two of which are given by the conditions

$$\sum_{i=1}^{n} a_i = 0 \tag{10}$$

and

$$\sum_{i=1}^{n} \frac{a_i}{i} = 1 \tag{11}$$

Equation (10) follows from equation (8) with the boundary condition (6) and equation (11) is obtained by averaging equation (8) over the cross section.

Solving for u from equation (2) and inserting this expression and equation (8) for w into equation (3) gives for $\partial P/\partial z$ a power series in η of order $2(n-1)$. But according to equation (4) $\partial P/\partial z$ must be independent of η. So all the $2(n-1)$ factors of the η powers must be zero, which gives $2(n-1)$ differential equations for $\partial P/\partial z$ and the a_i's. But from equations (8), (10), and (11) there are only $n-2$ unknown coefficients a_i. Therefore, with equation (8), only an approximate solution of the flow equations can be obtained and the question arises how to choose the a_i so that the radial variation of $\partial P/\partial z$ is minimized.

One possibility is to fulfill only the first $n-1$ of these differential equations, which makes $\partial P/\partial z$ fairly constant in the center part of the flow channel but leads to relatively large errors at the wall. One can improve the quality of the solution by substituting for the last two of these differential equations an equation for $\partial P/\partial z$ at the wall and the momentum equation (3) averaged over the cross section.

The set of differential equations is integrated by a Runge-Kutta scheme. The quality of the solution is monitored using a table in which, for each cross section, the local values of $\partial P/\partial z$ are compared with $\partial P/\partial z$ at the centerline. This is a simple and efficient way to detect inaccurate solutions.

In condensers with flow reversal, an impractically large number of terms is required in the continuous series described by equation (8) in order to maintain the quality of the solution near the wall. Alternatively, a good description of the flow can be obtained by using a continuous series of modest length m, plus one higher order term n, which is important only in the wall region. A guide to selecting n can be found by investigating the axial momentum equation (3) at the wall. Rewriting equation (3) in terms of dimensionless variables with $\eta = 1$ we have

$$\frac{R^2}{4\mu \bar{w}} \frac{dP}{dz} = \left[\left(\frac{\mathrm{Re}_r}{2} + 1\right) \frac{\partial}{\partial \eta} \frac{w}{\bar{w}} + \frac{\partial^2}{\partial \eta^2} \frac{w}{\bar{w}}\right]_{\eta=1} \tag{12}$$

In the case of pressure recovery, the term on the left-hand side is greater than zero and, thus, so must be the sum of the terms on the right-hand side. When flow reversal occurs, for the condition $|\mathrm{Re}_r| \gg 1$, with Re_r negative, both the slope and the curvature of the velocity profile are positive at the wall. Thus, the first term on the right-hand side of equation (12) is negative and the second is positive. To balance the pressure gradient, the sum must be positive. If term n controls the behavior at the wall, then a_n must be positive to give positive slope and equation (12) may be written as a condition for this dominant term

$$\left(\frac{\mathrm{Re}_r}{2} + 1\right)\left(\frac{\partial}{\partial \eta} \eta^{n-1}\right)_{\eta=1} + \left(\frac{\partial^2}{\partial \eta^2} \eta^{n-1}\right)_{\eta=1} > 0 \tag{13}$$

Large negative values of Re_r require large n to satisfy this inequality. One can rewrite the inequality as a condition for selecting the higher order term

$$n > 1 - \frac{\mathrm{Re}_r}{2} \tag{14}$$

The values calculated for $\partial P/\partial z$ near the wall are sensitive to the choice made for the highest order term in the velocity profile series. Experience has shown that the best wall description, i.e., the smallest radial variation in $\partial P/\partial z$, is obtained with a value of n equal to the minimum specified by equation (14). If this term is not included, the procedure may, in the worst case, fail to converge to a solution. For obtaining a high-quality solution it is usually sufficient, for large negative values of Re_r, to choose the terms in equation (8) according to $i = 1, 2, \ldots, m, n$ where n is the smallest integer that satisfies equation (14) and m is of the order of 5 to 10.

3 Condenser Pressure Recovery

It is convenient to define certain integral performance measures as an aid in comparing experimental measurements of condenser pressure recovery and the predictions of the laminar analysis. Averaging the momentum equation (3) over the cross section we get

$$\frac{dP}{dz} = -\frac{d}{dz}(\beta \rho \bar{w}^2) - \frac{f \rho \bar{w}^2}{R} \tag{15}$$

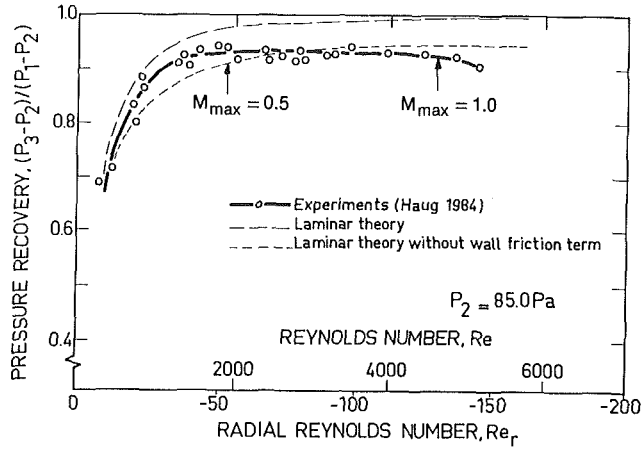

Fig. 3 Comparison between measured pressure recovery in a heat pipe and laminar theory: L_e = 210 mm; L_a = 150 mm; L_c = 210 mm; R = 23.8 mm

where the momentum factor β is defined as the average of $(w/\bar{w})^2$ over the cross section

$$\beta = \int_0^1 (w/\bar{w})^2 d\eta \tag{16}$$

and f is the Fanning friction factor

$$f = -\frac{8}{\mathrm{Re}(z)}\left(\frac{\partial}{\partial\eta}\frac{w}{\bar{w}}\right)_{\eta=1} \tag{17}$$

The average axial velocity $\bar{w}$ may be written in the form of an average Mach number

$$\bar{\mathrm{M}} = \frac{\bar{w}}{c} \tag{18}$$

For the case of constant radial Reynolds number $\mathrm{Re}_{r,c}$, equation (15) can be integrated from the condenser inlet at $z = z_3'$ to the end of the condenser at $z = z_3$ (see Fig. 1) to give the following expression for the condenser pressure rise

$$\frac{P_3 - P_3'}{P_3'} = \bar{\mathrm{M}}_3'^2\left(\beta_3' + \frac{\varphi_c}{8\mathrm{Re}_{r,c}}\right) \tag{19}$$

with the condenser wall friction parameter defined as

$$\varphi_c = \frac{2}{\bar{\mathrm{M}}_3' L_c}\int_{z_3'}^{z_3} f\,\mathrm{Re}(z)\bar{\mathrm{M}}dz \tag{20}$$

The wall friction parameter is a weighted average of (f Re) over the length of the condenser. For fully developed, incompressible, laminar flow in the absence of condensation $\varphi_c = f\,\mathrm{Re} = 16$. The two terms in the parentheses in equation (19) represent the contributions to pressure recovery of the inflowing momentum flux and the wall friction, respectively. β_3' is always positive but φ_c may be either positive or negative. For large $|\mathrm{Re}_{r,c}|$ and laminar flow, flow reversal will occur so at the wall $\partial(w/\bar{w})/\partial\eta$ will be positive and, from equation (17), f and thus φ_c will be negative.

The computer code AGATHE was employed, using the discontinuous series approximation in the condenser section, to analyze the heat pipe used by Haug (1984) in his measurements of pressure recovery. The cylindrical heat pipe, which contained dodecane as the working fluid, had the following geometry: L_e = 210 mm, L_a = 150 mm, L_c = 210 mm, and R = 23.8 mm. Water loops were used for heating and cooling the heat pipe. The vapor pressure was measured at the beginning of the evaporator (P_1), in the middle of the adiabatic zone (P_2), and at the end of the condenser (P_3) (see Fig. 1) at various heat flows and P_2 values. A description of the experiment and summary of the results have recently been presented (Haug and Busse, 1985). The relative pressure recovery is stated as the ratio of the pressure rise between the

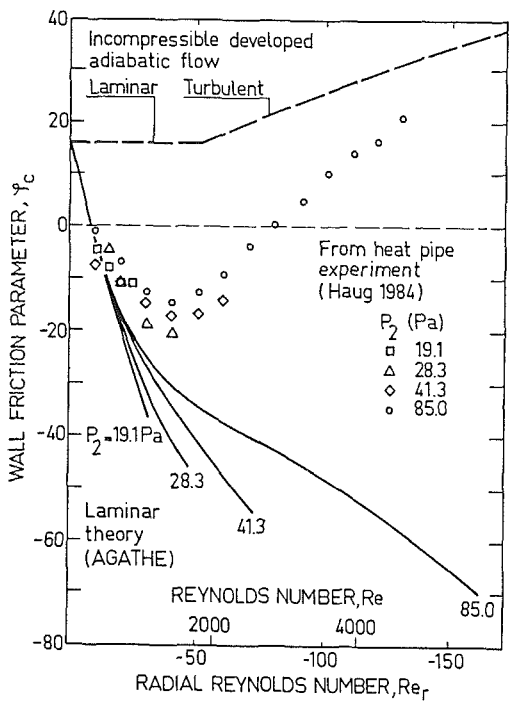

Fig. 4 Comparison between experimental wall friction parameter for the heat pipe condenser and laminar theory

center of the adiabatic section and the end of the condenser to the pressure drop from the beginning of the evaporator to the center of the adiabatic section. Haug presented his data as plots of the relative pressure recovery over an average radial Reynolds number, which by equation (5) is related to the axial Reynolds number at the entrance to the condenser, Re, by a constant determined by the condenser geometry ($\mathrm{Re} = -4L_c\mathrm{Re}_{r,c}/R$). Re itself was calculated from the measured total heat input rate to the evaporator. The experiment was designed and operated such that the axial variation of the radial Reynolds number in both the evaporator and the condenser was relatively small. In the present analysis, therefore, Re_r is considered as constant.

The measured data points shown in Fig. 3 are for a range of radial Reynolds numbers, with the pressure P_2 in the center of the adiabatic zone held constant. The data taken at other pressure levels follow essentially the same curve provided that the maximum Mach number (occurring on the centerline at the condenser inlet) is less than one. For higher Mach numbers the pressure recovery drops as additional losses from compression shocks come into play.

The pressure recovery predicted by the laminar model described previously lies above the measured recovery but approaches the measured recovery as $\mathrm{Re}_{r,c}$ approaches zero. A plausible explanation is that the condenser is operating in a regime of transition from laminar to turbulent flow and that the extent of the influence of turbulence increases with an increase in the magnitude of the Reynolds number. Referring to equation (19) one can see that the influence of the state of the flow, i.e., whether laminar or turbulent, on pressure recovery in the condenser is restricted to the φ_c term. An empirical wall-friction parameter may be deduced from the difference between the experimental data and the theoretical curve calculated for $\varphi_c = 0$ from equation (19) and a laminar-flow analysis of the evaporator and the adiabatic zone. Data points calculated in this way are plotted in Fig. 4. The different symbols are for different experimental runs made at different pressures in the center of the adiabatic zone. Only points for subsonic flow are plotted. The solid curves shown in Fig. 4 are the calculated values of φ_c' for laminar flow in the condenser at the various pressures of the experiment. These curves start

at $\varphi_c = f\,\mathrm{Re} = 16$ for $\mathrm{Re}_{r,c} = 0$ and decrease with decreasing $\mathrm{Re}_{r,c}$. Negative values of φ_c indicate finite sections of backflow at the wall and net positive contribution of the viscous force to pressure recovery.

A comparison between the measurements and the prediction of laminar theory indicates that the flow in the condenser is laminar at low $|\mathrm{Re}_{r,c}|$ but that transition to turbulent flow occurs within the condenser for $\mathrm{Re}_{r,c} \leq -6$ to -10. This conclusion is consistent with the experimental results of Quaile and Levy (1975) for flow of a single-phase fluid in a porous tube with suction. The fact that the axial Reynolds number at the inlet to the condenser was only 280 at the onset of transition indicates the strongly destabilizing effect of condensation on the vapor flow in a tube.

Figure 4 shows that significant reverse flow at the condenser wall also first appears at $-6 \geq \mathrm{Re}_{r,c} \geq -10$, giving rise to a positive contribution of wall shear to pressure recovery (φ_c negative). The range of significant backflow extends to $\mathrm{Re}_{r,c} \approx -80$. For $\mathrm{Re}_{r,c} < -80$, φ_c becomes positive again showing that turbulent momentum transfer is then sufficient to prevent significant backflow.

The broken line segments in Fig. 4 show for reference purposes the φ_c based on wall friction for a smooth cylindrical pipe with incompressible, fully developed flow without condensation. The laminar part is independent of Reynolds number ($f\,\mathrm{Re}(z) = 16$) while for turbulent flow $f\,\mathrm{Re}(z) = 0.078\,(\mathrm{Re}(z))^{3/4}$ and $\varphi_c \sim \mathrm{Re}^{3/4}$. The predicted laminar flow results for the condenser start at this line at $\mathrm{Re}_{r,c} = 0$ and fall with decreasing $\mathrm{Re}_{r,c}$. The experimental data follow this trend but then, for $\mathrm{Re}_{r,c} \lesssim -40$, turn up toward the broken line for turbulent pipe flow.

Although it is reasonable to expect that the value for fully developed, laminar pipe flow should be approached as $\mathrm{Re}_{r,c} \to 0$, it is not clear that the fully developed turbulent flow line will be an appropriate limit as $\mathrm{Re}_{r,c} \to -\infty$. In fact, calculations of fully developed turbulent flow (Kinney and Sparrow, 1970; Yeroshenko et al., 1984) have indicated that even small amounts of wall suction can dramatically increase the friction factor above that for flow in a tube with an impermeable wall. This conclusion is supported by the results of experiments with turbulent air flow through a porous tube with suction (Aggarwal et al., 1972). According to these experiments, φ_c should approach $K|\mathrm{Re}_{r,c}|$ in a fully turbulent condenser at high $|\mathrm{Re}_{r,c}|$ with K approximately equal to 2.8. The data points plotted in Fig. 4 not only fall well below this limit, but they also fall below the much lower limit, shown in Fig. 4, for turbulent flow without condensation or suction. This fact may be interpreted as indicating that the flow entering the condenser is laminar (or at least not fully turbulent) even at the highest Reynolds number of the experiments and that turbulence develops in the flow direction. At even higher Reynolds numbers, φ_c may rise above the level for adiabatic, developed turbulent flow, but, for the relatively short condenser used in the experimental heat pipe ($L_c/R = 8.8$), φ_c will probably remain below the level for developed flow with suction as long as the entering flow is laminar.

4 Conclusions

The numerical method for analyzing the vapor flow in a cylindrical heat pipe described by Busse and Prenger (1984) has been extended for use in analyzing condensers under conditions including strong flow reversal. The extension involves the use of a noncontinuous power series to describe the velocity profile. Criteria are presented for selecting the terms in the series to ensure that an approximate solution to the governing boundary-layer equations is obtained and that it is a good approximation. The resulting method for predicting laminar subsonic condensing flows is simple, fast, and requires only modest computing facilities.

The onset of turbulence at $\mathrm{Re}_{r,c} \approx -6$ at axial Reynolds numbers of only a few hundred is confirmed. It coincides with the appearance of significant flow reversal. Turbulence tends to eliminate flow reversal and to decrease pressure recovery.

For a prediction of subsonic recovery in the turbulent regime, an empirical wall-fraction parameter φ_c can be used. More experimental data are needed to generalize the method for condenser length to diameter ratios other than 4.4.

Acknowledgments

The authors gratefully acknowledge the contribution of J. Ligthart who assisted with the numerical calculations.

References

Aggarwal, J. K., Hollingsworth, M. A., and Mayhew, Y. R., 1972, "Experimental Friction Factors for Turbulent Flow With Suction in a Porous Tube," *Int. J. Heat Mass Transfer*, Vol. 15, pp. 1585–1602.

Berman, A. S., 1958, "Effects of Porous Boundaries on the Flow of Fluids in Systems With Various Geometries," *Proc. Int. Conf. on the Peaceful Uses of Atomic Energy*, Vol. 4, pp. 351–358.

Bourgarel, M., 1966, "Contributions to the Study of Flow at the Entrance of a Porous Cylindrical Tube With Suction" [in French], *Publications Scientifiques et Techniques du Ministere de l'Air*, No. 430.

Busse, C. A., 1967, "Pressure Drop in the Vapour Phase of Long Heat Pipes," *IEEE Conf. Record of the Thermionic Conversion Specialist Conf.*, Palo Alto, CA, pp. 391–398.

Busse, C. A., 1973, "Theory of the Ultimate Heat Transfer Limit of Cylindrical Heat Pipes," *Int. J. Heat Mass Transfer*, Vol. 16, pp. 169–186.

Busse, C. A., and Kemme, J. E., 1980, "Dry-out Phenomena in Gravity-Assist Heat Pipes With Capillary Flow," *Int. J. Heat Mass Transfer*, Vol. 23, pp. 643–654.

Busse, C. A., and Prenger, F. C., 1984, "Numerical Analysis of the Vapour Flow in Cylindrical Heat Pipes," *Proc. 5th Int. Heat Pipe Conf.*, Part I, JATEC, Tokyo, Japan, pp. 214–219.

Busse, C. A., 1987, "On the Development of Laminar Internal Flows With Mass Injection and Extraction," ASME *J. of Fluids Engineering*, Vol. 109, pp. 448–452.

Cotter, T. P., 1965, "Theory of Heat Pipes," Report No. LA-3246-MS.

Dunn, P. D., and Reay, D. A., 1982, *Heat Pipes*, Pergamon Press.

Faghri, A., 1987, "Analysis of the Effects of Vapor Pressure Drop on the Performance of the Double-Walled Concentric Heat Pipe," *6th Int. Heat Pipe Conf.*, Grenoble, May 25–29, Vol. 1, pp. 136–143.

Haug, F., 1984, "Druckrückgewinn in einem zylindrischen Wärmerohr bei hohen radialen Reynoldszahlen und hohen Machzahlen," Dr. Ing. Dissertation, Univ. Stuttgart, Federal Republic of Germany.

Haug, F., and Busse, C. A., 1985, "Pressure Recovery in a Cylindrical Heat Pipe at High Radial Reynolds Numbers and at High Mach Numbers," AIAA Paper No. 85-0980.

Hornbeck, R. W., 1963, "Laminar Entry Problem in Porous Tube," *Physics of Fluids*, Vol. 6, pp. 1649–1654.

Huesmann, K., and Eckert, E. R. G., 1968, "Investigation of Laminar Flow and the Transition to Turbulence in Porous Tubes With Uniform Injection through the Wall" [in German], *Wärme- und Stoffübertragung*, Vol. 1, pp. 2–9.

Kinney, R. B., and Sparrow, E. M., 1970, "Turbulent Flow, Heat Transfer and Mass Transfer in a Tube With Surface Suction," ASME JOURNAL OF HEAT TRANSFER, Vol. 92, pp. 117–125.

Quaile, J. P., and Levy, E. K., 1975, "Laminar Flow in a Porous Tube With Suction," ASME JOURNAL OF HEAT TRANSFER, Vol. 97, pp. 66–71.

Schlichting, H., 1979, *Boundary-Layer Theory*, 7th ed., McGraw-Hill, New York.

Weissberg, H. L., 1959, "Laminar Flow in the Entrance Region of a Porous Pipe," *Physics of Fluids*, Vol. 2, pp. 510–516.

Yeroshenko, U. M., Yershov, A. V., and Zaichik, L. I., 1984, "Heat Transfer for Turbulent Flow in a Circular Tube With Uniform Suction or Injection," *Int. J. Heat Mass Transfer*, Vol. 27, pp. 1197–1203.

B. L. Bhatt
Mem. ASME

G. L. Wedekind
Mem. ASME

Oakland University,
Rochester, MI 48063

K. Jung
Software Support Corporation,
Birmingham, MI

Effects of Two-Phase Pressure Drop on the Self-Sustained Oscillatory Instability in Condensing Flows

This paper presents the results of an extension of an experimental and theoretical investigation of an unstable flow phenomenon that leads to self-sustained limit-cycle-type oscillations of large amplitude, and which, under certain conditions, can involve flow reversals. The influence of two-phase pressure drop is examined and shown to have a stabilizing effect on the instability. Inclusion of the two-phase pressure drop as part of the downstream throttling allows the utilization of a previously developed linearized analysis, based on the system mean void fraction model, to predict successfully the experimentally observed stability boundary.

Introduction

This paper is concerned with horizontal in-tube condensing flows involving complete condensation in which the condensate completely fills the tube at the outlet. The stability of such flows is important in many energy conversion processes, including reheat, reboiler, and submerged evaporator systems associated with nuclear or conventional power plants. A sufficiently large excursion, or oscillation, could affect the performance of the processes taking place within these devices, cause damage to the mechanical equipment, and endanger the safety of such systems. For example, large oscillations in the subcooled liquid column at the end of the condensation process, including the possibilities of flow reversals, are likely to be associated with large impulse loads that may cause substantial damage to piping and various components involved in the overall system.

The condensation-induced instabilities are also known to have a dramatic effect during the bypass phase of the PWR loss of coolant accident (Lahey and Drew, 1980; Block, 1980). They are also associated with countercurrent (reflux) and cocurrent condensation inside the steam generator tubes of the PWR during a small break (without scram) loss of coolant accident (Calia and Griffith, 1981). Steam chugging within the condensation pipes of a pressure suppression system of a BWR (Pitts, 1980; Wang et al., 1981) is also due to condensation-induced instabilities. They might also be of importance in ocean thermal energy conversion systems, space power generation, and a host of other applications in refrigeration/air-conditioning and chemical process industries. The dynamic characteristics of condensing flows may be categorized into two classes. The first is the result of externally forced changes in a particular input variable, and the second is a phenomenon of internally induced self-sustained oscillations of large amplitude. For example, under the first category, externally forced small flow changes in the inlet vapor flow rate would result in very large surges in outlet liquid flow rate (Wedekind and Bhatt, 1977; Bhatt and Wedekind, 1980a), subcooled liquid temperature, condensing pressure, system pressure drop (Wedekind et al., 1986), and a variety of other system variables. Under the second category, the self-sustained oscillations are internally induced solely by the processes taking place within the condensing flow system and aided or hindered by the coupling that exists between the condenser and other system components. As the name implies, these oscillations are self-sustained and may come about without any external impetus. They represent a particular unstable mode of operation when the steady-state parameters of the condensing flow process assume some specific values. Once the condenser is left to itself at this operating level, one may see an initiation, a growth, and finally a limit-cycle type of sustained oscillations of a very large amplitude, including the possibility of flow reversals. More details are given in the authors' previous work (Bhatt and Wedekind, 1980b).

A systematic study of the sustained oscillatory condensing flow instability from a fundamental perspective led to the establishment of a number of physical mechanisms and parameters for the occurrence of this type of flow behavior (Bhatt and Wedekind, 1980b). These parameters include the condenser heat flux, liquid–vapor density ratio, downstream liquid inertia, upstream vapor volume, and upstream and downstream flow resistances. The experimentally observed linear stability boundary and the nonlinear limit cycle behavior were predicted by a comparatively simple, integrally formulated, system mean void fraction model. The above study represented an investigation of many of the fundamental mechanisms for the occurrence of instability. However, the effects of two-phase pressure drop were not considered. In that earlier work, it was observed that for a constant flow rate, one of the methods used for stabilizing the condenser was to increase the throttling in the subcooled liquid at the outlet of the condenser. Subsequently, however, it has also been experimentally observed that for a given constant heat flux and a constant outlet throttling, the condenser can operate in an unstable mode over a range of flow rates. Increasing the inlet vapor flow rate from a low value to a higher value has the effect of attenuating the amplitude of the self-sustained oscillations until a flow rate is achieved at which the condenser stabilizes. Experimental data representing such characteristics are depicted in Fig. 1 for two different test sections. The progression toward stability, for each case, is quite apparent. In each case, the experimentally observed stabilization could not be explained solely on the basis of outlet throttling, which was constant. Also, it could not be explained solely on the basis of a reduction in the outlet liquid inertia, due to the increase in the length of the two-phase region associated with an increased inlet flow rate. Furthermore, a comparison between the two tests, obtained for

Contributed by the Heat Transfer Division and presented at the 4th Miami International Symposium on Multi-phase Transport and Particulate Phenomena, Miami Beach, Florida, December 15–17, 1986. Manuscript received by the Heat Transfer Division March 9, 1987. Keywords: Condensation, Multiphase Flows, Transient and Unsteady Heat Transfer.

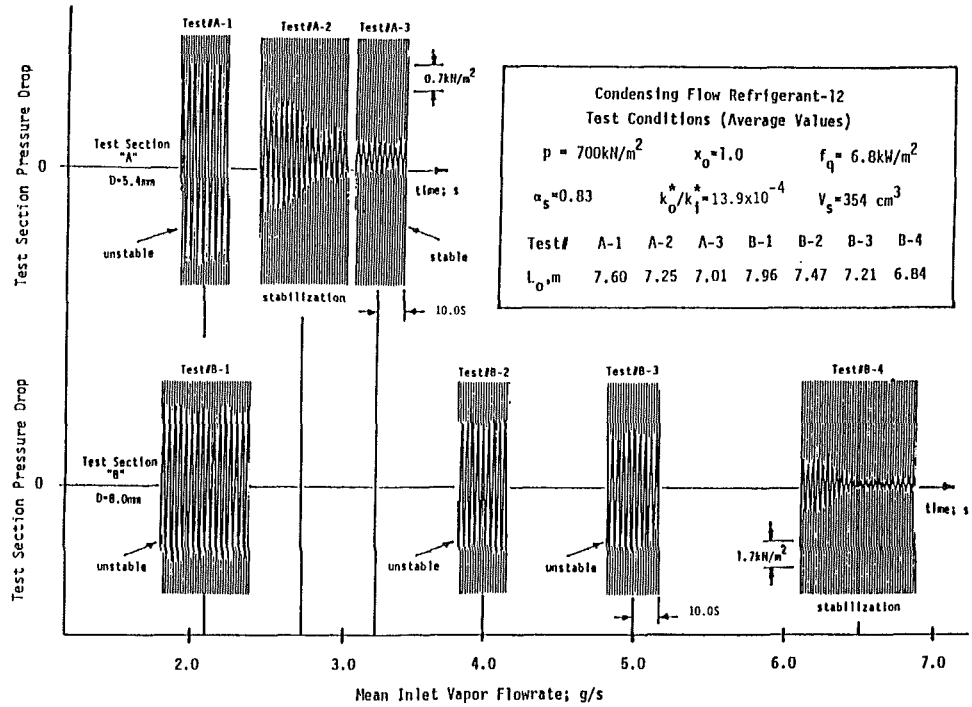

Fig. 1 Experimentally measured condensing flow instabilities: influence of inlet vapor flow rate

almost the same outlet throttling, reveals that the smaller diameter test section stabilizes at a lower flow rate than is the case for the larger diameter test section. Therefore, it would appear that the only logical mechanism that might explain the above experimentally observed stabilization would be the pressure drop in the two-phase region.

In view of the above, the primary focus of this paper is to study the effects of two-phase pressure drop on the self-sustained oscillatory flow phenomen. A numerical simulation of the set of nonlinear governing equations representing the theoretical model, including the effects of various pressure drop components, will be carried out. It will be shown that the

Nomenclature

A_t = total cross-sectional area of tube, m²
D = inside diameter of tube, m
f = single-phase friction factor, equation (18)
f_q = spatially averaged heat flux, W/m²
G = local total mass flux, g/m² • s
h = enthalpy of saturated liquid, J/kg
h' = enthalpy of saturated vapor, J/kg
k_i, k_o = inlet and exit orifice coefficients, $\Delta p/\rho_a' v^2$ and $\Delta p/\rho v^2$, respectively
k_i^* = linearized valve resistance at inlet = $2(k_i/\rho_a' A_t^2)m$, kN s/m² • g
k_0^* = linearized valve resistance at outlet = $2(k_o/\rho A_t^2)\ m$, kN s/m² • g
k_1 = parameter, equation (20)
k_o' = modified outlet orifice coefficient, equation (27)
L = total length of the condenser plus the length of piping between the outlet of condenser and inlet of the liquid receiver, m
L_o = $(L - \bar{\eta})$, m
$m_L(t)$ = $m(z, t)_{z=L} = m(z, t)_{z=\eta(t)}$, g/s
$m_o(t)$ = $m(z, t)_{z=0}$, g/s
$m_s(t)$ = total mass flow rate at inlet of upstream compressible volume, g/s
$m(z,t)$ = local instantaneous total mass flowrate of fluid, g/s
N_c,N_i = dimensionless numbers, equation (29)
N_o = dimensionless number, equation (30)
P = inside perimeter of tube = πD, m
Δp = pressure drop, kN/m²
p_c = pressure at inlet of condenser, kN/m²
p_f = pressure at point of complete condensation, kN/m²
p_i = pressure upstream of inlet throttling valve, kN/m²
p_o = pressure downstream of outlet throttling valve, kN/m²
r = dimensionless quantity, equation (16)
t = time, s
V_s = volume of vapor upstream of two-phase region, m³
V' = $(V_s + A_t\alpha_s\bar{\eta})$, m³
x = nonfluctuating flow quality
z = spatial coordinate in the axial direction, m
α_s = system mean void fraction
γ = $d\rho'/dp$ = vapor compressibility, g/m•kN
$\bar{\eta}$ = steady-state position of the effective point of complete condensation, m
$\eta(t)$ = effective point of complete condensation, m
μ = viscosity of liquid, N•s/m²
ξ = dimensionless spatial coordinate in axial direction = $z/\eta(t)$
ρ = density of saturated liquid, kg/m³
ρ' = density of saturated vapor, kg/m³
ρ_a' = density of saturated vapor at the average pressure across the upstream throttle valve, kg/m³
τ_c = time constant of condensing flow system, equation (11), s
ϕ = two-phase friction multiplier

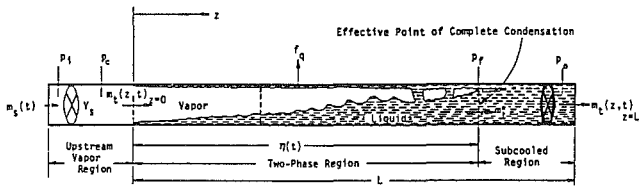

Fig. 2 Schematic of horizontal condensing flow system with upstream vapor region, upstream throttling, and downstream throttling

results of the numerical simulation are characteristically similar to these observed experimentally. A linearized version of the model, including the effects of two-phase pressure drop, will also be presented and shown to agree with the experimental data. Furthermore, the relationship of the instability under investigation to the well-known instabilities encountered in evaporating flows will also be discussed.

Theoretical Analysis

The theoretical analysis for this study of unstable condensing flows is an extension of one presented by Bhatt and Wedekind (1980). In this formulation, the concept of a system mean void fraction is used in conjunction with an integral formulation of the momentum principle, the conservation of mass, and the energy principles for the various regions of the condenser.

Figure 2 is a basic representation of the condensing flow system. The two-phase region in which this condensation takes place may vary in length depending on the transient conditions within the system.

In the theoretical development that follows, each region of the condenser, namely upstream vapor region, two-phase region, and the subcooled liquid region, will be analyzed in order.

Upstream Vapor Region. For simplicity, the vapor is assumed to be saturated and at the inlet condenser pressure $p_c(t)$. It is assumed to occupy a constant volume V_s, throughout which the density ρ' is uniform but time varying.

Pressure Drop Across the Inlet Throttling Valve. This is represented in terms of an inlet valve coefficient k_i as

$$P_i - p_c(t) = \frac{k_i}{\rho_a' A_t^2} m_s^2(t) \tag{1}$$

where p_i is invariant with time.

Conservation of Mass. The conservation of mass principle when applied to the upstream vapor region yields

$$V_s \frac{d\rho'}{dt} = m_s(t) - m_o(t) \tag{2}$$

Compressibility of Vapor. For small changes in the condenser pressure $p_c(t)$, the vapor density ρ' can be related to it by the equation of state

$$\rho' = \rho'_{t=0} + \gamma[p_c(t) - p_c(t)_{t=0}] \tag{3}$$

Two-Phase Region. The model for this region is built around the following assumptions:

1. System mean void fraction is assumed to be invariant with time.
2. Random fluctuations due to the stochastic nature of the two-phase flow process are assumed not to influence the deterministic transients.
3. Viscous dissipation, longitudinal heat conduction, and changes in kinetic energy are neglected.
4. The specific enthalpies and density of the liquid are considered to be saturated properties, independent of both axial position and time, and evaluated at the mean system pressure.
5. The density of the vapor phase is allowed to be a function of time, and assumed to be uniform and equal to the density of vapor in the upstream vapor region at all times.
6. The spatially averaged heat flux, for the entire two-phase region, is assumed to be invariant with time.
7. Transverse distribution of velocities and pressure within each phase is assumed to be uniform.

The implication of the time invariance of the system mean void fraction is that the concept of similarity (Wedekind and Bhatt, 1977; Wedekind et al., 1978) holds. In addition, the concept of similarity is extremely useful in the integration of the friction and inertia components of the transient pressure drop, leading to a closed-form solution for these components. The details of this analysis are presented by Wedekind et al. (1986). Only a summary of this analysis, relevant to the objectives of this paper, is presented below.

Momentum Principle. An application of the transient momentum principle in an integral form, to liquid and vapor within the two-phase region, leads to the following:

$$p_c(t) - p_f(t) = \Delta p_{\substack{2\phi, F}}(t) + \Delta p_{\substack{2\phi, M}}(t) + \Delta p_{\substack{2\phi, I}}(t) \tag{4}$$

The three terms on the right represent transient two-phase pressure drop due to friction, momentum, and inertia, respectively. Each one of these components will be considered in order.

It has become standard practice to represent the two-phase friction pressure drop in terms of a single-phase pressure drop for the total flow considered as liquid (Collier, 1972); thus

$$\Delta p_{\substack{2\phi, F}}(t) = \frac{2}{\rho D} \int_{z=0}^{\eta(t)} f\phi G^2(z, t) dz \tag{5}$$

For a uniform heat flux, the flow quality distribution, for an inlet quality of unity, can be represented by a linear function of z (Wedekind and Bhatt 1977; Wedekind et al., 1986); thus

$$x(z, t) = 1 - [z/\eta(t)] \tag{6}$$

Substitution of this equation into equation (5) changes the spatial integration to one involving flow quality, which is more convenient, as will be explained later; thus

$$\Delta p_{\substack{2\phi, F}}(t) = \frac{2\eta(t)}{\rho D} \int_{x=0}^{1} f\phi G^2 dx \tag{7}$$

where f is a single-phase friction factor for the total flow considered to be liquid, and $\phi = \phi(x, G)$ is the two-phase friction multiplier. $G = G(z, t)$ is the local mass flux within the two-phase region.

For an inlet flow quality of unity, the momentum pressure drop within the two-phase region, accounting for the moving boundary, $\eta(t)$, is given by

$$\Delta p_{\substack{2\phi, M}}(t) = \frac{1}{A_t}\left\{\left[\frac{1}{\rho} - \left(\frac{A_t}{m_L}\right)\frac{d\eta(t)}{dt}\right]\frac{m_L^2(t)}{A_t}\right\}_{z=\eta(t)} - \frac{1}{A_t^2\rho'} m_o^2(t) \tag{8}$$

The first term on the right-hand side represents the instantaneous momentum flux per unit area at the point of complete condensation relative to the tube. The second term represents the momentum flux per unit area at the entrance into the two-phase region.

The inertia pressure drop may be represented by

$$\Delta p_{\substack{2\phi, I}}(t) = \frac{d}{dt}\int_{z=0}^{\eta(t)} \frac{m(z, t)}{A_t} dz = \frac{d}{dt}\int_{z=0}^{\eta(t)} G(z, t) dz \tag{9}$$

The above expression represents the time rate of change of the integrated local momentum of the fluid per unit area within the two-phase region.

An examination of equations (4)–(9) indicates that in order to be able to determine the transient two-phase pressure drop, it is important to know the time-dependent local mass flux $G(z, t)$, the time-dependent motion of the effective point of complete condensation $\eta(t)$, and the response of the outlet liquid flow rate $m_L(t)$. To obtain this information, the concept of a time-invariant system mean void fraction, together with the conservation of mass and energy principles, was utilized. In addition, information regarding the two-phase friction multiplier $\phi(x, z)$, and the single phase friction factor f, is required.

Implicit in the above approach is the assumption that only a weak coupling exists between the transient form of momentum principle and the conservation of mass and energy. Therefore, independent solutions of the conservation of mass and energy principles, when incorporated into the momentum principle, should yield the prediction of the transient pressure drop. Such an approach has been followed for transient evaporating flows (Inayatullah and Nicoll, 1975, 1976; Hemphill et al., 1976). It is assumed that the same approach is valid for transient condensing flows.

Conservation of Mass and Energy. The combined conservation of mass and energy equations for the two-phase region in conjunction with the conservation of mass in the upstream vapor region, equation (2), leads to the governing differential equation for the effective point of complete condensation (Bhatt and Wedekind, 1980)

$$\frac{d\eta(t)}{dt} + \frac{1}{\tau_c}\eta(t) = \frac{m_s(t)}{\rho'\alpha_s A_t} - \left[\frac{V_s + A_t\alpha_s\eta(t)}{A_t\alpha_s\rho'}\right]\frac{d\rho'}{dt} \tag{10}$$

where τ_c is the condenser system time constant given by

$$\tau_c = \frac{A_t\,\alpha_s\,\rho'\,(h' - h)}{f_q P} \tag{11}$$

The conservation of mass equation for the whole condenser is given by (Bhatt and Wedekind, 1980)

$$m_L(t) = m_s(t) + (\rho - \rho')A_t\alpha_s\frac{d\eta(t)}{dt} - [V_s + A_t\,\alpha_s\eta(t)]\frac{d\rho'}{dt} \tag{12}$$

Substitution of equation (12) into equation (10) leads to an alternative form of equation (10) governing the effective point of complete condensation $\eta(t)$; thus

$$\frac{d\eta(t)}{dt} + \left(\frac{\rho'}{\rho}\right)\frac{1}{\tau_c}\eta(t) = \frac{1}{A_t\,\alpha_s\,\rho}\,m_L(t) \tag{13}$$

This form is convenient, as will be shown later.

Also, if equations (13) and (2) are substituted into equation (12), the vapor flow rate at the entrance to the two-phase region $m_o(t)$ is given by

$$m_o(t) = \frac{1}{\left[1 + \dfrac{A_t\,\alpha_s\,\eta(t)}{V_s}\right]}\left[\frac{A_t\,\alpha_s}{\tau_c}\left(\frac{\rho'}{\rho}\right)(\rho - \rho')\eta(t) + \left(\frac{\rho'}{\rho}\right)m_L(t) + \left(\frac{A_t\,\alpha_s}{V_s}\right)\eta(t)m_s(t)\right] \tag{14}$$

Local Mass Flux. The distribution of the local mass flux within the two-phase region is required for the evaluation of both the friction and the inertia pressure drop, as indicated in equations (7) and (9). An application of the conservation of mass and energy to a fixed subsystem, shown by the broken boundary within the two-phase region in Fig. 2, leads to the following equation (Wedekind et al., 1986):

$$G(z, t) = \frac{m_o(t)\{1 - r[z/\eta(t)]\}}{A_t(\rho'/\rho)\{1 + [(\rho/\rho') - 1]x\}} \tag{15}$$

where

$$r = \left[1 - \left(\frac{\rho'}{\rho}\right)\right]\frac{f_q\,P}{(h' - h)}\left\{\frac{\eta(t)}{m_o(t)}\right\} \tag{16}$$

In the derivation of equation (15), it was assumed that the compressibility effects do not affect the local mass flux distribution and they were accordingly ignored.

Evaluation of Pressure Drops. As indicated earlier, the solution to the conservation of mass and energy equations when substituted into the transient form of the momentum principle will yield the pressure drop response. Each component of the pressure drop will again be considered in order.

In the evaluation of the two-phase friction pressure drop from equation (7), it is necessary to have knowledge of the distribution of the two-phase friction multiplier, $\phi(x, t)$. The correlation proposed by Izumi et al. (1974) appears to represent the data well for both adiabatic and condensing flows involving Refrigerant-12 (Wedekind et al., 1986). In terms of the flow quantity, the two-phase friction multiplier is given by

$$\phi = 1.515(1 - x)^{0.18}\{1 + [(\rho/\rho')^{2/3} - 1]x\}^{1.57} \tag{17}$$

The single-phase friction factor f is assumed to be given by the Blausius formula for turbulent flow through smooth tubes; thus

$$f = \frac{0.079}{\left(\dfrac{GD}{\mu}\right)^{1/4}} \tag{18}$$

It is assumed that the form of ϕ and f during a transient is the same as in the steady state. However, both these quantities are dependent upon the local mass flow rate and flow quality, which are a function of both position and time during a transient.

Substitution of equations for f, ϕ, and G into equation (7) and the evaluation of the integral leads to the two-phase friction pressure drop. This necessitates a numerical integration. For details see Roslund (1981). However, if the concept of similarity (Wedekind and Bhatt, 1977; Wedekind et al., 1986) is extended further and the variable of integration is transformed into a similarity variable $\xi = z/\eta(t)$, then equation (7) yields a closed-form solution (Wedekind et al., 1986). For $r \simeq 1.0$, the solution is simplified even further yielding

$$\underset{2\phi,\,F}{\Delta p}\,(t) = k_1\eta(t)m_o^{1.75}(t) \tag{19}$$

where the constant k_1 is a function of fluid properties and flow geometry and is expressed as[1]

$$k_1 = \left(\frac{0.0696}{\rho D}\right)\left(\frac{\mu}{D}\right)^{0.25}[1 + (\rho/\rho')^{0.67}]^{1.57}\,(1/A_t)^{1.75} \tag{20}$$

It is interesting to note that a direct dependence of pressure drop on the condensing length has also been observed by Goodykuntz and Dorsch (1967).

Substitution of equation (13) into equation (8) leads to the following expression for the momentum pressure drop:

$$\underset{2\phi,\,M}{\Delta p}\,(t) = \left(\frac{1}{\rho A_t^2}\right)\left(\frac{\alpha_s - 1}{\alpha_s}\right)m_L^2(t) + \left(\frac{1}{A_t}\right)\left(\frac{\rho'}{\rho}\right)\frac{\eta(t)}{\tau_c}\,m_L(t) - \frac{1}{\rho' A_t^2}\,m_o^2(t) \tag{21}$$

Substitution of the mass flux from equation (15) into equation (9) and following a similar procedure as outlined for evaluation of the friction pressure drop, again for $r \simeq 1.0$, leads to the following expression:

$$\underset{2\phi,\,I}{\Delta p}\,(t) = \frac{1}{A_t}\left\{m_o(t)\frac{d\eta(t)}{dt} + \eta(t)\frac{dm_o(t)}{dt}\right\} \tag{22}$$

[1]For $(\rho/\rho') \gg 1$, $[1 + (\rho/\rho')^{0.67}]^{1.57} \approx (\rho/\rho')^{1.05}$.

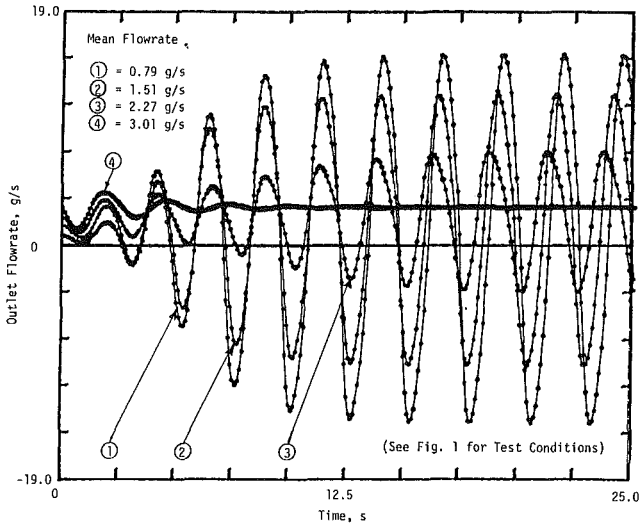

Fig. 3 Digital simulation of flow instability in 5.4 mm test section

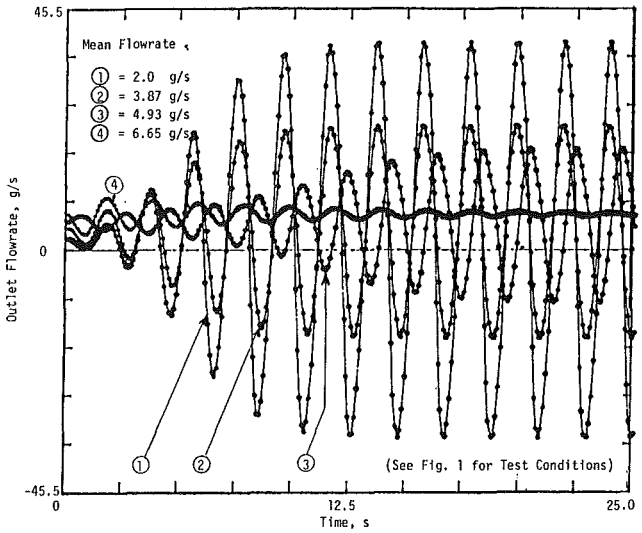

Fig. 4 Digital simulation of flow instability in 8.00 mm test section

The total two-phase pressure drop in the two-phase region is the sum of equations (19), (21), and (22)

$$p_c(t) - p_f(t) = k_1\eta(t)m_o^{1.75}(t) + \left(\frac{1}{\rho A_t^2}\right)\left(\frac{\alpha_s - 1}{\alpha_s}\right) m_L^2(t) + \frac{1}{A_t}\left(\frac{\rho'}{\rho}\right)\frac{\eta(t)}{\tau_c} m_L(t) - \frac{1}{\rho' A_t^2} m_o^2(t) + \frac{1}{A_t}\left\{m_o(t)\frac{d\eta(t)}{dt} + \eta(t)\frac{dm_o(t)}{dt}\right\} \quad (23)$$

Wedekind et al. (1986) have shown that the above model for the pressure drop transients, due to forced changes in inlet vapor flow rate, works reasonably well as confirmed by experimental data.

Subcooled Liquid Region. In a manner similar to what was done in the two-phase region, the sum of the friction, momentum, and inertia pressure drops in the single-phase liquid is given by

$$\Delta p_{1\phi}(t) = \frac{k_o}{\rho A_t^2} m_L^2(t) + \frac{[L-\eta(t)]}{A_t}\frac{dm_L(t)}{dt} \quad (24)$$

The first term on the right represents the total single-phase frictional pressure drop including piping, fittings, valves, etc., and the second term represents the inertia pressure drop. It should be noted that the contributions to the momentum and inertia pressure drops due to the movement of the effective point of complete condensation cancel each other (Wedekind et al., 1986).

Total System Pressure Drop. The total system pressure drop consisting of the pressure drops across the upstream throttling valve, the two-phase region, and the single-phase liquid region at the outlet of the condenser must add up to a constant pressure difference between the inlet and the outlet; thus

$$p_i - p_o = \text{const} \quad (25)$$

Nonlinear Analysis

The set of governing equations for the entire condensing flow system consists of equations (1)–(3), (13), (14), (23)–(25). There are eight unknowns, namely ρ', $m_s(t)$, $m_o(t)$, $m_L(t)$, $\eta(t)$, $p_c(t)$, $p_f(t)$, and p_i or p_o, since $(p_i - p_o)$ is a known parameter. There are also eight equations. This forms a complete set. The solution to this set of equations was obtained numerically using a Runge–Kutta integration technique. The simulation needs initial steady state input values. These were chosen to correspond to the values obtained experimentally. However, in situations where the steady state condensing length $\tilde{\eta}$ could not be measured experimentally, it was obtained from a simple model developed by the authors in an earlier work (Bhatt and Wedekind, 1984). The results of the simulation were similar to that depicted in Figs. 1(A) and 1(B). However, the stability limit, for example, at the conditions of Fig. 1(A), was achieved at roughly two and a half times the flow rate actually observed experimentally in Test #A-2. A further investigation of the simulation revealed that the system response was very sensitive to the outlet valve coefficient k_o. Therefore, it was decided to include the total two-phase flow resistance with the exit valve analytically. In view of this, a modified exit valve or orifice coefficient was determined, based on the steady-state values for each operating flow rate, as indicated below:

$$\Delta p_{1\phi,\ \text{valve}} + \Delta p_{2\phi,\ F,\ M} = \frac{k_o'}{\rho A_t^2} m^2 \quad (26)$$

where k_o' is the modified outlet orifice coefficient. A rearrangement of the above equation gives

$$k_o' = k_o + \left(\frac{\rho A_t^2}{m^2}\right)\Delta p_{2\phi,\ F,\ M} \quad (27)$$

With this modified outlet orifice coefficient substituted into equation (24) in place of k_o, the results of the numerical simulation for the conditions of the experimental tests shown in Fig. 1(A), for a 5.4 mm i.d. test section, lead to the responses depicted in Fig. 3. It is clear from this figure that as the flow rate increases, the simulated system stabilizes. In fact, the system proceeds to the stability limit in a manner similar to that observed experimentally, as shown in Fig. 1(A), and at about the same flow rate (3.0 g/s). The correspondence between the experimental and simulated flow rates at the stability limit is good. The results of another simulation, this time on a test section with an i.d. of 8.00 mm and at the conditions of Fig.1(B), leads to the results depicted in Fig. 4. Again the correspondence between the experimental and simulated flow rates at the stability limit is good (6.8 g/s). These observations lend support to the validity of the proposed procedure for including the effects of the two-phase pressure drop with the outlet throttling.

Linearized Model

In view of the procedures cited above under the nonlinear analysis, it would appear logical to attempt to incorporate the

two-phase pressure drop into the stability criterion that was developed by the authors in their previous work (Bhatt and Wedekind, 1980b). The simplified stability criterion for the condensing flow system is expressed by

$$\{N_i + N_c\} \geq N_o \tag{28}$$

where

$$N_c = \left(\frac{\tau_c}{V'\gamma k_i^*}\right), \quad N_i = \left(\frac{A_t k_o^* \tau_c}{L_o}\right) \tag{29}$$

and

$$N_o = \left\{\frac{1}{[(\rho/\rho')(k_o^*/k_i^*) + 1]} - \left(\frac{\rho'}{\rho}\right)\right\} \tag{30}$$

Including the effects of two-phase pressure drop, the linearized outlet valve resistance is given by

$$k_o^* = 2\left(\frac{k_o'}{\rho A_t^2}\right)m \tag{31}$$

where k_o' is the modified outlet orifice coefficient to be obtained from equation (27). The linearized stability plot, based on the criterion of equation (28), is shown in Fig. 5. The experimental tests displayed in Fig. 1(A) and 1(B) are plotted on the stability map in accordance with their appropriate dimensionless stability parameters N_c and N_i. Their distribution within the stable and unstable domains of the map is seen to be consistent with the experimental observations. That is, tests #A-1, #B-1, #B-2, and #B-3 are all located in the unstable domain. However, tests #A-2, #B-4, and #A-3 (off scale) are located in the stable domain. In fact, the flow rates at which the tests #A-2 and #B-4 are stabilized are seen to be very close to the stability boundary, as was the case in the nonliner solutions. This consistency between the nonlinear and linearized analysis lends further confidence in the method suggested for inclusion of the effects of two-phase pressure drop in determining the limit for stable operation of the condensing flow system.

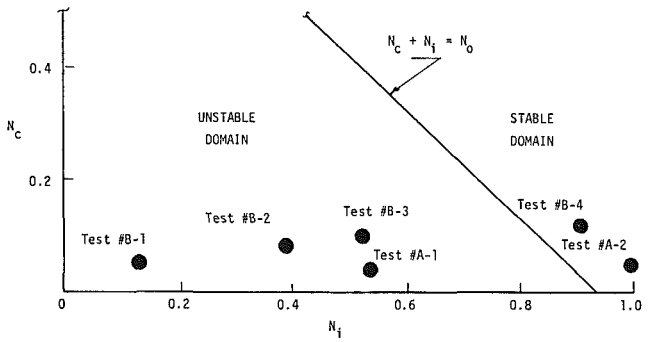

Fig. 5 Linear stability map of experimental tests displayed in Fig. 1

Experimental Apparatus

The experimental apparatus for the present studies is essentially the same as that described in the references (Wedekind and Bhatt, 1977; Wedekind et al., 1986). With slight modifications, it was possible to run the tests on a 5.4 mm i.d. test section or a 8.0 mm i.d. test section. Both were made of hard drawn copper tubing. A schematic of the closed-loop test facility is shown in Fig. 6 and is self-explanatory. The 8.0 mm i.d. test section had only one pressure transducer that was capable of measuring the pressure drop between the inlet and the outlet of the condenser, as shown in the figure. The 5.4 mm i.d. test section (Wedekind et al., 1986) had six pressure transducers mounted on it at about 48 cm intervals. The cooling water jacket was made of a 19.1 mm (34 in.) o.d. copper tube, to provide an annulus for water flow. At the pressure tap location, cooling water was bypassed through U-shaped sections (Wedekind et al., 1986) to facilitate the connection of the pressure tap fittings to the inner tube. The pressure tap itself was approximately 1.0 mm in diameter and was made by electrical discharge machining. There were seven pressure taps along the length of the condenser test section.

For each of the pressure transducers, one side of the diaphragm was connected to the test section inner tube while the other side was connected to a common manifold, which in turn was connected to the test section inlet (see Fig. 6). Thus, all six differential pressure transducers were referenced to the inlet pressure. For the transient experiment, great care was taken to ensure that liquid refrigerant existed on both sides of the transducer diaphragm. During testing, the saturation temperature at the system pressure was maintained at 2 to 8° C above the room temperature. This avoided vaporization of the liquid in the manifold. Static calibration of the pressure drop

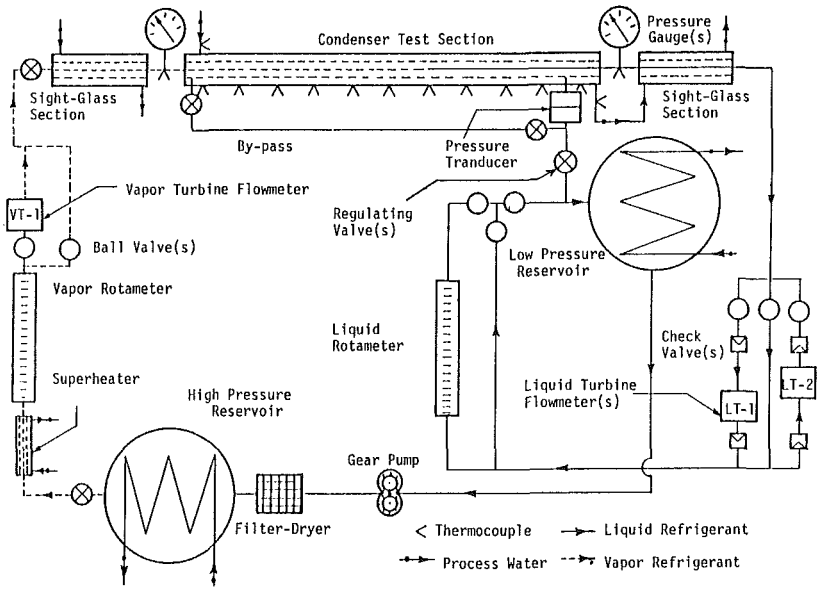

Fig. 6 Schematic of the experimental apparatus

instrumentation was performed using air and a dead weight tester.

The transient experimental data, with Refrigerant-12 as the working fluid, presented in Figs. 1(A), 1(B), and 5 for both the 5.4 mm i.d. test section and 8.0 mm i.d. test section, were obtained on the experimental apparatus described above. The experimental procedure that was followed consisted of establishing operating conditions at the lowest possible flow rate within the unstable domain of Fig. 5. System instability was indicated by the initiation, growth, and the subsequent self-sustained limit cycle oscillations. Next the flow rate was gradually increased to a higher value and the condenser left to operate at that level until various parameters assumed "steady" values. This process was continued until a flow rate was reached at which the system stabilized. The approaching stable limit was always reached within about ± 10 percent of the mean flow rate.

Relationship to Other Instabilities

Since the condensing flow instability considered in this paper is oscillatory, it is natural to question whether it is related to the density wave or pressure drop flow rate instabilities encountered in evaporating flows. There are a number of indicators that would eliminate it from being a density wave instability. First, the basic physics that exists in the typical evaporating flow system, experiencing density wave oscillations (Stenning and Veziroglu, 1965), is not present in a condensing flow system. This is also confirmed by Northern Research and Engineering Corporation (1965). This is so because density variations at the outlet, which have an important bearing on the existence of density wave oscillations, are practically absent in condensing flows. Another indicator is that the frequency of the condensing flow oscillations is strongly dependent upon the volume of vapor upstream of the two-phase region, whereas the frequency for density wave oscillations is normally related to the fluid transport time through the evaporator.

There are, however, some similarities between the observed condensing flow oscillatory instability, and the pressure drop–flow rate instabilities (Maulbetsch and Griffith, 1966) encountered in evaporating flows. The similarities are that the fluid inertia and compressibility form important energy storage mechanisms for both cases. Therefore, it was decided to investigate a possible relationship further.

An important requirement for the existence of pressure drop–flow rate instabilities in evaporating flows is that the operating point must lie on a negative sloping region on the overall pressure drop–flow rate curve. To verify if similar characteristics exist in condensing flow, steady-state tests were run on the 5.4 mm i.d. test section. The pressure drop measurements were made at six different locations along the axial length of the horizontal test section for flow rates of similar magnitude to those encountered in this instability study. Corresponding pressure drops are quite small, so relative experimental uncertainties are quite large. However, there did not appear to be a negative sloping region on the overall pressure drop–flow rate curve. Furthermore, the frequency of the oscillations under study in this paper appear to be much higher than the pressure drop–flow rate instabilities reported in the literature for evaporating flows. Although, because of potential experimental uncertainties, the above results can not be totally conclusive, it would appear that the condensing flow instabilities that have been under consideration in this paper are unique to condensing flow systems, and not related to the pressure drop–flow rate instabilities encountered in evaporating flows.

Summary and Conclusions

The studies presented in this paper were primarily concerned with an experimental and theoretical investigation of an unstable condensing flow phenomenon that leads to a self-sustaining limit-cycle-type oscillation of large amplitude, which under certain conditions can involve flow reversals. This unstable behavior normally exists for conditions of low outlet throttling.

Several physical mechanisms and parameters for the occurrence of this type of instability have been established from earlier studies. They are the condenser heat flux, liquid–vapor density ratio, downstream inertia, upstream vapor compressibility, upstream vapor volume, and downstream and upstream flow resistances. A particular interaction between these physical quantities leads to the unstable behavior. Upstream compressible volume and downstream inertia appear to be the dominant energy storage mechanisms for the self-sustained limit cycle oscillations.

In this paper, the mechanism and influence of two-phase pressure drop have been examined experimentally and analytically, and were shown to have a stabilizing effect on the instability. The paper demonstrated that inclusion of the two-phase pressure drop as part of the downstream throttling allows the utilization of a previously developed linearized analysis, based on the system mean void fraction model, to predict the experimentally observed stability boundary successfully.

Acknowledgments

The authors would like to acknowledge the National Science Foundation, Engineering Division, Mechanical Engineering and Applied Mechanics Section, Heat Transfer Program for its part in the support of this research under Grant No. MEA-8314966.

References

Bhatt, B. L., and Wedekind, G. L., 1980a, "Transient and Frequency Response Characteristics of Two-Phase Condensing Flows: With and Without Compressibility," ASME JOURNAL OF HEAT TRANSFER, Vol. 102, No. 3, pp. 495–500.

Bhatt, B. L., and Wedekind, G. L., 1980b, "A Self-Sustained Oscillatory Flow Phenomenon in Two-Phase Condensing Flow Systems," ASME JOURNAL OF HEAT TRANSFER, Vol. 102, No. 4, pp. 694–700.

Bhatt, B. L., and Wedekind, G. L., 1984, "An Experimental and Theoretical Study Into the Determination of Condensing Length," *Basic Aspects of Two-Phase Flow and Heat Transfer*, The 22nd National Heat Transfer Conference, Niagara Falls, New York.

Block, J. A., 1980, "Condensation-Driven Fluid Motions," *International Journal of Multiphase Flow*, Vol. 6, pp. 113–129.

Calia, C., and Griffith, P., 1981, "Modes of Circulation in an Inverted U-Tube Array With Condensation," *Thermal-Hydraulics in Nuclear Power Technology*, ASME HTD-Vol. 15, pp. 35–43.

Collier, J. G., 1972, *Convective Boiling and Condensation*, McGraw-Hill, New York.

Goodykuntz, J. H., and Dorsch, R. G., 1967, "Local Heat Transfer Coefficients and Static Pressures for Condensation of High-Velocity Steam Within a Tube," NASA TN D-3953.

Hemphill, F., Khater, H., Inayatullah, F., Raithby, G., Strong, A. B., and Nicoll, W. B., 1976, "A Finite-Interval Analytic Solution Technique for Transient Two-Phase Flows," *Two-Phase Transport and Reactor Safety*, Vol. II, Hemisphere Publishing Corporation, Proceedings of the Two-Phase Flow and Heat Transfer Symposium-Workshop, Fort Lauderdale, FL, pp. 815–837.

Inayatullah, G., and Nicoll, W. B., 1975, "A Suggestion Concerning a Possible Fast Solution Procedure for Transient Two-Phase Flows," *Letters in Heat and Mass Transfer*, Vol. 2, pp. 325–328.

Izumi, R., Ishimaru, T., and Matsuzaki, K., 1975, "Heat Transfer and Pressure Drop for Refrigerant R-12 Evaporating in a Horizontal Tube," *Heat Transfer—Japanese Research*, Vol. 4, No. 2, pp. 82–91 (translation of original paper published in *Kagaku Kogaku*, Vol. 38, 1974, No. 12, pp. 884–889).

Lahey, R. T., Jr., and Drew, D. A., 1980, "An Assessment of the Literature Related to LWR Instability Modes," NUREG/CR-1414, prepared for U.S. Nuclear Regulatory Commission, Washington, DC, 20555, NRC FIN NO:B6461.

Maulbetsch, J. S., and Griffith, P., 1966, "System-Induced Instabilities in Forced Convection Flows With Subcooled Boiling," *Proceedings of the Third International Heat Transfer Conference*, pp. 247–257.

Pitts, J. H., 1980, "Steam Chugging in a Boiling Water Reactor Pressure-Suppression System," *International Journal of Multiphase Flow*, Vol. 6, pp. 329–344.

Roslund, G. L., 1981, "A Generalized System Mean Void Fraction Model

Applied to Transient Two-Phase Condensing Flow," Ph.D. Thesis, Oakland University, Rochester, MI.

Stenning, A. H., and Veziroglu, T. N., 1965, "Flow Oscillation Modes in Forced-Convection Boiling," *Proceedings of 1965 Heat Transfer and Fluid Mechanics Institute*, Stanford University Press, CA, pp. 301–316.

"The Design and Performance Analysis of Compact Heat Exchangers," 1965, Northern Research and Engineering Corporation," Vol. 1, p. 204.

Wang, S. S., Sargis, D. A., Stuhmiller, J. H., and Masiello, P. J., 1981, "Numerical Simulation of Condensation Phenomena in Reactor Steam Suppression Systems," *AIChE Symposium Series No. 208*, Vol. 77, pp. 180–190.

Wedekind, G. L., and Bhatt, B. L., 1977, "An Experimental and Theoretical Investigation Into Thermally Governed Transient Flow Surges in Two-Phase Condensing Flow," ASME JOURNAL OF HEAT TRANSFER, Vol. 99, No. 4, pp. 561–567.

Wedekind, G. L., Bhatt, B. L., and Beck, B. T., 1978, "A System Mean Void Fraction Model for Predicting Various Transient Phenomena Associated With Two-Phase Evaporating and Condensing Flow," *International Journal of Multiphase Flow*, Vol. 4, pp. 97–114.

Wedekind, G. L., Bhatt, B. L., and Roslund, G. L., 1986, "An Experimental and Theoretical Study of Transient Pressure Drop in Two-Phase Condensing Flows," *4th Miami International Symposium on Multi-Phase Transport and Particulate Phenomena*, Miami Beach, FL; ASME JOURNAL OF HEAT TRANSFER, in press.

G. L. Wedekind
Mem. ASME

B. L. Bhatt
Mem. ASME

Oakland University,
Rochester, MI 48063

G. L. Roslund
General Motors Corporation,
Detroit, MI

An Experimental and Theoretical Study of Transient Pressure Drop in Two-Phase Condensing Flows

This paper presents the results of an experimental and theoretical investigation of the pressure drop associated with transient two-phase condensing flows involving complete condensation. Utilizing the system mean void fraction model, and the similarity relationships associated with it, an analytical prediction of the transient pressure drop is possible, including a simplified closed-form version. The capability of the proposed theory is demonstrated by comparison with experimental measurements of the transient pressure drop in a horizontal tube condenser following an exponential-type change in the inlet mass flow rate. Good agreement is shown to exist between the predicted and experimental results.

Introduction

Two-phase condensing flow phenomena occur in a variety of industrial applications including reheat and reboiler systems associated with nuclear and conventional power plants, space power generators, solar and ocean thermal energy conversion, vapor compression refrigeration, and chemical processing. The ability both to understand and to model the principle physical mechanisms associated with the transient response characteristics of condensing flows is of considerable importance as they relate to system design and control. The dynamic characteristics of two-phase condensing flows have received very little attention compared to their evaporating flow counterparts. A few studies that have been devoted to condensing flow transients have focused on the response of the outlet liquid flow rate to changes in inlet vapor flow rate (Wedekind and Bhatt, 1977; Bhatt and Wedekind, 1980a), frequency response of inlet pressure and the effective point of complete condensation (Schoenberg, 1966), theoretical analysis of the frequency response of the outlet liquid flowrate (McMorran and Moeck, 1976) and studies of flow instabilities (Soliman and Berenson, 1980; Williams et al., 1973; Bhatt and Wedekind, 1980b). In all of these studies, no consideration was given to the transient two-phase pressure drop. In addition to the importance of such a study on its own merit, the two-phase pressure drop in condensing flows has recently been shown (Bhatt et al., 1986) to have an important bearing on the instabilities involving such flows.

The objectives of this paper are to develop a simplified closed-form theoretical expression for the transient pressure drop response, to changes in inlet flow rate. This expression will then be compared both to a numerically integrated solution and to experimental data. It will be shown that the simplified closed-form expression predicts the measured two-phase pressure drop response quite adequately.

Model for Transient Pressure Drop

Consider the schematic of a tube-type condensing flow system involving complete condensation in which the condensate completely fills the tube at the outlet, as shown in Fig. 1. It is assumed that there is an effective position in the condenser where the last of the vapor is condensed. This position is denoted by $\eta(t)$, and represents the boundary between the two-phase region and the subcooled liquid region. The pressure drop within the two-phase region is denoted by

$$\Delta p_{2\phi}(t) = [p_c(t) - p_f(t)]$$

The focus of this paper is the consideration of the transient response of the two-phase pressure drop due to forced changes in the inlet vapor flow rate.

The model will be formulated using the conservation of mass and energy and the momentum principle in the integral form. In this formulation, the concept of a system mean void fraction (Wedekind and Bhatt, 1977) will be utilized. In addition, the following assumptions are being made.

Two-Phase Model Assumptions

1 System mean void fraction is assumed to be invariant with time.

2 Random fluctuations due to the stochastic nature of the two-phase flow process are assumed not to influence the deterministic transients.

3 Viscous dissipation, longitudinal heat conduction, and changes in kinetic and gravitational potential energy are neglected.

4 The specific enthalpies and densities of the liquid and vapor are considered to be saturated properties, independent of both axial position and time, and evaluated at the mean system pressure.

5 The spatially averaged heat flux, for the entire two-phase region, is assumed to be invariant with time.

6 Transverse distributions of velocities and pressures within each phase are assumed to be uniform.

An implication of the time invariance of the system mean void fraction is that the concept of similarity (Wedekind and Bhatt, 1977) holds. This will be extremely useful in the integration of the friction, gravitational, and inertial components of the transient pressure drop, leading to a closed-form solution, as will be demonstrated later.

Two-Phase Region. An application of the transient momentum principle in an integral form, applied to the liquid and vapor within the two-phase region, leads to the following:

$$p_c(t) - p_f(t) = \Delta p_{2\phi,\,F}(t) + \Delta p_{2\phi,\,M}(t) + \Delta p_{2\phi,\,I}(t) + \Delta p_{2\phi,\,g}(t) \quad (1)$$

where the four terms on the right represent the two-phase pressure drop due to friction, momentum, gravity, and inertia, respectively. Each one of these components will be considered in order.

Contributed by the Heat Transfer Division and presented at the 4th Miami International Symposium on Multi-phase Transport and Particulate Phenomena, Miami Beach, Florida, December 15-17, 1986. Manuscript received by the Heat Transfer Division March 9, 1987. Keywords: Condensation, Multiphase Flows, Transient and Unsteady Heat Transfer.

Friction Pressure Drop. The friction pressure drop may be represented in terms of a peripherally averaged wall shear stress as follows:

$$\Delta p_{2\phi,\,F}(t) = \frac{1}{A_t}\int_{z=0}^{\eta(t)} \tau_w P dz \tag{2}$$

However, as it has become a standard practice, the two-phase friction pressure drop may be expressed in terms of a single-phase pressure drop for the total flow considered as liquid (Collier, 1972). Thus

$$\Delta p_{2\phi,\,F}(t) = \frac{2}{\rho D}\int_{z=0}^{\eta(t)} f\phi G^2 dz \tag{3}$$

where the two-phase friction multiplier $\phi = \phi(x, G)$, and f is a single-phase friction factor for the total flow considered to be liquid. $G = G(z, t)$ is the local mass flux within the two-phase region and x is the local flow quality.

Momentum Pressure Drop. The momentum pressure drop within the two-phase region, accounting for the moving boundary $\eta(t)$, is given by

$$\Delta p_{2\phi,\,M}(t) = \frac{1}{A_t}\left\{\left[\frac{1}{\rho} - \left(\frac{A_t}{m_L}\right)\frac{d\eta(t)}{dt}\right]\frac{m_L^2(t)}{A_t}\right\}_{z=\eta(t)} - \frac{1}{A_t}\left\{\left[\frac{(1-x_i^2)}{\rho(1-\alpha_i)} + \frac{x_i^2}{\rho'\alpha_i}\right]\frac{m_o^2(t)}{A_t}\right\}_{z=o} \tag{4}$$

The first term on the right-hand side represents the instantaneous momentum flux per unit area at the point of complete condensation relative to the tube. The second term represents the momentum flux per unit area at the entrance into the two-phase region.

Inertia Pressure Drop. The inertia pressure drop may be represented by

$$\Delta p_{2\phi,\,I}(t) = \frac{d}{dt}\int_{z=0}^{\eta(t)} G(z, t) dz \tag{5}$$

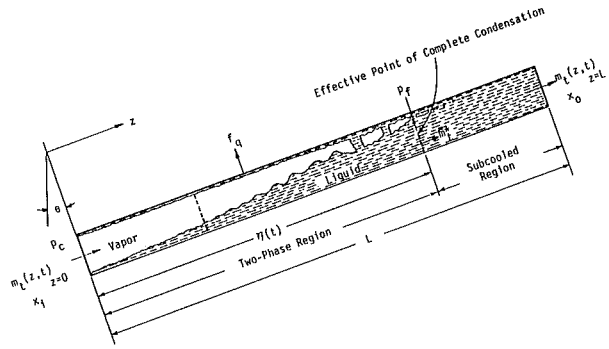

Fig. 1 Schematic of two-phase condensing flow system

The above expression represents the time rate of change of the integrated local momentum of the fluid per unit area within the two-phase region.

Gravitational Pressure Drop. The gravitational pressure drop can be represented in terms of a cross-sectionally averaged local area mean void fraction α, as follows:

$$\Delta p_{2\phi,\,g}(t) = \int_{z=0}^{\eta(t)} [\alpha\rho' + (1-\alpha)\rho] g \sin\theta dz \tag{6}$$

An examination of equations (3)–(6) indicates that in order to be able to determine the transient two-phase pressure drop, it is important to know the time-dependent local mass flux $G(z, t)$, the time-dependent motion of the effective point of complete condensation $\eta(t)$, and the response of the outlet liquid flow rate $m_L(t)$. To obtain this information, the concept of a time-invariant system mean void fraction, together with the conservation of mass and energy principles, will be utilized (Wedekind et al., 1978). In addition, information is needed regarding the two-phase friction multiplier $\phi(x, z)$, the single-

Nomenclature

A_t = total cross-sectional area of tube, m²
D = inside diameter of tube, m
f = single-phase friction factor, equation (21)
f_q = spatially averaged heat flux, W/m²
$G(z, t)$ = local total mass flux = $m(z, t)/A_t$, g/m² • s
$G_L(t)$ = $G(z, t)_{z=L}$
h = enthalpy of saturated liquid, J/kg
h' = enthalpy of saturated vapor, J/kg
k_1 = parameter, equation (25)
L = total length of the condenser, m
$m_L(t)$ = $m(z, t)_{z=L}$, g/s
$m_o(t)$ = $m(z, t)_{z=0}$; m_i, m_f = initial and final inlet flow rate, respectively, g/s
$m(z, t)$ = local instantaneous total mass flow rate of fluid, g/s
m_t^* = total mass flow rate relative to the moving boundary $\eta(t)$, g/s
$p(t, z)$ = local instantaneous pressure, kN/m²
P = inside perimeter of tube = πD, m
$\Delta p(t)$ = instantaneous pressure drop = $[p_c - p(z, t)_{z=Z}]$
Δp_i, Δp_f = initial and final steady-state pressure drop respectively, kN/m²
p_c = pressure at inlet of condenser, kN/m²
p_f = pressure at point of complete condensation, kN/m²
r = dimensionless quantity, equation (19)
t = time, s
x = nonfluctuating local flow quality
x_i = inlet flow quality
x_o = flow quality at outlet
z = spatial coordinate in the axial direction, m
Z = axial position of a specific pressure transducer, m
α = local area mean void fraction
α_s = system mean void fraction, equation (7)
$\bar{\eta}$ = steady-state position of the effective point of complete condensation, m
$\eta(t)$ = effective point of complete condensation, m
θ = angle of inclination of condenser tube
μ = viscosity of liquid, N•s/m²
ξ = dimensionless spatial coordinate in axial direction = $z/\eta(t)$
ρ = density of saturated liquid, kg/m³
ρ' = density of saturated vapor, kg/m³
$\bar{\rho}$ = mean density in two-phase region, kg/m³
τ_c = time constant of condensing flow system, equation (13), s
τ_w = wall shear stress, N/m²
ϕ = two-phase friction multiplier

phase friction factor f, and the distribution of the area mean void fraction α, within the two-phase region.

Implicit in the above approach is the assumption that only a weak coupling exists between the transient form of the momentum principle and the conservation of mass and energy. Therefore, independent solutions of the conservation of mass and energy, when integrated into the momentum principle, should yield the prediction of transient pressure drop. Such an approach has been followed for transient evaporating flows by Inayatullah and Nicoll (1975, 1976) and Wedekind et al. (1978). It is assumed that the same approach is valid for transient condensing flows as well.

System Mean Void Fraction. The system mean void fraction $\alpha_s(t)$ is expressed in terms of a local area mean void fraction $\alpha(z, t)$ within the two-phase region as follows:

$$\alpha_s = \frac{1}{\eta(t)} \int_{z=0}^{\eta(t)} \alpha(z, t)dz \tag{7}$$

As indicated earlier, the system mean void fraction α_s is assumed to be invariant with time. The implication of such an assumption (Wedekind and Bhatt, 1977; Bhatt and Wedekind, 1980a) is that the area mean void fraction $\alpha(z, t)$ is expressible as a function of a single dimensionless variable ξ; therefore

$$\alpha(z, t) = \alpha(\xi), \text{ where } \xi \equiv \frac{z}{\eta(t)} \tag{8}$$

For a uniform heat flux, the flow quality distribution during a transient can be represented by (Wedekind and Bhatt, 1977; Bhatt and Wedekind, 1980b)

$$x(z, t) = x_i - x_i \left(\frac{z}{\eta(t)}\right) = (1 - \xi)x_i \tag{9}$$

Substitution of equations (8) and (9) into equation (7) leads to a representation of the α_s in terms of flow quality (Wedekind et al., 1978).

Conservation of Mass and Energy. The conservation of mass principle, simultaneously applied to the liquid and vapor in the two-phase region, can be expressed as

$$\frac{d}{dt} \int_{z=0}^{\eta(t)} [\rho(1-\alpha) + \rho'\alpha]A_t dz = m_o(t) - m_t^* \tag{10}$$

Similarly, the conservation of energy in the two-phase region can be expressed as

$$\frac{d}{dt} \int_{z=0}^{\eta(t)} [\rho h(1-\alpha) + \rho' h'\alpha]A_t dz = -\int_{z=0}^{\eta(t)} f_q P dz + \{[h(1-x) + h'x]m_t(z, t)_{z=0}\} - hm_t^* \tag{11}$$

Equations (10) and (11) along with equation (7) and assumptions (1), (4), and (5), and an inlet flow quality of unity, yield the following governing differential equation, for $\eta(t)$:

$$\frac{d\eta(t)}{dt} + \frac{1}{\tau_c}\eta(t) = \left(\frac{1}{\rho'\alpha_s A_t}\right) m_o(t) \tag{12}$$

where the time constant τ_c is given by

$$\tau_c = \frac{A_t \alpha_s \rho'(h' - h)}{f_q P} \tag{13}$$

The response of the effective point of complete condensation $\eta(t)$ can be obtained from equation (12) for a given inlet flowrate change. If one also considers the conservation of mass in the subcooled liquid region, and it is combined with the conservation of mass in the two-phase region, the conservation of mass for the entire condenser leads to (Schoenberg, 1966)

$$m_L(t) = m_o(t) + (\rho - \rho')A_t\alpha_s \frac{d\eta(t)}{dt} \tag{14}$$

If equation (14) is substituted into equation (12), an alternative form of the differential equation for $\eta(t)$ is as follows:

$$\frac{d\eta(t)}{dt} + \left(\frac{\rho'}{\rho}\right)\frac{1}{\tau_c}\eta(t) = \left(\frac{1}{\rho A_t \alpha_s}\right) m_L(t) \tag{15}$$

This particular form is useful as will be demonstrated later on.

Local Mass Flux. The distribution of the local mass flux, $G(z, t)$, within the two-phase region is required for the evaluation of both the friction and inertia pressure drop as indicated in equations (3) and (5). Local mass flux can be obtained if attention is focused on a fixed subsystem within the two-phase region. As shown in Fig. 1, the extent of this subsystem is shown by position z on the figure. The conservation of mass and energy together with assumptions (4) and (5), and following a formulation similar to equations (10) and (11), lead to the following:

$$-(\rho - \rho')A_t \frac{d}{dt}\int_{z=0}^{z} \alpha dz = m_o(t) - m_t(z, t) \tag{16}$$

$$-(\rho h - \rho' h')A_t \frac{d}{dt}\int_{z=0}^{z} \alpha dz = [\{xh' + (1-x)h\}m_t(z, t)]_{z=0} - [\{xh' + (1-x)h\}m_t(z, t)]_z - f_q P \tag{17}$$

Substituting equation (16) into (17), and solving for $m(z, t)/A_t = G(z, t)$, leads to the following:

$$G(z, t) = \frac{m_o(t)\{1 - r[z/\eta(t)]\}}{(\rho'/\rho)A_t\{1 + [(\rho/\rho') - 1]x\}} \tag{18}$$

where

$$r = [1 - (\rho'/\rho)]\frac{f_q P}{(h' - h)} \cdot \frac{\eta(t)}{m_o(t)} \tag{19}$$

Evaluation of Pressure Drops. As indicated earlier, the solution to the conservation of mass and energy equations when substituted into the transient form of the momentum principle will yield the pressure drop response. Each component of the pressure drop will again be considered in order.

Friction. In the evaluation of two-phase friction pressure drop from equation (3), it is necessary to have a knowledge of the distribution of the two-phase friction multiplier $\phi(z, t)$. A number of empirical correlations, established at steady state, have been proposed. For evaporating steam–water flows, the correlations of Martinelli and Nelson (1948) and those proposed in Idsinga et al. (1977) are fairly well established. However, the one proposed by Izumi et al. (1974), again for evaporating flows, appears to represent the data well for both adiabatic and condensing flows involving Refrigerant-12. Therefore, this correlation will be utilized in the proposed model. In terms of the local flow quantity x, the two-phase friction multiplier is given by

$$\phi = 1.515(1-x)^{0.18}\{1 + [(\rho/\rho')^{2/3} - 1]x\}^{1.57} \tag{20}$$

A plot of the above correlation, and its capability to represent Sack's (1975) experimental data, are presented in Fig. 2.

The single-phase friction factor f can be assumed to be given by the Blasius formula for turbulent flow through smooth tubes

$$f = \frac{0.079}{\mathrm{Re}^{1/4}} = \frac{0.079}{(GD/\mu)^{1/4}} \tag{21}$$

It is assumed that the form of ϕ and f during a transient is the same as at steady state. However, both these quantities are dependent upon local mass flow rate and flow quality, which are a function of both position and time during a transient.

In order to determine the transient two-phase friction pressure drop, it is convenient to change the spatial integration in

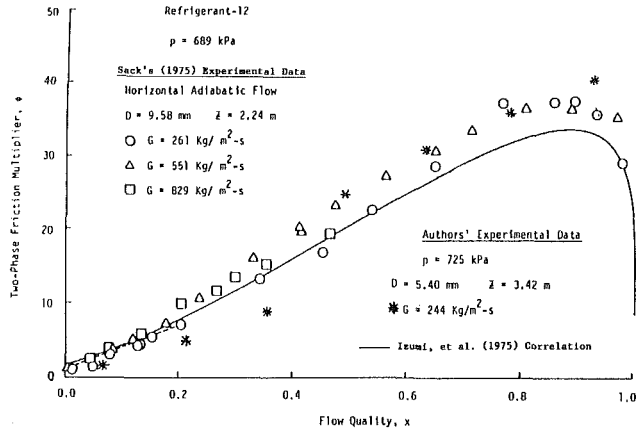

Fig. 2 Comparison of Izumi correlation for two-phase friction multiplier

equation (3) to integration in flow quality x. Using equation (9) for this purpose, equation (3) can be represented by

$$\Delta p_{2\phi,\,F}(t) = \frac{2\eta(t)}{\rho D x_i}\int_0^{x_i} f\phi G^2 dx \tag{22}$$

However, it is still necessary to integrate this equation numerically. For details regarding the numerical procedure see Roslund (1981).

Recently however, it became apparent that it is possible to get a closed-form solution, which is much easier to use and gives a better grasp of the parameters affecting the phenomena. The steps involved in finding such a solution are enumerated below.

From equations (8) and (9) it is possible to express flow quality and $z/\eta(t)$ in terms of the similarity variable ξ. Using this information in equations (18),(20), and (21), and subsequently equation (3), gives

$$\Delta p_{2\phi,\,F}(t) = \left(\frac{0.24}{\rho D}\right)\left(\frac{\mu}{D}\right)^{0.25}\left\{\frac{m_o(t)}{A_t}\right\}^{1.75}\left\{1+\left(\frac{\rho}{\rho'}\right)^{0.67}\right\}^{1.57} \eta(t)\int_{\xi=0}^{1}(1-r\xi)^{1.75}\left\{\frac{\xi}{(1-\xi)}\right\}^{0.18} d\xi \tag{23}$$

Introduction of the similarity variable has considerably simplified the integration process. Equation (23) leads to the following:

$$\Delta p_{2\phi,\,F}(t) = k_1[3.38(1-r) + r^2]\eta(t)m_o^{1.75}(t) \tag{24}$$

where[1]

$$k_1 = \left(\frac{0.0696}{\rho D}\right)\left(\frac{\mu}{D}\right)^{0.25}\left\{1+\left(\frac{\rho}{\rho'}\right)^{1.67}\right\}^{1.57}\left(\frac{1}{A_t}\right)^{1.75} \tag{25}$$

For most situations, it is likely that $r \simeq 1.0$. Therefore equation (24) gives

$$\Delta p_{2\phi,\,F}(t) = k_1\eta(t)m_o^{1.75}(t) = k_1 A_t^{1.75}\eta(t)G^{1.75}(z,\,t)_{z=0} \tag{26}$$

The above solutions represent a considerable simplification and obviate the need for a numerical solution. It will be shown later on that the above closed-form solution predicts results that are very close to those of the more complicated numerical solution.

Momentum. In the evaluation of momentum pressure drop, it is necessary to know the response of the effective point of complete condensation $\eta(t)$, as well as that of the outlet liquid flow rate $m_L(t)$. Substituting equation (15) into equation (4), for $x_i = 1.0$, leads to the following:

[1]For $(\rho/\rho')\gg 1$, $[1+(\rho/\rho')^{0.67}]^{1.57}\approx(\rho/\rho')^{1.05}$.

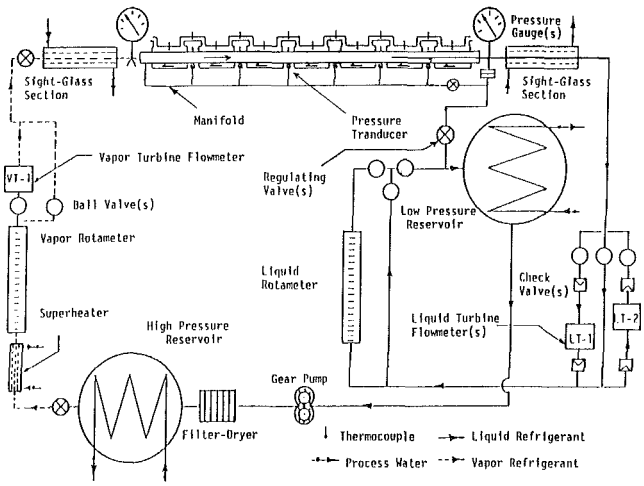

Fig. 3 Schematic of experimental apparatus

$$\Delta p_{2\phi,\,M} = \frac{1}{\rho}\left(\frac{\alpha_s-1}{\alpha_s}\right)G^2(z,\,t)_{z=L} + \left(\frac{\rho'}{\rho}\right)\frac{\eta(t)}{\tau_c}G(z,\,t)_{z=L} - \frac{1}{\rho'}G^2(z,\,t)_{z=0} \tag{27}$$

Inertia. Substituting equation (18) into (5) and using (9) to convert the variable of integration from spatial coordinate z to the similarity variable ξ leads to the desired result. For simplicity, if $r=1$, the inertia pressure drop takes the following form:

$$\Delta p_{2\phi,I} = G(z,\,t)_{z=o}\frac{d\eta(t)}{dt} + \eta(t)\frac{dG}{dt}(z,\,t)_{z=0} \tag{28}$$

Gravity. Inserting the definition of the system mean void fraction from equation (7) into equation (6) leads to the following simple result:

$$\Delta p_{2\phi,G} = \bar{\rho}g\sin\theta\eta(t) \tag{29}$$

where the mean density $\bar{\rho} = [\rho'\alpha_s + (1-\alpha_s)\rho]$.

Subcooled Liquid Region. In a manner similar to what was done in the two-phase region, the friction, momentum, inertia, and gravitational components of the pressure drop within the single-phase region are represented by

$$\Delta p_{1\phi,F} = \frac{P[L-\eta(t)]fG^2(t)}{2\rho A_t} \tag{30}$$

$$\Delta p_{1\phi,M} = \frac{G_L^2(t)}{\rho} - \left\{\left[\frac{1}{\rho} - \frac{1}{G(z,\,t)}\frac{d\eta(t)}{dt}\right]G^2(z,\,t)\right\}_{z=\eta(t)} \tag{31}$$

$$\Delta p_{1\phi,I} = [Z-\eta(t)]\frac{dG_L}{dt} - G_L\frac{d\eta(t)}{dt} \tag{32}$$

$$\Delta p_{1,\phi,g} = \rho g\sin\theta[L-\eta(t)] \tag{33}$$

Adding the above four equations to the respective friction, momentum, inertia, and gravity components for the two-phase region will determine the total transient pressure drop in a condenser where there is a subcooled liquid region.

Experimental Observations

The objective of the experimental program was to verify the theoretical model that was developed for the transient pressure drop in the previous section.

Experimental Apparatus. A schematic of the experimental apparatus is shown in Fig. 3. This facility is similar to the one used in earlier investigations (Wedekind and Bhatt, 1977); how-

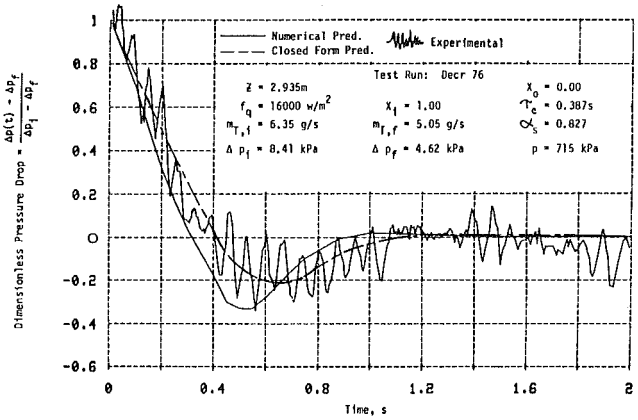

Fig. 4 Pressure drop response to flow rate decrease, complete condensation

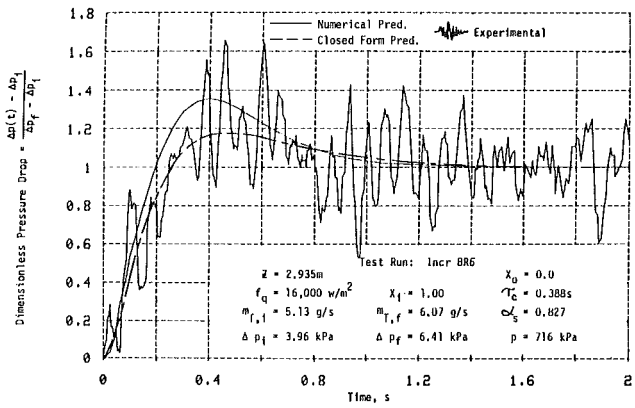

Fig. 5 Pressure drop response to flow-rate increase, complete condensation

ever major changes were made in the test section design. Refrigerant-12 vapor was generated in the high-pressure reservoir by circulating temperature-regulated hot water. A regulating valve located at the outlet of this reservoir controlled the flow rate of vapor, which passed in series through a superheater, vapor rotameter, vapor-turbine flow meter, precondenser, a sight glass, and into the test section. The subcooled liquid leaving the condenser was then passed through a sight glass and onward into the low-pressure reservoir with a minimum of resistance. Both the high-pressure and low-pressure reservoirs were maintained at constant pressures. At the end of each test, liquid was pumped back into the high-pressure reservoir.

The test section was a horizontal, all-copper condenser, approximately 3.42 m long. The inner tube was a single, uninterrupted copper tube with an o.d. of 7.94 mm and an i.d. of 5.4 mm. The cooling water jacket was made of a 19.1 mm o.d. copper tube, to provide an annulus for water flow. At the pressure tap location the cooling water was bypassed through U-shaped sections to facilitate the connection of the pressure tap fittings to the inner tube. The pressure tap itself was approximately 1.0 mm in diameter and was made by electrical discharge machining. There were seven pressure taps along the length of the condenser. The axial water temperature profile was measured by thermocouples mounted in the water passage at 15 axial locations along the test condenser as shown in Fig. 3. The condenser was horizontal; $\theta = 0$.

Pressure drop measurements were obtained by differential pressure transducers. Each pressure transducer had a diaphragm range of 138 kPa (20 psig). The transient pressure drop signals were recorded on a two-channel strip chart recorder. Later, these data were reduced with a digitizer and stored in a computer system for plot comparisons with predicted data.

For each of the pressure transducers, one side of the diaphragm was connected to the test section inner tube while the other side was connected to a common manifold, which in turn was connected to the test section inlet. Thus, all of the differential pressure transducers were referenced to the inlet pressure. For transient testing, great care was taken to ensure that liquid refrigerant existed on both sides of the transducer diaphragm. During testing, the saturation temperature at the system pressure was maintained 2 to 8°C above room temperature. This avoided vaporization of liquid in the manifold. Static calibration of the pressure drop instrumentation was performed using air and a dead weight tester.

In running a test, the condenser was initially allowed to reach steady-state operation. The transient was then initiated by varying the vapor flow rate at the inlet to the condenser by operating a regulating valve at the outlet of the high pressure reservoir. The output (pressure drop) from the transducer was measured as a function of time through a trace on a strip chart recorder, until the final steady state had been achieved.

For all tests, the vapor inlet flow rate was measured with a vapor-turbine flow meter. For transient flow conditions, the response time of the vapor turbine and frequency converter were considered carefully. Although the mechanical turbine meter itself has a relatively fast response time of about 10 ms, the frequency converter was found to be relatively slower with a response time of about 200 ms. This information was used to derive actual vapor flow rate. For further details see Roslund (1981).

Comparison of Theoretical Results With Experimental Data. Experimental data indicating the response of the transient pressure drop to changes in the inlet vapor flow rate are shown in Figs. 4 and 5 for the case of complete condensation. These data are accurate to within ±10 percent. In addition to the response of the two-phase pressure drop, these data also represent a slight contribution of the single-phase subcooled liquid between the effective point of complete condensation and the nearest pressure transducer within the single-phase region. For the initial steady-state situation, the length of this liquid column was less than 12.0 cm.

The major contributor to the pressure drop transient is the friction pressure drop within the two-phase region. It amounts to roughly 80 percent of the total magnitude. The momentum pressure drop, which is negative (pressure recovery), contributes 10 to 15 percent of the total magnitude and the rest is inertia pressure drop. In the single-phase region there is very little contribution of friction or momentum pressure drops. Single-phase inertia contributes less than 10 percent of the total pressure drop during the transient. Figure 4 depicts the transient condenser pressure drop response to an exponential-type flow-rate decrease in the inlet vapor flow rate. The magnitude of the flow change was 20 percent. The data have been plotted in terms of a dimensionless pressure drop as a function of time. The initial steady-state pressure drop for this test is within about 20 percent of the model predictions. This is good considering the complexity of the actual physical mechanisms involved. Superimposed on the graph is a plot of the pressure drop transient as predicted by the numerical solution (Roslund, 1981), as well as the closed-form solution presented in this work. The agreement between both models and the experimental data is quite reasonable. Both show a certain amount of overshoot, which appears to be related to a coupling of the overshoot in the liquid mass flow rate at the outlet of condenser (Wedekind and Bhatt, 1977).

Figure 5 depicts the results of the transient pressure drop response when the vapor flow rate at the inlet is increased by about 20 percent. Again agreement between the experimental data and the predictions of both models are very reasonable.

Considering the complexity of the physical phenomena involved, and the relative simplicity of the closed-form version of the theoretical model, the agreement between the experimental data and this model is very encouraging.

Summary and Conclusions

The principal purpose of this paper has been to present an extension of the system mean void fraction model for predicting transient pressure drop in two-phase condensing flow systems. Previous applications of the system mean void fraction model to transient condensing flows have been directed primarily at the transient flow surges in the outlet flow rate of the subcooled liquid, and at self-sustained oscillatory flow instabilities. These system responses are among the class of transient phenomena for which the system mean void fraction is time invariant, and the transient form of the momentum principle is not required. In this paper, the underlying concepts of the system mean void fraction model, including the integral formulation, were further exploited to include an investigation of its implications on the momentum principle. The result was an analytical model for transient pressure drop, expressed directly in terms of previously developed solutions for the transient response of the effective point of complete condensation and the corresponding outlet flow rate of subcooled liquid. The analysis was further simplified to allow for a closed-form solution.

Experimental measurements of the transient pressure drop for Refrigerant-12 flowing in a horizontal tube condenser subjected to a uniform and constant heat flux have been presented for comparison with the theoretical predictions. The transients were initiated by an exponential type change in the inlet mass flow rate. The theoretical predictions of the proposed model, including the completely closed-form version, which was based on a simplification of the analysis for two-phase friction and inertia pressure drop, compare favorably with the observed transient pressure drop response for both flow increases and decreases. These results provide additional experimental evidence as to the range of applicability of the system mean void fraction model in the analysis and prediction of transient two-phase condensing flow phenomena.

Acknowledgments

The authors would like to acknowledge the National Science Foundation, Mechanical Engineering and Applied Mechanics Section, Heat Transfer Program for its part in the support of this research under Grant No. MEA-8314966.

References

Bhatt, B. L., and Wedekind, G. L., 1980a, "Transient and Frequency Response Characteristics of Two-Phase Condensing Flows: With and Without Compressibility," ASME JOURNAL OF HEAT TRANSFER, Vol. 102, No. 3, pp. 495-500.

Bhatt, B. L., and Wedekind, G. L., 1980b, "A Self-Sustained Oscillatory Flow Phenomenon in Two-Phase Condensing Flow Systems," ASME JOURNAL OF HEAT TRANSFER, Vol. 102, No. 4, pp. 694-700.

Bhatt, B. L., Wedekind, G. L., and Jung, K., 1986, "Effects of Two-Phase Pressure Drop on the Self-Sustained Oscillatory Instability in Condensing Flows," *4th Miami International Symposium on Multi-Phase Transport and Particulate Phenomena*, Miami Beach, FL; ASME JOURNAL OF HEAT TRANSFER, this issue, pp. 538-545.

Collier, J. G., 1972, *Convective Boiling and Condensation*, McGraw-Hill, New York.

Idsinga, W., Todreas, N., and Bowring, R., 1977, "An Assessment of Two-Phase Pressure Drop Correlations for Steam-Water Systems," *International Journal of Multiphase Flow*, Vol. 3, pp. 401-413.

Inayatullah, G., and Nicoll, W. B., 1975, "A Suggestion Concerning a Possible Fast Solution Procedure for Transient Two-Phase Flows," *Letters in Heat and Mass Transfer*, Vol. 2, pp. 325-328.

Inayatullah, G., and Nicoll, W. B., 1976, "Prediction of Flashing Diabatic Steam-Water Flows," Waterloo Research Institute, Report No. 16.

Izumi, R., Ishimaru, T., and Matsuzaki, K., 1975, "Heat Transfer and Pressure Drop for Refrigerant R-12 Evaporating in a Horizontal Tube," *Heat Transfer—Japanese Research*, Vol. 4, No. 2, pp. 82-91 (translation of original paper published in *Kagaku Kogaku*, Vol. 38, 1974, No. 12, pp. 884-889).

Martinelli, R. C., and Nelson, D. B., 1948, "Prediction of Pressure Drop During Forced Circulation Boiling of Water," *Transactions, ASME*, Vol. 70, pp. 695-702.

McMorran, P. D., and Moeck, E. O., 1976, "Dynamic Model of Condensation in a Tube," AECL-5603, Chalk River Nuclear Laboratories, Chalk River, Ontario, Canada.

Roslund, G. L., 1981, "A Generalized System Mean Void Fraction Model Applied to Transient Two-Phase Condensing Flow," Ph.D. Thesis, Oakland University, Rochester, MI.

Sacks, P. S., 1975, "Measured Characteristics of Adiabatic and Condensing Single-Component Two-Phase Flow of Refrigerant in a 0.377-in. Diameter Horizontal Tube," ASME Paper No. 75-WA/HT-24.

Schoenberg, A. A., 1966,"Mathematical Model With Experimental Verification for the Dynamic Behavior of a Single-Tube Condenser," NASA TN D-3453.

Soliman, M., and Berenson, P. J., 1980, "Flow Stability of Gravitational Effect in Condenser Tubes," *Proceedings of the Fourth International Heat Transfer Conference*, Paris, France, Vol. VI, Paper No. Cs 1.8.

Wedekind, G. L., and Bhatt, B. L., Nov. 1977, "An Experimental and Theoretical Investigation Into Thermally Governed Transient Flow Surges in Two-Phase Condensing Flow," ASME JOURNAL OF HEAT TRANSFER, Vol. 99, No. 4, pp. 561-567.

Wedekind, G. L., Bhatt, B. L., and Beck, B. T., 1978, "A System Mean Void Fraction Model for Predicting Various Transient Phenomena Associated With Two-Phase Evaporating and Condensing Flow," *International Journal of Multiphase Flow*, Vol. 4, pp. 97-114.

Williams, J. L., Keshock, E. G., and Wiggins, C. L., 1973, "Development of a Direct Condensing Radiator for Use in a Spacecraft Vapor Compression Refrigeration System," ASME *Journal of Engineering for Industry*, Vol. 95, p. 1053.

Design and Calibration of a Local Heat-Flux Measurement System for Unsteady Flows

D. S. Campbell[1]

M. Gundappa
Assoc. Mem. ASME

T. E. Diller
Mem. ASME

Mechanical Engineering Department,
Virginia Polytechnic Institute and State University,
Blacksburg, VA 24061

A local heat-flux measurement system was built, calibrated, and tested for use in unsteady flows. The system was designed to maintain constant-wall-temperature boundary conditions. The measuring element is a thin-film heat flux gage made by sputter-coating gold onto a substrate. A constant-temperature anemometer is used to maintain the thin-film gage at a specified temperature under fluctuating conditions. A separate temperature control system maintains the surrounding boundary at the gage temperature. The system was calibrated for both steady and unsteady flows using a specially designed calibrator for local heat flux gages. The steady calibration was done with predominantly convective heat transfer. The unsteady calibration was achieved by adding oscillating radiant energy to the surface. Consequently, quantitative results can be obtained for both the mean and fluctuating components of the heat transfer. The frequency response was good to over 90 Hz. Sample results are presented of the unsteady heat transfer over a circular cylinder caused by natural vortex shedding at 70 to 80 Hz.

Introduction

Many different methods have been used to measure the time-averaged local convective heat transfer between a fluid and a surface. Very little experimental information has been collected, however, about the instantaneous heat transfer from surfaces. Many flows that have been traditionally treated as steady actually have significant components of unsteadiness. Examples include vortex shedding by cylinders in crossflow, the effects of rotor wakes on stator blades in turbomachinery, the growth of flow instabilities leading to turbulence, and the bubble flow regime of fluidized beds. In all of these cases understanding of the fundamental heat transfer mechanisms would be greatly aided by detailed time-resolved measurements of the heat flux.

Because most heat transfer measurement systems are designed for steady heat transfer, they are usually very limited in their frequency response. The miniature Gardon gage (Gardon, 1960) gives continuous output, but the thermal capacitance of the circular foil generally limits its response to less than 1 Hz (Keltner and Wildin, 1975; Kim et al., 1983). Thin layered gages of several designs have been used, but their frequency response is still generally below 20 Hz unless extensive signal processing is performed (Epstein et al., 1986). Thin-film gages have been developed to measure the heat flux from a surface by measuring the time-resistance (temperature) history (Vidal, 1956). Because they are passive, transient devices with time constants on the order of microseconds, however, they are limited to short-duration tests (Schultz and Jones, 1973). Moreover, since the heat flux is determined from the rate of change of the temperature, they are often only used to determine steady heat transfer. Some recent measurements, however, have included high-velocity flows with time-resolved heat flux (Doorly and Oldfield, 1985).

To allow longer tests using thin-film gages, some investigators (Boulos and Pei, 1974; Suarez and Figliola, 1983; Fitzgerald et al., 1981; Hayward and Pei, 1978) have used constant-temperature anemometers to supply power to the gages and maintain them at a fixed resistance (and, it is hoped, a fixed temperature). Although the construction of the gages is similar, the active and continuous resistance (temperature) control and the direct power measurement make their operation considerably different than the passive gages described. They have been used for measuring continuous unsteady heat flux from cylinders in fluidized beds (Suarez and Figliola, 1983; Fitzgerald et al., 1981) and the turbulent heat transfer fluctuations on the surface of a cylinder (Boulos and Pei, 1974) and a sphere (Hayward and Pei, 1978).

This type of thin-film gage with constant-temperature anemometer control has also been used with a large overheat to measure surface shear stress (Bellhouse and Schultz, 1968; Ramaprian and Tu, 1983). Because the temperature of the film is much higher than the surrounding surface, the gage actually measures the thermal boundary layer that develops only over the film strip itself. All of the surrounding surface is purposely made adiabatic to localize the thermal boundary layer development to the heated strip on the gage. Conversely, heat flux measurements are usually desired on a surface with a prescribed and continuous heating condition over the entire surface. The development of the thermal boundary layer over the surface is, therefore, a necessary part of the experiment. The difference, then, between a shear-stress measurement and a heat-flux measurement is the thermal boundary condition on the surface upstream of the gage (Van Heiningen et al., 1976).

In the previous work with thin-film heat flux gages, the temperature continuity of the boundary condition has often not been maintained. It is common to give the gage a temperature offset above the surrounding surface temperature to increase the operational stability (Fitzgerald et al., 1981). It is also common to leave unheated regions on the gage around the heated film. Although Suarez and Figliola (1983) left a significant area of their gage unheated, they covered the entire gage with a highly conductive protective covering. This acted like a fin to distribute the heat over the entire gage surface. A subsequent unsteady analysis demonstrated the effect of the unheated region on the transient gage response (Beasley and Figliola, 1988). Even though this analysis does not include the interaction of the control circuitry, it is clear that the response time decreases dramatically as the size of the unheated region is increased. Both the temperature offset and this unheated region make it difficult to account for the conduction losses through the substrate to obtain the absolute rate of heat flux or the effective gage area. The nonuniform temperature

[1]Present address: TRW Inc., 5203 Leesburg Pike, Falls Church, VA 22041.

Contributed by the Heat Transfer Division for publication in the JOURNAL OF HEAT TRANSFER. Manuscript received by the Heat Transfer Division April 28, 1986. Keywords: Forced Convection, Measurement Techniques, Transient and Unsteady Heat Transfer.

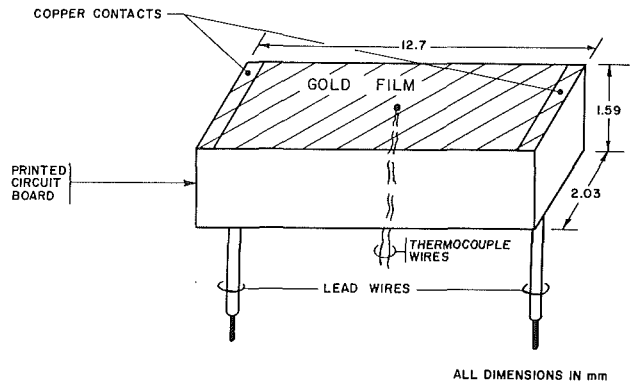

Fig. 1 Thin-film heat flux gage

around the gage makes calibration difficult, and calibration procedures have usually not been reported in detail.

The gage developed for the present work, like that of Boulos and Pei (1974), has a heated film that covers the entire surface of the substrate. There are no adiabatic surfaces to disturb the thermal boundary layer. Moreover, there are two additional differences from previous work. First, a small thermocouple is imbedded in the substrate immediately below the film. This is used to maintain the film temperature matched with the surrounding surface temperature to within ±0.1°C. Second, detailed heat flux calibrations are presented for *both* the steady and unsteady portions of the signal.

Gage Construction

The gage design is shown in Fig. 1. The gage is nominally 12.7 mm (0.5 in.) long by 2.03 mm (0.080 in.) wide by 1.6 mm (0.0625 in.) thick. It is constructed of a gold film sputter-coated onto a printed circuit board substrate. The lead wires are brought to the surface through the substrate and soldered to copper contacts at the surface. The gold film covers the substrate and the copper contacts, which eliminates problems in connecting the lead wires to the film. Also, a small thermocouple (0.076 mm wire) is mounted in the center of the surface of the substrate, approximately 0.13 mm (0.005 in.) below the film. A thin layer of epoxy is used to maintain electrical isolation between the thermocouple and gold film. The thermocouple is used as an external monitor of the film temperature. The periphery of the gage is coated with a thin layer of enamel paint as an electrical insulator. Sputter coating was chosen over other deposition methods because of the excellent uniformity and easy control of the surface thickness. The finished gage was installed in a machined slot, with the gage surface flush with the plate or cylinder surface.

Once installed in a surface the gage was connected to one leg of the bridge circuit of a TSI IFA-100 Constant Temperature Anemometer. A resistance calibration was done using the internal circuitry of the IFA-100. The surface was heated electrically with the heaters on the backside of the plate and with insulation covering the front surface to give a uniform temperature around the gage. The resulting temperature-resistance curve was used to establish the proper operating resistance. The IFA-100 was then used to maintain the gage at the operating temperature. Once this temperature was set, the surrounding plate was heated to the same temperature (within ±0.1°C) with a heater driven by a Eurotherm automatic controller, model 810. Matched thermocouples in the gage and plate were used to monitor the temperature difference and readjust the controller when necessary.

Steady Calibration

Two different methods were used for the time-averaged calibration of the thin-film gages. In each case the power input to the gage was compared with a known heat flux.

Impinging Flow Calibration. The flat plate apparatus of Borell and Diller (1987) was used for steady calibration of the heat flux gage in a convective environment. The estimated accuracy for determining local heat flux was ±2 percent. The heat flux gage was mounted in the center of the aluminum calibration plate with its top surface flush with the plate surface. The calibration plate was surrounded by four heated aluminum plates. The center plate and guard plates were heated with silicone-rubber resistance heaters supplied with power by a variable voltage autotransformer. The center plate was maintained isothermal to ±1°C and the guard plates were maintained to within ±0.2°C of the center plate temperature. The losses through the insulation strips between plates to the surrounding air, the losses through the insulation on the back of the plate, and the surface radiation were modeled and included in the heat transfer calculations. The equation used to obtain the surface heat transfer coefficient from the calibration plate power was

$$h_{av} = \frac{Q_{\text{htr}} - Q_{\text{loss}} - \sigma(\epsilon_p A_p)(T_p^4 - T_a^4)}{A_p(T_p - T_\infty)} \quad (1)$$

Further description of the calibration apparatus is given by Borell and Diller (1987).

All temperatures were read from a Doric 410A thermocouple readout, calibrated to ±0.1°C. The a-c rms voltage across

Nomenclature

A_p = surface area of calibration plate (without area of the gage)
A_{film} = surface area of gage film, including copper contacts
D = cylinder diameter
E_{br} = bridge voltage
f = frequency
h = heat transfer coefficient
$\bar{h}$ = time-averaged heat transfer coefficient
h_{av} = spatial-averaged heat transfer coefficient
h_g = heat transfer coefficient measured by gage
k = thermal conductivity of air
Nu = cylinder Nusselt number $= hD/k$
P_{film} = power dissipated in the film
Q_{htr} = power supplied to heater in calibration plate
Q_{loss} = losses through the back and the balsa wood for the calibration plate
R_{cable} = resistance of co-axial cable going to the gage
R_{gl} = resistance of the gage lead wires
R_{oper} = gage operating resistance
Re = cylinder Reynolds number $= U_\infty D/\nu$
St = Strouhal number $= fD/U_\infty$
T_a = ambient temperature, for radiation loss calculations
T_{film} = gage film temperature
T_m = mean air temperature for calculating air properties
T_p = plate mean temperature
T_∞ = free-stream temperature
U_∞ = free-stream velocity
Δ = change in variable
ϵ_{film} = gage film emissivity
ϵ_p = calibration plate emissivity
ν = kinematic viscosity of air
σ = Stefan–Boltzmann constant = 5.67×10^{-8} W/m^{2}K^4
τ = characteristic response time

the calibration plate heater and the heater resistance were measured with a Hewlett-Packard 3468A digital voltmeter. The gage operating temperature was adjusted until it matched the closest plate thermocouple temperature. Three readings of the bridge voltage (a-c true rms and d-c) were recorded along with the probe cable and operating resistances. These were used to calculate the power dissipated from the gage.

$$P_{\text{film}} = E_{br}^2 \frac{(R_{\text{oper}} - R_{gl})}{(R_{\text{oper}} + R_{\text{cable}} + 10\Omega)^2} \tag{2}$$

The square of the bridge voltage includes the square of the d-c voltage plus the square of the a-c true rms voltage. The corresponding heat transfer coefficient was calculated as

$$h_g = \frac{P_{\text{film}} - \sigma\epsilon_{\text{film}} A_{\text{film}} [T_{\text{film}}^4 - T_a^4]}{A_{\text{film}} (T_{\text{film}} - T_\infty)} \tag{3}$$

Cylinder Calibration Apparatus. The test cylinder was constructed from a hollow aluminum cylinder (6.0 cm o.d.), which was split lengthwise for ease of installation of instrumentation. This is the same test cylinder used by Borell et al. (1984) expect that a pair of 0.76 mm (0.003 in.) type-T thermocouples were mounted at the cylinder surface near the gage location. The thermocouples were soldered into brass tubing, which was press fit into holes drilled in the cylinder wall. The heat flux gage was fit into a slot milled in the center of one of the aluminum halves. The ends of the slot were rounded due to milling, but were made square by filling with Dupont Plastic Aluminum. The 2-mm-wide gage covered about 3 deg of arc on the cylinder.

The temperature of the cylinder was maintained by a wire resistance heater controlled by a Eurotherm 810 temperature controller and a Eurotherm 831 phase-angle-fired power supply. The controller stabilized the cylinder temperatures to $\pm 0.1°C$ in about 10 min from a cold start. The 0.55-cm-thick cylinder wall allowed good axial and circumferential conduction, which aided in maintaining the cylinder temperature uniform to $\pm 0.5°C$ over the entire center region.

The cylinder was placed into a wind tunnel with a 25 cm by 36 cm test section. This gave a blockage of 24 percent and a length-to-diameter ratio for the cylinder of 6. The free-stream turbulence was less than 0.5 percent and the flow uniformity was within ± 1 percent outside of the wall boundary layers. The free-stream velocity and temperature were measured upstream of the cylinder with a pitot tube and a thermocouple, respectively. The cylinder wall temperatures along with the free-stream temperature were read from a Doric 410A thermocouple readout, calibrated to $\pm 0.1°C$. During the tests the cylinder temperature was maintained about 35°C to 40°C above the free-stream temperature. The gage output was recorded as described for the impinging flow calibration and reduced using equations (2) and (3). All of the air properties were taken at the mean air temperature

$$T_m = \frac{T_{\text{film}} + T_\infty}{2} \tag{4}$$

Results. One of the questions about the gage operation was the match between the temperature determined from the gage thermocouple and the temperature from the operating resistance. A change of only 0.02 Ω in the resistance of these gages corresponds to a 1°C change in temperature. In addition, constant temperature anemometers generally have some bias voltage designed into their circuitry. The results of tests, however, showed a temperature match within $\pm 0.1°C$ between the temperatures indicated by the film thermocouple and the corresponding resistance calibration, when the controller and anemometer systems were properly adjusted and the gage resistance did not drift during the test. The resistance drift was seen as a change in thermocouple temperature during the test and a shift of the resistance-temperature curve between the beginning and end of a test. It is thought that the drop in resistance of a new gage is due to a slow structural collapse of the film. For this reason gages were always run at operating temperature for at least 25 hours before being used for measurements. After this break-in period, the resistance drop was usually less than 0.02 Ω (1.0°C) per hour, which is very slow compared to the duration of a measurement.

The steady calibration results are shown in Fig. 2. A different gage was used for the two sets of points in addition to the different calibration method. For the impinging flow calibration, the heat transfer coefficient determined from the thin-film gage is plotted versus the heat transfer coefficient determined from the steady-state power into the calibration plate. The estimated uncertainties are indicated for each measurement axis. The solid diagonal line represents the perfect one-to-one match between measurements and expected gage output. The dashed line is a least-square fit of the data points. This line is parallel with the expected correlation, but is shifted upward by about 10 W/m^2K or about 10 percent over the range of operation. The scatter of the points is about the same size as the estimated error. The largest component of the error was due to the uncertainty in matching the gage temperature with the surrounding surface temperature ($\pm 0.1°C$). A conduction analysis of the gage predicted a 5 percent uncertainty in the heat flux due to this 0.1°C temperature uncertainty (Campbell, 1985). It was observed that as more care was taken experimentally to match these temperatures, the data points came closer to the one-to-one correlation line.

Very similar results were found with the circular cylinder results, also as shown in Fig. 2. Here the comparison is made with the well-documented measurement and prediction for the Nusselt number at the stagnation point of a cylinder in an air crossflow (Kraabel et al., 1980)

$$\text{Nu} = 0.95\sqrt{\text{Re}} \tag{5}$$

The scatter and estimated uncertainty are about the same as the impingement calibration. Again, when the gage temperature was slightly higher than the surrounding plate temperature, the slope of the line fitting the data was increased and was displaced upward.

One of the operational difficulties with the present gage

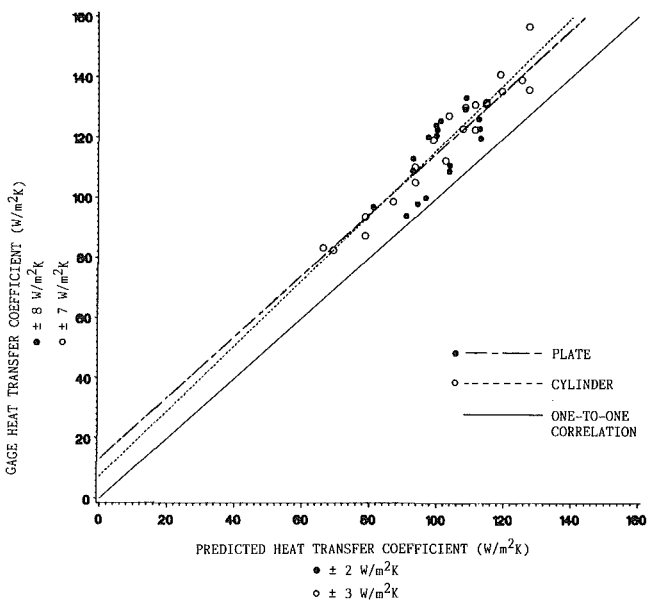

Fig. 2 Steady calibration results

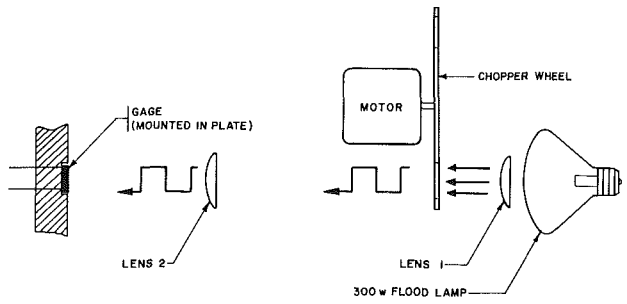

Fig. 3 Thermal square-wave apparatus for the unsteady calibration

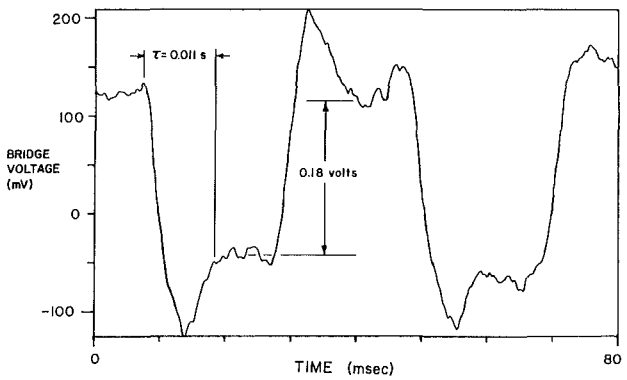

Fig. 4 Thermal square-wave test results

system was the inability to operate at low heat flux levels with large heat flux fluctations. This was a problem for both the impinging flow calibration apparatus because of the high free-stream turbulence levels (2 percent) and for the wake region of the cylinder model because of the vortex shedding. The fluctuations in the heat transfer signal due to the 2 percent turbulence were as high as ±10 percent. When the unsteadiness was much above this level the signal fluctuations caused the IFA-100 anemometer to shut off automatically.

Unsteady Calibration

Two methods were used to measure the frequency response of the gage system. Both used a square-wave perturbation of the system. In the first method this was done electronically, while in the second the gage was perturbed with a thermal radiation pulse.

Electronic Square-Wave Test Apparatus. The electronic square-wave test was used to give a step change to the gage anemometer system and to monitor the response. An electronic square wave is applied in parallel to the gage leg of the anomometer bridge and the bridge output voltage is observed on an oscilloscope or similar instrument. The test is often used to adjust the anemometer compensation controls to obtain maximum frequency response. Freymuth and Fingerson (1977) have defined the cutoff frequency for cylindrical hot-film sensors and wedge-type gages as the inverse of the observed response time of the bridge output. However, technical representatives from Thermo Systems Inc. (TSI) recommended a more conservative approximation for the frequency response of speciality probes such as used in this research, which is an order of magnitude less than what would be expected for a cylindrical hot-film sensor.

The test was conducted with the gage in the cylinder model since the low turbulence levels in the wind tunnel allowed clear viewing of the bridge voltage on an oscilloscope. In addition, a splitter plate was added to the cylinder to remove the effects of von Karman vortex shedding on the heat transfer signal.

Thermal Square-Wave Test Apparatus. The apparatus used for generating the chopped thermal radiation signal is shown in Fig. 3. The thermal radiation source is provided by a 300 W flood-lamp bulb with two plano-convex lenses used to focus the light. A wheel with two equally spaced slots, each spanning 90 deg of rotation, was used to chop the light. By mounting the chopper wheel between the two lenses, a sharp cutoff of the light was obtained. The chopper wheel was driven by a small d-c motor with a continuously variable d-c power supply. The maximum rotational speed was 2400 rpm, which corresponds to a maximum square-wave frequency of 80 Hz. This test was run on the calibration stand since the thermal radiation source could be easily directed at the gage while there was flow over the gage. However, since there was turbulence in the free stream, the signal was ensemble-averaged with a Hewlett-Packard 5420A digital signal analyzer to obtain a clear time record.

Results. A sample of the thermal square-wave test results is shown in Fig. 4. The time period for complete response, τ, is marked on the figure. For the test shown, the square-wave frequency was 25 Hz and the estimated frequency response was 91 Hz based on the measured time constant of 11 ms. This time constant for complete response is longer than that usually associated with the −3 dB hot-wire or hot-film time constants (Freymuth and Fingerson, 1977). It therefore provides a conservative estimate of the frequency response. Moreover, there was no measurable attenuation of the amplitude of the square-wave response compared to the steady-state on-off signal from the light. These results, however, were very sensitive to the cable compensation settings on the anemometer unit. When other TSI and DISA anemometer models were tried, the amplitude of the thermal square-wave test signal was attenuated by a factor of five to ten. Further testing in these cases revealed that the gage resistance was changing by the equivalent of up to 1°C by the changing heat flux. Because of the much lower overheat of this gage (~35°C) than for typical velocity probes, a much larger measurement error results.

The effect of this temperature change on the gage response is shown in Fig. 5. It should be noted that the time scale is much larger than in Fig. 4. Each curve shows the response of the anemometer bridge voltage as the radiation from the thermal square wave is turned off. The anemometer responds by increasing power to try to maintain the thin film at a constant temperature. In the upper curve (Fig. 5*a*) the anemometer responds properly as seen by the sharp change in voltage. Temperature measurements made by the thermocouple mounted in the gage also showed no change in gage temperature for this case. In the lower curve (Fig. 5*b*) the response of the anemometer to the thermal square wave occurs in two steps. After the initial sharp change the bridge voltage continues to drift toward the steady-state level. Beasley and Figliola (1988) found the same type of two-step response from a transient analysis of this type of gage. The fast response portion was due to the thin film and protective coating, while the slow response portion of the curve was due to the temperature change of the substrate. It is believed that the substrate response is also the reason for the slow response seen in Fig. 5(*b*). Measurements by the gage thermocouple indicated a corresponding decrease in gage temperature of 0.6°C due to this change in heat flux. Although such a temperature drift has only a small effect on the steady-state gage measurements, the effect on the transient response is a dramatic decrease in the measured amplitude of heat flux. The difference between the two responses seen in Fig. 5 can be achieved by simply changing the cable and bridge compensation settings on the anemometer. Therefore, the electronic compensation used in the bridge amplifier is very important, and a simple time-response measurement of the gage system is not sufficient to ensure accurate unsteady measurements. The amplitude of the

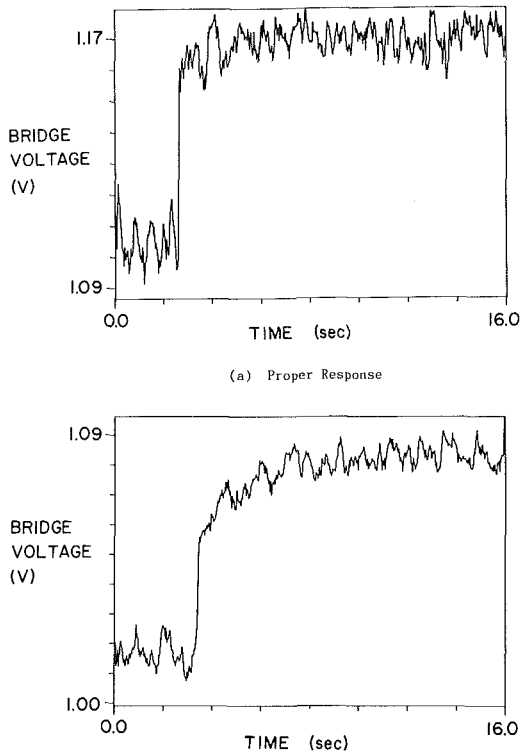

Fig. 5 Effect of bridge temperature control on transient response

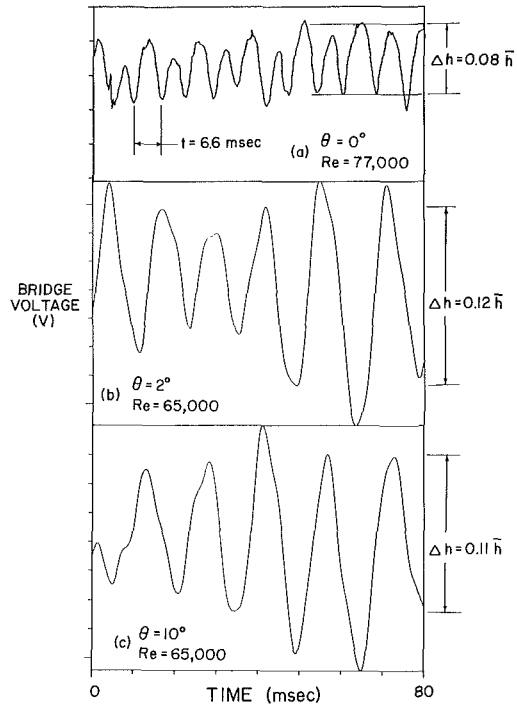

Fig. 6 Effect of vortex shedding on cylinder heat transfer

unsteady response must also be checked with the steady-state on-off values.

The frequency response of the gage was also dependent on the amount of copper cladding left on the front surface of the gage. Not only did this probably cause a nonuniform temperature distribution, but it also greatly increased the thermal inertia of the gage. The response time of the gold film was estimated to be ~ 1 ms, which is much faster than that measured for the gage. As the amount of copper left on the gage was increased, the frequency response dropped even further. Therefore, to maximize the frequency response of this type of gage the mass of the electrical contacts must be minimized.

Traces similar in shape to those in Fig. 4 were also obtained with the electronic square-wave test. The results, however, gave a time constant of about 20 μs. The corresponding -3dB cutoff frequency, as previously discussed, is estimated to be 5 kHz. The much faster response for the electronic test indicates that, even though the gage is included in the circuit, the true thermal response of the gage is not being measured.

Application to Cylinder Heat Transfer

As a demonstration of its potential, the gage was used to measure unsteady heat transfer from a cylinder in a steady crossflow. The free-stream turbulence level of the wind tunnel was less than 0.5 percent and the Reynolds number was varied from 65,000 to 77,000. The unsteadiness of the flow around the cylinder was due to the natural vortex shedding in the wake of the cylinder. This alternate shedding of vortices in the wake causes an oscillation of the front stagnation point by several degress of angle. The frequency of this oscillation is characterized by the Strouhal number, $St = fD/U_\infty$, which has a value of approximately 0.2 for a wide range of subcritical Reynolds numbers ($Re \lesssim 150{,}000$) (Achenbach and Heinecke, 1981).

The gage output for 0, 2, and 10 deg from the front stagnation point is shown in Fig. 6. These are the actual time records of the a-c component of the bridge voltage. Because the amplitude of the fluctuating voltage is small compared to the mean, the results shown are approximately proportional to the measured heat flux. The scale of the y axis is not the same for the three curves, however. Consequently, the size of the heat transfer coefficient fluctuation is marked on each curve, as calculated from the dissipated power. This also matched the results of calibrations like those shown in Figs. 2 and 4.

The results plainly show the effect of the vortex shedding on the local instantaneous heat transfer. The frequency of the heat flux oscillation at 2 and 10 deg from the stagnation point (Figs. 6*b* and *c*) matches that of the wake vortex shedding. These time records also indicate large variations of the amplitudes of the unsteady heat flux from cycle to cycle. This has also been observed in the unsteady fluid mechanics of vortex shedding (Blevins, 1985). To insure that the fluctuations actually were due to the vortex shedding, additional tests with a splitter plate installed immediately behind the cylinder were also performed for comparison. The only heat transfer fluctuations measured with the splitter plate in position were about 1 percent in amplitude and were due to 60 Hz noise and random turbulence.

The unsteady heat transfer measurements of Boulos and Pei (1974) did not show this regular pattern of heat transfer fluctuation in the attached boundary layer region. They only found this type of sinusoidal signal near separation (80 to 90 deg). This may be because they generally had higher levels of free-stream turbulence (up to 7 percent) and a lower Reynolds number ($Re < 10{,}000$). More importantly, however, they did not report a calibration of the amplitude of their fluctuating signal. As reported earlier in this paper, hot-wire anemometers tend to attenuate strongly the amplitude of the fluctuating portion of the signal from this type of gage. Because Boulos and Pei only performed an indirect dynamic calibration of their probe, the actual unsteady response was not determined.

At the front stagnation point (Fig. 6*a*), the heat flux signal shows that the fluctuations are at twice the shedding frequency of the signal at 2 deg (Fig. 6*b*). This is due to the heat transfer signal being rectified because of the zero net flow at the front stagnation point. This phenomenon has also been recorded in

skin friction measurements by Meier et al. (1981). When comparing the amplitude of the fluctuating heat transfer, it should be noted that because the signal at 0 deg is rectified, the lower portions of this curve have essentially been flipped. Therefore, the 6 to 8 percent amplitude at 0 deg should be compared with the zero-to-peak value of 6 percent at 2 deg.

Conclusions

The calibration and use of actively heated thin-film gages for measuring unsteady convective heat flux have been described. By coating the entire gage surface with the resistive film and by actively controlling both the gage temperature and the surrounding surface temperature, an isothermal boundary condition is maintained over the entire surface. Although the actual condition over the gage surface is constant heat flux, this produces very nearly a constant temperature for small spatial variations of the heat flux relative to the 2-mm width of the gage. The gage, therefore, is isothermal except for uses involving very small surfaces or very steep heat flux gradients as could occur at shock fronts. Consequently, no scaling of the results is necessary. The measured power can be directly related to the heat flux.

The time-averaged calibration results revealed a 10 percent uncertainty for different tests and gages. It is recommended, therefore, for accurate measurements to have another type of local gage to measure simultaneously the time-averaged heat flux.

A direct thermal calibration of the gage frequency response gave a much slower time response than the usual electronic test. However, the gage still gave complete response to a large-amplitude (10 percent) thermal square wave in 11 ms with no drop in amplitude. This gives confidence in the unsteady results up to at least 90 Hz.

As an example of the measurements possible using this gage, the effect on the heat transfer of cylinder vortex shedding was measured near the stagnation point of a cylinder in a low-speed wind tunnel. The time records of the gage output are demonstrated for shedding frequencies of 70 to 80 Hz. The characteristic double frequency is also shown at the stagnation point.

Acknowledgments

The support of the Department of Energy, Grant No. DE-A505-82ER12022, is gratefully acknowledged. This is a project in the program of Dr. Oscar P. Manley, Division of Engineering and Geosciences of the Office of Basic Energy Science.

References

Achenbach, E., and Heinecke, E., 1981, "On Vortex Shedding From Smooth and Rough Cylinders in the Range of Reynolds Number 6×10^3 to 5×10^6," *J. Fluid Mech.*, Vol. 109, pp. 239–251.

Beasley, D. E., and Figliola, R. S., 1988, "A Generalized Analysis of a Local Heat Flux Probe," *J. Phys. E: Sci. Instrum.*, Vol. 21, pp. 316–322.

Bellhouse, B. J., and Schultz, D. L., 1968, "The Measurement of Fluctuating Skin Friction in Air With Heated Thin-Film Gauges," *Journal of Fluid Mechanics*, Vol. 32, pp. 675–680.

Blevins, R. D., 1985, "The Effect of Sound on Vortex Shedding From Cylinders," *J. Fluid Mech.*, Vol. 161, pp. 217–237.

Borell, G. J., Kim, B. K., Ekhaml, W., Diller, T. E., and Telionis, D. P., 1984, "Pressure and Heat Transfer Measurements Around a Cylinder in Pulsating Crossflow," in: *Unsteady Turbulent Boundary Layers and Friction*, D. C. Wiggert and C. S. Martin, eds., ASME, New York, pp. 17–23.

Borell, G. J., and Diller, T. E., 1987, "A Convection Calibration Method for Local Heat Flux Gages," ASME JOURNAL OF HEAT TRANSFER, Vol. 109, pp. 83–89.

Boulos, M. I., and Pei, D. C. T., 1974, "Dynamics of Heat Transfer From Cylinders in a Turbulent Air Stream," *International Journal of Heat and Mass Transfer*, Vol. 17, pp. 767–783.

Campbell, D. S., 1985, "Design and Calibration of a Rapid-Response Thin-Film Heat Flux Gage," M.S. Thesis, VPI&SU, Blacksburg, VA.

Doorly, D. J., and Oldfied, M. L. G., 1985, "Simulation of the Effects of Shock Wave Passing on a Turbine Rotor Blade," ASME *J. Engineering for Gas Turbines and Power*, Vol. 107, pp. 998–1006.

Epstein, A. H., Guenette, G. R., Norton, R. J. G., and Cao, Y., 1986, "High-Frequency Response Heat-Flux Gauge," *Review of Scientific Instruments*, Vol. 57, pp. 639–649.

Fitzgerald, T. J., Catipovic, N. M., and Jovanovic, G. N., 1981, "Instrumented Cylinder for Studying Heat Transfer to Immersed Tubes in Fluidized Beds," *Industrial Engineering Chemistry, Fundamentals*, Vol. 20, pp. 82–88.

Freymuth, P., and Fingerson, L. M., 1977, "Electronic Testing of Frequency Response for Thermal Anemometers," *TSI Quarterly*, Vol. III, No. 4.

Gardon, R., 1960, "A Transducer for the Measurement of Heat Flow Rate," ASME JOURNAL OF HEAT TRANSFER, Vol. 82, pp. 396–398.

Hayward, G. L., and Pei, D. C. T., 1978, "Local Heat Transfer From a Single Sphere to a Turbulent Air Stream," *International Journal of Heat and Mass Transfer*, Vol. 21, pp. 35–41.

Keltner, N. R., and Wildin, M. W., 1975, "Transient Response of Circular Foil Heat Flux Gages to Radiative Fluxes," *Rev. Sci. Instrum.*, Vol. 46, pp. 1161–1166.

Kim, B. K., Borell, G. J., Diller, T. E., Cramer, M. S., and Telionis, D. P., 1983, "Pulsating Flow and Heat Transfer Over a Circular Cylinder," in: *Proceedings of the Symposium on Nonlinear Problems in Energy*, DOE CONF-830413, pp. 96–101.

Kraabel, J. S., Baughn, J. W., and McKillop, A. A., 1980, "An Instrument for the Measurement of Heat Flux from a Surface With Uniform Temperature," ASME JOURNAL OF HEAT TRANSFER, Vol. 102, pp. 576–578.

Meier, H. U., Kreplin, H. P., and Fang, L. W., 1981, "Experimental Study of Two- and Three-Dimensional Boundary Layer Separation," in: *Unsteady Turbulent Shear Flows*, R. Michel, J. Cousteix, and R. Houdeville, eds., Springer-Verlag, New York, pp. 87–99.

Ramaprian, B. R., and Tu, S. W., 1983, "Calibration of a Heat Flux Gage for Skin Friction Measurement," ASME *Journal Fluids Engineering*, Vol. 105, pp. 455–457.

Schultz, D. L., and Jones, T. V., 1973, "Heat-Transfer Measurements in Short Duration Hypersonic Facilities," AGARDograph, No. 165.

Suarez, E., and Figliola, R. S., 1983, "Instantaneous Azimuthal Heat Transfer Coefficients From a Horizontal Cylinder to a Mixed Particle Size Air-Fluidized Bed," ASME Paper No. 83-HT-93.

Van Heiningen, A. R. P., Mujumdar, A. S., and Douglas, W. J. M., 1976, "On the Use of Hot Film and Cold Film Sensors for Skin Friction and Heat Transfer Measurements in Impingement Flows," *Letters in Heat and Mass Transfer*, Vol. 3, pp. 523–528.

Vidal, R. J., 1956, "Model Instrumentation Techniques for Heat Transfer Measurements in a Hypersonic Shock Tunnel," Cornell Aeronautical Laboratory Report No. AD-917-A-1.

N. Akino
Principal Engineer.

T. Kunugi
Research Engineer.
Japan Atomic Energy Research Institute,
Tokai-mura, Naka-gun,
Ibaragi, 319-11 Japan

K. Ichimiya
Associate Professor.

K. Mitsushiro[1]
Graduate Student.
Department of Mechanical Engineering,
Yamanashi University,
Takeda-4, Kofu,
Yamanashi, 400 Japan

M. Ueda[2]
Graduate Student.
Department of Nuclear Engineering,
Kobe University of Mercantile Marine,
Kobe-shi, 658 Japan

Improved Liquid-Crystal Thermometry Excluding Human Color Sensation

A new liquid-crystal thermometry method is described to determine an isothermal map on a heat transfer surface coated with a cholesteric liquid-crystal layer that changes color according to temperature. This method is based on the use of a set of sharp band-pass optical filters, one of which is attached to a black-and-white video camera to take a monochromatic image having a specified color. From the image, an isothermal line was drawn with the aid of a digital image processing technique that excludes human color sensation. We obtain as many isothermal lines as band-pass filters and can determine an isothermal map. An experiment is presented as an application of the present method to measure temperature distributions on a heated surface cooled by air flow and disturbed by a short attached cylinder.

Introduction

During the development of the very high-temperature gas-cooled nuclear reactor, the authors have investigated the heat transfer and hydrodynamics caused by the spacer ribs, which protrude from the surface of the fuel rod to keep proper clearance between the fuel rod and the coolant channel. The protrusions disturb the coolant flow and may augment heat transfer. On the other hand, they may cause hot or cold spots, increase the pressure drop, and cause vibration problems by shedding the vortices. To understand such thermo-hydrodynamic phenomena, it is very informative to visualize the detailed distribution of the surface temperature.

For example, if thermocouples were employed, more than a hundred sensors should be attached to the surface and a large data acquisition system should be required. An infrared thermo-camera can also be used to measure surface temperature distributions. However, this device is expensive and the test section must be made of a material transparent to infrared radiation, for example, single crystals of Si, Ge, or other special materials, all of which are difficult to produce and machine. We preferred to choose a more economical and convenient method of thermometry that still provides the global characteristics of the heat transfer surface.

Some liquid-crystal materials (cholesteric or chiral-nematic type) exhibit beautiful colors with a visible spectrum when they are heated to the specified temperature ranges. Since the color change is reversible and repeatable, they can be calibrated accurately with proper care and used as temperature indicators. Fergason (1968) extensively reviewed the chemical, optical, and thermal properties, and the techniques important to the thermal mapping for nondestructive material testing. Recently, these thermochromatic liquid crystals have become commercially available in film or paint forms, in which liquid crystals are stabilized by micro-encapsulation. They can be easily attached or painted on a heat transfer surface, and two-dimensional temperature distributions can be directly visualized as a colored pattern.

Thus, thermosensitive liquid crystals have been successfully applied to heat transfer studies. As a qualitative measure, liquid crystal are very impressive, since they display the full picture of the temperature field. On the other hand, to evaluate temperature quantitatively, they are inefficient and unreliable, because human color sensation must be employed to quantify temperature from color. Consequently, errors may be caused by individual differences and temporal inconstancy of the human sensation, and the lack of reproducibility of color image recording methods such as photography and video systems. Moreover, a considerable amount of manual labor is required.

Goldstein et al. (1982) used liquid crystals to visualize the temperature distributions and measure the heat transfer coefficients on a heated plate cooled by impinging jets. To evaluate temperature distributions quantitatively, they made use of only one temperature, corresponding to the color boundary between green and blue, which was the sharpest to the naked eye. In this way the isothermal line was determined almost completely while avoiding ambiguous judgment of color by human sensation. Kasagi et al. (1981) improved the method in a study of film-cooling heat transfer. The monochromatic light source (a sodium lamp emitting light at 589 nm) was used selectively to illuminate the single isothermal line. By these methods, the isothermal line could be determined almost independently of human capabilities to judge colors, but they got only one isothermal line. Therefore, they obtained multiple isothermal lines, an isothermal map, by changing the temperature levels of the heat transfer surfaces by changing the heating rate. Unfortunately, this procedure required long waiting times before steady conditions were reached.

We have developed a new method by which we can deter-

[1]Present affiliation: Research engineer, Matsushita Electric Industry Co., Ltd., Kadoma, Osaka, 571 Japan.

[2]Present affiliation: Engineer, Nuclear Fuel Industries, Ltd., Tokai-mura, Naka-gunn, Ibaragi-kenn, 319-11 Japan.

Contributed by the Heat Transfer Division and presented at the ASME Winter Annual Meeting, Anaheim, California, December 7–12, 1986. Manuscript received by the Heat Transfer Division March 17, 1987. Keywords: Measurement Techniques.

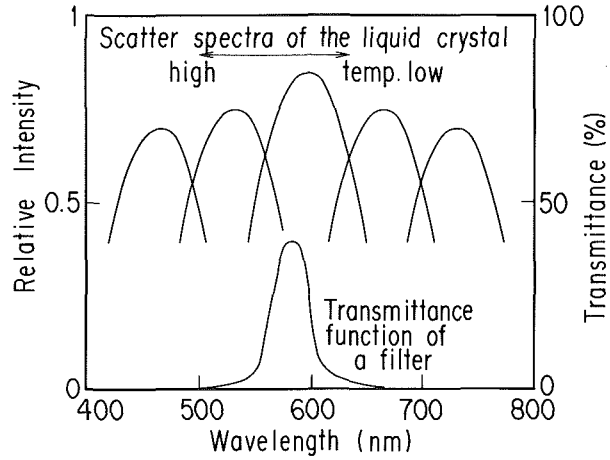

Fig. 1 Relation between light intensity, wavelength, and band-pass filter

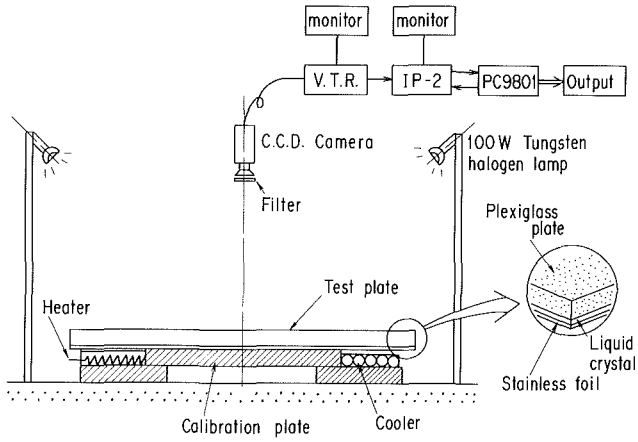

Fig. 2 Schematic view of the calibration apparatus

mine isothermal maps at a single heating condition, without the help of human sensation. This paper describes the fundamentals of the method, the calibration method, and application experiments to measure the temperature distributions on a heated surface cooled by air flow and disturbed by a short attached cylinder.

Fundamentals of this Method

The new method uses a set of optical filters having sharp band-pass transmittance characteristics to extract isochromatic regions and ordinary light sources having continuous spectral characteristics. Through the band-pass filter attached to a black-and-white video camera, the region showing the color specified by the filter can be observed selectively. A similar method was tried and presented briefly by Herold and Wiegel (1980).

The light scattered by the liquid-crystal layer has the spectral distribution described by the function $S(\lambda:T)$ of temperature T and wavelength λ, as shown in Fig. 1. The intensity $I_n(T)$ of the light filtered by the nth bandpass filter, with a transmittance function $f_n(\lambda)$, is represented by

$$I_n(T) = \int_0^\infty S(\lambda:T) f_n(\lambda) d\lambda \tag{1}$$

That is, the light intensity depends on both the temperature and the filter.

As the liquid-crystal layer is observed through one band-pass filter during the heating phase, the intensity becomes maximum around the temperature at which the peak wavelength of the light from the liquid-crystal layer coincides with the maximum wavelength of the transmittance of the band-pass filter. This temperature is specified for each filter, and called the peak intensity temperature hereafter.

When we observe a liquid-crystal layer having a monotonically distributed temperature through one filter, the intensity along the surface shows a distribution with a maximum at the point where its temperature coincides with the peak intensity temperature. That is, we can determine one isothermal line for each band-pass filter. By changing the filters, isothermal lines can be drawn and an isothermal map on the surface can be obtained.

Unfortunately, the filtered image is not always thin enough to draw an isothermal line directly, in spite of the sufficiently sharp characteristic of the band pass filters, because of the broad spectral characteristics of the light scattered and reflected from the liquid-crystal layer. As shown later, the light intensity depends not only on the temperature, but also on the width of the isochromatic region. Thus, the isothermal line has to be drawn connecting locally brightest points, with the aid of the digital image processing technique.

Calibration Tests

Before the quantitative determination of the isothermal lines, the peak intensity temperatures for each band-pass filter must be found by a calibration test. The liquid-crystal layer was painted on a plexiglass plate, which was placed on a calibration plate controlled to have a linearly distributed temperature profile. The video camera with one band-pass filter measured the light intensity distribution of the monochromatic image on the liquid-crystal layer, and the video signal was digitized by the image processor. Then a small computer was used to determine the location of the peak intensity. Because the temperature at all points was known from the embedded thermocouples, the peak intensity temperature could be determined. By changing the band-pass filters, the peak intensity temperature for each filter was determined.

Apparatus. A schematic view of the calibration apparatus and a diagram of the image processing system are shown in Fig. 2. The calibration plate was made of brass, with length of 300 mm, width of 80 mm, and thickness of 3 mm. One end was heated electrically and the other was cooled by water. Consequently, a linear temperature distribution was established within a length of 160 mm and was measured by three thermocouples buried in the plate.

Nomenclature

D = diameter of the circular cylinder
De = hydraulic diameter of test channel = $2H$
f = transmittance function
H = space of test channel
h = heat transfer coefficient = $q/(Tw-Tb)$
I = intensity of light
k = thermal conductivity of air
Nu = Nusselt number = hDe/k
q = heat flux
Re = Reynolds number = UDe/ν
T = temperature
Tb = bulk temperature of air
Tw = wall temperature
U = average velocity of air
X = streamwise distance toward downstream
X' = distance toward upstream
λ = wavelength
ν = kinematic viscosity of air

Table 1 Specifications of the band-pass filters

Filter No.	Wavelength (nm)	Transmittance (%)	Correction Factor	Half-width (nm)
1	401.5	35.0	1.30	10.0
2	427.0	31.5	1.44	9.0
3	451.5	42.0	1.08	10.5
4	477.0	40.5	1.12	9.0
5	500.0	37.0	1.23	7.0
6	524.0	40.5	1.12	7.5
7	537.5	39.5	1.15	7.0
8	548.5	37.0	1.23	7.5
9	561.5	40.0	1.14	9.0
10	577.0	39.0	1.16	7.5
11	589.0	36.0	1.26	8.0
12	598.5	36.5	1.25	7.5
13	627.0	37.0	1.23	7.5
14	651.0	45.5	1.00	9.0
15	672.0	41.5	1.10	9.0
16	700.0	36.5	1.25	8.0
17	729.0	42.5	1.07	10.0
18	747.0	35.5	1.28	8.0

The test plate was made from plexiglass and was 750 mm long, 330 mm wide, and 10 mm thick. One surface of the test plate was painted with the liquid-crystal ink, covered by black paint to absorb excess light, and attached to a 50-μm-thick stainless steel foil, which was used as the electric heater. The color distribution of the liquid-crystal layer was observed through the other side of the test plate.

The liquid crystal used in this study was a mixture of five cholesteric materials and was stabilized by the micro-encapsulation. The color of this liquid crystal changes at temperatures ranging from 27°C to 35°C, showing the colors red, orange, yellow, green, and blue.

The test plate was illuminated by four 100-W tungsten halogen lamps from a low angle so that light was not specularly reflected to the CCD camera. The lamps were equipped with infrared radiation absorbing filters to prevent radiative heating of the liquid crystal.

The color image was converted into an electric signal by a black/white CCD (Charge Coupled Device) video-camera located 700 mm above the test plate and the output from the camera was recorded by a video-recorder. A band-pass filter was mounted in front of the lens of the camera.

In this study, 18 interferential band-pass filters were used. Their central wavelengths were in the range of 401.5–747 nm and the full width at the half maximum (FWHM) of transmittance was 9($\pm$2) nm. The specifications of the filters are listed in Table 1.

Determination of Peak Intensity Temperature. The image signals were digitized with 8-bit gradations (i.e., 0 to 255) with 256×256 pixels per frame.

Using a small computer, the location of the pixel having the maximum intensity (peak intensity) was determined from each digital image for each filter. Because the temperature at the location of each pixel was known by interpolation of the thermocouple data, the relation between each filter and the temperature at the peak intensity (peak intensity temperature) was found.

Calibration Results. Photos 1(a)–(d) show photographs of monochromatic TV images of the liquid-crystal layer on the test plate under a temperature distribution with and without filters. Photo 1(a) was taken without filter, and the intensity distribution is relatively broad. Beside photo 1(a), the scale designated by W is the width of the calibration plate on the back side, H is the heater, C is the cooler, and LTR is the Linear Temperature Region. The region near the cooler is dark and cannot be observed. Photos 1(b)–(d) show the intensity distributions with band-pass filters corresponding to red, green, and blue. In photos 1(b) and 1(c), the brightness distributions in the LTR are relatively narrow and the peak-intensity lines can be distinguished by the naked eye. On the other hand, photo 1(d), with the blue (short-wavelength) filter, has a diffuse intensity distribution and peak-intensity positions cannot be found by the naked eye; the image processing technique is required.

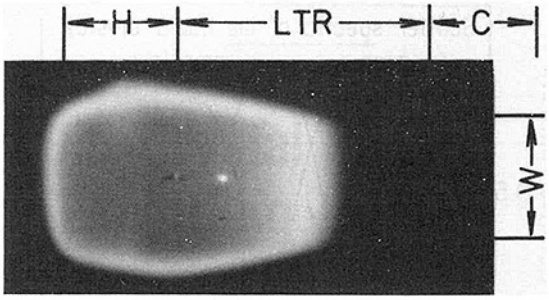

Photo 1(*a*) Image without filter

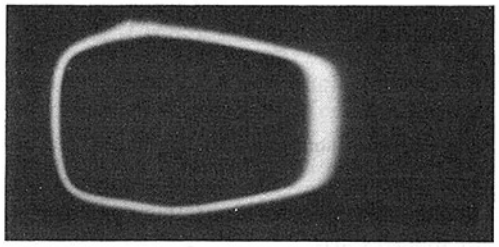

Photo 1(*b*) Image through a red band-pass filter

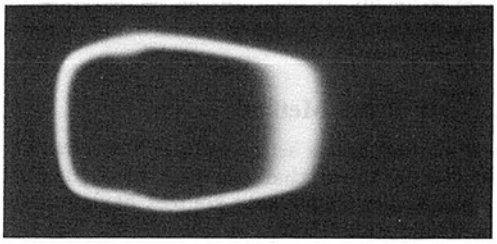

Photo 1(*c*) Image through a green band-pass filter

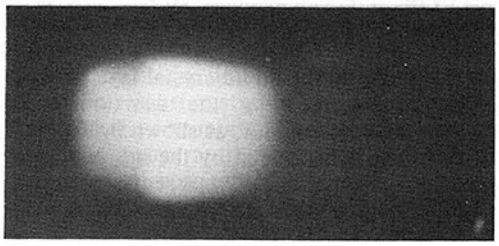

Photo 1(*d*) Image through a blue band-pass filter

Photo 1 Monochromatic TV images of the liquid-crystal layer on the test plate with and without band pass filters

Figure 3 shows the temperature distribution on the calibration plate and its corresponding location on the TV frame. Figure 4 shows two examples of the intensity distribution along the centerline of the test plate through band-pass filters with the center wavelengths of 561.5 and 477 nm. The vertical axis shows the intensity and two horizontal axes represent the location of pixels and the temperature. The error band symbols in the figure indicate the error caused by the flatness of the intensity profile near the peak, which corresponds to a factor of 2 (of the 8-bit gradations). This error causes an uncertainty of the peak intensity and peak intensity temperature. The error at 30.2°C is within 0.1°C for the band-pass filter having a 561.5 nm center wavelength, while that at 34°C is 0.5°C for the band-pass filter having a 477 nm center wavelength.

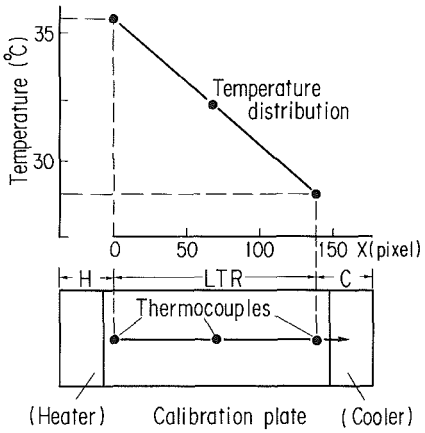

Fig. 3 Temperature distribution on the calibration plate

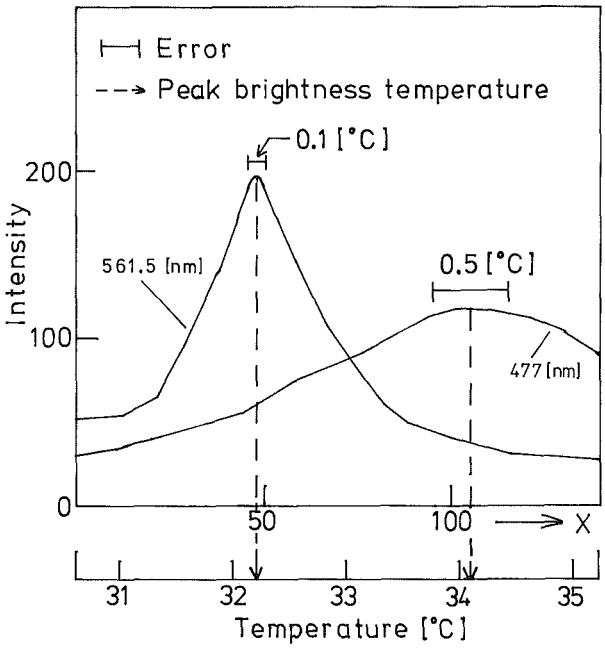

Fig. 4 Light intensity distribution along the test plate

The calibration test was carried out twice, with temperature gradients of 86 and 78°C/m. The relations between the central wavelength of the band-pass filters and the peak intensity temperature were obtained as shown in Fig. 5. The numbers in the figure (from No. 4 to No. 18) correspond to the number of the filters described in Table 1. For filters 1, 2, and 3, the peak intensity temperature could not be determined because the intensity profiles near the peak were too flat.

The two calibrations agreed within ±0.1°C in the temperature range 29–32°C. It was, however, difficult to determine the peak intensity temperature at the both extremes of the wavelength range, corresponding to temperatures below 29°C and above 35°C.

In the region where the filter wavelength has a clear functional relation to the peak intensity temperature (i.e., in the wavelength range of 524–700 nm, or in the temperature range 29°C–32°C), a temperature difference of 0.1°C corresponds to about an 8-nm difference of wavelength. Therefore, the error from the determination of the peak intensity temperature caused by the FWHM of the band-pass filters was found to be about 0.1°C.

The optical filter with a 627-nm wavelength (29.7°C) showed the least error of the peak intensity temperature

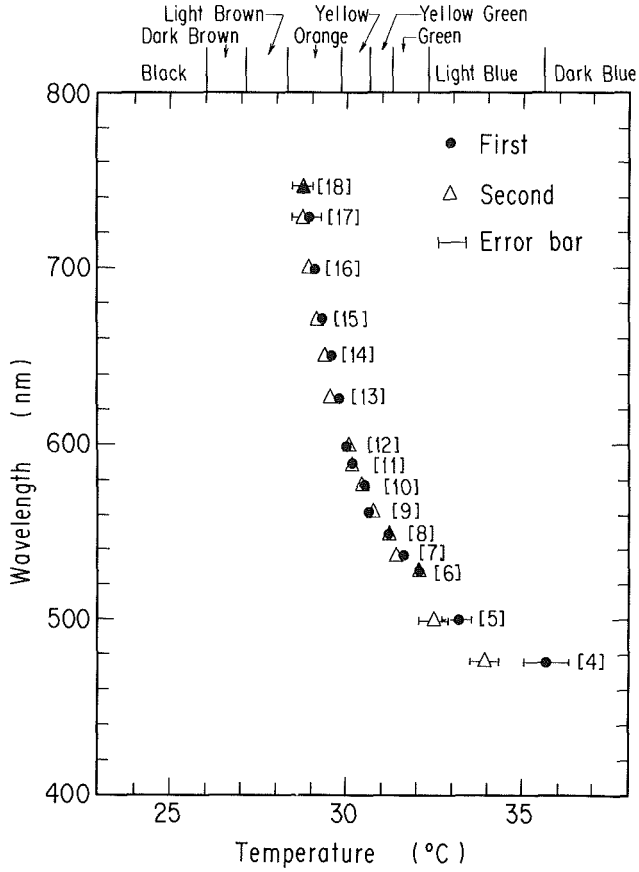

Fig. 5 Relationship between center wavelength of the band-pass filters and the peak brightness temperature

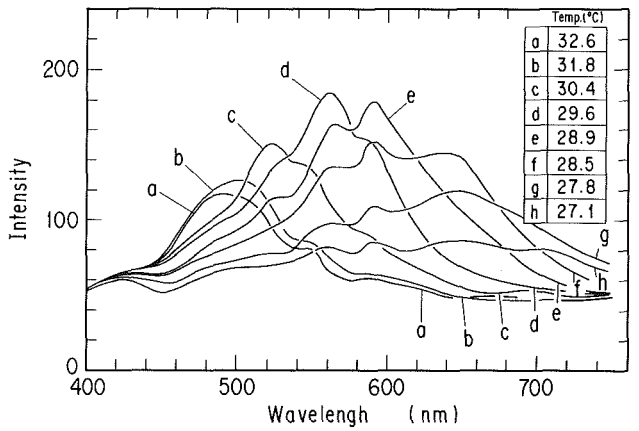

Fig. 6 Spectral characteristics of the micro-encapsulated liquid crystal

caused by the peaked profile of the intensity distribution; that error was about 0.1°C. The filter with 477 nm wavelength (34°C) showed the maximum error of about ±0.5°C.

Discussion of Calibration. Figure 6 shows the spectral characteristics of the light scattered by the liquid-crystal layer at several temperatures evaluated from the intensity of each pixel and wavelength of each filter. To the best of our knowledge, this is the first time that the spectral characteristics of micro-encapsulated liquid crystals were quantitatively measured. The differences of the transmittance among the optical filters were corrected by multiplying by the factors appearing in Table 1. The spectrum for each temperature was found for wavelengths from 400 nm to 750 nm.

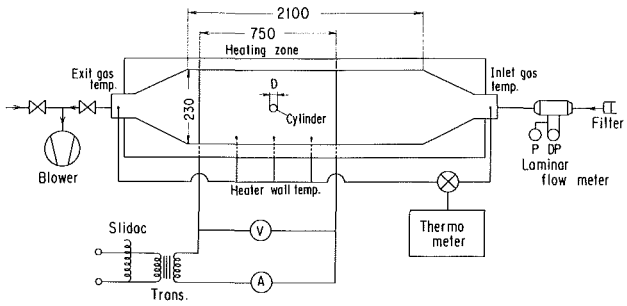

Fig. 7 Test channel for the application experiment

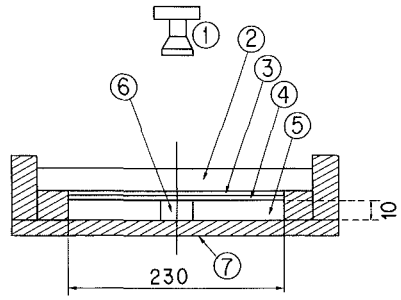

① C.C.D. Camera (with an optical filter)
② Upper plate (plexiglass, 10mm thick)
③ Liquid-crystal layer (about 0.1mm thick)
④ Stainless steel foil (50μm thick)
⑤ Flow passage (230min wide, 10mm high)
⑥ Cylindrical rod (brass, 20mm diameter)
⑦ Bottom plate

Fig. 8 Cross section of the test channel

The results shown in Fig. 6 illustrate the difficulty of finding the peak intensity temperatures without image processing at low and high-temperature conditions. At lower temperatures, that is, in the short wavelength range, the spectral distributions do not change beyond 35°C. Also the failure below 28.7°C can be explained by a considerable decrease in the spectral intensity of the scattering light. Further investigations on the spectral characteristics of other liquid-crystals are required to select the more suitable ones for the present method.

The halogen tungsten lamps were equipped with infrared absorption filters to prevent radiation heating by the lamps. This effect was confirmed by thermocouples fixed on the liquid-crystal layer. Consequently, the temperature on the test plate was not affected by the lamps. However, further investigation of the effect of the light source is necessary because the infrared absorption filter may have affected the spectral distribution in the low and high end regions.

The CCD camera used in this study has a relatively smooth sensitivity from 400 nm to 800 nm with a maximum in the range of 500–600 nm. The output of the camera in the calibration test was maintained above 70 percent of the saturation level of 8-bit gradations. Therefore, it can be concluded that the CCD camera did not effect the spectral distribution significantly.

It is believed that the liquid-crystal layer shows one color corresponding to one temperature. However, the light intensity is not always the same and changes according to the width of an isochromatic region, as shown in photos 1. This effect is not yet confirmed, but is inferred to be self-filtration. In the experimental configurations, the light sources were placed at a low angle position so as to avoid the glare light directly reflected from the surfaces of the plexiglass. Therefore, the light enters obliquely into the liquid-crystal layer, and a part of the light may be absorbed in neighboring regions before getting to the narrow isochromatic region. Consequently, the intensity depends on local conditions. This effect points out problems finding peak-intensity lines by simple image processing techniques.

Experimental Application

To demonstrate the present method, the distributions of temperatures and heat transfer coefficients on a heated plate of a parallel-plate channel, disturbed by a short cylinder, was measured. A new technique to determine isothermal lines was also developed.

Apparatus. A schematic drawing of the heat transfer test channel is shown in Fig. 7. The test channel was a parallel-plate channel, whose width, total length, and height were 230, 2100, and 10 mm, respectively. A single brass cylinder with a diameter of 20 mm and a height of 10 mm was mounted vertically on the test plate at the center.

The test plate was the same as that used in the calibration test (see Fig. 8). The relation between optical filter wavelength and peak intensity temperature had already been evaluated by the calibration test described earlier. The stainless steel foil attached to the liquid-crystal layer generated the ohmic heat uniformly by an electrical current. The local heat flux near and on the brass cylinder, however, is not constant. A thin silicone adhesive was used to connect the heating foil and the cylinder thermally.

The working fluid was filtered air. A 750-mm-long entrance length was placed before the heated section. The air flow rate was measured by a laminar flow meter.

The test section was thermally insulated except for the upper plate, from which, the color distribution of the liquid-crystal layer was observed by the CCD camera set 700 mm above the test plate.

Determination of Isothermal Lines. In the present experiment, a filtered image was sectioned into two or three square fields with 70×70 pixels. A package of interactive image processing programs written in BASIC language (Morimoto, 1984) was used, with some modifications by the present authors, to treat monochromatic images with 8-bit gradation and display intensity distributions as pseudocolored images with 16 levels.

As described earlier, the light intensity of a region with one color is not always the same and depends on the local width of the region; that is, the intensity depends on the local temperature gradient. Therefore, if necessary, one frame of a filtered image can be divided into a few sections having different peak intensities. Then, the lines can be determined by the repeated pseudocolor procedure.

The isothermal lines were determined using the following procedure:

1 The partial image (70×70 pixels) is converted into 16 levels by the pseudocolor process, retaining the original 8-bit gradation data.

2 The pixels having intensities less than a factor of 2 levels (of the 16 levels) below the peak intensity are eliminated.

3 The remaining pixels are again divided into 16 levels between the maximum and minimum intensities (of the 8-bit gradation data) of the remaining pixels by the pseudocolor process.

4 This pseudo color procedure is repeated two or three times until the difference of the intensity between the remaining pixel becomes less than a selected value (about 10 for the present experiment). Consequently, only the pixels having in-

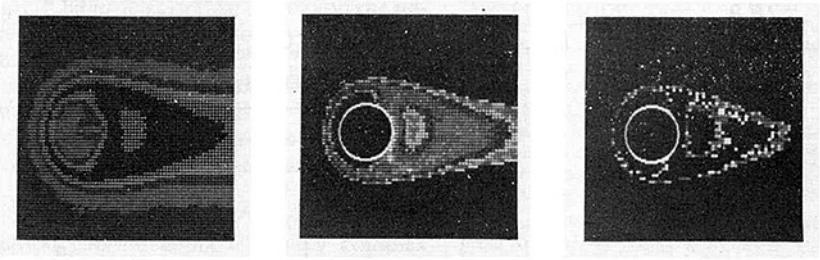

Photo 2(a) After the first pseudocolor procedure

Photo 2(b) After the second pseudocolor procedure

Photo 2(c) After the third (final) pseudocolor procedure

Photo 2 Images on the computer display during image processing

tensities near the peak intensity remain on the display showing the isothermal line.

The region having relatively low peak intensity was treated partially by the same process, and the partial isothermal lines were connected into a complete isothermal line using a digitizer board. Fifteen isothermal lines were obtained, corresponding to the optical filters. Finally, these isothermal lines were compiled into an isothermal map.

Photos 2(*a*)-(*c*) show the images on the computer display corresponding to each step of the procedure. Photo 2(*a*) shows the image after the first pseudocolor processing, photo 2(*b*) after the second pseudo-color processing, and photo 2(*c*) after the third pseudocolor processing and the final isothermal line.

Data Reduction. The experiments were carried out for the Reynolds number (Re) range of 1000–15,000. Re was based on the equivalent dimension equal to twice the channel spacing ($De=2H$), and the average velocity (U). The wall temperature distribution (Tw) was evaluated from the liquid crystal layer by the present method. The entrance and exit temperatures of air were measured directly by thermocouples, from which the mixed-mean-temperature distribution of air (Tb) was found. The local heat transfer coefficient (h) was evaluated by the following equation:

$$h=q/(Tw-Tb) \tag{2}$$

Heat conduction effects in the plexiglass plate, the stainless foil of the test plate, and the brass cylinder were not taken into account in this study, however, parasitic heat losses were evaluated at no flow rate. The air properties were evaluated at Tb.

The maximum error of wall temperature measurement by the present method is within ± 0.5°C as described in the previous section. The error of the bulk gas temperature is ± 0.5°C (at the lowest Reynolds number of 1000) caused by a heat loss evaluation, which also causes a 5 percent error in the heat flux. The film temperature differences are about 10°C. Therefore, the maximum uncertainty of Nusselt number is within ± 15 percent at the lowest Reynolds number, decreasing to ± 5 percent at the highest Reynolds number of 15,000. The uncertainty of Reynolds number is within ± 6 percent, caused by errors of flow rate, channel spacing, and air properties.

Experimental Results. Photos 3(*a*)-(*c*) show monochromatic photographs of the liquid-crystal layer at Reynolds numbers of 1000, 4000, and 10,000, respectively. Although color is not indicated, the temperature of each region is related to the darkness of the photographic pictures, the darker region having a lower temperature. Therefore, the lowest temperatures were observed around the cylinder, where

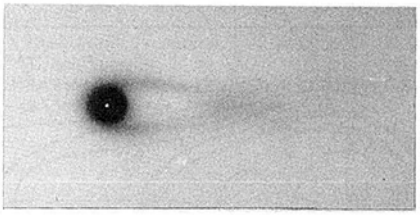

Photo 3(a) Re = 1000

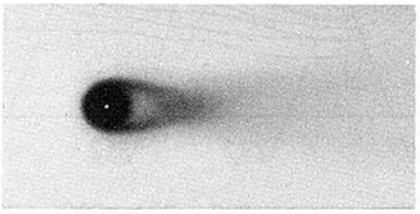

Photo 3(b) Re = 4000

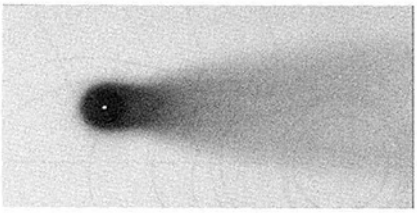

Photo 3(c) Re = 10,000

Photo 3 Photographs of the color distributions of the liquid-crystal layer on a heated plate disturbed by a cylinder

the air flow is disturbed by so-called horseshoe vortices surrounding the root of the cylinder (Baker, 1979; Akino et al., 1985) and heat transfer is augmented (Sobaya et al., 1974; Goldstein et al., 1985).

Figure 9 shows the isothermal maps of Re of 1000, 4000, and 10,000. In the region downstream of the cylinder, temperature gradient is gradual and the lines can be easily distinguished from each other. In the vicinity of the cylinder, however, the temperature gradient is large and the isothermal lines are too dense to identify as separate lines. The spatial resolution of the present method, however, is far better than the previous method depending on the human eyes (Ichimiya et al., 1986). Further, it has been confirmed that the maximum spatial resolution of the present method is about 1 mm and the maximum temperature resolution is about 0.1°C, which corresponds to the error in the calibration of the peak intensity temperature.

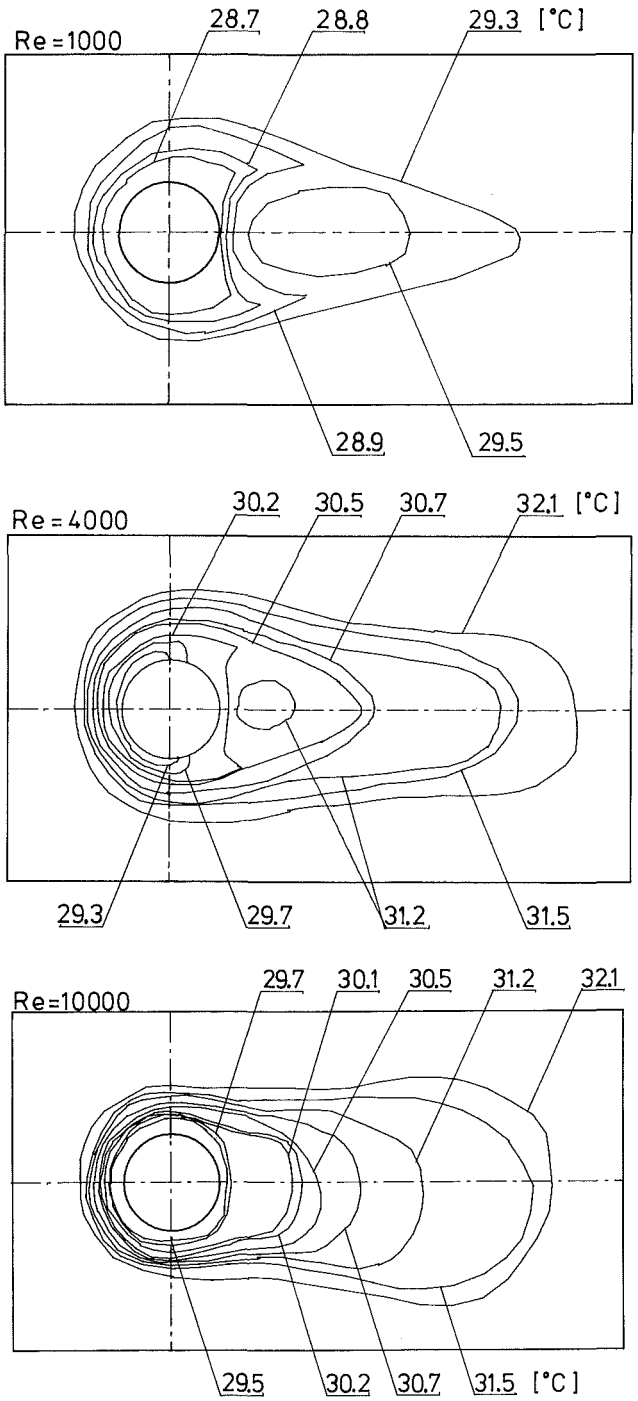

Fig. 9 Isothermal lines obtained by the present method for three Reynolds numbers of 1000, 4000, and 10,000

Heat transfer coefficients calculated from the isothermal maps are shown in Figs. 10. Figure 10(a) shows the Nusselt number distributions along the upstream side of the center line of the cylinder, parallel to the flow direction, at Re = 1000, 4000, and 10,000. Figure 10(b) shows the Nusselt number distributions in the centerline toward the downstream direction. In these figures, solid symbols show the results obtained by the present method, and open symbols show the results obtained using human color sensation (Ichimiya et al., 1986). The slashed regions show the error bands of ±15 percent by the latter method. It can be concluded that the results by both methods coincide within experimental uncertainty, except close to the cylinder, where the discrepancy becomes larger.

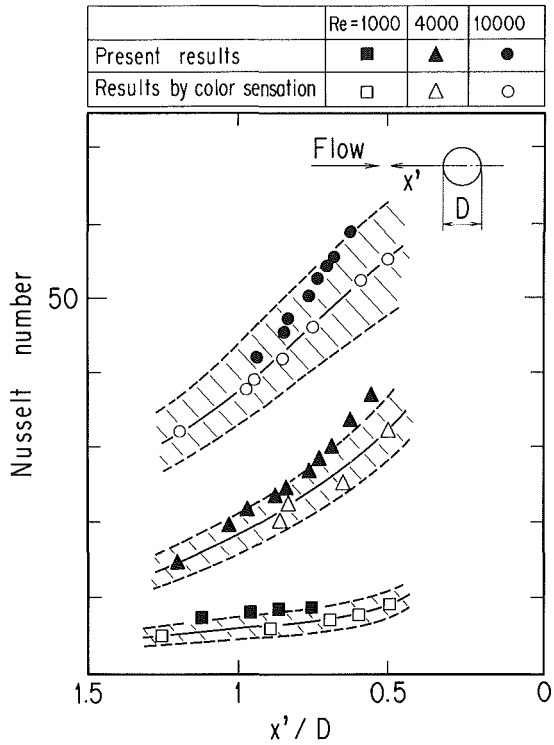

Fig. 10(a) Upstream direction

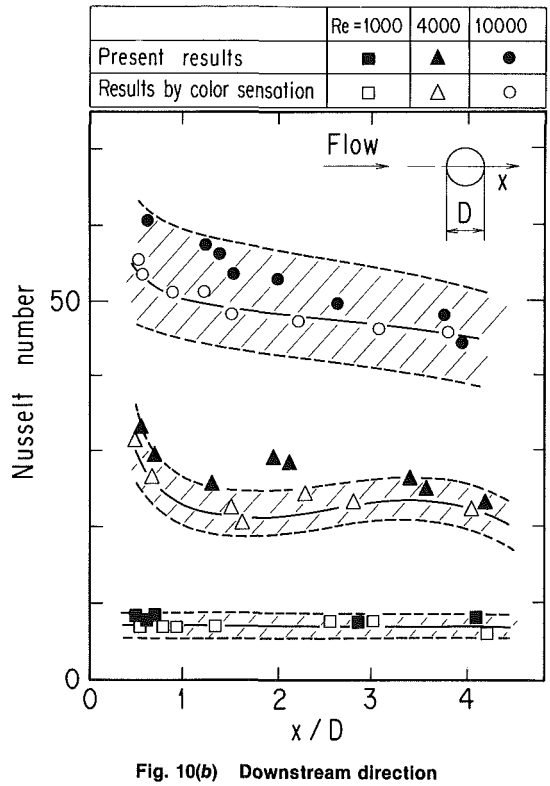

Fig. 10(b) Downstream direction

Fig. 10 Distribution of the Local Nusselt numbers determined by the previous method employing human color sensation and by the present method

Conclusions

The following conclusions were obtained from the present study:

1 A new method of liquid-crystal thermometry was

developed using the sharp band-pass optical filters and the image processing device. This method can exclude the employment of human color sensation.

2 A calibration method was established and the peak intensity temperature was accurately determined.

3 The accuracy of the temperature determination of the present method is $\pm 0.1°C$ in the temperature range of 29–32°C.

4 The present method can resolve to 0.1°C spatially.

5 The present method can be applied to very complex temperature distributions, located in a channel or a structural model, which would be problematical by ordinary methods such as thermocouples or infrared cameras.

Acknowledgments

The authors would like to thank Prof. Akira Kurosawa of Kobe University of Mercantile Marine for his valuable discussions and encouragement. We also would like to thank Mr. J. R. Haines of McDonnel Douglas/Oak Ridge National Laboratory and Dr. M. Hishida of JAERI for reading and commenting on the manuscript.

References

Akino, N., Kunugi, T., Takase, K., Okamoto, Y., and Ichimiya, K., 1985, "Observation of Flow Around a Vertical Cylinder in a Parallel Channel," *J. Flow Visualization Society of Japan*, Vol. 15, No. 18, pp. 193–198.

Baker, C. J., 1979, "The Laminar Horseshoe Vortex," *J. Fluid Mech.*, Vol. 95, Part 2, pp. 347–367.

Fergason, J. L., 1968, "Liquid-Crystal in Nondestructive Testing," *Applied Optics*, Vol. 7, No. 9, pp. 1729–1737.

Goldstein, R. J., Chyu, M. K., and Hain, R. C., 1985, "Measurement of Local Mass Transfer on a Surface in the Region of the Base of a Protruding Cylinder With a Computer-Controlled Data Acquisition System," *Int. J. Heat Mass Transfer*, Vol. 28, No. 5, pp. 977–985.

Goldstein, R. J., and Timmers, J. F., 1982, "Visualization of Heat Transfer From Arrays of Impinging Jets," *Int. J. Heat Mass Transfer*, Vol. 25, No. 12, pp. 1857–1868.

Herold, W. O., and Wiegel, D., 1980, "Problems of the Photographic Documentation of Liquid-Crystalline Thermographs," in: *Advances in Liquid-Crystal Research and Applications*, L. Bata, ed., Pergamon Press, Oxford, pp. 1255–1259.

Ichimiya, K., Akino, N., Kunugi, T., and Mitsushiro, K., 1988, "A Fundamental Study of the Heat Transfer and Flow Situation Around a Spacer (in Case of a Cylinder as a Spacer)," *Int. J. Heat Mass Transfer*, Vol. 31, No. 11, pp. 2215–2225.

Kasagi, N., Hirata, M., and Kumada, M., 1981, "Studies of Full-Converge Film Cooling: Part 1, Cooling Effectiveness of Thermally Conductive Wall," ASME Paper No. 81-GT-37.

Morimoto, Y., 1984, *Image Processing*, Baifukann Inc., Tokyo.

Sobaya, F. E. M., and Sparrow, E. M., 1974, "Local and Average Transfer Coefficients for One-Row Plate Fin and Tube Heat Exchanger Configuration," ASME JOURNAL OF HEAT TRANSFER, Vol. 96, No. 3, pp. 265–272.

Journal of Heat Transfer

Technical Notes

This section contains shorter technical papers. These shorter papers will be subjected to the same review process as that for full papers.

Two-Dimensional Heat or Mass Transfer in Laminar Flow Between Parallel Plates: Closed-Form Solution

A. R. Mansour[1]

Nomenclature

A = coefficients in equations (9), (24)
A_1 = coefficient in equation (18)
B = channel halfwidth, m
C_b = bulk concentration of species i, mol m^{-3}
C_i = concentration of species i, mol m^{-3}
C_o = surface concentration of species i, mol m^{-3}
D_i = diffusion coefficient of species i, m^2 s^{-1}
${}_1F_1$ = confluent hypergeometric function defined in equation (22)
K = constant in equation (12)
$K_{k,m}$ = Whittaker function defined in equation (21)
Nu = Nusselt number = $(\partial C_i/\partial y)_{y=B}$ $(2B/(C_b - C_o))$
V_x = axial component of the fluid velocity, m s^{-1}
X = axial coordinate, m
y = normal coordinate, measured from the center of the channel, m
Y = function of axial coordinate
ζ = axial coordinate defined in equation (4)
θ = concentration defined in equation (2)
λ = eigenvalue in equations (13), (14), (15), (20), (21), (23) and (24)
ξ = normal coordinate defined in equation (3)
Γ = gamma function used in equations (21) and (24)

Subscripts

b = bulk solution
i = particular species in solution
o = wall surface
-1 = wall located at $\xi = -1$
1 = wall located at $\xi = 1$
0 = asymptotic solution of Sellars et al. (1956)

Superscript

$*$ = dummy variable of integration

Introduction

The Graetz problem in heat or mass transfer in laminar flow of Newtonian fluids in noncircular ducts is well known in many engineering applications. It has been solved for some special cases (Graetz, 1883; Leveque, 1928; Newman, 1969; Brown, 1960; Sellars et al. 1956; Kay and Crawford, 1980; Norris and Streid, 1940; Yih and Cermak, 1951; Schenk and Beckers, 1954; Hatton and Turton, 1962; Cess and Shaffer, 1959; Edwards and Newman, 1985) but in this paper the case of a rectangular channel will be considered, where the surface concentration (or temperature) may differ on the two channel walls.

Problem Statement

The differential equation describing the dimensionless convective/diffusive mass transfer in a laminar flow in a channel, with negligible axial diffusion, is as follows (Edwards and Newman, 1985):

$$(1-\xi^2)\frac{\partial\theta}{\partial\zeta} = \frac{\partial^2\theta}{\partial\xi^2} \tag{1}$$

where

$$\theta = \frac{C_i - C_b}{C_o - C_b} \tag{2}$$

$$\xi = \frac{y}{B} \tag{3}$$

$$\zeta = \frac{X D_i}{\frac{3}{2} B^2 \langle V_x \rangle} \tag{4}$$

For the meaning of C_i, C_b, C_o, etc., see the nomenclature.

The boundary conditions needed to equation (1) are

$$\theta = 1 \text{ at } \xi = -1 \tag{5}$$

$$\theta = 0 \text{ at } \xi = 1 \tag{6}$$

$$\theta = 0 \text{ at } \zeta = 0 \tag{7}$$

Duhamle's superposition theorem can be used to express the flux N_i in terms of the solution to equation (1) with a step-

[1]Chemical Engineering Department, Jordan University of Science and Technology, Irbid, Jordan.

Contributed by the Heat Transfer Division for publication in the JOURNAL OF HEAT TRANSFER. Manuscript received by the Heat Transfer Division January 25, 1988. Keywords: Forced Convection, Mass Transfer.

function concentration for arbitrary boundary conditions as follows (Edwards and Newman, 1985):

$$N_{i,-1}(X) = \frac{D_i}{B}\int_o^x \frac{d\,C_{i,-1}}{dx}\bigg|_{x^*}\frac{\partial\theta}{\partial\xi}(\zeta-\zeta^*,\ \xi=-1)dx^* + \frac{D_i}{B}\int_o^x \frac{d\,C_{i,1}}{dx}\bigg|_{x^*}\frac{\partial\theta}{\partial\xi}(\zeta-\zeta,\ \xi=1)dx^* \tag{8}$$

Graetz Approach

The Graetz approach uses the separation of variables technique to solve equation (1). This leads to the following expression for the dimensionless concentration:

$$\theta = \frac{1}{2} - \frac{\xi}{2} + \sum_{k=1}^{\infty} A_k e^{-\lambda^2 k\zeta} Y_k(\xi) \tag{9}$$

The coefficients A_k, the eigenvalues λ_k, and the eigenfunctions Y_k, which are called Graetz functions, and are usually obtained numerically. The numerical solution of equation (9), however, is accurate only for large ζ.

Asymptotic Solutions for Large Eigenvalues

For the Graetz problem in a tube, Newman (1973) extended the asymptotic forms of Sellars et al. (1956) to obtain reasonable accuracy over a wider range of λ. Using a similar procedure, Edwards and Newman (1985) devised the following asymptotic form for the asymmetric Graetz problem for channel flow:

$$\lambda = \lambda_o + \frac{0.03254}{\lambda_o^{4/3}} - \frac{0.11}{\lambda_o^{14/3}} \tag{10}$$

where

$$\lambda_o = \frac{6k-1}{3} \qquad \text{for } k=1, 2, \ldots \tag{11}$$

This asymptotic form was modified (Edwards and Newman, 1985) to

$$A_k = (-1)^{k+1}\left(\frac{k}{\lambda_k^{1/3}}\right)(1+0.03\,\lambda_k^{-4/3} - 0.03\,\lambda_k^{-8/3}) \tag{12}$$

For $k \geq 6$, this asymptotic solution gives more accurate results as compared to other solutions (Edwards and Newman, 1985).

Nayfeh (1985) presented a new asymptotic solution for $Y_k(\xi)$ for large values of the eigenvalue.

The general solution is

$$Y_k(\xi) = \left[\int_\xi^1 (1-\tau^2)^{1/2}d\tau\right]^{1/2}[1-\xi^2)]^{-1/4} \times \left[C_1 J_{-1/3}\left(\lambda\int_\xi^1(1-\tau^2)d\tau\right) + C_2 J_{1/3}\left(\lambda\int_\xi^1(1-\tau^2)^{1/2}d\tau\right)\right] \tag{13}$$

where

$$\lambda_k = \left(k+\frac{11}{12}\right)\pi\left[\int_0^1(1-\tau^2)^{1/2}d\tau\right]^{-1} \tag{14}$$

C_1 and C_2 are two arbitrary constants of integration and $J_{-1/3}$ and $J_{1/3}$ are Bessel functions of the first kind.

This asymptotic solution gives results of almost the same accuracy as the previous asymptotic solution.

Closed-Form Solution

If we try a product solution of equation (1)

$$\theta = Z(\zeta)\,Y(\xi) \tag{15}$$

we obtain the following two ordinary differential equations:

$$\frac{dZ}{d\zeta} = -\lambda^2 Z \tag{16}$$

$$\frac{d^2Y}{d\xi^2} + \lambda^2(1-\xi^2)Y = 0 \tag{17}$$

The solution of equation (16) is

$$Z(\xi) = A_1 e^{-\lambda^2\xi} \tag{18}$$

where A_1 is an arbitrary constant.

Equation (17) is a Sturm–Liouville system with λ_k being real-numbered eigenvalues. $Y_k(\xi)$ are the eigenfunctions that form an orthogonal set with respect to the weight function $(1-\xi^2)$ over the interval of interest.

By introducing the transformation $t = -\lambda\xi^2$ into equation (17), it is readily converted into the form of a Schrödinger differential equation (see Slater, 1960)

$$y'' + (a^2 - b^2x^2)y = 0 \tag{19}$$

which has the following general solution:

$$Y_k(\xi) \simeq \xi^{-1/2}e^{-1/2\,\lambda_k\xi^2}(\lambda\xi^2)^{1/2\pm1/4}{}_1F_1\left[\frac{1}{2} - \frac{1}{4}\lambda_k - \frac{1}{4};\ 1\pm1/2;\ \lambda_k\xi^2\right] \tag{20}$$

or

$$Y_k(\xi) = \frac{\xi^{-1/2}}{\Gamma(1\pm1/2)}M_{\lambda_k/4\ \pm\ 1/4}(\lambda_k\xi^2) \tag{21}$$

where ${}_1F_1$ is a confluent hypergeometric function defined as follows (Slater, 1960):

$${}_1F_1(a;\ b;\ x) = \sum_{k=0}^{\infty}\frac{(a)_k X^k}{(b)_k k!} \tag{22}$$

$M_{m,k}$ is known as Whittacker's function (Slater, 1960).

The eigenvalues λ_k of equation (21) are evaluated from

$${}_1F_1\left[\frac{2-\lambda_k}{4};\ 1;\ \lambda_k\right] = 0 \qquad \text{for } k=1, 2, 3, \ldots \tag{23}$$

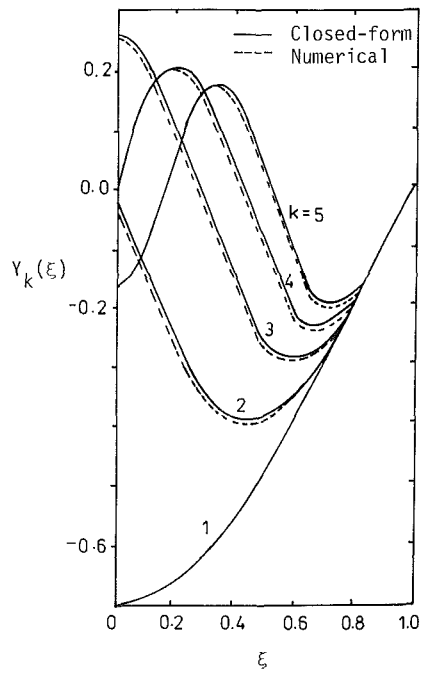

Fig. 1 Comparison of Graetz functions between present work and previous numerical solution

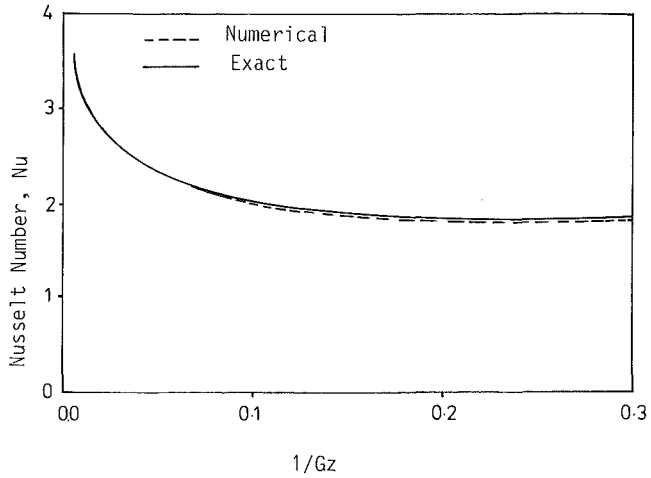

Fig. 2 Exact and numerical values of Nu versus 1/Gz for heat transfer in laminar flow between parallel plates

The complete solution to equation (1) that describes the concentration profile is

$$\theta(\xi, \zeta) = \sum_{k=0}^{\infty} A_k e^{-\lambda_k \zeta^2} \cdot \frac{\xi^{-1/2}}{\Gamma(1+1/2)} M_{\lambda_{k/4} \pm 1/4}(\lambda_k \xi^2) \quad (24)$$

Results and Discussion

The solution given in equation (21) is plotted versus ξ and compared with the finite-difference solution presented recently by Edwards and Newman (1985) in Fig. 1. It can be seen that a good agreement is obtained.

The closed-form solution given by equation (24) is also compared with numerical results published by Prins et al. (1951) in Fig. 2, and good agreement is found with their results as well.

References

Brown, G. M., 1960, "Heat or Mass Transfer in a Fluid in Laminar Flow in a Circular or Flat Conduit," *AIChE J.*, Vol. 6, pp. 179–183.

Cess, R. D., and Shaffer, E. C., 1959, "Laminar Heat Transfer Between Parallel Plates With Unsymmetrically Prescribed Heat Flux at the Walls," *App. Sci. Res.*, Vol. A9, pp. 64–70.

Edwards, V., and Newman, J., 1985, "The Asymmetric Graetz Problem in Channel Flow," *Int. J. Heat Mass Transfer*, Vol. 28, No. 2, pp. 503–505.

Graetz, L., 1983, "Über die Wärmeleitungsfähigkeit von Flüssigkeiten," *Annalen der Physik und Chemie*, Vol. 18, pp. 79–94; 1985, Vol. 25, pp. 337–357.

Hatton, A. P., and Turton, J. S., 1962, "Heat Transfer in the Thermal Entry Length With Laminar Flow Between Parallel Walls," *Int. J. Heat Mass Transfer*, Vol. 5, pp. 673–679.

Kays, W. M., and Crawford, M. E., 1980, *Convective Heat and Mass Transfer*, 2nd ed., McGraw-Hill, New York, pp. 88–132.

Lêvêque, M. A., 1928, "Les Lois de la Transmission de Chaleur par Convection," *Annales de Mines Memoires*, Ser. 12, 13, pp. 201–299, 305–362.

Nayfeh, A. H., 1985, *Problems in Perturbations*, Wiley, New York, pp. 450–451.

Newman, J., 1969, "Extension of the Lêvêque Solution," ASME JOURNAL OF HEAT TRANSFER, Vol. 91, pp. 177–178.

Newman, J., 1973, *The Fundamental Principles of Current Distribution and Mass Transport in Electrochemical Cells in Electroanalytical Chemistry*, Vol. 6, A. J. Bard, ed., Marcel Dekker, New York, pp. 196–221.

Norris, R. H., and Stried, D. D., 1940, "Laminar Flow Heat Transfer Coefficients for Ducts," *Trans. ASME*, Vol. 62, pp. 525–535.

Prins, J. A., Mulder, J., and Schenk, J., 1951, "Heat Transfer in Laminar Flow Between Parallel Plates," *App. Sci. Res.*, Vol. A2, p. 431.

Schenk, J., and Beckers, H. L., 1954, "Heat Transfer in Laminar flow Between Parallel Plates," *App. Sci. Res.*, Vol. A4, pp. 405–413.

Sellars, J. R., Tribus, M., and Klein, J. S., 1956, "Heat Transfer to Laminar Flow Around Tube or Flat Conduit," *Trans. ASME*, Vol. 78, pp. 411–448.

Slater, L. J., 1960, *Confluent Hypergeometric Functions*, Cambridge University Press, United Kingdom.

Yih, C. S., and Cermak, J. E., 1951, "Laminar Heat Convection in Pipes and Ducts," Civ. Eng. Dept., Colorado Agr. Mech. College, Fort Collins, CO, ONR Contract Report N90nr-82401, NR063-071/1-19-49.

Prediction of Heat Transfer in Turbulent Flow Over Rough Surfaces

R. P. Taylor,[1,3] H. W. Coleman,[2,3] and B. K. Hodge[2,3]

Nomenclature

A_x = area in y–z plane open to flow; Fig. 1
A_y = area in x–z plane open to flow; Fig. 1
C_D = roughness element drag coefficient defined in equation (1)
C_f = skin friction coefficient defined in equation (7)
C_p = specific heat
d = local roughness element diameter
F_D = local drag force due to a roughness element
H = time mean enthalpy
$H_{o,\infty}$ = free-stream stagnation enthalpy
H_w = enthalpy at the wall
h' = turbulent fluctuating value of enthalpy
K = conductivity
k = roughness element height
k_s = equivalent sandgrain roughness
l = roughness element spacing in z direction; Fig. 1
l_m = Prandtl mixing length
L = roughness element spacing in x direction; Fig. 1
Nu = Nusselt number
P = pressure
Pr = Prandtl number
Pr_t = turbulent Prandtl number
Q = heat transfer rate between element and fluid
Re = Reynolds number
St = Stanton number defined in equation (8)
T = time mean temperature
t' = turbulent fluctuating value of temperature
T_R = roughness element temperature
T^* = $(H_w - H_{o,\infty})\mathrm{St}/C_p\sqrt{C_f/2}$
u = velocity component in x direction
U = time mean value of u
u' = turbulent fluctuating value of u

Introduction

Because many systems of engineering interest have surfaces that are rough in the aerodynamic sense, there is considerable interest in the development of accurate predictive models for turbulent flows over rough surfaces. This work reports progress toward the development of a predictive approach for situations where the free-stream flow conditions, the macroscopic system geometry, and the surface roughness geometry are well described.

Two approaches are used to model turbulent flow over rough

[1]Associate Professor; Mem. ASME.

[2]Professor; Mem. ASME.

[3]Mechanical and Nuclear Engineering Department, Mississippi State University, Mississippi State, MS 39762.

Contributed by the Heat Transfer Division for publication in the JOURNAL OF HEAT TRANSFER. Manuscript received by the Heat Transfer Division March 24, 1987. Keywords: Forced Convection, Turbulence.

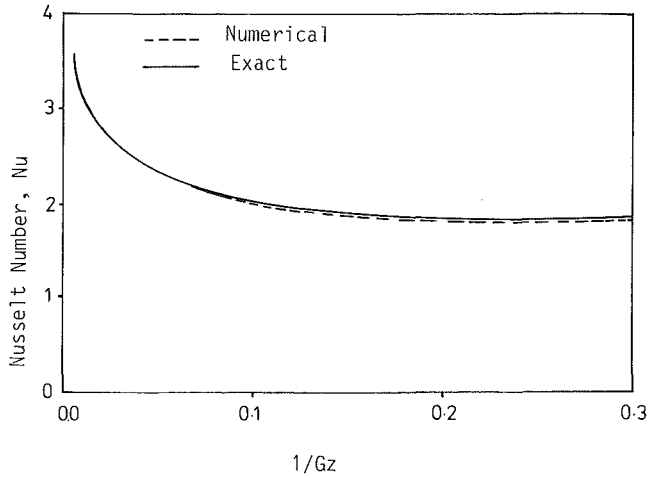

Fig. 2 Exact and numerical values of Nu versus 1/Gz for heat transfer in laminar flow between parallel plates

The complete solution to equation (1) that describes the concentration profile is

$$\theta(\xi, \zeta) = \sum_{k=0}^{\infty} A_k e^{-\lambda_k \zeta^2} \cdot \frac{\xi^{-1/2}}{\Gamma(1+1/2)} M_{\lambda_k/4 \pm 1/4}(\lambda_k \xi^2) \quad (24)$$

Results and Discussion

The solution given in equation (21) is plotted versus ξ and compared with the finite-difference solution presented recently by Edwards and Newman (1985) in Fig. 1. It can be seen that a good agreement is obtained.

The closed-form solution given by equation (24) is also compared with numerical results published by Prins et al. (1951) in Fig. 2, and good agreement is found with their results as well.

References

Brown, G. M., 1960, "Heat or Mass Transfer in a Fluid in Laminar Flow in a Circular or Flat Conduit," *AIChE J.*, Vol. 6, pp. 179–183.

Cess, R. D., and Shaffer, E. C., 1959, "Laminar Heat Transfer Between Parallel Plates With Unsymmetrically Prescribed Heat Flux at the Walls," *App. Sci. Res.*, Vol. A9, pp. 64–70.

Edwards, V., and Newman, J., 1985, "The Asymmetric Graetz Problem in Channel Flow," *Int. J. Heat Mass Transfer*, Vol. 28, No. 2, pp. 503–505.

Graetz, L., 1983, "Über die Wärmeleitungsfähigkeit von Flüssigkeiten," *Annalen der Physik und Chemie*, Vol. 18, pp. 79–94; 1985, Vol. 25, pp. 337–357.

Hatton, A. P., and Turton, J. S., 1962, "Heat Transfer in the Thermal Entry Length With Laminar Flow Between Parallel Walls," *Int. J. Heat Mass Transfer*, Vol. 5, pp. 673–679.

Kays, W. M., and Crawford, M. E., 1980, *Convective Heat and Mass Transfer*, 2nd ed., McGraw-Hill, New York, pp. 88–132.

Lêvêque, M. A., 1928, "Les Lois de la Transmission de Chaleur par Convection," *Annales de Mines Memoires*, Ser. 12, 13, pp. 201–299, 305–362.

Nayfeh, A. H., 1985, *Problems in Perturbations*, Wiley, New York, pp. 450–451.

Newman, J., 1969, "Extension of the Lêvêque Solution," ASME JOURNAL OF HEAT TRANSFER, Vol. 91, pp. 177–178.

Newman, J., 1973, *The Fundamental Principles of Current Distribution and Mass Transport in Electrochemical Cells in Electroanalytical Chemistry*, Vol. 6, A. J. Bard, ed., Marcel Dekker, New York, pp. 196–221.

Norris, R. H., and Stried, D. D., 1940, "Laminar Flow Heat Transfer Coefficients for Ducts," *Trans. ASME*, Vol. 62, pp. 525–535.

Prins, J. A., Mulder, J., and Schenk, J., 1951, "Heat Transfer in Laminar Flow Between Parallel Plates," *App. Sci. Res.*, Vol. A2, p. 431.

Schenk, J., and Beckers, H. L., 1954, "Heat Transfer in Laminar flow Between Parallel Plates," *App. Sci. Res.*, Vol. A4, pp. 405–413.

Sellars, J. R., Tribus, M., and Klein, J. S., 1956, "Heat Transfer to Laminar Flow Around Tube or Flat Conduit," *Trans. ASME*, Vol. 78, pp. 411–448.

Slater, L. J., 1960, *Confluent Hypergeometric Functions*, Cambridge University Press, United Kingdom.

Yih, C. S., and Cermak, J. E., 1951, "Laminar Heat Convection in Pipes and Ducts," Civ. Eng. Dept., Colorado Agr. Mech. College, Fort Collins, CO, ONR Contract Report N90nr-82401, NR063-071/1-19-49.

Prediction of Heat Transfer in Turbulent Flow Over Rough Surfaces

R. P. Taylor,[1,3] H. W. Coleman,[2,3] and B. K. Hodge[2,3]

Nomenclature

A_x = area in y–z plane open to flow; Fig. 1
A_y = area in x–z plane open to flow; Fig. 1
C_D = roughness element drag coefficient defined in equation (1)
C_f = skin friction coefficient defined in equation (7)
C_p = specific heat
d = local roughness element diameter
F_D = local drag force due to a roughness element
H = time mean enthalpy
$H_{o,\infty}$ = free-stream stagnation enthalpy
H_w = enthalpy at the wall
h' = turbulent fluctuating value of enthalpy
K = conductivity
k = roughness element height
k_s = equivalent sandgrain roughness
l = roughness element spacing in z direction; Fig. 1
l_m = Prandtl mixing length
L = roughness element spacing in x direction; Fig. 1
Nu = Nusselt number
P = pressure
Pr = Prandtl number
Pr_t = turbulent Prandtl number
Q = heat transfer rate between element and fluid
Re = Reynolds number
St = Stanton number defined in equation (8)
T = time mean temperature
t' = turbulent fluctuating value of temperature
T_R = roughness element temperature
T^* = $(H_w - H_{o,\infty})\mathrm{St}/C_p\sqrt{C_f/2}$
u = velocity component in x direction
U = time mean value of u
u' = turbulent fluctuating value of u

Introduction

Because many systems of engineering interest have surfaces that are rough in the aerodynamic sense, there is considerable interest in the development of accurate predictive models for turbulent flows over rough surfaces. This work reports progress toward the development of a predictive approach for situations where the free-stream flow conditions, the macroscopic system geometry, and the surface roughness geometry are well described.

Two approaches are used to model turbulent flow over rough

[1]Associate Professor; Mem. ASME.

[2]Professor; Mem. ASME.

[3]Mechanical and Nuclear Engineering Department, Mississippi State University, Mississippi State, MS 39762.

Contributed by the Heat Transfer Division for publication in the JOURNAL OF HEAT TRANSFER. Manuscript received by the Heat Transfer Division March 24, 1987. Keywords: Forced Convection, Turbulence.

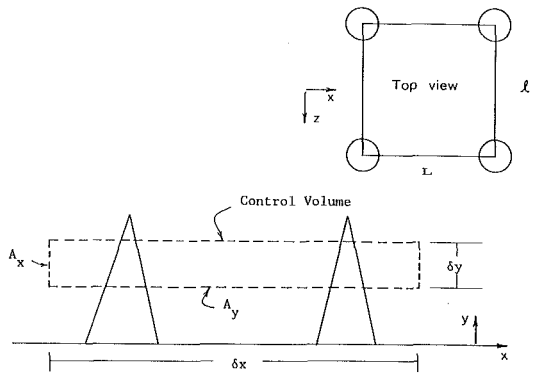

Fig. 1 Control volume for flow over a rough surface

surfaces: the equivalent sandgrain, k_s, approach and the discrete element approach. The sandgrain approach has its origin in the work of Nikuradse (1933) and Schlichting (1936). The idea is to define a single length scale k_s that characterizes the roughness and is used in various scaling laws for velocity profiles and friction coefficients. The original data base for the scaling laws is Nikuradse's sandgrain experiments—hence the name. The scale is based totally on fluid mechanics considerations, which contain momentum transport phenomena (drag forces) that have no heat transfer analog.

Schlichting (1936) also introduced the basic principles of the discrete element model; however, this concept has only been widely used since 1975. The idea is to treat the roughness as a collection of individual entities and to account for the form drag and heat transfer on the elements.

The discrete element roughness model discussed in this paper incorporates many features of the previous discrete element efforts and presents for the first time a completely consistent discrete element model for two-dimensional, nonisothermal turbulent boundary layers. The model is calibrated using data sets with well-described surface roughness geometries. Emphasis is placed on the heat transfer results, as results (velocity and Reynolds stress profiles and skin friction) for isothermal flows have been presented in a previous article (Taylor et al., 1985).

Discrete Element Roughness Model

The discrete element model presented herein is formulated for roughness elements with three-dimensional shapes (as opposed to transverse ribs, for example) for which the element cross section can be approximated as circular at every height y. In the following, attention is restricted to roughness elements of uniform shape and spacing. The current form of the discrete element model had its origins in the work of Finson and his co-workers (Finson, 1976, 1982; Finson and Wu, 1979; Finson and Clark, 1980). Other contributions have been made by Adams and Hodge (1977), Lin and Bywater (1980), Christoph and Pletcher (1983), and Taylor et al. (1984, 1985). Formulations for the case of general three-dimensional elements of random shape, height and spacing are presented by Taylor et al. (1984, 1985).

Derivation of the Differential Equations. The differential equations including roughness effects are derived by applying the basic conservation statements for mass, momentum, and energy to a control volume (CV) such as that shown in Fig. 1. Basic to this approach is the idea that the two-dimensional, time-averaged turbulent boundary layer equations can be applied in the flow region below the crests of the roughness elements. Therefore, the flow variables must be viewed as having been averaged over the transverse (z) direction and averaged in the longitudinal (x) direction over an appropriate x distance.

The physical effects of the roughness elements on the fluid in the CV are modeled by considering the flow blockage and the local element-fluid heat transfer and by postulating that the total force of the elements on the flow can be incorporated as a drag force. As is evident in Fig. 1, the fluid areas available for mass, momentum, and energy transport in the y-z plane (A_x) and the x-z plane (A_y) are decreased by the presence of the roughness elements. The areas on which shear stresses and pressures act are decreased in the same manner. This blockage effect is included using blockage factors β_x and β_y, which are defined as the fraction of the area open for flow through the y-z and x-z planes, respectively. In the most general case the blockage factors are functions of x and y. The drag force F_D on the CV due to the portion of a single element penetrating the CV is most conveniently handled by using a drag coefficient

$$F_D = \frac{1}{2}\rho u^2(y) C_D d(y) \delta y \tag{1}$$

Likewise, the rate of heat transfer Q between the portion of a single element penetrating the CV and the fluid is expressed using a local Nusselt number as

$$Q = K\mathrm{Nu}_d \pi \delta y (T_R - T) \tag{2}$$

Using the above ideas and noting that the number of roughness elements per unit area of the x-z plane is $1/(lL)$, the conservation of mass, momentum, and energy statements are applied to the CV in Fig. 1. Upon incorporating the boundary layer assumptions, the continuity, momentum, and energy equations for a steady (Reynolds-averaged), two-dimensional turbulent boundary layer are

$$\frac{\partial}{\partial x}(\rho\beta_x U) + \frac{\partial}{\partial y}(\rho\beta_y V) = 0 \tag{3}$$

$$\beta_x \rho U \frac{\partial U}{\partial x} + \beta_y \rho V \frac{\partial U}{\partial y} = -\frac{\partial}{\partial x}(\beta_x P) + \frac{\partial}{\partial y}\left[\beta_y\left(\mu \frac{\partial U}{\partial y} - \overline{\rho u' v'}\right)\right] - \frac{1}{2}\rho C_D d(y) \frac{U^2}{Ll}\left(1 + \frac{\overline{u'^2}}{U^2}\right) \tag{4}$$

and

$$\beta_x \rho U \frac{\partial H}{\partial x} + \beta_y \rho V \frac{\partial H}{\partial y} = \frac{\partial}{\partial y}\left[\beta_y\left(\frac{K}{C_p}\frac{\partial H}{\partial y} - \overline{\rho v' h'}\right)\right] + U\frac{\partial}{\partial x}(\beta_x P) + \beta_y \frac{\partial U}{\partial y}\left(\mu \frac{\partial U}{\partial y} - \overline{\rho u' v'}\right) + \frac{1}{2}\rho C_D \frac{d(y)}{Ll} U^3\left(1 + 3\frac{\overline{u'^2}}{U^2}\right) + \pi \frac{K\mathrm{Nu}_d}{Ll}(T_R - T) \tag{5}$$

Examination of equations (4) and (5) shows that empirical models for $-\overline{\rho u' v'}$, $\overline{u'^2}$, $-\overline{\rho v' h'}$, C_D, and Nu_d are necessary for closure.

The blockage parameters, β_x and β_y, and $d(y)$ require no empirical fluid mechanics input as they are determined solely from the geometry of the rough surface. Taylor et al. (1984, 1985) have shown for uniform three-dimensional roughness elements with circular cross section that

$$\beta_x = \beta_y = 1 - \frac{\pi d^2}{4Ll} \tag{6}$$

The boundary conditions for the discrete element approach for rough wall flows are identical to those for smooth wall flows. The wall location ($y = 0$) is the smooth surface on which the roughness elements occur. At $y = 0$, $U = V = 0$ and $H = H_w$. As $y \to \infty$, $U \to U_\infty$ and $H \to H_\infty$. (In the available data sets on well-defined rough surfaces, an exception to this is observed in the case of spherical roughness elements

packed in the most dense array. This special case is discussed in a following section.)

The "wall shear stress" is defined as the sum of the shear and drag forces on the wall in the mean flow direction divided by the plan area of the wall. The corresponding skin friction coefficient is then

$$C_f = \frac{(\beta_y)_w \mu \left.\frac{\partial U}{\partial y}\right|_w + \frac{1}{2}\frac{1}{Ll}\int_0^\infty (\rho d C_D U^2)\,dy}{\frac{1}{2}\rho_\infty U_\infty^2} \tag{7}$$

and the Stanton number is

$$\mathrm{St} = \frac{-(\beta_y)_w \frac{K}{C_p}\left.\frac{\partial H}{\partial y}\right|_w + \frac{\pi}{Ll}\int_0^\infty [K\mathrm{Nu}_d(T_R - T)]\,dy}{\rho_\infty U_\infty (H_w - H_{o,\infty})} \tag{8}$$

These definitions for C_f and St can be formulated from physical reasoning; however, they also arise naturally from equations (3)–(5) in the formulation of the integral boundary layer equations (Taylor et al., 1984).

Model Calibration. In order to solve equations (3), (4), and (5), turbulence models for $-\rho\overline{u'v'}$, $\overline{u'^2}$, and $-\rho\overline{v'h'}$ and roughness models for C_D and Nu_d are required. After consideration of the data base available for calibration of the roughness models and typical magnitudes of the turbulence intensity factor $(\overline{u'^2}/U^2)$, the authors elected to include the turbulence intensity factor in the drag term of the momentum equation in the drag coefficient C_D, thus avoiding a closure model for $\overline{u'^2}$. The added influence of $\overline{u'^2}$ in the fourth term of equation (5) was ignored.

The turbulence models were not modified to include roughness effects since the physical effects of the roughness on the flow were included explicitly in the differential equations. Both Pimenta (1975) and Coleman (1976) showed that nondimensionally the distributions of Reynolds stress and Reynolds heat flux in turbulent boundary layers are the same for both smooth and rough surfaces. Because of its wide acceptance and proven predictive capability for smooth surfaces, the Prandtl mixing length model (with van Driest damping) was selected for turbulent closure. Thus

$$-\overline{\rho u'v'} = \rho l_m^2 \left(\frac{\partial U}{\partial y}\right)\left|\frac{\partial U}{\partial y}\right| \tag{9}$$

where

$$l_m = 0.40y[1 - \exp(-y^+/26)]; \quad l_m < 0.09\delta \tag{10}$$

$$l_m = 0.09\delta; \text{ otherwise} \tag{11}$$

and

$$\mathrm{Pr}_t = 0.9 \tag{12}$$

The present authors, as did Lin and Bywater (1980), have chosen to formulate the C_D and Nu_d models as functions of the local element Reynolds number

$$\mathrm{Re}_d = U(y)d(y)/\nu \tag{13}$$

which includes roughness element size and shape information through $d(y)$. The *general shape* of the drag coefficient and Nusselt number versus Reynolds number curves of Zukauskas (1972) were used as starting points to determine the final expressions for C_D and Nu_D through comparison with calibration data sets from well-defined rough surfaces.

The data sets chosen for calibration of the C_D model were the corrected (Coleman et al., 1984) data of Schlichting for surfaces with roughness elements of spherical, spherical segment, and conical shapes at various spacings. As discussed by

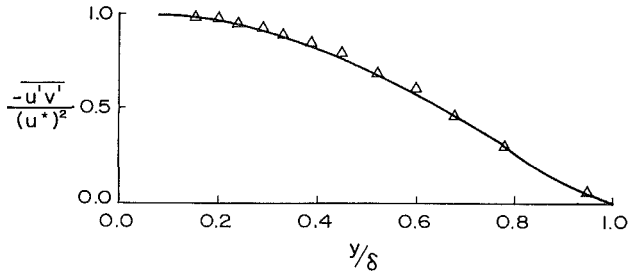

Fig. 2 Comparison of predicted and measured Reynolds stress (Pimenta, 1975); U_∞ = 27 m/s

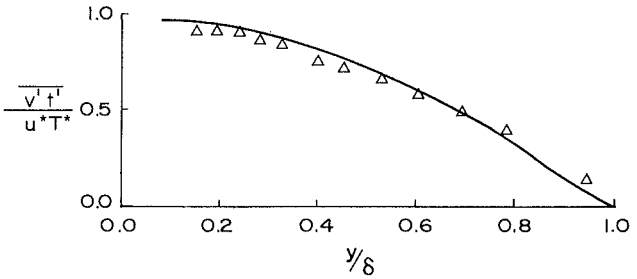

Fig. 3 Comparison of predicted and measured turbulent heat flux (Pimenta, 1975); U_∞ = 27 m/s

Taylor et al. (1984), the model that gave the best overall agreement was

$$\log_{10} C_D = -0.125 \log_{10}(\mathrm{Re}_d) + 0.375 \quad \mathrm{Re}_d < 6\times 10^4$$
$$C_D = 0.6 \quad \mathrm{Re}_d \geq 6\times 10^4 \tag{14}$$

The above expressions were used, unaltered, in all computations reported in this paper.

For surfaces composed of spheres packed in the most dense array, special treatment was found to be necessary. The flow evidently "sees" an apparent wall location well above the plane of the equators of the spheres due to the almost total flow blockage below this plane. The C_D model above was used in calculations with various assumed wall locations. After comparing these calculations with the corrected Schlichting data on the surface composed of most densely packed spheres, it was determined that the most appropriate wall location for the case of spheres in the most dense array is 0.2 D below the crests of the spheres, where D is the sphere diameter.

The data set chosen for calibration of the Nu_d model was the constant free-stream velocity (U_∞ = 27 m/s), constant wall temperature Stanton number data set of Pimenta (1975) taken in a boundary layer flow in the Stanford research apparatus with a rough surface of spheres packed in the most dense array. The model that gave the best overall agreement was found to be

$$\mathrm{Nu}_d = 2.475\ \mathrm{Re}_d^{0.4}\ \mathrm{Pr}^{0.36}, \quad \mathrm{Re}_d < 100$$
$$\mathrm{Nu}_d = 1.043\ \mathrm{Re}_d^{0.5}\ \mathrm{Pr}^{0.37}, \quad 100 < \mathrm{Re}_d < 1000 \tag{15}$$

The C_D model has been verified by comparisons with data (Taylor et al., 1985) for roughness element Reynolds numbers up to $\mathrm{Re}_d \approx 25{,}000$. The Nu_d model has been verified by comparisons with data (presented in the following section) only up to $\mathrm{Re}_d \approx 1000$.

Figures 2 and 3 show comparisons of measured and calculated profiles of nondimensional Reynolds shear stress and turbulent heat flux for Pimenta's U_∞ = 27 m/s run. The agreement seen in both figures is excellent. This agreement is of particular interest, as it reinforces the idea that the smooth wall turbulence model does not need modification if the interactions between the flow and the roughness elements are correctly included in the discrete element approach.

The numerical procedure used to obtain the solutions discussed above and the results that follow is discussed in detail

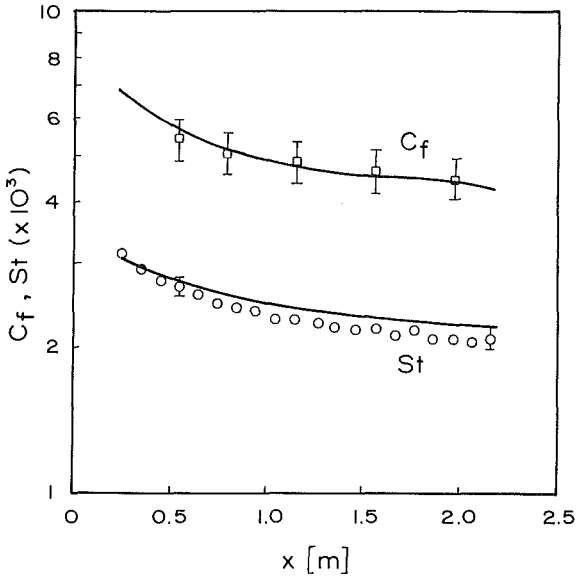

Fig. 4 Comparison of predictions with the data of Healzer (1974); U_∞ = 58 m/s, T_w = const

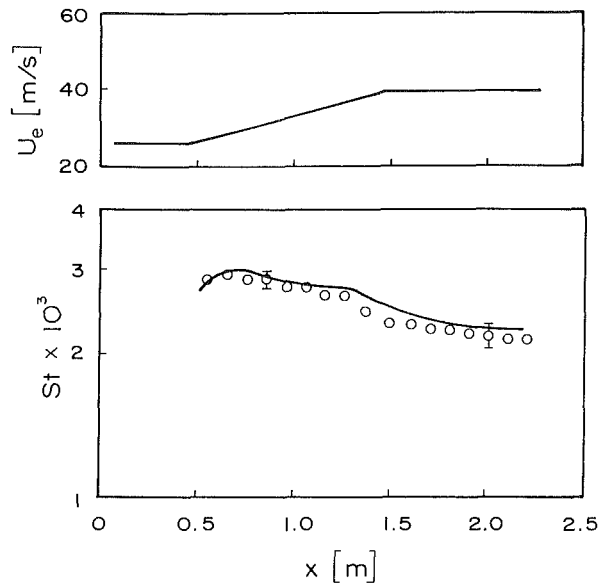

Fig. 6 Comparison of predictions with the data of Coleman (1976); equilibrium favorable pressure gradient, T_w = const

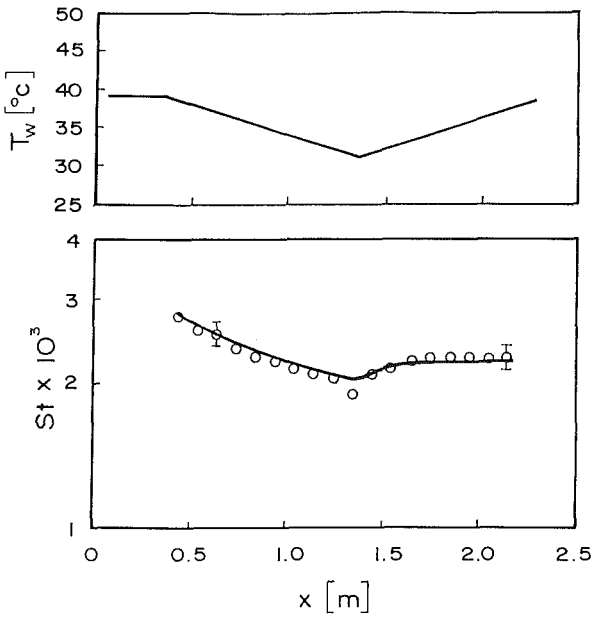

Fig. 5 Comparison of predictions with the data of Coleman (1976); bilinear wall temperature distribution, U_∞ = 26.8 m/s

by Taylor et al. (1984). An iterative marching, implicit finite difference method, adapted from the smooth wall approach of Adams (1973), was used to solve equations (3), (4), and (5). The solution was obtained on finer and finer grids until no differences were noted in the computed values of C_f and St to three significant digits. In addition, the code was verified by comparisons with known solutions of smooth wall turbulent and laminar flows.

Results and Discussion

Predictions of velocity and Reynolds stress profiles and skin friction coefficients have been reported in a previous paper (Taylor et al., 1985). Comparisons were presented with the corrected data (Coleman et al., 1984) of Schlichting, the fully developed pipe flow data of Chen (1971), and the boundary layer data of Healzer (1974), Pimenta (1975), and Coleman (1976). The comparisons of data and predictions were good to excellent in all cases.

Heat transfer predictions have been made and are compared below and in Taylor et al. (1984) with data from boundary-layer flows. The only detailed data sets for boundary-layer flows over a well-defined rough surface are those (Healzer, 1974; Pimenta, 1975; Coleman, 1976; Ligrani, 1979) from the research program at Stanford University. Boundary-layer profiles, skin friction coefficients, and Stanton numbers were reported for turbulent boundary-layer air flows over a flat plate constructed of 1.27-mm-dia spherical roughness elements packed in the most dense array.

Figure 4 shows comparisons between the calculated and measured values of C_f and St for Healzer's U_∞ = 58 m/s data set. The bars on the data points show a ±10 percent span for C_f and the reported uncertainty range for the Stanton numbers (±0.0001 St units). Inspection of the figures reveals that the agreement is very good: The predictions are almost everywhere within the data uncertainty.

Another zero pressure gradient comparison is shown in Fig. 5 for Coleman's U_∞ = 26.8 m/s run with a bilinear wall temperature variation along the test surface. The wall temperature variation and measured and predicted Stanton numbers are shown. Again, the agreement is excellent.

Figure 6 shows a comparison of predictions with data of Coleman for an equilibrium favorable pressure gradient case. The figure shows that the agreement is good.

Summary

A predictive discrete element approach for the effects of three-dimensional roughness elements on nonisothermal turbulent flow has been developed. The resulting partial differential equations explicitly include the physical effects of the flow blockage, the form drag of the elements, and the local heat transfer between the elements and fluid. The roughness element drag coefficient and Nusselt number models were calibrated using baseline sets of experimental data with well-described surface roughness and have subsequently been used for predictions of additional experimental cases.

If development of predictive models for turbulent flow and heat transfer over rough surfaces is to continue, there must be additional experimental results on both patterned and randomly rough surfaces. It is critical that the surfaces tested be well described, either with a mathematical description (for patterned roughness) or a sufficient number of surface traces (for random roughness).

Acknowledgments

This work was supported by the U. S. Air Force Armament Laboratory, Contract No. F08635-82-K-0062. The authors wish to thank Lt. Bruce Haupt and Drs. Lawrence Lijewski and Donald Daniel for their supprt and encouragement.

References

Adams, J. C., 1973, "Numerical Calculations of the Subsonic and Transonic Turbulent Boundary Layer on an Infinite Yawed Airfoil," AEDC-TR-73-112.

Adams, J. C., and Hodge, B. K., 1977, "The Calculation of Compressible, Transitional, Turbulent and Relaminarizational Boundary Layers Over Smooth and Rough Surfaces Using an Extended Mixing Length Hypothesis," AIAA Paper No. 77-682.

Chen, C. K., 1971, "Characteristics of Turbulent Flow Resistance in Pipes Roughened With Hemispheres," Ph.D. Thesis, Washington State University.

Christoph, G. H., and Pletcher, R. H., 1983, "Prediction of Rough-Wall Skin Friction and Heat Transfer," *AIAA Journal*, Vol. 21, No. 4, pp. 509-515.

Coleman, H. W., 1976, "Momentum and Energy Transport in the Accelerated Fully Rough Turbulent Boundary Layer," Ph.D. Thesis, Dept. Mech. Eng., Stanford University (also Report No. HMT-24).

Coleman, H. W., Hodge, B. K., and Taylor, R. P., 1984, "A Re-evaluation of Schlichting's Surface Roughness Experiment," ASME *J. Fluids Engineering*, Vol. 106, pp. 60-65.

Finson, M. L., 1976, "A Reynolds Stress Model for Boundary Layer Transition With Application to Rough Surfaces," AFOSR-TR-76-0322.

Finson, M. L., and Wu, P. K. S., 1979, "Analysis of Rough Wall Turbulent Heating with Application to Blunted Flight Vehicles," AIAA Paper No. 79-008.

Finson, M. L., and Clark, A. S., 1980, "The Effect of Surface Roughness Character on Turbulent Reentry Heating," AIAA Paper No. 80-1459.

Finson, M. L., 1982, "A Model for Rough Wall Turbulent Heating and Skin Friction," AIAA Paper No. 82-0199.

Healzer, J. M., 1974, "The Turbulent Boundary Layer on a Rough Porous Plate: Experimental Heat Transfer With Uniform Blowing," Ph.D. Thesis, Mech. Eng. Dept., Stanford University (also Report No. HMT-18).

Ligrani, P. M., 1979, "The Thermal and Hydrodynamic Behavior of Thick, Rough-Wall, Turbulent Boundary Layers," Ph.D. Thesis, Mech. Eng. Dept., Stanford University, Stanford, CA (also Report No. HMT-29).

Lin, T. C., and Bywater, R. J., 1980, "The Evaluation of Selected Turbulence Models for High-Speed Rough-Wall Boundary Layer Calculations," AIAA Paper 80-0132, 1980; also, *AIAA Journal*, Vol. 20, 1982, No. 3, pp. 325-333.

Nikuradse, J., 1933, "Stromungsgesetze in Rauhen Rohen," *VDI-Forchungsheft 361* (also "Laws of Flow in Rough Pipes," NACA TM 1292).

Pimenta, M. M., 1975, "The Turbulent Boundary Layer: An Experimental Study of the Transport of Momentum and Heat with the Effect of Roughness," Ph.D. Thesis, Dept. Mech. Eng., Stanford University (also Report HMT-21).

Schlichting, H., 1936, "Experimentelle Untersuchungen zum Rauhigkeitsproblem," *Ingenieur-Archiv*, Vol. VII, No. 1, pp. 1-34 (also "Experimental Investigation of the Problem of Surface Roughness," NACA TM 823).

Taylor, R. P., Coleman, H. W., and Hodge, B, K., 1984, "A Discrete Element Prediction Approach for Turbulent Flow Over Rough Surfaces," Report No. TFD-84-1, Mech. and Nuc. Eng. Dept., Mississippi State University.

Taylor, R. P., Coleman, H. W., and Hodge, B. K., 1985, "Prediction of Turbulent Rough-Wall Skin Friction Using a Discrete Element Approach," ASME *Journal of Fluids Engineering*, Vol. 107, pp. 251-257.

Zukauskas, A., 1972, "Heat Transfer From Tubes in Crossflow," *Advances in Heat Transfer*, Academic Press, New York.

Maximum Density Effects on Vortex Instability of Horizontal and Inclined Buoyancy-Induced Flows in Porous Media

Jiin-Yuh Jang[1] and Wen-Jeng Chang[2]

1 Introduction

Buoyancy-induced flows in a porous medium saturated with cold water are strongly affected by the occurrence of the density extremum associated with the temperature of 4°C in pure water at 1 atm. Such conditions occur commonly in a porous medium, such as the moist ground trapped under a layer of ice in winter, permeable soils flooded by cold lake or seawater, water-ice slurries, etc. Gebhart and Mollendorf (1977) developed a density relation, $\rho(T, s, p)$, as a function of temperature, salinity, and pressure for pure and saline water. The expression contains a single temperature term

$$\rho(T, s, p) = \rho_m(s, p)\{1 - \alpha_T(s, p)[T - T_m(s, p)]^{q(s, p)}\} \quad (1)$$

Using this density equation of state, Ramilison and Gebhart (1980) and Lin and Gebhart (1986) presented similarity solutions for buoyancy-induced flows adjacent to a vertical and a horizontal surface in porous media saturated with cold water. The vortex instability of buoyancy-induced inclined boundary layer flow in a porous medium saturated with a Boussinesq fluid or cold water has been studied, respectively, by Hsu and Cheng (1979) and Jang and Chang (1987), where the normal component of the buoyancy force is neglected. Thus, the main flow and instability results in Hsu and Cheng (1979) and Jang and Chang (1987) are not valid for angles of inclination from the vertical that are not small.

The present investigation uses equations (1) to re-examine conditions marking the onset of stationary longitudinal vortices in horizontal and inclined buoyancy-induced boundary layer flow in porous media with a maximum density effect. Both the streamwise and normal components of the buoyancy force are retained in the momentum equations. This is in contrast to our previous analyses (Jang and Chang, 1987). Thus the present study is applicable for angles ranging from 0 to close to 90 deg from the horizontal.

2 Analysis

2.1 Main Flow. Consider an inclined impermeable surface (T_o) embedded in a porous medium (T_∞) saturated with cold water as shown in Fig. 1. The wall temperature is assumed to be a power function of x, i.e., $T_o = T_\infty + Ax^m$, where A is a constant. The angle of inclination ϕ is measured from the horizontal. The variation of the buoyancy force across the thermal boundary layer depends primarily on the relationship between T_0, T_∞, and T_m (density extremum temperature) and the fluid density. It can be shown that when density extremum parameter $R = (T_m - T_\infty)/(T_o - T_\infty) \leq 0$, the buoyancy force and flow are invariably upward, and for $R \geq 1/2$, they are invariably downward. For $0 < R < 1/2$, the buoyancy

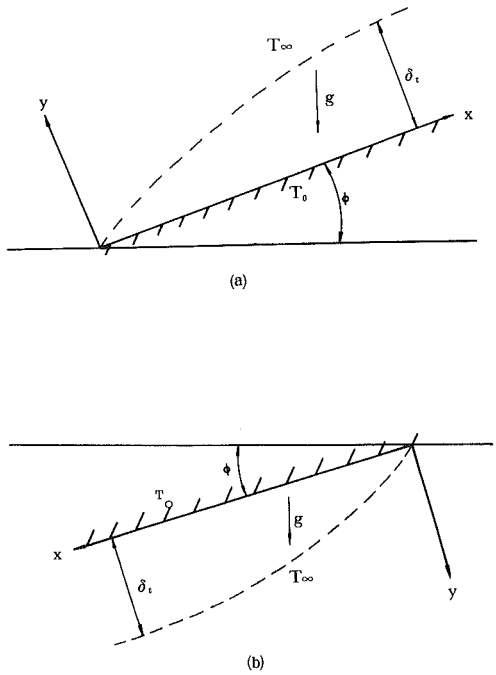

Fig. 1 Coordinate systems: *(a)* upward-facing surface with upflow ($R \leq 0$); *(b)* downward-facing surface with downflow ($R \geq 1/2$)

[1]Associate Professor, Department of Mechanical Engineering, National Cheng-Kung University, Tainan, Taiwan 70101.

[2]Graduate Assistant, Department of Mechanical Engineering, National Cheng-Kung University, Tainan, Taiwan 70101.

Contributed by the Heat Transfer Division for publication in the JOURNAL OF HEAT TRANSFER. Manuscript received by the Heat Transfer Division July 22, 1987. Keywords: Natural Convection, Porous Media.

Acknowledgments

This work was supported by the U. S. Air Force Armament Laboratory, Contract No. F08635-82-K-0062. The authors wish to thank Lt. Bruce Haupt and Drs. Lawrence Lijewski and Donald Daniel for their supprt and encouragement.

References

Adams, J. C., 1973, "Numerical Calculations of the Subsonic and Transonic Turbulent Boundary Layer on an Infinite Yawed Airfoil," AEDC-TR-73-112.

Adams, J. C., and Hodge, B. K., 1977, "The Calculation of Compressible, Transitional, Turbulent and Relaminarizational Boundary Layers Over Smooth and Rough Surfaces Using an Extended Mixing Length Hypothesis," AIAA Paper No. 77-682.

Chen, C. K., 1971, "Characteristics of Turbulent Flow Resistance in Pipes Roughened With Hemispheres," Ph.D. Thesis, Washington State University.

Christoph, G. H., and Pletcher, R. H., 1983, "Prediction of Rough-Wall Skin Friction and Heat Transfer," *AIAA Journal*, Vol. 21, No. 4, pp. 509-515.

Coleman, H. W., 1976, "Momentum and Energy Transport in the Accelerated Fully Rough Turbulent Boundary Layer," Ph.D. Thesis, Dept. Mech. Eng., Stanford University (also Report No. HMT-24).

Coleman, H. W., Hodge, B. K., and Taylor, R. P., 1984, "A Re-evaluation of Schlichting's Surface Roughness Experiment," ASME *J. Fluids Engineering*, Vol. 106, pp. 60-65.

Finson, M. L., 1976, "A Reynolds Stress Model for Boundary Layer Transition With Application to Rough Surfaces," AFOSR-TR-76-0322.

Finson, M. L., and Wu, P. K. S., 1979, "Analysis of Rough Wall Turbulent Heating with Application to Blunted Flight Vehicles," AIAA Paper No. 79-008.

Finson, M. L., and Clark, A. S., 1980, "The Effect of Surface Roughness Character on Turbulent Reentry Heating," AIAA Paper No. 80-1459.

Finson, M. L., 1982, "A Model for Rough Wall Turbulent Heating and Skin Friction," AIAA Paper No. 82-0199.

Healzer, J. M., 1974, "The Turbulent Boundary Layer on a Rough Porous Plate: Experimental Heat Transfer With Uniform Blowing," Ph.D. Thesis, Mech. Eng. Dept., Stanford University (also Report No. HMT-18).

Ligrani, P. M., 1979, "The Thermal and Hydrodynamic Behavior of Thick, Rough-Wall, Turbulent Boundary Layers," Ph.D. Thesis, Mech. Eng. Dept., Stanford University, Stanford, CA (also Report No. HMT-29).

Lin, T. C., and Bywater, R. J., 1980, "The Evaluation of Selected Turbulence Models for High-Speed Rough-Wall Boundary Layer Calculations," AIAA Paper 80-0132, 1980; also, *AIAA Journal*, Vol. 20, 1982, No. 3, pp. 325-333.

Nikuradse, J., 1933, "Stromungsgesetze in Rauhen Rohen," *VDI-Forchungsheft 361* (also "Laws of Flow in Rough Pipes," NACA TM 1292).

Pimenta, M. M., 1975, "The Turbulent Boundary Layer: An Experimental Study of the Transport of Momentum and Heat with the Effect of Roughness," Ph.D. Thesis, Dept. Mech. Eng., Stanford University (also Report HMT-21).

Schlichting, H., 1936, "Experimentelle Untersuchungen zum Rauhigkeitsproblem," *Ingenieur-Archiv*, Vol. VII, No. 1, pp. 1-34 (also "Experimental Investigation of the Problem of Surface Roughness," NACA TM 823).

Taylor, R. P., Coleman, H. W., and Hodge, B, K., 1984, "A Discrete Element Prediction Approach for Turbulent Flow Over Rough Surfaces," Report No. TFD-84-1, Mech. and Nuc. Eng. Dept., Mississippi State University.

Taylor, R. P., Coleman, H. W., and Hodge, B. K., 1985, "Prediction of Turbulent Rough-Wall Skin Friction Using a Discrete Element Approach," ASME *Journal of Fluids Engineering*, Vol. 107, pp. 251-257.

Zukauskas, A., 1972, "Heat Transfer From Tubes in Crossflow," *Advances in Heat Transfer*, Academic Press, New York.

Maximum Density Effects on Vortex Instability of Horizontal and Inclined Buoyancy-Induced Flows in Porous Media

Jiin-Yuh Jang[1] and Wen-Jeng Chang[2]

1 Introduction

Buoyancy-induced flows in a porous medium saturated with cold water are strongly affected by the occurrence of the density extremum associated with the temperature of 4°C in pure water at 1 atm. Such conditions occur commonly in a porous medium, such as the moist ground trapped under a layer of ice in winter, permeable soils flooded by cold lake or seawater, water-ice slurries, etc. Gebhart and Mollendorf (1977) developed a density relation, $\rho(T, s, p)$, as a function of temperature, salinity, and pressure for pure and saline water. The expression contains a single temperature term

$$\rho(T, s, p) = \rho_m(s, p)\{1 - \alpha_T(s, p)[T - T_m(s, p)]^{q(s, p)}\} \quad (1)$$

Using this density equation of state, Ramilison and Gebhart (1980) and Lin and Gebhart (1986) presented similarity solutions for buoyancy-induced flows adjacent to a vertical and a horizontal surface in porous media saturated with cold water. The vortex instability of buoyancy-induced inclined boundary layer flow in a porous medium saturated with a Boussinesq fluid or cold water has been studied, respectively, by Hsu and Cheng (1979) and Jang and Chang (1987), where the normal component of the buoyancy force is neglected. Thus, the main flow and instability results in Hsu and Cheng (1979) and Jang and Chang (1987) are not valid for angles of inclination from the vertical that are not small.

The present investigation uses equations (1) to re-examine conditions marking the onset of stationary longitudinal vortices in horizontal and inclined buoyancy-induced boundary layer flow in porous media with a maximum density effect. Both the streamwise and normal components of the buoyancy force are retained in the momentum equations. This is in contrast to our previous analyses (Jang and Chang, 1987). Thus the present study is applicable for angles ranging from 0 to close to 90 deg from the horizontal.

2 Analysis

2.1 Main Flow. Consider an inclined impermeable surface (T_o) embedded in a porous medium (T_∞) saturated with cold water as shown in Fig. 1. The wall temperature is assumed to be a power function of x, i.e., $T_o = T_\infty + Ax^m$, where A is a constant. The angle of inclination ϕ is measured from the horizontal. The variation of the buoyancy force across the thermal boundary layer depends primarily on the relationship between T_0, T_∞, and T_m (density extremum temperature) and the fluid density. It can be shown that when density extremum parameter $R = (T_m - T_\infty)/(T_o - T_\infty) \leq 0$, the buoyancy force and flow are invariably upward, and for $R \geq 1/2$, they are invariably downward. For $0 < R < 1/2$, the buoyancy

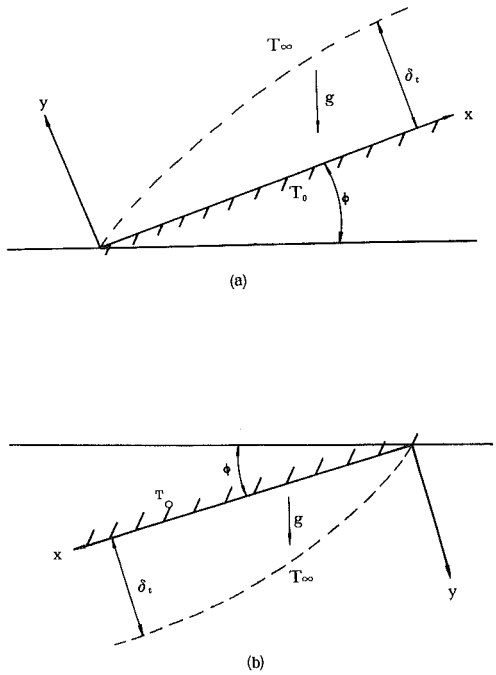

Fig. 1 Coordinate systems: *(a)* upward-facing surface with upflow ($R \leq 0$); *(b)* downward-facing surface with downflow ($R \geq 1/2$)

[1]Associate Professor, Department of Mechanical Engineering, National Cheng-Kung University, Tainan, Taiwan 70101.

[2]Graduate Assistant, Department of Mechanical Engineering, National Cheng-Kung University, Tainan, Taiwan 70101.

Contributed by the Heat Transfer Division for publication in the JOURNAL OF HEAT TRANSFER. Manuscript received by the Heat Transfer Division July 22, 1987. Keywords: Natural Convection, Porous Media.

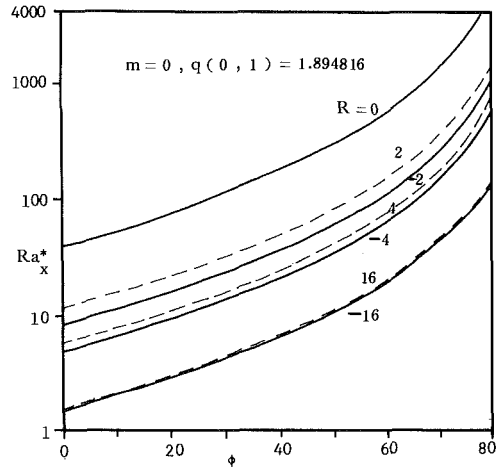

Fig. 2 Critical Rayleigh number versus ϕ for selected values of R and for $m = 0$, q (0, 1)

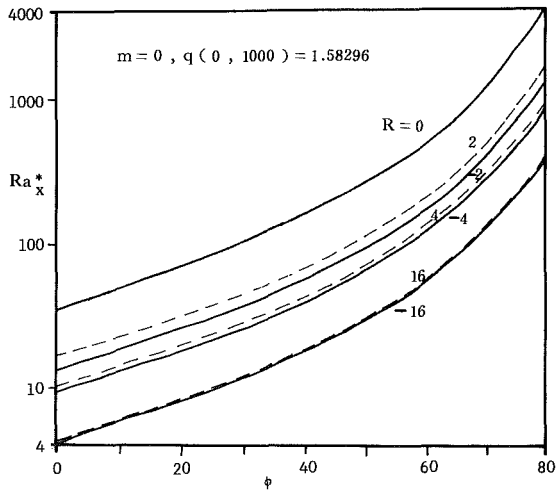

Fig. 3 Critical Rayleigh number versus ϕ for selected values of R and for $m = 0$, q (0, 1000)

force is bidirectional and a simple boundary layer analysis may not be directly applicable.

By applying Darcy's law and the boundary layer assumptions, the transformed equations and boundary conditions are given by

$$f'' \pm \frac{mq-2}{3} q\eta|\theta-R|^{q-1}\frac{\theta-R}{|\theta-R|}\theta' \pm mq(|\theta-R|^{q}-|R|^{q}) \mp \xi q|\theta-R|^{q-1}\frac{\theta-R}{|\theta-R|}\theta' = \mp\frac{mq+1}{3}\xi\frac{\partial}{\partial\xi}(|\theta-R|^{q}-|R|^{q}) \quad (2)$$

$$\theta'' + \frac{mq+1}{3} f\theta' - mf'\theta = \frac{mq+1}{3}\xi\left(f'\frac{\partial\theta}{\partial\xi} - \theta'\frac{\partial f}{\partial\xi}\right) \quad (3)$$

$$f(\xi, 0) = 0, \quad \theta(\xi, 0) = 1, \quad f'(\xi, \infty) = 0, \quad \theta(\xi, \infty) = 0 \quad (4)$$

where the pseudosimilarity variable $\eta(x, y)$, the parameter $\xi(x)$, the reduced stream function $f(\xi, \eta)$, and the dimensionless temperature $\theta(\xi, \eta)$ are given, respectively, by

$$\eta(x, y) = y(\mathrm{Ra}_x\cos\phi)^{1/3}/x, \quad \xi(x) = (\mathrm{Ra}_x\cos\phi)^{1/3}\tan\phi$$
$$f(\xi, \eta) = \psi(x, y)/\alpha(\mathrm{Ra}_x\cos\phi)^{1/3}, \quad \theta(\xi, \eta) = (T-T_\infty)/(T_o-T_\infty) \quad (5)$$

In equation (5), ψ is the stream function and the local Rayleigh number is defined as $\rho_m g K\alpha_T|T_o - T_\infty|^q x/\mu\alpha$, where K is the permeability, μ is the viscosity, and α represents the equivalent thermal diffusivity. The upper signs denote upflow, while the lower signs denote downflow. The primes denote partial differentiation with respect to η. Equations (2)–(4) are valid for all angles except $\phi = \pi/2$ because $\xi\to\infty$ as $\phi\to\pi/2$. They reduce to those equations for flow over a horizontal flat plate (Lin and Gebhart, 1986) when $\xi = 0$.

2.2 Disturbance Flow. Using standard methods of linear stability theory, one obtains the following dimensionless disturbance equation for the local similarity approximations (Hsu and Cheng, 1979):

$$(D^2-k^2)^2F - [B_1 \pm \xi B_3B_5](D^2-k^2)F - B_2D(D^2-k^2)F \pm B_3B_5\left(\frac{mq-2}{3}\eta F'' + \frac{2mq-1}{3}F'\right) \pm B_4B_5k^2(\mathrm{Ra}_x\cos\phi)^{2/3}F = 0 \quad (6)$$

where the coefficients $B_1(\xi, \eta)$ through $B_5(\xi, \eta)$ are given by

$$B_1 = mf', \quad B_2 = -\left(\frac{mq+1}{3}f + \frac{mq+1}{3}\xi\frac{\partial f}{\partial\xi}\right), \quad B_3 = \left(m\theta + \frac{mq-2}{3}\eta\theta' + \frac{mq+1}{3}\xi\frac{\partial\theta}{\partial\xi}\right), \quad B_4 = \theta', \quad B_5 = q\frac{\theta-R}{|\theta-R|}|\theta-R|^{q-1} \quad (7)$$

With the boundary conditions

$$F(0) = D^2F(0) = F(\infty) = D^2F(\infty) = 0 \quad (8)$$

where the D^n stands for d^n/d and k is the dimensionless wave number. Equation (6), along with its boundary conditions equation (8), constitutes a fourth-order system of linear ordinary differential equations for the disturbance amplitude distributions $F(\eta)$. For fixed m, q, and ϕ, the solution F is an eigenfunction for the eigenvalues k and Ra_x.

3 Results and Discussion

The system of equations (2)–(4) was solved by an implicit finite difference method similar to that described in Cebeci and Bradshaw (1977). The disturbance equation is solved by separatedly integrating two linearly independent integrals. The two integrals are integrated separately from the outer edge of the boundary layer to the wall using a sixth-order Runge–Kutta variable size integrating routine incorporated with the Kaplan filtering technique (Kaplan, 1964) to maintain the linear independence of the eigenfunctions.

The critical Rayleigh numbers as a function of inclination angles for $q(s, p) = q(0, 1) = 1.894816$ and $q(0, 1000) = 1.582950$ are plotted in Figs. 2 and 3, respectively, for various values of R. It is seen that the critical Rayleigh number is a rather strong function of ϕ and R. As expected, with increasing inclination angles ϕ, the flow is less susceptible to vortex instability. This is due to the fact that, as ϕ increases, the normal component of the buoyancy force, which is responsible for the occurrence of the longitudinal vortices, becomes smaller. Therefore, the flow is more stable. It is also seen that, for larger values of $|R|$, the critical Rayleigh number decreases. This trend agrees with the results of Mollendorf and Jahn

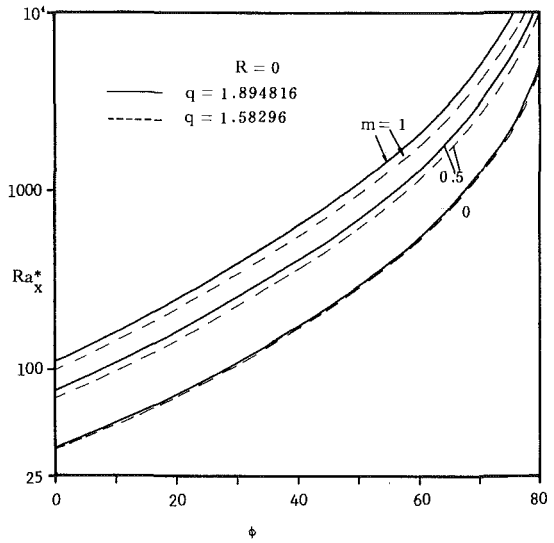

Fig. 4 Critical Rayleigh number versus ϕ for selected values of m and for R = 0, q (0, 1) and q (0, 1000)

(1983) for the thermal instability in a horizontal layer of cold water. However, for a given surface and ambient temperature, it can be shown that the flow is more stable in terms of the physical point of instability (x_{crit}). It is noted that, for increasing $|R|$, the critical Rayleigh numbers tend to merge for positive and negative values of R. Figure 4 shows that the critical Rayleigh number is a rather strong function of m. As the value of m increases, the critical Rayleigh number increases.

4 Conclusions

Linear stability analysis is used to study the vortex instability of the buoyancy-induced flow over horizontal and inclined surfaces embedded in a porous medium saturated with cold water. The neutral stability equation is derived to include the effect of pressure and salinity in the absence of saline diffusion up to a maximum of 1000 bars and 40 parts per thousand. The present results are valid for angles in the range of 0 to close to 90 deg from the horizontal. The results show that, as the angle of inclination from the horizontal increases, the susceptibility of the flow to the vortex instability decreases. As the density extremum parameter $|R|$ increases, the flow is more stable.

References

Cebeci, T., and Bradshaw, P., 1977, *Momentum Transfer in Boundary Layers*, Hemisphere Publishing Corp., Washington, DC, Chap. 7.

Gebhart, B., and Mollendorf, J. C., 1977, "A New Density Relation for Pure and Saline Water," *Deep-Sea Research*, Vol. 24, pp. 831–848.

Hsu, C. T., Cheng, P., and Homsy, G. M., 1978, "Instability of Free Convection Flow Over a Horizontal Impermeable Surface in a Porous Medium," *International Journal of Heat and Mass Transfer*, Vol. 21, pp. 1221–1228.

Hsu, C. T., and Cheng, P., 1979, "Vortex Instability In Buoyancy-Induced Flow Over Inclined Heated Surfaces in a Porous Media," ASME JOURNAL OF HEAT TRANSFER, Vol. 101, pp. 660–665.

Jang, J. Y., and Chang, W. J., 1987, "Vortex Instability of Inclined Buoyant Layer in Porous Media Saturated With Cold Water," *Int. Communications Heat and Mass Transfer*, Vol. 14, No. 4, pp. 405–416.

Kaplan, R. E., 1964, "The Stability of Laminar Incompressible Boundary Layers in the Presence of Complaint Boundaries," M. I. T. Aero-Elastic and Structures Research Laboratory, ASRL-TR 116-1.

Lin, D. S., and Gebhart, B., 1986, "Buoyancy-Induced Flow Adjacent to a Horizontal Surface Submerged in Porous Medium Saturated With Cold Water," *Int. J. Heat Mass Transfer*, Vol. 29, pp. 611–623.

Mollendorf, J. C., and Jahn, K. H., 1983, "Onset of Convection in a Horizontal Layer of Cold Water," ASME JOURNAL OF HEAT TRANSFER, Vol. 105, pp. 460–464.

Ramilison, J. M., and Gebhart, B., 1980, "Buoyancy Induced Transport in Porous Media Saturated With Pure or Saline Water at Low Temperature," *Int. J. Heat Mass Transfer*, Vol. 23, pp. 1521–1530.

Numerical Solution of Transient Natural Convection Around a Horizontal Wire

Y. W. Song[1]

Introduction

This work deals with transient natural convection around a horizontal wire having a constant heat flux. The problem arises from the determination of the thermal conductivity of fluids by the transient hot-wire method. Although finite difference solutions of natural convection heat transfer around a heated horizontal cylinder having a constant temperature at the surface of the cylinder were reported for steady-state (Kuehn and Goldstein, 1980) and transient conditions (Mitsuo, 1982), it appears that no detailed numerical results have been published on the transient heat transfer around a heated cylinder having a constant heat flux.

In this work the isotherms and streamlines for $\mathrm{Pr}=7$ and $0.12<\mathrm{Ra}^*<20$ are calculated from the beginning of heating to the time when a steady state is reached. The calculated transition time from conduction to convection agrees very well with experimental results obtained by other authors.

Analysis

Consider a cylinder of diameter d horizontally immersed in a layer of fluid. The system, initially at a uniform temperature T_0, is suddenly heated by a steady current passing through the cylinder. The heat generation per unit length of the cylinder is $\dot{q}_l = I^2 R_w/L$, where I is the magnitude of electric current, and R_w and L are the resistance and the length of the cylinder, respectively. It is well known that the whole process of heat transfer includes three stages, characterized as pure conduction, transient convection, and steady-state convection in a time sequence (Ostroumov, 1965; Vest and Lawson, 1972; Parsons and Mulligan, 1978).

In this numerical analysis, the following dimensionless variables are used:

$$R=r/d, \quad \tau=at/d^2, \quad U=ud/\nu, \quad V=vd/\nu,$$

$$\Psi=\psi/\nu, \quad \Omega=\omega d^2/\nu, \quad \Theta=(T-T_0)\lambda\pi/\dot{q}_l$$

where ν, λ, and a are the kinematic viscosity, the thermal conductivity, and the thermal diffusivity of the fluid, ψ and ω are the stream function and the vorticity, and u and v are the radial and circumferential components of velocity, respectively. The governing equations for the vorticity, the stream function, and the temperature in a two-dimensional natural convection flow for the Boussinesq approximations are as follows:

$$U=\frac{\partial\Psi}{R\partial\vartheta} \tag{1}$$

$$V=-\frac{\partial\Psi}{\partial R} \tag{2}$$

$$\Omega=-\nabla^2\Psi \tag{3}$$

$$\frac{\partial\Omega}{\partial\tau}+\mathrm{Pr}U\frac{\partial\Omega}{\partial R}+\mathrm{Pr}V\frac{\partial\Omega}{R\partial\vartheta} = \mathrm{Pr}\nabla^2\Omega+\mathrm{Ra}^*\left(\frac{\partial\Theta}{R\partial\vartheta}\cos\vartheta+\frac{\partial\Theta}{\partial R}\sin\vartheta\right) \tag{4}$$

[1]Institute of Thermodynamic and Heat Technology, Stuttgart University, 7000 Stuttgart 80, Federal Republic of Germany.

Contributed by the Heat Transfer Division for publication in the JOURNAL OF HEAT TRANSFER. Manuscript received by the Heat Transfer Division September 24, 1987. Keywords: Natural Convection, Numerical Methods, Transient and Unsteady Heat Transfer.

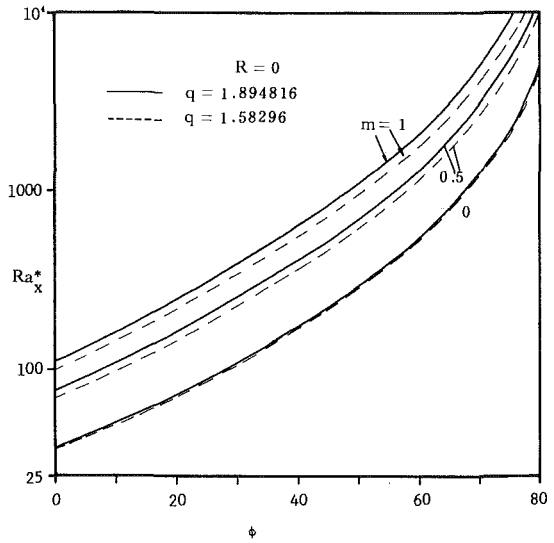

Fig. 4 Critical Rayleigh number versus ϕ for selected values of m and for R = 0, q (0, 1) and q (0, 1000)

(1983) for the thermal instability in a horizontal layer of cold water. However, for a given surface and ambient temperature, it can be shown that the flow is more stable in terms of the physical point of instability (x_{crit}). It is noted that, for increasing $|R|$, the critical Rayleigh numbers tend to merge for positive and negative values of R. Figure 4 shows that the critical Rayleigh number is a rather strong function of m. As the value of m increases, the critical Rayleigh number increases.

4 Conclusions

Linear stability analysis is used to study the vortex instability of the buoyancy-induced flow over horizontal and inclined surfaces embedded in a porous medium saturated with cold water. The neutral stability equation is derived to include the effect of pressure and salinity in the absence of saline diffusion up to a maximum of 1000 bars and 40 parts per thousand. The present results are valid for angles in the range of 0 to close to 90 deg from the horizontal. The results show that, as the angle of inclination from the horizontal increases, the susceptibility of the flow to the vortex instability decreases. As the density extremum parameter $|R|$ increases, the flow is more stable.

References

Cebeci, T., and Bradshaw, P., 1977, *Momentum Transfer in Boundary Layers*, Hemisphere Publishing Corp., Washington, DC, Chap. 7.

Gebhart, B., and Mollendorf, J. C., 1977, "A New Density Relation for Pure and Saline Water," *Deep-Sea Research*, Vol. 24, pp. 831–848.

Hsu, C. T., Cheng, P., and Homsy, G. M., 1978, "Instability of Free Convection Flow Over a Horizontal Impermeable Surface in a Porous Medium," *International Journal of Heat and Mass Transfer*, Vol. 21, pp. 1221–1228.

Hsu, C. T., and Cheng, P., 1979, "Vortex Instability In Buoyancy-Induced Flow Over Inclined Heated Surfaces in a Porous Media," ASME JOURNAL OF HEAT TRANSFER, Vol. 101, pp. 660–665.

Jang, J. Y., and Chang, W. J., 1987, "Vortex Instability of Inclined Buoyant Layer in Porous Media Saturated With Cold Water," *Int. Communications Heat and Mass Transfer*, Vol. 14, No. 4, pp. 405–416.

Kaplan, R. E., 1964, "The Stability of Laminar Incompressible Boundary Layers in the Presence of Complaint Boundaries," M. I. T. Aero-Elastic and Structures Research Laboratory, ASRL-TR 116-1.

Lin, D. S., and Gebhart, B., 1986, "Buoyancy-Induced Flow Adjacent to a Horizontal Surface Submerged in Porous Medium Saturated With Cold Water," *Int. J. Heat Mass Transfer*, Vol. 29, pp. 611–623.

Mollendorf, J. C., and Jahn, K. H., 1983, "Onset of Convection in a Horizontal Layer of Cold Water," ASME JOURNAL OF HEAT TRANSFER, Vol. 105, pp. 460–464.

Ramilison, J. M., and Gebhart, B., 1980, "Buoyancy Induced Transport in Porous Media Saturated With Pure or Saline Water at Low Temperature," *Int. J. Heat Mass Transfer*, Vol. 23, pp. 1521–1530.

Numerical Solution of Transient Natural Convection Around a Horizontal Wire

Y. W. Song[1]

Introduction

This work deals with transient natural convection around a horizontal wire having a constant heat flux. The problem arises from the determination of the thermal conductivity of fluids by the transient hot-wire method. Although finite difference solutions of natural convection heat transfer around a heated horizontal cylinder having a constant temperature at the surface of the cylinder were reported for steady-state (Kuehn and Goldstein, 1980) and transient conditions (Mitsuo, 1982), it appears that no detailed numerical results have been published on the transient heat transfer around a heated cylinder having a constant heat flux.

In this work the isotherms and streamlines for $\mathrm{Pr}=7$ and $0.12<\mathrm{Ra}^*<20$ are calculated from the beginning of heating to the time when a steady state is reached. The calculated transition time from conduction to convection agrees very well with experimental results obtained by other authors.

Analysis

Consider a cylinder of diameter d horizontally immersed in a layer of fluid. The system, initially at a uniform temperature T_0, is suddenly heated by a steady current passing through the cylinder. The heat generation per unit length of the cylinder is $\dot{q}_l = I^2 R_w/L$, where I is the magnitude of electric current, and R_w and L are the resistance and the length of the cylinder, respectively. It is well known that the whole process of heat transfer includes three stages, characterized as pure conduction, transient convection, and steady-state convection in a time sequence (Ostroumov, 1965; Vest and Lawson, 1972; Parsons and Mulligan, 1978).

In this numerical analysis, the following dimensionless variables are used:

$$R=r/d, \quad \tau=at/d^2, \quad U=ud/\nu, \quad V=vd/\nu,$$

$$\Psi=\psi/\nu, \quad \Omega=\omega d^2/\nu, \quad \Theta=(T-T_0)\lambda\pi/\dot{q}_l$$

where ν, λ, and a are the kinematic viscosity, the thermal conductivity, and the thermal diffusivity of the fluid, ψ and ω are the stream function and the vorticity, and u and v are the radial and circumferential components of velocity, respectively. The governing equations for the vorticity, the stream function, and the temperature in a two-dimensional natural convection flow for the Boussinesq approximations are as follows:

$$U=\frac{\partial\Psi}{R\partial\vartheta} \tag{1}$$

$$V=-\frac{\partial\Psi}{\partial R} \tag{2}$$

$$\Omega=-\nabla^2\Psi \tag{3}$$

$$\frac{\partial\Omega}{\partial\tau}+\mathrm{Pr}U\frac{\partial\Omega}{\partial R}+\mathrm{Pr}V\frac{\partial\Omega}{R\partial\vartheta} = \mathrm{Pr}\nabla^2\Omega+\mathrm{Ra}^*\left(\frac{\partial\Theta}{R\partial\vartheta}\cos\vartheta+\frac{\partial\Theta}{\partial R}\sin\vartheta\right) \tag{4}$$

[1]Institute of Thermodynamic and Heat Technology, Stuttgart University, 7000 Stuttgart 80, Federal Republic of Germany.

Contributed by the Heat Transfer Division for publication in the JOURNAL OF HEAT TRANSFER. Manuscript received by the Heat Transfer Division September 24, 1987. Keywords: Natural Convection, Numerical Methods, Transient and Unsteady Heat Transfer.

$$\frac{\partial \Theta}{\partial \tau} + \mathrm{Pr} U \frac{\partial \Theta}{\partial R} + \mathrm{Pr} V \frac{\partial \Theta}{R \partial \vartheta} = \nabla^2 \Theta \tag{5}$$

where $\mathrm{Pr} = \nu/a$ is the Prandtl number, $\mathrm{Ra}^* = g\beta \dot{q}_l d^3/\pi\lambda\nu a$, the Rayleigh number based on constant heat flow rate, g the gravitational acceleration, and β the coefficient of thermal expansion.

By symmetry, only the flow in the left side of the wire needs to be considered. Correspondingly, the boundary conditions are

$$U = V = \Psi = 0, \quad \Omega = -\frac{\partial^2 \Psi}{\partial R^2}, \quad \frac{\alpha d \Theta}{4 d\tau} = 1 - \frac{\partial \Theta}{\partial R}, \quad R = 0.5$$

$$V = \Psi = \Omega = \frac{\partial U}{\partial \vartheta} = \frac{\partial \Theta}{\partial \vartheta} = 0, \quad \vartheta = 0,\ 180$$

$$U = \Theta = \frac{\partial^2 \Psi}{\partial R^2} = 0, \quad \Omega = -\frac{\partial^2 \Psi}{\partial \vartheta^2}, \quad R = \infty$$

The initial conditions are

$$U = V = \Theta = \Psi = \Omega = 0$$

where $\alpha = (\rho c)_w/(\rho c)_f$ is the ratio of the heat capacity of an equivalent volume of the wire to that of the fluid.

Solution Technique

An explicit finite difference method is used to solve the energy and vorticity equations while a superoverrelaxation method is employed to determine the stream function at each time step. A power-law scheme suggested by Patankar (1980) is used to maintain the stability at large Rayleigh number. Equations (4) and (5) can be expressed in the following finite difference form:

$$f_{i,j}^{n+1} = f_{i,j}^{n} + (A f_{i+1,j} + B f_{i-1,j} + C f_{i,j+1} + E f_{i,j-1} - P f_{i,j} + H Q_{i,j})^n \tag{6}$$

where

$$Q_{i,j} = \frac{\Delta \Theta_{i,j}}{R \Delta \vartheta} \cos \vartheta + \frac{\Delta \Theta_{i,j}}{\Delta R} \sin \vartheta \tag{7}$$

and f can be either Ω or Θ. The coefficient A is calculated by

$$A = \left[\left[0,\ D_e \left(1 - \frac{0.1 F_e}{D_e}\right)^5\right]\right] + \left[\left[0,\ -F_e\right]\right] \tag{8}$$

where D_e is the diffusion conductance between nodes (i, j) and $(i+1, j)$; F_e is the strength of the convection in the i direction. While D_e always remains positive, F_e can be either positive or negative, depending on the direction of the fluid flow. The square brackets on the right side of the above equation denote that only the larger term in the brackets is to be chosen. Similar expressions can be obtained for the coefficients B, C, and E. They are all nonnegative and provide an extremely good approximation. The coefficient P can be written as

$$P = A + B + C + E \tag{9}$$

$H = 0$ for temperature and $H = \mathrm{Ra}^*$ for vorticity.

The successive overrelaxation technique for equation (3) can be described by the following iterative scheme:

$$(\Psi_{i,j})^{k+1} = \Psi_{i,j}^K + \mathrm{Relax}(A_1 \Psi_{i,j+1}^K + A_2 \Psi_{i,j-1}^K + A_3 \Psi_{i+1,j}^K + A_4 \Psi_{i-1,j}^K - A_0 \Psi_{i,j}^K - \Omega_{i,j}^K)/A_0 \tag{10}$$

The calculation procedure is outlined as follows. At any time, the instantaneous temperature and vorticity distributions are calculated using the data obtained from the previous time step except that at the initial instant they are prescribed by the initial conditions. The stream function is then calculated based on the vorticity distribution by solving equation (10) with an error allowance of 0.0001; the components of velocity can be calculated from equations (1) and (2) once Ψ becomes known.

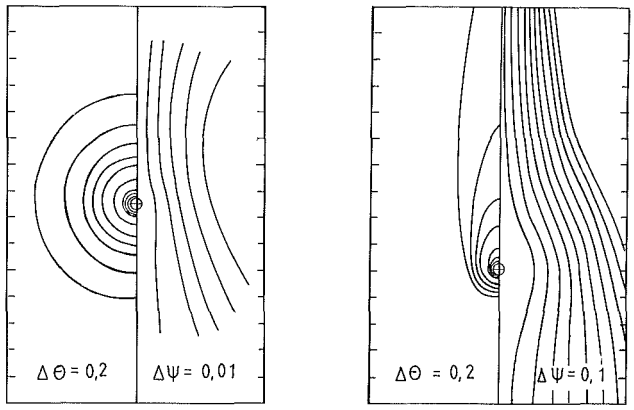

Fig. 1 Isotherms and streamlines for Ra* = 0.12 and Pr = 7

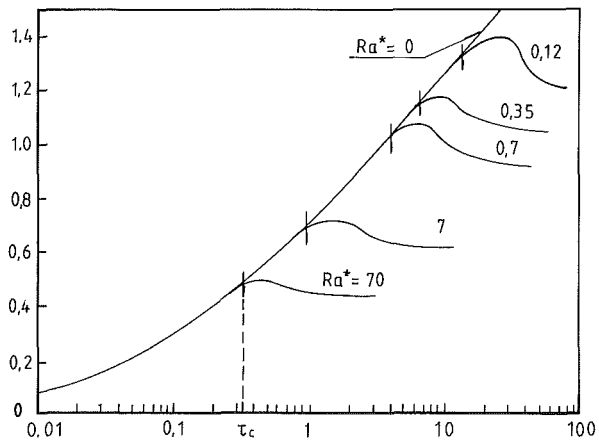

Fig. 2 Variations of the dimensionless temperature of the wire with dimensionless time

In order to examine the reliability of the solution technique a comparison of the steady-state results calculated by the above transient model with those obtained directly from the steady-state equations under the same conditions has been made. It is proved that these results are in very good agreement with each other.

Numerical Results and Discussion

Numerical solutions were obtained for $\mathrm{Pr} = 7$ and several different Rayleigh numbers ranging from 0.12 to 70. As an example, the isotherms and streamlines for $\mathrm{Ra}^* = 0.12$ at two different times, one at the initial stage and the other at steady state, are presented in Fig. 1. It can be seen that the isotherms are nearly coaxial within the first stage when only pure heat conduction takes place with very weak convective flow around the cylinder, Fig. 1(*a*). At a certain time, however, the isotherms in the upper part of the fluid begin to swell, followed by variations of thermal boundary layer with time. While the thermal boundary layer above the wire becomes thicker, that below the wire becomes thinner. Eventually, steady-state isotherms and streamlines are established as shown in Fig. 1(*b*). The flow field around the cylindrical heat source is also illustrated in this figure. The flow is essentially upward, convecting heat from the cylinder into a well-defined plume (Schorr, 1970).

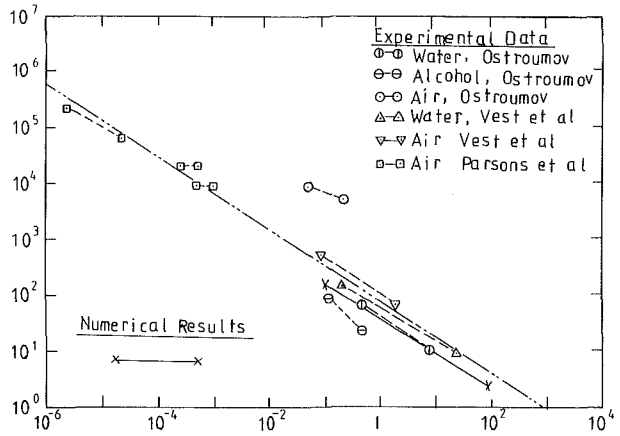

Fig. 3 Correlation of the transition time with Rayleigh number

The variations of the dimensionless temperature of the wire, θ_w, with the dimensionless time, for several Rayleigh numbers, are shown in Fig. 2. The curve for $Ra^* = 0$ is obtained from pure heat conduction theory, which takes the heat capacity of the wire into account. It can be seen again that during the initial stage, the temperature of the wire is the same as that obtained from pure heat conduction theory for all Rayleigh numbers considered. However, after a certain moment, denoted by τ_c in Fig. 2, the temperature deviates from that obtained from pure heat conduction theory, indicating the onset of significant convection. We refer to τ_c as the transition time.

It is evident from Fig. 2 that the transition time depends on the Rayleigh number. The larger the Rayleigh number, the shorter the transition time. The variation of dimensionless transition time with Rayleigh number is shown in Fig. 3. The solid line in this figure denotes the results of the present numerical analysis. For comparison, experimental results obtained by other investigators are also indicated by regression lines. There is excellent agreement between the numerical results and the experimental data, especially for liquids.

In the second stage the effect of natural convection becomes more important. If only pure heat conduction occurred, the temperature of the wire would increase monotonically. However, more heat will be transferred into surrounding fluid by natural convection occurring in this stage, which decreases the temperature of the wire. An equilibrium of the two effects leads to the occurrence of a maximum temperature of the wire at a certain time during this stage, as shown in Fig. 2. After this condition the temperature of the wire begins to decrease and finally a steady state is reached when another equilibrium, the equilibrium between the heat generated and that transferred by the combination of conduction and convection, is established.

Acknowledgments

The author wishes to thank Prof. Dr. E. Hahne for his guidance and the Alexander von Humboldt Foundation for financial support.

References

Kuehn, T. H., and Goldstein, R. J., 1980, "Numerical Solution to the Navier-Stokes Equations for Laminar Natural Convection Around a Horizontal Isothermal Circular Cylinder," *International Journal of Heat and Mass Transfer*, Vol. 23, pp. 971-979.

Mitsuo, S., and Tokuo, C., 1982, "Numerical Solution of Transient Natural Convective Heat Transfer From a Horizontal Cylinder," *Heat Transfer—Japanese Research*, Vol. 11(4), pp. 27-44.

Ostroumov, G. A., 1956, "Unsteady Heat Convection Near a Horizontal Cylinder," *Soviet Technical Physics*, Vol. 1, pp. 2627-2641.

Parsons, J. R., and Mulligan, J. C., 1978, "Transient Free Convection From a Suddenly Heated Horizontal Wire," ASME JOURNAL OF HEAT TRANSFER, Vol. 100, pp. 423-428.

Patankar, S. V., 1980, *Numerical Heat Transfer and Fluid Flow*, Hemisphere Publishing Corp., pp. 79-100.

Schorr, A. W., and Gebhart, B., 1970, "An Experimental Investigation of Natural Convection Wakes Above a Line Heat Source," *International Journal of Heat and Mass Transfer*, Vol. 13, pp. 557-571.

Vest, C. M., and Lawson, M. L., 1972, "Onset of Convection Near a Suddenly Heated Horizontal Wire," *International Journal of Heat and Mass Transfer*, Vol. 15, pp. 1281-1283.

Use of Heatlines for Unsteady Buoyancy-Driven Flow in a Cylindrical Enclosure

S. K. Aggarwal[1] and A. Manhapra[1]

Introduction

A novel approach to visualizing convective heat transfer is based on the concept of "heatline" as proposed by Kimura and Bejan (1983). As aptly discussed in the cited paper, this approach is the energy analog of the use of "streamlines" for fluid flow visualization. For a predominantly convective heat transfer situation, it provides a conceptually better visualization technique as compared to the traditional "isotherm" approach. Another useful feature of the "heatlines" patterns is that the value of Nusselt number is directly provided by the heatlines. In spite of its usefulness, the "heatline" flow visualization technique has not been accepted widely by the numerical heat transfer community. Kimura and Bejan (1983) and Bejan (1984), who first proposed it, illustrated its use for the classical problem of natural convection in a square enclosure heated from the side. Littlefield and Desai (1986) used the heatlines for visualizing the heat flow in a cylindrical annulus. The mass transfer analog of the same idea, through the use of "masslines," has also been employed by Trevisan and Bejan (1987). In this paper, we demonstrate the use of the "heatline" method for an unsteady buoyancy-driven flow in a cylindrical enclosure that is nonuniformly heated at the hot wall.

Physical Problem

An unsteady buoyancy-driven flow in a cylindrical enclosure is considered. As indicated in Fig. 1, the enclosure is nonuniformly heated at the top wall. The primitive forms of the time-dependent Navier-Stokes equations, along with the energy equations, are employed. The Boussinesq approxima-

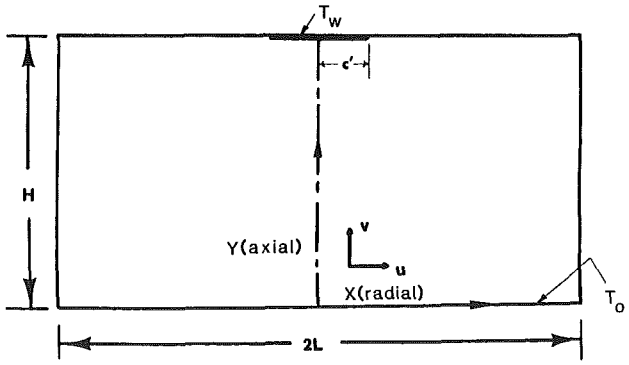

Fig. 1 Schematic of the physical model and the coordinate system

[1]Department of Mechanical Engineering, The University of Illinois, Chicago, IL, 60680.

Contributed by the Heat Transfer Division for publication in the JOURNAL OF HEAT TRANSFER. Manuscript received by the Heat Transfer Division March 16, 1988. Keywords: Natural Convection, Numerical Methods, Transient and Unsteady Heat Transfer.

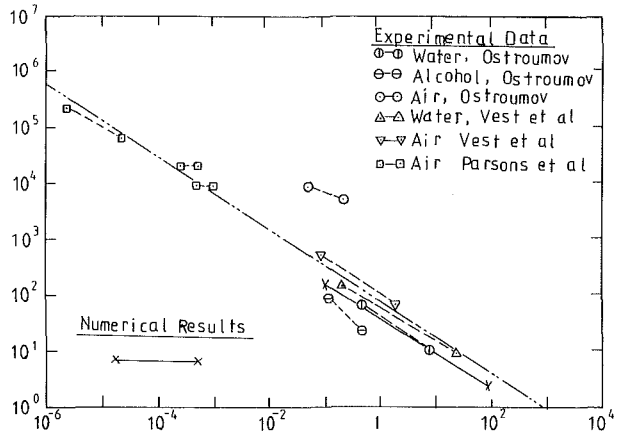

Fig. 3 Correlation of the transition time with Rayleigh number

The variations of the dimensionless temperature of the wire, θ_w, with the dimensionless time, for several Rayleigh numbers, are shown in Fig. 2. The curve for $Ra^* = 0$ is obtained from pure heat conduction theory, which takes the heat capacity of the wire into account. It can be seen again that during the initial stage, the temperature of the wire is the same as that obtained from pure heat conduction theory for all Rayleigh numbers considered. However, after a certain moment, denoted by τ_c in Fig. 2, the temperature deviates from that obtained from pure heat conduction theory, indicating the onset of significant convection. We refer to τ_c as the transition time.

It is evident from Fig. 2 that the transition time depends on the Rayleigh number. The larger the Rayleigh number, the shorter the transition time. The variation of dimensionless transition time with Rayleigh number is shown in Fig. 3. The solid line in this figure denotes the results of the present numerical analysis. For comparison, experimental results obtained by other investigators are also indicated by regression lines. There is excellent agreement between the numerical results and the experimental data, especially for liquids.

In the second stage the effect of natural convection becomes more important. If only pure heat conduction occurred, the temperature of the wire would increase monotonically. However, more heat will be transferred into surrounding fluid by natural convection occurring in this stage, which decreases the temperature of the wire. An equilibrium of the two effects leads to the occurrence of a maximum temperature of the wire at a certain time during this stage, as shown in Fig. 2. After this condition the temperature of the wire begins to decrease and finally a steady state is reached when another equilibrium, the equilibrium between the heat generated and that transferred by the combination of conduction and convection, is established.

Acknowledgments

The author wishes to thank Prof. Dr. E. Hahne for his guidance and the Alexander von Humboldt Foundation for financial support.

References

Kuehn, T. H., and Goldstein, R. J., 1980, "Numerical Solution to the Navier-Stokes Equations for Laminar Natural Convection Around a Horizontal Isothermal Circular Cylinder," *International Journal of Heat and Mass Transfer*, Vol. 23, pp. 971-979.

Mitsuo, S., and Tokuo, C., 1982, "Numerical Solution of Transient Natural Convective Heat Transfer From a Horizontal Cylinder," *Heat Transfer—Japanese Research*, Vol. 11(4), pp. 27-44.

Ostroumov, G. A., 1956, "Unsteady Heat Convection Near a Horizontal Cylinder," *Soviet Technical Physics*, Vol. 1, pp. 2627-2641.

Parsons, J. R., and Mulligan, J. C., 1978, "Transient Free Convection From a Suddenly Heated Horizontal Wire," ASME JOURNAL OF HEAT TRANSFER, Vol. 100, pp. 423-428.

Patankar, S. V., 1980, *Numerical Heat Transfer and Fluid Flow*, Hemisphere Publishing Corp., pp. 79-100.

Schorr, A. W., and Gebhart, B., 1970, "An Experimental Investigation of Natural Convection Wakes Above a Line Heat Source," *International Journal of Heat and Mass Transfer*, Vol. 13, pp. 557-571.

Vest, C. M., and Lawson, M. L., 1972, "Onset of Convection Near a Suddenly Heated Horizontal Wire," *International Journal of Heat and Mass Transfer*, Vol. 15, pp. 1281-1283.

Use of Heatlines for Unsteady Buoyancy-Driven Flow in a Cylindrical Enclosure

S. K. Aggarwal[1] and A. Manhapra[1]

Introduction

A novel approach to visualizing convective heat transfer is based on the concept of "heatline" as proposed by Kimura and Bejan (1983). As aptly discussed in the cited paper, this approach is the energy analog of the use of "streamlines" for fluid flow visualization. For a predominantly convective heat transfer situation, it provides a conceptually better visualization technique as compared to the traditional "isotherm" approach. Another useful feature of the "heatlines" patterns is that the value of Nusselt number is directly provided by the heatlines. In spite of its usefulness, the "heatline" flow visualization technique has not been accepted widely by the numerical heat transfer community. Kimura and Bejan (1983) and Bejan (1984), who first proposed it, illustrated its use for the classical problem of natural convection in a square enclosure heated from the side. Littlefield and Desai (1986) used the heatlines for visualizing the heat flow in a cylindrical annulus. The mass transfer analog of the same idea, through the use of "masslines," has also been employed by Trevisan and Bejan (1987). In this paper, we demonstrate the use of the "heatline" method for an unsteady buoyancy-driven flow in a cylindrical enclosure that is nonuniformly heated at the hot wall.

Physical Problem

An unsteady buoyancy-driven flow in a cylindrical enclosure is considered. As indicated in Fig. 1, the enclosure is nonuniformly heated at the top wall. The primitive forms of the time-dependent Navier-Stokes equations, along with the energy equations, are employed. The Boussinesq approxima-

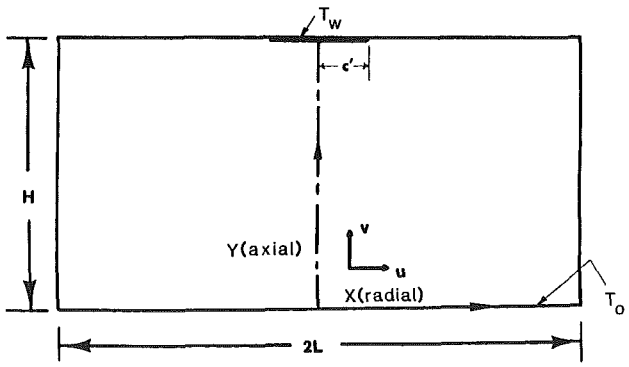

Fig. 1 Schematic of the physical model and the coordinate system

[1]Department of Mechanical Engineering, The University of Illinois, Chicago, IL, 60680.

Contributed by the Heat Transfer Division for publication in the JOURNAL OF HEAT TRANSFER. Manuscript received by the Heat Transfer Division March 16, 1988. Keywords: Natural Convection, Numerical Methods, Transient and Unsteady Heat Transfer.

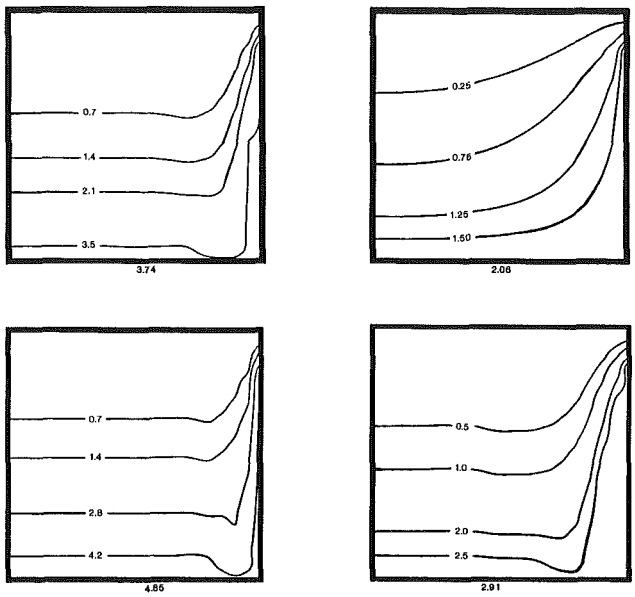

Fig. 2 Heatline: plots at steady state: (a) Ra = 70, (b) 7×10^5, (c) 7×10^6, (d) 7×10^7; Pr = 0.7; c′/L = 0.2

tion is employed to represent the buoyancy effect in the momentum equations. The governing equations in nondimensional form are as follows:

$$\frac{\partial v}{\partial y}+\frac{1}{x}\frac{\partial}{\partial x}(xu)=0 \tag{1}$$

$$\frac{\partial v}{\partial t}+\frac{\partial v^2}{\partial y}+\frac{1}{x}\frac{\partial}{\partial x}(x\,u\,v)=-\frac{\partial p}{\partial y}+T+\frac{1}{\mathrm{Gr}^{1/2}}\frac{\partial^2 v}{\partial y^2}+\frac{1}{A^2}\frac{1}{x}\frac{\partial}{\partial x}\left(x\frac{\partial v}{\partial x}\right) \tag{2}$$

$$\frac{\partial u}{\partial t}+\frac{\partial}{\partial y}(vu)+\frac{1}{x}\frac{\partial}{\partial x}(x\,u^2)=-\frac{1}{A}\frac{\partial p}{\partial x}+\frac{1}{\mathrm{Gr}^{1/2}}\frac{\partial^2 u}{\partial y^2}+\frac{1}{A^2}\frac{1}{x}\frac{\partial}{\partial x}\left(x\frac{\partial u}{\partial x}\right)-\frac{1}{A^2}\frac{u}{x^2} \tag{3}$$

$$\frac{\partial T}{\partial t}+\frac{\partial}{\partial y}(vT)+\frac{1}{x}\frac{\partial}{\partial x}(x\,u\,T)=\frac{1}{\mathrm{Gr}^{1/2}\mathrm{Pr}}\frac{\partial^2 T}{\partial y^2}+\frac{1}{A^2}\frac{1}{x}\frac{\partial}{\partial x}\left(x\frac{\partial T}{\partial x}\right) \tag{4}$$

where v and u are the axial and radial components of velocity, T the temperature, and p the pressure excluding the hydrostatic pressure. The normalization procedure is quite standard. The axial and radial distances are nondimensionalized by H and L, respectively (see Fig. 1). The characteristic velocities used for normalizing the axial and radial velocity components are $\mathrm{Gr}^{1/2}\,\nu/H$ and $\mathrm{Gr}^{1/2}\nu\,A/H$, where A is the aspect ratio. Then the characteristic time is given by $H^2/\nu\,\mathrm{Gr}^{1/2}$, where ν is the kinematic viscosity. The pressure is nondimensionalized by $\rho\,\nu^2\,\mathrm{Gr}/H^2$. The temperature is normalized as

$$T=\frac{T'-T'_o}{T'_w-T'_o}$$

where T'_w is the maximum temperature of the heated portion of top wall, and T'_o is the initial fluid temperature as well as the temperature of the bottom isothermal (cold) wall. The normalization gives rise to three dimensionless parameters, A, Pr, and Gr, which are, respectively, the aspect ratio, the Prandtl number, and the Grashof number based on the height.

A semi-implicit finite-difference technique is employed for solving equations (1)–(4). A staggered nonuniform grid is used in the computations. Further details are provided by Aggarwal and Manhapra (1988) and Manhapra (1987).

Definition of Heatline

The heatline is derived from a heat function that identically satisfies the steady-state energy equation, so that the net flow of energy across the heatline is zero. The heat function H' in a cylindrical coordinate system is defined as

$$-\frac{\partial H'}{\partial x'}=\rho\,c_p\,v'\,x'\,T'-k\,x'\frac{\partial T'}{\partial y'} \tag{5}$$

$$\frac{\partial H'}{\partial y'}=\rho\,c_p\,u'\,x'\,T'-k\,x'\frac{\partial T'}{\partial x'} \tag{6}$$

where ρ, c_p, and k are the fluid density, specific heat, and thermal conductivity. The nondimensional form of the above equations is

$$\frac{\partial H^*}{\partial x}=c_1\left[\mathrm{Gr}^{1/2}\mathrm{Pr}\,v\,x\,T-x\frac{\partial T}{\partial y}\right] \tag{7}$$

$$\frac{\partial H^*}{\partial y}=c_1\left[\mathrm{Gr}^{1/2}\mathrm{Pr}\,u\,x\,T-\frac{x}{A^2}\frac{\partial T}{\partial x}\right] \tag{8}$$

where

$$H^*=\frac{c_1 H' H}{L^2 K(T'_w-T'_o)} \tag{9}$$

and

$$c_1=\frac{4LA}{c'} \tag{10}$$

The constant c_1 is used in nondimensionalizing H' so that the maximum H^* directly provides the value of the Nusselt number of the top wall, which is defined as

$$\mathrm{Nu}=c_1\int_o^c\frac{\partial T}{\partial y}\,x\,dx \tag{11}$$

Note that the nondimensional heat function H^*, defined by equation (7) and (8) identically satisfies the steady-state form of the nondimensional energy equation (4). Thus, it is an analog of the stream function that identically satisfies the steady-state continuity equation. In addition, similar to the streamlines, which are lines of constant streamfunction, the heatlines are lines of constant H^*. In an unsteady flow, the streamlines provide an instantaneous flow visualization. Similarly, in an unsteady convection problem, the heatlines represent an instantaneous heat flow visualization.

Representative Results

Some representative results are now presented to illustrate the use of heatlines. The initial conditions for the case considered correspond to the fluid being at rest and at room temperature = 298 K at time $t=0$. No-slip velocity conditions are applied at the top wall ($y=1$), side wall ($x=1$), and bottom wall ($y=0$). Symmetry conditions are applied along $x=0$. In the heated part of top wall ($x<c$), the isothermal condition is used, whereas the adiabatic condition is used for the rest of top wall and the side wall. The bottom wall is considered as isothermal. The boundary conditions for the heat function H^* are that $H^*=0$ along the axis of symmetry, and $H^*=H_{\max}$ along the side wall. Along the top and bottom wall, H^* is computed by integrating equation (7) with $v=0$.

The heat function H^* (x, y, t) at any time t is computed by

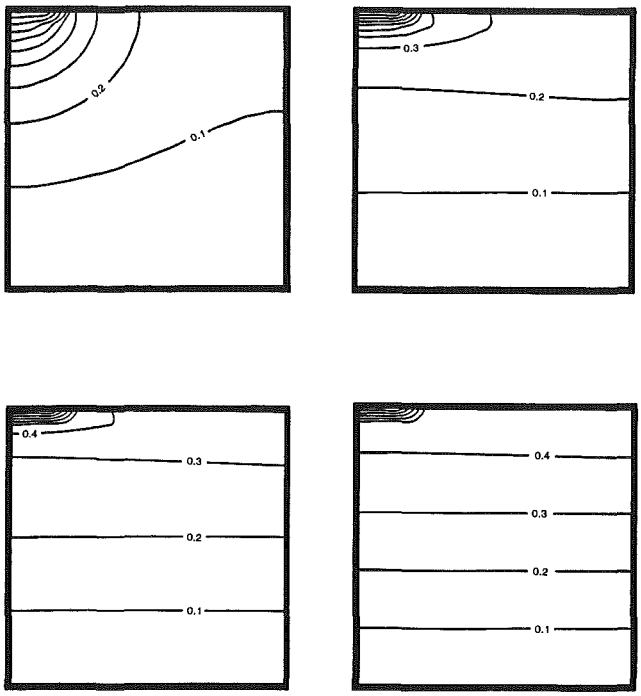

Fig. 3 Isotherms at steady state for the conditions of Fig. 2

using equations (7) and (8). The numerical solution of equations (1)–(4) is directly employed in the solution of equations (7) and (8). This procedure is different from that used by Kimura and Bejan (1983), who employed a Poisson-type equation for calculating H^*.

The results of heat flow visualization are illustrated in Fig. 2, where the H^* = constant lines or "heatlines" are plotted for the Rayleigh number (Ra) in the range of 70 to 7×10^7, which includes both conduction-dominated and convection-dominated regimes. The corresponding isotherm plots are shown in Fig. 3. There are several interesting observations:

1 For all the cases considered, the heatlines originate at the heated part of top wall, which extends radially outward from $x=0$ to $x=0.2$ or one fifth of the top wall, and terminate at the bottom wall, which is isothermal (cold). Thus, the heatlines indicate that the heat enters the enclosure at part of the top wall and leaves the enclosure from the bottom wall. Clearly, this provides a better visualization of heat transfer as compared to the isotherms.

2 As expected, the heatlines are parallel to the unheated portion of the top wall and the side wall since both these surfaces are assumed to be adiabatic. In fact, the unheated part of top wall and the side wall together form a heatline. For example, $H^* = 2.06$ for this line in Fig. 2(*a*).

3 For each case shown in Fig. 2, the maximum H^* directly provides the value of the Nusselt number (Nu) of the top wall. For example, for Ra = 70, the Nusselt number is 2.06, which indicates the dominance of conduction heat transfer (note that for the case of pure conduction, Nu = 2.0). The transition from a conduction-dominated to a convection-dominated regime occurs at a Rayleigh number of about 5×10^4. Thus the result in Fig. 2(*b*) represents a convection-dominated flow regime, where $\text{Ra} = 7 \times 10^5$. As indicated, the Nusselt number is 2.91 for this case. Also, the increase of Nu with Ra is vividly illustrated by the heatline plots.

4 With the aid of heatlines, we are also able to show how the rate of heat transfer in the enclosure is enhanced at higher Rayleigh number. Note, for example, the value of H^* for the first heatline, closest to the axis of symmetry. In addition, the heatlines indicate that the effect of convection is essentially confined to the upper part of the enclosure. In the lower part, which occupies more than two thirds of the enclosure, the heat transfer is mainly due to conduction. Thus, the upper boundary layer region at higher Rayleigh number and the pure conduction regime that persists in the core are very well identified by the heatlines.

To summarize, the usefulness of "heatline" plots in an unsteady heat transfer problem is clearly illustrated by the above example. Not only is a convenient instantaneous visualization of the heat flow provided, the value of the Nusselt number both as a function of time and of the Reynolds number is given by the heatlines. Also, the convection-dominated and conduction-dominated regimes can be identified. The use of "heatline" plots is strongly recommended for steady-state as well as transient convective situations.

Acknowledgments

The research was partially supported by a grant from the Office of Sponsored Research of the University of Illinois at Chicago.

References

Aggarwal, S. K., and Manhapra, A., 1988, "Transient Natural Convection in a Cylindrical Enclosure Non-uniformly Heated at the Top Wall," *Numerical Heat Transfer*, submitted.

Bejan, A., 1984, *Convection Heat Transfer*, Wiley, New York, pp. 21–23.

Kimura, S., and Bejan, A., 1983, "The 'Heatline' Visualization of Convective Heat Transfer," ASME JOURNAL OF HEAT TRANSFER, Vol. 105, pp. 916–919.

Littlefield, D., and Desai, P., 1986, "Buoyant Laminar Convection in a Vertical Cylindrical Annulus," ASME JOURNAL OF HEAT TRANSFER, Vol. 108, pp. 841–821.

Manhapra, A., 1987, "Transient Natural Convection in a Cylindrical Enclosure," M. S. Thesis, Department of Mechanical Engineering, The University of Illinois at Chicago.

Trevisan, O. V., and Bejan, A., 1987, "Combined Heat and Mass Transfer by Natural Convection in a Vertical Enclosure," ASME JOURNAL OF HEAT TRANSFER, Vol. 109, pp. 104–112.

High Rayleigh Number Experiments in a Horizontal Layer of Water Around Its Density Maximum

T. L. Spatz,[1] D. Poulikakos,[1] and M. J. Kazmierczak[1]

Nomenclature

A = area of heated surface, m^2
g = gravitational acceleration, m/s^2
H = enclosure height, m
k = thermal conductivity, W/mK
Nu = Nusselt number $= Q/(kA\ \Delta T/H)$
Pr = Prandtl number
q = exponent of density–temperature relationship
R = dimensionless parameter
Ra = Rayleigh number for natural convection of cold water, equation (5)
Ra_* = classical Rayleigh number, equation (4)
T = temperature, °C
T_B = bottom wall temperature, °C
T_M = density extremum temperature, °C

[1]Department of Mechanical Engineering, University of Illinois at Chicago, Chicago, IL 60680.

Contributed by the Heat Transfer Division for publication in the JOURNAL OF HEAT TRANSFER. Manuscript received by the Heat Transfer Division October 5, 1987. Keywords: Flow Instability, Natural Convection.

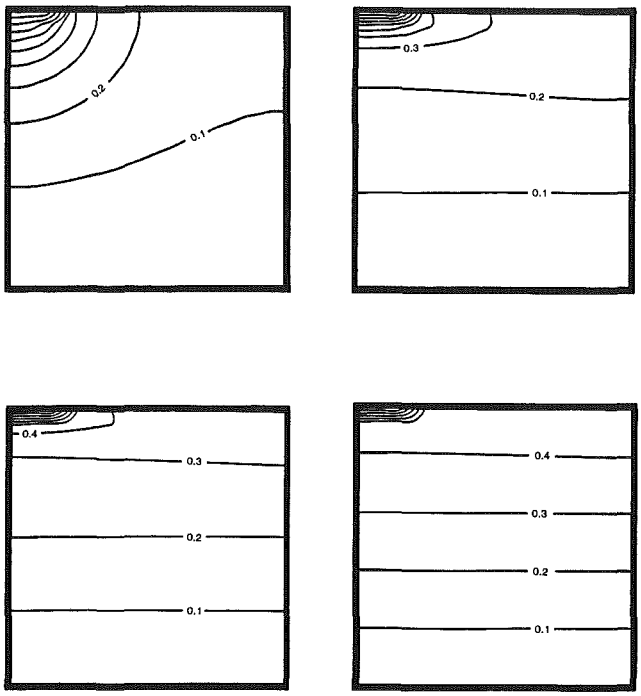

Fig. 3 Isotherms at steady state for the conditions of Fig. 2

using equations (7) and (8). The numerical solution of equations (1)–(4) is directly employed in the solution of equations (7) and (8). This procedure is different from that used by Kimura and Bejan (1983), who employed a Poisson-type equation for calculating H^*.

The results of heat flow visualization are illustrated in Fig. 2, where the H^* = constant lines or "heatlines" are plotted for the Rayleigh number (Ra) in the range of 70 to 7×10^7, which includes both conduction-dominated and convection-dominated regimes. The corresponding isotherm plots are shown in Fig. 3. There are several interesting observations:

1 For all the cases considered, the heatlines originate at the heated part of top wall, which extends radially outward from $x = 0$ to $x = 0.2$ or one fifth of the top wall, and terminate at the bottom wall, which is isothermal (cold). Thus, the heatlines indicate that the heat enters the enclosure at part of the top wall and leaves the enclosure from the bottom wall. Clearly, this provides a better visualization of heat transfer as compared to the isotherms.

2 As expected, the heatlines are parallel to the unheated portion of the top wall and the side wall since both these surfaces are assumed to be adiabatic. In fact, the unheated part of top wall and the side wall together form a heatline. For example, $H^* = 2.06$ for this line in Fig. 2(*a*).

3 For each case shown in Fig. 2, the maximum H^* directly provides the value of the Nusselt number (Nu) of the top wall. For example, for Ra = 70, the Nusselt number is 2.06, which indicates the dominance of conduction heat transfer (note that for the case of pure conduction, Nu = 2.0). The transition from a conduction-dominated to a convection-dominated regime occurs at a Rayleigh number of about 5×10^4. Thus the result in Fig. 2(*b*) represents a convection-dominated flow regime, where $\mathrm{Ra} = 7 \times 10^5$. As indicated, the Nusselt number is 2.91 for this case. Also, the increase of Nu with Ra is vividly illustrated by the heatline plots.

4 With the aid of heatlines, we are also able to show how the rate of heat transfer in the enclosure is enhanced at higher Rayleigh number. Note, for example, the value of H^* for the first heatline, closest to the axis of symmetry. In addition, the heatlines indicate that the effect of convection is essentially confined to the upper part of the enclosure. In the lower part, which occupies more than two thirds of the enclosure, the heat transfer is mainly due to conduction. Thus, the upper boundary layer region at higher Rayleigh number and the pure conduction regime that persists in the core are very well identified by the heatlines.

To summarize, the usefulness of "heatline" plots in an unsteady heat transfer problem is clearly illustrated by the above example. Not only is a convenient instantaneous visualization of the heat flow provided, the value of the Nusselt number both as a function of time and of the Reynolds number is given by the heatlines. Also, the convection-dominated and conduction-dominated regimes can be identified. The use of "heatline" plots is strongly recommended for steady-state as well as transient convective situations.

Acknowledgments

The research was partially supported by a grant from the Office of Sponsored Research of the University of Illinois at Chicago.

References

Aggarwal, S. K., and Manhapra, A., 1988, "Transient Natural Convection in a Cylindrical Enclosure Non-uniformly Heated at the Top Wall," *Numerical Heat Transfer*, submitted.

Bejan, A., 1984, *Convection Heat Transfer*, Wiley, New York, pp. 21–23.

Kimura, S., and Bejan, A., 1983, "The 'Heatline' Visualization of Convective Heat Transfer," ASME JOURNAL OF HEAT TRANSFER, Vol. 105, pp. 916–919.

Littlefield, D., and Desai, P., 1986, "Buoyant Laminar Convection in a Vertical Cylindrical Annulus," ASME JOURNAL OF HEAT TRANSFER, Vol. 108, pp. 841–821.

Manhapra, A., 1987, "Transient Natural Convection in a Cylindrical Enclosure," M. S. Thesis, Department of Mechanical Engineering, The University of Illinois at Chicago.

Trevisan, O. V., and Bejan, A., 1987, "Combined Heat and Mass Transfer by Natural Convection in a Vertical Enclosure," ASME JOURNAL OF HEAT TRANSFER, Vol. 109, pp. 104–112.

High Rayleigh Number Experiments in a Horizontal Layer of Water Around Its Density Maximum

T. L. Spatz,[1] D. Poulikakos,[1] and M. J. Kazmierczak[1]

Nomenclature

A = area of heated surface, m^2
g = gravitational acceleration, m/s^2
H = enclosure height, m
k = thermal conductivity, W/mK
Nu = Nusselt number = $Q/(kA\ \Delta T/H)$
Pr = Prandtl number
q = exponent of density–temperature relationship
R = dimensionless parameter
Ra = Rayleigh number for natural convection of cold water, equation (5)
Ra_* = classical Rayleigh number, equation (4)
T = temperature, °C
T_B = bottom wall temperature, °C
T_M = density extremum temperature, °C

[1]Department of Mechanical Engineering, University of Illinois at Chicago, Chicago, IL 60680.

Contributed by the Heat Transfer Division for publication in the JOURNAL OF HEAT TRANSFER. Manuscript received by the Heat Transfer Division October 5, 1987. Keywords: Flow Instability, Natural Convection.

T_T = top wall temperature, °C
α = thermal diffusivity, m^2/s
α_1 = coefficient of volumetric thermal expansion near the density, extremum temperature
β = coefficient of volumetric thermal expansion, K^{-1}
ΔT = temperature difference $= T_B - T_T$
ν = kinematic viscosity, m^2/s
ρ = density, kg/m^2
ρ_M = extremum density, kg/m^3

Subscripts

B = bottom (hot) wall
M = value corresponding to density extremum
T = top (cold) wall

1 Introduction

Natural convection of water has numerous thermal engineering applications ranging from heat exchangers and solidification or melting processes to water circulation in the sea, lakes, and estuaries. Unlike most of the fluids commonly used in engineering applications that possess monotonic, almost linear for small temperature ranges, density–temperature relationships, water possesses a density maximum at 4°C at atmospheric pressure. The presence of this density maximum greatly affects water natural convection and yields flows markedly different from those of other fluids, or even water for temperature ranges away from its density maximum.

Several relationships have been proposed and used by various investigators (Goren, 1966; Yen, 1974; Sun et al., 1969; Gebhart and Mollendorf, 1977) to describe the dependence of water density of temperature in the vicinity of the density maximum. For the present study we chose to adopt the most recent one proposed by Gebhart and Mollendorf (1977). The reason for this choice is that the abovementioned relationship holds for a rather large temperature range (between 0°C and 20°C), it is simple, and it appears to be at least as accurate as any other density–temperature relationship for the region of the density maximum of water. This relationship reads

$$\rho = \rho_M[1 - \alpha_1 |T - T_M|^q] \tag{1}$$

where the subscript M denotes the density maximum, $T_M = 4.02932$°C, $\rho_M = 999.972$ kg/m^3, $\alpha_1 = 9.297173\ 10^{-6}$ (°C)$^{-q}$, and $q = 1.894816$.

Several investigators have studied various aspects of the phenomenon of natural convection of cold water over the past few decades. For example, Robillard and Vasseur (1982) investigated numerically the transient cooling (through its side walls) of a rectangular container filled with cold water. Gebhart and Mollendorf (1978) reported interesting results of natural convection of cold water near a vertical flat plate. Flow reversals were observed, caused by the presence of the density extremum.

More relevant to the present study are investigations on natural convection in a horizontal layer of cold water heated from below. To this end, Sun et al. (1969) carried out linear stability analysis as well as experimental measurements to determine the critical Rayleigh number (at which convection first sets in the system) in a water layer heated from below and cooled from above. The presence of the density maximum yielded values for the critical Rayleigh number markedly different from those of the classical Benard problem. Recently, Blake et al. (1984) performed numerical simulations to determine the temperature and flow field in a layer of cold water for low and moderate Rayleigh numbers ($Ra < 2 \times 10^5$). They found a multicellular flow structure that changed depending on the value of the aspect ratio of the layer and the Rayleigh number. They also calculated numerically representative values of the critical Rayleigh number. These values agreed well with the findings of Sun et al. (1969).

Tien et al. (1972) performed a combined theoretical and experimental study that has some similarities as well as significant differences with the present work. More specifically, these authors investigated theoretically and experimentally natural convection of cold water in a thin horizontal water layer near its density extremum. Their theoretical analysis and part of the experimental findings focused on the "near onset" regime where convectioin first sets in the system. Experimental results were also obtained for higher Rayleigh numbers. The experimental model used in the work of Tien et al. (1972) was a *cylindrical shallow* water layer, which aimed to simulate convection in an infinitely long horizontal water layer. The physical height of this layer was of the order of 1 cm. The data obtained were correlated by using a cubic density–temperature relationship in place of the simpler equation (1) of the present study. As a result, the dimensionless parameters and relationships in Tien et al. (1972) are rather complicated. On the other hand, several important discoveries and observations were made showing that the effect of the density extremum is to suppress the onset of convection in the layer and to reduce the overall heat transfer across the layer. Comparisons between the present study and the work of Tien et al. (1972) are made whenever appropriate later in this paper.

The present experimental investigation focuses on the *high* Rayleigh number regime ($Ra > 10^9$). Unlike in previous investigations the flow in the system is *turbulent*. The experimental apparatus is a *rectangular enclosure* of height to length aspect ratio $\approx 1/2$ and height ≈ 25 cm. This arrangement is significantly different from the arrangement of Tien et al. (1972). The chief contribution of the present study, in addition to determining the temperature and flow fields in the enclosure, is that a general, easy to use correlation is proposed for the Nusselt number (representing the overall heat transfer through the layer). This correlation is accurate (when the density extremum exists in the system) regardless of the relative magnitude of the top wall temperature and the density extremum temperature.

2 Apparatus and Procedure

The setup for the experiment consisted of the test apparatus and three supporting devices: a data acquisition system, a power supply, and a bath refrigerator circulator. The internal dimension of the test apparatus measured $L = 48.3$ cm long by $H = 25.4$ cm tall by 12.7 cm deep. Plexiglas 1.27 cm thick was used to construct the side walls of the apparatus. The top and the bottom walls were constructed out of aluminum of thickness 2.54 cm and 1.27 cm, respectively. The bottom plate had 10 (T-type) thermocouples embedded 1.6 mm from the inside surface. Machined into the bottom plate was a cavity for a 3.2 mm thick high-density (10 W per sq. in.) flexible rubber electric heater. Highly conductive silicon paste was used to insure good conductivity between the heater and the aluminum plate. The heater was insulated from below with two layers of 8-mm-thick asbestos gasket material and a layer of 16-mm-thick rubber insulation. The top plate was machined to allow for 8 thermocouples, 21 access ports, and a counterflow heat exchanger. The access ports were designed so that a thermocouple probe could be inserted to any depth for temperature profile measurements. The counterflow heat exchanger was constructed by milling four channels into the top plate lengthwise. A 50 percent ethylene glycol/water solution precooled by the bath refrigerator was circulated through the heat exchanger. The direction of flow of the coolant was alternated in adjacent channels to establish isothermality (within ±0.5°C) along the top plate. The channels were sealed with a

1.27-cm-thick sheet of Plexiglas, which covered the entire top plate.

The apparatus was mounted on a 10 cm thick hardwood table and was insulated on the top and all sides by a 2.54-cm-thick layer of K-fac#19 insulating board. Finally, the apparatus was filled with distilled water.

Approximately nine steady-state experiments were run for each of three different top plate temperatures: 0, 4, and 8°C. For each top plate temperature, the power input to the heater was varied between 25 and 200 W in steps of 25 or 50 W so that the bottom wall temperature ranged from about 4 to 30°C. Between each setting steady state was re-established and top and bottom plate temperatures were recorded. For representative steady states complete temperature profiles were obtained by lowering thermocouple probes through the access ports of the top wall. These profiles allowed for the determination of the temperature field in the cavity.

Visualization of the flow field was accomplished by adding a rheoscopic suspension of microscopic crystalline disks to the fluid and passing a sheet of laser light through it. The disks are almost neutrally buoyant and thus have a very long settling time. The concentration of rheoscopic suspension was 0.1 percent. The laser sheet was created by passing the beam of a 5 mW helium–neon laser through a cylindrical lens. Light reflected off the crystalline disk enabled clear observation of the general flow pattern within the cavity.

3 Results and Discussion

Temperature measurements were taken during representative steady states, to improve understanding of the temperature field in the cavity. These measurements are not reported here for brevity. It was found that the temperature field in the system consisted of a practically isothermal core and two sharp thermal boundary layers along the top and bottom walls. Flow visualization helped explain these findings. For all steady states, a single turbulent cell was observed that filled the entire cavity. Flow traveled primarily horizontally along the bottom wall, rose on one vertical wall, traveled in the opposite horizontal direction along the top wall, and fell down the other vertical wall. Flow in the center (core region) was best characterized as turbulent shedding vortices that mixed the core region well and resulted in uniform temperature. Figure 1 (*a*) shows a comparison of our data for the case of $T_T = 8°C$ (when the density extremum effect is weakest) to two well-known correlations, one by Globe and Dropkin (1959) and the other by O'Toole and Silverston (1961). These correlations are valid in the absence of a density extremum and they read, respectively

$$\mathrm{Nu} = 0.069(\mathrm{Ra}_*)^{1/3}(\mathrm{Pr})^{0.074} \qquad 1.5\times 10^5 < \mathrm{Ra}_* < 6.8\times 10^8 \quad (2)$$

$$\mathrm{Nu} = 0.0104(\mathrm{Ra}_*)^{0.305}(\mathrm{Pr})^{0.084} \qquad 10^5 < \mathrm{Ra}_* < 10^9 \quad (3)$$

where

$$\mathrm{Ra}_* = \frac{g\beta(\Delta T)H^3}{\nu\alpha} \quad (4)$$

All quantities in the above equations are defined in the nomenclature and all properties are evaluated at the mean temperature between the top and bottom walls. The dependence of Nu on Ra_* is found to be similar in our data and in equations (2) and (3). Equation (3) agrees better with the present experimental data. The values of Nusselt number predicted by equations (2) and (3) are higher than the values of Nusselt number obtained in this study. There are several reasons for this fact. First, even though not dominant in our data for $T_T = 8°C$, the density extremum effect is present and tends to suppress the heat transfer relative to equations (2) and (3). Second, the ranges of validity of equations (2) and (3) are different (lower) than the range of Ra_* in the present work ($8.4\times 10^8 < \mathrm{Ra}_* < 7.3\times 10^9$). Third, equations (2) and (3) were obtained using other fluids in addition to water such as silicon oil and mercury. As shown by Globe and Dropkin (1959) and by O'Toole and Silverston (1961), respectively, equations (2) and (3) overestimate even their data for water.

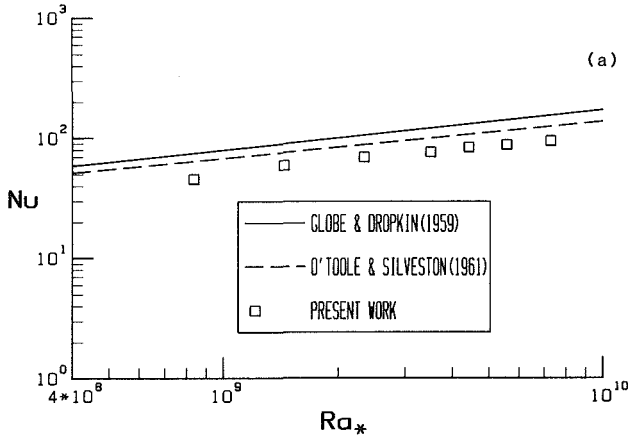

Fig. 1(*a*) Nu versus Ra_*: comparison of experimental data for $T_T = 8°C$ with equations (2) and (3) for natural convection without a density maximum

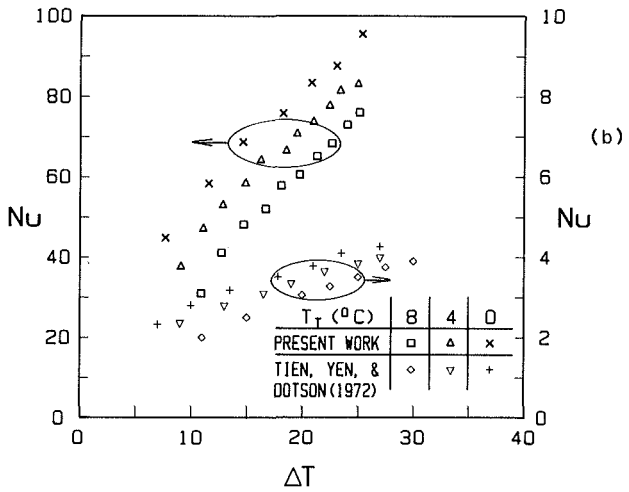

Fig. 1(*b*) Nu versus ΔT: comparison of the present data for $H = 25.4$ cm and data of Tien et al. (1972) for $H = 0.63$ cm

Comparisons between the present experiments and the results of Tien et al. (1972) are reported in Fig. 1 (*b*). The differences between the two studies outlined earlier are clearly reflected both in the actual values of Nusselt and in the dependence of Nu on Ra (the dependence of Nu or Ra in the results of Tien et al. (1972) appears to be weaker). Note that in addition to the differences between the two studies stated in the introductory section, the height of the water layer for the data presented in Fig. 1 (*b*) was 0.63 cm for the points of Tien et al. (1972) and 25.4 cm for the points of the present study.

In Fig. 2, Nusselt number versus Rayleigh number results are plotted for three representative top wall temperatures. The Rayleigh number appropriate for natural convection of cold water is based on the enclosure height and is defined as

$$\mathrm{Ra} = -\frac{g\alpha_1}{\alpha\nu}(T_B - T_T)^q H^3 \quad (5)$$

Figure 2 shows that as the top wall temperature decreases the heat transfer is reduced for a given Rayleigh number. Note also that this reduction is greater for lower Rayleigh numbers. This is clearly a result of the presence of the density maximum. The greater the portion of stably stratified fluid (because of the density extremum) present in the enclosure, the greater the reduction in heat transfer. It is worth mentioning that in the

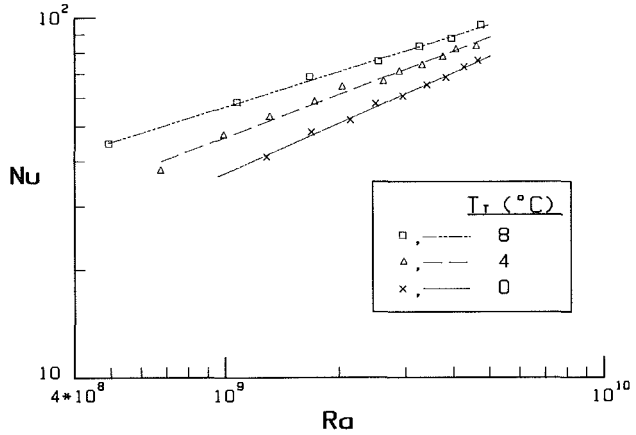

Fig. 2 Nu versus Ra for different top plate temperatures; 0, 4, and 8°C

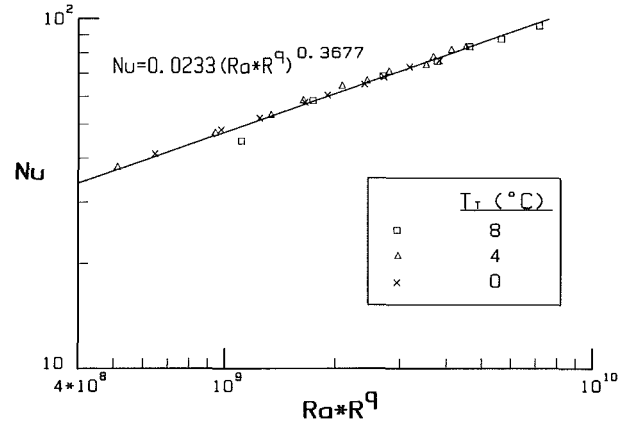

Fig. 3 Proposed general correlation for the heat transfer results

absence of the density maximum the Nu versus Ra graph is independent of the value of the top wall temperature. Finally, for a fixed value of the top wall temperature, Nu increases monotonically with Ra.

From an engineering standpoint, it is useful to produce a correlation for Nu, valid for all values of T_T in the vicinity of the density extremum temperature. This is achieved by introducing a new dimensionless parameter

$$R = (T_M - T_B)/(T_T - T_B) \tag{6}$$

For fixed values of the bottom and top wall temperatures, the parameter R gives an indication of the portion of the temperature field in the enclosure that is potentially unstable. Figure 3 shows the data of Fig. 2 but now plotted as Nu versus $\mathrm{Ra}R^q$. Clearly, all the data points fall on a single line and are correlated by

$$\mathrm{Nu} = 0.0233(\mathrm{Ra}R^q)^{0.368} \tag{7}$$

Correlation (7) is valid for all values of T_T. Note that the group $\mathrm{Ra}R^q$ represents an effective Rayleigh number that is based only on the unstable portion $(T_B - T_M)$ of the temperature difference across the enclosure $(T_B - T_T)$. It is this portion of the temperature difference that actively drives the flow and sustains the convection phenomenon. This argument is the theoretical basis for the proposed correlation (7).

4 Summary

This paper presented an experimental study of high Rayleigh number natural convection in a horizontal layer of water in the neighborhood of its density extremum. The layer was heated from below and cooled from above. The experiments focused on the high Rayleigh number regime. The flow field in the system consisted of a single turbulent cell. The temperature field featured two sharp thermal boundary layers along the two horizontal walls, bounding an isothermal core region.

The overall heat transfer through the layer was seriously depressed by the presence of the density extremum. The magnitude of this effect was controlled by the value of a dimensionless parameter (R), which placed the density extremum temperature with respect to the temperatures of the two horizontal walls. Finally, a general correlation was obtained for the Nusselt number in the presence of the density extremum in the high Rayleigh number regime.

4 Acknowledgments

We thank an anonymous reviewer who brought to our attention the related work of Tien et al. (1972). Support for this work from the National Science Foundation (Grant No. ENG-8451144) and from Amoco Co., through a graduate fellowship to T. L. Spatz, is gratefully acknowledged.

References

Blake, K. R., Poulikakos, D., and Bejan, A., 1984, "Natural Convection Near 4°C in a Horizontal Water Layer Heated From Below," *Phys. Fluids*, Vol. 27, pp. 2608-2616.

Gebhart, B., and Mollendorf, J. C., 1977, "A New Density Relation for Pure and Saline Water," *Deep Sea Res.*, Vol. 24, pp. 831-848.

Gebhart, B., and Mollendorf, J. C., 1978, "Buoyancy Induced Flows in a Liquid Under Conditions in Which Density Extrema May Arise," *J. Fluid Mech.*, Vol. 9, pp. 673-707.

Globe, S., and Dropkin, D., 1959, "Natural Convection Heat Transfer in Liquids Confined by Two Horizontal Plates and Heat From Below," ASME JOURNAL OF HEAT TRANSFER, Vol. 81, pp. 24-28.

Goren, S. L., 1966, "On Free Convection in Water at 4°C," *Chem. Eng. Sci.*, Vol. 21, pp. 515-518.

O'Toole, J. L., and Silverston, J. L., 1961, "Correlations of Convective Heat Transfer in Confined Horizontal Layers," *Chem. Eng. Progr. Symp. Ser.*, Vol. 57, pp. 81-86.

Robillard, L., and Vasseur, P., 1982, "Convective Response of a Mass of Water Near 4°C to a Constant Cooling Rate Applied on Its Boundaries," *J. Fluid Mech.*, Vol. 118, pp. 123-141.

Sun, Z. S., Tien, C., and Yen, Y.-C., 1969, "Thermal Instability of a Horizontal Layer of Liquid With Maximum Density," *AIChE J.*, Vol. 15, pp. 910-915.

Tien, C., Yen, Y.-C., and Dotson, J., 1972, "Free Convective Heat Transfer in a Horizontal Layer of Liquid—The Effect of Density Inversion," *AIChE Symposium Series*, Vol. 68, pp. 101-111.

Yen, Y.-C., 1974, "Effect of Density Inversion on Free Convective Heat Transfer in a Porous Layer Heated From Below," *Int. J. Heat Mass Transfer*, Vol. 17, pp. 1349-1356.

Effect of Wall Conduction on Combined Free and Forced Laminar Convection in Horizontal Tubes

R. S. Chen[1,2] and G. J. Hwang[1,3]

Nomenclature

A = a parameter $= \beta g \theta_c a^3/\nu^2$
a, d = tube radius and diameter
C = a dimensionless number $= -C_1 a^3/(4\nu\mu) = A^{1/2}\mathrm{Re}/8\bar{w}$
C_1, C_2 = axial pressure and temperature gradients

[1]Department of Power Mechanical Engineering, National Tsing Hua University, Hsinchu, Taiwan 30043.

[2]Instructor.

[3]Professor, Mem. ASME.

Contributed by the Heat Transfer Division for publication in the JOURNAL OF HEAT TRANSFER. Manuscript received by the Heat Transfer Division November 12, 1986. Keywords: Forced Convection, Mixed Convection, Natural Convection.

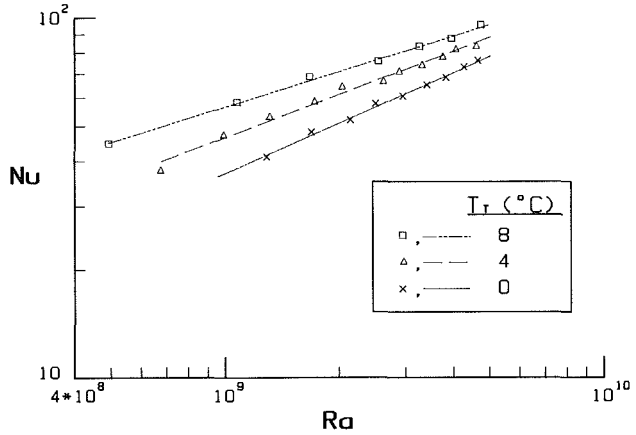

Fig. 2 Nu versus Ra for different top plate temperatures; 0, 4, and 8°C

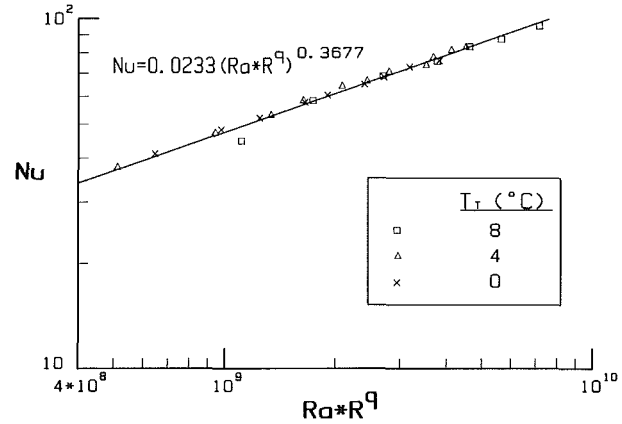

Fig. 3 Proposed general correlation for the heat transfer results

absence of the density maximum the Nu versus Ra graph is independent of the value of the top wall temperature. Finally, for a fixed value of the top wall temperature, Nu increases monotonically with Ra.

From an engineering standpoint, it is useful to produce a correlation for Nu, valid for all values of T_T in the vicinity of the density extremum temperature. This is achieved by introducing a new dimensionless parameter

$$R = (T_M - T_B)/(T_T - T_B) \tag{6}$$

For fixed values of the bottom and top wall temperatures, the parameter R gives an indication of the portion of the temperature field in the enclosure that is potentially unstable. Figure 3 shows the data of Fig. 2 but now plotted as Nu versus $\mathrm{Ra}R^q$. Clearly, all the data points fall on a single line and are correlated by

$$\mathrm{Nu} = 0.0233(\mathrm{Ra}R^q)^{0.368} \tag{7}$$

Correlation (7) is valid for all values of T_T. Note that the group $\mathrm{Ra}R^q$ represents an effective Rayleigh number that is based only on the unstable portion $(T_B - T_M)$ of the temperature difference across the enclosure $(T_B - T_T)$. It is this portion of the temperature difference that actively drives the flow and sustains the convection phenomenon. This argument is the theoretical basis for the proposed correlation (7).

4 Summary

This paper presented an experimental study of high Rayleigh number natural convection in a horizontal layer of water in the neighborhood of its density extremum. The layer was heated from below and cooled from above. The experiments focused on the high Rayleigh number regime. The flow field in the system consisted of a single turbulent cell. The temperature field featured two sharp thermal boundary layers along the two horizontal walls, bounding an isothermal core region.

The overall heat transfer through the layer was seriously depressed by the presence of the density extremum. The magnitude of this effect was controlled by the value of a dimensionless parameter (R), which placed the density extremum temperature with respect to the temperatures of the two horizontal walls. Finally, a general correlation was obtained for the Nusselt number in the presence of the density extremum in the high Rayleigh number regime.

4 Acknowledgments

We thank an anonymous reviewer who brought to our attention the related work of Tien et al. (1972). Support for this work from the National Science Foundation (Grant No. ENG-8451144) and from Amoco Co., through a graduate fellowship to T. L. Spatz, is gratefully acknowledged.

References

Blake, K. R., Poulikakos, D., and Bejan, A., 1984, "Natural Convection Near 4°C in a Horizontal Water Layer Heated From Below," *Phys. Fluids*, Vol. 27, pp. 2608-2616.

Gebhart, B., and Mollendorf, J. C., 1977, "A New Density Relation for Pure and Saline Water," *Deep Sea Res.*, Vol. 24, pp. 831-848.

Gebhart, B., and Mollendorf, J. C., 1978, "Buoyancy Induced Flows in a Liquid Under Conditions in Which Density Extrema May Arise," *J. Fluid Mech.*, Vol. 9, pp. 673-707.

Globe, S., and Dropkin, D., 1959, "Natural Convection Heat Transfer in Liquids Confined by Two Horizontal Plates and Heat From Below," ASME JOURNAL OF HEAT TRANSFER, Vol. 81, pp. 24-28.

Goren, S. L., 1966, "On Free Convection in Water at 4°C," *Chem. Eng. Sci.*, Vol. 21, pp. 515-518.

O'Toole, J. L., and Silverston, J. L., 1961, "Correlations of Convective Heat Transfer in Confined Horizontal Layers," *Chem. Eng. Progr. Symp. Ser.*, Vol. 57, pp. 81-86.

Robillard, L., and Vasseur, P., 1982, "Convective Response of a Mass of Water Near 4°C to a Constant Cooling Rate Applied on Its Boundaries," *J. Fluid Mech.*, Vol. 118, pp. 123-141.

Sun, Z. S., Tien, C., and Yen, Y.-C., 1969, "Thermal Instability of a Horizontal Layer of Liquid With Maximum Density," *AIChE J.*, Vol. 15, pp. 910-915.

Tien, C., Yen, Y.-C., and Dotson, J., 1972, "Free Convective Heat Transfer in a Horizontal Layer of Liquid—The Effect of Density Inversion," *AIChE Symposium Series*, Vol. 68, pp. 101-111.

Yen, Y.-C., 1974, "Effect of Density Inversion on Free Convective Heat Transfer in a Porous Layer Heated From Below," *Int. J. Heat Mass Transfer*, Vol. 17, pp. 1349-1356.

Effect of Wall Conduction on Combined Free and Forced Laminar Convection in Horizontal Tubes

R. S. Chen[1,2] and G. J. Hwang[1,3]

Nomenclature

A = a parameter $= \beta g \theta_c a^3/\nu^2$
a, d = tube radius and diameter
C = a dimensionless number $= -C_1 a^3/(4\nu\mu) = A^{1/2}\mathrm{Re}/8\bar{w}$
C_1, C_2 = axial pressure and temperature gradients

[1]Department of Power Mechanical Engineering, National Tsing Hua University, Hsinchu, Taiwan 30043.

[2]Instructor.

[3]Professor, Mem. ASME.

Contributed by the Heat Transfer Division for publication in the JOURNAL OF HEAT TRANSFER. Manuscript received by the Heat Transfer Division November 12, 1986. Keywords: Forced Convection, Mixed Convection, Natural Convection.

F = a function defined in equation (12)
f = friction factor $= 2\bar{\tau}_w/\rho\bar{W}^2$
Gr_b = Grashof number $= \beta g(\bar{T}_w - T_b)d^3/\nu^2 = 8A(\bar{\theta}_w - \theta_b)$
g = gravitational acceleration
h = heat transfer coefficient $= q/(\bar{T}_w - T_b)$
K_P = wall conduction parameter $= k_w t/ka$
k, k_w = thermal conductivities of fluid and tube wall
q = uniform wall heat flux
Nu = Nusselt number $= hd/k = qd/(\bar{T}_w - T_b)k$
p, p_c = pressure and characteristic pressure $= \rho A\nu^2/a^2$
p = dimensionless pressure
Pr = Prandtl number $= \nu/\alpha$
P_w = wall conduction parameter $= 2\mathrm{Nu}/K_p = hd^2/K_w t$
R, r = dimensional and dimensionless radial coordinates
Ra_b = Rayleigh number $= \beta g(\bar{T}_w - T_b)d^3/\nu\alpha$
Re = Reynolds number $= \bar{W}d/\nu$
T, T_r = temperature and reference temperature along the line $(a, \pi/2, Z)$
t = tube wall thickness
U, V, W = dimensional velocity components in R, ϕ, and Z directions
u, v, w = dimensionless velocity components in r, ϕ, and z directions
U_c = characteristic velocity in R and ϕ directions $= A^{1/2}\nu/a$
W_c = characteristic velocity in Z direction $= 4C(\nu/a)/A^{1/2}$
Z, z = dimensional and dimensionless axial coordinates
α = thermal diffusivity
β = coefficient of thermal expansion
ϵ = a small value defined in equation (10)
θ = dimensionless temperature difference
θ_c = characteristic temperature difference $= 4CC_2a/A$
ν = kinematic viscosity
ξ = vorticity function
ρ = density
τ_w = wall shear stress
ϕ = angular coordinate
ψ = stream function

Superscript

$^-$ = mean value

Subscripts

b = mixed mean value
c = characteristic quantity
r = reference
w = wall
0 = pure forced convection

Introduction

Combined free and forced laminar convection in ducts is encountered in a wide variety of engineering applications, including heat exchangers designed for viscous fluids in chemical processes, solar collectors, food industries, and biomedical engineering. In recent years, the combined convection in tubes and channels has been treated extensively. The boundary conditions posed for the analytical and experimental studies in the fully developed flow are: axially and circumferentially uniform heat flux (Bergles and Simonds, 1971; Newell and Bergles, 1970; Shannon and Depew, 1968), and uniform wall temperature at any axial position with linear axial wall temperature (Chou and Hwang, 1984; Hwang and Cheng, 1970; Sabbagh et al., 1976). It is noted that the former corresponds to the case of a thin wall and low wall thermal conductivity; the latter corresponds to the case of a thick wall and high wall thermal conductivity.

In many engineering applications, the boundary conditions for thermal convection in ducts cannot be considered uniform either for wall temperature or heat flux. In the thermally fully developed flow, the effect of peripheral wall conduction may be introduced by the nonuniform peripheral wall heat flux in noncircular ducts (Shah and London, 1978) and also introduced simultaneously by the secondary flow in rectangular channels (Hwang and Chou, 1987), or by the secondary flow alone in circular tubes (Morcos and Bergles, 1975). This paper investigates the effect of peripheral wall conduction on combined free and forced laminar convection in hydrodynamically and thermally fully developed flow in horizontal circular tubes with uniform heat input axially. A finite-difference power-law scheme is employed to solve the problem.

Analysis and Results

Consider a steady laminar convection in the hydrodynamically and thermally fully developed flow in a horizontal circular tube under an axially and peripherally uniform heat flux q on the outer surface of the tube wall. This situation can be realized as a steady laminar flow in a long circular tube with finite values of thermal conductivity k_w and wall thickness t heated electrically at the outer surface of the tube wall or heated electrically with a uniform internal heat generation q/t and insulated externally. The viscous dissipation and compressibility effects in the energy equation are neglected. The physical properties are constant and the Boussinesq approximation is valid.

For the convenience of numerical study, we may introduce the dimensionless transformation for the dependent and independent variables

$$U = U_c u, \quad V = U_c v, \quad W = W_c w, \quad P = P_c p,$$
$$T - T_r = \theta_c \theta, \quad R = ar \tag{1}$$

where the subscript r indicates the value along the reference line $(a, \pi/2, Z)$. The dimensionless continuity, momentum, and energy equations are

$$\xi = \nabla^2 \psi \tag{2}$$

$$u\frac{\partial \xi}{\partial r} + \frac{v}{r}\frac{\partial \xi}{\partial \phi} = \frac{1}{A^{1/2}}\nabla^2 \xi + \frac{1}{r}\frac{\partial \theta}{\partial \phi}\cos\phi + \frac{\partial \theta}{\partial r}\sin\phi \tag{3}$$

Table 1 Values of $\bar{w}$ and $\bar{\theta}_w - \theta_b$

Pr	A	$K_p = 10^4$		10		1.0		0.1		0	
0.72	100	1.221*	(1.951)†	1.221	(1.950)	1.223	(1.952)	1.225	(1.962)	1.225	(1.960)
	200	1.576	(3.127)	1.582	(3.139)	1.605	(3.244)	1.627	(3.432)	1.631	(3.455)
	300	1.793	(3.896)	1.804	(3.928)	1.851	(4.202)	1.891	(4.660)	1.903	(4.732)
	450	2.033	(4.818)	2.049	(4.877)	2.123	(5.414)	2.193	(6.297)	2.207	(6.475)
	600	2.218	(5.591)	2.239	(5.671)	2.333	(6.470)	2.424	(7.798)	2.443	(8.081)
	800	2.411	(6.453)	2.436	(6.555)	2.555	(7.714)				
	1000	2.563	(7.167)	2.593	(7.293)						
	1200	2.688	(7.777)	2.722	(7.928)						
10	10	0.3950	(2.687)	0.3951	(2.680)	0.3951	(2.656)	0.3951	(2.649)	0.3951	(2.638)
	20	0.5536	(4.472)	0.5573	(4.443)	0.5578	(4.472)	0.5581	(4.432)	0.5581	(4.648)
	30	0.6795	(5.861)	0.6801	(5.819)	0.6816	(5.984)	0.6824	(6.416)	0.6825	(6.495)
	40	0.7805	(7.024)	0.7819	(7.017)	0.7851	(7.364)	0.7865	(8.124)	0.7868	(8.286)
	60	0.9469	(9.073)	0.9507	(9.092)	0.9570	(9.890)	0.9598	(11.43)	0.9603	(11.80)
	80	1.083	(10.81)	1.089	(10.86)	1.100	(12.23)				
	100	1.200	(12.34)	1.208	(12.45)	1.224	(14.45)				
	130	1.352	(14.38)	1.364	(14.56)						

Pr	A	$K_p = 2.52$		0.34		Pr	A	$K_p = 6.30$		0.84	
3.08	10	0.3953	(0.8815)	0.3953	(0.8811)	50.97	10	0.3950	(8.247)	0.3951	(8.810)
	20	0.5585	(1.736)	0.5586	(1.729)		15	0.4833	(10.70)	0.4838	(11.92)
	30	0.6823	(2.490)	0.6826	(2.482)		20	0.5580	(12.86)	0.5584	(14.86)
	40	0.7844	(3.122)	0.7855	(3.142)		25	0.6237	(14.82)		
	60	0.9495	(4.169)	0.9541	(4.309)		30	0.6829	(16.63)		
	80	1.082	(5.035)	1.092	(5.372)						
	100	1.195	(5.828)	1.210	(6.373)						
	130	1.339	(6.898)	1.363	(7.800)						
	160	1.462	(7.869)								

* Value of $\bar{w}$, † value of $(\bar{\Theta}_w - \Theta_b)$, for $(f\mathrm{Re})_0 = 16.0$, $(\mathrm{Nu})_0 = 4.36$, $f\mathrm{Re} = 2A^{1/2}/\bar{w}$, $\mathrm{Nu} = \mathrm{Pr}A^{1/2}\bar{w}/(\bar{\Theta}_w - \Theta_b)$, $\mathrm{Gr}_b = 8A(\bar{\Theta}_w - \Theta_b)$, $\mathrm{Ra}_b = \mathrm{PrGr}_b$.

$$u\frac{\partial w}{\partial r} + \frac{v}{r}\frac{\partial w}{\partial \phi} = \frac{1}{A^{1/2}}\nabla^2 w + 1 \tag{4}$$

$$u\frac{\partial \theta}{\partial r} + \frac{v}{r}\frac{\partial \theta}{\partial \phi} = \frac{1}{A^{1/2}\mathrm{Pr}}\nabla^2 \theta - w \tag{5}$$

$$u = \frac{1}{r}\frac{\partial \psi}{\partial \phi} \quad \text{and} \quad v = -\frac{\partial \psi}{\partial r} \tag{6}$$

where $\nabla^2 = (1/r)\partial(r\,\partial/\partial r)/\partial r + (1/r^2)\partial^2/\partial\phi^2$ is the Laplace operator, and $A = \beta g\theta_c a^3/\nu^2$ is a factor similar to the Grashof number. $A^{1/2}$ appears in the denominators of the viscous terms in equations (3) and (4) and the denominator of the conduction term in equation (5) indicating that for a larger value of factor A, the viscous and conduction terms become less important in the core region, but this is not true near the pipe wall.

To derive the thermal boundary condition along the tube wall of thickness t, the following two cases are considered:
(1) a tube with uniform heat flux q,
(2) a tube with a uniform internal heat generation q/t and insulated externally.

With the assumptions of thin wall and small temperature difference across the tube wall, the thermal boundary condition for both cases is

$$\left.\frac{\partial \theta}{\partial r}\right|_{r=1} - K_p \left.\frac{\partial^2 \theta}{\partial \phi^2}\right|_{r=1} = \tfrac{1}{2}\bar{w}\mathrm{Pr}A^{1/2} \tag{7}$$

where $K_p = k_w t/ka$ is a parameter indicating the relative importance of heat transfer along the tube wall and the heat transfer from the tube wall to the fluid. Two limiting cases, $K_p = 0$ and ∞, yield the boundary conditions of uniform heat flux and uniform wall temperature, respectively.

Because of symmetry it is necessary to consider only half of the region $\phi = 0$ to π. The remaining boundary conditions are

$$\begin{aligned} &\psi = \frac{\partial \psi}{\partial r} = w = 0 && \text{at } r = 1 \\ &\psi = \xi = \frac{\partial w}{\partial \phi} = \frac{\partial \theta}{\partial \phi} = 0 && \text{along } \phi = 0 \text{ and } \pi \end{aligned} \tag{8}$$

Following the conventional definitions, the expressions for the product of the friction factor and the Reynolds number, and for the Nusselt number, are

$$f\cdot\mathrm{Re} = \frac{\bar{\tau}_w}{\frac{1}{2}\rho\bar{W}^2}\cdot\frac{\bar{W}d}{\nu} = 2A^{1/2}/\bar{w}$$

$$\mathrm{Nu} = \frac{hd}{k} = \frac{qd}{(\bar{T}_w - T_b)k} = \bar{w}\mathrm{Pr}A^{1/2}/(\bar{\theta}_w - \theta_b) \tag{9}$$

where the dimensionless forms are obtained by considering overall balances of force and thermal energy for $\bar{\tau}_w$ and q, respectively.

In order to have a convergent solution for a higher value of the factor A, the power law scheme of reference (Patankar, 1980) was employed. Computation of equations (2) to (7) will be repeated until the following convergence criterion is satisfied:

$$\epsilon = \max_{i,j} |\theta_{i,j}^{(n+1)} - \theta_{i,j}^{(n)}| / \max_{i,j} |\theta_{i,j}^{(n+1)}| < 10^{-5} \tag{10}$$

To assure the reliability of the present numerical solution, the mesh sizes 23×15, 31×19, and 25×27 in the radial and angular directions have been tried for $K_p = \infty$ and $\mathrm{Pr} = 0.72$ with various values of A. It is well understood that the nonlinear higher order numerical error mainly comes from the magnitudes of $A^{1/2}$ in equations (3) and (4) and $\mathrm{Pr}A^{1/2}$ in equation (5). As long as the solution is obtained under the convergence condition (10) within certain values of $A^{1/2}$ and $\mathrm{Pr}A^{1/2}$, the numerical experiment on the mesh size applies equally well to the solution with other values of Pr, A, and K_p. Therefore, the mesh size 31×19 is selected throughout the

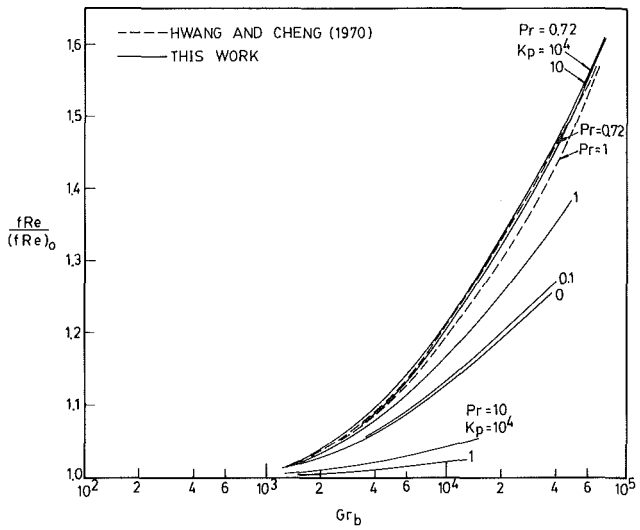

Fig. 1 $fRe/(fRe)_0$ versus Gr_b with parameters Pr and K_p

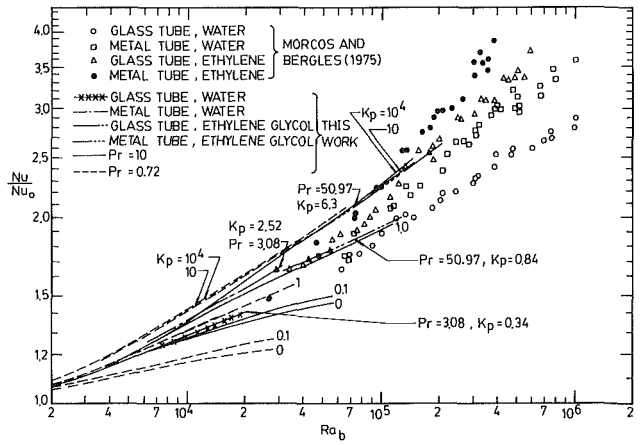

Fig. 2 Nu/Nu_0 versus Ra_b with parameters Pr and K_p

present study to have the values of f•Re and Nu with an accuracy of three significant figures. The result of $K_p = \infty$ and $Pr = 0.72$ is also confirmed with data in the literature (Hwang and Cheng, 1970).

The value of A can be converted to the value of Gr_b by using the relationship $8A\ (\bar{\theta}_w - \theta_b) = Gr_b$. Table 1 shows the values of $\bar{w}$ and $(\bar{\theta}_w - \theta_b)$ with the parameters Pr, A, and K_p. The values of f•Re and Nu can be obtained by the equations shown in this table.

To study the effect of peripheral wall conduction on the flow characteristics, $fRe/(fRe)_0$ versus Gr_b with parameters Pr and K_p is shown in Fig. 1. It is known that the ratio $fRe/(fRe)_0$ increases with the increase in the parameter Gr_b and the increase of $fRe/(fRe)_0$ is almost negligible for a large Pr, say $Pr \geq 10$ in the range of parameter Gr_b studied. We can see clearly for fixed Pr and Gr_b that the ratio $fRe/(fRe)_0$ decreases with the decrease in K_p. An appreciable decrease for the ratio $fRe/(fRe)_0$ between $K_p = 10$ and 0.1 is observed. For instance, at $Gr_b = 4 \times 10^4$ the ratio drops from 1.45 at $K_p = 10$ to 1.27 at $K_p = 0.1$, but the variations of the ratio are almost negligible in the ranges $K_p = 10 \sim 10^4$ and $K_p = 0 \sim 0.1$, in which the variations are less than 1 percent. Therefore, we may conclude that for the ratio of friction factor for the cases of $K_p \geq 10$ and $K_p \leq 0.1$ may be considered as the thermal boundary conditions of circumferentially uniform wall temperature and circumferentially uniform heat flux, respectively. Numerical data from Hwang and Cheng (1970) are also plotted in this figure. A good agreement is observed.

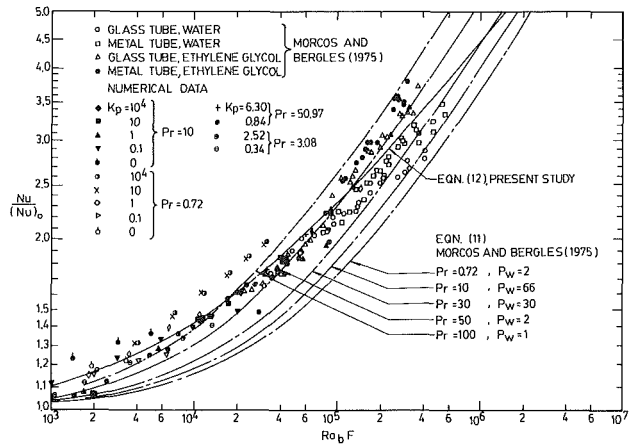

Fig. 3 Correlation for the Nusselt number

To investigate the effect of peripheral wall conduction on the heat transfer, Fig. 2 shows the variations of Nu/Nu_0 with varying Ra_b for various Pr and K_p. It is seen that the curve for $K_p = 10^4$, $Pr = 10$ is very close to the curve for $K_p = 10$, $Pr = 10$, and the curves for $K_p = 10^4$ and $K_p = 10$ with $Pr = 0.72$ are not far from those with $Pr = 10$. On the contrary, for small K_p, there are substantial deviations between the curves for $Pr = 10$ and $Pr = 0.72$. To make a comparison between the present numerical results and the existing experimental data (Morcos and Bergles, 1975), the experimental data are plotted in this figure and numerical data for the corresponding Pr and K_p are computed. The range of Rayleigh number in the experiment (Morcos and Bergles, 1975) is $Ra_b = 3 \times 10^4 \sim 10^6$. Some of the numerical data are computed up to $Ra_b = 2.0 \times 10^5$. It is seen that the measured ethylene data with both glass and metal tubes confirm reasonably well the computed data in the range of $Ra_b = 3 \times 10^4 \sim 2.0 \times 10^5$. Although the measured and computed water data are in different ranges of Ra_b, the measured water data lie on the extrapolations of the computed curves.

Correlation of experimental data for fully developed laminar convection in a uniformly heated horizontal tube with the effects of Prandtl number, Rayleigh number, and wall conduction parameter is a difficult task. However, Morcos and Bergles (1975) successfully correlated four sets of data with the equation

$$Nu = \left\{(4.36)^2 + \left[0.055\left(\frac{Ra_b Pr^{0.35}}{P_w^{1/4}}\right)^{0.4}\right]^2\right\}^{1/2} \qquad (11)$$

with all properties evaluated at $(\bar{T}_w + T_b)/2$, where $P_w = 2Nu/K_p$ was used. The advantages in using this equation are a smooth change of Nu from the value 4.36 for small Ra_b and a good correlation of data at high Ra_b. The ranges of parameters in their experiments (Morcos and Bergles, 1975) are approximately $Pr = 3.08 \sim 50.97$ and $K_p = 0.336 \sim 6.30$. It may not be desirable to use equation (11) with parameters beyond these ranges. It can be seen clearly that the value $Pr^{0.35}/P_w^{1/4}$ will be out of range for limiting values of Pr and K_p. Although equation (11) correlates well the data at a high value of Ra_b, it also seems to underestimate the value of Nusselt number at a small and intermediate range of the parameter $Ra_b Pr^{0.35}/P_w^{1/4} = 3 \times 10^3 \sim 2.5 \times 10^5$. This can be explained by replotting the measured and computed data, and equation (11) with a new variable $Ra_b F$. The term F will be defined later. Underestimations of 16 and 8 percent in the

value of Nu are observed at $Ra_b F = 10^4$ and 10^5, respectively, for $Pr = 10$ in equation (11).

With the help of the numerical data, equation (11) is modified by considering the asymptotic behaviors of large Prandtl number, constant wall temperature $K_p \to \infty$, and constant wall heat flux $K_p \to 0$. The new correlation is

$$Nu = \{(4.36)^2 + [0.23(Ra_b F)^{0.32}]^2\}^{1/2} \quad (12)$$

where $F = (Pr + 0.06)/(Pr + 0.6) \cdot (P_w + 200)/(5P_w + 200)$. It is seen that the value $(Pr + 0.06)/(Pr + 0.6)$ varies from 0.1 to 1 for $Pr = 0 \sim \infty$ and the value $(P_w + 200)/(5P_w + 200)$ varies from 1 to 0.2 for $P_w = 0 \sim \infty$. The value of F is 1.0 for the case of large Prandtl number $Pr \to \infty$ and constant wall temperature $K_p \simeq \infty$. The 0.32 power in equation (12) instead of the 0.4 power in equation (11) is expected to provide a better estimation of Nu in the small and intermediate range of Ra_b. The constant 0.23 is obtained by matching the value of Nu at a high value of Ra_b. The result of equation (12) is plotted in Fig. 3. The numerical data are plotted at each calculated datum and the calculated data are all within 11 percent of the value of equation (12). The experimental data (Morcos and Bergles, 1975) are also replotted in this figure. Equation (11) for various Pr and P_w is also plotted in this figure. It may be more desirable to use equation (12) particularly for $10^3 \le Ra_b \le 10^5$, $0.72 \le Pr < \infty$, and $P_w = 0 \sim \infty$ (or $K_p = 0 \sim \infty$).

Conclusions

1 The ratio $fRe/(fRe)_0$ increases with the increase in the parameter Gr_b and the increase of $fRe/(fRe)_0$ is almost negligible for a large Pr, say $Pr \ge 10$ in the range of Gr_b studied. For fixed Pr and Gr_b, the ratio $fRe/(fRe)_0$ decreases with the decrease in K_p, and an appreciable decrease between $K_p = 10$ and 0.1 is observed.

2 As shown in equation (12), a new correlating equation for the Nusselt number is proposed. The new correlating equation considers the asymptotic behaviors of large Prandtl number, large K_p, and small K_p. It is more desirable to use the equation particularly for $10^3 \le Ra_b \le 10^5$, $0.72 \le Pr < \infty$, and $P_w = 0 \sim \infty$ (or $K_p = 0 \sim \infty$).

References

Bergles, A. E., and Simonds, R. R., 1971, "Combined Forced and Free Convection for Laminar Flow in Horizontal Tubes With Uniform Heat Flux," *Int. J. Heat Mass Transfer*, Vol. 14, pp. 1989–2000.

Chou, F. C., and Hwang, G. J., 1984, "Combined Free and Forced Laminar Convection in Horizontal Channels for High ReRa," *Canadian J. of Chemical Engineering*, Vol. 62, pp. 830–836.

Hwang, G. J., and Cheng, K. C., 1970, "Boundary Vorticity Method for Convective Heat Transfer With Secondary Flow—Application to the Combined Free and Forced Laminar Convection in Horizontal Tubes," *Heat Transfer*, Vol. 4, Paper No. NC 3.5, Elsevier Publishing Company, Amsterdam.

Hwang, G. J., and Chou, F. C., 1987, "Effect of Wall Conduction on Combined Free and Forced Laminar Convection in Horizontal Rectangular Channels," ASME JOURNAL OF HEAT TRANSFER, Vol. 109, pp. 936–942.

Morcos, S. M., and Bergles, A. E., 1975, "Experimental Investigation of Combined Forced and Free Laminar Convection in Horizontal Tubes," ASME JOURNAL OF HEAT TRANSFER, Vol. 97, pp. 212–219.

Newell, P. H., and Bergles, A. E., 1970, "Analysis of Laminar Combined Free and Forced Convection for Fully Developed Laminar Flow in Horizontal Tubes," ASME JOURNAL OF HEAT TRANSFER, Vol. 92, pp. 83–93.

Patankar, S. V., 1980, *Numerical Heat Transfer and Fluid Flow*, Hemisphere, Washington, DC; McGraw-Hill, New York.

Sabbagh, J. A., Aziz, A., El-Ariny, A. S., and Hamed, G., 1976, "Combined Free and Forced Convection in Circular Tubes," ASME JOURNAL OF HEAT TRANSFER, Vol. 98, pp. 322–324.

Shah, R. K., and London, A. L., 1978, *Laminar Flow Forced Convection in Ducts*, Academic Press, New York.

Shannon, R. L., and Depew, C. A., 1968, "Combined Free and Forced Laminar Convection in a Horizontal Tube With Uniform Heat Flux," ASME JOURNAL OF HEAT TRANSFER, Vol. 90, pp. 353–357.

An Experimental Study of Direct Condensation on a Fragmenting Circular Jet

T. L. Lui,[1] H. R. Jacobs,[2] and K. Chen[1]

Nomenclature

- Cp = specific heat of liquid
- D = jet diameter
- Gz = Graetz number = $RePrD/x$
- h_{fg} = heat of vaporization
- Ja = Jakob number = $Cp(T_{sat} - T_o)/h_{fg}$
- k = thermal conductivity of liquid
- Pr = Prandtl number = $Cp\mu/k$
- Re = Reynolds number = $\rho UD/\mu$
- T = average jet temperature
- T_o = inlet temperature of jet
- T_{sat} = saturation temperature
- U = jet velocity (assumed uniform)
- W_∞ = molar fraction of noncondensible gas
- x = axial distance from nozzle exit
- μ = viscosity of liquid
- ρ = density of liquid

Introduction

Direct-contact heat exchangers have received increasing attention in recent years because of their simplicity of construction, compactness, and high heat transfer rate. Various types of direct-contact heat exchangers have been described and discussed by How (1956), Jacobs and Fanner (1977), and Sideman and Moalem-Maron (1982). Jet- and curtain-type condensers—in which the coolant is injected as a series of jets or solid sheets and falls down through a relatively quiescent vapor—have been studied analytically by Kutateladze (1952), Hasson et al. (1964a), and recently by Jacobs and co-workers (1984, 1987). Steam condensation on conical water sheets of swirl spray nozzles was experimentally studied by Weinberg (1952) using small probes inserted in the water sheets. An interferometric technique has been used (Hasson et al., 1964b) to measure local heat transfer coefficients of fan spray water sheets exposed to steam. Although a few experimental investigations of direct-contact condensers have been carried out in the past decade, there is still a significant lack of technical data for the design of direct-contact heat exchanger. This stimulated the present experimental investigation of direct condensation.

The present experiments were undertaken to provide technical data for the design of jet-type direct-contact heat exchangers in the laminar flow range. Flow instability and the transition from a circular jet to droplets were observed and discussed. A comparison between the measured heat transfer rate and the heat transfer rate predicted by Jacobs and Nadig's (1987) analytical models for a laminar circular jet is also given in the present investigation. It is found that the measured heat transfer rate is slightly lower than that predicted by Jacobs and Nadig's analytical model for pure vapor; however, the experimental data agree well with the analytical solution (Jacobs and Nadig, 1987) if the effects of the air content in steam are taken into account.

[1]Department of Mechanical and Industrial Engineering, University of Utah, Salt Lake City, UT 84112.

[2]Department of Mechanical Engineering, The Pennsylvania State University, University Park, PA 16802.

Contributed by the Heat Transfer Division for publication in the JOURNAL OF HEAT TRANSFER. Manuscript received by the Heat Transfer Division February 26, 1988. Keywords: Condensation, Direct-Contact Heat Transfer, Jets.

value of Nu are observed at $Ra_b F = 10^4$ and 10^5, respectively, for $Pr = 10$ in equation (11).

With the help of the numerical data, equation (11) is modified by considering the asymptotic behaviors of large Prandtl number, constant wall temperature $K_p \to \infty$, and constant wall heat flux $K_p \to 0$. The new correlation is

$$Nu = \{(4.36)^2 + [0.23(Ra_b F)^{0.32}]^2\}^{1/2} \quad (12)$$

where $F = (Pr + 0.06)/(Pr + 0.6) \cdot (P_w + 200)/(5P_w + 200)$. It is seen that the value $(Pr + 0.06)/(Pr + 0.6)$ varies from 0.1 to 1 for $Pr = 0 \sim \infty$ and the value $(P_w + 200)/(5P_w + 200)$ varies from 1 to 0.2 for $P_w = 0 \sim \infty$. The value of F is 1.0 for the case of large Prandtl number $Pr \to \infty$ and constant wall temperature $K_p \simeq \infty$. The 0.32 power in equation (12) instead of the 0.4 power in equation (11) is expected to provide a better estimation of Nu in the small and intermediate range of Ra_b. The constant 0.23 is obtained by matching the value of Nu at a high value of Ra_b. The result of equation (12) is plotted in Fig. 3. The numerical data are plotted at each calculated datum and the calculated data are all within 11 percent of the value of equation (12). The experimental data (Morcos and Bergles, 1975) are also replotted in this figure. Equation (11) for various Pr and P_w is also plotted in this figure. It may be more desirable to use equation (12) particularly for $10^3 \le Ra_b \le 10^5$, $0.72 \le Pr < \infty$, and $P_w = 0 \sim \infty$ (or $K_p = 0 \sim \infty$).

Conclusions

1 The ratio $fRe/(fRe)_0$ increases with the increase in the parameter Gr_b and the increase of $fRe/(fRe)_0$ is almost negligible for a large Pr, say $Pr \ge 10$ in the range of Gr_b studied. For fixed Pr and Gr_b, the ratio $fRe/(fRe)_0$ decreases with the decrease in K_p, and an appreciable decrease between $K_p = 10$ and 0.1 is observed.

2 As shown in equation (12), a new correlating equation for the Nusselt number is proposed. The new correlating equation considers the asymptotic behaviors of large Prandtl number, large K_p, and small K_p. It is more desirable to use the equation particularly for $10^3 \le Ra_b \le 10^5$, $0.72 \le Pr < \infty$, and $P_w = 0 \sim \infty$ (or $K_p = 0 \sim \infty$).

References

Bergles, A. E., and Simonds, R. R., 1971, "Combined Forced and Free Convection for Laminar Flow in Horizontal Tubes With Uniform Heat Flux," *Int. J. Heat Mass Transfer*, Vol. 14, pp. 1989–2000.

Chou, F. C., and Hwang, G. J., 1984, "Combined Free and Forced Laminar Convection in Horizontal Channels for High ReRa," *Canadian J. of Chemical Engineering*, Vol. 62, pp. 830–836.

Hwang, G. J., and Cheng, K. C., 1970, "Boundary Vorticity Method for Convective Heat Transfer With Secondary Flow—Application to the Combined Free and Forced Laminar Convection in Horizontal Tubes," *Heat Transfer*, Vol. 4, Paper No. NC 3.5, Elsevier Publishing Company, Amsterdam.

Hwang, G. J., and Chou, F. C., 1987, "Effect of Wall Conduction on Combined Free and Forced Laminar Convection in Horizontal Rectangular Channels," ASME JOURNAL OF HEAT TRANSFER, Vol. 109, pp. 936–942.

Morcos, S. M., and Bergles, A. E., 1975, "Experimental Investigation of Combined Forced and Free Laminar Convection in Horizontal Tubes," ASME JOURNAL OF HEAT TRANSFER, Vol. 97, pp. 212–219.

Newell, P. H., and Bergles, A. E., 1970, "Analysis of Laminar Combined Free and Forced Convection for Fully Developed Laminar Flow in Horizontal Tubes," ASME JOURNAL OF HEAT TRANSFER, Vol. 92, pp. 83–93.

Patankar, S. V., 1980, *Numerical Heat Transfer and Fluid Flow*, Hemisphere, Washington, DC; McGraw-Hill, New York.

Sabbagh, J. A., Aziz, A., El-Ariny, A. S., and Hamed, G., 1976, "Combined Free and Forced Convection in Circular Tubes," ASME JOURNAL OF HEAT TRANSFER, Vol. 98, pp. 322–324.

Shah, R. K., and London, A. L., 1978, *Laminar Flow Forced Convection in Ducts*, Academic Press, New York.

Shannon, R. L., and Depew, C. A., 1968, "Combined Free and Forced Laminar Convection in a Horizontal Tube With Uniform Heat Flux," ASME JOURNAL OF HEAT TRANSFER, Vol. 90, pp. 353–357.

An Experimental Study of Direct Condensation on a Fragmenting Circular Jet

T. L. Lui,[1] H. R. Jacobs,[2] and K. Chen[1]

Nomenclature

- Cp = specific heat of liquid
- D = jet diameter
- Gz = Graetz number = $RePrD/x$
- h_{fg} = heat of vaporization
- Ja = Jakob number = $Cp(T_{sat} - T_o)/h_{fg}$
- k = thermal conductivity of liquid
- Pr = Prandtl number = $Cp\mu/k$
- Re = Reynolds number = $\rho UD/\mu$
- T = average jet temperature
- T_o = inlet temperature of jet
- T_{sat} = saturation temperature
- U = jet velocity (assumed uniform)
- W_∞ = molar fraction of noncondensible gas
- x = axial distance from nozzle exit
- μ = viscosity of liquid
- ρ = density of liquid

Introduction

Direct-contact heat exchangers have received increasing attention in recent years because of their simplicity of construction, compactness, and high heat transfer rate. Various types of direct-contact heat exchangers have been described and discussed by How (1956), Jacobs and Fanner (1977), and Sideman and Moalem-Maron (1982). Jet- and curtain-type condensers—in which the coolant is injected as a series of jets or solid sheets and falls down through a relatively quiescent vapor—have been studied analytically by Kutateladze (1952), Hasson et al. (1964a), and recently by Jacobs and co-workers (1984, 1987). Steam condensation on conical water sheets of swirl spray nozzles was experimentally studied by Weinberg (1952) using small probes inserted in the water sheets. An interferometric technique has been used (Hasson et al., 1964b) to measure local heat transfer coefficients of fan spray water sheets exposed to steam. Although a few experimental investigations of direct-contact condensers have been carried out in the past decade, there is still a significant lack of technical data for the design of direct-contact heat exchanger. This stimulated the present experimental investigation of direct condensation.

The present experiments were undertaken to provide technical data for the design of jet-type direct-contact heat exchangers in the laminar flow range. Flow instability and the transition from a circular jet to droplets were observed and discussed. A comparison between the measured heat transfer rate and the heat transfer rate predicted by Jacobs and Nadig's (1987) analytical models for a laminar circular jet is also given in the present investigation. It is found that the measured heat transfer rate is slightly lower than that predicted by Jacobs and Nadig's analytical model for pure vapor; however, the experimental data agree well with the analytical solution (Jacobs and Nadig, 1987) if the effects of the air content in steam are taken into account.

[1]Department of Mechanical and Industrial Engineering, University of Utah, Salt Lake City, UT 84112.

[2]Department of Mechanical Engineering, The Pennsylvania State University, University Park, PA 16802.

Contributed by the Heat Transfer Division for publication in the JOURNAL OF HEAT TRANSFER. Manuscript received by the Heat Transfer Division February 26, 1988. Keywords: Condensation, Direct-Contact Heat Transfer, Jets.

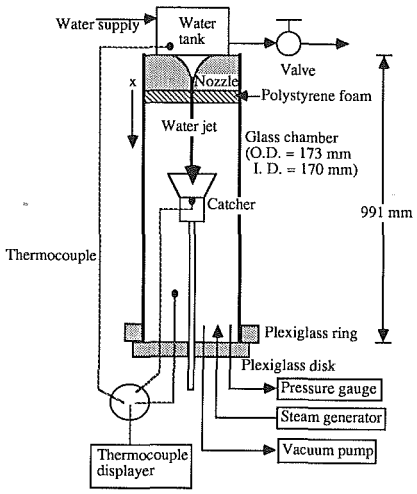

Fig. 1 Layout of experimental apparatus

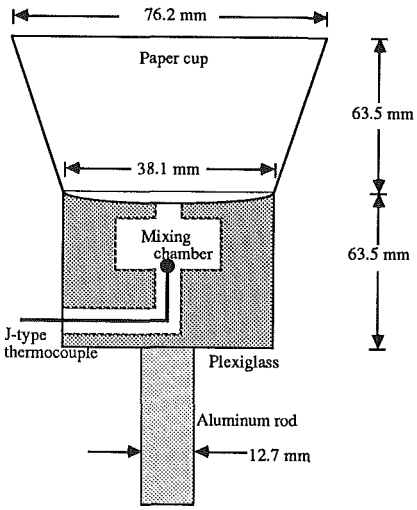

Fig. 2 Sketch of the probe for jet temperature measurement

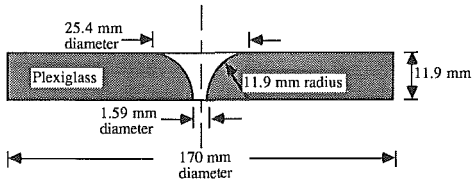

Fig. 3 Sketch of the top plexiglass disk

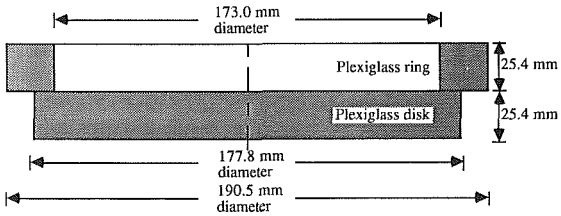

Fig. 4 Sketch of the bottom plexiglass disk

Experimental Apparatus and Procedure

The layout of the experimental apparatus is shown in Fig. 1. The essential components of the experimental system were an airtight glass chamber, a steam generator, a vacuum pump, and temperature and pressure measurement devices. A "catcher" made from plexiglass was used to measure the average temperature of the coolant jet. It can be inserted in the jet at any height by adjusting a clamp on the catcher support. The design and dimensions of the catcher are depicted in Fig. 2. The water gathered by the catcher is mixed in the mixing chamber in the base of the catcher. Thus, the water temperature measured by the embedded thermocouple is essentially the bulk mean temperature of the jet flow. Temperature fluctuations of less than 0.2°C were observed in the present experiments. The highest temperature measured at each location was recorded. The jet inlet temperature and the steam temperature were also measured. All the temperatures were measured using J-type thermocouples of 1.59 mm diameter.

Both ends of the glass chamber were sealed by plexiglass disks. A silicon sealant was applied around the edges of the plexiglass disks to keep the glass chamber airtight. The configurations and dimensions of the disks on top and bottom of the glass chamber are shown in Figs. 3 and 4, respectively. A nozzle with an exit diameter of 1.59 mm was machined at the center of the plexiglass disk on top of the glass chamber. The velocity of the water jet through the nozzle was determined by the head of water above the nozzle. To establish a constant jet flow rate, an overflow valve was attached to the water tank above the glass chamber to maintain a constant water level. A polystyrene foam insulator of approximately 48 mm was cemented under the top plexiglass disk to prevent the water in the nozzle from being heated by the steam.

Steam was generated by boiling water in a 2000 ml Ehrlenmeyer flask at atmospheric pressure. Connecting the glass chamber and the steam generator is a plastic tube of 6.35 mm diameter. An air pump was used to eliminate most of the noncondensible gases in the glass chamber. Prior to each experiment, the air in the glass chamber was first evacuated to approximately 50 mm Hg. Steam at about 95°C was then fed into the glass chamber while maintaining pump operation. The pressure in the glass chamber was measured in each experiment. The corresponding saturation temperature of the steam was determined from the steam table and compared with the measured steam temperature.

Results and Discussion

Two series of experiments were performed for inlet water temperature at 15, 31, 49, and 57°C. In the first series, the head of water is 12.7 mm, and in the second series, 50.8 mm. The velocity of the jet at the nozzle exit was calculated from the measured water supply rate divided by the product of the water density and the nozzle exit area. The Jakob numbers for the different inlet water temperatures were calculated. They range from 0.07 to 0.15. The Graetz numbers at different jet locations were also calculated based on the nozzle exit diameter.

Pictures of the jet with the glass chamber removed and without steam are shown in Figs. 5(*a*) and 5(*b*) for different heads of water. It is shown in these pictures that, due to the Vena contract effect, the jet diameter is slightly less than the exit diameter of the nozzle. The calculated Graetz numbers are therefore slightly greater. These photographs also show that the height at which the jet breaks into droplets is proportional to the inlet velocity of the jet, or the square root of the head of water on top of the nozzle. For 12.7 mm head of water, the jet broke into droplets at $x = 31$ mm while for 50.8 mm head of water, the jet length increased to 62.5 mm. Wavy instability occurred before the transition from a circular jet to droplets took place. Although the occurrence of waves on the jet surface may increase the heat transfer surface area, the droplets formed are approximately twice the diameter of the jet. For the same volume flow rate in the continuous jet and the drops, the surface area is about 10 to 20 percent less for drops of diameter two times the initial jet diameter than for the continuous jet. Although the external heat transfer resistance could be less, the internal resistance can increase. Thus, it was

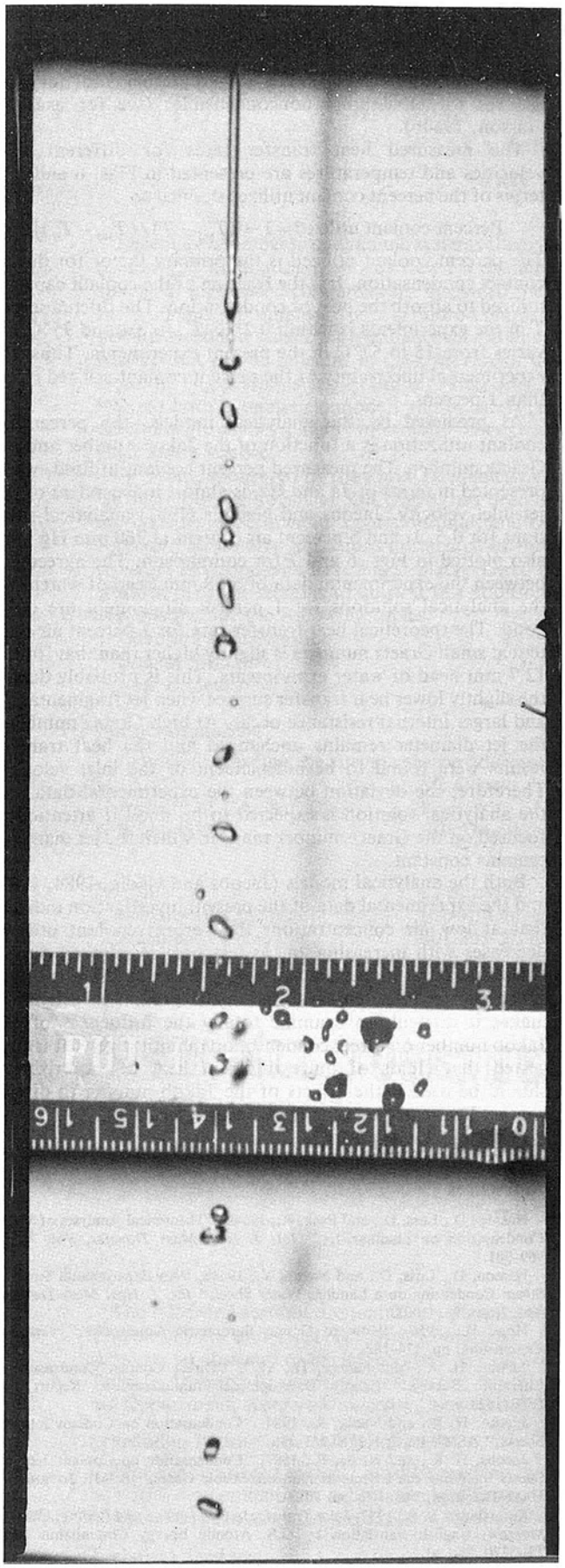

Fig. 5(*a*) 12.7 mm head of water

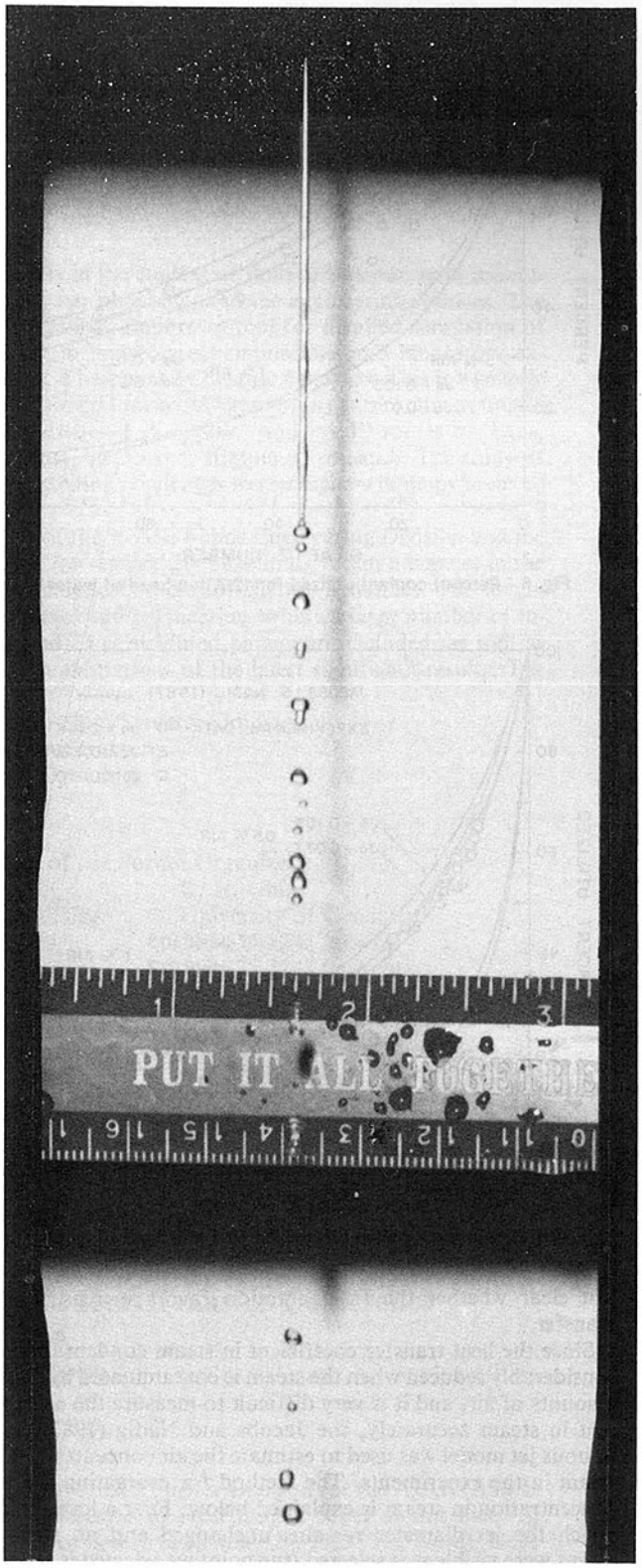

Fig. 5(*b*) 50.8 mm head of water

Fig. 5 Flow visualization results

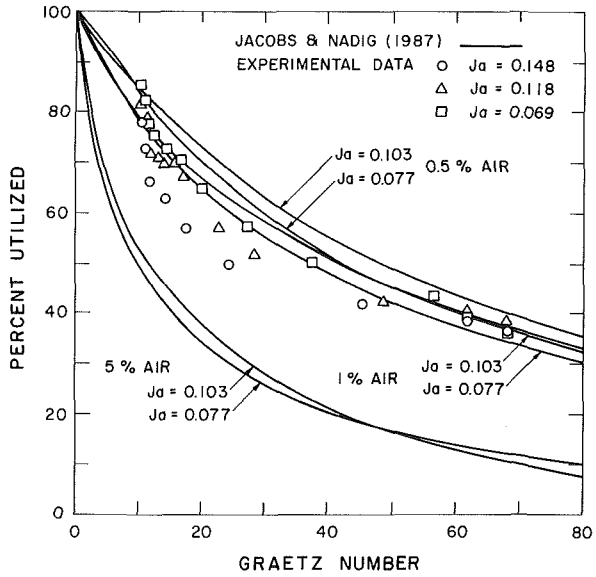

Fig. 6 Percent coolant utilized for 12.7 mm head of water

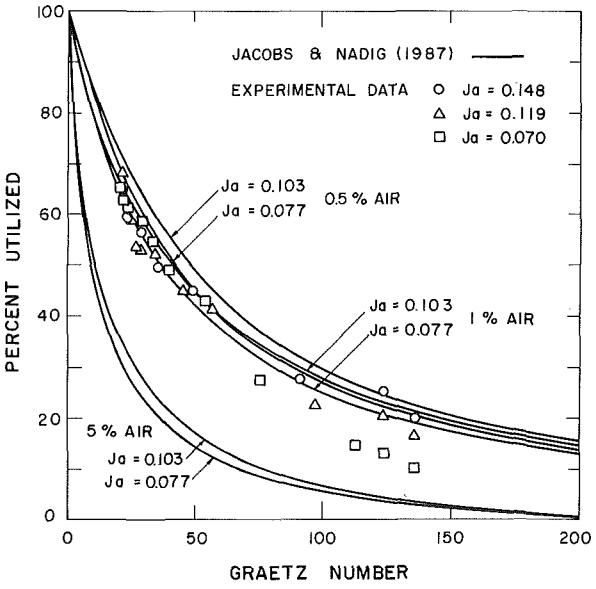

Fig. 7 Percent coolant utilized for 50.8 mm head of water

not clear whether the fragmentation favors increased heat transfer.

Since the heat transfer coefficient in steam condensation is considerably reduced when the steam is contaminated by slight amounts of air, and it is very difficult to measure the air content in steam accurately, the Jacobs and Nadig (1987) continuous jet model was used to estimate the air concentration in steam in the experiments. The method for estimating the air concentration in steam is explained below: First a location at which the jet diameter remains unchanged and no surface waves were visible was selected (the point we selected is Graetz number = 22 for Jakob number = 0.12 and head of water = 12.7 mm). The percent coolant utilized at that point was measured. The Graetz number of the same coolant utilization for pure vapor was then calculated according to Jacobs and Nadig's analytical solution (1984). The air content in steam can be estimated from Table 4 in Jacobs and Nadig (1987) if the ratio of the Graetz number with practically pure steam to the Graetz number with air in steam is known. The air content was estimated to be 1 percent by volume. The Ideal Gas Mixture model was also employed to estimate the air content in steam. Based on the measured pressure (636.8 mm Hg) and temperature (95°C) of the mixture, the air content is about 0.4 percent in our experiments. Such concentrations are typical of experiments similar to our design and our procedures for eliminating noncondensibles (see for example Hasson, 1964b).

The measured heat transfer rates for different inlet velocities and temperatures are presented in Figs. 6 and 7 in terms of the percent coolant utilized defined as

$$\text{Percent coolant utilized} = 1 - [(T_{\text{sat}} - T)/(T_{\text{sat}} - T_o)]$$

The percent coolant utilized is the primary factor for direct-contact condensation. It is the fraction of the coolant capacity utilized to absorb the heat of condensation. The fluctuation of T in the experiments is within 0.2°C. T_{sat} is around 95°C. T_o varies from 15 to 57°C in the present experiments. Thus, the experimental uncertainty of the percent coolant utilized is less than 1 percent.

As predicted by the analytical models, the percentage coolant utilization is a function of the Jakob number and the Graetz number. The measured percent coolant utilized, when presented in terms of Ja and Gz, is almost independent of the jet inlet velocity. Jacobs and Nadig's (1987) analytical solutions for 0.5, 1, and 5 percent air content at 760 mm Hg were also plotted in Figs. 6 and 7 for comparison. The agreement between the experimental data of 50.8 mm head of water and the analytical solutions for 1 percent air content are quite good. The theoretical heat transfer rate for 1 percent air content at small Graetz numbers is slightly higher than that for the 12.7 mm head of water experiments. This is probably due to the slightly lower heat transfer surface when jet fragmentation and larger internal resistance occur. At high Graetz numbers, the jet diameter remains unchanged and the heat transfer results were found to be independent of the inlet velocity. Therefore, the deviation between the experimental data and the analytical solution is expected to be small if attention is focused on the Graetz number range in which the jet diameter remains constant.

Both the analytical models (Jacobs and Nadig, 1984, 1987) and the experimental data of the present investigation indicate that at low air concentrations the percent coolant utilized decreases with increasing Ja, as less heat is released during condensation at higher Ja. However, the small difference between the jet inlet temperatures in the present investigation makes it difficult to examine totally the influences of the Jakob number on direct condensation quantitatively. It is suggested that fluids of quite different heat of vaporization should be used if the effects of the Jakob number in direct-contact heat exchange are to be investigated.

References

Hasson, D., Luss, D., and Peck, R., 1964a, "Theoretical Analyses of Vapor Condensation on Laminar Jet," *Int. J. Heat Mass Transfer*, Vol. 7, pp. 969–981.

Hasson, D., Luss, D., and Navon, V., 1964b, "An Experimental Study of Steam Condensing on a Laminar Water Sheet," *Int. J. Heat Mass Transfer*, Vol. 7, pp. 983–1001.

How, H., 1956, "How to Design Barometric Condensers," *Chemical Engineering*, pp. 174–182.

Jacobs, H. R., and Fanner, H., 1977, "Direct Contact Condensers: A Literature Survey," Energy Development Administration, Report No. DEE/1523.

Jacobs, H. R., and Nadig, R., 1984, "Condensation on Coolant Jets and Sheets," ASME Paper No. 84-HT-29.

Jacobs, H. R., and Nadig, R., 1987, "Condensation on Coolant Jets and Sheets Including the Effects of Noncondensible Gases," ASME JOURNAL OF HEAT TRANSFER, Vol. 109, pp. 1013–1020.

Kutateladze, S. S., 1952, *Heat Transfer in Condensing and Boiling*, Chap. 7, Moscow; English translation by U.S. Atomic Energy Commission AEC-TR-3770, 2nd ed.

Sideman, S., and Moalem-Maron, D., 1982, "Direct Contact Condensation," *Advance in Heat Transfer*, Vol. 15, pp. 227–281.

Weinberg, S., 1952, *Proc. Inst. Mech. Engrs., London*, Vol. 1B, pp. 240–244.